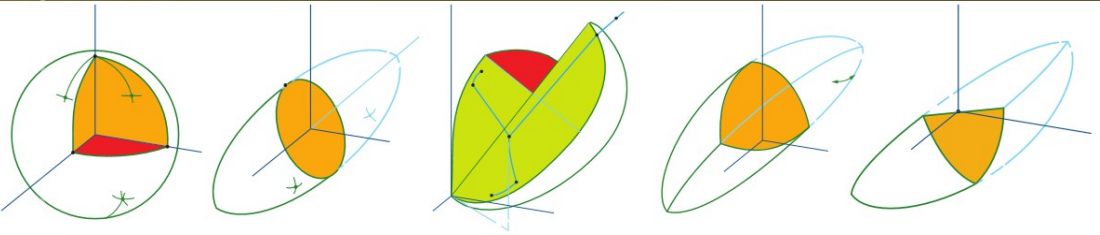


ADVANCES IN GEOPHYSICAL AND ENVIRONMENTAL MECHANICS AND MATHEMATICS



Gerd Gudehus

Physical Soil Mechanics

 Springer

Advances in Geophysical and Environmental Mechanics and Mathematics

Series Editor: Professor Kolumban Hutter

Gerd Gudehus

Physical Soil Mechanics

 Springer

Prof. Dr. Gerd Gudehus
Karlsruher Institut für Technologie
Inst. für Boden- und Felsmechanik
Campus Süd
Engler-Bunte-Ring 14
76131 Karlsruhe
Germany
gudehus@ibf.uka.de

Advances in Geophysical and Environmental Mechanics and Mathematics

ISSN 1866-8348

e-ISSN 1866-8356

ISBN 978-3-540-36353-8

e-ISBN 978-3-540-36354-5

DOI 10.1007/978-3-540-36354-5

Springer Heidelberg Dordrecht London New York

Library of Congress Control Number: 2010930660

© Springer-Verlag Berlin Heidelberg 2011

This work is subject to copyright. All rights are reserved, whether the whole or part of the material is concerned, specifically the rights of translation, reprinting, reuse of illustrations, recitation, broadcasting, reproduction on microfilm or in any other way, and storage in data banks. Duplication of this publication or parts thereof is permitted only under the provisions of the German Copyright Law of September 9, 1965, in its current version, and permission for use must always be obtained from Springer. Violations are liable to prosecution under the German Copyright Law.

The use of general descriptive names, registered names, trademarks, etc. in this publication does not imply, even in the absence of a specific statement, that such names are exempt from the relevant protective laws and regulations and therefore free for general use.

Cover design: deblik, Berlin

Printed on acid-free paper

Springer is part of Springer Science+Business Media (www.springer.com)

PROLOGUE

Soil is matter in its own right. Everybody will agree, but how to catch it scientifically? The first draft of this book, written with the intention to reconcile elastoplasticity and hypoplasticity, was more a cacophony than a symphony. Screening the literature I got tired by a jungle of data and a morass of equations. Thinking over the issue I got more and more aware that the *physis* of soils can be captured *more geometrico* by means of *attractors*. A look into history and a preview may show what is meant.

Physis (φύσις) means nature, early Greek philosophers coined the word physics (φυσικά) for the science of it. They thought that all matter is composed of the four elements fire (πυρ), water (ύδωρ), air (αήρ) and earth (γαία). Their mathematics (μαθηματικά) was mainly geometry (γεωμετεία), and their mechanics (μηχανική) was mainly statics (στατική). Using Apollonius' cone sections Kepler proposed his three Laws *more geometrico*, i.e. in a geometrical way. His *Astronomia Nova* begins with *durissime est hodie scribendo libros mathematicos* (it is very hard today to write mathematical books) and is full of ellipses, but void of algebra. Introducing gravity and inertia Newton derived Kepler's Laws *more geometrico*, hundred years later Euler proposed the differential equation of motion. Feynman proposed another geometrical proof of Kepler's Laws (Feynman and Goodstein 2000). Geometrical presentations and arguments will be used throughout this book for the ease of understanding, this is called *more geometrico*.

Astronomers discovered a group of galaxies which tend to one point. This 'Great Attractor' can be represented by a plot of radii vs. the inverse of velocities, therein the asymptotic line towards the origin represents an *attractor* which may be called *state limit*. It results from gravity, inertia and conservation of energy. More often cosmic clouds tend to collapse into lumps in orbits, as e.g. the Solar system. Such periodic attractors, which may be called *state cycles*, can also be obtained with Newton's Laws written as Euler's differential equation of motion. Poincaré discovered that calculated motions of three neighboured celestial bodies can already get chaotic, and won a prize for proving that the Solar system will remain stable. Recently a less known

mathematician found, however, that in the long run the Solar system will end in deterministic chaos. The trend to disorder can be represented by a *strange attractor*, but this is evidently hard to capture.

Other than celestial bodies atoms and molecules attract or repel each other according to their distance. At a thermodynamic equilibrium an ensemble of them has equal spatial and temporal averages. Due to the First and Second Laws this state is an attractor which can be attained by a closed ensemble. Phase transitions and reactions normally tend to thermodynamic equilibria with other molecules than at the onset, but under special circumstances such ensembles can also get into state cycles. There are no transition energies at *critical points*, then phase transitions and reactions occur spontaneously. Depending on the boundary conditions such a system is capable of pattern formation or deterministic chaos, then one may speak of strange attractors.

The interactions in these cases can be *conservative*, i.e. celestial bodies, molecules or atoms need not be changed by encounters and their interaction forces are given by the relative positions via potentials. Thus the governing differential equations are linear and the attractors for closed systems are *endogenous*. This is not the case with dissipative systems like rearranging soils. Their mineral particles are changed by each encounter, therefore no two of them are equal and their contact forces are not given via potentials. There is no thermodynamic equilibrium without conservative interactions (Feynman et al. 1966). So how can attractors be of any use for soils?

It is first shown in Chap. 1 that particulate models (e.g. grain by grain) and continuum solid models cannot suffice for soils, but can provide useful arguments. Therefore five following chapters begin with ‘preludes on solids’, and particulate dynamics will sometimes be considered qualitatively. The introduction deals then with continuum soil models in the light of *objectivity*. It is argued that such models can be validated and that related parameters can be calibrated objectively by means of attractors. Fabrics of solid particles are called *skeletons* although they have no hinges and thus no preferred configurations. I recommend to judge continuum soil models by means of numerical simulations and comparative plots. Without getting lost in equations and data one can *see* at a glance how well observed attractors and related benchmark tests are reproduced.

In experiments with sand in a box G.H. Darwin (1883) found that earth pressures did not obey the theories of Coulomb and Rankine as they depend on the kind of placement. He asked Maxwell, got the advice that sand has a *historical element* and believed that this eludes mathematical treatment. He observed that sand can be dilated or densified by shearing or shaking, respectively, but did not realize that this is the clue to the historical element. Maxwell was evidently aware that the non-conservative interaction of grains prevents a purely thermodynamic approach. Until now the historical element is widely ignored in geotechnical teaching and design, although Casagrande (1936) found an access. He realized that sand attains so-called

critical states by shearing with constant pressure independently of the onset, states with higher than critical void ratios by compression from a loose packing, and densest states by cyclic shearing with constant pressure. Roscoe et al. (1958) found critical and loosest states more precisely in triaxial tests with sand and clay. Combination with simple *elastoplasticity* led to Critical State Soil Mechanics (CSSM), this was the point of start for further elastoplastic models.

Critical and loosest states are driven or *exogeneous* attractors which can be reached independently of the onset by continued shearing or compression, respectively, with energy input for dissipation at the solid particle contacts. Roscoe (1970) proposed tests with initially loose samples in order to avoid shear localizations. A further exogeneous attractor was discovered by Gudehus et al. (1977): proportional strain paths always led to proportional stress paths. This was called *swept out memory* (SOM) as then internal variables are determined by stress and void ratio. Kolymbas (1978) proposed constitutive equations with this attractor, they produced also critical stress states. It took years until his *hypoplasticity* incorporated Casagrande's highest, critical and lowest void ratios. All that is outlined together with elastoplasticity in Chap. 2 for *psammoids* ($\psi\acute{\alpha}\mu\mu\omicron\varsigma$ = sand), i.e. sand-like soils. Therein driven attractors named state limits play the key role, they are mainly presented *more geometrico* and help to keep the requirements of objectivity.

As for Coulomb's dry friction rate-independence is a validated assumption for psammoids. *Peloids* ($\pi\eta\lambda\acute{\omicron}\varsigma$ = clay), i.e. clay-like soils, are *argotropic* ($\alpha\rho\gamma\acute{\omicron}\varsigma$ = fast), i.e. rate-dependent, however, as their particles are soft. It is outlined in Chap. 3 that this is due to thermally activated dislocations, which can also lead to creep and relaxation by endogeneous attractors. These attractors are nearly the same in elastoplastic and hypoplastic models with viscosity. They work for more than two components as required for objectivity and will first be presented *more geometrico*. The validation is focused on state limits as these attractors represent main properties. Post-peak states with localized shearing and dilation are avoided as then *representative soil elements* (RSEs) lose the desired uniformity.

The comparisons in Chaps. 2 and 3 exhibit bigger deviations for path reversals. This is shown by means of another kind of exogeneous attractors, viz. *state cycles* due to cyclic deformations or ratcheting, i.e. superimposed cyclic and isochoric monotonous deformations. One can conclude that the state of RSEs is not sufficiently characterized by void ratio and skeleton stress components if reversals have to be captured. The introduction of further state variables is difficult as these are hidden, i.e. they cannot be observed macroscopically. Elastoplastic and hypoplastic relations with hidden variables are not easily tractable and need a physical justification. After frustrating attempts I realized that state cycles can serve *more geometrico* to catch the nature of soils with reversals. Hidden variables are no more needed after sufficient monotonous deformations as they are then determined by the skeleton stress, the attained SOM-states were introduced above as driven attractors.

Constitutive relations of so-called simple materials can be represented by means of uniform RSEs, but soils are not always that simple. Contact forces of grain skeletons are often concentrated in force chains. This *force-roughness* can be reduced by small alternating deformations so that skeletons get almost *hypoelastic* (i.e. stress-dependent incrementally linear). It appears that hidden state variables needed for reversals represent the force-roughness implicitly in a probabilistic sense. They tend to cycles prior to the external variables of an RSE, viz. stress components and void ratio. State cycles including force-roughness can also be attained with peloid RSEs, they are argotropic as the solid particles due to thermal activation. Waiting times with creep or relaxation after reversals were often ignored so that reported state cycles are distorted with unknown amount by endogeneous attractors.

The *pore water* of saturated soils can be captured by two brilliant ideas of Terzaghi (Chap. 6). The *principle of effective stress* says that the total mean pressure p can be decomposed into mean skeleton pressure p_s and pore water pressure p_w by $p = p_s + p_w$, and that volume changes of solid particles are negligible. This neutrality of skeletons with respect to p_w requires pore-free solid particles. The *diffusion of pore water* has in common with the one of heat or dissolved matter that it is thermally activated. In Terzaghi's linear theory it is related with a poro-elastic solid, but it can as well occur with anelastic skeletons. Terzaghi proposed also a cohesive or bound pore water with higher density and far higher viscosity than free water. Research in physical chemistry revealed that there is a rather repulsive electro-capillary phase with higher density and viscosity, but it could not be quantified for soils.

The permeability cannot always be captured by Darcy's law because of capillary effects. The pore water of fat clays and of sands with a low degree of saturation can get stuck. Dissolved substances and pore gas can have so non-uniform distributions that continuum approaches fail. The diffusion of pore water is ever-present at least for peloids and implies an *attractor in the large*: with suitable conditions the skeleton and its pore water tend to a thermodynamic equilibrium and get thus more uniform. Such evolutions will be introduced by experiments and numerical simulations and will be presented mainly *more geometrico*.

I do not claim that all properties of soils can be captured by attractors, but some *gaps* can thus be bridged (Chap. 7). Saturated peloids can have a net repulsion ($p_n > 0$) or attraction ($p_n < 0$) for physico-chemical reasons. A decomposition into partial pressures by $p = p_s + p_w + p_n$ suggests a tensile strength and lower limit void ratios for $p_n < 0$. Actually void ratios are higher with net attraction due to macropores, and with them state limits get debatable. Soils with gas channels and suction have also a kind of net attraction and macropores. The desired uniformity of RSEs can rarely be achieved as such soils tend to a deterministic chaos. The cementation of soil particles may be modelled as an irreversible net attraction, but cracking and re-condensation can hardly be caught. Abrasion and fragmentation seem to prohibit state limits and state cycles as these imply permanence of average particle proper-

ties. This contradiction in terms can be circumvented by means of evolution equations for skeleton parameters, at least in principle.

RSEs can lose their uniformity spontaneously by *localizations* (Chap. 8). Coulomb assumed that shear bands arise with friction and such an inclination that earth pressures get extremal. Until now this theory is the base of design models, but it cannot generally be defended as it ignores Maxwell's historical element. Shear bands arise alongside with *polar* stresses and tend to localized state limits and patterns or rather chaotic evolutions. Such strange attractors occur with overcritical stress obliquities, i.e. ratios of mean deviatoric stress and pressure. Shear bands and polar stresses can be ironed out by reversals with subcritical obliquities, thus state cycle fields work as driven attractors in the large. Shear bands occur similarly in peloids, but depend on skeleton viscosity and pore water diffusion in an intricate manner. Therefore peloid models with polar terms are not yet available and test results with clay beyond peak can hardly be evaluated.

Cracks are localizations with capillary entry which can lead to patterns or chaotic rupture. They can disappear by flooding and swelling so that skeletons decay into a fluid-like mud. Such evolutions may be vaguely described by strange attractors, but can as yet hardly be quantified. *Fabrics* with shear bands and cracks seem therefore to elude mathematical treatment. To a certain extent, however, they are reproducible in experiments and may be captured by spatial averages (Chap. 9). Fabrics by composition are sometimes regular like a sandwich, but more often irregular, they occur over several orders of magnitude. Such products of nature could also be explained by means of attractors, but the ones proposed in this book can at best help to substitute fabrics by simpler composites.

Continuum soil models require conservation laws, constitutive relations, initial and *boundary conditions* (Chap. 10). Initial configurations and state fields are often but arbitrary snapshots of evolutions. Soils, solid bodies and water come and go, so conditions are needed for changing boundaries of skeleton and pore water. Finite element experts demand boundary stresses or velocities and prefer to simulate placement or removal by fictitious increase or reduction, respectively, of gravity and boundary stresses for suitable sections. Experience and intuition suggest that sizes, rates and order of evolution steps may be simplified, but not *ad libitum*. Attractors in the large can help to justify and delimit such approaches.

Symmetry plays a key role in systems with conservative interactions, mathematical models reflect symmetries of elementary particles with a stupendous precision. There is less order in the transient cosmos of soils, but symmetry may often be assumed and can be attained by technical operations due to attractors. As indicated further above RSEs can get more uniform by exogeneous or endogeneous attractors, but can also lose their uniformity by strange attractors. One-dimensional evolutions (Chap. 11) are often assumed for simplicity and can be approached with parallel layers and creep or shaking. Plane-parallel evolutions with filling or excavation can be approached

in model tests and in central cross sections in situ (Chap. 12). Conventional approaches with slip surfaces can thus be justified and delimited, the same symmetry may also be assumed for certain tectonic evolutions.

Plane-parallelity is often assumed for *soil-structure interactions* (SSIs, Chap. 13). Coulomb's earth pressure and Terzaghi's punching resistance are simple special cases. A number of lab and field observations are apt to validate plane-parallel models, this is also the case with several axi-symmetric evolutions (Chap. 14). Again the symmetry can be enhanced by exo- and endogeneous attractors and can get lost by bifurcations with shear localization or decay, i.e. by strange attractors. This can also happen with less symmetric evolutions which can arise by geotechnical operations (Chap. 15). Some lab and field tests of this kind provide further validations.

Critical phenomena are at the verge of predictability and will only be indicated at the end (Chap. 16). They are rather well understood for systems with conservative interactions at or near thermodynamic equilibria. Deforming soils far off equilibrium can similarly exhibit pattern formation or deterministic chaos. Experiments with minute sand avalanches (Bak et al. 1987) triggered a euphoria on 'self-organized criticality' and enhanced granular physics. In the meanwhile it was realized that strange attractors for soils are more complex. Conditions for critical points can be formulated for a number of cases, therein critical states in the sense of soil mechanics play a key role and seem to deserve this name. Decay and recombination of skeletons are also critical phenomena, but not in the reach of present models.

The progress in soil mechanics was and is hampered by inadequate *conventions*. Often pressure and shortening are called stress and strain, and notions like stiffness, strength and failure are unreflectedly taken over from solid mechanics. Rather intuitive expressions as softening, liquefaction and cyclic mobility are used without a convincing definition. Codes of practice tend to freeze conventions and are sometimes mixed up with science; they may be of use for contracts and routine work, but hamper innovations. This book was written for those who want to understand soils beyond conventional methods, the attribute 'physical' in its title is not a pleonasm. It is voluminous as many publications with different conventions had to be taken into account, and as soils are really complex matter. Impatient readers may start with interesting examples to see what can be done, find then in referred sections more on how and why this may be done, and can thus gradually acquire a deeper understanding. You will be fascinated by the fourth element although or just as it is so manifold.

Contents

1	INTRODUCTION	1
1.1	Potential of particulate and solid continuum models	2
1.2	Objectivity of continuum soil models	7
2	SIMPLE PSAMMOIDS	15
2.1	A prelude on solids	17
2.2	An introduction of simple psammoids	26
2.3	A shortcut of CSSM	37
2.4	A shortcut of hypoplasticity	44
2.5	Validations near state limits with cylindrical symmetry	50
2.6	Validation off state limits with cylindrical symmetry	56
2.7	Cuboidal deformations near state limits	64
2.8	Cuboidal deformations off state limits	75
2.9	Simple shearing at state limits	82
2.10	Shearing off state limits	93
2.11	General and outlook	100
3	SIMPLE PELOIDS	111
3.1	A second prelude on solids	112
3.2	An introduction of simple peloids	122
3.3	Cam clay plus viscosity with cylindrical symmetry	137
3.4	Visco-hypoplasticity with cylindrical symmetry	144
3.5	Validation near and at state limits with cylindrical symmetry ..	151
3.6	Validation off state limits with cylindrical symmetry	163
3.7	Cuboidal deformations	170
3.8	Simple shearing	174
3.9	General and outlook	185
4	PSAMMOIDS WITH REVERSALS	193
4.1	A third prelude on solids	194
4.2	Observed response of sand with reversals	206

4.3	Attractors with force-roughness	218
4.4	Elastoplasticity with back stress	227
4.5	Hypoplasticity with intergranular strain	235
4.6	Seismically activated viscous effects	243
4.7	General and outlook	252
5	PELOIDS WITH REVERSALS	259
5.1	A fourth prelude on solids	260
5.2	Observed response of peloids with reversals	267
5.3	Visco-elastoplasticity with back stress	275
5.4	Visco-hypoplasticity with intergranular strain	281
5.5	General and outlook	286
6	PORE FLUID	293
6.1	Interfaces of water with gas and solids	294
6.2	Pore fluid of psammoids	297
6.3	Pore fluid of peloids	304
7	BRIDGING GAPS	313
7.1	Saturated peloids with net pressures	313
7.2	Unsaturated soils	322
7.3	Cemented and transient particles	332
8	LOCALIZATION	343
8.1	A fifth prelude on solids	344
8.2	Shear localization in psammoids	354
8.3	Shear localization in peloids	368
8.4	Cracking and channelling	379
9	FABRIC	385
9.1	Fabrics by state	385
9.2	Fabrics by composition	391
10	BOUNDARY CONDITIONS	397
10.1	Soils at water and air	398
10.2	Boundaries in the ground	406
10.3	Soils at solids	415
10.4	Placement and removal	423
11	ONE-DIMENSIONAL EVOLUTIONS	437
11.1	A prelude on the diffusion of pore water	438
11.2	Standing psammoid columns	444
11.3	Standing peloid and composite columns	450
11.4	Standing soil columns with wave propagation	457
11.5	Psammoid columns in slopes	463

11.6	Peloid columns in slopes	470
11.7	Radial symmetry	478
12	PLANE-PARALLEL EVOLUTIONS WITHOUT SSI	485
12.1	Psammoid heaps upon a solid base	486
12.2	Peloid and composite heaps on a solid base	495
12.3	Heaps upon yielding ground	502
12.4	Excavations	513
12.5	In-plane and anti-plane shaking	522
12.6	Normal faulting	531
13	PLANE-PARALLEL EVOLUTIONS WITH SSI	539
13.1	Psammoids at rigid guided walls	540
13.2	Peloids and composites at rigid guided walls	554
13.3	Guided rigid strips upon yielding ground	563
13.4	Rigid structures at the ground	576
13.5	Deformable structures at the ground	590
13.6	Strutted and back-tied retaining structures	600
13.7	Cavities and underground structures	613
13.8	SSI with reversals	626
14	AXI-SYMMETRIC EVOLUTIONS	637
14.1	Triaxial tests	638
14.2	Fills, excavations and ring structures	649
14.3	Penetration	660
14.4	Piles	675
14.5	Silos	687
14.6	Torsion	699
15	LESS SYMMETRIC EVOLUTIONS	713
15.1	Two symmetry planes without SSI	713
15.2	Two symmetry planes with SSI	725
15.3	One symmetry plane and simple SSI	741
15.4	One symmetry plane and complex SSI	754
15.5	Tumbling and driving	773
16	CRITICAL PHENOMENA	789
16.1	Critical phenomena off soil mechanics	790
16.2	Pattern formation with soils	793
16.3	Deterministic chaos with soils	797
	EPILOGUE	803
	Symbols and Acronyms	807
	References	811
	Index	837

INTRODUCTION

In ΤΑ ΦΥΣΙΚΑ, the first ever book on physics, Aristoteles defined the difference of continuous and granular matter by means of *ενέργεια*, which denoted action and not energy in a modern sense (this statement was discovered by Th. Triantafyllidis). Ever since continuum approaches for soils were questioned as far as these are visibly particulate matter. One may be tempted to simulate granular aggregates grain by grain with a computer in order to understand their mechanical properties. On the other hand, engineers are inclined to take over continuum models from solids to soils, so they work with notions like stiffness and strength.

It is shown in Sect. 1.1 why both approaches cannot suffice to predict evolutions with soil. Particulate models have to be simplified, even when using big computers, to such an extent that they can at best yield qualitative insight. It is recommended to focus such attempts on attractors, namely state limits, state cycles and granular phase transitions. For the time being particulate models are hardly feasible with submicroscopic clay particles due to physico-chemical effects. One is inclined to catch clay instead as continuous matter like a solid.

Until present soils are often considered as elastoplastic like solids. Referring to Coulomb (1773) and Mohr (1914) their strength is attributed to friction and cohesion, and the bound theorems of plasticity (Koiter 1958) are taken for granted. The intricate dependence of soil stiffness on density, stress and direction of stretching is often neglected. Thus, however, soil bodies cannot properly be judged. Elastoplastic relations are not necessary for solids, these may as well be captured by hypoplastic relations. There is a vast variety of both kinds of constitutive models for soils, which cannot even be touched in Sect. 1.1. It is only shown that *no* solid-like continuum model can suffice for soils. This holds particularly true with respect to pore water and boundary conditions. For the same reason the preparatory sections of Chaps. 2, 3, 4, 5, 8 and 11 are entitled ‘preludes’, this is not a textbook on solids.

From a pragmatic point of view there is no way around continuum models for soils. They have to be tractable and feasible, however, and their *range of*

validity should be properly known and should be as wide as possible. Following Popper's (1959) 'Logic of Scientific Discovery' theories can catch parts of reality if they are logically consistent as long as the employed hypotheses are not refuted by observations. Popper proposed statistical measures for scattering phenomena so that these do not elude theories from the very beginning. We cannot take over this standpoint for two reasons. The continuum hypothesis cannot be proven with mathematical arguments, whatever sophisticated the employed statistics may be. Moreover, observational soil data will never suffice for sound statistical analyses, and simulated data from numerical models cannot compensate this lack.

We take over an argument by Babuška and Oden (2006) for solids to soils. They point out that numerical models should and can be mathematically consistent, i.e. that numerical artefacts can and have to be avoided by *verification*. They show, on the other hand, that currently used constitutive models for solids miss experimental results with many reversals outside the elastic range. They call this lack of *validation* a crisis in computational sciences. This book is focused on the validation of continuum models for soils, whereas the numerical verification is left aside. Following Popper the outlined models should not be mixed up with reality, they can at best catch parts of it.

General features of continuum models for soils are introduced in Sect. 1.1 in the light of their *objectivity*. Readers should have a textbook knowledge of continuum mechanics, notions of it are used throughout this book. The required smoothness can but vaguely be defended by means of representative statistical ensembles. Unit-invariance and frame-indifference can be achieved with suitably chosen quantities. Constitutive relations can be judged by means of attractors as thus the partial indeterminacy and arbitrariness of initial states can be ruled out. Not always, however, as localizations and decay (i.e. phase transitions at critical points) delimit the range of validity. This argument is extended to boundary value problems, for them *attractors in the large* can again reduce the indeterminacy and arbitrariness. Various kinds of symmetry, which will be used for simplifications and validations in following chapters, can thus be defended. Critical phenomena will also be introduced in Sect. 1.1 as they delimit the objectivity of continuum models, though in a cruder sense than meant by Popper.

1.1 Potential of particulate and solid continuum models

Following Jaeger et al. (1996) sand-like soils may be called *granular solids*, but with due caution. Grains are solid bodies, so why not simulate aggregates of them numerically and apply statistical mechanics? We will see that this cannot suffice. Grain skeletons may appear solid-like, so how far could they be captured with continuum models for solids? These do not suffice either, however, the more so with pore water and gas. Clayey soils may appear rather continuous like soft solids, but not when they are desiccated and cracked. Their

particles are not only grains and cannot clearly be identified due to physico-chemical effects (Sect. 6.1), so numerical simulations with them would be rather futile. Let us see how far particulate and solid continuum models can be of use for soils.

The *conservation laws* of mass, electric charge, energy and linear and angular momentum hold for arbitrary sections of space-time and with any kind of matter and evolutions (apart from relativistic and quantum effects). The behaviour of soils is distinguished by the interaction of solid particles with each other and with the fluid in between. This interaction is *not conservative*, i.e. soil particles are changed by encounters and energy is thus dissipated. Therefore no two soil particles are equal, and forces between them are not fully determined by mutual positions via potentials. This fact prevents a straightforward application of thermodynamics and causes enormous problems with statistical mechanics.

So what could be achieved by simulations with aggregates of particles as *representative soil elements* (RSEs)? Imagine an initially cubical RSE with grains of size d_g . They should not be equal spheres as these could get arranged in crystalline order, but a mixture of spheres with two sizes may serve as the simplest substitute. The interactions may be modelled by relations for elastic contact zones with friction (Johnson 1985), wear and cracking may be neglected. With due caution such relations may be substituted by non-linear springs and friction coefficients. As microseismic effects matter for redistributions in grain skeletons (Sect. 4.6) they should not be suppressed by a fictitious damping in order to make calculations easier. Mutual rotations should also not be excluded for simplicity as polar effects can play a role (Sect. 8.2).

How could many idealized grains be put together with contact forces so that we get an RSE with an *initial state*? Spatial averages make sense only with a sufficient number N of grains, i.e. the RSE-size d_e should exceed the mean grain size d_g . $d_e/d_g = 10$ will not suffice for stress components as the forces at ca. 10^2 grain contacts scatter strongly, so N should exceed ca. 10^4 . The grains could be placed with a desired void ratio which should not scatter spatially too much. A set of contact forces may be imposed along the RSE-boundary so that they sum up to desired initial stress components. This could be done with different spatial fluctuations, this force-roughness should be the same in a statistical sense throughout the RSE. We see that Maxwell was right stating that ‘sand when put together in different ways would exercise different thrusts’, i.e. that there is a *historical element* which could elude mathematical treatment (Darwin 1883).

Evolutions of shape and state of our RSE require changing *boundary conditions*. For a simple granular solid (more in Chap. 2) the RSE should remain statistically uniform so that it suits to equal neighbours. This excludes localizations (Chap. 8), and also strictly uniform distributions of displacements or contact forces along the boundary. In consistent simulations spatial fluctuations should be statistically uniform throughout the RSE during any evolution. Moreover, accelerations should occur at the boundaries as inside

the RSE, and the force-roughness should remain statistically uniform to be representative. Similar problems arise with representative elements which are composed of molecules, then a thermostat is needed to maintain the temperature T , but with T and conservative interactions the ‘historical element’ is less intricate.

Assuming that all these requirements could be satisfied, which succession of boundary conditions should be chosen in order to catch essentials of granular soils? Only those findings count which do not depend on the inevitable arbitrariness and indeterminacy of initial states. As far as both are *swept out* mechanical properties of our RSE may be called objective. In other words, simulations should be focused on attractors for evolutions of mean shape and state with suitable boundary conditions. As with other systems three topological kinds of attractors can be discerned, viz. monotonous ones (in particular points), cyclic or periodic ones, and strange attractors for pattern formation or chaos.

Such attractors may only be indicated here as the requirements formulated further above for simulations could as yet only partly be satisfied. So-called peak states (Sects. 2.2 and 3.8) were obtained with constant mean pressure (e.g. Thornton and Sun 1994), whereas stationary states for monotonous evolutions with constant volume (called critical states) could not be generated. State cycles were obtained with cylindrical RSEs and constant confining pressure (e.g. Alonso-Marroquin and Herrmann 2004). Simulations with parallel rods instead of grains are simpler, but provide less insight:

- force chains can indicate an increasing force-roughness (e.g. Cundall et al. 1982, Radjai et al. 1996, more in Sect. 4.3);
- proportional strain paths lead to proportional stress paths (Pena et al. 2006, supports Sect. 2.2);
- shear bands arise with constant mean pressure (e.g. Åstroem et al. 2000, D’Addetta et al. 2004, more in Sect. 8.2);
- seismic emissions arise with monotonous overall deformations (Tillemans and Herrmann 1995, Kondic and Behringer 2004, used in Sect. 4.6).

Experiments with bundles of rods provide less insight than such simulations as physical boundary conditions for RSEs cannot as well be realized. Force chains were discovered with photoelastic rods (Dantu 1957, Fig. 4.3.1). An increase of force-roughness was observed with torsional shearing (Behringer and Miller 1997). Polar effects were demonstrated with a torsional device (Bogdanova-Bontcheva and Lippmann 1975). Grains can also be observed in experiments with RSE-like granular aggregates, but hardly as many as needed for statistical evaluations. The collapse of force chains can be concluded from the acoustic emission (Hidalgo et al. 2001).

Simulations and experiments with simplified grains and RSE-like boundary conditions are thus of restricted use, at least until now. They can help to understand mechanisms and to formulate constitutive relations. More sophisticated simulations could help to establish attractors as those which will be

used in Chaps. 2 and 4 for granular soils. They could also help to understand *granular phase transitions*, viz.

- partial or complete decay of grain skeletons, which may be called granular melting or evaporation;
- recombination of skeletons, i.e. freezing of a granular fluid or condensation of a granular gas;
- creation and dwindling of polar quantities with shear localization and reversals, respectively (Sect. 8.2);
- formation and cracking of dry masonry (Sect. 2.2).

These may be called *critical phenomena* as they occur without transition energies at critical points over many length scales, and apparently with power laws (Bak et al. 1987, Kadanoff 1991). Critical phenomena may be related with strange attractors; this generic term will be used throughout this book without mathematical specification. They delimit the applicability of the methods outlined in subsequent chapters (Chap. 16). It will take a long time until statistical mechanics with non-conservative interactions can cope with such cases.

Taking into account *pore water* in simulations is easy only with full saturation, slow seepage and not too small grains. No problems arise as long as Darcy's law and Terzaghi's principle of effective stress hold valid. Turbulent flow of pore water and pressure waves therein are beyond the present reach, both can influence particularly granular phase transitions. Humid granular soils do not exhibit such kinetic effects, but capillary phenomena can elude mathematical treatment (Sects. 6.2 and 7.2). Granular dynamics and thermodynamics may be combined in simulations, but the desired stochastic uniformity of RSEs cannot easily be maintained. Wetting and drying fronts can exhibit fingering already with fixed grain skeletons, this indicates further critical phenomena.

Soils with *submicroscopic particles* are yet too complex for particulate numerical simulations. Dust grains with water may get stuck in a skeleton so that they are not affected by Brownian motion, but a net attraction depending on the ionic strength enables macropores which enhance spatial fluctuations (Sect. 7.1). Nano-sized layer silicates can form aggregates so that particles and skeletons with them can hardly be identified. The matter gets more intricate with solubles, condensates and pore gas, then thermodynamics may at best provide qualitative hints (Sects. 6.1, 6.3, 7.2 and 7.3).

Clays with invisible particles may appear like soft solids. *Continuum solid models* were often taken over for soils, let us see how far this could be legitimate. The simplest constitutive relations for solids are elastic. Only with them strain is a state variable, this is related with stress via the elastic energy. A viscous resistance may be added. The algebraic representation is easy if such relations are linear, but this has little to do with soils. These can be *plastic* (from $\pi\lambda\acute{\alpha}\theta\omega =$ to shape) like ductile solids. Elastoplastic relations are introduced *more geometrico* alongside with hypoplastic ones in Sect. 2.1

for pore-free solids. This is no more than a preparation for soils as these are porous.

Porous solids have changing densities and depend on pressure (imagine a sponge), i.e. they are *pyknotropic* and *barotropic*, but not like soils. Elastoplastic and hypoplastic relations represent another kind of pykno- and barotropy, this is outlined by means of attractors in Chap. 2. Ductile pore-free solids are *argotropic* (rate-dependent) by thermally activated dislocations, viscoplastic relations for them are presented in Sect. 3.1 for preparation. Porous ductile solids have another pykno- and barotropy than clayey soils, but their argotropy is nearly the same (Sect. 3.2).

Pore-free solids exhibit force-roughness which matters with reversals, this is outlined for preparation in Sect. 4.1 without and in Sect. 5.1 with argotropy. The required internal state variable can at best be captured indirectly by means of state cycles, these attractors will be presented only *more geometrico*. The presentation of constitutive relations with hidden state variables for sand-like and clay-like materials in Chaps. 4 and 5, respectively, is also mainly geometrical. It is focused on state cycles as the indeterminacy of initial states can thus be ruled out. Constitutive relations with hidden variables remain complex and rather arbitrary already for solids, algebraic details are left aside as they will be modified.

Solids with open pores can be saturated with water and can be elastic like a sponge. This model is used in Sect. 11.1 to introduce Terzaghi's (1925) diffusion of pore water, but relations for the pore fluid of soils (Chap. 6) differ from those for porous solids. Soils with net attraction or condensation bridges of particles appear more solid-like, but require other constitutive relations (Chap. 7). Sound differences arise also with localizations (Chap. 8). Pore-free solids serve for the introduction of polar quantities, cracking and erosion elude continuum approaches. Localizations in solids are often related with *failure*, which denotes the inability to meet requirements. This notion is less appropriate to characterize soils than solids and therefore largely avoided in the present book.

The issue of fabric exhibits further differences of solids and soils (Chap. 9). Dislocations and crystallites in solids have no counterparts for skeletons of mineral particles, and composites of solids differ fundamentally from those of soils. Soil fabrics *in situ* are less determinate than industrial solids. Little can also be taken over from solids for boundary conditions of soils (Chap. 10). Free soil boundaries enable phase transitions and are shifted by placement and removal. Solid bodies can interact with soils via interfaces (which can also arise within the ground), then separations into near- and far-fields are of use.

Continuum models for the *stability* of solid bodies and its loss cannot easily be taken over to soils. The sum of elastic and gravitational energy is minimal for a stable elastic solid, but not likewise for soil bodies. Upper and lower bound theorems (Koiter 1958) may at best be applied with due caution in a heuristic manner to soils (Gudehus 1972). Decay and recombination of soil

skeletons differ fundamentally from melting of solids and cooling of melts as granular phase transitions are driven and occur without transition energies. Critical phenomena delimit the applicability of continuum models for soils in other ways than with solids and fluids (Chap. 16). One may only speculate that strange attractors with common features for solids and soils could be of use for the verge of stability.

Summing up, particulate and continuum models with or for solids, respectively, can at best be of qualitative use for soils. Simulations with element-like grain aggregates are inevitably over-simplified, but can help to understand regular attractors and phase transitions. Such approaches are hardly feasible for soils with submicroscopic particles. Constitutive relations for solids may serve to prepare those for soils, but their pykno- and barotropy cannot be the same as for porous solids. Soils require also other initial and boundary conditions, and losses of stability differ markedly from those of solids.

1.2 Objectivity of continuum soil models

As always in science continuum models for soils should be objective. Requirements of objectivity are outlined in the sequel which will be needed throughout the book. The advantage of attractors will thus be illustrated, and also the inevitable indeterminacy of soil behaviour. Particulate models are left aside, but soil particles are considered again and again. The issue of objective continuum models is complex and can only be touched in this rather condensed section.

The *composition* of soil materials can be defined by volume or mass fractions of representative averages. The void ratio e is defined with the solid volume fraction α_s by $e = (1 - \alpha_s)/\alpha_s$. The water content is defined as $w = m_w/m_s$ with the mass fractions m_w and m_s of water and solid particles. With mass densities ρ_w and ρ_s of only these fractions w can substitute e by $w = e\rho_w/\rho_s$. A fraction of pore gas can be expressed by the degree of saturation $S_r = w\rho_s/e\rho_w$.

The kind of solid particles and pore water can be expressed by average sizes, shapes and minerals plus fractions of dissolved substance. Skeleton and pore fluid can be characterized by constitutive relations and parameters. Soils as materials are described by means of *representative elements* (RSE with S for soil or skeleton). RSEs are to represent ensembles in a probabilistic sense so that smooth average fields make sense. Mechanical skeleton properties are usually defined with uniform RSEs although these cannot exactly be achieved in experiments. Skeletons with polar quantities require RSEs with gradients (Sect. 8.2), and RSEs with a hydraulic gradient are needed for the permeability (Sect. 6.2). Finite elements are often also RSEs with gradients of state.

The kinematics can be formulated by means of thought marker particles which belong to the *skeleton* of solid particles. The word ‘skeleton’ is chosen although there are no hinges, contacts and neighbours of soil particles change

during rearrangements. Such skeletons may be fixed, but there are no preferred configurations as soils are amorphous (Greek for shapeless). Displacements of marker particles have to be referred to arbitrarily chosen reference configurations. Changes of shape of soil bodies can thus be identified as long as skeletons do not decay or lose their topological order.

Displacement fields have to be *smoothed* for continuum models so that derivatives can be defined. For this purpose the zig-zag paths of marker particles have to be substituted by averages of probabilistic ensembles. It is assumed that these are representative and thus objective, this assumption can only be justified indirectly by comparing predictions and observations. Differentiation of displacements with respect to time t leads to fields of the *skeleton velocity* \mathbf{v}_s . The *stretching tensor* \mathbf{D} is defined with the gradient $\nabla \mathbf{v}_s$ of \mathbf{v}_s as $\mathbf{D} = (\nabla \mathbf{v}_s + \mathbf{v}_s \nabla)/2$ (denoting the transpose of $\nabla \mathbf{v}_s$ by $\mathbf{v}_s \nabla$ and omitting components for brevity). Temporal changes \dot{e} of the void ratio e in convected RSEs are related with \mathbf{D} by $\dot{e}/(1+e) = \text{tr} \mathbf{D}$ if the solid density ρ_s is constant. Deformation tensors could be defined with gradients of displacements, but they are physically meaningless for soil skeletons. Only elastic bodies have deformation states, these are uniquely related with stress states and thus dispensable. Deformations of soil skeletons cannot be used to characterize their state, only *related changes of shape and state with time* are physically relevant.

For capturing rotations one may imagine marker particles which indicate their orientation. Again averaging and smoothing of ensembles is required so that derivatives get possible (more fictitious as rotations of particles scatter more than translations). As no configuration is distinguished only the rate of rotation $\boldsymbol{\omega}_s$ is relevant. It does not agree in general with the skew-symmetric part of $\nabla \mathbf{v}_s$, viz. $\mathbf{W}_s = (\nabla \mathbf{v}_s - \mathbf{v}_s \nabla)/2$. The difference $\boldsymbol{\omega}_c = \boldsymbol{\omega}_s - \mathbf{W}_s$ appears as additional quantity in polar continua. These can be used to capture shear localizations (Sect. 8.1), oriented particles in shear bands indicate that such polarizations occur (Sect. 8.3).

The *seepage velocity* of the pore water can be defined as the average volumetric flow relative to the skeleton, $\mathbf{v}_w - \mathbf{v}_s$. Imagine a grain skeleton at one instance along a plane and the flow of water through it per unit of cross section and time. Convected marker particles in the water would indicate diffusion in erratic open pore channels. Seepage can occur with a fixed skeleton ($\mathbf{v}_s = 0$) or can be negligible if skeleton and water move together ($\mathbf{v}_w = \mathbf{v}_s$). In case of full saturation the gradients of \mathbf{v}_s and \mathbf{v}_w are linked with \dot{e} via $e = w\gamma_s/\gamma_w$. With *pore gas* $\mathbf{v}_w - \mathbf{v}_s$ can likewise be defined, but is less representative because of stronger spatial fluctuations. Gas bubbles between particles may be harmless, but if they occur in macropores they can spoil skeletons. Soils with uniformly distributed gas channels have low S_r and often negligible $\mathbf{v}_w - \mathbf{v}_s$. With gas pockets or fingers $\mathbf{v}_w - \mathbf{v}_s$ can get chaotic so that averages are insufficient (Sect. 6.2).

Topological changes of solid particle skeletons confine the use of gradients. Skeletons get meaningless along edges of solid bodies or tips of cracks. They can no more be identified if their composition is changed by mixing or

segregation of solid constituents. Soil skeletons get lost by decay and can be recombined.

Internal forces of saturated soils can be represented by the fields of a symmetric *skeleton stress tensor* \mathbf{T}_s and of the *pore water pressure* p_w . According to the principle of effective stress they are linked with the total stress tensor \mathbf{T} by $\mathbf{T} = \mathbf{T}_s - p_w \mathbf{1}$ (traction positive). This implies $p = p_s + p_w$ for the mean pressures p and p_s and is justified by the neutrality of solid particles with respect to p_w (Sects. 2.2 and 3.2). Stress vectors $\mathbf{t}_s = \mathbf{T}_s \mathbf{n}$ represent average force densities of skeletons for thought cutting planes with normal \mathbf{n} . p_w can be substituted by the *hydraulic height* h_w of thought piezometers. The gradient ∇h_w is related with the seepage force \mathbf{f}_s between skeleton and pore water by $\mathbf{f}_s = \gamma_w \nabla h_w$ with the specific weight of water γ_w .

For understanding \mathbf{t}_s and h_w one may imagine solid particles along a plane grid or filter. This takes over the skeleton stress vector \mathbf{t}_s , whereas h_w is indicated as water height in a thought piezometric tube. Thus \mathbf{T}_s expresses the average density of contact forces of RSEs, i.e. of representative probabilistic ensembles. The spatial fluctuation of contact forces (which may be expressed by force chains) is thus not captured. This so-called *force-roughness* is an internal state property which cannot be captured easily (Sect. 4.3). Stronger spatial fluctuations of contact forces in shear bands may be described by a non-symmetric stress tensor and a couple stress. Such *polar stresses* can be used to model shear localizations, but their statistical interpretation is debatable (Sect. 8.2).

The pore pressure p_w is a sufficient state variable for the pore water of saturated granular soils if it is close to a thermodynamic equilibrium (Sect. 6.2). The pore water of saturated clayey soils can have other states, particularly near particle surfaces and contacts, then the effective stress principle can get insufficient (Sects. 6.3 and 7.1). Unsaturated and cemented soils may also be captured with additional partial stresses, but these are debatable because of stronger spatial fluctuations (Sects. 7.2 and 7.3). Soils with patterns of shear bands and cracks can hardly be captured by averages (Sect. 9.1). The desired uniformity of RSEs can get lost spontaneously by localizations at critical points (Chaps. 8 and 16). A decay of skeletons implies a loss of their mean pressure p_s while p_w remains.

If e and \mathbf{T}_s suffice as state variables of skeletons these are called *simple*. Then constitutive relations usually express how the stress rate, $\overset{\circ}{\mathbf{T}}_s = \overset{\circ}{\mathbf{T}}_s + \mathbf{W}\mathbf{T}_s - \mathbf{T}_s\mathbf{W}$ including convection by rotation, depends on the stretching tensor \mathbf{D} and on the state variables \mathbf{T}_s and e . This can be written $\overset{\circ}{\mathbf{T}}_s = \mathbf{F}_s(\mathbf{D}, \mathbf{T}_s, e)$ with a tensorial function \mathbf{F}_s which is non-linear in \mathbf{D} . \mathbf{F}_s should be an isotropic function of \mathbf{D} and \mathbf{T}_s in order to be independent of the reference frame. There is no reference time as t appears only in the rates. For unit-invariance reference quantities should be taken from the skeleton. This can be achieved by referring \mathbf{T}_s to a kind of hardness h_s and \mathbf{D} to a reference rate D_r .

Rate-independence is postulated for a class of idealized skeletons, i.e. $\mathbf{F}_s(\lambda\mathbf{D}, \mathbf{T}_s, e) = \lambda\mathbf{F}_s(\mathbf{D}, \mathbf{T}_s, e)$ for any $\lambda > 0$. These are called *psammoids* (sand-like) and further specified in Sect. 2.2. Therein \mathbf{F}_s is first represented graphically for cylindrical deformations by so-called response polars. It is shown with them how straight stretching paths lead towards state limits independently of the onset so that these are attractors. The same is achieved with algebraic representations of elastoplastic and hypoplastic relations, thus key properties of skeletons can be defined objectively. Without all algebraic details such attractors are then introduced for other than cylindrical deformations by means of associated paths and response polars, i.e. *more geometrico*.

Critical states are isochoric state limits which are related with a critical friction angle and a p_s -dependent critical void ratio e_c . Other limit void ratios range from p_s -dependent lower bounds e_d to upper bounds e_i . As state limits can be approached from different initial states they are particularly apt for validations by means of soil element tests. As long as samples remain uniform (which is not strictly the case) they can thus exhibit properties independently of the kind of placement. In other words, state limits are objective with respect to the starting point and can thus serve to identify simple psammoids.

Simple *peloids* are similarly introduced in Chap. 3 as representatives of clay-like soils. They are *argotropic* (rate-dependent) due to thermally activated dislocations in their solid particles. This can be expressed by state limits which are attained by proportional stretching with different amounts $D = \sqrt{\text{tr}\mathbf{D}^2}$. For them the dependence of stress directions on directions of stretching can be the same as for psammoids, but the solid hardness h_s depends on D so that a reference rate D_r is needed. Visco-elastoplastic and -hypoplastic relations are again represented *more geometrico* without all algebraic details.

Peloids are capable of creep and relaxation with constant skeleton stress or shape, respectively. Then the skeleton state tends to an endogeneous attractor by thermal activation, whereas state limits are exogeneous or driven attractors. Relaxation tends to a thermodynamic equilibrium, isochoric creep can get stationary and contractant creep leads to an equilibrium. Dilatant creep occurs with overcritical stress obliquities (i.e. ratios of mean shear stress and pressure) and leads to localizations so that the uniformity of RSEs gets lost. Waiting times should be taken into account in the execution and evaluation of experiments.

Because of the low permeability k_f pore pressure p_w and void ratio e of peloid samples are not generally uniform in element tests. Except for isochoric deformations p_w and e can get uniform by the diffusion of pore water in drained RSEs (Sects. 10.4 and 11.1). With suitable boundary conditions, creep and/or relaxation the skeleton can thus get uniform by thermal activation. This further endogeneous attractor works with subcritical stress obliquities of the skeleton so that this gets denser and tends to a state of rest. Skeletons with overcritical obliquities lose the desired uniformity spontaneously by localization as with psammoids.

Evolutions with several reversals are not sufficiently captured by assuming simple psammoids or peloids. This is revealed by *state cycles* of skeletons which are attained by stretching cycles without or with isochoric average stretching with constant amount D . Without average stretching these driven attractors can be symmetric in plots of stress components, and they are asymmetric in the other case which is called ratcheting. Hysteresis and ratcheting of simple psammoids are exaggerated with hypoplastic relations and underestimated with elastoplastic ones. It is shown in Chap. 4 for psammoids how this lack can be reduced by internal variables which can be related with the internal force-roughness. This approach works also for peloids, but their argotropy is as yet taken into account only in few constitutive relations (Chap. 5).

State cycles are proposed in order to validate constitutive relations for evolutions with reversals. If overcritical stress obliquities are avoided samples get more uniform by reversals in experiments with suitable boundary conditions. The force-roughness tends also to cycles, and its initial values due to placement are ironed out. This cannot be observed directly as the force-roughness is hidden, but is indicated indirectly by the asymptotic response to cyclic stretching or ratcheting. Elastoplastic relations with back stress and hypoplastic ones with intergranular strain can thus be judged although the employed internal variables cannot be observed.

Reversals in RSEs for applications are rarely regular, and experiments with sophisticated control reveal an inevitable intrinsic irregularity. Only many small cyclic deformations can lead to an almost elastic response with little hysteresis. Otherwise elastic fractions get smaller with bigger amplitudes and with higher average stress obliquities, and can hardly be separated in experiments. Numerical simulations get expensive with many anelastic reversals, and the accumulation of numerical errors is not easily avoided. A kind of seismically activated creep or relaxation can occur with many reversals. This is outlined for psammoids in Sect. 4.6 with a granular temperature and indicated for peloids in Sect. 5.5. These approaches are as yet heuristic so that their range of validity can hardly be judged.

The *pore fluid* is briefly treated in Chap. 6. For saturated psammoids Darcy's law and Terzaghi's principle of effective stress may suffice. Without saturation capillary effects can lead to the loss of uniformity of psammoid RSEs, and in more intricate ways of peloid RSEs. Pore fluids with gas and ions are heuristic substitutes which cannot be objective if deterministic chaos arises. Insufficiently understood influences of the pore fluid on skeletons are addressed in Chap. 7. A net attraction by electro-capillarity with full saturation, or by suction with gas channels, increases limit void ratios and can lead to irregular macropores. Cemented soils can hardly be captured with an irreversible net attraction, and such approaches are debatable because of the inherent chaos.

State limits and state cycles require permanence of skeleton properties. This is not really given as interactions of solid soil particles are not conservative. This contradiction in terms can be overcome by means of evolution

equations for skeleton parameters which change alongside with evolutions of skeleton shape and state. Such approaches are only indicated in Sect. 7.3 as it suffices that they are feasible.

The desired uniformity of RSEs can get lost by *localizations* (Chap. 8). The formation of shear bands can be modelled with polar quantities which arise in a kind of phase transition. Such models can at best be validated indirectly by comparing experiments and simulations. This works already with psammoids, but not yet with peloids due to skeleton viscosity and pore water diffusion. The formation of shear band patterns indicates a strange attractor with pattern formation or deterministic chaos. Only the onset at critical points may be predicted, but rarely further evolutions. This is much more so with the formation of cracks or hydraulic channels, such critical phenomena are not yet sufficiently understood.

It is often argued that soils have *fabrics* which can hardly be reconstituted so that undisturbed samples are needed. This argument seems to rule out the use of attractors. Well, not quite (Chap. 9). An RSE with a given kind of solid particles, void ratio and average skeleton stress can certainly have different fabrics. As indicated further above e and \mathbf{T}_s do not suffice as state variables if there are several reversals, then an internal variable is needed to catch the force-roughness. This occurs alongside with spatial fluctuations in the rearrangement of particles. More complex fabrics arise with localizations in patterns, these can get chaotic or can be ironed out by many reversals.

Fabrics by state are related with attractors and can thus be generated again and again, although not in arbitrary successions. Fabrics by composition can likewise principally be reproduced by placement and further treatment. Net attraction, cementation, transitory particles and mixing/unmixing are left aside, they cannot be captured by the attractors proposed in this book.

Modelling evolutions of shape and state requires a continuum framework for displacements and forces, conservation laws and constitutive relations, and also initial and boundary conditions. Due to necessarily non-linear constitutive relations of stress and stretching there is no way around numerical methods with discretization of space and time, and with iterations for solving incremental equations. Following Babuška and Oden (2006) numerical verification (how to avoid artefacts) and economy (proper use of capacity and effective equation solvers) may be taken for given. This book is focused on the *validation* of numerical models with physical arguments, and on the *identification* for applications. Identification of soil bodies means their representation by a composition into psammoids and peloids with boundaries including pore water and gas, and the specification of initial and boundary conditions.

State fields of skeleton and pore fluid in continuum models are generally not uniform. Only RSEs may be uniform by definition, but they can also have uniform gradients (needed e.g. for seepage or polar effects) or patterns (e.g. shear bands or sandwich). *Boundary conditions* have to be specified for skeleton and pore fluid according to the kind and state of both. As will be

outlined in Chap. 10 these conditions have to be simplified, attractors can help to justify and to delimit such approaches.

Skeletons at free surfaces (Sect. 10.1) can have pressure due to net attraction or suction. Otherwise they tend to decay or recombination so that such boundaries get fuzzy. This can be prevented by a skin or a mattress, i.e. a deformable solid which changes also the hydraulic boundary conditions. Boundaries in the soil interior can arise by separation or shear localization, they may also be assumed between different soils or between near- and far-fields. Their position is variable as it belongs to the evolution of shape and state, but sometimes it may be estimated or assumed. Complete conditions can hardly be given for internal boundaries, but transitions can often be specified along them. Shear bands with shearing resistance constitute a special case, usual assumptions for them will be discussed in Sect. 10.2.

Interfaces of solid and soil bodies are also internal boundaries (Sect. 10.3). They can be partly specified for skeletons and pore water according to roughness and permeability of solids. They can get less determinate by shear localization, opening, mixing or fluidization. The soil-structure interaction (SSI) requires a further specification of composition and boundary conditions of solid bodies at or in the ground. Placement and removal of soils and solids determine initial and boundary condition and have to be simplified for simulations (Sect. 10.4). Owing to attractors in the large natural and technical evolutions may be substituted by few steps with suitable order and duration. This could be justified by ground investigation and field monitoring, simulations with different steps can provide more insight. Judgement is needed as the ranges of attraction cannot be precisely specified, and as strange attractors for various critical phenomena are hardly known.

The subsequent chapters are organized by means of *symmetry*. The highest symmetry is assumed in Chaps. 2 and 3 for RSEs, viz. uniformity (in a probabilistic sense which cannot easily be specified). The variable spatial distribution of internal forces (force-roughness) employed in Chaps. 4 and 5 for reversals means already a lack of symmetry. This can be captured without internal lengths by means of state cycles so that the desired uniformity of RSEs is maintained. The uniformity gets lost spontaneously at critical points, critical phenomena (shear localization, cracking, decay) come in with pattern formation or deterministic chaos. In subcritical regimes the uniformity can be regained by contractant deformations, small deformation cycles, moderate ratcheting or the trend towards a thermodynamic equilibrium.

To a certain extent the gain or loss of symmetry can be judged by means of attractors in the large, one or the other may be naturally or technically given or may be assumed for simplification. One-dimensional evolutions are considered in Chap. 11. They are rarely given in situ, but can be approached with horizontal layers by thermal activation or seismic waves. Radial symmetry may be assumed for getting estimates of near-fields. Plane-parallel evolutions without SSI (Chap. 12) may be approached in model tests, or assumed in situ for oblong fills or cuts. Conventional models can thus be partly justified and

delimited by physical arguments. This kind of symmetry is also of use for evolutions by fast or slow tectonic far-field conditions. Plane-parallel evolutions with SSI (Chap. 13) are often considered for design. This symmetry was given in a number of lab and field tests which can therefore serve for validation. Design estimates can thus be judged and improved.

Axially symmetric evolutions can more easily be attained in the lab than in situ (Chap. 14). Triaxial and torsion tests can exhibit this symmetry except for localizations and collapse. Filling, excavation, penetration, pulling-out and silo flow will also be considered with this symmetry, but it can get lost spontaneously at critical points. Less symmetric evolutions are considered in Chap. 15. These kinds of symmetry are often assumed for geotechnical design, and sometimes attained to such an extent that validations can be achieved. Some cases are indicated for which the passage of solids past soils can lead to state limit or state cycle fields. Altogether the proposed attractors in the large enable to develop objective prediction models and to delimit their range of validity.

Principal limitations by *critical phenomena* are treated in the final Chap. 16. At critical points of thermodynamic systems at or near equilibrium pattern formation or deterministic chaos can arise spontaneously. Pattern formation can also occur in soils, but requires other models as the interactions of soil particles are not conservative. Like with other systems far off equilibrium, deterministic chaos can occur with soils at critical points. These may at best be recognized with the models outlined in this book, particularly by means of critical states, but then further predictions get fuzzy or unrealistic.

Summing up, continuum approaches for soils can be objective to a certain extent with the aid of attractors. The mechanical roughness, i.e. the fluctuation of interparticle displacements and forces, may be circumvented by means of representative averages. This is no more legitimate in the overcritical range wherein fluctuations grow spontaneously with localizations. Constitutive relations can be validated by means of attractors for representative elements as far as these are justified. Initial and boundary conditions can be simplified and justified by means of attractors in the large. This gets difficult or unfeasible at the verge of stability where critical phenomena arise. All that will be outlined in detail in the following chapters.

SIMPLE PSAMMOIDS

How to catch essentials of granular soils in a simple way? Allegedly Einstein said ‘theories should be as simple as possible, but not simpler’, so what is adequately simple? One can read in the Internet that Einstein’s philosophy of science was more subtle. He wrote ‘Our experience hitherto justifies us in trusting that nature is the realization of the simplest that is mathematically conceivable’, and ‘But what remains unsatisfactory in this is always the *arbitrariness in the choice* of those elements that one designates as a priori’ (translated by Howard 2004).

Truesdell and Noll (1965) call materials *simple* if their stress tensor is a frame-indifferent functional of a suitable stretching tensor. They give algebraic representations for fluids and elastic solids, but leave aside plastic materials. Representative elements (RSEs) of a pore-free solid are considered in Sect. 2.1 for preparation in this first chapter on constitutive relations for soils. Baro-, pykno- and argotropy (i.e. dependence on pressure, density and amount of strain rate) are neglected. The only state variable is the deviatoric stress tensor. Its rate is a function of deviatoric strain rate and stress. This function is not generally linear in strain rate (otherwise it would be hypoelastic), but homogeneous of degree one if rate-independence is assumed.

Such a function can be represented by a set of equations with two switch functions in the frame of elastoplasticity (*elp*), or by a single hypoplastic equation (*hyp*). I represent both *more geometrico* by response polars, and show with these how attractors are attained. Proportional stretching leads to roughly the same state limits by *elp* and *hyp*. Cyclic deformations with big amplitudes lead to nearly the same symmetric state cycles by *elp* and *hyp*, whereas such attractors are attained with small amplitudes only by *hyp*. Ratcheting, i.e. a combination of proportional and cyclic stretching, leads to asymmetric state cycles. This works for arbitrary deformations so that frame-indifference is granted. One could check the range of validity by means of these attractors, but this is not my intention in this preparatory section on solids.

Grains of *psammoids*, i.e. sand-like materials, may be assumed to consist of such a solid. These idealized soils are neutral with respect to pore water pressures, and their granulometric properties do not change although the grains are deformed. They are barotropic and pyknotropic, but not argotropic. Their properties will be introduced *more geometrico* in Sect. 2.2 for cylindrical RSEs (now S for soil) as then only two stress and two strain components are needed. State limits are again approached by proportional strain paths, but these can be contractant or dilatant. Stationary (so-called critical) states are approached by isochoric deformations, otherwise the stress paths get proportional with increase or decrease of pressure. Only at state limits the void ratio is determined by the skeleton stress components.

Psammoid skeletons are called simple if their state is fully characterized by stress components and void ratio. This implies that the memory of path reversals is *swept out* by sufficiently big monotonous deformations (Gudehus et al. 1977). The consequences for strain cycles and ratcheting are shown *more geometrico* in Sects. 2.2 and 2.6. The thus attained state cycles as attractors imply an exaggerated anelastic response if the amplitudes between reversals are small. Test results indicate (Sect. 2.6) that additional state variables are needed for evolutions with reversals in general (Sect. 4.3), so you have to pay a price for the proposed simplicity.

There is no need to repeat textbooks on CSSM (Critical State Soil Mechanics), this kind of elp is therefore presented only *more geometrico* in Sect. 2.3. You can see without algebra how state limits look like, how they are attained and in which range they work. In CSSM they are taken as boundaries of elastic ranges which change with void ratio, and hypoelastic relations are assumed inside. Hypoplastic relations for simple psammoids are also introduced *more geometrico* (Sect. 2.4), their algebraic representations are hardly more transparent than elastoplastic ones. The approach to state limits is shown by response polars and associated paths. In that respect the differences of elp and hyp appear minor, but hyp has a wider range of application. Bigger differences arise with reversals, in particular in the approach to state cycles as attractors due to strain cycles and ratcheting.

Cylindrical RSEs were chosen for the ease of presentation, but validation tests are not easy with them. So-called triaxial tests (I can see only one axis) tend to a loss of uniformity even if the sample is not slender and the plates are smooth (Sect. 14.1). State limits cannot be approached with the desired uniformity, particularly due to shear localization (Sect. 8.2). After evaluating the literature I came to the conclusion that state limits are better captured by hyp than by elp (Sect. 2.5). The uniformity is improved by reversals if overcritical stress obliquities are avoided, but only few tests of this kind were reported (Sect. 2.6). These confirm elp only for some aspects of single reversals, and hyp only for sufficient deformations between reversals.

If cuboidal RSEs are deformed without shearing three principal stress and strain components are needed. Then state limits can be represented by cuts

through and normal to the isotropic axis in the space of stress components (Sect. 2.7). Their approach by proportional strain paths is steered by three-dimensional response polars, only projections of them can be shown. Samples can remain uniform in biaxial devices with two pairs of smooth plates and a pressurized membrane. So-called truly triaxial devices can better maintain the desired uniformity, particularly if they work with nested smooth plates, reports with them are thus apt for validation. Elp and hyp are presented *more geometrico*, major deviations among them and from reality arise again with reversals (Sect. 2.8).

Simple shearing is not that simple as four stress and two strain components are needed, and as the required uniformity can hardly be maintained in experiments. State limits with elp and hyp, represented *more geometrico* by projections with only two components, are rather similar, but only few test reports are apt for validation (Sect. 2.9). Bigger differences of elp and hyp arise again with reversals, this is particularly revealed by asymptotic state cycles (Sect. 2.10). As with cylindrical deformations anelastic effects after reversals are underpredicted by elp and overpredicted by hyp. These lacks could not be removed by hybrids of elp and hyp.

General deformations of simple psammoids would require six stress and six strain components. In addition to graphical presentations with projections you will find tensor relations in Sect. 2.11. This is to show how objectivity (Sect. 2.2) can be achieved for arbitrary boundary value problems. Attractors for monotonous, cyclic and pulsating deformations can thus be introduced, but can hardly be validated in general. This chapter is rather long, and so is its introduction. On this base the following chapters on soil behaviour are shorter (I promise you) although the matter will not get easier.

2.1 A prelude on solids

Before dealing with skeletons of solid grains the solid itself may be considered in order to introduce some concepts. We begin with *uniaxial* deformations, i.e. cases where only one stress and one strain component suffice, say σ and ε (sign convention of mechanics, i.e. pressure and shortening negative). The rates $\dot{\sigma} = d\sigma/dt$ and $\dot{\varepsilon} = d\varepsilon/dt$ could be corrected for large strains, but this is not essential here. There is no radial stress, and volume changes are assumed to be negligible. A representative solid element (RSE) is assumed to be and remain homogeneous, thus bulging or necking and shear localization or cracking are excluded. Viscous effects (i.e. rate-dependence, creep and relaxation) and fatigue are also left aside.

With these idealizing restrictions the mechanical behaviour can be represented by σ - ε -curves as shown in Fig. 2.1.1a. For monotonous stretching (A) the response is first linear, then a plastification begins, finally σ remains at a strength limit (twice cohesion c). For monotonous shortening (B) a reflected

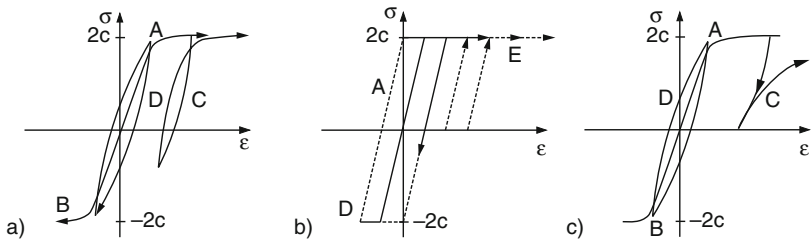


Fig. 2.1.1. Stress-strain curves of a pore-free solid (a), and of substitutes by an elastoplastic (b) and a hypoplastic relation (c)

plot is the simplest assumption. Un- and reloading with non-symmetric σ -changes leads to a stepwise increase of ε (called ratcheting, C). Cyclic deformation leads to increasing *hysteresis* for bigger amplitudes (D).

The simplest *elastoplastic* model works with a plastic strain rate $\dot{\varepsilon}^p$ via

$$\begin{aligned}
 \text{a)} \quad & \dot{\sigma} = E(\dot{\varepsilon} - \dot{\varepsilon}^p) \\
 \text{b)} \quad & \sigma^2 < 4c^2 & : & \dot{\varepsilon}^p = 0 \\
 \text{c)} \quad & \sigma^2 = 4c^2 & \& \quad \sigma \dot{\varepsilon} < 0 & : & \dot{\varepsilon}^p = 0 \\
 \text{d)} \quad & \sigma^2 = 4c^2 & \& \quad \sigma \dot{\varepsilon} > 0 & : & \dot{\varepsilon}^p = \dot{\varepsilon}
 \end{aligned} \tag{2.1.1}$$

and is represented by Fig. 2.1.1b. For a monotonous deformation starting from $\sigma = 0$ the response is linear for $|\sigma| < 2c$, and perfectly plastic for $|\sigma| = 2c$ (A, B). There is no hysteresis in case of $|\sigma| < 2c$ (C) for un- and reloading, and also for cyclic deformations. Hysteresis (D) or ratcheting (E) are only obtained if $|\sigma| = 2c$ is repeatedly reached.

The simplest *hypoplastic* model reads

$$\dot{\sigma} = E\left(\dot{\varepsilon} - \frac{\sigma}{2c} |\dot{\varepsilon}|\right) \tag{2.1.2}$$

and is represented by Fig. 2.1.1c. At the onset with $\sigma = 0$ the linear relation $\dot{\sigma} = E\dot{\varepsilon}$ is obtained by (2.1.2) as by (2.1.1). Fully plastic flow, i.e. $\dot{\sigma} = 0$ with $\sigma \dot{\varepsilon} > 0$, is obtained by (2.1.2) for $\sigma = 2c\dot{\varepsilon}/|\dot{\varepsilon}| = 2c\text{sgn}\dot{\varepsilon}$, again as by (2.1.1). For cases in between, i.e. for $0 < |\sigma| < 2c$, the slope of $\sigma - \varepsilon$ -curves changes smoothly in the range $2E \geq \dot{\sigma}/\dot{\varepsilon} \geq 0$ (A, B), whereas it is E by (2.1.1). For unloading the $\dot{\sigma}/\dot{\varepsilon}$ by (2.1.2) starts with $2E$ and reaches E for $\sigma = 0$, for reloading the response is the same as for first loading (C). This leads to exaggerated ratcheting for asymmetric σ -cycles. For cyclic deformation hysteresis is obtained which increases smoothly with increasing amplitude (D).

Both (2.1.1) and (2.1.2) relate evolutions of state and shape. The state is characterized by a single scalar variable, viz. the uniaxial stress σ . There is a

state limit, described by $|\sigma| = 2c$, for which the stress does not change with further energy input by imposed deformation, i.e. then $\dot{\sigma} = 0$ holds for $\sigma\dot{\varepsilon} > 0$. The range $|\sigma| \leq 2c$ cannot be left by deformations. The differential stiffness $\dot{\sigma}/\dot{\varepsilon}$ is determined by stress and direction of strain rate, i.e. by σ and $\text{sgn}(\sigma\dot{\varepsilon})$. In other words, $\dot{\sigma}$ is a function of σ and $\dot{\varepsilon}$, $\dot{\sigma} = f(\sigma, \dot{\varepsilon})$. Rate-independence is given by $f(\sigma, \lambda\dot{\varepsilon}) = \lambda f(\sigma, \dot{\varepsilon})$ for $\lambda > 0$. Differential non-linearity is implied as $f(\sigma, -\dot{\varepsilon}) \neq -f(\sigma, \dot{\varepsilon})$ holds in general.

Apart from these common features of (2.1.1) and (2.1.2) there are differences. The function $\dot{\sigma} = f(\sigma, \dot{\varepsilon})$ is represented by three equations and two switch functions in case of elastoplasticity, or by one hypoplastic equation without switch function. $\dot{\sigma}/\dot{\varepsilon}$ is the same in both cases for $\sigma = 0$, and for $|\sigma| = 2c$ with $\sigma\dot{\varepsilon} > 0$. For the range in between, $0 < |\sigma| < 2c$, elastic behaviour is obtained with (2.1.1), whereas (2.1.2) always yields anelastic effects. Hysteretic $\sigma - \varepsilon$ -cycles and ratcheting with asymmetric stress cycles are obtained with cycles by (2.1.1) only if $|\sigma| = 2c$ is repeatedly reached, and always by (2.1.2). A further difference appears for unloading from a state limit, i.e. for $\sigma\dot{\varepsilon} < 0$ with $|\sigma| = 2c$: (2.1.1) yields $\dot{\sigma}/\dot{\varepsilon} = E$, and (2.1.2) $\dot{\sigma}/\dot{\varepsilon} = 2E$.

The simplest *multiaxial* cases require two stress and two strain components. Deformations of cuboidal RSEs without rotation of principal axes belong to this group if only deviators are considered. Two of the three deviatoric stress components

$$\sigma_i^* = \sigma_i + p \quad (i = 1, 2, 3) \quad (2.1.3)$$

suffice as the mean pressure

$$p = -\frac{1}{3}(\sigma_1 + \sigma_2 + \sigma_3) \quad (2.1.4)$$

is assumed to have no influence, and two of the three deviatoric strain rate components

$$\dot{\varepsilon}_i^* = \dot{\varepsilon}_i - \frac{1}{3}\dot{\varepsilon}_v \quad (i = 1, 2, 3) \quad (2.1.5)$$

suffice if the rate of volume change

$$\dot{\varepsilon}_v = \dot{\varepsilon}_1 + \dot{\varepsilon}_2 + \dot{\varepsilon}_3 \quad (2.1.6)$$

is zero. Thus the asterisk may be dropped for strains, $\varepsilon_i^* = \varepsilon_i$. Their rates should be referred to the actual length for large deformations. Related evolutions of state and shape can be represented by associated stress and strain *paths*

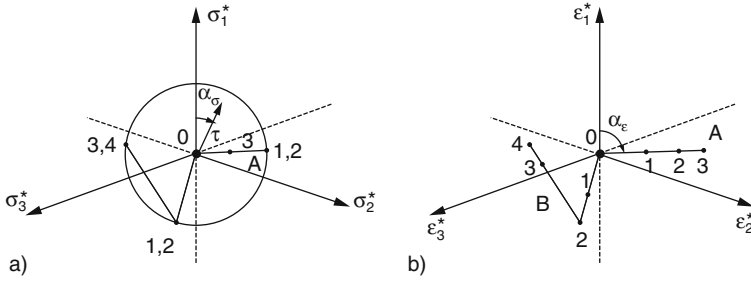


Fig. 2.1.2. Deviatoric stress paths (a) and related strain paths (b) of a pore-free solid

in deviator planes, Fig. 2.1.2, with Lode’s stress direction angle α_σ . Stress paths (a) cannot leave a certain range, its boundary represents state limits. In case of isotropy a change of principal components does not matter, with this symmetry one 60° -sector suffices. Thus two deviatoric stress invariants, viz. the mean shear stress

$$\bar{\tau} = \frac{2}{3} \sqrt{\sigma_1^{*2} + \sigma_2^{*2} + \sigma_3^{*2}} \quad (2.1.7)$$

and the Lode parameter

$$\cos 3\alpha_\sigma = \sqrt{\frac{2}{3}} \sqrt[3]{\sigma_1^{*3} + \sigma_2^{*3} + \sigma_3^{*3}} / \bar{\tau} \quad (2.1.8)$$

suffice as state variables, p by (2.1.4) is not needed. As plotted in Fig. 2.1.2a, state limits are assumed to be independent of $\cos 3\alpha_\sigma$ for simplicity.

Strain paths (Fig. 2.1.2b) are only restricted by $\dot{\epsilon}_v = 0$. Deviatoric strain invariants are not needed as they are no state variables. The amount of strain rate

$$D = \sqrt{\dot{\epsilon}_1^2 + \dot{\epsilon}_2^2 + \dot{\epsilon}_3^2} \quad (2.1.9)$$

and the strain rate direction angle α_ϵ suffice for the kinematics.

A proportional strain path (e.g. A) can be described by its direction α_ϵ and by numbers for the sequence (e.g. 1–3). The related stress path is likewise labelled. It may be straight up to a state limit, and remains there (which means *ductility*) with further proportional deformation. *Reversals* can be represented by further numbers at the considered lines (e.g. 2–3). It can happen that the related stress path also remains on the previous straight line (e.g. 2–3 in Fig. 2.1.2a). This may also work with a second reversal and with further ones.

Only then, i.e. with fixed α_σ and α_ε , stress-strain curves convey the same information as related stress and strain paths. For instance, Fig. 2.1.1 implies $\alpha_\sigma = \alpha_\varepsilon = 0$ and 180° .

For paths with sideward bends (e.g. B in Fig. 2.1.2) representations by stress-strain diagrams are insufficient and can be misleading. A strain path e.g. may consist of two straight sections making an acute angle. The stress path looks similar, but some steps in it may be confounded if they lie at a state limit. *Response polars* serve for graphical representation of stress-strain relations (Fig. 2.1.3). They represent stress rates related with strain rates of different directions α_ε (a) and unit amount, i.e. $D = 1$. The responses are polar diagrams of stress rates with directions α_σ and labels for the related α_ε (e.g. a, b...). They can be drawn in the stress plane (b). A polar should not have jumps or loops as for one strain rate there should be only one stress rate response. It should also be convex in order to secure physical and numerical robustness with respect to small changes of α_ε .

The simplest *elastoplastic relation* (abbreviated: elp) for cuboidal deformations can be written

$$\begin{aligned}
 \text{a)} \quad \dot{\sigma}_i^* &= 2G\dot{\varepsilon}_i^e = 2G(\dot{\varepsilon}_i - \dot{\varepsilon}_i^p) \\
 \text{b)} \quad f &= \Sigma \sigma_i^{*2} - \frac{4}{9}c^2 < 0 & : \quad \dot{\varepsilon}_i^p &= 0 \\
 \text{c)} \quad f &= 0 & \& \quad \sigma_i^* \dot{\varepsilon}_i < 0 & : \quad \dot{\varepsilon}_i^p &= 0 \\
 \text{d)} \quad f &= 0 & \& \quad \sigma_i^* \dot{\varepsilon}_i > 0 & : \quad \dot{\varepsilon}_1^p / \dot{\varepsilon}_2^p &= \sigma_1^* / \sigma_2^*
 \end{aligned}
 \tag{2.1.10}$$

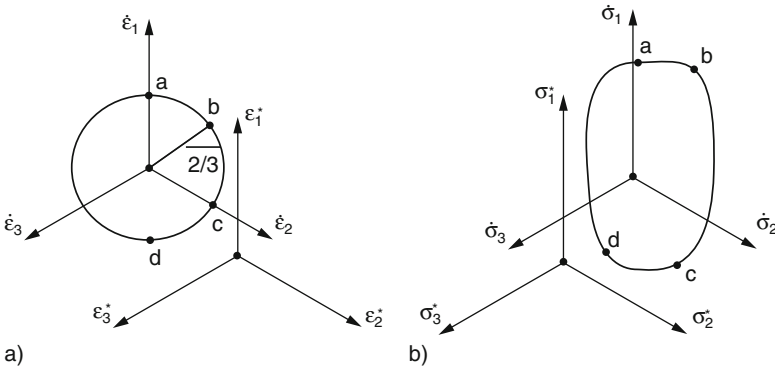


Fig. 2.1.3. Deviatoric stress response polar (b) for unit strain rates with different directions (a)

with $i = 1, 2, 3$ and the summation convention, e.g. $\sigma_i \dot{\epsilon}_i = \sigma_1 \dot{\epsilon}_1 + \sigma_2 \dot{\epsilon}_2 + \sigma_3 \dot{\epsilon}_3$. $E = 2G$ holds due to incompressibility. The strain rate is thus decomposed into elastic and plastic parts (a), the latter disappear in the elastic range (b). If the flow condition $f = 0$ holds and work is extracted (unloading) the response is again elastic (c). Plastic strains appear only for $f = 0$ if work is introduced (d). Their direction is given by the gradient of f (associated flow rule), here the directions of plastic strain rate and stress agree.

Figure 2.1.4a shows deviatoric stress paths by elp due to a proportional strain path (b). It suffices to consider one strain rate direction α_ϵ and two initial stress states, viz. A inside of and B at the boundary. The response polars by (2.1.10) are circles inside of and semicircles at the boundary. For B the stress path moves along the boundary until $\alpha_\sigma = \alpha_\epsilon$ is attained. With a longer transition case A leads to the same state limit, this is thus a driven attractor which depends only on α_ϵ . The transitions are steered by the response polars, thus a kind of fixed point theorem works *more geometrico*.

Figure 2.1.5a shows stress paths by elp due to strain cycles (b) with initial states A and B as before. A strain cycle with a small amplitude (I) leads to a stress cycle with the same shape, but different centres which are shifted differently. A big strain cycle (II) leads repeatedly to state limits, and to a unique stress cycle of another shape after different shifts for A and B. This *state cycle* is another driven attractor. With elp it arises only by sufficient amplitudes so that state limits are repeatedly attained. Imagine the response polars of Fig. 2.1.4 to see how this attractor works. According to shape and size of strain cycles the attained state cycles have different shapes. They are confined by state limits and only with them symmetric in the deviator plane.

Figure 2.1.6a shows stress paths by elp due to strain-controlled *ratcheting*, i.e. superposition of cyclic and proportional straining (b) with initial states as before. State limits are repeatedly attained in the direction of average straining. The state cycles are asymmetric therefore, and are attractors as

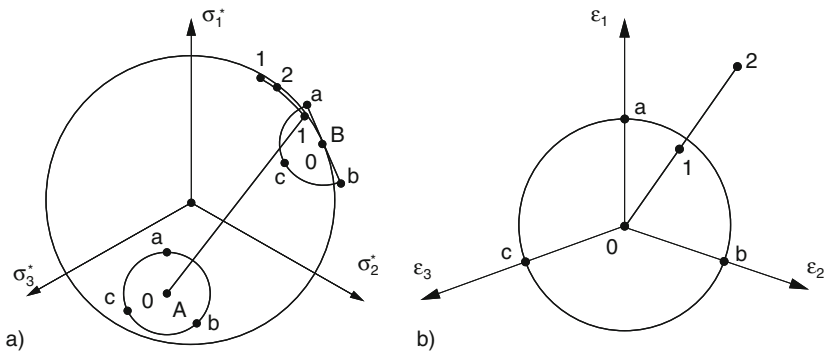


Fig. 2.1.4. Stress paths and response polars (a) by the elastoplastic relation (2.1.10) for proportional straining (b)

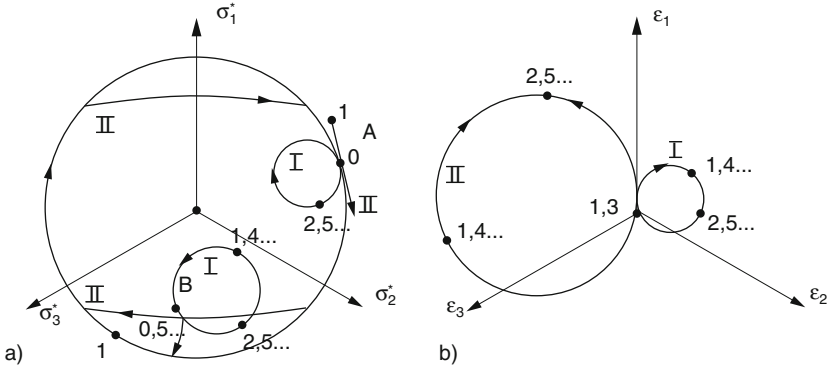


Fig. 2.1.5. Stress paths (a) by (2.1.10) for cyclic straining (b)

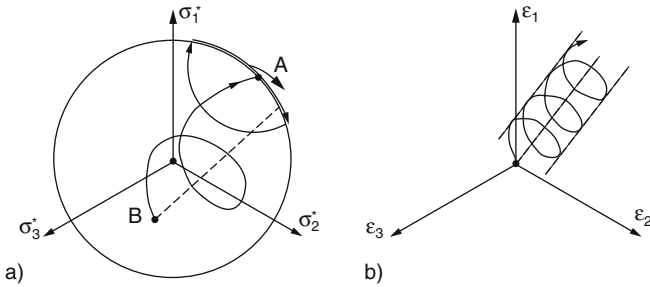


Fig. 2.1.6. Stress paths (a) by the elastoplastic relation (2.1.10) for forced ratcheting (b)

they are independent of the initial state. They have the same orientation as the average strain path, their shape depends on shape and size of the superimposed strain cycles. Imagine response polars to see that and how such state cycles are attained.

The simplest *hypoplastic relation* (abbreviated: hyp) for cuboidal deformations can be written

$$\dot{\sigma}_i^* = 2G(\dot{\epsilon}_i - \sqrt{\frac{9}{5}} \frac{\sigma_i^*}{2c} D) \quad (2.1.11)$$

with $i = 1, 2, 3$ and D by (2.1.9). It is strikingly simpler than (2.1.10). The transition to state limits by hyp is shown by stress paths in Fig. 2.1.7a for straight strain paths (b). The response polars are circles with radius $2G$. They are centric for $\sigma_i^* = 0$, touch the stress boundary for σ_i^* , and are eccentric between these bounds. For a strain path with the same direction as the initial stress, $\alpha_{\dot{\epsilon}} = \alpha_{\sigma}$, the stress path is straight and remains at a state limit (A).

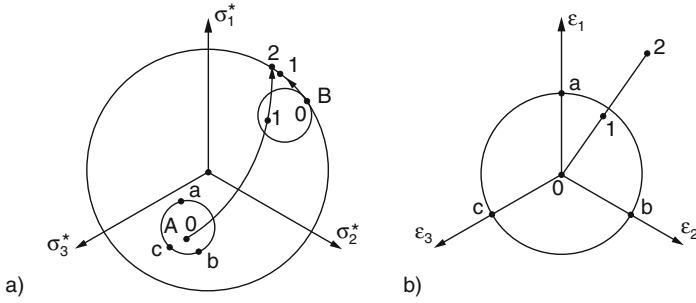


Fig. 2.1.7. Stress paths and response polars (a) by the hypoplastic relation (2.1.11) for proportional straining (b)

Otherwise the stress path is curved up to the limit (B). These attractors are thus the same as by elp, but transitions to them are smooth. Response polars reveal how transitions take place.

The asymptotic response to strain cycles with hyp is shown in Fig. 2.1.8 by associated stress (a) and strain paths (b). Imagine again response polars to understand transitions. Small centric stress cycles and associated strain cycles are similar (A). Other than with elp the attained cycles are always symmetric, transitions need more reversals for smaller amplitudes and wider distances of onset and asymptote. Asymptotic stress cycles due to bigger strain cycles are shaped by the stress boundary (B).

Non-symmetric stress cycles are attained by ratcheting (b) with small amplitude (I) so that the stress bound is never reached (Fig. 2.1.9a). State limits are repeatedly reached by ratcheting with big amplitude (II), thus stress cycles are shaped. The asymptotic response does not depend on the initial state (A or B as before), so the attained state cycles are attractors. This could be shown by means of the response polars of Fig. 2.1.7, whereas an algebraic proof would be hard with the non-linearity of (2.1.11).

Shearing requires in-plane and out-of-plane stress and strain components in general, Fig. 2.1.10a. Constitutive relations can be represented by associated stress paths (b) and strain paths (c). Similarly as shown above for

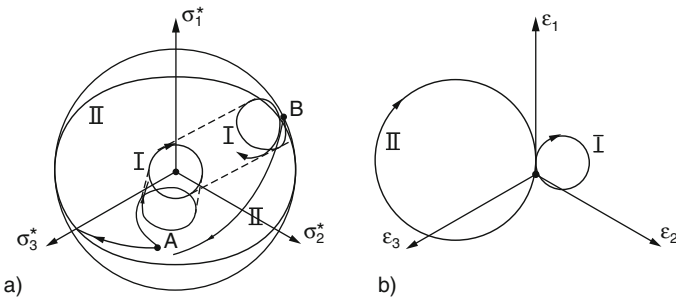


Fig. 2.1.8. Stress paths (a) by (2.1.11) for cyclic straining (b)

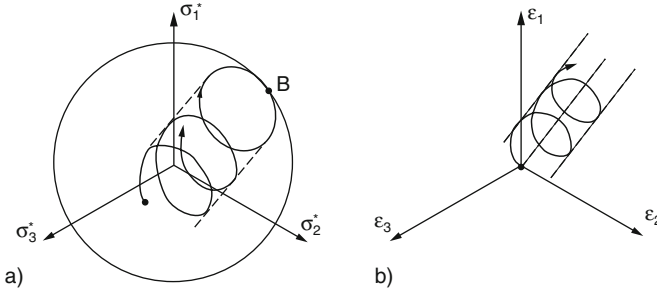


Fig. 2.1.9. Stress paths (a) by the hypoplastic relation (2.1.11) for ratcheting (b)

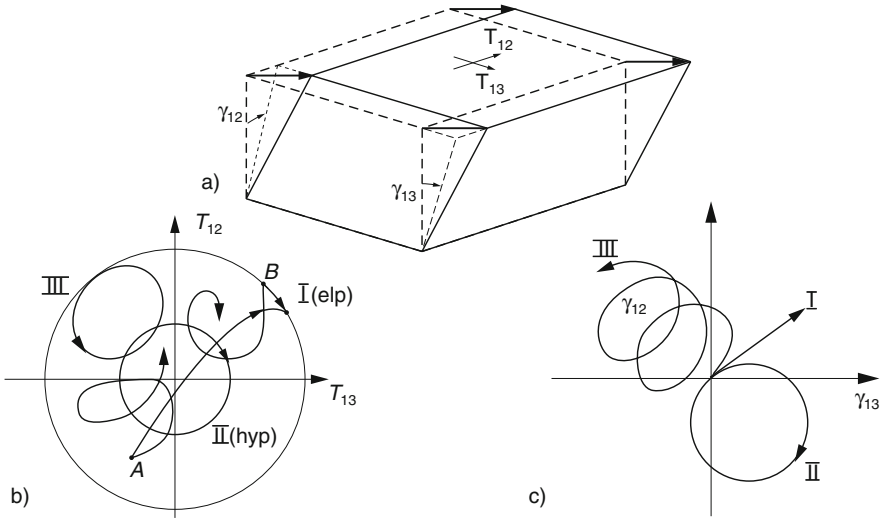


Fig. 2.1.10. Components for shearing (a), stress paths towards attractors (b) and related shearing paths (c)

cuboidal deformations driven attractors arise for proportional shear paths (I), cyclic shearing (II) and ratcheting (III). Differences of elp and hyp arise again in transitions, with small strain cycles and for ratcheting with small amplitudes. Approaches are only indicated *more geometrico* as algebraic representations will not be needed in the sequel.

One-dimensional stretching or shearing are implied as special cases where strain paths lie on a straight line. The stress paths tend to parallel lines. Only thereafter scalars suffice for strength and stiffness, otherwise these notions can be misleading. Only then ductility and hysteresis can be precisely defined as with Fig. 2.1.1. As shown e.g. in Fig. 2.1.10, shear ratcheting leads to a pulsating resistance in the direction of mean shearing which can scarcely be the one for monotonous shearing.

The outlined relations can be extended for arbitrary deformations. At state limits the deviatoric stress tensor \mathbf{T}^* is a function of the stretching tensor \mathbf{D}

only (with $\text{tr}\mathbf{D} = 0$). This function is isotropic due to frame-indifference, therefore \mathbf{T}^* and \mathbf{D} are coaxial and the function can be fully represented in the deviator plane. The objective stress rate $\overset{\circ}{\mathbf{T}}^*$ (Sect. 1.2) is related with \mathbf{D} and \mathbf{T}^* , this can be written as

$$\overset{\circ}{\mathbf{T}}^* = \mathbf{F}(\mathbf{T}^*, \mathbf{D}) \quad (2.1.12)$$

with an isotropic tensor function \mathbf{F} of \mathbf{T}^* and \mathbf{D} . Rate-independence requires $\mathbf{F}(\mathbf{T}^*, \lambda\mathbf{D}) = \lambda\mathbf{F}(\mathbf{T}^*, \mathbf{D})$ for any $\lambda > 0$. Irreversibility requires $\mathbf{F}(\mathbf{T}^*, -\mathbf{D}) \neq -\mathbf{F}(\mathbf{T}^*, \mathbf{D})$ in general, otherwise the response would be hypoelastic. State limits should be obtained as asymptotic solutions of (2.1.12) for $\mathbf{D} = \text{const}$. Algebraic representations of \mathbf{F} have to satisfy these requirements and to reproduce the relations for cuboidal deformations. This can be achieved by

$$\mathbf{F} = 2G(\mathbf{D} - \mathbf{D}^a) \quad (2.1.13)$$

with an anelastic stretching \mathbf{D}^a . For elp \mathbf{D}^a is linear in \mathbf{D} for sectors separated by two switch functions, for hyp \mathbf{D}^a is proportional to \mathbf{T}^* and to $D = \sqrt{\text{tr}\mathbf{D}^2}$, and thus nonlinear in \mathbf{D} .

The *range of validity* may only be touched by means of physical arguments as this section is a preparation for simple psammoids. Rate-independence is empirically justified for hard solids although any anelastic behaviour is at least slightly rate-dependent (Sect. 3.1). Incompressibility and pressure-independence are sufficiently given for mineral grains (Sect. 2.2), but cannot hold in general (Sect. 8.1). Anisotropy of grain materials may be neglected as it will scarcely influence grain skeletons. Ductility is certainly not given in general (Sect. 8.1), but implied by assuming granular permanence for psammoids (Sect. 2.2). Heating by rapid deformations is left aside (Sect. 3.1), and fatigue by reversals may be neglected as long as no pores or cracks arise (Sect. 8.1). The asymptotic response to strain cycles or ratcheting reveals substantial differences of elp and hyp, this will be further treated in Sect. 4.1.

To *sum up*, idealized solid elements serve to represent simple elastoplastic and hypoplastic relations. Semicircular and excentric circular response polars, respectively, lead to state limits for proportional deformations, and to state cycles for cyclic deformations and ratcheting. Neglecting pressure and density changes, and also rate-dependence and fatigue, this is a preparation for simple psammoids to be introduced in the sequel.

2.2 An introduction of simple psammoids

Consider a statistically homogeneous skeleton of solid grains as a representative soil element (RSE). It is called a *simple psammoid* ($\psi\acute{\alpha}\mu\mu\omicron\varsigma = \text{sand}$,

$\acute{o}\acute{\iota}\delta\acute{o}\varsigma = \text{similar}$) if its state is sufficiently represented by stress and density, and if the granular properties are permanent. Adhesion and cementation of grains are excluded. In the simplest case of cylindrical symmetry two principal components suffice, e.g. σ_{s1} and $\sigma_{s2} = \sigma_{s3}$ with subscript s for skeleton and the sign convention of soil mechanics, i.e. pressure positive. σ_{s1} and σ_{s2} may be imagined as grain contact force densities in axial and radial directions. These spatial averages represent internal forces in the simplest manner. Such a grain skeleton can only exist with pressure, i.e. $\sigma_{s1} > 0$ and $\sigma_{s2} > 0$. Other than for solids, the *mean skeleton pressure*

$$p_s = (\sigma_{s1} + 2\sigma_{s2})/3 \quad (2.2.1)$$

is evidently important: the bigger p_s , the stiffer and stronger the skeleton. This property is called *barotropy* ($\beta\alpha\rho\acute{\upsilon}\varsigma = \text{heavy}$, $\tau\rho\acute{o}\pi\acute{o}\varsigma = \text{kind}$).

Anisotropic stress states can be represented by points in a plane σ_{s1} vs. $\sqrt{2}\sigma_{s2}$, Fig. 2.2.1. Deviations from isotropic states with $\sigma_{s1} = \sigma_{s2}$ can be described by the deviator

$$\sigma_s^* = \frac{2}{3}(\sigma_{s1} - \sigma_{s2}) = \sigma_{s1}^* = -\sigma_{s2}^* \quad (2.2.2)$$

or by the *stress obliquity*

$$\tan \psi_s = \tan(\sigma_s^*/p_s) \quad . \quad (2.2.3)$$

This notion is taken over from Roscoe (1970) and will be substituted by an invariant in Sects. 2.7 and 2.11. In many papers p' is written for p_s , q for $(\sigma_1 - \sigma_2)$ and η for $(\sigma_1 - \sigma_2)/p'$. As far as these symbols were used in experimental reports they will be taken over in the sequel. Our notations are more appropriate for extensions later in this chapter. As traction is excluded, i.e. with $\sigma_{si} \geq 0$, ψ_s is bounded by

$$-1/\sqrt{2} \leq \tan \psi_s \leq \sqrt{2} \quad . \quad (2.2.4)$$

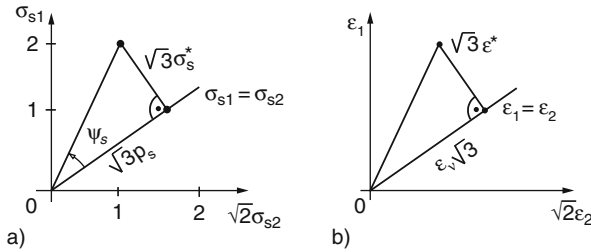


Fig. 2.2.1. Stress (a) and strain components (b) of a cylindrical grain skeleton

A water-saturated skeleton has an absolute pore water pressure p_w , this is often substituted by $u = p_w - p_a$ with the atmospheric pressure p_a . The total pressure components can be expressed by

$$p_1 = \sigma_{s1} + p_w \quad , \quad p_2 = \sigma_{s2} + p_w \quad , \quad (2.2.5)$$

or more conventionally by

$$\sigma_1 = \sigma'_1 + u \quad , \quad \sigma_2 = \sigma'_2 + u \quad , \quad (2.2.6)$$

wherein p_a is tacitly subtracted from σ_1 and σ_2 . The so-called *effective stress* σ' is thus identified as skeleton stress σ_s . Equation (2.2.5) states that a change of p_w in a fixed skeleton changes the total pressure components by the same amount. Imagine a skeleton kept under stress by filter plates to understand that the mean pressure of the grains changes by the same amount as p_w . Equation (2.2.5) holds true also if gas bubbles are trapped between the grains. For skeletons with gas channels or pockets other decompositions than (2.2.5) are needed (Sect. 6.2). Dry skeletons are included with $p_w = 0$ or $u = 0$.

As in Sect. 2.1 the solid grain material is assumed to be neutral with respect to its mean pressure and to have a constant density, so only deviators are relevant for the grain behaviour. Combined with (2.2.5), the skeleton is therefore neutral with respect to p_w . This is the so-called *principle of effective stress*. When proposing (2.2.6) Terzaghi (1936) used already the argument of neutrality of the grain solid.

As the grain volume is assumed to be constant the density of the skeleton can be substituted by the *void ratio* e , i.e. the ratio of void volume and solid volume. e can range within upper and lower p_s -dependent bounds. The *pyknotomy* ($\pi\nu\kappa\nu\acute{o}\varsigma = \text{dense}$), i.e. density-dependence of the skeleton is related with its barotropy, but uniquely only in cases which will be explained further below.

Deformations of our cylindrical RSE can be expressed by strain components ε_1 and $\varepsilon_2 = \varepsilon_3$ (positive for shortening by soil mechanics convention). Height h and diameter d of the RSE can change with time t . With $h = h_0$ and $d = d_0$ for $t = t_0$ the change of shape can be described by

$$\varepsilon_1 = \ln(h_0/h) \quad , \quad \varepsilon_2 = \ln(d_0/d) \quad . \quad (2.2.7)$$

These logarithmic strains work also for large amounts, for small ones they imply the simpler definition $\varepsilon = \Delta l/l$. The *strain rates*

$$\dot{\varepsilon}_1 = \frac{d\varepsilon_1}{dt} = -\frac{\dot{h}}{h} \quad , \quad \dot{\varepsilon}_2 = \frac{d\varepsilon_2}{dt} = -\frac{\dot{d}}{d} \quad (2.2.8)$$

are independent of the arbitrary reference size. A skeleton of grains has no preferred configuration as one of bones with joints, therefore its deformation is not a state variable. Spatial fluctuations of relative grain displacements are not captured by strain rates.

The *volumetric strain* and its rate are given by (densification positive)

$$\varepsilon_v = \ln(h_0 d_0^2 / h d)^2 \quad , \quad \dot{\varepsilon}_v = \dot{\varepsilon}_1 + 2\dot{\varepsilon}_2 \quad . \quad (2.2.9)$$

Due to the assumed constant grain density ε_v is related with e by

$$\dot{e} = -(1 + e)\dot{\varepsilon}_v \quad . \quad (2.2.10)$$

Deviations from isotropic deformations with $\dot{\varepsilon}_1 = \dot{\varepsilon}_2$ can be described by the deviatoric strain rate

$$\varepsilon^* = \frac{2}{3}(\dot{\varepsilon}_1 - \dot{\varepsilon}_2) = \dot{\varepsilon}_1^* = -\dot{\varepsilon}_2^* \quad , \quad (2.2.11)$$

or by the *strain rate obliquity*

$$\psi_{\dot{\varepsilon}} = \arctan(3\varepsilon^* / \dot{\varepsilon}_v) \quad , \quad (2.2.12)$$

this is shown in Fig. 2.2.1b.

Strain rates are assumed to be related with stress rates, this may be written as

$$\dot{\sigma}_{si} = f_i(\sigma_{si}, e, \dot{\varepsilon}_i) \quad (2.2.13)$$

with $i = 1$ and 2 for cylindrical symmetry. For simple psammoids the functions f_i are assumed to have the properties

$$\begin{aligned} \text{a)} \quad & f_i(\lambda\sigma_{si}) = \lambda^m f_i(\sigma_{si}) \quad , \quad \lambda > 0, \quad 1 \geq m > 0 \\ \text{b)} \quad & f_i(\lambda\dot{\varepsilon}_i) = \lambda f_i(\dot{\varepsilon}_i) \quad , \quad \lambda > 0 \\ \text{c)} \quad & f_i(-\dot{\varepsilon}_i) \neq -f_i(\dot{\varepsilon}_i) \quad . \end{aligned} \quad (2.2.14)$$

(a) reflects barotropy: due to increasing contact flats the skeleton is stiffer with higher p_s , (b) means rate-independence, which seems to be justified if the grain material is also rate-independent (otherwise cf. Sects. 4.2 and 4.6). Non-linearity in $\dot{\varepsilon}_i$ (c) means that the skeleton is not hypoelastic, otherwise $f_i(-\dot{\varepsilon}_i) = -f_i(\dot{\varepsilon}_i)$ would hold. Pyknotropy means that f_i depends also on e .

Algebraic representations of f_i should reflect mechanical properties. Before specifying the latter some selection criteria for the choice of representations may be listed:

S1: the explanation should be fully tractable,

S2: the representation should be objective and work for arbitrary deformations,

S3: a computer code of it should be freely available via Internet,

S4: the set of parameters should be robustly determinable and should cover the intended range of states and deformations.

As representations tend to be intricate S1 is not always a matter of course. Without S2 they could not be used in arbitrary boundary value problems. A user could hardly check the range of applicability without S3. S4 is needed for safety and economy, and is also reasonable as far as collective grain properties are permanent.

The most important properties are exhibited at *state limits*, which may be assumed as shown in Fig. 2.2.2. For them the stress and strain rate obliquities, expressed by ψ_s and $\psi_{\dot{\varepsilon}}$ via (2.2.3) and (2.2.12), are uniquely related (a). $\psi_s = \psi_{\dot{\varepsilon}} = 0$ holds in the isotropic case (i). *Critical states* are stationary for isochoric (constant volume) proportional deformations. This means $\dot{\varepsilon}_1 = -2\dot{\varepsilon}_2$ by (2.2.9) and (2.2.10), or $\psi_{\dot{\varepsilon}} = \pm 90^\circ$ instead (c and $-c$). For them the stress condition

$$(\sigma_{s1} - \sigma_{s2})^2 / (\sigma_{s1} + \sigma_{s2})^2 = \sin^2 \varphi_c \quad (2.2.15)$$

is postulated with a constant *critical friction angle* φ_c independently of p_s , e and sign of $\dot{\varepsilon}_1$. Contractant state limits between i and $\pm c$ have $|\psi_{\dot{\varepsilon}}| < 90^\circ$ and $\dot{p}_s > 0$. Cracking may be imagined for lower e -bounds (d and $-d$) with ψ_s -bounds by (2.3.4). $\psi_{\dot{\varepsilon}}$ is bounded by

$$-1 - 1/\sqrt{2} \leq \tan \psi_{\dot{\varepsilon}} \leq 1 + \sqrt{2} \quad . \quad (2.2.16)$$

Two critical stress obliquities $\tan \psi_{sc}$ are determined by (2.2.15). Stress states with $|\tan \psi_s| < |\tan \psi_{sc}|$ are called *subcritical*, those with $>$ *overcritical*. As the skeleton requires $\sigma_{si} > 0$ states with cracking are outside the allowed range, but they represent reasonable bounds. Dilatant state limits are close to *peak states* for which ε^* changes monotonously with constant σ_{s1} and σ_{s2} ,

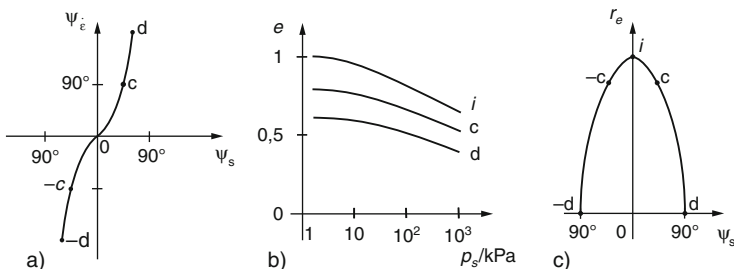


Fig. 2.2.2. State limits of simple psammoid cylinders: (a) obliquities, (b) limit void ratios vs. pressure, (c) relative void ratio vs. stress obliquity

and the amount of stress obliquity is maximal vs. strain. For them a peak friction angle φ_p can be defined by

$$(\sigma_{s1} - \sigma_{s2})_p^2 / (\sigma_{s1} + \sigma_{s2})_p^2 = \sin^2 \varphi_p \quad , \quad (2.2.17)$$

this dependent state variable is sometimes of use. Shear localization is left aside (Sects. 8.2 and 14.1).

Limit void ratios depend on p_s and ψ_s . They are lower with bigger p_s and with bigger $|\psi_s|$, Fig. 2.2.2b, as the grain contact flats get wider with bigger contact forces and with increasing deviations of them from the contact normals. p_s can be scaled by a granulate hardness h_s (Sect. 2.4). A logarithmic p_s – scale is chosen to cover the p_s – range from almost 0 to an upper bound due to grain crushing. For each p_s the upper e – bound is e_i for $\psi_s = 0$, the lower bound is e_d for ψ_s at one of the bounds by (2.2.4). The *critical void ratio* e_c for ψ_s by (2.2.15) and (2.2.3) is about halfway between e_i and e_d . As the e vs. $\log p_s$ curves are similar for different ψ_s the *relative void ratio*

$$r_e = (e - e_d) / (e_c - e_d) \quad (2.2.18)$$

with e_c and e_d for a given p_s is of use. r_e depends on ψ_s for state limits as plotted in Fig. 2.2.2c. As a consequence the peak friction angle φ_p by (2.2.17) depends on r_e and is nearly the same for axial shortening and extension with a given r_e .

State limits should not be mixed up with the so-called *failure* of initially cylindrical samples. This is usually defined by the maximum of an average deviator $|\sigma^*|$ ('peak') which is attained by axial shortening or extension with constant average confining pressure $\bar{\sigma}_{s2}$ ('drained') or constant average void ratio \bar{e} ('undrained') of saturated granular samples, Fig. 2.2.3. With $\bar{\sigma}_{s2} = \text{const}$ peaks in $\bar{\sigma}_s^*$ vs. \bar{e}^* plots (a) are higher with dense than with loose samples. Peak average stress circles lead to p_s - and e -dependent friction angles φ_p (b). Samples get non-uniform in many devices before a peak, and always beyond it (Sect. 14.1). φ_p depends on the average relative void ratio \bar{r}_e , this changes differently near a peak (c). With $\bar{e} = \text{const}$ peaks in $\bar{\sigma}^*$ vs. \bar{e}^* plots are enhanced by bulging or necking, more so with loose samples (d). Peak skeleton stress circles suggest different friction angles (e) instead of a single φ_c . \bar{r}_e attains different values at peak (f). Failure means the inability to meet requirements and may be used for structures at or in the ground (Chaps. 13 and 15), but this notion is not apt to characterize granular matter.

State limits can be approached with suitable deformations independently of the initial state. This can be shown graphically by means of *response polars* (Gudehus 1979), Fig. 2.2.4. These are polar diagrams of stress rates (a) for unit strain rates with different $\psi_{\dot{\epsilon}}$ (c). For the latter the magnitude of strain rate

$$D = \sqrt{\dot{\epsilon}_1^2 + 2\dot{\epsilon}_2^2} \quad (2.2.19)$$

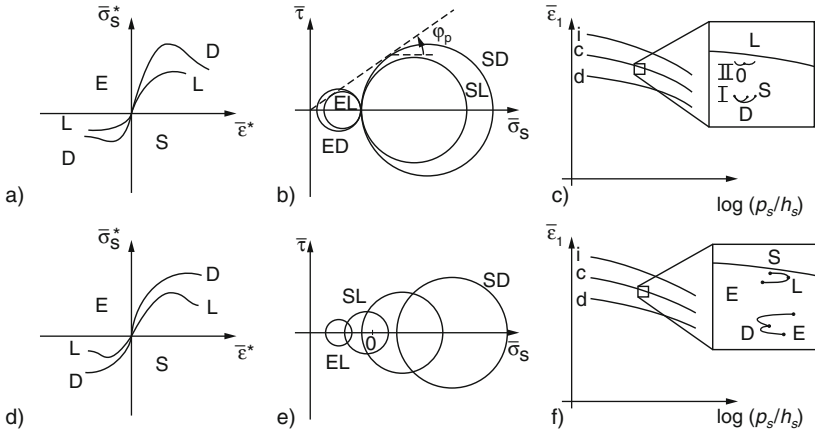


Fig. 2.2.3. Conventional ‘triaxial’ tests with axial shortening (S) or extension (E) of dense (D) or loose (L) saturated granular samples. Deviatoric stress-strain curves (a, d), peak stress circles (b, e) and plots of void ratio vs. pressure (c, f) with (*above*) and without drainage (*below*). All quantities are spatial averages of increasingly non-uniform samples, the plots are qualitative

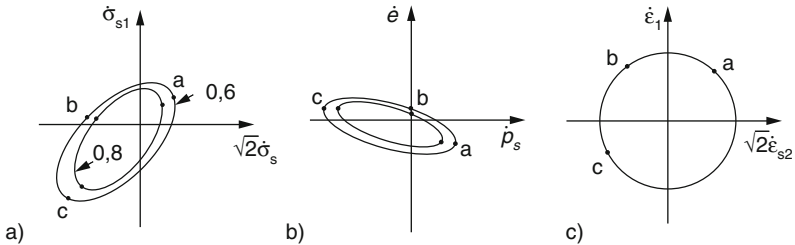


Fig. 2.2.4. Response polars of stress components (a) and void ratio vs. pressure (b) for unit strain rates (c). Labels a, b, c for directions of strain rate, numbers (e.g. 0.6 and 0.8) for relative void ratio, given stress components (qualitative)

is $D = 1$ so that $\psi_{\bar{\epsilon}}$ -labels suffice for a set of polars. Different $\dot{\sigma}_{si}$ -polars with labels for r_e exhibit pyknotropy; $\dot{\epsilon}$ by (2.2.10) and \dot{p}_s could be depicted by a further polar (b), but this is rarely needed. For representing a continuous and unique response the polars have to enclose the origin, and they should be convex and continuous. Barotropy and pyknotropy require bigger polars for higher p_s and lower e , respectively. The shape of $\dot{\sigma}_{si}$ -polars depends on ψ_s as the spatial distribution of grain contact forces depends on the skeleton stress components.

The approach to state limits can be shown by suitable associated strain and stress *paths* with the aid of response polars, Fig. 2.2.5. Straight strain paths (a) are chosen with constant $\psi_{\bar{\epsilon}}$ in the range by (2.2.16). A contractant

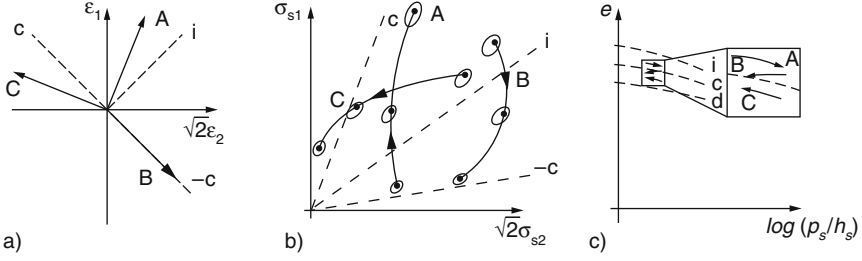


Fig. 2.2.5. Proportional strain paths (a) are related with stress paths (b) and void ratio vs. pressure paths (c) which lead to state limits (qualitative)

state limit between i and c or $-c$ as by Fig. 2.2.2 is approached with increasing p_s and constant r_e and ψ_s for the given ψ_ϵ (A). An isochoric (i.e. volume-conserving) path leads to a critical state with ψ_s by (2.2.15), $r_e = 1$ and p_s by Fig. 2.2.2b, and the state should not change afterwards. In the transition p_s decreases for initial $r_e > \text{ca. } 0.5$ (B), otherwise p_s increases. A dilatant state limit is approached with decreasing p_s , it has an overcritical $|\psi_s|$ and a lower than critical r_e by Fig. 2.2.2 between $\pm c$ and $\pm d$ (C).

An algebraic representation of f_i in (2.2.13) should reproduce state limits as *attractors*, i.e. asymptotic solutions independently of the start, for strain paths with constant ψ_ϵ in the range by (2.2.16). This is exhibited by response polars. The plot of e vs. $\log(p_s/h_s)$ (Fig. 2.2.2c) reveals that state limits cannot be approached with arbitrary initial relative void ratios r_e . Contractant and isochoric deformations can lead to grain crushing if they start with a too low e . Dilatant deformations with a too high e initially can lead to a decay of the skeleton before a state limit is reached. Isochoric deformations can lead to a decay if e exceeds the e_c for $p_s \rightarrow 0$.

Further well-known properties should be reproduced for certain *monotonous* strain paths, i.e. with constant sign of the deviatoric strain rate $\dot{\epsilon}^*$, viz. (Fig. 2.2.6)

- M1: isochoric (i.e. constant e) deformations with $r_e > 1$ initially lead to a critical state via a peak of $|\sigma_s^*|$,
- M2: isobaric (i.e. constant p_s) deformations with $r_e < 1$ initially lead to a critical state via a peak of $|\sigma_s^*|$,
- M3: for isobaric deformations the directions of stress and strain rate are nearly proportional to each other.

The response at the onset in such cases is less important as initial states in experiments are rather arbitrary, whereas the named properties count for the vicinity of state limits. M1 was observed with undrained saturated samples if they were looser than critical at the onset. M2 was observed with dry or

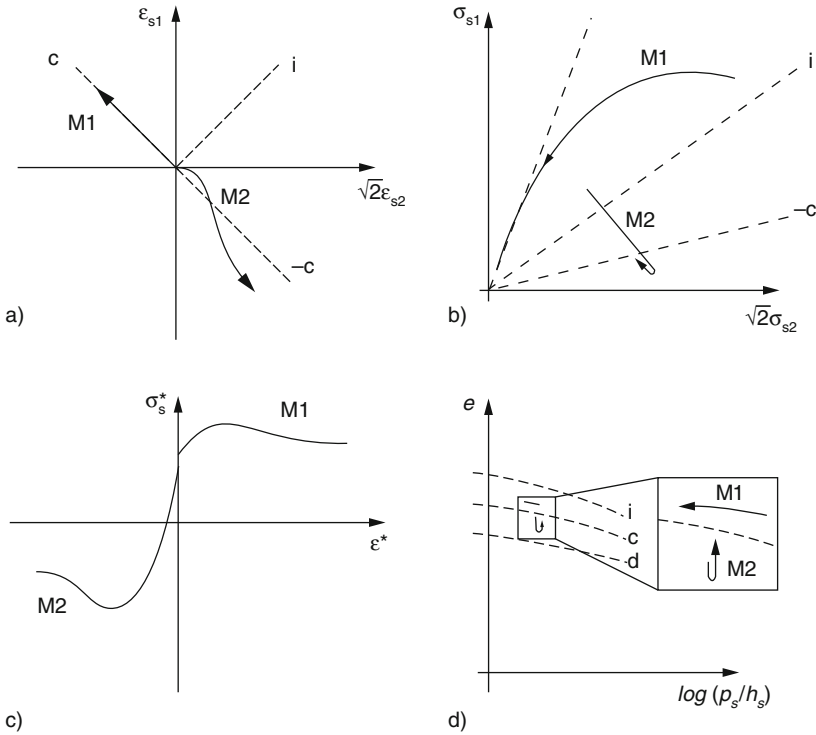


Fig. 2.2.6. Monotonous deformations (a) with constant e (A) or p_s (B) are related with stress paths (b) so that the curves of stress deviator vs. strain deviator (c) go through a peak if the initial void ratio is high or low enough, respectively (d) (qualitative)

saturated and drained samples, also if any linear combination of σ_{s1} and σ_{s2} instead of p_s was kept constant. As shear localizations cannot be avoided beyond a peak critical states appear in narrow shear zones (Sect. 8.2). This problem can be circumvented by assuming uniform deformations, i.e. by considering psammoids as simple materials in the sense of Sect. 3.2. M3 is often written as

$$\frac{\dot{\epsilon}_1^p}{\dot{\epsilon}_2^p} = -2 \frac{\sigma_{s2}}{\sigma_{s1}} \tan^2(45^\circ \mp \varphi_c/2) \tag{2.2.20}$$

with plastic strain rates and $+$ for axial shortening and $-$ for extension. Equation (2.2.20) was introduced as *stress-dilatancy* relation by Rowe (1962). He derived it by assuming a minimum of the ratio of ‘work in’ and ‘work out’, $\sigma_1 \dot{\epsilon}_1 / 2 \sigma_2 \dot{\epsilon}_2$, with respect to different sliding directions. De Josselin de Jong (1976) derived (2.2.20) without this extremum principle and pointed out that it cannot hold in general. A precursor of (2.2.20) was proposed by Taylor (1948) for simple shearing (Sect. 2.8). Extensions of (2.2.20) for other than cylindrical deformations will be treated in Sects. 2.7 and 2.8.

Plots like Fig. 2.2.6c are conventionally described by means of stiffness and strength. This is avoided here as it can be misleading due to barotropy and pyknotropy. The differential stiffness is so variable by (2.2.14) that it cannot be captured by a modulus. Peak stress deviators depend on the instantaneous e and p_s and the kind of deformation, e.g. isochoric or isobaric, therefore they should not be treated as shear strengths with given parameters. In a qualitative sense a psammoid may at best be called more or less *ductile* if a peak as in Fig. 2.2.6c is less or more marked.

Further properties are revealed by *reversals*, i.e. with sudden changes of path directions so that the sign of the mechanical power

$$P = \sigma_{s1}\dot{\epsilon}_1 + 2\sigma_{s2}\dot{\epsilon}_2 \quad (2.2.21)$$

changes. One may speak of loading for $P > 0$ just before a reversal, and of unloading for $P < 0$ just after it. Grain skeletons exhibit $\dot{p}_s < 0$ for isochoric and $\dot{e} < 0$ for isobaric unloading. This can lead to a cumulative decrease of p_s or e , respectively, for repeated reversals, and also to a cumulative deformation for stress cycles, i.e. ratcheting. The asymptotic response to paths with many reversals is particularly revealing, it can be represented by *state cycles*. As with simple solids (Sect. 2.1) these are attained by cyclic deformations or ratcheting, with big or small amplitudes so that state limits are repeatedly approached or not, respectively. The spectrum is wider than for solids due to barotropy and pyknotropy.

Strain cycles (Fig. 2.2.7a) may be big (I) or small (II) and rather isochoric (A) or isobaric (B). In case A (e.g. full saturation and no drainage) the stress path (b) tends to a double loop (butterfly), and the average asymptotic pressure (c) is lower for smaller amplitudes with a given void ratio. In case B the pressure p_s is kept nearly constant, this requires a butterfly-like strain cycle; then the asymptotic average e is lower for smaller amplitudes. Changes of paths with a reversal are intricate due to the non-linearity by (2.2.14c), this could be represented by response polars with labels for void ratio. Isochoric cyclic deformations can lead to skeleton decay if e is too high, and to grain crushing with big amplitudes if e is too low, in both cases asymptotic state cy-

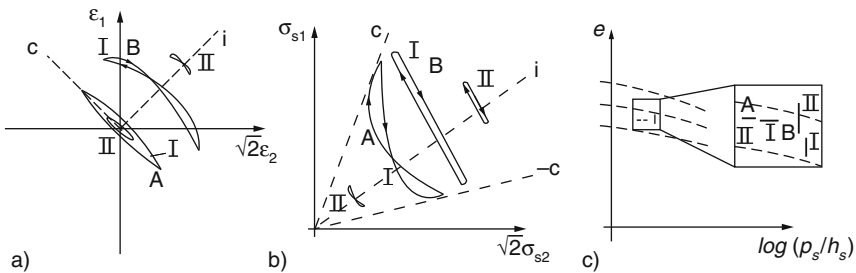


Fig. 2.2.7. Cyclic deformations (a) lead to cyclic stress paths (b) and cycles of e vs. p_s (c) (qualitative)

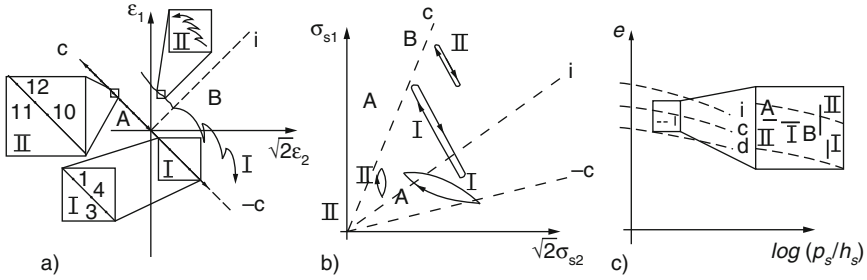


Fig. 2.2.8. Ratcheting (a) leads to stress cycles (b) and cycles of e vs. p_s (c) (qualitative)

cles are not reached. With small amplitudes e approaches the lower bound e_d for case B, and p_s tends to the value related with the given $e = e_d$ for case A. With so big amplitudes that the stress obliquity gets repeatedly overcritical the RSE can lose its uniformity by shear localizations, this is left aside here.

Ratcheting (Fig. 2.2.8a) can likewise occur with big (I) or small amplitude (II) and can be rather isochoric (A) or isobaric (B). In case A (saturated, no drainage) the stress path (b) tends to a lenticular cycle, and critical obliquities are repeatedly approached. With a given e the average asymptotic p_s is lower for smaller amplitudes. Asymptotic cycles cannot be reached due to skeleton decay with a too high e , and due to grain crushing with a too low e . In case B garland-like strain paths are needed to keep p_s constant, and the asymptotic average e is lower for smaller amplitudes, but not as close to e_d as with strain cycles. With very big amplitudes the amount of stress obliquity gets repeatedly overcritical, this leads to shear localizations and is left aside here (Sect. 8.2).

The state cycles attained by cyclic deformations or ratcheting are *driven attractors* of simple psammoid RSEs. As long as skeleton decay, degradation of grains and localizations are avoided skeletons could be driven to such state cycles and would remain uniform. By definition the state of simple psammoids is determined by stress components (σ_{s1} and $\sigma_{s2} = \sigma_{s3}$ in case of cylindrical symmetry) and void ratio e . The relation of stress rates and strain rates can be represented by response polars (Fig. 2.2.3) which depend on σ_{s1} , σ_{s2} and e only. Asymptotic state cycles are thus simplified as the variation of spatial force fluctuations (Sect. 4.3) is neglected.

Algebraic representations of the constitutive functions f_i by (2.2.13) and (2.2.14) will be outlined for cylindrical RSEs in the next two sections. It will be shown that big differences of asymptotic state cycles can arise for different constitutive relations even if their state limits are close to each other. One could reduce these differences by means of hybrid relations (Sect. 2.11), but the actual asymptotic response can thus not be captured much better. This can only be achieved with internal variables which are not determined by the external ones (here σ_{s1} , σ_{s2} and e) in general (Sect. 4.3).

The so-called *liquefaction* of saturated granular soils (e.g. Casagrande 1936, 1971) is not explicitly treated in this introduction. Instead of this rather subjective notion one should speak of *skeleton decay* with vanishing p_s . This can lead to a kind of suspension if a skeleton with $e > e_{co}$ for $p_s = 0$ is deformed monotonously without drainage. Cyclic isochoric deformations of a denser skeleton can lead to its temporary decay and recombination, the former should not be called liquefaction. The likewise rather subjective notion *cyclic mobility* (Castro 1975) should better be replaced by isochoric ratcheting with reduction of p_s . Decay and recombination cannot be modelled by means of simple psammoid relations.

To *sum up*, evolutions of shape and state of cylindrical simple psammoid RSEs can be captured by relations of stress rate and strain rate with stress and void ratio as state parameters. These relations can be represented graphically by response polars. Their asymptotic solutions or attractors are state limits for proportional straining, and state cycles for cyclic straining or ratcheting. Skeleton decay, degradation of grains, shear localization and internal state variables are left aside in this approach, which will be further considered in the next three sections and extended thereafter to more than two components.

2.3 A shortcut of CSSM

In their book on *Critical State Soil Mechanics* (CSSM) Schofield and Wroth (1968) propose essentially the concept of state limits – without using this name – for a peloid (Cam clay) and a psammoid (Granta gravel). The limit void ratios are approximated by Terzaghi’s (1925) formula (Fig. 2.3.1a)

$$e_i - e_{ir} = e_c - e_{cr} = e_d - e_{dr} = -\lambda \ln(p_s/p_r) \quad , \quad (2.3.1)$$

with a constant *compression index* λ and reference values e_{ir}, e_{cr}, e_{dr} for a reference pressure p which is arbitrarily chosen, e.g. $p_r = 100$ kPa. As this p_r has nothing to do with the material (2.3.1) is not unit-invariant. The lower bound e_d was added later by Schofield (2005) and linked with tensile cracking.

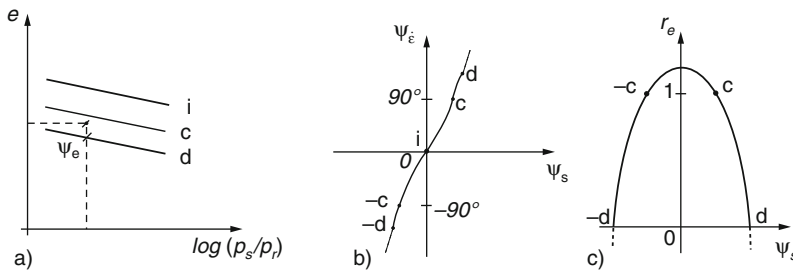


Fig. 2.3.1. State limits by CSSM: (a) void ratios, (b) obliquities, (c) relative void ratios (qualitative, dotted for tension)

Equation (2.3.1) works for a certain p_s -range, but fails evidently for $p_s \rightarrow 0$ and $p_s \rightarrow \infty$.

For critical states the stress ratio is given by (2.2.15). In some variants of CSSM another φ_c is assumed for axial extension than for shortening, this difference is left aside as there is no evidence for a substantial difference (Sect. 2.5). The dependence of strain rate direction on stress direction for state limits is plotted in Fig. 2.3.1b. It comes up to a nearly linear interpolation between isotropic compression (i) and critical states ($\pm c$). In CSSM state limits $\pm d$ as introduced in Sect. 2.2 do not occur explicitly, but tensile stresses (dotted) are excluded by a cut-off.

An *overconsolidation ratio*

$$OCR = p_e/p_s \quad (2.3.2)$$

can be introduced by means of an *equivalent pressure*

$$p_e = p_r \exp\left(\frac{e_{ir} - e}{\lambda}\right) \quad , \quad (2.3.3)$$

which substitutes e as proposed by Hvorslev (1937) by means of (2.3.1). For a given p_s one can take e_{cr} or e_{dr} in (2.3.3) instead of e_{ir} , the overconsolidation ratios may then be called $OCR_c = p_{ec}/p_s$ and $OCR_d = p_{ed}/p_s$. With them the relative void ratio by (2.2.18) can be written

$$r_e = \frac{\ln OCR_d - \ln OCR}{\ln OCR_d - \ln OCR_c} \quad (2.3.4)$$

by means of (2.3.1), (2.3.2) and (2.3.3). This r_e can be related with the stress obliquity for state limits as plotted in Fig. 2.3.1c. Beyond the bounds d and $-d$ the dotted lines plotted in Fig. 2.3.1b and c can be formally obtained by CSSM, but such states have to be excluded as they imply tensile stresses (more in Gudehus and Mašin 2010).

Been and Jefferies (1985) proposed a *state parameter* ψ_e which plays a similar role within CSSM as r_e . As shown in Fig. 2.3.1a it is the difference $e_c - e$ of the critical void ratio e_c for a given p_s and the actual one e . Without a lower bound e_d as by (2.3.4) ψ_e can replace e in a useful combination with p_s .

Elastoplastic relations (elp) are formulated in the frame of CSSM as shown in Fig. 2.3.2. State limits for a given void ratio e , or an equivalent pressure p_e by (2.3.3) instead, appear as a closed *state boundary curve* in a plot of σ_{s1}/p_e vs. $\sqrt{2}\sigma_{s2}/p_e$ and are assumed to bound elastic ranges. Usually this curve is taken as smooth everywhere (a), and the part of it with tensile stress (dotted) has to be cut off. This flaw can be avoided by means of an apex at the origin (b), e.g. Vermeer (1978). Plastic strain rates, with components $\dot{\epsilon}_1^p$ and $\dot{\epsilon}_2^p = \dot{\epsilon}_3^p$, were first assumed to be normal to the boundary curve (associated flow rule).

In later variants the flow rule for overcritical stress obliquities is not associated, but follows Rowe's (1962) stress-dilatancy relation (2.2.20). For critical states with stress ratios by (2.2.15) plastic deformations are isochoric, thus

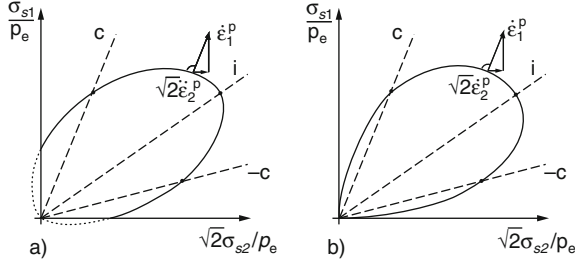


Fig. 2.3.2. State boundary curves by CSSM without (a) or with an apex (b), and with associated plastic strain rate (qualitative)

the tangents of the boundary line are parallel to the i -line $\sigma_{s1} = \sigma_{s2}$. For lower than critical amounts of stress obliquity $|\psi_s|$ plastic deformations are contractant. Their direction is taken as normal to the state boundary line, which is called *cap* in the contractant range. Plastic deformations are isotropic for isotropic stress states, then the tangent to the boundary line for $\sigma_{s1} = \sigma_{s2}$ is normal to the i -line. For higher than critical $|\psi_s|$ plastic deformations are dilatant.

The state boundary line is convex and essentially determined by the point for isotropic compression, the two points for critical states and a smooth shape or an apex at the origin $\sigma_{s1} = \sigma_{s2} = 0$. The indeterminacy of plastic strain rates near the origin does not matter as $p_s \rightarrow 0$ has to be avoided with (2.3.1) anyway.

Within the elastic range the relation of stress rates and strain rates assumed in several versions of CSSM is *hypoelastic*, viz.

$$\begin{aligned} \dot{p}_s &= \dot{\epsilon}_v p_s / \kappa \\ \dot{\sigma}_s^* &= \dot{\epsilon}^* \frac{p_s}{\kappa} \frac{\nu}{1 - \nu} \end{aligned} \quad (2.3.5)$$

with a *swelling index* $\kappa < \lambda$ and a Poisson ratio ν . Therein the volumetric and deviatoric components are defined by (2.2.1), (2.2.2), (2.2.9) and (2.2.11). Formally (2.3.5) is an isotropic linear elastic relation of $\dot{\sigma}_{si}$ and $\dot{\epsilon}_i$ with bulk modulus $K = p_s / \kappa$ and shear modulus $G = K\nu / (1 - \nu)$ which allows for barotropy in the simplest possible manner. The grain skeleton is thus substituted by a kind of sponge. Niemunis and Cudny (1998) have shown that such relations should be derived from a strain-dependent elastic energy. Only this approach is physically sound, other elastic relations which have been proposed for CSSM can lead to inconsistencies.

Strain rates have elastic and plastic parts by

$$\dot{\epsilon}_i = \dot{\epsilon}_i^e + \dot{\epsilon}_i^p \quad (2.3.6)$$

with $i=1$ and 2 for cylindrical symmetry. The elastic part $\dot{\epsilon}_i^e$ is related with the stress rate $\dot{\sigma}_{si}$ by (2.3.5). Plastic strain rates arise for ‘loading’ at state limits

and are directed as the normal of the boundary line (Fig. 2.3.2). ‘Loading’ means that the strain rate $\dot{\epsilon}_i$ would imply an elastic stress rate $\dot{\sigma}_{si}$ by (2.3.5) which leaves the elastic range. The volumetric strain rate $\dot{\epsilon}_v$ is related with the rate of void ratio \dot{e} by (2.2.10), and thus with changes of the equivalent pressure p_e by (2.3.3).

Vermeer (1978, 1984) replaced (2.3.5) by a power law like (4.5.2) this is advantageous for low p_s but does not remove the flaw of (3.3.1) for $p_s \rightarrow 0$. He proposes an associated flow rule for subcritical stress obliquities and the stress-dilatancy relation (2.2.20) otherwise. As other authors he uses the deviatoric plastic strain as a further state variable, but this is not physically tenable (Sect. 1.2). This so-called strain hardening enables an approach to state limits, but cannot produce state cycles by cyclic deformation or ratcheting. This lack could be revealed by numerical simulations, but software for Vermeer’s relation is not freely available.

Instead of algebraic expressions, which have been proposed for CSSM, this kind of elp is represented by *response polars* in Fig. 2.3.3 for two variants. As in Fig. 2.3.2 stress components are normalized by p_e . In the elastic range the polars are centric ellipses (Gudehus 1979, Vermeer 1984). According to (2.3.5) their long axis is aligned as the i-line, their shape is given by the assumed Poisson ratio ν and their size is proportional to p_s (e.g. A and B). This means that for a given p_s changes of stress deviator σ_s^* do not matter (e.g. B and C). For stress states along the state boundary curve the hypoelastic response holds only for unloading, this part of the response polar is thus a half-ellipse which is cut off by the tangent of the boundary curve.

The response polar for ‘loading’ is a section of an ellipse which is attached to the elastic half-ellipse (Gudehus 1979, Vermeer 1984). For critical states the outer half-ellipse degenerates to a straight line as the state is not changed by continued isochoric deformation (D and E). For an isotropic state the outer elliptic section is flatter than the inner one (F) by the factor λ/κ , this can be derived from (2.3.1) and (2.3.5). For states with subcritical stress obliquities response polars can be estimated by a monotonous interpolation (G). For states with overcritical stress obliquities the anelastic part of the response polar is an inwards elliptic section which is flatter than the elastic half-ellipse

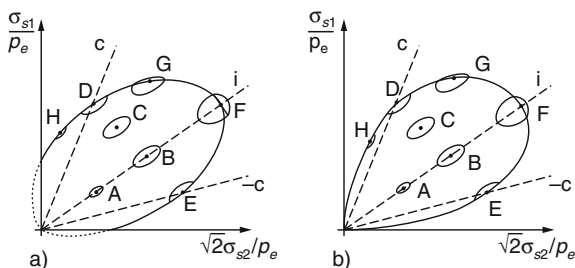


Fig. 2.3.3. Response polars by CSSM for state boundary curves without (a) and with apex (b) (qualitative)

(H). The notion ‘loading’ is thus ambiguous for softening by dilation. Differences between smooth (Fig. 2.3.3a) and bullet-shaped boundary lines (b) are more marked near the origin $\sigma_{si} = 0$. Niemunis (2003) gives algebraic details for such response polars.

Approaches to state limits are shown in Fig. 2.3.4. Proportional strain paths (a) may be contractant (A), isochoric (B) or dilatant (C). With the same initial state (0) the related stress paths (b) are straight in the assumed elastic range with different directions. With the assumed onset of plastification (1) the stress path turns to a straight line with p_s -increase (A), and tends to a critical stress point (B) or to a straight line with p_s -decrease (C), respectively. Response polars would indicate how state limits according to Fig. 2.3.1 work as driven attractors. This requires convex state boundary curves with an apex, otherwise the uniqueness gets lost and parts with tension have to be cut off. In the e vs. $\log p_s$ plot (c) the state path tends to the relative void ratio by Fig. 2.3.1c with increasing (A), stationary (B) or increasing p_s (C). Other than explained with Fig. 2.2.2b the skeleton cannot decay with constant e and limit void ratios by (2.3.1), whereas a contractant deformation would thus destroy grains if e is low.

Isobaric evolutions by elp within CSSM are shown in Fig. 2.3.5 for a higher (A) and a lower initial isotropic pressure (B) than the one related with the same initial e for critical states. In the elastic range (0–1) the strain paths (a) are isochoric until the stress paths (b) reach the state boundary line. A monotonous further deformation (1–2) leads to a critical state after contraction for A and dilation for B, thus the boundary curve gets wider or smaller (dotted curves). Un- and reloading thereafter (2–3–4) are elastic and isochoric. In the e vs. $\log p_s$ plot e tends to e_c for the given p_s (c). In a plot of stress deviator σ^* vs. strain deviator ε^* (d) straight lines appear for elastic sections. The response to a monotonous deformation is less ductile for B than for A. A plot of e vs. ε^* (e) exhibits contraction for A and dilation for B only during the first loading. The plots (d) and (e) are implied by the previous ones, but convey less information.

Isochoric evolutions by elp are shown in Fig. 2.3.6 for a higher (A) and a lower initial isotropic pressure (B) than the one related with the given e

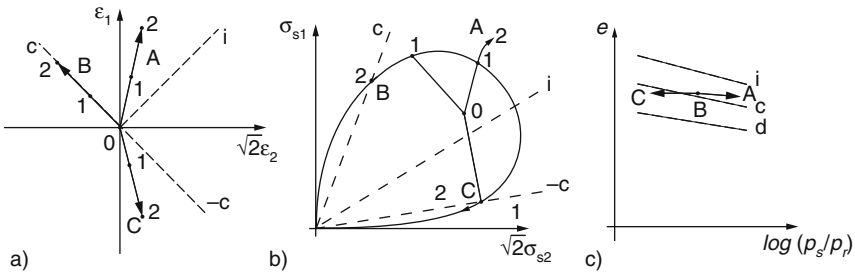


Fig. 2.3.4. Proportional strain paths (a) lead to state limits of stress components (b) and of e vs. $\log p_s$ (c) by elp within CSSM (qualitative)

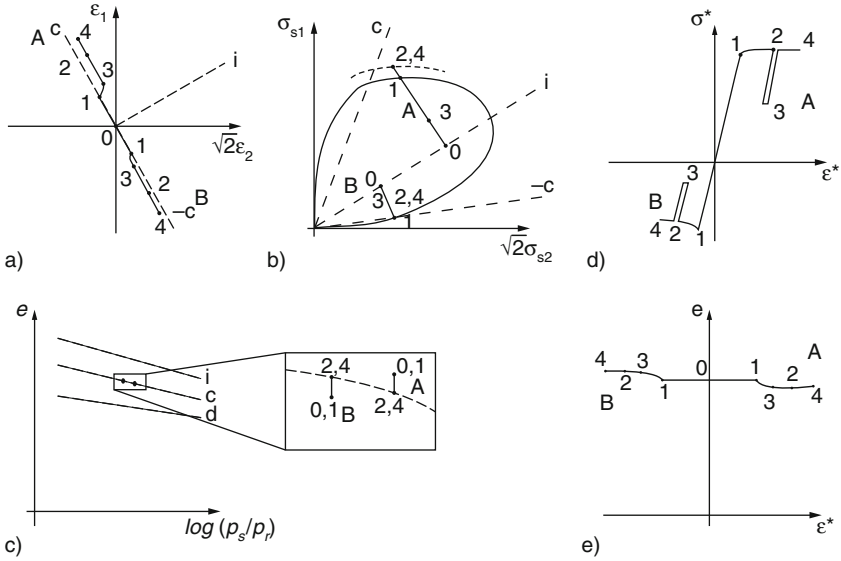


Fig. 2.3.5. Isobaric evolutions by CSSM (qualitative) (a) strain paths, (b) stress paths, (c) paths of e vs. $\log p_s$, (d) deviatoric stress-strain curves, (e) evolutions of void ratio with strain deviator

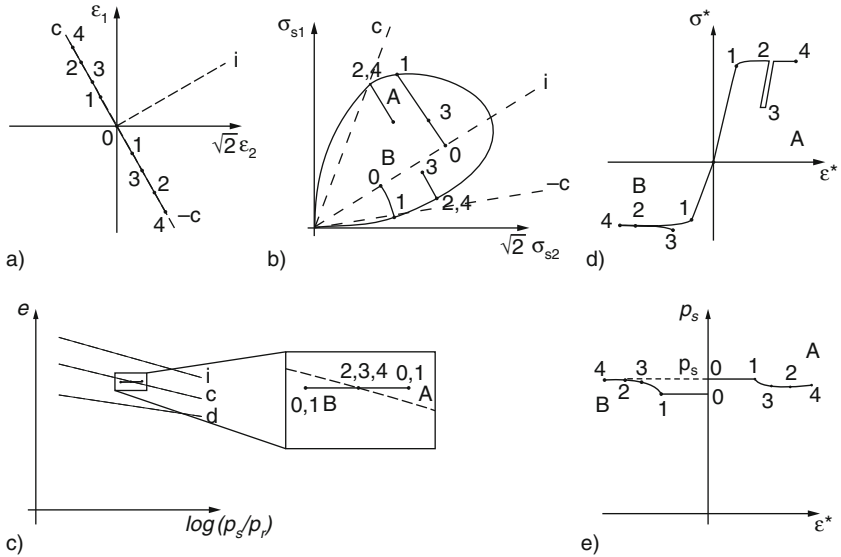


Fig. 2.3.6. Isochoric evolutions by CSSM (qualitative): (a) strain paths, (b) stress paths, (c) paths of e vs. $\log p_s$, (d) deviatoric stress-strain curves, (e) evolutions of pressure with strain deviator

for critical states. The strain paths (a) exhibit reversals (2–3–4, numbers for the sequence). The stress paths (b) show a reduction or an increase of p_s , respectively, for A and B in the sections with assumed plastification (1–2). This change appears also in the plot of e vs. $\log p_s$ (c). A deviatoric stress-strain plot (d) suggests hardening by plastification. A plot of p_s vs. strain deviator (e) shows a decrease or an increase of p_s by plastification. The plots (d) and (e) are implied by the former three, but are not as comprehensive.

Cyclic deformations (Fig. 2.3.7a) lead to asymptotic cycles of stress (b) and of e vs. $\log p_s$ (c) by consistent CSSM-elp relations. With a small amplitude (A) a stress cycle is attained near the onset, and a small e vs. $\log p_s$ cycle. This is achieved with the self-similarity by (2.3.1) and (2.3.5) for different initial p_e , the underlying elastic potential prevents cumulative changes of mean stress. With a bigger amplitude (B) the stress path tends to a cycle with elastic and anelastic sections, and with more marked e vs. $\log p_s$ cycles. This attractor is attained with different initial states (σ_{s1} , σ_{s2} and e) with bullet-shaped state boundary curves and suitable hypoelastic relations. In a periodic continuation the boundary curve is expanded and diminished in each cycle.

Ratcheting (Fig. 2.3.8a) leads to stress cycles (b) and cycles of e vs. $\log p_s$ in the asymptote. These attractors are obtained with consistent state boundary lines and hypoelastic relations. Critical states are periodically attained with small (A) or big amplitudes (B) of state cycles in the continuation. With a nearly isochoric deformation as chosen for A the asymptotic stress cycles are nearly isobaric. With wider garlands of the strain path as chosen for B both e and p_s cycle more markedly. State cycles cannot be achieved with elp if the deviatoric plastic strain is used as further state variable. This would increase indefinitely in case of ratcheting and would thus prevent an asymptotic state cycle.

Inserting response polars as in Fig. 2.3.3 into stress plots as in Figs. 2.3.4b, 2.3.7b, and 2.3.8b would reveal how the attractors are approached. This graphical version of a fixed point theorem cannot reveal all details, nor the range of attraction. Both could be achieved by numerical element tests. The range of

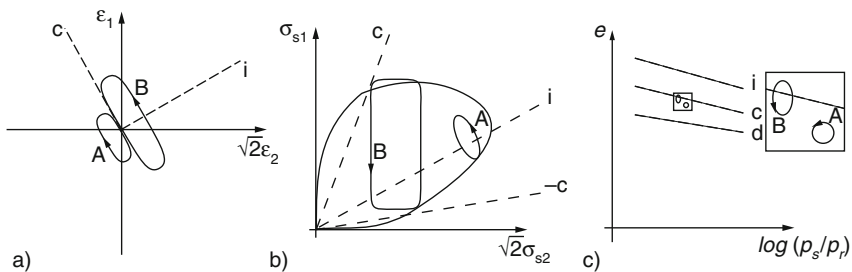


Fig. 2.3.7. Repeated strain cycles (a) lead to stress cycles (b) and e vs. $\log p_s$ cycles (c) by elp within CSSM (qualitative). The assumed elastic range is not left with a small amplitude (A), and repeatedly left with a big amplitude (B)

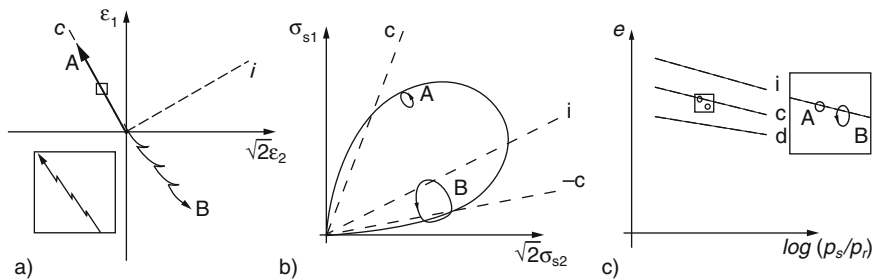


Fig. 2.3.8. Ratcheting (a) leads to stress cycles (b) and e vs. $\log p_s$ cycles (c) by a consistent elp within CSSM (qualitative)

validity will be discussed in Sects. 2.5 and 2.6 for cylindrical RSEs by means of experiments. As long as RSEs remain uniform and grain properties are not markedly changed consistent CSSM-elp relations should produce state limits and state cycles as shown in Figs. 2.3.4, 2.3.5, 2.3.6. The assumed elastic response to small strain cycles will be discussed in Sect. 4.2.

To *sum up*, elastoplastic relations within CSSM (elp) can reproduce observable attractors of psammoids to a certain extent. Contractant and isochoric state limits can be obtained except for low pressures p_s , dilatant ones without tension can be obtained with bullet-like state boundary curves. The flow rule, i.e. the direction of the plastic strain rate, is associated (i.e. normality rule) with the state boundary curve for subcritical stress oqliquities. In the overcritical regime Rowe's stress-dilatancy is more suitable than an associated flow rule. Hypoelastic relations with elastic potential and stiffness proportional to p_s lead to state cycles for strain cycles and for ratcheting. The deviatoric plastic strain is not tenable as further state variable because it excludes state cycles as attractors.

2.4 A shortcut of hypoplasticity

State limits of hypoplastic relations for simple psammoids are shown in Fig. 2.4.1. The limit void ratios (a) are approximated by Bauer's (1996) formula

$$\frac{e_i}{e_{i0}} = \frac{e_c}{e_{c0}} = \frac{e_d}{e_{d0}} = \exp \left[- \left(\frac{3p_s}{h_s} \right)^n \right]. \quad (2.4.1)$$

The exponent n ranges from ca. 0.3 for angular to ca. 0.6 for round grains. The *granulate hardness* h_s ranges from ca. 100 MPa for angular calcite to almost 10GPa for round quartz grains, and is bigger with less uniform grain sizes. Other than (2.3.1), (2.4.1) does not fail for $p_s \rightarrow 0$ and $p_s \rightarrow \infty$, and it is unit-invariant.

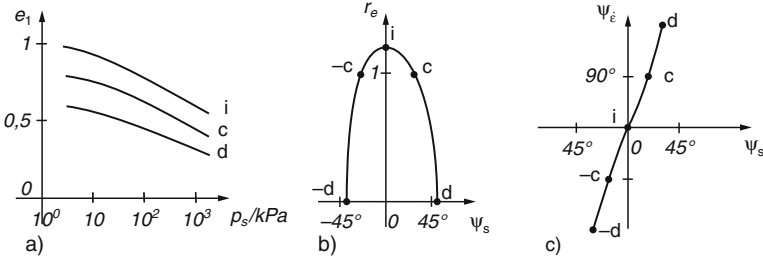


Fig. 2.4.1. State limits of a simple psammoid by hypoplasticity (qualitative): (a) limit void ratios, (b) relative void ratio vs. stress obliquity, (c) strain rate obliquity vs. stress obliquity

The limit void ratios e_{i0} , e_{c0} and e_{d0} for $p_s = 0$ are material parameters. As $e_{i0}/e_{c0} \approx 1.1\text{--}1.2$ and $e_{d0}/e_{c0} \approx 0.6\text{--}0.7$ holds for a wide range of granular soils e_{c0} is a key parameter. In the vicinity of $p_s = 0$ (2.4.1) can be approximated by the power law

$$p_s = \frac{1}{3} h_s (1 - e/e_0)^{1/n}, \quad (2.4.2)$$

wherein the subscript i, c or d may be added to e and e_0 . This indicates a kind of *percolation* (Guyon and Troadeck 1994): e is lower than e_0 for higher p_s due to wider contact flats. The exponent n may be related with the fractal dimension of the grain surface. If this is very smooth and thus two-dimensional $n = 2/3$ should hold as by the theory of Hertz (Johnson 1985). If the grain surface is very rough and thus three-dimensional $n \rightarrow 0$ appears more appropriate, but then (2.4.2) would fail. The turning point of e vs. $\log p_s$ at $p_s = h_s/3$ by (2.4.1) can scarcely be reached without fragmentation of grains (Sect. 7.3).

The relative void ratio r_e by (2.2.18) is plotted vs. the stress direction angle ψ_s by Fig. 2.2.1a for hypoplastic state limits in Fig. 2.4.1b. Its maximum $(e_{i0} - e_{d0})/(e_{c0} - e_{d0})$ holds for isotropic compression (i) from the highest possible void ratio e_{i0} and $p_s = 0$ onwards. $r_e = 1$ holds for critical states with axial shortening or extension (c or $-c$). For contractant state limits r_e ranges from $r_e > 1$ to the maximum for i. $r_e = 0$ holds for the extreme cases d and $-d$ with $\sigma_{s1} = 0$ or $\sigma_{s2} = 0$. For dilatant state limits r_e has values between 0 and 1.

Strain rate directions ψ_ε (Fig. 2.2.1) are plotted vs. stress directions ψ_s for hypoplastic state limits in Fig. 2.4.1c. For isotropic compression (i) $\psi_\varepsilon = \psi_s = 0$ is evident. Critical states with axial shortening (c) have $\psi_\varepsilon = 90^\circ$, $\psi_\varepsilon = -90^\circ$ holds with extension ($-c$). The related positive and negative critical values of ψ_s are determined by (2.2.15) with (2.2.2), and (2.2.3). The extreme state limits with ψ_s -bounds by (2.2.4) and ψ_ε -bounds by (2.2.16) are not explicitly represented by hyp, these states (d and $-d$) are unattainable asymptotes. The interpolations for contractant and dilatant state limits are nearly linear.

For cylindrical symmetry *hypoplastic relations* (hyp) can be written

$$\begin{aligned}\dot{\sigma}_{s1} &= f_s(L_{11}\dot{\epsilon}_1 + L_{12}\dot{\epsilon}_2 - f_d N_1 D), \\ \dot{\sigma}_{s2} &= f_s(L_{21}\dot{\epsilon}_1 + L_{22}\dot{\epsilon}_2 - f_d N_2 D).\end{aligned}\quad (2.4.3)$$

They are rate-independent, and non-linear in $\dot{\epsilon}_i$ as is the amount of stretching D by (2.2.19). The coefficients L_{ij} and N_i ($i, j = 1, 2$) are functions of the stress obliquity ψ_s with φ_c as material parameter, their order of magnitude is 1. The density factor f_d depends on the relative void ratio via

$$f_d = r_e^\alpha \quad (2.4.4)$$

with an exponent α ranging from ca. 0.1 for non-uniform to ca. 0.4 for uniform grain sizes. $r_e < 0$ has to be excluded. Peak states with vanishing stress rates come close to dilatant state limits; thus (2.4.3) yields relations of ψ_ϵ and r_e with ψ_s which are determined by φ_c and α . ψ_s may be substituted by a peak friction angle via (2.2.17). The stiffness factor f_s in (2.4.3) is given by (Herle and Gudehus 1999)

$$f_s = \frac{h_s}{n} \left(\frac{e_i}{e}\right)^\beta \frac{1 + e_i}{e_i} \left(\frac{3p_s}{h_s}\right)^{1-n} \left[3 + a^2 - \sqrt{3}a \left(\frac{e_{io} - e_{do}}{e_{co} - e_{do}}\right)^\alpha\right]^{-1} \quad (2.4.5)$$

with

$$a = \frac{\sqrt{3}(3 - \sin \varphi_c)}{2\sqrt{2} \sin \varphi_c}. \quad (2.4.6)$$

Using algebraic representations for L_{ij} and N_i by von Wolffersdorff (1996), f_s is derived from (2.4.1) and (2.4.3) for an isotropic compression as then both relations must coincide (Bauer 1996, Gudehus 1996). e_i in (2.4.5) depends on p_s by (2.4.1). As the exponent β ranges from ca. 1.1 to 1.2 the factor f_s depends on p_s mainly via $(p_s/h_s)^{1-n}$. Pyknotropy is thus linked with barotropy (Kolymbas 1991) as both f_d and f_s depend on e and p_s .

Equation (2.4.3) can be represented by *response polars* with labels for directions and r_e , Fig. 2.4.2. According to (2.4.3) they are ellipses with size by p_s and r_e , shape by ψ_s and eccentricity by f_d and ψ_s . The advantages of such

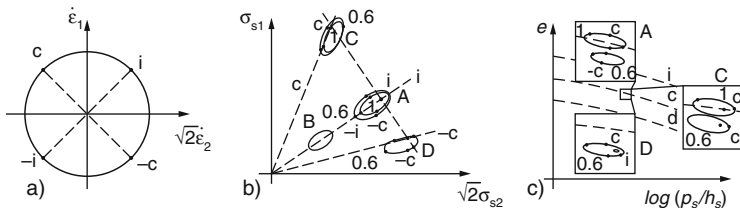


Fig. 2.4.2. Response polars by hypoplasticity (qualitative): (a) unit strain rates, (b) stress rates, (c) rates of e vs. $\log p_s$; with labels for r_e

ellipses were first shown by Wu (1992). Unit strain rates (a) with direction $\psi_{\dot{\varepsilon}}$ may in particular be isotropic compression (i) or expansion (–i), and isochoric with axial shortening (c) or extension (–c). Some response polars are shown in the stress plane (Fig. 2.4.2b) and in the e vs. $\log p_s$ plot (c).

For isotropic states the stress polars are aligned with the i-axis (e.g. A), wider and less eccentric with lower r_e , and smaller with lower p_s (B) by the power law in (2.4.5). In case of a critical stress obliquity (C) the stress polar touches the line by (2.2.15) for $r_e = 1$ and $\psi_{\dot{\varepsilon}} = 90^\circ$, and cuts it for $r_e < 1$. This means that critical states are stationary, whereas with lower than critical void ratios (i.e. $r_e < 1$) the stress obliquity $|\psi_s|$ can get bigger than critical. For a peak state (D) the polar passes the reference point, for it $\psi_{\dot{\varepsilon}}$ and ψ_s are related with r_e . This means that the peak friction angle φ_p by (2.2.17) is determined by the critical friction angle φ_c and the relative void ratio r_e . Response polars in the plot of e vs. $\log p_s$ (which are implied by stress polars plus (2.2.10) for isochoric grains) show that p_s can decrease by isochoric deformations for subcritical $|\psi_s|$ with $r_e > 1$, and increase for overcritical $|\psi_s|$ with $r_e < 1$.

Response polars are of use to demonstrate the *approach to state limits*, as was shown with Fig. 2.2.5. The evolution of state related with straight strain paths (a) in the sector by (2.2.16) is depicted by stress paths (b), evolutions of e vs. $\log p_s$ are also plotted (c). A proportional compression (A) leads to a proportional stress path asymptotically with r_e and ψ_s for the given $\psi_{\dot{\varepsilon}}$ by Fig. 2.4.1. This works without excessive p_s -increase if the initial r_e is not too low. A proportional extension (B) leads to a maximal $|\psi_s|$ which is related with the given $\psi_{\dot{\varepsilon}}$ and the achieved r_e via Fig. 2.4.1 with a low initial r_e . Isochoric stretching (C) leads to a critical state for $e < e_{co}$ as specified with Fig. 2.4.1, which remains with further stretching. The skeleton decays by isochoric stretching with $e \geq e_{co}$. State limits are thus attractors, i.e. asymptotic solutions of the hypoplastic relations. This can be seen from response polars, our geometrical consideration is a substitute of a fixed point theorem.

Isobaric evolutions by hyp are plotted in Fig. 2.4.3 for a higher (A) and a lower than critical (B) initial relative void ratio r_e and an isotropic initial stress. The strain path (a) is initially contractant (0–1), then (1–2) less contractant for A and dilatant for B. After deviatoric unloading (b, 2–3) it is more contractant, and with reloading (3–4) it is less dilatant for A than for B. In the e vs. $\log p_s$ plot (c) e reaches e_c for A and tends to e_c for B, therein contraction and dilation for deviatoric un- and reloading are hardly visible. In a plot of stress deviator σ^* vs. strain deviator ε^* (d) the response to unloading is seemingly elastic, but not in a plot of e vs. ε^* (e). Reloading (3–4) is related with nearly the same change of shape and void ratio as loading in the same stress range (1–2). With monotonous further deformation the state would remain critical for A and would go through a peak for B. These continuations are dotted in Fig. 2.4.4 as they cannot occur uniformly even in perfect testing devices because of shear localization (Sect. 8.2).

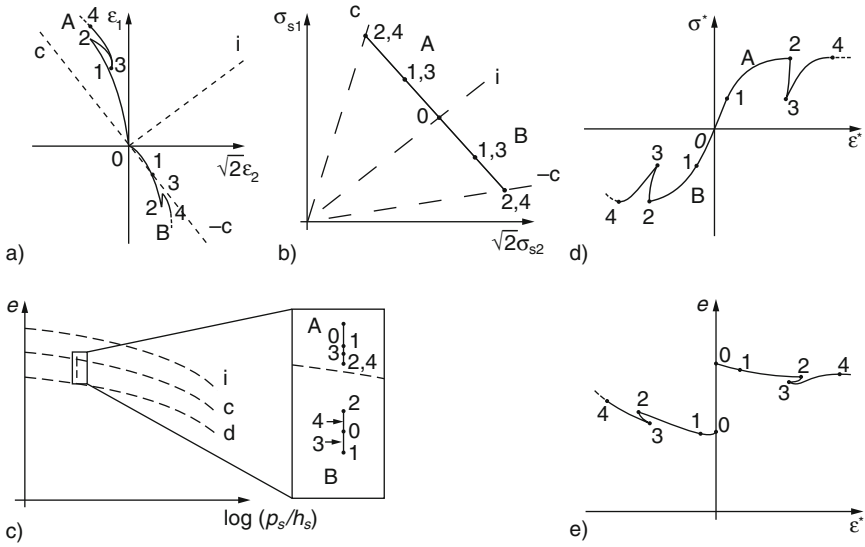


Fig. 2.4.3. Isobaric evolutions by hypoplasticity (qualitative): (a) strain paths, (b) stress paths, (c) e vs. $\log p_s$ paths, stress deviator (d) and void ratio vs. strain deviator (e); labels for the succession

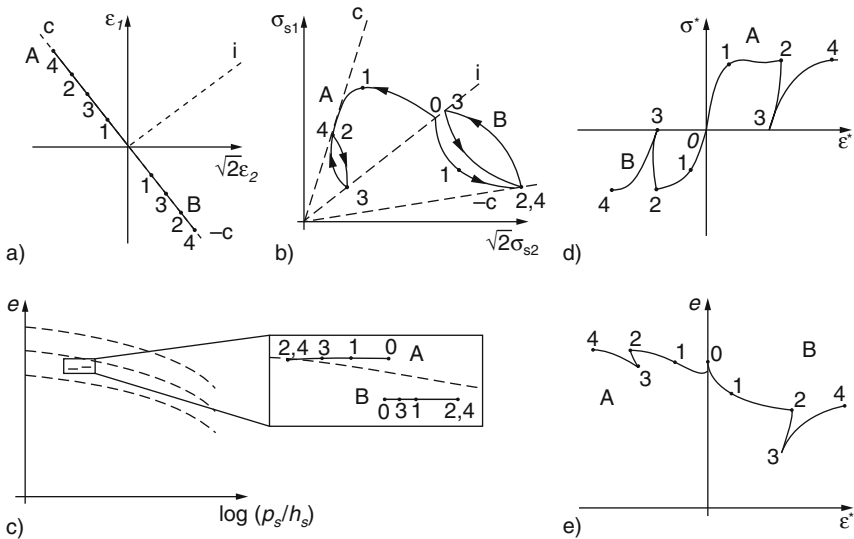


Fig. 2.4.4. Isochoric evolutions by hypoplasticity (qualitative): (a) strain paths, (b) stress paths, (c) e vs. $\log p_s$ paths, stress deviator (d) and mean pressure vs. strain deviator (e); labels for the succession

Isochoric evolutions by hyp are plotted in Fig. 2.4.4, again for a higher (A) and lower than critical initial r_e (B), and with an isotropic initial pressure. The strain paths (a) have two reversals. The stress paths (b) start with a reduction of p_s , this goes on for A and leads to a critical state if the skeleton does not decay due to $e > e_{co}$. For B p_s increases up to the value for a critical state, and two subsequent reversals lead to a stress loop as for A. In the e vs. $\log p_s$ plot (c) p_s -changes can better be seen in an insert. The plot of stress deviator σ^* vs. strain deviator ε^* (d) exhibits a peak for A, seemingly elastic unloading and anelastic reloading branches. The plot of p_s vs. ε^* (e) exhibits anelastic p_s -changes, particularly after reversals, which depend strongly on the instantaneous r_e . This behaviour cannot be characterized by notions like stiffness and strength, one may at best speak of a more or less ductile response for low or high initial void ratios.

The response by hyp with many reversals is revealed by asymptotic *state cycles*. These are shown already in Fig. 2.2.7 for strain cycles (a) with nearly constant void ratio e (A) or so that the mean skeleton pressure p_s gets nearly constant (B), both with lower than critical initial e . The skeleton stress path (b) tends to a double loop for A, whereas a lenticular asymptotic stress cycle with $p_s \approx \text{const}$ is achieved with a double strain loop (B). Evolutions tend to rather horizontal (A) or vertical cycles (B) in an e vs. $\log p_s$ -plot (c). Variants can be obtained with other amplitudes and shapes of strain cycles. As long as overcritical stress obliquities $|\psi_s|$ and too high or low relative void ratios are avoided state cycles are obtained as attractors which are determined by the strain cycle and the initial void ratio.

Ratcheting, i.e. strain cycles plus proportional isochoric straining, leads also to state cycles by hyp, this can be seen as for hyp in Fig. 2.2.8 for a nearly constant e (A) or so that p_s is nearly constant in the periodic asymptote (B). The strain path (a) remains nearly on the c-line (A) or resembles a garland (B). The stress path (b) tends to a lenticular loop which touches the c or $-c$ line and is wider for B than for A due to the chosen amplitude of pilgrim's steps. The e vs. $\log p_s$ paths (c) tend to lenticular loops with horizontal (A) or vertical alignment (B). Transitions to the attractors are omitted for simplicity, the sequence could be denoted in associated paths by numbers for reversals.

Algebraic representations of hyp have been proposed by Gudehus (1996), von Wolffersdorff (1996), and others. Niemunis (2003) discusses variants and limitations in mathematical detail. Software for numerical element tests can be found in his homepage (www Andrzej Niemunis). One can produce plots more quantitatively with assumed material parameters, initial states and boundary conditions of cylindrical RSEs. The approach to state cycles by strain cycles and ratcheting can thus be confirmed, this is a numerical substitute of a fixed point theorem. The latter could hardly be applied in a strict mathematical sense, but one can at least ascertain by means of response polars that state cycles are consistent.

To *sum up*, hypoplastic relations for cylindrical RSEs of simple psammoids produce state limits and state cycles as proposed in Sect. 2.2. The p_s -range

of limit void ratios and the range of stress obliquities are not restricted as by CSSM. Other than by *elp* there is no elastic range, thus state cycles are attained even by strain cycles with small amplitudes. Simply speaking, elastic effects after reversals are underestimated by *hyp* and overestimated by *elp*, but hybrids of *elp* and *hyp* won't do better. Differences of *elp* and *hyp* appear particularly after reversals for isobaric and isochoric evolutions.

2.5 Validations near state limits with cylindrical symmetry

The range of validity of the concepts outlined in Sect. 2.2, 2.3, and 2.4 can principally be explored by means of so-called oedometric, triaxial and cuboidal tests with granular samples. Some prerequisites are presented first, they will be referred to also in subsequent sections. State limits are then treated in the order of increasing deviation from isotropic states.

Granular samples in testing devices may be considered as RSEs (representative soil elements) of simple psammoids if the following *prerequisites* are satisfied:

PR1: homogeneity of composition and state at the onset,

PR2: validity of the effective stress principle,

PR3: permanence of granular properties,

PR4: exclusion of viscous effects,

PR5: compatibility of boundary conditions,

PR6: uniformity of changes of shape and state.

Careful selection and preparation are needed for PR1, ideally gravity should be compensated with a heavy pore fluid. PR5 and PR6 are already needed for producing a uniform initial state, which is arbitrary anyway. Neutrality of the grains with respect to pore water pressure p_w , as necessary for PR2, is achieved with pore-free grains. If a capillary skeleton pressure p_{cs} (Sect. 6.2) is employed to produce a high initial e flooding afterwards leads to $p_{cs} = 0$. With grain sizes below ca. 10^{-5} m a net intergranular attraction (Sect. 7.1) should be avoided by a suitable ionic strength. Uniformity of p_w requires a slow enough drainage.

Strictly speaking, PR3 is a contradiction in terms as grains are principally changed by encounters (Sect. 7.3). For the evolutions considered here, however, abrasion and fragmentation can be kept small enough so that the granular properties are not changed noticeably. PR4 can be achieved by keeping

the modulus of strain rate within one order of magnitude. Otherwise rate-dependance, creep and relaxation play a role even with hard grains (Sect. 4.6).

PR5 means average uniformity of displacements and state along the boundaries. In a perfect RSE relative grain displacements and contact forces should fluctuate around desired mean values along the boundary as in the interior. The shear stress along a boundary can be diminished by a smooth hard plate, but near it e is inevitably high. The latter can be avoided by a membrane, but this causes a variable penetration of grains and develops parasitary forces. Keeping these effects low requires careful compensation.

Even with PR1 and PR5 it is not generally possible to secure PR6 as the skeleton tends to lose its uniformity of itself. This bifurcation can be diffuse, and then called bulging or necking for axial shortening or extension (Sect. 14.1), and is not necessarily linked with a state limit. It is localized with the formation of shear bands near a peak (Sect. 8.2), then mean values of strain and void ratio can be misleading.

Proportional compressions, i.e. deformations with constant direction ψ_ε and $|\psi_\varepsilon| < 90^\circ$, require a high initial e for reaching a state limit without violating PR3. Ishihara (1993) reports on isotropic compression tests with a uniformly graded quartz sand and different initial e . His upper curve of e vs. p' , Fig. 2.5.1, comes close to a sequence of state limits e_i with the highest possible e . This was achieved by moist placement, i.e. by using the capillary skeleton pressure p_{cs} (Sect. 6.2). The onset of compression can be approximated by (2.4.2), but certainly not by (2.3.1). This indicates a percolation of the skeleton. Up to $p' = p_s \approx 4$ MPa a good approximation is obtained by (2.4.1) with $n = 0.5$, $h_s = 400$ MPa and $e_{io} = 1.06$. Equation (2.3.1) works

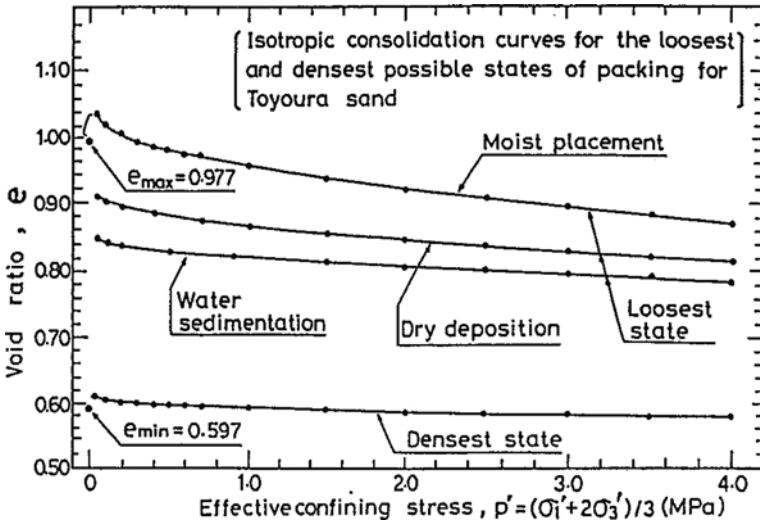


Fig. 2.5.1. Reduction of void ratios of a quartz sand by isotropic compression (Ishihara 1993)

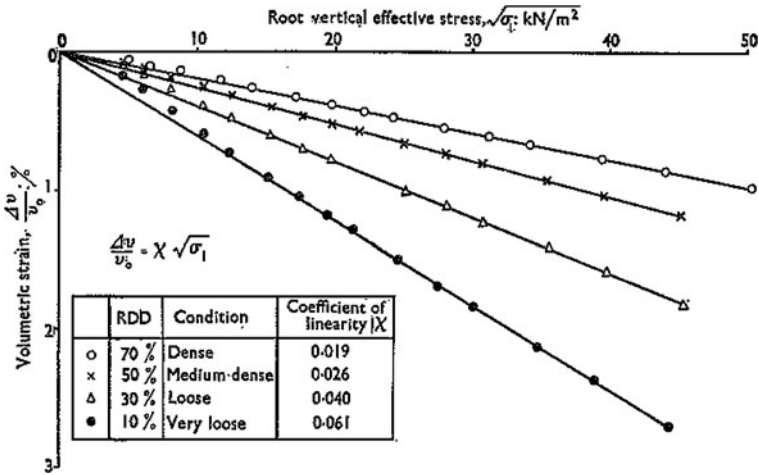


Fig. 2.5.2. Uniaxial compression ($\varepsilon_2 = 0$) of a quartz sand with different densities (Cornforth 1974)

with $p_r = 1$ MPa, $e_{ir} \approx 0.98$ and $\lambda \approx 0.02$ for p' from ca. 1 to 4 MPa. For the lower e given in Fig. 2.5.1 these approximations do not work as these void ratios do not belong to contractant state limits.

Cornforth (1974) reports on triaxial compression tests with $\varepsilon_2 = 0$, i.e. $\psi_\varepsilon = \arctan(1/\sqrt{2}) = 55^\circ$, with a non-uniformly graded quartz sand and different initial e . He found a linear increase of volumetric strain $\varepsilon_v = \varepsilon_1$ with $\sqrt{\sigma_1}$ for every initial e , Fig. 2.5.2. For initially very loose samples the line comes close to a sequence of contractant state limits. It confirms (2.4.2) with $n = 0.5$ and refutes (2.3.1). With Cornforth's data $e_0 \approx 0.75$ and $h_s \approx 1$ GPa can be estimated. Empirically the observed stress ratio can be approximated by $\sigma_{s2}/\sigma_{s1} \approx 1 - \sin \varphi_c$, thus ψ_s could be calculated and compared with the one by Fig. 2.3.1 or 2.4.1.

The approach to proportional stress paths by *proportional strain paths* was proposed by Gudehus et al. (1977), and confirmed by Goldscheider (1984) by means of cuboidal tests with high initial density. This property was called *swept-out of memory* (SOM) and was reproduced by Kolymbas (1978) with a rate-type constitutive relation. This led to hypoplasticity, but only years later state limits with relative void ratios were properly incorporated (Bauer 1992, Wu and Bauer 1993, Gudehus 1996). With the employed high density contractant state limits were not attained by Goldscheider (1984). His results will be used in Sect. 2.8 for evaluations off state limits.

Chu and Lo (1994) imposed proportional strain paths to initially dense quartz sand samples in triaxial tests. The stress paths tend to lines with constant component ratio. This holds true for different initial stress states, also after cyclic preloading. There is a unique dependence of the asymptotic stress ratio on the prescribed strain ratio. For bigger than critical stress ratios this is

fairly well approximated by Rowe's (1962) stress-dilatancy relation (2.2.20). For the biggest stress ratios and dilatancy ratios both relations agree with each other, and also with the observed peak ratio for isobaric stretching. A more detailed evaluation is not feasible as Chu and Lo (1994) do not communicate changes of void ratios.

Critical states can principally be approached by monotonous isochoric or isobaric stretching. Shear localization can be avoided by starting with higher than critical void ratios. Verdugo and Ishihara (1996) achieved that in a tri-axial setup with a saturated quartz sand and closed or open drainage. As plotted in Fig. 2.5.3 the critical stress ratio (a) and void ratio (b) are the same for both cases. This was obtained with axial shortening independently of the initial state. With short samples ($h \approx d$) and lubricated guided end plates the observed deformations were rather uniform (Sect. 14.1). The critical stress condition (2.2.15) is thus confirmed with $q = \sigma_{s1} - \sigma_{s2}$, it yields $\varphi_c = 31^\circ$. The observed dependency of e on $\log p'$ can be well approximated by (2.4.1) for $p' (= p_s)$ from ca. 0.02 to 1 MPa with $n = 0.5$, $h_s = 400$ MPa

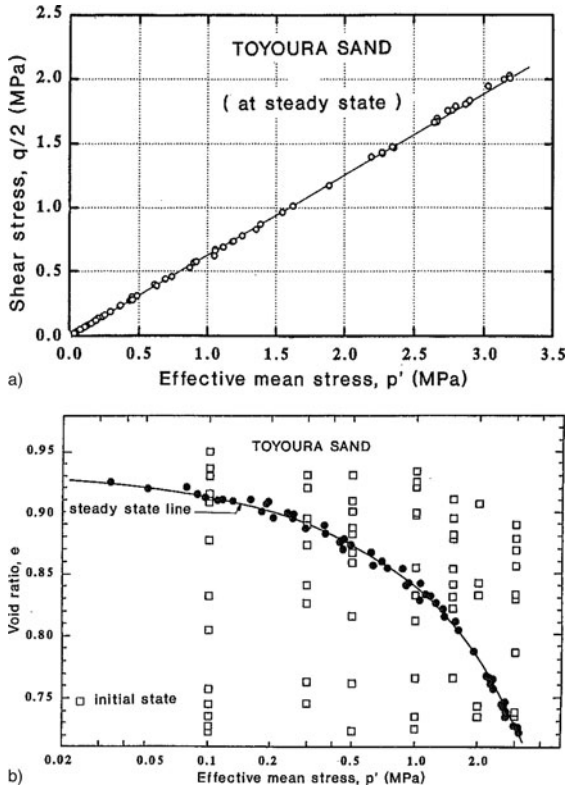


Fig. 2.5.3. Critical shear stresses (a) and void ratios (b) vs. effective mean pressure of a saturated quartz sand, from undrained triaxial tests by Verdugo and Ishihara (1996)

and $e_{co} \approx 0.96$. The highest isotropic compression line in Fig. 2.5.1, which was obtained with the same sand, is matched with the same n and h_s , and with $e_{io} = 1.06 \approx 1.2e_{co}$. This confirms (2.4.1), whereas (2.3.1) for CSSM works at best for p_s between ca. 0.2 and 1 MPa.

In the range $p_s > \text{ca. } 1 \text{ MPa}$ (2.4.1) is not apt for matching with the same parameters, whereas it serves to the purpose for isotropic compression up to ca. 4 MPa (Fig. 2.5.1). This indicates that the p_s -threshold by the degradation of grains is lower for bigger relative stress deviators $|\psi_s|$. For p_s beyond this threshold (2.3.1) enables a better matching than (2.4.1) up to ca. 50 MPa (e.g. Hirschfeld and Poulos 1963), but this is not the range of simple psammoids as then the grains are crushed (Sect. 7.3).

Miura and Toki (1982) produced asymptotic states in a triaxial setup with saturated quartz sand without drainage by axial shortening and extension, Fig. 2.5.4. For both cases the critical stress ratio can be described by (2.2.15) with nearly the same φ_c , which is thus confirmed. The same φ_c was obtained with different placement methods, i.e. there is no ‘inherent’ or ‘induced’ anisotropy (Sect. 9.1) for critical states.

So-called *peak states* were often produced in triaxial tests with monotonous isobaric stretching. With adequate boundary conditions in the sense of PR5 and PR6 spatial mean values may be used to describe peaks although shear band patterns arise already (Sects. 8.2 and 14.1). Barden and Khayatt (1966) observed nearly the same peak friction angle φ_p by (2.2.17) for axial shortening and extension with the same e and p_s , Fig. 2.5.5. Rowe’s stress-dilatancy relation (2.2.20) produces a good approximation. This confirms the concept of state limits outlined with Fig. 2.2.2. Unfortunately Barden and Khayatt do not report void ratios at peak, such data are rare in the literature. One can only conclude from Fig. 2.5.5 that the relative void ratio r_e at peak was lower

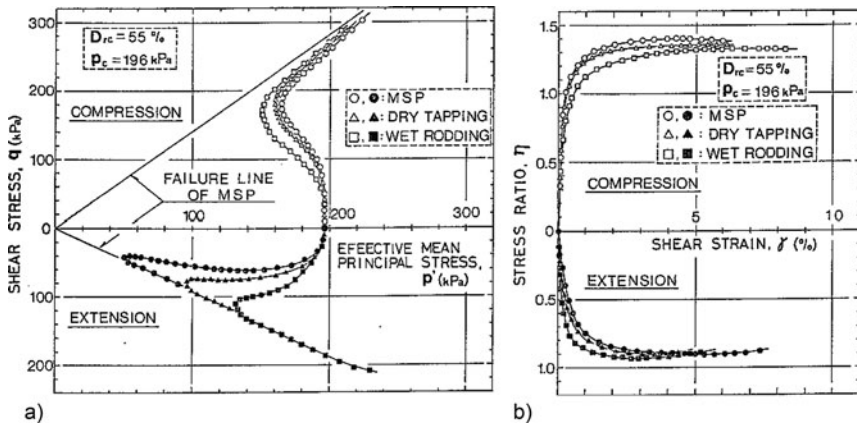


Fig. 2.5.4. Stress paths (a) and stress ratio vs. strain (b) of saturated undrained quartz sand samples in triaxial tests (Miura and Toki 1982); $q = \sigma_{s1} - \sigma_{s2}$, $p' = p_s$, $\gamma = (\varepsilon_1 - \varepsilon_2)/2$

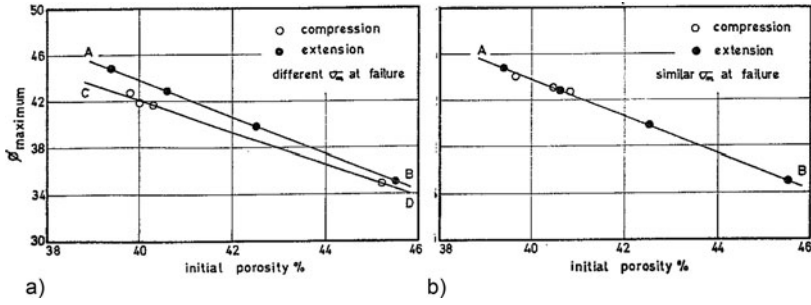


Fig. 2.5.5. Peak friction angles ($\varphi_{max} = \varphi_p$ by (2.2.17)) for different initial porosities ($n = e/(1 + e)$) in triaxial tests with different (a) or nearly equal (b) pressures ($\sigma_m = p_s$), Barden and Khayatt (1966)

for axial extension with a lower p_s (a) than with a constant p_s (b). Thus the second plot could better serve for calibration.

Triaxial tests by Lam and Tatsuoka (1988) indicate markedly different peak friction angles for axial shortening and extension, different aspect ratios h/d and different directions of σ_1 with respect to the previous placement, all that for the same relative density. Stress-dilatancy works only with different φ_c in (2.2.20). These findings seem to refute our concept of state limits, but they can be attributed to non-uniformity by placement and localization (Sects. 9.1 and 14.1) so that our prerequisites PR1 and PR6 are violated.

Cuboidal tests with plates, which will be described in Sect. 2.7, enable more uniform evolutions, in particular with cylindrical symmetry. Only Lanier et al. (1991) made such tests with an initially loose quartz sand. Stretching with constant p_s produced very flat peaks, so critical states were nearly reached. The friction angle was 30° for axial extension and 29° for shortening. This may be considered as validation of (2.2.15). Using a similar device, Goldscheider (1976) observed the peak friction angles $\varphi_p \approx 42^\circ$ for cylindrically symmetric axial shortening and $\varphi_p \approx 44^\circ$ for axial extension of a dense quartz sand. The initial void ratio was the same, but as with Fig. 2.5.5a p_s , and thus r_e , was lower at peak for axial extension than for shortening. Although void ratios at peak are not reported the small difference of φ_p may be considered as a further validation.

To *sum up*, the concept of state limits outlined for cylindrical symmetry in Sect. 2.2 is essentially validated, and its representation by hypoplasticity is more realistic than by CSSM. Bauer’s formula (2.4.1) for limit void ratios works from $p_s = 0$ up to a threshold by grain degradation, whereas the CSSM formula (2.3.1) works only in a narrower p_s -range without degradation. For a given relative void ratio peak friction angles are practically equal for axial shortening and extension. Rowe’s stress-dilatancy relation, which is approximately implied by *elp* and *hyp*, works in the vicinity of critical states. State limits can be approached by monotonous stretching in the direction sector by (2.2.16) independently of the initial state. They can be characterized by

equations of state which delimit the possible range of states. As they are driven the strain rate direction plays a decisive role. It appears that RSEs inevitably lose the defining uniformity near state limits.

2.6 Validation off state limits with cylindrical symmetry

The range of validity in case of cylindrical symmetry can be explored also off state limits with the devices and prerequisites outlined in Sect. 2.5. This will first be shown for proportional strain paths, then for monotonous isochoric and isobaric deformations. Path reversals exhibit bigger differences among CSSM, hypoplasticity and reality. They reveal that relations of stress rates with strain rates require more than the state variables σ_{s1} , σ_{s2} and e in general.

Let us first analyze again the response to *proportional compression* starting from $p_s = 0$ as shown in Sect. 2.5, but now with lower e than for state limits. Calculated e vs. $p' (= p_s)$ plots (Rebstock 2010) for the isotropic case agree pretty well with Fig. 2.5.1 when using hyp with $n = 1/2$, Fig. 2.6.1a, whereas

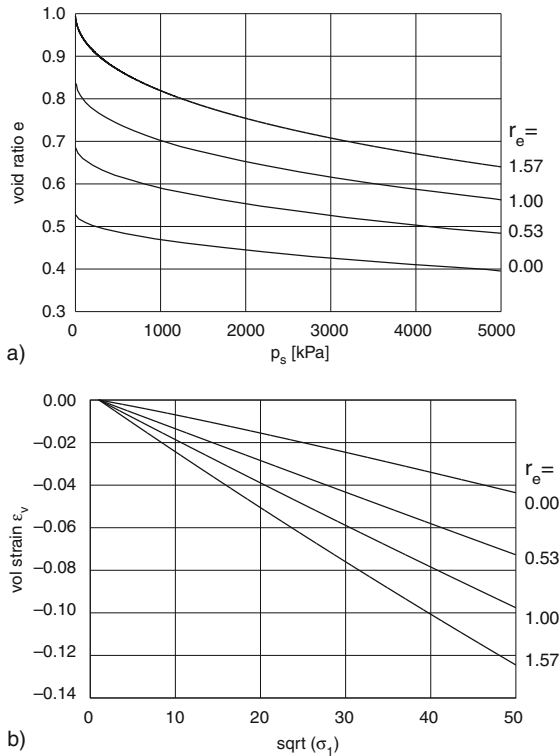


Fig. 2.6.1. Simulated compression with hyp (Rebstock 2010): (a) isotropic as by Fig. 2.5.1, (b) uniaxial as by Fig. 2.5.2

CSSM fails near $p_s = 0$. Close to $p_s = 0$ the power law (2.4.2) can be derived from (2.4.3) and (2.4.5), with the same exponent n and a bigger factor f_s for lower e , both is confirmed by Fig. 2.5.1. Good matching requires a suitable β in (2.4.5), this can thus be determined. Rather good predictions are also obtained for compression with $\varepsilon_2 = 0$ by hyp, Fig. 2.6.1b with calculated plots of ε_v vs. $\sqrt{\sigma_1}$ shows this by comparison with Fig. 2.5.2. This confirms $n \approx 1/2$.

Turning to *reversed isochoric* deformations, we can make further use of test results by Verdugo and Ishihara (1996). Figure 2.6.2 shows stress-strain curves (a) and stress paths (b) for different initial pressures and a lower than critical initial void ratio. The skeleton stress components in the nearly attained critical states are solely determined by e and φ_c as shown by Fig. 2.5.3. After the reversal the response is independent of the initial p' , this indicates that for critical states the only state variable relevant for the response is e . The ‘stiffness’ $dq/d\varepsilon_1$ and the initial reduction of p' ($= p_s$) are markedly higher for bigger initial p' . The increase of p_s is enhanced by the penetration of grains into the membrane so that the void ratio decreases, the decrease of p_s is likewise enhanced.

Stress-strain curves and stress paths calculated with hyp (Prada 2010) are shown in Fig. 2.6.2c, d. The observed onset with $dp'/d\varepsilon_1 = 0$ is not reproduced, but would be obtained with elp. The subsequent reduction of p' is

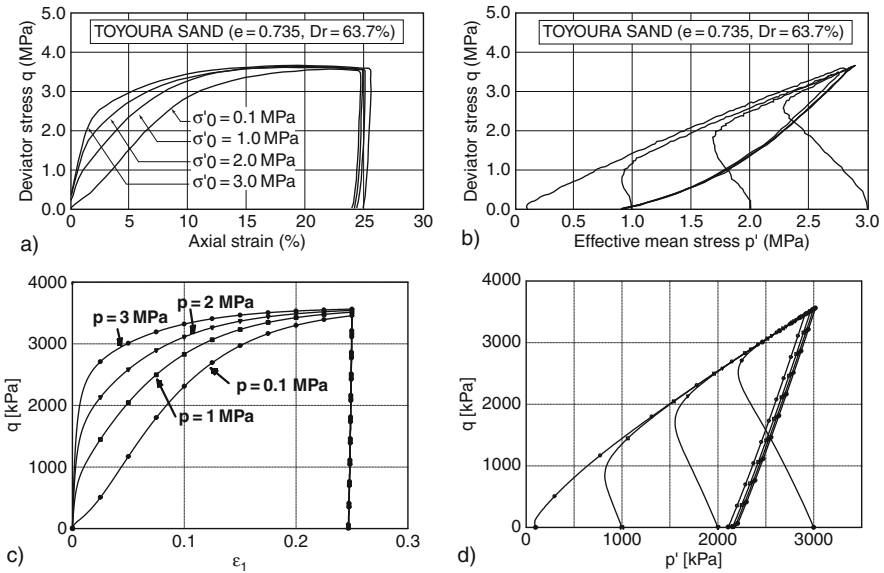


Fig. 2.6.2. Deviatoric stress-strain curves (a) and stress paths (b) of a saturated undrained quartz sand (Verdugo and Ishihara 1996), hypoplastic simulation (c and d. Prada 2010)

underestimated with hyp and cannot be reproduced by elp. The deviation can be partly attributed to the variable membrane penetration. Simply speaking, the response to monotonous isochoric deformations after a start with isotropic pressure and a lower than critical relative void ratio r_e is first rather elastoplastic and gets then rather hypoplastic, whereas close to critical states both theories work realistically. The response to a reversal from a critical state is apparently hypoelastic in the q vs. ε_1 plot, but rather hypoplastic in the stress path.

As proposed with Fig. 2.2.5 (B) the response of *loose undrained* saturated cylindrical sand samples to axial shortening implies a peak of the stress deviator $\sigma_1 - \sigma_3$. This can be seen from stress-strain curves and stress paths observed by Ishihara (1993) for rather high initial pressures. The samples bulge beyond such a peak (Sect. 14.1) so that this part should not be judged by assuming an RSE. The stress ratio at this peak is well below the so-called critical one by (2.2.15). The onset of bulging is a *critical point* far off a conventional critical state (Sect. 16.3). As indicated in Sect. 3.2 it may be related with a lack of ductility, but this notion is rather subjective. An observed p_s -increase beyond the peak indicates a slight dilation after a contraction with changing penetration of grains into the membrane, cf. Ramana and Raju (1981). Simulated stress-strain curves would have no peaks by CSSM (cf. Fig. 2.3.6a) and less marked peaks by hyp than in experiments. Peaks of deviatoric stress vs. strain could be reproduced with hyp, but not with elp. Observed purely deviatoric stress paths just after an isotropic onset could be reproduced by elp, but not by hyp.

Undrained triaxial experiments are no more feasible with very loose samples as then the skeleton tends to *decay*. This is predicted by hyp if e exceeds e_{co} in (2.4.1). After this phase transition into a suspension the lower part of a sample bulges by gravity, and simulations with psammoid relations get impossible. One may speak of a lack of ductility in the sense outlined with Fig. 2.2.6, or more vaguely of sensitivity. Evolutions near peaks could be captured by numerical simulations of a diffuse bifurcation (Sect. 14.1), but not up to a collapse with decay.

A typical response of sand to *monotonous isobaric* deformations, observed by Miura et al. (1998) in triaxial tests, can be seen in Fig. 2.6.3a. Hypoplastic simulations by Rebstock (2010) are shown in Fig. 2.6.3b. For the onset with $\sigma'_1 = \sigma'_2$ the observed initial contraction, $d\varepsilon_v/d\varepsilon_1 > 0$, is obtained with any initial relative void ratio r_e . The observed zero contraction for the critical stress ratio, $d\varepsilon_v/d\varepsilon_1 = 0$ for σ'_1/σ'_2 by (2.2.15) independently of r_e , is reproduced. The decreasing stiffness $d\tau_m/d\varepsilon_1$ prior to the peak for increasing stress obliquity $|\psi_s|$ is also reproduced by hyp. The lower attained $|\psi_s|$ for extension than for shortening is at variance with Fig. 2.5.5, it appears that both cases were mixed up by Miura et al. (1998). The continued dilation beyond peak is fairly well reproduced. A similar matching could be obtained with Vermeer's (1978, 1984) elp, but this is no proper validation as the employed deviatoric plastic strain as additional state variable is not physically tenable for repeated reversals up to state cycles.

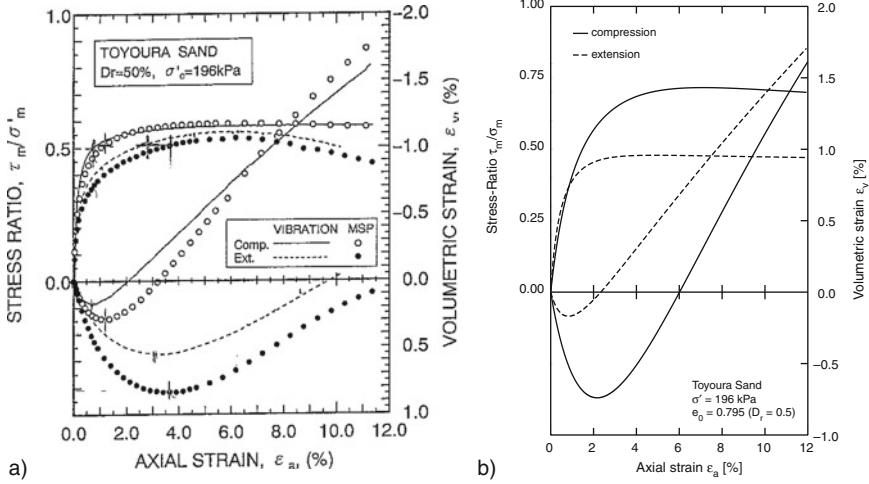


Fig. 2.6.3. Evolutions of stress ratio and volumetric strain with axial strain in drained triaxial tests and constant σ_{s2} (a) observed by Miura et al. (1998), (b) hypoplastic simulation by Rebstock (2010). $\sigma_m = p_s$, $\tau_m = |\sigma_{s1} - \sigma_{s2}|/2$, $\varepsilon_a = |\varepsilon_1|$; moderate densification by vibration or moist placement (MSP).

Lam and Tatsuoka (1988) investigated the influence of *different preparations* on the response to monotonous isobaric deformations. Prismatic quartz sand samples were pluviated with different orientations and nearly the same initial, lower than critical void ratio. For cylindrical shortening ($\sigma_{s1} > \sigma_{s2} = \sigma_{s3}$) σ_{s1} was transmitted by lubricated plates, σ_{s2} and σ_{s3} by membranes. The evolution of stress ratio σ_{s1}/σ_{s2} and volumetric strain with deviatoric strain depends on the orientation. This indicates an inherent anisotropy up to and beyond the peak. However, stress ratios and dilation are bigger for cuboidal than for flat samples, this indicates that the samples are not uniform as required for RSEs. The anisotropy can be explained by means of initial inhomogeneity and shear localization (Sect. 9.1).

Cylindrical shortening ($\sigma_{s1} < \sigma_{s2} = \sigma_{s3}$) with lubricated plates for σ_{s2} and membranes for σ_{s1} and σ_{s3} led to a wider variation of peaks and dilation with orientation and slenderness (Lam and Tatsuoka 1988). Shear bands arose beyond the peak at different sites depending on the slenderness of the sample. Then the uniformity of RSE gets evidently lost (Sect. 8.2). Shear localization occurs already prior to a peak (Sects. 8.2 and 14.1), and the inherent anisotropy can be attributed to an oriented non-homogeneity by placement (Sect. 9.1).

Drained reversals from critical or peak state limits are rarely described in ‘triaxial’ test reports, although they are usually carried out after a monotonous deformation. Jefferies (1997) imposed three cycles of deviatoric un- and reloading to dense saturated sand samples with constant lateral pressure, Fig. 2.6.4. The plot of stress ratio vs. deviatoric strain (a) looks rather elastoplastic. The

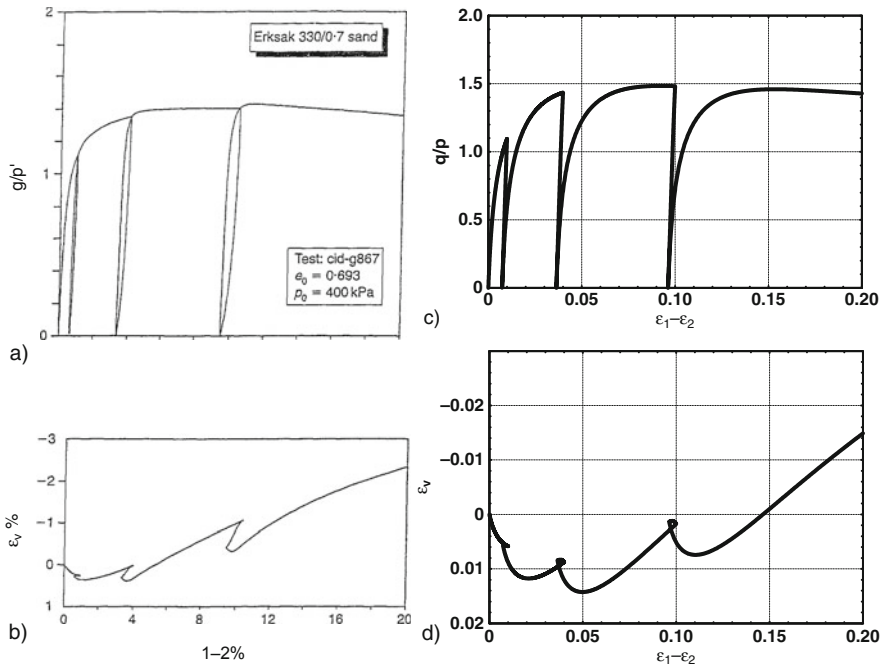


Fig. 2.6.4. Stress ratio (a) and volumetric strain (b) vs. deviatoric strain in triaxial experiments with quartz sand by Jefferies (1997), hypoplastic simulation (c and d, Prada 2010)

course of volumetric strain (b), however, exhibits contraction for deviatoric unloading and dilation for reloading. Jefferies made standard tests with slender samples and rough endplates, so his findings are biased by non-uniformities (Sect. 14.1). Wu (1992) obtained similar results with squat samples and lubricated plates, but even thus a loss of uniformity cannot be avoided near state limits (Sect. 14.1).

Plots simulated with hyp (Prada 2010) for stress ratio (c) and volumetric strain (d) vs. deviatoric strain differ substantially from the ones by Jefferies (1997). The calculated deviatoric stiffness for the second half of reloading is too low, and the contraction at the onset of unloading is missed. Simulations with elp would yield an elastic response for un- and reloading, this is more evidently refuted by Fig. 2.6.4b than by Fig. 2.6.4a. A qualitative flaw of hyp is that it produces no loop in the first plot and a loop in the second one. We will see in Sect. 4.5 that this flaw cannot be avoided with an additional hidden variable, and that the observed sharp bends at the end of reloading may be attributed to a sudden shear localization. We note that apparently familiar triaxial tests are rarely apt to judge constitutive relations, and that the ones by Jefferies (1997) do not convincingly support elp or hyp.

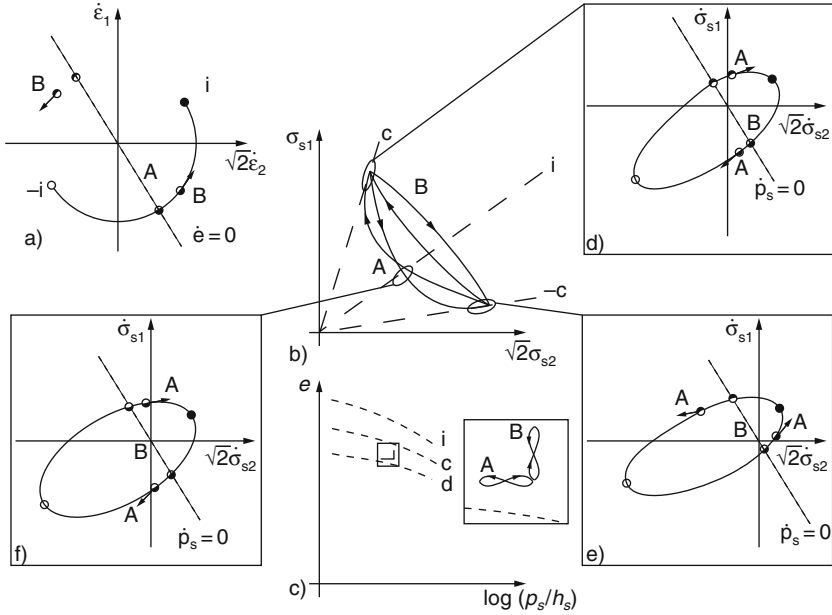


Fig. 2.6.5. Qualitative response to isochoric (A) and isobaric (B) large strain cycles: unit strain rates (a), stress paths (b), void ratio vs. pressure paths (c), response polars at upper (d) and lower reversals (e) and for $\sigma_{s1} = \sigma_{s2}$ (f)

Repeated reversals of simple psammoid RSEs will now be discussed *more geometrico* as this suffices for qualitative features known from the few acceptable experimental reports. Consider first rather large strain cycles with nearly constant void ratio e (isochoric, A) or skeleton pressure (isobaric, B), Fig. 2.6.5. ‘Rather large’ means that SOM-states are repeatedly reached by monotonous deformations between reversals so that the memory is swept out except for skeleton stress σ_{si} and e (Gudehus et al. 1977). Unit strain rates (a, moons for $\psi_{\dot{\epsilon}}$) are isochoric (A), or alternately dilatant and contractant (B, arrows for change by repetition). Stress paths (b) with response polars and e vs. $\log p_s$ paths (c) exhibit two reversals (cf. Figs. 2.2.7 and 2.2.8). According to the introduction by Fig. 2.2.4 the polars are assumed as rather hyp (cf. Fig. 2.4.2) than elp (cf. Fig. 2.3.3). Details will now be discussed by inserts and then by the sparse experimental results.

The upper reversal may be close to a critical state with $\sigma_{s1} > \sigma_{s2}$, thus the north-west point of its polar is closest to the reference point, Fig. 2.6.5d. More precisely speaking, for an isochoric deformation (A) the increase of p_s per unit of strain is bigger before the reversal than the decrease afterwards. As long as the attractor by Fig. 2.2.7 is not reached repeated strain cycles cause a gradual reduction of p_s and thus of r_e , the two isochoric points on the polar are thus shifted as indicated by arrows. For an isobaric deformation (B)

the rate of dilation ($\psi_\varepsilon > 90^\circ$) before the reversal is bigger than the rate of contraction afterwards. As long as a periodic attractor is not reached there is a gradual densification and thus again a reduction of r_e , this is indicated by arrows at the isobaric points on the unit strain rate cycle.

At the opposite reversal the south-east ($\psi_\delta = -90^\circ$) point of the response polar is closest to the reference point, Fig. 2.6.5e. The further specification for A and B is the same as above. Together with Fig. 2.6.5a this explains the stress path crossing near isotropic points and a gradual reduction of p_s for A, and a strain path crossing as in Fig. 2.2.7a (B) with a gradual reduction of e for B. One can thus see that state cycles are attained with response polars by Fig. 2.2.4, at least in case of rather big strain cycles.

Triaxial tests of this kind have not been carried out, but some reports with several stress reversals enable to judge the range of validity of the proposed asymptotic state cycles. Wichtmann (2005) imposed deviatoric stress cycles to a saturated sand. *Without drainage* alternations of $q (= \sigma_{s1} - \sigma_{s2})$ lead to a double-loop (butterfly) stress path which is only determined by e and $\max|q|$, Fig. 2.6.6a. In the transition the gradual reduction of p_s is faster without than with previous cycles. For parts of the butterfly the skeleton pressure p_s tends to zero between reversals, this indicates a temporary skeleton decay. This observed attractor is distorted and shifted due to the penetration of grains into the membrane which increases with higher p_s and reduces the void ratio. Without it the butterfly would have a bigger amplitude and a lower average of p_s .

A simulation with hyp (Fig. 2.6.6b) leads to a skewer and flatter than observed double stress cycle (butterfly) after less reversals than observed without precycling. The deviating shape of the butterfly cannot be attributed to the membrane penetration, this could be taken into account for a better validation and calibration. The influence of precycling cannot be captured by hyp.

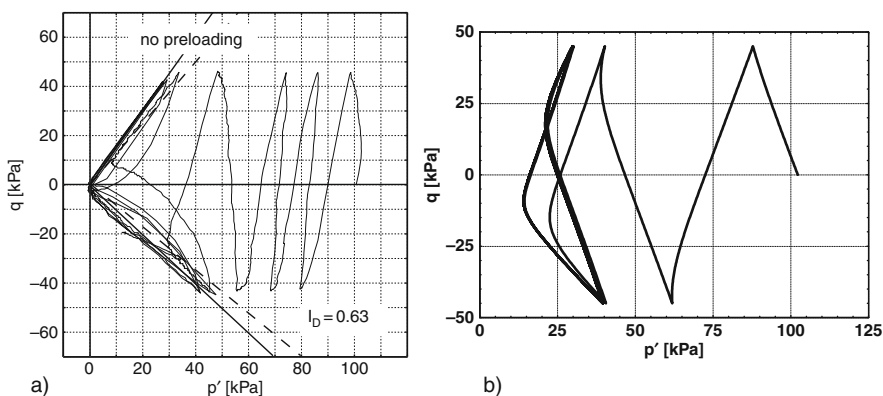


Fig. 2.6.6. Response of undrained saturated sand to an alternating stress deviator in a triaxial test (a, Wichtmann 2005), and in a hypoplastic simulation (b, Prada 2010)

We can conclude that further (internal or hidden) state variables are needed in general to capture the memory of previous reversals (Sect. 4.2). With the approach of a butterfly bigger monotonous deformations between reversals may suffice to sweep out this memory so that σ_{s1} , σ_{s2} and e suffice as state variables (SOM, Gudehus et al. 1977).

Stress cycles were imposed to saturated cylindrical sand samples *with drainage* by Luong (1982) and by Chang and Whitman (1988), and with more variants by Wichtmann (2005). If critical stress obliquities are not reached the skeleton is gradually deformed and densified, and the strain increments per cycle by hyp get smaller due to densification. No such accumulation is obtained by elp as the e -dependent elastic range is not left. The cumulative deformation is grossly overestimated by hyp, only an asymptotic void ratio near e_d is realistically obtained. One can conclude again that the memory of reversals is not swept out so much that the skeleton state is sufficiently captured by stress components and void ratio. Additional internal state variables are needed for small amplitudes to reduce the exaggerated hysteresis and double e - vs. $(\sigma_1 - \sigma_2)$ loops by hyp (Sect. 4.2).

Luong (1982) reports also on *ratcheting* ('cyclic mobility') with undrained triaxial tests, but this is no more than a qualitative finding. Hyodo et al. (1989) imposed stress deviators to undrained cylindrical quartz sand samples. With a rather dense sample ($r_e \approx 0.5$ initially) the stress path (Fig. 2.6.7a) tends to a lense as proposed in Fig. 2.2.8b, and the plot of deviator stress vs. deviator strain (b) indicates a transition to ratcheting. Loose samples decay repeatedly after a transition, the completely different diagrams are left aside therefore. A simulation with elp would produce an elastic response far off reality. hyp (Prada 2010) leads to wider stress cycles after a shorter transition than observed (c), and to an exaggerated ratcheting (d). It appears that the differential response is rather hypoplastic near maximal stress deviators, but not near isotropic states. One can again conclude that the skeleton state is not sufficiently captured by stress and void ratio only if monotonous deformations between reversals are not so big that the memory of previous reversals is swept out.

Ratcheting of cylindrical granular RSEs with stress control, particularly with constant p_s or σ_{s2} , was approached in triaxial tests as yet only with small amplitudes. This means that each forward deformation step is so small that the memory of previous reversals is not swept out (Sect. 4.2). The gradual densification or relaxation for deviatoric stress cycles with constant pressure or volume, respectively, and the cumulative deviatoric deformation is grossly overestimated by hyp and missed by elp. It will be shown in Sect. 4.3 how these lacks can be reduced by means of hidden state variables.

To *sum up*, the behavior of cylindrical psammoid RSEs can be better captured by hyp than by elp as long as deformations between reversals are not too small. Hyp works as long as the memory of previous reversals is swept out by sufficient monotonous deformations. Asymptotic state cycles by repeated strain cycles and ratcheting are at least qualitatively captured by hyp, but

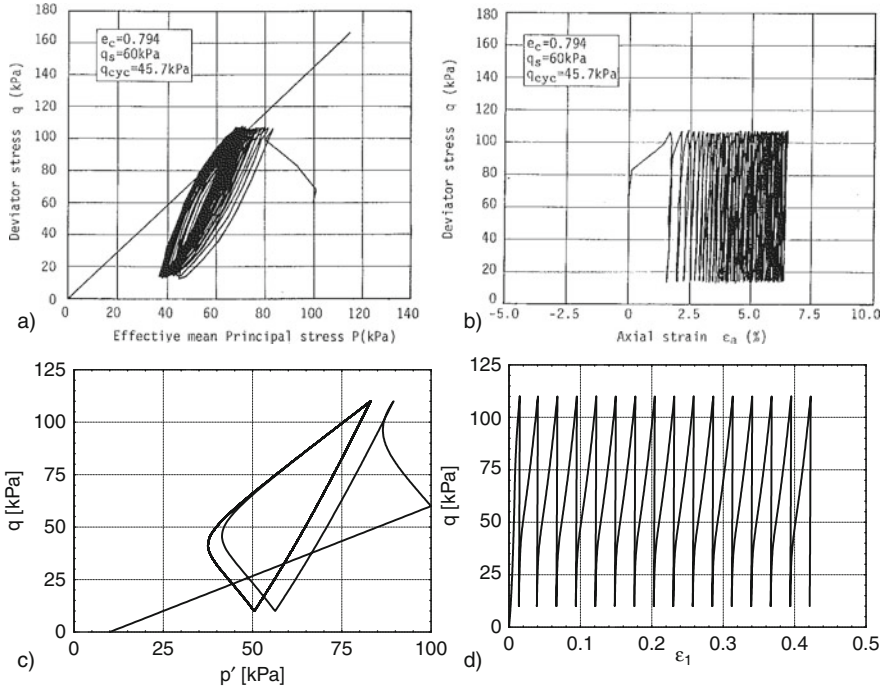


Fig. 2.6.7. Response of rather dense saturated cylindrical sand samples without drainage to a pulsating stress deviator: stress path (a) and stress-strain plot (b) observed by Hyodo et al. (1989), simulation by hyp (c and d, Prada 2010). $\epsilon_a = \epsilon_1$, $q = \sigma_1 - \sigma_2$, $p = p_s$

gradual changes of pressure or void ratio are thus overestimated. Ratcheting with small amplitudes is missed by elp and grossly over-predicted by elp. The loss of uniformity at state limits prevents a precise validation in their vicinity.

2.7 Cuboidal deformations near state limits

The three principal stress components σ_{s1} , σ_{s2} , σ_{s3} of a *cuboidal* grain skeleton may share with it the principal axes, Fig. 2.7.1a. Changes of the three edge lengths d_1 , d_2 , d_3 can be expressed as strains and strain rates by

$$\epsilon_i = \ln(d_{i0}/d_i) \quad , \quad \dot{\epsilon}_i = \dot{d}_i/d_i \quad , \quad i = 1, 2, 3. \quad (2.7.1)$$

Strain rates $\dot{\epsilon}_i$ are related with stress rates $\dot{\sigma}_{si}$, rate-independence is assumed. In a stress component space the deviator plane $p_s = \text{const}$ with the mean skeleton pressure

$$p_s = \frac{1}{3}(\sigma_{s1} + \sigma_{s2} + \sigma_{s3}) \quad (2.7.2)$$

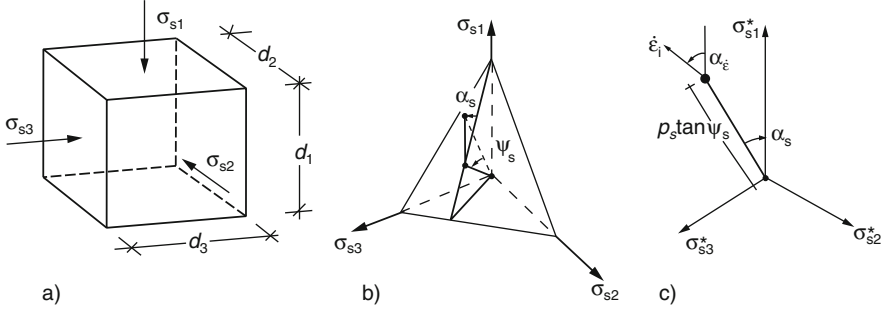


Fig. 2.7.1. Representation of three principal stress components: (a) cuboid, (b) component space, (c) deviator plane

cuts a triangle in the octant $\sigma_i \geq 0$ (b). The straight line connecting a point on it with the origin makes an angle ψ_s with the space diagonal. The straight line connecting a point $(\sigma_{s1}, \sigma_{s2}, \sigma_{s3})$ with the central point of the deviator plane makes an angle α_s with the bisectrix $\sigma_{s2} = \sigma_{s3}$ on the deviator plane.

In case of cylindrical symmetry with $\alpha_s = 0, \pm 60^\circ, \pm 120^\circ$ or $\pm 180^\circ$ p_s and ψ_s suffice to represent the skeleton stress state, state limits and evolutions can then be shown in a σ_{s1} vs. $\sqrt{2}\sigma_{s2}$ plane. Otherwise two projections are needed. The one onto a deviator plane shows α_s and ψ_s , Fig. 2.7.1c. Assuming e and $\sigma_{s1}, \sigma_{s2}, \sigma_{s3}$ to be sufficient state variables for simple psammoids, an interchange of the labels 1,2,3 does not matter due to frame-indifference (Sect. 1.2). One can see from Fig. 2.7.1 that $p_s, \cos 3\alpha_s$ and $\tan \psi_s$ are invariant with respect to this interchange. Thus the sector $0 \leq \alpha_s \leq 60^\circ$ suffices for representation. Analogous angles ψ_ε and α_ε can be defined for strain rates by means of the volumetric strain rate

$$\dot{\varepsilon}_v = \dot{\varepsilon}_1 + \dot{\varepsilon}_2 + \dot{\varepsilon}_3 \quad . \quad (2.7.3)$$

It can be of use to plot the deviatoric strain rate direction α_ε in the stress deviator plane.

The concept of *state limits*, introduced in Sect. 2.2 for cylindrical symmetry, can be extended as shown in Fig. 2.7.2. In a deviator plane (a) α_s and α_ε , as by Fig. 2.7.1, appear for states with equal r_e -dependent peak friction angles by (2.2.17). In a plot of $\cos 3\alpha_\varepsilon$ vs. $\cos 3\alpha_s$ (b) the influence of r_e may be neglected. The two lines of ψ_ε vs. ψ_s (c) for $\alpha_s = 0^\circ$ and 60° suffice as the interpolation is monotonous. The same holds true for the plot of r_e vs. ψ_s (d). Apart from the only positive sign of ψ_s by Fig. 2.7.1c the curves in Fig. 2.7.2c, d are the same as in Fig. 2.2.2a, c, this is indicated by the labels i, $\pm c$ and $\pm d$. Contractant state limits with $r_e > 1$ and dilatant ones with $r_e < 1$ are defined as for cylindrical symmetry, but now with related α_s and α_ε in the range from 0 to 60° via Fig. 2.7.2b, c.

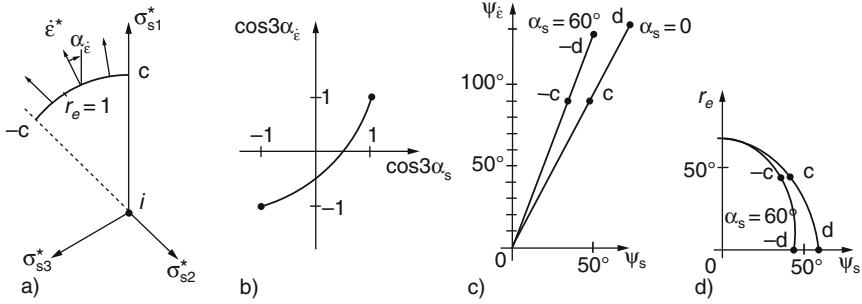


Fig. 2.7.2. State limits of a cuboidal psammoid RSE: (a) deviator plane, (b) relation of deviatoric invariants, (c) relation of strain rate and stress obliquities, (d) relative void ratio vs. stress obliquity

Biaxial deformations are defined by fixing one edge length of a cuboid, say $\varepsilon_2 = 0$. With this choice critical states have $\dot{\varepsilon}_1 = -\dot{\varepsilon}_3$, this means $\alpha_\varepsilon = 30^\circ$ and $\cos 3\alpha_\varepsilon = 0$ for any choice of axes. Then $\cos 3\alpha_s > 0$ can be read from Fig. 2.7.2b, i.e. $\alpha_s < 30^\circ$ holds for our choice of axes. A biaxial critical friction angle φ_{cb} can be defined by

$$(\sigma_{s1} - \sigma_{s2})_c^2 / (\sigma_{s1} + \sigma_{s2})_c^2 = \sin^2 \varphi_{cb}, \quad (2.7.4)$$

formally as φ_c for cylindrical symmetry by (2.2.15). Mohr (1914) assumed φ to be independent of α_s , this means a straight line in the deviator plot instead of the arc in Fig. 2.7.2a.

Biaxial peak states imply dilatancy, i.e. $\dot{\varepsilon}_1 + \dot{\varepsilon}_3 < 0$, and thus $\cos 3\alpha_\varepsilon > 0$. A biaxial peak friction angle φ_{pb} can be defined for them by

$$(\sigma_{s1} - \sigma_{s2})_p^2 / (\sigma_{s1} + \sigma_{s2})_p^2 = \sin^2 \varphi_{pb} \quad (2.7.5)$$

as φ_p by (2.2.17) for cylindrical symmetry, it is slightly bigger than φ_p for the same r_e . Similarly as (2.2.20) Rowe's (1962) *stress-dilatancy* relation can be written as

$$\dot{\varepsilon}_1^p / \dot{\varepsilon}_3^p = -\tan^2(45^\circ \mp \varphi_{cb}/2) \sigma_{s3} / \sigma_{s1} \quad (2.7.6)$$

with $-$ for $\dot{\varepsilon}_1 > 0$ and $+$ for $\dot{\varepsilon}_1 < 0$. This renders possible interpolations between critical and extremely dilatant state limits.

Cuboidal state limits should not be confused with so-called *failure conditions*, Fig. 2.7.3. Leaving aside the inherent anisotropy, the former can be represented in one sixth of a deviatoric stress plane (a). It is a straight line for the so-called Mohr-Coulomb condition, then the stress circles for a given p_s (b) have a tangent whose slope φ_p does not depend on the intermediate principal stress. Based on tests (some of which will be outlined below) variants of rounded envelopes have been proposed, with them φ_p is bigger for biaxial

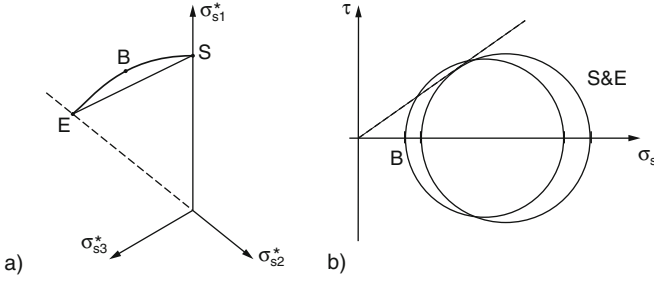


Fig. 2.7.3. Cuboidal ‘failure’ conditions in a deviator plane (a), and with stress circles (b), in particular for axi-symmetric extension (E) and shortening (S) or biaxial deformation (B)

deformations (B) than for axial shortening (S) and extension (E) with the same p_s and two equal stress components. As with ‘triaxial’ tests (Fig. 2.2.3) the loss of uniformity and changes of the relative void ratio r_e in cuboidal tests up to peak (=failure) are often ignored. Similarly as in Fig. 2.2.3c, f the average \bar{r}_e is rarely equal for a set of peak states, this is thus not apt for a proper validation of state limits.

Different extensions from cylindrical symmetry to cuboidal deformations have been proposed for *elastoplastic relations* (elp) with volumetric hardening in the framework of CSSM. Limit void ratios are taken by (2.3.1), *OCR* by (2.3.3) is normally used instead of r_e , both with p_s by (2.7.2). The stress condition for critical states can be written as

$$\tan \psi_s = \tan \psi_{sc} = f_c(\cos 3\alpha_s, \varphi_c) \tag{2.7.7}$$

with a function f_c representing the curve in Fig. 2.7.4a. In earlier versions of CSSM a bigger $\tan \psi_c$ by (2.2.15) was assumed for $\alpha_s = 90^\circ$ than for $\alpha_s = 0$. In improved CSSM versions ψ_s depends on φ_c by (2.2.15) for $\alpha_s = 0$ and 60° , i.e. the same critical friction angle holds for cylindrical shortening and

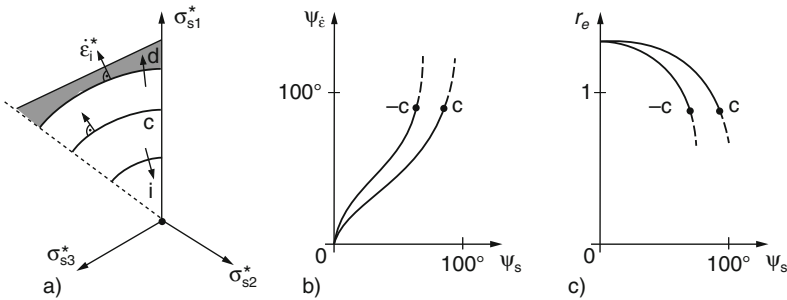


Fig. 2.7.4. State limits by CSSM: (a) deviator plane, (b) obliquities of strain rate and stress, (c) relative void ratios vs. stress obliquity (range with tension dotted)

lengthening. An associated *deviatoric flow rule*, as shown in Fig. 2.7.4a, can be represented by

$$\cos \alpha_{\dot{\epsilon}} = f_{\alpha}(\cos 3\alpha_s) \quad (2.7.8)$$

with a function f_{α} . $OCR = 1$ holds for isotropic first compression, and $OCR \approx 2$ for critical states.

Contractant state limits occur in the range $1 \leq OCR < \text{ca. } 2$, $0 \leq \tan \psi_s < \tan \psi_{sc}$ and $0 < \cos 3\alpha_{\dot{\epsilon}}$. Dilatant state limits by CSSM have $OCR > \text{ca. } 2$ and $\psi_{\dot{\epsilon}} > 90^\circ$. As shown in Fig. 2.7.4a a deviatoric flow rule with normality was repeatedly assumed, also for critical states and for proportional compressions with $OCR < \text{ca. } 2$. For big OCR tensile stresses can occur in some CSSM-versions, they are excluded by a cut-off for $\sigma_{si} \leq 0$. Tensile stresses lie outside the pyramid in Fig. 2.7.1b by (2.2.4), i.e. outside a straight line in the sector $0 \leq \alpha_s \leq 60^\circ$ of a deviator plane (Fig. 2.7.4a). Cross sections through the space diagonal exhibit state boundary lines as in Fig. 2.3.2a or b. For arbitrary α_s and constant void ratio e they represent a *state boundary surface*, this changes with e as outlined in Sect. 2.3. CSSM-versions with a tension cut-off imply similar plots of ψ_{ϵ} and r_e vs. ψ_s in the sector $0 \leq \alpha_s \leq 60^\circ$ as by Fig. 2.7.2c, d, but without the extreme state limits labelled $\pm d$ (Fig. 2.7.4b, c, dotted for tensile stress).

Transitions to state limits and *response polars* by CSSM are shown in Fig. 2.7.5. Therein planes appear uniformly grey and convex surfaces have a graded grey for giving a three-dimensional impression. The straight deformation paths (a) may be contractant (A), isochoric (B) and dilatant (C), now with other deviatoric directions than for cylindrical symmetry. These directions appear as points on the sphere $D = \sqrt{\dot{\epsilon}_1^2 + \dot{\epsilon}_2^2 + \dot{\epsilon}_3^2} = 1$ above, on and below the circle $\dot{\epsilon}_1 + \dot{\epsilon}_2 + \dot{\epsilon}_3 = 0$ (b). In the stress component space the state boundary surface is cut along the i-line $\sigma_{s1} = \sigma_{s2} = \sigma_{s3}$ and by the plane $p_s = \text{const}$ for critical states with a constant e (c). The chosen bullet shape corresponds to the state boundary line in Fig. 2.3.2b for $\alpha_s = 0$ and 60° , the extension of Fig. 2.3.2a would require a tension cut-off.

For a starting point 0 in the assumed elastic range, i.e. inside the bullet for the initial e , the response polar is a centric rotational ellipsoid (Fig. 2.7.5d). With the hypoelastic relation (2.3.5) it has the same shape and alignment throughout the elastic range, and its size changes in proportion with p_s . Thus the stress paths can be straight until the boundary surface is reached (0–1). Then the polars consist of an elastic half-ellipsoid and a flatter anelastic cap. With contraction the polar with a convex cap widens (e), and the stress path tends to a straight line with increasing p_s (A). Without volume change the cap gets flatter (f) until a stationary critical state is reached (B). With dilation the polar with a concave cap shrinks (g) and the stress path tends to a straight line with decreasing p_s (C). The latter attractor could not be achieved with a rounded state boundary surface near the origin. The void ratios tend to the state limit values shown in Fig. 2.3.4c as the latter do not depend on α_s .

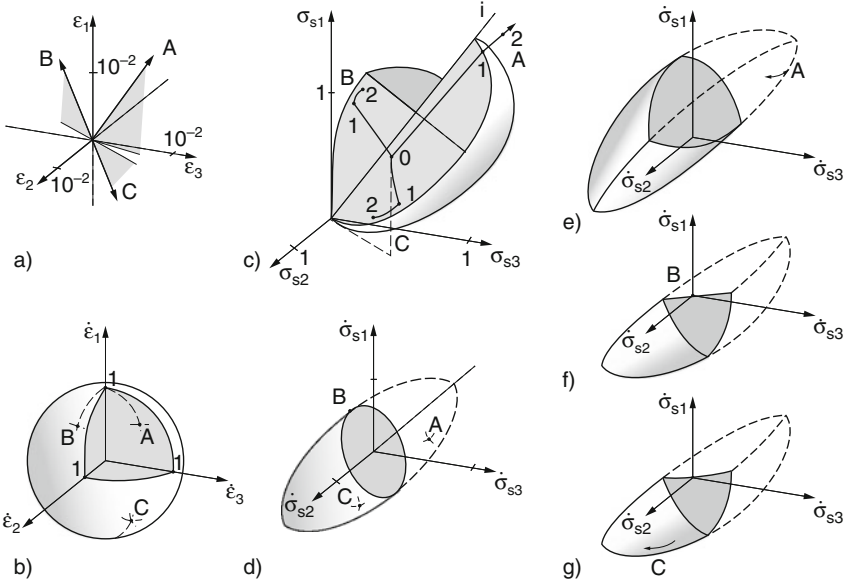


Fig. 2.7.5. Approach to state limits by CSSM (with a bullet-like elastic range): (a) strain paths, (b) strain rate directions, (c) stress space with state boundary surface and paths; response polars for onset (d) and contraction (e), and for isochoric (f) and dilatant (g) state limits

Extending (2.4.3) to three components, simple *hypoplastic* relations can be written as

$$\dot{\sigma}_{si} = f_s(L_{ij}\dot{\epsilon}_j - f_d N_i D) \quad (2.7.9)$$

with $i = 1, 2, 3$ and summation for repeated $j = 1, 2, 3$. Therein the modulus of strain rate is

$$D = \sqrt{\dot{\epsilon}_1^2 + \dot{\epsilon}_2^2 + \dot{\epsilon}_3^2} \quad (2.7.10)$$

The factors f_d and f_s depend on p_s and on e via (2.4.4) and (2.4.5). L_{ij} and N_i depend on ψ_s and α_s with φ_c as material parameter, representations were proposed e.g. by Gudehus (1996) and von Wolffersdorff (1996).

Relations between $\psi_s, \psi_{\dot{\epsilon}}, \alpha_s, \alpha_{\dot{\epsilon}}$ and r_e can be derived from (2.7.9) as follows. For critical states $\dot{\epsilon}_v = 0$ and $r_e = 1$ hold by definition, and $\dot{\sigma}_{si} = 0$ holds for $D > 0$. $\dot{\epsilon}_v = 0$ means $\psi_{\dot{\epsilon}} = \pm 90^\circ$, for any assumed $\alpha_{\dot{\epsilon}}$ the ψ_s and α_s can be calculated from (2.7.9). Peak states, which are close to dilatant state limits, have also $\dot{\sigma}_{si} = 0$ for $D > 0$, but $\dot{\epsilon}_v < 0$ and $r_e < 1$. Assuming any $\alpha_{\dot{\epsilon}}$ and an $r_e > 0$ one can calculate ψ_s, α_s and $\psi_{\dot{\epsilon}}$ from (2.7.9) with $\dot{\sigma}_{si} = 0$. For contractant state limits $\dot{\sigma}_{si}/\dot{\sigma}_{sj} = \sigma_{si}/\sigma_{sj}$ holds by definition,

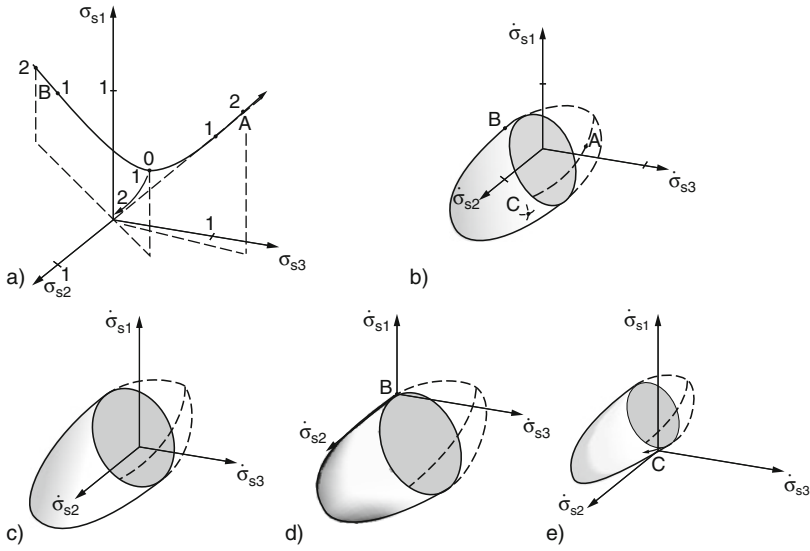


Fig. 2.7.6. Approach to state limits by hyp with strain paths as by Fig. 2.7.5a, b: stress paths (a), response polars for the onset (b) and near contractant (c), isochoric (d) and dilatant (e) state limits

and $r_e = \text{const} > 1$. This suffices to calculate ψ_s , α_s and r_e for any assumed strain path direction $\psi_{\dot{\epsilon}} < 90^\circ$ and $\alpha_{\dot{\epsilon}}$. Typical relations are shown in Fig. 2.7.2 which was used for introduction.

The *approach to state limits* and *response polars* by hyp are shown in Fig. 2.7.6. Strain paths and their directions may be the same as in Fig. 2.7.5a and b, stress paths (a) may start from the same point. The relative void ratios evolve as in Fig. 2.4.3c with negligible influence of α_s . The response polars are eccentric ellipsoids, labels for r_e are dropped for simplicity. They steer the stress paths from the very beginning. In case of contraction (A) the polars align the stress path with increasing p_s . Without volume change (B) the polars steer the stress path towards a critical state. With dilation (C) the polars align the stress path with decreasing p_s . A kind of state boundary surface could be constructed for state limits with constant e , but it is not needed for showing the approach to attractors.

True triaxial tests of three kinds are principally apt for validation, Fig. 2.7.7. Stress control by six pressurized membranes (a) requires separating edges, but these prohibit uniform large deformations. At best fairly uniform peak states can thus be approached, but no critical states. A better uniformity can be achieved by six nested and mutually guided smooth plates (b, Goldscheider and Gudehus, 1973). Rather uniform peak states may thus be attained, but in their vicinity shear localizations cannot be prevented (Sect. 8.2). Uniform critical states may be approached if e is high at the onset. Mixed devices with two oversized and two undersized plates and a pressurized membrane at two

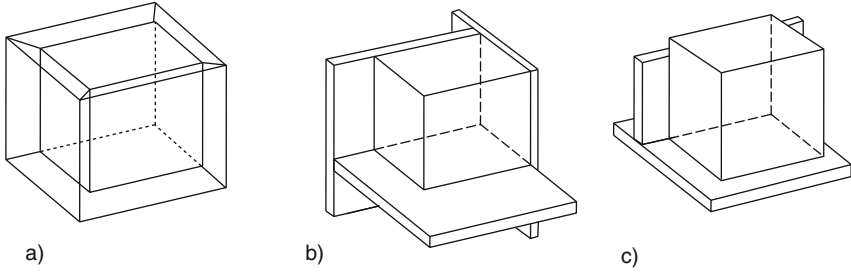


Fig. 2.7.7. True triaxial devices with (a) membranes and fixed edges, (b) nested plates (without top plate), (c) membranes and plates (two of them omitted)

faces (c) can at best produce fairly uniform small deformations up to peak. The penetration of grains into the membrane by up to about one third of a grain diameter should be taken into account.

Biaxial tests keep one edge length of a cuboidal sample constant via two fixed plates with membrane and lubrication, Fig. 2.7.8. With two mutually guided plates and two pressurized membranes (a) plane deformations can be rather uniform up to peak. With four mutually guided plates (b), smooth with membrane and lubrication, bigger uniform deformations are possible. With both devices shear localizations cannot be avoided near a peak (Sect. 8.2).

True triaxial tests are more expensive than biaxial ones, and much more than ‘triaxial’ tests. So they have rarely been made, and the few available reports are often incomplete. For all that such results are important for validation, in particular with respect to state limits, as the deformations can be more uniform than with ‘triaxial’ tests. The prerequisites PR1 to PR6 outlined at the beginning of Sect. 2.5 have to be kept in mind as with cylindrical symmetry.

Lanier et al. (1991) report on cuboidal tests with a quartz sand in a device as by Fig. 2.7.7b. Some tests with $\sigma_{s2} = \sigma_{s3} = 0.5$ MPa and $\varepsilon_1 < 0$ (Fig. 2.7.9)

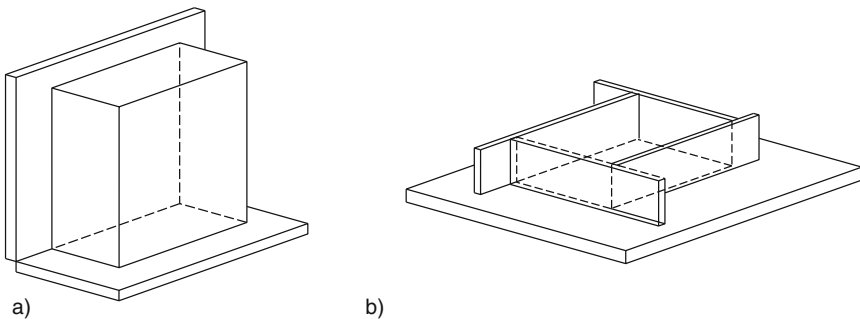


Fig. 2.7.8. Biaxial devices with (a) membranes and plates (without front and top plate), (b) nested plates (without top plate)

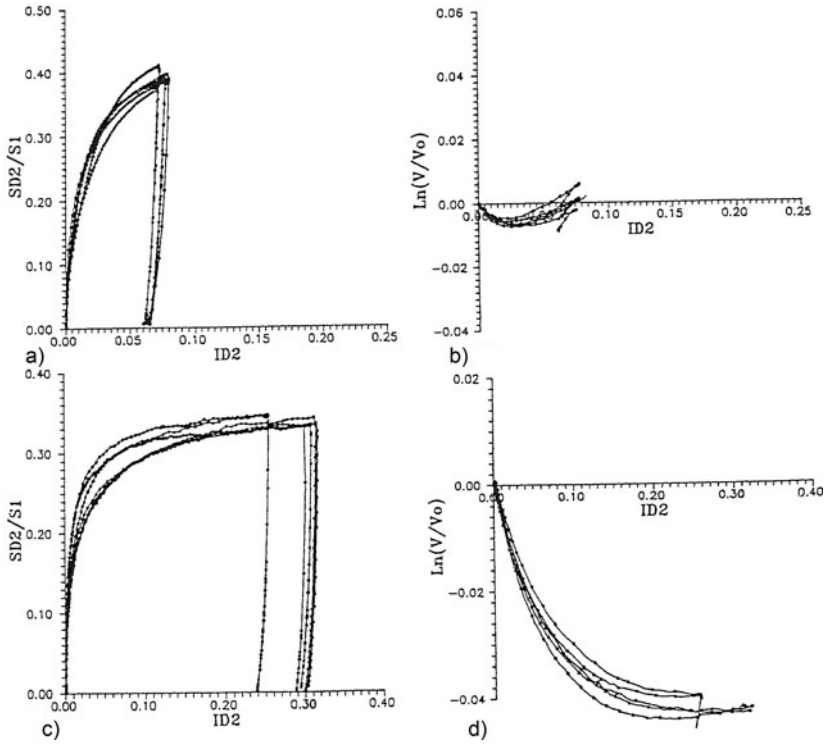


Fig. 2.7.9. Cuboidal test results by Lanier et al. (1991) with a differently bedded saturated quartz sand at $\sigma_{s1} = \sigma_{s2} = 0.5$ MPa and $\varepsilon_1 < 0$. Stress ratio and volume vs. strain deviator for dense (a, b) and loose samples (c, d)

exhibit a good repeatability of stress ratio and volume change vs. deviatoric strain with dense (a, b) and loose samples (c, d). These curves could be better matched by hyp than by elp, but they differ substantially for different orientations with respect to the bedding plane of placement. Dilatancy and stress ratios towards state limits get independent of the initial anisotropy (Sect. 9.1). As outlined in Sect. 2.5 loose samples yielded almost the same φ_c for cylindrically symmetric shortening and lengthening.

The memory of placement direction is also swept out by monotonous *isochoric* deformations (Lanier et al. 1991) from stress paths and stress ratio vs. strain deviator curves for axial shortening and lengthening with dense sand and $\sigma_{s2} = \sigma_{s3}$. The transitions cannot be matched with elp or hyp as both do not imply an inherent anisotropy (Sect. 9.1), but state limits as attractors are confirmed.

More cuboidal test results are available for peak states. Goldscheider (1976) observed relations of $\tan \psi_s$ with α_s and of $\alpha_{\dot{\varepsilon}}$ with α_s with a dense dry sand in a device as by Figs. 2.7.7b, 2.7.10a and b. Values of $\psi_{\dot{\varepsilon}}$ and e at peak are not given in the same publication, only one $\psi_{\dot{\varepsilon}}$ for one α_s is given

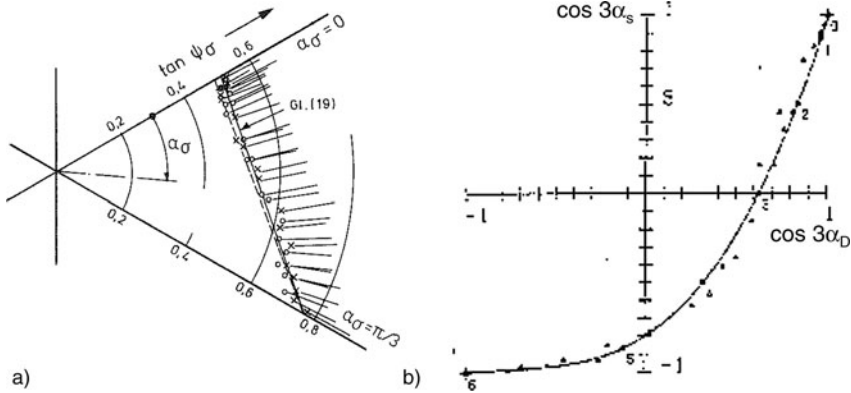


Fig. 2.7.10. Cuboidal test results by Goldscheider (1976) with a dense dry quartz sand at constant p_s : (a) stress obliquities and strain rate directions at peak, (b) Lode invariant of stress vs. the one of strain rate

elsewhere (Goldscheider 1975). With estimated void ratios, limit values e_c and e_d by (2.4.1) and data for the same sand $r_e \approx 0.4$ is obtained, but this is not precisely the same for the different peak states attained with the same initial r_e and constant p_s . Biaxial test results (type Fig. 2.7.8a) by Vardoulakis et al. (1978) with the same sand and about the same r_e yield nearly the same ψ_s for plane strains as by Fig. 2.7.10.

Other reports on peak states of sands do not render possible such precise conclusions. Arthur and Menzies (1972) worked with a device as by Fig. 2.7.7a and found that the orientation of the initial deposition of a dense sand influenced the stress obliquity ψ_s at peak by no more than $\pm 1^\circ$. Lam and Tatsuoka (1988) observed a bigger influence of the initial bedding direction on peak stress ratios and dilation ratios with a dense quartz sand in a device as by Fig. 2.7.7c. It appears, however, that the deformations near a peak were not uniform enough to disprove our concept of state limits without inherent anisotropy.

Lade and Duncan (1973) produced peak states with sand in a device as by Fig. 2.7.7a. The stress obliquity $\tan \psi_s$ depends on the deviatoric direction α_s (Fig. 2.7.11a), this could be expressed by peak friction angles φ_p . This depends markedly on e , but the latter is not the one of the onset. The plotted directions of deviatoric strain rates are nearly normal to the peak deviator curve. Ibsen and Praastrup (2002) observed $\tan \psi_s$ vs. α_s for peak states (Fig. 2.7.11b), and a reduction of ψ_s for higher p_s with a quartz sand in a device as by Fig. 2.7.6b. An influence of the bedding direction is visible, but not so strong that our concept of state limits is refuted. Relative void ratios r_e at peak cannot be concluded from the report, they were certainly not equal for all peaks. It appears that the inherent anisotropy was stronger than in Goldscheider's (1976) tests. Note, however, that peak states can at best come close to dilatant state

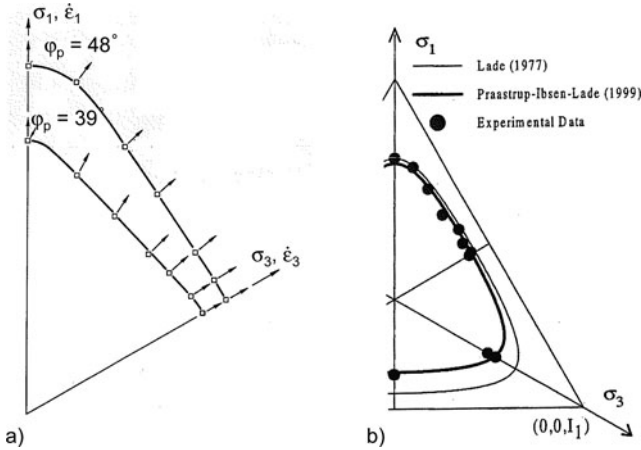


Fig. 2.7.11. Observed peak stress states of sand in a deviator plane; (a) by Lade and Duncan (1973), (b) by Ibsen and Praastrup (2002)

limits, and can be influenced by shear bands which depend on the orientation of placement (Sects. 8.2 and 9.1).

In a seminar talk 1982 Goldscheider (we have the manuscript) reported on cuboidal experiments where *extremely dilatant* state limits were approached. Dense dry sand samples were first brought to a stress state with $\sigma_{s2} > \sigma_{s1} = \sigma_{s3}$ and a slight densification. A reversed proportional deformation path was then imposed with $\epsilon_2 \approx \epsilon_3 \approx 0$ and dilation. The stress path tended to a straight line with a direction as for state limits. These states exhibit higher stress obliquities $\tan \psi_s$ than for the peak states shown in Figs. 2.7.10 and 2.7.11. Although relative void ratios r_e are not precisely known it appears that these states come close to state limits by Fig. 2.7.2 with an uncommonly high dilation. It would not make sense to characterize them by peak friction angles. Goldscheider mentions that eccentric normal forces observed at the plates indicate shear localizations (cf. Sect. 8.2).

Biaxial tests were less often carried out with sand than cuboidal ones although they are less expensive. Cornforth (1964) built a device as by Fig. 2.7.8a and produced different initial densities by a vibrator at the base, this led to uniform and rather isotropic saturated sand samples. In a typical drained test with medium density both major and intermediate principal stress go through a peak. A marked shear band arises at peak (Sect. 8.2) so that strains beyond it differ substantially from spatial averages. The void ratio decreases first and increases then, with a maximal dilation ratio $\dot{\epsilon}_v/\dot{\epsilon}_1$ at peak. This evolution could be matched by hyp, but not by elp.

Peak friction angles, volumetric and axial strains were thus determined for different initial porosities ($n = e/(1 - e)$), and compared with ‘triaxial’ test results with the same sand. These findings could be matched with elp or hyp, peak friction angles could also be reproduced by elp. Results by Tatsuoka et al.

(1990) with a device as by Fig. 2.7.8a, however, exhibit a marked influence of the bedding direction on peak values (cf. Fig. 2.6.5). This inherent anisotropy can be attributed to a sandwich fabric and arising shear bands (Sect. 9.1).

To *sum up*, cuboidal deformations of granular samples in the vicinity of state limits can be captured by simple psammoid models, better by hyp than by elp, but only few test reports reveal the range of validity. An approach to state limits by proportional strain paths was rarely observed. Observed peak states are debatable substitutes of dilatant state limits as their relative void ratio was rarely reported, and because of shear localization. The anisotropy by placement can be swept out by uniform deformations or increased by shear localization.

2.8 Cuboidal deformations off state limits

Aiming at uniformity, cuboidal and biaxial devices as by Figs. 2.7.7b and 2.7.8b were first built in Cambridge and used with clay (Roscoe 1970, more in Sect. 2.7). The first device of this kind for sand was built and used in Karlsruhe (Goldscheider and Gudehus 1973). It took some time to achieve controlled evolutions with a correction for the penetration of grains into the membrane, and with reversals a precise control turned out impossible. One morning the technician told me that he had started a test with an error, but corrected it without opening the device so that the error could not be detected. Thereafter Goldscheider (1975) discovered that proportional deformation paths lead to proportional stress paths independently of the initial stress, and that isobaric reversals cause a stronger contractancy than the previous dilatancy. On this base I postulated a *swept-out of memory* (SOM) by big enough monotonous deformations so that the skeleton state is sufficiently characterized by stress components and void ratio (Gudehus et al. 1977).

Proportional stress paths were again attained with proportional deformations by Goldscheider (1984), later also by Lanier et al. (1991) and by Chu and Lo (1994). SOM-states were attained with dense sand samples and so that limit void ratios were not reached, they are thus attractors *but no state limits*. More precisely speaking, the response for a succession of SOM-states can be captured by constitutive relations of the type

$$\dot{\sigma}_{si} = f_i(\sigma_{sj}, e, \dot{\epsilon}_j) \quad (2.8.1)$$

with $i, j = 1, 2, 3$ for cuboidal RSEs. This extension of (2.2.13) means that internal variables are not needed for simple psammoids. The void ratio is needed except for state limits where it is determined by p_s , ψ_s and α_s . The functions f_i can be represented algebraically, e.g. by elastoplastic or hypoplastic relations, or graphically by response polars. One can see from Figs. 2.7.5 and 2.7.6 that elp and hyp are similar for the approach to state limits, but less just after reversals and definitely not off state limits. We will see in the sequel how well

elp and hyp are confirmed by cuboidal test results off state limits, and when (2.8.1) cannot suffice.

Reversals from SOM-states were observed in some cuboidal tests as by Fig. 2.7.7b. Goldscheider (1975) observed that even dense dry sand contracts after isobaric reversals and that its p_s is reduced just after isochoric reversals. The same is obtained with hyp as can be seen with response polars (Fig. 2.7.5), but not with elp (Fig. 2.7.4). Later results with dense dry sand by Goldscheider (1984) are better apt for quantification. The samples were first isotropically compressed with 1 MPa and then decompressed to improve their homogeneity and isotropy. Results of a test with an isochoric reversal are shown in Fig. 2.8.1. Starting from $p_s \approx 0$ the sample was first compacted with $\sigma_{s2} = \sigma_{s3}$, then deformed with constant volume and reversed $\dot{\epsilon}_1$. The deviatoric strain path (c) and the plot of volume change vs. strain path length (d) consist of two nearly straight sections. The stress path in the deviator plane (a) and the plot of mean stress vs. deviator (b) is first also straight as with $p_s = 0$ at the onset. After the reversal the stress path bends before reaching a straight line, and exhibits a loop in one projection.

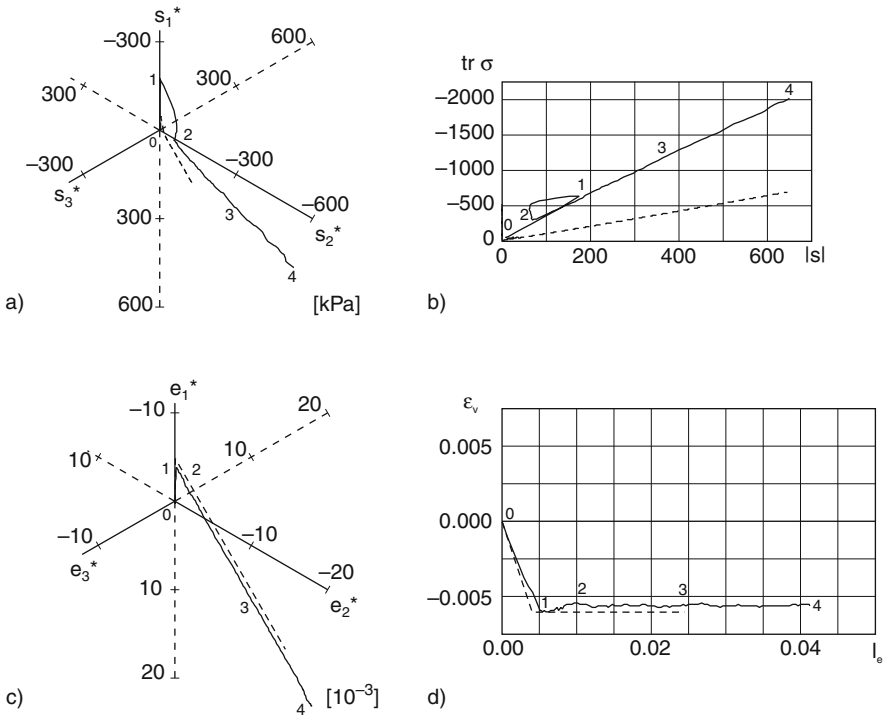


Fig. 2.8.1. Cuboidal test with dense dry sand by Goldscheider (1984): stress paths in a deviator plane (a) and in a plane through the space diagonal (b), deviatoric strain path (c) and volumetric strain vs. strain path length (d). Replotted and simulated with hyp (dotted lines) by Rebstock (2010)

A simulation with hyp, also plotted in Fig. 2.8.1, was carried out by Rebstock (2010) with smooth strain paths. It leads to a radial stress path after the reversal, but not quite with the observed directions and with other onsets (a, b). The latter may be attributed to the homogenization by isotropic prestressing which cannot be simulated by means of an RSE. The observed zig-zag cannot be reproduced, it results from manual corrections for the penetration of grains into the membrane and eludes a precise control.

Yamada and Ishihara (1982) tested *loose saturated undrained* sand samples with *one reversal* in a device as by Fig. 2.7.7a. Other than in Goldscheider's (1984) tests their samples were initially anisotropic by placement, and the changing penetration of grains into the membranes was not compensated. In three of their tests with nearly the same e and $\alpha_s = 30^\circ$, the angle between the major σ_{si} and the direction of sedimentation was $\theta = 30^\circ, 90^\circ$ and 150° . The stress paths depend markedly on θ . As with cylindrical samples they start with $\dot{p}_s = 0$, go on with $\dot{p}_s < 0$ and exhibit then $\dot{p}_s > 0$ with nearly constant obliquity. The latter can be attributed to a slight dilation by membrane penetration. The plots of ε_i vs. stress obliquity are different for $\theta = 30^\circ, 90^\circ$ and 150° . They do not reach a peak as in Fig. 2.6.3a, and indicate that nearly the same $\tan \psi_s$ is attained with bigger strains for $\theta = 90^\circ$ than for 30° and 150° .

This *inherent anisotropy* by placement is presumably due to a sandwich-like pattern of initial void ratios, the grains are too squat for preferred orientations (Sect. 9.1). With the reported strains of up to ± 0.02 the edges in the device by Fig. 2.7.7a could hardly spoil the uniformity, but the presumed sandwich could thus remain. The attained strains suffice to align the skeleton until its state is determined by σ_{si} and e in fine layers so that the overall behaviour exhibits anisotropy. Assuming a composite of two simple psammoid half-cuboids with different e on two sides of a skew separatrix (Sect. 9.1) one could match the plots by hyp. This would not yield the initial $\dot{p}_s = 0$, but at least roughly the subsequent $\dot{p}_s < 0$, then the $\dot{p}_s > 0$ with membrane penetration and the response just after the reversal for different inclinations θ of the separatrix. This is to say that the assumption of SOM-states could suffice to capture evolutions with monotonous deformation path sections of moderate amount (say ca. 0.01).

Goldscheider (1984) tested also *two isobaric reversals* with a dense dry sand, Fig. 2.8.2. The deviatoric stress path (a) and the p_s -level with changing ψ_s after an almost isotropic compression (b) could not be kept precisely on straight lines, an exact stress control with adaption of membrane penetration was impossible. The deviatoric strain path (c) exhibits more drift than the deviatoric stress path. The plot of volume change vs. strain path length (d) exhibits first densification and then dilation. This occurs mainly by the initial increase of isotropic pressure, the contraction after each reversal with nearly constant p_s exceeds the previous dilation (both referred to the same small deformation).

This evolution could be partly matched by Rebstock (2010) with hyp and smooth path sections (elp fails as with cylindrical symmetry), also in Fig. 2.8.2. The deviatoric strain path has another drift than observed (c),

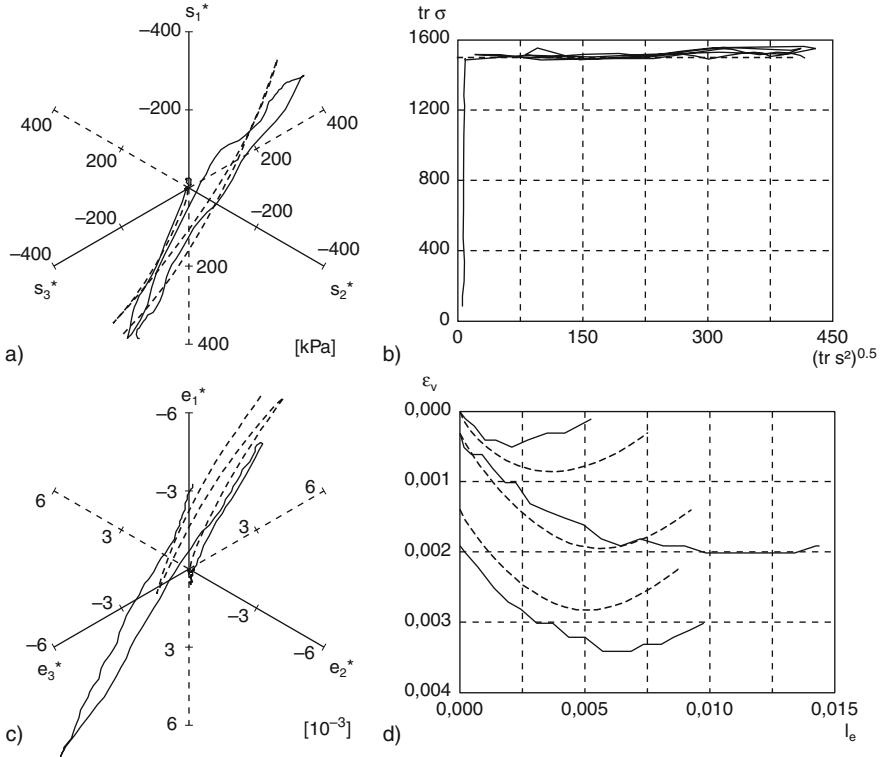


Fig. 2.8.2. Cuboidal test with dense dry sand by Goldscheider (1984): stress paths in a deviator plane (a) and in a plane through the isotropic axis (b), deviatoric strain path (c) and volumetric strain vs. strain path length (d). Replotted and simulated with hyp (dotted lines) by Rebstock (2010)

volume changes are better reproduced (d). This suggests again that the differential response is sufficiently determined by the state variables σ_{si} and e if and only if the previous deformation was monotonous and big enough (here $|\epsilon| > \text{ca. } 0.005$). Otherwise the internal state is no more determined by the named external state variables as assumed for SOM-states, thus hyp yields exaggerated anelastic effects.

Isochoric reversals with a dense sand were investigated in a cuboidal device as shown in Fig. 2.7.7b by Lanier et al. (1991), Fig. 2.8.3. The stress path (a) approaches $p_s = 0$ after reversals, this indicates temporary skeleton decay. The deviatoric stress-strain plot (b) exhibits sections without stiffness. This was similarly observed by Hyodo et al. (1989) and by Wichtmann (2005) with triaxial tests. One cannot capture decay and recombination of the skeleton by psammoid models, but for the other path sections with rather big deformations a sequence of SOM-states may be assumed. Off-decay parts could be captured with hyp.

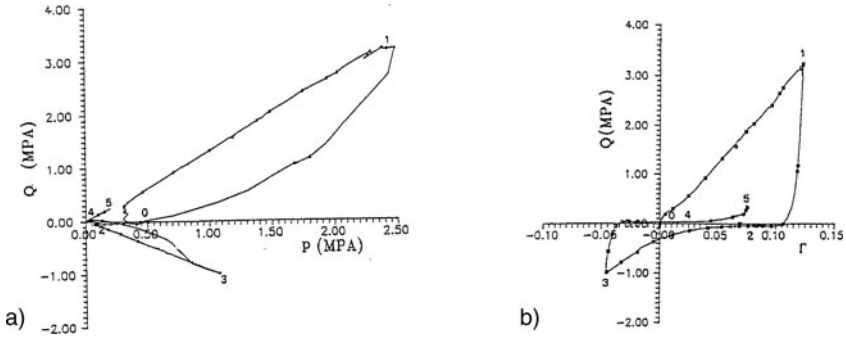


Fig. 2.8.3. Cuboidal test (Lanier et al. 1991) with undrained saturated dense sand. Stress path (a) and deviatoric stress-strain curve (b)

For lack of comprehensive experiments it is only briefly discussed now how far cuboidal deformations with *several reversals* could be captured by simple psammoid models. After the previous discussion elp can be left aside, and hyp can be expected to work at best if the deformations between reversals are so big that SOM-states are repeatedly attained. Then state cycles can be reached as attractors for cyclic deformation and ratcheting, but they are more intricate than with cylindrical RSEs. Stress cycles are no more in one plane in general, thus a constricted loop can be attained in a stress component space instead of a double loop in a stress plane. Asymptotic stress loops by ratcheting are presumably not constricted and will touch critical obliquities, but do not resemble lenses in three dimensions. One could explore such properties with response polars as in Figs. 2.7.5 and 2.7.6 or by numerical simulations.

It appears that only Lanier and Zitouni (1988) approached an attractor of this kind with a cuboidal device, Fig. 2.8.4. They worked with a dense saturated quartz sand. With a constant mean pressure the deviatoric stress path was first straight and then steered twice through a circle (a, with directions of strain rate). The deviatoric strain path approached a rounded triangle (c), the direction of the deviatoric strain rate (b) and the strain components (d) attained almost periodic changes with the deviatoric stress direction α_s . The volume change ε_v vs. α_s got nearly periodic during the second stress cycle (e). A plot of $\dot{\varepsilon}_v$ along the stress path exhibits three intermittent phases of dilation and contraction (f). This shows that a state cycle can be approached with two symmetric stress cycles, and that void ratio and shape tend to cyclic changes with three pulsations for one stress cycle.

A hypoplastic simulation by Rebstock (2010) is shown in Fig. 2.8.5. The strain path (a) tends to a similar cycle as observed. The calculated initial shift does not appear in Fig. 2.8.4c, it is rather indeterminate in the experiment as the initial state is not sufficiently known and as a precise stress control is impossible. The calculated volumetric strain (b) pulsates similarly as observed

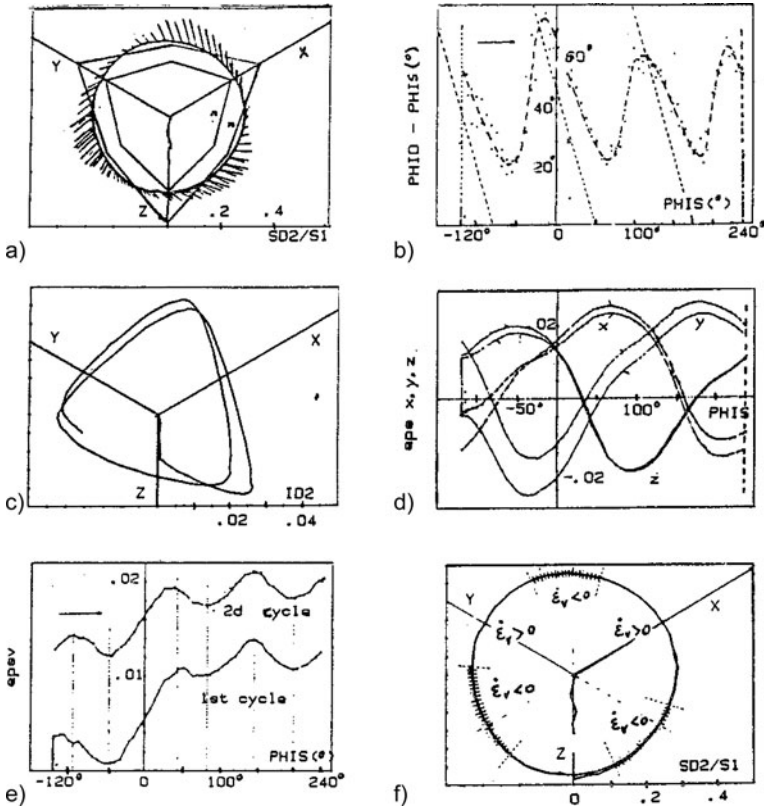


Fig. 2.8.4. Isobaric cuboidal test with saturated dense sand under stress cycles (Lanier and Zitouni 1988): deviatoric stress (a) and strain path (c), deviatoric strain rate direction (b) and strain components (d) vs. rotation of stress direction, volumetric change vs. rotation (e), signs of volumetric strain rates along the deviatoric stress path (f)

(cf. Fig. 2.8.4e), deviations may be attributed to the variable penetration of boundary grains into the confining membrane. The good reproduction of strain rates indicates a succession of SOM-states so that hyp is justified. Elastoplastic simulations would be less realistic.

It is a pity that *ratcheting* was not investigated with cuboidal devices. With constant p_s the deviatoric paths would resemble Fig. 2.1.9, and the plot of ε_v vs. α_s would presumably resemble Fig. 2.8.4e (cf. Sect. 2.6). With big reverse strain amplitudes this could be matched by hyp as the skeleton goes through SOM-states. Experiments by Yamada and Ishihara (1981) with initially loose quartz sand in a cuboidal device as by Fig. 2.7.7a help to clarify the issue. The deformations were so small that a loss of uniformity due to the fixed edges may be neglected. The deviatoric stress path consisted of radial sections with

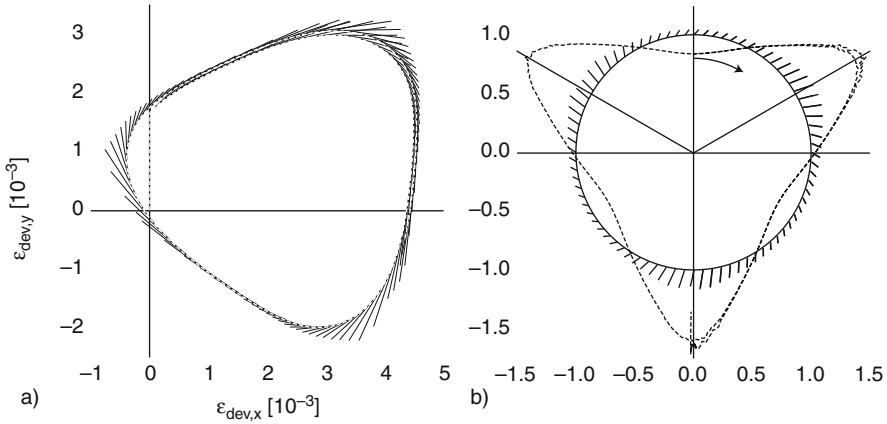


Fig. 2.8.5. Hypoplastic simulation (Rebstock 2010) of strain path (a) and volumetric strain (b) for comparison with Fig. 2.8.4. Bristles represent strain rates for equal amounts of stress rates, the circle in the right polar diagram denotes constant volume

reversals and increasing intensity. In a drained test with constant p_s the deviatoric strain path exhibited a kind of ratcheting with increasing amplitude, and the density increased gradually. In an undrained test the ratcheting was stronger and the mean pressure p_s was gradually reduced. The authors note that ‘the memory of previous load paths disappears almost completely’, this confirms the SOM-hypothesis by Gudehus et al. (1977).

Main features of these tests were reproduced in a hypoplastic simulation by Rebstock (2010). With constant p_s deviatoric strain path and density changes are rather realistic, but somewhat exaggerated. The deviations are bigger after α_s -reversals by 180° than with 60° . This shows that the SOM-hypothesis can work also for repeated reversals. In other words, with big enough deformation the skeleton is sufficiently determined by void ratio and stress components (Sect. 4.3). Elastoplastic simulations would be less realistic with the implied wide elastic range. The experiments by Yamada and Ishihara (1982) were planned and represented by assuming an elastoplastic response to imposed stress paths, the results show that this assumption is too restrictive. Rebstock (2010) deduces some objective qualitative conclusions and shows that such tests are not well apt for validations.

Summing up, the response of cuboidal psammoid RSEs can be captured by simple psammoid models, better by hyp than by elp, as long as deformations between reversals are not too small. Otherwise the skeleton state is not sufficiently characterized by stress components and void ratio. Then anelastic effects are overpredicted by hyp and underpredicted by elp. Experiments are better apt for validation and calibration with strain control than with stress control as the latter is earlier spoiled by loss of uniformity.

2.9 Simple shearing at state limits

Simple shearing means changing height h and obliquity γ of a parallelogram, Fig. 2.9.1a. For convenience the two deformation rates are called

$$\dot{\epsilon} = -\dot{h}/h \quad , \quad \dot{\gamma} = \dot{s}/h \tag{2.9.1}$$

with $\dot{\epsilon} > 0$ for compression and with shift s . For large deformations $\epsilon = \ln(h_0/h)$ may be used, the correct counterpart for γ is more intricate. $\dot{\epsilon}_1$ and $\dot{\epsilon}_2$ may be written here for the principal components $-D_1$ and $-D_2$ of D_{ij} . The default could be overcome with stretching components D_{ij} . Then $-\dot{\epsilon}$ and $\dot{\gamma}$ are replaced by D_{11} and $D_{12} = D_{21}$, the other D_{ij} are zero. The rate of volume change is

$$\dot{\epsilon}_v = \dot{\epsilon} = -D_{11} = -D_{ii} = -e/(1+e) \tag{2.9.2}$$

for isochoric grains, with summation for i . A dilatancy angle ν_s can be defined by

$$\tan \nu_s = -\dot{\epsilon}/\dot{\gamma} \tag{2.9.3}$$

In a Mohr diagram (Fig. 2.9.1b) the two principal strain rate components and the inclination $\chi_{\dot{\epsilon}}$ of $\dot{\epsilon}_1$ against the vertical are represented by a circle and a pole P.

There are four skeleton stress components, Fig. 2.9.1c. Two of them correspond to the conventional normal and shear stress,

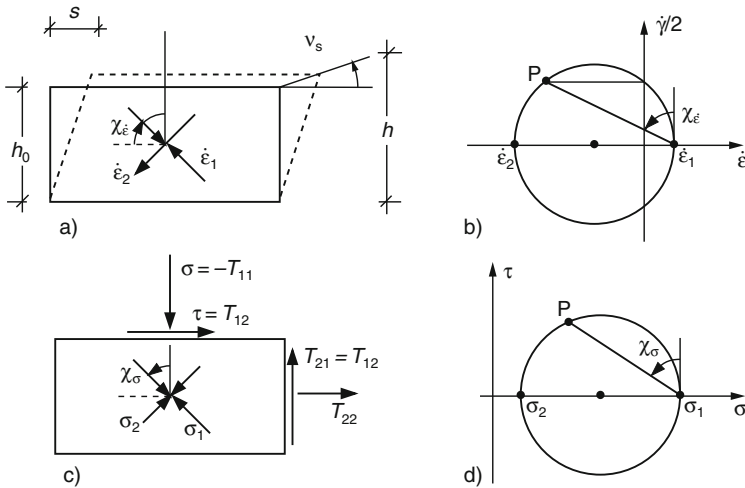


Fig. 2.9.1. Quantities for simple shearing: (a) RSE with strain rates, (b) strain rate circle, (c) RSE with stresses, (d) stress circle

$$\sigma_s = -T_{s11} \quad , \quad \tau = \tau_s = T_{s12} \quad , \quad (2.9.4)$$

$\tau = \tau_s$ holds as the pore water pressure is isotropic. $\sigma_3 = -T_{33}$ is normal to the considered plane. In a Mohr diagram (Fig. 2.9.1c, pressure positive) two principal skeleton stress components σ_{s1} , σ_{s2} and their inclination χ_σ appear in a circle with a pole. The intermediate principal stress can be related with the other two via

$$\sigma_{s3} = m(\sigma_{s1} + \sigma_{s2}) \quad (2.9.5)$$

with a factor m which varies in general.

For *state limits* coaxiality of stress and strain rate, i.e. $\chi_\sigma = \chi_{\dot{\epsilon}}$, and a constant m may be assumed (these assumptions will be discussed in the sequel). They can be represented by plots (Fig. 2.9.2) of ν_s (a), χ_σ (b) and r_e (c) vs. τ/σ_s . Negative $\dot{\gamma}$, τ and χ_σ refer to leftwards shearing. The e vs. $\log p_s$ relation is assumed as by Fig. 2.2.2b, now with $p_s \approx \sigma_s$ (justified further below). Three special cases are represented by Mohr circles with poles, assuming the same amount of strain rate (d) and the same vertical stress (e). For vertical compression (p) $\tau = 0$, $\nu_s = -90^\circ$ and $\chi_\sigma = 0$ hold with $\sigma_{s2}/\sigma_{s1} \approx 1 - \sin \varphi_c$ and r_e somewhere between 1 and $(e_{i0} - e_{c0})/(e_{c0} - e_{d0})$. For critical states (c) with $\nu_s = 0$ and $\chi_\sigma = \pm 45^\circ$

$$|\tau|/\sigma_s = \tan \varphi_{cs} = \sin \varphi_{cb} \quad (2.9.6)$$

holds with the critical friction angles φ_{cs} for shearing and φ_{cb} by (2.7.4) for biaxial deformation, this will be defended further below. In their vicinity the stress-dilatancy relation (Taylor 1948)

$$\tau/\sigma_s = \tan \varphi_{cs} + \tan \nu_s \quad (\dot{\gamma} > 0) \quad (2.9.7)$$

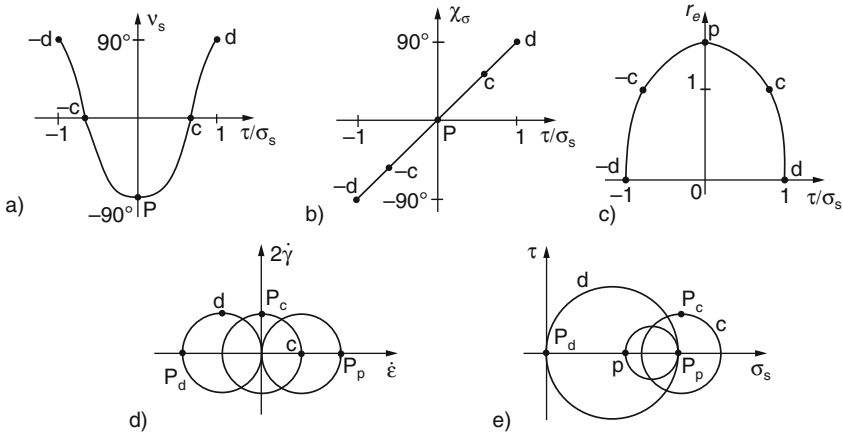


Fig. 2.9.2. State limits for simple shearing: (a) dilatancy angle vs. stress obliquity, (b) direction of major principal stress vs. stress obliquity, (c) relative void ratio vs. stress obliquity, (d) strain rate circles, (e) stress circles

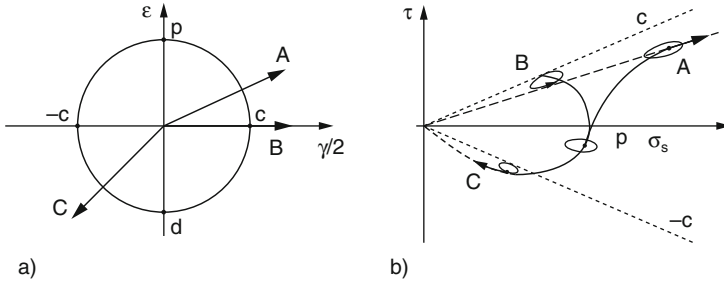


Fig. 2.9.3. Proportional strain paths with shearing (a) lead to state limits in a stress plane (b)

holds approximately. Extreme state limits with one zero principal stress (d), $\chi_\sigma = \pm 90^\circ$ and $\nu_s = \pm 90^\circ$ are fictitious as they cannot be reached.

Approaches to state limits are sketched in Fig. 2.9.3. Proportional strain paths (a) may be contractant (A), isochoric (B) or dilatant (C). The stress paths (b) tend to radial ones with σ_s -increase for A and with σ_s -decrease for C, and to a point for B. They are steered by the response polars which are indicated at four stress points, and are approached with different onsets so that the state limits are attractors. As in Fig. 2.2.5b the polars increase with σ_s (barotropy), as in Fig. 2.2.4 they are wider for lower r_e (pyknotropy), and limit void ratios are attained as in Fig. 2.2.5c. As the proper response polars are four-dimensional and depend on r_e the polars in Fig. 2.9.3b are sections for certain values of r_e , intermediate stress ratio m and inclination χ_σ of the major principal stress. For frame-indifference χ_σ must attain the given χ_ε (Sect. 2.11). As χ_ε -dependent stress component ratios are attained in a hyperspace of four stress components (which could be represented by sets of projected response polars) m tends to a constant for state limits, it ranges from ca. 0.3 to 0.5. This outline is not correct with large strains and co-rotated stress rates (Sect. 2.11).

In simple *elastoplastic* relations (elp) $m \approx 0.5$ and $\chi_\sigma = \chi_\varepsilon = 45^\circ$ (-45° for $\tau < 0$) is often assumed for state limits. These are taken as elastic range (cf. Sects. 2.3 and 2.7) which depends on e , and the limit void ratios depend on p_s by (2.3.1). A flow rule, i.e. $\dot{\varepsilon}^p/\dot{\gamma}^p$ vs. τ/σ_s , is assumed for critical and peak states. In some versions a tension cut-off is needed for high overconsolidation ratios *OCR*. A hypoelastic relation like (2.3.5) is often assumed for the elastic range. Analogously with Fig. 2.3.3 such constitutive relations may be represented in a stress plane, Fig. 2.9.4a, with response polars for unit strain rates (b). The stress components τ and σ_s are normalized by the equivalent pressure p_e by (2.3.3), the two further ones (or χ_σ and m instead) are thus not represented.

The elastic range, i.e. a section through the state boundary hyper-surface, resembles an ellipse or a drop. In the elastic range (e.g. I) the (cut of the) response polar is a horizontal centric ellipse which increases in proportion with σ_s . For a subcritical τ/σ_s and a σ_s at the boundary (A) the outer half of the

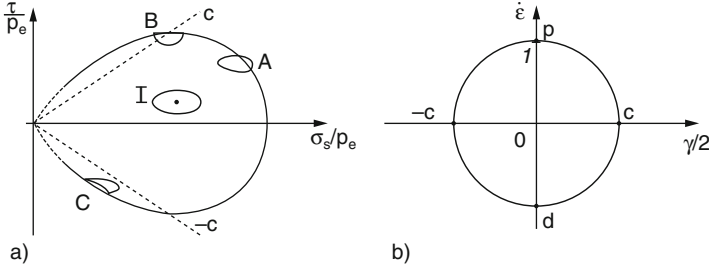


Fig. 2.9.4. State boundary line for simple shearing by CSSM (a) with response polars for unit strain rates (b)

polar is flatter, and the boundary is widened. At a critical state (B) one half of the polar is cut off, and the boundary is stationary. With an overcritical τ/σ_s and a σ_s at the boundary (C) the latter shrinks by dilation, thus the polar has a concave cap. Approaches to state limits as in Fig. 2.9.3 are thus rather evident (cf. Fig. 2.3.4). It is harder to imagine further projections of stress hyperspace and response polars, and to understand thus how the component ratios χ_σ and m come into play. This constitutive concept fails for $p_s \rightarrow 0$ due to (2.3.1).

Simple *hypoplastic* relations (hyp) can be written as

$$\begin{aligned}
 \dot{T}_{s11} &= f_s(L_{1111}D_{11} + L_{1112}D_{12} + f_d N_{11}D) \\
 \dot{T}_{s12} &= f_s(L_{1211}D_{11} + L_{1212}D_{12} + f_d N_{12}D) \\
 \dot{T}_{s22} &= f_s(L_{2211}D_{11} + L_{2212}D_{12} + f_d N_{22}D) \\
 \dot{T}_{s33} &= f_s(L_{3311}D_{11} + L_{3312}D_{12} + f_d N_{33}D)
 \end{aligned} \tag{2.9.8}$$

with the modulus of stretching

$$D = \sqrt{D_{11}^2 + 2D_{12}^2} = \sqrt{\dot{\epsilon}^2 + 2\dot{\gamma}^2}. \tag{2.9.9}$$

The stress rates $\dot{T}_{ij} = dT_{ij}/dt$ are taken without co-rotational terms here for simplicity (Sects. 1.2 and 2.11). The factors f_d and f_s depend on e and p_s by (2.4.4) and (2.4.5) as for cylindrical symmetry. The factors L_{ijkl} and N_{ij} depend on the *stress direction*

$$\hat{T}_{sij} = T_{sij}/p_s \tag{2.9.10}$$

with the mean pressure

$$p_s = -\frac{1}{3}T_{sii} = -\frac{1}{3}(T_{s11} + T_{s22} + T_{s33}) \quad , \tag{2.9.11}$$

in this dependence only φ_c appears as a material constant.

Relations for *state limits* can be obtained as follows. Using the hypoplastic relations by von Wolffersdorff (1996), Bauer (2000) derived $T_{s11} = T_{s22} = T_{s33} = -p_s$, $\chi_\sigma = \chi_{\dot{\epsilon}} = \pm 45^\circ$ and

$$\tan \varphi_{sc} = 2/\sqrt{1 + 3/\sin^2 \varphi_c} \quad (2.9.12)$$

for critical states. For peak states m , $\chi_\sigma \approx \chi_{\dot{\epsilon}}$, $\dot{\epsilon}/\dot{\gamma}$ vs. τ/σ_s and r_e vs. τ/σ_s can be calculated numerically with $\dot{T}_{sij} = 0$ from (2.9.8). With proportional compressions relations for the same quantities can be obtained iteratively from (2.9.8) by means of the proportionality of \dot{T}_{sij} and T_{sij} . These state limits are qualitatively represented by Fig. 2.9.2. Approaches to state limits by hyp look like Fig. 2.9.3b. The (sections of) response polars by (2.9.8) are ellipses with properties as outlined already in Sect. 2.4. $\chi_\sigma = \chi_{\dot{\epsilon}}$ is attained due to frame-indifference (Sect. 2.11) as at state limits the stress components suffice as state variables. A constant intermediate stress ratio m by (2.9.5) is attained as all asymptotic stress ratios tend to values which are determined by the direction of stretching.

Casagrande (1936) introduced a kind of state limits for simple shearing of sand. He explained the effect of shearing on the specific volume of sand with drawings, Fig. 2.9.5. For constant pressure σ an initially dense sand is dilated by shearing (a, b), whereas an initially loose sand is contracted (c, d). The shearing resistance tends to the same asymptotic value, after going through a peak in case of dilation. The void ratio tends to the same asymptotic value (porosity $n = e/(1 + e)$). Casagrande proposed (2.9.6) for critical states with a constant φ_{cs} , and a lower void ratio for higher σ_s . In the same diagram (e) he gives also an upper bound of n for ‘compression from loosest state’, and a lower bound named ‘compression for densest state’. Critical states are not named in this diagram, but certainly meant as in the text. The upper bound is nearly the same as e_i by Sect. 3.2, but our lower bound e_d is not the same as by Casagrande (cf. Fig. 2.5.1). Peak states were not explicitly recognized as state limits by Casagrande, let alone extremely dilatant state limits with vanishing pressure in one direction. For low $p_s \approx \sigma_s$ his limit void ratios cannot be approximated by (2.3.1), the power law (2.4.2) is more suitable.

Casagrande does not describe his experimental basis, he mentions only a report by Rutledge (1935). One figure therein (here Fig. 2.9.6) indicates shearing between two rough plates with a normal load, leading to dilation of dense sand with small displacement and to contraction of loose sand with bigger displacement. Leaving aside hints to fine-grained soils and clay, we note that this device cannot produce uniform stresses and strains as required for RSEs, particularly near the mutually displaced frames. The latter transmit unknown parasitic forces and impede contractant shearing (which occurs at the onset in better devices with any density). Rutledge’s findings are therefore at best qualitative.

May Casagrande’s statements nevertheless be considered as valid? His upper e -bound resembles the one observed by Ishihara (1993) after a moist

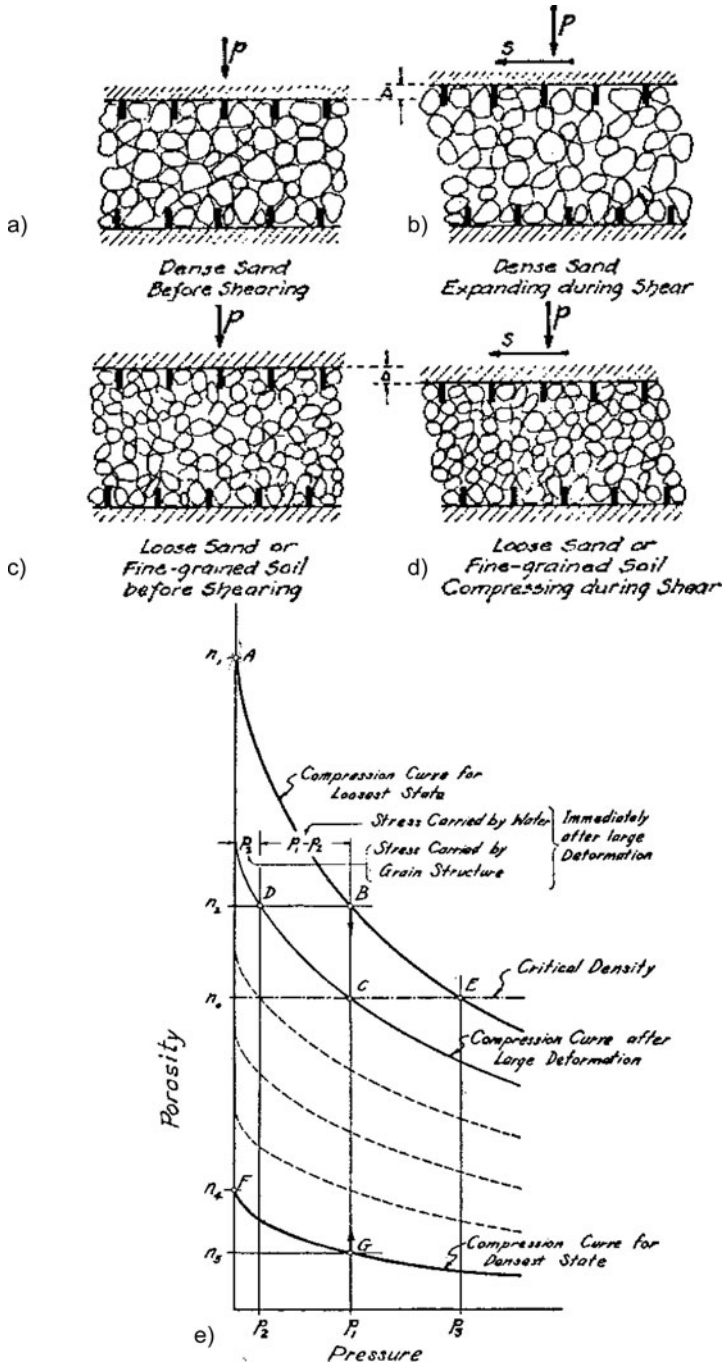


Fig. 2.9.5. Shearing behaviour (a-d) and void ratios vs. pressure (e) of sand by Casagrande (1936)

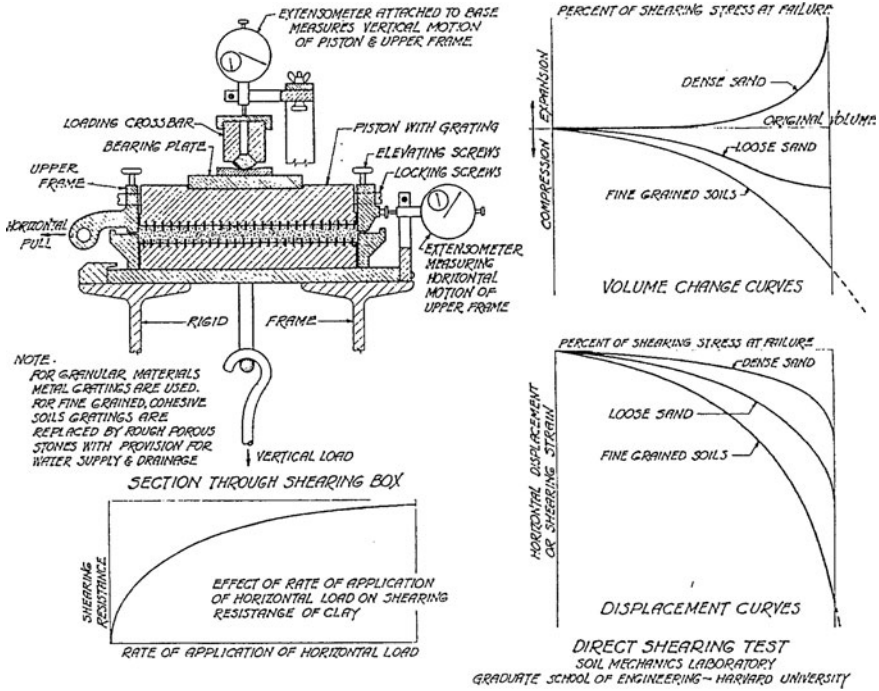


Fig. 2.9.6. Shearing device and behaviour by Rutledge (1935)

placement, Fig. 2.5.1. One can only conjecture that Casagrande and Rutledge applied a similar placement. A similar e_c vs. σ' dependence as in Fig. 2.9.5e was found by Verdugo and Ishihara (1996), Fig. 2.5.3b. The critical stress condition (2.9.6) with constant φ_{cs} was certainly observed by Casagrande, it is reported already by Terzaghi (1925) and was taken for granted earlier since Coulomb (1773). Casagrande does not mention shear localizations, so his statements on peak and dilation up to the same critical state as for contraction are conjectures. His lower e -bound is not explicitly related with cyclic shearing of suitable amplitude, but his hint to ‘vibratory densification’ is clear enough. So Casagrande may be called a pioneer of the concept of state limits.

In a so-called *simple shear apparatus* (SSA) the plates of a shear box consist of load cells so that mean lateral stresses and stress distribution in the top and base plates can be observed, Fig. 2.9.7. Roscoe (1970) reports that stresses and deformations (the latter observed with X-rays via lead shot markers) get non-uniform with increased shearing, so that only the middle third may be used for evaluations. He shows that the directions of spatially averaged principal strain rate and stress approach each other and get stationary at $\chi_\sigma \approx 45^\circ$. Budhu (1985) reports that the principal stress ratio m by (2.9.5) approaches ca. 0.4 both for loose and dense sand.

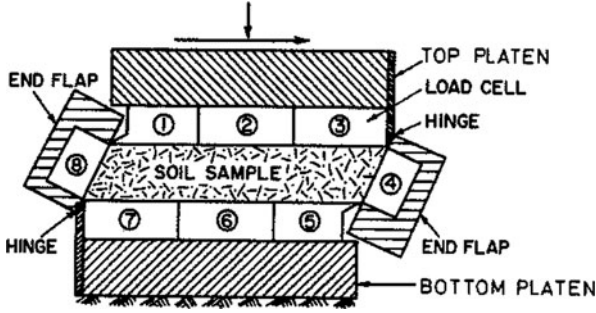


Fig. 2.9.7. Cambridge simple shear apparatus (Roscoe 1970)

Roscoe (1970) reports that the stress ratio $t/s = (\sigma_{s1} - \sigma_{s3})/(\sigma_{s1} + \sigma_{s3})$ increases with shearing under constant vertical pressure up to a peak which is higher and earlier for a lower initial e . Beyond it the reduction of t/s gets imprecise due to shear localization. After a slight initial decrease the void ratio e increases with shearing up to a maximal angle of dilatancy ν ($\approx \nu_s$ by (2.9.3)) at the peak of stress ratio. Beyond it void ratios observed with X-rays tend to critical values for the given σ_s in zones of localized shearing. A stationary t/s could not be attained. These findings support our concept of state limits as outlined further above, but simulations with *elp* or *hyp* with a single RSE are not legitimate. Non-uniform plane-parallel evolutions could be followed up with finite elements, but the shear localization starting from the corners would require polar quantities (Sects. 8.2 and 13.3).

Cylindrical shear tests are apparently simpler. An initially cylindrical sample was laterally confined by a membrane with a helical wire (Budhu 1985), by control of radial strain via pressure and membrane (Franke et al. 1979) or by a guided stack of ring disks (Bjerrum and Landva 1966). The sample was fixed at the bottom and sheared via a top plate, usually with constant normal force. As stresses and deformations are inevitably non-uniform, in particular near the edges, such tests can at best yield qualitative information. They are not apt for the validation of state limits and the determination of parameters for them.

Thin layer shear tests (Nasuno et al. 1997, Balthasar et al. 2006) are more appropriate, Fig. 2.9.8a. A granular sample with height h and far bigger length a and width b is kept and sheared via filter plates, its narrow rim is kept by capillary cohesion or by a soft rubber strip. Moist sand is filled with a high initial e , compressed by a normal force N and sheared with constant N . The shear force T increases, h decreases until both get almost stationary. The stresses calculated with hypoplasticity are uniform over the major part of the layer, and very small at the rim (b). One can thus determine φ_{cs} from T/N , and e_c from the sample size for the average pressure $\bar{p}_s \approx N/ab$. Therein the pressure $p_s = \sigma_s$ normal to shearing is justified as $T_{11} = T_{22} = T_{33}$ was proven by Bauer (2000) for critical states. The attained T/N and e confirm (2.9.12)

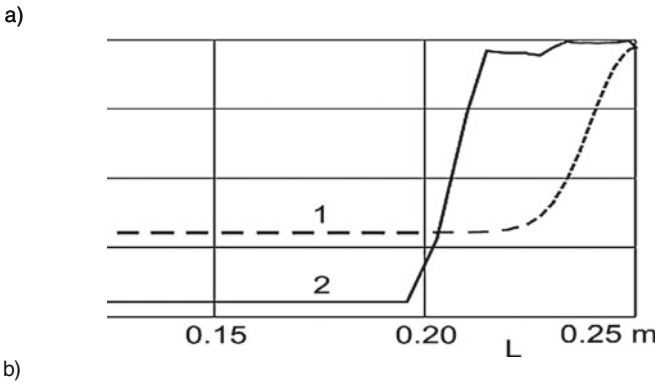
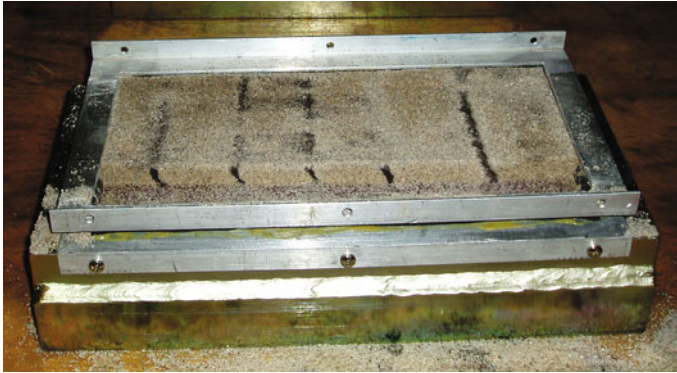


Fig. 2.9.8. Thin layer shear test with sand: (a) exposed sample with initially vertical markers (courtesy K. Balthasar), (b) simulated distribution (courtesy C. Slominski) of normal stress before (1) and after shearing (2)

and (2.4.1), respectively, with φ_c , e_{co} , h_s and n determined from triaxial tests with the same sand. The capillary skeleton pressure p_{cs} (Sect. 6.2) should be allowed for in case of $p_{cs}/\bar{p}_s > \text{ca. } 0.02$. The potential of thin layer tests will be further discussed in Sects. 2.11 and 3.9.

Ring shear devices of different kind have been developed (Bishop et al. 1971). The annular specimen with rectangular cross section has no end in the shearing direction, the ratio of width and radius is small so that changes along the radius may be neglected. Upper and lower halves of the sample are twisted past each other under constant axial force or constant height, average τ and σ are determined via torque and axial force. Radial displacements are prevented by outer and inner pairs of ring walls. For a more uniform shearing stacks of ring discs can be employed which slide past each other and the top and bottom ring plates. Often only two pairs of rings with a gap in between are used. The shearing is localized at the gap if the upper ring walls are fixed to the top plate. The height of the shear zone can be estimated afterwards by means of markers.

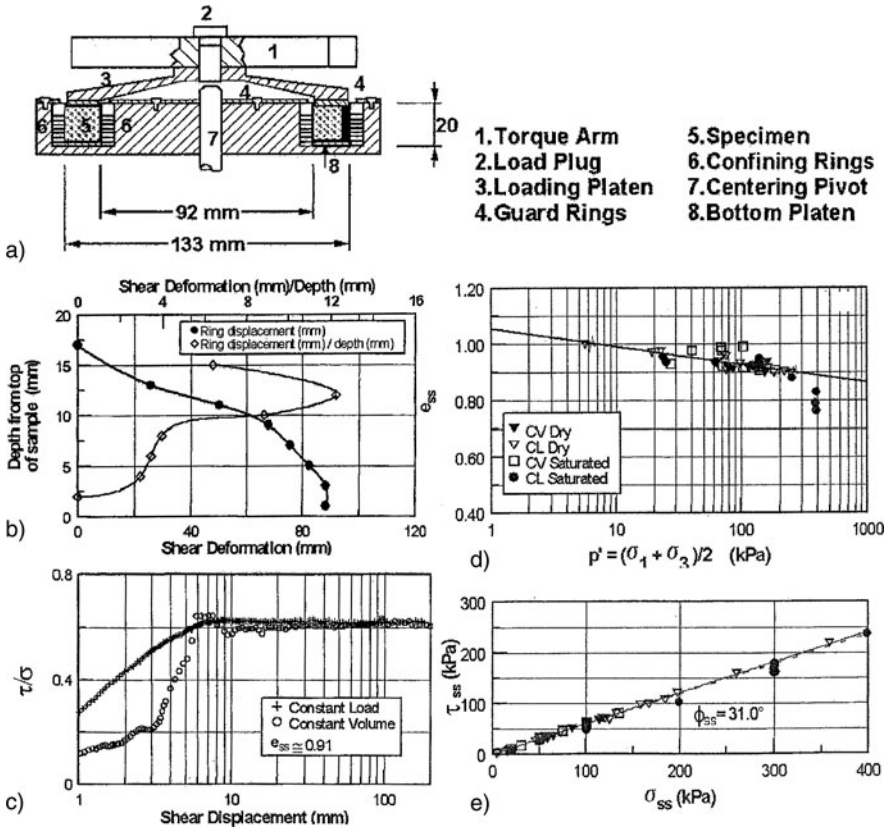


Fig. 2.9.9. Ring shear tests by Garga and Infante Sedano (2002); (a) device, (b) circumferential displacements vs. depth, (c) stress obliquity vs. shearing, (d) void ratio vs. pressure in the shear zone, (e) attained shear vs. normal stress

Hungry and Morgenstern (1984) carried out ring shear tests with different granular materials, pressures σ_s and shearing velocities \dot{s} . They observed stationary behaviour for constant σ_s , and a constant φ_{cs} for σ_s from ca. 20 to 200 kPa and \dot{s} from ca. 10^{-3} to 1 ms^{-1} . This supports the assumptions of Coulomb dry friction and granular permanence. Garga and Infante Sedano (2002) report on ring shear tests with constant σ_s (CL) and also with constant height (CV), Fig. 2.9.9a. Crushed quartz sand with fines was placed dry or under water with different densities. Cutting afterwards revealed a shear localization in the upper third (b), there considerable crushing was observed. For CL and CV the stress ratio τ/σ' attained the same plateau after ca. 60mm shearing (c). Asymptotic void ratio (d) and stress ratio (e) are the same for CL and CV both for dry and saturated samples.

These findings support the critical state concept for simple shearing. Shear localization could be allowed for by taking e from this zone. Crushing for

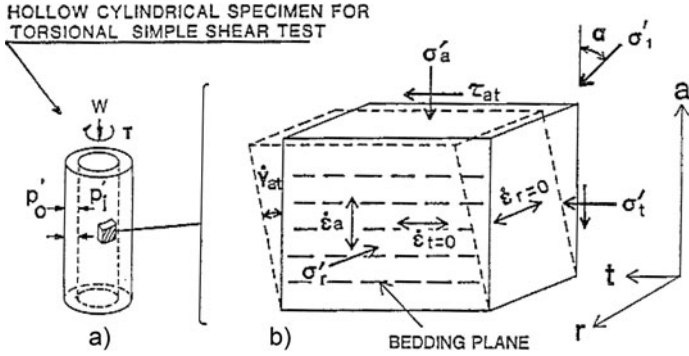


Fig. 2.9.10. Principle of torsional shearing (Pradhan et al. 1988a)

$\sigma_s \approx 250$ kPa reduces e_c more than with subrounded sand (Fig. 2.5.4b). For lower σ_s the rather scattering data in Fig. 2.9.9d can as well be matched by (2.3.1) and (2.4.1). e_c is evidently lower with more fines, whereas φ_{cs} is not changed by them. The reported $\varphi_c = 33^\circ$ from triaxial tests confirms (2.9.12) which yields $\varphi_{cs} = 31^\circ$ as observed.

More sophisticated devices enable *torsion of thick-walled tubes*, Fig. 2.9.10. The tube is sheared past its rough base by a rough top ring which keeps height or axial force constant. Radial pressures p_i and p_a are imposed via an inner and an outer membrane, so the sample can be saturated. p_i and p_a are controlled so that inner and outer radius are constant, grain penetration into the membranes can be allowed for. Saturated sand can be tested with or without drainage and pore pressure control. Average stresses and strains are calculated for a middle part wherein an RSE undergoes nearly simple shearing. Deformations are fairly uniform up to the peak of τ vs. γ , beyond it shearing gets markedly localized (Sect. 8.2).

Pradhan et al. (1988a) tested saturated quartz sand of different densities with and without drainage. For peak states they observed

- coaxiality of stress and strain rate, $\chi_\sigma = \chi_\varepsilon \approx 45^\circ$,
- nearly constant stress ratio m as by (2.9.5),
- same peak principal stress ratio σ_{s1}/σ_{s2} as for biaxial deformations with same density (and same bedding direction),
- same dilation ratio $\varepsilon_3/\varepsilon_1$ at peak as for biaxial deformations.

This supports the assumptions outlined further above with Fig. 2.9.2. These findings were confirmed by the same authors (Pradhan et al. 1988b) for lower pressures p_s . As shown by Fig. 2.5.5 for the same sand limit void ratios change only little with p_s , this is captured by (2.4.1) and not by (2.3.1). As plotted in Fig. 2.9.2 stress and strain rate obliquities for state limits are determined by the relative void ratio r_e , this was apparently almost the same in the two studies by Pradhan et al. (1988a, b).

Summing up, as far as uniform simple shearing can be attained in experiments these confirm the concept of state limits with four stress components, which is similarly implied by elp and hyp. With the same dilation angles and relative void ratios the principal stress ratios are the same as for biaxial deformations, and the directions of major principal stress and strain rate agree. The last two properties hold for state limits due to frame-indifference (Sect. 2.11), but not otherwise.

2.10 Shearing off state limits

Counting reversals is not correct if you don't know how many occurred already before you start. We will first discuss how far this problem can be avoided by sweeping out the memory of shear reversals. Another way out are state cycles as attractors for suitable repeated reversals. Available shear test results confirm this approach for big amplitudes, for small ones simple psammoids turn out insufficient (cf. Sects. 2.6 and 2.8).

Roscoe (1970) describes a shear test with dense dry sand in a so-called *simple shear apparatus* as by Fig. 2.9.7 with two reversals of shear stress τ under constant normal stress σ . The deviatoric stress-strain curves suggest an almost elastic response to un- and reloading. In between the directions of principal stress rate and strain rate agree as by isotropic elasticity. With monotonous further shearing the memory of the two reversals is apparently swept out: the stress-strain curve swivels towards the one as without reversals, and the directions of principal stress and strain rate tend to agree. These findings seem to support elp and to refute hyp. A plot of volumetric strain vs. shearing, however, would suggest the opposite (cf. Fig. 2.6.4a, b). Deviatoric unloading, i.e. $\tau\dot{\gamma} < 0$ with $\sigma_s = \text{const}$, densifies the skeleton, with reloading it is dilated if it is not loose. Simulations are not presented as Roscoe (1970) did not consider such volume changes, they would look like Fig. 2.6.4c, d. One can conclude again that anelastic effects between reversals are missed by elp and exaggerated by hyp. A state with swept-out memory (SOM, Gudehus et al. 1977) can be attained by sufficient monotonic shearing so that stress components and void ratio suffice as state variables.

If *thick-walled cylinders* are twisted back and forth they remain rather uniform as long as they do not approach state limits. This was achieved by Pradhan et al. (1989) with saturated drained sand which was sheared by an *alternating torque* with gradually increased amplitude and constant mean pressure p_s , Fig. 2.10.1. With a loose sample this led to a spiral plot of stress ratio vs. shear strain (a), and to a cumulative densification with minute dilation before the last two reversals (b). With a dense sample the spiral with kinks got wider (c), and the sample dilated and contracted between subsequent reversals with net contraction for small and net dilation for bigger amplitudes (d). The dilation is underestimated for overcritical stress obliquities as then it is localized to shear bands (Sect. 8.2).

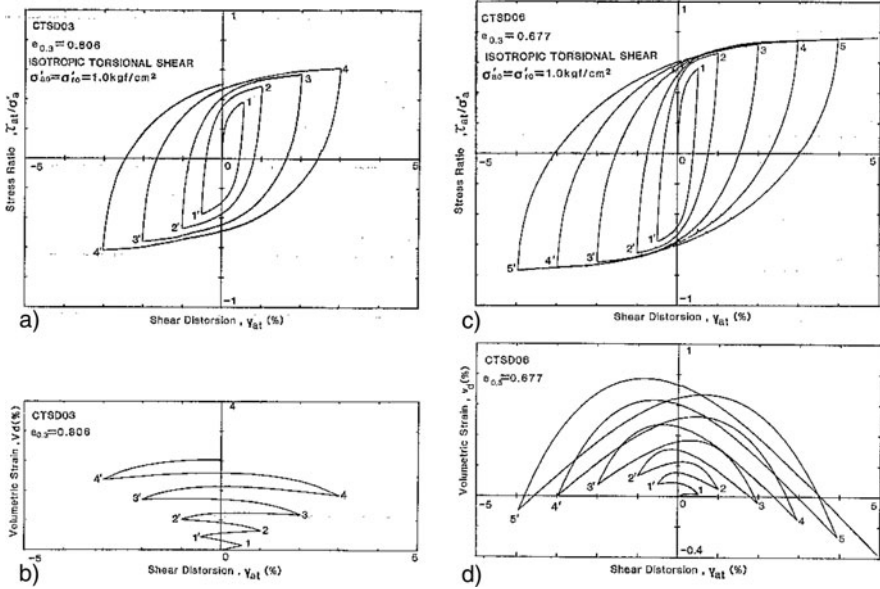


Fig. 2.10.1. Alternating torsion of drained thick-walled cylinders (Pradhan et al. 1989). Stress ratio and volumetric strain vs. shearing for loose (a, b) and dense sand (c, d)

Simulations by Prada (2010) with hyp and an RSE as by Fig. 2.9.10 show again that anelastic effects just after reversals are exaggerated by hyp, Fig. 2.10.2. They would be missed by elastoplastic simulations without internal state variables as the assumed elastic range is too wide. For loose sand the calculated spiral stress-strain plot (a) is fairly realistic (successive heights are given), and also the gradual densification except for a final dilation (b). For dense sand the simulated hysteresis loops are too wide (c), and the dilation is exaggerated after the initial contraction (d). The deviation is due to the localized dilation for overcritical stress obliquities (Sect. 8.2) which cannot be taken into account in such simulations. Some sections before reversals are better captured than those just thereafter. This indicates that SOM-states were repeatedly attained by the bigger deformations between later reversals, but not before. We will use the observations by Pradhan et al. (1989) in Sects. 4.4 and 4.5 as a touchstone for constitutive relations with internal variables.

Shear cycles of sand samples have been investigated in different devices, e.g. Fig. 2.10.3, but due to non-uniformities the observations are at best of qualitative use. In the device by Bjerrum and Landva (1966) a cylindrical sample is confined by a reinforced membrane (a) and sheared by translating the top plate. In a variant by Budhu (1985) load cells in the top and bottom plates (b) can indicate stress distributions. Wood et al. (1979) observed markedly non-uniform stress distributions from the very beginning of shearing.

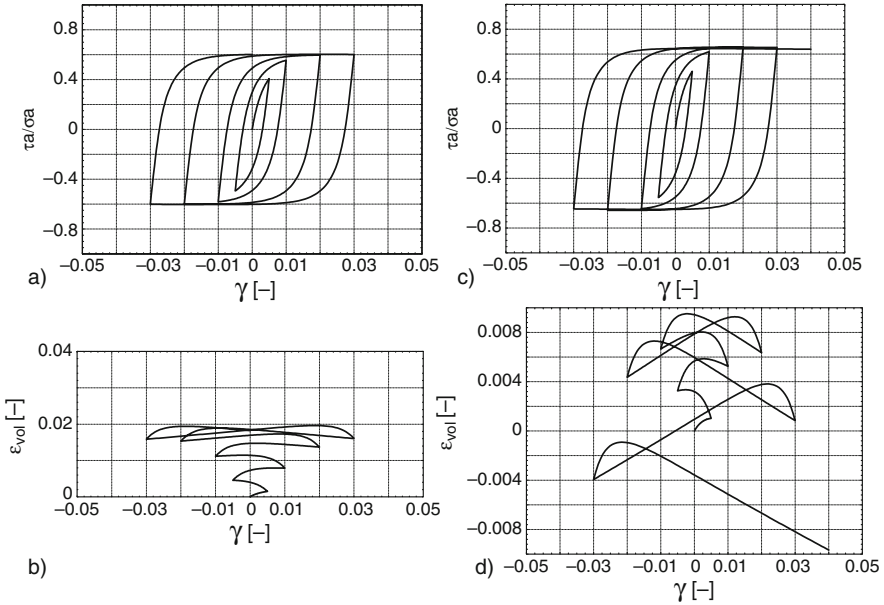


Fig. 2.10.2. Hypoplastic simulation (Prada 2010) of torsion tests by Pradhan et al. (1989), (a–d) as in Fig. 2.10.1

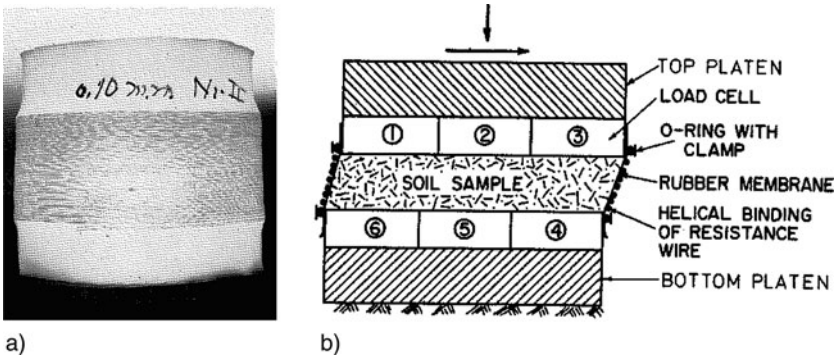


Fig. 2.10.3. Devices for shearing cylindrical samples with reinforced membrane; (a) enclosed sample (Bjerrum and Landva 1966), (b) cross section with load cells (Budhu 1985)

Youd (1972) describes isobaric tests with up to 10^5 cycles with saturated sand in a device as by Fig. 2.9.7, Fig. 2.10.4. In a typical test with medium initial density the sample was contracted after each reversal, less dilated thereafter and thus gradually densified (a). With a given pressure σ_s the densification is more rapid with a higher amplitude, but tends to the same asymptotic void ratio (b). With a given shear amplitude the asymptotic e is slightly reduced by a higher σ_s (c). The gradual change of e for any given σ_s

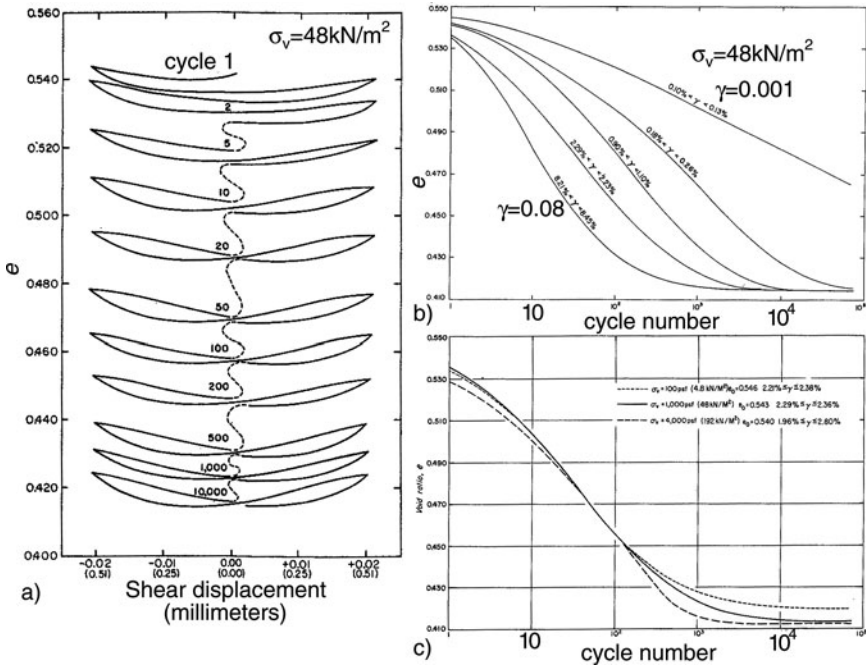


Fig. 2.10.4. Isobaric cyclic shear tests with sand by Youd (1972): (a) void ratio vs. shearing, void ratio vs. number of cycles for different shearing amplitudes (b) and different pressures (c)

and amplitude does not depend on the frequency, the response is thus rate-independent. The results with more than ca. 0.01 shear strain are certainly biased by shear bands (Roscoe 1970) and grain crushing therein (Fig. 2.9.9), and therefore not apt for validations.

The gradual densification is not obtained with elp as thus the skeleton would remain in the elastic range. A simulation of Fig. 2.10.4a with hyp (Prada 2010) exhibits contraction just after each reversal and dilation with further shearing, but a too rapid gradual densification, Fig. 2.10.5a. The asymptotic mean void ratio \bar{e} is higher for a bigger amplitude due to stronger dilation (b), which is suppressed by crushing in Fig. 2.10.3b, and is attained with too few cycles by hyp. For small amplitudes the calculated asymptotic \bar{e} approaches e_d by (2.4.1), its observed slight reduction with bigger σ_s could be obtained with a realistic h_s . The asymptotic double loop of e vs. γ (butterfly) is reproduced for the rather big amplitude of Fig. 2.10.4a, this indicates that SOM-states were repeatedly attained. Internal variables would be needed for smaller amplitudes as they are then no more determined by stress and void ratio (Sect. 4.3).

Budhu (1985) determined lateral stress components of dense sand in a device by Fig. 2.10.3b for shearing with big amplitude and constant mean vertical pressures. The normal stress components out of plane and in the

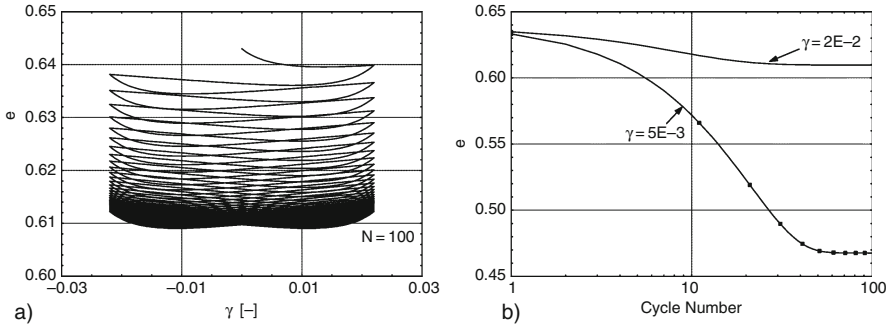


Fig. 2.10.5. Hypoplastic simulation (Prada 2010) of Youd's (1972) tests in Fig. 2.10.4a, b

plane of shearing attained double loops already in one cycle. Such loops could be similarly obtained with hyp by assuming a uniform RSE. The test results are debatable because of the observed non-uniformity, but provide a qualitative confirmation of hyp. It appears that cyclic shearing with constant σ_s and big amplitude leads to a periodic succession of SOM-states in state cycles after a transition which is too fast by hyp. Budhu (1985) indicates that stress ratios and void ratio get also nearly periodic after a few shear cycles, although he does not report on contraction after each reversal. As pointed out by Roscoe (1970) the big amplitudes lead to repeated shear localizations so that evaluations without them are misleading.

Ishihara and Towhata (1983) report on *isochoric cyclic* shear tests with torsion of thick-walled cylindrical samples as by Fig. 2.9.10. In a test with medium density and alternating shear stress τ the stress path tended to a symmetric butterfly (Fig. 2.10.6a), and the hysteresis loops attained sections without shearing resistance (b). The latter indicates repeated decay and recombination of the skeleton (cf. Figs. 2.6.6 and 2.8.3). As outlined with Fig. 2.6.6 the asymptotic response is distorted and shifted by the variable penetration of grains into the membrane.

The simulation by hyp (Prada 2010) exhibits a flatter butterfly after less reversals (c), and widening hysteresis loops (d) instead of partly concave loops which indicate a temporary decay. A similar behaviour was observed by Andersen and Berre (1999) with undrained shear cycles in a device as by Fig. 2.10.3a. A better validation could be achieved by taking into account the membrane penetration and by avoiding a temporary decay. It appears that an almost periodic succession of SOM-states was attained just before the skeleton decay, but that in the transition before the internal state was not sufficiently determined by skeleton stress and density (more in Sects. 4.4 and 4.5).

If strain cycles with shearing are imposed to a psammoid RSE this tends to state cycles by hyp (but not by elp) as long as the skeleton does not decay (shear localization and grain crushing are left aside), Fig. 2.10.7. Big enough amplitudes lead to a succession of SOM-states, whereas cycles with small

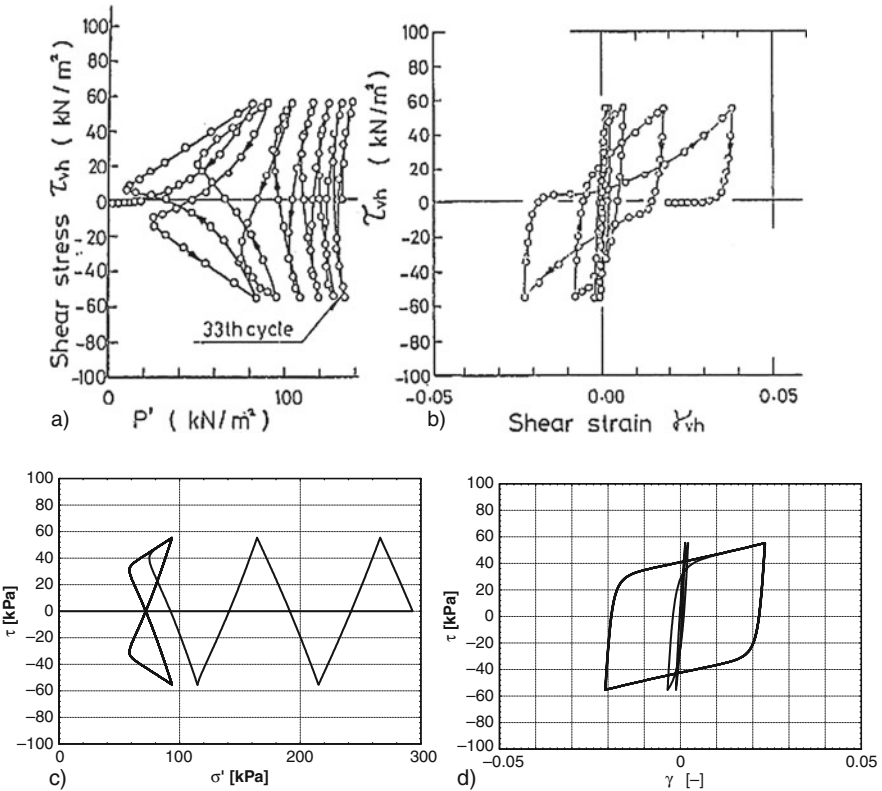


Fig. 2.10.6. Stress path (a) and stress-strain curve (b) of an undrained hollow cylindrical sand sample, observed with a cyclic torque by Ishihara and Towhata (1983) and by a hypoplastic simulation (c and d, Prada 2010)

amplitudes cannot be captured without internal variables. The strain cycle may be almost isochoric (A), or butterfly-like (B) so that a rather constant normal stress may be expected. The plots of $\tau (= T_{12})$ vs. γ tend to hysteresis loops after a reduction of height (and p_s) for A, and after an increase (by densification) for B (b). The plot of principal directions χ against the vertical vs. shearing (c) shows only the attractors. Just after each reversal the direction $\chi_{\dot{\epsilon}}$ of strain rate is near the direction of stress rate $\chi_{\dot{\sigma}}$, with further shearing $\chi_{\dot{\epsilon}}$ approaches the principal stress direction χ_{σ} . The paths of the two horizontal stresses σ_{s22} and σ_{s33} ($-T_{22}$ and $-T_{33}$ by Fig. 2.9.1c) tend to a double loop for A and B (d). In the plot of e vs. $\log p_s$ the state path tends to a minute double loop for A and B (e).

Uniform shear tests with measurement of all components are not possible, and state cycles could only be attained with granular permanence and periodic boundary conditions. Stress control on some boundaries, e.g. vertical for a thin layer or radial for a thick-walled cylinder, would require iterations

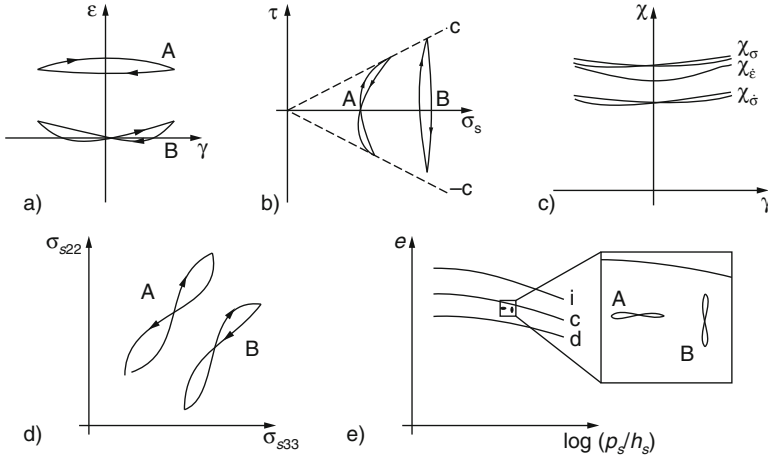


Fig. 2.10.7. Hypoplastic state cycles for almost isochoric (A) or isobaric (B) cyclic shearing (a): (b) shear stress vs. normal stress, (c) principal directions vs. shearing, (d) in-plane and out-of-plane horizontal stresses, (e) void ratio vs. mean pressure

both in physical and numerical tests, and would give more freedom for shear localization. In the range of subcritical stress obliquities the uniformity could be enhanced by shear cycles (Sect. 4.6), thus tests with them up to a cyclic response would be rewarding.

Andersen and Berre (1999) approached an *isochoric ratcheting* with a dense saturated quartz sand in a device as by Fig. 2.10.3a, Fig. 2.10.8. A pulsating shear stress $\tau > 0$ was imposed without drainage. The shear strain increased gradually with decreasing net amount per τ -cycle (a), but a stationary ratcheting was not attained. The stress path in a τ vs. σ_s plane tends to a skew loop which touches the critical line after a reduction of p_s (b). This test was simulated with hyp (Prada 2010) by assuming a single RSE with the same initial state and pulsating τ . The plot of τ vs. γ exhibits an exaggerated ratcheting (c). The simulated stress path tends to a nearly lenticular cycle at the critical line after a few reversals (d). As with cylindrical symmetry (Fig. 2.6.7) the cumulative anelastic effects are underestimated by elp and exaggerated by hyp. One can conclude again that small deformations between reversals do not suffice for sweeping out their relics.

This kind of ratcheting (called cyclic mobility by Castro 1975) was not investigated up to stationarity in simple shear tests. Thus the range of validity of hyp is unknown in that respect, simulations with other boundary conditions and more components would be premature. Tests in devices as by Fig. 2.9.7 or 2.10.3a could be made with imposed ratcheting, in spite of the inevitable loss of uniformity they could at least provide a qualitative validation. Thin layer tests (Fig. 2.9.8) could provide more insight as the major inner part of the flat sample remains uniform in case of subcritical stress obliquities (Sect. 8.2), particularly with reversals. As with other evolutions treated in this chapter

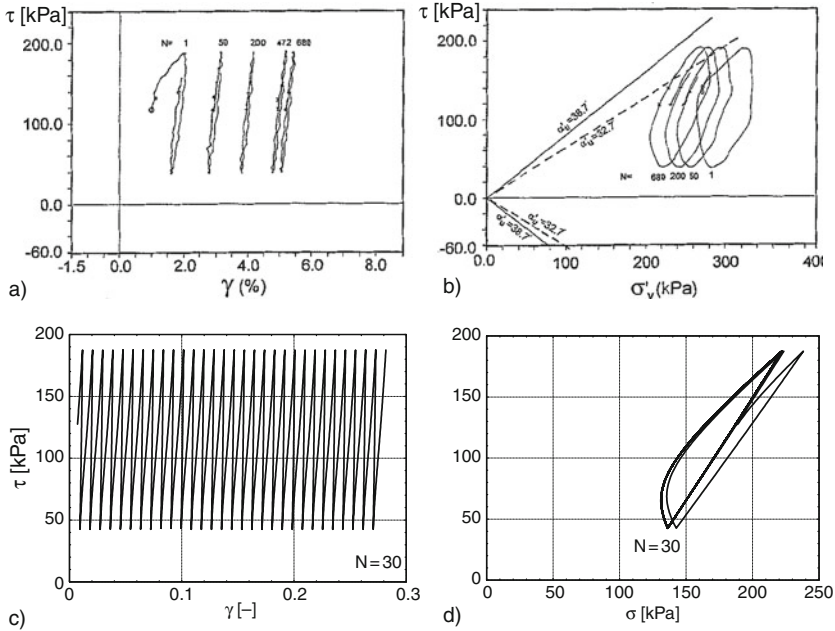


Fig. 2.10.8. Stress-strain plot (a) and stress path (b) of undrained sand under pulsating shear stress (Andersen and Berre 1999); hypoplastic simulation (c and d, Prada 2010)

one can expect a swept-out of memory for sufficient deformations between reversals so that internal variables are not needed.

Summing up, simple shearing off state limits can be captured by simple psammoid models as long as SOM-states may be assumed, but only crudely with reversals by hyp and hardly by elp. SOM-states require sufficient deformations between reversals, then the rather subjective number of cycles is not needed. Otherwise internal variables are no more determined by stress and void ratio, and are needed explicitly so that simple psammoid models cannot suffice. The desired uniformity of RSEs gets lost in shear tests so that these are not apt for precise validations. Tests with shear cycles and ratcheting will nevertheless be of use to better explore the range of validity. As always in this chapter skeleton decay, shear localization and grain crushing cannot be captured thus.

2.11 General and outlook

Imagine a tetrahedron in a deforming psammoid body, Fig. 2.11.1. As in a finite element mesh the velocity \mathbf{v}_s of the skeleton may be linearly distributed between the four convected corners or marker points (a). Thus the velocity

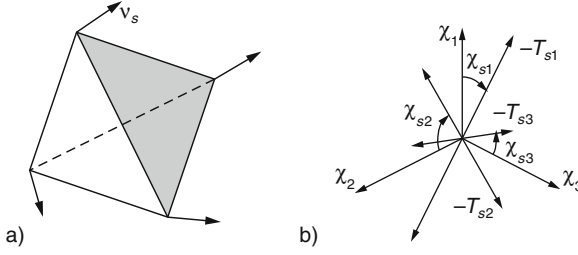


Fig. 2.11.1. General RSE with velocities (a) and principal stresses (b)

gradient $\nabla \mathbf{v}_s$ is constant within this general RSE, and so are the stretching $\mathbf{D} = (\nabla \mathbf{v}_s + \mathbf{v}_s \nabla)/2$ and the rate of rotation $\mathbf{W} = (\nabla \mathbf{v}_s - \mathbf{v}_s \nabla)/2$. The volumetric stretching is related with the change of void ratio of the convected RSE by

$$\text{tr} \mathbf{D} = \dot{e}/(1 + e) \quad (2.11.1)$$

with $\dot{e} = de/dt + \text{tr}(\nabla e \cdot \mathbf{v}_s)$ and isochoric grains. The amount of stretching $D = \|\mathbf{D}\| = \sqrt{\text{tr} \mathbf{D}^2}$ is another invariant of \mathbf{D} . As \mathbf{D} is symmetric it has three principal values (D_1, D_2, D_3) and three principal directions ($\chi_{D1}, \chi_{D2}, \chi_{D3}$) in general.

The symmetric (Cauchy) skeleton stress tensor \mathbf{T}_s may be uniform in our RSE (in a first approximation). It can be represented by three principal values T_{si} and three principal directions χ_{si} (Fig. 2.11.1b). The skeleton cannot have tension, thus $T_{si} < 0$ is needed and $T_{si} \rightarrow 0$ means its decay. The mean skeleton pressure $p_s = -\text{tr} \mathbf{T}_s/3$ is a first invariant. A saturated skeleton with pore pressure p_w has the total stress tensor

$$\mathbf{T} = \mathbf{T}_s - p_w \mathbf{1} \quad (2.11.2)$$

with unit tensor $\mathbf{1}$. The stress deviator is thus independent of p_w ,

$$\mathbf{T}_s^* = \mathbf{T}_s - p_s \mathbf{1} = \mathbf{T}^* = \mathbf{T} - (p_s + p_w) \mathbf{1} \quad (2.11.3)$$

Two suitable deviatoric invariants are

$$\tan \psi_s = \sqrt{\text{tr} \mathbf{T}_s^{*2}}/p_s \quad (2.11.4)$$

and

$$\cos 3\alpha_s = \sqrt{6 \text{tr} \mathbf{T}_s^{*3}}/(\text{tr} \mathbf{T}_s^{*2})^{3/2} \quad (2.11.5)$$

We call $\tan \psi_s$ *stress obliquity* and $\cos 3\alpha_s$ *Lode parameter*. The two angles ψ_s and α_s appear in the space of principal components as shown in Fig. 2.7.1. The state of our RSE can be represented independently of its orientation by two plots, Fig. 2.11.2, viz. e vs. $\log(p_s/h_s)$ (a) and $\tan \psi_s$ vs. $\cos 3\alpha_s$ (b). Isotropic

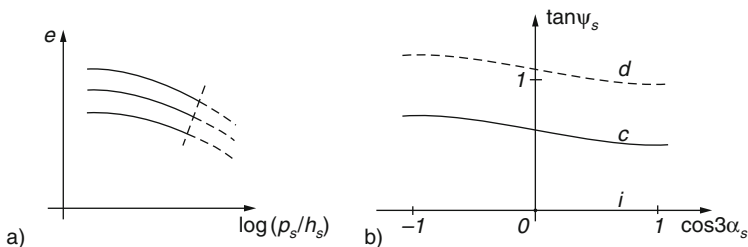


Fig. 2.11.2. State space with bounds of a general RSE: (a) void ratio vs. pressure (range with crushing *dashed*), (b) stress obliquity vs. Lode parameter (upper bound not attainable)

states have $\tan\psi_s = 0$, cylindrically symmetric ones have $\cos 3\alpha_s = \pm 1$. States with lower than critical stress obliquity $\tan\psi_s < \tan\psi_{sc}(\cos 3\alpha_s)$ are called subcritical, otherwise they are critical or overcritical. These are no state limits in general as the void ratios need not have the limit values. The latter are upper bounds for a given p_s , i.e. the relative void ratio r_e cannot exceed the $\tan\psi_s$ -dependent limit value (more further below).

The (debatable, Temmen et al. 2000) co-rotated stress rate

$$\dot{\mathbf{T}}_s = \dot{\mathbf{T}}_s + \mathbf{T}_s \mathbf{W} - \mathbf{W} \mathbf{T}_s \quad (2.11.6)$$

of our convected RSE is assumed to be related with the stretching tensor via

$$\dot{\mathbf{T}}_s = \mathbf{F}_s(\mathbf{T}_s, \mathbf{D}, e) \quad (2.11.7)$$

with an isotropic tensor function \mathbf{F}_s of \mathbf{D} and the state variables \mathbf{T}_s and e . This isotropy is due to frame-indifference (Sect. 1.2). Unit-invariance requires that \mathbf{T}_s is referred to a material property with the dimension of stress, this is achieved with the granulate hardness h_s (Sect. 2.2). For simple psammoids \mathbf{F}_s has the properties

- (a) $\mathbf{F}_s(\lambda \mathbf{T}_s, \mathbf{D}, e) = \lambda^m \mathbf{F}_s(\mathbf{T}_s, \mathbf{D}, e), \quad 0 < \lambda < 1, 0 < m \leq 1$
- (b) $\mathbf{F}_s(\mathbf{T}_s, \lambda \mathbf{D}, e) = \lambda \mathbf{F}_s(\mathbf{T}_s, \mathbf{D}, e), \quad \lambda > 0$ (2.11.8)
- (c) $\mathbf{F}_s(\mathbf{T}_s, -\mathbf{D}, e) \neq -\mathbf{F}_s(\mathbf{T}_s, \mathbf{D}, e)$ in general.

In this generalization of (2.2.14) the barotropy (a) enables SOM-states and state limits. The rate-independence (b) is not at variance with the non-linearity in \mathbf{D} (c). The pyknotropy via e in \mathbf{F}_s implies state limits as shown further below. As assumed for simple materials in the sense of Truesdell and Noll (1965) (2.11.8) holds also if \mathbf{T}_s and \mathbf{D} have gradients, this enables finite element calculations with other than linear interpolations of \mathbf{v}_s .

Algebraic representations of \mathbf{F}_s with the outlined properties may only be sketched here as they are so intricate in detail that the physics therein is hardly

visible, and also as they are subject to further improvements. *Elastoplastic* relations (elp) can be abbreviated as

$$\mathbf{F}_s = \mathbf{E}(\mathbf{D} - \mathbf{D}^p) = \mathbf{E}(\mathbf{D} - sh\mathbf{P}) \quad (2.11.9)$$

with a \mathbf{T}_s -dependent fourth-order stiffness tensor \mathbf{E} and a plastic stretching \mathbf{D}^p . \mathbf{E} is usually assumed as isotropic and proportional to $(p_s/p_r)^m$ with an exponent m between 1/2 and 1. The switch factor s disappears if \mathbf{T}_s is within an e -dependent elastic range, and also if $\dot{\mathbf{T}}_s$ with $\mathbf{D}^p = 0$ points there. The direction \mathbf{P} of \mathbf{D}^p (flow rule) depends on the stress direction \mathbf{T}_s/p_s . The factor h is determined by the change of e by (2.11.1) for continued plastification (volumetric hardening). In original CSSM a quadratic form is used as yield function which enables tensile stress and implies the same $\tan \psi_s$ for $\cos 3\alpha_s = \pm 1$, and \mathbf{P} is given by its normal (associated flow rule). In more recent versions the yield function is composed of quadratic forms so that the same $\tan \psi_s$ for $\cos 3\alpha_s = \pm 1$ and traction are avoided, and so that the flow rule is not associated for overcritical $\tan \psi_s$ (e.g. Vermeer 1978). \mathbf{T}_s and \mathbf{D}^p are coaxial, this is achieved by means of invariants.

Hypoplastic relations can be abbreviated by

$$\mathbf{F}_s = f_b(\mathbf{L}\mathbf{D} - f_d\mathbf{N}\mathbf{D}) \quad (2.11.10)$$

Other than by elp in the elastic range, i.e. for (2.11.9) with $s = 0$, (2.11.10) is always non-linear in \mathbf{D} by $D = \|\mathbf{D}\|$. The fourth-order tensor \mathbf{L} and the second order tensor \mathbf{N} depend on \mathbf{T}_s/p_s so that \mathbf{F}_s is isotropic in \mathbf{T}_s/p_s and \mathbf{D} , therein φ_c appears as material constant. The factor f_d is given by (2.4.4), thus (2.11.8a) holds with $m = 1 - n$. The pyknotropy is mainly captured with the factor f_d by (2.4.4).

Although (2.11.10) is formally easier without a switch function than (2.11.9), both representations of \mathbf{F}_s are not very transparent. Instead, \mathbf{F}_s can be represented graphically by generalized response polars, Fig. 2.11.3. Components therein are referred to the convected Cartesian system of instantaneous principal stresses, this is an objective base. A unit stretching, i.e. \mathbf{D} with $D = \|\mathbf{D}\| = 1$, is depicted by points on a sphere in the space of components (a) plus a point in a space of three principal directions of \mathbf{D} referred to the ones of \mathbf{T}_s (b). The stress rate response (for given \mathbf{T}_s and e) is represented by a polar in the space of three stress rate components (c) plus a point for the principal directions of $\dot{\mathbf{T}}_s$, these are also referred to the instantaneous principal axes of \mathbf{T}_s (d).

The response polars should be continuous and convex, this property survives projections from the six-dimensional hyperspace of $\dot{\mathbf{T}}_s$ -components to the three-dimensional component space of Fig. 2.11.3b. Their size increases with the mean pressure $p_s = -\text{tr}\mathbf{T}_s/3$ via $(p_s/h_s)^m$ with $0 \leq m < 1$. This barotropy satisfies (2.11.8a) and is the same as proposed in Sect. 2.2 for two components. elp means $m = 1$ by original CSSM and $m \approx 1/2$ in modified versions (the latter is not consistent with (2.3.1)). hyp means a constant exponent $0 < m < 1$ according to the increase of contact flats (Sect. 2.4).

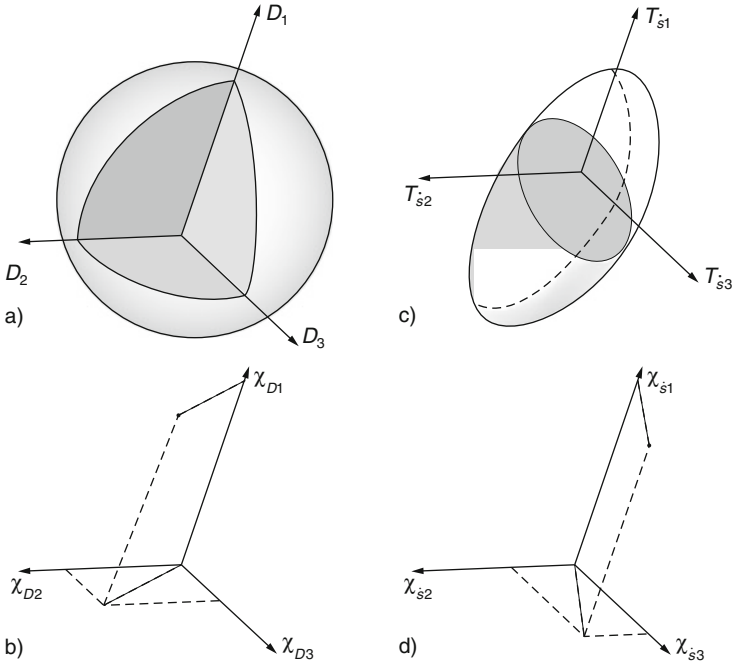


Fig. 2.11.3. Generalized response polars, referred to principal stress directions: (a) unit stretching components, (b) stress rate components, (c) stretching directions, (d) stress rate directions

The non-linearity by (2.11.8c) means that the polars are no centred ellipsoids in general. The latter holds only in the e -dependent elastic range by elp, then the principal directions of \mathbf{D} and $\dot{\mathbf{T}}_s$ agree in the sense of Fig. 2.11.3. Until present there is no stress-induced hypoelastic anisotropy in elp. Otherwise the polars by elp are composed of a centred half-ellipsoid and a non-centred one as in Fig. 2.7.5. The directions of $\dot{\mathbf{T}}_s$ and \mathbf{D} agree in the elastic range by elp, whereas for plastification the direction of \mathbf{T}_s agrees with the one of the plastic stretching \mathbf{D}^p . For hyp the polars are eccentric ellipsoids as in Fig. 2.7.6, and the direction of \mathbf{D} does not agree with those of \mathbf{T}_s and of $\dot{\mathbf{T}}_s$ in general. Thus the response polars for hyp are less intricate than the ones for elp. Both depend on the stress direction \mathbf{T}_s/p_s as for cuboidal deformations (Figs. 2.7.5 and 2.7.6), but the additional influence of changing principal directions cannot easily be visualized. The response polar for a given \mathbf{T}_s depends also on the relative void ratio, this could be represented by nested polars as in Fig. 2.2.4.

State limits of our general RSE are characterized by relations of stress direction and stretching direction, i.e.

$$\mathbf{T}_s/p_s = \mathbf{G}_s(\mathbf{D}/D), \quad (2.11.11)$$

and of limit void ratio with mean pressure and stress obliquity, i.e.

$$e = f_e(p_s/h_s, \tan\psi_s). \quad (2.11.12)$$

\mathbf{G}_s is isotropic in \mathbf{D}/D due to frame-indifference, thus \mathbf{T}_s and \mathbf{D} are coaxial for state limits and (2.11.11) can be expressed by relations of deviatoric invariants. The third stretching invariant $\cos 3\alpha_D$, defined by (2.11.6) with $\mathbf{D}^* = \mathbf{D} - (1/3)\text{tr}\mathbf{D}$ instead of \mathbf{T}_s^* , depends on $\cos 3\alpha_s$ as shown in Fig. 2.7.2b, therein the influence of $\tan\psi_s$ may be neglected. The stretching obliquity $\tan\psi_D$ by (2.11.5) with \mathbf{D} and $-\text{tr}\mathbf{D}/3$ instead of \mathbf{T}_s and p_s depends on $\tan\psi_s$ and $\cos 3\alpha_s$ as shown in Fig. 2.7.2c with ψ_ε instead of ψ_s .

Equation (2.11.12) can be represented by plots of e vs. $\log(p_s/h_s)$ and of r_e vs. $\tan\psi_s$ as Fig. 2.11.2a and 2.7.2d. Isochoric (or critical) state limits are stationary, then a convected RSE has $\dot{e} = 0$, $\dot{p}_s = 0$ and the critical stress obliquity $\tan\psi_{sc}$ which depends on $\cos 3\alpha_s$ (Fig. 2.11.2b). Invariant relations could be calculated from the stationarity condition $\dot{\mathbf{T}}_s = \mathbf{F}_s = 0$ with a given representation of \mathbf{F}_s and a given \mathbf{D} . Contractant state limits are subcritical with increasing pressure, i.e. with $\text{tr}\mathbf{D} < 0$ they have $\tan\psi_s < \tan\psi_{sc}$ and $\dot{p}_s > 0$. Dilatant state limits are overcritical with decreasing pressure, i.e. with $\text{tr}\mathbf{D} > 0$ they have $\tan\psi_s > \tan\psi_{sc}$. Invariant relations could be calculated for $\text{tr}\mathbf{D} \pm 0$ from the proportionality of stress and stress rate, i.e.

$$\dot{\mathbf{T}}_s/\dot{p}_s = \mathbf{F}_s/\dot{p}_s = \mathbf{T}_s/p_s \quad (2.11.13)$$

with a given representation of \mathbf{T}_s and a given \mathbf{D} . The obtained $\tan\psi_s$ and $\cos 3\alpha_s$ could be used to calculate the relation of \dot{p}_s with \dot{e} by (2.11.1) and (2.11.11).

Representations of \mathbf{F}_s by elp and hyp are essentially formulated so that observed state limits are captured. As was shown with cylindrical symmetry in Sect. 2.2 the range of stretching directions is bounded to avoid tensile stresses. elp is further bounded as small p_s are not captured by (2.3.1). State limits are assumed to be attainable by stretching with constant \mathbf{D} and suitable initial r_e . This is achieved with the response polars as shown in Figs. 2.7.5 and 2.7.6, plus an alignment of the principal direction of \mathbf{T}_s to the one of \mathbf{D} , which could be shown with a sequence of plots as Fig. 2.11.3. Using algebraic representations of \mathbf{F}_s as by (2.11.9) or (2.11.10) one could also obtain these attractors by numerical element tests, whereas a strict mathematical proof is not yet in sight.

The *range of attainable states* is restricted. If the initial r_e is too high for a given $\text{tr}\mathbf{D}$ the skeleton decays before a state limit is reached with a constant \mathbf{T}_s/p_s . If r_e is too low for a given $\text{tr}\mathbf{D}$ stretching with constant \mathbf{D} can crush the grains so that a state limit is not approached with the initial granular properties. State limits can nearly be attained with a constant stretching deviator $\mathbf{D}^* = \mathbf{D} - (1/3)\text{tr}\mathbf{D}$ and a constant p_s . This can lead to a generalized peak state with bigger $\tan\psi_s$ and dilation ratio $\text{tr}\mathbf{D}/D$ than before and afterwards. These are no exact state limits as \mathbf{D} is not constant in alignment with $bf\mathbf{T}_s$,

and as shear bands with polar quantities arise spontaneously (Sect. 8.2). One may call a peak of $\tan\psi_s$ or $p_s \tan\psi_s$ strength, but this depends on the actual r_e and direction of stretching and is thus not objective. Therefore hardening, softening and ductility are rather vague notions.

Void ratios in the possible range by Fig. 2.11.2a cannot be attained arbitrarily by deformations with constant \mathbf{D} or \mathbf{D}^* . Very loose skeletons, say with $e > e_{co}$ by (2.4.1), cannot be obtained by decompression or isobaric stretching, but by moist placement with capillary attraction. Densification by monotonous contractant deformations is limited by grain crushing. As shown e.g. with Fig. 2.10.4 skeletons can get denser by isobaric *reversals*, but how can this behaviour be captured objectively with the six degrees of freedom of our RSE?

Changes of sign of the power

$$P = \text{tr} \mathbf{T}_s \mathbf{D} \quad (2.11.14)$$

indicate reversals objectively, but little specifically. *Deformation cycles* may be imposed from an inevitably arbitrary initial configuration and state. More precisely speaking, starting with a set \mathbf{T}_s and e in the allowed range an evolution $\mathbf{D}(t)$ may lead to a deformation \mathbf{H} with $d\mathbf{H}/dt = \mathbf{D}$ (Hencky strain tensor \mathbf{H}) which returns to zero after a period $t = t_p, 2t_p$ etc. This may be represented by a closed curve in a six-dimensional component space of \mathbf{H} , but how to describe it objectively? An amplitude may be defined by a norm $\|\mathbf{H}\|$, but when is this small or big? The shape of a \mathbf{H} -component-path may be described by means of a circumscribing hyper-ellipsoid, but are properties as slenderness or convexity of physical use? How could reversals be defined invariantly, and how could the arbitrariness of the onset be ruled out?

These questions cannot be answered without the associated evolution of \mathbf{T}_s and e , and restrictions are needed for focussing on key properties of simple psammoids. To begin with, let us confine to deformation cycles which imply only two changes of $\text{sgn}P$. Furthermore the cycles may be isochoric or isobaric, i.e. $\dot{e} = 0$ or $\dot{p}_s = 0$. Initial states and deformation cycles may be chosen so that skeleton decay ($p_s \rightarrow 0$), peak states with marked shear localization and crushing (by too high p_s) are avoided. This can hardly be judged in advance, but would be exhibited by physical or numerical RSE-tests so that trial and error could show what is allowable.

Within this frame deformation cycles may be repeated so often that state cycles are attained. These do not depend on the arbitrary reference shape, but only on the deformation cycles and the average void ratio \bar{e} or pressure \bar{p}_s . These attractors could be represented by three associated plots of $\tan\psi_s$ vs. $\cos 3\alpha_s$ (Fig. 2.11.4a), e vs. $\log(p_s/h_s)$ (b) and principal directions of \mathbf{T}_s in two projections (c). The third plot is objective by referring the angles to the principal axes of the average stress $\bar{\mathbf{T}}_s$ for one deformation cycle. Taking angles in rad and normalizing the e vs. $\log(p_s/h_s)$ plot so that both range from ca. 0 to 1, one can define the *amplitude* of a state cycle by

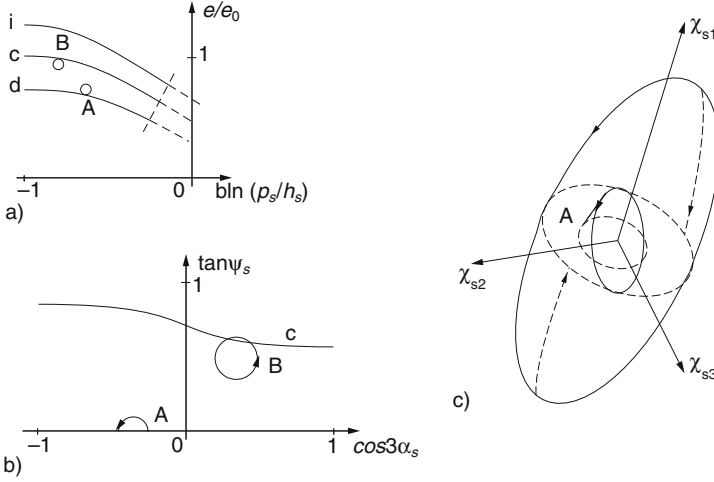


Fig. 2.11.4. State cycles for cyclic deformation (A, e.g. with small amplitude), and ratcheting (B, e.g. with big amplitude): (a) void ratio vs. pressure (normalized), (b) stress obliquity vs. Lode parameter, (c) principal stress directions relative to mean values (two projections)

$$a_s = \frac{1}{\sqrt{7}} [(\Delta \tan \psi_s)^2 + (\Delta \cos 3\alpha_s)^2 + \Sigma(\Delta \chi_i)^2 + (\Delta e/e_o)^2 + (\Delta b \ln(p_s/h_s)^2)]^{1/2} \quad (2.11.15)$$

with ranges Δ and normalizing factors e_o and b . As indicated in Fig. 2.11.4 one can speak of big and small cycles if a_s attains 1 or does not exceed 0.1 (say). Mean state values are more evident for small cycles, but could also be calculated for bigger ones with representations of \mathbf{F}_s in (2.11.7).

We can now characterize the response of simple psammoids to deformation cycles more generally than in previous sections. Observations indicate that isochoric deformation cycles with two changes of $\text{sgn } P$ cause a reduction of the average pressure \bar{p}_s and lead to state cycles with a double cycle of p_s , whereas isobaric deformation cycles cause a reduction of the mean void ratio \bar{e} and lead to a double cycle of e . Furthermore, the average stress obliquity $\tan \bar{\psi}_s$ tends to almost zero, i.e. \mathbf{T}_s tends to cycles around $p_s \mathbf{1}$. These properties are missed by elp as \mathbf{T}_s remains in the elastic range after at most two reversals. Hyp reproduces reduction and double cycles, but with the more exaggerated progression and hysteresis the smaller the amplitude is. As observed the average asymptotic relative void ratio \bar{r}_e by hyp is closer to zero for smaller amplitudes. The average principal directions of average stress $\bar{\mathbf{T}}_s$ agree with the ones of average stretching $\bar{\mathbf{D}}$ for state cycles. This result of alignment is necessary for frame-indifference, but as yet not confirmed.

The work per unit of skeleton volume which is dissipated in one state cycle, viz.

$$W_{sc} = \oint P dt = \oint \text{tr} \mathbf{T}_s \mathbf{D} dt, \quad (2.11.16)$$

is always positive by hyp and observations. An objective *hysteresis ratio* can be defined by referring it to the mean pressure \bar{p}_s in one cycle, i.e. as

$$r_h = W_{sc} / \bar{p}_s \quad . \quad (2.11.17)$$

It is rate-independent by (2.11.8b) and implies that the work is dissipated by dry friction. For big amplitudes, i.e. $a_s > \text{ca. } 1/2$ by (2.11.15), r_h is apparently captured by hyp, this means that the skeleton passes through SOM-states. For convex slender deformation cycles with smaller amplitudes (say $a_s < 1/4$) r_h is grossly overestimated by hyp. Then the internal state of the skeleton is no more determined by \mathbf{T}_s and e so that hidden variables are needed (Sect. 4.7). It appears that the threshold amplitude for a more hypoelastic than hypoplastic behaviour is lower for concave and squat state cycles, but this could not yet be quantified in an objective way.

Ratcheting can be defined for our general RSE by a superposition of a cyclic deformation and an isochoric stretching with constant direction. For objectivity the reference configuration has to be updated after each deformation cycle according to the simultaneous shift. This ratcheting can in particular be isochoric or isobaric. Both elp and hyp predict an alignment of average principal stress $\bar{\mathbf{T}}_s$ and stretching $\bar{\mathbf{D}}$ as required for frame-indifference. State cycles can be represented by three associated plots, this is also shown with Fig. 2.11.4. An amplitude could again be expressed by (2.11.15), the shift per cycle is bigger with a bigger average obliquity $\bar{\psi}_s$. As observed the asymptotic $\tan \psi_s$ attains repeatedly $\tan \psi_{sc}$ both by elp and hyp. Observations indicate a lower asymptotic average relative void ratio \bar{r}_e for smaller amplitudes, but higher than without shift. The latter is not obtained with elp, whereas shift and hysteresis are overpredicted by hyp for smaller amplitudes.

It appears that available experimental data and simulations of them do not enable a further quantification. Ratcheting with big amplitude and shift may be captured by hyp as then successions of SOM-states may be assumed. Otherwise hidden variables have to be taken into account explicitly, but such approaches are preliminary (Sect. 4.7). The dissipated work by (2.11.16) and the hysteresis ratio by (2.11.17) have to be taken for the cyclic part of deformation, the dissipation by the simultaneous shift has also to be taken into account.

Numerical simulations with elp and hyp could exhibit when and how the proposed state cycles are attained by cyclic deformations or ratcheting. The range of these attractors can as yet only be explored by trial and error, generalized response polars may be of use, but a strict mathematical proof is not in sight. The range of validity can be judged objectively by these attractors as the arbitrary onset is ruled out, but experiments with uniform general RSEs are hardly feasible. Such attractors could also be attained with gradients of stretching and state in shearing, torsion and tumbling experiments (Sects. 2.9,

14.6, and 15.5). Simulations of them with simple psammoid relations may indicate their range of validity, but less precisely than with element tests as boundary conditions require additional assumptions (Sect. 10.3).

So how can *material parameters* be determined as far as simple psammoids may be assumed, i.e. how can these be identified? This can be achieved by means of attractors without and with reversals as thus the partial indeterminacy of initial states can be ruled out. State limits come first, and among them critical states play the key role. The critical friction angle φ_c of a dry or submerged granular soil can be determined from the slope of a loose cone (Sect. 14.2) or by simple shearing (Sect. 2.9), whereas uniform cylindrical samples are an expensive exception (Sect. 14.1). The critical void ratio e_c for $p_s \approx 0$ can be estimated with a loose free fill, and more precisely determined with uniform cylindrical samples, thus parameters for (2.3.1) or (2.4.1) can be adapted.

As shown with Fig. 2.5.1 upper bound void ratios e_i can be determined by isotropic compression of loose samples, but this is expensive and not reliable. Oedometric compression tests with loose samples by moist placement are easier and may suffice to catch the p_s -dependence by (2.3.1) or (2.4.1). One can only guess when SOM-states are attained, and when these go over into state limits. This cannot be judged with elp as (2.3.1) fails for $p_s \rightarrow 0$, and as the assumed elastic ranges are not realistic. Plotting volume changes ε_v vs. $(p_s/h_s)^{1-n}$ with tentative h_s and n can reveal n by hyp for SOM-states as the power law holds approximately by (2.4.3) with (2.4.5). Variation of the initial e can reveal the approach to a contractant state limit, cf. Fig. 2.5.2. SOM-sections for different initial e , recognizable from $\varepsilon_v \approx (p_s/h_s)^{1-n}$ with a single n , enable to estimate β in (2.4.5) by matching.

Dilatant state limits with $\tan\psi_s > \tan\psi_{sc}$ and $e < e_c$ for a given p_s may be captured by peak states as far as marked shear localizations are avoided when approaching them. Void ratio and dilatancy ratio $\text{tr}\mathbf{D}/D$ at peak are needed for different stress obliquities $\tan\psi_s$. Matching such data yields parameters for dilatant yielding by elp and for α in (2.4.4) by hyp. The samples should be densified by vibration or slow isobaric cycling under pressure, not by pluviation as this can produce an anisotropic sandwich (Sect. 9.1). The lower bound e_d can be approached by isobaric shaking or cycling, but not precisely. This is excluded by elp, whereas the extreme state limits enabled by hyp cannot be attained. As e_d cannot be determined exactly it may suffice to estimate e_{do} for $p_s = 0$ by shaking with a free surface, and to take for given the same n and h_s by (2.4.1) as for smaller $\tan\psi_s$. The differential deviatoric stiffness $d\sigma^*/d\varepsilon^*$ from triaxial tests may be used to improve the identification if the assumption of uniform SOM-states is justified. An objective differential stiffness, e.g. $\|\dot{\mathbf{T}}_s\|/\|\mathbf{D}\|$, is of little use as it varies extremely with p_s , e and the directions \mathbf{T}_s/p_s plus \mathbf{D}/D .

Apart from preparatory compaction, experiments with reversals can contribute to the identification as they can reveal the range of validity of simple psammoid models. Hypoelastic parameters for elp may be estimated from the

response to a reversal after a state limit, but even then the absence of an elastic range should not be ignored. Experiments with strain cycles or ratcheting can indicate how far SOM-states may be assumed, preferably after attractors have been attained. Alignment of average stress and double frequency of p_s or e may be observed in sophisticated experiments, but the desired uniformity can hardly be maintained with so big amplitudes that a sequence of SOM-states may be assumed. This means that the validity range of simple psammoid models for evolutions with several reversals cannot be specified precisely.

Summing up, stress and void ratio may suffice as state variables for big enough monotonous deformations of general RSEs, but with reversals anelastic effects are missed by elp and exaggerated by hyp. An alignment of stress and stretching occurs near state limits due to frame-indifference, tests with cylindrical symmetry suffice therefore to determine state limit parameters. An alignment of average stress and stretching is also obtained by objectivity in the asymptotic response to deformation cycles and ratcheting. Average reduction and asymptotic double frequency of pressure or void ratio are obtained by hyp for isochoric or isobaric ratcheting, respectively, but exaggerated except for big amplitudes. The range of validity of simple psammoid models without hidden variables cannot easily be demarcated.

SIMPLE PELOIDS

Mach (1912) stated ‘The economy of communication and perception belongs to the essence of science’. Which are the essentials of soils like clay, and how can they be captured in Mach’s sense? Which properties and concepts can be taken over from psammoids, what should be added in the first place, and what could be left aside?

Imagining a lump of clay one is tempted to name *cohesion* as primary property. However, the tensile strength of clays is mainly due to the suction of pore water. The net attraction of solid clay particles in water (Sect. 6.3) is often negligible against the mean pressure p_s of the skeleton. Nevertheless it can enable higher void ratios, this cannot easily be captured (Sect. 7.1) and is left aside here. Terzaghi (1931) attributed the observed cohesion to the bound pore water, but this turned out as an error (Sect. 6.1). Cracking of clays suggests also cohesion, but is due to the cavitation of pore water (Sect. 6.3). We leave aside unsaturated and cemented clays as they are intricate (Sects. 7.2 and 7.3).

Remoulded clays can have much higher void ratios e than granular soils, and their e is far more reduced by increasing the effective pressure $p' (= p_s)$. This could be expressed by higher reference values e_o and a lower granulate hardness h_s in (2.4.1), and would be a quantitative difference. However, saturated clays exhibit also *viscous effects* which cannot be attributed to the pore water. For preparation it is outlined in Sect. 3.1 how rate-dependence, creep and relaxation of a pore-free solid can be captured by two parameters, and how it can be attributed to thermally activated dislocations.

Introducing *simple peloids* (from $\pi\eta\lambda\acute{o}\varsigma$ =clay, i.e. clay-like materials) in Sect. 2.2 the skeleton viscosity is likewise captured with only two parameters. Rate-dependence and creep could be modelled with an argotropic solid hardness, but relaxation requires a viscosity factor as for solids. In visco-elastoplastic and -hypoplastic relations (*v-elp* and *v-hyp*, Sects. 2.3 and 2.4) this factor depends on the ratio p_s/p_e of actual and equivalent pressures p_s and p_e and on a viscosity index I_v . Thus state limits and state cycles can be nearly the same as for psammoids in case of a constant stretching rate D .

Differences arise with dramatic changes of D , viz. jumps or waiting intervals. As with solids v-elp and v-hyp are similar for monotonous evolutions, but differ in case of reversals.

The range of validity of v-elp and v-hyp is first discussed in Sects. 3.5 and 3.6 for cylindrical samples. These are not uniform with diffusion of pore water, therefore undrained tests are preferred, drained ones can also be more intricate due to shear localization. The few available reports with reversals indicate that internal variables are needed as for psammoids in case of small amplitudes.

The concept of simple peloids can be extended to cuboidal deformations (Sect. 3.7), simple shearing (Sect. 3.8) and arbitrary deformations (Sect. 3.9). Although pore water diffusion and skeleton viscosity come into play this chapter is shorter than Chap. 2 as there are less experimental reports. The state of simple peloid RSEs is again characterized by skeleton stress and void ratio, but the amount of stretching D is also needed.

3.1 A second prelude on solids

Other than assumed in Sect. 2.1 ductile solids – e.g. lead at room temperature – exhibit *viscous effects*. For uniaxial cases the resistance to monotonous stretching is markedly bigger if the strain rate $|\dot{\epsilon}|$ is increased by orders of magnitude, Fig. 3.1.1a. After a jump to another $\dot{\epsilon}$ the σ vs. ϵ curve tends to the one for the new $\dot{\epsilon}$ from the very beginning, this is indicated by dotted curves. The observed *argotropy* (i.e. rate-dependence, $\alpha\varrho\gamma\acute{o}\varsigma = \text{fast}$) of the resistance can be approximated by

$$\begin{aligned} \text{(a)} \quad |\sigma| &= 2c_r[1 + I_v \ln(|\dot{\epsilon}| / |\dot{\epsilon}_r|)] \\ \text{(b)} \quad &\approx 2c_r(|\dot{\epsilon}| / |\dot{\epsilon}_r|)^{I_v} \end{aligned} \tag{3.1.1}$$

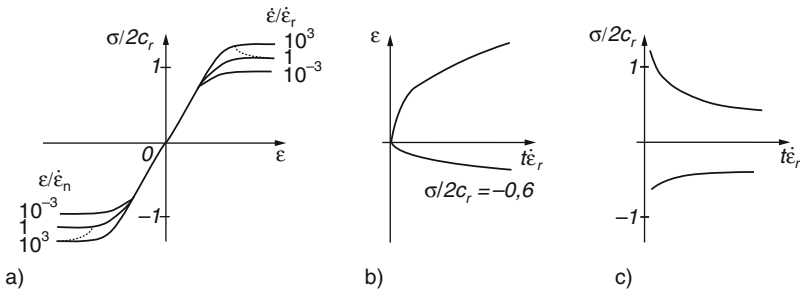


Fig. 3.1.1. Viscous behaviour of a pore-free solid: (a) rate-dependence, (b) creep, (c) relaxation

with a reference cohesion c_r for a convenient reference rate $\dot{\varepsilon}_r$. Following Leinenkugel (1976), I_v is called *viscosity index*, it ranges from ca. 0.01 to 0.1. Equation (3.1.1a) fails for $|\dot{\varepsilon}| \rightarrow 0$, and $\sigma \rightarrow 0$ for $|\dot{\varepsilon}| \rightarrow 0$ by (3.1.1b) cannot be observed as the low I_v would require extremely low $|\dot{\varepsilon}|$. Equation (3.1.1a, b) agree fairly well for some decades of $|\dot{\varepsilon}| / \dot{\varepsilon}_r$. *Creep* is obtained if σ is kept constant (Fig. 3.1.1b). The time t can be replaced by the dimensionless $t\dot{\varepsilon}_r$. After a transition the creep rate $\dot{\varepsilon}$ is the one by the inversion of (3.1.1), and its sign agrees with the one of σ , i.e.

$$\begin{aligned} \text{(a)} \quad \dot{\varepsilon} &= \dot{\varepsilon}_r \cdot \text{sgn}(\sigma) \cdot \exp\left(\frac{|\sigma| / 2c_r - 1}{I_v}\right) \\ \text{(b)} \quad &\approx \dot{\varepsilon}_r \cdot \text{sgn}(\sigma) \cdot \left(\frac{|\sigma|}{2c_r}\right)^{1/I_v}. \end{aligned} \quad (3.1.2)$$

Equation (3.1.2b) is empirically known as Norton's (1929) law. *Relaxation*, i.e. reduction of $|\sigma|$ with time t for $\varepsilon = 0$ occurs as indicated by Fig. 3.1.1c. It happens the more rapidly the bigger $|\sigma| / 2c_r$ initially is. An asymptotic σ for $t \rightarrow \infty$ cannot be observed, only with big I_v observations indicate $\sigma \rightarrow 0$.

The response after *reversals* resembles the one of Fig 2.1.1a. With constant $|\dot{\varepsilon}|$ hysteresis loops are obtained, but $\max |\sigma|$ depends on $\dot{\varepsilon}$ as by (3.1.1). The loops get wider if $|\dot{\varepsilon}|$ is reduced just before a reversal and increased just after it. Nearly elastic behaviour is observed for $|\sigma| / 2c_r < \text{ca. } 0.5$ with $|\dot{\varepsilon}| / |\dot{\varepsilon}_r| > \text{ca. } 10^{-3}$.

Prandtl (1928) explained these viscous effects by means of *thermally activated dislocations*. His mechanistic model may be substituted by the one shown in Fig. 3.1.2. Imagine a pendulum with a magnet above a row of repulsive magnets upon an incline (a, you can easily assemble it). The free energy F of the suspended magnet has a maximum in the middle due to repulsion, and two sideways minima with a lower F on the lower side due to gravity (b).

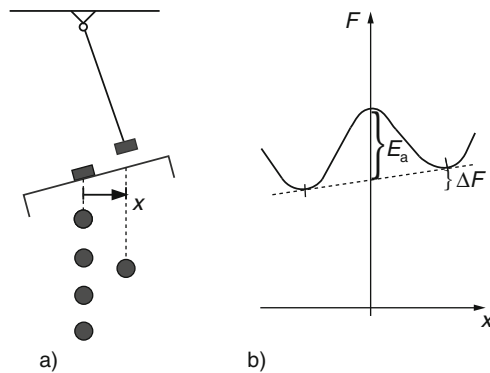


Fig. 3.1.2. A mechanistic model of thermal activation: (a) pendulum with repulsive magnets, (b) free energy vs. distance from middle position

The energy difference between upper and lower minimum may be called *drift* ΔF . The excess of the maximum against the gravitational part is called *activation energy* E_a . The released pendulum experiences a chaotic motion which comes to an end by damping. The base may now be shaken chaotically with an average kinetic energy E_k . Every now and then the pendulum crosses the middle gate, far more often downwards than upwards and more often with bigger E_k/E_a .

The magnets are to represent groups of molecules and may be named *dislocation units*. The forces acting between them are conservative, i.e. they are determined by the relative positions via potentials. A system of such units is capable of chaotic oscillations with leading frequencies, here we take only the lowest one f_c (imagine the pendulum without magnets under it). The average chaotic kinetic energy may represent the absolute temperature T via $E_k = k_B T$ with the Boltzmann constant k_B . The probability distribution of the kinetic energy E is exponential,

$$p = \frac{k_B T}{e} \exp(1 - E/k_B T) \quad (3.1.3)$$

with $e = 2.7183$ and the prefactor from $\int p dE = 1$. Thus the entropy, i.e. a measure of missing information or disorder,

$$S = \int_0^{\infty} p \ln p dE \quad , \quad (3.1.4)$$

is bigger than with any other distribution, this means maximal disorder. Our shaking base represents a thermostat that keeps T constant, otherwise E_k would disappear by radiation of waves. The average number ν of passages down- (+) or upwards (-) through the gate, i.e. of dislocations, per unit of time can be derived with (3.1.3) as

$$\nu \approx f_c \frac{k_B T}{E_a} \exp\left(\frac{\pm \Delta F - E_a}{k_B T}\right) \quad . \quad (3.1.5)$$

For $\Delta F > k_B T$ the upwards part may be neglected. Comparison of (3.1.5) with (3.1.1) yields

$$\begin{aligned} I_v &\sim k_B T/E_a, \\ \dot{\varepsilon}_r &\sim f_c k_B T/E_a. \end{aligned} \quad (3.1.6)$$

Thus Prandtl (1928) concluded that the two parameters called I_v and $\dot{\varepsilon}_r$ in (3.1.1) are proportional to the absolute temperature, and that an internal frequency is needed to get an objective reference rate.

Persson (2000a) derived similar relations with modern condensed matter physics and achieved further conclusions. The dislocation units are imagined as nano-sized blocks of length d_d with shear modulus G and cohesion c_d .

This means a dislocation energy $E_a \approx c_d d_d^3$ and a reference frequency $f_c \approx \sqrt{G/\rho}/d_d$ with mass density ρ . For stationary stretching with $\sigma > 0$ and $\dot{\epsilon} > 0$ Persson gets

$$\sigma = 2c_d \left[1 + \frac{k_B T}{E_a} \ln \left(\frac{3G}{c_d} \frac{E_a}{k_B T} \frac{\dot{\epsilon}}{f_c} \right) \right] \quad (3.1.7)$$

in the range

$$\exp \left(\frac{-E_a}{k_B T} \right) \ll \frac{3G}{c_d} \frac{E_a}{k_B T} \frac{\dot{\epsilon}}{f_c} \ll 1 \quad . \quad (3.1.8)$$

Towards the upper bound by (3.1.8) the dissipated energy leads to heating and melting so that σ is lower than by (3.1.7). Towards the lower bound (3.1.7) has to be replaced by a linear relation of σ with $\dot{\epsilon}$ as for a viscous fluid. Evaluation of published creep test results with different T by means of (3.1.7) leads to activation energies up to $E_a \approx 5 \text{ eV}$ (electron volt) for steel ($1 \text{ eV} = 40 k_B T$ holds for $T = 293 \text{ K}$).

Comparison of (3.1.7) with (3.1.1) confirms (3.1.6). As the reference rate implied by (3.1.7) is extremely high, and as the variation of T is small in most geotechnical applications, it is of use to transform (3.1.7) into

$$\sigma = 2c_d \left[1 - \frac{k_B T}{E_a} \ln \left(\frac{f_c}{m \dot{\epsilon}_r} \right) \right] \left[1 + \frac{k_B T / E_a}{1 - (k_B T / E_a) \ln(f_c / m \dot{\epsilon}_r)} \ln \left(\frac{\dot{\epsilon}}{\dot{\epsilon}_r} \right) \right] \quad (3.1.9)$$

with $m = (3G/c_d)(E_a/k_B T)$ and a convenient reference rate $\dot{\epsilon}_r$ in the working range of $\dot{\epsilon}$. $\dot{\epsilon}_r$ is a suitable fraction of f_c and thus likewise objective, though somewhat arbitrary as the size d_d of dislocation units is not precisely known. The crude estimates $3G/c_d \approx 10$, $E_a/k_B T \approx 10^2$ and $f_c/\dot{\epsilon}_r \approx 10^{12} \text{ s}^{-1}/10^{-6} \text{ s}^{-1} = 10^{18}$ lead to $\ln(f_c/m\dot{\epsilon}_r) \approx \ln 10^{15} \approx 35$. This means that the average resistance c_r for $\dot{\epsilon} = \dot{\epsilon}_r$ is well below the one of dislocation units, and that I_v by (3.1.1) with a convenient $\dot{\epsilon}_r$ and the usual T is related with the activation energy by

$$I_v = \frac{k_B T / E_a}{1 - (k_B T / E_a) \ln(f_c / m \dot{\epsilon}_r)} \quad . \quad (3.1.10)$$

I_v can be determined from σ -changes due to changes of $\dot{\epsilon}$ with constant T via (3.1.1), viz.

$$I_v = \frac{\sigma - 2c_r}{\ln(\dot{\epsilon}/\dot{\epsilon}_r)} \quad (3.1.11)$$

with σ for $\dot{\epsilon} \neq \dot{\epsilon}_r$. Thus the argotropy of the resistance for isothermal stationary stretching reveals the dislocation energy via the inversion of (3.1.10) if $\ln(f_c/m\dot{\epsilon}_r)$ can be estimated.

A constitutive relation for the *uniaxial* case can be written as

$$\dot{\sigma} = E(\dot{\epsilon} - \dot{\epsilon}^a) \quad (3.1.12)$$

with the anelastic stretching rate

$$\dot{\varepsilon}^a = Af_v \text{sgn}(\sigma) \dot{\varepsilon}_r \tag{3.1.13}$$

and the *viscosity factor*

$$f_v = \exp\left(\frac{|\sigma|/2c_r - 1}{I_v}\right) \approx \left(\frac{|\sigma|}{2c_r}\right)^{1/I_v}. \tag{3.1.14}$$

The prefactor $A = 1$ is assumed for *visco-hypoplastic* relations (abbreviated v-hyp in the sequel). For *visco-elastoplastic* relations (v-elp) the switch condition

$$\begin{aligned} \text{a)} \quad & A = 1 \quad \text{for } \sigma \dot{\varepsilon} \geq 0, \\ \text{b)} \quad & A = 0 \quad \text{for } \sigma \dot{\varepsilon} < 0 \end{aligned} \tag{3.1.15}$$

is proposed, cf. Sect. 3.1 This can be abbreviated as $A = H(\sigma \dot{\varepsilon})$ with the Heaviside function

$$H(x) = \begin{cases} 1 & \text{for } x \geq 0, \\ 0 & \text{for } x < 0. \end{cases} \tag{3.1.16}$$

For monotonous evolutions with $\sigma \dot{\varepsilon} \geq 0$ there is no difference between v-elp and v-hyp due to $A = 1$. Stationary stretching means $\dot{\sigma}=0$ for $\dot{\varepsilon}=\text{const}$, i.e. $\dot{\varepsilon} = \dot{\varepsilon}^a$ by (3.1.12). With (3.1.13) and (3.1.14) this leads to (3.1.1) and its inversion (3.1.2). This is achieved as f_v is the inversion of the factor in (3.1.1). Depending on the sign of σ and $\dot{\varepsilon}$ there are two *argotropic state limits* for uniaxial stationary deformations. They are described by (3.1.1) or its inversion and correspond to (3.1.7) or (3.1.9), i.e. viscoplastic deformations are thermally activated.

Typical evolutions which could be calculated with (3.1.12), (3.1.13) and (3.1.14) for $A = 1$ are shown in Fig. 3.1.3. With an imposed constant stretching rate, and independently of the initial stress, the stress tends to an argotropic state limit which is thus a driven attractor (a). This is achieved with (3.1.12) as f_v by (3.1.14) tends to $|\dot{\varepsilon}|/\dot{\varepsilon}_r$ so that $\dot{\varepsilon}^a \rightarrow \dot{\varepsilon}$ is produced by (3.1.13). If $\dot{\varepsilon}$ is suddenly changed by $\Delta\dot{\varepsilon}$ from a state limit the stress rate switches to an elastic $\dot{\sigma} = E\Delta\dot{\varepsilon}$ and disappears thereafter with further stretching. Creep with constant σ tends to the state limit with $\dot{\varepsilon}$ by (3.1.2), depending

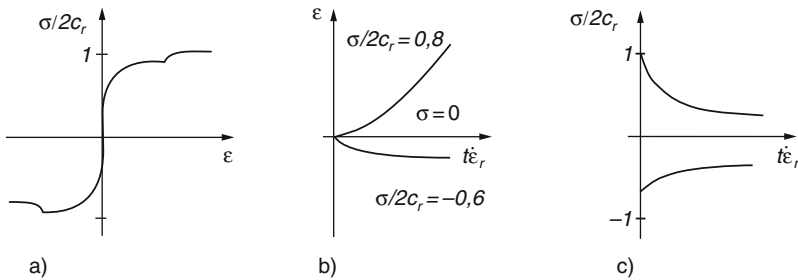


Fig. 3.1.3. Viscous behaviour by (3.1.12) to (3.1.14): (a) argotropy, (b) creep, (c) relaxation

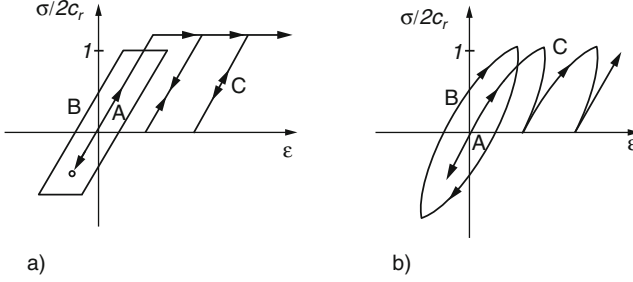


Fig. 3.1.4. Hysteresis and ratcheting with visco-elastoplastic (v-elp) (a) and visco-hypoplastic (v-hyp) relations (b)

on the initial σ and $\dot{\epsilon}$ the transition exhibits acceleration or deceleration (b). Relaxation according to

$$\dot{\sigma} = -E f_v \operatorname{sgn}(\sigma) \dot{\epsilon}_r \quad (3.1.17)$$

is obtained for $\dot{\epsilon}=0$ (c). A similar relation was derived by Persson (2000a). The similarity of observed and predicted monotonous evolutions (Figs. 3.1.1 and 3.1.3) confirms the proposed constitutive relation.

Differences among v-elp and v-hyp arise with *reversals*, Fig. 3.1.4. For v-elp the response is elastic after each reversal as long as $\sigma\dot{\epsilon}$ is negative, thus $\dot{\epsilon}^a=0$ holds by (3.1.15a). ϵ -cycles with constant $|\dot{\epsilon}|$ and a small amplitude, so that $|\sigma|$ remains well below the limit value by (3.1.1), lead to a practically elastic response (A). For intervals with $\sigma\dot{\epsilon} \geq 0$, and thus $A = 1$ by (3.1.15), $\dot{\epsilon}^a$ is negligible against $\dot{\epsilon}$ as then (3.1.16) yields $f_v \ll 1$. That's why only one switch function is needed for A , not two as in (2.1.1). ϵ -cycles with constant $|\dot{\epsilon}|$ and bigger amplitude lead to a markedly hysteretic asymptotic cycle (B). The response to small stress cycles is practically elastic. Non-symmetric bigger stress cycles lead to ratcheting (C). Hysteresis and ratcheting are increased by waiting intervals due to relaxation or creep, respectively.

With v-hyp (Fig. 3.1.4b) the response to small strain cycles (A) is nearly the same as with v-elp due to $f_v \ll 1$. For bigger strain cycles the asymptotic hysteresis is smaller than with v-elp (B), whereas ratcheting due to non-symmetric stress cycles is bigger (C). Hysteresis and ratcheting increase again with waiting intervals. It appears that the plots for strain cycles produced with v-hyp are somewhat more realistic than with v-elp, whereas ratcheting is apparently better modelled by v-elp.

For *cuboïdal* deformations we use the same notations and representations as in Sect. 2.1, but now with allowance for viscous effects. *Argotropic state limits* appear in associated deviator planes with strain rate and stress components, Fig. 3.1.5. The $\dot{\epsilon}_i$ are represented by the deviatoric direction angle α_ϵ and the normalized intensity $(D/D_r)^{I_v}$ with reference rate D_r (b). Cycles for equal D are markedly different only for a variation of D over several decades due to $0 < I_v \ll 1$. Associated limit stress states (b) have the same direction due to the assumed isotropy, $\alpha_\sigma = \alpha_\epsilon$, and have the intensity

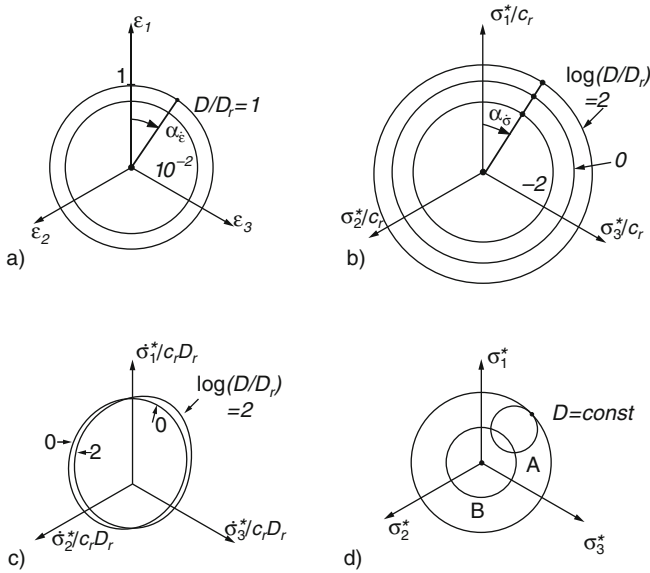


Fig. 3.1.5. Deviatoric argotropic response of a solid cuboid: (a) substitute strain rates, (b) state limits, general (c) and special (d) response polars

$$\sigma^* = \sqrt{\sum \sigma_i^{*2}} = \frac{4}{\sqrt{5}} c_r (D/D_r)^{I_v} . \quad (3.1.18)$$

With the factor $4/\sqrt{5}$ this implies the uniaxial version (3.1.1) for $\cos 3\alpha = \pm 1$.

Argotropic response polars represent stress rates, Fig. 3.1.5c, related with strain rates as shown in Fig. 3.1.5a. Strain rates with constant D can be represented by directions α_ε and circles in a deviator plane with $d_i = (2|\dot{\varepsilon}_i|/3D_r)^{I_v} \text{sgn}(\dot{\varepsilon}_i)$ (a). The polars should be convex and continuous and are eccentric in general (c). They can be plotted in the stress plane, two evident cases are shown in Fig. 3.1.5d. For a state limit the polar with the same D touches the limit stress circle with $\alpha_\sigma = \alpha_\varepsilon$ so that $\dot{\sigma}_i=0$ holds (A). For the state $\sigma_i=0$ the polar is circular with the assumed isotropy (B).

The extension of (3.1.12), (3.1.13) and (3.1.14) can be written as

$$\dot{\sigma}_i^* = G(\dot{\varepsilon}_i - \dot{\varepsilon}_i^a) \quad (3.1.19)$$

with the anelastic stretching rate

$$\dot{\varepsilon}_i^a = A f_v \sqrt{\frac{5}{4}} \frac{\sigma_i^*}{c_r} D_r \quad (3.1.20)$$

and the viscosity factor

$$f_v = \exp\left(\frac{4\sqrt{5}\sigma^*/c_r - 1}{I_v}\right) \approx \left(\frac{4}{\sqrt{5}} \frac{\sigma^*}{c_r}\right)^{1/I_v} . \quad (3.1.21)$$

The uni-axial case is implied for $\cos 3\alpha_\sigma = \pm 1$ with $G = E/2$ and σ^* by (3.1.18). The prefactor in (3.1.20) is $A = 1$ for v-hyp and $A = H(\sigma_i^* \dot{\epsilon}_i)$ for v-elp with H by (3.1.16) and Einstein's abbreviation $\sigma_i^* \dot{\epsilon}_i$ for $\sum \sigma_i^* \dot{\epsilon}_i$. (3.1.20) implies a simple flow rule, viz. the same direction of $\dot{\epsilon}_i^a$ and σ_i^* . Response polars exhibit the differences due to factor A , Fig. 3.1.6, labels for α_ϵ and D refer to Fig. 3.1.5. Only with an isotropic initial state (A) the polars by v-elp (a) and v-hyp (b) agree due to $\sigma^* = 0$ (cf. Fig. 3.1.5d). For an argotropic state limit the polars by v-elp are semicircles plus arcs which are flatter for lower D . The polars by v-hyp are circles which are more eccentric with bigger D . The polars touch the state limit circle with the same D , as shown for a low (B) and a big D (C) the deviator σ^* can thus only increase with a higher D .

Interpolations between the depicted cases are rather evident. The response by (3.1.19), (3.1.20), and (3.1.21) is almost elastic for $\sigma^*/c_r < ca.0.01^{I_v}$ and markedly viscoplastic for $\sigma^*/c_r > 0.5^{I_v}$. There is an upper D -bound due to mechanical heating by (3.1.8), its experimental value could be used to estimate the factor m in (3.1.9). A lower D -bound can hardly be observed, it can be introduced by a cut-off in (3.1.21), say $f_v = 0$ for $\sigma^*/c_r < 10^{-3I_v}$. Thus relaxation for $D = 0$ is implied and could also be represented by response polars.

Approaches to state limits are shown in Fig. 3.1.7. Straight strain paths are assumed with constant rates in different directions (a). The initial stress

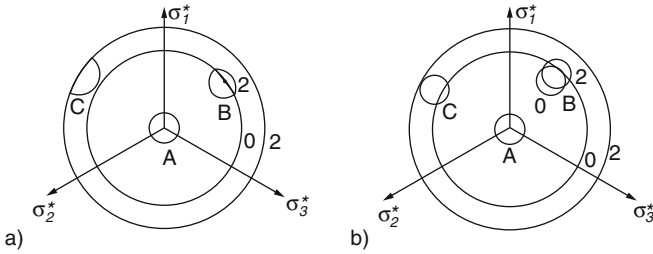


Fig. 3.1.6. Response polars of v-elp (a) and v-hyp (b) for cuboids. Numbers indicate strain rate by $\log(D/D_r)$

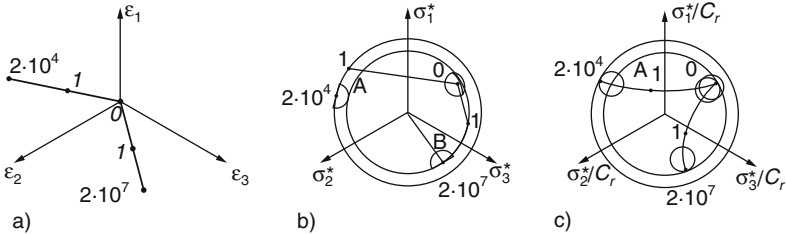


Fig. 3.1.7. Proportional strain paths (a) lead to argotropic state limits by v-elp (b) and v-hyp (c). Labels for dimensionless time tD_r

state is arbitrary within the range by Fig. 3.1.6. The stress paths tend to state limits as outlined with Fig. 3.1.5 with differences of v-elp (b) and v-hyp (c) in the transition. They are streamlined by the argotropic response polars, these show that the argotropic state limits are attractors for monotonous stretching.

Creep and *relaxation* are almost the same by v-elp and v-hyp as $A=1$ holds for both. Figure 3.1.8 shows associated paths of strain (a) and stress (b) with labels for the dimensionless time tD_r . With constant stress (A) the strain path direction tends to the stress direction and D tends to the state limit value by (3.1.18). The initial strain rate is forgotten in the transition, only therein v-elp and v-hyp are slightly different. With fixed strain (B) the stress path points to the centre. Plots of strain and stress vs. tD_r would look like Fig. 3.1.3b, c for the uniaxial case, but are incomplete.

Typical responses to *strain cycles* are shown in Fig. 3.1.9. Elliptic strain paths (a) may be imposed repeatedly with constant D and small (A) or big amplitude (B). The stress path by v-elp (b) remains near the onset (A) or tends to a symmetric cycle with the same alignment as the strain path (B), thus the amplitude is defined as big. The stress path by v-hyp (c) tends to a symmetric aligned cycle both for A and B. With a small amplitude the transition by v-hyp needs more reversals if the onset is farther off the

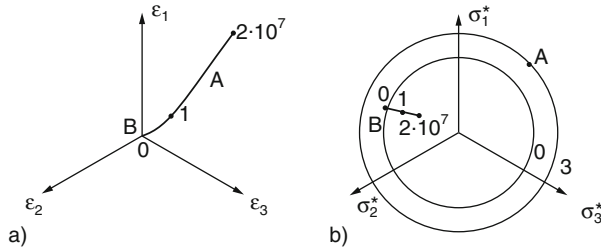


Fig. 3.1.8. Strain (a) and stress paths (b) for creep (A) and relaxation (B). State limits with labels for $\log(D/D_r)$

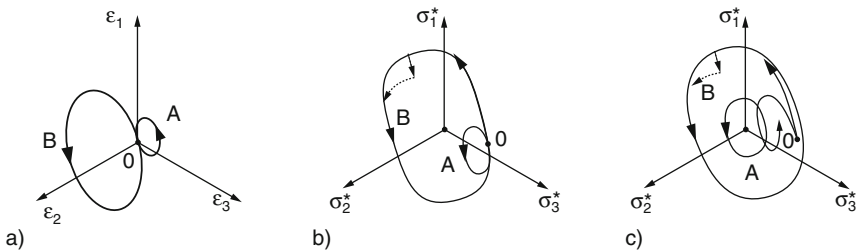


Fig. 3.1.9. Repeated strain cycles (a) with constant D lead to stress cycles by v-elp (b) and v-hyp (c). An interruption causes relaxation, thereafter the state cycle is again attained (*dotted paths*)

asymptotic state cycles. With a big amplitude the asymptote is reached before the first reversal. Argotropic response polars as in Fig. 3.1.6 or simulations with (3.1.19), (3.1.20), and (3.1.21) reveal how the attractors are attained. An interruption of stretching causes relaxation, continuation with the previous D leads back to the related path (dotted). Stressing along state cycles with the same stress rates would lead to strain cycles after creep, the latter would increase by waiting with constant stress.

Typical responses to *ratcheting* are shown in Fig. 3.1.10. The strain paths are composed of strain cycles and stretching with constant direction (a), e.g. with small amplitude and low D (A) or big amplitude and higher D (B). The stress path attains the D -dependent state limit and touches it repeatedly with the same average deviatoric direction as the strain path. With v-elp (b) the asymptotic state cycle resembles the strain path in the range of unloading ($\Sigma\sigma_i^*\dot{\epsilon}_i < 0$), this similarity holds also for the transition. With v-hyp (c) the attractor is smoother and the return stress paths are less similar to the related strain path sections. This could be shown more in detail with response polars or simulations. An interruption would cause a relaxation, after a continuation the driven attractor is again attained. Asymmetric stress cycles with constant mean rate would also lead to ratcheting, waiting intervals with constant stress would cause creep in addition.

The common feature of evolutions by (3.1.19) is the directional agreement of anelastic strain rate and stress by (3.1.20) and the viscosity factor f_v by (3.1.21) for the intensity of anelastic strain rates, and thus the intensity of creep and relaxation. With I_v from ca. 0.02 to 0.1 $f_v < 0.01$ is obtained for σ^*/c_r from ca. 0.5 to 0.3, then the response is almost elastic. Differences of v-elp and v-hyp are thus only marked for cyclic straining with small amplitude.

For *arbitrary deformations* (3.1.19) can be substituted by

$$\mathbf{T}^* = G(\mathbf{D} - \mathbf{D}^a) \quad (3.1.22)$$

with the co-rotated deviatoric stress rate $\overset{\circ}{\mathbf{T}}^*$ by (2.11.6) and the anelastic stretching

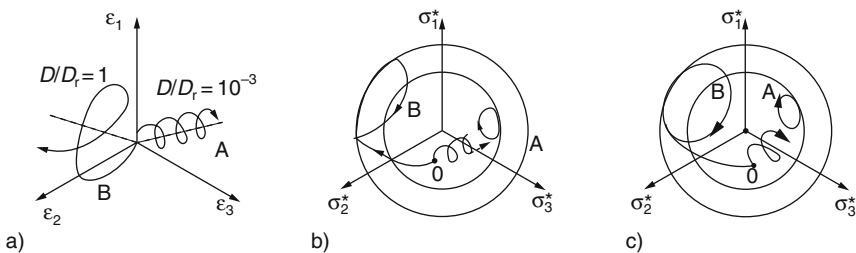


Fig. 3.1.10. Imposed ratcheting with constant D (a) leads to asymmetric stress cycles by v-elp (b) and v-hyp (c)

$$\mathbf{D}^a = Af_v \sqrt{\frac{5}{4} \frac{D_r}{c_r}} \mathbf{T}^* \quad . \quad (3.1.23)$$

The viscosity factor f_v is determined by (3.1.21) with the invariant $\sigma^* = \sqrt{\text{tr} \mathbf{T}^{*2}}$, the prefactor $A = H [\text{tr}(\mathbf{T}^* \mathbf{D})]$ (H by (3.1.15)) for v-elp and $A = 1$ for v-hyp. State limits and stationary creep mean $\mathbf{D} = \mathbf{D}^a$ with the same direction as \mathbf{T}^* . f_v determines the intensity of creep and relaxation as outlined further above, viscous effects get negligible for $\sigma^*/c_r < \text{ca. } 0.3\text{--}0.5$. Equation (3.1.22) is frame-indifferent, thus the material parameters are already determined by cuboidal deformations. Shearing as in Fig. 2.1.10 could be treated with (3.1.22), except for argotropy the response to shear cycles and ratcheting would be similar for constant $D = \sqrt{\text{tr} \mathbf{D}^2}$. Stress-strain-time plots are evidently insufficient, notions like strength and ductility can at best make sense for monotonous stretching with $D = \text{const}$.

The *range of validity* may only be touched as this section is to prepare for simple peloids. Neglect of volume changes and pressure influence is justified for high enough pressures and very low void fractions. This is sufficient for the principle of effective stress (Sect. 3.2). The argotropy due to thermally activated dislocations is physically well established. The proposed argotropic state limits require ductility, this cannot hold for D above a threshold that depends on pressure and temperature. The neglect of the invariant $\cos 3\alpha$ by (2.11.5) is minor for our purpose.

The most restrictive assumption is that states of solid RSEs are fully characterized by stresses and change with strain history via a constitutive relation of stress rate with stretching and stress. For being consistent this relation should be continuous and should imply argotropic state limits as attractors. As without viscosity internal state variables will be needed for evolutions with many reversals and small amplitudes (Sect. 5.1). Shear localizations require polar quantities in addition and spoil the uniformity of RSEs (Sect. 8.1). The spatial distribution of different crystallites causes an inherent anisotropy. All that is left aside as it will not be needed in the sequel.

To *sum up*, the behaviour of pore-free solids with thermal activation can be captured with visco-elastoplastic or -hypoplastic relations. Therein a viscosity index and a reference stretching rate characterize rate-dependence, creep and relaxation, both parameters are proportional to T . Both relations agree for monotonous evolutions and differ with reversals. They will be used in the sequel to explain viscous effects of clay-like soils with much softer particles than quartz grains.

3.2 An introduction of simple peloids

A homogeneous skeleton of mineral particles may be called a *simple peloid* (i.e. clay-like, $\pi\eta\lambda\delta\zeta = \text{clay}$) RSE if it has the following properties:

P1: the solid particles are surrounded by water with ions and are so small that electro-capillary effects are relevant;

P2: the voids are completely filled with water which may contain solubles below saturation;

P3: the state is sufficiently characterized by the effective stress components and the void ratio;

P4: the solid particles are soft and their collective properties are permanent.

Without going into details these simplifying assumptions can be justified as follows.

Given P2 as outlined further below, P1 means that the pore water is less mobile in narrow voids than in the bulk (Sect. 6.3). This is due to the adsorption of water and ions at the particle surfaces and contacts. As was discovered by Terzaghi (1920) and investigated at length by Derjaguin (1971), the absorbed pore water with higher ion concentration has a higher density and a far bigger viscosity than ordinary water. Following Derjaguin this bound pore water may be called *polywater* as it resembles polymers. With absorption films of a few nm thickness the polywater influences the mechanical behaviour if the solid particles are smaller than about 10^{-6} m. Then the kind of mineral, the shape of the particles and the ion concentration of the free pore water play a role.

P2 excludes gas bubbles, pockets or channels and also condensation bridges among the particles. Gas bubbles appear if the pore water is saturated with dissolved gas, and gas channels arise by capillary entry (Sect. 6.3). Liquid condensation bridges appear with low degrees of water saturation, solid condensation bridges play a role with high concentrations of dissolved minerals (Sects. 7.2 and 7.3). In these cases the solid partial stress is no more given by Terzaghi's (1936) equation (2.2.6), and adaptations for partial saturation or condensation bridges do not suffice in general (Sects. 6.3 and 7.2).

Given P1 and P2, net particle forces and internal variables are excluded by P3. The effective stress by (2.2.5) or (2.2.6) for cylindrical symmetry, or by (2.11.2) in general, agrees with the solid partial or skeleton stress if the van der Waals attraction is compensated by the osmotic repulsion of the particles (Sect. 6.3). This is not the case in general. An excess of attraction causes higher void ratios, an excess of repulsion enhances swelling (Sect. 7.1). Apart from the neglect of such interparticle forces the influence of the spatial fluctuation of contact forces (Sect. 5.2) is neglected by P3.

P4 means that thermal activation plays a role for changes of particle shape during evolutions of state and shape of a peloid RSE. As outlined for solids without pores in Sect. 3.1 the particles are neutral with respect to the pore water pressure p_w , therefore the skeleton stress by (2.2.5) or (2.11.2) is effective. Other than assumed for simple psammoids, however, the skeleton is *argotropic* as are its particles, therefore these may be called soft. With softer particles

barotropy and pyknotropy of peloids are more marked than for psammoids. We thus leave aside saturated soils with fine hard grains, these can better be modelled as psammoids. With soft particles the assumed permanence of the skeleton is apparently a contradiction in terms, even more than for psammoids. However, very small particles can be reconstituted by thermal activation if the particle encounter times are not too short (Sect. 7.3).

Shear localization with polar quantities (Sect. 8.3) is left aside by P3, as with simple psammoids the RSE is assumed to be and remain uniform so that spatially averaged void ratios and non-polar stresses and strains suffice. Experimental results may therefore be used up to peaks, beyond them at best with data for narrow shear zones. As therein interparticle forces are partly bigger and relative particle motions are faster than in the average of the RSE the permanence by P4 is more restricted.

In the sequel we will consider evolutions of RSEs with cylindrical symmetry by using the stress and strain quantities as in Sect. 3.2. Constitutive relations may again be abbreviated by (2.2.13), and selection criteria are taken over from Sect. 2.2. The general properties described by (2.2.14), however, have to be modified due to the argotropy. For the function f_i in (2.2.13) we postulate now, with $i = 1$ and 2,

$$\begin{aligned}
 \text{a) } f_i(\lambda\sigma_{si}) &= \lambda^m f_i(\sigma_{si}) & \text{with } \lambda > 0 & \quad \text{and } 0 < m \leq 1 \text{ for } D = \text{const} \\
 \text{b) } f_i(\lambda\dot{\epsilon}_i) &= \lambda^m f_i(\dot{\epsilon}_i) & \text{with } \lambda > 0 & \quad \text{and } m > 1 \quad \text{for } D = \text{const} \\
 \text{c) } f_i(-\dot{\epsilon}_i) &\neq -f_i(\dot{\epsilon}_i) & \text{in general} & \quad .
 \end{aligned}
 \tag{3.2.1}$$

The amount of stretching rate, D by (2.2.19) for cylindrical symmetry, is assumed to be constant for (a) and (b). Then the barotropy is reflected by (a), this means that skeletons of soft particles are stiffer with bigger pressure p_s due to wider contact flats. Rate-independence is no more given with (b), it may at best be assumed with constant D in a certain range of D as m ranges from about 0.5 to 1 (m is not necessarily constant). Non-linearity by (c) does not exclude hypoelastic behaviour as a special case. (b) Enables creep with $\dot{\epsilon}_i \neq 0$ for $\dot{\sigma}_{si} = 0$ and relaxation with $\dot{\sigma}_{si} \neq 0$ for $\dot{\epsilon}_i = 0$, both is excluded by (2.2.14b) for psammoids. Equation (3.2.1) restricts representations of the constitutive functions f_i , but further restrictions are needed to model essentials of peloid behaviour.

Argotropic state limits are defined for constant strain rates similarly as in Sect. 2.2 without argotropy, but now the amount of stretching D has to be allowed for, Fig. 3.2.1. The relation of stress and strain rate directions ψ_s and ψ_ϵ (a) looks like the one for psammoids and does not depend on D . In particular (2.2.15) holds for critical states, i.e. isochoric state limits, with a D -independent critical friction angle φ_c . This can be lower than for psammoids if flat clay particles slide past each other, and bigger if diatomaceous relics produce a felt-like soil. $\psi_s = \psi_\epsilon = 0$ is evident for isotropic compres-

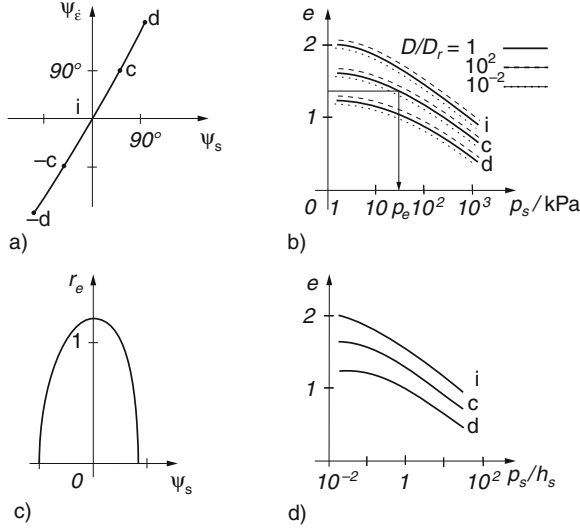


Fig. 3.2.1. State limits of cylindrical peloid RSEs: strain rate direction (a) and relative void ratio vs. direction of stress (c), void ratio vs. pressure p_s for different strain rates (b) and with p_s referred to an argotropic solid hardness (d)

sion, proportional compression holds for lower than critical $|\psi_s|$. Extremely dilatant state limits at the bounds by (2.2.4) and (2.2.16) are less fictitious than for psammoids as clay-like soils can more easily be cracked. Peak states come close to dilatant state limits, and a continued deformation beyond them leads to a marked shear localization (Sect. 8.3).

Limit void ratios decrease with bigger mean skeleton pressure p_s and bigger stress obliquity $|\psi_s|$ by (2.2.3) similarly as for psammoids, Fig. 3.2.1b. The range is wider as squat angular particles cause bigger voids for low p_s and are more squashed for high p_s than hard grains. As the particles are harder for bigger amounts of strain rate D due to their argotropy (Sect. 3.1) the limit void ratios are bigger for bigger D . This can be represented by *isotachs* ($\tau\alpha\chi\acute{\upsilon}\zeta$ =fast) for different D , some of them are drawn in Fig. 3.2.1b (Suklje 1969). If D varies by several decades these isotachs cannot convey a clear picture as the ones for different stress obliquities overlap each other. One can plot instead e vs. $\log(p_s/h_s)$ with an *argotropic solid hardness* as by (3.1.1), viz.

$$\begin{aligned}
 h_s &= h_{sr} [1 + I_v \ln(D/D_r)] \\
 &\approx h_s(D/D_r)^{I_v} \quad .
 \end{aligned}
 \tag{3.2.2}$$

As for solids I_v is named *viscosity index* (Leinenkugel 1976), and D_r is a reference strain rate so that h_s equals the reference value h_{sr} for $D = D_r$. Extremely small or big D have to be excluded as for solids. D_r can be chosen conveniently (e.g. 10^{-6} s^{-1}), the I_v for matching test results depends on this

choice. I_v and D_r are thus not the same as for a solid, the transfer to it requires assumptions on spatial distributions of forces and displacements (Sect. 3.5). As with solids by (3.1.1) and (3.1.6) both I_v and D_r are proportional to the absolute temperature T due to thermal activation. There is an upper D -bound by mechanical heating, and a lower one below which the viscosity gets linear. The power law in (3.2.2b) agrees with the logarithmic one (3.2.2a) in a range which depends on I_v . I_v ranges from ca. 0.02 to 0.05 for clay-like soils.

As shown in Fig. 3.2.1d the isotachs are assumed to coincide by means of (3.2.2) for any ψ_s . This is justified as the argotropy of the solid particles does not depend on skeleton stress and void ratio. Thus the upper and lower bounds and the critical void ratios are barotropic as for psammoids, but they are also argotropic. A relative void ratio r_e can again be defined by (3.2.18), but now the reference values e_c and e_d depend on D via (3.2.2). The argotropy does not appear in the dependence of r_e on ψ_s , Fig. 3.2.1c. Together with the dependence of $\psi_{\dot{\varepsilon}}$ on ψ_s this means that for a state limit with a given $\psi_{\dot{\varepsilon}}$ both ψ_s and r_e are functions of $\psi_{\dot{\varepsilon}}$, the argotropy influences only the mean pressure via (3.2.2).

The mechanical behaviour can be represented by *argotropic response polars*, Fig. 3.2.2. The kind of stretching can be captured by substitute rates $s_i = (|\dot{\varepsilon}_i|/D_r)^{I_v} \text{sgn} \dot{\varepsilon}_i$ with constant amounts D and different directions $\psi_{\dot{\varepsilon}}$ (a). Differences of D by orders of magnitude can be captured by scaling with $(\dot{\varepsilon}_i/D_r)^{I_v}$, the argotropy by (3.2.2) is only significant if D varies substantially. The stress rate response in the associated polar diagram (b) depends on the state variables σ_{s1} , σ_{s2} and e (or any substitute, e.g. p_s , ψ_s and r_e as for psammoids), but also on D . Convexity and continuity are needed, exceptionally the polar can be centric. As for psammoids a second polar in the plane \dot{e} vs. \dot{p}_s/p_s (c) can be of use. $\dot{e}(-\psi_{\dot{\varepsilon}}) = -\dot{e}(\psi_{\dot{\varepsilon}})$ follows from (2.2.10) with (2.2.12), but $\dot{p}_s(-\psi_{\dot{\varepsilon}}) \neq -\dot{p}_s(\psi_{\dot{\varepsilon}})$ holds by (3.2.1c). Argotropy is represented by D -dependent size, shape and/or eccentricity, this will be specified in Sects. 3.3 and 3.4. Creep with $\dot{\sigma}_{s1} = \dot{\sigma}_{s2} = 0$ requires polars which go through the origin for certain $\psi_{\dot{\varepsilon}}$ and D . Relaxation with $\dot{\varepsilon}_1 = \dot{\varepsilon}_2 = 0$ can be depicted by a point for a lower bound of D (cf. Sect. 3.1) as then there is no influence of $\psi_{\dot{\varepsilon}}$.

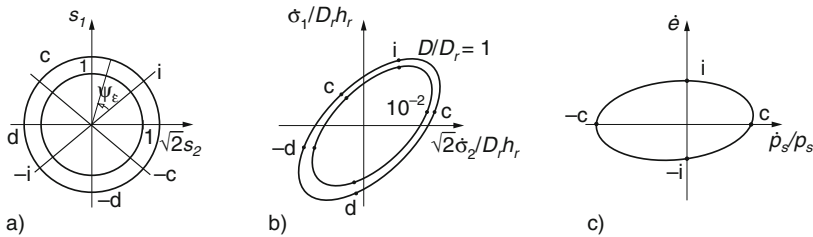


Fig. 3.2.2. Response polars of stress rates (b) and rates of void ratio and pressure (c) for substitute strain rates with constant D (a)

Analogously with (3.1.19) the function f_i by (2.2.13) and (3.2.1) may be represented by

$$f_i = M_{ij}(\dot{\varepsilon}_j - \dot{\varepsilon}_j^a) \quad (3.2.3)$$

with an elastic stiffness matrix M_{ij} and summation on j , and an anelastic stretching rate

$$\dot{\varepsilon}_j^a = A f_e f_v P_j D_r \quad . \quad (3.2.4)$$

Therein A is 0 or 1 in v-el_p (Sect. 3.3) and 1 in v-hyp (Sect. 3.4), f_e is an e -dependent factor and P_j denotes different ψ_s -dependent directions in both approaches. The *viscosity factor* f_v depends on the *consolidation ratio* p_e/p_s via

$$f_v \approx \left(\frac{p_s}{p_e}\right)^{1/I_v} \approx \exp\left(\frac{p_s/p_e - 1}{I_v}\right) \quad (3.2.5)$$

with an *equivalent pressure* p_e . The latter is defined as the p_s at a state limit for the actual e and $|\tan \psi_s|$ with $D = D_r$, as indicated in Fig. 3.2.1b for a critical stress obliquity. p_e was introduced for shearing by Hvorslev (1937), he mentions already the viscosity and the dependence on stress obliquity (more in Sect. 3.8). p_e/p_s should not be confused with the overconsolidation ratio *OCR* which ignores the influence of ψ_s and D (Sects. 2.3, 3.3 and 3.8). The factor f_e is determined by the coincidence of limit void ratios with those for an isotropic compression with $D = D_r$ by (3.2.3).

The stiffness matrix M_{ij} in (3.2.3) should be proportional to $(p_s/h_s)^m$ for a given D in order to model the barotropy by (3.2.1a), and depends also on the stress direction ψ_s in general. Some features of (3.2.3), (3.2.4), and (3.2.5) are shown in Fig. 3.2.3 by argotropic response polars. Strain rates with different directions and $D/D_r = 10^{-3}$, 1 and 10^3 are represented by circles with radius $(D/D_r)^{I_v}$ and labels for ψ_ε (a). For $D \approx D_r$ and $p_e \approx p_s$ the polars exhibit barotropy and depend on the stress obliquity nearly as for psammoids (b, cf. Fig. 2.2.5). For $D \gg D_r$ and/or $p_e/p_s > \text{ca. } 2$ the polars are nearly centric ellipses which are bigger for higher p_s (c), this indicates an almost hypoelastic behaviour. For $D \ll D_r$ and $p_e \approx p_s$ the polars are nearly straight lines which are longer for higher p_s and have a bigger $-\dot{p}_s/p_s$ and a lower $\dot{\psi}_s/\psi_s$ for a lower $|\tan \psi_s|$ (d). This behaviour comes close to relaxation with $\dot{\varepsilon}_1 = \dot{\varepsilon}_2 = 0$.

As for solids D_r has to be chosen conveniently because a reference frequency of the particles cannot be strictly identified (Sect. 3.1). This apparent lack of unit-invariance (Sect. 1.2) can be overcome by adapting the reference hardness h_{sr} to a chosen D_r in the observed validity range of (3.2.2). Thus p_e denotes p_s for a state limit with given e and ψ_s and suitably chosen D_r in the D -range where state limits can occur (cf. Sect. 3.1). The response outlined with Fig. 3.2.3 is psammoid-like near state limits with the same D (b), and rather hypoelastic for a drastic increase of D and/or a consolidation ratio $p_e/p_s > \text{ca. } 2$ (c). The normalized rate of relaxation $\dot{p}_s/p_s D_r$ is substantial only if it starts near state limits with D near D_r (d). Other than with rate-independent psammoids the response of simple peloids is thus determined by

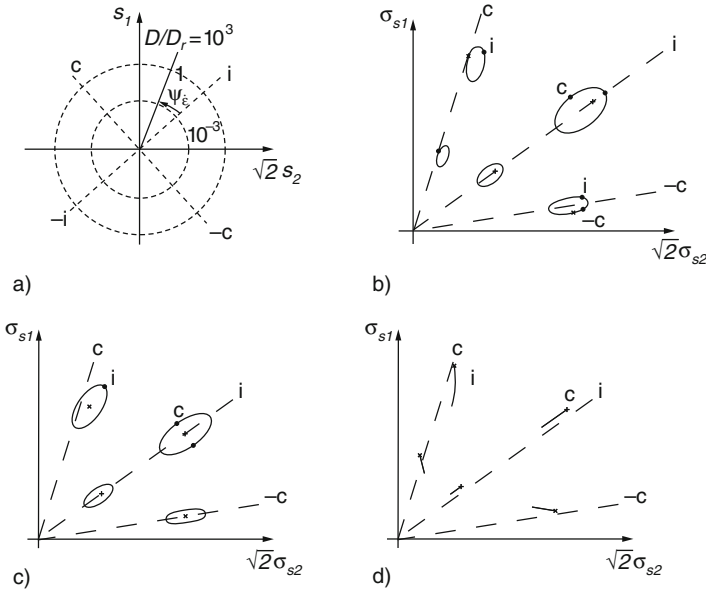


Fig. 3.2.3. Argotropic response polars: (a) substitute strain rates, (b) stress response from state limits with $D = D_r$, (c) response with $D \gg D_r$ and/or high consolidation ratio, (d) relaxation from state limits with $D = D_r$.

the strain rate ratio D/D_r and the consolidation ratio p_e/p_s , whereas pressure p_s and stress obliquity $\tan \psi_s$ have the same qualitative influence. The relative void ratio r_e , which depends on the actual e and the argotropic state limit values e_c and e_d by (2.2.18) and Fig. 3.2.1, is less useful than p_e/p_s as long as one is far off extremely dilatant state limits with e near the lower bound.

Approaches to state limits are shown in Fig. 3.2.4. A straight contractant (A), isochoric (B) or dilatant (C) strain path may be imposed with section-wise constant rate D (a, labels for $\log(D/D_r)$). The deformation time may exceed by far the time needed for the diffusion of pore water so that the RSE

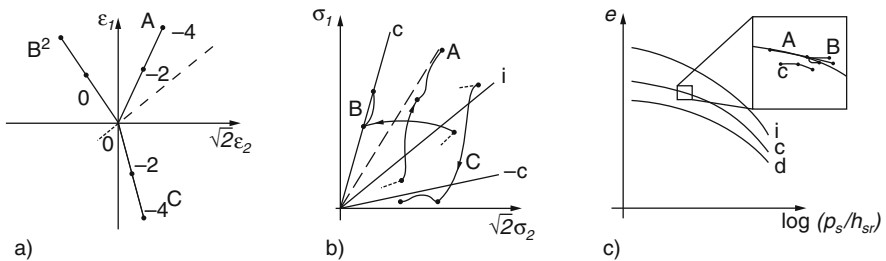


Fig. 3.2.4. Approach of cylindrical RSEs to argotropic state limits: (a) strain paths with labels for $\log(D/D_r)$, (b) stress paths, (c) void ratio vs. pressure paths and limit void ratios for $D = D_r$.

can remain sufficiently uniform (Sects. 6.2 and 11.1). The stress paths tend to $\psi_{\dot{\epsilon}}$ -dependent obliquities by Fig. 3.2.1a with kinks after D -jumps and $\dot{p}_s > 0$ (A), $\dot{p}_s = 0$ (B) and $\dot{p}_s < 0$ (C) in the continuation (b). The stress path kink depends on the previous strain rate, this could be indicated by dotted lines. The paths in the plot of e vs. $\log(p_s/h_{sr})$ tend to ψ_s - and D -dependent limit void ratios by Fig. 3.2.1b (c). Thus the consolidation ratio p_e/p_s tends to 1 for $D = D_r$, but to a constant > 1 for $D < D_r$ and < 1 for $D > D_r$.

These transitions are steered by argotropic response polars as shown in Fig. 3.2.3. Thus the argotropic state limits are attractors for deformations with constant rate $\dot{\epsilon}_1$ and $\dot{\epsilon}_2$. Similarly as with psammoids (Sect. 2.2) state limits cannot be attained with a too high initial void ratio e_o because of skeleton decay, and can be prevented by particle crushing with a too low e_o . Isobaric peak states come close to dilatant state limits, but their continuation leads to shear localization (Sect. 8.3). Cracking could be linked with extremely dilatant state limits (Sect. 8.4).

The *isobaric creep* of cylindrical peloid RSEs is shown in Fig. 3.2.5 with labels for dimensionless time tD_r . Paths of strain (a), stress (b) and e vs. $\log(p_s/h_{sr})$ (c) represent typical evolutions. Previous strain rates and stress paths are indicated by dotted lines, they are forgotten in the sequel. Plots of e vs. $\log(tD_r)$ (d) and of strain deviator ϵ^* vs. tD_r (e) convey a partial information. With a subcritical stress obliquity, i.e. $|\tan \psi_s| < |\tan \psi_{sc}|$ by (2.2.3) and (2.2.15), the creep is contractant and D gets smaller (A). It tends to a succession of contractant state limits, the transition takes more time for a higher initial consolidation ratio p_e/p_s (1) than for a lower one (2). Near the asymptote the direction of strain rate $\psi_{\dot{\epsilon}}$ is determined by ψ_s as for state

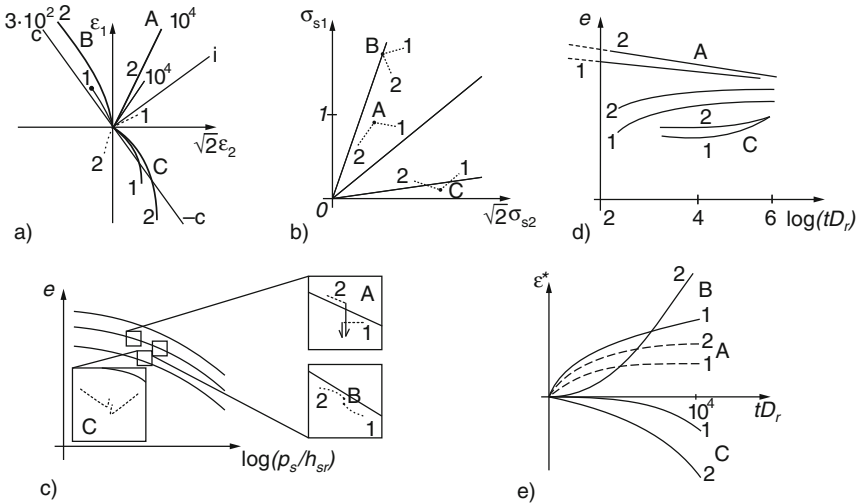


Fig. 3.2.5. Isobaric creep of cylindrical peloid RSEs: (a) strain paths (labels for tD_r), (b) stress paths (dotted before creep), (c) void ratio vs. pressure (limit void ratios for $D = D_r$), (d) shortening vs. time, (e) deviatoric strain vs. time

limits by Fig. 3.1.1a, and the gradual densification can be approximated by

$$e \approx e_o - \lambda I_v \ln(1 + tD_r). \tag{3.2.6}$$

Therein e_o denotes e for $t = 0$, and λ the slope of e vs. $\ln(p_s/h_{sr})$ in the given range. As shown in Fig. 3.2.5d the initial evolution is not described by (3.2.6), this asymptote is not attained with an initial $p_e/p_s > \text{ca. } 2$ within relevant times. Only after a very long time the densification by creep comes to an end.

With a critical stress obliquity the creep gets stationary (B) after a longer transition for a higher initial p_e/p_s (1) than for a lower one (2). The asymptotic strain rate is isochoric with an amount D which is determined by (3.2.2) via Fig. 3.2.1d and (3.2.4). For the transition this means an acceleration if D and p_e/p_s are initially low (1) and a deceleration in the opposite case (2). With an overcritical stress obliquity (C) the creep is dilatant and more accelerated with high (1) than with low initial p_e/p_s (2). In case C the uniformity of the RSE gets lost by shear localization or cracking (Sects. 8.3 and 8.4). As with a lower stress obliquity the creep is negligible within relevant times if the initial p_e/p_s exceeds ca. 2, and cannot occur with constant σ_{s1} and σ_{s2} if the pore water diffusion time is not far shorter than the deformation time.

Some evolutions of cylindrical peloid RSEs with *isochoric creep* and constant stress deviator $\sigma^* = 1(\sigma_{s1} - \sigma_{s2})/3$ are shown in Fig. 3.2.6. Stress paths just before this kind of creep are indicated by dotted lines. Thereafter the

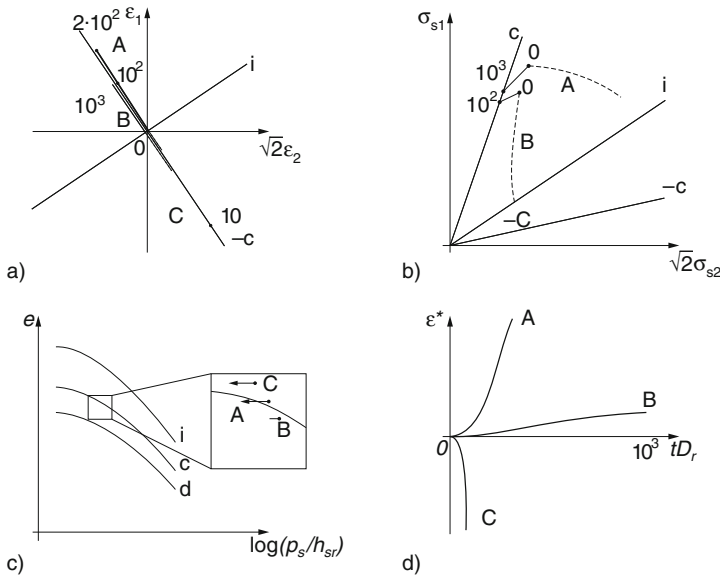


Fig. 3.2.6. Isochoric creep of cylindrical peloid RSEs: (a) strain paths (labels for tD_r), (b) stress paths (dotted for $t < 0$), (c) void ratio vs. pressure (limit void ratios for $D = D_r$), (d) deviatoric strain vs. time

strain paths (a) are isochoric, the skeleton stress paths (b) and the plot of e vs. $\log(p_s/h_{sr})$ (c) exhibit a gradual reduction of p_s . This is related with different increases of deviatoric strain with time (d). Stationary creep can be attained with a low initial p_e/p_s (A), whereas the creep rate can remain minute with a higher initial p_e/p_s (B). If both p_e/p_s and p_s/h_{sr} are initially low isochoric creep can lead to $p_s \rightarrow 0$, i.e. skeleton decay and transition to a suspension (C). Except for such a decay RSEs with constant stress deviator tend to an isochoric state limit with D by (3.2.2) for $e = e_c$.

Some evolutions with *relaxation* are shown in Fig. 3.2.7. The strain paths (a) are halted (dotted for $t < 0$). The stress paths (b) tend towards the isotropic line and the origin. As shown in the plot of e vs. $\log(p_s/h_{sr})$ (c) the initial void ratio is assumed as overcritical (A), critical (B) or subcritical (C) for $D = D_r$. The mean pressure p_s gets more markedly smaller with time (d) for A and B than for C. The stress obliquity $|\tan \psi_s|$ is little reduced with time for A and C, and markedly for B (e). The relaxation gets so slow anyway that asymptotic states of rest cannot be explored. One may call such states endogeneous attractors as they are attained solely by thermal activation.

Some common features of creep and relaxation, which may appear rather complex in Figs. 3.2.5, 3.2.6, and 3.2.7, can be explained by means of (3.2.3), 3.2.4, and (3.2.5) and Fig. 3.2.3. Isobaric creep means $\dot{\epsilon}_j = \dot{\epsilon}_j^a$ by $\dot{\sigma}_{si} = 0$. Its direction $\psi_{\dot{\epsilon}}$ is determined by the stress direction ψ_s . Its intensity D is

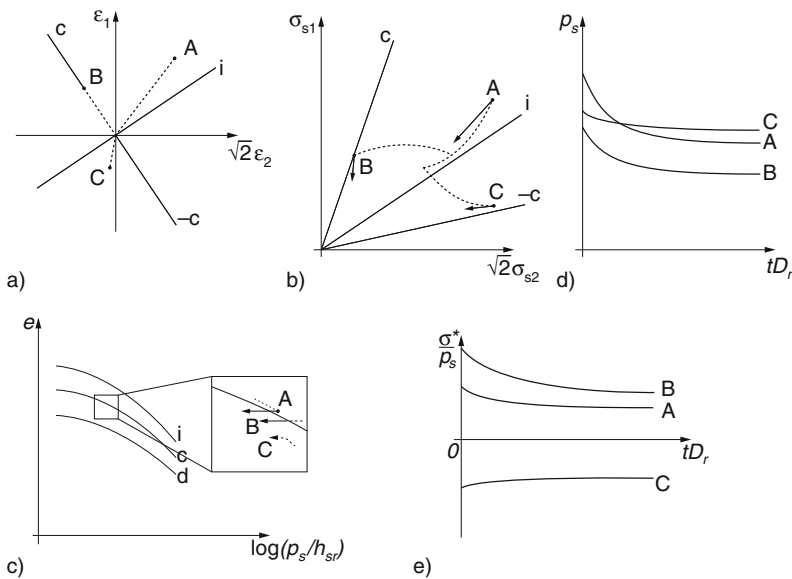


Fig. 3.2.7. Relaxation of cylindrical peloid RSEs: (a) strain paths (*dotted* for $t < 0$), (b) stress paths, (c) void ratio vs. pressure (limit void ratios for $D = D_r$), (d) mean pressure vs. time, (e) stress obliquity vs. time

given by the viscosity factor f_v , which is negligible if the consolidation ratio p_e/p_s exceeds ca. 1.5–2. The equivalent pressure p_e is given by e and ψ_s for the chosen reference rate D_r . With a subcritical stress obliquity ($|\tan \psi_s| < |\tan \psi_{sc}|$) the creep is contractant and decelerated as p_e increases. With a critical stress obliquity the creep is isochoric and gets stationary after an adaption of the stretching rate D . With an overcritical stress obliquity the creep is dilatant and accelerated, and depending on the initial p_e its amount D/D_r can be extremely variable.

The rate of relaxation, i.e. $\dot{\sigma}_{si} = f_i = M_{ij}\dot{\epsilon}_j^a$ by (3.2.3) with $\dot{\epsilon}_j = 0$, can be expressed by the dimensionless pressure rate $\dot{p}_s/p_s D_r$ and the rate of stress obliquity $\tan \psi_s$. With the barotropy by (3.2.1) the pressure rate is

$$\dot{p}_s/p_s D_r \approx -b f_v (h_{sr}/p_s)^{1-m}. \quad (3.2.7)$$

Therein the exponent $1 - m$ ranges from about 0 to 0.5 and $b \approx 1$ can be estimated from (2.4.5). The dominant factor in (3.2.7) is the viscosity factor f_v , as with creep the rate of relaxation is thus negligible for $p_e/p_s > \text{ca. } 1.5$ to 2. The stress path directions in Fig. 3.2.3d indicate that the amount of stress obliquity $|\tan \psi_s|$ is the more slowly reduced the smaller it is. This can also be explained with f_v by (3.2.5): p_e increases with a reduction of $|\tan \psi_s|$ while p_s decreases by (3.2.7), thus f_v dwindles strongly.

Isochoric creep implies a relaxation of p_s by (3.2.7) so that f_v dominates both \dot{p}_s and D . The stretching intensity D dwindles with a constant deviator σ^* as p_e decreases due to the increase of $|\tan \psi_s|$, whereas p_s dwindles. The viscosity factor f_v by (3.2.5) is always dominant for the rate of creep and/or relaxation. What counts is thus the consolidation ratio p_e/p_s , i.e. a combination of void ratio, mean pressure and stress obliquity, and the change of p_e/p_s with time. We will see in following sections how this works with visco-elastoplastic and -hypoplastic relations, and that our statements are not confined to cylindrical RSEs.

Evolutions with *reversals* may only be touched here as little is known from experiments or can be concluded with physical arguments. We restrict ourselves to isochoric evolutions as deformation times with reversals are usually much shorter than pore water diffusion times, and presume that the gas content is so small that density changes without diffusion of pore water are negligible. As with psammoids (Sect. 2.2) amplitudes are called small if the amount of stress obliquity remains subcritical, and big otherwise. Because of the viscosity the stretching rate D and its reference value D_r play a role if they change by orders of magnitude. We consider mainly evolutions with $D/D_r = 1$, and briefly also with $D/D_r \ll 1$ or $\gg 1$. Apart from the latter we will focus on asymptotic responses, i.e. state cycles as driven attractors.

Responses to isochoric *deformation cycles* are indicated in Fig. 3.2.8. Strain paths with big (A) or small amplitude (B) are depicted as flat lenses for visibility (a). The stress path with D/D_r for A tends to a butterfly which touches the critical lines, whereas for B with $D = D_r$ its shift towards an

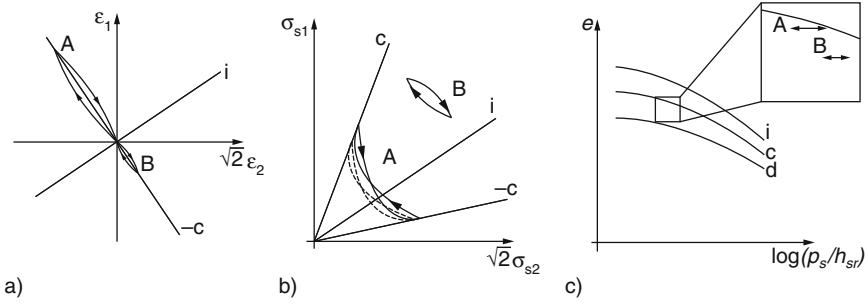


Fig. 3.2.8. Response of cylindrical peloid RSEs to isotachic cyclic strain paths (a): asymptotic cycles of stress components (b) and of void ratio vs. pressure (c)

argotropic attractor is hardly detectable (b). As shown in a plot of e vs. $\log(p_s/h_{sr})$ this shift is due to a low p_e/p_s for A (repeatedly $p_e/p_s \rightarrow 1$), and to a higher p_e/p_s for B (c). As outlined further above with (3.2.3), (3.2.4), and (3.2.5) the response is thus rather hypoplastic for $p_e \approx p_s$ and rather hypoelastic for $p_e/p_s > \text{ca. } 2$. In the transition the average pressure \bar{p}_s is rapidly reduced for $p_e \approx p_s$, and hardly for $p_e/p_s > \text{ca. } 2$. The asymptotic average \bar{p}_s is markedly lower for a constant $D/D_r \ll 1$ and higher for $D/D_r \gg 1$ (dotted), but visibly only in case A. Waiting intervals would lead to a marked relaxation for A, continuations with constant D lead again to the previous attractor.

Responses to isochoric *ratcheting* are indicated in Fig. 3.2.9. Strain paths with big (A) and small amplitude (B) are depicted by saw-tooths for visibility (a). The stress paths (b) for $D = D_r$ tend to lenticular cycles which touch one critical line and are wider for A than for B. In the plot of e vs. $\log(p_s/h_{sr})$ the asymptotic state cycle is farther off the c-line for B than for A (c). In the transition to an argotropic attractor the average pressure \bar{p}_s is more rapidly reduced for A than for B, and also for a lower initial p_e/p_s . With a constant

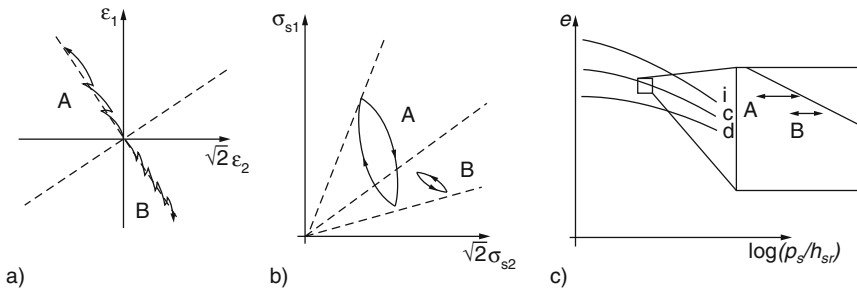


Fig. 3.2.9. Ratcheting of cylindrical peloid RSEs: (a) strain paths (volume changes exaggerated), asymptotic state cycles of stress components (b) and void ratio vs. pressure (c) for constant strain rate magnitude D

$D \ll D_r$ the asymptotic pressure \bar{p}_s gets smaller as the solid hardness is lower by (3.2.2), and with $D \gg D_r$ the \bar{p}_s gets bigger. A halt leads to relaxation, thereafter the argotropic attractor is reached again.

By definition hidden variables are not needed to characterize the state of the RSE-skeleton of a simple peloid. In other words, stress rates are assumed to be functions of stress, strain rate and void ratio only, these are specified by (3.2.1), (3.2.2), and (3.2.5). As with psammoids hidden variables are needed for reversals with small amplitudes in between. This will be discussed in Sect. 5.2, but not as thoroughly as for psammoids in Sect. 4.2 for two reasons: simple peloids can be nearly hypoelastic for $p_e/p_s > \text{ca. } 1.5$ and/or $D/D_r > \text{ca. } 10^2$, and the experimental data do not suffice to separate these effects from those of reversals with small amplitudes. Polar stresses can arise as another kind of hidden variable in narrow shear bands (Sect. 8.3), but are left aside for simple peloids. As they are often met, but can hardly be analyzed in detail, they may be captured by means of spatial averages, but this approach can be misleading (Sect. 9.1).

Clay-like soils can hardly be characterized by stiffness and strength of cylindrical samples in an objective way, Fig. 3.2.10. In a usual *compression test* with lateral confinement ($\varepsilon_2 = 0$) the sample is axially loaded, un- and reloaded in steps of axial stress $\Delta\sigma_1$ with pauses for the diffusion of pore water (a). Assuming $\Delta\sigma_1 = \Delta\sigma'_1$ and $u = u_a$ by (2.2.6) after diffusion in each step one can calculate a stiffness modulus $E_s = \Delta\sigma'_1/\Delta\varepsilon_1$ with the strain increment $\Delta\varepsilon_1$ of each step. Evidently this stiffness depends on e and σ'_1 and is different for first, un- and reloading. The skeleton stress path (b) exhibits a variable component ratio σ_{s2}/σ_{s1} which influences E_s . At the onset (0) $\sigma_{s1} \approx \sigma_{s2}$ may act by suction, with loading σ_{s2}/σ_{s1} tends to a constant, it rises with unloading and tends again to the previous constant value.

As σ_{s2} and a solid hardness h_{sr} are rarely determined e is usually plotted vs. $\log(\sigma'_1/p_a)$ (c) instead of $\log(p_s/h_{sr})$. Following Terzaghi (1925) a pre-consolidation pressure σ_c is often estimated from a bend in this plot, and substituted by an overconsolidation ratio $OCR = \sigma_c/\sigma'_1$. Hvorslev (1937) proposed instead $OCR = \sigma_e/\sigma'_1$ with an e -equivalent pressure σ_e for first compression, and argued that it does not matter how the soil has attained a given e . He mentions already the influence of σ_{s2}/σ_{s1} and of creep on σ_e . Bjerrum (1973) points out that with geological resting times e can be reduced as by preloading. We will see in Sect. 3.6 that this behaviour can be captured by v-elp or v-hyp, whereas stiffness moduli E_s are inadequate and can be misleading.

The response to *undrained* axial shortening or stretching with constant D is often plotted as $(\sigma_1 - \sigma_2)/2$ vs. $(\varepsilon_1 - \varepsilon_2)/2$, Fig. 3.2.10d. Bulging or necking of too slender samples leads to a peak (A) even if this would not occur with uniform deformations (Sect. 14.1). Without such diffuse bifurcations the maximum of $|\sigma_1 - \sigma_2|/2$, often called *undrained cohesion* c_u , is different for shortening and stretching with a given e (cf. Fig. 3.2.4 for isochoric state limits). After a drastic change of D $\max|\sigma_1 - \sigma_2|$ tends to another value

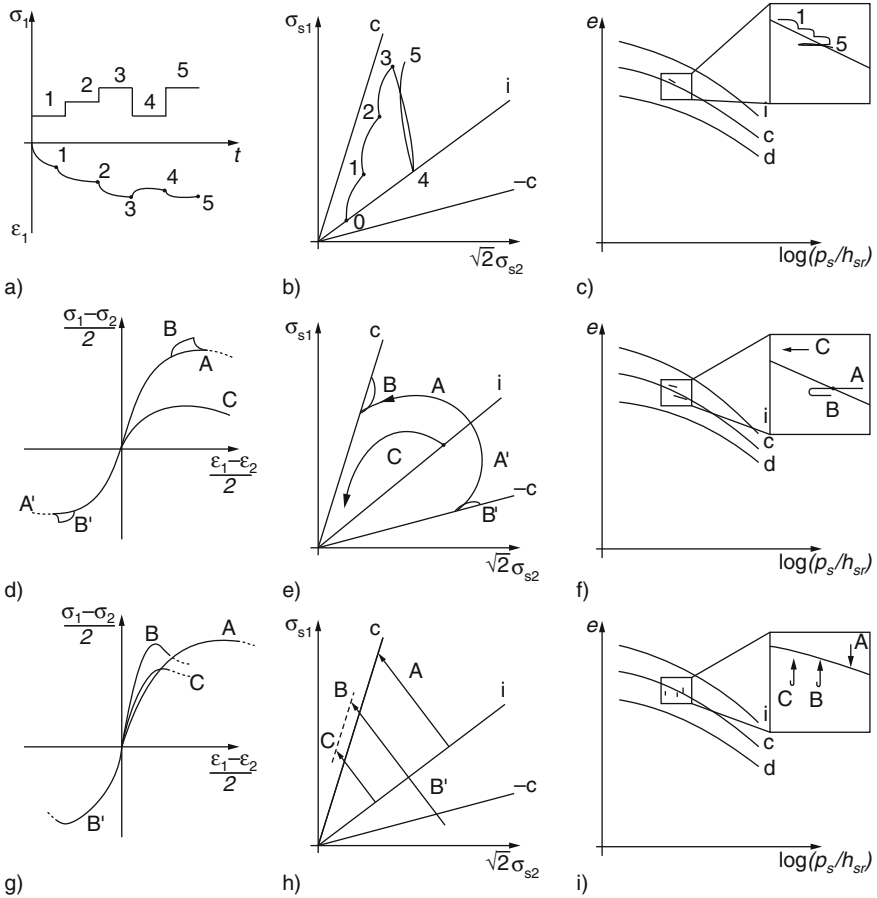


Fig. 3.2.10. Cylindrical peloid samples in usual tests: (a) compression and swelling by load steps with $\varepsilon_2 = 0$, related stress path (b) and evolution of void ratio vs. pressure (c); (d) deviatoric response to undrained deformations, related stress paths (e) and e vs. $\log p_s$ -paths (f); (g) deviatoric response to isobaric deformations, related stress paths (h) and e vs. $\log p_s$ -paths (i)

(B), and this part of the stress path (b) can also be attributed to argotropy as in Fig. 3.2.4. If the peloid has hard grains, a rather low p_s and $e > e_c$, $|\sigma_1 - \sigma_2|$ goes through a peak without diffuse bifurcation before a critical state is reached (C). Such a soil may be called *collapsible*, like a loose psammoid its skeleton can decay by monotonous deformation (liquefaction, cf. Sect. 2.2).

The notion strength is of limited use for isochoric deformations and can be misleading, nevertheless one may speak of a more or less *ductile* behaviour. A peloid may be called ductile if the amount of its stress deviator is not reduced by a monotonously continued deformation with constant D . After a reduction of D its $|\sigma_1 - \sigma_2|$ is first reduced due to argotropy and then gets stationary.

If an argotropic critical state is reached via a peak of $|\sigma_1 - \sigma_2|$ the peloid is less ductile, and it may be called collapsible (or extremely sensitive) if the skeleton decays by monotonous isochoric deformations.

The ductility can be judged from a plot of e vs. $\log(p_s/h_{sr})$, Fig. 3.2.10f, without any notion of strength. An undrained peloid may be called ductile if it attains a critical state by a monotonous deformation with constant D with a growth of stress obliquity $|\tan \psi_s|$ up to the critical value $|\tan \psi_{sc}|$ by (2.2.15). The related asymptotic mean pressure p_s is determined by $e = e_c$ with the given e and D . This definition can be extended to arbitrary deformations and is thus objective (Sect. 3.9). Opposed to this an undrained stiffness modulus $E_u = \Delta(\sigma_1 - \sigma_2)/\Delta(\varepsilon_1 - \varepsilon_2)$ is rather subjective and possibly misleading. It depends on the state variables (at least σ_{s1} , σ_{s2} and e), the sign of $(\sigma_1 - \sigma_2)(\dot{\varepsilon}_1 - \dot{\varepsilon}_2)$ and the stretching rates $\dot{\varepsilon}_1$ and $\dot{\varepsilon}_2$. As shown with Fig. 3.2.3 the differential stiffness of simple peloids cannot be represented by a modulus.

The response to *isobaric* deformations (i.e. constant p_s or σ_{s2}) may also be represented by a plot of $(\sigma_1 - \sigma_2)/2$ vs. $(\varepsilon_1 - \varepsilon_2)/2$, Fig. 3.2.10g. The peak deviator $\max|\sigma_1 - \sigma_2|$ is often called *drained strength*, and related with shear parameters c' and φ' from a plot of skeleton stress components (h). Even without bulging or necking the peak is exaggerated by shear localization (Sect. 14.1), beyond it the assumption of uniform cylindrical RSEs is no more justified. A plot of e vs. $\log(p_s/h_{sr})$ (i) is thus only legitimate up to peak. Serious triaxial tests are carried out so slowly that the diffusion of pore water can hardly impair the required uniformity, and the argotropy of the skeleton should not be ignored.

If the sample tends to contract for the given p_s (or σ_{s2}) and initial e it could approach a uniform critical state (A). One can evaluate for φ_c by (2.2.15) and for e_c by Fig. 3.2.1. Apart from differences of φ_c for axial shortening and lengthening, which can be attributed to diffuse bifurcation (Sects. 3.5 and 14.1), the φ_c from good experiments is e - and p_s -independent. The argotropy of e_c could be observed with different low enough rates $|\dot{\varepsilon}_1|$, this is far more expensive than undrained tests with differences of p_s for different $|\dot{\varepsilon}_1|$ at critical states. With stress control and critical obliquity a contractant sample creeps until a critical state with constant strain rate is reached. As shown with Fig. 3.2.5 (B) the stationary creep rate and the related $e = e_c$ depend on the initial creep rate and void ratio. As such creep tests should be slow to avoid a loss of uniformity by diffusion they are not economic to determine the argotropy of e_c .

If the sample tends to dilate the peak for a given p_s (or σ_{s2}) and $\dot{\varepsilon}_1$ is higher for a big initial consolidation ratio p_e/p_s (B) than for a lower one (C). This can be explained with Fig. 3.2.4 (C) as dilatant state limits are close to peak states. Two of them suffice formally to determine so-called *effective shear strength* parameters c' and φ' as indicated by a dashed line in Fig. 3.2.10h, but this is physically dubious. As proposed by Hvorslev (1937) for shearing (Sect. 3.8) c' may be assumed to be proportional to an e -equivalent pressure p_e , but this should be taken at peak. This p_e is not the same for two peaks

in general and should also depend on the stress obliquity as outlined with Fig. 3.2.5. A peak friction angle φ_p could be determined with $c' = 0$ by (2.2.17) as for psammoids, it depends on the void ratio (or r_e or p_e instead) at peak. This evaluation is more adequate than the one for c' with an arbitrary φ' as clay-like soils without net attraction or cementation (i.e. simple peloids) have no skeleton tensile strength, i.e. *no effective cohesion* (Schofield 2005).

The characterization of overconsolidated peloids by shear strength parameters c' and φ' is thus not physically tenable. It is anything but objective, there is no unique c' and φ' for arbitrary deformations, let alone the actual argotropy. In spite of the inadequacy of c' and φ' the *ductility* of peloids can be defined objectively for isobaric deformations. If these are monotonous and isotachic (i.e. $D = \text{const}$) the peloid may be called ductile if the stress obliquity $|\tan \psi_s|$ does not decrease. Contractant peloids are ductile as they tend to an argotropic critical state. Dilatant peloids are not ductile as their $|\tan \psi_s|$ goes through a maximum, and then tends to $|\tan \psi_{sc}|$ with shear localization. The ductility limit can be judged by means of an initial consolidation ratio p_e/p_s and the direction of deviatoric deformation, i.e. by $\text{sgn} \dot{\epsilon}_1$ for cylindrical symmetry. This definition can be extended to arbitrary deformations, but works at best as precisely as p_e/p_s and the direction of stretching are given (Sect. 3.9).

To *sum up*, simple peloids are viscoplastic if their consolidation ratio p_e/p_s is low for a given reference rate D_r and/or if their amount of strain rate D does not exceed D_r by far, otherwise they are rather hypoelastic. State limits with constant D are psammoid-like, but the limit void ratios are argotropic via the solid hardness h_s . The viscosity index I_v therein is determined by the solid and thus not baro- and pyknotropic. D_r can be chosen conveniently without loss of unit-invariance. Creep and relaxation are marked for the chosen D_r if p_e/p_s is lower than ca. 1.5–2. The response to big strain cycles and ratcheting with constant e and D is psammoid-like, whereas small strain cycles can lead to a rather hypoelastic response. Hidden variables are needed for reversals with small amplitudes and also to capture shear localizations. Usual parameters for stiffness and strength are rather subjective, whereas the ductility can be defined in an objective way.

3.3 Cam clay plus viscosity with cylindrical symmetry

In the framework of Critical State Soil Mechanics (CSSM, Schofield and Wroth 1968) elastoplastic relations for clay are named *Cam clay* models. They exist in several variants and belong to peloids as far as the properties given in Sect. 3.2 are implied. Most of them presume rate-independence, which is only justified if the amount of strain rate D does not vary substantially. As such constitutive models were already introduced in Sect. 2.3 the following outline of Cam clay is kept short. There are quantitative differences to psammoids because of softer particles. Plots of $q (= \sigma_1 - \sigma_3 = \sigma_{s1} - \sigma_{s3})$ vs. $p' (= p_s)$ are used together with σ_{s1} vs. $\sqrt{2}\sigma_{s2}$ as the former are often employed for

experimental reports, whereas the latter are better apt for generalizations. Extremely dilatant state limits (subscript d) are not captured by Cam clay models.

State limits of Cam clay are represented in Fig. 3.3.1. Limit void ratios (a) depend on the mean pressure p_s by (2.3.1), this excludes $p_s \rightarrow 0$ and $p_s \rightarrow \infty$. As usual in CSSM p_s is referred to the atmospheric pressure p_a although this is not objective. For substantially bigger or smaller D than the reference value D_r the limit void ratios are markedly higher or lower, this is indicated by dashed and dotted lines as in Fig. 3.2.1b. Effective stress components are normalized by the equivalent pressure p_{ei} from (2.3.3) for $D = D_r$ and e_i , and represented in the planes q vs. p' (b) or σ_{s1} vs. $\sqrt{2}\sigma_{s2}$ (c). Dashed and dotted lines indicate a wider or narrower elastic range for much bigger or smaller D . The relation between stress and strain rate directions (d) is rate-independent, cf. Fig. 3.2.1a. Extremely dilatant limits are not comprised, and the stress boundary can approach the no-tension lines $\sigma_{s1}=0$ or $\sigma_{s2}=0$. An associated lower bound void ratio e_d is plotted in Fig. 3.3.1a as proposed by Schofield (2005) although it does not occur explicitly in Cam clay models.

In early versions of Cam clay state limits for a constant e (i.e. $p_{ei} = \text{const}$) are approximated by an ellipse in the q vs. p' -plot. Later two half-ellipses were proposed so that (2.2.15) holds with a single φ_c for critical states. As shown in Fig. 3.3.1b the part of the boundary line with tension has to be cut off. This

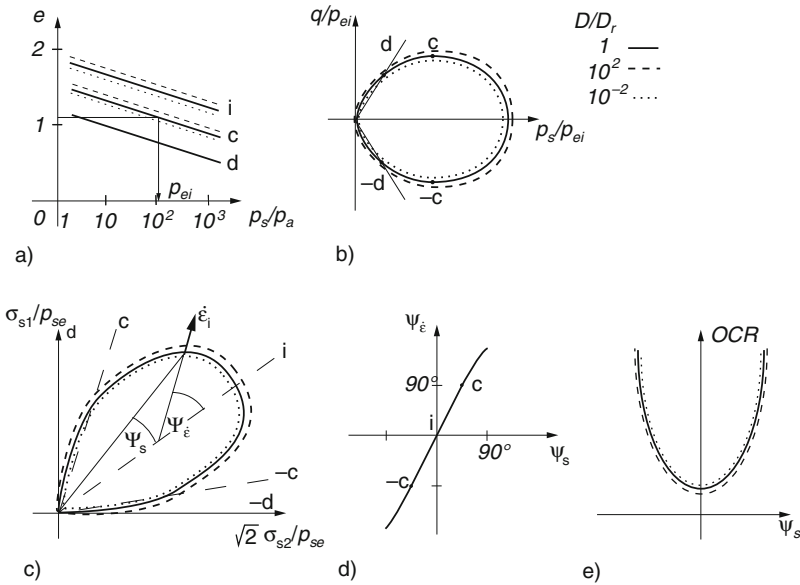


Fig. 3.3.1. State limits by Cam clay with argotropy: Limit void ratios (a), state boundaries in Roscoe-type (b) and Rendulic-type (c) stress planes, dependence of strain rate on stress direction (d), overconsolidation ratio vs. stress direction (e).

is avoided by bullet-shaped boundaries as shown in Fig. 3.3.1c. Near a tension cut-off the dependence of strain rate and stress directions is not consistent, therefore it is not shown up to $\pm d$. A plot of relative void ratio r_e vs. stress direction ψ_s as by Fig. 2.3.1 is not suitable for Cam clay as these models work without a lower bound void ratio e_d . Instead, an overconsolidation ratio $OCR = p_{ei}/p_s$ as by (2.3.2) and (2.3.3) can be plotted vs. ψ_s for state limits, Fig. 3.3.1e. Therein OCR is not shown up to $\pm d$ because of the inconsistency near tension cut-offs. As p_{ei} is determined by e for isotropic state limits with $D = D_r$ (Fig. 3.3.1a), and as p_s increases with D by argotropy for a given e , OCR is smaller for higher D_r , this is indicated in Fig. 3.3.1e.

As outlined for psammoids with Fig. 2.3.2 state limits with constant e (i.e. $p_{ei}=\text{const}$) are taken in CSSM as boundaries of elastic ranges. Inside of them the isotropic hypoelastic relation (2.3.5) may be assumed with much bigger compression index λ and swelling index κ , and a bigger ratio κ/λ than for psammoids. In early versions of Cam clay the deviatoric relation (2.3.5b) is replaced by $\sigma^* = G\varepsilon^*$ with a constant modulus G , but this is not justified for a wide p_s -range. In more recent versions (2.3.5) is replaced by a power law, viz.

$$\begin{aligned}\dot{p}_s &= K_r(p_s/p_r)^m \dot{\varepsilon}_v \\ \dot{\sigma}_s^* &= K_r(\nu/(1-\nu))(p_s/p_r)^m \dot{\varepsilon}^*\end{aligned}\quad (3.3.1)$$

with an exponent $0 < m < 1$ instead of 1 as by (2.3.5). Therein p_r denotes a reference pressure, K_r a compression modulus for $p_s = p_r$ and ν a Poisson ratio. As for a sponge this hypoelastic relation can be extended by another stress-dependence, but this should imply an elastic potential for being consistent (Niemunis and Cudny 1998).

As by (2.3.6) strain rates can be decomposed into elastic and anelastic ones, viz.

$$\dot{\varepsilon}_i = \dot{\varepsilon}_i^e + \dot{\varepsilon}_i^a \quad (3.3.2)$$

with $i = 1$ and $2 = 3$ for cylindrical RSEs. The elastic part $\dot{\varepsilon}_i^e$ is related with the stress rates $\dot{\sigma}_{si}$ by (2.3.5) or (3.3.1). The anelastic part $\dot{\varepsilon}_i^a$ arises only for loading at the boundary of the elastic range, and its direction $\dot{\varepsilon}_2^a/\dot{\varepsilon}_1^a$ or ψ_ε^a is determined by the stress direction σ_{s2}/σ_{s1} or ψ_s . As shown for psammoids with Fig. 2.3.2 the directional dependence can be specified by an associated flow rule (normality), for overcritical stress obliquities ($|\tan \psi_s| > |\tan \psi_{sc}|$) it can instead be expressed by the stress-dilatancy relation (2.2.20). Writing P_i for the normalized $\dot{\varepsilon}_i^a$ -direction (i.e. $P_1^2 + 2P_2^2 = 1$) one can write

$$\dot{\varepsilon}_i^a = f_e H_1 H_2 P_i D \quad (3.3.3)$$

with the amount of strain rate D by (2.2.19) and a factor $f_e > 0$, and two switch functions H_1 and H_2 as by (3.1.16). $H_1 = 0$ holds inside the elastic range, and $H_1 = 1$ along its boundary. $H_2 = 1$ holds for stress rates which

point out of the elastic range (plastification for loading), otherwise $H_2 = 0$ means $\dot{\epsilon}_i^a = 0$ for unloading or neutral loading. The factor f_e is determined from the $\dot{\epsilon}$ for plastification by (2.2.10) (consistency condition).

Apart from renaming (3.3.1), (3.3.2), and (3.3.3) and (2.2.10) constitute elastoplastic relations with volumetric hardening and rate-independence as in Sect. 2.3. As outlined in Sect. 3.1 plastic deformations of solids are actually viscoplastic due to thermally activated dislocations. Peloids are visco-plastic as are their solid particles, so their viscosity can be captured with a reference rate D_r and a viscosity index I_v which do not depend on e and p_s (Sect. 3.2). Rate-independent elastoplastic relations can nevertheless be of use for solids (Sect. 2.1), a viscoplastic response comes close a plastic one if D/D_r ranges within few decades so that $(D/D_r)^{I_v}$ deviates only little from 1, but the relaxation is thus missed (Sect. 3.1). So how far may elastoplastic relations like Cam clay be used for peloids although these are non-linearly viscous?

Writing (3.3.1) for elastic strain rates and combining with (3.3.2) and (3.3.3) leads to

$$\begin{aligned} \text{(a)} \quad \dot{p}_s &= \kappa_r (p_s/p_r)^m [\dot{\epsilon}_v - f_e H_1 H_2 P_v D] \\ \text{(b)} \quad \dot{\sigma}_s^* &= \kappa_r (p_s/p_r)^m [\dot{\epsilon}^* - f_e H_1 H_2 P^* D] \end{aligned} \quad (3.3.4)$$

with the volumetric and deviatoric parts P_v and P^* of the strain rate direction, the switch functions H_1 and H_2 and the factor f_e as explained after (3.3.3). Equation (3.3.4) satisfies the general requirements (3.2.1), but (3.2.1b) is thus only fulfilled with rate-independence. Equation (3.3.4) resembles (3.2.3) with (3.2.4) and $A = H_1 H_2$, but therein D_r stands instead of D . A formal agreement can be achieved by means of the argotropic reference pressure

$$p_r = p_{rr} (D/D_r)^{I_v} \quad (3.3.5)$$

with $p_r = p_{rr}$ for $D = D_r$. Thus p_r can replace the solid hardness h_s by (3.2.2b). With an e -equivalent pressure p_{ei} instead of p_e and with p_r instead of p_s the viscosity factor by (3.2.5) is thus $f_v = (p_{sr}/p_{ei})^{I_v} = D/D_r$, so insertion into (3.2.4) and then into (3.2.3) with $\dot{\sigma}_{si} = f_i$ leads to

$$\dot{\sigma}_{si} = M_{ij} \left[\dot{\epsilon}_{ij} - \left(\frac{p_{rr}}{p_{ei}} \right)^{I_v} A P_j D \right]. \quad (3.3.6)$$

This agrees with (3.3.4) wherein M_{ij} and A are more specified. The prefactor M_{ij} is thus barotropic as stated by (3.2.1a), and argotropic via p_r by (3.3.5). $A = H_1 H_2$ means two switch functions instead of one for A in (3.2.4), the factor $(p_{sr}/p_{ei})^{I_v}$ replaces f_e .

The argotropy by (3.2.3), (3.2.4), and (3.2.5) is formally eliminated in (3.3.6), but this is rather a sleight of hand. The prefactor M_{ij} is argotropic via p_r by (3.3.5), but not strongly as $(D/D_r)^{I_v}$ ranges from ca. 0.9 to 1.2 if D/D_r ranges from ca. 10^{-2} to 10^2 with I_v from 0.02 to 0.05. More debatable

is the oversimplification of f_v by taking p_r/p_{ei} in (3.2.5) instead of p_s/p_e . It was shown in Sect. 3.2 that only in the vicinity of state limits $p_s \approx p_e$ may be assumed for $D = D_r$, whereas $f_v \approx 0$ is obtained for p_e/p_s from ca. 1.5 to 2 and hypoelastic behaviour results also for $D \gg D_r$, but relaxation for $D \ll D_r$. One can conclude that the formally rate-independent Cam clay relation (3.3.4) is at best legitimate if monotonous plastic deformations are nearly isotachic and un- or reloading occur much faster. Equation (3.3.4) fails for substantial changes of D (e.g. sudden decrease), creep (where D can change by several orders of magnitude) and relaxation ($D = 0$).

A *visco-elastoplastic* relation (v-elp) on the base of Cam clay was proposed by Adachi and Oka (1982). With our renaming it can be written for cylindrical RSEs as

$$\begin{aligned}
 \text{(a)} \quad \dot{p}_s &= \frac{p_s/\kappa}{1+e} \left[\dot{\varepsilon}_v - \left(\frac{p_s}{p_e} \right)^{1/I_v} f_e H_1 H_2 P_v D_r \right] \\
 \text{(b)} \quad \dot{\sigma}_s^* &= (p_s/\kappa(1+e))(\nu/(1-\nu)) \cdot [\dot{\varepsilon}^* - (p_s/p_e)^{1/I_v} f_e H_1 H_2 P^* D_r]
 \end{aligned}
 \tag{3.3.7}$$

with a swelling index κ and a Poisson ratio ν as in (2.3.5), and with switch functions H_1 and H_2 as in (3.3.4). The plastic strain rate direction (P_v and P^*) is normal to the boundary of the elastic range, this is an ellipse for $e=\text{const}$ as in Fig. 3.3.1b. The equivalent pressure p_e is determined by e and by the stress obliquity as indicated in Fig. 3.3.1a, thus it depends also on the choice of D_r . The factor f_e is given by (2.2.10), i.e. by the conservation of solid particle volume, for on-going plastic deformations.

Equation (3.3.7) with specified factors is no simple algebraic representation, and the mathematical outline of Adachi and Oka (1982) is more complex. (3.3.7) is a special case of (3.2.3) with M_{ij} by (2.3.5), anelastic strain rate by (3.2.4) and viscosity factor by (3.2.5b). More insight could be gained by numerical RSE-tests, particularly with the aid of attractors, if software for simulations would be freely available, but some features can already be read from (3.3.7). The following examples follow the outline in Sect. 3.2.

Approaches to *argotropic state limits* resemble Fig. 3.2.4. The strain paths (a) with section-wise different D are contractant (A), isochoric (B) or dilatant (C). The critical friction angle φ_c is bigger for axial extension than for shortening, and the tension cut-off prevents extreme obliquities. The p_s -decrease is weaker with the linear $e\text{-log}p_s$ -relation by (2.3.1), and there is a tension cut-off instead of a lower e -bound e_d .

Some features can be read from the shortcut (3.3.7). After the elastic boundary is reached $H_1 H_2 = 1$ holds for monotonous continuations. For state limits $p_s/p_e = (D/D_r)^{I_v}$ holds, thus the viscosity factor by (3.2.5b) gets D/D_r so that (3.3.7) gets formally rate-independent as (3.3.6). Then p_s increases by proportional compression with constant D via (2.3.1) with p_r by (3.3.5), thus f_e is determined. The attained proportional stress path has a

constant ratio of rates $\dot{\sigma}_s^*/\dot{p}_s$, its direction ψ_s determines the anelastic strain rate direction P^*/P_v , thus (3.3.7) determines the strain rate ratio $\dot{\epsilon}^*/\dot{\epsilon}_v$ as shown by Fig. 3.3.1d.

Isochoric state limits are stationary for constant D , they have $P_v = 0$ and $P^* = 1$. Thus (3.3.7a) is satisfied with $\dot{p}_s = 0$ and $\dot{\epsilon}_v = 0$, and (3.3.7b) with $\dot{\sigma}_s^* = 0$ yields

$$\dot{\epsilon}^* = \left(\frac{p_s}{p_e}\right)^{1/I_v} f_e D_r \quad (3.3.8)$$

with a constant f_e as outlined further above, and an e -dependent p_e from (2.3.3) with e_{cr} and p_{rr} by (3.3.5). With $\dot{\epsilon}^* = \dot{\epsilon}_1/3$, and $p = p_s$

$$q_c = (\sigma_1 - \sigma_3)_c = p_s \frac{6 \sin \varphi_c}{3 - \sin \varphi_c} \quad (3.3.9)$$

holds for the critical stress deviator q_c by (2.2.15) in case of axial shortening. With p_s by (2.3.1) and with (3.3.5) one can substitute (3.3.9) by

$$q_c = p_{rr} \frac{6 \sin \varphi_c}{3 - \sin \varphi_c} \exp\left(\frac{e_{cr} - e}{\lambda}\right) f_e^{-I_v} \left(\frac{\dot{\epsilon}_1}{3D_r}\right)^{I_v}. \quad (3.3.10)$$

Apart from renaming this kind of argotropic strength was proposed by Leinenkugel (1976), only without the factor $f_e^{-I_v}$. Renaming constants and calling $q_c = 2c_u$ one can write

$$c_u \approx p_{ec} f_c (D/D_r)^{I_v} \quad (3.3.11)$$

instead of (3.3.10) for the *undrained cohesion* with $p_{ec} = p_s$ for $D = D_r$ and a factor f_c that depends on φ_c and I_v .

For dilatant state limits with constant pressure D the pressure p_s decreases by an almost proportional decompression. As shown further above for contractant state limits one can conclude from (3.3.7) that the directions of strain rate and stress are directly related. This corresponds to Fig. 3.3.1d with a confined range by tension cut-off.

Isobaric creep by v-elp resembles Fig. 3.2.5, the stress obliquity is subcritical (A), critical (B) or overcritical (C), but for each case only one initial state and strain rate is assumed. Instead of a lower e -bound the stresses for expansive creep are bounded by a tension cut-off. Such evolutions tend to argotropic state limits. With a critical stress obliquity, i.e. $\tan \psi_s = \tan \psi_{sc}$ by (2.2.15), the attained strain rate is isochoric with amount D by (3.3.8). Therein p_s is given, but p_e for $\tan \psi_s = \tan \psi_{sc}$ can change during the transition if this implies a change of e . The latter occurs if the initial strain rate is not isochoric, thus the attained amount D is not fully determined by the initial e . The change of e is reduced if the deformation time does not suffice for the diffusion of pore water, but then an RSE is no more uniform.

With a subcritical stress obliquity, i.e. $|\tan\psi_s| > |\tan\psi_{sc}|$, an isobaric creep by v-elp tends to a succession of contractant state limits. The strain rate ratio $\dot{\epsilon}_2/\dot{\epsilon}_1$ or direction $\psi_{\dot{\epsilon}}$ is determined by the stress ratio σ_{s2}/σ_{s1} or direction ψ_s as was outlined further above. Inserting (2.2.10) and p_e by (2.3.3) with $p_s = p_r$ by (3.3.5) into (3.3.7a) yields a decreasing void ratio by

$$\dot{e} = -\frac{b}{1+e} D_r \exp\left(\frac{e-e_r}{\lambda I_v}\right) \quad (3.3.12)$$

with a constant $b > 0$ and a reference void ratio e_r for the given $\tan\psi_s$. For small changes of e the factor $1/(1+e)$ is nearly constant, then (3.3.12) is satisfied by (3.2.6) which is thus confirmed. Both relations are no more justified if e is lower than the limit void ratio for the given σ_{s1} and σ_{s2} and the decreasing D_r . This slower densification with time can no more be estimated algebraically. Equation (3.3.12) and (3.2.6) cannot work for substantial reductions of e and extremely long times. Then a lower bound void ratio e_d is needed, but this does not occur in Adachi and Oka's (1982) theory.

With an overcritical stress obliquity, $|\tan\psi_s| > |\tan\psi_{sc}|$, isobaric creep by v-elp tends to dilatant state limits. In their continuation (3.3.12) would formally hold with $b < 0$, and (3.2.6) would hold with $-t$ instead of t , but actually the RSE gets non-uniform by shear localization and by diffusion of pore water (Sects. 3.5 and 14.1). If e is lower than the limit void ratio for the given σ_{s1} and σ_{s2} the strain rate can be extremely low at the beginning, but sooner or later the dilation leads to a substantial acceleration. One can at best estimate an initial D via state limits as v-elp gets invalid for much lower than critical void ratios. The time up to a delayed substantial acceleration can hardly be determined with a uniform RSE.

Evolutions by v-elp with *isochoric creep* resemble Fig. 3.2.6. Critical states are attained with argotropic limit void ratios according to the asymptotic amounts of strain rate. The plot of deviatoric strain vs. time tends to straight lines with different slopes. The latter could be calculated with (3.3.8), whereas the initial strain rate depends on the rate of previous deviatoric loading. Other than in Fig. 3.2.6c, and in reality with hard particles and overcritical void ratios, the skeleton cannot decay by Adachi and Oka's (1982) v-hyp.

Relaxations by v-elp resemble Fig. 3.2.7. For lack of lower e - and D - bounds Adachi and Oka's (1982) v-elp cannot produce realistic asymptotes for $t \rightarrow \infty$. The initial amount of pressure reduction could be estimated by (3.2.7) with f_v by (3.2.5b). It changes strongly with slight changes of p_e/p_s , therefore the initial reduction of pressure and stress obliquity cannot be quantified by (3.3.7). Evolutions with *strain cycles* resemble Fig. 3.2.8. With constant amount of strain rate $D = D_r$ the stress path tends to a flat lense which touches the two critical state lines, or a flat lense inside the critical lines. Both stress cycles are attained after the first reversal as the theoretical response is repeatedly or always hypoelastic. The plot of e vs. $\log(p_s/p_{rr})$ exhibits a constant p_s after the first reversal.

The response by v-elp to *ratcheting* resembles Fig. 3.2.9. Waiting intervals lead to relaxation, thereafter the same stress cycles are attained again by strain cycles with constant rate. These attractors are argotropic and touch one critical line, but v-elp does not produce a cumulative reduction of p_s in the transition to state cycles by imposed ratcheting.

The v-hyp relation by Adachi and Oka (1982) could be modified and extended. One could change the boundary of an elastic range so that the same φ_c by (2.2.15) holds for axial shortening and extension, and could install a vertex at $p_s = 0$ so that a tension cut-off is not needed. One could replace (2.3.1) for limit void ratios by Butterfield's (1979) relation

$$\ln\left(\frac{1+e_r}{1+e}\right) = \lambda \ln(p_s/p_r) \quad (3.3.13)$$

with another compression index λ and a reference void ratio e_r for $p_s = p_r$ which depends on $\tan\psi_s$ as indicated in Fig. 3.3.1a. Equation (3.3.13) works for a wider p_s -range than (2.3.1), but fails likewise for $p_s \rightarrow 0$ and $p_s \rightarrow \infty$. A lower bound void ratio e_d could be introduced and related with $\sigma_{s2} \rightarrow 0$ or $\sigma_{s1} \rightarrow 0$. The reference pressure p_r could be replaced by an objective solid hardness h_s , this could be argotropic by (3.2.2)a or b. The plastic flow rule in the dilatant regime need not be associated, a stress-dilatancy relation could be employed. The hypoelastic relation (3.3.1) with power law can be taken instead of (2.3.5). Extensions beyond cylindrical symmetry will be treated in following sections.

To *sum up*, visco-elastoplastic relations can capture features of simple peloids as proposed in Sect. 3.2, and rate-independent Cam clay models may serve to the purpose if the amount of strain rate D does not change by many decades. The hypoelastic response by Cam clay for un- and reloading is justified for $D/D_r > 10^2$ if the elastic range is referred to $D = D_r$. Argotropy, creep and relaxation as proposed in Sect. 3.2 are produced by Adachi and Oka's (1982) v-elp. This does not yield a gradual p_s -reduction and asymptotic state cycles as proposed in Sect. 3.2 for strain cycles and ratcheting.

3.4 Visco-hypoplasticity with cylindrical symmetry

Various attempts were made to extend hypoplastic relations for the viscosity of the solid particle skeleton. Kolymbas (1978) proposed a rate-type relation with the acceleration of strains which can be written

$$\sigma_{si} = f_s \left[L_{ij} \dot{\epsilon}_j - N_i D - \frac{c_1 \ddot{\epsilon}_i}{\sqrt{c_2 + D^2}} \right] \quad (3.4.1)$$

with $i, j = 1$ and $2 = 3$. c_1 and c_2 are constants, the factors f_s , L_{ij} and N_i depend on σ_{s1} and σ_{s2} similarly as in (2.4.3). He could thus reproduce the response to isochoric jumps of strain rate as observed by Leinenkugel (1976),

and the contractant creep as approximated by (3.2.6). Except for contractant creep (Klobe 1992) this model was not further employed as the additional parameters for the term with $\ddot{\varepsilon}_i$ could not easily be identified, and as the second derivative $\ddot{\varepsilon}_i$ causes numerical problems and requires further initial conditions which are hardly available.

After substantial improvements of the scalar factors f_s and f_d and the tensorial factors L_{ij} and N_i in (2.4.3) (outlined in Sect. 2.4) further attempts were made in the nineties to incorporate viscosity into hypoplastic relations. Wu et al. (1993) proposed

$$\dot{\sigma}_{si}/f_i = L_{ij}\dot{\varepsilon}_{ij} + N_i[D/\log(1 + a/D/D_r)^b + c \exp(-dl)^e] \quad (3.4.2)$$

with material parameters a, b, c, d, e and strain path length l . Other than in (3.4.1) this relation works without the rate of strain rate $\dot{\varepsilon}_i$, nevertheless it reproduces argotropy, creep and relaxation. Equation (3.4.2) was given up as barotropy and pyknotropy could not be properly built in. After the latter was achieved without argotropy by Wu and Bauer (1993) and Gudehus (1996) proposed an argotropic solid hardness h_s by (3.2.2) in the hypoplastic relations (2.4.3). Argotropy and creep can thus be captured, but no relaxation as (2.4.3) yields $\dot{\sigma}_{si} = 0$ for $\dot{\varepsilon}_i = 0$ with any f_s .

Niemunis (1992, 2003) achieved a breakthrough by proposing an equation of the type (3.2.3). His *visco-hypoplastic* relation (v-hyp) can be written

$$\dot{\sigma}_{si} = \frac{p_s(1+e)}{\kappa} L_{ij} \left[\dot{\varepsilon}_j - \left(\frac{p_s}{p_e} \right)^{1/I_v} L_{ij}^{-1} N_j D_r \right] \quad (3.4.3)$$

with $i, j = 1$ and $2 = 3$ for cylindrical symmetry and summation in j . The dimensionless factors L_{ij} and N_j are the same as for psammoids in (2.4.3) without argotropy, they depend only on the stress direction ψ_s and the critical friction angle φ_c . Other than in hyp the barotropy factor $p_s(1+e)/\kappa$ is proportional to p_s as by (3.3.7), this was taken over from Cam clay. Without the viscoplastic or anelastic strain rate

$$\dot{\varepsilon}_i^a = \left(\frac{p_e}{p_s} \right)^{-1/I_v} L_{ij}^{-1} N_j D_r \quad (3.4.4)$$

Equation (3.4.3) would be hypoelastic and should have an elastic potential as outlined by Niemunis and Cudny (1998).

Equation (3.4.4) agrees with (3.2.4) for $A = 1$ and the viscosity factor f_v by (3.2.5a) if the direction P_i of the anelastic strain rate is taken as

$$P_i = L_{ij}^{-1} N_j / f_e \quad . \quad (3.4.5)$$

It may suffice to state that the factors therein have the order of magnitude 1 so that P_i is almost a unit vector ($P_1^2 + 2P_2^2 \approx 1$). Thus (3.4.5) means that the direction of the anelastic strain rate is determined by the one of stress,

which could be expressed by a relation of $\psi_{\varepsilon a}$ with ψ_s . The intensity D^a of the anelastic strain rate is determined by the viscosity factor f_v via

$$D^a = f_v D_r = \left(\frac{p_e}{p_s} \right)^{1/I_v} D_r \quad . \quad (3.4.6)$$

As shown with Fig. 3.4.1a Niemunis (1996, 2003) combines Butterfield's (1979) relation (3.3.13) for limit void ratios with the influence of stress obliquity from a version of Cam clay to determine an equivalent pressure p_e . He writes

$$f_v = OCR^{-1/I_v} = \left(\frac{p_{ei}}{p_s^+} \right)^{1/I_v} \quad (3.4.7)$$

with an overconsolidation ratio $OCR = p_{ei}/p_s^+$ and a modified pressure $p_s^+ = p_s f_c$. The factor f_c depends on the stress direction ψ_s in such a manner that p_s is smaller with increasing obliquity $|\tan \psi_s|$ as for isochoric deformations after isotropic first consolidation by Cam clay. This reduction is calculated by means of an elliptic state boundary line (Fig. 3.4.1b) and quantified by a material constant β .

In this book the symbol OCR in Niemunis' v-hyp is replaced by p_e/p_s for getting f_v , thus p_e/p_s is written instead of p_{ei}/p_s^+ . The notion overconsolidation ratio is often used for special stress obliquities, in particular isotropic ($\varepsilon_1 = \varepsilon_2$) or oedometric ($\varepsilon_2 = 0$), and the argotropy is usually ignored. Our *consolidation ratio* p_e/p_s compares an obliquity-dependent equivalent pressure p_e with the actual mean pressure p_s . As proposed with Fig. 3.2.1 p_e depends on the actual e and ψ_s for $D = D_r$. This definition of p_e/p_s implies the ones by Adachi and Oka (1982) and by Niemunis (1996, 2003), it can be taken over to other viscoplastic relations and extended to arbitrary deformations. It is of use for judging the viscoplastic behaviour of arbitrary RSEs and is of importance for boundary value problems.

Niemunis' v-hyp can be represented by *argotropic response polars* as shown in Fig. 3.2.3. Stretching rates with different directions ψ_ε are normalized by

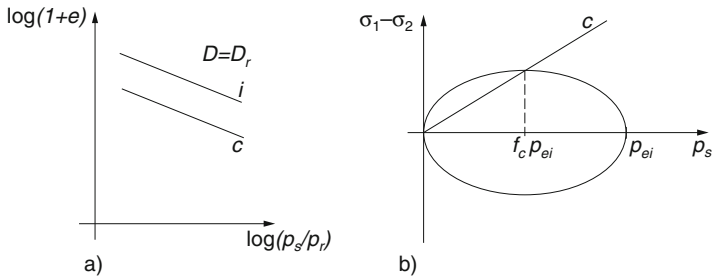


Fig. 3.4.1. Modified Cam clay elements used in Niemunis' (1996, 2003) visco-hypoplastic relation: (a) limit void ratios by Butterfield (1979), (b) state boundary line and equivalent pressures

$\log(D/D_r)$ to capture several decades of amount D (a). The polars by (3.4.3) are ellipses which are determined by the state variables σ_{s1} , σ_{s2} and e (or substitutes of them, e.g. p_s , ψ_s and p_e) and by D . Labels for $\psi_{\dot{\epsilon}}$ can show the influence of strain rate direction. For $p_s/p_e = (D/D_r)^{-I_v}$, and thus $f_v = D/D_r$ by (3.2.5b), (3.4.3) goes over into the hypoplastic relation (2.4.3) with $n = 0$ and $f_d = 1$. The polars are increasingly eccentric with bigger stress obliquity $|\tan\psi_s|$, and their size is proportional to the mean pressure p_s (b). Other than with hyp by (2.4.3) there is no lower bound void ratio e_d and no extreme obliquity $|\tan\psi_s|$ with v-hyp by (3.4.3). The latter gets invalid for too high consolidation ratios, roughly $p_e/p_s > 3$, as it would then lead to tensile skeleton stresses.

Very low or high mean pressures are also not captured by (3.4.3) as then the employed relation (3.3.13) by Butterfield (1979) fails. The hypoelastic response for negligible anelastic strain rates, i.e. $D^a \ll D$, is represented by centred ellipses, Fig. 3.2.3c. Again their shape depends on ψ_s , and their size is proportional to p_s . They cannot occur with extreme stress obliquities as explained further above. As was outlined more generally with Fig. 3.2.3c, (3.4.3) yields a hypoelastic response for $D \ll D_r$ and/or $f_v D/D_r$. If the anelastic fraction of strain rate dominates, i.e. for $D^a \gg D_r$, the response polars are so slender and eccentric ellipses that they can be replaced by straight line sections, Fig. 3.2.3d. Such degenerated polars characterize the onset of relaxation. They indicate a reduction of p_s and $|\tan\psi_s|$, their amount gets negligible if p_e/p_r exceeds about 2.

The response polars in Fig. 3.2.3 are meant for a conveniently chosen reference rate D_r . As far as the power laws (3.2.2b) and (3.2.5a) are empirically validated one may change the arbitrary time scale D_r^{-1} , this causes a change of the viscosity index I_v . The unit-invariance needed for objectivity (Sect. 1.2) can be achieved by a relation of D_r with I_v (Leinenkugel 1976). It was shown in Sect. 3.1 for solids how this could be done with an objective oscillation frequency of thermally activated nano-sized dislocation units. It suffices for applications to choose D_r conveniently and to determine the related I_v by experiments, oscillation frequencies are at best needed to estimate activation energies (Sect. 3.5) and to modify v-hyp for seismic activations (Sect. 4.6).

Argotropic state limits for v-hyp by (3.4.3) are represented in Fig. 3.4.2 (cf. Figs. 3.2.1 and 3.3.1). The relation of strain rate and stress directions (a) is rate-independent, extreme obliquities are excluded as explained further above. As shown in Sect. 3.3 for v-elp this rate-independence is achieved by the dependence of L_{ij} and N_i on ψ_s with $p_s/p_e = (D/D_r)^{I_v}$ for state limits. The limit void ratios by (3.3.13) are argotropic and coincide for different D by straight lines (b) in a plot of $\log(1+e)$ vs. $\log(p_s/p_r)$ with an argotropic reference pressure p_r by (3.2.2b). Their dependence on the stress direction ψ_s (or obliquity) can be represented by a plot of reference void ratios e_r in (3.3.13) vs. ψ_s (c). e_r holds for $D = D_r$ and is not given for extreme ψ_s as there is no lower bound e_d in (3.4.3). The argotropic state limits by (3.4.3) can be expressed aswell with other D_r and I_v in an empirically allowed range.

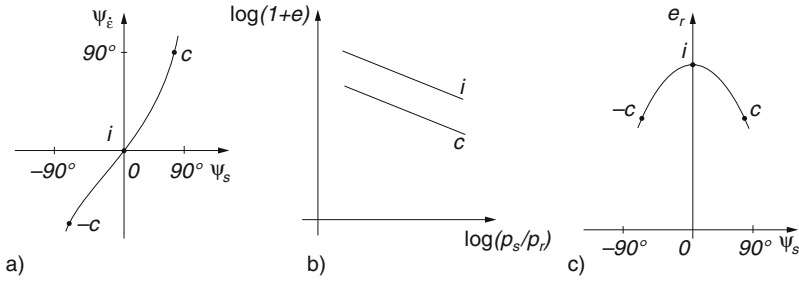


Fig. 3.4.2. State limits by v-hyp: (a) directions of strain rate and stress, (b) void ratios vs. normalized pressure, (c) reference void ratios vs. stress direction

Approaches to state limits by (3.4.3) can be represented like in Fig. 3.2.4. Extreme pressures and obliquities have to be avoided. With constant intensity D and direction $\psi_{\dot{\epsilon}}$ of strain rate p_s/p_e tends to $(D/D_r)^{I_v}$, thus f_v tends to D/D_r and (3.4.3) gets apparently rate-independent. The stress paths are then steered towards radial increase, standstill or radial decrease by the response polars with contractant, isochoric or dilatant deformations, respectively. If D is suddenly changed to a much higher or lower value and then maintained there is first a hypoelastic response or a relaxation, respectively, then the state limit for the new D is attained. Argotropic state limits are thus driven attractors as postulated for simple peloids in Sect. 3.2.

Isobaric creep is produced by (3.4.3) as shown in Fig. 3.2.5. The range is not only confined by shear localization and diffusion of pore water, but also as low void ratios and high stress obliquities are not covered by (3.4.3). As shown for v-elp in Sect. 3.3 creep leads to a succession of state limits with decreasing or increasing D for sub- and overcritical stress obliquities, respectively. The approximate asymptote (3.2.6) can again be derived via (3.3.12), it can formally also be applied for dilatant creep with $-\lambda$ and $-t$ instead of λ and t . Isochoric creep leads to critical states with stationary D after a reduction of p_s . This occurs with any initial state and constant stress deviator, but other than shown as case C in Fig. 3.2.6 a peloid by (3.4.3) cannot collapse.

Relaxations by v-hyp proceed as shown by Fig. 3.2.7. The reduction of p_s and $|\tan\psi_s|$ can be derived from (3.4.3) with $\dot{\epsilon}_i = 0$. As described by (3.2.7) the rate of pressure reduction $\dot{p}_s/p_s D_r$ is proportional to f_v , and thus negligible for $p_e/p_s > \text{ca. } 2$. The range of possible ψ_s is not known for lack of a lower e -bound. As shown for v-elp contractant creep and relaxation would not come to an end by (3.4.3). A peloid RSE should tend to a thermodynamic equilibrium, but the transition times are usually extremely long so that this lack of (3.4.3) will hardly matter.

Bigger differences by v-hyp and v-elp arise with strain cycles, this is shown qualitatively in Fig. 3.4.3. Like in Fig. 3.2.8 a small volumetric fraction is assumed for the strain paths (a), and the amplitude is big (A) or small (B) so that state limits are touched repeatedly or not. The stress paths exhibit a

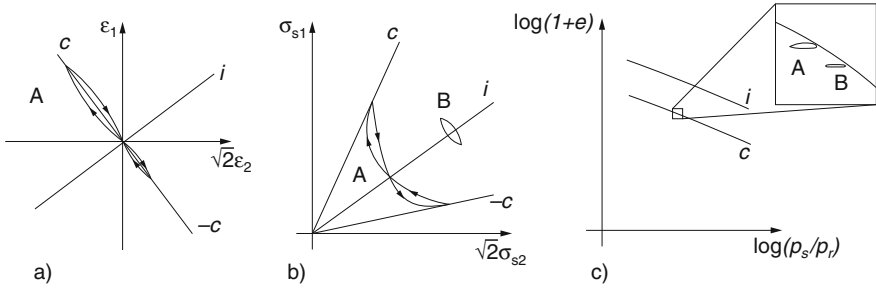


Fig. 3.4.3. Response to strain cycles (a) by v-hyp: asymptotic cycles of stress (b) and void ratio vs. normalized pressure (c)

gradual reduction of the average pressure \bar{p}_s in the transition and an asymptotic butterfly for A, and an almost hypoelastic response for B (b). The log-log plot of void ratio vs. pressure (c) shows that the consolidation ratio p_e/p_s approaches repeatedly the state limit value $(D/D_r)^{-I_v}$ for A, but remains above ca. 1.5 for B. As proposed in Fig. 3.2.8 the asymptotic state cycle for A is rather hypoplastic, whereas it is rather hypoelastic for B. Other than with v-elp, however, the minute anelastic fractions by (3.4.3) lead to a slow gradual reduction of average pressure and stress obliquity for case B. After a great many cycles with moderate amplitude a butterfly attractor can thus be attained which touches twice the critical lines. As in Fig. 3.2.8 waiting intervals would cause relaxation and lead to the same asymptotic state cycles thereafter, whereas faster or slower strain cycles with the same average e would lead to similar state cycles with higher or lower average p_s .

Differences of v-elp and v-hyp arise also for *ratcheting*. This is shown qualitatively in Fig. 3.4.4 with big (A) and moderate amplitude (B) of the cyclic strain fraction and a small volumetric average-free fraction (a). After a gradual reduction of the average pressure \bar{p}_s the stress paths tend to lenticular asymptotic cycles with higher p_s where these touch one critical line (b). Waiting intervals would cause relaxation, but no change of the attractor thereafter.

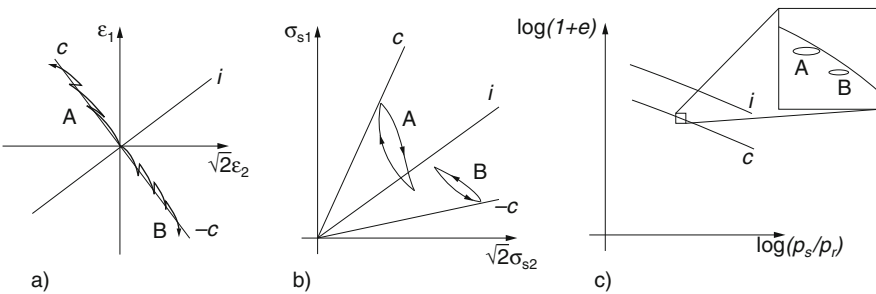


Fig. 3.4.4. Response to ratcheting (a) by v-hyp: asymptotic cycles of stress (b) and void ratio vs. normalized pressure (c)

The repeated approach of an argotropic state limit is also visible in the plot of void ratio vs. pressure (c). With a higher or lower constant D the average pressure \bar{p}_s of the attractor is higher or lower by factor $(D/D_r)^{I_v}$.

Software for numerical element tests with Niemunis' (1992, 2003) v-hyp is freely available (www Andrzej Niemunis). One can explore with it the approach to attractors more in detail. Conventional tests can thus be simulated, the results resemble Fig. 3.2.10. Nearly the same as by v-elp is obtained for compression, de- and recompression with $\varepsilon_2 = \varepsilon_3 = 0$. Axial shortening and lengthening leads to curves as in Fig. 3.2.10d, but $|\sigma_1 - \sigma_2|$ gets bigger for $\varepsilon_1 > 0$ than for $\varepsilon_1 < 0$ with a given e as L_{ij} and N_i in (3.4.3) imply a single φ_c by (2.2.15). There is no peak prior to critical states as for case C in Fig. 3.2.10d, thus peloids by (3.4.3) are ductile for $e = \text{const}$. With drainage and $p_s = \text{const}$ or $\sigma_{s2} = \text{const}$ dilation leads to peaks as in Fig. 3.2.10g. The range of consolidation ratios p_e/p_s is restricted as outlined further above, and again the description of peak states by c' and φ' is dubious.

A *modified* visco-hypoplastic relation (mv-hyp) was proposed by Gudehus (2004b). It can be written

$$\dot{\sigma}_{si} = f_s(L_{ij}\dot{\varepsilon}_j - f_d f_v N_i D_r) \quad (3.4.8)$$

with $i, j = 1$ and $2 = 3$ for cylindrical RSEs. L_{ij} and N_i are the same as for hyp by (2.4.3), they depend on the stress direction ψ_s and the critical friction angle φ_c . The stiffness factor f_s is given by (2.4.5) as for hyp, but now with the argotropic hardness h_s by (3.2.2a). This holds for the range

$$\exp\left(\frac{\alpha_r - 1}{I_v}\right) \leq D/D_r < \exp\left(\frac{1 - \alpha_r}{I_v}\right) \quad (3.4.9)$$

with a relaxation factor α_r in the range $0 < \alpha_r \leq 1/2$. For D/D_r below this range h_s is taken as for the lower bound, for D/D_r beyond the upper bound heating would reduce h_s as by (3.1.8) for solids. The limit void ratios are approximated by Bauer's (1996) formula (2.4.1) with h_s by (3.2.2a). With them the relative void ratio r_e is given by (2.2.18) for the instantaneous D , and the density factor f_d by (2.4.4). The viscosity factor in (3.4.8) is

$$\begin{aligned} f_v &= \exp((p_s/p_e)/I_v) & \text{for } p_s/p_e \geq \alpha_r \\ f_s &= 0 & \text{for } p_s/p_e < \alpha_r \end{aligned} \quad (3.4.10)$$

with a ψ_s -dependent e -equivalent pressure p_e for $D = D_r$ as indicated in Fig. 3.2.1b. The dependence of p_e on $\tan \psi_s$ is expressed by an interpolation formula so that a lower bound e_d with extreme $\tan \psi_s$ is implied.

Whereas (3.4.3) contains elements of Cam clay (3.4.8) is purely hypoplastic. The p_s -range is not restricted as for (2.3.1) and (3.3.13), but extremely low p_s have to be exempted because of net pressures (Sect. 7.1), and with big p_s clay particles are no more permanent. The turning point by (2.4.1) is

in the usual p_s -range with low h_s , therefore (2.3.1) or (3.3.13) may be used in its vicinity with an objective $p_r = h_{sr}/3$. Limit void ratios can exceed the asymptote e_o by (2.4.1) for a given ψ_s , thus isochoric deformations can lead to skeleton decay.

The exponential relation (3.2.2a) for h_s works for a wider range of D/D_r than the power law (3.2.2b), it corresponds to (3.1.7) for solids. Bounds as by (3.4.9) correspond to (3.1.8). Within them the viscosity index I_v depends on the chosen reference rate D_r , but as before this lack of objectivity does not matter if I_v is properly determined. The viscosity factor f_v by (3.4.10) yields $f_v = D/D_r$ for $p_s/p_e = h_s/h_r$ by (3.2.2a), as for (3.2.3b) and (3.4.3) this is needed to get argotropic state limits. The lower bound $f_v = 0$ for very low D/D_r produces asymptotes of contractant creep and relaxation for $t \rightarrow \infty$. Extremely dilatant state limits with the lower bound void ratio $e = e_d$ can be closer approached than by (3.4.3), but not attained. Due to the factor f_e lower void ratios than e_d cannot be attained with a given pressure p_s (by contractant creep) or average pressure \bar{p}_s (by deviatoric cycles). As with hyp, however, a strong decompression could lead to $e < e_d$, then (3.4.8) fails or has to be modified (Niemunis 2003).

In the range $\text{ca. } 10^{-2} \leq D/D_r < \text{ca. } 10^2$ and $|\tan\psi_s| < \text{ca. } 1.2|\tan\psi_c|$ the differences of v-hyp and the modified version mv-hyp are unimportant. mv-hyp comes into play for a wider range, particularly for contractant creep or relaxation over long times and with extreme stress obliquities. As this wider range was not yet explored by RSE-experiments and boundary value problems applications of mv-hyp are not given in this book. mv-hyp could be of interest for very slow deformations in the earth crust, and for very fast ones which can lead to cracking by cavitation of pore water (Sect. 6.3).

To *sum up*, visco-hypoplastic relations can capture simple peloids as introduced in Sect. 3.2 for a range of states and amounts of strain rates D which can be widened. The relation by Niemunis (1992, 2003) contains elements of v-elp, but shapes of response polars and directional relations of strain rate and stress are rather hypoplastic. Argotropic state limits, creep and relaxation resemble those by v-elp, but asymptotic state cycles due to strain cycles and ratcheting come closer to those proposed in Sect. 3.2. The modified relation by Gudehus (2004b) works for a wider range of strain rates, pressures and stress obliquities, and it implies a lower bound of void ratios. With it consolidation ratios are less restricted. The viscosity index I_v holds only for a chosen reference strain rate D_r .

3.5 Validation near and at state limits with cylindrical symmetry

As for psammoids the range of validity can be explored with oedometric, triaxial and cuboidal tests, but the prerequisites listed in Sect. 2.5 have to be modified with respect to the properties of simple peloids outlined in Sect. 3.2.

Water-saturated homogeneous samples with fine mineral particles and without net attraction, repulsion or condensation bridges should be deformed without loss of homogeneity. This excludes macropores (Sect. 7.1) and gas pockets (Sect. 6.3). With the low permeability uniform pore pressures p_w can best be achieved without drainage, or with so slow volume changes that gradients of p_w are negligible. The argotropy has to be allowed for, it can only be suppressed by choosing hard particles and/or by keeping the strain rate D within a few decades. The desired permanence of collective particle properties, which cannot strictly be given, can principally be checked by repeating tests with the same samples.

Void ratio and skeleton stress components should suffice to characterize the state of RSE skeletons, at least after sufficient monotonous deformations. As the state limits are argotropic the rate-dependence of limit void ratios has to be allowed for. Critical states will first be treated as there are no drainage problems with them. Compressions will then be considered in the range of negligible p_w -gradients. Peak states which lead to shear localization with sudden local changes of D and p_w are treated with due caution. As with psammoids uniform peak states can at best be nearly achieved with suitable boundary conditions.

Only few test reports are therefore apt for validation, and some famous ones cannot yield more than a qualitative support. Rendulic (1937) observed creep and shear band patterns, and discovered changes of pore water density with kaolin samples in triaxial tests (Sect. 14.1). Plotting void ratios as contours in a plane σ_{s1} vs. $\sqrt{2}\sigma_{s2}$, he found that e was rather path-independent and neutral with respect to p_w . These findings were confirmed by Henkel (1960). They do not strictly prove the principle of effective stress, however, as e is determined by σ_{s1} and σ_{s2} only for state limits with a given D . Roscoe et al. (1958) likewise left aside the argotropy in their Cam clay concept. They worked with p' , the deviator $q = \sigma'_1 - \sigma'_2$ and the specific volume $v = 1 + e$ instead of σ'_1 , σ'_2 and e .

The majority of test reports is written with p' , q' and v , amounts of stress and strain rates are rarely indicated. The rather subjective notion failure is often employed instead of critical or peak state limits, losses of homogeneity were rarely documented. The inevitability of diffuse bifurcation in triaxial tests (Sect. 14.1) and of shear localization even in cuboidal tests (Sect. 8.3) is often ignored. Several reports confirm the concept of argotropic state limits proposed in Sect. 3.2, and some also the thermal activation as outlined in Sect. 2.1. A more quantitative validation can be obtained with numerical simulations; these are presented only with v-hyp as software for v-elp is not freely available.

Henkel (1959) carried out triaxial tests with moderately plastic clays. For contractant, isochoric and dilatant deformations he proposed and demonstrated path-independent relations of the instantaneous state variables σ'_1 , σ'_2 and e . His plot of limit water contents ($e = w\gamma_s/\gamma_w$) vs. p' , Fig. 3.5.1, supports (2.3.1) and shows $e_i > e_c$. Very low or high p' were not investigated, so

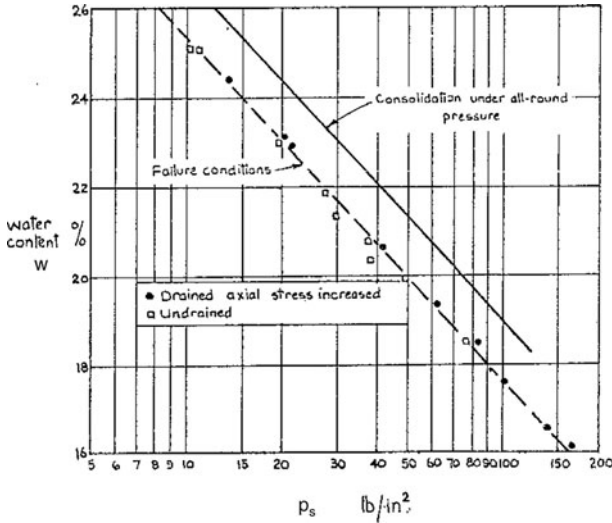
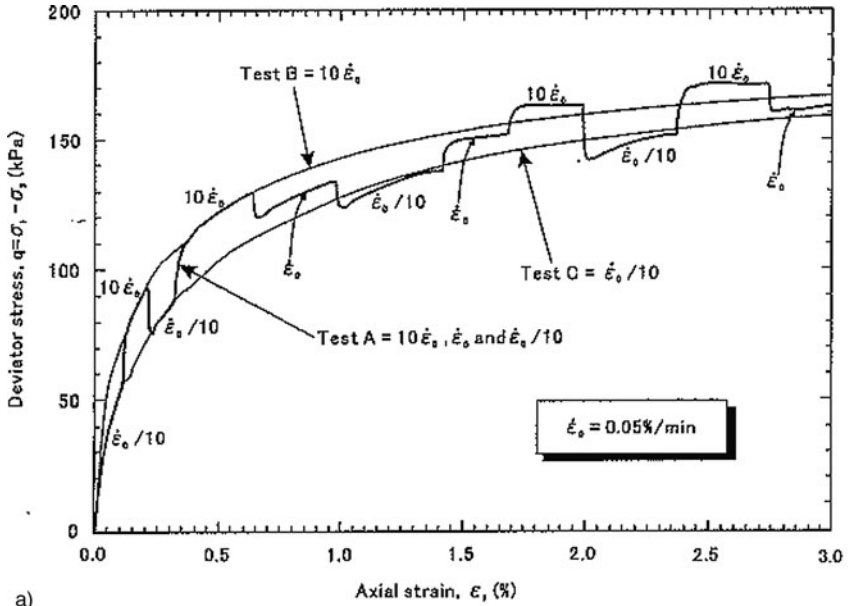


Fig. 3.5.1. Water contents vs. log pressure for isotropic first compression (*upper line*) and subsequent critical states (*lower line*), from triaxial tests with a clay by Henkel (1959)

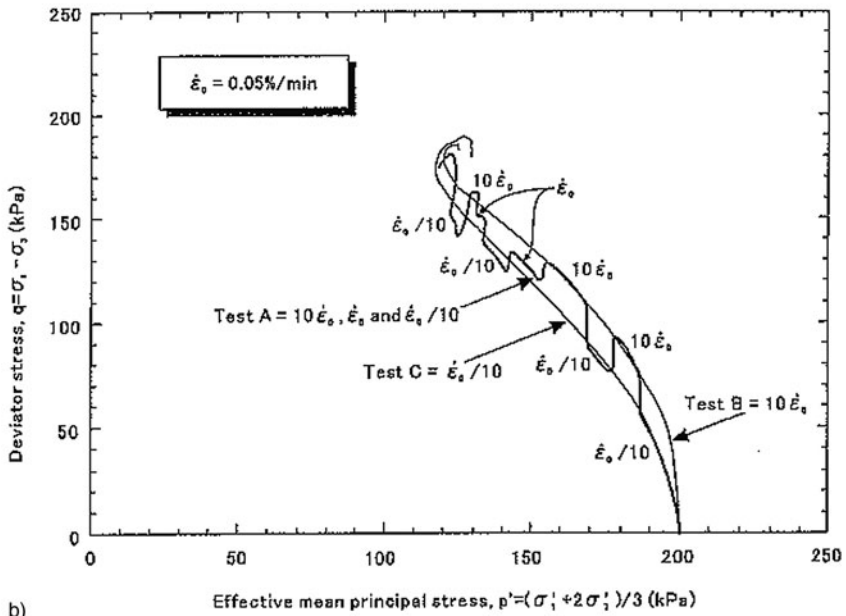
the failure of (2.3.1) for $p' \rightarrow 0$ and $p' \rightarrow \infty$ did not appear. Amounts of strain rates D were not reported, they were certainly decreasing during compression and far bigger during undrained shortening. An allowance for argotropy as by Fig. 3.2.1b would change Fig. 3.5.1.

Henkel (1959) found that the critical friction angle φ_c does not depend on p_s and is the same without and with drainage. His results suggest a lower φ_c for axial extension than for shortening, whereas Schofield and Wroth (1968) propose the opposite. Shear localization does not occur without decompression after consolidation as then the sample tends to contract, this was called ‘wet side’ by Roscoe et al. (1958). Bulging and necking cannot be avoided even with short samples and hard smooth end plates and soft membranes (Sect. 14.1). Uniform critical states can at best be produced in cuboidal devices as by Fig. 2.7.7b. With the first apparatus of this kind Pearce (1972) observed the same φ_c for axial extension and shortening with kaolin (more in Sect. 3.7).

The argotropy of state limits was first observed by Bjerrum (1973), and more in detail by Leinenkugel (1976). It is revealed with monotonous isochoric deformations after first compression (normal consolidation) with step-wise different rates D , as shown e.g. in Fig. 3.5.2. With every increase or decrease of D there is an increase or decrease of stress deviator (a) and mean skeleton pressure (b). After a transition critical stress ratios by (2.2.15) are again reached. The stress deviator increases linearly with $\log D$. With a lower e , i.e. a higher e -equivalent pressure p_e , the p_s in a critical state increases in proportion to p_e . This was expressed by Leinenkugel (1976) as



a)



b)

Fig. 3.5.2. Deviatoric stress-strain curve (a) and effective stress path (b) from an undrained triaxial test with normally consolidated clay and different strain rates (Oka et al. 2003)

$$\begin{aligned}
 q_c &= p_e \tan \varphi_c [1 + I_v \ln(\dot{\epsilon}/\dot{\epsilon}_r)] \\
 &\approx p_e \tan \varphi_c (\dot{\epsilon}/\dot{\epsilon}_r)^{I_v}
 \end{aligned}
 \tag{3.5.1}$$

for the stress deviator q_c at stationary shearing, with viscosity index I_v and reference strain rate $\dot{\epsilon}_r$. Such argotropic critical states were introduced in Sect. 3.2 and are reproduced by visco-elastoplastic and -hypoplastic relations, Sects. 3.3 and 3.4. Plots like Fig. 3.5.2 were reproduced with v-hyp by Niemunis (2003), this could similarly be achieved with v-elp. The differences of v-elp and v-hyp for extremely low or high p_s and D cannot be judged by means of usual tests.

Undrained creep up to a critical state cannot easily be attained in triaxial tests as the deviatoric stress $\sigma_1 - \sigma_2$ should be kept constant with on-going deformations. Otherwise and with a conventional interpretation test results can be misleading. Campanella and Vaid (1974) determined creep curves with undrained cylindrical clay samples after consolidation with a manual step-wise increase of the axial force. Samples cut in situ got first ductile by compression, the axial force was then increased in a short time without drainage and kept constant for a while. Thus $\sigma_1 - \sigma_2$ decreased as the sample radius increased, so the creep slowed down (coventionally called primary creep). Then the axial force was increased to regain a desired $\sigma_1 - \sigma_2$, and the creep rate $\dot{\epsilon}$ got nearly constant ('secondary'). After a stronger increase of the axial force $\dot{\epsilon}_1$ grew substantially ('tertiary') up to a loss of control. This occurred after a longer time and a smaller deformation if the average $\sigma_1 - \sigma_2$ was smaller.

Tests of this kind could be simulated with v-hyp. An initial state is produced by isotropic consolidation, then $\sigma_1 - \sigma_2$ is increased by a rapid isochoric deformation. As long as the axial force is fixed, i.e. for $(\sigma_1 - \sigma_2)(1 - \epsilon_2^2) = \text{const}$, $\dot{\epsilon}_1$ decreases with increasing ϵ_1 . Thereafter $\sigma_1 - \sigma_2$ is further increased so that $\dot{\epsilon}_1$ increases up to an apparent divergence. This occurs earlier with more deformation after the same previous consolidation if $\sigma_1 - \sigma_2$ attains higher amounts without drainage. This shows that Campanella and Vaid's (1974) results are subjective: their (often employed) creep phases depend on a rather arbitrary axial force control. With a given $\sigma_1 - \sigma_2 = \text{const} > 0$ the creep rate would tend to

$$\dot{\epsilon}_1 - \dot{\epsilon}_2 = a [(\sigma_1 - \sigma_2)/p_{ei}]^{1/I_v}
 \tag{3.5.2}$$

with the e -equivalent pressure p_{ei} after isotropic consolidation, and a φ_c -dependent constant a by (3.3.8) and (3.3.9) or (3.4.3). Such an argotropic state limit could be achieved by a servo-control with lubricated endplates and so squat samples that bulging is prevented (Sect. 14.1).

The *thermal activation* of undrained creep was investigated by Mitchell et al. (1968) with a saturated soft clay in a triaxial setup, Fig. 3.5.3. Creep was observed for different temperatures T with a constant stress deviator (a). After a transition a higher stationary creep rate $\dot{\epsilon}$ was obtained for a higher

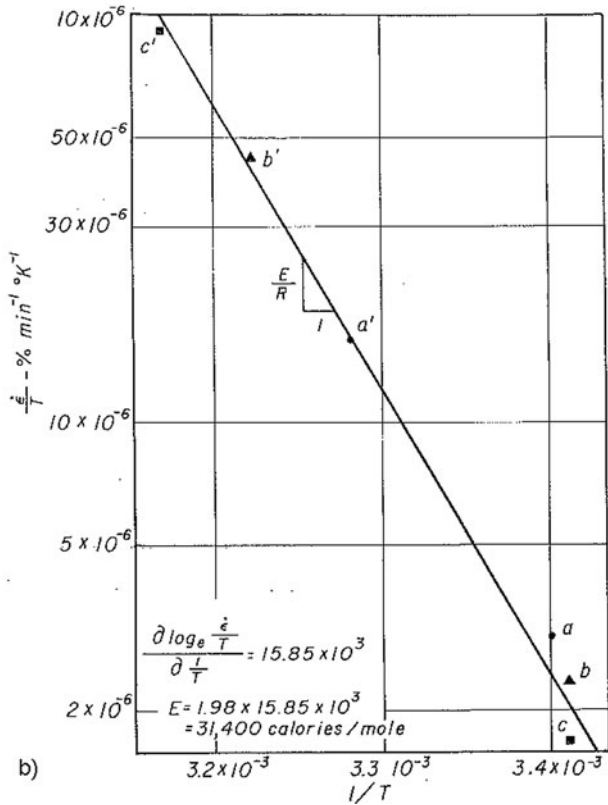
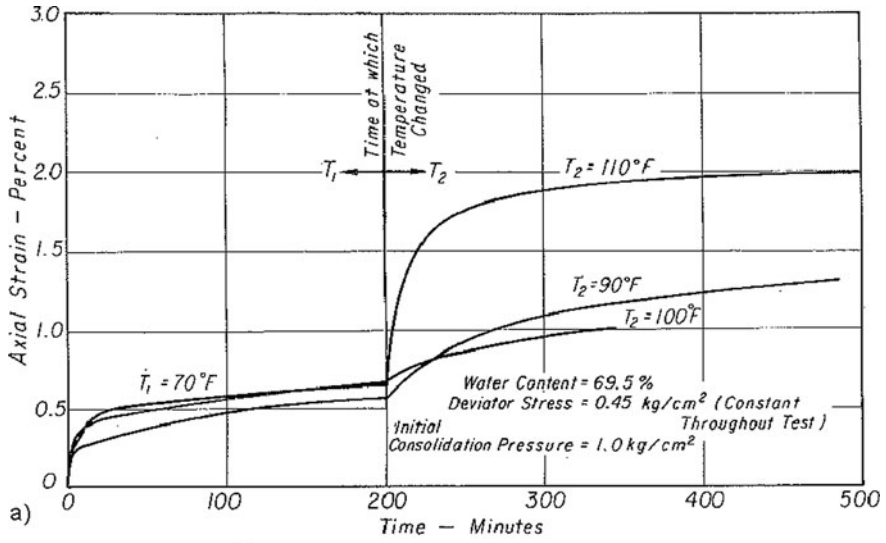


Fig. 3.5.3. Results of undrained creep tests by Mitchell et al. (1968) with a soft clay and different temperatures T : (a) shortening vs. time, (b) $\log \dot{\epsilon}/T$ vs. $\log(1/T)$

T . A plot of $\log(\dot{\varepsilon}/T)$ vs. $1/T$ yields a straight line (b). The strain rate by thermal activation can be written as

$$\dot{\varepsilon} = m f_c \frac{k_B T}{E_a} \exp\left(\frac{c_s \sigma_s^* - E_a}{k_B T}\right) \quad (3.5.3)$$

on the base of (3.1.5) or (3.1.9). The drift energy ΔF in (3.1.5) is proportional to the deviator $\sigma_s^* > 0$ with a suitable constant c_s . This is justified as both ΔF and σ_s^* are proportional to the work dissipated for stationary creep by a fictitious amount $\varepsilon^* = 1$. As in (3.1.9) the skeleton strain rate $\dot{\varepsilon}$ is proportional to the average dislocation frequency of the solid particles with a suitable constant m . This assumption is reasonable as the deformed skeleton acts like a kinematic chain. Equation (3.5.3) can be substituted by

$$\frac{\partial \ln(\dot{\varepsilon}/T)}{\partial(1/T)} = \frac{c_s \sigma_s^* - E_a}{k_B}, \quad (3.5.4)$$

this is confirmed by Fig. 3.5.3b. Mitchell et al. (1968) worked with energies per mole, then the Boltzmann constant k_B has to be replaced by the universal gas constant R . They could not specify a mole of ‘flow units’, but supplied an argument for thermal activation. The obtained activation energies, in calories per mole, are typical of ceramic substances, so creep is seated in the skeleton of solid particles. The bound pore water has far lower activation energies than the solid (Sect. 6.3), and its thermal expansion does not matter in undrained tests with soft samples.

Using the stress condition (2.2.15) for critical states, Mitchell et al. (1968) argue that the number of ‘flow units’ is proportional to the mean skeleton pressure p_s , and try to estimate this number. A similar argument was proposed by Terzaghi (1925) to justify Coulomb’s law of friction: the solid contact surface is $A_s = N'/c$ with cohesion c (Sect. 2.1) and normal force minus water pressure N' , the shear force is proportional to A_s and thus to N' . Prandtl (1928) proposed the same argument and pointed out that the rate-dependence of c by (3.1.1) does not influence the friction coefficient. For solid contact friction this idea is usually attributed to Bowden and Tabor (1954). In his book on sliding friction Persson (1998) shows why Coulomb’s law holds although there is rapid stick-slip with thermal oscillation. The rate-independence of φ_c was often observed, e.g. Fig. 3.5.2b.

Combining (3.5.3) with (3.1.9) the activation energy per dislocation unit can be estimated (Gudehus 2004b) as

$$E_a \approx (k_B T / I_v)(1 + 12 I_v) \quad (3.5.5)$$

for the range $0.02 \leq I_v < 0.07$. Equation (3.5.5) is based on Persson’s relation (3.1.7) and implies an estimate of m in (3.5.3). With $k_B T \approx 0.025$ eV (electron Volt) for $T = 298$ K dislocation energies from about 1 to 3 eV are obtained with (3.5.5). This seems to be realistic for broken mineral particles (steel has ca. 5 eV).

Proportional compressions up to argotropic state limits were more often investigated with $\varepsilon_2 = 0$ (oedometric) than with $\varepsilon_1 = \varepsilon_2$ (isotropic). Isotropic first compressions were carried out with remoulded clay under stress control in triaxial devices, but strain rates were rarely reported. As explained with Figs. 3.5.1 and 3.2.10 the e vs. $\log p_s$ lines with equal D (isotachs as by Fig. 3.2.1b) have another shape than those with equal stress rate. Big deviations arise with overconsolidation as then the creep can be so slow that state limits are not reached. Strain rate control would be better, but it should be slow enough to get drainage with negligible gradients of p_s .

A wealth of oedometer test reports is available with stress control, few were made with strain rate control and very few with temperature control. A first compression was defined by Terzaghi (1925) as the range where (2.3.1) holds, he ignored argotropy as later Roscoe et al. (1958) did with Cam clay. Buisman (1941) discovered a simpler precursor of (3.2.6). With C_α instead of λI_v (3.2.6) is widely used for oedometric creep, which is often called *secondary consolidation*. Mesri (1973) discovered that C_α/λ is a constant, Leinenkugel (1976) derived $C_\alpha = \lambda I_v$ with I_v from isochoric deformations with D -jumps. Suklje (1969) introduced oedometric isotachs and derived (3.2.6). He pointed out that e vs. $\log p_s$ lines for compressive creep of equal duration (isochrones) are equivalent to isotachs. This can be seen with

$$\dot{e} = -\lambda I_v D_r / (1 + t D_r) \quad (3.5.6)$$

from (3.2.6), thus the same t means the same \dot{e} .

Figure 3.5.4a shows isotachs of e vs. $\log \sigma_{s1}$ determined from stress-controlled oedometer test results with a remoulded organic clay by Den Haan and Kamao (2003). Strain rates are indicated by exponents of D/D_r . Using further parameters from this report Grandas-Tavera (2010) made a simulation with v-hyp (b). The argotropy is visibly reproduced, this confirms the normalization in Fig. 3.2.1d with h_s by (3.2.2). In the σ_{s1} -range from ca. 30 to 900 kPa the σ_s -dependence is likewise modelled by the relations (2.3.1), (3.3.13), or (2.4.1) with D -dependent p_r or h_s , respectively.

Similar isotachs or isochrones of e vs. $\log \sigma_{s1}$ have often been observed with natural clays. Such reports cannot be used for validation, however, as the state of natural samples is not sufficiently characterized by e and σ_{si} in general. The vicinity of $p_s = 0$ cannot properly be explored as an exact compensation of attractive and repulsive interparticle forces cannot be achieved (Sect. 6.3). Sedimentation experiments by Been and Sills (1981) indicate a power law for low p_s as by (2.4.2).

Compression tests with *different temperatures* exhibit lower void ratios for higher T (e.g. Yashima et al. 1998). Oedometer tests with temperature jumps imposed to a diatomaceous mud by Krieg (2000) indicate a marked T -dependence, Fig. 3.5.5a. This would be far weaker with (3.1.6) for I_v and D_r by (3.3.7) or (3.4.3). Compressive creep (b) shows a substantial drop of e after a T -increase. Other than with undrained tests (Fig. 3.5.3) the creep

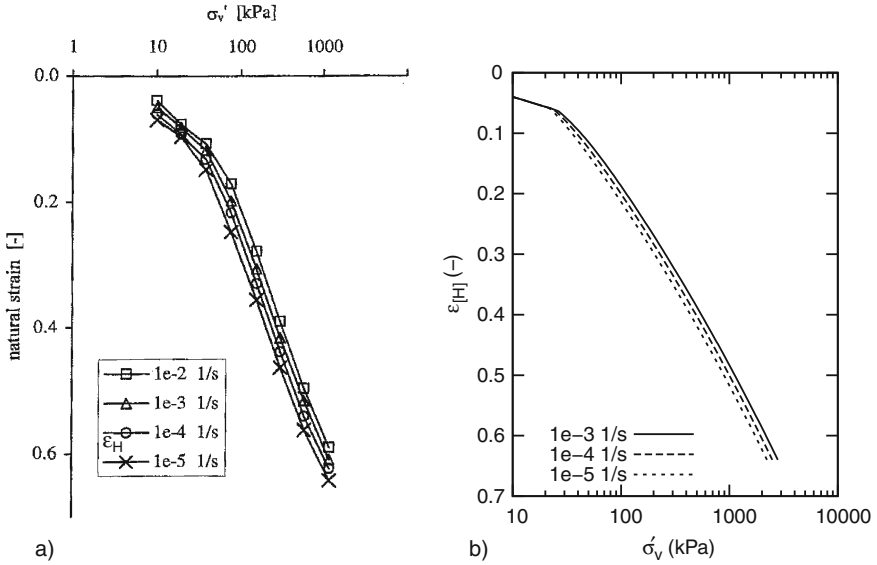


Fig. 3.5.4. Isotachs of shortening vs. pressure for compression with $\varepsilon_2 = \varepsilon_3 = 0$: (a) observed with organic clay by Den Haan and Kamao (2003), (b) simulated with v-hyp by Grandas-Tavera (2010)

rate some time after a T -increase is nearly the same, which confirms (3.3.8) with (3.1.4). Following Towhata et al. (1993) one can conclude that the solid particles are less T -dependent than the pore water. The latter is denser and less mobile in diffuse interfaces (Sect. 6.1), it dilates and gets less viscous by heating. Its osmotic repulsion and mobility grow by a T -increase.

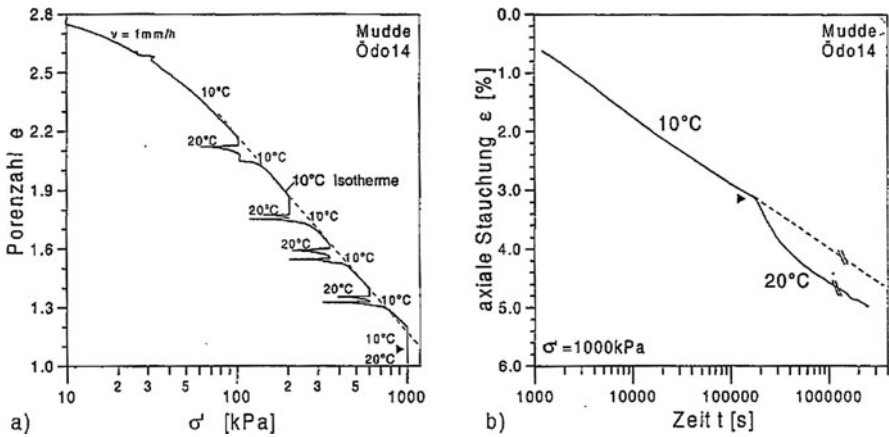


Fig. 3.5.5. Densification of a mud observed in triaxial tests with different temperatures by Krieg (2000): (a) void ratio vs. pressure, (b) axial shortening vs. time

Reports on *peak states* of clays with determination of strength parameters are abundant, but they are rarely apt for validations. Even with smooth, hard and guided endplates cylindrical samples get non-uniform at peak due to diffuse and localized bifurcation (Sect. 14.1). The required dilation is often impeded by the low permeability, localized p_w -changes cannot be observed at the sample boundary. The argotropy of peaks was rarely investigated, let alone the influence of temperature and bound pore water.

Shimizu (1982) investigated differently overconsolidated remoulded silty clay samples in drained triaxial tests. The behaviour for isotropic compression and decompression was like in Fig. 3.5.1, the decompression was faster, the argotropy can only be guessed for lack of D -data. With open drainage and constant mean pressure p_s the deviator $\sigma_{s1} - \sigma_{s2}$ was increased rapidly and kept constant afterwards. This led to a more or less delayed *creep rupture* if the stress ratio

$$\eta = (\sigma_{s1} - \sigma_{s2})/p_s \quad (3.5.7)$$

exceeded about 1.4. v-elp and v-hyp predict contractant and thus stabilizing creep if η is below the critical value

$$\eta_c = 6\sin\varphi_c/(3 - \sin\varphi_c) \quad (3.5.8)$$

as by (2.2.15) for axial shortening, and dilatant accelerated creep for $\eta > \eta_c$. With the reported $\varphi_c \approx 26^\circ$ and $\eta_c \approx 1.4$ this is confirmed by Shimizu's tests. The strain rate ratios were found to depend on the stress ratios by Rowe's (1962) stress-dilatancy relation (2.2.20). This suits to the relation of ψ_ε with ψ_s by Fig. 3.2.1a, which is thus confirmed. The samples were mainly dilated in a dominating shear band. This localization does not change the strain rate ratio $\dot{\varepsilon}_2/\dot{\varepsilon}_1$ when calculating it from boundary displacements.

Water contents determined in the shear zone after the test are plotted in Fig. 3.5.6a, they scatter spatially. These values suit to the dependence of limit void ratios on p_s and stress ratio by Fig. 3.2.1d. They were used by Shimizu (1982) to calculate an equivalent pressure p_e as for Cam clay (Sect. 3.3). State paths in the plane $(\sigma_{s1} - \sigma_{s2})/p_e$ vs. p_s/p_e can be seen in Fig. 3.5.6b. Except for $OCR = p_e/p_s = 1$ at the onset, where an immediate contraction increases p_e , the paths start vertically. With the given $p_s = \text{const}$ this means an isochoric initial response. Later there is dilation, visible from a decrease of p_e , for $OCR > 2$ initially. A critical stress ratio is reached for $OCR \leq 2$, and also a critical void ratio as shown in Fig. 3.5.5a. For $OCR > 2$ the plotted paths tend towards critical states. Strain rates or creep times are missing in Fig. 3.5.6 and cannot be reconstructed from Shimizu's paper.

Simulations of these tests with v-hyp by Grandas-Tavera (2010) are shown in Fig. 3.5.7. Waiting times were partly guessed for lack of data, partly calculated step by step for creep. Compression, decompression and dilation yield a similar e vs. $\log p_s$ plot (a) as in Fig. 3.5.6a. The calculated paths in a $(\sigma_{s1} - \sigma_{s2})/p_e$ vs. p_s/p_e plane (b), with $p_e = p_s$ for state limits with $\sigma_{s1} = \sigma_{s2}$ and $D = D_r$, resemble those in Fig. 3.5.6b. In the simulated plot p_e is thus

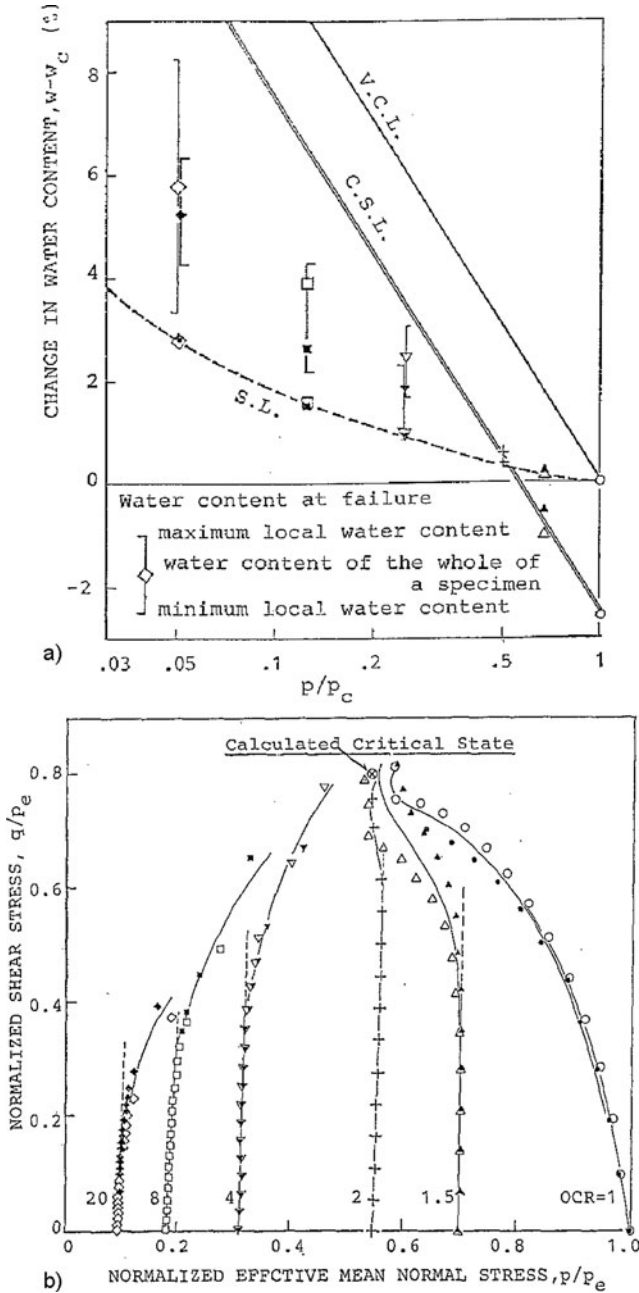


Fig. 3.5.6. Evolution of silty clay samples in drained triaxial tests with constant stress after different consolidation (Shimizu 1982): (a) changing water contents vs. ratio of actual and consolidation pressures, (b) stress paths normalized by an equivalent pressure

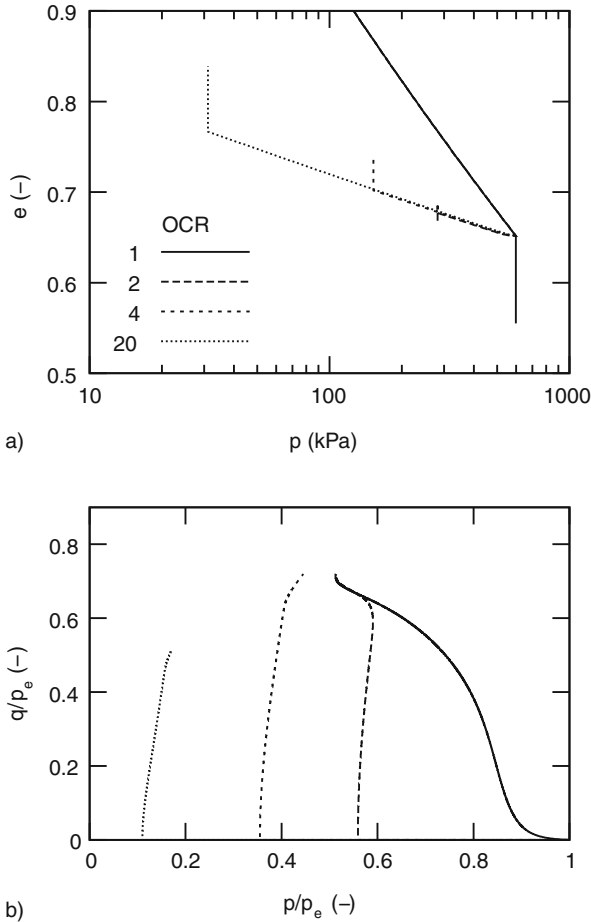


Fig. 3.5.7. Simulation of Shimizu's (1982) tests (Fig. 3.5.6) by v-hyp (Grandas-Tavera 2010): void ratios vs. pressure (a), normalized stress paths (b)

the equivalent pressure by Hvorslev (1937) as used by Shimizu (1982). As in the experiments the simulated creep could no more be controlled when it got fast near a critical state. Such a fair agreement could not be obtained with extremely different loading times. The smaller reported than simulated strains in the overcritical regime with acceleration can be attributed to the actual shear localization.

To *sum up*, visco-hypoplastic relations are validated near state limits of cylindrical remoulded clay samples. The argotropy may be neglected if the temperature is constant and the amount of strain rate D does not change substantially for loading and is much higher for unloading. The relations proposed for argotropic state limits by Fig. 3.2.1 are confirmed. The experimental support is better in the contractant than in the dilatant regime. The usual

evaluation of stress-controlled tests is insufficient: during compression and decompression D varies by several orders of magnitude so that isotachs or isochrones are often missed. The delayed rupture for isochoric or isobaric creep with constant stress deviator can be reproduced with v-hyp. Experiments speak for thermally activated dislocations of the solid particles.

3.6 Validation off state limits with cylindrical symmetry

The requirements for peloid RSE tests outlined in Sect. 3.5 hold also off state limits. We consider results of experiments satisfying these conditions in order to reveal the range of validity of constitutive relations introduced in Sects. 3.3 and 3.4. Transitions to state limits will be considered again, equivalent pressures will be further discussed. While the relations for state limits differ only for very low or high pressures p_s and high stress obliquities $\tan \psi_s$ bigger differences appear for reversals. Acceptable reports with the latter are scarce, strain rates and waiting times are rarely given, so the conclusions will be less consistent than with psammoids (Sect. 2.6). This holds also true for the few available relaxation tests. Observations with natural samples are at best of qualitative use as their composition and state is often more complex than presumed for simple peloid RSEs (Chap. 9).

We begin with *isotropic* compression and decompression. It is usually carried out with control of total pressure p and drainage, sometimes the pore pressure p_w is measured. The skeleton pressure $p_s = p - p_w$ cannot be uniform as the drainage requires gradients of p_w , the uniformity of the sample is at best regained after equalization of p_w (often called *primary consolidation*). The subsequent volumetric creep under nearly constant p_s (*secondary consolidation*) was rarely recorded, the strain rate D at the end of primary consolidation can at best be estimated from reported data. A uniform decompression can likewise only be approached after a sufficient waiting time. This is shorter as swelling is smaller than compression for the same p_s -range, so D can be bigger after equalization of p_w than for compression.

Roscoe and Burland (1968) report on such tests with kaolin. The samples were placed between smooth plates with central porous stones for drainage. Waiting times of 12 h for each p -increment secured 95% equalization of p_w . For a back-analysis p_s could be imposed as function of time t in 12 h-steps. The change of p_s with t in each step could be adapted to the one by the theory of primary consolidation (pore water diffusion, Sects. 6.3 and 11.1). The observed initial straight part of e vs. $\log p_s$ confirms (2.3.1). With the empirical relation (3.2.6) for compressive creep this section is an isochrone, and also an isotach via

$$D = \sqrt{3}\dot{\epsilon}_i = \dot{\epsilon}_v/\sqrt{3} = -\frac{\dot{e}/\sqrt{3}}{1+e} = \frac{\lambda I_v D_r}{(1+e)(1+tD_r)}. \quad (3.6.1)$$

Thus (2.3.1) would also work with an argotropic reference pressure by (3.3.5), this confirms (3.3.13). For un- and reloading, however, (3.2.6) does not hold and D can no more be estimated in this way.

There are many experimental reports on *oedometric* tests ($\varepsilon_2 = 0$) which include de- and recompression. Usually the evolution of axial stress with time $\sigma_1(t)$ is controlled and $\varepsilon_1(t)$ is observed, but p_w and $\sigma_2 = \sigma_3$ are rarely measured. $\varepsilon_2 = 0$ is achieved by a stiff ring or by servo-control in a triaxial device. Axial drainage can be achieved by guided filter plates, radial drainage is prevented. Large strains ε_1 cause no problem, they can be properly allowed for via (2.2.9) and (2.2.10) if the initial void ratio is known. Only fresh remoulded samples are apt for validation tests as initial states with cementation and fabric cannot be captured as simple peloids (Sects. 7.3 and 9.1). The net interparticle attraction or repulsion should be negligible as against the effective pressure (Sect. 6.3). One can at best guess from reports whether the net attraction or repulsion may be neglected (Sect. 7.1).

Oedometer test results by Hvorslev (1937, 1960) are acceptable in the sense of the requirements given above and in Sects. 3.4, Fig. 3.6.1. Wiener Tegel (a) is less porous, compressible and expansive than Kleinbelt clay (b) as its solid particles are bigger and harder. The material was mixed with fresh water, consolidated samples decayed slowly in fresh water, so cementation and net attraction were negligible. Osmotic repulsion could play a role for Kleinbelt clay, but presumably not much as the ionic strength was kept low and constant

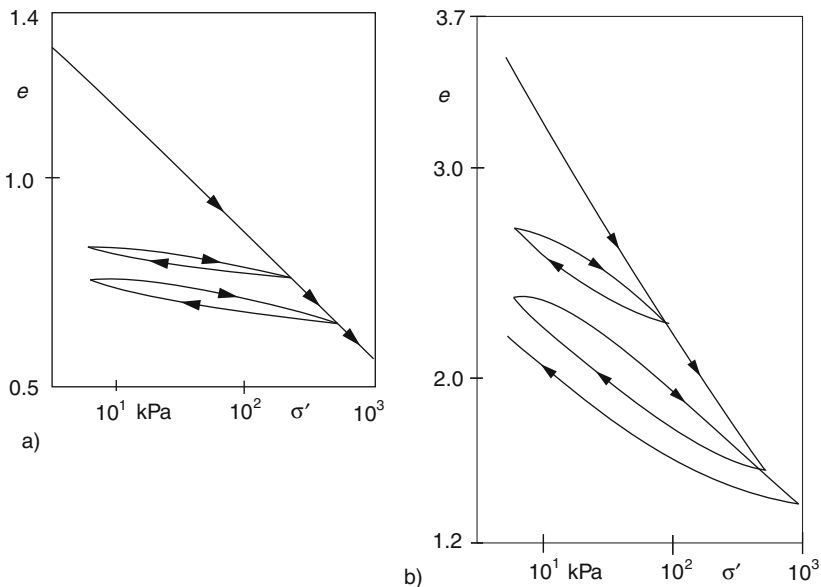


Fig. 3.6.1. Oedometer test results by Hvorslev (1937, replotted) with a moderately plastic clay (a) and a highly plastic clay (b)

(Sect. 6.3). σ_1 was gradually doubled or halved and kept constant for 24 h in each step, thus the samples did not come to a complete rest.

Results of back-analyses with v-hyp (Grandas-Tavera 2010) are shown in Fig. 3.6.2. Compression parameters were adapted to fit the experimental curves, further parameters were estimated by empirical correlations. The pore water diffusion leads to a slight non-uniformity of state after each change of σ_1 which is equalized within the subsequent interval. The initial void ratios are the ones given by Hvorslev, the initial isotropic skeleton stress was assumed as for an isotropic first consolidation with $p_s = p_e$. The load steps were chosen as indicated by Hvorslev.

The isotachs for the ends of the intervals compare fairly well with Hvorslev's curves. Deviations at the onset are minor, realistic variations of the assumed small initial skeleton stress had no influence on the subsequent evolution. The obtained oedometric first compression is an argotropic attractor of v-hyp. For Wiener Tegel Terzaghi's (1925) relation (2.3.1) yields a good fit in the σ_{s1} -range from ca. 5 kPa to 1 MPa, but also Butterfield's (1979) and Bauer's (1996) relations (3.3.13) and (2.4.1) could be adapted. For Kleinbelt clay a deviation from a linear e vs. $\log \sigma_{s1}$ relation is visible for $\sigma_{s1} > \text{ca. } 100 \text{ kPa}$, then (3.3.13) works for $\sigma_{s1} < \text{ca. } 500 \text{ kPa}$ and (2.4.1) up to ca. 1 MPa.

Bigger differences of theoretical and experimental e vs. $\log \sigma_{s1}$ curves appear for un- and reloading. The re-entry into a contractant state limit suits to the experiment. For lower σ_{s1} the theoretical response is nearly hypoelastic, though not with a straight line of e vs. $\log \sigma_{s1}$ as by (2.3.5). The hysteresis at the onset of reloading is not reproduced. For Kleinbelt clay the argotropy of state limits produces a better fit near the maximal previous σ_{s1} as the argotropy is more pronounced.

The observed hysteresis is not well reproduced, deviations are bigger for the Kleinbelt clay with finer particles. It appears that there is almost no volume change just after a reversal. For the onset of unloading this could be

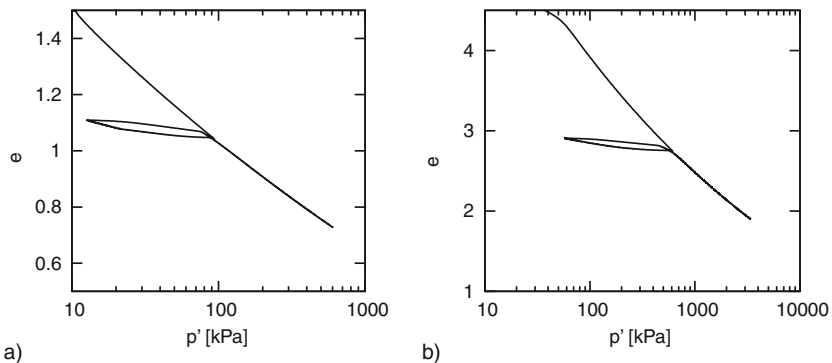


Fig. 3.6.2. Visco-hypoplastic simulation of Hvorslev's findings (Fig. 3.6.1) by Grandas-Tavera (2010) for a moderately (a) and a highly plastic clay (b)

explained by relaxation if the top plate was fixed for a while. For reloading the relaxation is negligible and would also mean a decrease of σ_1 (cf. Fig. 3.2.7). For Kleinbelt clay swelling goes on with constant σ_{s1} ($= \sigma'_1$) after the third unloading (Fig. 3.6.1b). This is not obtained with v-hyp and could presumably not be produced by a skeleton with constant σ_{s1} and $\varepsilon_2 = 0$. This indicates a net interparticle repulsion (Sect. 7.1) which plays a bigger role for a stronger decompression. The bound pore water then causes a very low and non-linear permeability (Sect. 6.3). Thus almost no pore water is squeezed out at the onset of reloading, the pore pressure increases without immediate filtration. The influence of the bound pore water is also revealed by oedometric deformations with changing temperature (Fig. 3.5.5). We will see in Sect. 6.1 how the bound pore water can be explained by electro-capillarity.

The *oedometric lateral stress* σ_{s2} is treated in some reports, but these are hardly apt for validation. Brooker and Ireland (1965) compressed and decompressed remoulded saturated clay samples with different particles and apparently negligible net attraction. The axial pressure σ_1 was imposed in steps and kept constant to enable primary consolidation, strain rates are not reported. The lateral pressure σ_2 was determined by keeping $\varepsilon_2 = 0$ via a metal membrane and a pressure chamber. The observed evolution of stresses is shown in Fig. 3.6.3 for a fat clay with rather soft and small particles. In each interval with constant axial stress the radial stress decreased for loading and increased for unloading (a). The stress path (b) exhibits a constant σ_2/σ_1 for loading towards the end of an interval and an increase of σ_2/σ_1 for unloading.

Brooker and Ireland's (1965) findings could be simulated with v-hyp. With step-wise constant σ_1 the calculated σ_2 decreases during 24 h intervals for loading and increases for unloading. Calculated stress paths are garland-like due to skeleton viscosity, only a smooth interpolation of 24 h-points would resemble Fig. 3.6.3b. Calculated stress ratios σ_2/σ_1 would depend on φ_c and *OCR*. With longer waiting times the ratio of effective horizontal and vertical stress would tend to the one without preloading because of relaxation. Results like Fig. 3.6.3b for short lab times should not be transferred therefore to field situations with far longer resting times.

The *overconsolidation ratio* was introduced by Hvorslev (1937) as *OCR* = p_e/p_s with the equivalent pressure $p_e = p_s$ for first consolidation. He noted that p_e works for arbitrary origins of e and should depend also on the stress ratio σ_{s2}/σ_{s1} , but he left aside the influence of strain rate. A consolidation pressure p_c instead of p_e is often estimated from the transition into a straight e vs. $\log \sigma_{s1}$ line in oedometer tests, and sometimes from such a transition for an isotropic compression. Hvorslev (1937) realized that e can be lower than by first consolidation up to a certain σ_{s1} not only after a decompression, but also after desiccation or cyclic shearing. Bjerrum (1973) pointed out that long resting times lead also to a kind of overconsolidation. In the visco-elastoplastic and -hypoplastic relations of Sects. 3.3 and 3.4 p_e depends on e and ψ_s (i.e. σ_{s2}/σ_{s1}), and the consolidation ratio p_e/p_s plays a key role. One should not

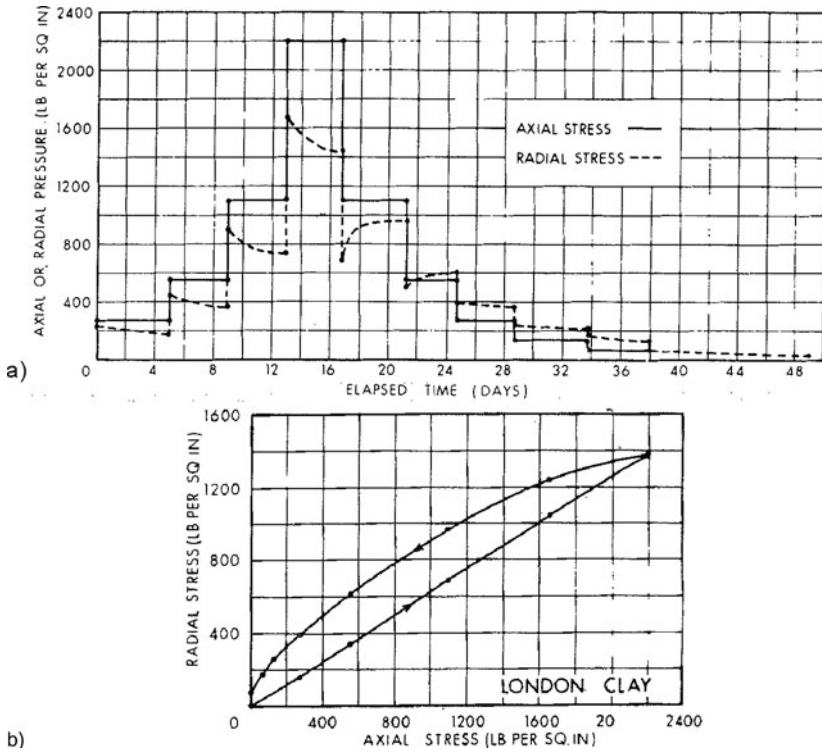


Fig. 3.6.3. Confining pressures of clay samples with $\epsilon_2 = 0$, observed by Brooker and Ireland (1965): (a) axial and radial stress vs. time, (b) stress path

write OCR for p_e/p_s as this symbol could be misleading and insufficient, and as it is dispensable in general. The symbol OCR is only used with due caution in this book as far as it appears in experimental reports which are acceptable for validations.

Creep with constant σ_{s1} and σ_{s2} , or with constant $\sigma_{s1}-\sigma_{s2}$ and e , was already treated in Sect. 3.5. The unique dependence of strain rate ratio on stress ratio, i.e. of ψ_ϵ on ψ_s , which is implied by v-elp and v-hyp as outlined in Sect. 3.3. and 3.4, is supported by Krieg's (2000) test results with a calcareous mud, Fig. 3.6.4. For constant σ_{s1} and σ_{s2} the strain paths tend to straight lines (a). This leads to a dependence of ψ_ϵ on ψ_s which compares pretty well with the one by Fig. 3.2.1a for state limits. Plots of axial strain vs. $\log t$ tend to straight lines (b) as by (3.2.6). The onset of this stabilizing creep with lower than critical obliquity $|\psi_s|$ and the transition to argotropic state lines cannot as well be reproduced. A main reason is that the viscosity factor f_v varies extremely with p_s/p_e before a state limit is reached.

Uniaxial consolidations by constant pressure as in oedometer tests are first delayed by the diffusion of pore water and later by the viscous resistance to

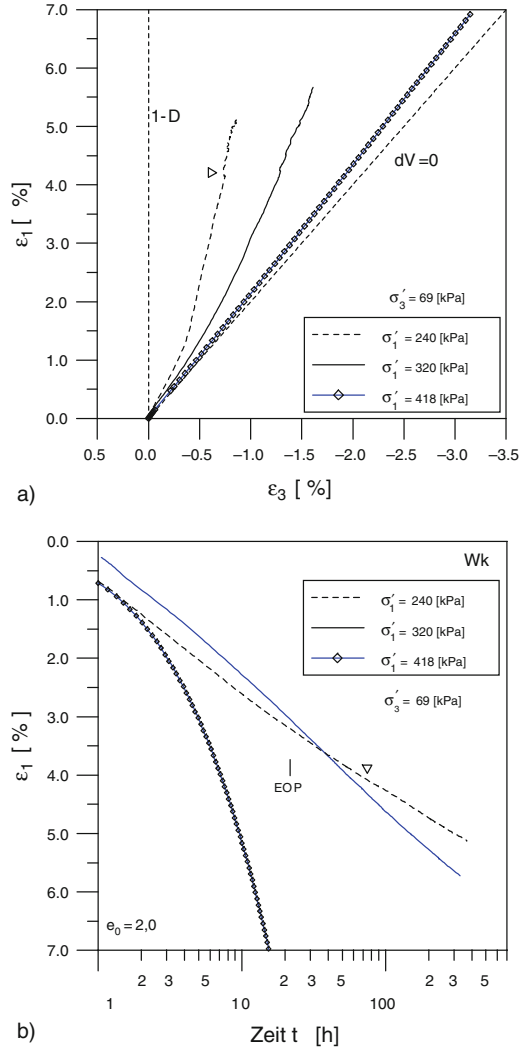


Fig. 3.6.4. Drained creep test results by Krieg (2000) with a calcareous mud and different confining pressures: strain paths (a), axial strains vs. time (b)

compression. Sturm (2009) simulated two such tests by Barden (1969) with the same clay and two different sample heights, Fig. 3.6.5. Observed and calculated plots are nearly the same, and converge after the excess pore pressure has faded away by diffusion. The further compressive creep dominates earlier for the shorter sample, and comes close to a succession of uniform contractant state limits as proposed in Sect. 3.2.

Creep with acceleration due to pore pressure increase or dilation is less predictable. Shear localization cannot be avoided near a peak (Sects. 8.3 and 14.1),

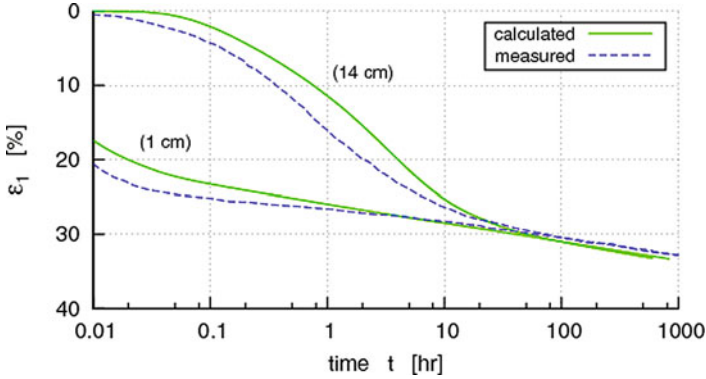


Fig. 3.6.5. Compression of a high (*above*) and a low clay sample with constant pressure, observed by Barden (1969) and simulated with v-hyp by Sturm (2009)

and arises before even with minor imperfections in the sample and along its boundaries. Thus the waiting time up to a delayed collapse can hardly be predicted and cannot be used for validations.

Relaxation was rarely observed, it is not easy to keep samples fixed and to observe stress changes with time. The initial state is rarely uniform, net interparticle forces and condensation can also play a role. Oda and Mitachi (1988) observed the relaxation of saturated kaolin samples in triaxial tests, Fig. 3.6.6. Different initial stress deviators $q = \sigma_1 - \sigma_2$ were produced before by isochoric axial shortening with different strain rates after an isotropic consolidation ($p' = p_s$). For constant ε_1 and ε_2 the stress deviator got smaller almost linearly vs. $\log t$ (a). The stress paths for constant ε_1 and ε_2 (b) exhibit a simultaneous reduction of p' only for low initial stress ratios q/p' . The observed relaxation could be roughly reproduced with v-hyp. Deviations for long times may be attributed to bound pore water and cementation (Sect. 6.1 and 7.3), these effects are not covered by the concept of simple peloids as introduced in Sect. 3.2.

Only few experimental reports on the response of saturated clays to *several reversals* are acceptable for validation. Observed and simulated evolutions with isotropic de- and recompression indicate that cumulative anelastic effects are missed by v-elp and overestimated by v-hyp (more in Sect. 5.2).

To *sum up*, the concept of simple peloids can cover the observed behaviour of saturated clays in case of cylindrical symmetry to a certain extent also off state limits. The observed nearly elastic behaviour for un- and reloading well off state limits is reproduced. Creep is well reproduced if the onset is near a state limit, then v-hyp yields a succession of state limits. The few relaxation test reports could also be matched fairly well if the onset is near a state limit. The anelastic response to cycles beyond the nearly elastic range and off state limits is missed by v-elp and caught by v-hyp with an exaggerated degradation.

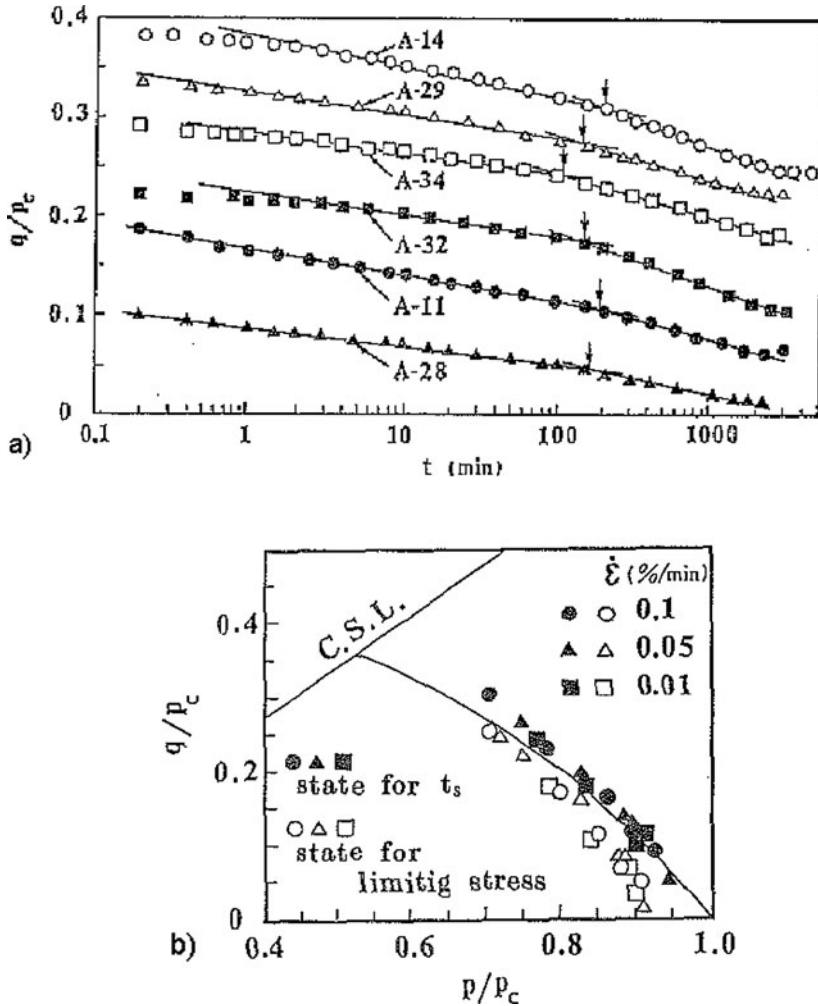


Fig. 3.6.6. Relaxation test results with kaolin (Oda and Mitachi 1988): decrease of stress deviator with log time (a), stress paths (b)

3.7 Cuboidal deformations

Visco-elastoplastic and -hypoplastic relations work also for cuboidal deformations, now with $i = 1, 2, 3$ for three principal components. Cuboidal tests, and biaxial ones in particular, were carried out with devices as indicated by Figs. 2.7.7 and 2.7.8 with remoulded saturated clay, but less often than with sand. Experimental reports are rarely apt for validations as stress and strain rates were usually not recorded. One may use observed state limits in the vicinity of critical states as for them strain rates have always the same order of magnitude. For other evolutions only biaxial test data by Topolnicki (1987)

are of use as he recorded times continuously. Other reports will be mentioned as they could possibly be used for evaluation with estimated times. Again only simulations with v-hyp are presented as software for v-elp is not freely available.

Argotropic state limits can be represented by combining Figs. 2.7.2 and 3.2.1. The invariants $\tan \psi_s$, $\cos 3\alpha_s$, $\tan \psi_\varepsilon$ and $\cos 3\alpha_\varepsilon$ play the same role as for psammoids. The argotropy can be taken into account by a D -dependent reference pressure p_r by (3.3.5) in the plot of e vs. $\log p_s$. For lack of a lower bound e_d a plot of reference void ratios e_r vs. ψ_s (Fig. 3.4.2c) may be used instead of r_e vs. ψ_s (Fig. 2.7.2d). The relations of $\tan \psi_s$ and $\cos 3\alpha_\varepsilon$ with $\cos 3\alpha_s$ are apparently the same as for psammoids. Cuts of response polars with the planes $\sigma_{s1} = \sigma_{s2}$ and $p_s = \text{const}$ could reveal the approach to attractors for deformations with constant rates, this could be demonstrated for v-elp and v-hyp as in Figs. 2.7.5 and 2.7.6.

Shibata and Karube (1965) tested a normally consolidated clay in a cuboidal device as by Fig. 2.7.7a. Central projections of achieved stress limits onto a deviator plane, Fig. 3.7.1a, resemble Fig. 2.7.2a. Nearly the same was observed by Pearce (1972), Fig. 3.7.1b, with a device as by Fig. 2.7.7b. Kirkgard and Lade (1993) observed similar state limits in a device as by Fig. 2.7.7c, and plotted also strain rate directions, Fig. 3.7.1c. The visible lack of invariance against 120° -rotations could reflect a similar lack of symmetry of the apparatus, or may be due to a sandwich-like fabric (Sect. 9.1). The argotropy does not appear in these representations of stress-controlled tests.

Nakai and Matsuoka (1983) employed a device as by Fig. 2.7.7a both with saturated sand and normally consolidated clay. They observed a linear

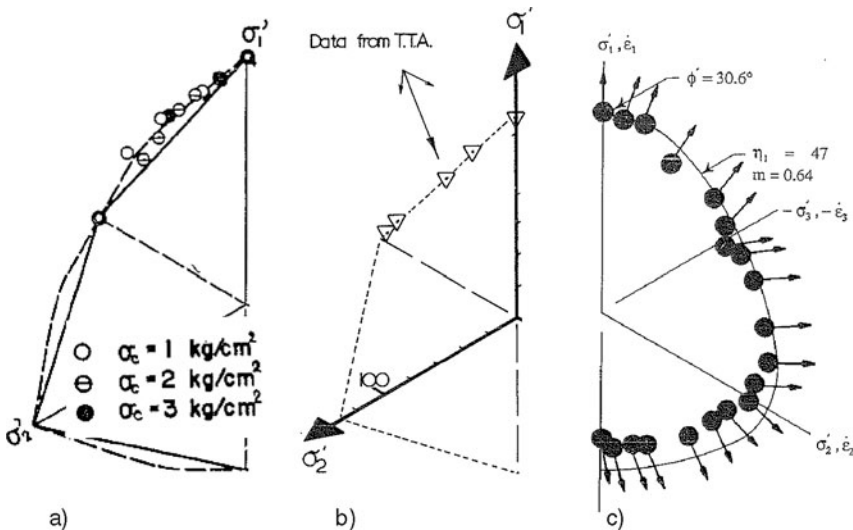


Fig. 3.7.1. Peak states of saturated clays in cuboidal tests, observed by Shibata and Karube (1965) (a), Pearce (1972) (b) and Kirkgard and Lade (1993) (c)

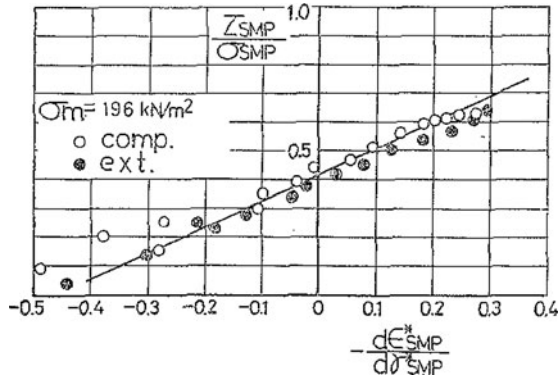


Fig. 3.7.2. Dependence of invariant stress ratios on strain rate ratios at state limits, observed with clay in cuboidal tests by Nakai and Matsuoka (1983)

dependence of invariant stress and strain rate ratios with clay (Fig. 3.7.2) as with sand, this confirms Fig. 2.7.2c for both materials. They found the same limit stress ratios for $\sigma_{s2} = \sigma_{s3}$ as in triaxial tests with short samples and smooth hard end plates. Their limit stress condition

$$\frac{J_1 J_2}{J_3} = \text{const} \tag{3.7.1}$$

with

$$\begin{aligned} J_1 &= \sigma_{s1} + \sigma_{s2} + \sigma_{s3} = 3p_s \\ J_2 &= \sigma_{s1}\sigma_{s2} + \sigma_{s2}\sigma_{s3} + \sigma_{s3}\sigma_{s1} \\ J_3 &= \sigma_{s1}\sigma_{s2}\sigma_{s3} \end{aligned} \tag{3.7.2}$$

is embedded in the hypoplastic and visco-hypoplastic relations by von Wolfersdorff (1996) and by Niemunis (1996, 2003). It implies (2.2.15) for cylindrical symmetry and is confirmed by the test results shown in Fig. 3.7.1.

Peak states of overconsolidated clay samples, observed with $p_s = \text{const}$ in a device as by Fig. 2.7.7a, were presented in a plane $p_s = \text{const}$ by Prashant and Penumadu (2005). Therein the initial overconsolidation ratio is $OCR = p_{ei}/p_s$ with the isotropic consolidation pressure p_{ei} prior to decompression. This is not the OCR at peak as the void ratio changes with deviatoric loading and drainage. The reported peak states cannot be used for evaluation as related simultaneous void ratios are not given.

Wood (1975) worked with kaolin and a cuboidal device as by Fig. 2.7.7b in order to judge constitutive relations, Hambly (1972) did the same with a biaxial device as by Fig. 2.7.8b. As they do not report strain and stress rates their results cannot be used for evaluations with the ever-present argotropy. This lack could possibly be removed by means of estimated times, but this could not be achieved for the present book.

Topolnicki et al. (1990) published results of strain-controlled biaxial tests with a similar apparatus as by Hambly (1972), further details are given by Topolnicki (1987). Sturm (2009) back-analyzed them with v-hyp. A first attempt with the documented strain rates led to disappointing deviations just after reversals, in a second one waiting times at reversals were taken into account. Thus observed evolutions could far better be reproduced, two examples are given in Fig. 3.7.3. Both plots show paths of stress and strain in the upper right and lower left quadrants, respectively, and stress-strain curves in the other two quadrants. Kaolin samples were first consolidated from mud by

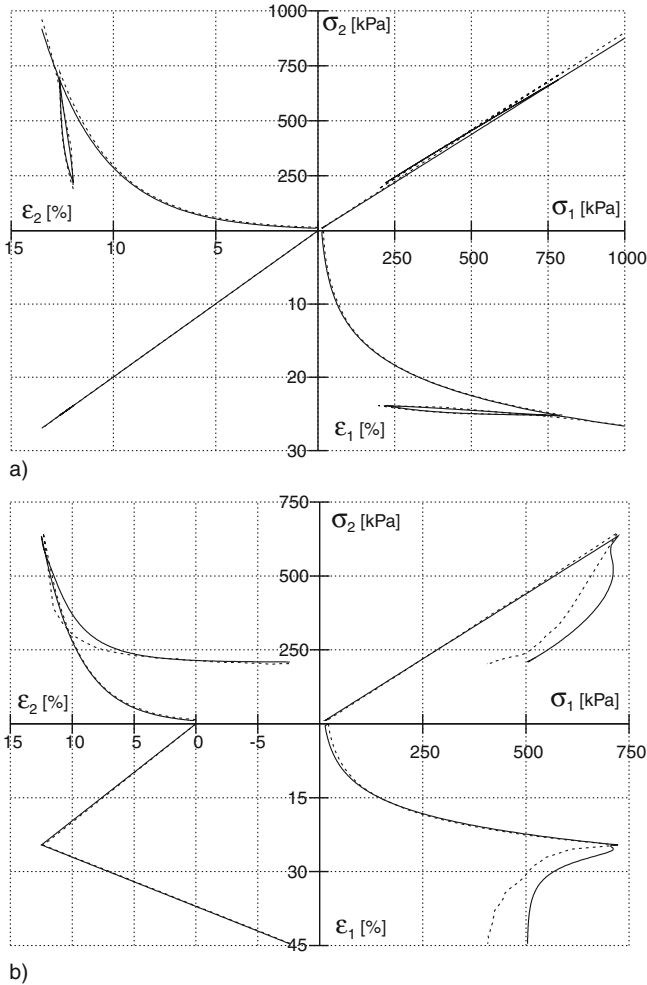


Fig. 3.7.3. Simulation of biaxial tests with a clay (dotted, Topolnicki 1987) by v-hyp (Sturm 2009); (a) uni-directional shortening and stretching, (b) bi-directional stretching; *left below* imposed strain path, *right above* stress path response

proportional compression and then deformed with another direction, always so slowly that the observed pore pressure remained nearly hydrostatic. Dots with labels for the elapsed time are dropped for simplicity, but could be added for completeness.

The initial proportional compression led to a proportional stress path, this succession of argotropic state limits is well reproduced by v-hyp. In one case (Fig. 3.7.3b) the subsequent deformation had the same amount D as before, but reversed signs of the rate components and a slight dilation. The stress path indicates first a strong reduction of obliquity and turns then to a straight line towards the origin. Except just after the reversal with unknown precise waiting time and relaxation this transition to a state limit is fairly well modelled. Stress-strain curves for this case are also reproduced, but are not so instructive as the path directions change substantially. In another case (a) two strain reversals were imposed with 180° changes, the latter would appear in the lower left quadrant with labels. Observed and calculated stress paths remain almost on the straight line as for the previous compression. The two stress-strain curves have nearly the same hysteresis loops in the experiment as by v-hyp with reasonably assumed waiting times after reversals. They indicate an almost hypoelastic behaviour for the higher consolidation ratios shortly after reversals. The same good agreement (Sturm 2009) for other biaxial tests by Topolnicki (1987) validates v-hyp and shows that viscous effects during waiting times should not be ignored.

Relaxation after first uniaxial compression was also observed by Topolnicki et al. (1990) with a saturated kaolin clay in a biaxial device. The major part occurs in the first 20 min where a certain fraction of the initial σ'_i disappears, $\sigma'_2 \approx \sigma'_3$ reflects the symmetry due to previous deformation. In-plane stress paths with t -labels would indicate that the mean stress p' ($= p_s$) decays faster than the stress obliquity. Simulations with v-hyp could at best produce a crude confirmation. It appears that friction in the apparatus enhanced the sharp bend in the σ'_i vs. t -lines and prevented a significant further stress reduction.

To *sum up*, the constitutive relations outlined in Sects. 3.3 and 3.4 are not refuted by true triaxial and biaxial test results with remoulded saturated clay. The concept of argotropic state limits is only confirmed for the vicinity of critical states with roughly constant strain rates. Only one report on biaxial tests gives complete evolution times, including waiting times with relaxation and reversals thereafter the results are reproduced with v-hyp. Further simulations could be worth the effort if evolution times could be estimated in hindsight.

3.8 Simple shearing

Stress and deformation components for simple shearing can be taken over from Fig. 2.9.1. As always in this book the subscript s denotes solid partial stress components, neglecting net attraction or repulsion and cementation they are

identical with effective stress components. Full saturation is taken for given. Thus only remoulded clays with suitable ionic strength are apt for validation tests, but the influence of bound pore water has to be kept in mind (Sect. 6.3). The shearing devices described in Sect. 2.9 are also principally apt for clays. The uniformity required for RSEs is questionable as with granular samples, and also because of pore water diffusion with low permeability. Changes of strain rate and waiting times are relevant as without rotation of principal axes, this was often not sufficiently noticed. For all these reasons only few reports are acceptable.

Argotropic state limits can be defined again with invariants by means of Figs. 2.7.2 and 3.2.1, this implies *coaxiality* of stress and strain rate, i.e.

$$\frac{T_{s12}}{T_{s11} - T_{s22}} = \frac{D_{12}}{D_{11} - D_{22}} \quad (3.8.1)$$

For peak states $\tau/\sigma_s = T_{s12}/T_{s11}$ is maximal, this leads to shear localization (Sect. 8.3). The limit void ratios depend on the mean skeleton pressure p_s as shown in Fig. 3.2.1, their argotropy is again allowed for by means of a rate-dependent reference pressure. Other representations of peak state limits will be taken over from publications. A more comprehensive representation with invariants will be given in the following Sect. 3.9.

An extension of the *visco-elastoplastic* relations (v-elp) by (3.3.7) for simple shearing requires four equations for stress rate components, and one equation for the direction of anelastic strain rates. Invariants of stress and strain rates can be employed as for cuboidal deformations. Argotropic state limits of v-elp correspond to the ones by Figs. 2.7.2 and 3.2.1 for the range from isotropic compression to peaks, and for p_s from ca. 50 to 500 kPa. A tension cut-off is needed for $|\tau/\sigma_s|$ well above the critical amount $\tan \psi_c$. Very low or high p_s have to be excluded as then (2.3.1) fails. State limits serve as boundaries of an elastic range and as plastic potential. The void ratio is the only hardening parameter, it can be substituted by the equivalent pressure p_{ei} for isotropic states as shown in Fig. 3.3.1a for $D = D_r$ with D by (2.9.9). The viscosity factor f_v for the anelastic strain rate by extensions of (3.2.4) is given by (3.2.5). $f_v = D/D_r$ holds again for argotropic state limits with given strain rate directions. The direction ν_s^a of anelastic strain rate depends on the stress obliquity τ/σ_s as for psammoids (Fig. 2.9.2a). The factor f_e for the anelastic strain rate is given by the extension of (3.3.7) for a continued state limit with (2.2.10) for conservation of solid mass. The switch functions for the viscoplastic strain rate in the extension of (3.3.7) give zero in the elastic range and for unloading from state limits.

The *visco-hypoplastic* relations by Niemunis (2003) (v-hyp) can be written for simple shearing as

$$\begin{aligned} T_{s11} &= f_s [L_{1111}(D_{11} - D_{11}^a) + D_{1112}(D_{12} - D_{12}^a)] \\ D_{11}^a &= f_v D_r L_{11ij}^{-1} N_{ij} / \|L_{ijkl} N_{kl}\| \end{aligned} \quad (3.8.2)$$

and similar expressions for the other three components. The summation convention holds for repeated subscripts ij and kl . The factors L_{ijkl} and N_{ij} depend on the stress direction components $\hat{T}_{sij} = T_{sij}/p_s$ and the critical friction angle φ_c as by hypoplasticity in (2.9.8). The viscosity factor is given by (3.2.5b) with $p_s/p_e = (D/D_r)^{I_v}$ for state limits. f_s is determined by comparison of (3.8.2) with (3.3.13) for isotropic first compression with $D = D_r$. The visco-hypoplastic relations by Gudehus (2004) can be written as

$$T_{s11} = f_s(L_{1111}D_{11} + L_{1112}D_{12} + f_d f_v N_{11} D_r) \quad (3.8.3)$$

and three further components for simple shearing, cf. (2.9.8). L_{ijkl} and N_{ij} are the same functions of \hat{T}_{sij} and φ_c as for hyp. f_d and f_s are given by (2.4.4) with (2.2.18) and by (2.4.1) with (3.8.3) for isotropic first compression, respectively, both for $D = D_r$. f_v and p_e therein have the same meaning as for cuboidal deformations.

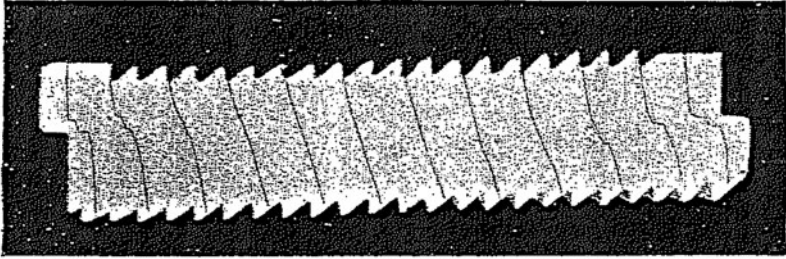
Hvorslev (1937, 1960) carried out *direct shear tests* in a device nearly as by Fig. 2.9.6 with two kinds of remoulded saturated clays (cf. Sect. 3.6). The samples were first compressed and decompressed in oedometer tests as shown with Fig. 3.6.1. Hvorslev introduced the equivalent pressure p_e and the overconsolidation ratio $OCR = p_e/p'$ for this case. He noted already that p_e should also depend on the ratio of stress components. Under constant average vertical pressure $\bar{\sigma}$ the average shear stress $\bar{\tau}$ was gradually increased via a load frame. In each step $\bar{\tau}$ was kept constant so that pore pressure differences could disappear by diffusion, the required time was estimated as for compression and decompression.

Shear creep was observed by Hvorslev (1937) after the end of pore water diffusion. The creep rate increased more than linearly with increasing $\bar{\tau}$, at a ‘failure load’ $\bar{\tau}_f$ the shear creep got stationary or accelerated. The vertical displacement of the upper plate indicated that the sample contracted for $OCR < \text{ca. } 2$ initially. Then a kind of stationary creep was attained with

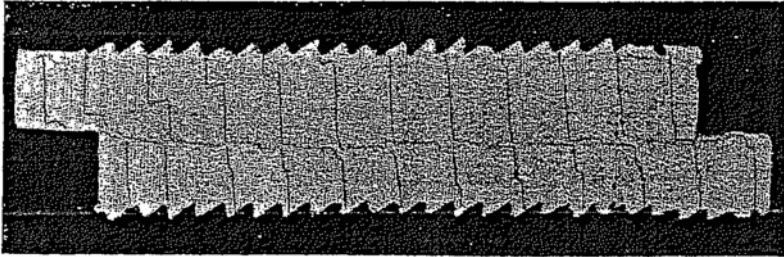
$$\bar{\tau} = \tau_f = \bar{\sigma}' \tan \varphi_{cs} \quad (3.8.4)$$

and constant sample height. The critical friction angle was σ' -independent for the silty Wiener Tegel, $\varphi_{cs} = 26^\circ$. The more plastic Kleinbelt clay had a far lower φ_{cs} which decreased noticeably with higher $\bar{\sigma}'$. For $OCR > \text{ca. } 2$ initially the samples dilated and exhibited acceleration at $\bar{\tau} = \tau_f$. Some samples had vertical markers and were cut after the test, Fig. 3.8.1. With $OCR < \text{ca. } 2$ the shear deformation was uniform in the middle part (a). With $OCR > \text{ca. } 2$ shearing was localized near the middle plane (b).

Hvorslev (1937, 1960) carried out also *ring shear tests* with the same clays. Using different confining rings, shearing was revealed by vertical markers and cuts after the test, Fig. 3.8.2. Up to peak states the behaviour was nearly the same as with the shear box tests. Beyond peaks shearing was localized near the middle plane with free rings, and near the top with fixed rings. A reduced



a) Mitte $p = 2$ $T_s = 88$ $H = 2,0$ $\Delta L = 3,5$ $\Delta L' = 4,0$
A



b) Mitte $p = 5-0-\frac{1}{2}$ $T_s = 390$ $H = 2,2$ $\Delta L = 4,0$ $\Delta L' = 13,0$

Fig. 3.8.1. Cut clay samples after shearing with an initial $OCR < ca. 2$ (a), and with $OCR > ca. 2$ (b), Hvorslev (1937)

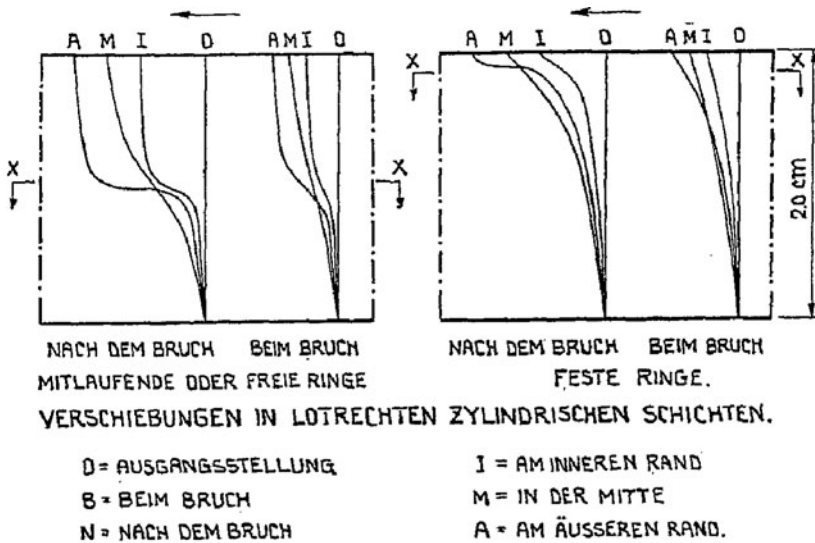


Fig. 3.8.2. Distribution of shearing in clay samples cut after ring shear tests (Hvorslev 1937) with free (left) and fixed lateral rings (right)

shearing resistance was observed beyond the peak. Without previous decompression the peak of Wiener Tegel was reached with ca. 10% shear strain. Beyond it τ had to be reduced to avoid acceleration. With slower τ -loading the sample was softer, but it got stiffer by a τ -cycle. After decompression the peak shear strain was smaller than without, and bigger with slower loading. With Kleinbelt clay the peak strain was smaller or bigger without or with decompression, respectively, and the τ -reduction to avoid acceleration beyond the peak was bigger than with Wiener Tegel.

Void ratios were determined by means of cuts after each test. Other than Casagrande (Fig. 2.9.5) Hvorslev believed that beyond the peak a critical state is not reached independently of the state at the onset of shearing. Roscoe et al. (1958) concluded instead that critical states are reached in narrow shear bands, which were not investigated in detail by Hvorslev and ignored by Casagrande. Hvorslev's peaks without decompression and his different τ -asymptotes after peaks without or with it are not covered by CSSM, these findings cannot be explained without shear localization (Sect. 8.3).

Hvorslev's complicated diagrams for peak states are simplified in Fig. 3.8.3. Limit shear stresses τ_p (a) and related void ratios (b) are plotted vs. vertical effective stress σ' . After first compression (0–1) shearing with unchanged σ' (1-1P) leads to a void ratio decrease Δe and a strength by (3.8.4). After decompression by reduction of σ' by ca. 50% (1–2) shearing up to peak (2–2P) leaves e almost unchanged, whereas τ_p is bigger than τ_f by (3.8.4). After a stronger decompression (1–3) shearing up to the peak (3–3P) is dilatant, and τ_p/τ_f is bigger than after less decompression. The difference of void ratios at peak and after first compression with the same σ' is nearly independent of OCR. Hvorslev's approach for shear strength can be written as

$$\begin{aligned}
 \text{a)} \quad \tau_p &= \sigma' \tan \varphi'_s + \kappa_c \sigma_e (= \sigma' \tan \varphi'_s + c'), \\
 \text{b)} \quad \tau_p &= \sigma' (\tan \varphi_{cs} + \tan \varphi'_s - \tan \varphi_{cs} + \kappa_e \sigma' \sigma_e / \sigma'), \\
 \text{c)} \quad \tau_p &= \sigma' (\tan \varphi_{cs} + \tan \nu_s), \\
 \text{d)} \quad \tan \nu_s &= \tan \varphi' - \tan \varphi_{cs} + \kappa_e \sigma_e / \sigma'.
 \end{aligned} \tag{3.8.5}$$

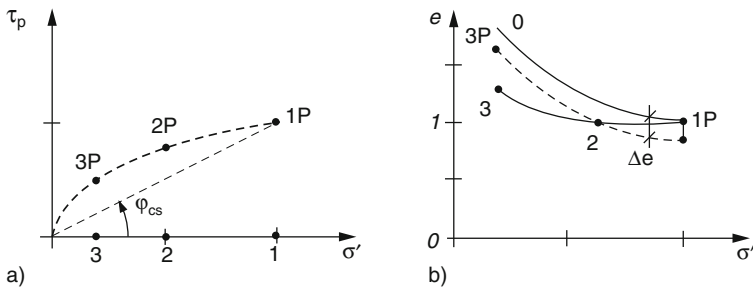


Fig. 3.8.3. Simplified representation of Hvorslev's (1937) shear strength concept: (a) shear strength vs. normal stress, (b) void ratios vs. normal stress

In the Coulomb-Mohr expression (a) employed by Hvorslev a friction angle $\varphi'_s < \varphi_{cs}$ is determined from the inclination of shear bands in uniaxial shortening tests. The effective cohesion c' is proportional to the equivalent pressure σ_e , $c' = \kappa_e p_e$, with a constant factor $\kappa_e = \tan \varphi_{cs} - \tan \varphi'_s$. This can be rewritten (b), and renamed (c) with a dilatancy angle ν_s (d) so that Taylor's (1948) expression (2.9.7) is obtained. Hvorslev's σ_e is given by the e at peak via Terzaghi's (1925) compression law (2.3.1) with a suitable e_r . Thus his c' is variable so that $\tau_p = \tau_f$ is obtained with $OCR = 1$ initially, and $\tau_p > \tau_f$ for $OCR > 1$.

Following Terzaghi (1931), Hvorslev (1937) justified the effective cohesion c' by an overlap of bound pore water near contacts of solid particles. Actually this overlap causes a repulsion (Sect. 6.1) which is more or less compensated by van der Waals attraction (Sect. 7.1). Schofield (2005) defends (3.8.5c) without c' by means of CSSM, arguing that τ_p exceeds τ_f only due to dilation and not because of an effective cohesion. Within our concept of state limits (3.8.3c) holds in the vicinity of critical states, cf. Figs. 2.9.2a and 3.2.1a. The dilatancy angle ν_s of simple peloids increases with bigger strain rate D due to the viscosity of the solid particles (Sect. 3.1). For a given σ' and e harder particles cause more dilation. With argotropic state limits the relative void ratio r_e by (2.2.18) is lower with a higher D for given e and σ' as then e_c and e_d are bigger, cf. Fig. 3.2.1b. Thus τ_s and τ/σ_s are bigger, as shown by Fig. 2.9.2a and c, if r_e is lower with a higher D .

For the initial compression and decompression Hvorslev's void ratios are nearly as good as from oedometer tests. Shearing without decompression before was rather uniform in the middle third of the samples, cf. Fig. 3.8.1a. After decompression shearing with constant σ' was first contractant and then dilatant, and localized beyond the peak. As the sample got non-uniform Hvorslev's e -values can no more be representative. A back-analysis of his tests with allowance for localization and sharp edges is not yet feasible (Sect. 8.3).

Hvorslev's ring shear test results suggest a *residual strength* τ_r below the critical one by (3.8.5) for continued shearing. This was confirmed by Skempton (1985) and will be discussed in Sect. 8.3. *Thin layer shear* tests (Balthasar et al. 2006) as by Fig. 2.9.8 do not exhibit this kind of softening, Fig. 3.8.4. A highly plastic clay was compressed between filter plates with a mean vertical pressure up to $\bar{\sigma}' = 15$ MPa, and then sheared with constant $\bar{\sigma}'$ and different velocities v_s (a). With a layer thickness of ca. 1.5 mm and free vertical mobility excess pore pressures can be avoided, and the major part of the sample with up to ca. 25 cm length and 15 cm breadth is not influenced by the free rim. The shearing resistance beyond a flat peak increases or decreases just after an increase or decrease of v_s , respectively (b). With further shearing it returns to a v_s -independent stationary value which depends on $\bar{\sigma}'$ by (3.8.4), with $\varphi_{cs} \approx 10^\circ$ in this case.

Libreros-Bertini (2006) carried out a back-analysis with v-hyp, Fig. 3.8.5. The thin layer is divided into finite elements with allowance for diffusion of pore water, contact at the filter plates and capillary pressure along the rim (a).

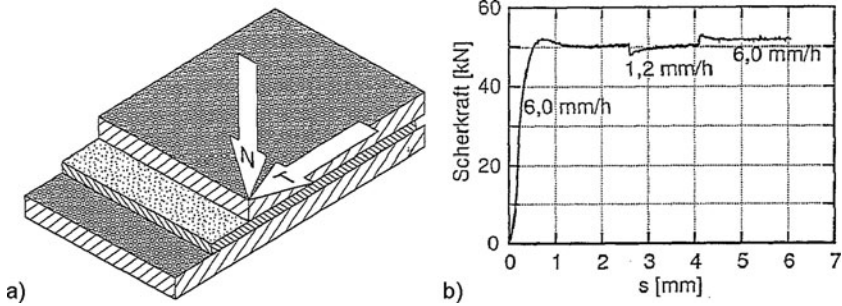


Fig. 3.8.4. Thin layer shearing of a highly plastic clay with constant pressure (Balthasar et al. 2006): simplified system (a), shear force vs. displacement with different velocities (b)

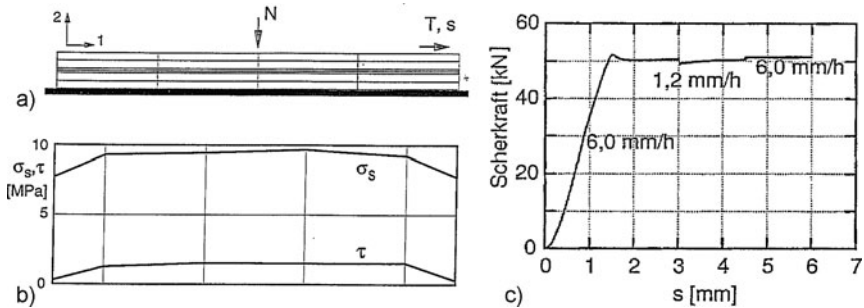


Fig. 3.8.5. Simulation of thin layer shearing with v-hyp (Librerios-Bertini 2006): mesh (a), stress distribution (b), shear force vs. displacement (c)

After compression and shearing the calculated σ' and τ are uniform over the major part of the thin layer (b), and excess pore pressures are negligible. The calculated shearing resistance for different v_s (c) comes close to the observed one (cf. Fig. 3.8.4b). This confirms the state limit concept with a pressure- and rate-independent φ_{cs} by (3.8.4) up to high p_s . Argotropy matters after each change of shearing velocity v_s , which causes dilation or contraction until the new e_c for the higher or lower D as by Fig. 3.2.1b is attained. Even with the high σ' and the soft particles the material is permanent, at least as far as parameters for argotropic state limits are concerned.

Apparently lower residual friction angles were observed with the same clay and almost the same range of σ' by Goldscheider and Böisinger (1989). This reduction of shearing resistance can be explained by means of excess pore pressures in narrow shear bands which cannot be detected at the sample boundaries (Sect. 8.3). Softening beyond a peak may also be attributed to the dilation of bound pore water (Sect. 6.3) which is more pronounced with more plastic and less porous clays, it occurs even without decompression be-

fore shearing. The lower than critical residual shearing resistance observed by Hvorslev (1937), Skempton (1985) and others is thus not a property of the skeleton of solid particles only.

Similarly as with sands (Sect. 2.9) attempts were made to produce uniform shearing in the sense of an RSE, but less often. Airey and Wood (1987) sheared initially cylindrical kaolin samples after consolidation in a *confined cylindrical device* with wire rings as by Fig. 2.10.3. The vertical stress measured by five pressure sensors (load cells) in the top plate was not uniform and indicated that only an inner third of the sample may be considered as RSE. The friction condition (3.8.4) was confirmed, but $\tan \varphi_{cs}$ was about 10% higher than in a device with two frames sheared against each other. In spite of friction at the confirming rings void ratios after consolidation were markedly lower than in an oedometer. The radial stresses determined via elastic strains of the rings were realistic for consolidation, but so imprecise for shearing that inclinations of principal stress could not be determined.

Hong and Lade (1989) report on torsion tests with *thick-walled cylindrical* remoulded kaolin samples without or with drainage in a device as by Fig. 2.9.10. After compression with negligible horizontal strains the deviatoric stress components $\tau_{z\theta}$ and $\sigma_z - \sigma_\theta$ for $\sigma_z = 98 \text{ kPa}$ were changed, whereas the other components were kept constant. The attained state limits (Fig. 3.8.6) can be captured by Lade's (1977) limit stress condition

$$(I_\sigma^3 / III_\sigma - 27)(I_\sigma / p_a)^m = \eta_1 \tag{3.8.6}$$

with the invariants $I_\sigma = 3p'$ and

$$III_\sigma = \sigma'_1 \sigma'_2 \sigma'_3 = \sigma'_2 \sigma'_3 \sigma'_\theta - \sigma'_r \tau_{z\theta}^2 \quad . \tag{3.8.7}$$

With the atmospheric pressure $p_a = 98 \text{ kPa}$ the constants in (3.8.6) are $m = 0.42$ and $\eta_1 = 27.1$ for the given clay. In a 3-dimensional stress space

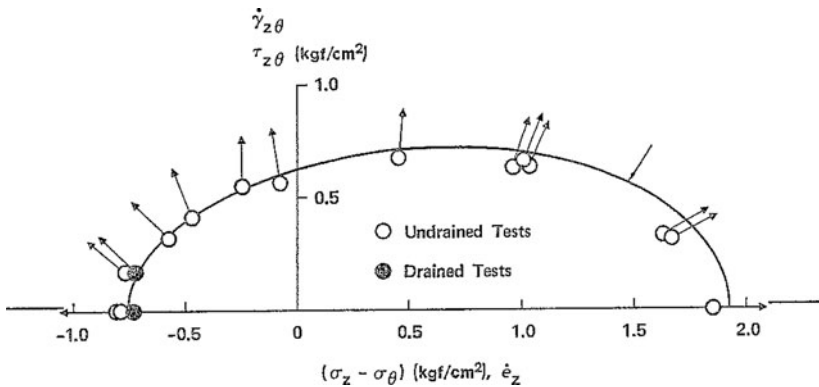


Fig. 3.8.6. Torsional resistance of thick-walled clay cylinders (Hong and Lade 1989): stresses and strain rate directions at peak

(3.8.6) is represented by a cone, its projection appears in the plane $\tau_{z\theta}$ vs. $\sigma'_z - \sigma'_\theta$. Strain rate directions are shown in the same plot.

Using data from triaxial tests by Hong and Lade (1989) with the same clay, Fig. 3.8.6 could be reproduced with v-hyp. For critical states stresses are on a cone with a near-elliptical cross section. The observed coaxiality of principal stress and strain rate means

$$\begin{aligned} \text{(a)} \quad & \tan(2\chi_\sigma) = \tan(2\chi_{\dot{\epsilon}}), \quad \text{i.e.} \\ \text{(b)} \quad & 2\tau_{z\theta}/(\sigma_z - \sigma_\theta) = 2\dot{\gamma}_{z\theta}/\dot{\epsilon}_z \end{aligned} \tag{3.8.8}$$

with the direction angles χ_σ and $\chi_{\dot{\epsilon}}$ of principal stress and strain rate, and $\dot{\epsilon}_\theta = 0$. With lower or higher than critical void ratios the cone is inside or

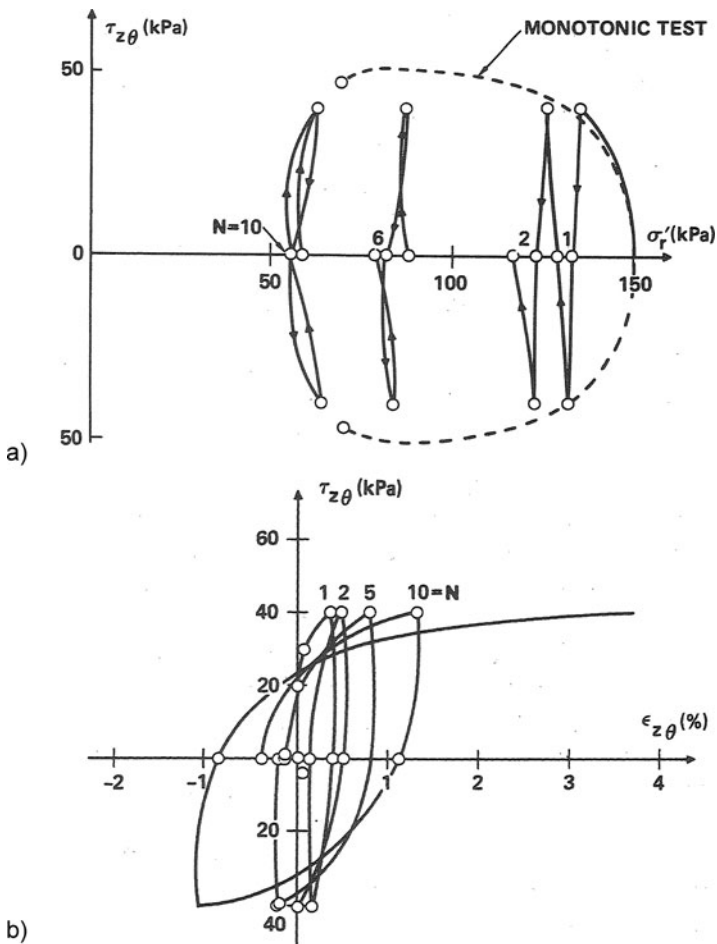


Fig. 3.8.7. Response of thick-walled clay cylinders to torsion with reversals (Hicher and Lade 1987): stress path (a) and stress-strain plot (b) with alternating torque

outside the critical one, but (3.8.8) holds again. This is confirmed by the torsion tests, minor deviations are probably due to bifurcation and argotropy which was not allowed for by Hong and Lade (1989). Lade's condition (3.8.6) does not explicitly allow for the void ratio, but this influences his m and η_1 . Coaxiality by (3.8.8) is obtained for state limits by frame-indifference (Sects. 2.11 and 3.9). A more detailed validation with respect to void ratios is not possible with the test results, these are apparently close to critical states.

There are very few publications on shear tests *with reversals* which are apt for validation as it is difficult to satisfy the criteria at the beginning of Sect. 2.5. Hicher and Lade (1987) imposed cyclic torsion to hollow cylindrical samples of the same clay and with the same apparatus as Hong and Lade (1989). After uniaxial consolidation the drainage was closed, vertical and radial stresses were kept constant, the shearing rate was nearly constant between the reversals. In all tests the mean skeleton pressure was reduced and got almost stationary after 10–15 load cycles. With an alternating torque the effective stress path tends to a double loop (butterfly, Fig. 3.8.7a), while the

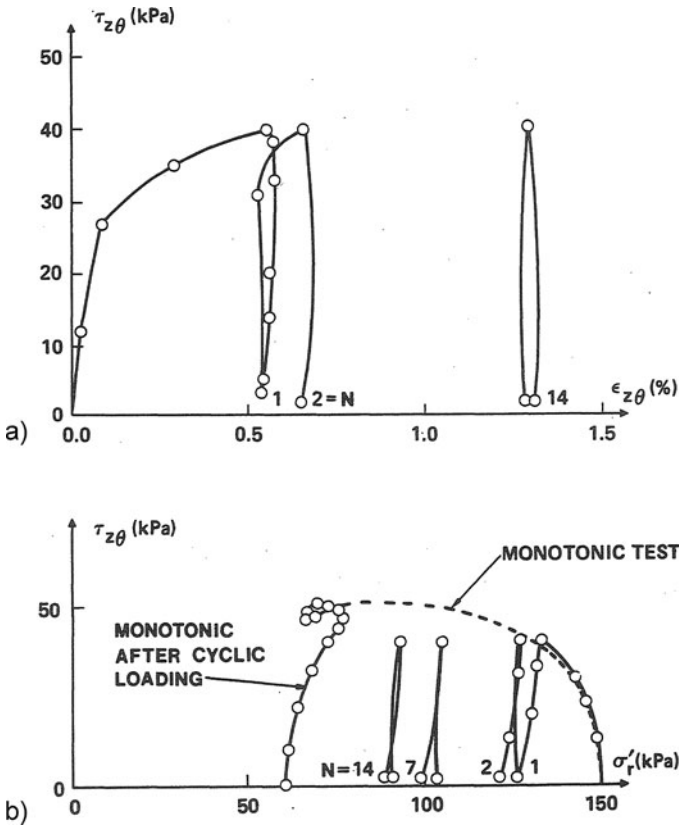


Fig. 3.8.8. Response of thick-walled clay cylinders to torsion with reversals (Hicher and Lade 1987): stress path (a) and stress-strain plot (b) with pulsating torque

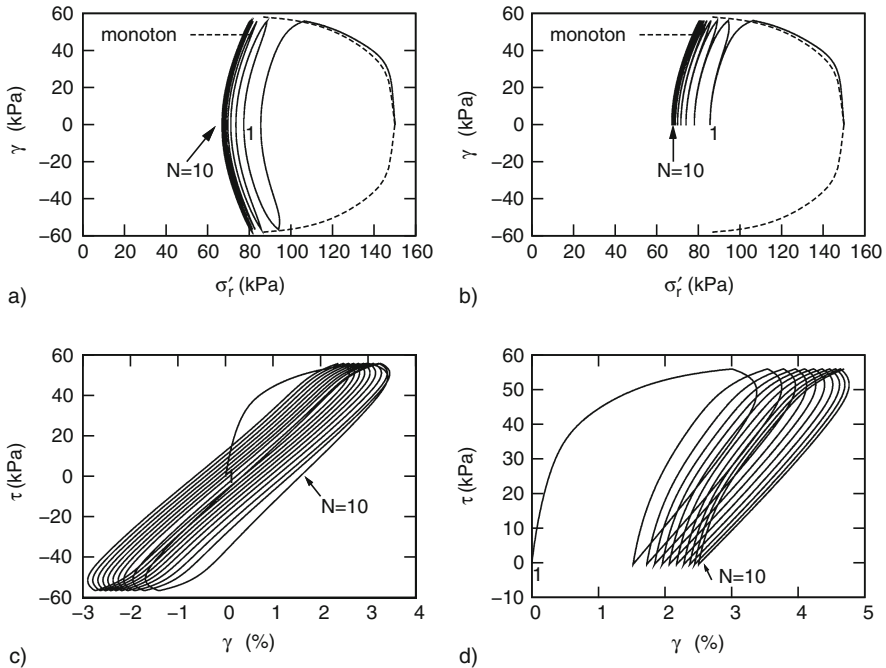


Fig. 3.8.9. Simulation of undrained torsional shear tests as shown in Figs. 3.8.7 and 3.8.8 with v-hyp by Grandas-Tavera (2010): stress paths for alternating (a) and pulsating torque (b), related stress-strain curves (c, d)

plot of shear stress vs. strain exhibits increasing hysteresis (b). With a pulsating torque the stress path tends to a lenticular cycle (Fig. 3.8.8a), and the stress-strain plot indicates ratcheting (b). Both attractors are psammoid-like for the given nearly constant amount of stretching. The stress paths would be different by relaxation with waiting intervals at reversals, cf. Fig. 3.7.3.

Simulations with v-hyp by Grandas-Tavera (2010) are shown in Fig. 3.8.9. An acceptable agreement with the plots by Hicher and Lade (1987) is only obtained up to the second reversal, this can hardly be improved by taking into account the relaxation at the first reversal. The further cyclic deviatoric loading does not lead to the observed butterfly or lenticular attractor, respectively, but to arc-like asymptotic stress cycles. The simulated hysteresis and ratcheting curves have other shapes than the observed ones. These deviations remain with relaxation by pauses at reversals, so there is no convincing validation of v-hyp with several reversals. It is questionable whether an improvement could be achieved with the modified v-hyp by Gudehus (2004b). The deviations are even stronger with v-elp as this would produce an elastic response after the first reversal. A hybrid of v-elp and v-hyp would not do better, it appears that the concept with a viscosity factor (Sect. 3.2) gets insufficient for several

reversals. A better agreement can only be expected with reversals if state limits are repeatedly approached so that the consolidation ratio p_e/p_s does not exceed ca. 1.5.

Experimental reports on shear creep and relaxation after simple shearing are not available with saturated clay. The ductility for undrained shearing can be impaired by localized dilation or by the transition to a skeleton collapse. Both is not captured by v-elp and v-hyp, nor can these models cover the localized dilation for drained shearing (cf. Sect. 8.3).

To *sum up*, the concept of argotropic state limits and state cycles is confirmed by the few acceptable reports on shear tests. In particular, the critical friction angle is pressure- and rate-independent, and limit principal stresses are coaxial with stretching rates. Only tests with hollow cylindrical samples can produce sufficient uniformity up to a peak. Void ratios at state limits were rarely reported, so their influence is not well confirmed. As outlined already in Sects. 3.3, 3.4, 3.5, the conventional concept of shear strength with φ' , c' and OCR is not physically justified and can be misleading. With repeated shear reversals anelastic effects are missed by v-elp and v-hyp if the consolidation ratio p_e/p_s exceeds ca. 1.5.

3.9 General and outlook

The general outline of peloid behaviour may be kept rather short as a lot can be taken over from psammoids (Sect. 2.11). We will see how the peculiarities of peloids due to skeleton viscosity and pore water diffusion can be characterized for arbitrary deformations in an objective way. It is not known how far the response with reversals can be captured without hidden state variables. Simple peloid models are also restricted by localizations in the range of overcritical stress obliquities, and near upper and lower bound void ratios.

A tetrahedron as in Fig. 2.11.1 may be taken as a general RSE of a simple peloid. The principle of effective stress can be formulated with (2.11.1) and (2.11.2). The state can again be represented (cf. Fig. 2.11.2) in plots of void ratio e and of stress obliquity $\tan \psi_s$ vs. Lode parameter $\cos 3\alpha_s$. The argotropy of state limits is captured by referring p_s to a D -dependent solid hardness h_s by (3.2.2) with $D = \sqrt{\mathbf{D}^2}$. The viscosity index I_v holds for a suitable reference rate D_r within D -bounds as for solids. Less objectively h_s can be substituted by an argotropic reference pressure p_r by (3.3.5). Too low and too high p_s have to be excluded because of net pressures (Sect. 6.3) and degradation (Sect. 7.3), respectively. Shear localization with overcritical $\tan \psi_s$ (Sect. 8.3) is left aside with simple peloids, and also cracking with extremely high $\tan \psi_s$ (Sects. 8.3 and 8.4).

The constitutive relation of the co-rotated skeleton stress rate $\overset{\circ}{\mathbf{T}}_s$ with the stretching tensor \mathbf{D} may again be expressed by (2.11.7), but the properties of the function \mathbf{F}_s of \mathbf{T}_s , e and \mathbf{D} are different. The barotropy by (2.11.8a) holds

only for constant D , and the exponent m for the influence of p_s is higher than for psammoids. The barotropy exponent $m = 1$ was often assumed for v-elp and v-hyp, this may suffice for an empirical range of p_s . Generalizing (3.2.1b) and (2.11.8b) can be replaced by

$$\mathbf{F}_s(\mathbf{T}_s, \lambda \mathbf{D}, e) = \lambda^n \mathbf{F}_s(\mathbf{T}_s, \mathbf{D}, e), \lambda > 0 \quad (3.9.1)$$

with $n > 1$ for argotropy. The argotropy exponent n is not constant, $n \approx 1 + I_v$ may serve as approximation. \mathbf{F}_s is generally non-linear in \mathbf{D} as by (2.11.8c), but can be nearly linear (hypoelastic) after over-consolidation or for fast stretching.

\mathbf{F}_s can be represented rather generally by

$$\mathbf{F}_s = \mathcal{L}(\mathbf{D} - \mathbf{D}^a) \quad (3.9.2)$$

with a fourth-order elastic stiffness tensor \mathcal{L} and an anelastic stretching

$$\mathbf{D}^a = H f_e f_v \mathbf{P} D_r \quad (3.9.3)$$

Its direction \mathbf{P} with $\|\mathbf{P}\| = 1$ depends only on the direction $\hat{\mathbf{T}}_s$ of the skeleton stress tensor. \mathcal{L} depends on \mathbf{T}_s , e and \mathbf{D} , thus the hypoelastic response for $\mathbf{D}^a = 0$ is baro-, pykno- and argotropic. Due to the barotropy outlined above \mathcal{L} is proportional to $(p_s/h_s)^m$ with $0 < m \leq 1$.

The viscosity factor f_v in (3.9.3) depends on the consolidation ratio p_e/p_s by (3.2.5). Therein the equivalent pressure p_e is determined by e and $\tan \psi_s$ for $D = D_r$ as indicated in Fig. 3.2.1. $\cos 3\alpha_s$ enters via $\tan \psi_s$ for state limits so that it is not needed explicitly for p_e . The factor f_e depends on e and p_s so that for an isotropic compression with $D = D_r$ (3.9.2) and (3.9.3) yield the limit void ratio $e_i(p_s)$. More in detail there are differences of visco-elastoplastic and -hypoplastic relations (v-elp and v-hyp).

For v-elp by Adachi and Oka (1982) limit void ratios depend on p_s by Terzaghi's (1925) (2.3.1) with p_r by (3.3.5) and $e_r(\tan \psi_s)$ as indicated by Fig. 3.3.1a. Therein the influence of $\cos 3\alpha_s$ on $\tan \psi_s$ is neglected for state limits so that the deviatoric boundary by Fig. 2.7.2a is a circle. Thus φ_c by (2.2.15) is bigger for $\cos 3\alpha_s = -1$ than for $\cos 3\alpha_s = 1$. State limits with $e = \text{const}$ are expressed by a quadratic form of p_s and $\tan \psi_s$ and are taken as elastic range. This is assumed as potential for \mathbf{P} (normality condition) and determines the switch function H in (3.9.3): $H = 0$ holds in the elastic range and for unloading, $H = 1$ for continued plastification. $\tan \psi_s$ is bounded by a tension cut-off, and there is no lower bound void ratio e_d .

Limit void ratios for Niemunis' (1992, 2003) v-hyp depend on p_s by Butterfield's (1979) compression law (3.1.13). Therein p_r depends on D by (3.3.5), and e_r on $\tan \psi_s$ as indicated by Fig. 3.3.1a. $\cos 3\alpha_s$ is implied by Nakai and Matsuoka's (1983) limit stress condition (3.7.1). Thus p_e is determined from e and $\tan \psi_s$ for $D = D_r$, and p_e/p_r determines f_v by (3.2.5). \mathcal{L} and $\mathbf{P} = \mathcal{L}^{-1} \mathbf{N}$

depend on $\hat{\mathbf{T}}_s$ as in (2.11.8) for hyp. The factor $H = 1$ can be dropped in (3.9.3), nevertheless hypoelastic behaviour is obtained for $p_e/p_s > \text{ca. } 2$ and thus $f_v \ll D/D_r$. There is no lower e -bound, and too high $\tan \psi_s$ should be avoided as they would lead to tensile stress.

These viscoplastic relations could be represented by 3-dimensional response diagrams (cf. Fig. 2.11.3). Normalized stretching with $D=\text{const}$ and different directions $\hat{\mathbf{D}}$ appears as spheres, but with $\log(D/D_r)$ -labels as in Fig. 3.2.3a plus principal directions referred to the ones of stress. Stress rate components appear as polars for three components plus direction angles relative to those of principal stress, now with $\log(D/D_r)$ -labels for argotropy. Such diagrams can help to understand the approach to attractors, i.e. asymptotic solutions of (3.9.2) with (3.9.3) for different conditions of stretching, stress and void ratio. Suitable attractors with rather arbitrary deformations exhibit the behaviour of simple peloids in an objective way.

State limits by v-elp and v-hyp are attained with $\mathbf{D}=\text{const}$ and can be contractant ($\text{tr}\mathbf{D} < 0$), isochoric ($\text{tr}\mathbf{D} = 0$) or dilatant ($\text{tr}\mathbf{D} > 0$). In the approach to them p_s/p_e tends to $(D/D_r)^{I_v}$, thus f_v tends to D/D_r . The skeleton stress gets stationary (critical) for $\text{tr}\mathbf{D} = 0$, and the direction of stress rate and stress tend to coincide with $p_s > 0$ for $\text{tr}\mathbf{D} < 0$, and with $\dot{p}_s < 0$ for $\text{tr}\mathbf{D} > 0$. At state limits \mathbf{T}_s is determined by \mathbf{D} and e , thus \mathbf{T}_s and \mathbf{D} are coaxial due to frame-indifference. The dependence can be expressed by relations of $\tan \psi_s$ with $\text{tr}\mathbf{D}/D$, of $\cos 3\alpha_s$ with $\cos 3\alpha_D$ (by (2.11.15) with $\text{tr}\mathbf{D}/D$ instead of \mathbf{T}_s^*), and of e with p_s with $\tan \psi_s$. Too high dilatancy ratios $\text{tr}\mathbf{D}/D$ have to be left aside as they would lead to tensile stress.

Creep is attained with $\overset{\circ}{\mathbf{T}}_s = 0$, then (3.9.2) means $\mathbf{D}^a = \mathbf{D}$. With (3.9.2) the direction of stretching $\hat{\mathbf{D}}$ is thus determined by the one of stress $\hat{\mathbf{T}}_s$ via $\mathbf{P}(\hat{\mathbf{T}}_s)$. As the factor f_e has the order of magnitude 1 the intensity of creep is

$$D = D^a \approx f_v D_r = \left(\frac{p_s}{p_e} \right)^{1/I_v} D_r \quad . \quad (3.9.4)$$

As I_v ranges from ca. 0.02 to 0.05 D changes drastically with changes of p_e . D dwindles for subcritical stress obliquities ($\tan \psi_s < \tan \psi_{sc}$), gets stationary for critical $\tan \psi_s$ and diverges for overcritical ones. Depending on the evolution prior to a constant \mathbf{T}_s the initial creep rate goes over into the one by $\overset{\circ}{\mathbf{T}}_s = 0$.

With the low permeability of peloids a rapid creep is nearly isochoric, particularly in case of a constant deviator \mathbf{T}_s^* by (2.11.3). Its amount D is again given by (3.9.4), but p_s is reduced via

$$\dot{p}_s/p_s \approx - \left(\frac{p_s}{p_e} \right)^{1/I_v} D_r \quad . \quad (3.9.5)$$

With constant \mathbf{T}_s^* and e the equivalent pressure p_e is more reduced than p_s as $\tan \psi_s$ increases, thus the intensity of creep increases via (3.9.4). In case

of *relaxation* with $\mathbf{D} = 0$ the pressure p_s is also reduced by (3.9.5), and the stress obliquity $\tan \psi_s$ gets smaller simultaneously.

More generally and less precisely speaking, the intensities of creep and relaxation depend on the consolidation ratio p_e/p_s by (3.9.4) and (3.9.5). Creep tends to a succession of state limits so that the directional invariants $\text{tr} \mathbf{D}/D$, $\cos 3\alpha_D$, $\tan \psi_s$ and $\cos 3\alpha_s$ are related. Relaxation means a reduction of \dot{p}_s by (3.9.5), and a more rapid reduction of $\tan \psi_s$ the bigger $\tan \psi_s$ still is. Contractant creep and relaxation get extremely slow by v-elp and v-hyp, but cannot attain an equilibrium. Estimates of rates by (3.9.4) and (3.9.5) are crude as p_e depends sensitively on the instantaneous e and $\tan \psi_s$ as p_s can be rather indeterminate and as p_e/p_s enters with the power $-1/I_v$.

Response to *sudden changes of stretching* \mathbf{D} can be judged by its intensity D and direction $\hat{\mathbf{D}} = \mathbf{D}/D$, and depend on the instantaneous state \mathbf{T}_s and e as for any \mathbf{D} . If an RSE is first near a state limit, with $p_s/p_s \approx (D/D_r)^{I_v}$ and thus $f_v \approx D/D_r$ by definition, a drastic rise of D causes a nearly hypoelastic response as then D exceeds D_r by far. In monotonous continuations with the new D the response gets viscoplastic as f_v tends to the new D/D_r . With the same previous state a drastic reduction of D causes first a relaxation, in a continuation with the lower D the response gets viscoplastic. With high enough consolidation ratios, say $p_e/p_s > 2$, f_v is so small that the response by (3.9.2) is nearly hypoelastic as long as D is not reduced by several decades. Differences of v-elp and v-hyp arise with directional changes of \mathbf{D} in the vicinity of argotropic state limits. Then the response is hypoelastic by v-elp within an assumed elastic range and if the stress tends towards this range, and rather hypoplastic by v-hyp.

Cam clay models are elastoplastic without rate-dependence as by (2.11.8) in general. They can be justified by the viscoplastic relations (3.9.2) and (3.9.3) if D/D_r does not change drastically for continued anelastic deformations, and if D/D_r is much higher for un- and reloading. As outlined further above f_v is close to D/D_r for a continuation of state limits, and $D^a \ll D$ holds after a drastic increase of D . Argotropy, creep and relaxation are not captured by Cam clay models, they are often ignored in the evaluation of experiments with such models.

Differences and limitations of v-elp and v-hyp are revealed by *state cycles* and transitions to these attractors by repeated reversals. We restrict ourselves to isochoric evolutions with constant D as then the diffusion of pore water may be neglected, and as changes of D are not given in the few test reports with many reversals.

Isochoric *strain cycles* of our general RSE can be referred to the initial or co-rotated principal directions of \mathbf{T}_s for objectivity as proposed in Sect. 2.11. v-elp yields a shakedown to hypoelastic behaviour with small amplitudes and to a succession of state limits and hypoelastic response with bigger amplitudes. The mean pressure p_s does not change after the transition before the first reversal. More realistically v-hyp leads to a gradual reduction of p_s and $\tan \psi_s$, though with minute rate for low p_s/p_e , and to state cycles with two p_s -cycles

for one strain cycle. The gradual reduction of p_s and $\tan \psi_s$ is exaggerated by v-hyp, but not as much as by hyp in case of moderate amplitudes.

Isochoric *ratcheting* means cyclic plus monotonous isochoric deformation with constant rate D . An updating of reference configurations is needed in general as for psammoids. Ratcheting leads to stress cycles in convected RSEs asymptotically both by v-elp and v-hyp. An argotropic state limit is attained by the forward steps. With v-elp the asymptotic cycles have constant p_s , whereas with v-hyp p_s makes a cycle alongside with two stretching reversals which seems to be more realistic. In the transition to a state cycle p_s changes by v-elp only up to the first reversal, and gradually with further reversals by v-hyp. The latter is more realistic, but observations with clays do not suffice for a more precise validation.

By definition the state of a simple peloid RSE is sufficiently characterized for its mechanical response by stress \mathbf{T}_s and void ratio e . Even without net attraction and cementation this cannot generally suffice, in particular with repeated reversals and with shear localization or cracking. As with psammoids one may imagine states of *swept-out memory* (SOM) which are attained by monotonous deformations (Gudehus et al. 1977), now with constant rate D because of argotropy, so that hidden variables are determined by \mathbf{T}_s and e and are thus not needed explicitly. Argotropic SOM-states are not state limits in general as for these e is determined by \mathbf{T}_s and D , but state limits are special SOM-states. As indicated further above viscoplastic effects with many reversals are missed by v-elp and exaggerated by v-hyp. The few experimental reports do not suffice to quantify how far SOM-states are justified for such evolutions. It will be shown in Chap. 6 that SOM-states cannot suffice in general, but are of use as attractors for hidden variables. These do not suffice with overcritical stress obliquities, then polar stresses are needed for localizations (Sect. 8.3).

Modifications of v-elp and v-hyp are available or at least feasible for arbitrary deformations. The reference pressure p_r can be replaced by an objective hardness h_r , its argotropy can be captured by (3.2.2a) which works for a wider range of D/D_r than (3.2.2b). The pressure dependence of limit void ratios can be expressed by Bauer's (1996) formula (2.4.1) with an argotropic h_s . This works for a wider p_s -range than (2.3.1) and (3.3.13), and yields skeleton decay with overcritical void ratios for low p_s and isochoric stretching. A lower bound void ratio e_d could be related with extreme state limits for which one or two skeleton stress components vanish. This could be achieved approximately by relating the prefactor e_o in (2.4.1) with the stress obliquity $\tan \psi_s$ (Gudehus 2004). Therein the triangle in the deviator plane for vanishing stress with $p_s = \text{const} > 0$ (Fig. 2.7.1b) could be replaced by Nakai and Matsuoka's (1983) relation (3.7.1) with a suitable constant.

Other than introduced in Sects. 3.3 and 3.4 the argotropic stiffness tensor \mathcal{L} can depend on p_s , e and \mathbf{D} and on the stress direction $\hat{\mathbf{T}}_s = \mathbf{T}_s/p_s$. The exponent m for barotropy with constant D as by (2.11.8a) can be smaller than 1, as was assumed by Adachi and Oka (1982) for v-elp and by Niemunis

(1992, 2003) for v-hyp. This barotropy should agree with the one of limit void ratios for a sufficiently wide p_s -range, which can be achieved by (2.4.1). As \mathcal{L} yields a hypoelastic response for isotachic deformations with negligible anelastic part, i.e. $D = \text{const} \gg D^a$, it should be derived from a \mathbf{T}_s -dependent elastic energy (Niemunis and Cudny, 1998). Otherwise stretching cycles with $D = \text{const} \gg D^a$ could produce inconsistent gradual changes of \mathbf{T}_s . The direction \mathbf{P} of the anelastic stretching \mathbf{D}^a by (3.9.3) could depend on the stress direction $\hat{\mathbf{T}}_s$ in an other way than proposed by v-elp and v-hyp.

Modifications will be more important in the vicinity of argotropic state limits. Then the viscosity factor f_v by (3.2.5) plays the dominant role, therefore the equivalent pressure p_e has to be defined carefully. The elastic range of v-elp for $f_v = D/D_r$ and constant e and D is shaped by \mathcal{L} and \mathbf{P} . Instead of the Cam clay shape employed by Adachi and Oka (1982) the boundary may be bullet-like near $p_s = 0$ in the space of principal stress components (Fig. 2.7.5), so that a tension cut-off is not needed. Cuts of this boundary with $p_s = \text{const}$ can exhibit a dependence of $\tan \psi_s$ on $\cos 3\alpha_s$ so that φ_c by (2.2.15) agrees for $\cos 3\alpha_s = -1$ and $+1$, e.g. by (3.7.1). The switch function H for v-elp may be dropped as the observed response with reversals and $D = \text{const}$ is not hypoelastic near argotropic state limits. The general viscoplastic relation (3.9.2) produces hypoelastic behaviour already with $f_v \ll D/D_r$ by $p_e/p_s > \text{ca. } 1.5\text{--}2$, and also with a drastic increase of D .

The *range of applicability* could be widened and properly bounded by modifications of v-elp and v-hyp. This was indicated already further above for the p_s -dependence of limit void ratios, whereas the exclusion of net attraction and of collective particle degradation belongs to simple peloids by definition. The argotropic solid hardness h_s by (3.2.2) may be used within the bounds by (3.4.9), these could be specified more precisely. The dependence of the viscosity index I_v on the choice of the reference rate D_r could be captured as for solids by (3.1.9). Such an objective relation requires an oscillation frequency and nano-micro factors for stress and stretching which cannot easily be quantified. The relation of overcritical stress obliquities $\tan \psi_s$ with reference void ratios by (2.3.1), (2.4.1), or (3.1.13) could be improved if more data on peak states were available, although shear localizations cannot be captured with v-elp or v-hyp (Sect. 8.3). Extreme state limits with $e = e_d$ could be related with splitting or cracking, this implies the cavitation of pore water (Sect. 6.3).

Objective and economic procedures are needed to *determine the parameters* of simple peloids. Thin layer shear tests with drainage via filter plates (Balthasar et al. 2006) can supply the critical friction angle φ_{cs} , this can be transformed into φ_c by (2.9.12). Undrained triaxial tests with axial shortening $D_{11} = -D_r$ and low initial p_e/p_s can provide e_c for different p_s , short samples between smooth plates can remain uniform (Sect. 14.1). Jumps of D with the same device and sample exhibit the argotropy, I_v can be determined from changes of the stress deviator via (3.3.11). Parameters for the barotropy of limit void ratios are best determined by compression of mud with $D_{22} = 0$ in an oedometer, the argotropy and the diffusion of pore water have to be taken

into account. Parameters for dilatant state limits can be estimated from peak states in triaxial tests which prevent marked shear localizations (Sect. 14.1). Isotropic compression tests to find e_i are expensive and extreme state limits with e_d cannot be attained, but e_i/e_c and e_d/e_c may be guessed empirically as for psammoids. The parameter κ for unloading by v-elp, or its counterpart by v-hyp, can be determined from decompression tests, but argotropy and diffusion should be taken into account.

Conventional *limit water contents* w can help to estimate limit void ratios, Fig. 3.9.1. With full saturation e depends on w via $e = w\gamma_s/\gamma_w$. The pore water should have the same ionic strength as in the intended application which should imply a negligible net attraction (Sects. 6.3 and 7.1). Amounts of stretching D should be estimated so that the argotropy can be allowed for. The shrinkage limit w_s arises by capillary entry after an isotropic compression with constant D (Sect. 11.1). The related p_s can be estimated from the undrained cohesion c_u via (3.3.10). The liquid limit w_L belongs to an isochoric state limit with $c_u \approx 2$ kPa, w_L can also be determined with a shear vane and may be used to estimate p_s (Sect. 14.6). The plasticity limit w_P implies a capillary entry by splitting with $e \approx e_d$ (Sect. 6.3), the related p_s can again be estimated via c_u with the same D . More *plastic clays* have a higher w_P .

More than with psammoids conventional notions of *stiffness and strength* are hardly apt to characterize simple peloids in general. The stiffness modulus $E_s = \dot{T}_{s1}/D_1$ for uniaxial deformations ($D_1 \neq 0, D_2 = D_3 = 0$) varies with \mathbf{T}_s , e and D_1 so that a single E_s is not relevant. A Poisson ratio ν as by (3.3.1) is rather arbitrary, it cannot be determined via the velocities of shear and compression waves as the latter are confined by the pore water. The undrained cohesion c_u depends on e and D by (3.3.10) for monotonous isochoric deformation, but also on the stretching invariant $\cos 3\alpha_D$. It may at best be used for the evaluation of shearing or penetration resistances in situ (Sects. 14.3 and 14.6), and for design estimates. If stationarity is related with

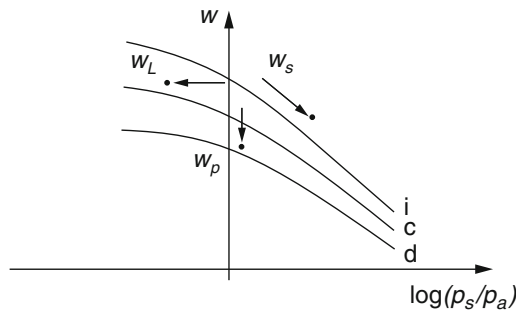


Fig. 3.9.1. Conventional limit water contents and argotropic limit values; the latter for $D = D_r$, the former for higher stretching rates and pressures p_s

c_u this may be called ductility, this is not always given as was outlined in Sect. 3.5.

Except for skeleton decay the shearing resistance tends to $p_s \tan \varphi_{cs}$ as for psammoids (Sect. 2.9), but $p_s = p - p_w$ can hardly be estimated via total and pore water pressures p and p_w as both are unknown in general. The assumption of free drainage with given p_w may at best be justified along pervious boundaries of peloid bodies. Even then the often assumed shearing resistance $\tau_f = c' + \sigma' \tan \varphi'$ cannot be defended as the shear strength parameters c' and φ' are subjective (Sects. 3.5 and 3.8), and as σ' can hardly be estimated. The frequently proposed degradation of strength by cyclic loading via increasing p_w is also dubious: the solid particles do not feel changes of p_w so that only the gradual reduction of p_s counts, this is not the same for cyclic deformations and ratcheting, and the latter has little in common with monotonous shearing up to a maximal resistance. In other words, the so-called cyclic mobility cannot be specified in an objective way by a reduction of strength.

As with psammoids viscoplastic relations like v-elp and v-hyp cannot be *validated* by RSE-tests in general, but only by special element tests and via suitable boundary value problems. Element tests as outlined in Sects. 3.5 to 3.8 are necessary for confirmation or refutation, but more general deformations cannot be produced with the uniformity required for RSEs. Initial and boundary conditions can be realized in certain model tests so that their back-analysis reveals the range of validity. This will be shown with v-elp by examples in Chaps. 11, 12, 13 and 14. Hydraulic conditions have also to be considered.

To *sum up*, viscoplastic models can capture the behaviour of clayey soils in an objective way for a wide range which can be explored and extended. Viscoelastoplastic and hypoplastic relations (v-elp and v-hyp) can be formulated with frame-indifferent tensors so that they work for arbitrary deformations. Argotropic state limits can be represented by means of invariants and serve to determine the main constitutive parameters. Rate-dependence, creep and relaxation are dominated by the consolidation ratio p_e/p_s , therein the equivalent pressure p_e cannot easily be determined. Hypoelastic behaviour is obtained with $p_e/p_s > \text{ca. } 2$ and just after a dramatic rise of stretching. The assumption of elastic ranges and switch functions for v-elp and Cam clay models is thus supported in a rather subjective manner. Anelastic effects with cyclic stretching and ratcheting are underestimated by v-elp and overestimated by v-hyp. The range of application of v-elp and v-hyp can be widened by modifications. Extreme stress obliquities and lower bound void ratios could be incorporated, but without shear localization and cracking. Conventional notions of stiffness and strength are rather subjective.

PSAMMOIDS WITH REVERSALS

It was shown at length in Chap. 2 that the behaviour of psammoids with reversals cannot generally be captured without internal state variables. But how to introduce and justify hidden quantities? Babuška and Oden (2006) show that the uniaxial anelastic response of metals with some hundred cycles is not satisfactorily captured by widely used elastoplastic relations with internal variables. It is not my intention to overcome this misery for solids in Sect. 4.1, but to prepare *more geometrico* a way out for soils. The hidden state can be related with the spatial fluctuation of internal forces, this is called *force-roughness*. This oriented quantity is particularly indicated by the asymptotic response to strain cycles and ratcheting (cf. Sect. 2.1). The proposed additional attractors of force-roughness are inevitably heuristic, but may help to secure objectivity.

Because of the partly hidden state the introduction of psammoids with reversals cannot be as straightforward as in Sect. 2.2. An ample discussion of experimental results shows how the invisible can be traced indirectly (Sect. 2.2). State variables for the force-roughness are then proposed by means of attractors (Sect. 2.3). This approach is rather heuristic, but photoelastic experiments and numerical simulations provide at least a qualitative support. The force-roughness can be related with erratic and variable force chains.

With this background elastoplastic relations with back stress ($elp-\alpha$) are introduced in Sect. 2.4. Algebraic representations will not be outlined in detail as they are intricate and preliminary. Instead it is shown with diagrams how attractors with reversals are approached in numerical simulations, and how far experimental results can be matched. The same is shown for hypoplastic relations with intergranular strain ($hyp-\delta$) in Sect. 2.5, they are likewise intricate and preliminary. The stress- or strain-like internal variables are interpreted as representations of force-roughness.

A closer inspection reveals seismically activated viscous effects during strong changes of stretching, particularly near reversals (Sect. 2.6). The often assumed rate-independence can at best be defended for hypoelastic and hypoplastic limits of granular solids, and for quasi-static evolutions with many

reversals. This can be explained by means of a granular temperature which arises during rearrangements. Heuristic models for cumulative anelastic effects should thus be substituted by a unified physical concept wherein attractors play a key role (Sect. 4.7).

4.1 A third prelude on solids

For preparing the subsequent sections we consider first evolutions of pore-free solid RSEs which are and remain uniform (in a statistical sense) by definition. As in Sect. 2.1 barotropy, argotropy, brittleness and fatigue are neglected, but it is no more assumed that the state is sufficiently defined by stress components only. Observations with path reversals indicate that additional internal state variables are needed. It is shown in the sequel how this can be achieved, first for uniaxial and then for cuboidal deformations, and both with elastoplasticity (elp) and hypoplasticity (hyp). Use is made of suitable attractors, and the outline is more graphical than algebraic.

For *uniaxial* cases some σ - ε -curves with reversals were shown already in Fig. 2.1.1. Observed lenticular hysteresis loops are not reproduced by elp and exaggerated by hyp. Ratcheting, i.e. cumulative anelastic deformation, is obtained with asymmetric stress cycles by elp only if the stress limit is attained repeatedly, and is exaggerated by hyp. These lacks cannot be overcome by combining elp and hyp (Fig. 4.1.1a). First loading in an elastic range (OA) can similarly be modelled by elp and hyp, but the diffuse observed elastic limits prohibit improvements. The transition to a state limit (AB) can better be captured by hyp than by elp. The response to a reversal (BC) can be captured by elp or hyp with a switch function of $\sigma\dot{\varepsilon}$, the difference of the differential stiffness $\dot{\sigma}/\dot{\varepsilon}$ by factor 2 (Sect. 2.1) could be removed by modifying hyp. A reloading (CD) eludes such an approach, however, as then $\dot{\sigma}/\dot{\varepsilon}$ is not only determined by σ and $\text{sgn}(\sigma\dot{\varepsilon})$. An additional state variable has to be employed, but how?

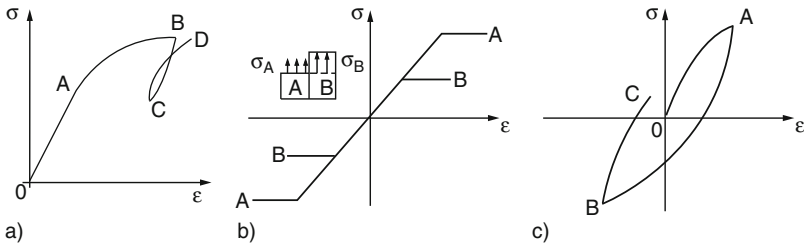


Fig. 4.1.1. Stress-strain curves with un- and reloading (a), with a composite model (b), and for alternating stress (c)

Masing (1926) proposed a bundle of elastoplastic rods with equal deformation to explain this behaviour. In the simplest version two components have the same cross section and modulus E , but different plastic limits (Fig. 4.1.1b, insert). Thus an *eigenstress* $\sigma_A - \sigma_B$ can occur with zero total or external stress $\sigma = \sigma_A + \sigma_B$ if one component was plastified, so that $\dot{\sigma}/\dot{\varepsilon}$ is different with a certain σ and $\text{sgn}(\sigma\dot{\varepsilon})$ for different $\sigma_A - \sigma_B$. This model can be formulated with a bundle of several rods to get rather smooth $\sigma - \varepsilon$ curves between reversals (Fig. 4.1.1c). Masing concluded that the branch of the $\sigma - \varepsilon$ curve after a second reversal (BC) equals the inverted branch after the first reversal (AB) as long as the composite does not attain a state limit with $\dot{\sigma}/\dot{\varepsilon} = 0$. In experiments with ductile brass he observed, however, bigger $\dot{\sigma}/\dot{\varepsilon}$ than by this rule after a second reversal, and concluded that the eigenstress is not a suitable hardening quantity.

A similar composite model was proposed by Iwan (1966), this is simplified in Fig. 4.1.2. Working with different distributions of component stresses σ_i and of plastic limits c_i with the same averages (a) one obtains always the same state limits with $\dot{\sigma}/\dot{\varepsilon} = 0$ for monotonous stretching (b). The transitions depend on c_i and the initial distribution of σ_i (the sketch is qualitative). This indeterminacy is overcome with the *asymptotic response to cyclic deformations* (c). Then the distribution σ_i gets independent of the initial one and tends to a periodic change. This depends only on the strain amplitude and the assumed distribution of c_i . The latter can be chosen so that observed hysteresis loops are reproduced.

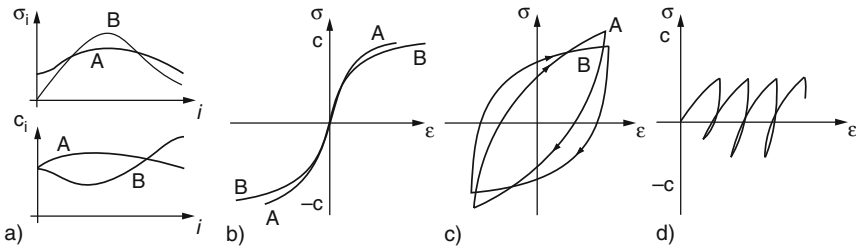


Fig. 4.1.2. Response with parallel elastoplastic rods: (a) distributions of internal stress and strength, (b) stresses for monotonous stretching and shortening, (c) asymptotic stress cycles for cyclic straining, (d) stress-strain plot for imposed ratcheting

Although not considered by Iwan (1966) one can also capture *ratcheting* with his model, Fig. 4.1.2d. Imposing monotonous plus cyclic strains asymmetric stress cycles are attained after a transition. These depend only on the amplitude and the step-wise increase of strain. The distribution of eigenstress $\sigma - \sigma_i$ gets also periodic and is asymmetric independently of the onset. The distribution of c_i can be adapted to match ratcheting test results.

We can thus identify three kinds of attractors for which an initial state is erased: state limits for monotonous stretching, symmetric stress cycles for cyclic straining and asymmetric ones for ratcheting. They characterize the mechanical behaviour in an objective manner (in uniaxial cases) and serve to confine internal variables and their parameters, e.g. σ_i and c_i in case of Fig. 4.1.2. Composites with distributions like c_i may be chosen so that the observed asymptotic response is reproduced, but this approach is cumbersome and could hardly be extended to multi-axial cases in an objective way.

Instead of inevitably arbitrary composites one can introduce a heuristic internal state variable, discuss it with physical arguments and adapt it to experimental findings. For uniaxial cases the spatial deviations from an even stress distribution may be captured by a quantity h . This *force-roughness* has an intensity $|h|$, say a standard deviation, and a sign so that plastifications are differently enhanced with a given $|h|$. We postulate that h gets maximal at state limits and is then determined by σ . With strain cycles h may tend to a symmetric cycle alongside with a symmetric σ -cycle, both should be smaller for smaller ε -amplitudes. With ratcheting h is assumed to tend to asymmetric cycles alongside with asymmetric σ -cycles. Such attractors of force-roughness h could be justified indirectly by matching test results. As h is a hidden variable it cannot be determined directly, simulations with composites can at best provide qualitative hints. We will see below how one-dimensional constitutive models with hidden variables could work and be judged by means of h .

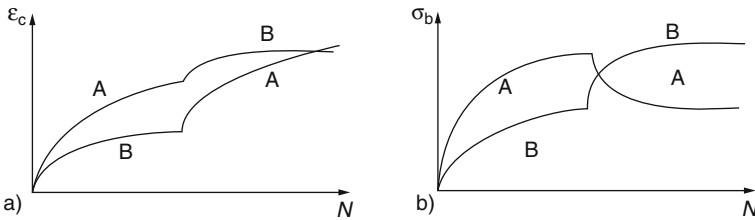


Fig. 4.1.3. Ratcheting with two different intensities in different orders: cumulative strain (a) and upper stress (b) vs. number of cycles

Symmetric stress cycles in an allowable range would lead to strain cycles after a shift of strain, and to symmetric cycles of the hidden state variable h . Asymmetric stress cycles would lead to an accumulation of anelastic strain and to asymmetric cycles of h . Such evolutions can be partly represented by a plot of cumulative strain ε_c vs. number of stress cycles N . This is shown in Fig. 4.1.3a for two sequences (AB and BA) of different stress cycles. When state cycles are attained ε accumulates by the same amount with each cycle. If the order of different stress cycles is interchanged the cumulative ε agrees for a suitable N . This empirical *Miner's rule* (1945) cannot work for quite different numbers of different stress cycles. Imposed ratcheting with exchanged

sequences of different intensity (AB and BA) can similarly lead to the same stress bound σ_b for a certain N (Fig. 4.1.3b), but not otherwise. Such equivalence rules are not apt to catch arbitrary transitions, whereas attractors can be objective.

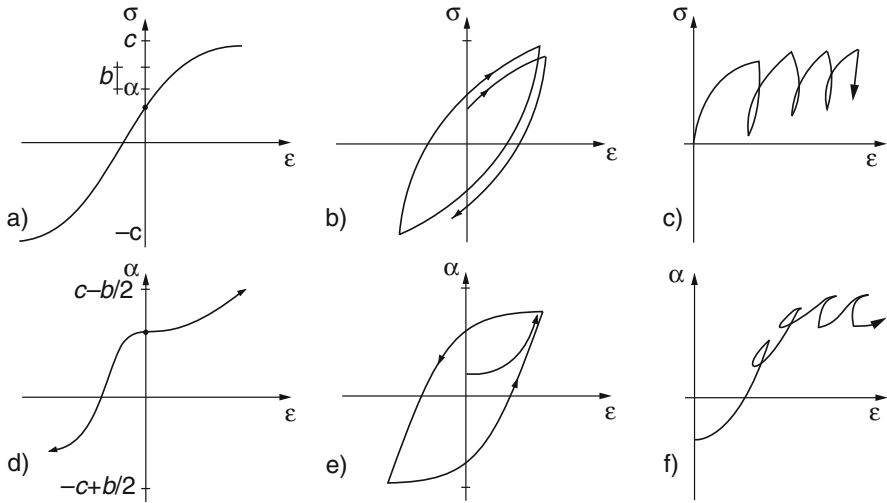


Fig. 4.1.4. Uniaxial elastoplastic response with back stress α : (a) $\sigma - \varepsilon$ curve with initial α , stress response to strain cycles (b) and to ratcheting (c), evolutions of back stress for monotonous (d) and cyclic deformation (e) and for ratcheting (f)

An elastoplastic model with a so-called *back stress* α (elp- α) is represented in Fig. 4.1.4 (simplified after Mróz 1967). The centre α of an elastic range with size $b < c$ is variable between $\pm(c - b/2)$. The behaviour is elastic ($\dot{\varepsilon} = \dot{\varepsilon}^e = \dot{\sigma}/E$) as long as σ is in this range. If the stress is at its boundary $\dot{\varepsilon} = \dot{\sigma}/E$ holds only for $\dot{\sigma}$ towards its interior. Otherwise a plastic strain rate $\dot{\varepsilon}^p$ occurs with the sign of $\dot{\sigma}$, and the elastic range is shifted via $\dot{\alpha} = \dot{\sigma}$. This *kinematic hardening* is bounded at state limits with $\dot{\alpha} = \dot{\sigma} = 0$ and $\sigma\dot{\varepsilon} > 0$ as then $\pm(\sigma - \alpha) = b/2$ holds. Monotonous stretching leads to one of these values of stress (a) and back stress (d) as both are independent of the initial values σ and α , these states are thus attractors.

Cyclic straining with amplitudes between b/E and $(c - b)/E$ leads to symmetric cycles of stress (b) and back stress (e) in the periodic asymptote. For a smaller amplitude than b/E the elastic range would not be left, for a bigger one than $(c - b)/E$ the hysteresis loops would have sections with constant σ and α . Ratcheting with not too big strain sections leads to asymmetric asymptotic cycles of stress (c) and back stress (f) with sections having $\dot{\sigma} = 0$ and $\dot{\alpha} = 0$. The parameter c can be determined from the asymptotic resistance to monotonous stretching, the additional one b can be adapted so that

observed asymptotic σ -cycles are matched. As the back stress α produces the cannot be interpreted as an eigenstress.

A *hypoplastic* model with a so-called *internal strain* δ (hyp- δ) is represented in Fig. 4.1.5 (simplified after Niemunis and Herle, 1997). δ evolves with ε by $\dot{\delta} = \dot{\varepsilon}$ for $\delta\dot{\varepsilon} \leq 0$ and by $\dot{\delta} = (1 - |\delta|/R)\dot{\varepsilon}$ for $\delta\dot{\varepsilon} > 0$ (a). This means that δ attains one of the bounds $\pm R$ for monotonous deformations, with $\dot{\delta} = 0$ for a continuation with $\delta\dot{\varepsilon} > 0$, and that δ changes like ε after a reversal with $\delta\dot{\varepsilon} \leq 0$. σ evolves elastically with ε by $\dot{\sigma} = E\dot{\varepsilon}$ for $\delta\dot{\varepsilon} \leq 0$ in case of $\delta = 0$, and follows the hypoplastic relation (2.1.2) for $\delta\dot{\varepsilon} > 0$ with $|\delta| = R$. An interpolation is employed between these cases for $|\delta| < R$. The approach to state limits by monotonous stretching is shown in the same plots, they are attractors as the initial values of σ and δ are erased.

Strain cycles lead to symmetric asymptotic cycles of internal strain (c) and of stress (d). Other than by elp- α the asymptotic amounts of σ/c and δ/R get arbitrarily small for smaller ε -amplitudes, but the transition to the attractor requires more cycles than by hyp. Ratcheting leads to asymmetric cycles of internal strain (e) and stress (f) up to $\dot{\sigma} = 0$ and $\dot{\delta} = 0$ in forward sections. This attractor reaches state limits of σ and δ repeatedly, and remains close to them in case of small amplitudes. The parameters E and c can be determined by small cycles and big stretching, respectively. The parameter R and the interpolation functions for $\dot{\delta}$ and $\dot{\sigma}$ have to be adapted to match observed

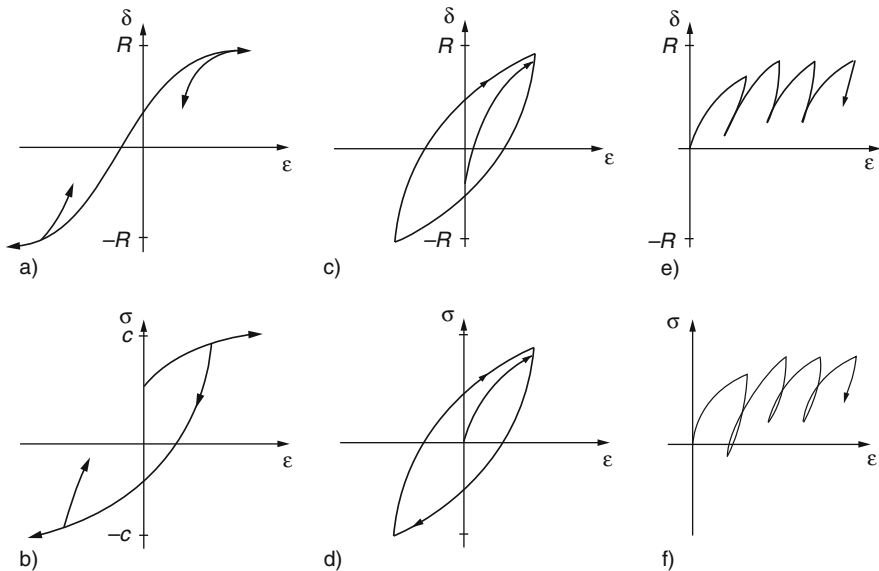


Fig. 4.1.5. Uniaxial hypoplastic response with internal strain δ : changes of δ by stretching and shortening with reversals (a), by strain reversals (b) and by ratcheting (c); associated σ - ε curves with two reversals (d), strain cycles (e) and ratcheting (f)

asymptotic cycles. The internal strain δ leads to the same asymptotic effects as the proposed force-roughness h , this can thus be represented by δ . δ is formally treated like a strain, but cannot be physically interpreted as such.

For going beyond uniaxial evolutions *biaxial* RSEs with zero out-of plane stress and force-roughness are sketched in Fig. 4.1.6. The drawn normal stress distributions at the flanks may have average wavelengths as the sizes of crystallites. The average amplitudes of spatial stress fluctuations are different in general for orthogonal flanks and change with deformations. Their magnitudes h_1 and h_2 are oriented, e.g. an interchange of h_1 and h_2 changes the orientation by 90° (a, b). As the crystallites feel only differences $\sigma_1 - \sigma_2$ we assume that only differences $h_1 - h_2$ matter. Thus two RSEs with different h_1 and h_2 and the same $h_1 - h_2$ have the same hidden state (e.g. c and d). This assumption may be justified by considering ensembles of cuts, but is not necessary and could at best be supported by simulations with composites of crystallites.

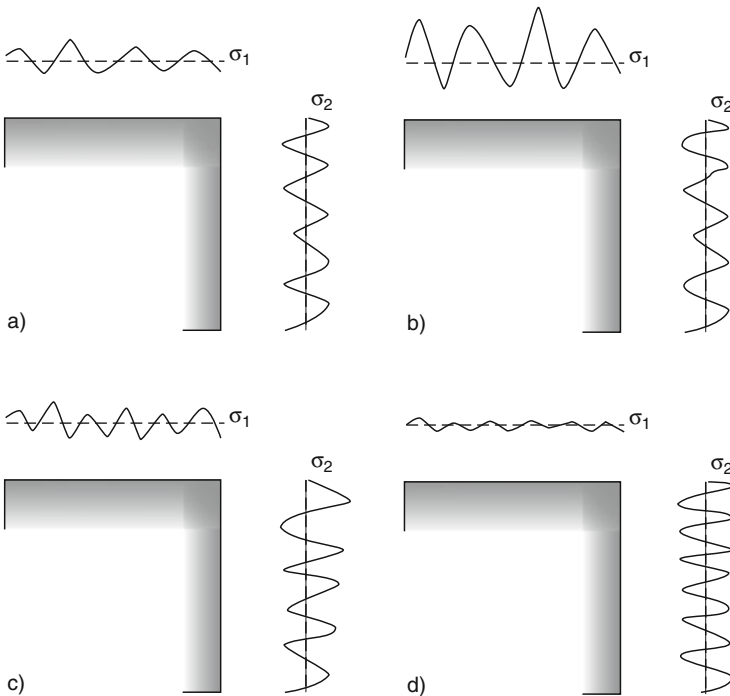


Fig. 4.1.6. Stress distributions of solid biaxial RSEs with different force-roughness and same mean values. Components of force-roughness interchanged (a, b), and an equivalent with same difference (c, d)

One can imagine similar stress fluctuations for *cuboidal* RSEs. They have three components of force-roughness h_i ($i = 1, 2, 3$), but only the deviators $h_i^* = h_i - \Sigma h_i/3$ matter. The crystallites may be so small that mean values and standard deviations of their stress components make sense. Their sizes are not further specified, considerations with fractals are left aside as these could as yet not be quantified.

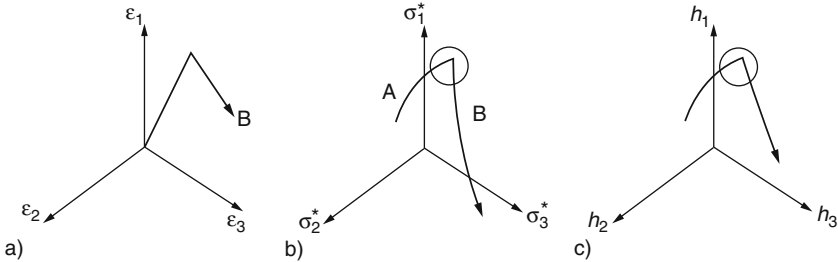


Fig. 4.1.7. Associated deviatoric paths of strain (a), stress (b) and hidden force-roughness (c), with response polars at a reversal

Cuboidal evolutions of shape and state can be represented by associated paths in deviator planes, Fig. 4.1.7 (cf. Fig. 2.1.2). A strain path (a) is related with a stress path (b) and a hidden path of the deviatoric components of force-roughness h_i^* (c). The latter has an intensity $h = \sqrt{\Sigma h_i^{*2}}$ and an orientation α_h . Evolution equations relating $\dot{\sigma}_i$ and h_i^* with $\dot{\varepsilon}_i$, σ_i^* and h_i^* can be represented by response polars for unit strain rates ($\Sigma \dot{\varepsilon}_i^2 = 1$), now also for the hidden state. These polars are of use to represent the approach to attractors and other features of constitutive relations.

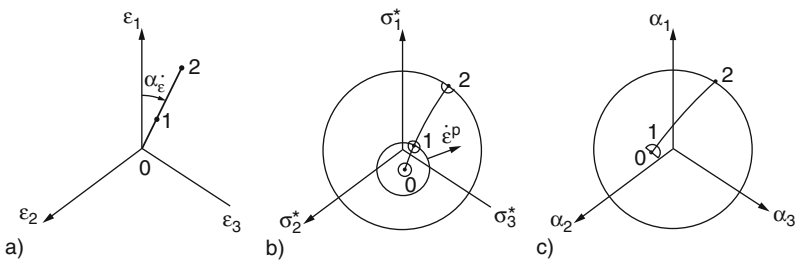


Fig. 4.1.8. Approach to a state limit by an elastoplastic relation with back stress (elp- α): (a) strain path, paths and boundaries of stress (b) and back stress (c)

Elastoplastic relations with back stress (elp- α) are represented in Fig. 4.1.8 (simplified after Mróz, 1967). In the deviatoric stress plane (b) an elastic range is a circle with diameter b and centre α_i inside the bounding circle for state

limits. Plastic strain rates $\dot{\varepsilon}_i^P$ occur when σ_i is at the elastic boundary and $\dot{\sigma}_i$ tends to leave it. $\dot{\varepsilon}_i^P$ is normal to the elastic boundary, this is shifted in the same direction. This *kinematic hardening* is bounded as the elastic range cannot cross the bounding circle. An approach to a state limit by a straight strain path (Fig. 4.1.8a) is shown by means of associated stress (b) and back stress paths (c).

Response polars reveal how the state paths tend to points with the same orientation ($\alpha_{\dot{\varepsilon}} = \alpha_{\sigma} = \alpha_{\alpha}$) and limit radius independently of the beginning, i.e. to an attractor. The evolution in Fig. 4.1.8 starts (0) in an elastic range so that the response polar for $\dot{\sigma}_i^*$ is a circle and the one for $\dot{\alpha}_i$ is a point. At the onset of plastification (1) the stress response gets weaker and agrees with the one of back stress. At a state limit (2) the stress response exhibits a cut-off (cf. Fig. 2.1.4) and the back stress changes only with sideways paths. A monotonous interpolation is assumed for kinematic hardening (1–2).

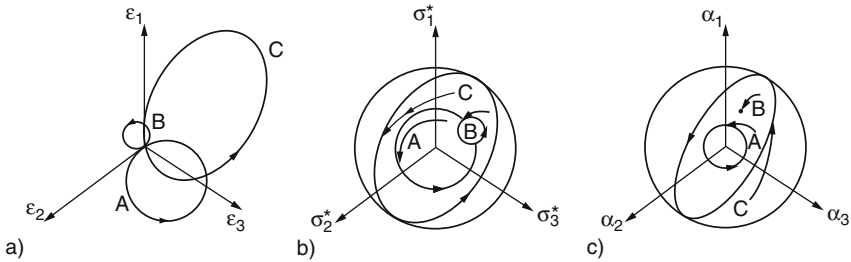


Fig. 4.1.9. Deviatoric response to strain cycles (a) by elp- α : paths and boundaries of stress (b) and back stress (c)

Strain cycles of moderate amplitude (A in Fig. 4.1.9a) lead to symmetric asymptotic cycles of stress (b) and back stress (c) with the same shape. With amplitudes below b/G the elastic range shifts slightly inwards and remains eccentric as the further response is elastic (B). With a big amplitude the state cycles are cut off by the conditions for state limits and thus distorted. Elliptic strain cycles (e.g. C) lead to symmetric state cycles with the same alignment, i.e. the same average Lode angles $\bar{\alpha}_\sigma$, $\bar{\alpha}_h$ and $\bar{\alpha}_\varepsilon$.

Ratcheting (Fig. 4.1.10a) leads to asymmetric asymptotic cycles of stress (b) and back stress (c). The average obliquities get the same, i.e. $\bar{\alpha}_\sigma = \bar{\alpha}_\alpha = \bar{\alpha}_\varepsilon$, and the state limit amounts of σ_i^* and α_i are attained in the forward sections. This holds for small (A) and big amplitudes (B). The back stress α_i has the properties proposed with Figs. 4.1.6 and 4.1.7 for the components h_i^* of force-roughness, which is thus represented. α_i is formally an internal stress, but not physically.

Mróz (1967) points out that the elastic range can have another shape than circular, and that its size can be variable by means of an isotropic hardening parameter. Its translation with plastic strain (kinematic hardening) can be

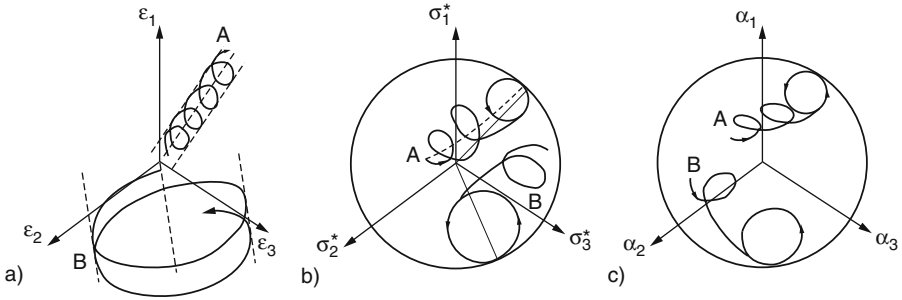


Fig. 4.1.10. Deviatoric response to imposed ratcheting (a) by elp- α : paths and boundaries of stress (b) and back stress (c)

approximated differently in detail, but so that it cannot cross the bounding line of state limits. The elastic stiffness can depend on the back stress so that a variable anisotropy is allowed for. Uniaxial deformations are implied as special cases with the constant Lode angles $\alpha_{\dot{\varepsilon}} = \alpha_{\sigma} = \alpha_{\alpha} = 0 \pm 60^\circ$. Reversals appear as extremely slender ellipses representing the cyclic parts of strain paths and the limit cycles of σ_i^* and α_i . Uniaxial cases do not suffice for validation and identification.

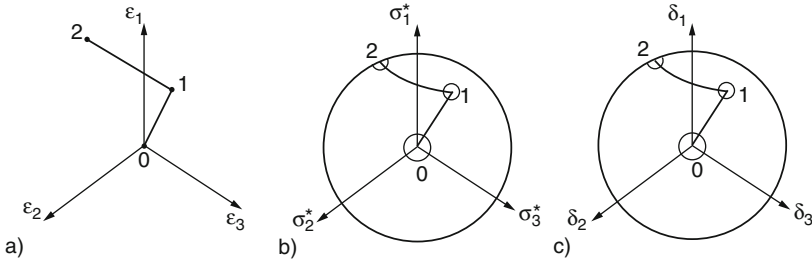


Fig. 4.1.11. Deviatoric response to a strain path (a) by a hypoplastic relation with internal strain (hyp- δ): paths and boundaries of stress (b) and internal strain (c)

Hypoplastic relations with internal strain (simplified after Niemunis and Herle 1997) are represented in Fig. 4.1.11. In deviator planes paths of strain ε_i (a) are related with those of stress σ_i^* (b) and internal strain δ_i (c). δ_i changes with ε_i by $\dot{\delta}_i = \dot{\varepsilon}_i$ for $\sum \delta_i \varepsilon_i < 0$ and by $\dot{\delta}_i = \dot{\varepsilon}_i - \delta_i \delta / R$ otherwise, with $\delta = \sqrt{\sum \delta_i^2}$ so that δ cannot exceed R . σ_i^* changes with ε_i by the elastic relation $\dot{\sigma}_i^* = G \dot{\varepsilon}_i$ for $\delta_i \dot{\varepsilon}_i < 0$, otherwise by the hypoplastic relation (2.1.12) for $\delta = R$ and by an interpolation function for $\delta < R$. These differential relations can be represented by response polars. They steer the paths of σ_i^* and δ_i towards a state limit if the strain path is straight. For these attractors the Lode angles are equal, $\alpha_{\sigma} = \alpha_{\delta} = \alpha_{\varepsilon}$, $\sigma^* = \sqrt{\sum \sigma_i^{*2}}$ and δ are at the upper bounds c and R . Only for an onset with $\sigma_i = 0$ and $\delta_i = 0$ the polars

are circles (0). Otherwise (1) they consist of two circular arcs, at state limits (2) one of them gets a straight cut-off.

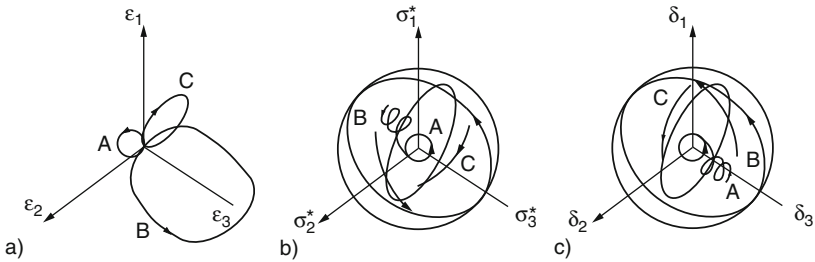


Fig. 4.1.12. Response to strain cycles (a) by hyp- δ : paths and boundaries of deviatoric stress (b) and internal strain (c)

Strain cycles, Fig. 4.1.12a, lead to symmetric limit cycles of stress (b) and internal strain (c). Other than for elp- α these attractors are attained with arbitrarily small amplitudes (e.g. A), depending on the initial state the number of cycles required for the transition is again bigger for a lower amplitude. As with elp- α the asymptotic cycles are cut off by limit conditions in case of big amplitudes (e.g. B). Again elliptic strain cycles lead to symmetric state cycles with aligned average Lode angles, i.e. $\bar{\alpha}_\sigma = \bar{\alpha}_\delta = \bar{\alpha}_\varepsilon$.

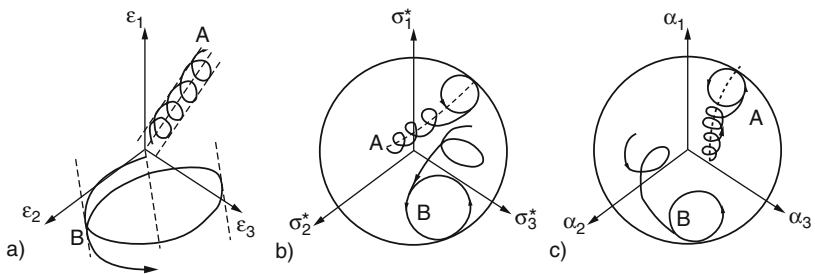


Fig. 4.1.13. Response to forced ratcheting (a) by hyp- δ : paths and boundaries of deviatoric stress (b) and internal strain (c)

Ratcheting (Fig. 4.1.13a) leads to asymmetric cycles of stress (b) and internal strain (c). This holds true for small (A) and big amplitudes (B) of the circular parts of strain paths. The asymptotic average Lode angles agree, $\bar{\alpha}_\sigma = \bar{\alpha}_\delta = \bar{\alpha}_\varepsilon$, and the state limit amounts of σ_i^* and δ_i are repeatedly attained in the forward sections. Except for small amplitudes this is the same as with elp- α , cf. Fig. 4.1.10.

Following Niemunis and Herle (1997) one could modify the evolution equations by means of other limit state conditions and other interpolation

functions. The only must is that attractors are obtained as indicated by Figs. 4.1.11, 4.1.12, and 4.1.13, i.e. state limits by proportional deformations, symmetric state cycles by strain cycles and asymmetric ones by ratcheting. Like with $\text{elp-}\alpha$ uniaxial cases are implied as extremely slender elliptic or lenticular paths, the apexes of which represent reversals. Such cases do not suffice for validation and identification.

The outline with deviator planes would evidently not be influenced by an interchange of the order of subscripts i . In other words, the statements are invariant with respect to adding any integer multiple of 120° to the Lode angles. With *arbitrary deformations* frame-indifference requires coaxiality of stress and hidden state tensors with the stretching tensor for state limits. Coaxiality should also hold for the average state and stretching tensors in case of aligned state cycles by stretching cycles and ratcheting. Thus both for $\text{elp-}\alpha$ and $\text{hyp-}\delta$ biaxial experiments with fixed principal axes suffice for validation and identification.

Biaxial tests have been carried out and simulated for improving constitutive theories, Fig. 4.1.14. A rectangular sheet of metal is pulled in orthogonal directions (a) with stress or strain control in various successions. The out-of-plane stress is zero, without volume changes the out-of-plane strain is given by the in-plane strain components. Buckling prohibits compressive stresses, necking and shear banding cannot be avoided with big strains. Thus uniform state limits can scarcely be attained, but only be estimated by extrapolation.

Simulations can be obtained with composites of perfectly elastoplastic polygonal domains (crystallites), Fig. 4.1.14b. As with uniaxial cases (Figs. 4.1.1b and 4.1.2) it is usually assumed that all domains experience the same strain path. So the stress distribution is uneven with jumps at the domain boundaries, only spatial average stress vectors are further considered. This implies a kind of force-roughness as proposed further above which characterizes the hidden internal state. The idealized crystallites should be convex and far smaller than the RSE. The submicroscopic force-roughness related with dislocations is more complicated and can as yet scarcely be captured.

Results of such simulations by Kuroda and Tvergaard (2001) are shown in Fig. 4.1.14c. 160 domains were assumed with such a distribution of plastic resistance that realistic stress-strain curves are reproduced (cf. Fig. 4.1.2). The lines are stress paths due to biaxial stretching, first isotropically ($\varepsilon_1 = \varepsilon_2$) and then uniaxially in the 1 or 2 direction. Yield curves from calculated plastic strains are indicated as rows of equal points. The also indicated directions of plastic stretching rate are not normal to the yield curves and lie in the fan of a vertex at the sharp bend of stretching paths. This indicates that $\text{elp-}\alpha$ models as introduced with Fig. 4.1.8 are oversimplified.

Approaches with some hundred domains could deepen the understanding, but could scarcely be used in applications. So there is no way around heuristic constitutive relations with internal state variables. The latter are simplified substitutes of the actual force-roughness and the variable fabric. Attractors

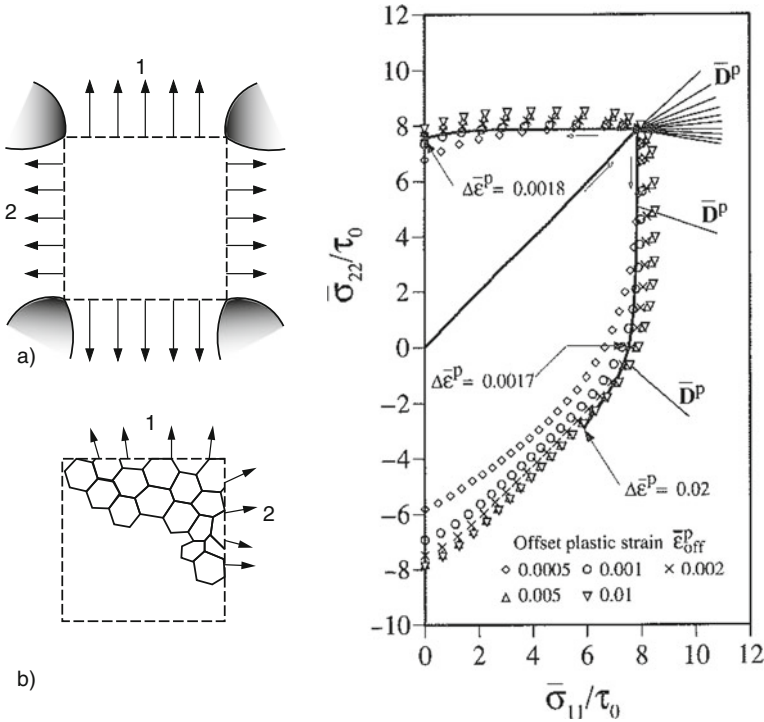


Fig. 4.1.14. Biaxial deformations: pulling device (a), composite model (b), simulation results (c) by Kuroda and Tvergaard (2001)

are necessary to get rid of always partially unknown initial states, otherwise constitutive models and related experiments would not be objective. It is evident for biaxial deformations that a hidden state variable should have at least two components, say h_1 and h_2 . Their ratio h_2/h_1 represents an internal orientation, their intensity $h = \sqrt{h_1^2 + h_2^2}$ should be bounded from below and above. This is *nota bene* at best a crude substitute of force-roughness and fabric, a direct validation is out of reach.

Back stress α and internal strain δ in elp- α and hyp- δ , respectively, are special cases of tensorial hidden state variables \mathbf{h} . Both are deviatoric second order tensors, so three principal axes and two invariants (amount and Lode angle) suffice to quantify them. Coaxiality of stress and stretching follows from frame-indifference for state limits, also with average stress and stretching for aligned stretching cycles and ratcheting. A physical interpretation of the tensors α and δ beyond these general requirements is hardly possible. Mind that α or δ is a kind of stress or strain merely in a formal, not in a physical sense. One can only speculate that both represent oriented spatial fluctuations.

Validation and identification of such models as elp- α and hyp- δ are inevitably heuristic. Attractors are necessary to get rid of unknown initial states,

but they cannot easily be attained in experiments. Most revealing is the response to a reversal from a state limit or in a state cycle as then initial states are *erased*. Still the improvement of constitutive relations with hidden state variables is a cumbersome sequence of trial and error. Only on the base of validations the determination of parameters (identification) makes sense. The neglect of barotropy, pyknotropy, argotropy, brittleness and fatigue is certainly not always justified.

To *sum up*, the behaviour of pore-free solids with reversals may be captured with elastoplastic or hypoplastic relations with hidden variables, these are stress- or strain-like and could represent the internal force-roughness. Stress cycles as asymptotic response to cyclic deformations and ratcheting are attractors which enable an objective validation and calibration. Interpolations between such attractors and state limits are only indicated *more geometrico* as this section is to prepare for sand-like soils with reversals.

4.2 Observed response of sand with reversals

As can be seen in Fig. 2.6.2a, b, Verdugo and Ishihara (1996) observed that the response to deviatoric unloading without volume change depends solely on e if a critical state was attained before. The same can be expected for the response to reversals with a given direction of stress path from other critical states, and also from contractant or dilatant state limits. This behaviour was rarely checked and reported, but is often tacitly assumed to get repeatable test results. Initial states are often produced by imposing a proportional stress path to dense cylindrical samples. Subsequent axial shortening or lengthening with constant skeleton pressure σ_{s2} or p_s (conventionally σ'_2 or p') produces evolutions of σ_{s1} and e which get more repeatable with the approach of peak states.

As long as the internal state is determined by skeleton stress components and void ratio, i.e. for states of swept-out memory (SOM), it cannot be revealed by the response to an isobaric or isochoric reversal. The response to repeated reversals off SOM-states is more revealing as then the state is not sufficiently determined by skeleton stress components and void ratio, but irreproducible relics of preparation should be *erased by repetitions*. Test results of this kind are outlined in the sequel, first with rather symmetric and then with asymmetric deviatoric stress cycles of different kinds. Only tests with reconstituted samples and clean hard quartz grains are taken into account as only then abrasion and fragmentation, cementation and rate-dependence can be of minor importance. Published test reports refer preferably to cyclic deviatoric loading with constant skeleton pressure (σ' , σ'_2 or p') or constant void ratio e . The following selection and discussion is focused on that part of the behaviour which does not depend on the initial state except for density.

Small symmetric shear cycles with isotropic average stress are produced with cylindrical samples in *resonant column tests*, Fig. 4.2.1. After preparation

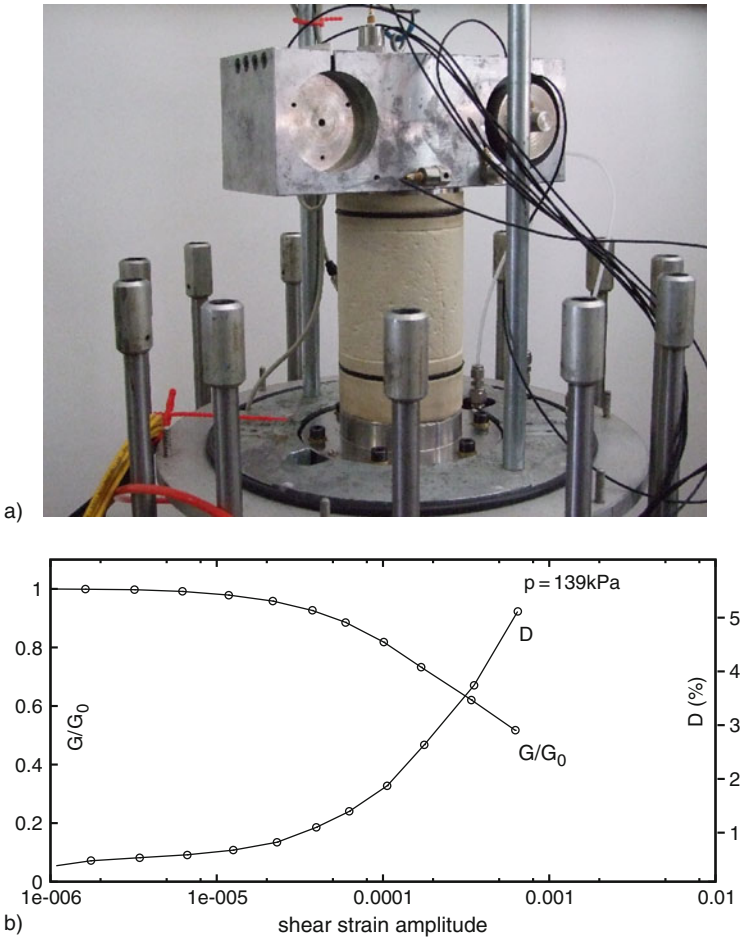


Fig. 4.2.1. Dismantled setup for resonant column tests with a sand (a), shear moduli and damping ratios vs. amplitude (b, courtesy G. Huber)

with an initial e and pressurizing with $\sigma_{s1} = \sigma_{s2} = p_s$ torsional vibrations are imposed by a crosshead with electromagnetic control of the torque (a), and a resonance frequency so that the amplitude is bigger than with other frequencies for the same torque. Assuming a linear response with a shear modulus G_s and a hysteretic damping ratio D_s for the evaluation, G_s and D_s are obtained for different shear strain amplitudes γ_a as shown in Fig. 4.2.1b. If γ_a is lower than a threshold γ_e that ranges from ca. 10^{-7} for big angular to ca. 10^{-5} for small round grains G_s and D_s depend hardly on the amplitude. For this range the dependence of G_s on e and p_s can be described by the empirical formula (Hardin and Drnevich 1972)

$$G_s = K_s \frac{(e_r - e)^2}{1 + e} \left(\frac{p_s}{p_r} \right)^m \quad (4.2.1)$$

with an exponent m ranging from ca. 0.4 to 0.6, a reference pressure $p_r = 1\text{kPa}$, a reference void ratio e_r and a factor K_s ranging from ca. 3 to 7 MPa for quartz sands. Equation (4.2.1) could be made unit-invariant by taking p_r and K_s proportional to a strength or stiffness of the grain mineral. It suggests hypoelastic behaviour, but D_s indicates hysteresis even for minutest amplitudes. The Hertz-Mindlin theory of elastic spheres in contact with sliding friction would yield $m = 2/3$ in (4.2.1) and also hysteresis, a more realistic $m \approx 0.5$ is obtained with contacts of angular and round grains (Iwasaki et al. 1978).

The decrease of G_s and increase of D_s with bigger amplitudes visible in Fig. 4.2.1b appears reasonable, but more in detail it is contestable. With an increasing hysteresis for bigger amplitudes the evaluation with a linear theory is no more consistent, it can at best yield an average secant modulus \bar{G}_s and an average damping ratio \bar{D}_s . Richart et al. (1970) point to a minute gradual decrease of e with drainage and of p_s without it, both are ignored in the routine evaluation of resonant column tests. These cumulative effects tend apparently towards a periodic response if the average e or p_s and the amplitude are not too big. This was confirmed by Huber (2010) with sophisticated resonant column tests. These show more precisely than Fig. 4.2.1b that only with very small amplitude and high density the response gets almost elastic. It appears therefore that sand has at best an infinitesimal elastic range near stable states of rest.

Small shear cycles with anisotropic average stress reveal *anisotropic* G_s , Fig. 4.2.2. Roesler (1979) observed the propagation of shear waves through a cubical dry sand sample under an axisymmetric anisotropic stress state (a). With dense samples the empirical relation (4.2.1) was confirmed, but G_s was increasingly anisotropic with increasing stress ratio σ_1/σ_2 . Kuwano and Jardine (2002) imposed shear waves of small amplitude to cylindrical samples with $\sigma_{s1} > \sigma_{s2}$ by means of so-called bender elements (Fig. 4.2.2b). They confirmed (4.2.1) and observed again an increasing anisotropy of G_s , calculated from wave travel times, with increasing skeleton stress ratio σ_{s1}/σ_{s2} . These findings suggest a hypoelastic approach as if the skeleton was a kind of solid after an adaption by stationary mean stress components and shear cycles. There is at least as much hysteresis as indicated by Fig. 4.2.1b for $\sigma_{s1} = \sigma_{s2}$, however, and although cumulative anelastic effects have not been recorded with the devices of Fig. 4.2.2 they must occur.

Moderate symmetric shear cycles with constant effective pressure σ' normal to shearing were investigated in different devices, this was outlined already in Sects. 2.9 and 2.10. Without describing tests Casagrande (1936) proposed a lower bound void ratio e_d attained by shear cycles that decreases with bigger σ' as e_c for critical states (Fig. 2.9.5e). Youd (1972) confirmed this finding more in detail (Fig. 2.10.4): e tends to asymptotic butterfly loops, these are

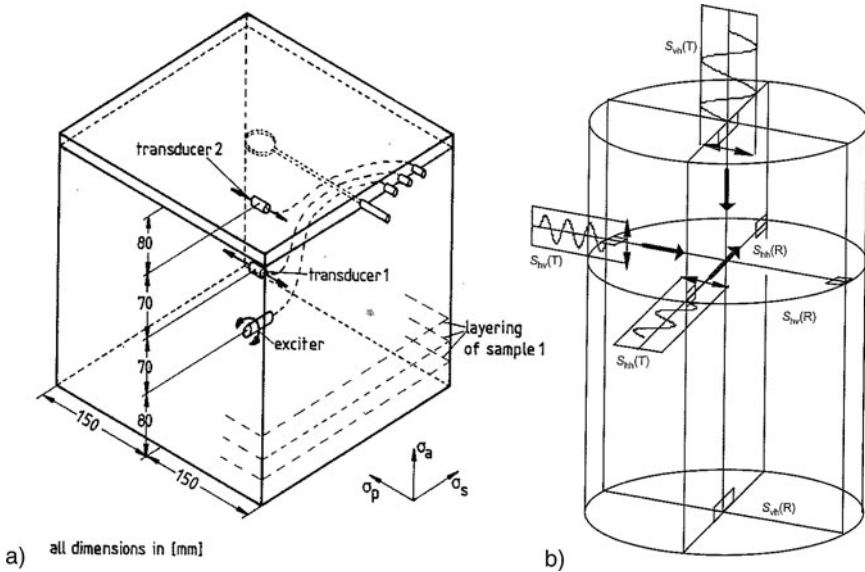


Fig. 4.2.2. Arrays to observe the propagation of shear waves in sand samples: (a) by Roesler (1979), (b) by Kuwano and Jardine (2002)

reached with a lower number of cycles if the amplitude is bigger, e_d does not depend on frequency and water content and is lower for bigger σ' . The observed periodic asymptotic response indicates that the grain properties are rather permanent in the tested range. The simulations shown in Fig. 2.10.5 reveal that the cumulative effects observed by Youd (1972) are overestimated with a simple hypoplastic model.

Youd (1972) used a device as sketched in Fig. 2.9.7 which inevitably produces non-uniform stress distributions. So his results can at best support constitutive relations with an internal variable, but are not apt to quantify the latter. Isochoric cyclic shear tests (e.g. Franke et al. 1979) with saturated undrained samples in devices as sketched in Fig. 2.10.3 have the same shortcoming. They produce a gradual decrease of σ_s and thus of shear stiffness, which is often related with the so-called *cyclic mobility* (Castro 1975). This anelastic effect is not obtained with simple elastoplasticity and exaggerated by simple hypoplasticity (Sect. 2.10). With the inevitable lack of uniformity such test results cannot suffice to quantify an internal state variable, let alone how this is related with spatial fluctuations of intergranular forces.

Results of *cyclic torsional shear tests* with saturated drained hollow cylindrical samples by Pradhan et al. (1989) provide more insight as stress and deformation are more uniformly distributed. The authors show that nearly the same dependence of τ/σ_s on $\dot{\epsilon}^p/\dot{\gamma}^p$ is obtained with loose and dense samples. This suggests that a kind of stress-dilatancy relation holds as a plastic flow rule. This was already proposed by Rowe (1962) and by Roscoe (1970).

The former showed that (2.2.20) works also for monotonous deformations prior to state limits. This may be taken over to (2.9.7) for monotonous shearing. The sections with the same signs of τ and $\dot{\gamma}$ can be fairly well matched by (2.9.7) with $\dot{\varepsilon}^p/\dot{\gamma}^p$ instead of $\tan \nu_s = \dot{\varepsilon}/\dot{\gamma}$. In particular, for critical stress ratios $\tau/\sigma_s = \pm \tan \varphi_{sc}$ zero dilation is obtained, i.e. $\dot{\varepsilon}^p/\dot{\gamma}^p = 0$.

This seems to support Rowe's (1962) idea of a sliding mechanism in the grain skeleton which is dominated by the stress ratio σ_{s1}/σ_{s2} and the direction of the principal stress σ_{s1} independently of the void ratio. In the sections with different signs of τ and $\dot{\gamma}$, however, the experiments reveal *two* branches for shearing before and after a reversal. At each reversal $\dot{\varepsilon}^p/\dot{\gamma}^p$ jumps to a bigger amount just after it. In other words, two values of $\dot{\varepsilon}^p/\dot{\gamma}^p$ hold for one value of τ/σ_s if τ and $\dot{\gamma}$ have a different sign.

Thus the concept of a unique flow rule fails just after a reversal, but can get valid again when τ and $\dot{\gamma}$ obtain the same sign by monotonously continued shearing. This behaviour after a reversal suggests a *gradual adaption* of the internal state by a monotonous deformation until it is determined by the external state, i.e. by skeleton stress components and void ratio. This adaption was called swept-out of memory (SOM) by Gudehus et al. (1977) and was discussed in Sect. 2.5. Thus the influence of the internal state is only revealed during small deformations just after a reversal. This argument is not refuted by the uncertainty of elastic strain rates, $\dot{\varepsilon}^e$ and $\dot{\gamma}^e$ in case of simple shearing. Pradhan et al. (1989) determined $\dot{\varepsilon}^e$ and $\dot{\gamma}^e$ from test sections with isotropic or isobaric unloading, but their stress-dilatancy relation is not substantially influenced by the inaccuracy of elastic strain rates.

The findings of Pradhan et al. (1989) refute the idea of a single plastic flow rule, i.e. a unique relation of the directions of stress and strain rate, but they do not suffice to establish an internal state concept. A more quantitative evidence, though again indirectly as a unique definition and determination of internal state variables is apparently out of reach, can be obtained by cumulative effects with repeated reversals. One can see from Fig. 2.10.1 that there was no drift of the average shear stress and strain, i.e. the cycles investigated by Pradhan et al. (1989) were rather symmetric. So the only cumulating quantity in this case is volumetric strain or void ratio e . As in Youd's (1972) tests (Fig. 2.10.4) e decreases gradually if $|\tau/\sigma_s|$ never gets so big that dilation dominates and peak states would lead to shear localization. The gradual decrease is stronger if the relative void ratio r_e is higher, and e can also increase with bigger amplitudes.

At first sight the isobaric hollow cylinder shear test results in Fig. 2.10.1 reveal a stronger cumulative densification than the ones by Pradhan et al. (1989) with negligible radial and circumferential strain. Up to the first three reversals the samples with an isotropic initial stress state are stiffer than the ones with an anisotropic initial stress state. After an adaption in the first few cycles there is no significant influence of the previous stressing on the differential and cumulative response. Thus the initial state except for e and p_s can be swept out with a few reversals. The external and internal state can tend to

periodic changes by imposing repeated cycles independently of the onset. This asymptotic behaviour was attained in the tests by Youd (1972), Fig. 2.10.4, but not in the ones by Pradhan et al. (1989).

Cyclic triaxial tests with saturated quartz sand have been carried out in many variants, none of them led to a periodic response. Pradhan et al. (1989) report on drained isobaric tests with the same sand as for their shear tests, again with gradually increasing amplitudes, Fig. 4.2.3. A loose sample reveals a gradual increase of differential stiffness $\dot{\tau}/\dot{\gamma}$ for each τ/σ_s (a) due to the densification (b). A dense sample has a bigger $\dot{\tau}/\dot{\gamma}$ for each τ/σ_s (d) than a loose one, and this stiffness exhibits less gradual increase as dilation and contraction are nearly equal (e). The plots of q/p_s vs. $-\dot{\epsilon}^p/\dot{\gamma}^p$, calculated with elastic strain rates from unloading, are almost the same for loose (c) and dense sand (f).

A vanishing dilation is obtained for critical stress ratios before reversals, i.e. for σ_{s2}/σ_{s1} by (2.2.15) with $(\sigma_1 - \sigma_2)(\dot{\epsilon}_1 - \dot{\epsilon}_2) > 0$, this is also obtained by the stress-dilatancy relation (2.2.20). As for shearing one can conclude that a

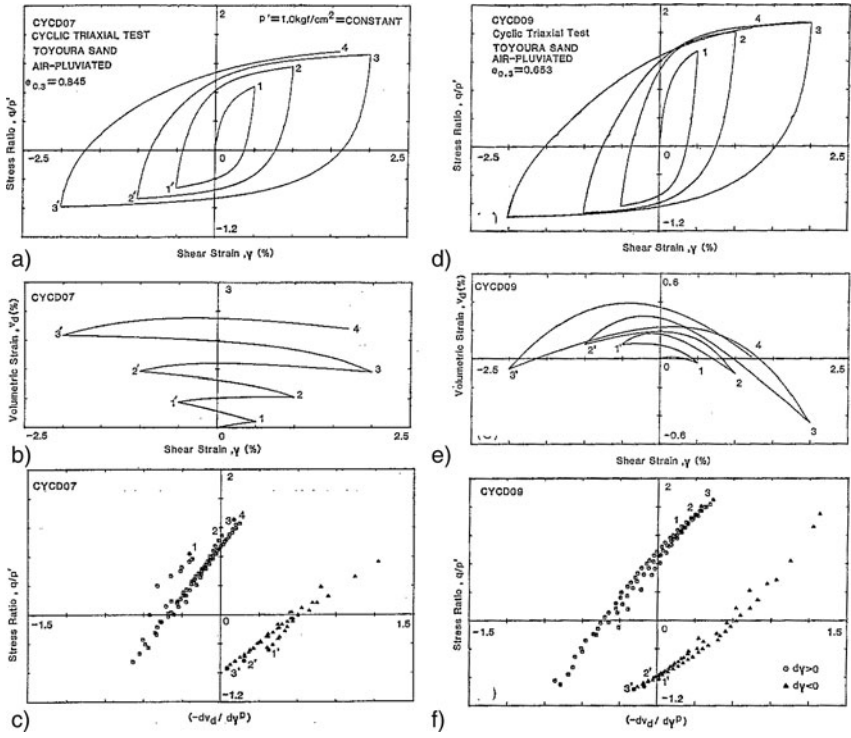


Fig. 4.2.3. Isobaric behaviour of saturated sand samples with pulsating and gradually increasing amplitudes in triaxial tests (Pradhan et al. 1989). Loose sample: stress ratio (a) and volumetric strain vs. shear strain (b), stress ratio vs. plastic strain rate ratio (c); same with a dense sample (d, e and f)

unique stress-dilatancy relation works as a plastic flow rule only if $(\dot{\sigma}_1 - \dot{\sigma}_2)$ and $(\dot{\epsilon}_1 - \dot{\epsilon}_2)$ have the same sign. The plots are not as symmetric as for shearing or for biaxial deformations, but there is again no drift of the average deviators $(\bar{\sigma}_1 - \bar{\sigma}_2)$ and $(\bar{\epsilon}_1 - \bar{\epsilon}_2)$.

There are only few consistent reports on *cumulative deformations* observed with cylindrical samples of saturated sand. Luong (1982) observed cumulative volume changes due to 20 cycles of $(\sigma_1 - \sigma_2)$ with constant average (σ_1, σ_2) and open drainage. Independently of pressure and initial density there was always contraction when the average stress obliquity $(\sigma_1 - \sigma_2)/p'$ was below the critical threshold by (2.2.15), and always dilation in the opposite case. Luong found critical stress obliquities separating contractant and dilatant regimes both for positive and negative average stress deviators. He proposed that without drainage cycles of $(\sigma_1 - \sigma_2)$ should lead to the same critical obliquity $(\sigma_1 - \sigma_2)/p'$, and to an increase or decrease of p' in the transition depending on the given e and the initial p' .

Chang and Whitman (1988) extended this concept by evaluating results of cyclic triaxial tests with free drainage, Fig. 4.2.4. In the plane of $(\sigma_1 - \sigma_2)$ vs. p' (a) the average $(\sigma_1 - \sigma_2)/p'$ and the amplitude $\Delta(\sigma_1 - \sigma_2)/p'$ were kept constant with different σ'_2 . The directions of the cumulative strain increments for up to 10^3 stress cycles (b) are determined by the average $(\sigma_1 - \sigma_2)/p'$. The plastic potential associated with this kind of flow rule (dashed lines) agrees with the one for state limits by CSSM (Sect. 2.3). Chang and Whitman (1988) do not communicate void ratios and their evolution. It appears that as for isobaric cyclic shearing the average e is lower than critical for critical average obliquities $(\sigma_1 - \sigma_2)/p'$, and that the gradual densification saturates at a lower bound of e for lower than critical average stress ratios $(\sigma_1 - \sigma_2)/p'$.

Wichtmann et al. (2006) continued this investigation with different kinds of saturated sand samples, also with negative average stress deviators and gradual axial extension, Fig. 4.2.5. Keeping the average stress components $\bar{\sigma}'_1$ and $\bar{\sigma}'_2$ constant, up to 10^5 cycles of $\bar{\sigma}'_1$ and $\bar{\sigma}'_2$ were imposed with an

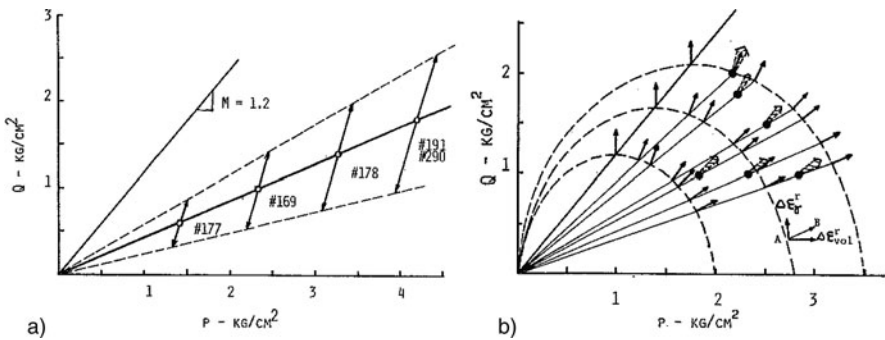


Fig. 4.2.4. Response of saturated sand samples in drained triaxial tests (Chang and Whitman 1988): cycles of stress deviator vs. mean pressure (a), directions of cumulative strain increments in the same stress plane (b)

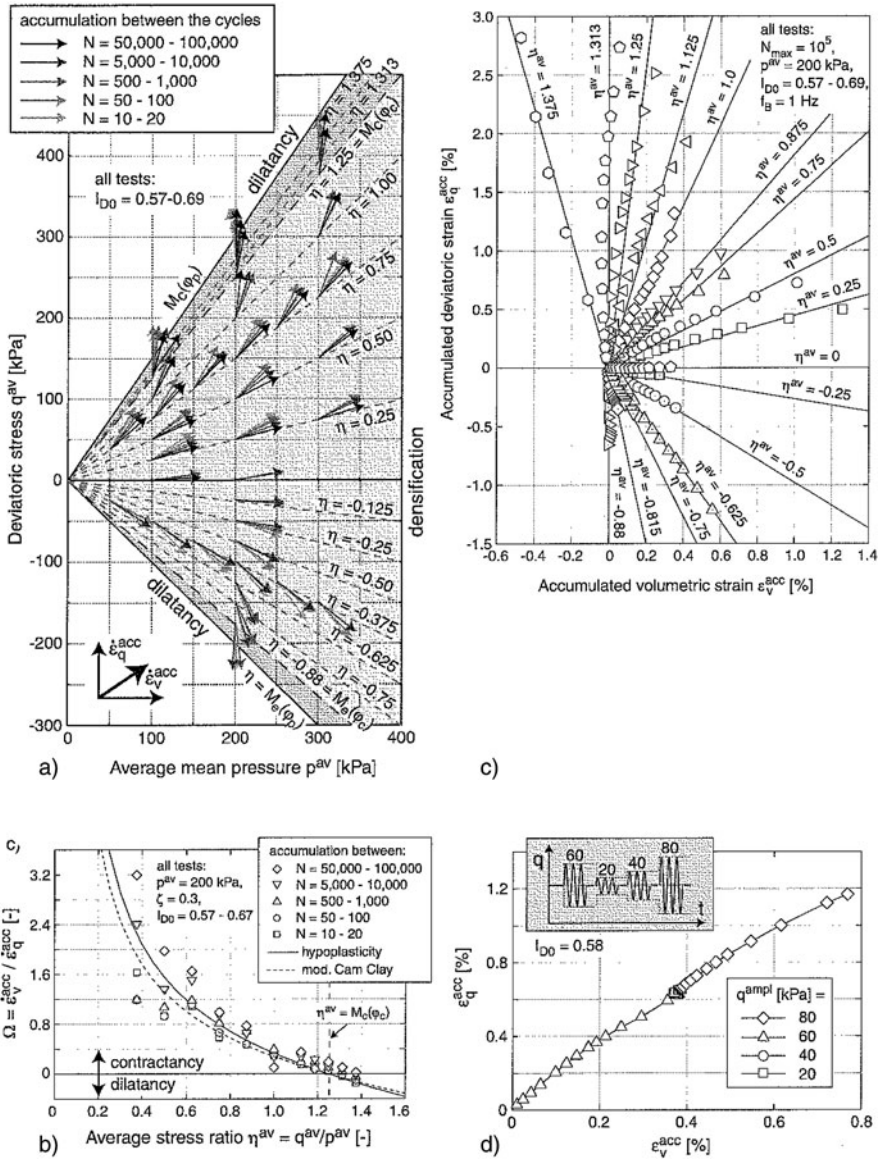


Fig. 4.2.5. Response of saturated sand to stress cycles in drained triaxial tests (Wichtmann et al. 2006): stress components and directions of cumulative strain rates (a), flow rule for cumulative strain rates (b), cumulative strains (c), influence of the amplitude on the intensity of accumulation (d)

elliptic stress path of constant shape in each test. similarly as in Fig. 4.2.4a the amplitude $\Delta(\sigma_1 - \sigma_2)/(\bar{\sigma}_1 - \bar{\sigma}_2)$ was kept rather small. The direction of the average cumulative strain rate is essentially determined by the average stress obliquity (a). This kind of flow rule can be approximated by the one for state limits according to CSSM or hypoplasticity (b). This is a more precise substitute of what Luong (1982) and Chang and Whitman (1988) discovered.

The cumulative strains follow nearly the same kind of flow rule (Fig. 4.2.5c). They do not depend systematically on the frequency in the tested range from 0.05 to 2 s⁻¹. The accumulation increases or decreases with an increase or decrease of the amplitude, respectively (d). A detailed analysis revealed that the rate of accumulation depends only on the instantaneous stress cycle and the average state $\bar{\sigma}'_1$, $\bar{\sigma}'_2$ and \bar{e} . It is maximal with circular cyclic stress paths and minimal with a constant ratio $\Delta\sigma'_2/\Delta\sigma'_1$ of the cyclic stress fractions. This indicates that the grain skeleton can be adapted to a nearly hypoelastic response if stress cycles are polarized, but not otherwise.

Wichtmann et al. (2006) observed a linear increase of cumulative strains with the logarithm of the number of cycles up to $N \approx 10^4$. The observed stronger increase for $N > \text{ca. } 10^4$ indicates a gradual abrasion. Without it the densification should attain an asymptote as for cyclic shearing (Fig. 2.10.4). The void ratios were always lower than critical. In the dilatant regime with an overcritical average stress obliquity the tests had to be stopped after an amplitude-dependent low number of cycles because of shear localization and bulging or necking. As Luong (1982) and Chang and Whitman (1988) Wichtmann et al. (2006) do not report on the evolution of e more in detail.

More recently Wichtmann et al. (2009) presented the *gradual relaxation* of a rather dense undrained sand sample by cyclic deformation with small

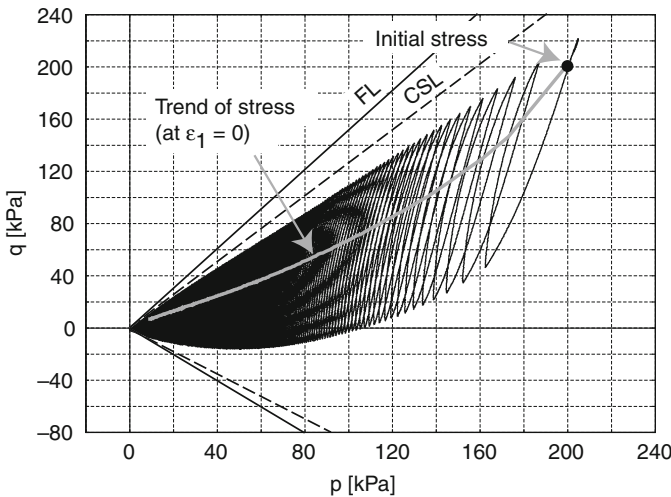


Fig. 4.2.6. Stress path of a saturated undrained medium-dense cylindrical sand sample by isochoric cyclic deformation with small amplitude (Wichtmann et al. 2009)

amplitude, Fig. 4.2.6. The effective stress disappeared similarly with different initial stress states, and after less cycles for higher void ratios. This may be considered as the counterpart of the gradual densification by small deviatoric strain cycles with constant skeleton pressure. A complete relaxation cannot be expected, however, with very dense samples, then small isochoric strain cycles should lead to a butterfly attractor.

Ibsen (1994) tested *undrained* saturated sand samples of different densities with cyclic stress deviator $\sigma_1 - \sigma_2$ and constant average $\bar{\sigma}_1 - \bar{\sigma}_2$, Fig. 4.2.7. He demonstrated that consistent results can be obtained in a triaxial setup with short samples ($h \approx d$) and hard lubricated endplates (Sect. 14.1). With a medium density the stress path tends to a cyclic asymptote (a), and the pore pressure tends to stationary cycles after an increase (b). Hysteresis loops of

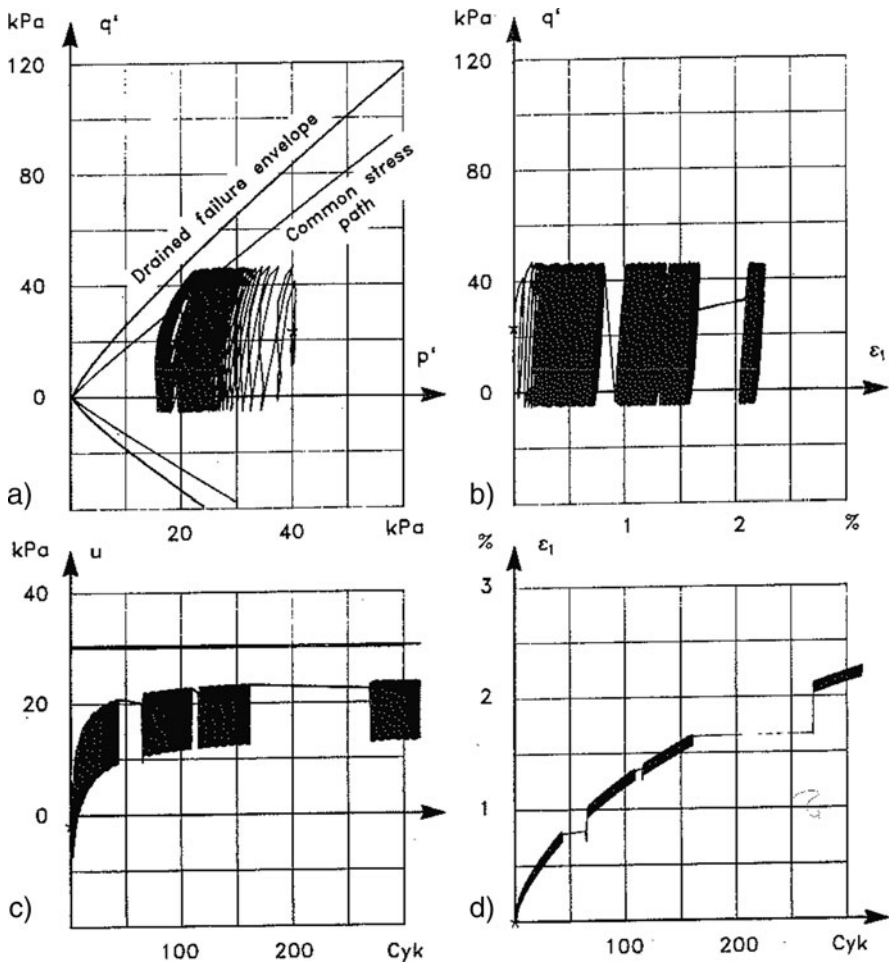


Fig. 4.2.7. Response of saturated sand to a pulsating deviatoric stress in an undrained triaxial test (Ibsen 1994): effective stress path (a), stress deviator vs. axial strain (b), pore pressure (c) and axial strain vs. number of cycles (d)

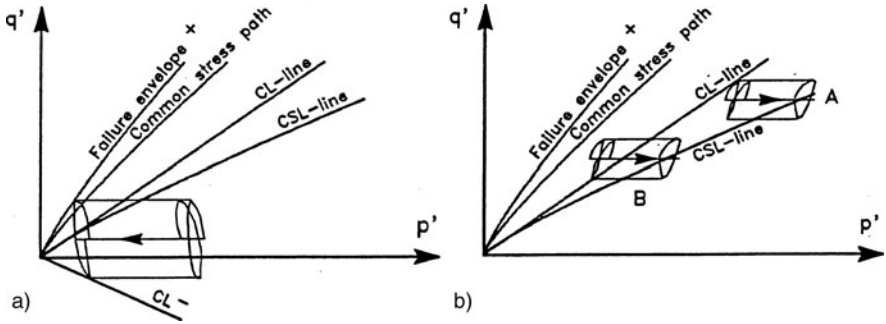


Fig. 4.2.8. Asymptotic stress cycles for tests of Fig. 4.2.7 with moderately (a) and very dense (b) samples (Ibsen 1994)

decreasing width appear in the plot of $\sigma_1 - \sigma_2$ vs. ε_1 (c), the cumulative ε_1 tends to a linear increase with the number of cycles (d). As shown in Fig. 4.2.8 the asymptotic stress paths are lenticular with a lower than critical average ratio $(\bar{\sigma}_1 - \bar{\sigma}_2)/p'$ this is somewhat lower for higher p' . The average pressure \bar{p}' decreases (a) or increases, respectively, to an asymptote (b) if the sample has a high or a lower density. The variable membrane penetration, which was introduced with Fig. 2.6.7, makes the lenses flatter and wider and enhances their shift.

These findings confirm Luong's (1982) opinion, they are a counterpart of the results by Chang and Whitman (1988) and by Wichtmann et al. (2006), but there are differences. Ibsen (1994) attained stationary ratcheting and stress cycles, so his sand was not abrasive in the tested range. The stationary average pressure \bar{p}' is determined by e , its dependence on the amplitude was not recorded. The stationary average stress ratio is lower than critical and lower with bigger \bar{p}' , its dependence on the amplitude can be guessed from Fig. 4.2.8. The flow rule by Wichtmann et al. (2006), on the other hand, implies a critical average stress ratio with φ_c for ratcheting, cf. Fig. 4.2.5a, b. This could work at best with small amplitudes. Ibsen (1994) did not report on void ratios in detail. One may presume that his p' attained an asymptotic average \bar{p}' so that e was closer to the lower bound e_d than to the the critical value e_c for this \bar{p}' .

Similarly as Ibsen (1994), Hyodo et al. (1989) investigated saturated undrained cylindrical sand samples under cycles of $\sigma_1 - \sigma_2$ (Fig. 2.6.7). With low density and non-zero average deviator they obtained a gradual decrease of p' and increase of $\varepsilon_1 - \varepsilon_2$. A periodic asymptote with stationary ratcheting was not attained as the samples had $h \approx 2d$ and rough endplates so that they got inhomogeneous. An increasing lack of homogeneity blurs many test results so that they are hardly apt for objective conclusions. For example, Ishihara and Towhata (1983) could not avoid the collapse of samples by a diffuse bifurcation in triaxial and torsional tests with saturated undrained sand. Even so some of their findings are of use. With shear strains above ca. $2 \cdot 10^{-2}$ they observed coaxiality of stress and strain rate and a subsequent

response to reversals that did not depend on previous smaller shear cycles. This shows that SOM-states were repeatedly attained. Just before a decay of the grain skeleton butterfly-shaped stress paths were attained both in triaxial and torsional tests without ratcheting.

Katzenbach and Festag (2004) obtained an *isobaric ratcheting* of dry quartz sand samples with more than 10^6 cycles, Fig. 4.2.9. The sand was dense, with $\sigma_2 = 150\text{kPa}$ cycles of σ_1 from 200 to 350kPa were imposed once per second, a critical stress ratio was never attained. The average $\varepsilon_1 - \varepsilon_2$ grows in proportion to the number of cycles N (a), occasional kinks indicate abrasion. Slender hysteresis loops (b) exhibit a gradual shift with increasing N . Other than in the tests by Wichtmann et al. (2006) the deviatoric stress amplitude was rather big compared to the average deviator. As with Ibsen's

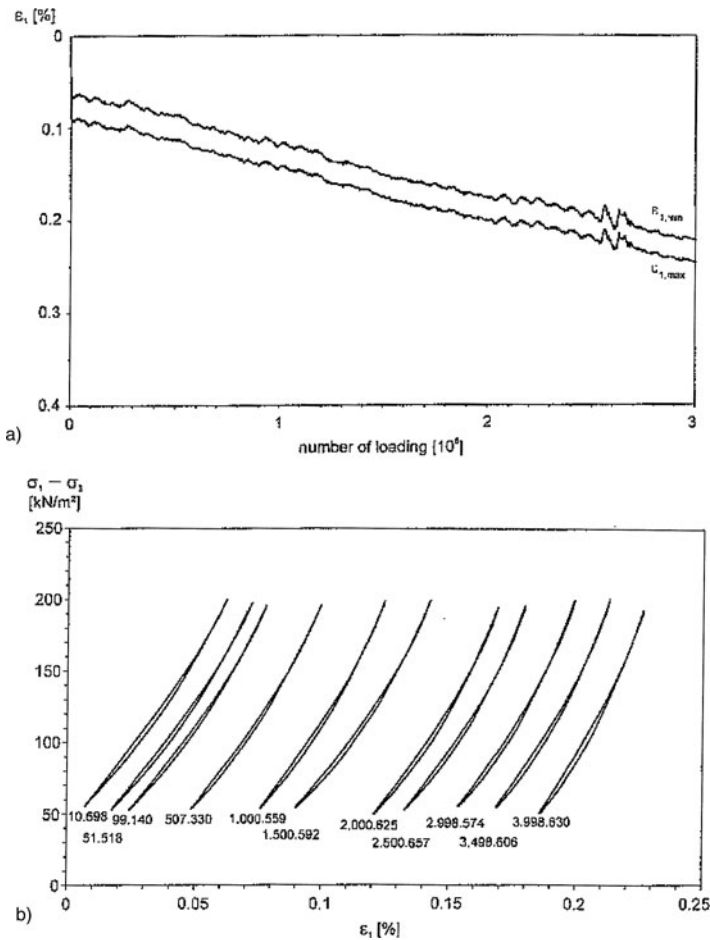


Fig. 4.2.9. Response of dense dry sand samples to axial stress cycles with constant σ_2 in triaxial tests (Katzenbach and Festag 2004): axial strain vs. number of cycles (a), axial stress vs. strain after different numbers of cycles (b)

(1994) tests stationary ratcheting can thus be achieved with a lower than critical average stress obliquity.

Summing up, the response of sand samples to reversals is almost hypoelastic for small amplitudes in the subcritical range, but anelastic effects play a role for bigger amplitudes, with many reversals and in the overcritical range. Anelastic strain rates just before and after reversals indicate two different flow rules. The cumulative strain for small stress cycles obeys a flow rule as by *elp* or *hyp*, its intensity cannot as easily be captured. A flow rule does not work with bigger amplitudes, but then asymptotic state cycles can serve for an objective characterization. Isochoric strain cycles cause a cumulative relaxation up to a decay except for high densities. The desired uniformity of RSEs gets lost in the overcritical range so that the behaviour with reversals can hardly be judged.

4.3 Attractors with force-roughness

It was outlined in Chap. 2 that the state of psammoid RSEs is not sufficiently captured by void ratio and stress components in case of repeated reversals. The cumulative effects shown in Sect. 4.2 would be grossly underestimated with *elp* and overestimated with *hyp*. Better constitutive models require additional state variables which are hidden, i.e. not observable from outside as stress and void ratio. They can be related rather heuristically with the *force-roughness* of grain skeletons. Their initial indeterminacy can be swept out by suitable strain paths which lead to attractors (cf. Sect. 2.1 for objectivity). This will be outlined *more geometrico* in the sequel for proportional and cyclic deformations and for ratcheting. Asymptotically attained stress paths can serve as benchmarks for constitutive relations although the force-roughness remains hidden. As with simple psammoids granular permanence and rate-independence are presumed, the latter will be discussed in Sect. 4.6.

Dantu (1957) observed strong spatial fluctuations of contact forces in an assembly of photoelastic rods which was deformed in a shearing device, Fig. 4.3.1. The major part of the average stress is transferred by *force chains*, neighboured rods with far lower forces prevent their buckling. Force chains come and go with continued deformation, they can be more or less marked and can have different orientations. They are related with the skeleton stress components which represent average contact forces, but are not determined by them in general. A skeleton of rods is more prone to rearrange with sliding, opening and closing of contacts if the force chains are more erratic, and more prone to an elastic response in the opposite case. Thus the hidden state may be related with the force-roughness of the skeleton. As with solids (Sect. 4.1) it appears that the fabric, i.e. the spatial arrangement of particles, could thus also be captured (Sect. 9.1).

Cundall et al. (1982) calculated force chains for an assembly of discs with a simplified interaction allowing for elastic deformation and sliding friction,

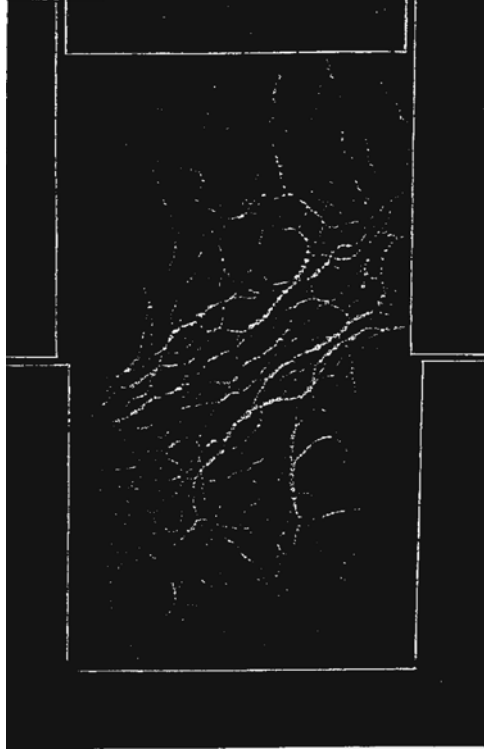


Fig. 4.3.1. Force chains in a sheared assembly of photoelastic rods (Dantu 1957)

Fig. 4.3.2 (also Radjai et al. 1976). A stress path (σ_1, σ_2) with fixed principal axes was imposed from the boundary. Force chains (a) are marked for a peak state (above) and remain partly after unloading to $\sigma_1 = \sigma_2$ (below). This is also visible with polar histograms of grain contact normals which represent the fabric, i.e. the relative positions of discs (b). The inner histograms belong to force chains, the outer ones to nearly force-free supporting discs. After the initial isotropic loading the force chains have no preferred orientation (above). At the peak state the force chains are less regular and more marked in the σ_1 direction (middle). After deviatoric unloading the force chains retain this orientation, though less marked (below). The locked-in forces make the sample stiffer for deviatoric reloading than for first deviatoric first loading.

Simulations with RSE skeletons composed of spheres with different sizes produce also force chains which change alongside with the boundary conditions. Calvetti et al. (2003) calculated histograms of spatially fluctuating grain contact forces and show that the differential stiffness, represented by response polars, varies substantially for a given average force density (i.e. stress) and void ratio. The findings are biased as mutual rotations of grains were suppressed. The differential stress response to strain rates is weaker with more

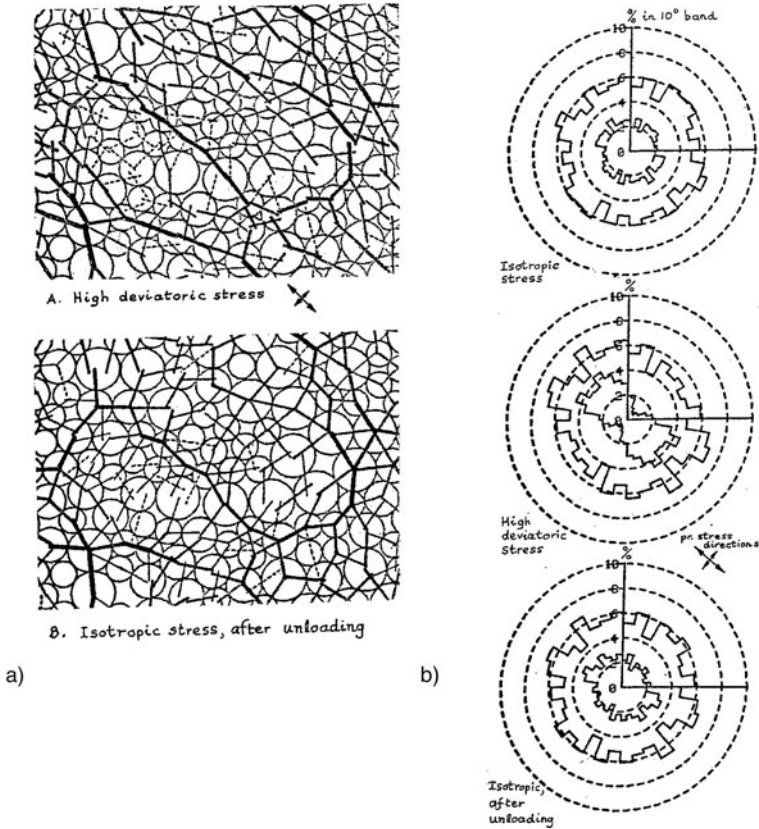


Fig. 4.3.2. Force chains (a) and distribution of contact normals (b) after loading and unloading of a simulated assembly of discs (Cundall et al. 1982)

marked force chains as these are more prone to buckle. The stiffest nearly hypoelastic response is obtained with the smallest possible force chains, i.e. with a minimal force-roughness. The softest rather hypoplastic response can be expected after a sufficient monotonous deformation which produces the biggest possible force-roughness with given average forces and void ratio. Force chains are strongest in certain directions (Fig. 4.3.1), the force-roughness has thus a variable intensity and orientation.

Physicists speak of differently *jammed* grains which remain unchanged in a resting skeleton. Howell et al. (1999) observed strong temporal stress fluctuations with a transducer at the base of a sheared annular sample of glass beads. The power spectrum was rather fractal and rate-independent, i.e. the progression of stress kinks was proportional to the rate of shearing. This suggests that force chains are produced and destroyed with the same rate as kinematic chains. The kinetic energy released by buckling chains is dissipated with an average rate which is proportional to the rate of shearing. The

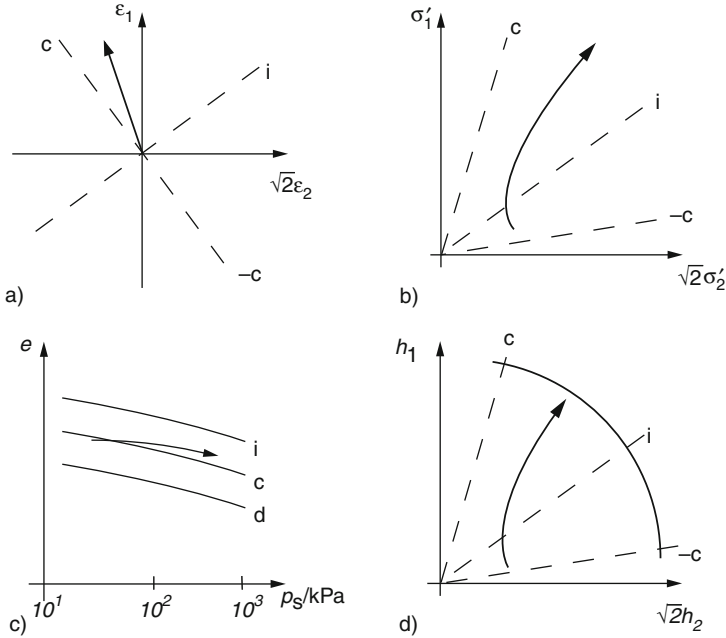


Fig. 4.3.3. Associated paths towards a state limit: strain (a), stress (b), void ratio vs. pressure (c) and hidden state (d)

force-roughness is enhanced by the resistance to mutually rotating grains, the consequences for mean values could be modelled with polar quantities (Sect. 8.2). Kondic and Behringer (2004) simulated such evolutions and calculated the additional elastic energy of force chains, it is far bigger than the average kinetic energy and enhances the buckling of chains in case of slow shearing. Taking over thermodynamic relations they interpret this additional energy as a kind of temperature.

Consider now a cylindrical psammoid RSE with variable void ratio, stress components and force-roughness. The latter may be represented by two positive components h_1 and $h_2 = h_3$, which can be replaced by an intensity $h = \sqrt{h_1^2 + 2h_2^2}$ and an obliquity $\tan\psi_h$ as by (2.2.3). This substitute of force chains may serve as hidden state variable for the response to strain rates. With given void ratio and stress components h_1 and h_2 can have different values in an allowed range; they cannot be observed and are indeterminate if the past is unknown. A *proportional deformation*, Fig. 4.3.4a, leads to paths of stress (b), void ratio vs. pressure (c) and force-roughness (d). The initial hidden state is swept out by the imposed rearrangement so that the subsequent response is determined by stress and void ratio. For such so-called SOM-states (Swept Out Memory, Gudehus et al. 1977) the stress path gets radial, and the hidden state is not needed explicitly (Sect. 2.2). A continued proportional

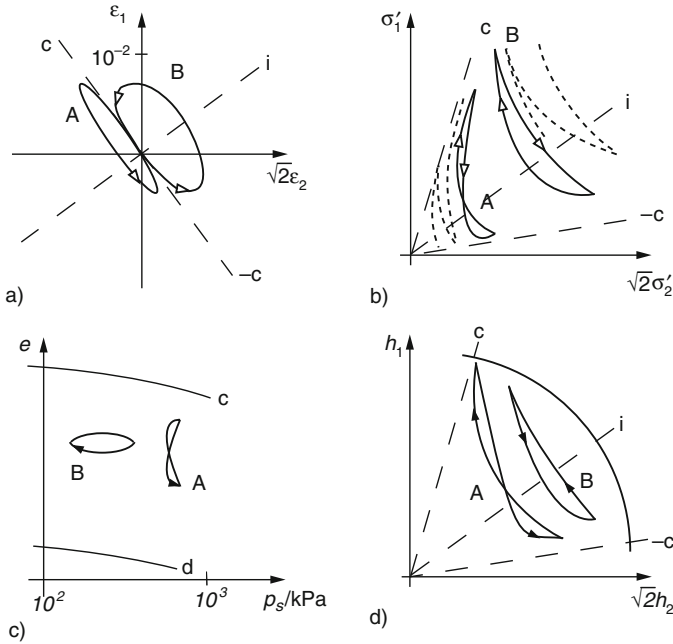


Fig. 4.3.4. Strain cycles (a) of a cylindrical psammoid RSE; associated paths of stress (b), void ratio vs. pressure (c) and hidden state (d) up to state cycles

deformation leads towards a state limit for which the void ratio is determined by the stress components and thus no more needed explicitly.

SOM-states by proportional deformations are thus attractors for the hidden force-roughness. This is indirectly revealed by the differential stress response if it gets determined by stress and void ratio, or by stress only at state limits. For instance, Fig. 2.6.4 shows that near an isochoric state limit (critical state) the response to continued or reversed deformation is determined by the void ratio and thus by the stress components. Figure 2.7.9 indicates the same for isobaric deformations. Less precisely Fig. 2.6.3 shows that near a dilatant state limit the isobaric response to continued or reversed deformations is determined by stress and void ratio.

The concept of simple psammoids without hidden state may be used for monotonous deformations which suffice to sweep out an indeterminate initial force-roughness. As indicated in Fig. 4.3.4 one may assume for simplicity that its intensity gets maximal in transitions to SOM-states. It is also reasonable, though not necessary, to assume that the obliquities of stress and force-roughness agree for SOM-states. This kind of alignment may likewise be assumed for non-cylindrical monotonous deformations with sufficient amount. The objective of Fig. 4.3.4 is to show that the invisible force-roughness may be ignored if it has attained a SOM-attractor by a sufficient monotonous deformation.

If our cylindrical RSE is *cyclically deformed*, Fig. 4.3.4a, the paths of stress (b), void ratio vs. pressure (c) and force-roughness (d) tend to cycles. The initial indeterminacy is swept out when these attractors are attained. The mean pressure tends to a lower value or the skeleton decays, and the mean stress obliquity tends to zero. As this gradual relaxation is assumed to be rate-independent it comes to an end after a sufficient number N of cycles, this assumption means that frequency and waiting intervals do not matter. As shown qualitatively with the plots the asymptotic state cycles exhibit double cycles for each strain cycle. Except for special cyclic changes of void ratio the attained double cycles of stress components and of void ratio vs. pressure resemble a butterfly. One can only guess that a butterfly is also obtained for the hidden state.

Asymptotic *state cycles* due to cyclic deformations should be quantified. We leave aside so big deformations that state limits are attained repeatedly as then our cylindrical RSE loses the desired uniformity and the grains are more easily crushed. As without hidden variables (Sects. 2.2 and 2.6) big amplitudes may be defined by asymptotic stress cycles which approach critical obliquities repeatedly. Small amplitudes may be defined by asymptotic hidden state cycles which never attain their bound, i.e. so that SOM-states are not reached. Small deviatoric strain cycles with constant pressure lead to a maximal densification and to double cycles of void ratio vs. strain (Fig. 2.10.4). Small isochoric strain cycles lead to a minute double stress cycle in case of high density, otherwise the skeleton is relaxed up to a decay (Fig. 4.2.6).

Some further properties can be concluded from the few available reports. Almost all triaxial tests were stress-controlled, in case of closed drainage with controlled stress deviator. Asymptotic state cycles were rarely attained. This is a pity as the findings are less objective and more intricate, and as the reports are often biased by constitutive relations which were not properly validated and calibrated. Nearly hypoelastic responses with small amplitudes have been observed in triaxial setups with bender elements (Fig. 4.2.2b). With deviatoric stress cycles the skeleton stress path tends to a butterfly-like double cycle, and the skeleton can decay repeatedly (Fig. 2.6.6). The gradual reduction of the mean pressure is smaller just after some previous deviatoric stress cycles, but their trace is swept out when the stress obliquity gets almost critical.

Cyclic attractors were approached, but not reached in isobaric triaxial tests (Fig. 4.2.3). The plots of stress ratio vs. strain deviator are nearly the same for an initially loose sand without and with a precompression (Pradhan et al. 1989). This indicates that the trace of a precompression is swept out by a monotonous deformation of sufficient amount. The last two hysteresis loops were nearly the same without and with precompression, and a state cycle was not quite reached as the cumulative densification was not completed. Continuations of such tests up to periodic responses would be rewarding as the attractors would only depend on the chosen amplitude and mean pressure.

Ratcheting of a cylindrical psammoid RSE is represented in Fig. 4.3.4. The strain path (a) is composed of cyclic and monotonous isochoric straining. The

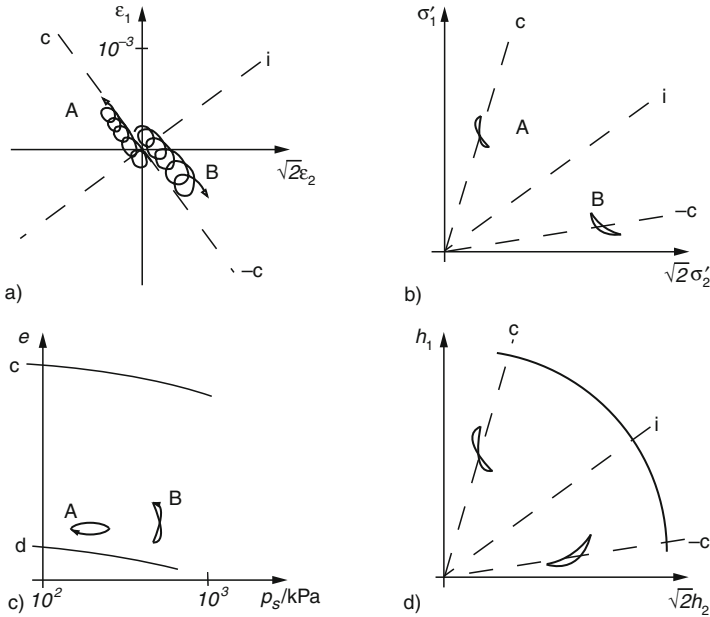


Fig. 4.3.5. Ratcheting (a) of a cylindrical psammoid RSE with smaller (A) and bigger volume changes (B), associated paths of stress (b), void ratio vs. pressure (c) and hidden state (d)

stress path (b) tends to a lenticular loop which touches a critical obliquity. The path of void ratio vs. pressure (c) tends to a lenticular loop well below the critical line. The path of force-roughness (d) should also tend to a lenticular loop which touches the bound and has the same average obliquity as the stress. One may call a stationary ratcheting strong if the stress obliquity varies strongly, and mild otherwise. It could be further quantified by the ratios of stepwise strain decrease and increase for deviatoric and volumetric parts. One may call such a cumulative deformation *intermittent creep*, and a transitory reduction of average stress *intermittent relaxation*.

Transitions to state cycles by cyclic deformation or ratcheting can also be expected for *cuboidal deformations*, but were scarcely observed. Representations with deviator planes as for solids in Figs. 4.1.9 and 4.1.10 may be qualitatively adequate, but cannot suffice. With a constant average void ratio the pressure p_s will first decrease or increase according to the void ratio e , and then pulsate with twice the frequency of deformation pulses. With constant p_s the void ratio will first decrease or increase according to the onset, and then pulsate with double frequency. Figure 2.8.3 indicates the transition to an attractor with so big deformations that a succession of SOM-states may be assumed, thus a hidden force-roughness is possibly not needed.

The database is better for *shearing* with reversals although this can hardly be uniform. It may suffice to plot the two easily visible stress components

(Sect. 2.9) although the additional stress ratios are no more determined by them as for monotonous shearing. It is reasonable to assume also four components for the hidden force-roughness, plotting only two of them does not mean that the other two are determined in general. *Cyclic shearing* (Fig. 4.3.6a) will lead to a symmetric stress cycle (b) and a cycle of void ratio vs. pressure with a relative void ratio near the lower bound (c). The hidden state should also tend to a symmetric cycle (d), and should touch its bound repeatedly if the amplitude suffices to attain SOM-states temporarily. Big amplitudes can be defined by temporarily critical stress obliquities. The ratio of volumetric and deviatoric strains could be further specified for cases in between isochoric and isobaric evolutions. Transitions to attractors exhibit intermittent relaxation.

Test reports with pressure control provide a further support. The isobaric tests shown in Figs. 2.10.1 and 2.2.3 imply temporary SOM-states due to sufficient amplitudes, and a gradual densification except for big amplitudes with a low relative void ratio. Attractors could not be attained with the employed increasing amplitudes, but the path in Fig. 4.2.3e tends to a butterfly. Figure 2.10.3 indicates approaches to an attractor with moderate amplitudes and shows an asymptotic butterfly of void ratio vs. shearing. The transition may be called contractant intermittent creep, its dependence on amplitude and pressure may serve for quantification of constitutive models. Resonant column tests (Fig. 4.2.1) imply small amplitudes and a periodic response after a transition. The small hysteretic damping for small amplitudes suggests a rate-independent nearly hypoelastic behavior. Huber (2010)

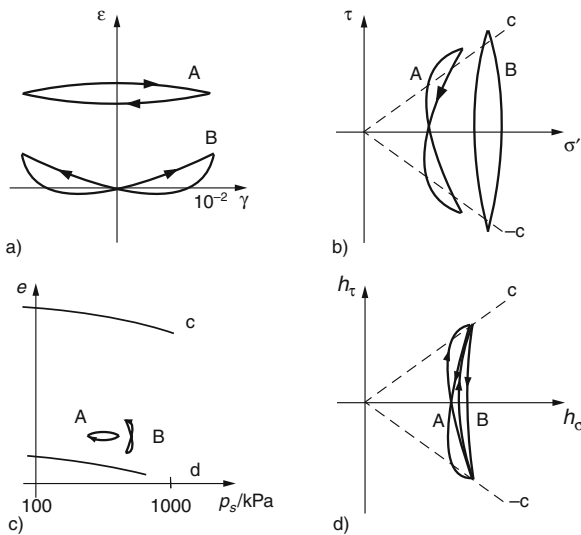


Fig. 4.3.6. Shear cycles with big amplitude (a) lead to state cycles including state limits: stress components (b), void ratio vs. pressure (c) and hidden state (d) in nearly isochoric (A) and isobaric (B) evolutions

observed a gradual densification with constant pressure up to an amplitude-dependent saturation, and double cycles of void ratio even with small amplitudes. Richter (2006) observed pulsating skeleton pressures after a reduction with saturated undrained corundum powder in resonant column tests with small amplitudes. This confirms the postulated intermittent relaxation up to an attractor with low pressure and force-roughness.

Shear ratcheting (Fig. 4.3.7a) can lead to lenticular stress cycles (b), cycles of void ratio vs. pressure below critical states (c) and asymmetric cycles of force-roughness (d). Critical stress obliquity and maximal force-roughness are repeatedly attained, the transversal components change sign in case of big amplitudes. The attractor may be named stationary intermittent creep, this is an objective substitute of Castro's (1975) 'cyclic mobility'. Depending on initial stress and void ratio transitions exhibit an intermittent relaxation or a built-up of mean skeleton stress. Figure 2.10.7 serves for validation: an almost stationary isochoric ratcheting is attained after a gradual relaxation up to a lenticular stress cycle with low relative void ratio. A bigger uniform shearing could be obtained with a thin layer (Fig. 2.9.8) or an annular sample (Fig. 2.9.9). It is reasonable to assume then coaxiality of average stretching, stress and force-roughness. Huber (2010) notes that sand samples in resonant column tests with axial traction would be gradually extended. This kind of ratcheting is composed of cyclic shearing and isochoric stretching with constant anisotropic mean pressure.

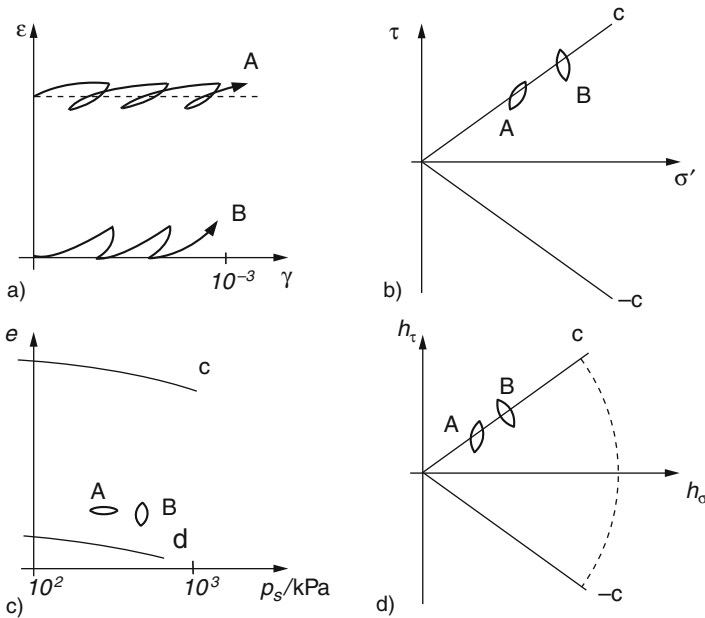


Fig. 4.3.7. Shear ratcheting (a) with smaller (A) or bigger volume changes (B) leads to state cycles of stress (b), void ratio vs. pressure (c) and hidden state (d) asymptotically

Summing up, the skeleton response to many quasi-static reversals can be captured with rate-independent asymptotic state cycles including the hidden force-roughness, transitions to them may be interpreted as intermittent creep or relaxation. An unknown initial force-roughness is swept out by suitable deformations up to attractors, thus the force-roughness gets determined although it cannot be observed. Cyclic deformations cause a gradual loss of the mean stress deviator, whereas the mean skeleton pressure can tend to a decay or to a lower stationary value. Ratcheting leads to a lower than critical mean stress obliquity, whereas the mean pressure can increase or decrease according to the void ratio. Asymptotic state cycles exhibit pulsations of pressure or void ratio with twice the frequency of reversals, this could also hold true for the hidden force-roughness.

4.4 Elastoplasticity with back stress

We consider first psammoid RSEs with cylindrical symmetry. According to Manzari and Dafalias (1997) they may have the following elastoplastic properties, Fig. 4.4.1. A narrow conical elastic range is assumed with its apex at the origin in the plot of σ'_1 vs. $\sqrt{2}\sigma'_{s2}$ (a). Its mean direction ψ_α is the only internal state variable, it may be called *back stress direction*. The cone width is assumed to be a material constant, which is rather arbitrary as sand has at best an infinitesimal elastic range.

Within the elastic range the hypoelastic relations

$$\begin{aligned}
 \text{(a)} \quad \dot{\varepsilon}_1 - \dot{\varepsilon}_2 &= \dot{\varepsilon}_1^e - \dot{\varepsilon}_2^e = G_r(p'/p_r)^m (\dot{\sigma}_{s1} - \dot{\sigma}_{s2}) \\
 \text{(b)} \quad \dot{\varepsilon}_1 + 2\dot{\varepsilon}_2 &= \dot{\varepsilon}_v = \dot{\varepsilon}_v^e = K_r(p'/p_r)^m (\dot{\sigma}_{s1} + 2\dot{\sigma}_{s2})
 \end{aligned}
 \tag{4.4.1}$$

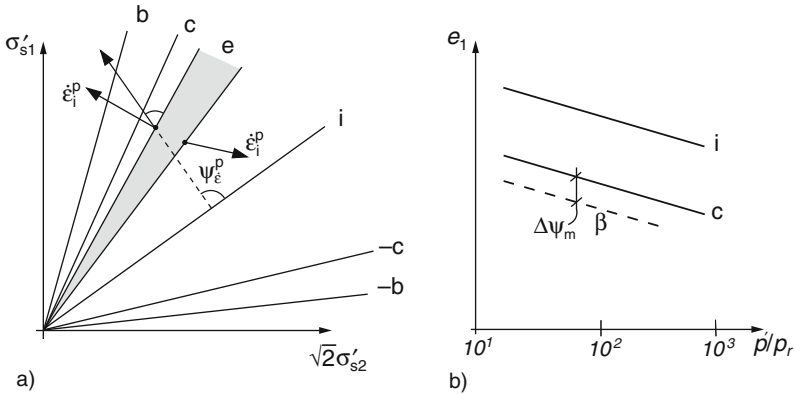


Fig. 4.4.1. Stress ranges (a) and related void ratios (b) of a cylindrical psammoid RSE in the model by Manzari and Dafalias (1997)

are assumed, then strain rates are elastic ($\dot{\varepsilon}_i = \dot{\varepsilon}_i^e$). The exponent is taken as $m = 1/2$, the reference moduli are related with a Poisson ratio $\nu < 1/2$ via

$$K_r/G_r = (1 + \nu)/(1 + 2\nu) \quad . \quad (4.4.2)$$

The reference pressure in (4.4.1) is chosen at will, e.g. $p_r = 100\text{kPa}$. Equation (4.4.1a) suits to (4.2.1), thus the dependence of G_r on e could be allowed for, but the anisotropy explained with Fig. 4.2.2 is neglected. Equation (4.4.2) was also used by Pradhan et al. (1989) for the evaluation of triaxial test results which are shown in Sect. 4.2. As outlined with Fig. 4.2.3 the parameters in (4.4.1) cannot be determined precisely: an elastic range does not really exist, its choice is inevitably arbitrary.

Plastic strain rates $\dot{\varepsilon}_i^p = \dot{\varepsilon}_i - \dot{\varepsilon}_i^e$ occur when the stress point leaves the elastic range. Two flow rules are assumed for the ratio $\dot{\varepsilon}_2^p/\dot{\varepsilon}_1^p$, or the direction ψ_ε^p instead (Fig. 4.4.1a). Rowe's (1962) stress-dilatancy rule (2.2.20) is taken for deviatoric loading, i.e. for increasing $|\psi_s|$. A contractancy of bigger amount than the dilatancy for loading is assumed for deviatoric unloading, i.e. a bigger $|\psi_\varepsilon^p|$ for decreasing $|\psi_s|$. In both cases ψ_ε^p depends on ψ_s , but not on e . This double flow rule corresponds to what Pradhan et al. (1998) found by triaxial tests with reversals, cf. Fig. 4.2.3.

Two hardening rules are needed for volumetric and deviatoric parts. Assuming isochoric grains the void ratio changes with the skeleton volume by (2.2.10) as for simple psammoids. The back stress angle ψ_α changes alongside with the one of stress in case of plastic deformations by a relation of ψ_α with ψ_α , ψ_s and the state parameter ψ_e shown in Fig. 4.4.1b which replaces e . An increase of $|\psi_\alpha|$ is limited by the CSSM bounding cone for the actual e , it gets wider by contraction. Plastic strain rates for stress paths with constant direction ψ_s inside the CSSM bounding cone are neglected in Manzari and Dafalias' (1997) model. This is completed by an interpolation with the requirement of continuous elastoplastic transitions (consistency condition).

Gajo and Muir Wood (1999) proposed an extension of this model. Using the CSSM-frame for state boundaries, they work also with Been and Jefferies' (1985) state parameter and the hypoelastic relations (4.4.1). The elastic range consists of a cone as in Fig. 4.4.1a and a cap like the one by CSSM. Two different flow rules are again employed for the cone flanks, the related hardening rules are kinematic and volumetric. Additional flow and hardening rules are proposed for the assumed cap, they depend on e and p' . The back stress has thus one more component than the model introduced with Fig. 4.4.1. In both models the back stress characterizes an elastic range inside the one by CSSM, thus they resemble Mróz' (1967) model for solids (Fig. 4.1.8). Interpreting the back stress as a representation of force-roughness, the one shown with Fig. 4.4.1 neglects the barotropy for the hidden state as for a solid (Sect. 4.1), whereas this barotropy is captured by Gajo and Muir Wood (1999).

Pestana and Whittle (1999) propose similar relations. In a stress plane the elastic ranges are bounded by a bullet-like curve as in Fig. 2.3.2b. Skew lemniscates are employed so that tensile stresses are excluded, and so that critical

stress obliquities correspond to the same friction angle for axial shortening and lengthening. The direction of plastic strain rates (flow rule) is associated (normality rule) for increasing pressures, and non-associated by different stress-dilatancy relations for increasing and decreasing stress obliquities. Changes of the back stress values, which characterize the variable elastic range, are related with plastic strain rates by kinematic and volumetric hardening rules. Hypoelastic relations like (4.4.1) are assumed for the elastic range. As always with elastoplastic relations the amount of plastic strain rate is determined by the continuity of response for elastoplastic transitions (consistency).

Algebraic representations of such elastoplastic relations with back stress (elp- α) are intricate already in case of cylindrical symmetry. Publications are rarely so tractable that one could write a computer code, and it is difficult to discover subtle defects. Variants were proposed with improvements, but it is hard to understand them in all detail. Given a complete and consistent set of equations or even a computer code, one is still left alone with the calibration of material parameters. Given a computer code and a realistic range of parameters, however, one could judge such constitutive relations *more geometrico* by means of attractors. The following plots were produced by Niemunis and Prada (2010) with a more recent elp- α by Taiebat and Dafalias (2007), called *Sanisand*, which works with a second tensorial hidden variable and had to be corrected in some details for getting feasible. Authors of similar theories should provide software with instructions in their homepage so that potential users can judge the range of validity without getting confused by intricate algebra and numerics. If simulated attractors are realistic they may be used for the calibration of parameters.

Evolutions by elp- α with *proportional deformations* look like Fig. 4.3.6. The asymptotic state limits are the same as without back stress (Sect. 2.3). A plot of void ratio vs. log pressure shows the evolution of two key state parameters, but not the one of back stress. A plot of back stress obliquity vs. stress obliquity would reveal a gradual adaption well before state limits are attained. This means that the rather arbitrary initial back stress is swept out by a sufficient deformation, thereafter the response gets determinate as is the hidden state.

Turning to *reversals*, we consider first evolutions of saturated cylindrical RSEs with *free drainage*. Figure 4.4.2 shows a simulation of Jefferies' (1997) experiment which was plotted in Fig. 2.6.4. The stress-strain curve (a) and the plot of volumetric vs. axial strain (b) are partly realistic. The deviatoric deformation by un- and reloading is fairly well captured except for the approach to the previous deviator. A peak state with maximal dilation is not obtained as in the experiment. The calculated elastic dilation just after the onset of deviatoric unloading is less realistic than the subsequent contraction with further unloading. The further contraction and the following dilation by reloading is well captured. The elastic dilation just after unloading could be avoided with another hypoelastic relation.

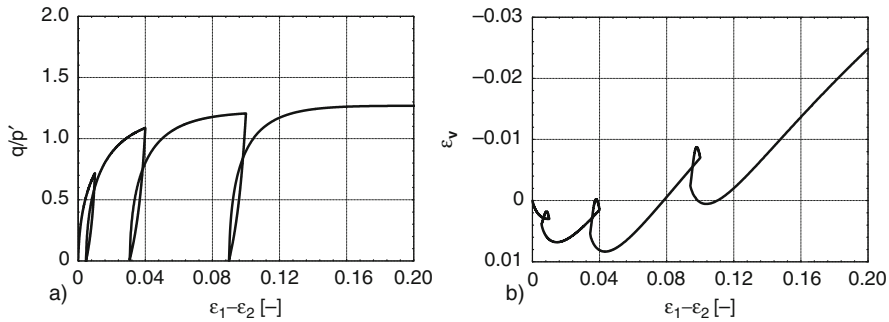


Fig. 4.4.2. Simulation of Jefferies' (1997) drained triaxial tests with reversals (Fig. 2.6.4) with Sanisand (Niemunis and Prada 2010); stress ratio (a) and volumetric strain (b) vs. deviatoric strain

The observed evolutions near the end of reloading are not apt for such evaluations as Jefferies' (1997) triaxial tests imply a loss of uniformity at least near state limits. Slender samples with rough endplates get less deformed near the plates (conical dead zones) and more than the average in the middle (bulges and shear bands, Sect. 14.1). The reported sharp bends at the end of reloading suggest the verge of an elastic range, but the observed simultaneous volume changes are markedly anelastic. It appears that the reloaded sample is stiffer by a kind of eigenstress from the rough plates, and that the sharp bend is due to a spontaneous shear localization. The peak is exaggerated therefore in standard tests. Sanisand cannot reproduce these effects if uniformity is assumed, but simulations without it will be cumbersome or hardly feasible with localization.

Even with short samples and lubricated endplates a loss of uniformity cannot be avoided near state limits (Sect. 14.1). Wu (1992) obtained similar results as Jefferies (1997) with short samples and lubrication. He did not observe shear bands, but a diffuse bifurcation near the plates (Sect. 14.1). Patterns of shear bands need not appear at the confining membrane, but they arise inevitably with overcritical stress obliquities (Sect. 8.2). Unloading from a state with shear bands means that these are contracted by reverse shearing, this could explain the overall contraction with high stiffness in Wu's and Jefferies' tests. Reloading can lead to a sudden reactivation of dilating shear bands, this could explain the high stiffness before and its sudden drop after the end of reloading observed by both authors. Evaluations without localizations are evidently misleading if they really happen. The polarization needed to determine the thickness of shear bands means a higher force-roughness (Sect. 8.2), this cannot be covered by a hidden variable like back stress in $\text{elp-}\alpha$.

We consider now simulated evolutions of *undrained* saturated cylindrical RSEs. Figure 4.4.3 shows that the findings with *one reversal* by Verdugo and Ishihara (1996), which were plotted in Fig. 2.6.2, can be well reproduced. The

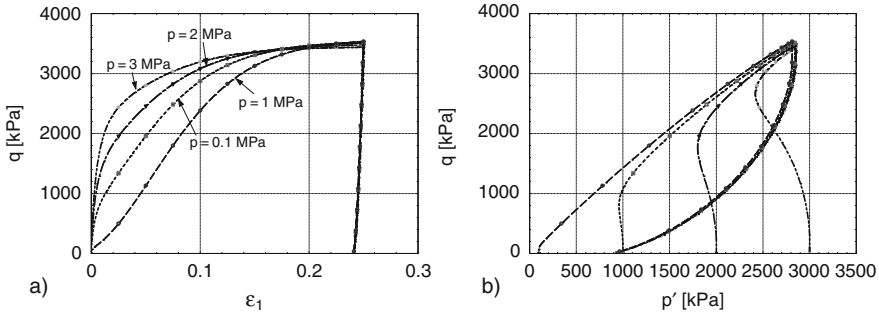


Fig. 4.4.3. Simulation of undrained triaxial tests (Verdugo and Ishihara 1996) with one reversal (Fig. 2.6.2) by means of Sanisand (Niemunis and Prada (2010); deviatoric stress vs. axial shortening (a) and vs. effective mean pressure (b)

onset was isotropic with different pressures for the same void ratio e , the initial back stress was estimated by simulating previous evolutions with drainage. With a suitable e the stress-strain curves (a) depend on the initial pressure as observed, lead to the same critical state and have a single unloading branch. The stress paths (b) start without change of mean pressure p' , exhibit then a reduction of p' and tend to a common point on the critical line as observed. The calculated paths for unloading do not reproduce the immediate pressure reduction, this lack could be removed with a better hypoelastic relation. As outlined with Fig. 2.6.2 the subsequent reduction of p' is reduced by the decreasing membrane penetration, its reproduction by Sanisand is even more realistic than suggested by the plots. Shear bands may be neglected as the evolution remained in the subcritical range.

A simulation of Wichtmann's (2005) undrained triaxial tests with an *alternating deviator* of stress is plotted in Fig. 4.4.4. The skeleton is rather dense and isotropic at the onset, the initial back stress is guessed. The stress path (a) tends to a stationary double cycle with temporary critical obliquities as in Fig. 2.6.6a. As outlined with the same figure this attractor is flatter than the observed one as the latter is distorted by the variable penetration of grains into the membrane. After a deviatoric preloading the transition to this attractor requires more reversals as observed. The deviatoric stress-strain curve exhibits an increasing hysteresis up to a loop with changing sign of curvature between reversals. This was similarly observed by Hyodo et al. (1989), the sample decayed likewise repeatedly in these experiments. The calculated cumulative deviatoric strain appears to be negligible, observed ones were not reported.

The above simulations suggest that 'Sanisand' as representant of $elp-\alpha$ is well validated. It is unable, however, to reproduce the *intermittent relaxation* by small isochoric strain cycles shown in Fig. 4.2.6. Niemunis and Prada (2010) obtain thus first a gradual reduction of stress components, but the mean value p' does not converge to zero for any initial void ratio e . This shortcoming is

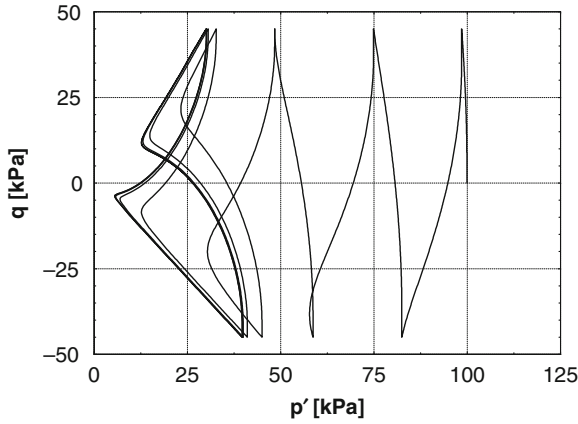


Fig. 4.4.4. Simulation of Wichtmann’s (2005) undrained triaxial tests with symmetric deviatoric stress cycles (Fig. 2.6.6a) with Sanisand (Niemunis and Prada 2010)

due to the assumed p' -dependence of limit void ratios by CSSM (Sect. 2.3) without a lower bound. It could be avoided by using Bauer’s (1996) formula (2.4.1) including the lower bound e_d .

An evolution up to a rather realistic *ratcheting* is obtained by Sanisand with an undrained RSE under a pulsating stress deviator, Fig. 4.4.5. The skeleton cannot decay temporarily with the employed limit void ratios by CSSM, the initial stress may be isotropic, an initial back stress is chosen at will in the allowed range. The stress path (b) tends to a lense which touches the line of critical obliquity, the deviatoric stress-strain curve tends to a stationary ratcheting (a). Both plots resemble Fig. 2.6.7a, b from triaxial tests by Hyodo et al. (1989), but the anelastic response is exaggerated by Sanisand. It appears that the deviations cannot be avoided with the same data set which produces

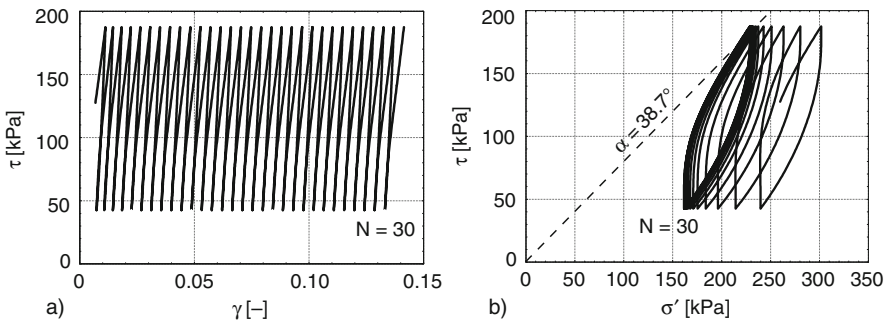


Fig. 4.4.5. Simulation of Hyodo’s et al. (1989) undrained triaxial tests with one-sided deviatoric stress cycles (Fig. 2.6.7) with Sanisand (Niemunis and Prada 2010); (a) stress-strain curve, (b) stress path

a reasonable fit in the first two simulations shown above. The influence of the variable membrane penetration on the attainable agreement is not yet known.

The extension of elastoplastic relations with back stress to *cuboidal deformations* is straightforward in principle, but intricate in detail. Niemunis and Prada (2010) detected that Sanisand can produce a discontinuous response to changing directions in the deviator plane. This may be attributed to an artificial loss of stability with the intricate equations. Therefore it was not possible to reproduce cuboidal test results with reversals as the ones given in Sect. 2.8. The models by Gajo and Muir Wood (1999) and by Pestana et al. (2002b) cannot be judged in that respect as the papers are not fully tractable and as software for simulations is not freely available.

As *simple shearing* requires four stress components (Sect. 2.9) three back-stress components arise in Sanisand (and a fourth one with a cap). The assumed elastic range is a narrow hyper-cone with constant width and variable axial direction which is bounded by state boundary surfaces. The evolution of the hidden back stress with plastic deformations is modelled by a rather intricate combination of kinematic and volumetric hardening, this could hardly be represented graphically by projections. Two different flow rules are again assumed for increasing and decreasing stress obliquity, with the additional directional freedom this requires arbitrary specifications and caution for changing path directions. As with less degrees of freedom the assumed elastic response depends only on p_s and e , and the intensity of plastic deformations is determined by the requirement of continuity.

Simulations of the *alternating torsion* tests with saturated sand by Pradhan et al. (1989), which were given in Fig. 2.10.1, are shown in Fig. 4.4.6. With loose sand the nested hysteresis loops (a) are fairly well reproduced, but the strain path (b) exhibits an unrealistic sudden change of drift. With dense sand the nested loops are not as well captured (c) and the calculated strain path (d) shows an exaggerated dilation. The latter is due to shear localization for overcritical stress obliquities (Sect. 8.2). The observed interchange of dilation and contraction before and after reversals, respectively, is qualitatively reproduced. This unrealistic change of drift may be attributed to the unstable response mentioned above, it cannot be deduced from or easily removed in the Sanisand equations.

The response of sand to *isobaric shear cycles* as observed by Youd (1972) and shown in Fig. 2.10.3 cannot be reproduced with Sanisand (Niemunis and Prada 2010). This lack could be overcome with a lower bound void ratio e_d . Youd's tests with big amplitudes may be left aside as with them the stress obliquity got repeatedly overcritical so that shear bands arose. His tests with undercritical obliquities, however, may serve as a benchmark attractor as the inevitable non-uniformity is repeatedly reduced by reversals which break force chains.

Niemunis and Prada (2010) simulated also the *isochoric cyclic shear* test with a thick-walled cylinder by Ishihara and Towhata (1983) which was depicted in Fig. 2.10.6. The given alternating deviator without drainage leads

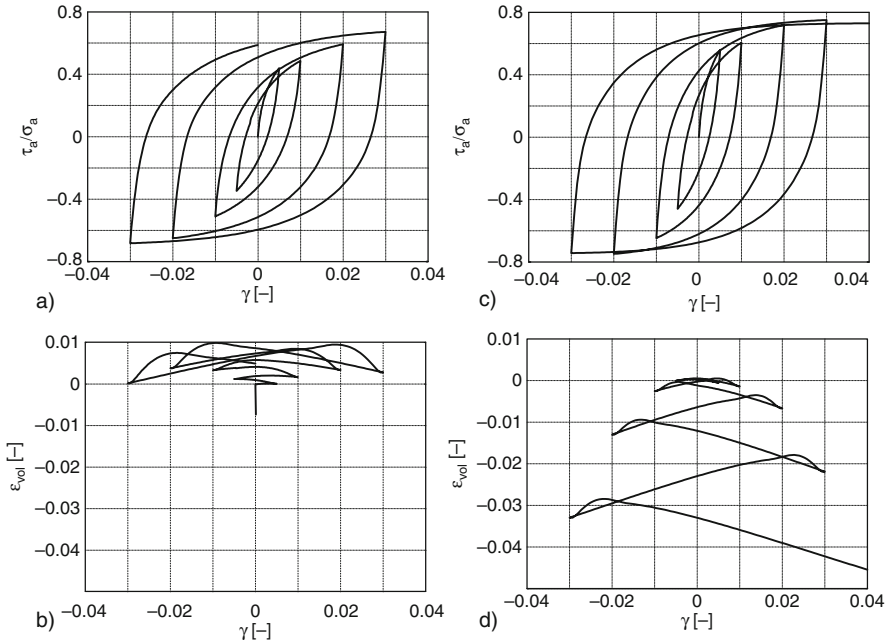


Fig. 4.4.6. Simulation of Pradhan’s et al. (1989) drained hollow cylinder tests with increasing alternating torque (Fig. 2.10.1) with Sanisand (Niemunis and Prada 2010); stress ratio (a) and volume change (b) vs. shear strain for loose sand, same for dense sand (c, d)

to a butterfly with Sanisand, Fig. 4.4.7a, with an apparently realistic stress path. However, as outlined with Fig. 2.6.5 the observed attractor is widened and shifted by the penetration of grains into the membrane. The simulated hysteresis curves (b) are apparently close to the observed ones, but distorted by membrane penetration and temporary decay. Sanisand parameters were apparently adapted to such tests.

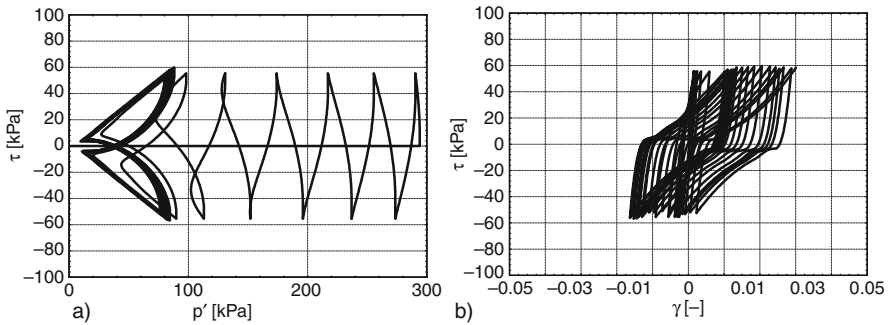


Fig. 4.4.7. Simulation of Ishihara and Towhata’s (1983) undrained hollow cylinder tests with alternating torque (Fig. 2.10.6) with Sanisand (Niemunis and Prada 2010); (a) skeleton stress path, (b) deviatoric stress-strain curve

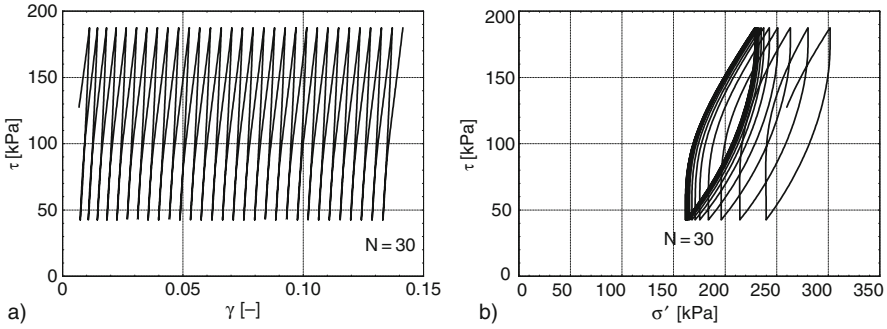


Fig. 4.4.8. Simulation of undrained ratcheting in a shearing device (Andersen and Berre 1999, Fig. 2.10.8) with Sanisand (Niemunis and Prada 2010); (a) stress-strain curve, (b) stress path

It appears that only Andersen and Berre (1999) observed *shear ratcheting* (Fig. 2.10.8), though not uniformly with a device as by Fig. 2.10.2a. This is qualitatively reproduced with Sanisand, Fig. 4.4.8. The calculated plot of shear stress vs. shearing (a) and the simulated stress path (b) could be improved by matching parameters, but such a calibration is debatable with the inevitable non-uniformity. As far as a stationary ratcheting is attainable in such tests the model may be considered as validated. The experiment cannot reveal elastic ranges as the device produces a force-roughness which enhances anelastic effects.

To *sum up*, the range of validity of elastoplastic relations with back stress (elp- α), here represented by a recent version of Sanisand, is rather restricted and could not easily be extended. Drained and undrained triaxial tests with few reversals can be fairly well reproduced, some deviations could be avoided with a better hypoplastic relation. The double flow rule before and after reversals observed by Pradhan et al. (1989) is a part of Sanisand, but there is a strange deviation from these tests which may be attributed to an unintended discontinuity. The simulated approach to butterfly- and lense-like stress cycles by symmetric and asymmetric deviatoric stress cycles, respectively, is apparently realistic, but such observed attractors are distorted by the penetration of grains into the membrane. The intermittent relaxation and densification by isochoric and isobaric deformation cycles, respectively, is not reproduced with elp- α . These attractors could be obtained with limit void ratios as in hyp. The calibration for Sanisand could be improved with attractors. Shear localizations with polarisation (Sect. 8.2) cannot be captured with elp- α .

4.5 Hypoplasticity with intergranular strain

Niemunis and Herle (1997) proposed a hypoplastic model with a hidden variable (abbreviated hyp- δ) for sand-like soils. This is outlined and discussed here first for cylindrical RSEs. The components h_1 and $h_2 = h_3$ of the hidden

state tensor as introduced in Sect. 4.3 are written δ_1 and $\delta_2 = \delta_3$ and named *intergranular strain*. Although this name is contestable we will use it in the sequel as in reports on applications. We will see how δ_i can be interpreted as a kind of force-roughness. Apart from δ_i or h_i the idealizing assumptions for psammoids are taken over from Sect. 2.2.

The amount $\delta = \sqrt{\delta_1^2 + 2\delta_2^2}$ is assumed to have an upper bound, $\delta \leq R$, with a material constant R ranging from ca. 10^{-5} to 10^{-3} for fine to coarse grains and depending on the grain roughness. The relative amount is abbreviated as $\varrho = \delta/R$. The direction of intergranular strain is expressed by

$$\hat{\delta}_1 = \delta_1/\delta \quad , \quad \hat{\delta}_2 = \delta_2/\delta \quad (4.5.1)$$

or by an angle ψ_δ as ψ_s for stress by (2.2.3). Evolutions of the hidden state can be represented by paths in a plane δ_1 vs. $\sqrt{2}\delta_2$, Fig. 4.5.1a. They are related with the strain path as indicated with Fig. 4.5.1b. It is assumed that a proportional strain path (e.g. A) leads to an intergranular strain of maximal amount R and the same orientation, $\psi_\delta = \psi_\varepsilon$, independently of the initial δ_1 and δ_2 . It is further assumed that strain cycles of smaller amplitude than R always lead to cycles of δ_i (e.g. B). These asymptotic properties are achieved by the evolution equations

$$\dot{\delta}_i = \dot{\varepsilon}_i - \varrho^\beta \delta_i \quad \text{for} \quad \delta_1 \dot{\varepsilon}_1 + 2\delta_2 \dot{\varepsilon}_2 > 0 \quad , \quad (4.5.2)$$

and

$$\dot{\delta}_i = \dot{\varepsilon}_i \quad \text{for} \quad \delta_1 \dot{\varepsilon}_1 + 2\delta_2 \dot{\varepsilon}_2 \leq 0 \quad , \quad (4.5.3)$$

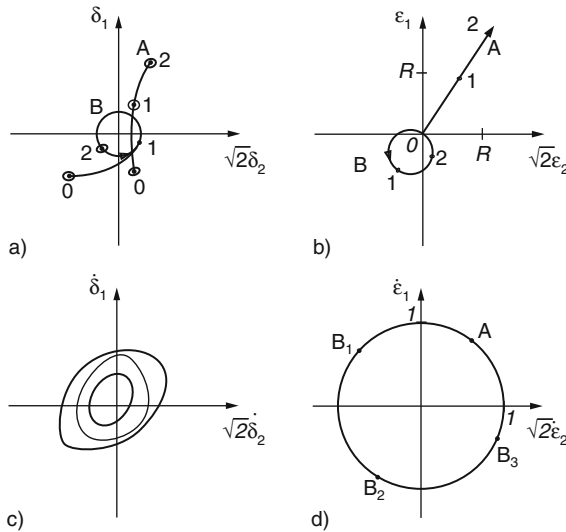


Fig. 4.5.1. Paths of intergranular strain (a) and related strain paths (b); bounded response polars of intergranular strain (c) for unit strain rates (d)

i.e. with a switch function of $\Sigma\delta_i\dot{\epsilon}_i$, $i = 1$ and 2 or 3 and an exponent $0 < \beta \leq 1$.

Cudmani (2010) showed with comparative calculations that β should range from ca. 0.05 to 0.2. The paths in Fig. 4.5.1 reflect these equations, and they have the attractors proposed in Sect. 4.3. This is visible with response polars for $\dot{\delta}_i$ (Fig. 4.5.1c) due to unit strain rates (d) as indicated in the δ_i -plot (a). Bounding curves for maximally and minimally elastic responses are also indicated. With a straight strain path (A) the polars steer the δ_i -path towards a SOM-state (swept-out memory, cf. Sect. 4.3) with $\psi_\delta = \psi_\epsilon$ and $\delta = R$. With a circular strain path (B) the δ_i -path is steered towards a state cycle.

The evolution equations by Niemunis and Herle (1997) for the stress components read

$$\begin{aligned} \dot{\sigma}_{si}/f_s &= \{[\varrho^\chi m_T + (1 - \varrho^\chi)m_R]L_{ij} + \varrho^\chi(1 - m_T)L_{ik}\delta_k\delta_j + \varrho^\chi f_d N_i\delta_j\}\dot{\epsilon}_j \\ &\text{for } \delta_1\dot{\epsilon}_1 + 2\delta_2\dot{\epsilon}_2 > 0 \end{aligned} \quad (4.5.4)$$

and

$$\begin{aligned} \dot{\sigma}_{si}/f_s &= \{[\varrho^\chi m_T + (1 - \varrho^\chi)m_R]L_{ij} + \varrho^\chi(m_R - m_T)L_{ik}\delta_k\delta_j\}\dot{\epsilon}_j \\ &\text{for } \delta_1\dot{\epsilon}_1 + 2\delta_2\dot{\epsilon}_2 \leq 0 \end{aligned} \quad (4.5.5)$$

for $i = 1$ and 2 or 3. The factors f_s and f_d , the matrix L_{ij} and the vector N_i are the same as in (2.4.3) for simple psammoids. f_s is given by (2.4.3) and f_d by (2.4.4), L_{ij} and N_i depend only on the stress direction ψ_s . The relative amount $\varrho = \sqrt{\delta_1^2 + 2\delta_2^2}/R$ and the switch function are the same as in the evolution equations (4.5.2) and (4.5.3) for the intergranular strain components δ_i . Niemunis and Herle (1997) propose a range from ca.1 to 10 for the exponent χ , but Cudmani (2009) found that the narrower range from 0.8 to 1.5 suffices.

In some cases the intricate equations (4.5.4) and (4.5.5) get simpler. For $\delta_i = 0$ and $\delta_1\dot{\epsilon}_1 + 2\delta_2\dot{\epsilon}_2 \leq 0$ they shrink to the hypoelastic relation

$$\dot{\sigma}_{si} = f_s m_R L_{ij} \dot{\epsilon}_j. \quad (4.5.6)$$

As δ_i arises again by (4.5.2) with any deformation this means that hyp- δ implies an infinitesimal elastic range. Cudmani (2009) shows that the factor m_R in (4.5.4) ranges from about 2 to 7. If δ_i has attained a SOM-state with $\varrho = 1$ and $\psi_\delta = \psi_\epsilon$ the stress response by (4.5.4) to a strain rate ψ_ϵ reduces to

$$\dot{\sigma}_{si} = f_s (L_{ij} \dot{\epsilon}_j - f_d N_i D) \quad (4.5.7)$$

with $D = \sqrt{\dot{\epsilon}_1^2 + 2\dot{\epsilon}_2^2}$, i.e. (4.5.4) goes over into the hypoelastic relation (2.4.3). Thus the evolution equations for stress components (4.5.4) and (4.5.5) with intergranular strain constitute a kind of interpolation between hypoelastic and hypoplastic relations. For transverse deformations with $\sum \delta_i \dot{\epsilon}_i = 0$ (4.5.5) shrinks to

$$\dot{\sigma}_{si} = f_s [\varrho^X m_T + (1 - \varrho^X) m_R] L_{ij} \dot{\varepsilon}_j \quad , \quad (4.5.8)$$

which is not hypoelastic except for $\varrho = 0$ as it holds only for the two strain rate obliquities $\psi_{\dot{\varepsilon}}$ with $\sum \delta_i \dot{\varepsilon}_i = 0$. Cudmani (2010) showed that the factor m_T ranges from ca. 2 to 7.

For validation we consider first simulations of triaxial tests with saturated sand as in Sect. 4.4. The hypoplastic parameters are the same as in Sect. 2.6, the parameters for the intergranular strain were chosen in the range given above. Figure 4.5.2 shows a back-analysis of Jefferies' (1997) test with *free drainage* which was shown with Fig. 2.6.3. The plots of stress ratio (a) and volumetric strain vs. deviatoric strain (b) are partly realistic, but in another way than with *elp- α* . The deviatoric stiffness for unloading is overestimated, the reported simultaneous contraction is not reproduced. For reloading the deviatoric stiffness is increasingly underestimated, whereas subsequent volume changes are qualitatively captured. As outlined with Fig. 4.4.2 Jefferies' tests, and also the similar ones by Wu (1992) with smooth endplates, imply a loss of uniformity near state limits so that deviations near the end of reloading cannot be judged by assuming element tests.

Other deviations cannot be avoided by changing the model parameters in the empirically allowed range. One may conclude that a hypoplastic relation with intergranular strain (*hyp- δ*) can capture the response just after reversals from SOM-states, but is less realistic otherwise, in particular for low stress obliquities. In the latter case the real behavior is apparently not hypoelastic as by *hyp- δ* with small relative intergranular strain ρ (and as by *elp- α* with well-adapted back stress), in particular for deviatoric reloading. It appears that the force-roughness, which might be represented by the intergranular strain, is not as strongly reduced by deviatoric unloading in the experiment as by *hyp- δ* .

Turning to evolutions of *undrained* saturated cylindrical sand samples, Fig. 4.5.3 shows a *hyp- δ* -simulation of the experiments by Verdugo and Ishihara (1996) with *one reversal* which were plotted in Fig. 2.6.2a, b. The stress-

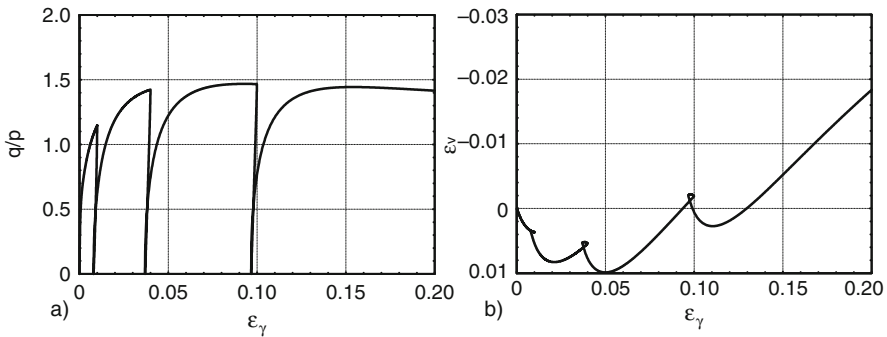


Fig. 4.5.2. Simulation of Jefferies' (1997) test (Fig. 2.6.3) with *hyp- δ* (Niemunis and Prada (2010)); stress ratio (a) and volumetric strain (b) vs. deviatoric strain

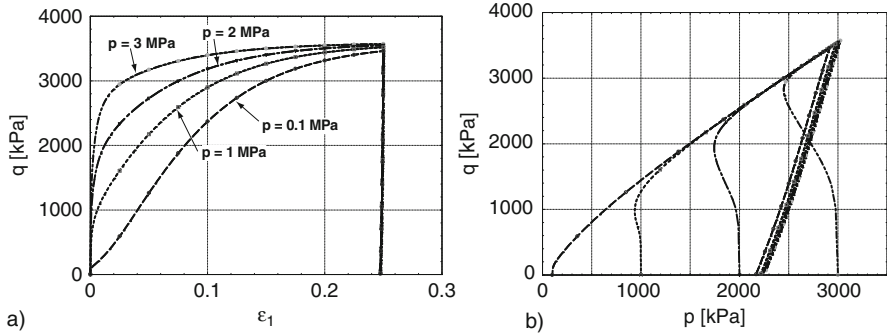


Fig. 4.5.3. Simulation of Verdugo and Ishihara's (1996) undrained triaxial tests (Fig. 2.6.2) with hyp- δ (Niemunis and Prada 2010); (a) deviatoric stress-strain curves, (b) skeleton stress paths

strain curves after different precompressions up to the same void ratio (a) are rather realistic. The single curve just before and after the reversal means that the trace of the isotropic preloading was swept out like in the experiments. The simulated stress paths (b) exhibit first a too weak pressure reduction, but are then realistic up to and after the reversal. As without intergranular strain the pressure reduction just after the reversal is underestimated, this cannot be attributed to the variable membrane penetration. A comparison with Fig. 2.6.2c, d shows that the intergranular strain can improve the hypoplastic simulation, but is not needed close to a critical state.

A simulated evolution of an undrained cylindrical RSE with an *alternating deviator* is shown in Fig. 4.5.4. At the beginning the skeleton is rather dense

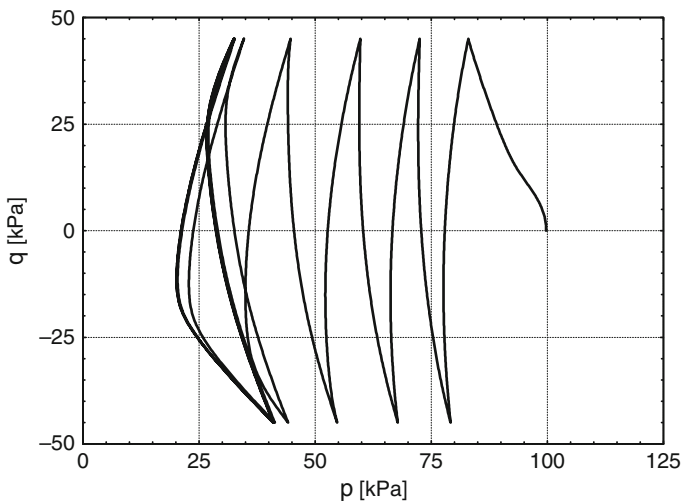


Fig. 4.5.4. Simulation of Wichtmann's (2005) undrained triaxial test with alternating stress deviator (Fig. 2.6.6a) with hyp- δ (Niemunis and Prada 2010)

with an isotropic stress, the intergranular strain is chosen as for a SOM-state. The stress path tends to a double cycle (butterfly) with a reduced mean pressure and temporary critical obliquities. The asymptotic butterfly appears skewer and flatter than in Fig. 2.6.5a from tests by Wichtmann (2005). The transition to a state cycle needs less reversals than observed, this means that cumulative anelastic effects are still underestimated with hyp- δ . The deviatoric stress-strain curve exhibits an increasing hysteresis up to a stationary loop, other than observed this is nowhere concave. The asymptotic loops reported by Hyodo et al. (1989) and by Wichtmann (2005) should not be used for validation and calibration, however, as they are distorted by temporary decay and by the variable penetration of grains into the membrane. The latter should be taken into account for validation and calibration, a decay should be avoided by low enough void ratios.

The *intermittent relaxation* by small isochoric deformation cycles shown in Fig. 4.2.6 is reproduced with hyp- δ (Niemunis and Prada 2010), whereas it is missed with elp- α . It leads to a skeleton decay if the void ratio exceeds the lower bound e_{d0} for vanishing pressure by (2.4.1), otherwise it leads to a butterfly. The simulated intensity of stress reduction is still exaggerated, but not as much as without intergranular strain. It appears that this deviation cannot be avoided by adapting parameters (Prada 2010).

A simulated *ratcheting* of an undrained cylindrical RSE is shown in Fig. 4.5.5. The stress path tends to a thinner and steeper than observed lense, cf. Fig. 2.6.7 by Hyodo et al. (1989) and Fig. 4.2.7 by Ibsen (1994). The deviation can be partly attributed to the variable membrane penetration outlined further above. With a low enough initial relative void ratio the simulated mean skeleton pressure would increase in the transition to the attractor as in Fig. 4.2.8b by Ibsen (1994). The calculated cumulative increase of deviatoric strain with the number of cycles (b) gets linear as observed by Ibsen (1994).

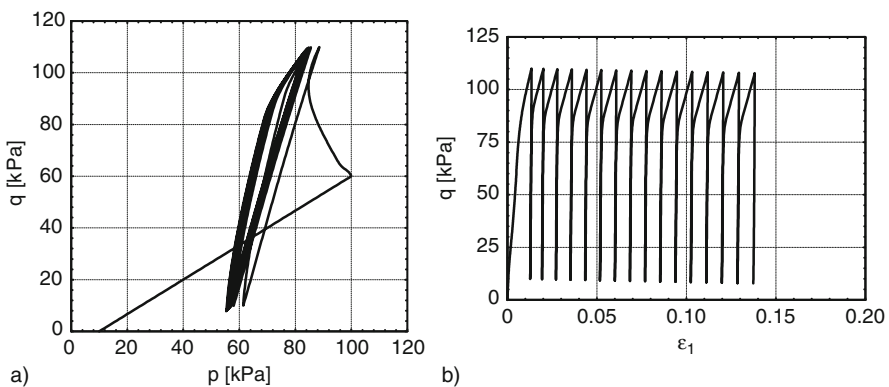


Fig. 4.5.5. Simulation of Hyodo's et al. (1989) ratcheting (Fig. 2.6.7) with hyp- δ (Niemunis and Prada 2010); (a) skeleton stress path, (b) deviatoric stress-strain plot

It is significantly bigger than observed (cf. Fig. 4.2.7d), so cumulative effects are overpredicted by hyp- δ . These deviations cannot be avoided with a better calibration.

The extension of hyp- δ to *cuboidal deformations* is straightforward. Approaches to attractors by deformations without or with reversals look like the ones for cylindrical symmetry if the direction in the deviator plane is rather constant. That was the case e.g. in the experiment shown in Fig. 2.8.2, but this is not apt for a quantitative validation as the manual compensation of grain penetration into the membrane produced an erratic zig-zag. Other than with hyp (Fig. 2.8.5) the isobaric experiment with a deviatoric stress cycle (Fig. 2.8.4) could not be simulated with hyp- δ (Rebstock 2010). This indicates an unintended discontinuous response, but on the other hand the intergranular strain is not needed as a sequence of SOM-states occurred evidently in this case.

The hyp- δ equations get more intricate for *simple shearing*, and then complete graphical representations would be expensive. Proportional deformations lead again to SOM-states for which the intergranular strain is maximal and aligned, and then to state limits as without intergranular strain. Cyclic shearing leads to symmetric cycles of stress and intergranular strain, whereas ratcheting leads to asymmetric state cycles. Such attractors were rarely approached in experimental reports.

Niemunis and Prada (2010) made a back-analysis of Pradhan's et al. (1989) tests with thick-walled cylinders and alternating torque shown in Fig. 2.10.1. For loose sand the nested loops of shear stress vs. strain (Fig. 4.5.6a) and the gradual densification (b) are pretty realistic. For dense sand the nested loops (c) are less realistic, and the gradual dilation (d) is exaggerated. The latter is due to shear localization for overcritical stress obliquities (Sect. 8.2). The observed interchange of dilation before and contraction just after reversals is reproduced. SOM-states with maximal and aligned intergranular strain are repeatedly attained, that's why simulations without intergranular strain are quite similar (Fig. 2.10.2).

Niemunis and Prada (2010) simulated also Youd's (1972) *isobaric cyclic shear* tests which were shown in Fig. 2.10.4. Other than with elp- α the gradual densification leads close to a lower bound void ratio e_d and to an asymptotic butterfly of e vs. shearing, Fig. 4.5.7a. As observed this occurs almost independently of the shearing amplitude, but with exaggerated progression in the simulations (b). Youd's tests with big amplitudes should be left aside because of repeated shear localization and grain crushing. The better simulation otherwise than without intergranular strain (Sect. 2.10) can hardly be improved with modified parameters.

A further simulation with hyp- δ by Niemunis and Prada (2010) refers to the *isochoric cyclic shear* test by Ishihara and Towhata (1983) which was shown in Fig. 2.10.6. The effective stress path due to an alternating stress deviator (Fig. 4.5.8a) leads to a flatter than observed butterfly after an intermittent relaxation. The simulated hysteresis loops (b) remain convex whereas

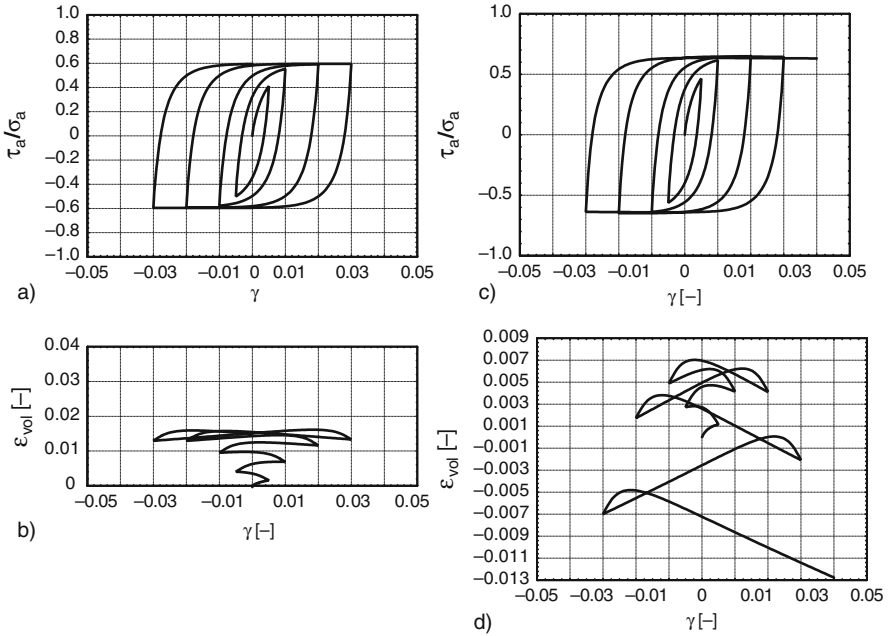


Fig. 4.5.6. Simulation of Pradhan’s et al. (1989) shear test with reversals (Fig. 2.10.1) by hyp- δ (Niemunis and Prada 2010); stress ratio (a) and volumetric strain (b) vs. shear strain for a dense sand, same for a loose sand (c, d)

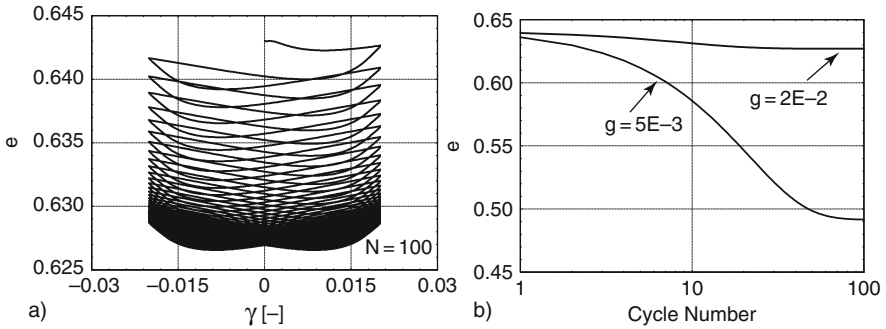


Fig. 4.5.7. Simulation of Youd’s (1972) findings (Fig. 2.10.4) with hyp- δ (Niemunis and Prada 2010): (a) void ratio vs. shearing, (b) void ratio vs. number of cycles for a small and a bigger amplitude

the observed ones get temporarily concave. The deviations can be partly attributed to the variable penetration of grains into the membrane, and possibly also to a temporary skeleton decay. A better validation and calibration could be obtained by taking into account the membrane penetration, and by means of a so low void ratio that the skeleton cannot decay.

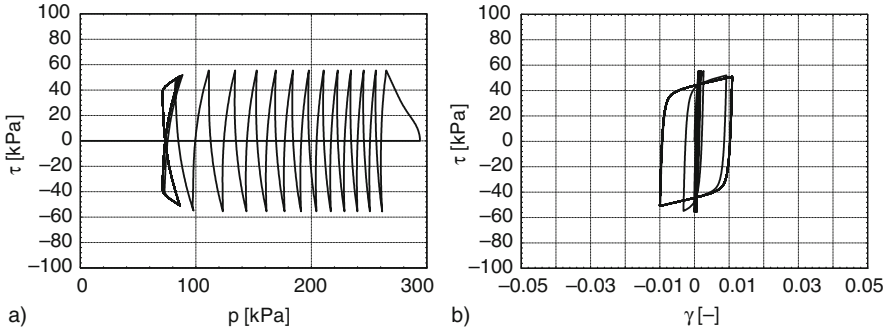


Fig. 4.5.8. Simulation of Ishihara and Towhata's (1983) undrained cyclic shear tests (Fig. 2.10.6) with hyp- δ (Niemunis and Prada 2010): (a) skeleton stress path, (b) deviatoric stress-strain curve

To *sum up*, hypoplastic relations with intergranular strain (hyp- δ) are apt to reproduce at least qualitatively key experiments with sand under reversals. As far as asymptotic state cycles can be deduced from test reports it appears that double loops can be fairly well reproduced for isobaric and isochoric cycles of deviatoric deformations, and also lenticular stress loops for isochoric ratcheting. Lower bounds of relative void ratios can be approached with hyp- δ as in isobaric and isochoric experiments, which is impossible with present elp- α . The calibration of parameters is feasible, but with it an exaggerated progress of intermittent creep and relaxation cannot be avoided. The impossibility to simulate the cuboidal test with deviatoric cycles shown in Fig. 2.8.4 indicates an artificial instability. The equations are less intricate than the ones of elp- α , but can likewise only be judged by numerical simulations. The spontaneous localization and polarization (Sect. 8.2) in the overcritical range is not captured.

4.6 Seismically activated viscous effects

Consider a block upon a plate with a lower inclination β than the friction angle φ_w , Fig. 4.6.1a. If the plate is kicked erratically from its sides with frequency f_c the block moves downwards in irregular steps (b) with average-free sideways fluctuations. This kind of *seismic creep* or erratic ratcheting can be observed easily, and could be simulated by solving the equations of motion with dry friction and random excitation. Vielsack (1991) showed that for a slight periodic shaking the motion can be captured with a linear *pseudo-viscosity* which is proportional to the frequency f_c of shaking. Evidently the motion stops without shaking as the block stands due to $\beta < \varphi_w$.

The average kinetic energy E_k transmitted per cycle to the block may be interpreted as a kind of *seismic temperature*. In case of erratic shaking

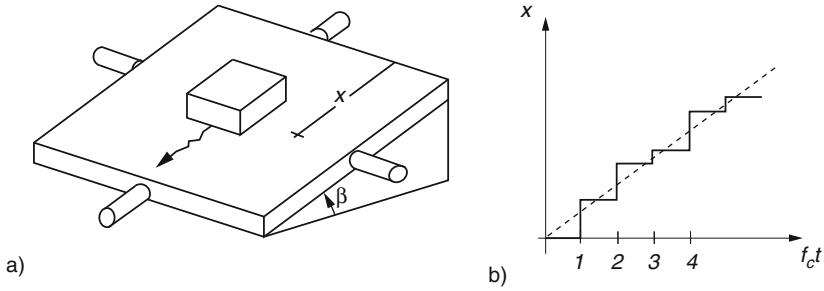


Fig. 4.6.1. Erratic displacements (b) of a block upon a shaken incline (a)

a heuristic analogon of (3.1.5) for thermally activated dislocations may be written as

$$v = a f_c \frac{E_k}{E_a} \sinh \left(\frac{\Delta F - E_a}{b E_k} \right). \tag{4.6.1}$$

Therein v denotes the average sliding velocity, and f_c the frequency of shaking. The activation energy E_a for the onset of sliding is proportional to $W \tan \varphi_w$ with the weight W of the block. The shift energy ΔF according to the loss of height is proportional to $W \tan \beta$, a and b are empirical constants. For small amplitudes with $\Delta F/bE_k < ca. 0.5$ the v by (4.6.1) gets proportional to ΔF , this corresponds to the linear viscosity by Vielsack (1991). For bigger amplitudes (4.6.1) can be replaced by

$$v = \frac{1}{2} a f_c \frac{E_k}{E_a} \exp \left(\frac{\Delta F - E_a}{b E_k} \right). \tag{4.6.2}$$

This corresponds to (3.1.7) for thermally activated creep, but now the frequency f_c is exogeneous from shaking and not endogeneous from elastic oscillations. If the shaking is totally erratic the configurational entropy gets maximal so that the exponential probability distribution by (3.1.3) is justified.

The transition to granular materials is anything but straightforward. Barkan (1962) proposed a *vibro-viscosity* by means of experiments. A metal sphere sunk into dry sand in a box when this was shaken with an acceleration $a > g$. Shearing with constant pressure was enhanced by shaking the base, its acceleration reduced the resistance of the grain skeleton. Barkan could not quantify his findings by constitutive relations. His first experiment can be explained by means of a *granular gas* (e.g. Pöschel and Luding 2001). Therein grains collide incessantly so that their number per unit of volume, i.e. the gross density, is lower than for a loose skeleton. The average kinetic energy per unit of mass is called *granular temperature* T_g . Analogously with a molecular gas an equation of state

$$p_g v_g = a_g T_g \tag{4.6.3}$$

is postulated with pressure p_g and specific volume v_g of the granular gas. The factor a_g , which replaces the universal gas constant R , is adapted to pressure and shaking of walls which serve as a kind of granular thermostat. Other than a molecular gas a granular gas comes to rest in a closed box when this is fixed. There is no adiabatic equilibrium as the encounters of grains are not conservative, therefore seismic energy cannot be stored like heat. A linear viscosity was proposed for a sheared granular gas by taking over Einstein's relation for a molecular fluid. As experiments are hardly possible numerical simulations were made to get more insight. The statistical mechanics of a granular gas is not the same as for a molecular one, relations like (4.6.3) are rather heuristic and should be checked by experiments.

Various attempts were made with a granular temperature T_g for denser granular materials. Haff (1983) proposed relations for *granular fluids* with linear viscosity and T_g . Jaeger and Nagel (1996) speak of *granular solids* in case of grain skeletons. Herrmann (1993) defined T_g as the chaotic part of the kinetic energy for granular solids and employed the formalism of equilibrium thermodynamics. In another approach Edwards and Oakeshott (1989) worked with entropy and changes of density, but did not completely specify equations of state. Kondic and Behringer (2004) proposed a T_g in proportion to the elastic energy of spatial stress fluctuations in a skeleton. This kind of T_g , which is justified by numerical simulations and observed fluctuations of stress in a ring shearing device (Behringer and Miller 1997), can be frozen in a resting skeleton and changes only during deformations, so it is rate-independent. It corresponds to the force-roughness which was introduced in Sect. 4.3, so this may be understood as latent seismicity.

Gudehus (2006) proposed *seismo-hypoplastic* relations (s-hyp) for shaking with small amplitudes. The average kinetic energy represented by T_g is assumed to play the same role as T in visco-hypoplasticity (Sect. 3.3), i.e. reference rate D_r and viscosity index I_v are taken as proportional to T_g . For monotonous evolutions an endogeneous T_g is assumed to be a fraction of the dissipated energy per unit of deformation, and thus proportional to the mean skeleton pressure p_s . Results of biaxial tests by Matsushita et al. (1999) can be matched by v-hyp with suitable D_r and I_v . The observed response to jumps of strain rate (argotropy), constant mean stress (creep) and fixing the shape (relaxation) was apparently *seismically activated*. The activation energy estimated from the required $I_v = 0.02$ by (3.5.5) is lower than the one known for quartz, so there is not only thermal activation. Baro- and pyknitropy could be reproduced by means of argotropic limit void ratios as in v-hyp. The critical friction angle φ_c is not argotropic, this is confirmed by shear tests for two decades of shearing rates by Hungr and Morgenstern (1984).

The granular temperature T_g is revealed by an *acoustic emission*, this was observed in triaxial tests with a dry corundum granulate by Huber and Wienbroer (2005), Fig. 4.6.2a. Keeping σ_2 constant by vacuum, every increase of σ_1 causes a noise which may be attributed to the buckling of force chains (Figs. 4.3.1 and 4.3.2). Figure 4.6.2b exhibits a fluctuation of σ_1 with constant

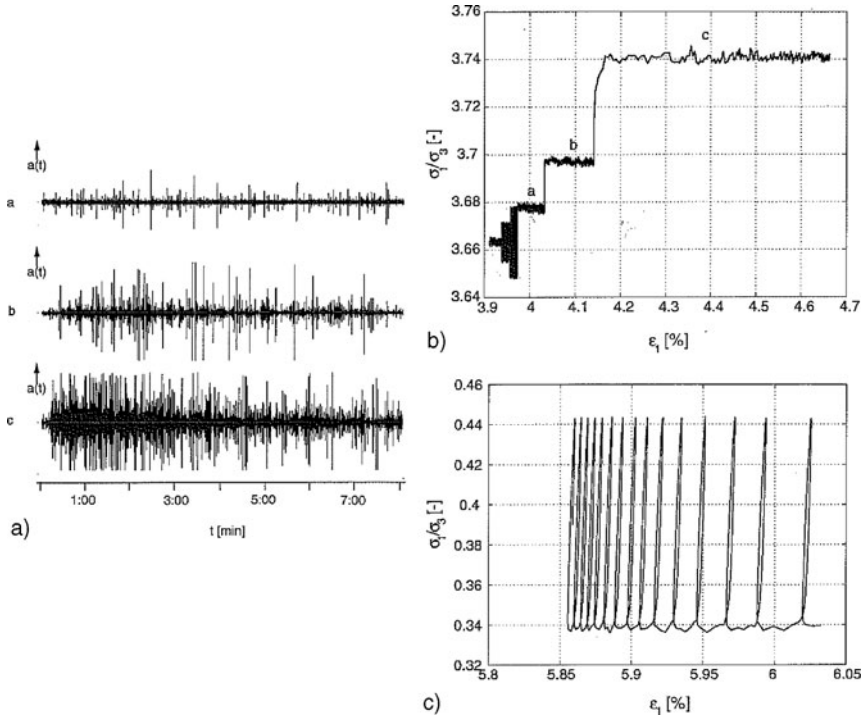


Fig. 4.6.2. Results of triaxial tests with a corundum granulate (Huber and Wienbroer 2005): acoustic emission vs. time (a) for a low (*above*) and a nearly critical stress deviator (*below*), axial strain with axial stress cycles for average axial shortening (b) and stretching (c)

σ_2 which is reduced by densification. The seismic activity gets more marked when σ_1/σ_2 approaches the critical amount by (2.2.15) whereas the void ratio is lower than critical. A stationary flow could not be attained uniformly as the sample bulged with increasing seismicity, a constant σ_1 could not be maintained any more and shear bands arose.

Figure 4.6.2b shows the response to axial stress cycles with a small amplitude as compared with the average $\bar{\sigma}_1$. They cause a kind of ratcheting or intermittent seismic creep. According to the flow rule by Wichtmann et al. (2006) for cumulative deformations due to small stress cycles the creep is contractant for lower than critical average ratios $\bar{\sigma}_1/\bar{\sigma}_2$ (cf. Sect. 4.2), thus the creep rate is reduced by densification. As Matsushita et al. (1999) and Huber and Wienbroer (2005) found it impossible to keep σ_1 precisely at a desired value, and to impose precisely small σ_1 -cycles. This may be attributed to the random buckling of force chains in the skeleton which elude an exact control. Figure 4.6.2b exhibits a smooth transition between endogeneous and exogeneous fluctuations, the average creep is apparently the same without

and with imposed cycles. As without stress cycles the skeleton comes to rest after a short while under stresses with a lower than critical average stress ratio.

Figure 4.6.2c shows the response with a pulsating $\sigma_1 < \sigma_2$, i.e. with an average axial extension. Again acoustic emission and seismically activated creep increase when the average stress obliquity approaches the critical amount by (2.2.15), come to rest by densification and are enhanced by σ_1 -cycles. The latter can iron out a bulge from previous axial shortening: the sample got almost cylindrical again and shear bands were apparently swept out (cf. Sects. 8.2 and 14.1). Overcritical stress ratios as by (2.2.17) were not attained so that necking and new shear banding up to a loss of control were avoided (Sect. 14.1).

An exogeneous granular temperature T_g is proposed for imposed cycles in the seismo-hypoplastic relations (s-hyp) by Gudehus (2006). With a constant frequency f_c the time t can be replaced by the number of cycles $N = tf_c$ (cf. Fig. 4.6.1b). Thus the cumulative deformation ϵ_c increases by

$$\epsilon_c = bT_g N \exp\left(\frac{p'_s/p_e - 1}{I_v}\right) \quad (4.6.4)$$

in case of a critical average stress ratio, with a constant prefactor b and a viscosity index I_v which is proportional to T_g . Apart from renaming (4.6.4) corresponds to (4.6.2). The equivalent pressure p_e is lower for a higher exogeneous T_g , similarly limit void ratios of a peloid are higher for a higher temperature T (Fig. 3.5.5).

In case of subcritical stress obliquities the seismically activated creep is contractant, and thus reduced by densification if the average stress is constant. Taking over (3.2.6) for contractant creep the gradual densification may be captured with $I_v \sim T_g$ and $N = tf_c$ by

$$e = e_0 - c_1 \ln(1 + c_2 T_g N) \quad . \quad (4.6.5)$$

Therein e_0 is the initial e , and the factors c_1 and c_2 depend on the average stress ratio. The direction of seismic creep rates is given by the flow rule of Wichtmann et al. (2006) shown in Fig. 4.2.5 which is part of s-hyp. For overcritical stress obliquities the same argument leads to a seismic creep collapse after a cumulative dilation (cf. Sect. 3.2). With a constant average shape of the skeleton s-hyp predicts a reduction of p_s with the number of cycles N by

$$p_s \approx p_0(1 - cT_g \ln N), \quad (4.6.6)$$

with $p_0 = p_s$ at the onset and a constant c . This can be derived from (3.2.7) with $f_v = \text{const}$, $I_v \sim T_g$ and replacing the time t by N/f_c .

These relations with N are qualitatively confirmed by observations, but can hardly be quantified. An average stationary ratcheting as by (4.6.4) could be achieved in a ring shear device or by shearing a thin layer (Figs. 2.9.8 and 2.9.9). The gradual densification by (4.6.5) appears reasonable, but would not

come to a saturation. A weaker accumulation occurs for a lower p_s/p_e , i.e. a lower e/e_c , but tests as shown in Fig. 2.10.3 do not suffice to quantify it. The seismic relaxation by (4.6.6) corresponds to the observed p_s -reduction of cyclically deformed saturated sand without drainage (Fig. 4.2.6), but again only qualitatively and without an asymptote as observed. The rate-independence implied by the relations with N is often observed and taken for granted, but refuted e.g. by Duttine et al. (2008).

A more serious shortcoming of s-hyp is the difficulty to determine T_g and the quantities D_r , I_v and p_e depending on it. The seismically dissipated energy, including exogeneous fractions, could be estimated from experiments, and cumulative changes of e could be measured more precisely than until now. This could also be achieved with controlled random fluctuations of σ_1 and σ_2 in a sophisticated triaxial setup. One could thus check whether the same accumulation occurs with different erratic cycles which provide the same average seismic energy. The control gets difficult or even impossible with small amplitudes, and also in the vicinity of critical stress ratios as then the sample tends to deterministic chaos. A further problem is the specification of the reference strain rate D_r . It should be endogeneous without and exogeneous with imposed cycles, but actually there is a mixture of both. The choice of an external frequency f_c is often arbitrary, real seismic events have a rather fractal spectrum as the acoustic emission during monotonous deformations (Tillemans and Herrmann 1995).

Viscous effects as reported by Matsushita et al. (1999) are overestimated for two reasons. First, the grease between the membrane around a sand sample and at translating or confining plates is viscous. Second, a servo-control of stresses or displacements produces fluctuations which enhance seismic creep and relaxation. Working without grease and servo-control, Wienbroer (2010) observed rate-independent stress changes for isochoric stretching with constant amount D , and a far more rapid and less intensive relaxation than with grease thereafter. It appears that the endogeneous granular temperature T_g is proportional to D , as is the number of buckling force chains per unit of time. The matching of Matsushita's et al. (1999) results with suitable I_v and D_r is no more than a qualitative support of s-hyp, so this model will only be used in later chapters for a qualitative judgment.

In case of repeated reversals with resting intervals the granular temperature T_g arises temporarily and vanishes in between. This requires a stable psammoid body, otherwise it would generate seismicity by releasing free energy, and long enough pauses so that propagating seismic waves cannot overlap. Then the response is rate-independent except for the short times where changes are propagated, so the number of reversals may be taken instead of time with frequency. The gradual relaxation towards state cycles by an intermittent seismicity is more or less compensated by an elastic regain of stress (Sect. 4.3). T_g is endogeneous as it is produced by rearrangements with reversals. The seismic energy represented by T_g arises and dwindles in packages during the deformation and vanishes in pauses. This does not exclude

rate-dependence near reversals with strong changes of D , but the latter does not matter apparently for cumulative changes.

Seismo-hypoplastic relations (s-hyp) are heuristic as averages and frequencies of an intermittent granular temperature T_g are not equivalent to a continuous T_g . An intermittent T_g is called exogeneous in s-hyp if the excitation is heat-like, i.e. erratic with a leading frequency. This may be assumed not only for earthquakes and storms, but also for the vicinity of vehicles or machines. An erratic shaking could be represented by average T_g -values along boundaries of psammoid bodies, which may be called *seismostats*, and by means of the field equation

$$T_g = s\Delta T_g, \quad (4.6.7)$$

with a spreading factor s which depends on the stress obliquity $\tan\psi_s$. With the Laplace operator $\Delta = \text{divgrad}$ and with seismostats this equation produces a stationary T_g -field which may be of use for estimates with s-hyp. Equation (4.6.7) may be interpreted as the local balance of seismic energy: its transition into heat is compensated by a kind of diffusion along the gradient of T_g . Imagine a shaking plate at a psammoid body with uniform average stress: the spreading factor s will be maximal for $\tan\psi_s = 0$, and will vanish if $\tan\psi_s$ is critical as then seismic waves can no more be propagated. With empirical adaptations this approach could produce estimates.

A quantification for quasi-static reversals is achieved with the *high-cycle accumulation model* (h-cyc) by Niemunis et al. (2005). The flow rule for visco-hypoplastic creep (Sect. 3.4) is applied to cumulative deformations of sand due to rather small stress cycles as observed in triaxial tests (Fig. 4.2.8). The intensity of such kind of seismic creep is captured by factors which depend on pressure, void ratio, amplitude and shape of stress cycles. For applications stress cycles are repeatedly calculated by explicit calculations with hyp- δ and a few reversals. This approach led to realistic results in some cases (Wichtmann 2005, Niemunis et al. 2009), but the determination of the intensity factors is expensive. It is advantageous for big numbers of reversals where applications of hyp- δ get too expensive and can produce cumulative numerical errors.

h-cyc is more sophisticated than s-hyp, but also debatable for physical reasons. The flow rule in both models cannot hold for substantial temporal fluctuations of stress due to repeated reversals: stationary ratcheting can occur with subcritical average stress obliquities for moderate amplitudes (Figs. 4.2.7 and 4.2.9). For small enough amplitudes seismically activated state limits can be attained with s-hyp, but not with h-cyc. Quantifications in that respect would require RSE-experiments with repeated reversals up to state cycles. Erratic slow temporal stress fluctuations cannot be captured with h-cyc and could hardly be quantified for s-hyp. RSE-experiments with slow proportional average plus erratic stretching would be rewarding, they could lead to state limits which are influenced by an intermittent T_g .

In the papers mentioned further above the granular temperature T_g was assumed to be proportional to the microseismic kinetic energy of trembling grains. This works for granular gases and is also acceptable for granular fluids, but is debatable for granular solids near states of rest. The thermodynamic temperature T is similarly only proportional to the kinetic energy of molecules for an ideal gas, but less for a liquid and definitely not for a solid. A granular solid is close to $T_g = 0$ by definition, then T_g need not be proportional to the microseismic energy. The *seismodynamics* of psammoids will therefore be as intricate as the thermodynamics near $T=0$, even more so as both have to be combined. Seismometers can only feel parts of T_g , so they are not as representative as thermometers. Different kinds of *granular entropy* S_g were proposed as a measure of disorder (e.g. Edwards and Oakeshott 1989, Herrmann 1993), but not in combination with the thermal entropy S .

A *ceaseless seismicity* can be generated by sufficiently rapid and intensive shaking. This is more easily achieved with dry sand than with pore water as this absorbs a substantial part of seismic energy, more so with finer grains (one can hear crackling gravel under water, but not sand). Sufficiently shaken sand in a vessel tends to an isotropic pressure according to gravity without average flow. The pressure in such *seismodynamic equilibria* is purely entropic: the trembling grains repel each other and have almost no average elastic energy, so there is no grain skeleton. With a sufficiently intensive shaking the sand boils up, this transition to a granular fluid may be called granular melting with $T_g = T_m$. Barkan (1962) observed a reduction of shearing resistance τ with sand by shaking vertically from below, this can be captured by

$$\tau = (p - p_d) \tan \varphi, \quad (4.6.8)$$

with the total pressure p , a *seismic pressure* p_d and a friction angle φ . p_d may be understood as an entropic pressure due to T_g , and $p - p_d$ as reduced skeleton pressure instead of σ in (2.9.6) for quasi-static shearing. Other than in a seismodynamic equilibrium the grains are not fully relaxed, but jammed again and again in skeletons which are continuously rearranged. Rao (1966) proposed (4.6.8) with an unquantified ‘dynamic pressure’ p_d on the base of shear tests with dry sand shaken vertically from above. Mogami and Kubo (1953) observed a similar reduction of the shearing resistance of dry sand by horizontal shaking. I played with a thin layer of fine dry sand between an inclined rough shaking base and a rough heavy plate; steady sliding occurred independently of size and weight with higher velocity for more intensive shaking or more inclination. These observations could be captured with

$$p_d = p(T_g/T_m)^m, \quad (4.6.9)$$

with total pressure p and a granular melting temperature T_m so that $\tau = 0$ holds by (4.6.9) for $T_g = T_m$. The exponent $m > 0$ would be 1 if T_g were proportional to the microseismic energy, which as said above is debatable, and could be determined with thin layer tests. The seismostat in experiments

should be so strong that it is not impaired by the sand, only then it can produce a desired T_g independently of the shaken masses. The seismic activation of shearing should not be called liquefaction for $T_g < T_m$ as there is still a kind of skeleton with jammed grains, i.e. a state between granular solid and granular fluid. The proposed experiments cannot produce uniform RSEs as T_g has a gradient by (4.6.7), but may suffice for approximations.

Experiments with thin layers on a horizontal shaken base could also be made under *water* with constant pressure p_w and total pressure p . The resistance to stationary shearing could be measured with different rates, the thus revealed viscosity should be related with (not easily observable) void ratios. As the grains are neutral with respect to p_w one has to replace p in (4.6.8) and (4.6.9) by $p - p_w$; mind that this is not an effective or skeleton pressure as without shaking. The same intensity of shaking as without water causes (apart from the reduction of the granular surface energy) the same reduction of τ by (4.6.8) with (4.6.9), but requires more power as the sheared water between the grains absorbs kinetic energy. The seepage of pore water is determined by the gradient of the hydraulic height (Sect. 6.2), the permeability k_f is not changed by T_g . Changes of skeleton density imply seepage which absorb substantial parts of seismic energy. A decay of the grain skeleton is not only produced by a loss of $p - p_w$, but can also occur by an increase of T_g .

Returning to evolutions of saturated psammoids with intermittent seismicity, we face a couple of open questions. Transitions to asymptotic state cycles (Sect. 4.3) may be interpreted with average stress obliquities $\tan\bar{\psi}_s$ including an entropic pressure as by (4.6.9). Strain cycles mean thus relaxation by \bar{T}_g up to an isotropic pressure $p - p_w - p_d$, whereas ratcheting leads to a critical obliquity $\tan\bar{\psi}_{sc}$ with $p - p_w - p_d$ instead of $p - p_w$. One could employ s-hyp with a suitable average granular temperature \bar{T}_g and with a number of cycles $N = tf_c$ instead of time t and frequency f_c . The high-cyclic model (h-cyc) could be modified by means of a seismic pressure and attractors with \bar{T}_g , thus both models would no more be restricted to small amplitudes. One could estimate T_g -fields with (4.6.7) by an empirical matching of the spreading factor s and of boundary conditions for T_g (seismostats).

Such heuristic approaches may be of use for estimates, but are physically debatable. As outlined further above T_g arises temporarily during quasistatic evolutions with reversals, and may get proportional to the amount of stretching D when SOM-states are reached. This causes an intermittent relaxation and a regain of elastic stress which resembles the one with continuous T_g , but is not the same. A novel theory is needed which embraces rate-independent approaches and enables to calculate adequate averages of T_g and p_d on a better physical base than s-hyp and h-cyc. This should also enable to judge and calculate spreading factors and seismostats for estimating average granular temperatures.

The matter gets more intricate with *wave propagations*. Even quasistatic evolutions have dynamic interplays as changes of the skeleton state are transmitted by seismic waves, in particular near reversals. T_g arises alongside with

any propagation as this is never only elastic, the microseismic energy is heat-like and is transformed into heat. The balance of this energy is not properly captured by (4.6.8) as it is not conducted like heat. In case of repeated quasi-static reversals an average heat-like seismicity is generated by seismic waves and consumed by dissipation. More often propagations occur in rather erratic swarms during which the skeleton does not rest. Simulations with hyp- δ have been validated for vertically propagated plane waves (Sect. 11.2) and may be used to estimate gain and loss of T_g , but extensions to two or three dimensions would be too expensive. Simplified approaches as with (4.6.8) are at best qualitatively reasonable, but may suffice if psammoid bodies and seismic boundary conditions are rather indeterminate.

Such approaches are limited by *phase transitions*. Shear localizations in psammoids mean that polar quantities arise, these can disappear again with reversals (Sect. 8.2). Active shear bands can prevent the propagation of shear waves, the stability of psammoid bodies may thus be judged, but this is at best feasible for one-dimensional evolutions (Osinov and Wu 2005). Skeletons decay with a loss of $p - p_w - p_d$, the resulting suspension is an intricate fluid. The pore water can evaporate into bubbles or cracks, the behavior of skeletons and suspensions is changed by such cavitations. The mechanical roughness can get so strong that continuum models are no more justified. Nevertheless novel hydrodynamic theories will be welcome, they should combine thermo- and seismodynamics and could indicate the fractality of deterministic chaos. This will clearly go beyond our concept of psammoids with reversals.

Summing up, the seismically activated viscosity of psammoids can at best be estimated with present mechanical models. A continuous heat-like seismicity may be captured with a granular temperature T_g and a related entropic pressure p_d . Granular solids can have an intermittent seismicity with low temporary T_g , then the seismodynamics is more intricate. The rate-independence of elp- α and hyp- δ seems to be justified, and may be taken over for the seismically activated creep and relaxation in seismo-hypoplastic and high-cycle accumulation models. Such approaches may be quantified for estimates by matching with experiments and simulations by hyp- δ , therein averages of T_g and p_d may be of use. They are debatable with seismic waves in the over-critical range with granular phase transitions, such cases are at the verge of predictability.

4.7 General and outlook

Applications to field problems require tensorial relations for frame-indifference (Sect. 1.2). The mechanical roughness with grains and water can impair continuum approaches, in particular with reversals, but other models are hardly feasible (Sect. 2.1). Following Jaeger et al. (1996) one may employ notions like granular solids, liquids and gases, but with caution as granular interactions are not conservative and as water plays a role. We will argue with attractors

for the validation and calibration of models although general RSEs are fictitious. Present models are intricate and preliminary, they should be delimited and substituted with physical arguments.

Resting aggregates of hard grains are delicate solids, nearly resting ones may be called *granular solids*. Stable grain skeletons, i.e. aggregates with lower than critical stress obliquity and relative void ratio, can be nearly hypoelastic, i.e. capable of non-dissipative oscillations and propagations with minute amplitudes. The required low force-roughness may be achieved by previous shaking, even then the elastic range is infinitesimal. Resonant column tests (Fig. 4.2.1) reveal the dependence on stress and void ratio and a slight hysteretic damping, they suggest rate-independence. It is reasonable to neglect the force-roughness for the hypoelastic limit with infinitesimal amplitudes. This corresponds to a vanishing intergranular strain in hypoelastic models (hyp- δ), the back stress in elastoplastic models (elp- α) is also minimal in such cases.

Consider first a general RSE as by Fig. 4.1.11 with *small deformation cycles*. Small means that the stress obliquity $\tan\psi_s$ remains subcritical, and that the force-roughness remains small as SOM-states are not reached. This requires so low relative void ratios that the grain skeleton cannot decay. After a transition (which will be treated further below) the response gets periodic (as long as the degradation of grains is negligible). Assuming rate-independence this attractor may be represented by a cyclic path in a hyperspace of state components and void ratio. Such attractors can serve to define objective properties, other than in Sect. 2.11 they include the hidden force-roughness. It is postulated that the mean stress deviator vanishes in the asymptote, and that the asymptotic relative void ratio is near the lower bound and exhibits double cycles. This is at variance with the hypoelastic behaviour often assumed for small cycles (Figs. 4.2.1 and 4.2.2), but Huber (2010) observed double cycles even with minute amplitudes.

The observed hysteresis cannot be quantified without hidden state variables. It appears that the amount of force-roughness pulsates at a low level, this can be modelled with back stress or intergranular strain. Further specifications require thought experiments as general RSE-tests with small deformation cycles are not feasible. Imagine a cyclic shearing, without or with cyclic changes of void ratio, with another alignment than for a previously attained state cycle. After a transition a state cycle is again attained with the new alignment. The variability of such attractors suggests a symmetric second-order tensor for the force-roughness as for stress and strain, so it has three principal directions and three invariants. It is rather obvious that principal directions and Lode parameters of strain and force-roughness agree in the asymptote.

With *moderate deformation cycles* our RSE will tend to state cycles with temporary SOM-states, and $\tan\psi_s$ can get repeatedly critical. A skeleton decay can be avoided with low enough void ratios, overcritical $\tan\psi_s$ may be excluded to avoid shear localizations. The asymptotic stress cycles imply a

stronger hysteretic dissipation than with small amplitudes, their average deviator will not vanish exactly, and they get but approximately aligned. The asymptotic relative void ratio attains a higher average and pulsates more markedly with twice the deformation frequency than for small amplitudes. The hysteresis ratio by (2.11.17) is lower than by hyp, i.e. for assumed successions of SOM-states. These statements suggest a tensorial force-roughness with temporarily maximal amount, and show that the energetics should be taken into account.

Turning now to *moderate ratcheting*, one should update the reference configuration for big average deformations as in Sect. 2.11. With small amplitudes of the cyclic deformation part the asymptotic stress cycles have a nearly critical obliquity $\tan\psi_s$, but the average relative void ratio r_e is lower than critical. While $\tan\psi_s$ pulsates alongside with the deformation r_e pulsates with the two-fold frequency. A tensorial force-roughness gets obviously aligned by the average stress and deformation, but its amount need not temporarily attain the upper bound as SOM-states are not reached with small deformations between reversals. An attractor of this kind could be attained in resonant column tests with an axial dead load (Huber 2010).

Strong ratcheting of our RSE produces temporary SOM-states, but state limits (for which the desired uniformity gets lost) should be avoided. The stress obliquity $\tan\psi_s$ gets about critical near reversals relative to the average stretching, and can get almost critical near opposite reversals. The relative void ratio pulsates with twice the frequency of the cyclic deformation part, its asymptotic average is lower than critical and higher than for moderate ratcheting. Beyond cylindrical symmetry and simple shearing such states could be approached with cyclically twisted and simultaneously extended thick-walled cylindrical samples. Such experiments could be of use to further validate and calibrate $\text{elp-}\alpha$ and $\text{hyp-}\delta$ although the force-roughness remains hidden.

To a certain extent the indicated generalized attractors may be assumed as *rate-independent*. This is justified near the hypoelastic limit of granular solids, even with rapidly shaken skeletons. The hysteretic damping in resonant column tests has a phase shift which can be attributed to elastic grains with dry friction (Richart et al. 1970). Rate-independence is also empirically legitimate for successions of SOM-states. The stress-strain curves observed by Matsushita et al. (1999) for constant D exhibit a minute rate-dependence, but this could be caused by the grease in the device. A marked rate-dependence was observed at jumps of stretching intensity D in isobaric shear tests without grease (Duttine et al. 2008). Reversals require also drastic changes of D , so the response in their vicinity can exhibit rate-dependence. This could influence asymptotic state cycles near reversals with big amplitudes, but cannot be controlled in detail, therefore rate-independent relations should be taken with a pinch of salt.

Within these limitations *transitions* of general RSEs exhibit intermittent relaxation and creep wherein the time may be replaced by the number of reversals. For small stress amplitudes the direction of the cumulative anelastic

deformation depends on the direction of average stress as for thermally activated creep (Sects. 3.2 and 3.9). The intensity of cumulative deformations may be captured by a high-cycle model (h-cyc) or by a seismo-hypoplastic relation (s-hyp). Applications to boundary value problems (Wichtmann 2005, Niemunis et al. 2009) show that h-cyc models work for general deformations, whereas s-hyp requires a more arbitrary matching. Seismically activated attractors for general deformations are not obtained with h-cyc and could not be quantified with s-hyp. The seismic creep as in Fig. 4.6.2 is enhanced by a servo-control which works as a seismostat. For bigger stress amplitudes both models could be extended by an average entropic pressure \bar{p}_d so that $p - p_s$ is replaced by $p - p_s - \bar{p}_d$, otherwise transitions to strong ratcheting could only be captured by going through all reversals with hidden variables (Sect. 4.6). Erratic slow rearrangements with a smooth average trend may be judged with an intermittent granular temperature, but quantifications have not yet been achieved.

These considerations call for a *unified concept* for quasi-static evolutions of granular solids. This cannot be a hybrid of $\text{elp-}\alpha$ and $\text{hyp-}\delta$ as a kind of seismically activated viscosity arises during rapid changes of stretching. Rate-independence may be justified in hypoelastic and hypoplastic limits, and also for cumulative effects if resting intervals occur between reversals. State limits may at best be captured approximately as for them the desired uniformity of RSEs gets lost. In a subcritical regime, which has to be defined by combined bounds of stress obliquity and relative void ratio, cumulative effects with many reversals could be captured with an intermittent granular temperature T_g . Employing also entropic pressures for bigger amplitudes, this could substitute rather heuristic concepts like s-hyp and h-cyc by means of a consistent average T_g . Unified concepts should also enable to derive average T_g -fields from average stress and void ratio fields for quasi-static boundary conditions with reversals. Needless to explain that this cannot work with seismic waves and in the overcritical regime.

The remarks in the previous section on seismodynamics hold rather in general so that little need to be added. Rearranged granular solids, i.e. psammoids with a kind of skeleton, exhibit an intricate *mechanical roughness*, in particular in case of many reversals with big deformations in between. Quasi-static rearrangements are jerky with rate-independent seismic kinks: force chains arise and buckle alongside with deformations. The force-roughness gets frozen in pauses, then it means latent seismicity. As long as shear localization and decay are avoided smooth averages are legitimate for velocities and their gradients (Sect. 2.2), although a continuous force-roughness seems to be paradoxical. This is no more than a heuristic approach, however, which may help to understand and to delimit models like $\text{elp-}\alpha$ and $\text{hyp-}\delta$. A closer look shows that asymptotic state cycles proposed for validation and calibration are not really rate-independent and cannot be precisely obtained. The need of physically viable theories is more evident with many irregular reversals which occur often in situ.

To be more specific, the mechanical roughness may be neglected for stable grain skeletons, i.e. in case of subcritical stress obliquities $\tan\psi_s$ and relative void ratios r_e . Then repeated reversals can even smooth the response as $\tan\psi_s$ and r_e can be reduced by stress redistribution and densification. This kind of seismic relaxation and stabilizing creep occurs also with erratic reversals in the subcritical regime, and evolutions with time can be more erratic due to boundary conditions. Low intermittent granular temperatures may then be substituted by temporal averages without explicit force-roughness, but such heuristic approaches deserve a better physical base. The roughness tends to increase in the overcritical regime, then shear localization or decay imply a spontaneous growth of seismicity. Such critical phenomena (Sect. 16.3) are beyond the reach of continuum models, these may at best help to catch the onset of deterministic chaos. The force-roughness rises dramatically by shear localizations, this can be captured with polar quantities (Sect. 8.2).

The *pore water* can play a passive or active role. The granular temperature T_g in the hypoplastic SOM-regime, i.e. for slow monotonous deformations, is enhanced by a lower surface energy and reduced by viscous damping with water. Both effects seem to compensate each other as hypoplastic parameters are rather water-independent. The grains do not feel the pore water pressure p_w , but the skeleton feels $p_s = p - p_w$ and the pore water cavitates if p_w vanishes (Sect. 6.2). A skeleton decay with $p_s \rightarrow 0$ is enhanced by a rise of p_w and hindered by its reduction except for cavitation when the continuity gets lost. A subsequent suspension flow is beyond the reach of present theories. Pressure waves in water can produce a significant T_g in case of big amplitudes or if the granular body is beyond the verge of stability (i.e. for overcritical $\tan\psi_s$ and/or r_e). A turbulent seepage in gravel or rockfill generates T_g and can thus mobilize the skeleton.

Strong seismicity by intensive shaking or impacts means so high granular temperatures that the entropic pressure p_d plays a role (Sect. 4.6). This can lead to a granular liquid or gas without water, and with it to a kind of suspension which has little in common with ordinary fluids. Such cases are enigmatic in the light of present soil mechanics and hydromechanics, they require novel physical approaches. There is no way around continuum models and conservation laws, but there is no need to catch mixtures of mineral grains and water by ‘simple materials’ in the sense of Truesdell and Noll (1965). The clue could lie in the fractal energetics.

To *sum up*, psammoids with reversals may be captured by elastoplastic or hypoplastic models with hidden variables (elp- α or hyp- δ), and also with seismo-hypoplastic (s-hyp) or high-cycle accumulation models (h-cyc), but there are limitations. Rate-independence is justified for vibrations and propagations near stable states of rest, and also for slow monotonous deformations. Asymptotic stress cycles due to cyclic deformations or ratcheting are apt to judge elp- α and hyp- δ . The hidden state for them may be related with spatial fluctuations of inner forces, this force-roughness can be represented by a

symmetric tensor. Cumulative changes of shape and state with many reversals and pauses in between may be understood as a kind of creep and relaxation in heuristic rate-independent models like s-hyp or h-cyc. Grain skeletons exhibit a kind of viscosity with an intermittent granular temperature. This works in the subcritical regime, so far pore water plays the usual role. In the overcritical regime and with stronger seismicity the named constitutive models for psammoids and pore water get meaningless, novel energy-based approaches will be needed.

PELOIDS WITH REVERSALS

This fourth chapter on constitutive relations is more comprehensive and should therefore be longer than the preceding ones, but it is not and is still possibly too long. Peloids with reversals exhibit viscosity and require hidden variables as skeleton stress and void ratio do not suffice in general to characterize their state.

For preparation I begin again with pore-free solids (Sect. 5.1). The viscosity is captured as in Sect. 3.1, and the force-roughness as in Sect. 4.1, but the combination of both is not straightforward. Back stress and internal strain, which may represent the force-roughness, should dwindle after fixing skeletons, but visco-elastoplastic and -hypoplastic relations (*v-el p - α* and *v-hyp- δ*) do not capture this kind of relaxation. It is shown without algebra how one can produce argotropic state limits and asymptotic state cycles. These could be adapted to experimental results so that an assumed hidden state variable is indirectly captured. Viscoplastic relations without hidden variable can already produce a nearly elastic response without a switch function (Sect. 3.1). Relations with a hidden variable need at least one switch function for reversals, but this is rather arbitrary. It appears that this uncertainty cannot be removed by experiments only.

The outline of experimental results with clays under reversals (Sect. 5.2) is kept shorter than for psammoids as there are less reports and as these are less revealing. Viscous effects were ignored almost throughout, in one publication they were even suppressed by choosing rock flour with hard particles. The observed response to un- and reloading without drainage could be explained without a hidden variable, the response to many small strain cycles is also not conclusive in that respect. The observed response of undrained clay to several deviatoric stress cycles appears to be sand-like, but asymptotic state cycles were rarely achieved. Some cuboidal and biaxial tests were carried out with drainage and few slow reversals, but waiting times with creep or relaxation after reversals were not recorded. One recent report indicates a sand-like response to cyclic shearing with drainage. Altogether this is not a good base for validations.

There are several elastoplastic relations with back stress for clay which ignore viscous effects. I take the freedom to introduce them in Sect. 5.3 as visco-elastoplastic as the assumed rate-independence may be justified for slow loading and rather fast un- and reloading. The thus achieved matching of test results does not suffice to select back stress approaches. Numerical simulations up to asymptotic state cycles could at least demonstrate limitations of such approaches. Properly visco-elastoplastic relations are only mentioned as they are intricate, and as software for numerical RSE-tests with them is not freely available. The latter is the case with visco-hypoplastic relations, but these are not less intricate. So they are introduced in Sect. 5.4 only by means of associated paths including an intergranular strain. Simulated asymptotic state cycles are not convincing, whereas experimental results with only one reversal can be fairly well matched. Comparison and discussion with v-elp- α and v-hyp- δ are as yet rather interpretations than validations.

General aspects are considered only briefly therefore in Sect. 5.5, explicit models for cumulative effects and critical phenomena are also discussed in this final section. The force-roughness could get visible for longer wavelengths of spatial stress fluctuations, thus attempts with boundary value problems could be more rewarding. Seismo-viscous effects may be assumed for explicit models as with psammoids, but quantifications will be more difficult because of the simultaneous thermal activation. Shear localization, cracking and decay delimit the range of applications.

5.1 A fourth prelude on solids

Maintaining the prerequisites of Sect. 4.1 except rate-independence, we now allow for *viscous effects*, i.e. argotropy, creep and relaxation. As explained in Sect. 4.1 and other than in Sect. 3.1, hidden state variables are needed. This will be shown with graphical representations of visco-elastoplastic approaches with back stress, and of visco-hypoplastic ones with internal strain. The attractors for proportional and non-monotonous deformations are argotropic, in addition there are endogeneous attractors for creep and relaxation. Algebraic representations are left aside in this preparatory section, physical interpretation and validation will be discussed briefly at the end.

As without viscosity (Sect. 4.1) the hidden state can be related with the *force-roughness*, i.e. with oriented spatial fluctuations of stress. This enables an interpretation of the generally tensorial back stress and internal strain. The force-roughness should attain state limits and state cycles alongside with those for stress, can increase by creep and should be more strongly reduced than the stress by relaxation. This should be reflected by evolution equations for back stress or internal strain, but will only be indicated graphically in the sequel as the corresponding viscoplastic relations for soils in the following sections are preliminary. Nearly elastic behaviour is already obtained without hidden variables for low ratios of actual and limit stress deviators, and with

a sudden rise of strain rates (Sect. 3.1). The force-roughness comes into play only for evolutions with many reversals and repeated approaches to argotropic SOM-states.

Monotonous uniaxial evolutions are shown in Fig. 5.1.1. Stretching with constant $|\dot{\epsilon}|$, which may be referred to a material parameter $\dot{\epsilon}_r$, leads to state limits of stress σ (a), back stress α (b) and internal strain δ (c). The limit σ is argotropic as described in Sect. 3.1 by Fig. 3.1.1 and (3.1.1). The hidden limit of α should have the same argotropy by the factor in (3.1.1) as otherwise the hardening concept shown with Figs. 4.1.5 and 4.1.6 would not work. The limit of δ need not be argotropic, so $|\delta| \leq R$ may be taken over from Fig. 4.1.5b. Transitions from one strain rate $\dot{\epsilon}$ to another one are indicated by dotted lines, they do not appear in δ .

With constant σ uniaxial creep (d) tends to a state limit with constant $\dot{\epsilon}$ by (3.1.2). The back stress α tends likewise to a state limit in the course of time (e). Depending on σ/c_r and the initial α the transition requires different

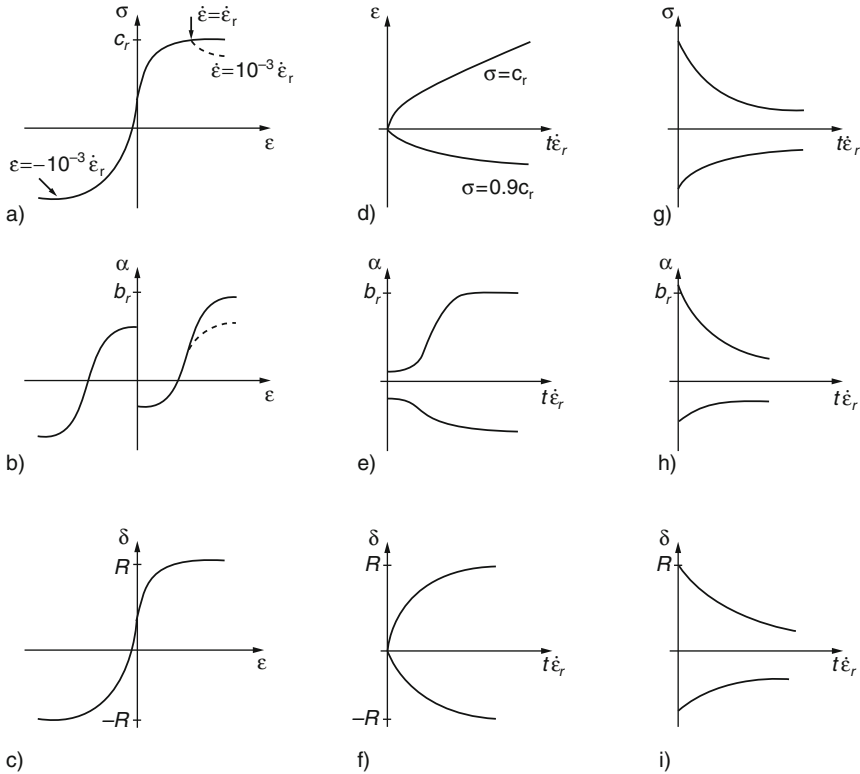


Fig. 5.1.1. Uniaxial evolutions of a viscous solid RSE with hidden state: argotropic stress-strain curves (a), creep (b) and relaxation (c); related evolutions of back stress (d-f) and internal strain (g-i)

times. The internal strain δ tends likewise to a state limit within variable times (f). With constant shape relaxation should be exhibited by σ (g), α (h) and δ (i). The proposed asymptotic low amounts cannot be attained in realistic times, the initial rates $\dot{\sigma}$, $\dot{\alpha}$ and $\dot{\delta}$ depend on the initial σ and α or δ . These are endogeneous attractors due to thermal activation. Creep tends to a steady state with a stationary energy input $\sigma\dot{\epsilon}$, whereas relaxation tends to a thermodynamic equilibrium.

Uniaxial strain cycles and ratcheting may lead to asymptotic responses as shown in Fig. 5.1.2. A moderate amplitude is chosen so that neither elastic cycles nor state limits are attained. The argotropy is shown by bigger amplitudes of σ and α , dotted for different amounts of strain rate $|\dot{\epsilon}|$, whereas δ (c) may be rate-independent. The argotropic asymptotic cycles of σ (a), α (b) and δ (c) for strain cycles should be symmetric. For ratcheting with moderate amplitude and two different $|\dot{\epsilon}|$ the state cycles should be asymmetric and argotropic for stress (d) and back stress (e), but may be rate-independent for internal strain (f). State limit values are repeatedly approached, with small amplitudes the stress remains close to them.

Algebraic representations according to Figs. 5.1.1 and 5.1.2 could be formulated as follows. In visco-elastoplastic relations with back stress (v-elp- α) the width and the bounds of the elastic range (cf. Sect. 4.1) are likewise argotropic by (3.1.1). A viscoplastic strain rate $\dot{\epsilon}^v$ reduces the stress rate $\dot{\sigma}$ from $E\dot{\epsilon}$ to $E(\dot{\epsilon} - \dot{\epsilon}^v)$ if thus the elastic range is left. This can be shifted up to an argotropic bound, thus the evolution of α is determined (kinematic hardening). Apart from switch functions as in Sect. 4.1 $\dot{\epsilon}^v$ can be modelled similarly as by

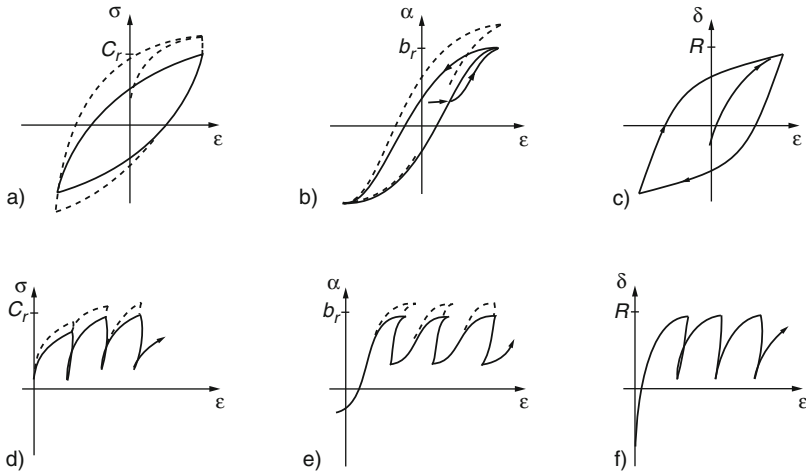


Fig. 5.1.2. Evolutions of a viscous solid RSE with reversals: asymptotic hysteresis of stress (a), back stress (b) and internal strain (c) by strain cycles; transition to ratcheting (d) with related back stress (e) and internal strain (f)

(3.1.13) with a reference rate $\dot{\epsilon}_r$ and a viscosity factor f_v by (3.1.14). Thus the state limits of σ and α get likewise argotropic, and endogeneous attractors for creep and relaxation are also obtained. The hardening rule has to be formulated so that realistic symmetric and asymmetric state cycles are produced as attractors for strain cycles and ratcheting. In visco-hypoplastic relations with internal strain (v-hyp- δ) $\dot{\sigma} = E(\dot{\epsilon} - \dot{\epsilon}^v)$ holds without switch function, and δ may evolve with ϵ as proposed in Sect. 3.1. Argotropic state limits, creep and relaxation are obtained as with v-elp- α . State cycles could similarly be attained with both models for ratcheting, whereas state cycles with zero average could only be reached by v-hyp- δ and not by v-elp- α .

Evolutions with *monotonous cuboidal* deformations are shown in Fig. 5.1.3 by means of deviator planes. Strain paths (a) may be straight lines with labels for the amount of strain rate D , which is referred to an objective reference rate D_r . In the stress plane (b) argotropic state limits are attained as introduced with Fig. 3.1.7. With v-elp- α (A) the elastic range has a likewise argotropic size. Its position, described by back stress, is shifted to an argotropic state limit value with the same Lode angle as the strain rate (c). The response polars, which steer the approach to the attractors, are cycles within the elastic range. At its rim they consist of an elastic semi-cycle and an argotropic arc which gets straight at a state limit with constant D .

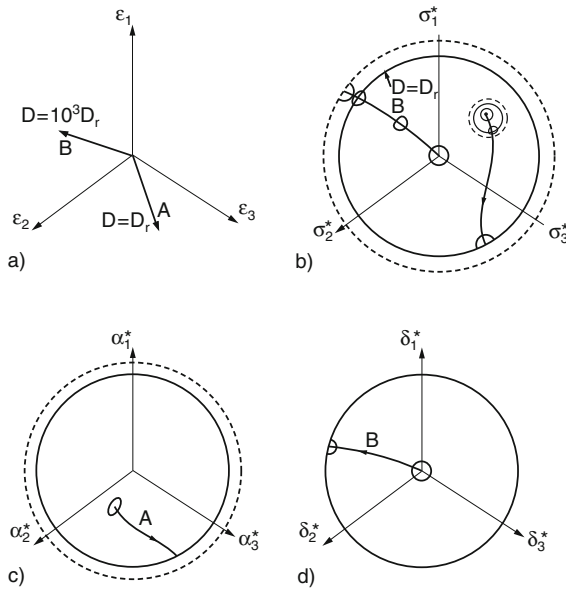


Fig. 5.1.3. Evolutions of solid cuboids in deviator planes towards argotropic state limits: paths of strain (a), stress (b), back stress (c) and internal strain (d). Dotted circle for $D = 10^3 D_r$

With $v\text{-hyp-}\delta$ (B) the response polar is a centered circle only if both stress and internal strain are zero. Otherwise it consists of an elastic semi-cycle for $\delta_i \dot{\epsilon}_i < 0$, and an argotropic arc depending on σ_i and δ_i which gets straight at a state limit. For the internal strain (d) the response polars consist likewise of centered semi-circles and argotropic arcs, these state limits may be assumed as rate-independent. The alignment at a state limit should agree with the one of the strain rate. Transitions from a state limit to another one with another D imply an increase or reduction of σ and α for an increase or reduction of D , whereas δ_i may remain unchanged. Transitions require an interpolation.

Cuboidal *creep* and *relaxation* are proposed in Fig. 5.1.4 by means of deviatoric paths of strain (a), stress (b), back stress (c) and internal strain (d). With constant stress (A) the strain path gets straight with constant D if σ_i is not in an elastic range in case of $v\text{-elp-}\alpha$. The transition to state limits of α_i or δ_i takes different times depending on σ_i and the initial α_i or δ_i . With constant shape (B) stress σ_i and back stress α_i remain unchanged for $v\text{-elp-}\alpha$ if σ_i is in an elastic range, otherwise σ_i and α_i tend to zero. For $v\text{-hyp-}\delta$ the state variables σ_i and δ_i should then tend to zero. The approach to an autogeneous attractor by relaxation is fast for an onset near a state limit, and is slowed down otherwise to non-observable rates. Relaxation of δ_i may be neglected for simplicity.

The proposed asymptotic response to *cuboidal strain cycles* is represented in Fig. 5.1.5. In the strain plane (a) the amplitude may be small (A) or

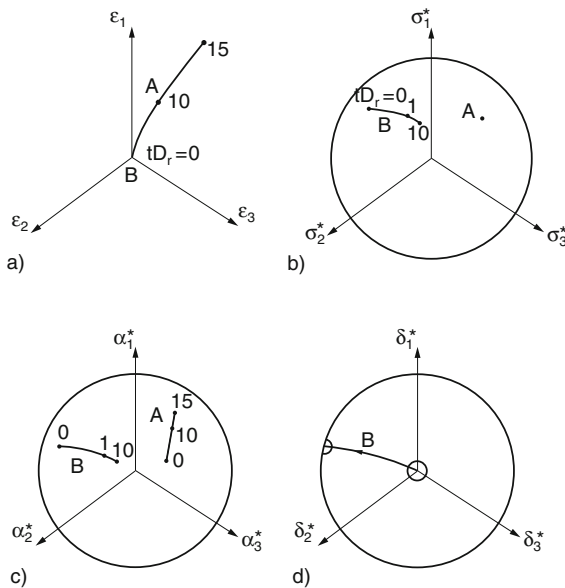


Fig. 5.1.4. Creep and relaxation of cuboids: paths in planes as Fig. 5.1.3

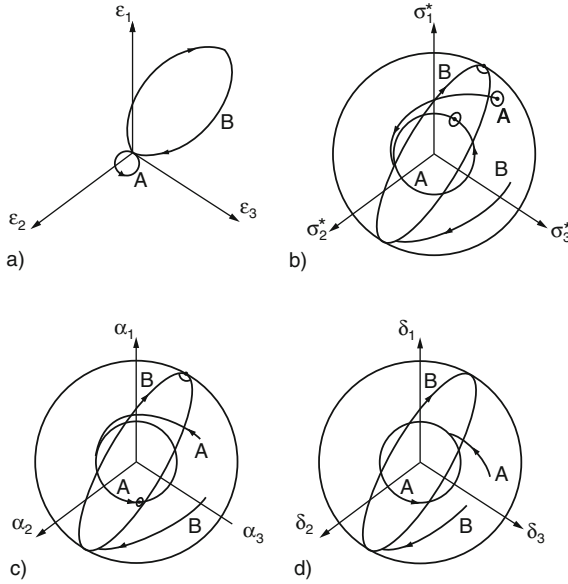


Fig. 5.1.5. Asymptotic response of cuboids to strain cycles: paths in planes as by Fig. 5.1.3

moderate (B), the amount D of strain rate may be constant. For v-elp- α the deviatoric paths of stress (b) and back stress (c) should be symmetric in the asymptote, except for so small amplitudes that the elastic range is not left. For v-hyp- δ the asymptotic cycles of stress (b) and internal strain (d) should always be symmetric. If the strain path is elliptic, as for case B e.g., the asymptotic state paths should have the same alignment. Evolutions with reversals can be represented by lenticular paths (e.g. B) which are flat for uniaxial deformations. The asymptotic cycles should be wider for bigger D , and these attractors should be argotropic (except for v-elp- α with small amplitude). Some response polars indicate that the asymptotic state paths are not left.

Cuboidal ratcheting is proposed in Fig. 5.1.6. In the strain plane (a) the amplitude of the periodic fraction may be small (A) or moderate (B), D may be constant. The stress path (b) should tend to asymmetric cycles which are always (A) or periodically close to an argotropic state limit (B). The asymptotic cycles of back stress (c) and internal strain (d) should have the same property, with v-elp- α the elastic range would be left repeatedly. These attractors are argotropic as the former ones, some response polars indicate how the driven attraction works. Elliptic or lenticular periodic strain path fractions should lead to state cycles of similar shape (e.g. B), thus uniaxial deformations can also be captured.

Algebraic representations could be formulated so that evolutions as shown in Figs. 5.1.3, 5.1.4, 5.1.5 and Fig. 5.1.6 are reproduced. As indicated by

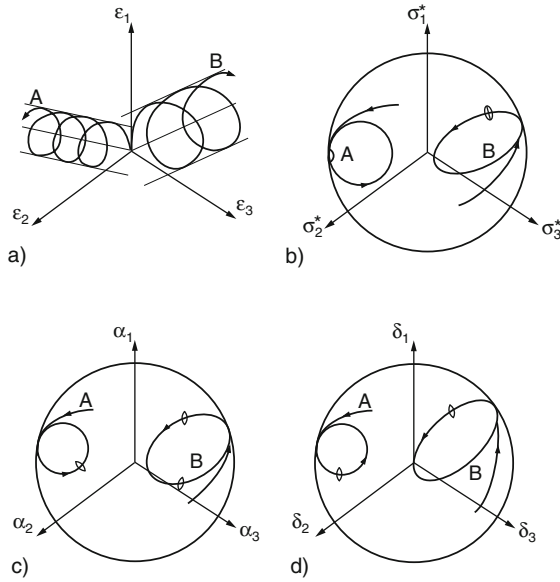


Fig. 5.1.6. Asymptotic response of cuboids to ratcheting; paths in planes as Fig. 5.1.3

response polars they should be differentially non-linear (e.g. via switch functions) and argotropic. The latter can be achieved by the viscosity factor f_v as in Sect. 4.1, now also for the evolution of the hidden state variable α_i or δ_i . State limits can easily be achieved, but only few representations can lead to acceptable asymptotic cycles. As without argotropy elastic ranges need not be circular, and their size can be variable by means of a further state variable. The range of variation is wider with creep and relaxation, but then changes of the hidden variable can hardly be judged. The extension to other than cuboidal deformations with tensors is a minor formal problem, cf. Sects. 2.1, 3.1 and 4.1.

Some arguments may be given for a *physical interpretation*. As outlined in Sect. 3.1 anelastic effects seem always to be thermally activated. Hidden state variables representing the force-roughness can also exhibit thermally activated viscosity. With v-elp- α argotropy and relaxation of α_i are implied alongside with those of σ_i due to the formalism of kinematic hardening. With v-hyp- δ the evolution of δ_i can be formulated without viscosity, then the amount δ can have a rate-independent upper bound. However, relaxation should also reduce δ_i as the force-roughness is reduced by thermal activation if the shape is fixed. A similar kind of annealing at room temperature can be achieved by many small strain cycles. Approaches with α_i or δ_i are heuristic anyway, thus dislocations and crystallite fabric cannot fully be captured.

A few remarks on validation may be added for preparing the next sections, they may serve also as a *summary*. Apart from the uniformity needed for all element tests, the argotropy requires a control of strain rates, any waiting

time changes state and subsequent behaviour. Strain rates should be small enough so that pores are not generated spontaneously, and so that mechanical heating is avoided. The argotropy is marked near state limits, but then shear localization can scarcely be avoided. The indeterminacy of the initial hidden state can be overcome by means of many strain cycles or ratcheting. Moderate amplitudes with low enough stretching rates for self-healing are advisable as then state cycles can be attained after a reasonable number of reversals without cracking and heating. Extremely slow tests are not worth the long duration if they do not start from an attractor so that the initial hidden state is determined. These qualitative hints may suffice for introduction.

5.2 Observed response of peloids with reversals

Simple peloids have been introduced in Sect. 3.2. We now drop one simplifying assumption, namely that the state of an RSE is sufficiently captured by skeleton stress components and void ratio. This is necessary with more than one path reversal, as was shown in Sects. 3.6, 3.7 and 3.8 by back-analyses with visco-elastoplastic and -hypoplastic relations. In the sequel the argotropy is first left aside as it is often ignored and may sometimes be neglected, thereafter it is allowed for. Some arguments for hidden state variables of psammoids can be taken over to peloids, but the experimental base is narrower. Thus the outline is shorter although peloids have a wider range of attractors due to argotropy.

A *neglect of argotropy* is justified if the amount of stretching D remains in a suitable range. For a given void ratio and direction of stretching without drainage the mean skeleton pressure p_s ($= p'$) varies with D by (3.3.5) as with a solid by (3.1.1) due to thermal activation. The viscosity index I_v of clays ranges from ca. 0.02 to 0.05, so p_s changes by less than 15% when D ranges between ca. 10^{-2} and 10^2 times the reference value D_r . In the majority of tests with control of strain rate or stress after consolidation D varies in this range, then its influence is moderate and may often be ignored.

With *cylindrical symmetry* the typical response to a second reversal was discussed already in Sect. 3.6. In a test by Roscoe and Burland (1968) the sample was normally consolidated, they concluded that its response to un- and reloading was rather elastic, but that a distinct bound of an elastic range can hardly be identified. Tests by Sangrey et al. (1969) with several reversals reveal a more complicated reality, Fig. 5.2.1. Undisturbed samples of a saturated, uncemented, moderately plastic clay were reconsolidated isotropically, then loaded and unloaded deviatorically without drainage. With the rather low and constant $|D| \approx 10^{-6} \text{ s}^{-1}$ the pore water pressure p_w changed rather uniformly so that it could be observed at the plates. Some samples were axially shortened without drainage up to a state limit with a plateau of $\sigma_1 - \sigma_2$ and p_w .

Cycles of $\sigma_1 - \sigma_2$ between zero and ca. 80% of the state limit value lead to a kind of ratcheting: the axial strain ε_1 increases gradually (Fig. 5.2.1a), p_w increases mainly in the first cycles (b), the stress path tends to a loop

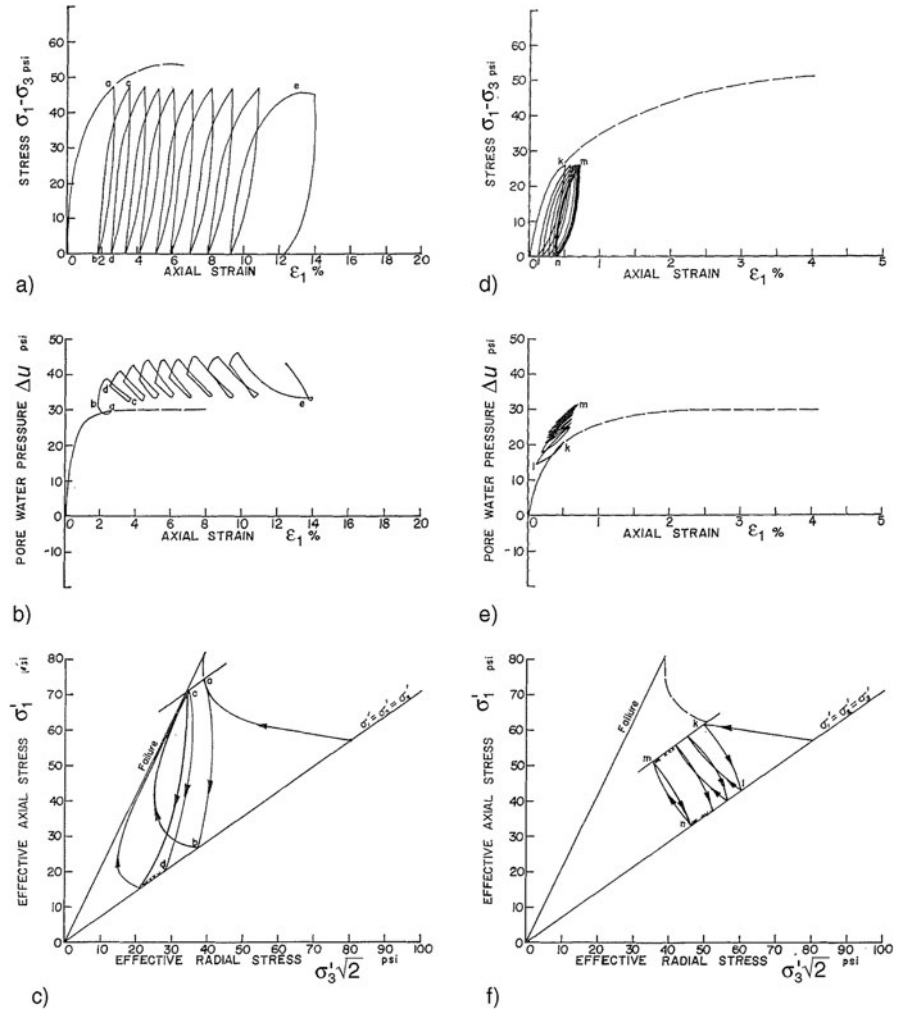


Fig. 5.2.1. Response of clay to some deviatoric stress reversals in undrained triaxial tests (Sangrey et al. 1969): axial stress (a) and pore water pressure (b) versus axial shortening and effective stress path (c) with stress deviators up to 80% of their limit value; same with 50% (d-f)

that approaches a state limit condition repeatedly (c). It appears that with ϵ_1 beyond ca. 5% the sample lost its uniformity due to bulging and friction at the plates, so this part cannot be used as element test. Cycles of $\sigma_1 - \sigma_2$ between zero and ca. 50% of the state limit value lead to a kind of stabilization: hysteresis cycles are reached in the plots of $\sigma_1 - \sigma_2$ vs. ϵ_1 (d) and of p_w vs. ϵ_1 (e), the stress path (f) reaches a cycle which remains well off a state limit. With ϵ_1 below 1% the sample remains rather uniform.

As outlined in Sect. 4.2 for psammoids one can conclude that the differential stiffness $d(\sigma_1 - \sigma_2)/d\varepsilon_1$ is not sufficiently determined by the external state variables σ'_1 , σ'_2 and e . An internal or hidden state variable is needed in addition, with two components h_1 and h_2 in case of cylindrical symmetry. h_1 and h_2 are indeterminate at the onset, but get determined with the approach to SOM-states or by reversals of sufficient number. It appears that in the tests by Sangrey et al. (1969) two kinds of attractors were nearly reached, viz. state limits and *asymmetric state cycles*. Bulging and plate friction prevented uniform big deformations (Sect. 14.1), parameters for state limits could only be estimated with the few data on e and consolidation.

Similarly as in Ibsen's (1994) tests with sand (Fig. 4.2.7) stationary ratcheting was nearly reached with the bigger $\sigma_1 - \sigma_2$, so Fig. 5.2.1c exhibits a similar asymmetric state cycle as observed with sand. With the lower $\sigma_1 - \sigma_2$ of Fig. 5.2.1d the accumulation of p_w (e) gets so small that it is not visible with some cycles. The one-sided asymptotic stress cycle of Fig. 5.2.1f should lead to stationary ratcheting after a sufficient number of cycles with a bigger p_w , so that the limit stress condition for axial shortening would be approached repeatedly. Sangrey et al. (1969) did not attain this ratcheting with ca. 20 cycles. Brown et al. (1975) tested remoulded, undrained clay cylinders with up to 10^6 asymmetric deviatoric stress cycles. In the subcritical range stationary ratcheting was apparently reached, but the report does not suffice to identify asymptotic state cycles.

Hyodo et al. (1999) imposed *symmetric deviatoric cycles* to undrained cylindrical clay samples up to a periodic response, Fig. 5.2.2. Undisturbed samples had been reconsolidated before to estimated in situ stresses. With a lowly plastic clay the stress path (a) tends to a butterfly, and the stress-strain curve (b) tends to a hysteresis loop as observed with sand (cf. Fig. 2.6.6a). In the periodic asymptote the skeleton attains repeatedly critical stress obliquities for axial stretching and shortening, in between the skeleton pressure approaches zero. With a more plastic clay the stress path (c) tends to a butterfly without these two features. The attained hysteresis loop (d) has no almost horizontal sections. Asymptotic state cycles were not attained with a more plastic clay after about 200 reversals.

Hyodo et al. (1999) interpret their observations in terms of cyclic strength, stiffness and mobility without mentioning viscous effects. As outlined in Sects. 2.2 and 3.2 this conventional approach is not objective, empirical correlations proposed by Hyodo et al. are therefore left aside. The only objective feature is the attractor visible in Fig. 5.2.2. This is determined by void ratio, amplitude and strain rate D . As the samples were slender ($h/d = 2$) and the deformations got big the samples lost the desired uniformity (Sect. 14.1). The rather qualitative findings show that the asymptotic response of undrained peloids with reversals gets psammoid-like if state limits are approached repeatedly. The argotropy did not appear as D was roughly constant.

Nearly *symmetric state cycles* were also attained in triaxial tests by Matsui et al. (1980). They imposed alternating $\sigma_1 - \sigma_2$ without drainage to saturated

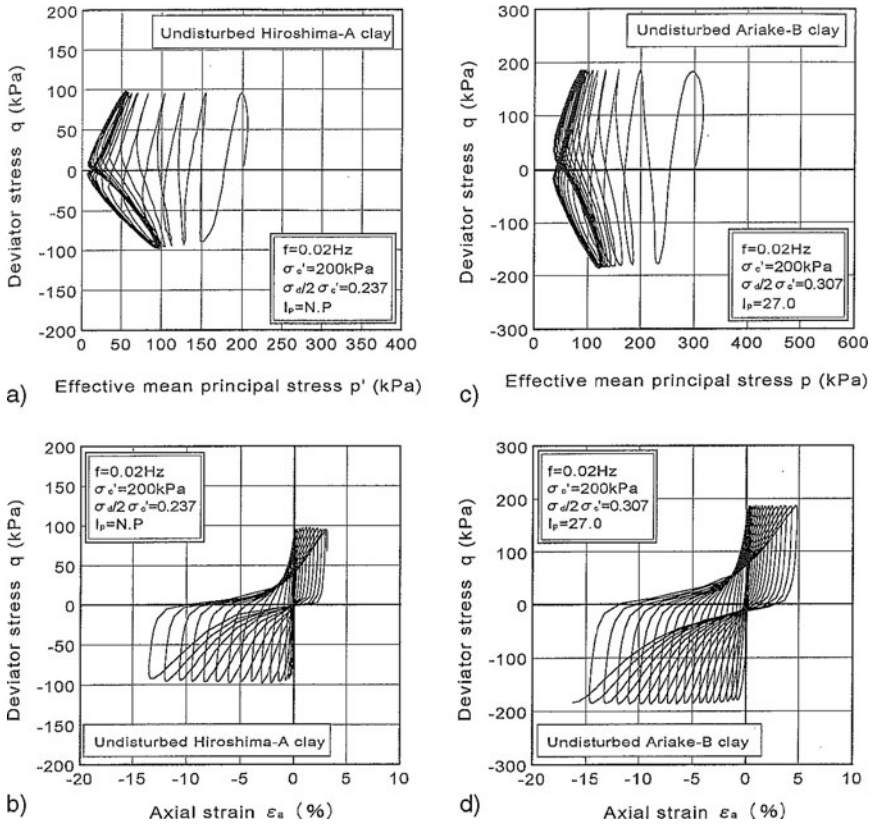


Fig. 5.2.2. Response of undrained saturated cylindrical clay samples to deviatoric stress cycles (Hyodo et al. 1999): stress path (a) and stress-strain curve (b) with low plasticity; same with a more plastic clay (c, d)

samples of a remoulded rather plastic clay after isotropic compression, and also after decompression. With $(\sigma_1 - \sigma_2)$ -amplitudes below ca. 50% of the attainable maximum a periodic response was reached after more than 10^3 cycles. This is shown in Fig. 5.2.3 for tests without decompression with different frequencies f_c . The average pore pressure \bar{p}_w increases up to a saturation value which is higher for a lower f_c (a). The strain amplitude increases alongside with the increase of p_w (b). The argotropy is significant for a frequency increase by factor 20, and stronger than what (3.1.1) and (3.2.2) yield with $I_v = 0.05$. This may be attributed to the wider almost elastic range for more rapid deformations as outlined in Sect. 3.2.

Test results with constant frequency are shown in Fig. 5.2.4. Without precompression the average pore pressure \bar{p}_w increases up to a saturation value that grows with the stress deviator (a). With precompression the asymptotic p_w decreases first and has lower asymptotes (b). Results with

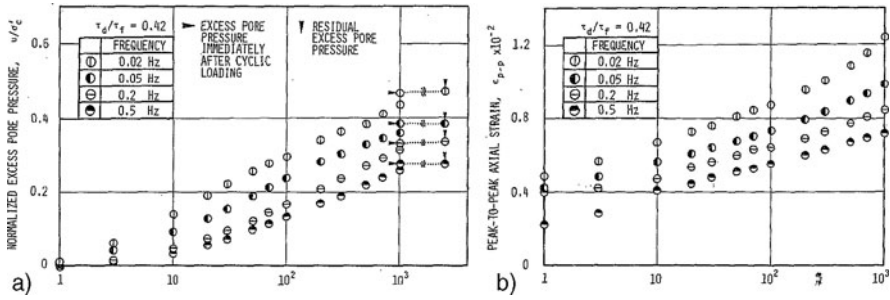


Fig. 5.2.3. Response of a moderately plastic clay after first compression to many deviatoric stress cycles in undrained triaxial tests (Matsui et al. 1980); growth of pore water pressure (a) and strain amplitude (b) with log number of cycles for different frequencies

($\sigma_1 - \sigma_2$)-amplitudes referred to the attainable deviator are left aside as then the sample gets non-uniform. There is no \bar{p}_w -increase (c) after stronger pre-compression and lower than 50% deviatoric stress amplitude. The asymptotic \bar{p}_w increases linearly with the logarithm of the asymptotic strain amplitude and is lower with more precompression (d).

Asymptotic state cycles according to Figs. 5.2.1 and 5.2.4 are proposed in Fig. 5.2.5. Stress components are normalized by the isotropic equivalent

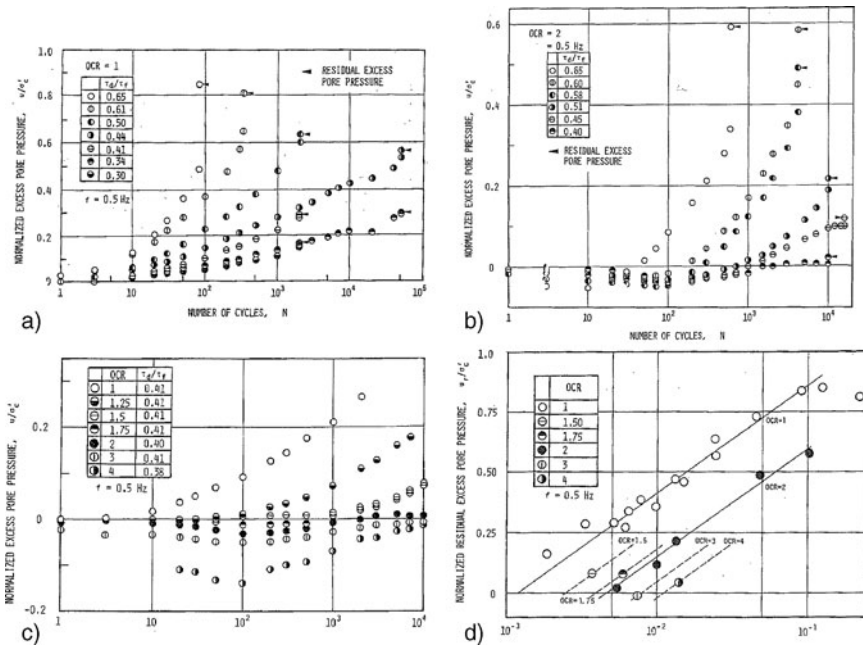


Fig. 5.2.4. Further results of Matsui et al. (1980): change of pore pressure with number of cycles without (a) and with previous decompression (b), evolution of pore pressure after stronger decompression and with lower stress amplitudes (c), averages of asymptotic pore pressure versus log strain (d)

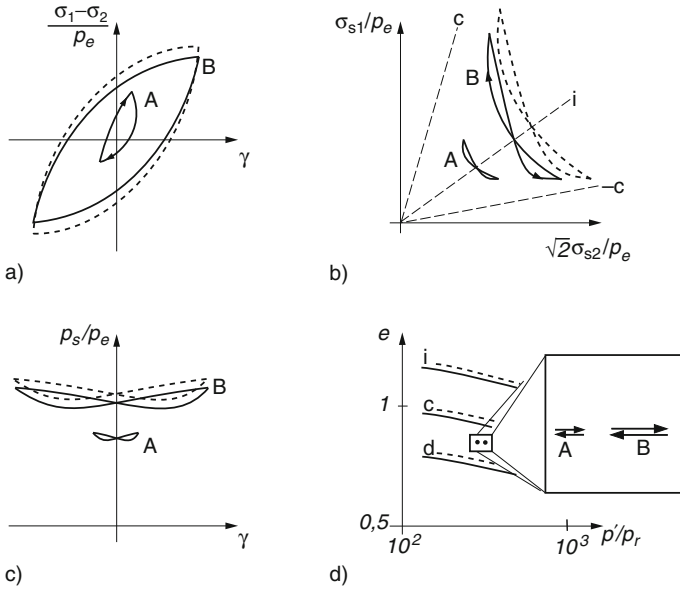


Fig. 5.2.5. Proposed asymptotic state cycles for the tests shown in Fig. 5.2.2: normalized stress deviator versus deviatoric strain (a); normalized stress paths (b), normalized pressure versus deviatoric strain (c), void ratio versus pressure (d). *Dotted* for higher strain rate

pressure p_{ei} in plots of stress deviator (a) and mean pressure (b) vs. axial strain and in the plane σ_{s1} vs. σ_{s2} (c), but not in the plot of e vs. $\log p_s$ (d). With $D = D_r$ and small amplitude (A) the hysteresis (a) is smaller than with big amplitude (B). Butterfly loops indicate two cycles of p_s with one cycle of ε_1 and $\sigma_s - \sigma_2$. They are wider with a bigger amplitude and get closer then to state limit values. Transitions after compression with p_c , and also after decompression to $p_s = p_c/OCR$, indicated in Fig. 5.2.4d by arrows, correspond to the asymptotic \bar{p}_w in Fig. 5.2.3. Dotted loops indicate the asymptotic response for $D > D_r$, this argotropy corresponds to Fig. 5.2.2 qualitatively. Hypothetic asymptotic cycles of the hidden state are similar as in Fig. 4.3.4d. Their amount is lower for lower amplitude and for bigger D , this indicates a more elastic response. The transitions need more cycles with lower amplitude, their onset is as indeterminate as the initial hidden state.

Matsui et al. (1980) opened the drainage of samples with excess pore pressure after many deviatoric cycles, and observed a consolidation. A drainage during the cycles would require extremely low strain rates, therefore isobaric poly-cyclic triaxial tests with saturated clay are hardly feasible. Hyde and Ward (1985) report on undrained triaxial tests with up to 10^4 cycles of $\sigma_1 - \sigma_2$ between zero and up to ca. 80% of the attainable maximum. Remoulded saturated samples of a lowly plastic clay had been consolidated, and were decompressed by different amounts. The observed pore pressure increase with

cycles is similar as the one of highly plastic clays under constant $\sigma_1 - \sigma_2$. Hyde and Ward (1985) do not report on the evolution of strains nor on the asymptotic response, thus their results do not imply ratcheting with asymmetric state cycles.

Matsui et al. (1980) and Hyde and Ward (1985) used elastoplastic models for planning and evaluation of their tests, as almost all other authors. Thus stress paths were imposed without drainage, empirical relations were proposed for the excess pore pressure as softening parameter, failure (i.e. a drastic loss of uniformity) was described with strength parameters depending on an overconsolidation ratio, and viscous effects were often ignored. Lewin and Burland (1970) chose a powder with harder particles than kaolin in order to get less creep, and tried in vain to find elastic ranges. Atkinson et al. (1990) evaluated triaxial test results with a moderately plastic clay and conclude that its behaviour is 'largely inelastic and highly non-linear'. Tavenas et al. (1979) determined lines of equal strain energy around points in a stress component plane which depend also on stress rate or strain rate, Fig. 5.2.6. Thus elastic ranges cannot be identified, and flow rules can only be guessed. The test results with low $\sigma_1 - \sigma_2$ by Matsui et al. (1980) and by Hyde and Ward (1985) demonstrate also that elastic ranges of clays can hardly be identified.

Only few *cuboidal tests* including path reversals have been made with saturated clays. With volume changes the strain rates should be small enough for drainage, so the attainable number of reversals is low. Thus Wood (1975)

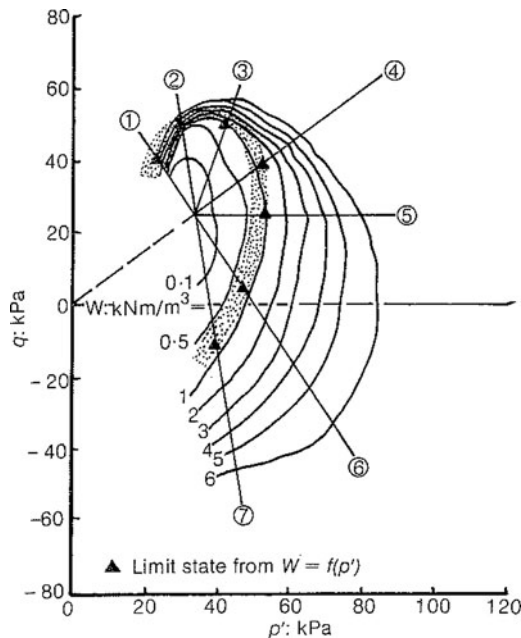


Fig. 5.2.6. Lines of equal strain energy in a stress component plane, determined from triaxial tests with clay by Tavenas et al. (1979)

and Topolnicki et al. (1990) worked with at most two reversals in true triaxial and biaxial tests, respectively, with saturated kaolin. Their results, which were discussed in Sect. 3.7, are apt for validation although the deformations between reversals are big enough to sweep out the internal state, and as amounts of strain rates are given at least by order of magnitude. No observations are available up to argotropic state cycles for cuboidal deformations.

The response of clays to *cyclic shearing* was likewise not as often investigated as with sand. For *small amplitudes* resonant column tests indicate a dependence of the shear modulus G_s on p_s and e as by (4.2.1). Kagawa (1992) obtained a fairly good fit with an exponent $m \approx 0.9$, whereas Hardin and Black (1968) succeeded with $m = 0.5$ as for sand. Accumulations of p_w or e without or with drainage were not observed, so they are presumably low in the usual range of resonant column tests. Callisto and Rampello (2002) observed anisotropic G_s -values via propagation of shear waves similarly as with sand (cf. Fig. 4.2.1). This finding is merely qualitative as the samples had been cut in situ, and as their initial fabric and force-roughness is unknown (Sect. 9.1).

Bigger shear cycles have been imposed to saturated clay samples in devices as by Fig. 2.9.7a. The findings can only indicate qualitative trends as the edges prohibit uniformity of stress and strain. Thiers and Seed (1968) observed a reduction of stiffness and strength with strain amplitudes beyond a threshold of ca. 1%, this is at best a crude estimate. Hsu and Vucetic (2002) sheared samples of a lowly plastic clay in a device as by Fig. 2.10.3, with rather free drainage due to low sample height and frequency, Fig. 5.2.7. With ca. 1.5% strain amplitude the hysteresis is significant (a), and there is a slight gradual densification (b, initial sample height 18 mm). With ca. 15% strain amplitude hysteresis (c) and densification (d) are bigger and approach a periodic

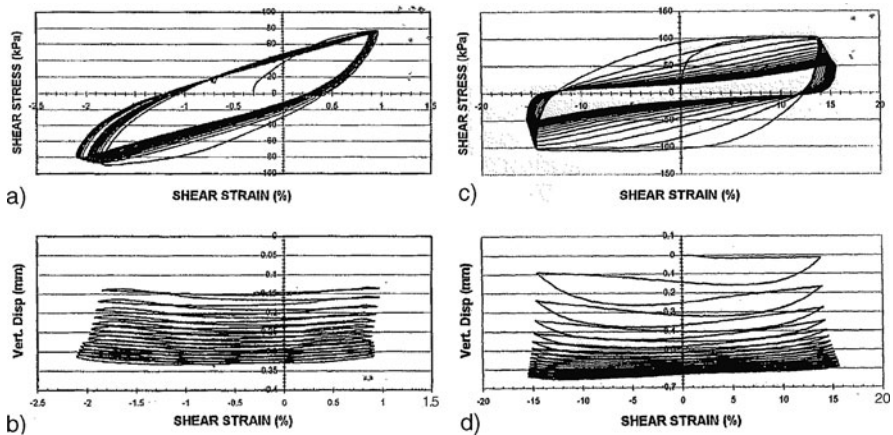


Fig. 5.2.7. Response of a clay to isobaric cyclic shearing (Hsu and Vucetic 2002): shear stress versus shear strain (a) and densification (b) with moderate amplitude; same with big amplitude (c, d)

response. These findings resemble those by Youd (1972) with sand for lower shearing amplitudes, cf. Fig. 2.10.3, and they are likewise impaired by shear localization.

Torsional cyclic shear tests with thick-walled hollow cylindrical samples of saturated clay are rare. Hicher and Lade (1987) worked with a remoulded moderately plastic clay and different kinds of consolidation. The observed response to moderate shear stress cycles without drainage was shown already in Fig. 3.8.7. The evolution of pore pressures and shear strain is more uniform than in simple shear tests. The results are also better apt for validation as it appears that the hidden state gets independent of the onset after a few moderate cycles (cf. end of Sect. 4.2 for sand).

As for solids (Sect. 5.1) it is proposed that the required hidden state variable represents the *force-roughness*. This can be expressed by a symmetric tensor \mathbf{h} , other than for pore-free solids (Sect. 4.1) its isotropic part $\text{tr}\mathbf{h}$ is not negligible due to barotropy. Monotonous deformations with constant D lead to states of swept-out memory (SOM) for which \mathbf{h} is determined by the skeleton stress, and is thus not needed explicitly. Argotropic state limits are SOM-states for which e is determined by p_s , $\tan\psi_s$ and D . Strain cycles and ratcheting lead to state cycles including force-roughness, but the latter is no more always determined by stress and therefore needed. Apart from argotropy this behaviour agrees qualitatively with the one of psammoids, but the skeleton viscosity of peloids influences also their force-roughness. This may get negligible for creep if this tends to a succession of SOM-states (Sect. 3.2), but transitions before can hardly be predicted. As the force-roughness represents spatial fluctuations of stress it gets smaller by relaxation if the shape is fixed. This transition to an equilibrium may be called cold annealing.

To *sum up*, remoulded saturated clays reveal a similar response to reversals as sand. Without drainage strain cycles cause an accumulation of pore pressure, except for strong overconsolidation plus small amplitude, with drainage the gradual densification is significant for the same exception. Symmetric asymptotic state cycles due to strain cycles can be deduced from some test results, an asymmetric state cycle for ratcheting can only be deduced from a single report. Except for lowly plastic clays the argotropy is significant if D changes by orders of magnitude. Some triaxial, cuboidal and shear test results with few reversals are apt for validation as D is known or can be estimated. The relaxation at reversals can matter, but waiting times needed for simulations were rarely recorded. As with sand the cumulative response with many reversals is apparently quasi-viscous and nearly rate-independent.

5.3 Visco-elastoplasticity with back stress

This section is focused on elastoplastic relations, mainly with cylindrical symmetry. As in Sect. 4.5 it is assumed that the internal state can be represented by two back stress components, say α_1 and $\alpha_2 = \alpha_3$. Constitutive relations

are presented *more geometrico* instead of algebraic representations which are intricate and rather preliminary. The argotropy is neglected in most of them, this may be justified if the strain rate D remains in suitable ranges. Extensions with viscosity are treated rather briefly, again *more geometric* as otherwise they are hardly tractable. Back-analyses of some triaxial test results are added for validation.

Based on Mróz' (1967) concept of kinematic hardening which was indicated with Fig. 4.1.8, so-called *bubble models* were proposed for clays with barotropy and pyknotropy, but without argotropy. A plot from Mróz et al. (1979) may indicate what can thus be done, Fig. 5.3.1. In a $p - q$ plane (p instead of p') the elastic range is a smaller ellipse within an elliptic state boundary of the same aspect ratio. Two back stress components defining the position of the elastic range (bubble) can be shifted (kinematic hardening) up to the boundary. The latter depends on e as by Cam clay (Sect. 3.3), thus q and p can be normalized by an e -equivalent pressure p_{ei} (isotropic hardening or softening by contraction or dilation). Critical states with isochoric deformation are implied, and also consolidation with lower than critical obliquity $|q|/p$. Tensile stresses could occur in the dilatant range, therefore a cut-off is needed (cf. Sect. 2.3).

Rather realistic evolutions are obtained for monotonous deformations. The dilatant peak states after strong overconsolidation are debatable as peloids in the sense of Sect. 3.2 cannot have tensile skeleton stress. q -cycles without

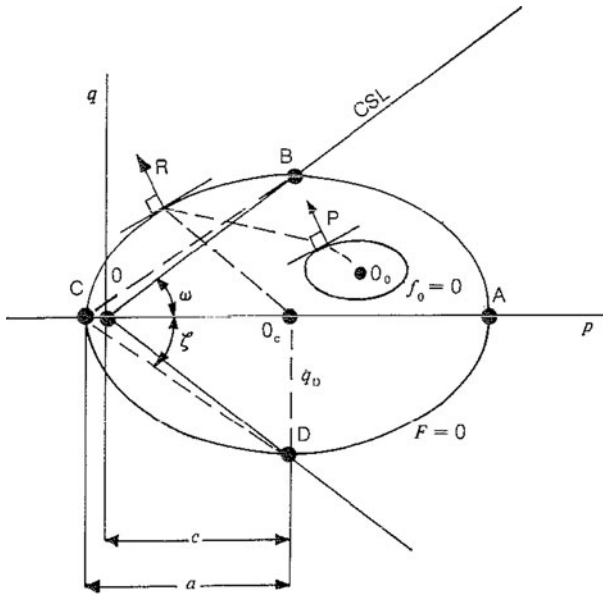


Fig. 5.3.1. Bubble model by Mróz et al. (1967): plane of stress deviators versus mean pressure

drainage lead to a reduction of p without overconsolidation and to an increase with it. This is qualitatively realistic, cf. Fig. 5.2.4. With drainage q -cycles lead to gradual densification and ratcheting. In extensions with rotated boundaries the elastic range is co-rotated so that it can only touch, but not cross the boundary. Shift and inclination of the boundary require two further internal state variables. Mróz et al. (1979) indicate how these can be chosen so that data from uniaxial consolidation tests can be matched.

Attractors for such bubble models cannot be given as software for numerical element tests is not available and could not be worked out from the publications. The bubble model by Rouainia and Muir Wood (2000) allows also for cementation (Sect. 7.3). Stallebrass and Taylor (1997) proposed an extension with *two bubbles*, Fig. 5.3.2. In addition to the boundary and a small elastic range there is a ‘history surface’ which depends on the most recent reversal. The plastic flow rule is the same for the three ellipses (black arrows), the inner surfaces are shifted by plastic deformation (white arrows). The outline by Stallebrass and Taylor (1997) is not easily tractable, but Mašin et al. (2008) worked out software for numerical tests by asking the authors for additional information. Their simulations are not convincingly close to test results.

Whittle and Kavvas (1994) proposed another kind of elastoplastic model with two nested yield surfaces, Fig. 5.3.3. A bounding surface appears as an ellipse in a $q - p'$ plane (left), and as a bubble inside a circle for critical states in a deviator plane (right). Its size and orientation are internal state variables which may be called back stress, two components are needed in case of cylindrical symmetry. They change with plastic strains via a flow rule and a hardening rule with a volumetric (isotropic) and a deviatoric (kinematic) part. An inner yield surface is assumed with the same orientation and flow

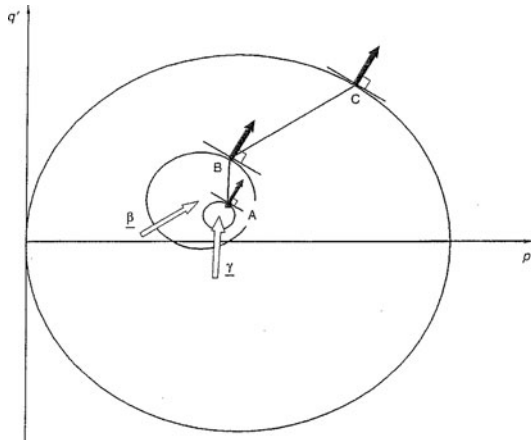


Fig. 5.3.2. Two bubble model by Stallebrass and Taylor (1997) in a plane of stress deviator versus mean pressure

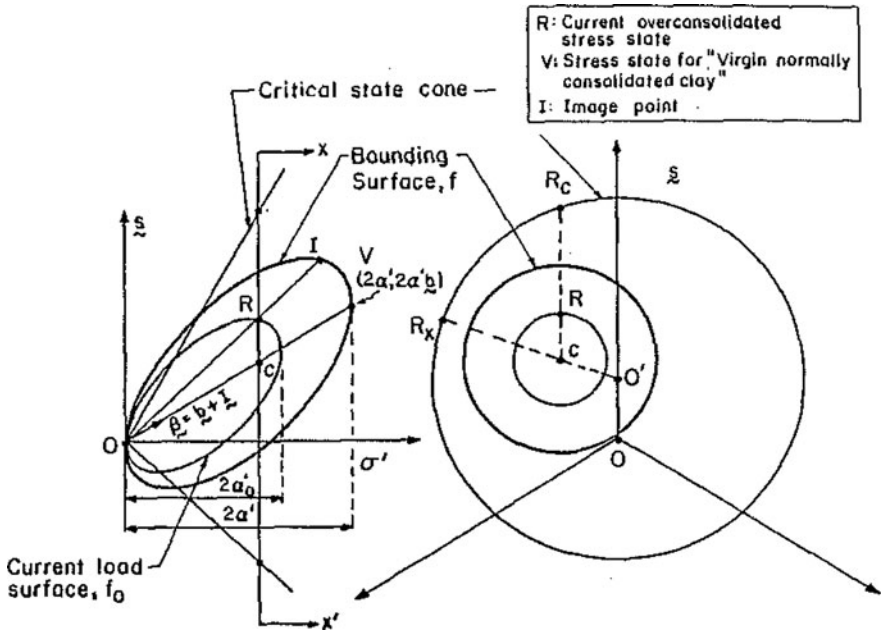


Fig. 5.3.3. Elastoplastic model with nested yield surfaces by Whittle and Kavvas (1994), stress deviator versus mean stress (left), deviatoric stress plane (right)

rule, its size depends on the stress at the last reversal. Combined with an isotropic hypoelastic relation as by (4.4.1), this leads to a response to stress cycles with increasing hysteresis for increasing amplitude. This is achieved by different elasticity parameters for loading and unloading, which are defined by $\dot{\sigma}'_1 \dot{\epsilon}_1 + 2\dot{\sigma}'_1 \dot{\epsilon}_2 \geq 0$ and < 0 respectively.

Whittle and Kavvas (1994) propose procedures for determining the numerous material parameters. The ones for the bounding surface are obtained by matching triaxial test results with proportional compression, critical and peak states. The initial orientation of back stress is adapted so that stress ratios for compression with $\epsilon_2 = 0$ are reproduced (cf. Fig. 3.6.5). The parameters for the hypoelastic-hysteretic response are fitted by means of cyclic triaxial test results. As software is not freely available for this model an in-depth investigation by means of attractors cannot be presented here.

This model was improved by Pestana et al. (2002b), Fig. 5.3.4. In a $q - p'$ plane (a) the bounding and yield surfaces are approximated by lemniscates so that tensile stresses are avoided. In a deviator plane (b) the bounding surface and the cone for critical states are rounded hexagons by Nakai and Matsuoka's (1983) condition (3.7.1). Thus the critical stress condition (2.2.15) holds with the same φ_c for axial extension and shortening. Width and orientation of the elastic range change with plastic strains as for sand (cf. Fig. 4.4.1). The yield surface has the same orientation as the bounding surface, the flow rule is the same for the same stress obliquity. As with the precursor model by

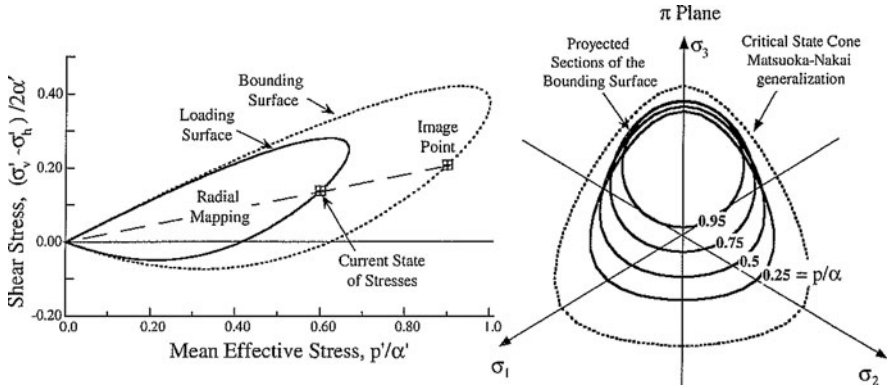


Fig. 5.3.4. Improvement of the model by Fig. 5.3.3 (Pestana et al. 2002)

Whittle and Kavvas (1994) the size of the inner yield surface depends on the last stress reversal, thus an amplitude-dependent hysteresis is obtained with different elasticity parameters before and after a reversal.

Pestana et al. (2002a) propose a procedure to determine the material parameters. They achieve a good matching for monotonous cylindrical deformations of remoulded saturated clays, Fig. 5.3.5. In the plane of $\sigma'_1 - \sigma'_2$

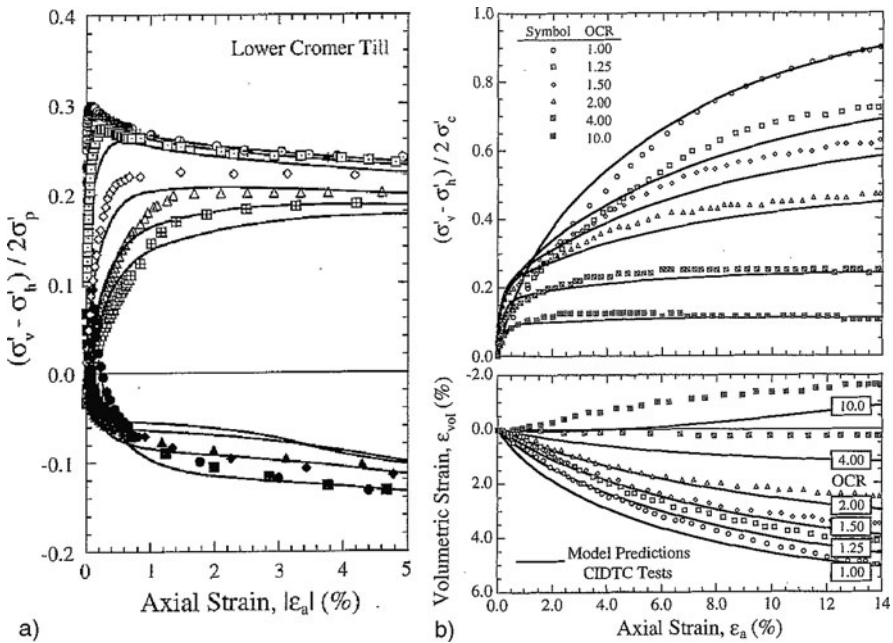


Fig. 5.3.5. Back-analysis of monotonous triaxial tests (Pestana et al. 2002a); normalized stress paths and stress-strain curves without drainage (a); stress deviator and volumetric strain versus axial strain with drainage (b)

vs. $\sigma'_1 + \sigma'_2$, normalized by the consolidation press σ'_p , realistic stress paths are obtained both for axial shortening and extension without drainage (a). Curves of stress deviator vs. $\log |\varepsilon_1|$ reveal a good fit for small and large strains. With drainage the evolution of stress deviator (b) and volumetric strain with axial shortening and constant σ'_2 is also well reproduced. The samples were consolidated with $\varepsilon_2 = 0$, and decompressed by an overconsolidation ratio with different amounts as expressed by *OCR*. In the investigated range peaks appear only with minute amounts for calculations with higher *OCR*. Pestana et al. (2002a) do not outline how they could match stronger peaks, as reported e.g. by Henkel (1956). They argue that the observed hysteretic response to small stress cycles can be reproduced, but do not consider cumulative effects.

The *viscosity* due to thermally activated dislocations in the soft particles could be taken into account with different degrees of precision. If the amount of strain rate D remains within about two decades for loading it may suffice to determine the parameters with D in the range of the intended application, or to correct the reference pressure by (3.3.5) with the viscosity index I_v and the reference rate D_r from tests with different D . This comes up to argotropic bounding surfaces and elastic ranges, whereas flow rules and stress obliquities are not argotropic as for simple peloids (Sect. 3.2).

Thus creep can at best be captured crudely as then D often varies by several orders of magnitude, whereas relaxation with $D = 0$ is missed. As with visco-elastoplastic relations (Sect. 3.3) this lack could be removed by means of a viscosity factor f_v . This depends on the mean stress p_s and an e -equivalent pressure p_e due to combined barotropy and pyknotropy. p_e depends also on the stress obliquity $\tan \psi_s$ as otherwise consistent argotropic state limits cannot be obtained. With f_v plastic strain rate components $\dot{\varepsilon}_1^p$ and $\dot{\varepsilon}_2^p = \dot{\varepsilon}_3^p$ are substituted by viscoplastic ones, $\dot{\varepsilon}_1^v$ and $\dot{\varepsilon}_2^v = \dot{\varepsilon}_3^v$. Taking over the hypoelastic relations (4.4.2) for psammoids, the stress rates are given by

$$\begin{aligned} \dot{\sigma}'_1 - \dot{\sigma}'_2 &= G_r(p'/p_r)^m [(\dot{\varepsilon}_1 - \dot{\varepsilon}_2) - (\dot{\varepsilon}_1^v - \dot{\varepsilon}_2^v)] \quad , \\ \dot{\sigma}'_1 + 2\dot{\sigma}'_2 &= K_r(p'/p_r)^m [(\dot{\varepsilon}_1 + 2\dot{\varepsilon}_2) - (\dot{\varepsilon}_1^v + 2\dot{\varepsilon}_2^v)] \quad . \end{aligned} \tag{5.3.1}$$

The ratio K_r/G_r may be given by (4.4.2) with a rate-independent Poisson ratio ν (which has nothing to do with dilatancy). The exponent m may be rate-independent, whereas the reference pressure p_r could be argotropic by (3.3.5). The flow rule which determines the direction $\dot{\varepsilon}_2^v/\dot{\varepsilon}_1^v$ is rate-independent, it may be given by the normal of the elastic boundary. Kinematic hardening can be formulated similarly with argotropic bounding surfaces and elastic ranges (cf. Fig. 5.1.3). Isotropic hardening and softening by densification or dilation gets argotropic via an argotropic reference pressure by (3.3.5). Visco-elastoplastic-relations with back stress can thus be formulated in variants according to elastoplastic ones. This was done e.g. by Oka (1985), Matsui et al. (1980) and Kaliakin and Dafalias (1990). These models are not outlined here as they are hardly tractable and as software for numerical element tests is not freely available.

Some authors tried to capture isochoric evolutions with many reversals by means of *explicit accumulation models* for the pore pressure p_w . The latter is treated therein like an isotropic back stress in elastoplastic relations. Observed p_w -accumulations were approximated empirically by Van Eekelen and Potts (1978) on the base of cyclic triaxial tests by Andersen (1976). Thus simple methods of elastoplasticity can be used with p_w as empirical hardening or softening parameter. Similar approaches were proposed e.g. by Fujiwara et al. (1985) and Hyodo et al. (1992). Qualitatively a saturated clay behaves like a more overconsolidated one after a p_w -increase due to many isochoric cycles. It is not possible, however, to obtain thus a realistic ratcheting with the same empirically accumulated p_w , let alone other than cylindrical deformations. Heuristic approaches for cumulative anelastic effects with a kind of seismically activated viscosity (cf. Sect. 4.6 for psammoids) appear to be empirically justified, this was noticed already by Hyde and Ward (1985). The pore pressure p_w should not be taken as a kind of temperature, however, as its accumulation has little in common with a seismic relaxation (more in Sect. 5.5).

Not quite as for psammoids in Sects. 4.4 and 4.5, the back stress variants outlined in the present section may be interpreted as representations of *force-roughness*, cf. the end of Sect. 5.2. Apart from argotropy peloids may be assumed to be similar as psammoids in that respect if the amount of strain rate D does not vary extremely. In other words, the argotropy of back stress may be neglected for almost isotachic evolutions. Creep and relaxation cannot be captured by extended Cam clay models with nested yield surfaces and back stress. As the force-roughness can increase by creep and decrease by relaxation the neglect of both can impair back-analyses with Cam clay models which are extended with bubbles in a stress space.

To *sum up*, some elastoplastic relations with back stress produce partly realistic state limits and asymptotic state cycles of remoulded saturated clays. Such relations can work at best for strain rates within few decades as then viscous effects are neglected. They fail for a too high initial overconsolidation as they have no lower e -bound, and also as some of them need a tension cut-off. Argotropy, creep and relaxation could principally be modelled with a viscosity factor as in Sect. 3.4 without back stress. As these models are hardly tractable and as software for numerical tests is not freely available further investigations with argotropic and autogeneous attractors are not yet feasible. Approaches with an empirical accumulation of pore water pressure are physically debatable.

5.4 Visco-hypoplasticity with intergranular strain

Combining the concepts outlined in Sects. 3.4 and 4.6, Niemunis (2003) proposed a visco-hypoplastic relation with intergranular strain (v-hyp- δ), this is introduced here for cylindrical RSEs. The outline is more geometrical than

algebraic, some back-analyses with the freely available software are discussed with physical arguments for validation.

It is assumed for *cylindrical symmetry* that two intergranular strain components δ_1 and $\delta_2 = \delta_3$ evolve with ε_1 and $\varepsilon_2 = \varepsilon_3$ as explained in Sect. 4.5. This is contestable as a relaxation with $\dot{\varepsilon}_1 = \dot{\varepsilon}_2 = 0$ can also reduce the δ_i which represent the force-roughness (Sects. 5.1 and 5.2), but is justified on the other hand by a couple of applications. The evolution equations for the skeleton stress components can be written

$$\dot{\sigma}_{si} = f_b M_{ij} (\dot{\varepsilon}_j - \dot{\varepsilon}_j^v) \quad (5.4.1)$$

with 1 and 2=3 both for i and j , the summation convention, a barotropy factor f_b , a stiffness matrix M_{ij} and a *viscous strain rate* $\dot{\varepsilon}_j^v$. The latter is assumed as

$$\dot{\varepsilon}_j^v = B_j f_v D_r \quad (5.4.2)$$

with the direction

$$B_j = L_{ij}^{-1} N_i / \|L_{ij}^{-1} N_i\| \quad (5.4.3)$$

determined by the non-linear term of the visco-hypoplastic relation (3.4.3), the viscosity factor f_v by (3.2.5a) and a reference stretching rate D_r . $\dot{\varepsilon}_j^v$ is thus the same as without the internal variable δ_i (cf. Sect. 3.4), this is justified by Persson's (2000a) argument that thermally activated creep and relaxation in solids do not depend on the spatial stress fluctuation due to dislocations. The matrix M_{ij} is related with L_{ij} as without argotropy in Sect. 4.5. This is an interpolation between hypoelastic and visco-hypoplastic relations by means of the switch function depending in $\delta_i \dot{\varepsilon}_i$ as in (4.5.4) and (4.5.5). The prefactor f_b is determined by Butterfield's (1979) formula (3.3.13) for first compression. So it is proportional to p_s/p_r , therein the reference pressure p_r depends on D by (3.3.5).

Approaches to *state limits* by v-hyp- δ are rather hypoplastic for constant stretching rates D . The stress paths tend to obliquities $\tan \psi_s$ with the same dependence on the strain rate obliquity as by simple hypoplasticity (Sect. 2.4). The argotropy appears in plots of e vs. $\log p_s$, but not with the paths of intergranular strain. The trend towards the attractors can be visualized by argotropic response polars which consist of two elliptic arcs.

Creep and relaxation by v-hyp- δ are nearly the same as without intergranular strain. With constant skeleton stress components σ_{si} the strain path is straight and contractant with deceleration, isochoric with constant D or dilatant with acceleration, with the same directional dependence of ψ_ε on ψ_s as for state limits. D depends strongly on the void ratio and its evolution. This creep behaviour can be read from (5.4.1) to (5.4.2) with (5.4.3) for $\dot{\sigma}_{si} = 0$, it is essentially the same as shown in Sect. 3.4 without intergranular strain. The latter tends to state limit values without dependence on the rate D . With constant shape the stress path exhibits relaxation which is stronger for a low initial ratio p_e/p_s than for a higher one. This appears also in a plot of e vs. $\log p_s$. A relaxation of δ_i is not allowed for by Niemunis (2003).

The intergranular strain comes into play in the response to *strain cycles*. Stress paths tend to asymptotic cycles which are small and centered, butterfly-like or lenticular. Elliptic cycles for small amplitudes would indicate a nearly hypoelastic response due to a very small viscosity factor f_v . The hysteresis for bigger amplitudes is smaller than without intergranular strain. The argotropy is visible in an e vs. $\log p_s$ plot for bigger amplitudes, but does not appear in an intergranular strain plot. Asymptotic cycles are changed significantly by relaxation in pauses for consolidation ratios $p_e/p_s > \text{ca. } 1.5$. The response to *ratcheting* with constant D resembles the one by hyp- δ . As for v-hyp the argotropy enters via the solid hardness by (3.2.2). The skeleton stress path tends to lenticular cycles which are close to the limit condition.

A back-analysis with v-hyp- δ by Grandas-Tavera (2010) of the *undrained cyclic* tests by Sangrey et al. (1969), which were presented in Fig. 5.2.1, is shown in Fig. 5.4.1. Parameters for the lowly plastic clay were estimated by means of data in this report and from tests with similar clays. With a big deviatoric stress amplitude the stress-strain curve (a), the evolution of pore pressure (b) and the stress path (c) are fairly well reproduced. With a smaller amplitude the diagrams of the same kind (d, e, f) deviate more from the experimental ones, the gradual increase of deformation and pore pressure is underpredicted. Grandas-Tavera (2010) shows that visco-hypoplastic simulations without intergranular strain are nearly as good. The relaxation during reversals plays a role for big amplitudes, but can hardly be taken into account as waiting times were not reported. A back-analysis of the undrained cyclic tests by Matsui et al. (1980) could lead to a further validation, but this report is hardly apt for a quantification.

The neglect of argotropy for the intergranular strain in v-hyp- δ may be accepted for evolutions with roughly constant stretching intensity D as then spatial stress fluctuations of peloids could be similar as those of psammoids. States of swept-out memory (SOM), for which the hidden state is determined by the skeleton stress and thus not needed explicitly (Gudehus et al. 1977), can be attained by monotonous deformations with constant D . SOM-states could be recognized by the response just after reversals with the same D . An almost hypoelastic response is obtained with a sudden increase of D and with consolidation ratios above ca. 1.5 (Sect. 3.2). Contractant decelerating creep can also be captured without hidden state parameters, but observed transitions can hardly reveal the force-roughness. Dilatant accelerated creep leads to shear localization, this requires another kind of internal state variable (Sect. 8.3).

Grandas-Tavera (2010) tried to simulate the *isochoric cyclic* triaxial tests by Hyodo et al. (1999) shown in Fig. 5.2.2. The observed asymptotic butterfly stress paths and concave parts of hysteresis loops could not be reproduced. The underestimation of anelastic effects can be attributed to the nearly hypoelastic response by v-hyp and v-hyp- δ for the attained consolidation ratios (Niemunis and Grandas-Tavera 2010), and as the relaxation near reversals could only be estimated with guessed waiting times (cf. Sect. 3.7). The obser-

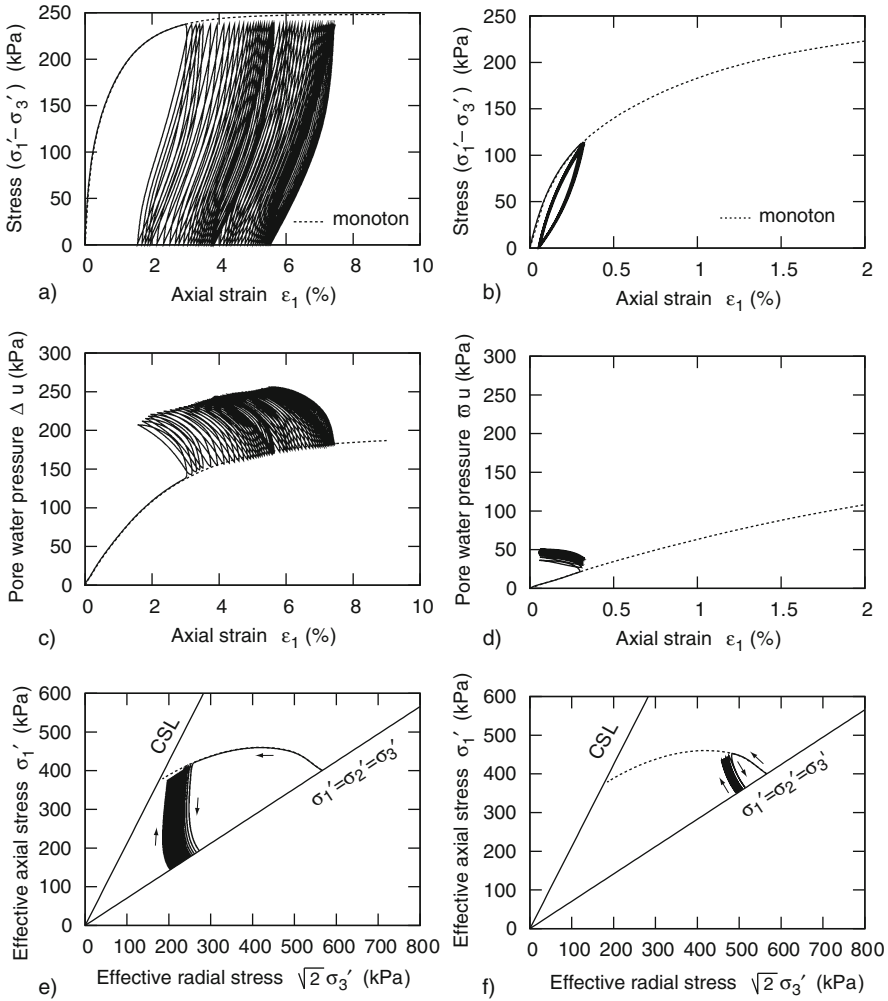


Fig. 5.4.1. Back-analysis of Sangrey’s (1969) tests (Fig. 5.2.1) with v-hyp- δ (Grandas-Tavera 2010); stress-strain curve (a), evolution of pore pressure (b) and stress path (c) for big deviatoric stress cycles; same with small deviatoric stress cycles (d–f)

vations by Hyodo et al. are not apt for a detailed validation as the samples could not remain uniform with the attained big amplitudes, and as strain rates and waiting times are not reported. One cannot judge with them whether the progressive reduction of the skeleton pressure can be better captured with an intergranular strain, let alone the lack of relaxation of the force-roughness by v-hyp- δ .

Niemunis’ (2003) model works also for *cuboidal deformations*, then the subscripts i and j are 1, 2 and 3. Deviator planes with centrally projected

paths of stress and intergranular strain have to be added, whereas the projections onto planes through the space diagonals may be omitted here as they resemble the ones for cylindrical symmetry. The latter holds also for plots of e vs. $\log p_s$, but these must not be dropped. Labels of $(D/D_r)^{I_v}$ may again be used to indicate the argotropy, and labels for $(tD_r)^{I_v}$ for creep and relaxation. Approaches to state limits resemble the ones by hyp- δ . The dependence of the asymptotic directions of stress and intergranular strain on the strain rate direction is the same as without argotropy (Sect. 4.6). The argotropy enters via the solid hardness h_s by (3.2.2).

Creep and relaxation resemble the ones by v-hyp. With constant stress the deviatoric strain path has the same Lode angle α_ε and dilation ratio as for state limits, so it is contractant and decelerating, isochoric and stationary or dilatant and accelerating for a subcritical, critical or overcritical stress obliquity $\tan \psi_s$, respectively. The amount of strain rate is determined by the ratio of the ψ_s -dependent equivalent pressure p_e and p_s via (5.4.2) and (3.2.5). With a constant shape of the skeleton the deviatoric stress path is nearly radial, and the rate of relaxation is far bigger for lower consolidation ratios p_e/p_s . The intergranular strain cannot relax by v-hyp- δ although the force-roughness represented by δ can relax considerably. The response to strain cycles or ratcheting with constant amount of stretching D resembles again the one by hyp- δ .

The tests by Hicher and Lade (1987) with undrained cyclic *isochoric shearing* of hollow cylindrical samples of saturated remoulded clay (Figs. 3.8.7 and 3.8.8) are apt for a more detailed investigation. Stress paths and stress rates were taken from the publication. Simulations by Grandas-Tavera (2010) exhibit nearly the same deviations as the ones without intergranular strain (Sect. 3.8). The agreement is hardly better with relaxation in reasonably assumed waiting times. The simultaneous relaxation of the force-roughness cannot be captured with v-hyp- δ , so the benefit of an intergranular strain is debatable for peloids.

An apparent validation was achieved for a kind of ratcheting with a *thin layer shear test* by Balthasar et al. (2006). The device, the clay and the previous consolidation were described in Sect. 3.8. Anti-plane shear cycles were imposed in addition to section-wise constant shear forces in the direction of average shearing, the normal force was constant. The ca. 1.5 mm thin clay layer was accelerated and dilated slightly after each increase of the shear force. During the anti-plane shear cycles with 1 s^{-1} frequency a drainage was scarcely possible, thereafter the shear rate was reduced strongly by densification. Nearly the same evolution was obtained with a finite element calculation, this allowed for the free rim of the thin layer with capillary skeleton pressure and for filtration.

This agreement holds for the evolution of shear force and shear displacement. The findings suggest that the major inner part of the thin layer remained rather uniform (cf. Fig. 3.8.5b), so this was almost an element test. However, this is not a validation of v-hyp- δ as the same agreement is obtained with

v-hyp (Libreros-Bertini 2006). v-hyp can capture several reversals if the consolidation ratio p_e/p_s does not exceed ca. 1.5 and if the relaxation in waiting intervals is taken into account (Sect. 3.8). An improvement by means of the intergranular strain δ for several reversals with $p_e/p_s < \text{ca. } 1.5$ is questionable, also as there is no relaxation of δ in v-hyp- δ .

Thin layer shear tests with ratcheting were also carried out with higher than critical constant shear forces. A dramatic acceleration occurred shortly after anti-plane shaking with ratcheting. The threshold for this kind of collapse is $F_c \approx N \tan \varphi_{cs}$ with the critical friction angle φ_{cs} . With the very low permeability the dilation necessary for the acceleration must have occurred in the pore fluid. The observations by Balthasar et al. (2006) do not suffice to decide whether this dilation stems from cavitation and crack extension or from shear thinning of bound pore water (Sect. 6.3). Thus the starting time of a dilatant and accelerated skeleton response cannot be predicted, one can only state that it occurs for $|F| > N_s \tan \varphi_{cs}$ with a delay which is shortened by disturbance.

Grandas-Tavera (2010) tried also to simulate the *isobaric cyclic shear* tests by Hsu and Vucetic (2002) shown in Fig. 5.2.7, but rather in vain. The obtained asymptotic hysteresis and mean void ratio were artificial as Niemunis' (2003) v-hyp has no lower bound void ratio e_d , and as anelastic effects are underestimated for consolidation ratios p_e/p_s above ca. 1.5. These shortcomings could be reduced with the modified visco-hypoplastic relation by Gudehus (2004b). The biggest amplitudes employed by Hsu and Vucetic should be left aside, however, as with them shear bands were certainly produced.

To *sum up*, the visco-hypoplastic relation with intergranular strain (v-hyp- δ) by Niemunis (2003) is not convincingly more realistic for evolutions with reversals than v-hyp without intergranular strain. Like with v-hyp observed state cycles are missed for consolidation ratios $p_e/p_s > \text{ca. } 1.5$, and without relaxation near reversals for $p_e/p_s < \text{ca. } 1.5$. Isobaric cyclic shear tests cannot be reproduced as v-hyp and v-hyp- δ have no lower bound void ratio. A certain improvement could be achieved with the modified visco-hypoplastic relation by Gudehus (2004b). The advantage of an intergranular strain representing the force-roughness is questionable as its relaxation is excluded by v-hyp- δ . Some available test reports are debatable as the samples lost the desired uniformity with the attained big amplitudes.

5.5 General and outlook

The viscoplastic relations with hidden state variable which were introduced in this chapter can be formulated with tensors, and can thus be applied in boundary value problems with arbitrary deformations. This will be discussed in the sequel only briefly as the available relations are preliminary, and as successful applications are rare. It is indicated and discussed also how so-called explicit relations could be formulated for evolutions with many reversals. There are

limitations, however, for relations connecting evolutions of shape and state of peloid RSEs with reversals.

A general peloid RSE may be imagined as in Fig. 2.11.1, and can be enriched by an internal state tensor \mathbf{h} for the force-roughness as outlined in Sect. 4.7. The ‘external’ state is objectively characterized by void ratio, mean pressure and deviatoric stress invariants as shown for psammoids with Fig. 2.11.2. The hidden state can be characterized by three invariants of \mathbf{h} , further mixed invariants of \mathbf{h} and \mathbf{T}_s are needed in general if \mathbf{h} is not aligned by the skeleton stress \mathbf{T}_s . Monotonous deformations can lead to SOM-states for which \mathbf{h} is determined by \mathbf{T}_s , and are then not needed explicitly. Otherwise the force-roughness is smaller and less aligned by \mathbf{T}_s , further specifications of the hidden state remain arbitrary and can at best be justified indirectly.

The general response of RSEs with internal state can as yet hardly be quantified beyond the one of simple peloids (Sect. 3.9). This is due to the almost hypoelastic response just after a rapid rise of stretching D , and with consolidation ratios p_e/p_s above ca. 1.5 to 2. Only for constant D and low p_e/p_s the response with reversals can be markedly different from the one with SOM-states. This can be recognized objectively from asymptotic cycles of stress and void ratio by stretching cycles and ratcheting with constant D . It appears that these argotropic attractors, as also state limits for monotonous stretching, resemble those of psammoids (Sect. 4.7). In particular, isochoric repeatedly reversed stretching with moderate amplitudes leads to stress cycles with negligible average deviators, and the mean pressure p_s pulsates with double frequency around an average \bar{p}_s which is mainly determined by the void ratio e . Isochoric ratcheting with small amplitude leads to stress cycles which attain repeatedly the critical obliquity, whereas \bar{p}_s is lower than for critical states with the given e and D . The attained hysteresis, which may be defined by (2.11.16) also for ratcheting with the cyclic fraction of stretching, is smaller than for sequences of SOM-states as assumed for simple peloids. The latter could not yet be quantified for lack of experimental results.

Asymptotic state cycles with changing e can hardly be attained in RSE-experiments with many reversals as the diffusion of pore water prevents the desired uniformity with realistic frequencies and sample sizes. The few published experiments with slow reversals and drainage did not lead to state cycles which clearly reveal deviations from SOM-states. One can as yet only conjecture that periodic attractors with $D=\text{const}$ are psammoid-like. Because of long diffusion times in situ isochoric evolutions with reversals are more often relevant for applications than isobaric ones. Waiting times can suffice for drainage, then gradients of pore pressure p_w generated by isochoric reversals dwindle alongside with changes of e . This consolidation or swelling (Sect. 11.1) is influenced by the viscoplastic skeleton behaviour. Temporal changes and spatial redistributions of the skeleton stress field contribute to a stabilization if the average stress obliquities are subcritical. Then the force-roughness is reduced over several length scales alongside with a densification.

The response to subsequent disturbances without drainage is thus less anelastic initially, but with moderate amplitudes the force-roughness grows again and gets aligned. With overcritical average stress obliquities disturbances lead to subsequent dilation and acceleration up to a creep collapse, then the force-roughness rises and is accompanied by shear localization. It appears that the cumulative response to repeated moderate disturbances can be estimated without an explicit force-roughness.

Visco-elastoplastic and -hypoplastic relations with hidden state variables can lead to similar argotropic state limits and creep, then the internal state is determined by the skeleton stress and thus not needed explicitly (Sect. 3.9). Differences of v-elp- α and v-hyp- δ arise with repeated reversals with so small amplitudes that SOM-states do not prevail, and with relaxation during states of rest. The assumed tensors α of back stress or δ of intergranular strain are at best reasonable substitutes of the invisible force-roughness. Most of the present elastoplastic models ignore the skeleton viscosity, this may be justified for loading with rather constant D and for un- and reloading with far higher D (Sect. 3.9). The relaxation is thus missed, and the judgment of repeated reversals is rather arbitrary. The algebraic representations of more sophisticated versions of v-elp- α and v-hyp- δ are intricate and preliminary due to rather arbitrary switch functions and interpolations.

Numerical simulations as presented in Sects. 5.3 and 5.4 may help to clarify the issue, but can only lead to validations if attractors are attained with them and with adequate RSE-experiments. Some of the presented observations indicate an approach to SOM-states or to state cycles, but cannot be considered as ample evidence of experimental attractors including the hidden state. An apparently acceptable agreement may be achieved by an ad-hoc adaption of parameters. Pitfalls can be avoided by focusing on argotropic attractors which reveal also the influence of force-roughness. This requires explorations in a wide range of stretching and amplitudes, and could lead to improved constitutive relations by trial and error.

Similarly as for psammoids (Sects. 4.6 and 4.7), cumulative anelastic effects of peloids may be captured by so-called *explicit constitutive relations*. Therein cyclic fractions of evolutions are bundled by measures of intensity and duration, thus only averages over many reversals are needed in simplified relations. Attempts of this kind were as yet focussed on the evolution of excess pore pressures (Matsui et al. 1980), this was used as internal variable in elastoplastic relations (van Eekelen and Potts, 1978). Andersen (1976) observed a kind of reduced strength in undrained triaxial and shear tests with clay, and proposed to use it for plastic limit states. Hyde and Ward (1985) noticed that cyclically loaded clay samples exhibit a kind of creep. Let us discuss how far such approaches could be defended and extended.

As the skeleton feels only differences $p - p_w = p_s$ of total and pore pressures, p and p_w , a decrease of the skeleton pressure p_s by isochoric shaking may be interpreted as a kind of osmotic (i.e. entropy-increasing) *net repulsion* (Sect. 6.3). This can be attributed to an average *seismic temperature* T_s ; the

subscript s is chosen instead of g for a granular temperature T_g as peloid particles are not only grains. The repulsion pressure p_r due to T_s (not to be confused with a reference pressure) resembles the seismic pressure p_d proposed in Sect. 4.6. As can be seen from Matsui's et al. (1980) results (Fig. 5.2.3) p_r evolves gradually up to an asymptotic value and is thus cumulative, whereas p_d is thought to result from the instantaneous shaking. Focussing on asymptotic values for stationary shaking this difference is only quantitative, however, the slower growth of p_r than of p_d may be understood as slower seismic 'heating'.

A qualitative difference of p_r and p_d seems to arise with substantially lower than critical void ratios. Matsui et al. (1980) observed no increase of p_w after sufficient overconsolidation (Fig. 5.2.3), whereas the stationary stretching of dense sand (Fig. 4.2.9) reported by Katzenbach and Festag (2004) can be interpreted with $p_d > 0$ (Sect. 4.6). On the other hand, however, p_w decreases to an asymptotic average for dense undrained sand samples (Fig. 4.2.8) in triaxial tests with deviatoric stress cycles (Ibsen 1994). This indicates a kind of net attraction (Sect. 6.3) by isochoric shaking, whereas a net repulsion can arise by isobaric seismic heating alongside with dilation. Both is also possible with thermodynamic equilibria of colloids (Sect. 6.1), thus the analogy of T and T_g or T_s is viable. The remaining difference is the skeleton viscosity, which is both thermally and seismically activated for peloids and only seismically activated for psammoids. We need thus *two* temperatures T and T_s for shaken peloids, but how to combine them?

Consider first the average *directions* of average stress and cumulative deformation rates for shaken peloid RSEs. They are apparently related with each other as for simple peloids and psammoids, but now p_s has to be replaced by $\bar{p}_s - p_r$ with the average skeleton pressure \bar{p}_s and a repulsion pressure p_r by shaking. Thus peloids can exhibit argotropic resistance, creep and relaxation due to combined thermal and seismic activation. They may be judged by means of a generalized stress obliquity, viz.

$$\tan \bar{\psi}_s = \sqrt{\text{tr} \bar{\mathbf{T}}_s^{*2}} / (\bar{p}_s - p_r) \quad , \quad (5.5.1)$$

which depends on the average Lode parameter $\cos 3\bar{\alpha}_s$ as outlined in Sect. 2.11, and by a *generalized consolidation ratio* $\bar{p}_e / (\bar{p}_s - p_r)$ wherein \bar{p}_e depends not only on e and $\tan \psi_s$ for $D = D_r$, but also on T_s . As without shaking stationary flow (average stretching $\bar{\mathbf{D}} = \text{const}$) requires a critical $\tan \bar{\psi}_s$, but now also a stationary repulsion pressure p_r . As with psammoids (Sect. 4.7) the generalized critical void ratio \bar{e}_c is lower due to the seismic temperature T_s which represents shaking (except for big amplitudes as considered further below). \bar{e}_c is similarly reduced by T_e as e_c by a higher T , the particles approach each other more easily for a given \bar{p}_s , heating without drainage would also reduce p_s and soften peloids. The dependence of p_r and \bar{p}_e on T_s may be formulated quasi-thermodynamically, but such a heuristic approach could only be quantified by means of experiments.

With lower than critical stress obliquities by (5.5.1) shaking would cause a gradual increase of the generalized consolidation ratio $p_e/(\bar{p}_s - p_r)$. Without drainage, i.e. for constant e with full saturation, the average skeleton pressure \bar{p}_s would decrease, while the generalized \bar{p}_e is less increased by stationary shaking. This reflects the experience that undrained clay gets more overconsolidated by shaking (Andersen 1976). With drainage and constant \bar{p}_s the average void ratio \bar{e} decreases gradually by shaking, this raises \bar{p}_e via e more than it reduces \bar{p}_s via T_s . With overcritical generalized stress obliquities shaking would cause a reduction of \bar{p}_s without drainage, and a dilation alongside with it. This leads to shear localization, cracking and/or skeleton decay. The thermally activated argotropy causes higher \bar{p}_s for bigger stretching rates D , and enhances the seismic creep if the average stress $\bar{\mathbf{T}}_s$ or its deviator $\bar{\mathbf{T}}_s$ is constant. $\bar{\mathbf{T}}_s$ is more relaxed than with T only by shaking with constant average shape. This is visible from undrained experiments with deviatoric stress cycles with zero average (Figs. 5.2.2 and 5.2.3).

The indicated directional relations require quantifications of repulsion p_r and generalized equivalent pressure \bar{p}_e for different stress obliquities $\tan \bar{\psi}_s$. Experiments are needed with different kinds of shaking, only thus a seismic temperature T_s could be quantified. As with psammoids (Sects. 4.6 and 4.7) the intensity of seismically activated evolutions is lower if the shaking is not random, but rather ordered and polarized. Keeping in mind also the thermally activated viscosity and the diffusion of pore water the required variety of experiments could scarcely be explored. Simulations with v-elp- α or v-hyp- δ would be of little use as these relations with hidden variables are far from being properly validated.

As with psammoids (Sect. 4.6) investigations with a seismic temperature T_s should be focussed on *attractors*. In one group of them samples should tend to a state with constant average shape and imposed fluctuations. If the latter were periodic the skeletons would tend to state cycles with zero average deviators. Erratic fluctuations of shape with constant stationary intensity lead to an isotropic average state. T_s can be defined via the dissipated energy, like T_g it can be referred to \bar{p}_s and to an average number of reversals. In another group of experiments samples should attain a stationary average stretching rate which is necessarily isochoric. With periodic changes of shape around the average deformations, the skeleton would tend to state cycles with non-zero average deviators. With erratic fluctuations this kind of ratcheting leads to a critical stress obliquity by (5.5.1), it exhibits thus a repulsion pressure p_r by T_s . As for psammoids T_s could be defined via the dissipated energy of the fluctuating fraction of deformations.

There are some open questions. By referring T_s to an average number of reversals it would be rate-independent, but the response is argotropic due to thermal activation. As T_s is a kind of temperature its definition should not depend on the kind of soil and excitation. The first group of experiments proposed above corresponds to thermodynamic equilibria, but the dissipation requires a stationary average input of seismic energy and excludes a

seismic heat capacity. The second group corresponds to flow equilibria with stationary drift and thermal activation as outlined e.g. for solids in Sect. 3.1. The combined baro-, pykno- and argotropy should resemble the one of simple peloids (Sect. 3.2). The dependence on T_s could resemble the one on T (Sect. 3.5). Time-averages of T_s could be used for different erratic excitations with the same mean dissipation of energy. For unit-invariance the average excitation frequency \bar{f}_c should be referred to the reference rate D_r for viscosity (Sect. 3.2). All that could better work for random shaking, then the force-roughness is maximal and aligned by the average skeleton stress. Regular shaking implies a lower and less stress-aligned force-roughness, cumulative effects can then be captured by asymptotic state cycles. As flow rules for viscoplastic strains are essentially the same as for simple peloids (Sect. 3.9) one may conjecture that such cases can be captured by seismo-hypoplastic approaches.

Explicit relations can thus at best provide crude estimates of cumulative anelastic effects for shaken peloids. For a rather qualitative judgment later in this book we will only assume that viscosity index I_v and reference stretching rate D_r rise, whereas the equivalent pressure p_e decreases with higher T_s (i.e. stronger shaking) similarly as with higher T . Reversals with *big amplitudes* impair the uniformity of skeletons, so these can even decay. Shear localizations may be principally captured with polar quantities, but can as yet not be quantified (Sect. 8.3). Cracking means cavitation and loss of saturation (Sect. 6.3), it can at best be approached qualitatively (Sect. 8.4). Both lead to changes of fabric which influence the subsequent behaviour (Sect. 9.1). The skeleton can thus decay and go over into mud, which can again become a peloid. Such critical phenomena can only be touched in this book (Sect. 16.3). With them the otherwise presumed continuity goes over into a kind of multifractality so that continuum models with RSEs fail.

To *sum up*, evolutions of peloid RSEs can be captured to a certain extent by viscoplastic relations with a hidden variable, and cumulative effects may be estimated by explicit models, but with big amplitudes both kinds of approaches fail due to critical phenomena. Visco-elastoplastic relations with back pressure are as yet hardly available, extended Cam clay models without viscosity are at best justified for slow loading and rapid un- and reloading. Visco-hypoplastic relations with intergranular strain capture viscous effects, but the relaxation of intergranular strain is ignored. Both kinds of models may serve for matching certain experimental findings, but exhibit shortcomings in the asymptotic behaviour.

The latter can as yet only partly be judged by rather few experimental reports with repeated reversals. The invisible internal state may be understood as force-roughness, this is determined by skeleton stress and void ratio for SOM-states and is indirectly indicated by asymptotic state cycles. Explicit models may be formulated with a seismically activated viscosity via a seismic temperature. With erratic shaking the force-roughness could be maximal and aligned with the average skeleton stress. Such heuristic models may at best

serve to estimate cumulative anelastic effects. The issue gets more intricate than with psammoids due to skeleton viscosity and pore water diffusion. With big amplitudes, i.e. repeatedly overcritical stress obliquities, peloids experience localizations and tend to deterministic chaos for which continuum models fail altogether.

PORE FLUID

For saturated soils the interaction of skeleton and pore water can be captured by the effective stress principle and by means of Darcy's law. In case of partial saturation it is convenient to work again with a kind of *pore fluid*, and with partial stresses and a permeability relation. A moist soil is glued by capillary water which can scarcely flow. Terzaghi (1920) observed that water in narrow slits between glass plates is less mobile. He called it *bound pore water* and proposed later that this glues particles in saturated clay (Terzaghi 1931). Derjaguin and Churaev (1973) postulated a denser and more viscous '*polywater*' in narrow gaps. The DLVO-theory by Derjaguin, Landau, Verwey and Overbeck explains equilibria with interparticle attraction and repulsion in colloids. The interactions of soil particles are more complicated and beyond the present reach of thermodynamics, molecular dynamics and microscopy. So there is no way around heuristic approaches with pore fluid, partial stresses and transport relations, but caution is required.

Liquid and gas in soil pores are not a proper fluid mix, but a compound that is kept by the fabric of solid particles. There are interfaces between liquid and gas and/or solid and in slits with liquid between solids (Sect. 6.1). Thermodynamics works for smooth plane or curved interfaces, but gets already intricate with solutes and electric charges. Soil particles are far from smooth, uniformly charged and inert, and they can be changed by encounters so that their interaction forces are not determined by potentials. Even with simplifying assumptions partial stresses and transport relations for unsaturated psammoids (Sect. 6.2) are problematic as the pore gas tends to non-uniform distributions.

Peloids (Sect. 6.3) are more difficult already with full saturation due to electro-capillary effects. Rather heuristic partial stresses are proposed which depend on the ionic strength. A kind of polywater seems to be justified by observations, but not as imagined by Terzaghi. A net attraction, i.e. an effective tensile strength of the skeleton can occur, surprisingly it raises the limit void ratios. The influence of changing ionic strength is far from being well understood. For peloids with low degrees of saturation the notion of an

average pore fluid gets meaningless. This chapter is kept short as little could be done with more details in the sequel.

6.1 Interfaces of water with gas and solids

The *interface of water and gas* is a skin of roughly $d_w \approx 10^{-9}$ m thickness. Therein H_2O -molecules are polarized and more densely arranged than in bulk water, there is a surface energy $\gamma_{wg} \approx 7 \cdot 10^{-5} \text{ kNm}^{-1}$ which is changed by ions. At thermodynamic equilibrium the balance of linear momentum requires

$$p_g - p_w = \gamma_{wg} (1/r_1 + 1/r_2) \quad (6.1.1)$$

with the pressures p_g and p_w of gas and water. r_1 and r_2 denote the principal radii of curvature, r_i is positive for a concave water surface. Equation (6.1.1) was proposed by Laplace for a *capillary*, it works likewise for slits, necks, bubbles or drops. It holds as long as the skin is thinner than its radius of curvature, i.e. for

$$p_g - p_w \leq \text{ca.} \gamma_{wg}/d_w \approx 7 \cdot 10^{-5}/10^{-9} \approx 10^5 \text{ kPa} \quad . \quad (6.1.2)$$

The gas constituents are H_2O , O_2 , N_2 etc., their partial pressures add up by

$$p_g = p_v + p_{g2} + \dots \quad (6.1.3)$$

with the vapor pressure p_v . The liquid consists of H_2O , dissolved gas and other solutes which are partly dissociated into ions. The liquid partial pressures add up to the water pressure

$$p_w = p_{l1} + p_{l2} + \dots \quad (6.1.4)$$

with the partial pressure p_{l1} of H_2O . The partial pressures are proportional to the mass or mol fractions via equilibrium relations. For low fractions of dissolved gas its concentration or partial pressure is proportional to the partial gas pressure of the same species (Henry's law). This cannot hold at saturation as then an increase of p_{g2} cannot lead to more intake of gas.

Zero net exchange of H_2O through the skin is expressed by Kelvin's law

$$p_g - p_w = -\frac{RT}{V_w} \ln \psi_w \quad (6.1.5)$$

with the relative humidity ψ_w , the specific volume of water V_w and the universal gas constant R . $RT/V_w \approx 1.3 \cdot 10^5$ kPa holds with the usual temperature $T \approx 280$ K. As ions are shielded by the skin they exert an osmotic pressure

$$p_{oi} = -\frac{RT}{V_i} C_i \quad (6.1.6)$$

for a ionic fraction with specific volume V_i and concentration C_i . Similarly as Henry's law this cannot hold near saturation. The equilibrium of coexistent different ions (H^+ and OH^- , Na^+ and Cl^- etc.) is captured by additional relations expressing the average balance of charge. The skin of an electrolyte can have an electric charge at equilibrium, thus e.g. an air bubble in sea water is charged. The equilibria of chemical reactions are also other at the skin than in the bulk. With curved skins there is an even wider variety of capillary equilibria.

Surfaces of hydrophilic *solids* are not smooth in general, and even then they are more complex than skins between liquid and gas. An amorphous glass can have a smooth surface and a boundary layer of aligned molecules, so there is a surface energy and a surface charge. A perfect crystal can have a plane surface with uniformly distributed energy and charge. As both depend on the crystal order an edge separates surfaces with different energy and charge. Real mineral surfaces have steps, dislocations and cracks. Mineral particles in water or air have also adsorbates which are not removed under usual geotechnical conditions. This complexity of shape and composition can principally be captured by thermodynamic relations (Gelb et al. 1999), but these can at best convey qualitative hints.

Diffuse layers of water with ions can be imagined along charged smooth solid surfaces, Fig. 6.1.1. There is an excess of counterions so that the gross charge is zero. Along a plane (a) the equilibrium distribution of the voltage potential ψ is given by the electron charge, the ion valence, the dielectric constants of water and vacuum, the number density of ions at the wall and the

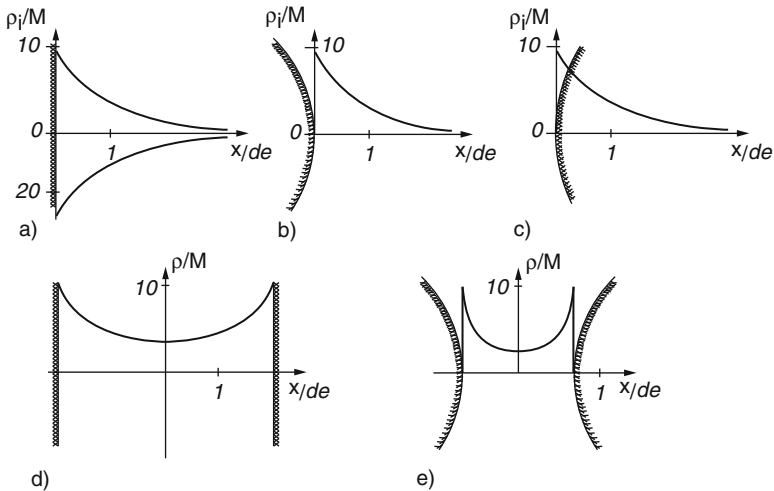


Fig. 6.1.1. Ion concentrations in water near solid surfaces which are plane (a), convex (b) or concave (c), in a slit between planes (d) and between convex solids (e)

distance from the wall (Israelachvili 1995). H_2O molecules are more polarized and more densely arranged near the solid. The thickness of the diffuse layer ranges from ca. 10^{-9} to $5 \cdot 10^{-9}$ m for far-field NaCl-concentrations from zero to 0.5 M \approx 3% by mass. The electrolyte in a diffuse layer has a lower average free energy and a higher average density than in the bulk.

Along a convex solid surface (Fig. 6.1.1b) a lower counterion concentration suffices for the compensation of charge, so the distance to half the maximum excess concentration is bigger than at a plane. The opposite holds for a concave solid surface (c), so there is a kind of *electro-capillary suction* for counterions. In a slit between two planes (d) two diffuse layers interfere and cause an *osmotic repulsion* which is stronger for a narrower slit. A similar interference with osmotic repulsion acts between cylinders or spheres (e).

The situation at contacts of mineral soil particles in water is more intricate as the solid surfaces are not smooth nor uniformly charged, and as there are always adsorbates and often also condensation bridges. Therefore the DLVO theory for colloids is not outlined here, it could at best provide qualitative hints for soils. *Triple interfaces* of solid, liquid and gas in soils are almost beyond the reach of thermodynamics. It may suffice to state that soil minerals are hydrophilic and nowhere on earth free of H_2O at usual temperatures.

The *kinetics* of interfaces is thermally activated (Gelb et al. 1999), cf. Fig. 3.1.2. With a drift energy ΔF which causes dislocations of molecules and/or ions past each other the average rate of dislocations by (3.1.5) can be written as

$$r_t = 2f_c N_o \frac{\Delta F}{E_a} \exp\left(-\frac{E_a}{k_B T}\right) . \quad (6.1.7)$$

Therein r_t denotes the molar transport per unit of time, f_c the average frequency of thermal motion, N_o the Avogadro number, E_a the activation energy per molecule and k_B the Boltzmann constant. One can also refer E_a to one mol and replace k_B by the gas constant R , then ΔF and E_a mean spatial averages per mol in an interface.

For the bulk liquid or gas (6.1.7) determines the rates of shearing and diffusion (and also of heat conduction and chemical reactions which are left aside). Due to lower E_a all rates are far bigger for a gas. For shearing (6.1.7) can be replaced by Newton's relation $D = \tau/\eta$ with shear rate D , shear stress τ and viscosity η . The latter is thus

$$\eta = \frac{E_a}{a_m^3 f_c N_o} \exp\left(\frac{E_a}{k_B T}\right) \quad (6.1.8)$$

with the average molecular distance a_m , and the drift energy $\Delta F = \tau a_m^3$ is dissipated by a unit shear displacement. Coefficients of diffusion can similarly be derived with a drift ΔF due to the gradient of concentration, and an activation energy E_a for the dislocation of a solute molecule past the liquid. This E_a is evidently related with the one for viscosity.

There is a bigger manifold of kinetics with *interfaces*. They have bigger activation energies than the bulk liquid as their density is higher, they are anisotropic as their molecules are polarised, and surface energy is needed or released to reduce or increase their number, respectively. Thus there are various kinds of *capillary condensation* (Evans 1990) towards one of the equilibria outlined further above. For instance, vapor is attracted by a water neck, ions migrate towards a solid surface with ions of lower valence, and two bubbles without charge unite to a bigger one with lower free energy.

Shearing and diffusion along interfaces of liquid and solid are slowed down by higher activation energies due to bigger densities (Israelachvili 1995). *Shear thinning* (Xue and Grest 1990) occurs if the shear stress suffices to dilate and disorder denser molecular arrays in interfaces. Then the viscosity by (6.1.8) is strongly reduced as E_a gets lower. This approach to polywater cannot produce more than a crude estimate as the energy needed for shear thinning exceeds $k_B T$ so that the linear relation $D = \tau/\nu$ is no more justified.

Summing up, only simple interfaces and fluid dislocations, in narrow pores can as yet be captured with thermodynamic relations. Capillary and electrocapillary equilibria can be quantified only with smooth interfaces, not with rough mineral soil particles. The kinetics of water and ion transport is understood except for interfaces with nano-sized curvature.

6.2 Pore fluid of psammoids

Imagine a grain skeleton as RSE which is fixed by rigid filters, Fig. 6.2.1a. The filters take over the skeleton stress components σ_{s1} and $\sigma_{s2} = \sigma_{s3}$ in case of a cylinder, these are constant if the relaxation of the skeleton is negligible. The pore fluid is controlled via the filters and can be at equilibrium or flow. The skeleton can have different degrees of saturation

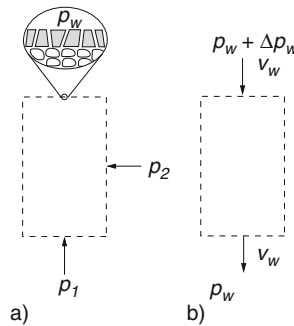


Fig. 6.2.1. Psammoid RSEs fixed by filters, with resting (a) and flowing pore water (b)

$$S_r = \frac{w\gamma_w}{e\gamma_s} \quad (6.2.1)$$

with the water content w per weight of skeleton, void ratio e and specific weights γ_w and γ_s of water and solid. The concentration of solutes may be so low that its influence on γ_w is negligible. Van der Waals attraction and osmotic repulsion at the grain contacts can be neglected for typical grain sizes of psammoids, say $d_g \geq 10^{-4}$ m, if very low skeleton pressures are excluded.

For a *saturated* psammoid the pore water pressure p_w is related with the total and skeleton pressure components p_i and p_{si} by

$$p_i = p_w + p_{si} \quad . \quad (6.2.2)$$

This was introduced in Sect. 2.2 as principle of effective stress. In (6.2.2) p_{si} and p_w are referred to vacuum so that the atmospheric pressure is a part of them. The skeleton pressure p_{si} is called effective pressure σ'_i in soil mechanics. Terzaghi (1936) argued that stiffness and strength are controlled by σ'_i as the solid particles are *neutral* with respect to p_w . Equation (6.2.2) resembles (6.1.4) for a liquid with partial pressures, so p_{si} may be called solid or *skeleton partial pressure*, but other than with a liquid it can be anisotropic and is not proportional to the solid mass fraction. Osmotic repulsion, van der Waals attraction and partial pressures of solutes are neglected by (6.2.2), this is no more generally legitimate for peloids (Sects. 3.5 and 7.1).

The rate of *seepage* per unit skeleton volume and time is proportional to the hydraulic gradient, this is Darcy's law

$$v_w = k_f i = k_f \Delta p_w / \Delta s \quad . \quad (6.2.3)$$

The seepage velocity v_w has to be replaced by $v_w - v_s$ with the velocity v_s of the skeleton if this moves. The quantities in (6.2.3) hold for the direction of seepage. In an objective formulation \mathbf{v}_w , \mathbf{v}_s and the gradient ∇h_w of hydraulic height h_w (instead of $\Delta p_w / \Delta s$) are vectors (Sect. 1.2). Δp_w is the difference of p_w between water entry and outlet minus the one by gravity, Δs is the length of the RSE (Fig. 6.2.1b). This is no more homogeneous with respect to p_w , but may still be called RSE. The skeleton pressure by (6.2.2) has also a gradient due to the specific seepage force $\gamma_w \Delta h / \Delta s$ (in general $\gamma_w \nabla h_w$).

The permeability k_f , which is empirically isotropic for psammoids, is related with the void ratio e and a representative grain size d_g by

$$k_f \approx f_s d_g^2 \frac{n^3}{(1-n)^2 \nu} \quad (6.2.4)$$

with the pore volume fraction $n = e/(1+n)$, $g = 9.81 \text{ ms}^{-2}$ and the viscosity $\nu \approx 10^{-6} \text{ m}^2\text{s}$. The empirical factor $f_s \approx 5 \cdot 10^{-3}$ depends on the shape of the grains and the grain size distribution. Equation (6.2.3) was derived by Carman (1956) by considering laminar flow in channels, their estimated width is a certain fraction of d_g . The pore water flows along open zig-zag paths which

cannot precisely be modelled. The viscosity $\nu = \eta/\rho_w = \eta g/\gamma_w$ depends on activation energy and temperature by (6.1.8).

Thus (6.2.3) and (6.2.4) are based on thermal activation, the proportionality of v_w and Δp_w indicates that the drift ΔF in (6.1.7) is proportional to Δp_w (cf. Fig. 3.1.2, where ΔF is due to gravity). Permeability tests are still needed, but with (6.2.4) the influence of changing void ratio can be estimated, and via (6.1.7) also the one of changing temperature. As outlined further above with equilibria the influence of solute transport on k_f can be neglected for skeletons of saturated psammoids.

Consider now a psammoid RSE with *gas bubbles* between the grains. Their diameter d_b ranges from ca. $0.1d_g$ to $0.4d_g$ for grains with uniform size d_g . The difference of gas and water pressures by (6.1.1) with $d_b \geq \text{ca.} 0.1d_g$ and $\gamma_{wg} = 7 \cdot 10^{-5} \text{ kNm}^{-1}$ is bounded by

$$p_g - p_w \approx \gamma_{wg}/d_b \approx 10\gamma_{wg}/d_g \leq 10 \cdot 10^{-5}/10^{-4} = 1 \text{ kPa} \quad (6.2.5)$$

with $d_g \geq 10^{-4} \text{ m}$ for psammoids. This is negligible against $p_w \geq p_a \approx 100 \text{ kPa}$. The elastic compressibility of a bubble is sufficiently given by the ideal gas equation $pV = \text{const.}$ With the volume fraction $1 - S_r$ of bubbles in the pore fluid its average compressibility is thus approximately

$$K_f \approx p_w/(1 - S_r) \quad (S_r < 1) \quad (6.2.6)$$

for $p_g - p_w \ll p_w$. As long as the concentration of dissolved gas is well below its saturation the gas fraction $1 - S_r$ is proportional to $p_w = p_g$ by Henry's law, but even then (6.2.6) is a crude estimate. One can determine S_r via (6.2.6) by compression tests without seepage, and can attain $S_r \approx 0$ by a high enough p_w to dissolve all the gas if its initial fraction is low enough.

The permeability k_f is reduced by gas bubbles as they work like additional smaller grains, so k_f should be measured with realistic p_w and S_r . The influence of dissolved salt on the compressibility of a pore fluid with gas bubbles may be neglected for psammoids. The salt content can play a role, however, in case of a skeleton decay as then bubbles are no more caught by the grains and unite more easily without a surface charge due to salt.

Consider now psammoid RSEs with *gas channels*. If these are interconnected (Fig. 6.2.2a) the gas and vapor pressures p_g and p_v in them are uniform as long as gas and vapor transport may be neglected. If pore water and vapor are at equilibrium this means p_w by (6.1.5), and a constant curvature $1/r_1 + 1/r_2$ of the water-gas interface by (6.1.1). For a given degree of saturation S_r thus $p_g - p_w$ should be proportional to $1/d_g$ if all lengths are proportional to the grain size d_g . With lower S_r the curvature of capillary water bridges must be bigger, whereas with $S_r \rightarrow 1$ gas channels get impossible.

It is convenient to plot $p_a - p_w$ in a log scale versus S_r , Fig. 6.2.2b. The suction $p_a - p_w$ should objectively be scaled by γ_{wg}/d_g , but usually it is

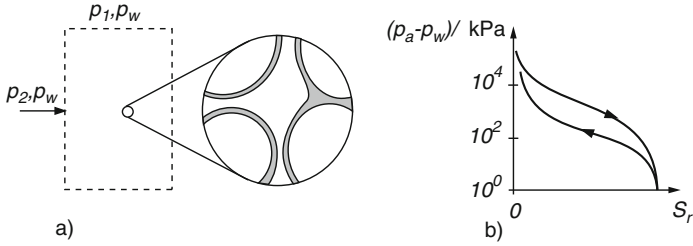


Fig. 6.2.2. Psammoid RSEs with gas channels (a), suction versus degree of saturation (b)

scaled by 1 kPa or 100 kPa. The $p_a - p_w$ for such so-called pF -curves can be determined via filters with known capillary entry pressure or via the relative humidity ψ_w in (6.1.5), salt effects may be neglected for psammoids. $p_g - p_w$ increases from zero for $S_r = 1$ to incredibly high values for $S_r \rightarrow 0$, an upper bound is given by (6.1.2) and by asperities as indicated in Sect. 6.1. For each S_r a bigger $p_a - p_w$ is obtained by removing water than by adding it, this is due to *capillary hysteresis* (Evans 1990).

Wetting and drying up to a certain S_r lead to different spatial equilibrium distributions and to different average suctions. More unique pF -curves can be obtained if H_2O is spread as vapor. Otherwise metastable less uniform distributions with higher free energies are obtained with so high energy barriers that they can be practically permanent. Close to full saturation pF -curves are no more justified as then the gas fraction sits in bubbles and not in channels.

The *permeability* of unsaturated psammoids can formally be described by an S_r -dependent reduction factor to k_f in (6.2.4) as long as the pore water is inter-connected. The gradient of suction $p_a - p_w$ works like the one of p_w , but the average cross section with water is reduced by lower S_r . The permeability is lower for adding water than for removing it, this hysteresis is due to metastable less uniform distributions. Seepage gets impossible if liquid water sits only in islands at grain contacts and as adsorbate on the grains. Therefore the permeability of psammoids with gas channels is low and can at best be crudely estimated.

A *capillary entry* can be produced by increasing the outward gradient of $p_g - p_w$ at an initially saturated RSE. We leave aside suction with $p_w < p_a = p_g$ as then vapor bubbles arise in the pore space. A first gas channel percolates according to the Laplace condition (6.1.1) with the biggest opening between grains at the RSE surface. The capillary entry pressure can thus be estimated by (6.2.5), it is often negligible for psammoids. With a further increase of $\Delta(p_g - p_w)/\Delta s$ more gas channels break through, a new equilibrium can be achieved (and used for porosimetry). The spatial distribution of pore water gets less uniform as outlined further above. Thus a drying front gets more and more non-uniform, this is called *fingering*. The entry of water into an ini-

tially dry skeleton can be more uniform if the skeleton is rather homogeneous. Otherwise the water intrudes faster along wider pore channels and includes pore gas in pockets.

Consider now *skeleton pressures of unsaturated psammoids*, Fig. 6.2.3. A cross section through grain contacts close to a plane (a) cuts water and gas in general. It can go around gas bubbles so that (6.2.2) holds again. With interconnected gas channels having pressure p_g a fraction χ of the cross section projected to the plane cuts water with pressure $p_w < p_g$. Following Jennings and Burland (1962) one may then replace (6.2.2) by

$$p_i = p_{si} + p_f = p_{si} + [\chi p_w + (1 - \chi)p_g] \tag{6.2.7}$$

with $i = 1$ and $2 = 3$ for a cylindrical RSE. A kind of mean pore fluid pressure p_f is thus proposed as weighted average of water and gas pressures. The weighting factor χ depends on the degree of saturation S_r . In a random aggregate average surface fractions agree with volume fractions (e.g. Guyon et Troadec 1994), this would mean $\chi = S_r$. If the gas channels are in equilibrium with the atmosphere, i.e. for $p_g = p_a$, $\chi = S_r$ leads to

$$\sigma_{si} = \sigma_i + S_r(p_a - p_w) \tag{6.2.8}$$

instead of (6.2.7), therein $\sigma_i = p_i - p_a$ denotes total minus atmospheric pressure. The suction $p_a - p_w$ depends on S_r and a representative grain size d_g by the pF-curve.

Equations (6.2.7) and (6.2.8) are no more than estimates. Wavy cross sections cut interfaces of water and gas with surface tension, this raises $-p_w$ and thus σ_{si} . $\chi = S_r$ holds only for plane cross sections, not for wavy ones

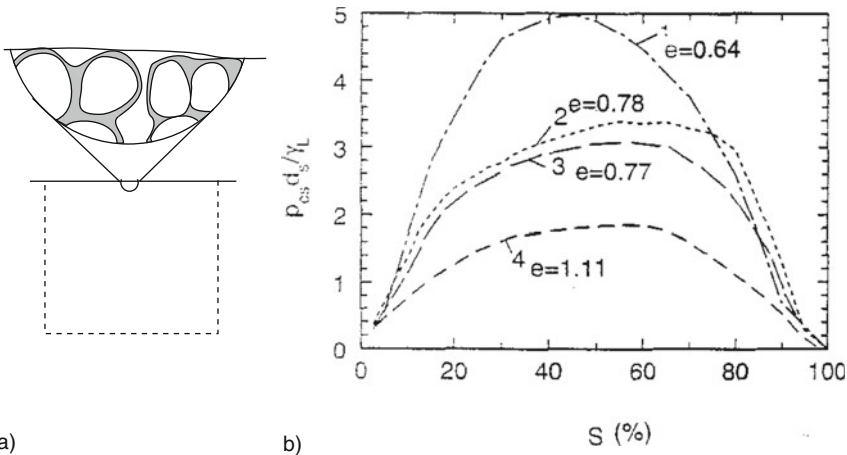


Fig. 6.2.3. Wavy cut through a psammoid RSE with gas channels (a), normalized capillary tensile strength of granular samples versus degree of saturation (b) observed by Mikulitsch and Gudehus (1995)

avoiding grains. As explained with Fig. 6.2.2b the pF-curve is not unique, the water fraction given by S_r can be arranged differently. Equation (6.2.8) gets invalid for S_r near 1 as then the pore gas is in bubbles and not in channels. Altogether the composite of water and gas in the pore space is not really a fluid, so (6.2.7) is rather heuristic.

Skeleton stress components for different S_r could be measured via filter plates with control of vapor pressure to get rather uniform distributions. An indirect determination via compressibility and shear strength, as employed e.g. by Jennings and Burland (1962), is contestable as further constitutive assumptions are needed which should be validated separately. In particular, limit void ratios are higher with gas channels (Sect. 7.2).

Mikulitsch and Gudehus (1995) report on biaxial tests and uniaxial tension tests with fine sand and silt and S_r -control via vapor. Observed tensile strengths p_{cs} for different S_r and e are normalized by γ_{wg}/d_g , Fig. 6.2.3b. This strength is called *capillary skeleton pressure* p_{cs} , it acts in the cross section where the sample is pulled apart. The curves for sand and silt with the same e agree, this confirms that for a given S_r the curvature of water-gas interfaces is proportional to $1/d_g$. p_{cs} is maximal for $S_r \approx 1/2$ and tends to zero for $S_r \rightarrow 0$ and $S_r \rightarrow 1$ as then there is no water or no suction. For a given S_r the p_{cs} is bigger for a lower e and smaller for a higher e as then the curvature is higher or lower. p_{cs} is a kind of negative mean pore fluid pressure p_f , so

$$\sigma_{si} = \sigma_i + p_{cs} \tag{6.2.9}$$

is a better substitute of (6.2.2) or (6.2.7) with the aid of a pF-curve. Figure 6.2.3b may be used for estimates with due caution as the relevant d_g is well below the mean grain size if the grain size distribution is far from uniform.

A capillary entry into a *free surface* of a saturated psammoid determines the partial pressures, Fig. 6.2.4. $p_i = p_a$ normal to the free surface means (a)

$$p_{si} = p_{ce} \tag{6.2.10}$$

with the capillary entry pressure $p_{ce} = \max(p_a - p_w)$. As a channel can get through like a bubble $p_{ce} \approx 10\gamma_{wg}/d_g$ can be estimated with (6.1.1). Without

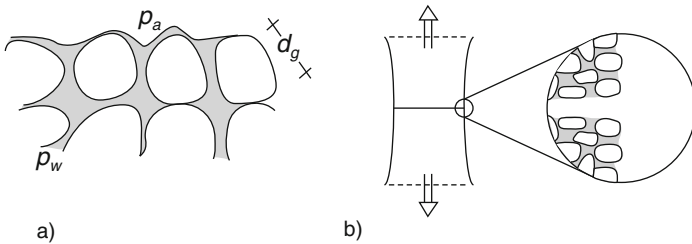


Fig. 6.2.4. Capillary entry at a free psammoid surface by evaporation (a) and traction (b)

net attraction and cementation p_{ce} is identical with the tensile strength as opening of a tensile crack means capillary entry and creation of two free surfaces (b). This tensile strength is bigger than the one by Fig. 6.2.3b as with $S_r \approx 0.5$ and gas channels the curvature of the water-gas interface is roughly the same as at the previously treated free psammoid surface, but the water cross section is smaller. With a continued capillary entry a dewatered psammoid gets less uniform, so its capillary skeleton pressure can only be estimated.

The *coupling* of skeleton deformations and seepage depends on many factors, for some of them crude estimates are obtained with a saturated RSE under simple shearing. The total pressure p may be constant, the RSE-base may be impervious and $p_w = p_e$ is kept at the top. Shearing with a higher velocity v_s leads to a change of skeleton pressure Δp_s nearly as without volume change. As shown in Sect. 2.9 this Δp_s can be negative or positive depending on the relative void ratio r_e , and its amount can reach or even surpass the initial pressure p_{so} , so we have roughly $|\Delta p_s| \approx p_{so}$. The vertical seepage velocity at the top is roughly $v_w \approx k_f \Delta p_w / \gamma_w d$ by (6.2.3) with RSE-height d . It has the same magnitude as the vertical skeleton velocity, $v_{sv} = -v_w$, if water and grains are isochoric. It should be well below the velocity of shearing if this is almost isochoric, say $v_{sv} \leq v_s/100$. $\Delta p_w = -\Delta p_s$ holds by (6.2.2) with the assumed constant p . Combining the assumptions leads to the condition

$$v_s > \text{ca.} 10^2 k_f \frac{p_{so}}{\gamma_w d} \quad . \quad (6.2.11)$$

This may be used to estimate the order of magnitude of v_s for cases with roughly given total pressure, and a mean initial skeleton pressure if seepage may be neglected (*no drainage*). A further estimate is obtained for shearing with nearly constant $p_s = p_{so}$. The ratio of dilatancy $\tan \nu = v_{sv}/v_s$ can be negative or positive, its amount can scarcely exceed about 10^{-1} (Sect. 2.9). For keeping $|\Delta p_w|$ below $10^{-2} p_{so}$, i.e. negligibly small, the shearing velocity has to satisfy the condition

$$v_s < \text{ca.} 10^{-1} k_f \frac{p_{so}}{\gamma_w d} \quad (6.2.12)$$

if excess pore pressures may be neglected (*free drainage*).

For skeleton velocities between these bounds the coupling of skeleton and pore water has to be considered more in detail. If there are gas bubbles (6.2.11) holds with a lower factor than 10^2 as the skeleton can change its volume without seepage, whereas (6.2.12) may be used again. With gas channels skeleton volume changes are not impeded by the pore water as long as S_r is low enough. Near a critical degree of saturation S_{rc} , however, gas channels can be closed by contraction or new ones can be opened by dilation of the skeleton. There is a fuzzy range around S_{rc} for this loss or gain of

skeleton pressure $p_s = p_a - p_w > 0$ as pore water and gas tend to be unevenly distributed.

Cavitation occurs in a dilating saturated skeleton if p_w attains zero (McManus and Davis 1997), i.e. bubbles of vapor and formerly dissolved gas arise. Negative absolute pore pressures cannot occur in saturated psammoids as the rather coarse grains enhance the cavitation.

Summing up, the role of the pore water in psammoids is well understood only for certain degrees of saturation S . For $S_r > \text{ca. } 0.9$ gas bubbles between grains do not impair the principle of effective stress and reduce the permeability only little. Remnants of water for $S_r < \text{ca. } 0.1$ are rather immobile and do not matter for skeleton pressures in the geotechnical range. Skeletons with S_r around ca. 0.5 have an additional capillary pressure which can matter and may be estimated. However, gas channels and pockets need not be uniformly distributed so that RSEs get contestable.

6.3 Pore fluid of peloids

Consider first *saturated peloids with hard grains*. As proposed in Sect. 3.2 their grain size d_g is so small that intergranular forces are not always sufficiently captured with the skeleton stress $p_{si} = p_i - p_w$, which is also called effective stress $\sigma'_i = \sigma_{si}$. The straightforward extension of (6.2.2) reads

$$p_i = p_w + p_{si} + p_{ni} \quad (6.3.1)$$

with a *net repulsion* pressure p_{ni} . Imagine a cross section through grain contacts as in Fig. 6.2.1, and add up repulsive and attractive contact forces similarly as for (6.2.7). The interference of diffuse zones with counterions causes a repulsion which changes with the ionic strength. The interaction of dipoles in solid particles leads to a van der Waals attraction which does not depend on the ionic strength (Israelachvili 1995).

For a colloid of spherical particles without solid contact the net repulsion may be calculated with the DLVO-theory. Israelachvili (1995) shows that the interaction of mineral particles in electrolytes is more complicated. It appears that as yet the net repulsion pressure p_n of peloids cannot be calculated, so there is no way around experiments. As outlined already in Sect. 3.2, $p_n = 0$ is indicated by a submerged saturated sample if it decays without swelling. Fig. 6.3.1 shows sedimented aggregates of corundum powder (grain size $d_g \approx 5 \cdot 10^{-7}$ m) in water with different pH, i.e. logarithm of concentration of H^+ -ions. With pH=4 the sediment has $e \approx 0.6$ and no cohesion, the water above is cloudy, this indicates $p_n > 0$. With pH=9 the sediment has $e \approx 1.6$ and a cohesion of ca. 1 kPa, the water above is clear which indicates $p_n < 0$. With dissolved NaCl a decay indicating $p_n \approx 0$ is obtained for another pH (more in Sect. 7.1).

Such tests can at best indicate the sign and the order of magnitude of p_n and its dependence on the ionic strength. Rather sophisticated resonant

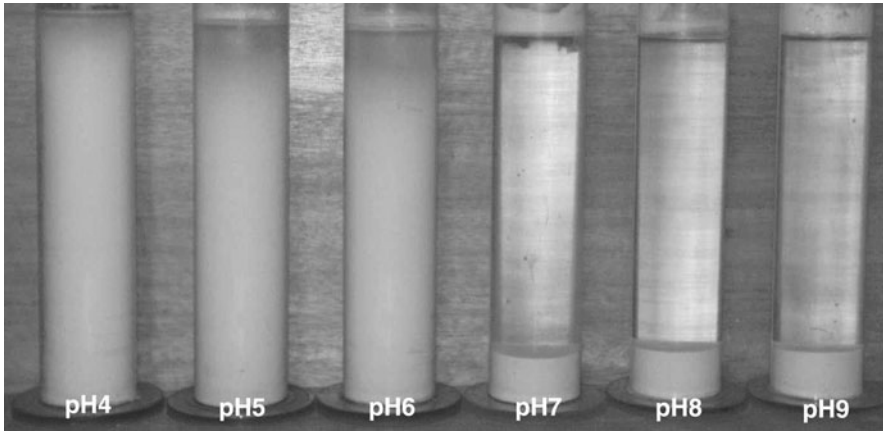


Fig. 6.3.1. Mixtures of corundum powder and water with different pH after sedimentation (Richter 2006)

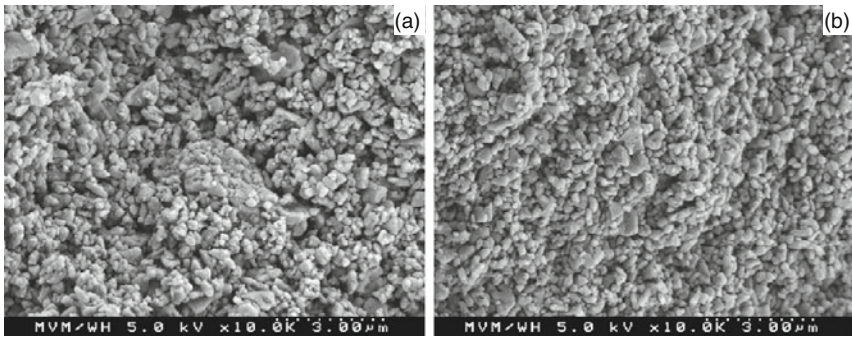


Fig. 6.3.2. Scanning electron micrographs (Richter and Huber 2006) of corundum aggregates with net attraction (a) and repulsion (b)

column tests lead to $p_n \approx 12$ kPa and $p_n \approx -6$ kPa for corundum aggregates as in Fig. 6.3.1 with pH=4 and 9, respectively, after consolidation with $p - p_w$ from ca 50 to 300 kPa (Richter and Huber 2004). A *net attraction* $p_n < 0$ could also be determined as tensile strength under water if the pore water pressure p_w is kept constant. An access of air has to be avoided, the gradient $\Delta p_w / \Delta s$ must be low by slow deformation. A net attraction $p_n < 0$ is a genuine cohesion of the skeleton. It increases the skeleton pressure via (6.3.1), and also the void ratio as shown with Fig. 6.3.1. This apparent paradox (Horn 1990) can be explained by the stability of pores, Fig. 6.3.2. With net repulsion (b) the skeleton pressure is transferred by grain chains in a simple skeleton. With net attraction (a) *macropores* bigger than one grain can stand between grain chains. It will be shown in Sect. 7.1 that limit void ratios are bigger with net attraction.

Filter plates fixing a saturated peloid RSE would indicate changes of p_n due to changes of the ionic strength via diffusion with constant p_w . The filter plates take over $\sigma_{si} = p_{si} + p_{ni}$, the skeleton pressure p_{si} is constant as with resting hard grains their relaxation is negligible. Condensation bridges may be excluded. For instance, the corundum aggregate of Fig. 6.3.1 with pH=9 could be consolidated to $e = 1$ and fixed; after transition to pH=4 the filter plates would indicate $p_s = 0$ due to skeleton decay. An aggregate with pH=7 and 0.5 M NaCl could be densified and brought to $p_s = 0$ by a minute expansion; an increase of p_s after transition to nearly no NaCl would indicate $p_n > 0$. Such experiments have not yet been carried out, but only thus the influence of changing ionic strength could be determined precisely.

Without changing the ionic strength of the pore fluid a net attraction $p_n < 0$ could be estimated via tension tests. A net repulsion $p_n > 0$ could be observed at filter plates after a minute expansion which leads to $p_{si} = 0$. Strictly speaking, this requires comparative tests with $p_n = 0$ and the same e to get the expansion needed to attain $p_s = 0$. Compression and shear tests could at best lead to crude estimates of p_n as the evaluation would require a validated constitutive relation including p_n . We are far from this state of knowledge, at best limit void ratios for different p_n are in the reach (Sect. 7.1).

The *permeability* of saturated hard-grained peloids can be determined as with psammoids. This is justified as long as flow channels in the pore space are scarcely influenced by the lower mobility of H₂O in diffuse zones at the grains. Seepage tests should be carried out with the same ionic strength of the pore water, otherwise the skeleton could change with changing p_n . The influence of grain size and void ratio on k_f may be estimated with (6.2.3). The diffusion is similar as with psammoids, but is accompanied by adsorption or desorption as the specific surface is bigger.

Turning now to *saturated peloids with soft particles*, one has to face stronger electrocapillary effects. A relevant fraction of the solid particles consists of layer silicates, i.e. platelets of a few nanometer thickness with negative face and positive edge charges. Depending on the void ratio and the ionic strength platelets can form various aggregates and can be differently combined with grains which can constitute a skeleton or not. The *bound pore water* near the solid is denser and less mobile, it can be dilated and thinned by shearing. The DLVO theory is even qualitatively insufficient as the particles are far from spherical and uniformly charged. Even in geometrically simple situations the interparticle forces are intricate (Israelachvili 1995). Molecular dynamics simulations are difficult already with dilute aggregates of uniform laponite discs of ca. 2 nm thickness and ca. 25 nm size (Dijkstra et al. 1997).

So for a long while there will be no way around heuristic approaches with idealized RSEs kept by filters similarly as with hard fine grains. With a sufficiently low void ratio e one may assume a skeleton of solid particles, their spatially averaged solid contact forces are captured by skeleton stress components $\sigma_{si}(= p_{si})$. For simple peloids as introduced in Sect. 3.2 the partial stress $\sigma_{si} = \sigma_i - p_w$ is postulated to be effective for the skeleton. This was proposed

by Terzaghi (1936) by means of the neutrality of the skeleton with respect to the water pressure p_w , and was often confirmed by tests with saturated clay.

A wavy cross section through particle contacts of a skeleton (Fig. 6.3.3a) leads to (6.3.1) with a net repulsion pressure p_n , or p_{ni} for direction i , as with hard grains. This was proposed by Sridharan and Venkatappa Rao (1971), whereas Fam and Santamarina (1996) argue that the constituents could also work in series and not in parallel as assumed with (6.3.1). The second assumption would refute the concept of a solid particle skeleton for peloids. Only such skeletons, however, can have argotropic state limits with solid friction as outlined in Sect. 3.2. The activation energies of roughly 1 eV given in Sect. 3.5 point also to solid contacts, the ones of the bound pore water are far lower as will be shown further below. Assuming a skeleton as the seat of stiffness and strength via p_{si} , and neutrality with respect to the pressure p_w of the pore water, (6.3.1) is justified by a cut as in Fig. 6.3.3a. The net repulsion pressure $p_n > 0$ or attraction $p_n < 0$ is thus defined by (6.3.1). So how could p_n be determined and used, and how far is it justified?

One may take over the arguments pointed out further above with hard grains, but there are additional limitations. A consolidated clay sample has a negligible p_n if it is close to decay without filters in water with the same ionic strength as the free pore water (Fig. 6.3.3b). With $p_n > 0$ it expands to a suspension, with a $p_n < 0$ far below the consolidation pressure it breaks under its weight. One has to wait so that p_w gets uniform by seepage, at the onset the sample stands by suction. Changes of the ionic strength in the range of technical interest indicate an increase of net repulsion or attraction with more swelling or higher uniaxial strength.

The resistance to a slow expansion after densification could lead to a more quantitative p_n (Fig. 6.3.3c). Again the surrounding water should have the same ionic strength as the free pore water, and p_w -gradients should be kept low. In case of a net attraction the pressure $p_1 - p_w$ registered by the filter plate drops from the one after consolidation to a negative peak that indicates $p_n < 0$, then it disappears with opening of a crack. In case of net repulsion

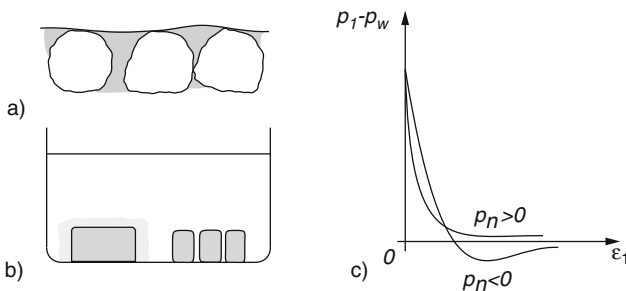


Fig. 6.3.3. Peloids with net pressures: wavy cross section (a), swelling or cracking under water (b), response to extension under water (c)

$p - p_w$ drops sharply down to $p_n > 0$ by decay of the skeleton, then slowly by decreasing osmotic repulsion.

This method could suffice to detect the influence of p_n on state limits (Sect. 7.1). It appears that for them the ratio of net repulsion components p_{n1}/p_{n2} is roughly the same as the skeleton stress ratio p_{s1}/p_{s2} , and that the critical friction angle φ_c is not influenced by the ionic strength. It appears also that the ratio p_n/p_s does not exceed ca. 10% for state limits, thus crude estimates of p_n may suffice. As shown for hard grains in Fig. 6.3.1, however, a net attraction $p_n < 0$ can substantially raise limit void ratios because of macropores.

The proposed determination of p_n and of its influence on state limits could be carried out with different ionic strengths, but an evaluation would overextend the present reach. The clay particles and their spatial arrangement, depending on granular constituents and the sample preparation, are strongly influenced by the ionic strength. A pragmatic way out will briefly be treated in Sect. 9.1 where differences of undisturbed and reconstituted samples are discussed. p_n may be considered as additional state variable, but as yet its dependence on the ionic strength is scarcely known. So one should care for the same ionic strength in experiments as in situ.

Gradients of the electric potential in the free pore water cause its *electrophoresis* past the skeleton. This can imply faster seepage and diffusion of pore water in highly plastic clays than attained with purely hydraulic boundary conditions. With the ever-present ions in the pore water a flux of electric charge is also induced by seepage, the coupling of water and ion transport in the pore space is symmetric (Sect. 16.1).

The *permeability* may be estimated again with (6.2.4), but with another prefactor f_s than for psammoids. The choice of a representative grain size d_g is rather arbitrary as clay particles cannot all be identified as grains. The particle size distribution determined via sedimentation depends strongly on

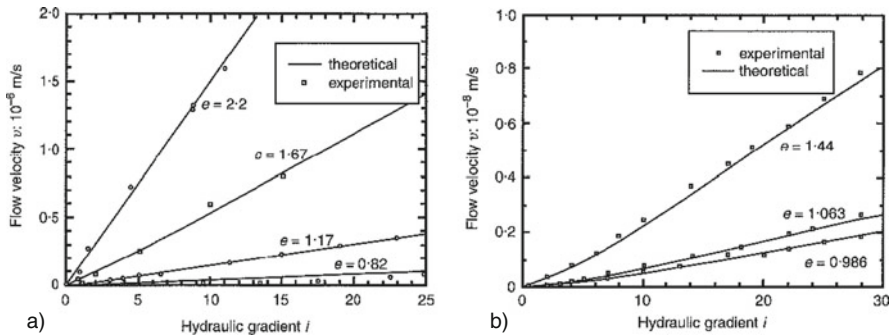


Fig. 6.3.4. Dependence of seepage velocity on hydraulic gradient for a silt (a) and a clay (b), modelled by Zou (1996)

the ionic strength as net attraction leads to flocs that sink faster. The influence of changing void ratios on k_f may be captured by (6.2.4), but what about the less mobile pore water near the particles? Permeability tests show that Darcy's law does not always hold for low gradients, Fig. 6.3.4. While for a silt (a) (6.2.3) and (6.2.4) are confirmed, a clay (b) exhibits a non-linear dependence. Below a kind of stagnation gradient i_o the seepage velocity is well below $k_f i$ with a k_f as for bigger gradients i . i_o increases with lower e and with smaller particles.

These observations show the influence of the *bound pore water*. Zou (1996) explains the non-linear permeability by assuming a kind of shear thinning near the solid particle surfaces. Thus the higher viscosity of the bound pore water is reduced with an increasing seepage force so that the permeability as by (6.2.3) increases. Using (6.1.8) for the influence of E_a on viscosity, and comparing with experimental permeability relations, Zhou estimates activation energies of the bound pore water of up to $E_a \approx 8k_B T = 0.2$ eV for $T \approx 300$ K, whereas for shearing of free water E_a is lower than $k_B T$. For low gradients $\Delta p_w / \Delta s$ the bound pore water is not thinned, this causes the stagnation visible in Fig. 6.3.4.

Results of oedometer tests with saturated clay, as shown e.g. in Fig. 3.6.3b, indicate the same kind of stagnation just after loading reversals. A certain pore pressure difference Δp_w with respect to the water outside the filter plates can occur with negligible seepage according to Fig. 6.3.4, so far a volume change of the skeleton is prevented. For bigger amounts of Δp_w the permeability is reduced by shear thinning of bound pore water, skeleton deformations are no more prevented.

Following Derjaguin et al. (1986) shear thinning can lead to a dilation of the bound pore water by up to ca. 2%. This would mean a minute dilation of saturated clay by undrained shearing, and a minute excess of pore water by contractant drained shearing. As only a small fraction of the pore water is bound in the usual geotechnical range of peloids their dilation can scarcely be measured in RSE tests. Rendulic (1937) observed an excess of pore water beyond the densification of the skeleton in drained triaxial tests with kaolin. Topolnicki (1987) indicates a minute dilation or contraction of the pore water in biaxial test with saturated kaolin. However, Külzer (2010) could not confirm these findings with more sophisticated biaxial tests.

Some observations in triaxial and shear tests with saturated clay point to dilation and thinning of bound pore water although this was not measured directly. A back-analysis of triaxial test results by Henkel (1956) with a visco-hypoplastic relation (Gudehus 2004b) leads to an exaggerated peak with drainage and an initial $OCR \approx 20$. This could be explained by assuming localized shearing without seepage so that the dilation of the skeleton is controlled by the one of the pore water. It will be outlined in Sect. 8.3 that changes of void ratio observed in shear bands could be explained with the same assumption. Thin layer shear tests (Balthasar et al. 2006) with a highly plastic

clay, consolidated and kept under $\sigma = 15$ MPa, exhibited a substantial acceleration under a constant slightly overcritical τ after nearly stationary shear creep. The volume fraction of bound pore water was certainly bigger than for the usual geotechnical range, and seepage was scarcely possible during the acceleration, so the skeleton was apparently dilated by the pore water.

These few observations do not suffice to justify and quantify constitutive relations for and with the bound pore water. Derjaguin's polywater occurs only in narrow zones near solid particles, it depends on surface charges and ion concentrations in an as yet unpredictable manner. It is not a bulk phase, so working with shear-dependent average viscosity and density is contestable. For the present, however, only such approaches are feasible.

The bounds (6.2.11) and (6.2.12) may be taken over to saturated or almost saturated peloids. The order of magnitude of skeleton velocity v_s for assuming no or free drainage is shifted with the one of k_f . As k_f can vary substantially the influence of bound pore water may be neglected in that respect. This is not the case with *cavitation*, however. Temperley and Chambers (1946) observed with water in a thermally expanded glass ball that the suction $p_a - p_w$ can attain ca. 4 MPa before a cavitation. It appears that $-p_w$ can attain almost 100 MPa in narrow gaps, this would mean a radius of curvature of about 10^{-9} m by (6.1.1), i.e. ca. five diameters of a water molecule. Rübél (2010) compressed a bentonite sample up to 150 MPa and observed that it remained saturated after decompression (Fig. 14.1.7). Its strength suggests a suction of $p_a - p_w \approx 50$ MPa, this suits to $\psi \approx 50\%$ humidity by (6.1.5) and to $r \approx 10^{-9}$ m by (6.1.1). Peloids with coarser particles cannot develop such a high suction, thus 50 MPa is an upper bound.

Models with a volume-averaged pore fluid are more disputable for *unsaturated peloids*. Gas bubbles between the solid particles may be allowed for by a reduced permeability and an increased compressibility in comparison with full saturation. Parameters should be determined by experiments with the same solutes as in situ, thermodynamics does not suffice for predictions (Sect. 6.1). Peloids with gas bubbles bigger than the solid particles can occur in mud which thus gets softer (Sect. 7.2).

Interconnected gas channels can arise in a skeleton of hard grains. Other than with psammoids such states are reached if the water content w is below the *shrinkage limit* w_s . Shrinkage with full saturation means isotropic compression with a constant seepage rate $v_w - v_s$ normal to the free surface, Fig. 6.3.5a (Külzer 2010). v_w is given by the rate of evaporation, it can be measured via the weight loss of the sample and is determined by the humidity of the neighboured air via (6.1.5) and (6.1.7). With isochoric solid particles and water $v_s = -v_w$ holds due to the mass balance. The consolidation for $w > w_s$ can be calculated with this boundary condition (Sects. 10.1 and 11.7). The capillary entry at $w = w_s$ is indicated by a change of brightness and a reduction of shrinkage rate (Fig. 6.3.5b) as the further evaporation is reduced by an increase of suction $p_a - p_w$. At the shrinkage limit

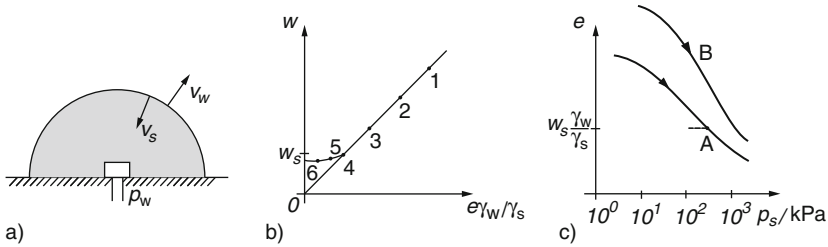


Fig. 6.3.5. Shrinkage of peloids: hemispherical sample (a), actual water content versus the one for full saturation (b), void ratio versus pressure (c)

$$p_a - p_w = p_s = p_{ce} \tag{6.3.2}$$

holds with the pressures of air, pore water skeleton and capillary entry. p_{ce} can be determined via the tensile strength at $w = w_s$ as outlined with Fig. 6.2.4. Thus a limit void ratio $e_i = w_s \gamma_s / \gamma_w$ is given for $p_s = p_{ce}$ and a strain rate via $v_s = -v_w$ (cf. Fig. 3.9.1). A net attraction or repulsion as by (6.3.1) is neglected in this approach, this could be justified via decay in water as outlined further above.

For $w < w_s$ a unique relationship between e and p_s can hardly be obtained, Fig. 6.3.5c. There are no macropores without net attraction prior to the capillary entry, then the skeleton follows the state limit line for isotropic compression (A). The p_s may be determined from e by means of an isotropic first compression test with $S_r = 1$ and $p_s > p_{ce}$. With an average pore fluid pressure as by (6.2.7) this would lead to the net suction

$$p_a - p_w = p_s / \chi \tag{6.3.3}$$

with the area fraction χ with water in a cross section as in Fig. 6.3.3. One could determine $p_a - p_w$ from the relative humidity by (6.1.5) and then χ by (6.2.7). This is incorrect, however, as the ion concentration increases with the evaporation so that (6.1.5) is no more valid. Equation (6.2.7) is also contestable as the surface tension is neglected in the cut.

The net attraction can get bigger due to an increasing salt concentration. For low S_r and longer waiting times a cementation can also get relevant. Compression of dry powder leads to higher void ratios as then the net attraction causes macropores, curve B in Fig. 6.3.5c. The contributions of suction $p_a - p_w$ and of net attraction $p_n < 0$ to p_s may be negligible, this could be checked by comparing the tensile strength with the p_s deduced from e as outlined further above. Only for pressures above the usual geotechnical range curves B and A come together, then capillary gas-water effects could be neglected. With this lack of uniqueness constitutive relations for peloids with gas channels can scarcely produce more than crude estimates (Sect. 7.2).

Without a sufficient fraction of hard grains the desiccation of peloids leads to *shrinkage cracks*, Fig. 6.3.6. A shrinkage limit w_s cannot be identified, the

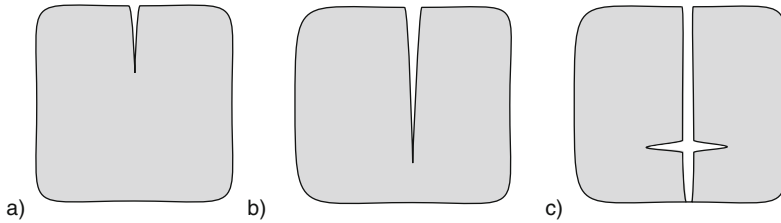


Fig. 6.3.6. Succession of cracks by shrinkage of a highly plastic clay

evolution of cracks depends on the sample size and the vapor transport. The onset of a crack indicates a capillary entry (a), cracks get deeper and wider due to shrinkage between them (b), secondary cracks start from the primary ones (c) and so on. The evolution of such fractal patterns is determined by the coupled transport of water by seepage from the shrinking skeleton and of vapor by diffusion and convection. It is beyond the reach of present prediction models and can get unpredictable (deterministic chaos, Sect. 16.3).

Surface water fills the cracks rapidly, the soil gets softer by the loss of suction and by swelling, the cracks close under gravity as far as the saturated skeleton has not enough net attraction. Thus swelling is enhanced by neutral rain water, and air can be enclosed by wetting in narrower cracks. Depending on the overburden and the remaining permeability a soil with cracks can thus get quite soft after flooding. Evolution and consequences of such cracks were already described by Terzaghi (1925). Soils with many cracks may be modelled as composites (Sect. 9.1), but not without tests on undisturbed samples. Continuum approaches with an average pore fluid and an average skeleton may be used for numerical predictions, but the physical limits should not be ignored.

To *sum up*, the pore fluid of saturated peloids is better understood with hard grains than with soft particles, whereas there are open questions with pore gas. Net repulsion or attraction can be captured with hard-grained saturated peloids. Saturated peloids with soft particles are influenced by bound pore water; therefore skeletons of layer silicates cannot always be identified. Shrinkage and capillary entry are better understood with hard grains than with layer silicates. Desiccated peloids cannot be captured with a pore fluid and skeleton pressure.

BRIDGING GAPS

The title of this chapter was chosen for two reasons. Solid particles can stick together by net attraction (Sect. 7.1), and similarly by capillary (Sect. 7.2) or solid bridges (Sect. 7.3), this attraction enables macropores. In spite of higher skeleton pressures the limit void ratios can be higher by net attraction. The influence and evolution of *particle bridges* can be captured by extended constitutive models, these will but briefly be indicated as there are only few validations.

The intention of this chapter is also to bridge gaps to *other disciplines*. Ceramic masses are of interest in various branches of engineering, and soils are the object of pedology and sedimentology. Soil particles are not permanent as their interactions are not conservative, this is apparently at variance with state limits and state cycles. These attractors will be defended in Sect. 7.3, and further ones could be of use to catch particle bridges. Bridging attempts are limited by strange attractors, however, which can as yet hardly be captured.

7.1 Saturated peloids with net pressures

As outlined in Sect. 6.3 peloids can have a *net pressure* from the difference of interparticle van der Waals attraction and osmotic repulsion. With the aid of cuts through ensembles of contacts ('wavy planes') one can define a net pressure tensor \mathbf{P}_n with mean values $p_n = \frac{1}{3}\text{tr}\mathbf{P}_n$ and direction quantities as for the skeleton pressure tensor \mathbf{P}_s ($= -\mathbf{T}_s$, Sect. 2.11) with mean value p_s . With the total pressure tensor $\mathbf{P} = (-\mathbf{T})$, the pore water pressure p_w and the unit tensor $\mathbf{1}$ (6.3.1) can be written as

$$\mathbf{P} = p_w\mathbf{1} + \mathbf{P}_s + \mathbf{P}_n \quad (7.1.1)$$

which includes

$$p = p_w + p_s + p_n \quad (7.1.2)$$

This decomposition into partial pressures is neither cogent nor generally sufficient, but sophistications are hardly feasible.

With a *net repulsion* of particles a suspension remains turbid above the sediment, which is a rather dense skeleton due to gravity and Brownian motion (Fig. 6.3.1 left). Then p_n is positive and reduces p_s by (7.1.2) for given p and p_w . An increase of p_n means osmotic swelling and can enhance a decay of the skeleton. It can occur by a change of the ionic strength of the pore water, i.e. of acidity or alkalinity (pH) and/or of salinity, i.e. concentration of NaCl and other salts. \mathbf{P}_n , or at least p_n , can principally be determined with an RSE the skeleton of which is fixed by filter plates via the pressure changes at the latter. In such a thought experiment the osmotic repulsion is changed by changing the ionic strength via seepage and solute diffusion, whereas the partial pressure of the fixed skeleton and the van der Waals attraction are not necessarily changed.

With a *net attraction* a suspension gets clear as flocs sink in spite of Brownian motion, and the sediment gets macropores and is thus less dense (Fig. 6.3.1 right). Then p_n is negative and increases p_s for given p and p_w . An increase of $-p_n$ should compress the skeleton, so why is it more porous than for $p_n > 0$ and the same p_s ? This apparent paradox (Horn 1990) can be explained with the solid bridges of attractive particles around macropores. These bridges are not totally destroyed by an increase of the so-called effective pressure $p' = p - p_w$, and can be regained during skeleton rearrangements due to the interparticle attraction. A peloid with $p_n < 0$ does not decay by gravity at an inclined free surface under water with $p = p_w$. A net attraction tensor \mathbf{P}_n with $p_n < 0$ can principally be determined by the experiment described above, but only as long as the skeleton does not decay when the macropores implode due to the loss of interparticle attraction.

State limits of peloid RSEs with net pressure may be defined as follows. The net pressure tensor may be proportional to the skeleton pressure tensor, i.e.

$$\mathbf{P}_n = \kappa_n \mathbf{P}_s \quad (7.1.3)$$

including

$$p_n = \kappa_n p_s \quad (7.1.4)$$

is assumed with a factor κ_n . κ_n depends on the ionic strength and ranges from ca. -0.15 to $+0.15$ by Richter and Huber (2004). Equation (7.1.3) means that the principal directions of \mathbf{P}_n and \mathbf{P}_s agree, $\hat{\mathbf{P}}_n = \hat{\mathbf{P}}_s$, i.e. that the net pressure is aligned by the one of the skeleton. The directional invariants of \mathbf{P}_n and \mathbf{P}_s may therefore agree, i.e. $\tan \psi_n = \tan \psi_s$ and $\cos 3\alpha_n = \cos 3\alpha_s$ (Sect. 2.11) may be assumed. Thus $\cos 3\alpha_n$ ranges from -1 to $+1$ for axial stretching or shortening of cylindrical RSEs, respectively. $\tan \psi_n$ ranges from zero for isotropic states to the upper bound by (2.2.4) for states with one or two zero components, i.e. axial splitting or discing of cylindrical RSEs.

One may imagine solid contact islands with additional net forces from van der Waals attraction and osmotic repulsion to understand (7.1.4). This

hypothesis is debatable as is the assumed alignment of \mathbf{P}_n and \mathbf{P}_s , also in combination with the assumed decomposition of the total pressure into partial pressures by (7.1.2). The latter would yield $p_s = -p_n$ at a free surface under water with $p = p_w$, and thus $\kappa_n = -1$ by (7.1.4) independently of the ionic strength. Actually a skeleton could not exist with net repulsion $p_n > 0$ near a free surface. A peloid can stand with gravity and any inclination due to net attraction $p_n < 0$ up to sizes

$$h_n \approx -p_n / (\gamma - \gamma_w) \tag{7.1.5}$$

with specific gravity minus uplift $\gamma - \gamma_w$ (cf. Sects. 11.2 and 11.3). This does not imply a state limit, however, as the latter can hardly be achieved at a free surface. The uniformity assumed for RSEs requires skeleton pressure levels well above the net pressure, say $|p_n|/p_s < \text{ca. } 0.1$. Otherwise the uniformity would get lost in element tests by decay or cracking.

Limit void ratios may be assumed to depend on skeleton pressure p_s and stress obliquity $\tan \psi_s$ similarly as without net pressure p_n , but in addition on the latter, Fig. 7.1.1. For isotropic state limits e is assumed to be higher with net attraction $p_n < 0$, but to be independent of a net repulsion $p_n > 0$ (a). The regime of muds with low skeleton pressures (say $p_s < 5$ kPa) is left aside for the reasons indicated above. The regime of mudstones with high pressures (say $p_s > 50$ MPa) is also left aside as then skeletons with solid friction are hardly justified. The e vs. $\log p_s$ plots may be similar for different $p_n < 0$, thus the same ratio of macro- and micropores may be assumed for different p_s and a given ionic strength. The influence of the latter on p_n and e cannot yet be quantified by physical arguments (cf. Sect. 6.3). One may only state that the e vs. $\log p_s$ plot is hardly stretched or shortened horizontally with $|p_n| < 0.1p_s$, but can be stretched vertically by substantial amounts due to the net attraction.

Similar e vs. $\log p_s$ plots may be assumed for different stress obliquities $\tan \psi_s$ and a given ratio of net and skeleton pressures p_n/p_s , Fig. 7.1.1b. As without p_n isotropic state limits (i) constitute an upper bound, a lower e -bound (d) may hold for extreme obliquities, and critical void ratios for stationary deformations (c) should be in between. The influence of the Lode

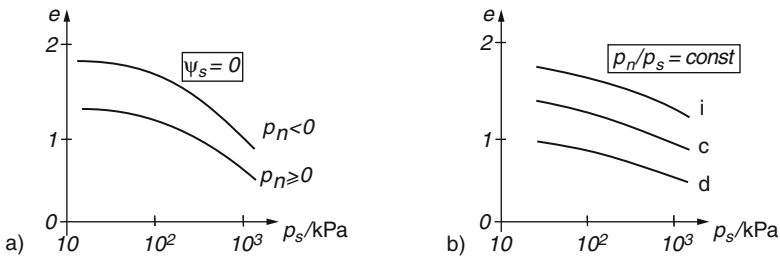


Fig. 7.1.1. Limit void ratios versus skeleton pressures of peloids with net pressure: isotropic compression (a), different stress obliquities (b)

invariant $\cos 3\alpha_s$ on limit void ratios may be neglected as without net pressures. The assumed similarity implies the same volume fraction of macropores for different orientations of the skeleton for given p_s and p_n . As with (7.1.3) and (7.1.4) this assumption is not cogent, but may suffice for the time being.

The *argotropy* of state limits due to thermally activated dislocations at solid particle contacts may be assumed as without net pressure p_n (Sect. 3.2). This means that e vs. $\log p_s$ plots for different stretching D are confounded if p_s is normalized by a reference pressure p_r which depends on D via (3.2.2). Therein a reference D_r and the related p_{rr} for $D = D_r$ should be material properties in order to secure unit-invariance. The net pressure is not argotropic for the D -range which can thus be captured: the van der Waals attraction is given by the relative position of particles, and likewise the osmotic repulsion for a given ionic strength of the free pore water. The latter requires that the diffusion of solubles near particle contacts takes far less time than the rearrangement of skeletons. This is justified for peloids as the activation energies of bound pore water (Sect. 6.3) are well below the ones of dislocations at the contact (Sect. 3.5), and as the diffusion lengths are minute.

The *barotropy* including p_n may be approximated similarly as without p_n , Fig. 7.1.2. In the framework of CSSM (Sect. 2.3) one can write (a)

$$e = e_r - \lambda \ln [(p' + p_n)/p_r] \tag{7.1.6}$$

with $p' = p - p_w$ and a reference void ratio e_r which depends on p_n and p_r . As without p_n one can express the influence of the stress obliquity by a Δe which depends on ψ_s . The influence of p_n could be expressed by a p_n -equivalent pressure p_{ne} which appears as horizontal shift of the e vs. $\log p_s$ line. As without p_n (7.1.6) fails for very low or high skeleton pressures $p_s = p' - p_n$. Other than by CSSM the reference pressure p_r can be argotropic and objective as indicated in Sect. 3.5, and a lower bound e_d can be added.

Bauer's formula (2.4.1) may be used instead of (7.1.6) with a prefactor e_o which is bigger for $p_n < 0$ than without p_n , and not changed by repulsion $p_n > 0$. The same exponent n and hardness h_s may be assumed as without p_n because both represent skeleton properties which do not depend on the

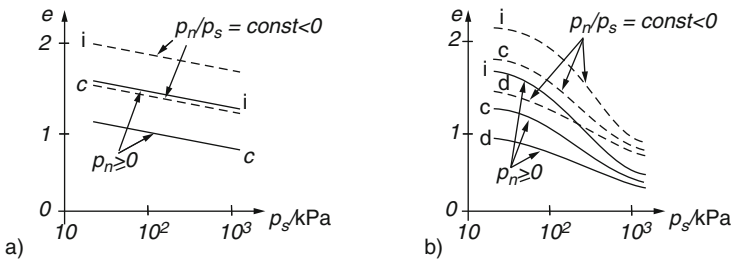


Fig. 7.1.2. Limit void ratios of peloids with net pressures in the framework of CSSM (a) and of hypoplasticity (b)

ionic strength. Thus a relative void ratio r_e can be introduced by (2.2.18), now with critical and lower bound values e_c and e_d which depend on p_s and p_n . The objective h_s can depend on D by (3.2.2) so that r_e is argotropic for a given e . This representation could work for a wider range than (7.1.6) and reflects the assumed similarity of state limits.

The relative void ratio r_e may now be assumed to depend on the obliquity invariants $\tan \psi_s$ and $\cos 3\alpha_s$ as without net pressure (Sect. 2.11), particularly for cylindrical symmetry (Sect. 2.2). Plots of e vs. $\log p_s$ as by Fig. 7.1.2b can thus be confounded by means of a prefactor e_o which depends on $\tan \psi_s$ and p_n/p_s . Less consistently a p_n -dependent relative void ratio difference $\Delta e/e_c$ may be referred to ψ_s in the framework of CSSM. Both representations work only as far as the influence of $\cos 3\alpha_s$ on limit void ratios may be neglected.

State limits with net pressure p_n may be related with a dilatancy ratio $\tan \psi_D$, and with further quantities characterizing the stretching direction (Sect. 2.11). It is proposed that $\tan \psi_D$ depends on $\tan \psi_s$ and $\cos 3\alpha_s$ as without p_n (Fig. 2.7.2). This is rather evident with net repulsion $p_n > 0$ as this cannot influence the dilatancy for a given skeleton stress. With net attraction $p_n < 0$ this assumption means that macropores for a given skeleton stress do not influence the dilatancy ratios of state limits. More specifically it means that macropores do not prevent isotropic state limits, that their volume fraction is stationary for continued critical states of given orientation, and that at bounding state limits with extreme obliquities macropores take part with a characteristic volume fraction.

As without net pressure p_n state limits are assumed to be attractors of RSEs for proportional isotachic deformation paths, i.e. for uniform deformations with constant stretching \mathbf{D} in the range by (2.2.16). Now not only the skeleton stress is determined by the actual D and e , but also the net pressure p_n for a given ionic strength of the free pore water. With the assumed

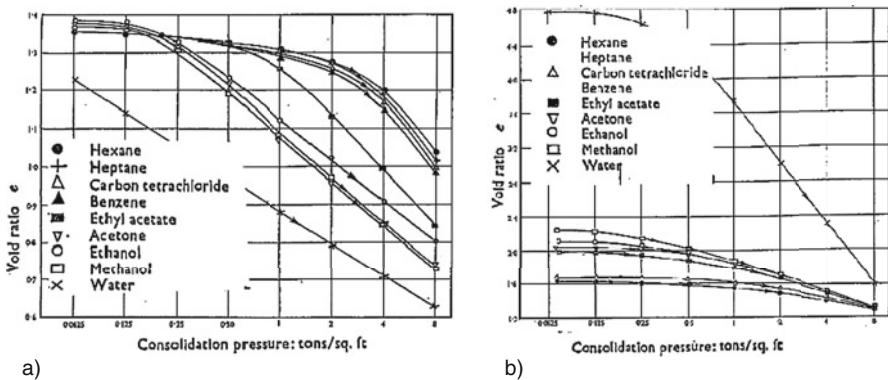


Fig. 7.1.3. Void ratios versus consolidation pressure by first compression of kaolinite (a) and bentonite (b) with water (x) and with less polarized liquids (Sridharan and Venkatappa Rao 1971)

directional agreement, $\hat{\mathbf{P}}_n = \hat{\mathbf{P}}_s$, only p_n is needed as additional state variable, *nota bene* for state limits. Transitions to such distinguished states are left aside, and also localizations which can arise from them alongside with additional state quantities (Sect. 8.3).

Compression tests with different pore fluids by Sridharan and Venkatappa Rao (1971) show how far the proposed concept could be valid, Fig. 7.1.3. Void ratios with kaolinite are higher for less polarized liquids than water (a), this can be attributed to a lower repulsion with organic liquids. The pressure dependence could be described as outlined with Figs. 7.1.1 and 7.1.2 by means of a net attraction $p_n < 0$ from tension tests (Sect. 6.3). Void ratios with bentonite, however, are *lower* with less polarized liquids than water (b). This

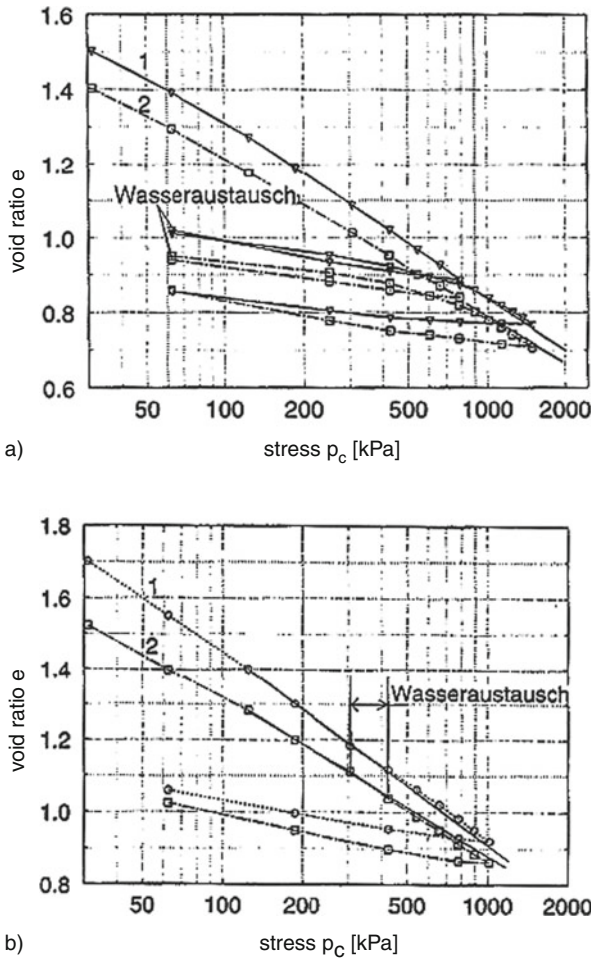


Fig. 7.1.4. Void ratios versus consolidation pressure of saturated quartz powder (a) and kaolin (b) with $5 \cdot 10^{-3}$ M (1) and ca. 10^{-1} M (2) salt content (Zou 1998)

cannot be explained with a skeleton of solid particles with net attraction, both notions are no more justified. Particles and force-transmitting contacts of them can hardly be identified for highly compressible and expansive aggregates of ultra-fine layer silicates and water. Such materials cannot be captured with partial pressures as by (7.1.1), it appears that the constituents work in series and not in parallel (Fam and Santamarina 1996). The neutrality with respect to p_w can still justify the use of effective pressure $p' = p - p_w$, but skeleton and net pressures can no more be defended. Such rather exotic cases are left aside in the sequel.

Zou (1998) reports on oedometric compression tests with saturated kaolin and different ionic strengths of the free pore water, Fig. 7.1.4. Both with NaCl (a) and with CaCl_2 (b) e is higher for a given σ' with a higher ionic strength. This is known for marine sediments with such minerals, their particles coagulate and sink in river suspensions when these reach the sea with about M1 NaCl-concentration. As also shown in Fig. 7.1.4 Zou (1998) changed the ionic strength by seepage and diffusion, and continued the compression afterwards. With each reduction of ionic strength e gets lower under constant σ' , but with a rising and afterwards constant σ' a rise of e is not noticeable. Continued compression leads to the e vs. $\log \sigma'$ plot as for the new ionic strength from the very beginning. This shows that a contractant state limit is attained as outlined further above, whereas states during and just after a change of ionic strength are not state limits.

Külzer (2010) attained state limits with mixtures of Al_2O_3 powder (d_g from ca. $5 \cdot 10^{-7}$ to $5 \cdot 10^{-6}$ m) with water of different ionic strength, Fig. 7.1.5. Depending on pH and NaCl content fresh mixtures were sols or gels due to net repulsion or attraction (a). Such phase diagrams can be explained qualitatively by the DLV-theory, but not the related void ratios. Oedometric compression tests without NaCl exhibit higher void ratios for lower pH and pressures $\sigma' = \sigma - p_w$ up to ca. 1 MPa (b). Slightly higher void ratios are obtained with the same pH-dependence by the rather isotropic shrinkage of hemispherical samples up to a capillary entry (c). The results with repulsion for pH4 can be well approximated by (2.4.1), the ones for pH9 less well with the same n and h_s , but higher prefactors. This confirms Fig. 7.1.2b, but shows also that saturated peloids with a high fraction of macropores cannot be captured precisely.

Shear tests with thin layers of the same material between filter plates led to stationary states with a shearing resistance τ_c proportional to $\sigma' = \sigma - p_w$ (c). As this is valid for different pH and salinities in the range of σ' from ca. 50 to 500 kPa it supports the postulated concept for critical states: τ_c , σ' and p_n are proportional to each other. Related critical void ratios could not be measured, but it was at least observed that e_c is lower for a given σ' than e after compression. A densification up to a lower e -bound was obtained by shear cycles with constant σ' . τ -peaks for subsequent shearing with constant σ' alongside with dilation exhibit the postulated dilatant state limits, but the ionic strength was not varied in these tests.

Tests with various peloids and ionic strengths will be needed for further quantification. Net pressures p_n cannot be determined directly for state limits. Fixing an RSE by filter plates and changing the ionic strength as proposed further above can lead off state limits, cf. Fig. 7.1.4. The resistance to a slow extension under water as proposed in Sect. 6.3 can only yield the order of magnitude of $p_n < 0$ as cracking means loss of uniformity. Triaxial tests with short samples, smooth plates and closed drainage can at best approach uniform critical states (Sect. 12.1). This can lead to e_c and related $p - p_w$, but not directly to p_n . Extrapolations from resonant column tests with Al_2O_3 peloids by Richter and Huber (2004) lead to $p_n \approx 12$ kPa for pH4 and $p_n \approx -7$ kPa for pH9. With a consolidation pressure of $p - p_w = 100$ kPa this suggests that p_n/p_s ranges from ca. -0.1 to 0.1 , but this is only a crude estimate as state limits were thus not attained. It appears that even for state limits the net pressure cannot be determined precisely.

Constitutive relations could be formulated with p_n so that state limits are attractors for proportional deformation paths (cf. Sects. 2.2 and 3.2). The net pressure tensor \mathbf{P}_n , which may be considered as an internal state variable, requires an additional evolution equation. This should produce aligned attractors so that \mathbf{P}_n is proportional to $\mathbf{P}_s (= -\mathbf{T}_s)$ for state limits. This could be achieved by the same stress and stretching rate dependence of net pressure rates as the one of the skeleton pressure rate. With suitable net pressure parameters \mathbf{P}_n is thus not always proportional to \mathbf{P}_s . The argotropy could be modelled by a viscosity factor depending on a consolidation ratio as without p_n . Evolutions with reversals could principally be captured with hidden state variables so that state cycles are obtained as further attractors. Spatial fluctuations of net pressures could be imagined for an additional interpolation.

Such constitutive relations are not outlined here in any detail as they could not yet be applied for lack of experimental data. Some physical arguments may help to illustrate what could and should be done. So-called element tests, i.e. experiments with uniformly composed and deformed samples, should be focussed on attractors as only then the results are objective and apt for validations. A wider spectrum of peloids than indicated by Figs. 7.1.1, 7.1.2, 7.1.3, 7.1.4 and 7.1.5 should be tested, but pH and salinity should only be varied in the intended range of application. The latter can be done also during tests, Fig. 7.1.4 shows that attractors can again arise. Having in mind the complexity of pore fluids (Sect. 6.1) one may hope that this will be better understood with the aid of associated attractors of skeleton and pore fluid.

One may ignore p_n in applications except for free boundaries as long as pH and salinity are constant. With the low presumed ratios p_n/p_s and the indeterminacy of material parameters the neglect of p_n is hardly detectable for skeleton pressures from about 10 kPa to 10 MPa. Conditions for free boundaries, and for filters with wide gaps, may be specified with p_n estimated from the uniaxial strength under water. The issue is different with changes of ionic strength, however. To begin with, state limit parameters determined with

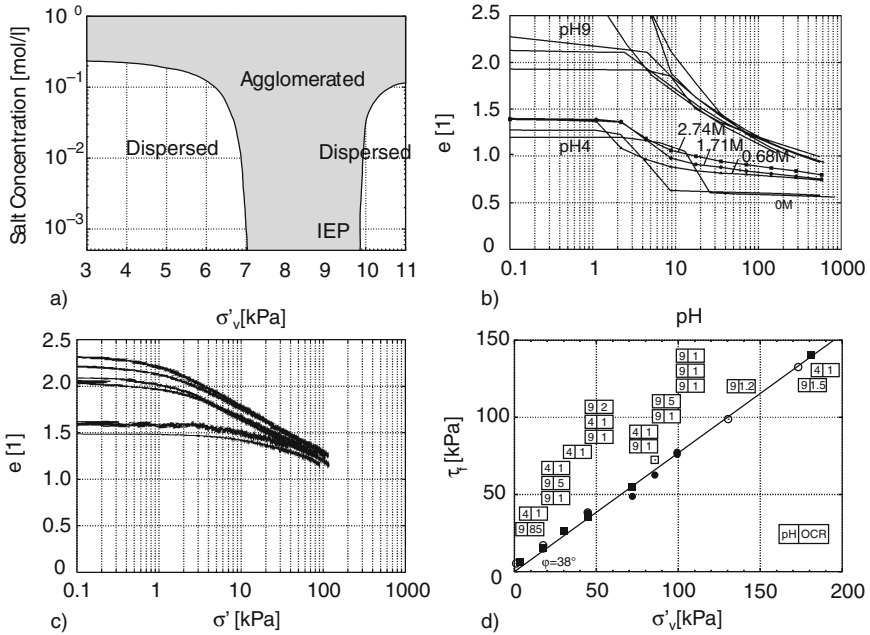


Fig. 7.1.5. State limits of saturated corundum powder with different ionic strengths (Külzer 2009): phase diagram (a), oedometric (b) and isotropic compression (c), stationary shearing resistance with free drainage (d)

fresh water can be misleading if the pore water in situ is different. For instance, a quick clay decays into a suspension by shearing and gets ductile by adding salt (Bjerrum 1955).

Salt concentrations and pH may be uniform in samples, but in general they change with position and time so that p_n is not constant. Even with a single species the *solute transport* by convection and diffusion is influenced by adsorption and desorption, let alone reactions. The coupled transport of several species can as yet only be modelled for fixed skeletons. The equations get non-linear by coupling with changes of void ratio, i.e. with diffusion of pore water. Thus predictions of pH- and salinity-dependent net pressures p_n can at best be crude and are impeded by critical phenomena (Sect. 16.1). It will be a long way therefore up to validations.

To *sum up*, the influence of net pressures p_n on the mechanical behaviour of saturated peloids can principally be captured by means of attractors, but quantifications and validations will need a lot more work. State limits have been observed in some element tests, the influence of p_n can be represented graphically and algebraically. This may be neglected in applications with constant ionic strength except for free surfaces and filters. Changes of p_n with position and time due to solute transport can as yet hardly be modelled, but can be important for the stability of skeletons in situ.

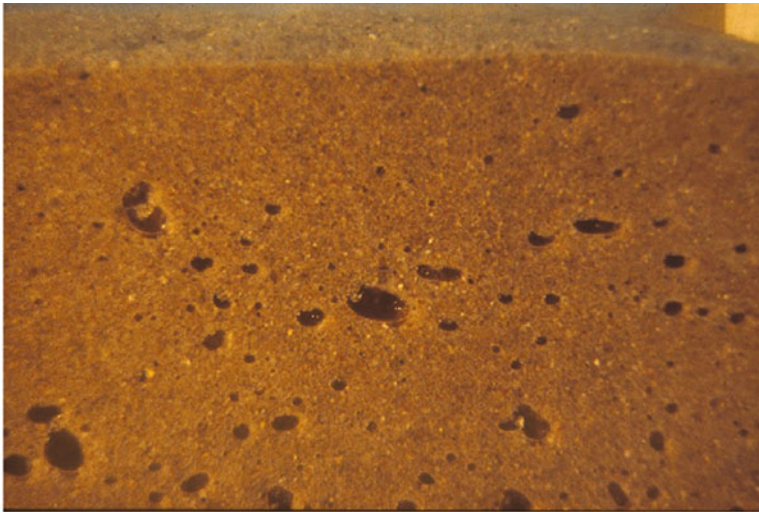
7.2 Unsaturated soils

Pore gas can occur in skeletons of psammoids and peloids as bubbles and channels, often with little spatial order (Sects. 6.2 and 6.3). Even with simplified spatial distributions, so that RSEs make sense, the influence of pore gas can at best be captured for state limits and asymptotic cycles. Without considering constitutive relations it will be indicated in the sequel what could and should be done, and what is hardly feasible because of critical phenomena.

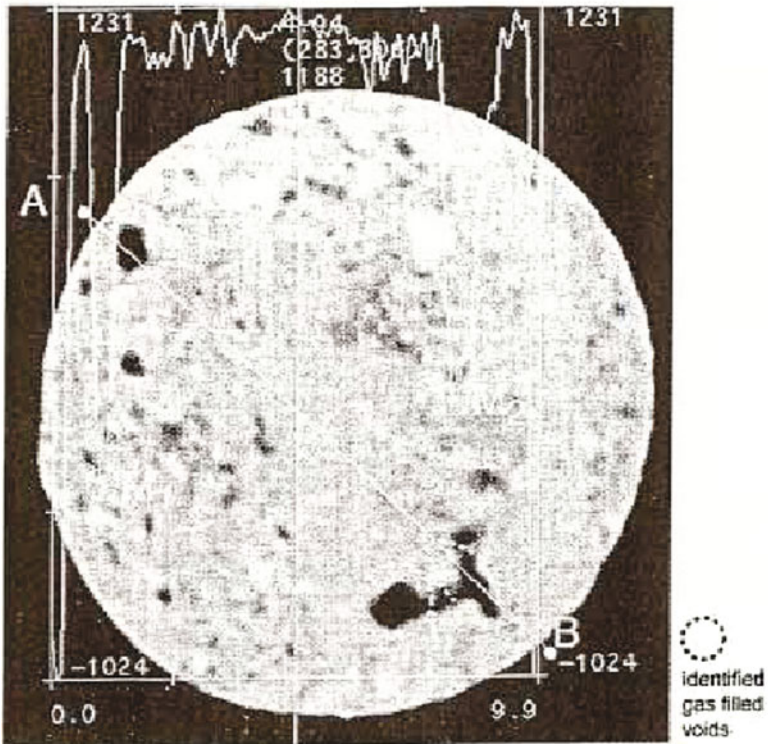
Consider first *psammoid* RSEs with a rather uniform distribution of pore gas so that relations with spatial averages suffice to catch the mechanical behaviour. As without gas net pressures may be negligible. The skeleton state is captured by void ratio e and stress tensor $\mathbf{T}_s (= -\mathbf{P}_s)$, particularly by mean pressure p_s and obliquity $\tan\psi_s$ (Sects. 2.2 and 2.11). Due to the pore gas and its interfaces with pore water and solid particles (Sect. 6.1) the skeleton can have *macropores*. These can be bigger than grains in skeletons with gas channels, e.g. Fig. 7.2.1a from a model test. Then the pore water with suction according to the vapor pressure forms intergranular capillary bridges. Gas bubbles can also support macropores (b, X-ray tomography after freezing in situ). Their excess gas pressure $p_g - p_w$ depends on curvature and surface energy (Sect. 6.1). Macropores are evidently reduced by increasing total pressure p , but need not disappear in the geotechnical pressure range.

Skeletons with macropores are complex even in case of rather uniform distributions and nearly equal grain size d_g . The pore water can flow more easily around gas bubbles than via capillary bridges, in both cases its spatial distribution can be and remain far from uniform. Gas bubbles can be kept between grains with so small diameters, say $d_b < \text{ca. } d_g/4$, that the skeleton does not feel them directly. One may then assume a simple skeleton (Sect. 2.2) with reduced permeability and increased compressibility of the pore fluid for lower degrees of saturation S_r than 1 (Sect. 6.2). With a lower S_r bubbles are distorted by grains and could support macropores. According to (6.1.2) the excess gas pressure $p_g - p_w$ can hardly exceed 1 kPa for grain sizes $d_g \geq 10^{-4}$ m. This could suffice to support a dense surrounding skeleton, whereas a loose one would collapse (Wheeler 1988).

More insight can be gained by considering attractors of psammoid RSEs with gas bubbles. Isochoric stretching with constant \mathbf{D} , e.g. cylindrical shortening or simple shearing, should lead to a stationary state limit. With not too small grains and a low fraction of *small bubbles* among them, say $0.9 < S_r < 1$, $d_g > 10^{-4}$ m and bubble size $d_b \leq 0.1d_g$, skeleton rearrangements are hardly impeded by bubbles so that these increase only the compressibility of the pore fluid. Contractant deformations with $\mathbf{D} = \text{const}$ would slightly squeeze small bubbles if these are not reduced by increasing p_w . Dilatant ones would not be impeded by bubbles, and these would increase by decreasing p_w (Sect. 6.2). Leaving aside localizations (Sects. 8.2 and 8.4) and skeleton decay, small bubbles can thus be captured by an S_r -dependent compressibility of the pore fluid.



a)



b)

Fig. 7.2.1. Gas bubbles trapped in sand: model test (a), X-ray tomography (b) of a frozen sample (Pralle 2002)

With *bigger bubbles* and small grains around them, say $d_g < 10^{-4}$ m and $d_b > 0.1d_g$, state limits can be markedly changed by macropores. p_w is constant along a wavy cross section around grains and bubbles (cf. Fig. 6.2.3), but the gas-water interfaces produce a kind of hydraulic net attraction pressure $p_n < 0$, or tensor \mathbf{P}_n in general. One can decompose the total pressure into partial ones by (7.1.1) and (7.1.2), but now p_n or \mathbf{P}_n does not depend on p_s or \mathbf{P}_s and S_r in the same way as without big bubbles. p_n can be crudely estimated by (6.1.2), viz.

$$-p_n \leq \text{ca.} 10\gamma_{wg}/d_g \quad , \quad (7.2.1)$$

as bridging gas-water interfaces are curved with $1/r_1 + 1/r_2 \approx d_g/10$. This is an upper bound as the volume fraction of macropores cannot be big (Fig. 7.2.1), and as p_n is small compared with skeleton pressures p_s in the usual geotechnical range. So why could this p_n and its influence on limit void ratios not be neglected?

Other than with peloids grains of psammoids and bubbles between them are so big that they are not rearranged by Brownian motion. The simplest *state limits* can be achieved by isochoric monotonous stretching. In a stationary overall deformation gas-filled macropores would disappear and arise by rearrangements of the skeleton with the same average. One can imagine that the critical void ratio e_c for a given p_s , which is somewhat bigger by $p_n < 0$, is increased by the distortion of bubbles with narrow gas-water interfaces. However, relatively big bubbles can thus be split into smaller ones which can no more support macropores so that these can hardly survive. Contractant and dilatant state limits could be approached with less rearrangement so that gas-filled macropores need not be excluded for them.

Rearrangements with *reversals* (Sect. 4.2) would destroy gas-filled macropores if the amplitudes in between are big and/or in case of ratcheting. So why not neglect such macropores anyway? In a humid loose granular fill macropores can arise up to such a high degree of saturation S_r that the pore gas is trapped. As then the suction $p_a - p_w$ disappears and p_w can get higher than hydrostatic, however, macropores could at best survive a monotonous compaction, but hardly a more effective one with reversals. If a humid granular fill is flooded part of the pore gas is caught with less uniform spatial distribution, rather dry islands of erratic shape and size can more easily arise than gas-filled macropores. A monotonous intrusion of pore gas into initially saturated skeletons can cause fingering (Sect. 6.2) and channelling (Sect. 8.4) with erosion (Sect. 16.3). Loose skeletons are more collapsible with gas inclusions (Wheeler 1988) and can lose their uniformity by skeleton decay (cf. Fig. 16.3.1).

The contradiction between the imagined uniformity of gas inclusions in RSEs and the actual non-uniformity in situ can be overcome in pragmatic approaches. The influence of a capillary pressure difference $p_g - p_w$ on p_s for given p and p_w may be neglected. Critical void ratios e_c can be higher with fine grains due to gas bubbles, this could be quantified by element tests

with mixtures having p_s , p_w and S_r in the range of the intended application. One is on the safe side by neglecting this rise of e_c if the void ratios are lower than critical in situ, i.e. $e < e_c(p_s)$. Otherwise spatial averages of e over sizes of earthworks, structures and/or layers (Chaps. 12 and 13) may suffice without elevated e_c for gas inclusions. This assumption is on the safe side up to the onset of a collapse with a continuous mud flow as shear zones are spread by diffusion (Sect. 8.2). The subsequent progressive localization by an accumulation of gas into a cushion after a skeleton decay is beyond the present reach (Sect. 16.3). An enhanced decay by reversals with gas inclusions can as yet also hardly be captured.

Randomly uniform psammoid RSEs with *gas channels* have a kind of net attraction which was introduced as capillary skeleton pressure p_{cs} in Sects. 2.2 and 6.2. This can be determined by pressure changes at fixing filters with wetting or drying via vapor, or estimated from the tensile strength (Mikulitsch and Gudehus 1995). It can be anisotropic so that a capillary skeleton pressure tensor \mathbf{P}_{cs} with first invariant $p_{cs} = \text{tr}\mathbf{P}_{cs}/3$ may be assumed. Analogously with (7.1.1) and (7.1.2) one can decompose the total pressure tensor \mathbf{P} via

$$\mathbf{P} = p_g \mathbf{1} + \mathbf{P}_s - \mathbf{P}_{cs} \quad , \quad (7.2.2)$$

including

$$p = p_g + p_s - p_{cs} \quad (7.2.3)$$

with a pore gas pressure p_g which need not agree with the atmospheric pressure p_a . A change of p_g with constant \mathbf{P}_s and \mathbf{P}_{cs} , i.e. fixed skeleton and adherent pore water, would change $p_w (< p_g)$ by the same amount (Sects. 6.1 and 6.2). As with full saturation there is no area correction factor (χ in Sect. 6.2) due to the neutrality of water and solid particles with respect to p_w . One may thus treat the capillary skeleton pressure similarly as a net attraction of peloids in Sect. 7.1.

At *state limits* the skeleton is aligned by its pressure \mathbf{P}_s , and capillary bridges are also wider at contacts along force chains (Figs. 4.3.1 and 4.3.2). It is reasonable therefore to postulate

$$\mathbf{P}_{cs} = \kappa_{cs} \mathbf{P}_s \quad (7.2.4)$$

including

$$p_{cs} = \kappa_{cs} p_{cs} \quad (7.2.5)$$

with a factor κ_{cs} analogously to (7.1.3) and (7.1.4). This is evident for isotropic states, and also for states with one or two zero stress components (Sect. 2.2) as capillary bridges break in a splitting skeleton. Critical states with constant S_r could be achieved by shearing of thin layers, but data of this kind have not yet been produced. Heaps of flowing humid granular material, and thus with critical states near the surface (Sect. 14.2), exhibit slope angles which do not depend on humidity and slope height. This is implied by (7.2.4) which is

thus further justified as interpolations to isotropic and splitting state limits are monotonous.

Capillary bridges may be aligned with the skeleton, but their resultant forces cannot be proportional to the solid contact force as with its increase the liquid bridges change their shape. Other than κ_n in (7.1.3) the factor κ_{cs} in (7.2.4) cannot be constant therefore, but it changes with S_r and p_s . Fig. 6.2.3 with p_{cs} from the tensile strength indicates that κ_{cs} is maximal for $S_r \approx 1/2$, and vanishes for $S_r \rightarrow 0$ (no water) and $S_r \rightarrow \text{ca. } 0.9$ (no gas channels). Imagine a fixed skeleton and thus fixed p_s with a change of S_r from an initial $S_r = 1/2$ to understand that p_{cs}/p_s can change substantially with given p_s , i.e. given solid contact flats.

Limit void ratios are higher with capillary attraction as with a net attraction of saturated peloids, Fig. 7.2.2 (cf. Fig. 7.1.1). Isotropic compressions of humid loose skeletons start with $p_s = p_{cs}$, i.e. $p = p_g$ by (7.2.3), the degrees of saturation S_r can be different at the onset and increase if no H₂O is extracted. As in Fig. 6.2.3 the instantaneous p_{cs} may be referred to γ_{wg}/d_g and used as objective state variable for presentation, although p_{cs} cannot be determined precisely. The e vs. $\log p_s$ -curves (a) are higher and start with a higher p_s for bigger $p_{cs}d_g/\gamma_{wg}$, and converge with increasing p_s . A set of similar plots may be assumed for different stress obliquities $\tan \psi_s$ and constant $p_{cs}d_g/\gamma_{wg}$ (b). For each $\tan \psi_s$ the curve is blown up by bigger $p_{cs}d_g/\gamma_{wg}$ as for $\psi_s = 0$.

Relations for limit void ratios can be differently quantified, but available data can only provide a partial validation. Extensions of CSSM with special cases of (7.2.2) have been proposed and investigated (Fredlund and Rahardjo 1993). The suction $p_g - p_w$ is usually determined via (6.1.5) by measuring the relative humidity ψ_w of the pore gas. Ridley et al. (2003) measured $p_g - p_w$ also with other methods and found deviations. Experiments with different gas pressures p_g confirmed the neutrality with respect to p_w which is implied by (7.2.2). A unique relation of suction with the degree of saturation S_r , i.e.

$$p_g - p_w = f_{gw}(S_r) \tag{7.2.6}$$

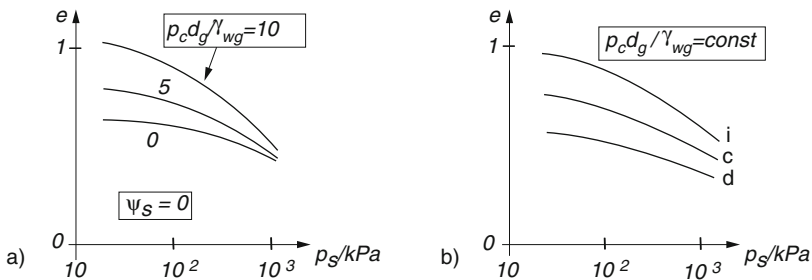


Fig. 7.2.2. Limit void ratios versus skeleton pressures of psammoids with gas channels for isotropic compression (a) and different stress obliquities (b)

with a monotonous function f_{gw} of S_r , is often tacitly assumed. This would be correct for a skeleton fixed by filters through which the relative humidity ψ_w is controlled up to equilibrium (Sect. 6.2). Even with fixed skeletons, however, so-called pF-curves of $\log(p_g - p_w)$ versus S_r , exhibit differences due to *capillary hysteresis* (Fig. 6.2.2). Depending on the kind of adding or removing liquid H_2O there are different metastable equilibrium distributions of pore water for the same overall S_r . In other words, there are pockets with higher or lower S_r so that the assumption of a uniform RSE with gas channels is no more justified. Even a uniform fixed RSE exhibits different excess gas pressures $p_g - p_a$ for different void ratios e and given S_r or vice versa, this is evident by considering skeletons with different capillary bridges. For these reasons experimental reports and evaluations via (7.2.6) and pF-curves are often debatable.

Capillary skeleton pressures, i.e. \mathbf{P}_{cs} and p_{cs} in the sense of (7.2.2) and (7.2.3), are not uniquely related with $p_g - p_w$ or S_r even for a given e , and have rarely been determined in experiments. The ones obtained with fine sand and silt (Fig. 6.2.3b) by Mikulitsch and Gudehus (1995) do not refer to state limits. The latter are at best approached by uniaxial tensions, but not in biaxial tests with slow changes of S_r . The extension of hypoplastic relations with an isotropic \mathbf{P}_{cs} by Gudehus (1995) cannot suffice as the rise of e by suction is neglected.

Without knowing p_{cs} observed void ratios are usually plotted versus $\log(p - p_g)$. Maatouk et al. (1995) report on triaxial tests with reconstituted silt samples of different S_r , Fig. 7.2.3. For isotropic compression e is markedly higher with more suction $u_a - u_w$ (b). For a given suction the e vs. $\log(p - p_g)$ plots converge with increasing pressure (a), but state limits are hardly attained. Anisotropic compression tests exhibit a similar influence of suction, but state limits are not attained so that the influence of stress obliquity as

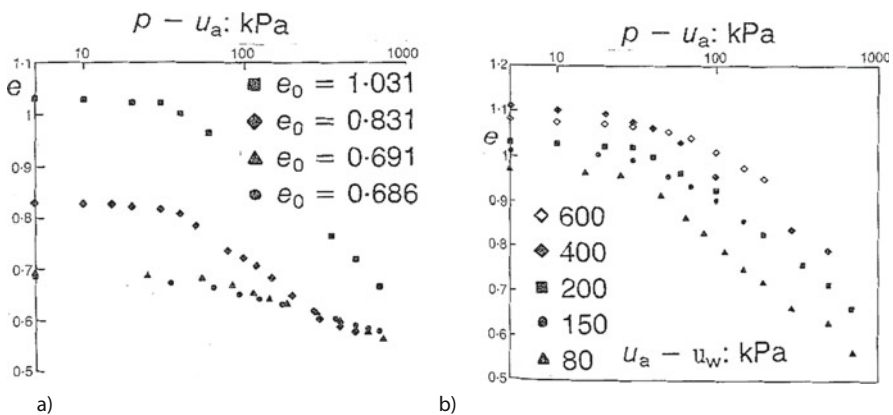


Fig. 7.2.3. Void ratios of silt with gas channels, observed in triaxial tests by Maatouk et al. (1995) with different initial void ratios (a) and different suctions (b)

by Fig. 7.2.2b cannot be judged. Maatouk et al. (1995) discuss also critical states, but do not communicate critical void ratios e_c . It appears that they did not attain uniform stationary state limits (cf. Sect. 14.1).

With this provisional experimental background it may suffice to mention *constitutive relations* just briefly. Alonso et al. (1990) proposed elastoplastic relations with suction (abbreviated by c-elp in the sequel) on the base of CSSM. State limits i and c are thus captured for a certain range of $p - p_g$, also transitions with at most one reversal, overcritical states are implied without a lower e -bound and splitting (cf. Sect. 2.3). A hypoplastic counterpart (c-hyp) could be formulated with a suction-dependent prefactor e_o in Bauer's formula (2.4.1). Relative void ratio r_e and dilatancy ratios could depend on the stress obliquity as without suction, \mathbf{P}_{cs} may be proportional to \mathbf{P}_s as by (7.2.4). Evolution equations with rates of \mathbf{P}_s and \mathbf{P}_{cs} could be formulated so that the proposed state limits are attractors for proportional stretching paths. To catch evolutions with several reversals one could also introduce hidden state variables and judge this approach by means of asymptotic cycles.

Applications are difficult not only due to the identification with suction, but also due to the complexity of spatial evolutions with time. The migration of water in fixed unsaturated grain skeletons can be captured by Richard's (1931) equation. This expresses the mass balance of water for an RSE with a suction-dependent permeability and degree of saturation (cf. Sect. 6.2). The transition from gas channels to bubbles is inevitably fuzzy and can get chaotic, thus wetting or drying fronts can hardly be predicted (cf. Sect. 16.1). This is a pity as wetting of a loose skeleton with gas channels can lead to a collapse, whereas drying can stabilize it more by suction than by densification.

The approaches employed for unsaturated psammoids in subsequent chapters are tentative therefore. An isotropic p_{cs} is proposed for free surfaces with given S_r , also for cracks which can thus open and stand. Sufficiently far from free surfaces p_s is often so big that p_{cs} may be neglected as partial pressure by (7.2.2), but hardly in model tests. Limit void ratios should be determined with the suction as in situ, thus deformations with this suction can be reasonably predicted without taking into account changes of p_{cs} . The loss of suction by densification and/or water access cannot yet properly be predicted, but is clearly indicated by p_w -transducers in situ. The inclusion of gas cushions is indicated for arbitrary shapes by a rise of p_w . Thus one can judge a loss of stability by a decay of the skeleton. The loss of suction by evaporation via random gas channels may be captured by continuum approaches, and also its gain via access of vapor. The opening of new gas channels in zones without previous suction is too chaotic for predictions (cf. Sects. 6.2 and 16.3), but p_w -monitoring could serve as a partial substitute.

Unsaturated *peloids* are more complex as capillary effects are stronger with the smaller particles, and as net pressures (p_n , Sect. 7.1) can play a role. We assume first $p_n = 0$ and will discuss the influence of p_n further below. As without pore gas the viscosity of softer particles leads to argotropy, creep and relaxation (Sect. 3.2), this property is not changed by pore gas. In spite

of the low permeability the diffusion of pore water and of pore gas therein should not be neglected, even for fast deformations in the sense of (6.2.11), as gas inclusions are narrow. Thus their close vicinity can take up or release water and/or solubles in short times. More than with psammoids cracks and voids between lumps are preferred sites of pore gas. Only few kinds of spatial distribution will be treated in the sequel.

Gas bubbles can arise in peloids from mixing, compaction of moist fills, cavitation due to decompression and/or decay of organic constituents. They support macropores with far bigger sizes than the smallest neighbored particles, and are so small and wrinkled that their excess gas pressure $p_g - p_w$ is not negligible against the mean pressure of the neighbored skeleton. The latter may be saturated and ductile without filtration due to the softness of the particles (Sect. 3.2). With a solid volume fraction $\alpha_s = 1/(1+e) \approx 1/2$ an average bubble distance of 10 bubble diameters would yield $S_r \approx 0.98$. Then the bubbles can hardly interfere each other, this may be assumed from five bubble diameters distance onwards, i.e. for $S_r > \text{ca. } 0.9$ which is often met.

State limits of such peloid RSEs can be imagined as follows. For stationary stretching, e.g. cylindrical shortening or simple shearing, the bubbles are deformed and displaced past each other, whereas their average volume and distance are constant. The bubble shape is adapted to the average skeleton stress. The near-fields of bubbles have higher p_s than the average because of more rapid deformations and viscosity. Given ductility, viscosity by the power law (3.2.2b) and stationarity the average argotropy is the same as without bubbles (Winter 1979). The pressure decomposition $p = p_s + p_w$ is justified with spatial averages (only these can be observed by means of cuts around the bubbles). One may thus work with critical states as for $S_r = 1$, but with higher critical void ratios e_c for lower S_r . The S_r -dependence of e_c has to be observed in experiments with $p_s - p_w$ in the range of application so that S_r is not changed.

Contractant state limits could be achieved by oedometric or isotropic compression tests with drainage. The volume fraction of gas bubbles should be kept constant, this can be controlled via volume change and mass of squeezed out water. Shrinkage tests up to a capillary entry can serve to the purpose if the reduction of weight and volume is measured. Dilatant state limits cannot be controlled similarly because of shear localization and cracking. Both are enhanced by bubbles, their volume fraction can at best be determined via compressibility up to a capillary entry which leads to gas channels. S_r - and p_s -dependent limit void ratios can thus be well captured in the contractant range, less precisely observed for critical states and only estimated in the dilatant range.

The argotropy and the dependence of relative void ratios and dilatancy ratios may be assumed for state limits as without gas bubbles (Sect. 3.2). Constitutive relations by v-elp or v-hyp with a compressible pore fluid may suffice as a substitute therefore. The compressibility may be estimated by (6.2.6) as p_w and S_r cannot be determined precisely. The permeability k_f

may be taken as for $S_r = 1$, the influence of bubbles on the diffusion of pore water (but not of soluble gas) is captured by the compressibility. The range of application is limited by capillary entry, this can be estimated via shrinkage and plasticity limits (Sect. 6.3).

Peloids with gas channels are fissured due to shrinkage, or they consist of lumps with contact flats after compaction. A sufficiently uniform RSE should be wider than about ten fissure distances, but this cannot be easily judged (Sects. 6.3 and 9.1). Imagining boundary filters to support the skeleton and to control pore water and gas, one may again assume the decomposition into partial pressures by (7.2.2) and (7.2.3). The solid partial pressures need not fluctuate more than in grain skeletons with force chains, so spatial averages may be justified. The pore gas pressure p_g is constant in the connected channels, so the pore water pressure at equilibrium with vapor by (6.1.5) is also constant. p_w can be different in narrow slits (Sect. 6.1), but this could hardly be observed and seems to be negligible for the RSE-behaviour. The neutrality of solid and liquid constituents with respect to p_w may again be assumed, it was confirmed by tests with different p_g and constant $p_g - p_w$ via humidity (Fredlund and Rahardjo 1993).

Leaving aside net pressures (p_n , Sect. 7.1) *state limits* of peloid RSEs with gas channels could be principally treated as for psammoids. The capillary skeleton pressure p_{cs} may be determined via the tensile strength, it should be replaced by a tensor \mathbf{P}_{cs} in general. The proportionality of \mathbf{P}_{cs} and \mathbf{P}_s by (7.2.4) and (7.2.5) may be assumed again. This is evident for isotropic states, could principally be checked for critical states and is rather evident for extreme state limits with cracking. Other than for psammoids the factor κ_{cs} could depend mainly on the suction $p_g - p_w$, this could be checked via tensile strength after isotropic compression. The argotropy of limit void ratios could be captured as proposed in Sect. 7.1 without pore gas.

Extending the definition of simple peloids in Sect. 3.2, state limits may be sufficiently determined by the (spatially averaged) skeleton stress tensor and the suction $p_g - p_w$, or the factor κ_{cs} by (7.2.4) instead. Critical states are likewise approached by monotonous isochoric deformations with cracks or lumps at the onset. Because of the net attraction the critical void ratios e_c are higher for the same p_s than without p_{cs} (or suction instead). Limit void ratios are higher for compressions with the same stretching rate D up to the same p_s . Such contractant state limits could be achieved in shorter times because of a more rapid drainage via gas channels as long as these are not closed. The latter could be seen from a rise of p_w , which could thus no more be kept nearly constant. Dilatant state limits could hardly be approached with the desirable uniformity, suction control and uniqueness. The smaller required deformations do not suffice to sweep out differences of samples with cracks or lumps (Sect. 9.1).

Experiments of this kind are feasible and desirable, whereas published results do not exhibit clearly enough unique asymptotic responses, and capillary skeleton pressures p_{cs} cannot be derived from them. Therefore the issue of *con-*

stitutive relations may only be touched, also as spatial evolutions of suction can yet hardly be predicted. The elastoplastic relations with suction (c-elp) proposed by Alonso et al. (1990) imply state limits according to CSSM, they could be modified for p_{cs} and extended for argotropy. A hypoplastic counterpart (c-hyp) could be formulated with a suction-dependent prefactor in (2.4.1). An additional evolution equation for \mathbf{P}_{cs} is needed in both variants (cf. Sect. 7.1). Evolutions with reversals could principally be captured by asymptotic cycles, these could favour the desired uniformity.

Mašin and Khalili (2008) proposed a hypoplastic model with variable suction (c-hyp). Therein the void ratio by isotropic first compression decreases less with higher effective stress for higher suction, Fig. 7.2.4 (cf. Figs. 7.2.2 and 7.2.3). Test results (a) with a clay by Sun et al. (2007) are well matched (b)

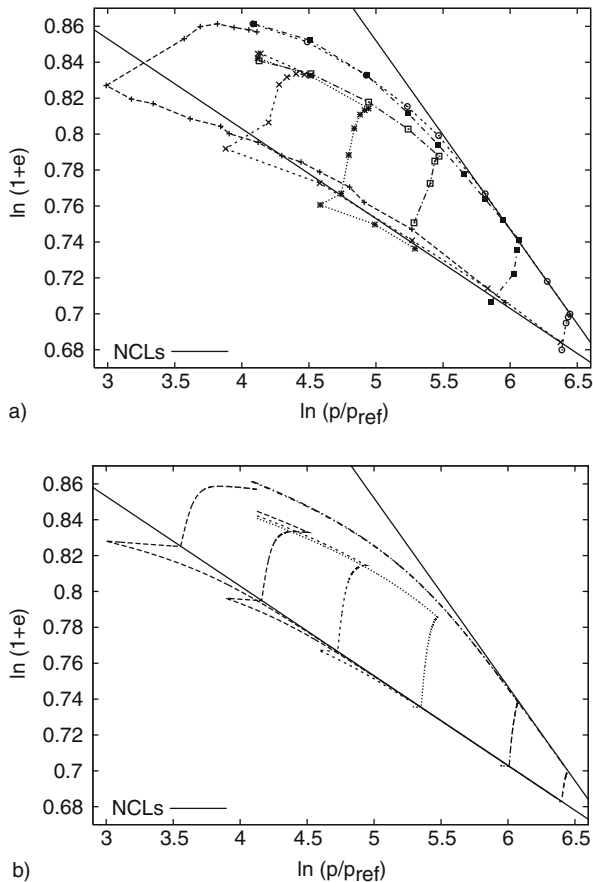


Fig. 7.2.4. Void ratios versus isotropic effective pressure of an unsaturated clay with variable suction: (a) experiments by Sun et al. (2007), (b) simulation by Mašin and Khalili (2008)

both with constant suction (monotonous curves) and with decreasing suction by wetting (vertical lines with kink). The curves show also that with further compression after wetting the same void ratios are attained as with a new suction from the very beginning. These are thus limit void ratios including suction which work as attractors. The model by Mašin and Khalili (2008), which is organized as indicated above with Fig. 7.2.1, works also satisfactorily for monotonous evolutions off state limits. Alonso et al. (1990) obtain similarly good agreements with their c-elp, state limits can thus likewise be captured as with c-hyp. The range of validity for unsaturated clays with reversals has not yet been explored.

Last but not least *net pressures* p_n of saturated peloid regions should be taken into account. In case of gas bubbles it may suffice to determine parameters with the same ionic strength as in situ (Sect. 7.1). With gas channels changes of salinity can matter in narrow slits between solid particles (Sect. 6.1). With a desiccation the NaCl-concentration increases, particularly near growing cracks, so that the net attraction $p_n < 0$ grows. Wetting via vapor or rain water would soften the peloid more than with salt water. Suction can no more suffice as state variable, whereas the capillary skeleton pressure p_{cs} with control of the ionic strength could serve to the purpose.

To *sum up*, unsaturated soils can principally be captured by means of partial pressures and attractors, but more experiments will be needed for quantification and limitation. Gas bubbles may be captured by a higher average void ratio and compressibility of the pore fluid. Soils with randomly uniform gas channels have higher limit void ratios because of capillary attraction (cf. Sect. 7.1), but only simple substitutes could as yet be quantified. The spatial evolution of wetting and drying can at best be estimated or observed, but critical phenomena are not yet properly understood.

7.3 Cemented and transient particles

Skeletons of mineral particles can have higher void ratios with solid condensate bridges. Such bridges break and often cannot arise again during geotechnically typical deformations. This can be captured by an irreversible net attraction, and a recondensation can principally be taken into account. The concept of state limits and state cycles gets debatable if bridges of particles cannot arise again. This objection will also be discussed for the particles themselves as their encounters are not conservative, nevertheless the attractors proposed in this book are consistent.

Cementations may be first considered for *psammoids*. Imagine cross sections through idealized grain skeletons, Fig. 7.3.1. With *full saturation* solubles can be condensed around the contact flats so that solid bridges arise (a). This happens even with pure water and corundum grains, and matters if these are fine (Richter 2006). Solubles are produced by the pressure at the contact flats and are condensed around them. The thermodynamic equilibrium

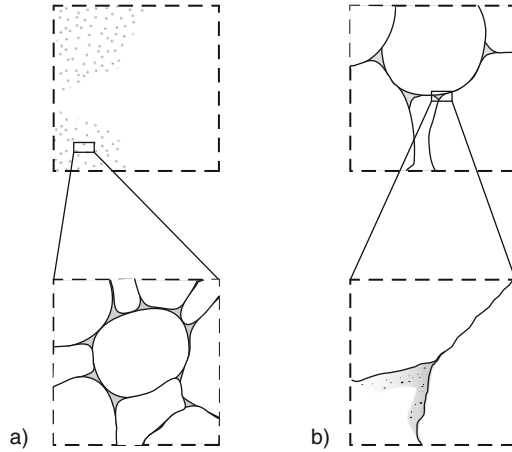


Fig. 7.3.1. Contact flats of grain skeletons with solid condensate (a) and smaller particles (b)

is determined by surface energies and curvatures of narrow necks (Sect. 6.1), the condensate in the bridges has a kind of capillary suction. The time needed for the formation of such bridges is controlled by diffusion towards the necks. The growth time t_g depends on concentrations of solubles and the sizes of contact necks, t_g can vary in a wide range therefore.

Much smaller solid particles than the grains tend to accumulate at grain contacts (Fig. 7.3.1b). Minute particles can stem from abrasion of the grains or are intruded by seepage. They precipitate preferably at necks and can condense into an amorphous solid with the aid of crystallizing solubles. This occurs particularly if cement particles were suspended in the pore water, but the notion cementation is also used for other solid condensation bridges. Their growth times are longer with the confined Brownian motion of fine particles in narrow necks. At equilibrium such bridges exhibit again a kind of capillary suction, but their surface is less regular. Minute particles are also adsorbed off the contacts on the grain surfaces, and these are rarely smooth.

Such bridges *break* by skeleton rearrangements. They open by cavitation, parts of them fall aside and others stick so that the grains get rougher and more fragile. The encounter time t_e of grains, i.e. the lifetime of their contacts, is determined by the stretching tensor \mathbf{D} of the skeleton. With isochoric stretching nearly equal grains find new neighbours after shearing by $\tan \gamma = 1$ (Fig. 2.9.1), the encounter time is thus $t_e < 1/D$ ($D = \|\mathbf{D}\|$). t_e is longer for contractant and shorter for dilatant stretching, and can at best be crudely estimated anyway. The cementation is *brittle* if the encounter time does not suffice for recondensation, i.e. for $t_e < t_g$.

State limits of saturated psammoid RSEs with cementation bridges cannot generally be defended. Continued stationary (i.e. critical) states could only occur with $t_e = t_g$, i.e. with so slow deformations that bridges arise in

the average with the same rate with which they disappear. Then the skeleton pressure p_s and the related critical void ratio e_c would be and remain higher due to the net attraction. Otherwise solubles and fines would be convected with the pore water and could influence critical states only via the pore water pressure p_w . Contractant state limits can more often occur with so low stretching that the fraction of bridges is not reduced. In this case the related limit void ratios are higher than without bridges. Dilatant state limits may also be imagined with net attraction, i.e. effective tensile strength, and higher limit void ratios than without bridges. The desired uniformity of an RSE gets lost by cracking, then the argument with t_g and t_e should be adapted to the opening and healing of cracks.

State cycles may also be discussed by comparing encounter and condensation times. Cyclic deformations with small enough deformations do not destroy solid bridges, then the skeleton is a solid in its elastic range. With moderate amplitudes and usual frequencies cyclic deformations can weaken bridges without their total loss. Cyclic deformations with bigger amplitudes destroy all bridges so that they should be neglected after this kind of fatigue. Solid bridges can survive ratcheting if the amplitudes are small and the cumulative stretching is slow enough for repeated recondensation. The latter is prevented by a more intensive ratcheting. Thus asymptotic cycles as proposed in Sect. 4.2 are no more justified for skeletons with solid condensation bridges.

Constitutive relations with attractors including solid bridges are more debatable therefore than the ones indicated in Sects. 7.1 and 7.2. Except for extremely small or slow deformations the brittleness of bridges prevents the kind of permanence which is implied by state limits and state cycles. It is difficult to judge the range of validity by experimental reports as the grains themselves often break alongside with their bridges. For instance, Lagioia and Nova (1995) carried out triaxial tests with samples of a saturated calcareous sand cut *in situ*, Fig. 7.3.2. For isotropic compression the e vs. p' plot (a) exhibits a collapse at a threshold pressure where the bridges break. For axial shortening with constant σ'_2 the e vs. p' plot reveals a collapse at a lower threshold pressure (b).

Axial shortening with different constant σ'_2 leads to a less brittle response for higher σ'_2 . The $q = \sigma'_1 - \sigma'_3$ vs. ε_1 plot (c) exhibits jumps for a low σ'_2 and a monotonous increase for higher σ'_2 . The volume reduction vs. ε_1 (d) is small for a low σ'_2 , strong for an intermediate σ'_2 and not as marked for the highest σ'_2 . With the attainable shortening the ratio q/p' gets constant as for critical states, but e is further reduced due to grain crushing. The response is less brittle with higher σ'_2 as then the bridges were already destroyed by the previous isotropic compression.

The response exhibited by Fig. 7.3.2 is typical for a soft porous rock or a cured mortar. Lagioia and Nova (1995) could partly capture it by elastoplastic relations with two components p_{n1} and p_{n2} of a net attraction as internal variable. In addition to volumetric hardening as by CSSM (Sect. 2.3) they assume that the net attraction decays exponentially with increasing deformations. In

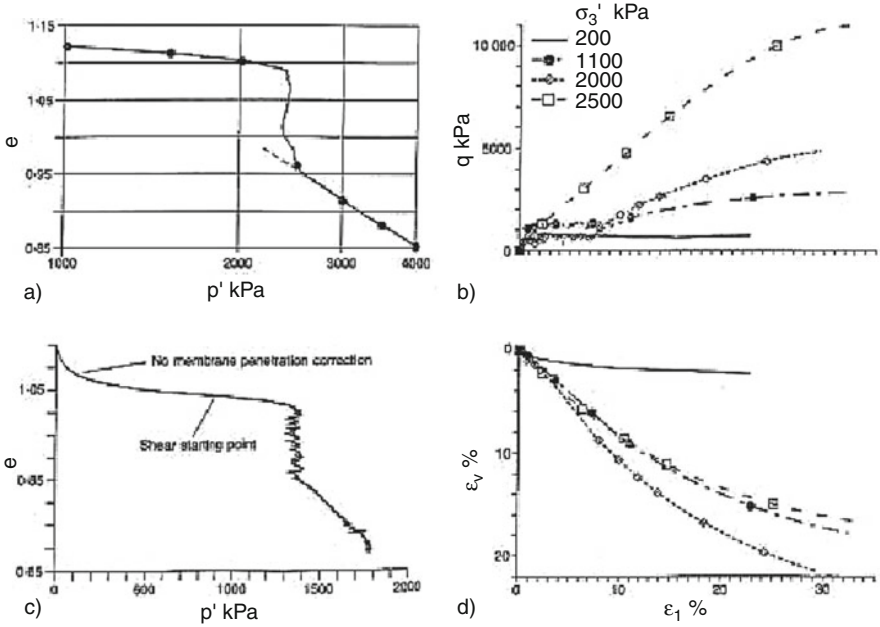


Fig. 7.3.2. Triaxial test results with a calcarenite (Lagoia and Nova 1995) : (a) void ratio for increasing isotropic pressure, (b) compression by shortening with different confining pressures σ_3' , (c) void ratio versus log pressure for constant σ_3' , (d) void ratio versus axial shortening for different σ_3'

extended hypoplastic relations for cylindrical RSEs Gudehus and Mikulitsch (1996) work similarly with p_{n1} and p_{n2} . The decay with deformation is described by a differential evolution equation with a threshold elastic energy of the bridges. Without using strains as state variables, as proposed by Lagoia and Nova (1995), the observed response without and with reversals can thus be fairly well matched.

Both approaches could be extended objectively for arbitrary deformations by means of tensors, but are not further outlined here as they do not suit into the scope of this book. State limits and state cycles do not appear so that the identification depends on insufficiently known initial states. As in Sect. 7.1 the net attraction should lead to higher limit void ratios, this is indicated by Fig. 7.3.2a, but not explicitly taken into account in the named approaches. These capture the loss of bridges, but not their possible recovery by condensation. The more erratic response exhibited by Fig. 7.3.2c for low confining pressures indicates a loss of the uniformity which is needed for RSEs. Simply speaking, cemented skeletons are not as plastic as typical granular soils.

The issue of cementation is not easier with *unsaturated psammoids*. Gas channels enhance the evaporation so that the higher concentration of solubles in intergranular capillary bridges eases the growth of solid bridges. The

capillary water can easily follow skeleton rearrangements by diffusion in the pores, whereas broken solid bridges can hardly be regained. Attractors as without cementation (Sect. 7.2) are no more justified therefore. One could again match test results by heuristic approaches as the ones indicated above, but the range of validity could scarcely be judged in an objective manner. It may suffice therefore in geotechnical applications to neglect cementation bridges as long as the tensile strength is well below the mean pressure. At free surfaces an isotropic net attraction may be assumed to avoid a skeleton decay in calculations, but a loss of attraction by the rupture of solid bridges is not captured by such simplified models.

Cemented peloids can be plastic in a certain range of pressures and stretching, otherwise the notion peloid would be a contradiction in terms. With *full saturation* a cementation causes a kind of net attraction pressure, say $p_{nc} < 0$ or \mathbf{P}_{nc} more generally, which increases the skeleton pressure by (7.1.1) and (7.1.2) for a given ‘effective’ pressure $p' = p - p_w$ or $\mathbf{P}' = \mathbf{P} - p_w \mathbf{1}$ in general. As the net attraction $p_n < 0$ in Sect. 7.1 this p_{nc} causes an effective tensile strength and should increase limit void ratios. As outlined further above for psammoids, however, this net attraction disappears by other than extremely slow deformations so that state limits and state cycles are no more justified.

Similarly as in Sect. 7.1 and further above for psammoids, one could formulate various heuristic *constitutive relations* with p_{nc} . Mašin (2007) proposed an irreversible excess equivalent pressure within the framework of CSSM, Fig. 7.3.3a. For isotropic compressions of a loose skeleton the p' related with an instantaneous e is higher by a factor $f_c > 1$ due to cementation (a). This is equivalent to (7.1.6) with a higher reference void ratio e_r due to $p_n < 0$. As brittle bridges disappear during a compression the factor f_c tends to 1 (e.g. path 0-1). Higher void ratios with bridges can also be captured by this factor f_c which fades away by isochoric shearing (b, e.g. path 0-1). With evolution equations for f_c Mašin (2007) can better match triaxial test results than without this extension.

In spite of successful matching and practical need the range of validity of such constitutive relations can hardly be judged with physical arguments. Saturated peloids with hard grains can be collapsible with an excess of van der

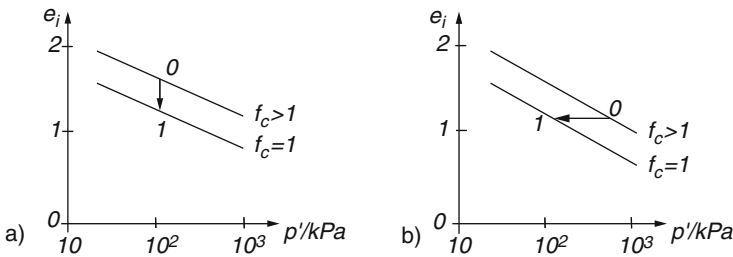


Fig. 7.3.3. Limit void ratio of a saturated peloid without and with cementation, pressure-dependent by CSSM (a) and by hypoplasticity (b)

Waals attraction (Sect. 7.1), and this kind of cohesion can hardly be separated from the one by cementation (Richter and Huber 2004). With layer silicate platelets and different solubles even thermodynamic equilibria in narrow slits are beyond the present reach (Sect. 5.1). Condensation bridges can scarcely be identified so that a decomposition into partial pressures as by (7.1.1) is debatable. State limits and state cycles of RSEs could only be attained with so low stretching rates that condensation bridges decay and grow with the same average rate. The less plastic behavior with more rapid stretching is accompanied by cracking so that the desired uniformity of RSEs gets lost. Triaxial test results indicate that cracks can be healed again at such critical points (e.g. Fig. 14.1.7), but the role of cementation is not yet understood.

For the time being there is no way around ad hoc-approaches. Saturated clay samples may be considered as cemented if they have an effective tensile strength which gets lost by isochoric deformations. Strictly speaking this requires a zero net attraction in the sense of Sect. 7.1, and so slow deformations that the pore pressure p_w is hydrostatic. Even with artificial samples this separation is difficult as the diffusion of pore water is coupled with the one of solubles, and as a net attraction cannot be measured directly. Samples should have the same composition and state as in situ, but then they are at best little disturbed. Only effective pressures, i.e. $p' = p - p_w$ and $\mathbf{P}' = \mathbf{P} - p_w \mathbf{1}$ in general, can be observed as long as the samples are and remain so uniform that RSEs may be assumed. Critical void ratios and stress ratios would indicate a net attraction (Sect. 7.1), but except for very slow deformations the assumption of critical states with cementation is a contradiction in terms.

Mašin (2006) achieved a good matching with an internal attraction which gets lost by deformations. This could also work with variants of elp and hyp for different clays. The internal variable representing a net attraction is hidden anyway, it has to be matched so that it raises the limit void ratios and dwindles by deformations. An irreversible part of a net attraction cannot be captured by state limits and state cycles, therefore the identification of material parameters by matching remains partly subjective as the partial indeterminacy of initial states cannot be ruled out. The smoothness of elp- and hyp-type approaches with a density-dependent hardening or softening seems to be justified for contractant or isochoric deformations. This can already lead to localizations, however, which cannot yet be captured. Localized shear dilation could principally be taken into account (Sect. 8.3), but cracking with cementation is out of reach (Sect. 8.4).

Applications within the fuzzy possible range of validity are impeded by progressive spatial changes of concentrations of solubles. As without cementation (Sect. 7.1) the redistribution by coupled convection, diffusion and sorption can at best be predicted for fixed skeletons. The coupling with skeleton rearrangements is beyond the present reach, so there is no way around drastic simplifications. As without cementation the main issue is softening up to the collapse of undrained skeletons with overcritical void ratios. To be on the safe side it may suffice to work with limit void ratios within elp or hyp, determined

by RSE-tests with given or anticipated ionic strength. A hardly separable cementation which gets lost by rearrangements is thus neglected, deformations would thus be overestimated.

The issue is so complex for *unsaturated peloids* that a brief demarcation may suffice. Gas bubbles can be bigger with a cementation of the skeleton, thus a peloid can get collapsible. As without cementation it may suffice to work with higher average void ratios and a more compressible pore fluid (Sect. 7.1), but deformations can thus be overestimated. With gas channels, which have a wider variety of shapes than for psammoids, higher concentrations of solubles due to evaporation can ease a cementation. This could only be assessed by means of a remaining effective tensile strength after saturation with a ionic strength, so that a net attraction in the sense of Sect. 7.1 would get negligible. Such a separation is less feasible, however, with pore gas as its spatial distribution can hardly be controlled. Wetting of a peloid sample with gas channels leads to rather chaotic gas inclusions and to a complex coupled diffusion of pore water and solubles.

Combinations of pore gas and cementation cannot yet be taken into account therefore in applications. For the time being it may suffice to capture peloid crusts with gas channels by capillary skeleton pressures and average void ratios in the same way as humid psammoids. Material parameters should be determined with samples which are big enough with respect to fissures and lumps (Sect. 9.1). Wetting with suitable ionic strength can be investigated by similar tests, these may be evaluated with spatial averages of skeleton and pore fluid. This approach is no more legitimate for rock-like and concrete-like materials, but these are left aside in this book.

Turning now to the often assumed *permanence of solid particles*, let us first consider *psammoids*. As indicated already in the Prologue interactions of grains are not conservative, i.e. they are changed by dislocations and cavitation. Therefore no two grains are equal, the grains are worn by encounters with solid contact and the interaction forces cannot be derived from a potential (which would be called Hamiltonian in statistical mechanics). That's why equations of state cannot be identified as for thermodynamic systems, and why phase transitions of grain skeletons have little in common with thermodynamic phase transitions. Equations of state may at best be postulated for state limits of skeletons, but a kind of granular permanence is thus implied (Sect. 2.2). Asymptotic state cycles of grain skeletons with reversals require the same permanence.

This is apparently a contradiction in terms: the desired objectivity of the attractors proposed in this book for psammoids is at variance with the actual degradation of grains. But there is a way out of this dilemma as one can take into account, at least principally, granular changes via evolution equations for the constitutive parameters which are defined for state limits and state cycles. To begin with, the critical friction angle φ_c may be permanent, whereas the p_s -dependent critical void ratio e_c gets lower by degradation during monotonous isobaric or monotonous deformations. Us-

ing Bauer's formula (2.4.1) this means that the prefactor e_{co} , i.e. e_c for $p_s \rightarrow 0$, the granulate hardness h_s and the exponent n change with on-going deformations.

Some possible evolutions are indicated in Fig. 7.3.4 for monotonous thin layer shearing with constant pressure p_s of different levels in each test (a, cf. Fig. 2.9.8). As assumed further above the stress ratio may get stationary (b), i.e. $\tau/p_s \rightarrow \tan \varphi_{sc}$ with a p_s -independent φ_{sc} . This seems to be realistic as long as the degradation leads again to grains with the same surface properties which are relevant for sliding friction (Persson 1998). p_s may be at a low (A), moderate (B) or high level (C). This means such a ratio p_s/h_s of pressure and granulate hardness that the void ratio e is hardly changed with shearing (c) by abrasion (A), markedly reduced by chipping of grain parts (B) or drastically diminished by fragmentation (C).

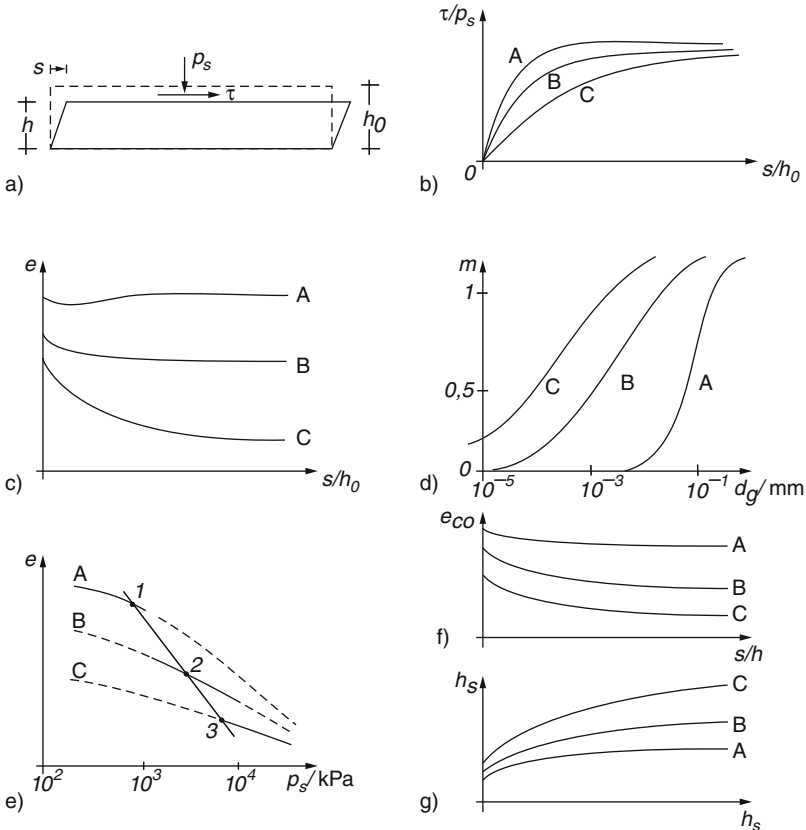


Fig. 7.3.4. Thin layer shearing (a) of psammoid, resistance with degradation of different extent (b), void ratios versus shearing (c), grain size distributions (d), void ratios versus pressure (e), void ratio prefactor (f) and granulate hardness (g) versus shearing

The plots of e vs. s/h_o tend apparently to asymptotes, i.e. the further degradation could get negligible in the considered range. This appears also in the plots of mass fraction m vs. grain size $\log d_g$ (d). These tend to log-normal distributions if the comminution is a multiplicative random process (Kolmogorov 1941). In our case a sand may be initially uniform with rounded grains as at a beach (A). Shearing with moderate pressure produces smaller and more angular grains in a wider range (B), therefore e gets smaller. With high pressure the grains get smaller and harder as otherwise they would not survive, and the dispersion of their sizes increases further (C). Thus the grain size distribution dominates skeleton properties for a given mineral and pore fluid, but grain shapes play also a role.

Plots of critical void ratios e versus $\log p_s$ get rather hypothetical in the light of the comminution (e). Plot A may represent e_c as if the grains were permanent, by they are so only for a low p_s . Plot B refers to the product of comminution by a moderate p_s , and C to the one for a high p_s . A sequence of void ratios after comminution with different p_s (e.g. 1–2–3) cannot yield an e_c vs. $\log p_s$ plot, and cannot produce related parameters therefore. For matching with (2.4.1) evolutions of e_{co} and h_s with shearing have to be assumed. The prefactor e_{co} decreases with the increasing dispersion of grain sizes (f). The granulate hardness h_s increases (g) as smaller grains have less imperfections and more contacts with neighbours due to the bigger dispersion. The adaption of e_c -parameters gets partly subjective therefore, this is also the case with (2.3.1) in the framework of CSSM.

The role of comminution with *reversals* may only be touched as the spectrum for different amplitudes without or with ratcheting is very wide. With a low pressure p_s the abrasion can already reduce the lower bound void ratio e_d , whereas the produced dust would hardly influence the skeleton and could be eroded easily. With higher p_s an increasing dispersion of grain sizes will reduce e_d much more, the granulate hardness h_s can rise substantially, and more fines reduce the permeability k_f . The determination of parameters for state cycles with assumed granular permanence gets the more subjective the more rapidly the grains are damaged. Thought and real experiments may help to quantify the loss of granular permanence, but the major part of this work is still ahead of us.

Evolution equations for the change of granular properties could be formulated as follows, at least in principle. Skeleton parameters as h_s , e_{co} , etc. change irreversibly with deformations according to the skeleton state. This change can be represented for rate-independent psammoids by

$$\dot{h}_s = \text{tr}(\mathbf{L}_h \mathbf{D}) + N_h D \quad (7.3.1)$$

and similar relations for e_{co} etc. with the stretching tensor \mathbf{D} and $D = \|\mathbf{D}\|$. The factors \mathbf{L}_h and N_h depend on p_s/h_s , $\tan \psi_s$ and r_e in such a manner that nearly asymptotic changes with big deformations and/or many reversals are captured. It suffices for the scope of this book that such relations could be formulated and adapted. Schünemann (2006) has proposed an example

with $\mathbf{L}_h = 0$ for simplicity. Constitutive relations for skeleton state variables would thus get further terms which could be derived by means of relations like (7.3.1) from the ones with granular permanence. The latter assumption could be principally delimited, and even left aside so that the postulated attractors do not lead into a dead-end.

The permanence of *peloid* particles appears to be more debatable because of the far lower solid hardness h_s (Sect. 3.4), but this is not the case. Thin layer shear tests by Balthasar et al. (2006) exhibit stationarity for pressures p_s up to almost 15 MPa (Fig. 3.8.4). The argotropy is the same as for lower p_s , so it is an invariable property of the solid constituent (Sect. 3.1). The critical friction angle φ_{cs} is ca. 2° smaller than in the usual geotechnical range of p_s from ca. 0.1 to 1 MPa. p_s -dependent critical void ratios e_c could not be measured precisely, but they were doubtlessly smaller for higher p_s , and the layer height did not change with further shearing. Anti-plane shaking with the same device led to a nearly stationary ratcheting, this indicates that the tested clay is capable of state cycles for p_s up to ca. 10 MPa. The material was brittle for overcritical stress ratios, i.e. $|\tau|/p_s > \tan \varphi_{sc}$, but after remoulding with added water and reconsolidation repeated shear tests produced the same results.

It appears thus that there are rather permanent primary clay particles, and secondary ones or aggregates of primary particles which come and go with deformations in the considered range of p_s and e . Both kinds of particles cannot and need not be more specified in this working hypothesis. Its range of validity can as yet only be determined by experiments, these can at best exhibit argotropic state limits and state cycles for a certain range of pressures and stretching rates. The ionic strength of the pore water should stay in a given range, otherwise physico-chemical changes would impair the desired permanence. As long as not even thermodynamic equilibria of clay-like materials are properly understood (Sect. 6.1) microscopic theories are not available to justify the proposed attractors for evolutions far off equilibrium.

More conventionally speaking, constitutive concepts with state limits and state cycles may work for reconstituted clays as far as the postulated asymptotic properties are observed in RSE-tests. The softness of aggregates – whatever shapes they may have – enhances their reconstitution with deformation-induced rearrangements. The much harder grains of psammoids are less permanent as they are not recombined by deformations. The observable brittleness of reconstituted clays is not ruled out by the postulated permanence which is implied by state limits and state cycles. Dilatant deformations with cavitation were observed by Balthasar et al. (2006) for overcritical stress ratios. Such dilatant state limits can be attained repeatedly, i.e. cavitation cracks can be closed again. The evolution of cracks is hardly predictable, at best critical points for the onset can be specified (Sects. 8.4 and 16.3).

To *sum up*, the brittleness of solid particles and cementation bridges excludes state limits and state cycles if deformation-induced encounter times do not suffice for recondensation. This can principally be captured for psammoids

by heuristic relations for the decay of bridges and the degradation of grains with deformations, so that the proposed attractors are still consistent. The softer and smaller aggregates of peloids are more easily recombined by thermal activation, but cementation and other kinds of net attraction can hardly be separated via experiments. The observed behaviour of natural clay samples can be better captured with a net attraction which gets lost by deformations. The thermally activated recovery should be taken into account in order to bridge the gap between natural and reconstituted clays. The cracking of clays by cavitation of pore fluid need not impair the permanence of primary clay particles.

LOCALIZATION

Localized shearing, cracking and decay were mentioned in previous chapters as limitations of constitutive models. How far could they be captured by extended continuum models, and on which physical base? As throughout this book attractors will be presented *more geometrico* for this purpose, we will see that some critical phenomena can thus be indicated or even predicted.

A fifth prelude on solids (Sect. 8.1) begins with a sheared solid strip, this is the simplest way to introduce *polar quantities* without a lot of algebra. Localized phase transitions off thermodynamic equilibrium are also indicated for biaxial tests in which patterns of shear bands can arise. Such cases may be captured with spatial mean values of RSEs so that polar quantities are averaged out, but this is not always justified. Cracking of solids is only mentioned in Sect. 8.1, it can at best partly be predicted with continuum models.

Shear bands in soils were first described by Coulomb (1773), they are usually related with ‘failure’ in soil mechanics. It is thus left aside why and how they arise. We will see in Sect. 8.2 how polar quantities can evolve in a sheared granular strip. Extended hypoplastic relations with polar terms (*p-hyp*) are apt to predict forced and spontaneous localizations in bands of some grain diameters thickness. This theory produces strikingly similar patterns of shear bands as observed in biaxial tests. This is but a partial validation, the enhanced force-roughness remains hidden and is at best indirectly indicated. We will see in Sects. 12.6, 13.1 and 13.3 that some model test results can be reproduced with *p-hyp*, but that problems with bigger lengths (referred to the grain size) and/or less symmetry are still out of reach. Fortunately polar terms may be neglected in many cases, this can be justified and delimited with *p-hyp*.

Shear localizations in peloids are more intricate due to skeleton viscosity and pore water diffusion (Sect. 8.3). Evolutions with polar quantities are again introduced by means of an endless sheared strip, but now the time enters via argotropy and seepage. Thin layer shear tests indicate a localized polarization and could be simulated by means of extended visco-hypoplastic relations (*pv-hyp*). More than with psammoids this could lead at best to a partial

validation as hidden polar quantities cannot strictly be separated by observations. Biaxial tests exhibit similar shear band patterns as with psammoids, but simulations with pv-hyp are not yet feasible. With subcritical stress obliquities viscous and polar effects can compensate each other, and the localization is impeded by spreading due to pore water diffusion. Then polar effects may be neglected, but with overcritical stress obliquities this is no more justified and predictions can altogether get impossible.

Cracking and hydraulic localization are briefly addressed in Sect. 8.4. Cracking may be considered as an extreme kind of shear localization, which is often accompanied by the cavitation of pore water. More than for solids continuum approaches are hardly feasible for such phase transitions. They can at best indicate the onset of cracking, but not its further evolution. Models with spatial averages may be justified up to critical stress obliquities (more in Sect. 9.1), but fail beyond. Hydraulic localizations will only be mentioned, they can particularly occur after a skeleton decay and can hardly be captured by continuum models.

This chapter is an excursion into so-called critical phenomena with pattern formation and deterministic chaos. Strange attractors are only touched, this notion is used throughout my book in a rather vague sense. It appears that often only the onset of localizations can be predicted, but not their further evolution. This issue will be further discussed in the final Chap. 15.

8.1 A fifth prelude on solids

Similarly as in Sects. 2.1, 3.1, 4.1 and 5.1 idealized solids are considered in this section in order to introduce some concepts. The use of polar quantities for shear localizations is justified by means of diagrams. This qualitative presentation implies extended state limits, whereas other attractors are not treated in detail. The evolution of cavities and cracks in solids is only touched as little can be taken over in that respect to soils.

Consider an infinite *solid strip* which is fixed at base and top and sheared via a rigid top plate, Fig. 8.1.1. Without pores the height h is constant. With increasing top displacement u_{2h} the shearing resistance T_{12} may increase up to a peak and get slightly smaller thereafter (a). Up to the peak the shearing profile u_2 vs. x_1 may appear nearly linear, but beyond it the further shearing is *localized* to a narrow band somewhere in the middle (b). With a constitutive relation between the rates of shearing $\dot{\gamma} = \partial \dot{u}_2 / \partial x_1$ and of resistance $\dot{\tau} = dT_{12}/dt$ the differential stiffness $\dot{\tau}/\dot{\gamma}$ would be negative beyond the peak. In a numerical simulation with a minute initial fluctuation the shearing would concentrate in the finite element row where the peak is reached first. This result is as subjective as the choice of elements and gets absurd with extremely thin elements.

A closer look reveals why this approach is physically wrong, and how merely numerical attempts (regularizations) could be substituted by a

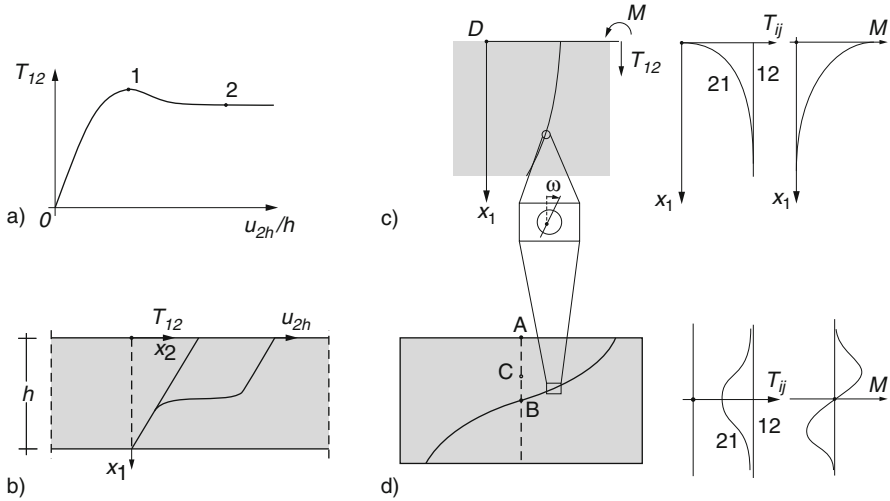


Fig. 8.1.1. Shearing of a solid strip with polar quantities: stress-strain curve (a), subsequent profiles of shearing (b), profiles of shearing and polar stresses (c); shearing with rotation and polar stresses in the mid-plane (d)

physically sound concept. A rate-independent relation of $\dot{\tau}$ with $\dot{\gamma}$ such as elp or hyp in Sect. 2.1 could not produce shear softening, i.e. $\dot{\tau}/\dot{\gamma} < 0$. An internal state variable would be needed, but how should it be defined? Consider a close-up near the top plate with markers for displacement u_2 and rotation ω , Fig. 8.1.1c. $\partial u_2/\partial x_1$ and ω vanish at the fixing wall, there an orthogonal shearing resistance T_{21} cannot arise. Thus the stress tensor is no more symmetric, we have $T_{12} \neq T_{21}$ and the difference $T_{12} - T_{21}$ is a candidate for an internal variable. Off the wall the rotation need not agree with the slope of shearing, i.e. $\omega \neq \partial u_2/\partial x_1$ can hold in a boundary zone. The stronger curvature $\partial \omega/\partial x_1$ near the wall wakes a resisting *couple stress* M , thus the width d_b of the boundary zone cannot get arbitrarily small.

A close-up of the inner *shear band* is more complex, Fig. 8.1.1d. The rotation ω is stronger than outside of the band and need not agree with the gradient $\partial u_2/\partial x_1$. The curvature $\partial \omega/\partial x_1$ has opposite signs above and below the middle of the band, and wakes a couple stress M so that the band cannot get arbitrarily thin. Associated shear stress components are not equal throughout the band, $T_{12} - T_{21}$ varies with x_1 while T_{12} is constant. The middle of the band works like a rough wall, but with lower resistance as it is sheared.

Polar quantities as indicated in Fig. 2.1.1c and d were proposed in an extended continuum theory by Cosserat and Cosserat (1909). Therein the tensors of stress and stretching are no more symmetric, and skew-symmetric tensors are added for couple stress and rotation. With this framework and extended linear elastic relations Günther (1958) could deepen the understanding

of boundary conditions and of dislocations. Mühlhaus (1987) proposed a polar continuum with elastoplastic relations and could thus capture shear localizations. These approaches demonstrate also how frame-indifference can be achieved with rate-type relations. The ones by Mühlhaus (1989) and Vardoulakis et al. (1992) are debatable, however, as plastic strain is used as a state variable.

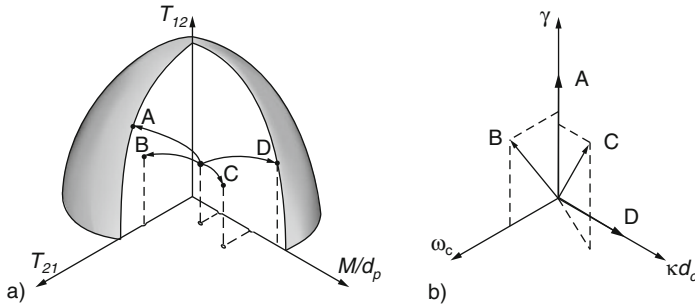


Fig. 8.1.2. Component spaces of transversal and couple stress (a) and strains (b)

Returning to our sheared strip a constitutive concept may now be represented by means of related paths, Fig. 8.1.2. While such paths are restricted to two planes for simple shearing (Sect. 2.1) two further statical and two kinematical polar quantities require three-dimensional component spaces, but only few projections can be shown. In a stress space (a) T_{12} and T_{21} are not equal in general, and the couple stress M is divided by a material length d_c to be commensurate. *Extended state limits* may be represented by a symmetric ellipsoid so that two component ratios suffice as additional polar parameters. The ellipsoid represents a positively definite quadratic form of the three stress components. Similarly three stress components. Similarly as with non-polar components (Sect. 2.1) an extended deviatoric stress energy attains thus a critical value for state limits. This energy threshold is related with on-going dislocations in composites of crystallites, but microscopic In the related space of deformations (b) a curvature κ and a Cosserat rotation ω_c appear in addition to shearing γ . ω_c is the difference of the total rotation and the one given by the gradient of displacement $\gamma = \partial u_2 / \partial x_1$. The curvature $\kappa = \partial \omega_c / \partial x_1$ is made dimensionless by the material length d_c . In our sheared strip the polar quantities κ and ω_c arise only along the boundaries and in the middle shear band. The sketched related paths for some material points in Fig. 8.1.1 are schematic as the real paths are not independent and can at best be guessed.

Outside the shear bands a continued simple shearing would lead to a non-polar state limit (A). Minor polar stress components (remnants from previous evolutions as outlined further below) are swept out by such a non-polar deformation. In the middle of the free shear band (B) T_{21} gets smaller than T_{12} ,

and M does not arise due to symmetry (Fig. 8.1.1d). A straight generalized deformation path leads to a state limit with a lower shearing resistance T_{12} than in case A. This state limit is attained with different initial states. The shear softening of Fig. 8.1.1a arises thus through a *localized bifurcation* with polar quantities. Close to the middle of the shear band (C) the ‘external’ shear stress T_{12} attains the same amount and differs less from T_{21} while M arises. T_{12} tends to a state limit value alongside with the couple stress M . At the boundary (D) a purely polar deformation without shearing leads to a state limit with $T_{21} = 0$ and a bigger M than for C, whereas T_{12} is the same as in the middle due to static equilibrium.

Elastoplastic or hypoplastic relations with polar terms (*p-el*p or *p-hyp*) could be formulated as shown in Sect. 2.1 without polar components so that the proposed state limits are asymptotes (attractors) which are determined by the directions of generalized stretching, viz. by $\dot{\omega}_c/\dot{\gamma}$ and $\dot{\kappa}/\dot{\omega}_c$ or by equivalent direction angles. Together with generalized equilibrium and compatibility conditions and boundary conditions evolutions of a sheared strip could thus be simulated numerically. The spatial uniformity of simple shearing without polar terms gets lost at the boundaries from the very beginning, this may be called *forced polarization*. A peak and a subsequent shear localization in the middle can be obtained by means of minute initial fluctuations, this may be called *spontaneous polarization*. The thickness of the boundary zones and the inner shear band come close to d_c , this internal length should therefore be smaller than the strip height h .

Tentative variants of p-el and p-hyp should first reproduce the qualitative features of Figs. 8.1.1 and 8.1.2. After a trial and error procedure thin layer shear tests could serve for quantification. The axis ratios of the proposed state limit ellipsoid determine the ratio of peak and residual shearing resistance, but not vice versa. The material length d_c could be adapted by a repeated back-analysis so that an observed shear zone thickness is matched. d_c is presumably determined by the size of crystallites, not by the far smaller size of dislocations. Even if the sample is initially uniform and if the free lateral ends do not matter this identification cannot be unique: the thin layer loses its uniformity and internal shear bands are not necessarily plane. This lack of precision with shear localization is principally inevitable.

The thermally activated *viscosity* of our sheared strip could rather easily be taken into account, Fig. 8.1.3. Plots of T_{12} vs. u_{2h} for constant top velocities \dot{u}_{2h} exhibit the same argotropy as without polar effects up to the peak (a). Beyond it the residual resistance is less reduced than without argotropy as the rate of deformation increases with the localization. Argotropic extended state limits could be formulated as shown with Fig. 8.1.2, now with argotropic generalized deviators as by (3.1.19) and the same component ratios as without argotropy. Rate-tape relations as (3.1.19) could be extended by polar terms, and the viscosity factor f_v by (3.1.21) could also be generalized. This is legitimate as thermally activated dislocations exhibit always the same argo- and thermotropy (Persson 2000a). The generalized stress energy works

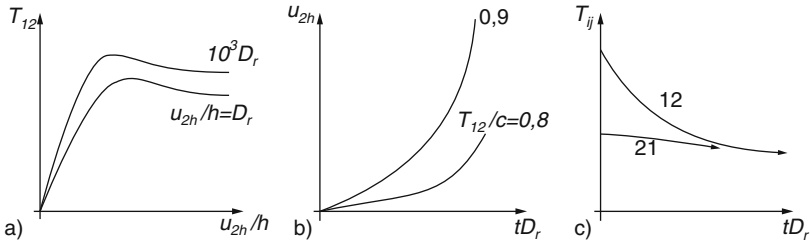


Fig. 8.1.3. Shearing of an argotropic solid strip: stress-strain curves (a), creep (b) and relaxation (c)

as a drift (Sect. 3.1) for any ratio of components (i.e. mechanism of sliding and rotation).

An identification could again be obtained by means of thin layer shear tests, now with velocity control. It is more realistic than without argotropy as there is no plasticity and ductility without viscosity: dislocations are always thermally activated (Sect. 3.1). Creep (Fig. 8.1.3b) is achieved with constant T_{12} , it leads also to localization and tends to a stationary extended state limit. Constitutive relations with polar terms and f_v (abbreviated *vp-el* and *vp-hyp*) can only work in the range of generalized stretching rates D by (3.1.8). For lower D the viscosity tends to be linear, for too high D the dissipated heat increases the temperature T . Relaxation is obtained after fixing the boundaries (Fig. 8.1.3c). The polar stresses are more rapidly reduced than the external shear stress, thus the drift energy is diminished and f_v gets very small. This cold annealing tends to a thermodynamic equilibrium, but such an endogenous attractor is only attained after extremely long times if T is well below the melting point.

Other evolutions can occur in our sheared strip with *reversals*, Fig. 8.1.4. Plots of T_{12} vs. u_{2h}/h tend to cycles (a) nearly as without hysteresis for small amplitudes (A), with marked hysteresis for moderate amplitudes (B) and with alternating peaks beyond (C), provided that there is no fatigue.

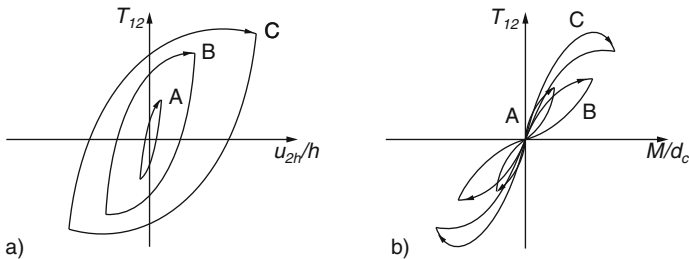


Fig. 8.1.4. Asymptotic response of a solid to cyclic shearing: hysteresis loops (a) and polar stress cycles (b)

State cycles are attained at certain material points, e.g. for T_{12} vs. couple stress M at the boundary (b). Small amplitudes lead to flat double loops after a reduction of M (A), this works also for other polar stresses and may be called *mechanical annealing*. With moderate amplitudes the asymptotic cycles may be wider double loops (B), but with big ones their shape is changed (C) as state limits are attained repeatedly. Such evolutions could be principally captured by extended hidden state variables, i.e. by kinds of p-elp- α or p-hyp- δ (cf. Sect. 4.1). The viscosity could also be taken into account, but such attempts are hardly worth the effort as an identification by means of thin layer shear tests would scarcely be feasible. Shear localizations should first be captured without reversals, with them drastic simplifications are needed anyway.

A wider manifold of shear localizations can occur with initially uniform solid samples under *biaxial* boundary conditions, Fig. 8.1.5. A single shear band arises in a slender rectangle with lateral pressure control by shortening via two smooth plates (except for a central fixing) which can translate past each other (a). After the spontaneous polarization at a random height the deformation goes on only in the band wherein a state limit with polar stresses is attained. As in thin layer tests the uniformity gets gradually lost with large displacements which start from the free boundaries. Such evolutions could be simulated with p-elp or p-hyp, also including viscosity, therein more components are needed than for an endless sheared strip so that frame-indifference is secured. The localized bifurcation is enhanced by a minute initial fluctuation, the identification remains again imprecise.

If a squatter rectangle is flattened via two smooth plates two shear bands can arise which meet at one of the smooth plates, Fig. 8.1.5b. In a reflection zone at the wall (insert) polar terms of the two bands compensate each other. With further convergence of the plates further bands arise from boundary zones which are weakened by polar effects (indicated by dotted lines). A zig-zag line of shear bands arises in a flat rectangle (c) with arbitrary onset,

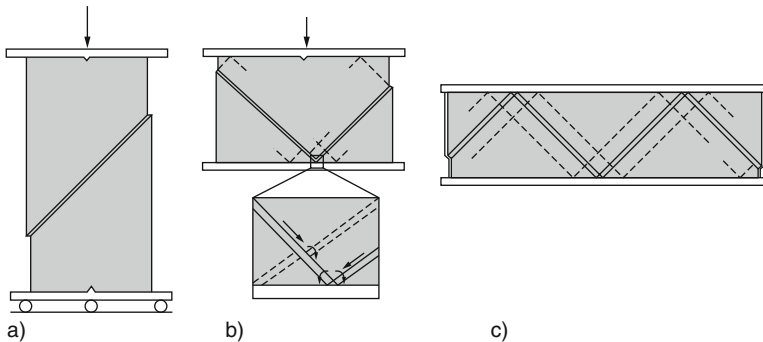


Fig. 8.1.5. Shear localization in a solid rectangle: single band (a), two bands (b) and pattern (c)

reflection, compensation and successive bands. Such evolutions could principally be simulated with p-elp or p-hyp and initial fluctuations, the identification by means of biaxial tests would again remain imprecise.

Patterns of shear bands can differ from the ones shown in Fig. 8.1.5c and could not be captured in general by simulations as indicated above. They can arise from random initial fluctuations with suitable boundary conditions, and their order can get lost with continued stretching via the boundary. As indicated further above for endless sheared strips the polar stresses in patterns are reduced by relaxation or by reversals with suitable amplitudes.

One may consider a rectangle with polarized bands as a kind of RSE with spatial fluctuation of stresses including polar quantities. This kind of force-roughness resembles the one discussed in Sects. 4.1 and 5.1 which can likewise be reduced by relaxation or reversals. There is a difference in the boundary conditions: an RSE can be split into two or more RSEs by shear localization, whereas the force-roughness of Sects. 4.1 and 5.1 can just grow or fade and change its orientation. In both approaches internal variables cannot be determined directly, but this uncertainty can at least partly be ruled out by means of state cycles.

Two kinds of attractors, viz. state cycles for reversals and thermodynamic equilibria for relaxation, can thus enhance the spatial uniformity which is desired for RSEs. State limits as another kind of attractor (isochoric for a pore-free solid) impair this uniformity by shear localizations. Polar quantities arise in various hardly predictable patterns which depend on assumed boundary conditions. In other words, the apparently simplest attractor for monotonous deformations (Sects. 2.1 and 3.1) goes over into a *strange attractor* which can as yet hardly be captured. Even for idealized solids constitutive models without polar terms (like elp, hyp, v-elp or v-hyp) therefore have a limited range of validity which cannot be judged easily. Extended models with polar terms can principally provide more insight, but the identification by test results will never be complete and the required amount of calculation work is too big for applications.

Cylindrical samples can lose the desired uniformity of RSEs with a wider manifold than biaxial ones. Test results with initially uniform paraffin cylinders may serve for a qualitative illustration, Fig. 8.1.6. The material resembles an amorphous solid like glass or ice, but typical losses of uniformity can be produced more easily. If a paraffin cylinder of equal height as its diameter is shortened via smooth plates with low velocities it is deformed into a barrel without change of opaqueness (a). The plot of axial stress versus shortening exhibits argotropy and slight peaks (b). The barrelling can be interpreted as a diffuse bifurcation: the radial shearing due to barrelling in addition to isochoric axial shortening weakens the axial resistance, this reduction is not compensated by an increasing viscous resistance as the amount of stretching D is hardly changed. This behavior could be captured with arbitrary components and frame-indifference by means of a critical stress energy for state limits (Sects. 2.1 and 3.1). It can also occur with a sheared endless strip if

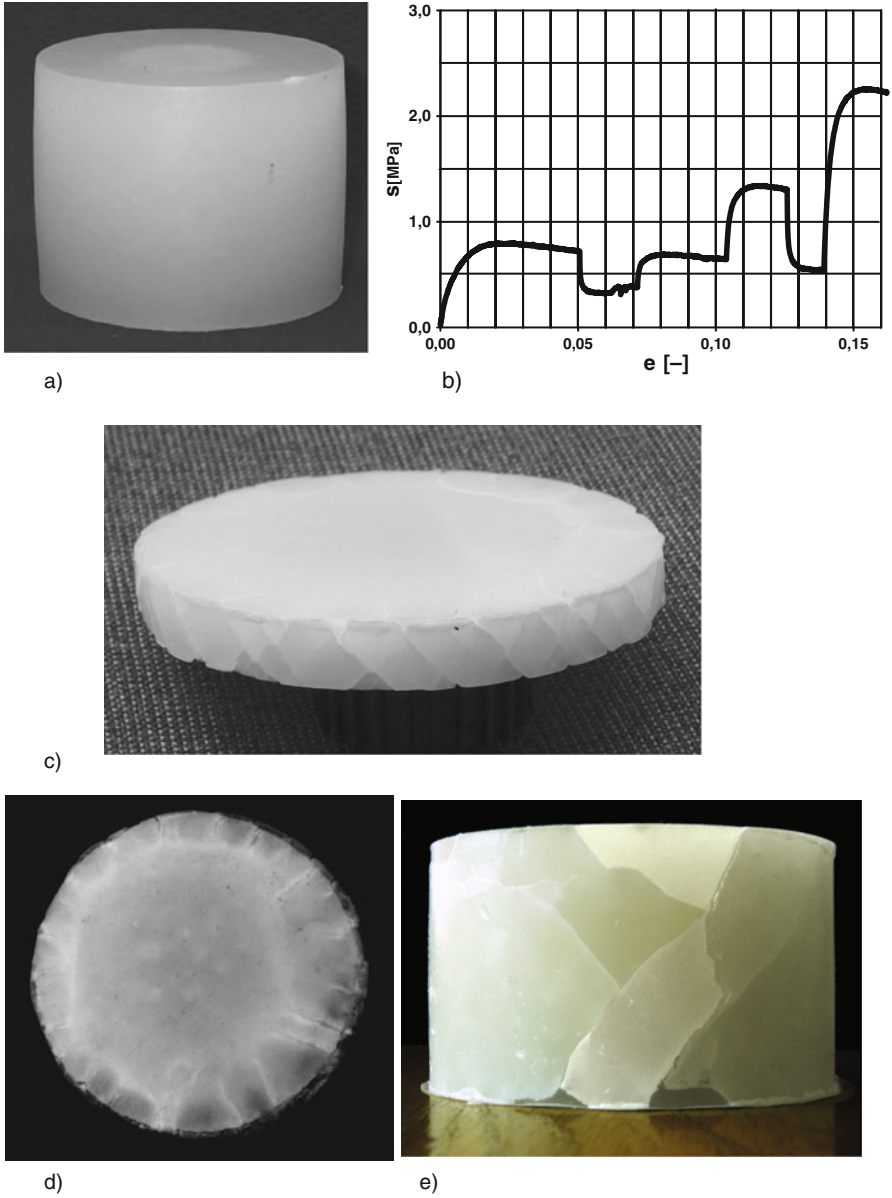


Fig. 8.1.6. Response of paraffin samples to uniaxial shortening (Rübel 2010): **a** barrel after slow shortening, **b** related stress-strain curve, **c** shear bands at the rim of a flattened disc, **d** shear bands at the spread horizontal surface, **e** cracks after rapid shortening

the resistance to in-plane shearing gets smaller by an additional anti-plane shearing (Fig. 2.1.10).

If a paraffin disc is flattened much faster via smooth plates than shown by Fig. 8.1.6a and b zig-zag shear bands arise at the perimeter, and the sample gets more opaque (c). The horizontal surface exhibits radial shear bands in an outer ring (d). This pattern resembles the one in a flattened biaxial strip (Fig. 8.1.5c) although the symmetry is different. The plot of axial pressure versus shortening has a peak. It appears that the shear softening due to localized shearing with polar effects is not compensated by the viscous increase due to the faster stretching in shear bands. This indicates that the constitutive model proposed further above for sheared strips does not suffice. It appears that the paraffin develops micropores in bands and that it gets softer therefore and more opaque.

A higher paraffin sample with the same diameter and rate of shortening would simultaneously bulge and develop a pattern of shear bands. Needless to explain that a back-analysis with polar terms and viscosity is beyond the present reach. Therefore the outline here is at best qualitative, and caution is required with so-called triaxial tests (Sect. 14.1). This is also the case with the axial splitting of a paraffin disc by rapid shortening via smooth plates, Fig. 8.1.6e. This kind of local dilation may be interpreted as a driven growth of pores into cracks, i.e. a continued cavitation. The uniformity desired for RSEs gets evidently lost, and a crack pattern can hardly be identified. Simply speaking, the material response is no more plastic and viscous without or with shear localization, but *brittle*.

Constitutive relations of the kind indicated further above are no more applicable. The aim here is only to demarcate the range of validity with respect to cracking. Solids with crystallites, or amorphous ones, have often a small volume fraction of micropores, say $\alpha_p < 1/200$, with widths below 10^{-6} m. They are therefore barotropic and pyknotropic, but of minor extent if the mean pressure p remains within one order of magnitude. Plastic deformations are enhanced by micropores as around them deviator stresses are higher than in the spatial average. If the stress response to isochoric or isobaric stretching with constant ratios of overall components tends to get stationary state limits may be conceived as without micropores (Sect. 2.1). The argotropy could similarly be taken into account (Sect. 3.1), but what will happen with micropores in such cases?

With constant gross density ρ and/or pressure p a continued stretching does not change the volume fraction α_p of pores, nor their average shape if all RSE-averages are stationary. A single micropore gets flatter or rounder by deformations, however, and can disappear or arise. The pore surface and the related surface energy can be stationary in the spatial average, but can rise and sink by the evolution of each pore. Thus energy is taken up from or released into the near-field of a micropore where the stress deviators decrease or increase. If one pore would be totally flattened the near-field stress deviators would vanish, and closing surfaces could release energy which could trigger

the widening of a neighbored pore. All the time energy is consumed by deformations which could at best be crudely estimated. Such evolutions are argotropic due to thermal activation (Sect. 3.1), but now surface energies come into play (Sect. 6.1).

Stationarity means that micropores grow and dwindle with the same average rate. For a given pore fraction α_p or pressure p and temperature T this requires a suitable stretching D_s so that the times for growth t_g and reduction t_r of micropores agree in the average. With given p and T the α_p would decrease for $D < D_s$ and increase for $D > D_s$. Due to the exponential dependence of rates on energies by (3.1.5) the order of magnitude of the threshold D_s may suffice for this discrimination. D_s can be represented in a plot of α_p versus p for a given T and mode of stretching (e.g. cylindrical extension or simple shearing), Fig. 8.1.7. This plot may suffice here for discussion, experiments would be needed for quantification. Theories of thermally activated dislocations and cavitations (Sects. 3.1 and 6.1) can at best support the dependence of D_s on T , but activation energies can hardly be separated.

With a sufficiently high p and low D micropores dwindle by stretching. As their volume fraction α_p is minute anyway one may neglect volume changes and pressure effects, as was assumed in Sect. 3.1 and further above in this section. In this regime solid particles may be considered as neutral with respect to changes of pore water pressure p_w so that Terzaghi's principle of effective stress (Sects. 2.2 and 3.2) is justified. For faster stretching than the threshold, i.e. $D > D_s$, α_p increases by isobaric stretching with various kinds of arising pores, then barotropy and pyknotropy play a role for solids. This merely qualitative demarcation may suffice for this prelude as the brittleness of soils is not well understood.

For the sheared strip of Fig. 8.1.1 dislocations are faster in bands with polar quantities. If the overall stretching rate is below the threshold D_s for a given p and T it can exceed it in polarized bands. Micropores can arise and grow there, and their volume fraction α_p can attain a p - and T -dependent threshold if the response of the strip gets stationary after a shear localization. With this kind of dilation the constitutive model indicated with Fig. 8.1.2 would get insufficient as barotropy and pyknotropy should no more be neglected.

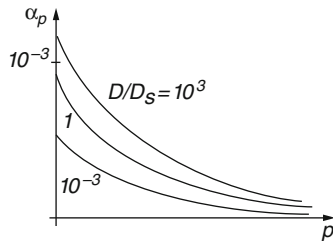


Fig. 8.1.7. Volume fraction of micro-pores versus pressure for different strain rates

Extended state limits should imply α_p and T via D as before. p - and α_p -effects could principally be observed in experiments, one could also investigate whether micropores remain closed. Figure 8.1.6e may illustrate what is meant although paraffin is not really a solid.

As indicated by Fig. 8.1.6e growing micropores turn into cracks if the overall stretching exceeds the threshold by orders of magnitude, say $D/D_s > 10^3$. A growing flat pore is metastable in the sense of Griffith (1921) and Irwin (1957) for a given overall stress as more elastic energy is released by the growth than the increase of surface energy. This concept is oversimplified as viscoplastic effects and crystallites are neglected. Both can pin a growing crack, this can at best be qualitatively explained by means of continuum models so that experiments are indispensable. The adsorption at a growing free surface exposed to a fluid reduces the surface energy so that a crack can grow more easily. The rate of growth can be so high that inertia plays a role, continuum models have been proposed for such dynamic crack propagations.

Persson (1998) points out that continuum models do not suffice for crack tips, and that simplified atomistic models can produce qualitatively different crack propagations. Quantitative atomistic simulations are beyond the present reach as too many atoms and degrees of freedom would be needed. Persson and Brener (2005) considered the crack propagation in viscoelastic solids from a continuum approach down to the molecules. In spite of the complexity the derived relations of the crack-tip radius with surface energy and velocity of propagation agree with experimental findings.

The thermally activated healing of cracks can principally be captured by combining atomistic and continuum approaches (Persson 1998). There is a long way to the quantification of such models, let alone the evolution of crack patterns. It may suffice here to state that sophisticated models exist for the propagation of a single crack in solids, but not (at least not yet) for the appearance and disappearance of crack patterns.

To *sum up*, evolutions of solid RSEs with shear localization can principally be captured by means of polar quantities, and micropores may also be taken into account, but the evolution of cracks leads outside the reach of continuum approaches. Polar quantities arising in narrow bands can impair the desired uniformity of RSEs, but this can be regained by relaxation or reversals. Micropores impair the often assumed pressure-independence, they arise preferably in shear bands. The restricted ductility with shear localization gets lost by a more rapid overall stretching if pressure or temperature are lower than critical. The brittle response with the propagation of cracks can no more be captured by constitutive relations of spatial averages for RSEs.

8.2 Shear localization in psammoids

Other than pore-free solids grain skeletons are pyknotropic and barotropic, therefore they can exhibit shear softening with constant void ratio e or mean skeleton pressure p_s , and the pore water pressure $p_w = p - p_s$ is involved.

An extended hypoplastic model with polar terms (p-hyp) is introduced in the sequel by diagrams for a sheared strip, then biaxial RSEs are treated similarly as in Sect. 8.1. The discussion includes the influence of pore water and relative void ratio r_e , other than with solids the shear localization can thus be enhanced or impeded.

Tejchman and Gudehus (2001) simulated evolutions of a *dry sheared strip* with *polar quantities* and spatial variation only along the normal (here x_2). Quantities of a polar continuum are indicated with RSEs in Fig. 8.2.1, apart from renaming they appear already partly in Fig. 8.1.1. In addition to two displacement components u_1 and u_2 there is an excess rotation ω_c (a) with respect to the one by u_1 and u_2 ($(\partial u_1/\partial x_2 + \partial u_2/\partial x_1)/2$ for small displacements). As there are no changes along x_1 changes of the void ratio e are related with $\partial u_2/\partial x_2$ by (2.11.1) for isochoric grains. ω_c is not the same throughout the RSE, thus the curvature $\partial \omega_c/\partial x_2$ describes twisting. In addition to shearing ($0.5\partial u_1/\partial x_2$) and dilation ($\partial u_2/\partial x_2$) there are thus two polar deformation quantities, ω_c and $\partial \omega_c/\partial x_1$. For large displacements velocities v_1 , v_2 and $\partial \omega_c/\partial t$ and their gradients $\partial v_1/\partial x_2$. $\partial v_2/\partial x_2$ and $\partial^2 \omega_c/\partial x \partial t$ are more appropriate.

There are four in-plane stress components (Fig. 8.2.1b, traction positive). The out-of plane normal stress σ_{33} has to be kept in mind, and all components refer to the skeleton. The couple stress m_1 vanishes for the considered strip without changes along x_1 . The non-vanishing couple stress m_2 may be imagined as the moment of an eccentric pressure in the x_2 -direction, thus the stress is no more uniform along x_1 in our RSE. m_2 is statically compensated by the asymmetric shear stress, i.e.

$$\frac{\partial m_2}{\partial x_2} + \sigma_{21} - \sigma_{12} = 0 \tag{8.2.1}$$

holds without a field of external torque and without acceleration.

The *constitutive relations* proposed by Tejchman and Gudehus (2001) are hypoplastic with polar terms (*p-hyp*). Similarly as in Fig. 8.1.2 they may

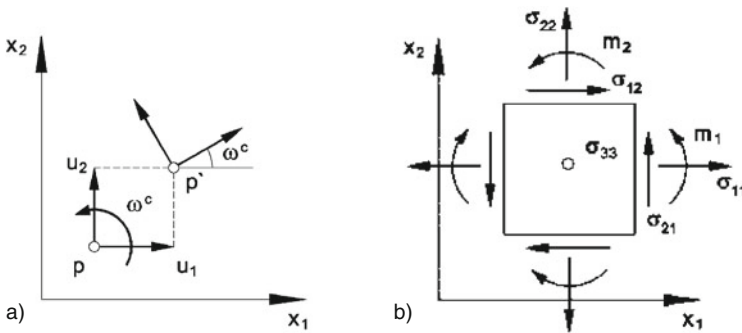


Fig. 8.2.1. RSEs with polar kinematic (a) and static quantities (b), Tejchman and Gudehus (2001)

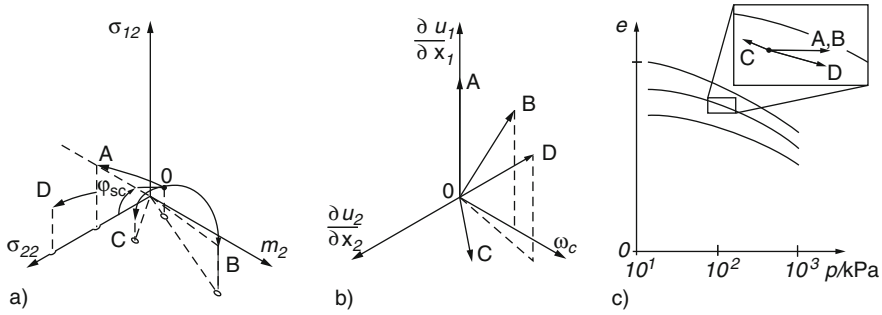


Fig. 8.2.2. Evolutions of a granular RSE with polar quantities towards extended state limits: paths of stress (a), deformation (b) and void ratio versus pressure (c)

be represented by means of related paths, but now with barotropy and pyknotropy, Fig. 8.2.2. In a stress component space (a) one skeleton pressure $-\sigma_{22}$ appears, and only the ‘external’ shear stress component σ_{12} and the couple stress m_2 can also be shown. Further stress components do not appear with three-dimensional paths as projections from a higher-dimensional component space, so the representation is incomplete and merely qualitative. Generalized deformation paths appear in a space of shearing, dilation and rotation (b), thus the curvature cannot be shown. A plot of e versus $\log p$ (c) is needed for pyknotropy, labels for stress obliquity are omitted for simplicity.

The initial state (O) may have small polar components and a lower than critical relative void ratio, $r_e < 1$. Pure shearing without rotation (A) leads to a critical state with $-\sigma_{12}/\sigma_{22} = \tan \varphi_{cs}$ and $r_e = 1$, the polar stress is swept out. Pure shearing plus rotation leads to a critical state with polar stress (B). The stress component ratios of such *extended state limits* are related by

$$(\sigma_{12}/p \tan \varphi_{cs})^2 + (m_2/pd_g a_c)^2 = 1 \tag{8.2.2}$$

with a representative grain size d_g and a dimensionless parameter a_c . Without the couple stress m_2 (8.2.2) is reduced to (2.9.6) for non-polar shearing. The quadratic form (8.2.2) can be extended for further stress components, with a further one it can be represented by an ellipsoid. As shown by Fig. 8.1.2a for a pore-free solid this means that the deviatoric stress energy is a certain fraction of the isotropic one for state limits. The relation of generalized stress and stretching component ratios for state limits is not given by (8.2.2), it could be expressed by a kind of flow rule.

As shown in Fig. 8.2.2c it is assumed that the critical void ratio e_c depends on p like without polar quantities, this simplification may suffice for the time being. A rotation with dilation leads to an extended dilatant state limit (C) and a decay thereafter. A path with monotonous contraction leads to a contractant state limit with p -increase and constant stress component ratios (D).

The extended state limits are thus assumed to be attractors for straight generalized deformation paths. The latter cannot generally be realized in element tests as extended RSEs (Fig. 8.2.1) cannot be controlled arbitrarily. The proposed asymptotic response is needed for consistency and cannot be validated directly nor completely.

The p-hyp relations by Tejchman and Gudehus (2001) are formulated so that such generalized state limits are obtained as asymptotes. The algebraic representation is similar as without polar terms for plane-parallel evolutions (Sects. 2.4 and 2.11). Only two further material constants are needed, viz. an average grain size d_g and the factor a_c introduced by (8.2.2). a_c can be determined by matching the observed thickness of shear bands as will be shown further below.

Figure 8.2.3 shows calculated snapshots of state and shape after large shearing ($u_{2h} = h$) with medium initial density and constant pressure. The height is $h = 100d_{50}$ (d_{50} for d_g) so that the shear band with dilation constitutes a significant fraction (a). The Cosserat rotation ω_c arises only in the shear band which can thus be identified (b). The void ratio rises mainly in the shear band (c). The couple stress has an anti-symmetric distribution with peaks in the shear band and forced values near the walls (e). The normal stress components are almost the same everywhere, the shear stress is asymmetric ($\sigma_{12} \neq \sigma_{21}$) in the shear band and at the plates (d). The inner zone with polar stresses is a little bit wider than the one with ω_c and dilation.

Similar plots are obtained with a lower initial relative void ratio r_e . After a displacement $u_2 = h$ the shear band is narrower and exhibits more rotation ω_c , the stronger dilation leads to the same critical void ratio $e = e_c$ in the middle, the polar stresses are bigger as mutual rotations of grains are more impeded. With a high initial r_e (loose skeleton) the shearing gets uniform except for boundary zones, so there is no more a spontaneous shear localization. There is a small Cosserat rotation ω_c , but polar stresses arise only near the rough boundaries (cf. Fig. 8.1.1), and except for these zones $e = e_c$ is attained throughout the strip.

A simulated evolution of some state variables in a sheared strip with $r_e \approx 1/2$ (medium dense) initially is plotted in Fig. 8.2.4. One normal stress component is constant, the two further ones tend to nearly the same value in the middle, the shear stress there gets and remains asymmetric (a). The couple stress arising at the rough plates gets stationary beyond a slight peak (b). The stress obliquity $\varphi_w = \tan(\sigma_{12}/\sigma_{22})$ rises to a peak and attains a slightly lower asymptote than the critical value without polar terms (φ_{cs} by Sect. 2.9) thereafter (c). The void ratio at mid-height decreases slightly first, and attains $e = e_c$ thereafter (d). The state is stationary for shearing beyond ca. 50%, this extended state limit is represented in Fig. 8.2.2.

Without polar quantities the sheared granular strip would remain uniform as required for an RSE (Sect. 2.9) and would tend to a uniform critical state. The uniformity gets lost by polarization at the boundaries and in the middle. With a higher initial density and the same external pressure $-\sigma_{22}$ the peaks

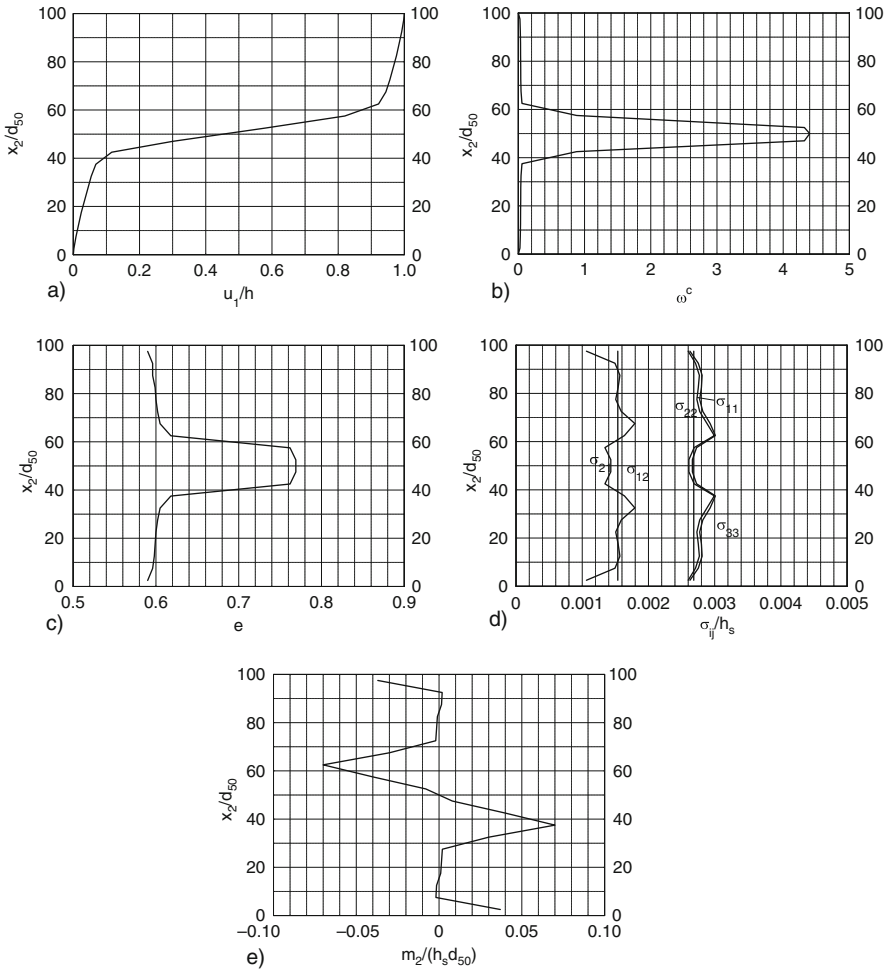


Fig. 8.2.3. State and shape of a sheared granular strip, simulated by Tejchman and Gudehus (2001) with a polar hypoplastic relation (p-hyp) : profiles of shearing (a), Cosserat rotation (b), void ratio (c), normal and shear stresses (d) and couple stress (e)

of stress obliquity φ_w and of couple stress are more marked. The stationary extended state limit beyond the peak exhibits the same $\varphi_w = \varphi_{cs}$ and $e = e_c$ at mid-height, but stronger polar stresses in a narrow shear band.

The calculated *shear band thickness* t_s depends on the initial relative void ratio r_e , Fig. 8.2.5, and on the mean grain size (d_{50} for d_g). For a low initial r_e (dense skeleton) it amounts about 20 grain diameters, for $r_e \rightarrow 1$ (loose) it reaches the height of the strip as there is no localization. As can be seen from the spatial distribution of polar quantities in Fig. 8.2.3 the band width is somewhat fuzzy. Thin layer shear test results (Fig. 2.9.8) could be used for

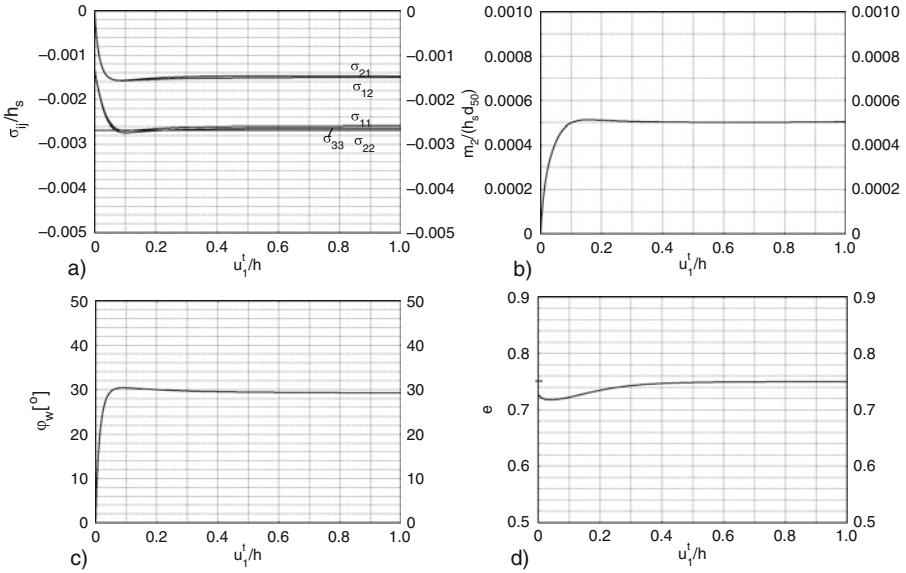


Fig. 8.2.4. Evolution of state variables with shearing of a strip, simulated with p-hyp (Tejchman and Gudehus 2001): normal and shear stresses (a), couple stress (b), stress obliquity (c) and void ratio at mid-height (d)

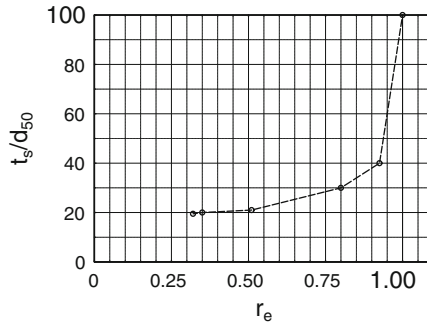


Fig. 8.2.5. Shear band thickness in a sheared strip, calculated with p-hyp by Tejchman and Gudehus (2001)

matching, but at best with moderate precision. Shear bands could be observed by means of markers for different initial r_e and h/d_g , whereas observable peak stress obliquities and local void ratios are principally imprecise and hardly repeatable. The polar rotation can at best be observed in an assembly of rods instead of grains (Bogdanova-Bontcheva and Lippmann 1975), but thus polar stresses could hardly be measured.

Huang and Bauer (2003) simulated evolutions of a sheared granular strip with a modified p-hyp relation. Therein a generalization of (8.2.2) holds for extended state limits, and associated generalized stretching component ratios

are derived (a kind of flow rule). Thus the numerical robustness is improved, and the adaptability is wider than with the version by Teichman and Gudehus (2001). With a low initial relative void ratio ($r_e \approx 0.2$) shearing with constant pressure leads again to peaks of stress obliquity and couple stress, and to an extended state limit beyond. The state quantities evolve as in Fig. 8.2.4 and are similarly distributed as in Fig. 8.2.3, but with one exception: the profiles of void ratio and shear stress skewness $\sigma_{12} - \sigma_{21}$ exhibit two peaks in the shear band, not one.

The shear band thickness t_s by Huang and Bauer (2003) increases with higher initial r_e as in Fig. 8.2.5. For a given r_e it grows nearly in proportion to the grain size d_g , only for strip heights $h < \text{ca.} 50d_g$ the ratio t_s/d_g gets higher as then the boundary layers interfere with the inner band. For a given r_e our t_s/d_g decreases if the polar constant (a_c in (8.2.2) or an equivalent) increases. This relationship helps for matching test results and could lead to a physical interpretation of the polar material constant a_c , presumably via the angularity of grains. Thin layer shear test results could serve for clarification, but single or double peaks in shear bands as mentioned above could scarcely be discriminated. Strict validations can hardly be obtained and the estimation of parameters remains partly subjective, let alone the specification of initial states with polar quantities which will be treated further below.

A snapshot of an idealized granular strip may serve for a *microscopic interpretation* of polar quantities, Fig. 8.2.6. For simplicity grains are substituted by rods so that parallel cross sections are equal, but the following argument could be extended to three dimensions. The contact flats where forces are transferred are much smaller than the grain diameters so that contact couples (moments) may be neglected. Otherwise the grains would be soft or crushable for the considered average skeleton pressure p , this is excluded for psammoids by definition (Sect. 2.2). RSEs in the sense of Fig. 8.2.1 should be almost as small as one grain, boundary zones and shear bands are only a few grain diameters thick (Fig. 8.2.5). Forces at RSE-boundaries, which can be derived from contact forces, scatter strongly therefore so that stress components (i.e. force densities) should be understood as averages along strips.

Grains at a rough boundary (wall) are fixed, but their neighbours can rotate and slide past them. The resultant forces at the wall-side RSE-boundary

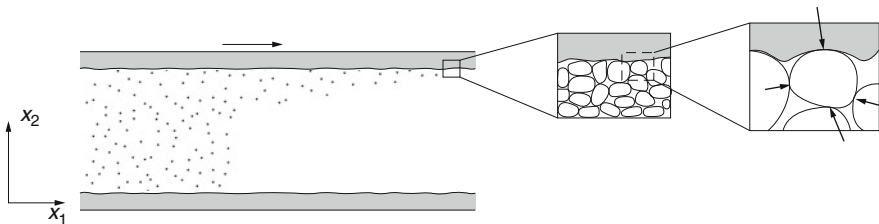


Fig. 8.2.6. Grains with contact forces at the rough boundary of a sheared strip

are eccentric and skew. Their average values per unit of strip length have the components σ_{22} , σ_{12} and m_2 by the rotations of Fig. 8.2.1a. The resultant forces at the RSE-boundaries normal to the wall are not eccentric and less skew in the average, this is represented by $m_1 = 0$ and $\sigma_{21} \ll \sigma_{12}$. The forces at the wall-parallel RSE-boundaries are more eccentric and skew in the average, but less than at the wall. In a state of rest with negligible weight the forces at each RSE are at equilibrium for their spatial average, this means $\partial\sigma_{22}/\partial x_2 = 0$, $\partial\sigma_{12}/\partial x_2 = 0$ and (8.2.1). Fluctuations in the x_1 -direction are averaged out, this necessitates also $m_1 = 0$, otherwise the independence of stress components on x_1 could not be assumed. The void ratio along the wall is also a spatial average for an ensemble of RSEs in our thin strip. It can hardly change as the grains are fixed by the rough wall.

An RSE in a thin strip near the middle of a shear band exhibits a higher void ratio as all grains rotate and slide past each other. The mean normal and shear forces per unit of length (σ_{22} and σ_{12}) at wall-parallel RSE-boundaries do not depend on x_2 by equilibrium, i.e. erratic deviations of these forces are averaged out. The eccentricity of the normal force at the wall-parallel RSE-boundary is lower in the average than at the wall as the mutual rotation is less impeded. Likewise the average force obliquity at wall-normal RSE-boundaries is less reduced than at the wall. With wider RSEs the polar stresses m_2 and $\sigma_{12} - \sigma_{21}$ would get smaller by averaging. If an RSE comprises the complete shear band or even the whole granular strip m_2 and $\sigma_{12} - \sigma_{21}$ would disappear, this can be seen from Fig. 8.2.3.

Polar stresses can thus represent the resistance of grains against mutual rotations in boundary zones and internal shear bands with a thickness of a few grain diameters. RSEs which are nearly as small as grains represent spatial fluctuations along normals to bands with polar effects. There is no need of grain contact couples, but an averaging of contact forces over wider strips would rule out polar stresses. These arguments are outlined with statistics and tensors by Vardoulakis and Georgopoulos (2005). They show that polar stresses may be considered as internal state variables in strongly sheared zones so that these cannot be thinner than a few grains. The grain contact forces in such zones of sufficient length can be represented by average force densities which include polar stress components. The spatial fluctuation of contact forces is higher in polar zones than outside, this force-roughness can enhance the crushing of grains (Buchholtz and Pöschel 1997).

The response of a granular strip to *reversals* may only be touched as simulations with them have not yet been made, let alone thin layer shear tests. The initial state may be non-uniform with state quantities as shown in Fig. 8.2.3. With a first reversal under constant pressure all shear and polar stress components are reduced and the dilated shear band gets denser. Continued isobaric shearing in the new direction would lead to shear and polar stress components of opposite sign and nearly the same amount as at the onset (except for a minor difference of void ratio). Isobaric cyclic shearing with moderate amplitude, so that overcritical stress obliquities ($\varphi_w > \varphi_{cs}$ provided) are not

reached, would lead to a further densification and to alternating shear and polar stress components along the rough plates. A shear localization would no more occur in the middle. With small isobaric shear cycles the skeleton would attain the lower bound void ratio e_d (Sect. 2.2), whereas the deviatoric and the polar stress components would almost disappear. This is shown in detail by Niemunis et al. (2007).

The indicated asymptotic response to shear reversals could principally be captured by *extended state cycles*. If the pressure or strip height is constant, respectively, the height or pressure oscillates with twice the frequency of shearing (cf. Sects. 2.10 and 4.3). The polar stress components alternate similarly as the shear stress components, and their averages over one shear cycle are nearly constant if the pressure is constant. Big amplitudes lead to an alternating shear localization which could be simulated by p-hyp. With smaller amplitudes, so that overcritical stress obliquities are never reached, the shearing is no more localized and polar stresses are swept out except for a slight oscillation along rough boundaries.

Ratcheting can be similarly judged. A shear band with polar stresses arises repeatedly if overcritical stress ratios are attained. Otherwise polar stresses are swept out except for one-sided cycles along rough boundaries. Thus there is no need for hypoplastic relations with polar terms plus hidden state variables in the sense of Sect. 4.3. The uneven spatial distribution of internal forces can be captured either by p-hyp or by hyp- δ as polar quantities are either dominant or negligible. There is apparently no need of a combination (p-hyp- δ) in applications. It will be a long way until critical phenomena are better understood so that the origin of force-roughness can be explained (Sect. 16.3). Boundary conditions of psammoid bodies have to be simplified anyway (Sects. 10.2 and 10.3).

Consider now an endless granular strip with *pore water*, again so thin that its weight may be neglected. Apart from the somewhat lower hardness of wet grains a constant pore pressure p_w raises only the total pressure via $p = p_s + p_w$. Deviatoric and polar stress components occur only in the skeleton, thus the relations outlined above can be written with generalized skeleton stress components (subscript s). For rapid shearing p_w could deviate from the average if the velocity of shearing exceeds the bound by (6.2.11). The ratio $p_{so}/\gamma_w d$ therein should be replaced by $p_s/\gamma_w d_s \approx 0.1 p_s/\gamma_w d_g$ with the shear band thickness $d_s \approx 10 d_g$. With $p_s \geq 10$ kPa and $d_g \leq 10^{-3}$ m this leads to the bound $v_s < \text{ca.} 10 k_f$.

Gradients of pore pressure $\partial p_w/\partial x_2$ can thus at most influence the shear localization of fine-grained skeletons as their permeability k_f can be lower than 10^{-4} ms^{-1} . Their dilation is impeded as p_s rises, thus deviatoric and polar stress components increase until an extended state limit without further dilation is attained. Grains are more easily crushed in a shear band with higher contact forces due to polar effects (imagine how easily a grain is damaged by rotating it past a hard surface). p_w can attain zero so that the pore water cavitates (Sect. 6.2), after that the dilation is no more impeded.

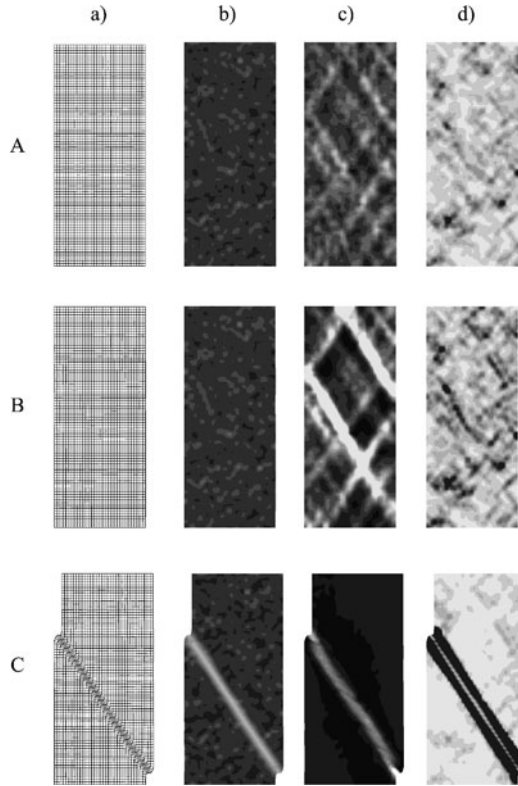


Fig. 8.2.7. Evolution in a biaxial test simulated with p-hyp (Gudehus and Nübel 2004): shape (a), void ratios (b), dilation (c) and couple stress (d) by small (**A**), moderate (**B**) and big shortening (**C**)

Shear localizations in *biaxial tests* can arise in many variants which depend on the boundary conditions. p-hyp simulations (Gudehus and Nübel 2004) for a slender sample with lateral pressure and shortening via smooth plates are shown in Fig. 8.2.7. The weight is neglected. At the onset the skeleton has an isotropic pressure and a low relative void ratio r_e with a minute spatial fluctuation. After a small shortening (A) a pattern arises in the plot of volumetric strain (c). With further shortening (B) the dilation dominates in some bands (c), and the plot of couple stress indicates the same pattern (d). Continued shortening (C) leads to a shear band (a) with dominant dilation (b, c) and two bands of couple stress (d).

The evolution of some state variables with shortening ε_2 for the same case is plotted in Fig. 8.2.8. The overall deviatoric stress $\sigma_1 - \sigma_2$ (a) goes through a peak (A, B) and tends to an asymptote (C). The void ratio e (b) starts to grow near the peak and tends to the critical value e_c in the shear band (b). The rotation ω (c) arises after the peak and increases mainly in the shear band. The spatial variance s_e of e (d) grows mainly in the shear band. The

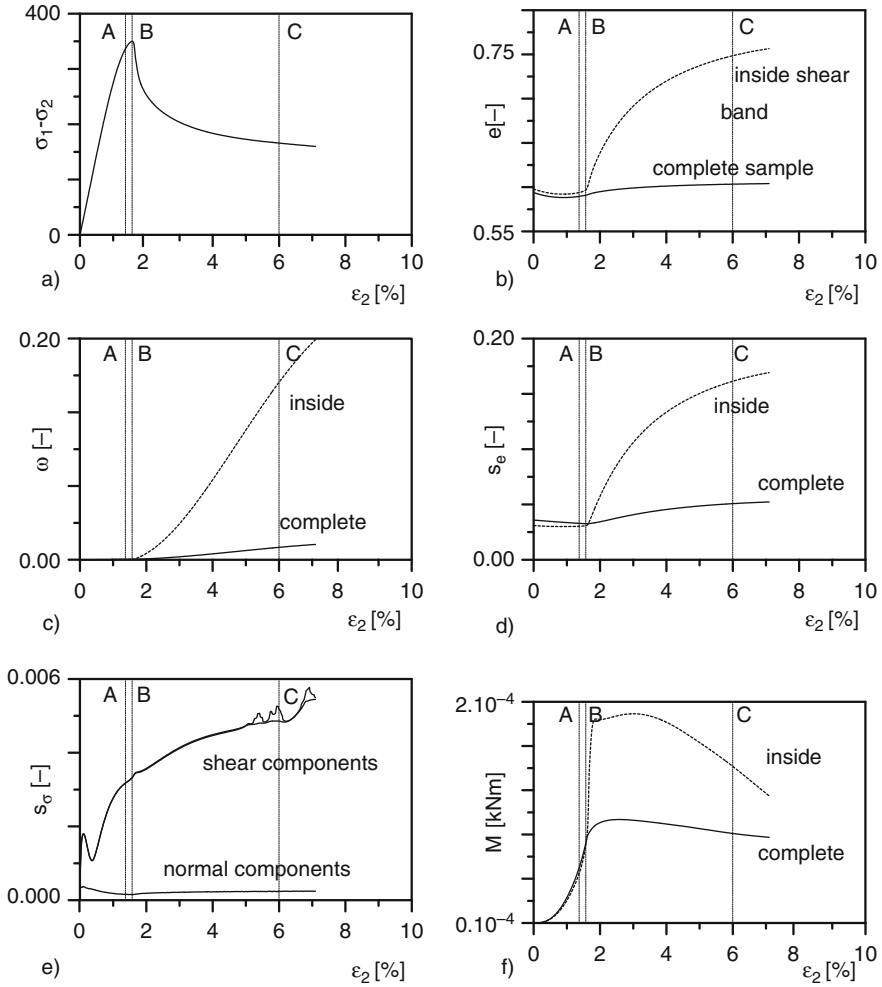


Fig. 8.2.8. Evolutions with shortening by Fig. 8.2.7: stress deviator (a), void ratios (b), rotations (c), fluctuations of void ratio (d) and stress (e), couple stresses (f)

spatial variance s_σ (a measure of force-roughness) of stress (e) remains low for the normal components and rises for the shear components. The amount M of couple stress (f) grows up to the $(\sigma_1 - \sigma_2)$ -peak and gets smaller beyond it, more so inside the shear band.

Single shear bands as in Fig. 8.2.7C have often been observed in biaxial tests since Vardoulakis et al. (1978). In this paper their inclination is estimated as a mode of bifurcation from biaxial shortening into dilated shearing. The grain-size dependent band width was first estimated with elastoplastic relations including polar terms (p-el-p) by Mühlhaus and Vardoulakis (1987). The more precise estimate by Gudehus and Nübel (2004) is still inevitably

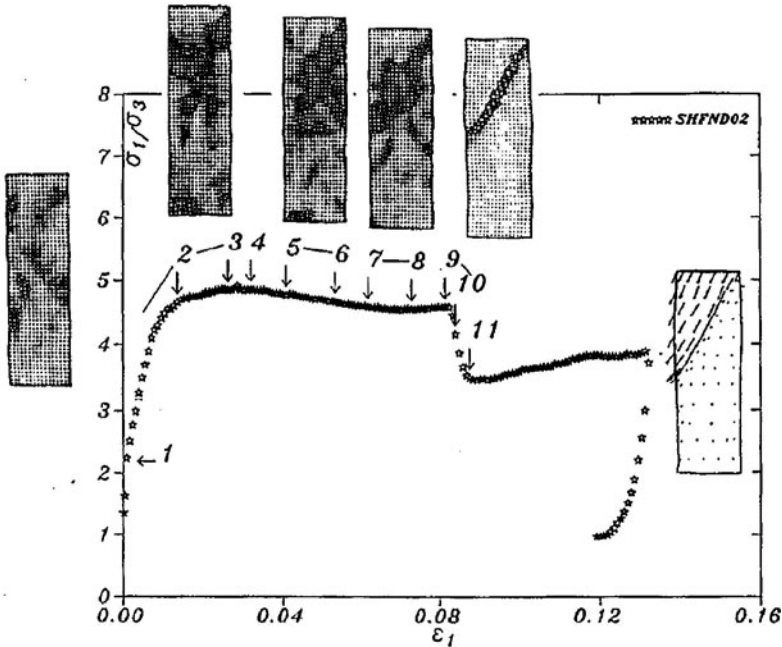


Fig. 8.2.9. Observed shear localization in a biaxial test with sand (Mokni and Desrues 1989)

fuzzy, but in fair agreement with observations (cf. Fig. 8.2.5). A single shear band gets visible near the peak of $\sigma_1 - \sigma_2$. Mokni and Desrues (1998) observed an evolution of patterns nearly as in Fig. 8.2.7 by means of X-ray tomography, Fig. 8.2.9. Radiographs by Oda and Kazama (1998) exhibit a dilation up to the critical void ratio with substantial fluctuations in shear bands.

Gudehus and Nübel (2004) report also on biaxial tests with smooth nested plates, Fig. 8.2.10 (cf. Fig. 2.7.8b). A rectangular skeleton of corundum grains was deformed with constant pressure and observed via a top glass plate. Volume changes obtained by particle image velocimetry (PIV) exhibit a pattern of shear bands (a), this is fairly well reproduced by a simulation with p-hyp (b). After further stretching three dominating shear bands are revealed by PIV, similar but thinner ones are reproduced with p-hyp. The reflection of shear bands with compensation of polar effects at smooth boundaries (cf. Fig. 8.1.5b) was not perfect in the experiment as the plates were not quite smooth.

The experience that biaxial test results can be fairly well matched by p-hyp is not a complete validation as with a sheared granular strip polar quantities can hardly be observed and the width of shear bands remains fuzzy. The following interpretation is referred to biaxial RSEs without and with polar quantities. It appears that for isobaric stretching of dense skeletons arising shear band patterns are rather uniform prior to the peak (Figs. 8.2.7 and

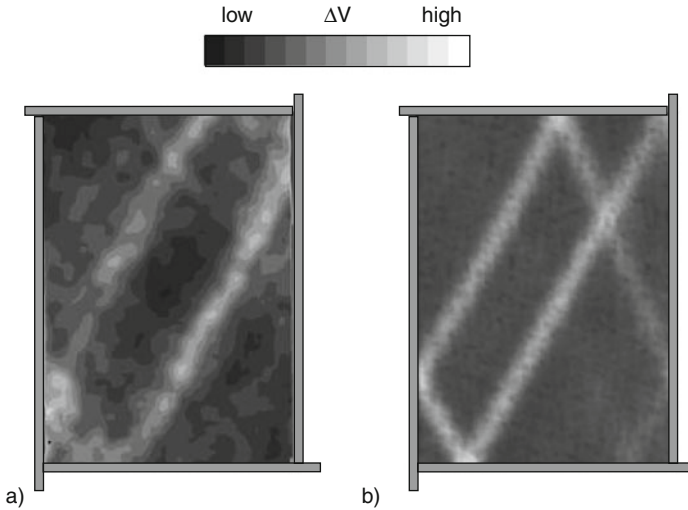


Fig. 8.2.10. Volume changes observed in a biaxial setup (a) and simulated with p-hyp (b), Gudehus and Nübel (2004)

8.2.9). Beyond it shear bands with polar effects lead to a stronger loss of uniformity which is partly chaotic and depends on the kind of boundaries.

There are always spatial fluctuations of the void ratio, more with higher relative void ratio r_e (Shahinpoor 1981), and of intergranular forces which are scarcely visible along the RSE-boundaries. It appears that polar quantities grow spontaneously when the stress obliquity gets overcritical. The shearing is thus favoured in two directions and enhanced while the obliquity rises with dilation and polarization. This positive feedback is first as irregular as the spatial fluctuation, then few shear bands win in the competition. This leads to an offset at boundaries with pressure control and to a reflection at smooth boundaries with displacement control. With a deformable boundary an extended critical state is reached in shear bands nearly as in an infinite strip except for the offsets. With nested rigid plates a succession of overlapping shear bands can lead to an overall critical state without average polar stresses, but with fractal spatial fluctuations.

Two kinds of RSE may thus be justified for predicting evolutions of grain skeletons. For lower than critical stress obliquities (invariants in Sect. 2.11) shear localization and polar quantities may be neglected. Remnants of them are captured by spatial averages, element tests with stress and/or displacement control suffice as long as the uniformity is not impaired by diffuse bifurcations (e.g. bulging) or boundary defects (e.g. wrinkles or gaps). The spatial fluctuation of internal forces, which is particularly exhibited by the response to reversals, can be captured by a hidden force-roughness (Sect. 4.3). The same fluctuation cannot be achieved along sample boundaries, but this defect of element tests can be kept minor. The spectrum of fluctuation

wavelengths seems to be rather self-similar (fractal), thus a material length is not needed.

For higher than critical stress obliquities the desired uniformity of RSEs gets lost by shear localizations with polar quantities which can no more be averaged out beyond a peak. This spontaneous loss of uniformity can lead to a deterministic chaos. The interactions of grains in a psammoid RSE are not conservative, shear localizations require continued energy input due to dissipation. Beyond a peak state with constant mean pressure p_s the rate of dissipation per unit rate of stretching gets smaller by definition, but does not vanish as in a thermodynamic system. Therefore our strange attractor is driven, and a polarized non-uniform skeleton can be frozen by fixing the boundaries. A collapse would occur with dead loads, but critical phenomena could then at best be observed at the onset. The generic term ‘strange attractor’ is used to denote representations of such critical phenomena, mainly *more geometrico* and without claim for mathematical rigour.

The spontaneous growth of polar stresses at critical points may be called a *granular phase transition*. This is necessarily localized and grain-size dependent so that a previous uniformity without polar quantities gets lost. It can be captured by extended RSEs with polar terms and sizes of about two grains. This is at best feasible for the back-analysis of model tests with lengths of a few hundred grain diameters (Sects. 13.1 and 13.3). Even then the numerics get hard, and boundary conditions with polar terms can as yet hardly be specified in general. With smaller grains and/or bigger body lengths polar effects have to be substituted by interfaces (Sects. 10.2 and 10.3) or to be neglected altogether.

For sake of completeness pore water and non-biaxial RSEs may at least be mentioned. As outlined above for a sheared strip p_w is taken into account by $p = p_s + p_w$. Finno et al. (1997) observed similar patterns as in Fig. 8.2.7 in undrained biaxial tests with rather loose saturated sand. At the onset e was almost critical for the initial p_s , say $r_e \approx 0.9$, but with isochoric stretching p_s decreased (cf. Sect. 2.5) so that r_e got smaller. This suffices for a localized dilation with contraction nearby so that the total volume is constant. Shear bands in triaxial (Sect. 14.1), cuboidal (e.g. Chu et al. 1996) and torsional tests (Sect. 14.6) impair the uniformity, simulations with p-hyp would be expensive, but RSEs may be judged as outlined above.

To *sum up*, deformed psammoid RSEs get non-uniform by shear localization if overcritical stress obliquities are attained, this can principally be captured by means of polar quantities. A grain size and a further constant are needed in extended hypoplastic relations (p-hyp). Simulations of lab experiments with p-hyp are realistic, but the physical interpretation is difficult. Polar stresses are swept out by reversals in the subcritical regime so that the force-roughness may be captured by a hidden state variable without polar terms. If an RSE is subdivided by shear localizations extended RSEs are needed for simulations. This is not feasible with too many of such RSEs, then substitute interface elements or remeshing will be needed.

8.3 Shear localization in peloids

Observed shear localizations in peloids can be similar as in psammoids, but closer inspections reveal differences. Pore pressure gradients are rarely negligible, argotropy plays a role and phase transitions can also occur in the pore water. Because of this complexity the following outline is rather qualitative, validated models are not yet at hand.

Consider first a *thin endless strip* which is sheared so slowly via filter plates that the pore pressure p_w is constant. Balthasar et al. (2006) approached such conditions with highly plastic clay layers of ca. 3 mm thickness after consolidation under up to 14 MPa (cf. Sect. 3.8). The normal skeleton pressure $-T_{s22}$ ($-\sigma_{22}$ in Fig. 8.2.1, more precisely speaking its spatial average $-\bar{T}_{s22}$) was kept constant, and the top shearing velocity v_{sh} was kept below the threshold by (6.2.12) so that changes of p_w were negligible. The shearing resistance T_{s12} for constant v_{sh} (properly \bar{T}_{s12}) got stationary beyond a slight peak and attained the same value after changing v_{sh} (Fig. 8.3.1a). The stationary resistance was proportional to the solid partial pressure and independent of v_{sh} (b), this rate-independence is part of Coulomb's friction law (Persson 2000b).

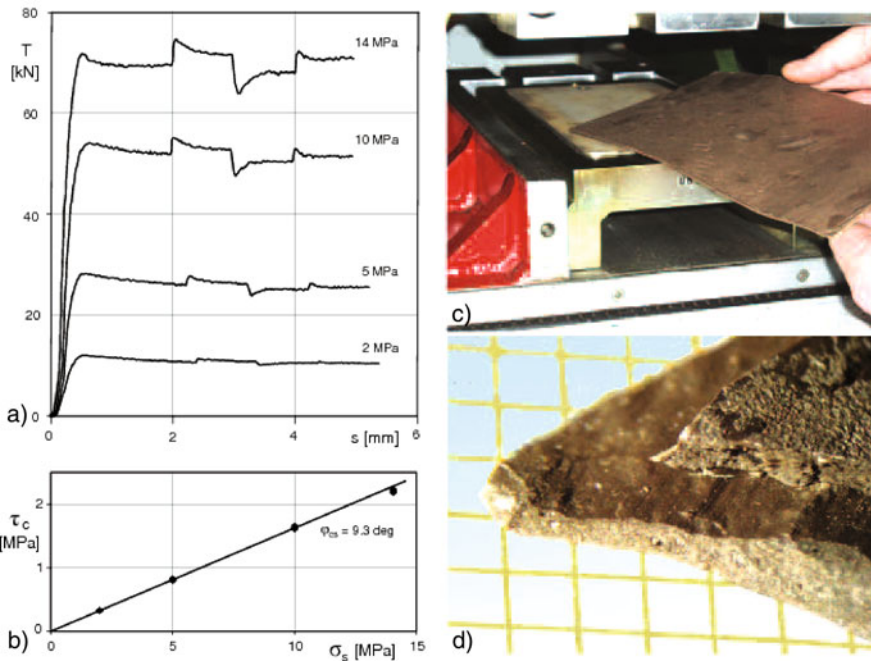


Fig. 8.3.1. Shearing resistance of a thin clay layer (Balthasar et al. 2006) versus shearing (a), stationary resistance versus pressure (b), placement of a thin layer (c), broken sample after a test (d)

The sheet-like samples were visibly uniform after consolidation, during the installation they were kept together by suction without capillary entry (Fig. 8.3.1c). After shearing and breaking off a part they exhibited a band of aligned clay particles (d). This kind of slip surface is known as *slickenside*, as observed in situ it is a wavy band of ca. 10^{-5} m thickness. Its exposition indicates a lower suction $p_a - p_w$ than in the broken parts above and below. Grooves and weals due to convected grains appear in the direction of shearing, aligned layer silicates are indicated by optical reflection. The fabric may be changed by the exposition, but such snapshots prove that shearing can be localized to thin bands with oriented particles.

The argotropy visible in Fig. 8.3.1a is reproduced by v-hyp and is not at variance with the non-argotropic friction of Fig. 8.3.1b (Sect. 3.8). The particles get harder or softer by an increase or decrease, respectively, of stretching D like a pore-free viscoplastic solid (Sect. 3.1). For a given skeleton pressure p_s , and with $T_{s11} = T_{s22} = T_{s33} = -p_s$ in case of stationary shearing (Sect. 3.8), the critical void ratio e_c is higher with a bigger D as then the solid hardness h_s is higher (Sect. 3.2). After a jump of D to a higher or lower value the skeleton dilates or contracts, respectively, until the new higher or lower e_c is reached. Apart from the first one the peaks in Fig. 8.3.1a are thus of argotropic origin.

Following the argument in Sects. 8.1 and 8.2 any reduction of resistance with further shearing, i.e. a peak in a τ vs. γ plot, leads to a shear localization which is confined by polar effects. Alongside with this bifurcation from uniform into localized shearing with rotation and curvature the amount of stretching D (including polar terms) increases even if the driving velocity v_{sh} is constant. The reduction of shearing resistance after such a bifurcation can thus be compensated more or less by a gain of viscous resistance. Therefore peaks as in Fig. 8.3.1a are not sufficient for a shear localization. The repeatedly attained stationary response may thus be related with *extended argotropic critical states*. According to (8.2.2) the shearing resistance $|\sigma_{s12}/p_s|$ should be smaller than without polar stresses, but with given p_s this reduction is apparently compensated by the resistance to the mutual twisting of particles. As with psammoids (Sect. 8.2) the critical friction angle φ_{cs} is thus not changed by a localized polarization.

One could extend visco-hypoplastic relations by polar terms (*vp-hyp*), but attempts with validation and identification lead to a dilemma. Following Sect. 3.4 vp-hyp relations could be written with a p_e/p_s -dependent viscosity factor f_v so that extended argotropic state limits are obtained, and also creep and relaxation with polar terms. A back-analysis of isobaric thin layer shear tests with vp-hyp, however, cannot be conclusive. Without polar terms (as in Sect. 3.8) one would obtain a critical friction angle φ_{cs} and a critical void ratio e_c for the given p_s , but the assumed uniformity gets lost by shearing. As outlined above the onset of polarization need not be indicated by a peak, and as in Sect. 8.2 a polar parameter a_c for extended critical states can at best be estimated by matching.

Moreover, a particle size and a shear band width cannot be identified as distinctly as for psammoids. Aggregates of clay particles are rather fuzzy, thus an objective size d_g can hardly be defined. For the same reason a band width t_s cannot easily be determined after a test (Fig. 8.3.1d). One can at best recognize a band with a higher void ratio from a lower capillary entry pressure (Sect. 6.3), but could hardly determine e_c therein. The visibly preferred orientation of flat clay particles in a shear band is a clear sign of polarization. Similarly as with Fig. 8.2.6 polar stresses could be interpreted as spatial averages of contact forces over narrow strips. These may be imagined in the direction of shearing, but the stochastic lateral waviness of shear bands (Fig. 8.3.1d) would require three-dimensional averages. One has to concede therefore that even an observed stationary isobaric shearing could as yet only principally be captured by argotropic state limits with polar terms.

Consider now *dilatant state limits* of a sheared peloid strip with constant pore pressure p_w (although they can hardly be attained in thin layer test as will be discussed further below). For them the stress obliquity and the ratios of polar stress and p_s are overcritical. Taking over (8.2.2), this may be expressed by

$$(\sigma_{12}/p_s \tan \varphi_{cs})^2 + (m_2/p_s d_g c_c)^2 = K \quad (8.3.1)$$

with a parameter $K > 1$, or by an extended formula with further polar and non-polar skeleton stress components. K depends on the extended stretching direction which implies a dilation ratio. p_s depends on the instantaneous void ratio and the amount D of stretching, it is thus argotropic as the solid particles. Such extended state limits could be produced as attractors of vp-hyp relations, formally as without polar terms (Sect. 3.4). A continuation with the same stretching would lead to a decay of the skeleton.

Isobaric shearing (i.e. $T_{s22} = \text{const}$ or $p_s \approx \text{const}$) with constant boundary velocity v_{sh} would lead to dilatant state limits if the initial void ratio is lower than the critical one for the given pressure, i.e. for $e_o < e_c(p_s)$. Without polar terms this can be judged by means of a threshold of the initial consolidation ratio p_e/p_s (Sect. 3.4), say $p_{eo}/p_s \geq \kappa_o$ with κ_o around ca. 5. The argotropy is thus not captured, with it e_c grows with bigger D as without polar quantities (Sect. 3.2). As with psammoids a peak due to dilation, which comes close to a dilatant state limit, leads to a shear localization as the softening is thus enhanced. This localization is confined by the polar resistance to increasing rotation and curvature, but also by the increasing viscous resistance as D grows by a localization with unchanged v_{sh} .

Simulations with vp-hyp, $e_o < e_c$, $v_{sh} = \text{const}$ and $p_s \approx \text{const}$ could produce similar plots as in Figs. 8.2.3 and 8.2.4 for psammoids, but now these would be v_{sh} -dependent due to argotropy. The void ratio would increase in the shear band and would hardly change outside (where a rather uniform dilation is nearly compensated by an initial contraction). Similarly as in Fig. 8.2.5 the calculated ratio t_s/d_g of shear band width t_s and particle size d_g would increase with the relative void ratio r_e . This can at best be a crude estimate

as the limit void ratios e_c and e_d needed for r_e are not precisely known, and as a representative particle size d_g has to be chosen at will. The dilemma with validation and identification is less evitable therefore than with psam-moids as outlined further above. And there is more frustration due to the pore water!

Depending on the initial e/e_c (or p_e/p_s or r_e instead) *pore pressure gradients* $\partial p_w/\partial x_2$ can impede or enhance a shear localization, Fig. 8.3.2. For getting substantial $\partial p_w/\partial x_2$ the rough boundaries of our saturated peloid strip can be closed hydraulically (undrained), or sheared so rapidly past each other that a driven diffusion can hardly occur in the pore water (Sects. 6.2 and 11.1). If the skeleton would contract by isobaric shearing, i.e. for $e > e_c$ initially, p_w rises in a sheared zone so that it has outwards gradients (a). If the boundary shearing is continued and/or slowed down the driven diffusion produces a spreading of pore water by densification with a reduction of p_w and $|\partial p_w/\partial x_2|$. A shear localization, which may start with unchanged e as explained further above, can thus be compensated by spreading.

Except for boundary zones with polar constraint there is thus no need to consider localized polarizations if the void ratio is higher than critical for the initial skeleton pressure ($e > e_c(p_{so})$). If the shearing produces spreading by pore water diffusion contractant state limits can be attained for which polar terms are swept out. Otherwise polar quantities can arise in narrow bands with unchanged void ratio and overall shearing resistance, but such localizations are not felt along the boundaries so that polar terms may again be neglected.

If the skeleton would dilate by isobaric shearing, i.e. for a low enough $e < e_c$ initially, the localization is enhanced by gradients of p_w towards the band, Fig. 8.3.2b. The diffusion gets faster if the band gets narrower (Sect. 11.1), but with the increasing local stretching D the skeleton pressure p_s can grow substantially by the viscous resistance to shearing. Without drainage, cavitation and change of pore water density the strip height is constant, but the pore water can get redistributed by localized dilation and contraction nearby. Then the localization is confined by polar and viscous effects. This coupling of skeleton and pore water could principally be taken into account, but it impedes simulations with vp-hyp which could as yet hardly be validated anyway.

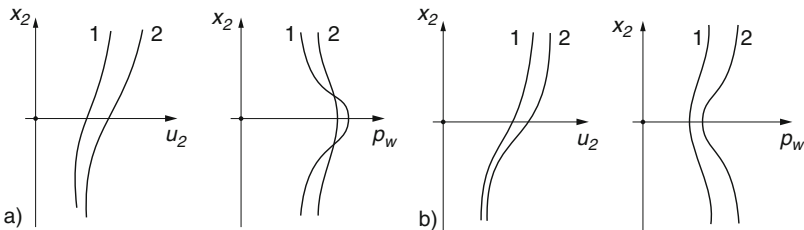


Fig. 8.3.2. Localized shearing with diffusion of pore water: profiles of shearing and pore pressure (a) with contracting skeleton; same with dilating skeleton (b)

Phase transitions of pore water may at least be touched although they cannot yet be quantified. With a given total pressure p the suction $p_a - p_w = p_a - p + p_s$ by shearing can lead to cavitation (Sects. 6.3 and 8.4). Thereafter a dilatant shearing can proceed without seepage, but additional polar effects and particle degradation occur with cracks (Sect. 7.3). The denser resting pore water in narrow slits (Sect. 6.1) is dilated and thinned by shearing (Sect. 3.8). A skeleton with $e < e_c$ for the initial pressure can thus be dilated by shearing without seepage until the pore water attains its ordinary density. Simulations with vp-hyp and coupling of skeleton and pore water would thus get more intricate, let alone validation and identification.

Creep can also play a role for a saturated endless peloid strip. With draining boundaries and given boundary stresses T_{s22} and T_{s12} the stability of creep depends on the obliquity $|T_{s12}/T_{s22}|$ as without polar terms (Sect. 3.8). The creep rate depends on the initial consolidation ratio p_{e0}/p_s and on the diffusion of pore water (Sect. 11.1). With subcritical obliquities, i.e. $|T_{s12}/T_{s22}| < \tan \varphi_{cs}$, polar stresses are swept out by stabilizing creep and get negligible therefore. In critical cases with $|T_{s12}/T_{s22}| = \tan \varphi_{cs}$ the shearing gets stationary and localized, i.e. extended argotropic state limits arise. The asymptotic creep velocity v_{sh} is determined by the skeleton pressure after diffusion, i.e. $p_s = T_{s22}$, and the void ratio or its equivalent p_e in the shear band, so v_{sh} depends on the initial p_e/p_s and the parameters that control the diffusion of pore water.

With overcritical obliquities, i.e. $|T_{s12}/T_{s22}| > \tan \varphi_{cs}$, the creep for constant T_{s12} and T_{s22} with boundary drainage leads to a *delayed collapse* with localization. The dilation is enhanced by cavitation and by stripping of bound pore water, whereas the diffusion cannot keep pace in case of rapid shearing. Thus the attained high creep velocity is determined by the void ratio in the shear band at collapse without further diffusion. The delay time increases with a higher initial p_e/p_s and is reduced by cavitation and thinning of bound pore water, so it is hardly predictable. Without boundary drainage and with constant $T_{s12}(= T_{12})$ the creep tends to stationary localized shearing as long as the pore water does not cavitate. The asymptotic creep velocity is principally determined by T_{s12} and the initial e or p , but can as yet hardly be quantified with localized polarisation.

Relaxation occurs in a fixed peloid strip similarly as in a solid (Sect. 8.1), but now pyknotropy, barotropy and pore water play a role. Deviatoric and polar stresses dwindle qualitatively as in Fig. 8.1.3c, the rates are roughly proportional to $(p_s/p_e)^{1/I_v}$ as without polar quantities. With $1/I_v > \text{ca. } 20$ even minor changes of p_s/p_e matter a lot. As outlined in Sect. 3.4 p_s is reduced by relaxation, and p_e increases for constant e by the reduction of stress obliquity. Therefore the relaxation including polar stresses is slowed down far more than in a pore-free solid. Pore pressure gradients fade away by diffusion, so e and p_s get more uniform with fixed boundaries. A minor part of the pore water, particularly in shear bands, returns to a denser state in narrow slits (Sect. 6.1). This does not influence the average p_s of the fixed skeleton, the

average p_w would only increase without boundary drainage, but the diffusion of pore water is enhanced by this kind of adsorption.

Waiting intervals matter more with longer duration because of relaxation and creep. This is also the case with *reversals* which may now be addressed for a saturated peloid strip. As with psammoids (Sect. 8.2) polar stresses are swept out (except for boundary zones) by alternating deformations with small to moderate amplitudes so that critical stress obliquities are not attained. Then polar effects may be neglected, and many reversals produce a kind of relaxation or annealing. With big amplitudes, so that stress obliquities get repeatedly overcritical, reversals produce repeated polarizations and can lead to a deterministic chaos. The response to strong cyclic shearing via the top plate can lead asymptotically to average state cycles, but the strip cannot get uniform. Waiting intervals at reversals with fixed boundaries change the response by relaxation. With constant time averages of boundary stresses T_{s12} and T_{s22} the creep is enhanced by reversals which can be in-plane or anti-plane. With subcritical $|T_{s12}/T_{s22}|$ and moderate amplitudes polar effects are or get negligible, otherwise a delayed collapse is enhanced (Balthasar et al. 2006).

Leaving aside gas inclusions for brevity, possible *validations* of models for sheared peloid strips may now be discussed. Shear box tests with rigid walls attached to mutually sheared rough plates cannot produce the required uniformity in the direction of shearing. Hvorslev (1937) showed with initially vertical markers that a forced lateral offset is not continued in the interior (Fig. 3.8.1). Morgenstern and Tchalenko (1967) observed successions of shear band patterns in such devices, with little symmetry and without asymptotic response. Clays have rarely been tested in a so-called simple shear apparatus with tilting lateral walls (Fig. 2.9.7a), but the non-uniformity known with sand (Sect. 2.9) refutes the assumption of uniformity in the direction of shearing.

Samples in ring shear devices (e.g. Fig. 2.9.9a) are endless strips, but the radial uniformity is debatable. Hvorslev (1937) found with markers (Fig. 3.8.2) that tangential displacements were differently non-uniform with differently movable lateral rings although these were smooth. It appears that a succession of shear bands arose in his tests, and that his shearing was too fast for getting uniform pore pressures with free boundary drainage. Based on improved slow drained ring shear tests and comparable field experience, Skempton (1985) proposed that overconsolidated clays are first locally dilated by shearing up to a critical state, and then further softened up to a residual resistance due to the alignment of flat particles. This idea is supported by observed slickensides and may suffice for an interface model (Sects. 11.2 and 10.3), but is at variance with the concept of localized polarization and diffusion proposed further above.

Goldscheider and Böisinger (1989) sheared inclined thin layers, which were already inside or cut into cylindrical clay samples, in triaxial tests. Equally consolidated samples were then sheared along the cuts (Fig. 8.3.3a) with different confining pressures and a so low velocity ($v_s = 3 \cdot 10^{-7} \text{ ms}^{-1}$) that excess pore pressures were presumably negligible. The shearing resistance got stationary and depended on the normal pressure σ on the cut so that

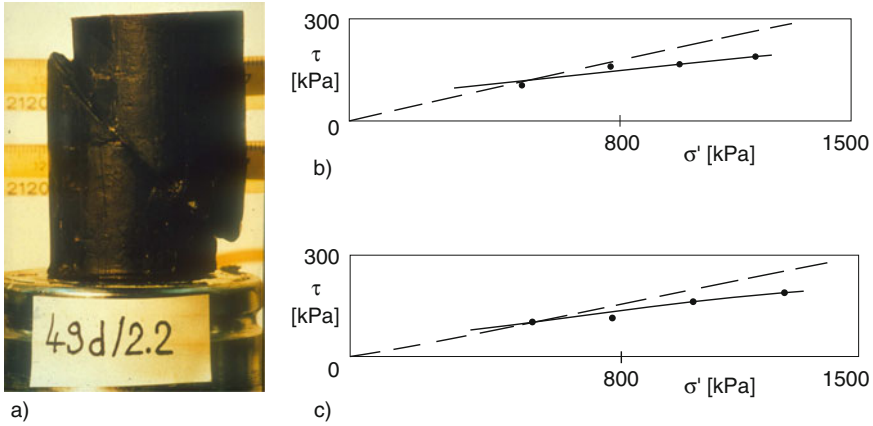


Fig. 8.3.3. Sample with a pre-existing shear band after a triaxial test (a), shearing resistance of a cut (b) and a natural shear band (c); Goldscheider and Bösinger (1989)

a cohesion c and a friction angle φ could be identified (b). Similar values were obtained with natural slickensides of the same orientation (c), these were confirmed by the back-analysis of slips in situ. The shearing resistance calculated with the friction angle 11° , determined for the same clay in thin layer tests (Balthasar et al. 2006), is lower for low σ and higher otherwise in the tested range (dashed). This shows that an under- or overpressure of pore water occurred in the shear band which could not be observed at the top and bottom plates (and certainly not in situ).

Thin layer shear tests can provide further insight. The free lateral boundaries with skeleton pressure by suction have little influence on the major interior part as length and breadth exceed the height by far ($a/b/h \approx 250/130/2$). Thus averages over the ground area are legitimate, and only changes of them along the normal and with time have to be considered. The results in Fig. 8.3.1a and b show that stationary states can be achieved by isobaric shearing with rate-independent component ratios, and Fig. 8.3.1d proves a shear localization in the middle of the thin layer. The polarized fabric in a narrow band (slickenside) is evident, a higher void ratio than nearby can be concluded from cracks due to the lower capillary entry pressure. The argotropy is exhibited by the transitory response after changes of shearing velocity v_{sh} , it is the same as without localization. This suggests higher stationary void ratios for faster shearing, but these could not yet be observed.

In the middle of a representative average shear band the skeleton stress tensor is asymmetric ($T_{12} \neq T_{21}$) and the couple stress vanishes ($m_2 = 0$), cf. Figs. 8.1.1 and 8.2.3. At a state limit the skeleton state is determined by the stress state, the ratios of stress and stretching rate components are uniquely related, with argotropy the limit void ratio is determined by skeleton stress

and an argotropic solid hardness (Sect. 3.2). This holds in particular for stationary states (called critical) and makes sense also with polar effects. The skew-symmetric stress tensor in the middle of the shear band represents its orientation and void ratio, it is related with isochoric shearing plus Cosserat rotation with the same orientation. Off the mid-plane couple stress and curvature occur in the band (Figs. 8.1.1 and 8.2.2) and determine its width, this requires a material length. The width increases with a higher relative void ratio in the vicinity (Fig. 8.2.4), and is argotropic as the implied limit void ratio.

More thin layer tests and their simulations with vp-hyp will be needed for a quantification with the following main points. $T_{s11} = T_{s22} = T_{s33} = -p_s$ may be assumed for extended critical states as shown by Bauer (2000) without polar terms, for convenience and because T_{s11} and T_{s22} cannot be measured. It appears that a localization can occur without a peak of T_{s12} as the reduction of T_{s12} by polarization is compensated by the viscous increase from localization with constant v_{sh} . This assumption could be built into an extended limit stress condition with tentative ratios T_{s12}/T_{s21} and band widths t_s , and could be checked by tests with constant p_s and v_{sh} but slightly different initial void ratios (e.g. through waiting times). The couple stress m_2 (M in Fig. 8.1.1) cannot be observed, but the ratio $m_2/T_{s12}d_g$ could be chosen so that observed band widths are reproduced. According to (8.3.1) with $K = 1$ this would enable a matching of the product $d_g c_c$ of two polar parameters. As a particle size d_g cannot be identified microscopically it could be matched by adapting observed t_s (Fig. 8.3.1d) for different initial e with calculated ones as in Fig. 8.2.4.

As mentioned already further above such a quantification cannot lead to a complete and unique validation. The unchanged alignment with continued shearing in the band is compatible with an increasing Cosserat rotation ω_c . Thickness and void ratio of a shear band cannot be determined precisely after a test because of spatial fluctuations and changes by preparation. Mean values of T_{s12} and T_{s22} over the whole sample area are lower than interior values, but ratio and argotropic changes of both are hardly influenced by the free rim. Within the assumptions proposed above the simplest representations of vp-hyp should be chosen so that two parameters d_g and c_c suffice for matching observed t_s . The crucial hypothesis that e_c is determined by p_s and by the amount of stretching D , likewise without or with polar effects, could be checked by monitoring e during tests, but this is still out of reach. The proposed matching of t_s with different initial e will not enable a precise discrimination. Nevertheless such efforts will deepen the physical understanding and can help to justify and delimit non-polar approaches for common use.

Thin layer tests with insufficient drainage will also be instructive, but less quantitative as pore pressures p_w cannot be monitored in shear bands. Back-analyses with vp-hyp and seepage as proposed further above could at best help to delimit the cases with free or negligible drainage, and to understand the diffusion of pore water in and near shear bands. This could again delimit

non-polar approaches and would clarify the role of localizations with p_w -gradients in usual tests. For instance, the softening in Hvorslev's (1937) ring shear tests could thus be quantified by means of a gradually reduced suction.

For the time being thin layer tests in the overcritical regime can produce merely qualitative validations. A stronger dilation in case of higher initial consolidation ratios can hardly be observed during tests, and after them void ratios in bands are impaired by swelling and cracking. Localized suction and cavitation cannot be observed during a test. Skempton's (1985) opinion that first critical states are reached in shear bands with dilation, and that thereafter the shearing resistance decreases further by alignment, is at variance with the concept proposed here. One could open and cut the thin layer just after a peak and could observe a localized alignment which could hardly be explained without polarization. The subsequent drop of shearing resistance can be explained through a drop of suction by the diffusion of pore water. Unfortunately this can hardly be observed during thin layer tests, and their back-analysis with changes of permeability (and even of water density) is inevitably imprecise.

Biaxial tests with clay samples can produce similar shear bands as with sand (Sect. 8.2), but such evolutions are more complex because of skeleton viscosity and pore water diffusion. Kolymbas (1978) shortened Kaolin prisms with vertical dye markers, which were confined by a pair of perspex plates and by silicone oil pressure at two free surfaces, via two smooth plates. This led to a dislocation along one band (Fig. 8.3.4, left) or to several intersecting bands (right). This localization was not accompanied by a peak of deviator stress versus shortening. The bands were about 10^{-5} m thick, the further shortening of sample height occurred mainly by dislocation along them.

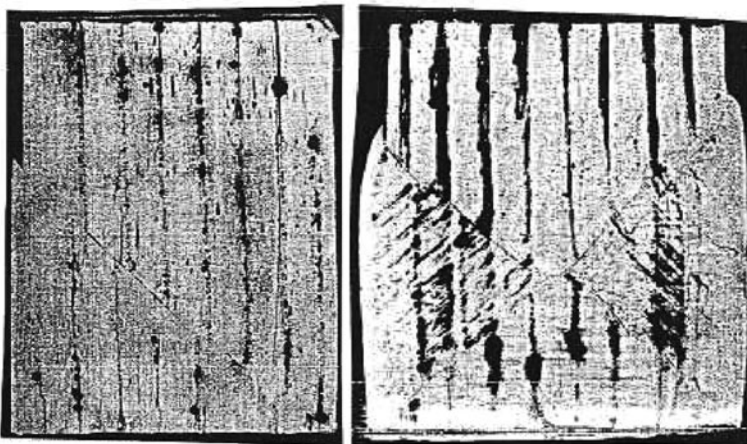


Fig. 8.3.4. Shear bands in biaxial tests with clay (Kolymbas 1978)

Such shear bands could principally be reproduced by vp-hyp with pore water diffusion as outlined above with endless strips. Crossing and reflected bands could be captured principally as for psammoids (Fig. 8.2.10), but because of their low width the available computer capacity would only suffice with remeshing. The numerical problems increase by taking into account the diffusion of pore water, particularly along narrow bands and with variable permeability.

Kuntsche (1982) observed shear bands in Kaolin samples after biaxial tests with nested smooth plates as in Fig. 2.7.8b. Isochoric deformations led to a stationary stress deviator after ca. 25% shortening in the direction of the previous uniaxial compression. After dismantling the sample was cut with a wire, and shortly after exposure a rhomboidal pattern of grooves appeared in side-light. The more rapid evaporation and shrinkage at shear bands may be attributed to a higher pore pressure, void ratio and permeability than in the vicinity. The pattern was less marked if the sample had been shortened isochorically along the normal to the previous uniaxial compression.

Similar patterns are reported by Topolnicki (1987). He observed that the bands nearly reached the smooth walls, could be reflected there and had different distances with the same inclinations, Fig. 8.3.5. Other than observed by Kuntsche (1982) the direction of previous consolidation had no systematic influence. Again and more precisely there was no peak of stress deviator versus shortening. It may be legitimate therefore to neglect the localization in simulations, but one should care for argotropy and relaxation (Sect. 3.7). The

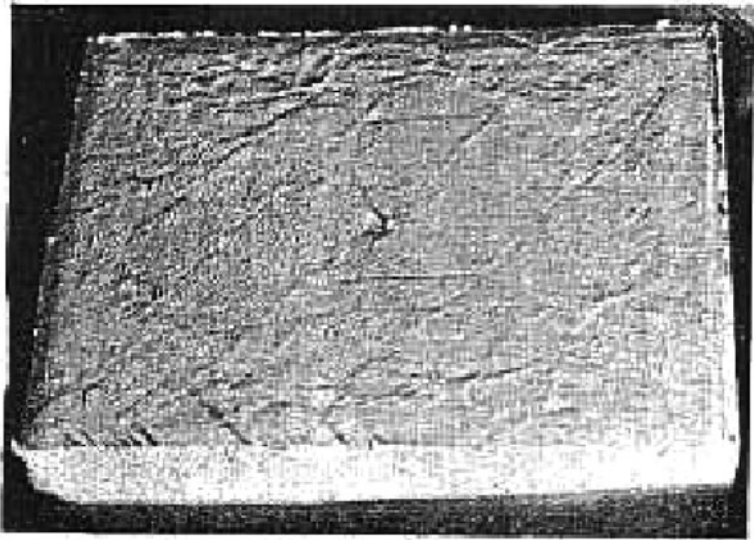


Fig. 8.3.5. Pattern of shear bands from a biaxial test with clay (Topolnicki 1987)

latent polarization could principally be simulated by vp-hyp with pore water diffusion, but not yet with available computer capacity. The lack of determinacy and repeatability can be attributed to partly erratic imperfections and waiting times.

Lizcano (2004) investigated remoulded moderately plastic clay samples in a biaxial apparatus as by Fig. 2.7.8a, and in cuts of them afterwards. After uniaxial consolidation the sample was shortened without drainage via guided plates so that a shear band could develop freely. This happened after normal consolidation, i.e. without initial excess pore pressure or decompression, whereas samples with initial excess pore pressure remained cuboidal. The dislocation started near the peak of the stress deviator versus shortening, whereas the pore pressure at the bottom plate did not change. The response got almost stationary although the sliding motion was impeded by the rubber membrane. The observed relative displacements indicate isochoric shearing along the bands. Their inclination was nearly repeatable, $\theta \approx 60^\circ \pm 5^\circ$, their position was random. A critical friction angle $\varphi_{cs} \approx 24^\circ$ was derived by assuming a uniform pore pressures p_w .

Dismantled samples exhibited shear zones of ca. 5 mm width. Scanning micrographs of cuts reveal much thinner shear bands (Fig. 8.3.6a). Close-ups

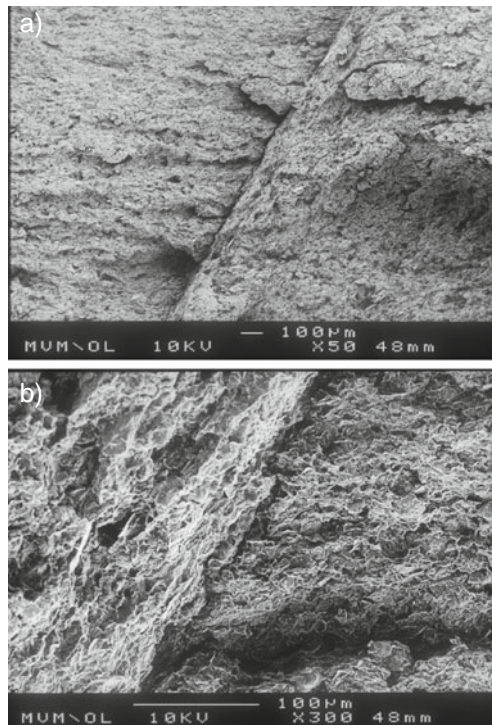


Fig. 8.3.6. Scanning micrographs of a shear localization with clay in a biaxial test (courtesy A. Lizcano), band (a) and close-up (b)

exhibit a less regular alignment in bands of ca. 10^{-5} m width (b), but particles can hardly be identified. Following the outline on sheared strips further above a localized polarization may be stated, and a localized reduction of p_w so that the φ_{cs} calculated without it is too high. It appears that a peak which necessitates a shear localization was caused by a diffusive loss of suction, but that this did not lead to a uniform p_w . As with other biaxial tests a back-analysis with vp-hyp and diffusion is beyond the present reach.

Triaxial tests with clay samples can lead to shear band patterns which are more complex than with biaxial tests (Sect. 14.1). This can also be said about cuboidal and torsional tests (Sects. 3.7 and 3.8) although shear localizations have hardly been studied with them. Transferring the experience with biaxial tests one may presume that localizations do not occur or do not matter in so-called RSE-tests if the initial consolidation ratio p_e/p_s is low enough. Otherwise localizations with dilation and cavitation spoil the desired uniformity, but quantifications with polar terms, diffusion and phase transitions of pore water are not yet at hand.

To sum up, evolutions with shear localization observed in clay samples can be principally captured by polar quantities, but quantifications are difficult due to skeleton viscosity, changes of pore water state and limited computer capacity. Observations with thin layer shear tests demonstrate a localized polarization and could be used to examine visco-hypoplastic relations with polar terms (vp-hyp). This is debatable as pore pressures and void ratios can hardly be observed in narrow bands, and as the bound pore water can get thinned or cavitated. Evolutions with shear band patterns in other tests can as yet only be interpreted qualitatively, back-analyses with vp-hyp and pore water diffusion are not yet feasible. The usual evaluation with assumed uniformity is legitimate up to critical stress obliquities, but gets dubious otherwise, all the more as then pore pressure gradients enhance localizations.

8.4 Cracking and channelling

The uniformity of RSEs can get lost by cracking and/or by spontaneously arising channels in case of pore pressure gradients. Such localizations are briefly described in the sequel in order to delimit approaches with spatial averages. Continuum approaches as for shear localizations are not at hand and not always legitimate, but the issue arises repeatedly in this book and some common features can be identified.

The skeleton of a *very dense psammoid* RSE can dilate almost like a dry masonry. This was related in Sect. 2.2 with dilatant state limits with extreme stress obliquities so that one or two skeleton pressure components vanish. One may also speak of an anomalous shear localization with extreme dilation. Chains of grains (cf. Fig. 4.3.1) along a cleft may be imagined to buckle with polar effects. This rather chaotic localization (Sect. 16.3) is at variance with the uniformity assumed for psammoid RSEs. The problem can arise after

a reduction of skeleton pressure p_s so that the void ratio e is lower than the lower bound $e_d(p_s)$ for simple skeletons. Niemunis (2003) modified hypoplastic relations so that they still work with assumed uniformity, this could suffice for many applications. The capability of continuum approaches with polar terms for splitting was demonstrated by Mühlhaus (1989).

The splitting of dense grain skeletons can be enhanced by localizations in the *pore water*. With full saturation and a hydraulic gradient the water transport can be concentrated onto a crack, then the skeleton at its flanks is supported by sideways seepage forces. The critical hydraulic gradient for a breakthrough is thus not only determined by e and p_s , but also by the vicinity to a dilatant state limit. Given a sufficient hydraulic gradient the localized dilation enhances the transport of water, and a subsequent collapse of grain chains can lead to an inner erosion. Mean-field approaches for seepage (Sect. 6.2) and for stability of filters (Sect. 10.3) cannot suffice. One may determine critical gradients in experiments with adequate skeleton state and boundary conditions, but subsequent evolutions with such kind of channeling are apparently beyond the present reach (Sect. 16.3).

A gas channel can stabilize a crack by suction and enhances the vapor transport. It can arise spontaneously in a previously saturated dense skeleton by splitting alongside with a capillary entry (Sect. 6.2). This can happen with fine grains and low enough total pressures so that capillary entry and skeleton pressures have the same order of magnitude, provided the deformation is too fast for the diffusion of pore water. Axial splitting or discing can then be produced by shortening or lengthening, respectively, of cylindrical samples. Constitutive relations with spatial averages of RSEs can at best indicate conditions for such a localization, but cannot catch its further course.

Without contact with the atmosphere skeletons can crack alongside with a cavitation of the pore water. With saturated gravel and sand this occurs by vanishing water pressure, $p_w \rightarrow 0$, with finer grains p_w can get negative by evaporation or by rapid deformation of dense skeletons. Relations with mean values can again at best indicate the onset, but cannot catch further evolutions. With bubbles of air or vapor between the grains and given total pressure the water pressure p_w is hardly reduced by further deformations of the skeleton, this could only crack then if it is very dense.

Unsaturated psammoid samples with interconnected pore gas can crack with suitable initial and boundary conditions. Uniaxial tension opens the capillary bridges along a single crack, the capillary skeleton pressure p_{cs} can thus be determined (Sect. 6.2). Splitting or discing can be produced in cylindrical samples by axial shortening or stretching, respectively, if the skeleton is denser than critical. The buckling of grain chains along crack flanks is prevented by p_{cs} , but this is reduced by dilation so that further cracks arise. This kind of localization can happen near free boundaries with total pressures $p \approx p_{cs}$, it enhances the de- or increase of water content.

The decay of looser than critical and fully or nearly saturated psammoid skeletons can lead to *channelling* in initially uniform RSEs. If the skeleton is

deformed via filters without or with reversals (Sects. 2.2 and 4.2) its mean pressure p_s can vanish so that the grains can move freely. If the skeleton velocity is too high for drainage and the total pressure p is nearly constant the pore water pressure p_w rises. The seepage force by the gradient of p_w (Sect. 6.2) widens preferred pore channels. The positive feedback by sideways seepage from channels enhances the localization of pore water outflow and leads to erosion (more in Sect. 16.3). Evidently this cannot be captured by psammoid approaches with mean field relations only.

If a gradient of p_w is imposed to our RSE a similar localization can occur even if a loose skeleton is kept by boundary filters. Other than with lower than critical void ratios the skeleton can collapse along widening channels although the average skeleton stress obliquity is low. Critical hydraulic gradients should be determined with the same average e and p_s as with intended applications. This can help to judge a hydraulic breakthrough in skeletons which are kept at boundaries, but hardly the further evolution. With more kinematic freedom loose wet skeletons can slump into suspensions, therein released gas bubbles can unite to gas cushions. The flow of avalanches is thus enhanced until gas breaks out in channels (Gudehus 1998). Thus p_w is suddenly reduced and grains are recombined into skeletons which are denser than critical (more in Sect. 16.3).

Cemented granular RSEs can be split with overcritical stress obliquities if they are denser than critical. Otherwise macropores disappear rather uniformly alongside with the condensation bridges and the net attraction by them (Sect. 7.3). If high skeleton velocities prevent drainage (roughly by (6.2.11)) the loss of cementation can lead to a decay if the skeleton is loose. The more marked brittleness due to cracking without grain crushing implies a localized dilation with buckling chains of grains. Similarly as with humid skeletons the void ratio may be initially higher than the lower bound e_d , but the acoustic emission is stronger. Constitutive relations with spatial averages may capture the onset of cracking, but not its further evolution (Sect. 7.3).

Peloid RSEs can exhibit a wider spectrum of cracking and channelling as their particles are argotropic and can have net attraction, and as the diffusion of pore water plays a dominant role. The evolution of *cracks* by the cavitation of pore water can hardly be captured by presently available models (Sect. 6.3). The tensile strength without net attraction may be identified as capillary entry pressure if its change by localized dilation is neglected. As with psammoids the splitting or discing of cylindrical RSEs by axial shortening or extension, respectively, may be interpreted as an anomalous extreme shear localization. As long as even the latter cannot be quantified (Sect. 8.3) this interpretation is of little use. Conditions with spatial averages may at best serve to specify the loss of uniformity, but further evolutions can hardly be captured by continuum approaches.

The evolution of *crack patterns* cannot yet be quantified even in case of shrinkage near free surfaces. As outlined with Fig. 6.3.6 the fractal succession is determined by diffusion in and near the cracks, and is coupled with

anisotropic contractant skeleton deformations. The complexity grows if the peloid RSE has anisotropic average stresses, net attraction and/or gas inclusions. Shear bands can occur alongside with cracks, the latter can be closed as long as the pore gas is not dissolved or squeezed out, through-going cracks enhance the transport of pore water and solubles.

Such complex evolutions could be observed in thin layer (Sect. 8.3) or tri-axial tests (Sect. 14.1), but they are beyond the present reach of continuum models. RSE-tests with stiff fissured clays require samples with such patterns of cracks, shear bands and gas inclusions that spatial averages are legitimate. This necessitates rather big samples, a good reconstitution after cutting them *in situ*, and boundary conditions in experiments so that the moderate uniformity is not lost without control (Sect. 9.1).

Baro-, pykno- and argotropy are essentially the same as without fissures as these do not change the solid particles. Similarly as shear bands fissures cause an *inherent anisotropy* which changes with the evolution of crack patterns. Other than with simple peloids the state of RSEs is not sufficiently captured by spatially averaged skeleton stress components, pore pressure and void ratio. The spatial fluctuations with cracks cannot be captured by hidden state variables as proposed for reversals in Sect. 5.2. Crack patterns can get so chaotic that their fluctuations cannot be captured by continuum quantities. Therefore constitutive relations for peloids with crack patterns which include their evolution are not in sight.

For the time being it may suffice to work with state limit parameters from matching of test results with the precautions indicated further above. This is an apparent contradiction in terms as states of stiff fissured clay samples are not sufficiently determined by the average skeleton stress. In other words, fabrics with fissures and shear bands cannot arbitrarily be reconstituted by feasible RSE boundary conditions. State limits cannot uniquely be recognized from the response, so the identification of parameters in the framework of v-el-p or v-hyp is not objective. This shortcoming will hardly matter in the contractant regime as then cracks and shear bands are not activated, and may be minor for isochoric evolutions as then cracks are smeared and shear bands will hardly influence the average response (cf. Sect. 8.3). In the dilatant regime validation and identification are debatable due to localizations anyway, but the inherent anisotropy could then be of minor importance.

Spatial averages may suffice for the skeleton response, but *localizations in the pore fluid* should not be neglected for stiff fissured clays. If there are no inter-connected gas channels the overall permeability \bar{k}_f is higher with partly open fissures, this \bar{k}_f can be determined by element tests with skeleton stresses and gas inclusions as *in situ*. The average effective skeleton stress components are related with the total ones and with the average pore pressure \bar{p}_w as without fissures. Deviations of \bar{p}_w from the observable p_w in fissures may be neglected for amounts of overall stretching

$$D < 10^{-1} k_f \bar{p}_s / \gamma_w d_f^2 \quad . \quad (8.4.1)$$

Therein k_f denotes the permeability without fissures and d_f their average distance. According to (6.2.11) the seepage may be neglected if D exceeds 10^3 times this amount, with the same k_f as then fissures are smeared.

With inter-connected gas channels the situation is different due to *suction*. A network of shrinkage cracks is not generally closed by overburden pressures so that an adjacent saturated clay has $p_g - p_w > 0$ according to gas and vapor pressures in the fissures. An anisotropic capillary skeleton pressure \mathbf{P}_{cs} and state limits with higher void ratios according to its isotropic part p_{cs} were proposed in Sect. 7.2. This is debatable for stiff fissured clays as they can have zero tensile strength and inherent anisotropy. Triaxial tests with big samples (Gudehus and Wichter 1977) exhibit a ductile response with cohesion c and friction angle φ in conventional terms, but rock-like fabrics. Axial splitting occurs with low confining pressures σ_2 , whereas the suction can get lost with so high σ_2 that the pore gas gets trapped. c and φ are anisotropic and depend on the average pressure and suction, so they are by no means material constants.

Formal extensions of elp or hyp with anisotropy and suction are of little use because of the indeterminacy by random cracks. It is difficult and expensive to cut samples with representative fissures, to reconstitute in situ states and to impose RSE-like boundary conditions including suction. Sophisticated constitutive relations including the evolution of inherent anisotropy could only be validated by means of artificial samples with reproducible crack patterns (e.g. Fig. 14.1.10). Such attempts are beyond the scope of this book, and may turn out not feasible as relations with spatial averages can be principally insufficient (Sect. 9.1).

More than without fissures (Sects. 11.3, 12.2 and 13.3) plastic limit states with c and φ are at best necessary, but not sufficient for the *stability* of peloid bodies with fissures. With further drying and overcritical average stress obliquities, e.g. at steep cuts, main cracks run ahead and are followed by secondary and tertiary cracks until the clay gets a debris of crumps. Wetting proceeds first along wider cracks, these are closed by swelling under overall pressure, part of the pore gas is enclosed in the further deforming mass, this can collapse into a suspension. Calculations with v-elp or v-hyp and spatial averages may provide crude estimates of deformations and stability. As the irregular pore water transport is hardly predictable the suction should be monitored in situ alongside with drainage and/or hydraulic insulation (e.g. Sect. 12.2). Thus the indeterminacy with cracks cannot be ruled out, but an unexpected delayed collapse can be avoided.

Zou (2000) investigated the *hydraulic breakthrough* in differently prepared and kept clay samples. After consolidation some samples were flattened via smooth plates so that they got a pattern of shear bands. Hydraulic gradients were imposed via filter plates in oedometric and triaxial setups. With a given average void ratio e and axial skeleton pressure σ'_1 the critical gradient for a breakthrough was lower with shear bands, lower stress ratios σ'_2/σ'_1 and wider filter openings. Position and orientation of the breakthrough channels

are random, erosion widens the channel which always start at the downstream filter.

Zou (2000) proposes an estimation formula for the dependence of the critical gradient i_c on conventional strength parameters (c' and φ'). It may suffice here to state that i_c depends on initial and boundary conditions of the RSE and that the hydraulic breakthrough starts at the downstream boundary. One can conclude that this kind of hydraulic localization with skeleton decay is a boundary effect. It could not start spontaneously in the interior like a shear band or a crack, so it is not a localized bifurcation which can be attributed solely to the state of skeleton and pore water.

Saturated peloids with *net attraction* (Sect. 7.1) are certainly capable of cracking and channeling, but such cases have hardly been investigated. Uniaxial extension leads to a tensile crack, and splitting can occur in the direction of maximal shortening. This was described for model tests by Pralle et al. (2003) with a mixture of quartz powder, salt water and gas bubbles. Total pressure pulses lead to a local skeleton decay and to mud volcanos. Such critical phenomena are beyond the reach of this book (more in Sect. 16.3).

Peloids with *cementation* may merely be mentioned for sake of completeness. As outlined in Sect. 7.3 bridges by condensation and by net attraction cannot clearly be separated for cemented clays, otherwise these should be called claystones. Tensile cracking and splitting can certainly occur, but could hardly be captured as with solids or psammoids. Cracks can heal by thermally activated rearrangement and recondensation, this can be observed in experiments, but certainly cannot be captured by methods treated in this book. A hydraulic breakthrough is impeded by cementation and may therefore be left aside.

To *sum up*, cracking and channeling are localizations which influence the mechanical behaviour of soils, but can hardly be captured by constitutive relations. For contractant and isochoric deformations elp or hyp relations may suffice as without crack patterns, particularly if these are smeared out. In this regime a control of suction via open cracks can be of use. The argotropy is not changed by cracks. The onset of crack growth in the dilatant regime may at best be indicated by relations for spatial averages. The transport of pore water and gas gets chaotic with cracks and can lead to skeleton decay and inner erosion.

FABRIC

The notion ‘fabric’, which is often used instead of ‘structure’ for geo-materials, has two different meanings. If a skeleton is homogeneous with respect to the kind of solid particles these can be differently arranged according to the *state* of an RSE. The outline in Sect. 9.1 deals with the issue of remoulded, reconstituted and undisturbed samples. It may help to understand limitations of constitutive relations and of microscopic approaches.

The spatial distribution of statistically different solid particles in RSEs characterizes fabrics by *composition*. It will be indicated in Sect. 9.2 that the mechanical response can strongly depend on the spatial distribution so that spatial averages do not suffice. This requires careful identifications and/or composite RSEs. The attractors proposed in this book get invalid by mixing and segregation of solid particles so that evolutions of skeletons can no more be followed up.

9.1 Fabrics by state

By definition the grains of a *psammoid* RSE constitute a skeleton with contact forces which sum up to skeleton stress components. These force densities define the state of simple psammoids together with the void ratio e (Sect. 2.2). In a statistical sense the relative positions and the contact forces of the grains should thus be sufficiently determined. Let us briefly discuss how far this simplifying assumption could be justified. For simplicity the pore space may be saturated and have a constant water pressure p_w , as always p_w may influence the pore-free grains only via $p_s = p - p_w$.

The *preparation* of psammoid RSEs as samples for experiments can lead to different fabrics even if average skeleton stress and void ratio are the same at the onset of RSE tests. A layer-wise placement leads to spatial fluctuations of e which are aligned by gravity, let alone inobservable skeleton stress fluctuations (Sect. 4.3). Such fabrics can be ironed out by alternating deformations with moderate amplitudes. Shear band patterns could be produced in dense

skeletons so that these get a kind of fabric. Skeletons can be fixed in situ by grouting or freezing, then cut and unfixed after imposing RSE boundary stresses. Such expensive samples have at best nearly the spatial distribution of e as before in situ, but not the same force-roughness. Their state including fabric is not reproducible, their uniformity will rarely suffice for spatial averages.

Only at *state limits* the skeleton state is fully determined by the skeleton stress components, then the void ratio is determined by p_s and the stress obliquity (Sects. 2.2 and 2.11). This assumption implies that the fabric, i.e. the configuration of grains with contact forces, is sufficiently given by the skeleton stress tensor. In other words, density and orientation of the skeleton are so strongly adapted to the skeleton stress components that these determine the relation of stress rates and stretching, and that the fabric need not be considered explicitly. So-called element tests with uniform RSEs support this assumption (Sects. 2.5, 2.7 and 2.9), but would it stand a microscopic inspection?

Imagine a kind of microscope which yields the positions of all grains and their contact forces and flats, or the same data set from a numerical simulation with granular interactions. Imagine further a stochastically uniform skeleton which is deformed without loss of uniformity, i.e. an RSE. These are thought experiments: no tomography and no preparation is perfect, simulations are always over-simplified, and statistically uniform fluctuations cannot be achieved. Anyway, a data set of grain positions and forces for a resting skeleton could be summed up into void ratio, skeleton stress components and a *fabric tensor* \mathbf{S} . The latter could capture the distribution of grain contact normals and/or of orientations of oblong grains (Lätzel et al. 2000). Reasonably \mathbf{S} is a symmetric second-order tensor, thus the fabric has three principal axes in general, three positive principal values and three invariants. These are also the properties of the Cauchy skeleton stress tensor \mathbf{T}_s , thus one may analogously define a fabric vector \mathbf{s} which is related with a direction \mathbf{n} by the fabric tensor via $\mathbf{s} = \mathbf{S}\mathbf{n}$.

\mathbf{S} is an internal or hidden state variable which can principally be fully determined by microscopy or simulations. Fabric effects may at best be indirectly exhibited by observed evolutions of skeleton stress, void ratio and shape as far as samples are and remain uniform enough so that spatial averages are justified and sufficient. Constitutive relations could be formulated with a fabric tensor \mathbf{S} so that objective rates of \mathbf{T}_s and \mathbf{S} are tensorial functions of e , \mathbf{T}_s , \mathbf{S} and stretching \mathbf{D} , viz.

$$\overset{\circ}{\mathbf{T}}_s = \mathbf{F}_s(e, \mathbf{T}_s, \mathbf{S}, \mathbf{D}) \quad (9.1.1)$$

and

$$\overset{\circ}{\mathbf{S}} = \mathbf{F}_f(e, \mathbf{T}_s, \mathbf{S}, \mathbf{D}) \quad . \quad (9.1.2)$$

Frame-indifferent representations of the functions \mathbf{F}_s and \mathbf{F}_f should be homogeneous of first order and non-linear in \mathbf{D} . They are necessarily more

complicated than without \mathbf{S} (Sect. 2.11), tentative approaches by trial and error would be boundless. Even isochoric state limits get complex: for them $\mathbf{F}_s = 0$ and $\mathbf{F}_f = 0$ may be expressed as

$$\mathbf{T}_s = \mathbf{G}_s(e, \mathbf{S}, \hat{\mathbf{D}}) \quad (9.1.3)$$

and

$$\mathbf{S} = \mathbf{G}_f(e, \mathbf{T}_s, \hat{\mathbf{D}}) \quad , \quad (9.1.4)$$

but the inversions of the functions \mathbf{G}_s and \mathbf{G}_f have two tensorial arguments instead of only the direction $\hat{\mathbf{D}}$ of \mathbf{D} as for simple psammoids (Sect. 2.11). In the latter case \mathbf{S} is determined by \mathbf{T}_s as both \mathbf{T}_s and \mathbf{S} are determined by $\hat{\mathbf{D}}$ (monotonous functions provided for uniqueness). Then \mathbf{S} is no more needed, i.e. the fabric is fully determined by the skeleton stress.

Goddard (2005) proposed relations like (9.1.3) and (9.1.4) as for a liquid with an internal structure, but without evolution equations as (9.1.1) and (9.1.2). Skeletons of ablong grains are certainly aligned at isochoric state limits, but then their fabric is not necessarily determined by the stress tensor. Frame-indifferent representations of (9.1.3) and (9.1.4) may be specified with physical arguments, but could hardly be validated by element tests. As outlined in Sects. 2.5, 2.7 and 2.9 uniform critical states can hardly be produced in triaxial or shear tests, an inherent anisotropy could not be detected therefore with isochoric state limits attained after different preparations.

The feasibility of approaches with a fabric tensor is more questionable for non-isochoric state limits of psammoids. Contractant state limits with hard grains require a capillary net attraction for stabilizing sufficiently loose skeletons, and cannot properly be attained with increasing skeleton pressure p_s as then grains are crushed and as this effect can hardly be separated (Sect. 7.3). As far as such state limits can be identified it suffices therefore to assume that the fabric is determined by the skeleton stress. Attempts with cuboidal samples and differently oriented placement suggest an inherent anisotropy for dilatant state limits (Sect. 2.7). This is not a sufficient evidence, however, as the relative void ratio r_e is not uniformly distributed, as the spatial average \bar{r}_e is not the same for the compared peak states, and also as \bar{r}_e cannot precisely be deduced from the reports. A stress-independent fabric tensor could thus not be specified even for state limits.

Evidently *shear localizations* produce a kind of fabric in psammoid RSEs, but models for such fabrics are hardly feasible and justified. A single shear band in an RSE would divide this into two RSEs and a narrow interface with higher e and polar stresses. The interface could be substituted by a band without polar quantities if only its evolution is to be captured. Such simplifications may be justified if the data for initial state and boundary conditions are incomplete and details of localization do not matter. If the size of granular bodies prohibits a comprehensive meshing simulations without polar terms may still capture evolutions of fabric in the large. It will be shown

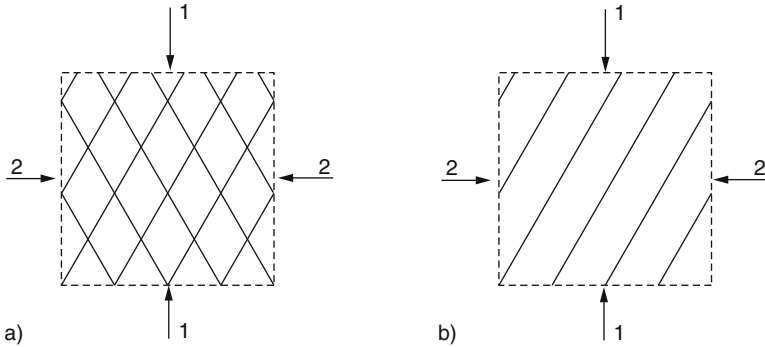


Fig. 9.1.1. Shear band patterns of psammoid RSEs without (a) and with overall skewness (b)

in Sect. 12.6 that the so-called normal faulting in the earth crust can thus be modelled, but scaling and validation are debatable.

RSEs with *shear band patterns* can be imagined which constitute a kind of fabric with an inherent anisotropy, Fig. 9.1.1. For instance, two overlapping swarms of bands from biaxial shortening in the 1-direction would exhibit a not only stress-induced anisotropy by shortening in the 2-direction (a). This could be captured by relations of RSE-averages without polar terms as these can cancel each other (Sect. 8.2), but now with an evolving fabric tensor. With a single swarm of shear bands the fabric is no more aligned with the stress field (b). If polar quantities are not cancelled by crossing bands the average stress tensor gets non-symmetric, and average couple stresses are required so that our RSE is no more uniform with respect to its pressure distributions.

Tejchman and Niemunis (2006) simulated evolutions of biaxial RSEs with p-hyp and oriented fluctuation patterns of the initial void ratio. They could reproduce the observed influence of bedding directions on peak stress ratios and shear band inclinations, and the independence of residual stress ratios on the kind of bedding. This can be helpful to interpret biaxial test results and to understand the inevitable loss of uniformity with overcritical stress obliquities (Sect. 8.2). Such simulations could elucidate how far fabric tensors \mathbf{S} as indicated above could serve to the purpose. Evolution equations for \mathbf{S} should produce attractors which reflect repeatable features, but this seems to be a contradiction in terms as the evolution of multifractal patterns indicates a deterministic chaos (Fig. 8.2.7).

Fabrics of shear band patterns can scarcely be taken into account in applications. The expense for finding initial shear bands in situ may at best be justified if they could lead to a collapse or a hydraulic breakthrough which could not be avoided by cheaper means. Otherwise spatial averages without polar quantities and fabric tensors do suffice, a good specification of initial and boundary data is difficult enough (Sects. 9.2 and 10.2). One should at

least keep in mind the lower determinacy of evolutions in lab tests and in situ due to localizations. A lot more research will be needed until evolving fabrics by localization and polarization are better understood and can be technically controlled.

Some further fabric effects with psammoid RSEs may at least be mentioned. As indicated further above fabrics can be ironed out by moderate alternations of shape and may then be ignored. The capillary skeleton pressure p_{cs} due to gas channels enables fabrics with cracks (Sect. 7.3) or with lumps of grains. As long as the mean pressure p exceeds p_{cs} in subsequent evolutions fabrics by p_{cs} are swept out and may therefore be ignored. For $p < p_{cs}$ near free boundaries capillary-induced fabrics can be stable, so p_{cs} is of use for boundary conditions (Sect. 10.1). Cementations enable also cracks and lumps, but fabrics with them are rather chaotic (Sect. 7.3).

Turning to *peloid* RSEs we first leave aside net attraction and pore gas (Sects. 7.1 and 7.2). State limits are again determined by the skeleton stress components only, they are argotropic as the soil particles (Sect. 3.2) and can only be uniform after the diffusion of pore water so that its pressure p_w is uniform. The latter requires a slow consolidation by (6.2.12), the observed uniqueness of the argotropic response indicates that then further state variables are not needed (Sect. 3.5).

The neglect of fabric is more debatable for isochoric state limits of peloids, i.e. for rate-dependent critical states. It is necessary for their uniformity to avoid diffuse and localized bifurcations (let alone initial non-uniformity and boundary conditions which enforce a loss of uniformity). As outlined in Sect. 8.3 even initial and boundary conditions which favour the uniformity can lead to shear bands, but the response can be the same as without this localization. One may therefore ignore such fabrics as long as the average stress obliquity of RSEs is not overcritical.

A *localized dilation* cannot be avoided when trying to attain dilatant state limits in saturated peloid RSEs. A localization is enhanced by the positive feedback with suction in dilating bands (Sect. 8.3), and by inevitable fluctuations of permeability which are thus increased. Patterns of shear bands constitute a kind of evolving fabric. As outlined further above for psammoids a symmetric fabric tensor \mathbf{S} could be insufficient because of polar effects, and evolution equations with \mathbf{S} would hardly be feasible.

Pore gas enables a wider variety of peloid fabrics as capillary effects are stronger with the smaller particles than for psammoids. Gas inclusions, left back e.g. after the compaction of lump aggregates with anisotropic total stress, can be flat and aligned. This may be interpreted as a kind of fabric with anisotropy, but again evolution equations with a tensor \mathbf{S} could hardly be quantified. For the time being it may suffice therefore to work with v-elp or v-hyp and a more compressible pore fluid according to the degree of saturation S_r and to the pore water pressure p_w . Validations presented later in this book indicate that the partial indeterminacy of S_r and p_w (Sects. 6.1 and 6.3) need not spoil predictions.

The opening or closing of *gas channels* is paramount due to the loss or gain of suction in adjacent saturated peloid zones (Sects. 6.3 and 7.2). Crack patterns constitute a kind of fabric which evolves with boundary conditions, often alongside with shear band patterns (Sect. 8.4). In spite of poor statistical uniformity one may speak of a variable anisotropy, but this can hardly be captured by constitutive relations. The same holds true for compacted composites of lumps with suction. The overall permeability is evidently higher with channels, but so variable and irregular that its quantification is hardly feasible.

A *net attraction* in peloids enables fabrics with macropores (Sect. 7.1) which are oriented in general. A cementation can have similar effects and cannot clearly be separated from net attraction (Sects. 7.3 and 8.4). The quantification of such fabrics is beyond the present reach, indirect approaches via variable net attraction are more promising. As with psammoids peloid fabrics can be ironed out by *alternating deformations* as long as the average skeleton stress obliquity is not higher than critical. This holds also true with pore gas and/or net attraction, but then hidden state variables as outlined in Sect. 5.2 will not suffice and the coupled diffusion of pore water, gas and soluble minerals in narrow slits between solid particles cannot yet be captured (Sect. 6.1). The microscopic investigation of peloid fabrics is of little practical use therefore.

The outline in this section shows that the widespread distinction of *induced and inherent anisotropy* can hardly be defended. Fabrics can be generated to a certain extent via boundaries of RSEs, patterns of shear bands and cracks may thus be included with due caution. Fabrics of statistically uniform particles result from placement and subsequent evolution, they are not more inherent than states of RSEs in general. An ordered non-uniformity can principally be captured by composites of RSEs. Certainly fabric and state of RSEs with statistically uniform particles cannot be reconstituted in general, but both can never be fully determined. So-called undisturbed samples may also exhibit ordered gas inclusions and condensates which cannot be captured by mean values only, but then no constitutive relation could serve to the purpose.

To *sum up*, fabrics of RSEs with rather uniform solid particles can represent the state in addition to average mass fractions and partial pressures, but constitutive models with fabric are as yet hardly quantifiable. The fabric at state limits is determined by the skeleton stress and therefore not needed explicitly. The inherent anisotropy due to layer-wise placement and evolving shear bands can be principally simulated, but cannot be captured by fabric tensors. Fabrics with gas bubbles and channels, which can be overlain by shear band patterns, are beyond the present reach of models. Therefore drastic simplifications are needed for applications. Fabrics can be ironed out by alternating deformations if the average skeleton stress obliquity is subcritical.

9.2 Fabrics by composition

Consider first *psammoids* which are composed of two fractions with different grain sizes. In a *mixture* these can constitute a composite grain skeleton wherein the coarser grains float in the finer fraction (Fig. 9.2.1a), or form a skeleton with fines inside (b). Such mixtures can be produced by stirring, their grain contacts can have forces which sum up to stresses, and their composition is not changed with suitable rearrangements. Then they may be modelled as simple psammoids (Sect. 2.2), and for reversals a hidden state variable may capture the spatial fluctuation of contact forces (Sect. 4.3). One could also model localized polarizations as outlined in Sect. 8.2, but representative grain sizes and rotations could not as clearly be identified as with more uniform grain sizes.

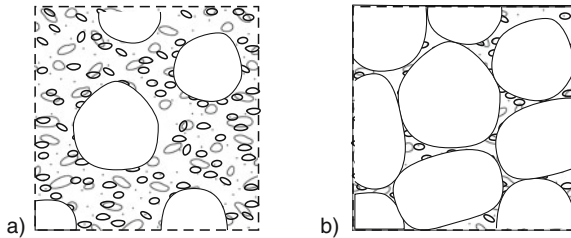


Fig. 9.2.1. Psammoids with floating (a) or skeleton-forming coarser grains (b)

State limits of such granular mixtures can be defined and handled as outlined in Sects. 2.2–2.11. For a given mean skeleton pressure p_s limit void ratios are evidently lower than those of the coarse and fine fractions, but the ratios of bounding and critical values e_i/e_c and e_d/e_c are hardly changed. The granulate hardness h_s exceeds the ones of the fractions: coarse grains have more force-transferring contacts by the finer ones, and the skeleton of fines is reinforced by coarse grains. If both fractions have grains with the same average hardness and roughness the critical friction angle φ_c would hardly depend on the mass fraction of fines. The angles of peak friction and dilation for isobaric stretching are smaller than those of the coarse and fine fractions (Sect. 2.2), shear localizations are less marked therefore (Sect. 8.2). Such considerations can help to estimate material parameters, but RSE-tests with mixtures are indispensable.

The *pore water* can have other effects in such mixtures than in its constituents. The pressure $p_s = p - p_w$ is relevant for the skeleton again if the grains are neutral with respect to the pore water pressure p_w (Sect. 2.2). With gas channels the capillary skeleton pressure p_{cs} (Sect. 6.2) is dominated by the fines. The permeability k_f is also dominated by the fines as long as there are no pore channels along coarser grains. The seepage force can move fines

past a coarser skeleton so that the mass fraction of fines can de- or increase. Such rearrangements by inner erosion cannot be captured with constitutive relations for skeletons, but changes of their parameters by seepage forces may be used for estimates. For instance, a skeleton of coarse grains gets loose and collapsible if fines are flushed out. Filter rules as for interfaces can help to judge the mobility of fines (Sect. 10.2).

A sandwich with coarse and fine grains cannot be sufficiently captured by a single RSE, Fig. 9.2.2. It can arise by sedimentation from periodically changing suspensions as coarser grains sink faster, or by segregation during a granular flow (e.g. Koeppel et al. 1997). Thus it can be aligned horizontally (a) or along a previous slope (b), but often this order is disturbed (c) as granular rearrangements under water can get wavy or chaotic (Sect. 16.3). Similar fabrics can arise by filling and compaction of humid granular materials, then macropores due to p_{cs} can play a role (Sect. 7.2). Aeolian sediments can also exhibit kinds of sandwich, these are influenced by lumps due to p_{cs} . The spatial distribution of pore gas is evidently aligned in a sandwich.

The anisotropy of a granular sandwich can be captured by composites of RSEs. The simplest substitute is a pair of finite elements with different psammoid parameters and an orientation according to horizontal (Fig. 9.2.2d) or inclined fine layers (e). According to the size of the granular body the pairs can be wider than the sandwich bands, but should have the same mass fraction of fines. The thus modelled inherent anisotropy is changed with large deformations. The spatial scattering of sandwiches is left aside, evolutions with

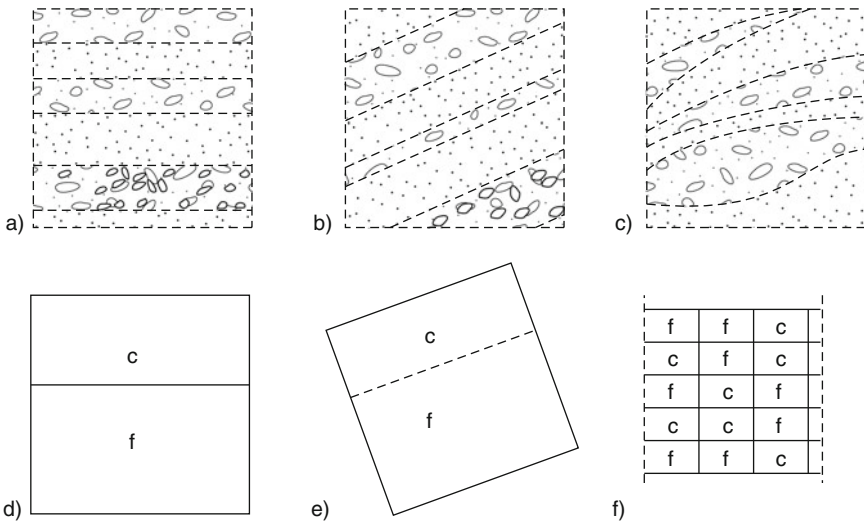


Fig. 9.2.2. Sandwich of psammoids by sedimentation (a) and by segregation with granular flow (b) and by irregular sedimentation (c), representative composites for horizontal (d) and inclined layers (e), and for less regular sediments (f)

small sizes are smoothed (e.g. penetration, Sect. 11.7). A disturbed sandwich can principally be represented by a coarser inhomogeneous mesh (e). In spite of the lower determinacy overall responses of large bodies may thus be captured.

Even a rather disordered sandwich exhibits another overall behaviour than a granular mixture with the same mass fractions. The anisotropy of a distorted composite may be neglected, but its void ratios are higher and their isobaric changes are stronger than with a mixture of the same grains. Gradients of the hydraulic height h_w have less predictable effects in sandwiches than in mixtures as the permeability k_f is proportional to the square of the grain size d_g (Sect. 6.2). The orthotropic permeability of a sandwich can be captured by pairs of elements, but the distinction of coarse- or fine-grained lenses and bands in situ remains incomplete. Thus spatially averaged permeabilities can be quite imprecise, and hydraulically influenced skeleton rearrangements cannot be well predicted.

Turning now to *peloids*, let us first consider again *mixtures*. These can arise *in situ* by the flow of mud and in building sites by placement and/or stirring. With the wider variety of solid particles by size, shape and hardness, and with a plethora of physico-chemical effects (Sects. 7.1 and 7.3), peloid mixtures can exhibit quite different fabrics. It appears, however, that fabric tensors for peloid mixtures can hardly be quantified and are not even necessary. Peloid mixtures may be considered just as peloids, many validations were achieved with such mixtures and parameters were determined for them. Certainly fabrics of peloid mixtures are not fully determined by skeleton stress and void ratio (Sect. 3.2), and additional internal state variables for reversals (Sect. 5.2) can hardly be related with fabric. For the time being it appears that investigations into the fabric of peloid mixtures are of little practical use.

This standpoint cannot as easily be defended for a *sandwich* of different thin peloid layers. It can arise by sedimentation from seasonally changing lacustrine or marine suspensions. An RSE with such a sandwich is anisotropic, as shown in Fig. 9.2.2 it may be represented by a pair of finite elements due to different peloid parameters. This simplification is somewhat arbitrary, but may suffice to match the experimentally observed anisotropy of samples cut in situ. As with psammoids a peloid sandwich is rarely regular, therefore finite element meshes with partially random anisotropy can be more appropriate and predictions get less determinate. One may replace such a sandwich by a peloid without inherent anisotropy for design purposes with substitute parameters chosen on the safe side.

Composites of psammoids and peloids occur in a wide range of spatial distributions, some of them may be considered as soils with fabric. A *sandwich* (deserving this name more than with only psammoids or peloids) can occur with various sizes, Fig. 9.2.3. So-called varved clays contain several bands of clay and fine sand in one sample (a). Sand grains sink more rapidly than finer particles in a suspension with periodic variation from annual floods. The anisotropy can be represented by pairs of peloid and psammoid elements (b). With the volume fraction α_p of psammoid the average permeability is thus

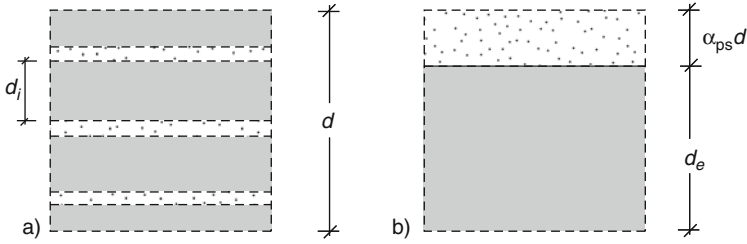


Fig. 9.2.3. Sandwich of psammoids and peloids with different sizes (a), simplified substitute composite (b)

$$k_{ft} \approx \alpha_p k_{fs} \quad (9.2.1)$$

in the direction of bands with the permeability k_{fs} of the psammoid. The average permeability across the bands is

$$k_{fn} \approx (\alpha_p - 1)k_{fp} \quad (9.2.2)$$

with k_{fp} for the peloid. Both (9.2.1) and (9.2.2) are obtained by placing substitute pairs of elements with orientation and psammoid fraction as in situ. This may be appropriate for average seepage velocities and forces, but not for the diffusion of pore water in peloid bands. As diffusion times are proportional to the square of the layer thickness (Sect. 11.1) the equivalent permeability k_{fe} for peloid elements of width d_e should be

$$k_{fe} = k_{fp}(d_e/d_i)^2 \quad (9.2.3)$$

with the peloid band width d_i in situ. Thus the transversal permeability is overestimated by (9.2.2) with k_{fe} instead of k_{fp} , but hardly too much as the average permeability is dominated by the one of psammoid bands.

Sandwich-like formations are more or less *disordered* over different scales, Fig. 9.2.4. For instance, a sample of a lacustrine sediment exhibits different fine clay bands in different cuts (a). A more regular sandwich can be produced in the lab (e.g. Fig. 11.3.2), but the sedimentation in situ is never that regular and often disturbed by erosion. Thus bands get wavy and fuzzy so that their lateral extension cannot easily be identified. In one site sand bands with over 100 m length may work as horizontal drains in clay, but not in another one with up to 10 m long sand lenses which exhibit the same profiles from boreholes. Substitute element pairs as proposed above should form therefore a finite element mesh which is partially random. This requires geological and geotechnical judgment, the investigation and representation of peloid-psammoid fabrics cannot be mastered by mathematical rules only.

At the scale of ca. 10^2 – 10^3 m depth and ca. 10^3 – 10^5 m width sandwich-like formations occur in various compositions. For instance, marine deposits off Osaka exhibit pleistocene clay lenses in sand and a holocene soft clay layer on top (Fig. 9.2.4b). They were investigated for the construction of an

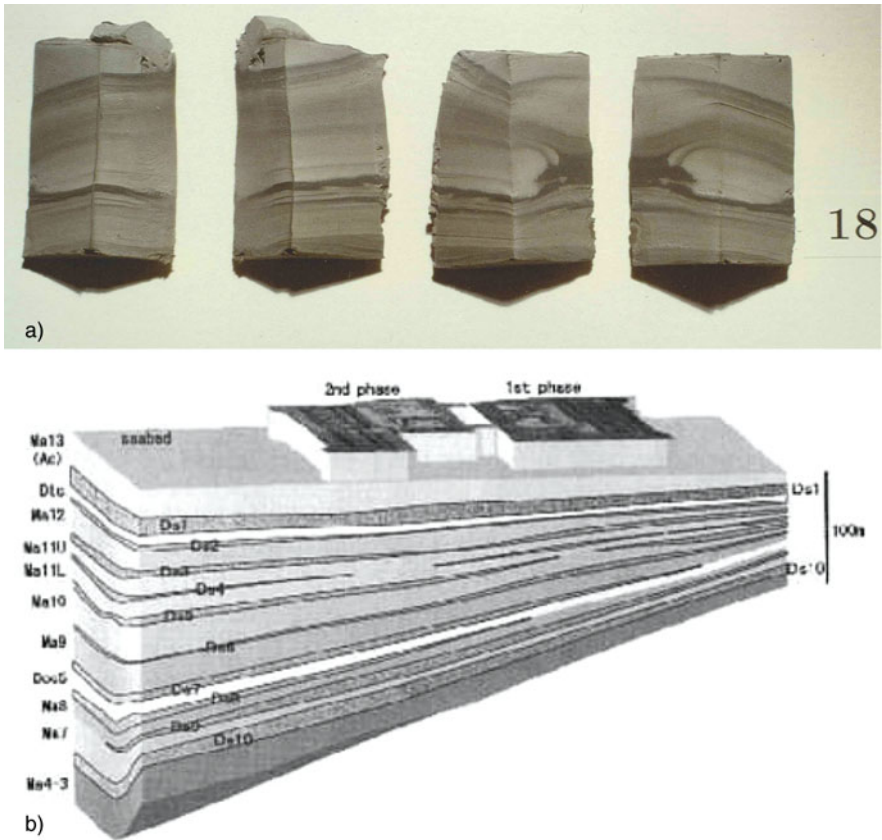


Fig. 9.2.4. Disordered sandwich: cut samples of a lacustrine sediment (a, Jagau 1990), a cross section from the Osaka bay (b, courtesy T. Adachi)

airport island. Settlement and spreading during and after placement could be calculated with a substitute composite mesh including granular columns in the soft layer, the indeterminacy could be bounded by comparative simulations. The delay of displacements by the diffusion of pore water is indeterminate due to irregular psammoid channels, the subsequent creep is more predictable if average peloid parameters are well known (Sect. 12.3).

The large-scale fabric of psammoid-peloid composites is different with *faults*. For instance, a cross section West of Cologne exhibits dislocations of psammoid and peloid layers along normal faults with some 10^3 m distance (Fig. 13.4.7a). Single boreholes can suggest a rather regular sandwich which may be simplified for the prediction of settlements due to lowering the groundwater table. The calculated delay by diffusion can be uncertain as horizontal changes of a sand-clay sandwich are hardly known. Faults with dislocated clay seams can work as slip planes after an excavation and should be taken into account in simulations (Fig. 13.4.7).

The issue is actually more complex as parallel cross sections will rarely exhibit the same fabric in the large. Three-dimensional variations of composition can principally be represented by element meshes without any symmetry, but then the numerical expense would often be too big for applications. The same argument holds true for other kinds of ground fabric with a wide spectrum of lengths, e.g. from erosion by rivers or from weathering of rock with cracks. This lack of homogeneity and isotropy is a commonplace, and it is then more an art than a science to assume symmetries for predictions without ignoring the physics.

To *sum up*, soil fabrics by composition may be captured by composites of substitute elements, but their partial disorder causes an inevitable indeterminacy. Mixtures of different psammoids or peloids may be modelled as simple psammoids or peloids with suitable parameters. Composites with different psammoid and peloid zones are not equivalent to mixtures with the same mass fractions. A sandwich of psammoids and peloids may be represented by coarser elements than bands in situ. The disorder of bands due to erosion or faulting cannot fully be captured, fabrics over many length scales require geological judgment.

BOUNDARY CONDITIONS

Given a system composed of psammoids and/or peloids with pore fluid and of solids, the evolution of its shape and state can be considered as a *boundary value problem*. For setting the scene imagine marked skeleton and solid particles (Sect. 1.2) at nodes of a finite element mesh which indicate displacements and deformations, and transducers between neighbored markers which indicate skeleton or solid stresses and pore pressures. An *evolution* can be represented as a succession of snapshots of positions and state fields which are ordered by time t . $t = 0$ may be taken for an onset with an initial state field including the void ratio e_o . This onset is chosen at will and not physically distinguished, i.e. the skeleton does not start at a state limit or at the verge of a suspension in general. Changes of position and shape are thus referred to arbitrary initial configurations.

For simulating evolutions the set of conservation equations (mass, linear and angular momentum, energy) and constitutive relations (e.g. elp or hyp for the skeleton and Darcy's law for seepage) has to be supplemented by *boundary conditions*. The conservation of solid mass determines the rate of void ratios \dot{e} by (2.11.8) in case of isochoric particles. The conservation of pore water with constant density is expressed by the so-called continuity equation with variable e and degree of saturation S_r . The conservation of linear momentum may often be reduced to the equation of static equilibrium, the one of angular momentum is not needed in its differential form if the stress tensor is symmetric. The conservation of energy is needed if changes of temperature and granular or seismic temperature come into play. Along the boundary the displacement or stress vector of the skeleton has to be given as function of t , and also velocity or pressure of the pore fluid.

Such boundary conditions are known for continuum models of solids and fluids, but they are more complex in general for soils. First, the conditions depend on the state at the boundary and should take into account the coupling of skeleton and pore fluid. Second, the soil can gain or lose pore fluid and solid particles so that the composition is changed. Such changes along the boundary have little in common with condensation and melting or evaporation of solids

and liquids, respectively. Various kinds of *boundary zones* can occur along soil boundaries. Their composition and state have to be specified in order to define boundary conditions. The natural or technical gain or loss of skeleton and pore fluid has to be represented by specifying a simultaneous change of composition and boundary conditions. This requires empirical simplifications as soil boundary zones with suspensions, cracks or polar quantities cannot be well modelled and as their origin is rarely well known.

Free soil boundaries are treated in Sect. 10.1 with various simplifications of boundary zones. Internal boundaries of skeletons can arise by shearing and separation, or are assumed for symmetry and/or as substitute for far-fields (Sect. 10.2). Interfaces of skeletons and solid bodies have to be specified for the interaction of both (Sect. 10.3). Approaches for the gain or loss of skeletons and solids are indicated in Sect. 10.4, therein attractors will appear again which constitute the backbone of this book.

10.1 Soils at water and air

Soils at free surfaces are in contact with water or/and air which are at rest or moving. This can be expressed by boundary conditions for skeleton and pore fluid of psammoids and peloids. Limitations arise from decay and recombination of skeletons and can be circumvented by technical measures and/or simplifying assumptions. Suspensions and filter cakes are also treated in this section, whereas gaps in and at soils are only touched. Their opening and closing will be part of Sects. 10.2 and 10.3, whereas removal and adding of soils and solids belong to Sect. 10.4.

We begin with *saturated psammoids* under *resting water*, Fig. 10.1.1. The skeleton may be stress-free at its surface and therefore at the verge of decay or recombination. Constitutive relations for evolutions of skeleton shape and state are not possible without skeleton pressure p_s (Sect. 2.2). At a horizontal free surface the skeleton pressure increases in proportion with depth by

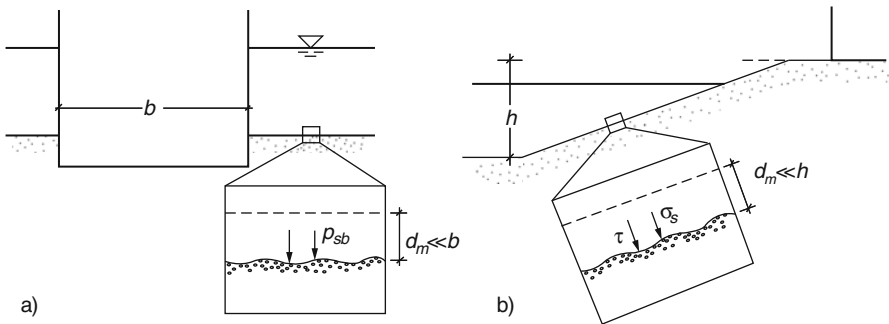


Fig. 10.1.1. Free horizontal (a) and inclined surfaces (b) of psammoid bodies with resting pore water

gravity (more in Sect. 11.2). Numerical simulations require the assumption of a fictitious boundary skeleton pressure p_{sb} to avoid $p_s = 0$. One may imagine a *mat* on top with thickness d_m and specific weight minus uplift γ_m so that $p_{sb} = \gamma_m d_m$ is obtained (a). $\gamma_m = \gamma_r - \gamma_w$ may be assumed as for psammoids (Sect. 11.2), d_m should be much smaller than the psammoid body considered in simulations. This may suffice for the back-analysis of lab and field experiments and should be checked by comparative calculations.

The skeleton at a horizontal free surface can have any void ratio e within the bounds for state limits with $p_s \rightarrow 0$ (Sect. 2.2). This part of the *initial conditions* depends on placement and further previous actions which cannot fully be captured by constitutive models for skeletons, so for the time being initial e -values have to be assumed suitably. For an *inclined* free psammoid surface under water (Fig. 10.1.1b) the inclination β is bounded. The normal skeleton pressure $\sigma_{sn} = -T_{sn}$ increases again in proportion with depth, but there is also a shear stress $\tau_s = \tau$ by gravity (Sect. 11.2). The stress ratio $|\tau|/\sigma_s$ cannot exceed the critical one $\tan \varphi_c$ (Sect. 2.9). Steeper slopes cannot stand, with lower than critical void ratios they collapse with dilatant shearing (Sect. 12.1).

A fictitious boundary skeleton pressure p_{sb} , which is needed for simulations with elp or hyp, may again be justified by assuming a mat on top with thickness d_m and net specific weight γ_m . Statical equilibrium requires $\sigma_m = \gamma_m d_m \sin \beta$ and $\tau = \gamma d_m \cos \beta$, other stress components are bounded by state limits (Sect. 11.2). If the mat can take over normal forces these can change τ (more in Sect. 10.3). As long as resting water may be assumed artificial boundary pressures for avoiding $p_s = 0$ can be justified by comparative calculations.

Psammoid skeletons near *flowing water* have gradients of the hydraulic height h_w and can exhibit other features than with resting water, Fig. 10.1.2a. If clear water flows into the skeleton this is kept by seepage forces so that the free surface can be steep (more in Sects. 12.1 and 14.2). A substitute skin may be assumed for calculations with a skeleton boundary pressure p_{sb} from seepage force, gravity and uplift. An outwards seepage would drive grains from

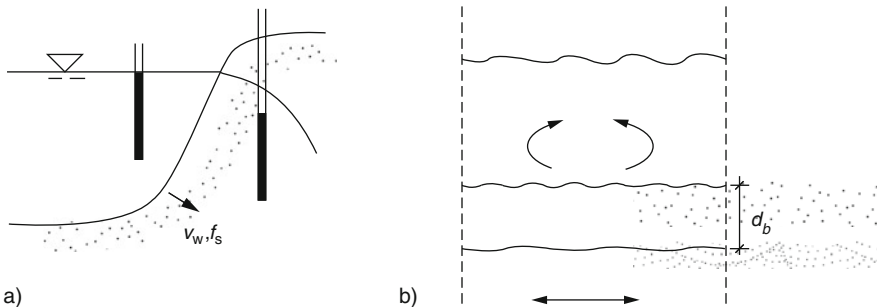


Fig. 10.1.2. Free surfaces of psammoid bodies with moving pore water: steep slope with inwards seepage (a), fluidized bed (b)

the surface into the free water, this decay of skeletons is left aside. The erosion by transversal water flow will be touched further below.

A *fluidized bed* can arise above a horizontal skeleton boundary, Fig. 10.1.2b. Its void ratio exceeds the upper bound of a skeleton with $p_s \rightarrow 0$, i.e. $e > e_{io}$ (Sect. 2.1). The grains are in chaotic motion, their average kinetic energy (e.g. per unit of solid mass) means a granular temperature T_g . The water in the fluidized bed is also in chaotic motion, its average kinetic energy is proportional to an equivalent temperature T_w by turbulence ($T_w = T_g$ for dynamic equilibrium). The grains constitute a granular gas with an entropic partial pressure p_d , this can be related with T_g and e (or a substitute) by a kind of gas equation (Sect. 4.6). Similarly the average water pressure p_w has a kinetic fraction which can be related with T_w . The balance of average momentum yields $p = p_d + p_w$ with the total pressure $p = \gamma_b d_b$ from specific weight γ_b and thickness d_b of the fluidized bed.

The underlying skeleton has a boundary pressure $p_{sb} = p_d$ from the fluidized bed, and a downwards seepage force from the gradient of p_w . The fluidized bed is excited erratically from above or below, otherwise it would settle and densify into a saturated skeleton. A turbulent motion of the free water without average shift causes a ‘seismic heating’ near the boundary of a saturated psammoid, so this is dilated to a fluidized bed. Stationary turbulence can lead to a kind of equilibrium with stationary bed depth d_b and equipartition of chaotic kinetic energy. Seismic waves propagating from the base of the skeleton (Sect. 11.4) cause its decay near the free surface. Their repetition with stationary average kinetic energy, i.e. stationary T_g (Sect. 4.6), leads again to a fluidized bed with a kind of flow equilibrium. In this case chaotic kinetic energy is continuously conducted upwards as thus T_g is higher below than above.

The thickness d_b and the granular base pressure $p_{sb} = p_{db}$ of a fluidized bed are evidently bigger with a stronger erratic excitation. Theories for quantification are hardly available and outside the scope of this book. Boundary values for the adjacent skeleton, i.e. p_{sb} and $p_w = \gamma_b d_b - p_{sb}$, may at best be estimated by matching observational data. This approach is inevitably imprecise and requires caution. d_b and p_{sb} cannot be measured precisely, both are only indicated by higher e and p_w in a mobile boundary zone. Fluidized beds can get stationary in the lab or in a factory, but they are transient in situ so that d_b and p_{sb} can hardly be predicted.

Various kind of *granular flow* can occur near free surfaces of saturated psammoid bodies under water. A fluidized bed with initially horizontal surface can be shifted aside by streaming water so that its surface gets uneven. Such displacements are as yet not predictable, therefore position and state of skeletons under moving fluidized beds can hardly be specified. The mobility is evidently enhanced by shaking. A zone of granular mud with inclined surface flows like an avalanche. It can arise by turbulent water flow or by shaking, and also by the collapse of skeletons with high void ratio or overcritical

inclination (Sect. 12.4). Such transient mud zones cannot yet be quantified by validated continuum models. Empirical specifications of their thickness and base stress components can at best provide estimates, position and state of skeleton boundaries are rather fuzzy.

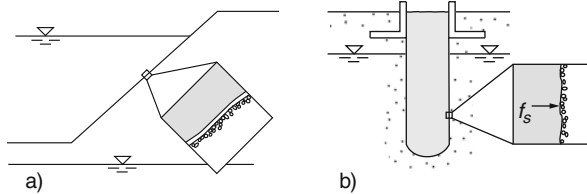


Fig. 10.1.3. Psammoid bodies with a skin: slope with cover (a), trench with slurry and filter cake (b)

Free psammoid surfaces under water can be kept in place by an inwards gradient of water pressure p_w via different kinds of *skins*. Figure 10.1.3. A skeleton boundary pressure is produced by a hydraulic pressure difference, $p_{sb} = \Delta p_w$ holds with a soft skin. A *membrane* (a) can be almost impervious, adjacent grains are punched in by p_{sb} and thus immobilized nearly as by an adjacent skeleton. p_{sb} deviates from Δp_w by longitudinal force and curvature of the membrane (more below), this can impede the use of membranes in so-called element tests. A membrane is evidently lifted by an outwards hydraulic gradient, then p_{sb} disappears and the skeleton decays. Rather elastic membranes can occur as base seals for the storage of fluids, except for the rim p_{sb} along seals is well defined. Seals with asphalt are anelastic, they can creep, melt or crack so that an adjacent psammoid boundary is less well determined.

A *filter cake* (b) consists of finer particles which are fixed at a psammoid skeleton by an inwards seepage force $f_s = \Delta p_w / d_f$. As long as Δp_w acts the thickness d_f grows with fines from an adjacent suspension. This accretion is reduced by densification of the filter cake which gets a peloid zone with low permeability k_f . An intrusion of the cake into the adjacent skeleton can be prevented by empirical filter rules (more in Sect. 10.2). Normal forces in filter cakes are bounded by state limits, but their influence on the skeleton boundary pressure p_{sb} via curvature is negligible. Filter cakes can seal water reservoirs and stabilize excavations (Sects. 12.4 and 14.2).

Mats are more pervious and less deformable than skins, in many variants they can keep in place psammoid surfaces under water, Fig. 10.1.4. A mattress of stones in a grid (a) can prevent a fluidized bed by providing a boundary skeleton pressure $p_{sb} = \gamma_m d_m$ (specific weight minus uplift γ_m , thickness d_m). p_{sb} is lower or higher if the mattress gets concave or convex, respectively, but this anelastic response can hardly be quantified (Sect. 10.3). The rim of

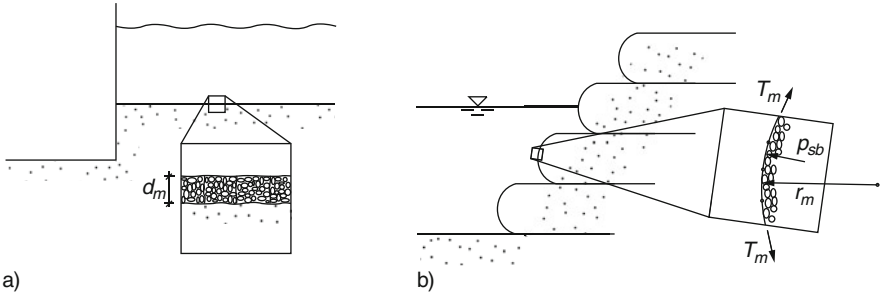


Fig. 10.1.4. Psammoid bodies with a mattress (a) or bulging membranes (b)

a mattress should slide along a solid surface without opening so that p_{sb} is maintained. A free rim can break by scours in an adjacent fluidized bed.

Geotextile mats (b) are more flexible than mattresses, they need a tensile force T_m and a curvature $1/r_m$ to produce a boundary skeleton pressure p_{sb} via

$$p_{sb} = 2T_m/r_m \quad (10.1.1)$$

in case of plane-parallelity. With double curvature and anisotropic resistance

$$p_{sb} = 2T_{m1}/r_{m1} + 2T_{m2}/r_{m2} \quad (10.1.2)$$

holds instead of (10.1.1) with two principal values of T_m and r_m . These are only estimates as T_m changes with the interaction of psammoid body and mat (Sect. 10.3). Curved mats have to be anchored in the ground and should be stressed by placement.

Consider now free psammoid surfaces *at the air*. With *full saturation* the suction $p_a - p_w$ cannot exceed the capillary entry pressure p_{ce} (Sects. 6.2). According to (6.1.2) p_{ce} is so small for psammoids that these are at best briefly saturated when they are exposed to the air. The low suction at the free surface, $p_a - p_w = p_s \leq \text{ca. } 1 \text{ kPa}$, may suffice to keep the grains together for a short while. An increase of $p_w - p_a$ by evaporation, lowering of groundwater-table or rapid shear dilation leads to capillary entry. The boundary condition $p_s = p_a - p_w$ may thus at best be of use for well-controlled model tests.

Humid psammoids have a capillary skeleton pressure at a free surface, $p_{sb} = p_{cs}$, which is determined by fines. It depends on the relative void ratio r_e and is maximal for a degree of saturation $S_r \approx 0.5$ (Sect. 6.2). p_{cs} enables steep and even overhanging free surfaces, but such parts of psammoid bodies tend to collapse by cracking. This may be controlled in model tests and can deepen the understanding of cracks (Sects. 12.4 and 13.7). Overcritical inclinations should be avoided in situ except for controlled excavations in small sections. Changes of p_{cs} by wetting or desiccation and by changes of density can hardly be avoided. With subcritical inclinations ($\beta < \varphi_{cs}$) it may suffice to assume a lower bound of $p_s = p_{cs}$ for free surfaces as long as p_{cs} has little influence on results of interest.

The sensitivity of humid free psammoid surfaces requires a kind of protecting cover anyway. A light flexible skin could serve as a rather impervious membrane with vacuum inside, but hardly in situ. Geotextile nets work with curvature, anchoring and prestressing as indicated further above. p_{cs} is needed to bridge coarse meshes and can be better maintained by adding humus and grass. A felt of living roots and psammoid with humus can maintain an optimal pore vapor pressure in dry and wet seasons. Only after having cared for a good skin numerical simulations including substitute skeleton boundary pressures can be worth the effort.

Pavements can work as skin or mat upon a humid psammoid body. They may be represented by simplified boundary conditions including traffic loads if their stiffness is negligible for the overall behaviour. For instance, a water-tight pavement between a strutted retaining wall and a building (Fig. 10.1.5a) may be substituted by a skeleton boundary pressure, viz.

$$p_{sb} = p_{cs} + \gamma_m d_m + p_t \quad . \quad (10.1.3)$$

Therein the capillary skeleton pressure p_{cs} may be neglected if the psammoid has no fines. One should keep in mind that p_{cs} is lost by desiccation or water access. The pressure $\gamma_m d_m$ by the pavement weight suffices to keep the skeleton together. A uniform traffic pressure p_t may be assumed for the design of the retaining structure, but not of the pavement (Sect. 10.3).

A layer of stones with a filter mat upon a psammoid slope (Fig. 10.1.5b) may be substituted by the normal and shear boundary stresses

$$\sigma_{sb} = \gamma_m d_m \sin \beta \quad (10.1.4)$$

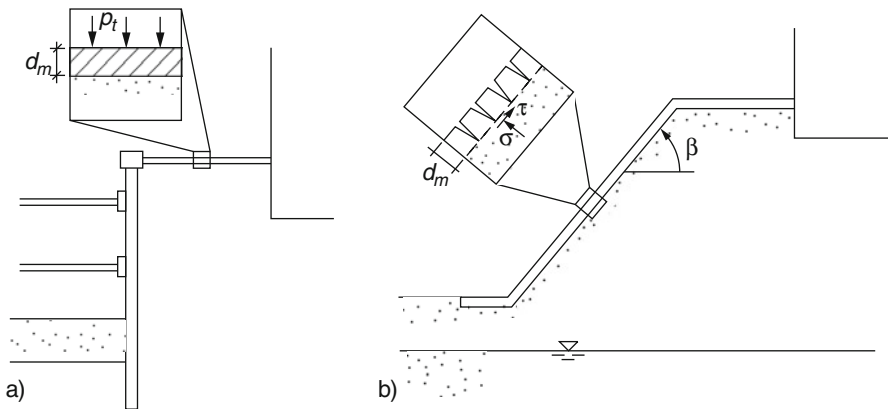


Fig. 10.1.5. Psammoid bodies with horizontal (a) and inclined pavement (b)

and

$$\tau_{sb} = \gamma_m d_m \cos \beta \tag{10.1.5}$$

as proposed already further above. A traffic load is thus left aside, the p_{cs} of the psammoid and the normal force in the pavement are neglected. As outlined further above p_{cs} is not warranted with respect to erosion, filter rules serve to avoid the penetration of stones (Sect. 10.3). Equation (10.1.4) and (10.1.5) may suffice for calculating displacements of neighboured structures by excavations and subsequent actions, but not for the pavement design. The access of water into the ground has to be prevented, otherwise the slope could collapse by a loss of suction.

Turning to surfaces of *peloids* we presume first *full saturation*. With soft particles and low permeability k_f changes of void ratio e by diffusion of pore water cause transient changes of skeleton pressure p_{sb} and pore pressure p_{wb} under boundary zones of variable thickness d_b . *Under water* a horizontal peloid surface without net attraction ($p_n \geq 0$, Sect. 6.3) is covered by mud (Fig. 10.1.6a). With resting water this cover grows by sedimentation from above or by swelling of the peloid below. The mud is easily shifted by moving water so that the surface gets uneven. With net attraction ($p_n < 0$) a free surface can be inclined at rest (b) although e is higher by sedimentation than with $p_n = 0$ (Sect. 7.1). Submerged peloids with $p_n < 0$ tend to crack at slopes, thereafter they go over into mud which flows down. Moving water cannot as easily mobilize a peloid with $p_n < 0$ as a mud. The ion transport by convection and diffusion via a free surface can change the ionic strength and can thus influence the peloid skeleton (Sects. 6.3 and 7.1).

Evolutions of mud covers cannot yet be predicted by validated calculation models, so they have to be judged empirically. Evolutions of adjacent peloid bodies may be simulated with v-elp or v-hyp and pore water diffusion by means of substitute pressures for free boundaries, viz. an estimated low p_{sb} for the skeleton and p_w from the water depth. This may suffice to estimate

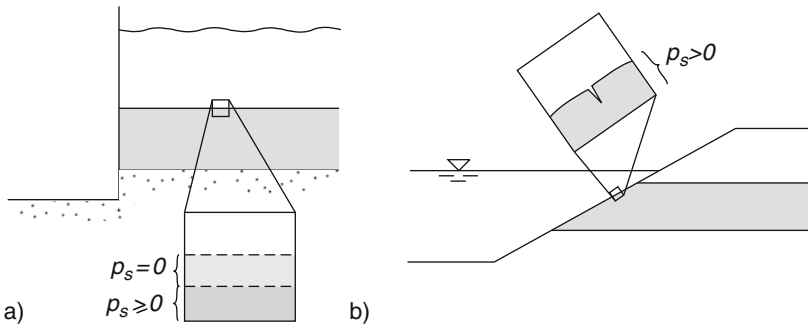


Fig. 10.1.6. Horizontal (a) and inclined (b) free boundary of peloid under water

evolutions with excavation (Sects. 12.4 and 14.2) or with structures which are hardly influenced by changes at free peloid surfaces (Sects. 12.4 and 14.2). Judgment is vital as the formation and flow of mud can endanger the stability. One had better cover submerged free peloid surfaces by pervious mats, thus a sufficient boundary skeleton pressure p_{sb} can be attained and mud problems can be avoided. Simulations with $p_{sb} = \gamma_m d_m$ (as outlined above for submerged psammoid) will then be more legitimate as the p_s -range of validated constitutive relations is not left.

Saturated peloids *at the air* have more suction than psammoids and can thus exhibit a substantial skeleton boundary pressure from the difference of air pressure p_a and negative pore water pressure p_w , $p_{sb} = p_a - p_w$. The neighboured relative humidity ψ_w and the net radius of curvature r_w of the pore water surface are related with $p_a - p_w$ by thermodynamic equilibrium conditions (Sects. 6.1 and 6.3). Often $p_a - p_w$ is determined by evaporation via ψ_w , which is enhanced by wind. Shrinkage with increasing p_{sb} grows into the interior by diffusion of pore water, the thickness d_b of the shrunk boundary zone increases with time t via. $d_b \approx \sqrt{t c_v}$ with a diffusion factor c_v which ranges from ca. 10^{-6} to $10^{-10} \text{ m}^2 \text{ s}^{-1}$ (Sect. 11.3). Peloids swell at a wetted free surface and turn into mud if they have no net attraction. The thickness d_b of the swollen zone grows again by $d_b \approx \sqrt{t c_v}$, but with a lower c_v (about 20 to 50% of the c_v for shrinkage). Repeated evaporation and wetting with period time t_p can lead to a boundary zone with $d_b \approx \sqrt{t_p c_v}$ and a nearly stationary peloid boundary beneath.

These estimates for boundary zones may be of use for controlled experiments. These may be considered as undrained in simulations, i.e. with constant e of RSEs, if d_b remains well below depth and breadth of the engaged soil body. The state limit value for the given e and isotropic compression with rate $D = D_r$ may be taken as initial p_s . Imposing gravity and boundary conditions including $p = p_{sb} + p_{wb} = p_a$ at free surfaces leads to a changing field of hydraulic height h_w in simulations with v-elp or v-hyp. Depending on the initial consolidation ratio p_e/p_s , the kind of isochoric deformation and the humidity ψ_w , gradients of h_w lead to seepage, particularly at free boundaries. Simulations with seepage could be carried out with measured rates of evaporation at shrinking boundaries, or with $p_w = p_a$ at swelling ones, in both cases $p = p_a$ gives $p_s = p_a - p_w$.

A *capillary entry* occurs at a free peloid surface if the suction attains the entry pressure, i.e. for $p_a - p_w = p_{ce}$ (Sect. 6.3). This happens by continued evaporation and/or with rapid isochoric deformations with high consolidation ratio p_e/p_s so that p_w drops strongly (Sect. 3.2). As long as a boundary zone is uniformly desiccated and its thickness d_b is well below the size of the whole soil body one may assume d_b and a capillary boundary skeleton pressure ($p_{sb} = p_{cs}$) for simulations. Otherwise evolutions with desiccation get rather chaotic by fingering of air fronts (Sect. 7.3) and/or by successions of cracks (Sect. 6.3). Then simulations with v-elp or v-hyp would be of little use as the soil bodies are not sufficiently defined. This lack of knowledge could be

reduced by experiments, but critical phenomena can principally confine the use of continuum models (Sect. 16.3).

Peloids near the air in situ are mostly *unsaturated and fissured*. A thin crust (i.e. $d_b \ll$ body size) may be substituted in simulations by a mat with empirical thickness d_m and suction $p_a - p_w$. Both values can hardly be predicted, and observations can be misleading. This inevitable indeterminacy grows with deeper air channels as these tend to be chaotic. Only in exceptional cases the evolution of cracks can be reasonably estimated (Sect. 10.2). Stiff fissured clays with suction may be considered as peloids with experimentally matched average parameters (Sects. 7.3 and 9.1). Boundary skeleton and pore water pressures may be matched empirically, but the predictability is rather poor.

Flooding of unsaturated peloid bodies leads to the inclusion of air and the formation of mud, both can hardly be quantified. A collapse with mud flow in situ can be prevented by a flexible and permeable skin. A felt of humus with living roots can serve to the purpose, thus natural slopes can survive dry and wet seasons. Synthetic mats with psammoid-peloid mixtures may also be of use if the humidity (and thus the suction) at their base is controlled. Simulations with empirical boundary pressures of skeleton and pore water may be justified if the stability is secured by a skin. Skins with curvature and anchoring may be judged as outlined further above for psammoids. Reinforced shotcrete covers are no skins in this sense, but brittle solids that interact with the ground (Sect. 10.3), so the suction behind them should be controlled.

To *sum up*, boundary conditions can be formulated for free surfaces of psammoid and peloid skeletons with pore water and/or gas, also with skins or mats, but decay or cracking of skeletons can cause indeterminacy and collapse. Thin boundary zones may be represented by assumed pressures of the adjacent soil. Fluidized boundary zones cannot yet be modelled and should be avoided by skins or mats. The boundary suction above the water table should be controlled to avoid cracking and fluidization. Model tests can help to better formulate boundary conditions.

10.2 Boundaries in the ground

New free boundaries can arise in psammoid and peloid bodies by the opening of gaps or cracks, as in Sect. 10.1 pore water and gas come into play. Shear bands may be considered as internal boundaries with interface conditions. Boundaries between psammoid and peloid zones can exhibit mutual penetration and mixing. Fictitious boundaries in the ground can be of use with symmetry or for separating near- and far-fields. Such cases are treated in the sequel, whereas interfaces of soils and solids are postponed to Sect. 10.3.

With suitable conditions *gaps* can open in *saturated ground* so that boundary conditions can be specified. For instance, a horizontal peloid layer upon a psammoid base can be *lifted* by rising the hydraulic height h_w in the base,

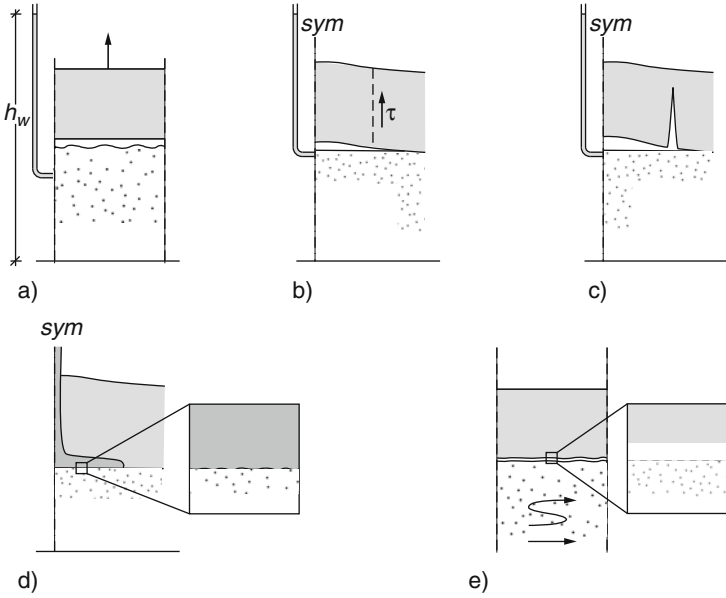


Fig. 10.2.1. Fluids between a peloid layer and a psammoid base: artesian water (a), injection of water (b), onset of hydraulic breakout (c), injection of a suspension (d), water film by base shaking (e)

Fig. 10.2.1. With horizontal uniformity this would occur if the total pressure at the peloid base is taken over by a water cushion (a). Without net attraction this determines p_w and means $p_s = 0$ while the skeletons below and above such a gap need not decay. The psammoid remains in place by gravity, the peloid is kept together by the upwards seepage force. The peloid swells in a lower boundary zone which widens by diffusion (Sect. 10.1) until a new equilibrium is attained.

A rather axi-symmetric *bulge* is lifted by injection of water via a vertical tube into a fine-grained base layer (b). The gap widens and p_w exceeds the overburden pressure as a shearing resistance τ is waked near the rim of the bulge. $\tau = c_u$ (undrained cohesion, Sect. 3.2) may be assumed along a thought cylinder (dashed in Fig. 10.2.1b), but a statical equilibrium with it is only necessary and not generally sufficient for stability. A rapid injection can lead to an almost cylindrical *crack* which grows from the rim of the gap where the peloid is more extended than elsewhere (c). Given an instantaneous gap with water pressure and rate of extension one may estimate whether a crack could arise (Sect. 6.3), but not what would happen thereafter (Sects. 8.4 and 16.3).

Prior to an outburst the indicated gaps would evidently close if the pore water pressure is reduced in the psammoid base. A gap would similarly arise by *injecting a suspension* from a tube that reaches the interface between peloid layer and psammoid base (d). The suspension does not penetrate into the

psammoid if its fines form a filter cake (cf. Fig. 10.1.3b). Similarly as an injection of water the one with a suspension produces a bulge and can lead to an outburst after cracking the peloid base. The outburst pressures are higher with the same quantity of injected fluid than with water as the suspension is more viscous, and as its spreading is impeded by the filter cake. If the injection is halted the enclosed suspension releases water and gets a peloid. Boundary conditions for skeleton and pore water along the gap with mud or peloid inside cannot be formulated precisely (cf. Sect. 10.3).

A gap with a *water film* is also produced between a peloid layer and its psammoid base by *shaking*, Fig. 10.2.1e. If the void ratio of the psammoid is higher than its lower bound (i.e. $e > e_d$) and the skeleton is shaken moderately it is densified and releases pore water rapidly near its surface. Seismic shear waves cannot propagate any more into the peloid layer, but can dilate the psammoid near its new free surface (Sect. 11.4). The water film closes after the end of shaking as the adjacent peloid can swell and consolidate thereafter. Stronger shaking can transform an upper part of the psammoid into a fluidized bed (cf. Fig. 10.1.2a). This kind of skeleton loss and regain cannot be captured precisely by boundary conditions, the formation of water films by shaking has to be judged empirically (Kokusho 1999). The impossibility of shear wave propagation thereafter is evident, the reconsolidation after shaking could be simulated.

Horizontal changes of such water films with spreading and closing are left aside for simplicity. The gaps outlined with Fig. 10.2.1 have in common that their shape is transient and not known in advance. They are thus *changing internal boundaries*, and boundary conditions for skeleton and pore fluid along them are also transient. The indeterminacy increases by a temporary loss or gain of skeletons along gaps. The issue gets more complex with large monotonous *shearing along gaps* between saturated psammoid and peloid bodies. This is indicated in Fig. 10.2.2 with an inclined peloid layer upon a psammoid base, for simplicity only with gravity and without lateral changes up to the onset of sliding.

When a water film arises by injection or shaking the peloid slides with acceleration even if the inclination is small. This leads to *shear mixing* in a fluidized bed of increasing thickness. The peloid layer floats and warps until it

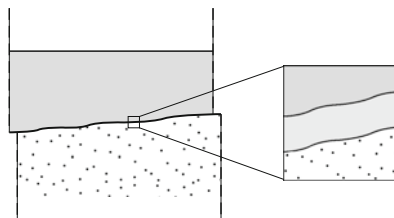


Fig. 10.2.2. Sliding of an inclined layer upon a fluidized zone

breaks so that the water bursts out and loses its excess pressure. An injected suspension can enhance sliding like a grease. It can be mixed with the adjacent peloid and/or psammoid, more so as an initial lateral uniformity gets lost. Sliding of a peloid layer along a looser than critical psammoid base can also lead to a fluidized bed, this gets mixed with adjacent peloid and can break out. Boundary conditions with such phase transitions and changes of composition cannot be formulated precisely for skeleton and pore water. For sake of completeness it may be mentioned that changing free surfaces of saturated peloid bodies with net attraction (Sect. 10.1) get more easily cracked and less easily mixed.

Turning now to *gaps in unsaturated soils*, we have to face more complex and less well-defined boundary conditions, Fig. 10.2.3. A crack can open in a *psammoid* body by extension, for instance in the shoulder of a steep slope by excavation (a). The normal skeleton pressure along its flanks equals the capillary skeleton pressure, $\sigma_{ns} = p_{cs}$, which depends on relative void ratio r_e and degree of saturation S_r (Sects. 6.2). (The capillary entry with full saturation will be considered below.) The tangential skeleton pressure σ_{ts} is bounded by state limits of the skeleton, which in turn imply changes of e and thus of p_{cs} even without change of water content w . With changing w , be it by seepage or via vapour, p_{cs} will change even more. Cracks in unsaturated psammoids are thus rather indeterminate internal boundaries which can at best be estimated (Sect. 12.4).

Flooding of unsaturated psammoids can lead to *gas inclusions* which may be considered as internal boundaries. A *macropore* (Fig. 10.2.3b) can have an excess gas pressure according to the capillary entry pressure, $p_g - p_w = p_{ce}$. It can arise by the access of water into a crack which disappears thus. The surrounding psammoid dilates easily if it is denser than critical with the low $p_s = p_{ce}$ at the macropore. A psammoid body with many macropores can arise from many cracks or a heap of lumps, it has a higher than critical overall void ratio and is therefore collapsible. Macropores in it can unite into *gas cushions* under a cover with finer particles and thus a much higher p_{ce} . Such cushions can enhance avalanches without shearing resistance as long as they do not break out (Gudehus 1998). Evolutions of gas cushions and of neighbored fluidized beds can as yet hardly be predicted.

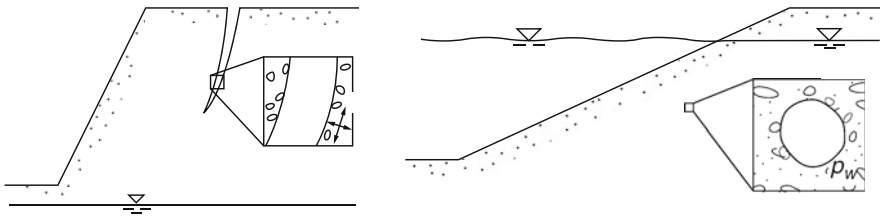


Fig. 10.2.3. Gas inclusions in psammoid bodies with cracks (a) or macropores (b)

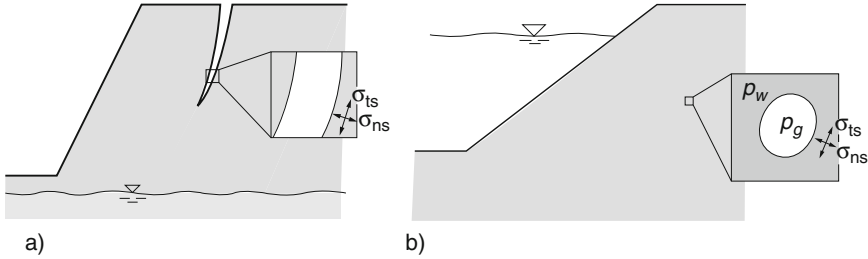


Fig. 10.2.4. As Fig. 10.2.3 with peloid

Various *cracks* can arise in *peloid* bodies which are exposed to the atmosphere. Shrinkage leads to a fractal succession of cracks with capillary entry and multiple diffusion (Sect. 6.3). A single crack can arise by extension, e.g. in the shoulder of a steep slope (Fig. 10.2.4a), and may be considered as a transient internal boundary. Without net attraction and other gas channels than cracks the normal skeleton pressure at a crack equals the capillary entry pressure, $\sigma_{sn} = p_{ce}$. It approaches the tensile strength and is determined by particle sizes and void ratio (Sect. 6.3). Tangential skeleton pressures σ_{ns} at cracks are bounded by argotropic state limits (Sect. 3.2), this may help to estimate such internal boundaries (Sect. 12.4). With gas channels in cracking peloids their capillary skeleton pressure determines the normal skeleton pressure, $\sigma_{sn} = p_{cs}$, but not precisely as there are many erratic cracks. Tangential skeleton pressures are again bounded by argotropic state limits, but limit void ratios therein depend also on p_{cs} (Sect. 7.2). Evolutions of cracks in peloid bodies with evaporation or water access along them are beyond the reach of present models.

Gas inclusions in otherwise saturated peloid bodies may also be considered as transient internal boundaries, Fig. 10.2.4b. They can arise by flooding of peloids with gas channels, particularly via cracks or between lumps, or by reactions which produce e.g. methane. Without net attraction ($p_n = 0$, Sect. 7.1) the skeleton normal pressure along them is determined by the capillary entry pressure, $\sigma_{sn} = p_g - p_w = p_{ce}$. As p_{ce} varies with particles sizes and void ratio, and as the other skeleton stress components can vary within wide bounds with a given σ_{sn} , gas inclusions can have various shapes. Assuming spheres may at best provide crude estimates of bubble sizes (Wheeler 1988). As with psammoids gas-filled macropores can enhance the decay of peloids into mud and can unite into gas cushions, particularly with hard particles and overcritical void ratios. With soft particles and high initial consolidation ratios gas inclusions enhance the swelling of neighbored peloid bodies so that the whole body gets softer, but this can hardly be quantified.

Shear bands are often considered as internal boundaries in order to judge the stability of equilibrium states. Their position and shape are assumed empirically, and varied to find unfavourable configurations so that soil bodies can

move like kinematic chains (sliding mechanismus). The shear stress τ along them is often assumed to be determined by cohesion and friction with normal stress σ via

$$\tau = c + \sigma \tan \varphi \quad , \quad (10.2.1)$$

or with pore pressure $u = p_a + p_w$ by an 'effective cohesion' and an 'effective friction' via

$$\tau = c' + (\sigma - u) \tan \varphi' \quad . \quad (10.2.2)$$

Let us briefly discuss how far these internal boundary conditions may be justified. For *psammoid* bodies under the groundwater table p_w may be given by hydraulic conditions and (10.2.2) is used with $c' = 0$, above the groundwater table (10.2.1) may be taken with $c = p_{cs} \tan \varphi'$. A peak friction angle φ_p may be taken for φ' , but this depends on the instantaneous relative void ratio r_e (Sect. 2.9) as does p_{cs} . Actual shear bands are snapshots of evolutions, the instantaneous r_e along them is not uniform and higher than before the localization (Sect. 8.2). With certain plane-parallel evolutions assumed shear bands with r_e may suffice for design estimates (Chaps. 12 and 13), but otherwise such assumptions can be misleading.

For saturated *peloid* bodies (10.2.2) is often used with assumed shear bands and $c' > 0$, but this is rarely justified with the combined pyknotropy, barotropy and argotropy (Sect. 3.8). Without diffusion of pore water τ would be determined already by the void ratio e and the stretching rate D as long as the peloid is ductile. With dilation, and thus with diffusion including a drift (Sect. 11.1), $\sigma' = \sigma - u$ can hardly be predicted, φ' has to be chosen rather at will and the matched 'effective cohesion' c' depends on the rate of dilation. As with psammoids shear bands with their non-uniform states evolve by initial and boundary conditions (Sect. 8.3), only in some plane-parallel cases they may be reasonably assumed. Equation (10.2.1) may sometimes be justified for peloid bodies with gas channels, but at best as far as the suction required for c is warranted and if c and φ are determined with suitable samples and test conditions. More than for psammoids (10.2.1) and (10.2.2) are otherwise irrelevant for the stability of peloid bodies. This holds also true for composites of psammoid, peloid and solid bodies.

The advice to abandon conventional assumptions for so-called limit equilibria with shear bands, except for design estimates in certain cases, may be considered as a sacrilege, but may help to avoid a dead end. It will be shown in Chaps. 11, 12, 13, 14 and 15 that practically relevant evolutions including shear localizations can be predicted with validated models wherein (10.2.1) and (10.2.2) do not occur. Evolving shear bands may therein be considered as transient internal boundaries, also with polar terms (Sects. 8.2 and 8.3) and re-meshing, but there is no need any more to assume them alongside with rather arbitrary stress conditions.

Filter criteria can be formulated for interfaces of different psammoid and/or peloid zones, Fig. 10.2.5. They are to assure that different skeletons

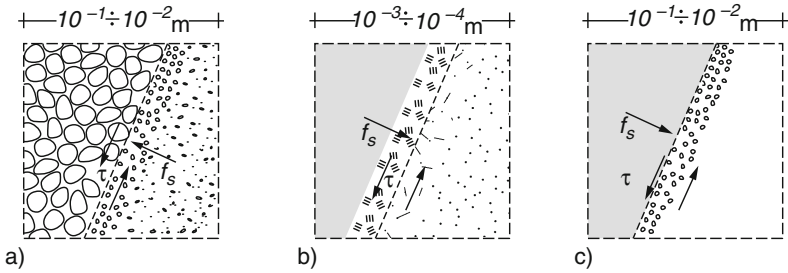


Fig. 10.2.5. Filter effects at interfaces in the ground at different scales: gravel at sand (a), peloid at granular peloid (b), peloid at psammoid (c)

do not mix with each other so that such internal boundaries would get fuzzy, particularly by seepage forces f_s . The boundary between two different psammoids (a) can remain sharp if finer grains cannot intrude into a coarser skeleton. This may be judged via grain size distributions and requires a skeleton pressure p_s . Two neighbored grain skeletons can still get mixed by mutual shearing and by deformations with reversals. Rapid alternating deformations can produce a kind of diffusion of different grain fractions by a granular temperature (Sect. 4.6), then skeletons can no more be clearly identified. With gas channels finer grains are better kept in place by capillary bridges (Sect. 6.2).

Interfaces of different saturated peloids (b) cannot be judged only by shapes and sizes of adjacent particles. The boundary gets fuzzy by thermally activated diffusion of neighbored pore fluids (Sect. 6.1), and also of small particles without net attraction. This diffusion is enhanced by rapid and/or alternating deformations, then peloid skeletons can hardly be identified near interfaces. Filter criteria for such cases may at best be established by experiments with realistic initial and boundary conditions including the fractions of solubles. Fortunately the mutual diffusion is so slow in many cases that it may be neglected.

Interfaces of psammoids and peloids (Fig. 10.2.5c) may be judged by mechanical criteria for both sides, they can get fuzzy in different ways. Without net attraction and pore gas the peloid can intrude gradually into the psammoid skeleton by swelling and creep. The intrusion can be slow as long as the peloid has a high consolidation ratio p_e/p_s (Sect. 3.2), then the pore water pressure p_w in the peloid is lower than in the psammoid. The intrusion can be halted by the accumulation of less fine peloid particles in denser bridges between psammoid grains. A filter cake can thus be produced from a suspension by seepage towards the psammoid (Fig. 10.1.3b). Peloids without intermediate fines can form bridges by means of net attraction $p_n < 0$ (Sect. 7.1).

A cut through particle contacts along an interface (dashed in Fig. 10.2.5c) would reveal a high force-roughness of the peloid and a lower one of the

psammoid. Therefore the peloid gets easily mobilized if it has no intermediate fines and/or no $p_n < 0$. With high gradients of p_w and coarse psammoids the seepage force f_s can transform stiff clays into mud (Sects. 8.4 and 16.3). Mixing along the interface is enhanced by shearing, more so by alternations which lead to diffusion by a kind of temperature (Sect. 5.5). Interfaces can evidently remain sharp with suction in the peloid, this requires open gas channels in the adjacent psammoid. With all these effects filter criteria for psammoid-peloid interfaces can only be quantified by experiments. Therein boundary conditions off the interface for the skeleton (stress and/or displacement components) and the pore fluid (water with solubles and gas) should be adapted to the intended application. In the majority of cases as considered in the following chapters such interfaces may remain sharp, but this should not always be taken for granted (Sect. 16.3).

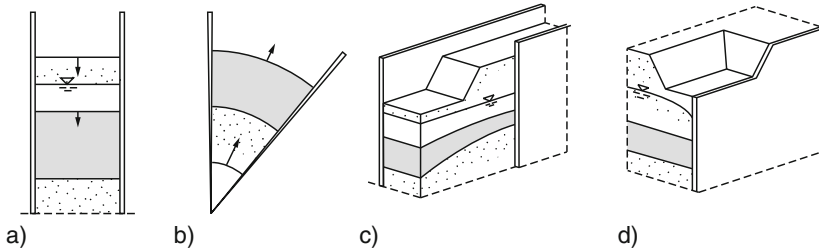


Fig. 10.2.6. Symmetries: soil column (a), radial symmetry (b), plane-parallelity (c), vertical symmetry plane (d)

Fictitious boundaries may be assumed in soil bodies with *symmetry*, Fig. 10.2.6. One-dimensional evolutions are considered in Chap. 11 with soil columns which are confined by thought smooth rigid walls (a). These substitute the absence of lateral changes, particularly without lateral stretching. Lateral seepage is excluded with this symmetry, so the fictitious walls are impervious. Radial symmetry (Sect. 11.7) comes up to a smooth cylindrical or spherical wall (b) which expands or shrinks by assumed amounts, while pore pressure or seepage velocity are assumed with the same symmetry. For plane-parallel evolutions (Chap. 12) soil discs may be imagined with two smooth fixed confining walls (c), but not in case of anti-plane shaking (Sect. 12.5). A vertical symmetry plane, which will repeatedly be assumed in Chaps. 12 and 16, may be considered as a smooth fixed wall (d).

Fictitious boundaries for symmetry must not be confused with real ones. The assumed symmetry may be attained by favourable initial and boundary conditions, but it can get lost by bifurcation with localization and/or collapse. A desired symmetry may be approached in experiments with real boundaries which resemble fictitious ones, but full equivalence can thus hardly be achieved.

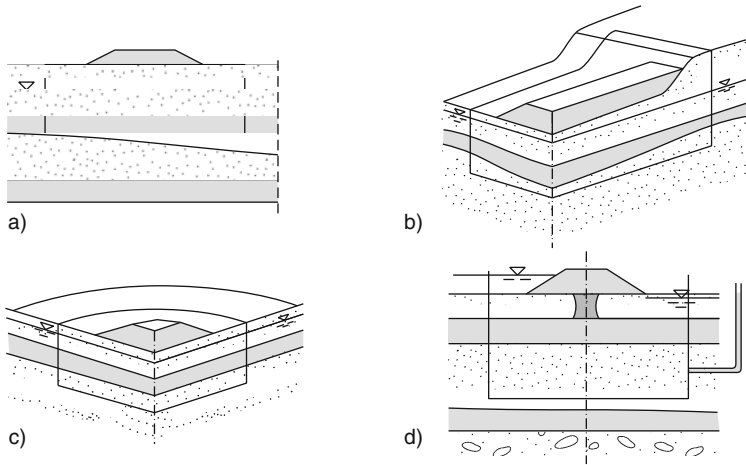


Fig. 10.2.7. Fictitious boundaries between near- and far-fields with a long (a) or short dam (b), with a heap (c) and with axial symmetry (d)

Fictitious boundaries may also be introduced in order to *separate near- and far-fields*, Fig. 10.2.7. By definition a far-field is not influenced by the near-field, but the latter depends on the former. The boundary between both and conditions for it have to be assumed, such assumptions can only be justified by considering boundary value problems without such separations.

It may often suffice to bound the near-field by a fixed base and a smooth or rough fixed wall. The wall appears twice for plane-parallel evolutions, in general without a vertical symmetry axis (a). Base and walls may be assumed so far away from the near-field range of action (and of major interest) that along them changes of state variables are negligible. Plane-parallelity may be justified if the near-field exhibits nearly the same cross sections over a reasonable length, but the fictitious boundary is not really fixed (b). The slenderer a near-field with equal cross sections, the more would the ground move under its fictitious base, and the farther off should fictitious walls be placed. With axial symmetry base and wall could be assumed closer to the range of action (c).

Appropriate near-field boundaries should also depend on the composition of the ground and on the kind of actions. Their choice and specification require judgment, comparative calculations for justification without the desired symmetry are often too expensive. Hydraulic conditions along assumed near-field boundaries should likewise be chosen with care. It may often suffice to assume hydraulic heights at psammoids and no seepage normal to peloid sections (d), natural compositions are partly indeterminate anyway (Sect. 9.2).

Absorbing boundaries may be assumed for near-fields in order to substitute the radiation of waves into a far-field. Within the theory of elasticity frequency-dependent dampers can serve to this purpose. This may suffice for far-fields of soils with repeated propagations with small amplitudes as then

the response can get nearly elastic (Sects. 4.2 and 5.2). The position of an absorbing boundary should be chosen so that outside of it the amplitudes are small enough. This choice requires judgment and monitoring for control, comparative calculations for justification would be too expensive.

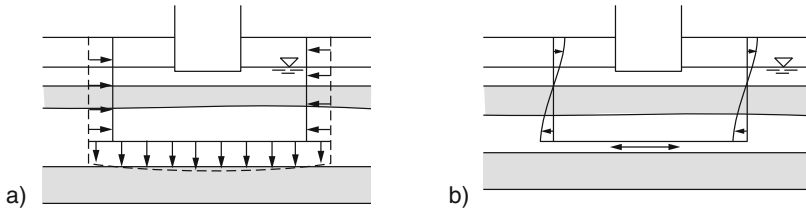


Fig. 10.2.8. Near- and far-field boundary with slow displacements (a) and shaking from below (b)

Active far-fields may be represented by choosing and specifying their boundaries around affected near-fields, Fig. 10.2.8. A deep-seated removal of solids or fluids may be substituted by imposing a depression of a base and a changing distance of opposed walls (a). Seismic far-fields may be represented by a shaking base and walls with propagating waves (b). Such substitutes may be justified by field data, more comprehensive seismic boundary value problems are hardly feasible. Such simplifications are no more justified to capture the influence of neighbored technical actions. If construction activities in or at the adjacent ground could impair existing structures they should and can be incorporated into a more comprehensive boundary value problem.

To *sum up*, positions of and conditions for boundaries in soils can rarely be specified precisely, but the required assumptions can be supported by observations and/or more comprehensive models. Evolutions of gaps, cracks and peloid-psammoid interfaces with coupled diffusion of constituents can at best be estimated empirically. Shear bands with shearing resistances may be assumed for design estimates, but such assumptions are debatable and not needed with better models. Fictitious boundaries and conditions for them may be of use to represent symmetries or to separate near- and far-fields, they can be justified by considering more comprehensive systems.

10.3 Soils at solids

Only few models for interfaces of psammoids and peloids with solids are ready for use. They cannot catch all details of composition and state, and their validity is restricted as skeletons can decay and arise again. Interface models are needed for the *soil-structure interaction* (SSI), their choice depends also on the deformations of solid bodies and on their displacements relative to the ground.

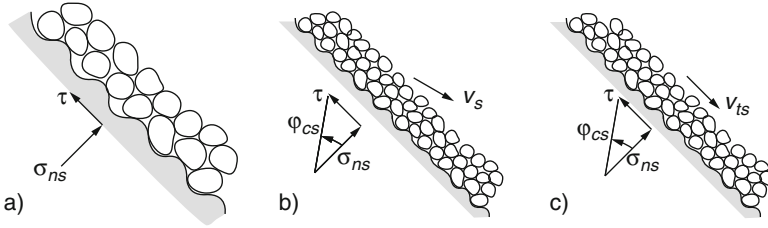


Fig. 10.3.1. Interfaces of psammoid and rough solid; grains fixed at a rough surface (a), boundary zone with (b) and without dilation (c)

The grains of *saturated psammoids* in contact with *rough surfaces* cannot be shifted and rotated past the solid, Fig. 10.3.1. Often the solid is far less permeable than the psammoid, then the relative normal seepage velocity is negligible, $v_{nw} = 0$ (a). The void ratio near the surface can range within the p_s -dependent bounds of skeletons (Sect. 2.2), but is less variable as the grains at the solid are fixed. The skeleton stress vector with normal and shear components, σ_{ns} and τ (for simplicity only in-plane), is transferred to the solid with a less uniform spatial distribution, i.e. a higher force-roughness (Sect. 4.3) than off the surface. Polar stresses can occur near the solid and can be related with the force-roughness at the interface (Sect. 8.2).

Simplified models are often justified as details of psammoid boundary zones are rarely known nor important for the overall behaviour (SSI). With lower than critical stress obliquities, i.e. for $|\tau|/\sigma_{ns} < \tan\varphi_{sc}$ (Sect. 2.9), simple psammoid RSEs may be assumed along the interface which are displaced and deformed together with the solid. With reversals the force-roughness may be assumed to be the same as off solid surfaces although it is higher (Sect. 4.6). Overcritical obliquities ($|\tau|/\sigma_{ns} > \tan\varphi_{sc}$) can occur in denser than critical dilating *shear bands* at rough solids (Fig. 10.3.1b) alongside with polar stresses (Sect. 8.3). Evolutions up to peak stress obliquities and dilation ratios may be modelled by RSEs without polar terms. SSIs may thus be captured as long as the grain size d_g is well below the solid body size d_b , say $d_g/d_b \leq 10^{-3}$ (Tejchman 1997). Otherwise simulated SSIs can depend on chosen element sizes.

Sliding along rough solids implies critical states in boundary zones of some grain diameters thickness, Fig. 10.3.1c. It may be captured by the *stick-slip condition*

$$\begin{aligned} |\tau|/\sigma_{ns} &= \tan\varphi_{sc} & \text{for } v_{ts} \neq 0 & \quad , \\ |\tau|/\sigma_n &< \tan\varphi_{sc} & \text{for } v_{ts} = 0 & \quad . \end{aligned} \quad (10.3.1)$$

Therein v_{ts} denotes the tangential velocity of the skeleton at the shear band relative to the solid. Equation (10.3.1) may suffice if the band is thin against the body size and as details of the band do not matter, particularly for continued sliding. The onset of sliding or its reversal can thus at best be roughly captured. This simplification is also justified if the initial skeleton state at the solid is not well known.

Rough pervious solids in contact with psammoids can work as filters. As with Fig. 10.3.1a the solid pores should be small enough to keep adjacent grains, particularly if the skeleton experiences reversals. Elastic *membranes* are rough by the penetration of grains and rather impervious (Sect. 10.1). If they are stretched with curvature the normal pressure of the adjacent skeleton is changed by the longitudinal membrane force via (10.1.2). Adjacent psammoid RSEs may be assumed as off the interface although the skeleton is changed by the membrane.

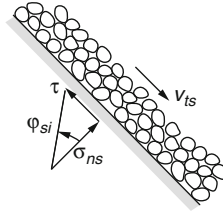


Fig. 10.3.2. Stationary sliding along a smooth surface

Psammoid grains can be rotated and shifted past a *smooth* solid surface, Fig. 10.3.2. The void ratio is higher near the surface and the grains along it are more ordered than in an RSE. A smooth solid cannot have open pores so that its permeability is quite low and often negligible. For a given mean skeleton pressure p_s shear and polar stresses cannot get as big as at rough solids (Tejchman 1997). A stick-slip condition can be formulated as

$$\begin{aligned} |\tau|/\sigma_{ns} &= \tan \varphi_{si} & \text{for } v_{ts} \neq 0 &, \\ &< \tan \varphi_{si} & \text{for } v_{ts} = 0 &, \end{aligned} \quad (10.3.2)$$

with a lower interface friction angle than the critical one in (10.3.1), $\varphi_{si} < \varphi_{sc}$. Outside a boundary zone of usually negligible thickness simple psammoid RSEs may be assumed which are fixed or slide along the wall according to (10.3.2). Evidently a solid is harder than the grains at a smooth surface, its slight p_s -independent waviness dominates φ_{si} .

Fluidized zones can arise in saturated psammoid near a solid, Fig. 10.3.3. If the solid body is shaken a part of the neighboured skeleton can be diluted into a granular fluid with negligible shearing resistance (a). A strong earthquake can produce a fluidized bed (cf. Fig. 10.1.2b) so that a solid body can tilt and sink (b). The pressure in a fluidized zone is nearly isotropic, this results from the pore water and the granular temperature (Sect. 4.6). For lack of validated models the extent of fluidized zones has to be estimated empirically. Because of the danger one should avoid fluidized zones, e.g. by a pervious mattress. Their influence on displacements of solid bodies cannot be predicted with models for grain skeletons as these get lost partly and temporarily.

Gaps along and *edges* at solid surfaces can lead to a dilation of saturated psammoid skeletons, Fig. 10.3.4. An opening gap produces a free surface of

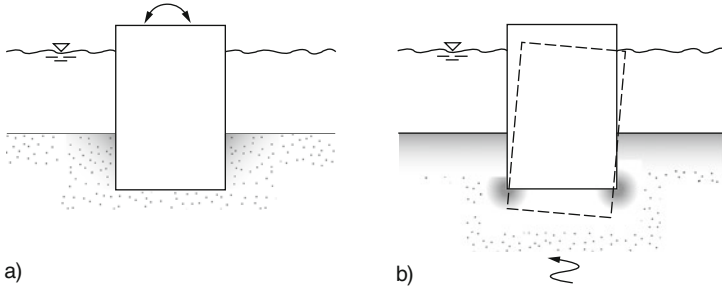


Fig. 10.3.3. Fluidized zones in saturated psammoid near solid bodies by shaking from above (a) and below (b)

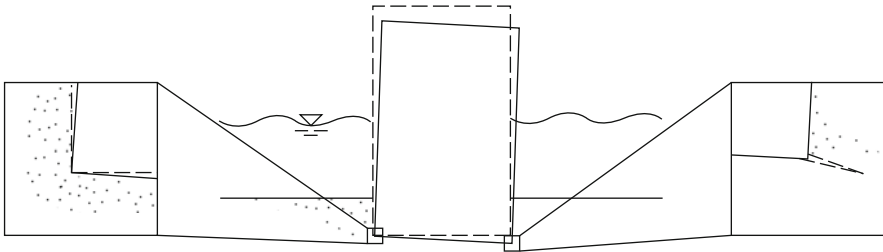


Fig. 10.3.4. Localizations at edges of a tilting solid in psammoid: gap (*left*), shear band (*right*)

the skeleton (left insert). Depending on inclinations, void ratios and hydraulic gradients the skeleton is deformed and can get dilated up to decay (Sect. 10.1). If an edge is shifted into a denser than critical skeleton this is dilated along a shear band which evolves from the edge (right insert). The onset of this evolution may be modelled (Sect. 8.2), but hardly its further course (Sect. 13.4). Repeated opening and closing of gaps or penetration and retreat of edges enhance the dilation, particularly with so short periods that the average pore pressure increases. Thus fluidized zones can arise temporarily which cannot be captured with psammoid models. Empirically they may be kept within harmless bounds, the re-densification with many small alternations (Sect. 4.7) is of advantage.

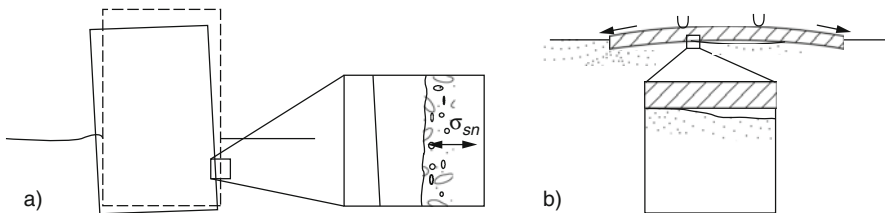


Fig. 10.3.5. Gap between psammoid and solid by tilting (a), or by bending with traffic (b)

Pore gas in psammoids has no effect on interfaces with solids if it sits in bubbles between grains, only the pore fluid gets more compressible (Sect. 6.2). Gas-filled *gaps* along interfaces matter differently when they are open or closed, Fig. 10.3.5. Gaps with gas channels up to the atmosphere can open without dilation of the skeleton as far as this is kept by the capillary skeleton pressure p_{cs} (a). Such evolutions may be modelled by *contact elements* which open if the skeleton normal stress σ_{ns} disappears and then switches to $\sigma_{ns} = p_{cs}$ (Sect. 15.4). Repeated opening and closing of such gaps can densify skeletons and increase p_{cs} as long as gas channels are not closed due to high degrees of saturation (Sect. 6.2).

Enclosed *gas cushions* along solid surfaces can arise and lead to dilation or even decay of psammoid skeletons. For instance, air can be enclosed under a slightly convex plate upon psammoid if this is flooded from the sides, Fig. 10.3.5b. Densification by traffic can lead to a gas cushion upon saturated psammoid so that subsequent traffic punches the plate and dilates the skeleton. Such cases should be avoided by design and maintenance.

Turning now to *saturated peloids*, we first consider stick-slip conditions. Along a *rough impervious* solid surface

$$\begin{aligned} |\tau| &= c_u & \text{for } v_{st} &\neq 0 \\ |\tau| &< c_u & \text{for } v_{st} &= 0 \end{aligned} \quad (10.3.3)$$

may be assumed with the cohesion c_u for undrained shearing without drainage (Sect. 3.8) and the slip velocity v_{st} . Fixed elements ($v_{st} = 0$) can be modelled with v-el-p or v-hyp, thus c_u is proportional to the e -equivalent pressure p_e and to $(D/D_r)^{I_v}$ by (3.3.11) with stretching rate D , reference rate D_r and viscosity index I_v . A shear band arises with slip ($v_{st} \neq 0$), the reduction of τ by polarization can be compensated by its increase from viscosity (Sect. 8.3). Thin layer shear tests with appropriate e and different shearing velocities can provide c_u and I_v .

Equation (10.3.3) may also be used for peloids at a *rough pervious* solid surface. This is justified by thin layer shear tests with hydraulically open filter plates (Sect. 8.3). The pore water pressure p_w or the normal seepage velocity v_{wn} has to be given, v_{wn} or p_w is determined by the coupling of skeleton and pore water in the adjacent peloid. Rapid shearing would lead to (10.3.3) as then the seepage cannot cope so that p_w changes. Simulations should incorporate the permeable solid body with its hydraulic conditions. In the simplest case of slow shearing p_w at the interface is determined by the hydraulic conditions.

Filter criteria can be formulated for rough pervious solid surfaces in contact with saturated peloids similarly as outlined with Fig. 10.3.1b. Peloid particles are more easily mobilized by seepage forces if the solid is deformed, particularly with reversals. For a saturated peloid at a *smooth solid*

$$\begin{aligned} |\tau| &= c_a & \text{for } v_{st} &\neq 0 \\ |\tau| &< c_a & \text{for } v_{st} &= 0 \end{aligned} \quad (10.3.4)$$

may be assumed with an *adhesion* $c_a \leq c_u$. Fixed elements ($v_{st} = 0$) can again be modelled by v-elp or v-hyp. The sliding resistance c_a is a lower fraction of c_u if more flat particles are aligned at a hydrophilic solid. c_a depends also on the ionic strength and is lower at a hydrophobic solid, so it can only be found by experiments. Evidently smooth solids are impervious, p_w along them is determined by the interaction of skeleton and pore water in the adjacent peloid.

Elastic *membranes* are more often rough than smooth with respect to saturated peloids as harder particles are penetrated and softer fine ones adhere. The permeability of membranes is mostly lower than the one of peloids, but seepage through them can matter with high hydraulic gradients. A difference of normal pressures inside and outside of a membrane is given by its curvature and longitudinal forces via (10.1.2).

Fluidized zones can arise in peloids near solids similarly as in psammoids (cf. Fig. 10.3.3). Alternating deformations with higher amplitudes than for psammoids are needed for the transformation into mud, alongside with it pore pressures get more irregular due to cracks and breaking lumps. *Gaps* and *edges* at saturated peloids can lead to dilation up to skeleton decay similarly as indicated with Fig. 10.3.4. With viscosity and net attraction or repulsion of particles prediction models are farther out of reach than for psammoids. Experiments can provide some insight. Bühler (2006) found e.g. that fluidized zones near piles moving into and from clay under water can hardly be avoided near free surfaces (Sect. 15.4). Empirically their influence may be kept small, but more research into fluidized zones will be needed to overcome their present indeterminacy.

Pore gas can matter in peloid-solid interfaces as capillary entry pressures p_{ce} are far higher than for psammoids. Small gas bubbles in a peloid can hardly accumulate along a solid, therefore they should only be taken into account for the compressibility of the bulk peloid. Gas-filled gaps along solids can be longer and wider than with psammoids. They can open along a cracking solid by capillary entry from a free surface or by cavitation at a base. The required suction is lower at a smooth surface than at a rough one. As long as the peloid is saturated the difference of gas and pore pressure equals the capillary entry pressure, $p_g - p_w = p_{ce}$ (Sect. 6.3).

The widening or closing of such gaps may be estimated by means of contact elements as for psammoids. Desiccation or stretching can lead to cracks in the peloid which are hardly predictable (Sect. 6.3). Irregular gas channels can open and enhance the dewatering. Closing of gaps at such peloids can lead to their densification as long as pore gas can evade. Otherwise, particularly if such peloids are flooded, *gas cushions* can be enclosed along solids with excess gas pressure $p_g = p_w + p_{cs}$. The SSI can thus get rather indeterminate and more detrimental than without gas cushions, particularly with repeated widening and closing of gaps. These should therefore be avoided by empirical design, monitoring and counter-measures.

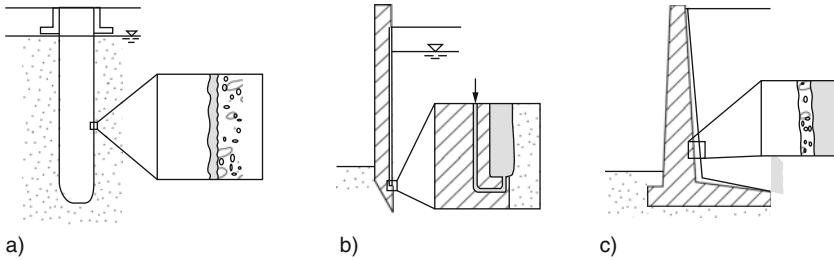


Fig. 10.3.6. Fine-grained interfaces between psammoids and solids: remnant of filter cake (a), grout injected for sliding (b), drainage cover (c)

Interface zones with various compositions can arise from placement of solids and soils and from subsequent evolutions, Fig. 10.3.6. A filter cake along a psammoid from a suspension (cf. Fig. 10.1.3b) is densified into a peloid zone after placement and curing of fresh concrete (a). Depending on the surface roughness the stick-slip behaviour may thus be captured by (10.3.1) with an intermediate critical friction angle φ_{cs} , whereas p_w can be determined via the psammoid.

Injection of mud via openings in solids leads to wider and less uniform peloid interface zones (b). Spreading of gaps and sliding with injected mud may be judged by means of (10.3.3) without seepage. The latter can occur along psammoids already during the injection, however, and the influence of this densification can hardly be predicted. Injected mud can break through towards a free surface (cf. Fig. 10.2.1c), such chaotic evolutions are hardly predictable (Sect. 16.3).

A psammoid zone can be placed between a solid and a peloid for controlling the pore water pressure p_w (c). In addition to filter criteria for the psammoid-peloid interface (cf. Fig. 10.2.5c) sufficient widths and outlets are needed for the psammoid so that p_w cannot rise too much in it. Mixing by placement and by reversals afterwards can spoil such a drain, the psammoid is better enclosed by a grid or substituted by a filtrating solid.

Shearing of solids past soils can lead to an accumulation of fines in an interface zone. Softer and flatter peloid particles can more easily adhere to a hydrophilic smooth solid than fine grains. Softer grains and aggregates of peloid particles are more decomposed in a shear zone due to its stronger force-roughness than the soil farther off the solid. Such evolutions are not predictable yet with validated models, one has to assume therefore composition and state of resulting boundary zones. These may then be captured by the stick-slip relations (10.3.2) or (10.3.3) with experimentally determined parameters.

Topological changes require additional concepts for modelling interactions of solids and soils, Fig. 10.3.7. It was outlined further above how transient gaps can spoil the usually desired SSIs without loss of contact. Their numerical sim-

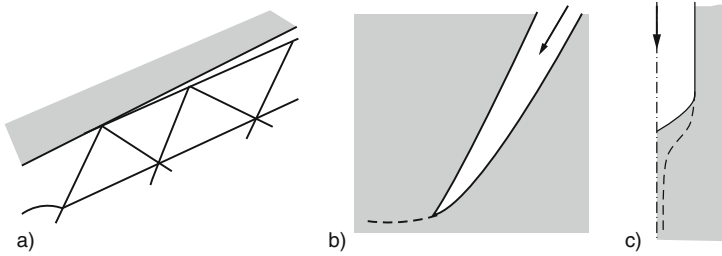


Fig. 10.3.7. Topological changes by opening (a), cutting (b) and penetration (c)

ulation requires changing finite element meshes (a) with transition conditions for the loss or gain of contact. Such continuum models with a changing tip of a gap are as debatable as those for cracks in solids (Sects. 8.1 and 15.4).

Cutting of soil by a sharp solid edge means separation and lateral soil displacement (b). A shear band or a crack can run ahead and reach a free surface if the solid body is guided like a shovel. The separation of the soil skeleton by an edge may at best be modelled for saturated peloids without seepage and cavitation as one may then assume a non-linearly viscous fluid (Winter 1979). Otherwise a changing tip can hardly be captured by continuum models, these may at best provide qualitative estimates. For instance, the driving resistance of psammoid at the edge of a sheetpile or a tube is higher with harder grains and denser skeletons, and lower with reversals or torsion respectively, but this cannot be quantified without observations.

The *penetration* of a solid into soil does not require an edge or a tip, but implies lateral displacements not only in one plane. Even with radial symmetry (Fig. 10.3.7c) RSEs at the penetration front cannot be followed up as their deformations are unlimited. One may at best capture saturated peloids without seepage in a kind of stationary fluid flow. Peloids with seepage, and psammoids without or with the same, may be captured by a substitute smaller central cylinder and an hour-glass transition (dashed in the sketch, more in Sect. 14.3). A proper simulation of topological changes of soils by penetration is outside the reach of present models.

Solid gaps can open or close so that adjacent soil moves in or out. For instance, if two adjacent edges spread a psammoid with not too big grains can flow in between and could not be fully extruded if the edges approach again. The grains would move more easily with seepage forces and reversal, then the skeleton can decay. A peloid could flow more easily into or out of a gap as long its equivalent pressure p_e is low and does not increase by consolidation. Needless to explain that such evolutions can hardly be captured by continuum models. As with filters one should avoid such gaps by design, monitoring and counter-actions.

To *sum up*, interfaces of solids and soils can be fairly well modelled for successions of stick and slip, but not as well for variable openings or penetration and hardly if the skeleton decays temporarily. Roughness, permeability

and deformations of solid bodies have to be taken into account. Numerical simulations are hardly feasible for tips and edges where skeletons open.

10.4 Placement and removal

Placement and removal of soils and solids imply complex evolutions which cannot be caught in all details by the methods outlined in this book. It is necessary and legitimate, however, to capture average changes of composition, shape and state by means of simplified substitutes. This can be justified to a certain extent by attractors in the large with the aid of observations and simulations. The following overview with psammoids, peloids, pore fluids and solids is rather condensed, more will be said in later chapters without exhausting the issue.

Consider first *psammoids under water* with different degrees of homogeneity. A so-called *element* is produced by filling into a solid device and can be brought to a homogeneous initial state (Fig. 10.4.1a, numbers for steps of the evolution). A skeleton arises by placement and attains thus a non-homogeneous field of void ratio and stress components (as far as these can be defined by configuration and contact forces of grains). Subsequent changes of skeleton and pore water are produced via solid sample boundaries. With suitable boundary conditions the skeleton can approach uniform state limits or state cycles. These attractors and transitions between them serve to identify psammoids (Chaps. 2 and 4). Even with uniform boundary conditions

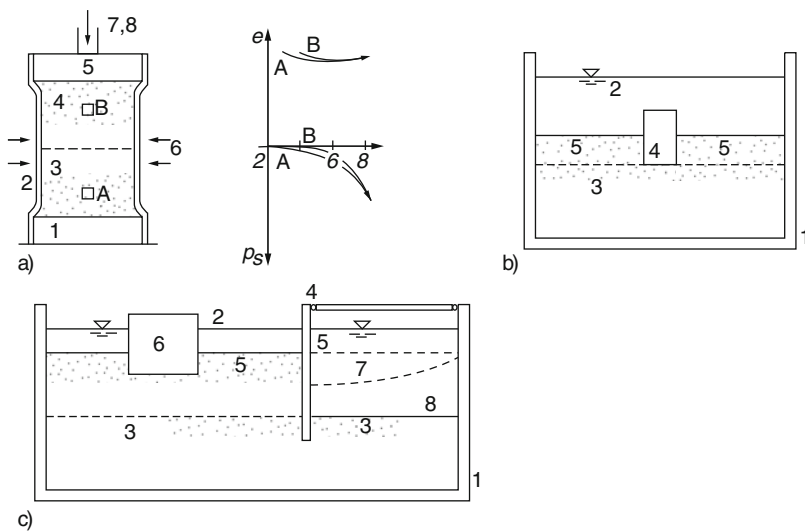


Fig. 10.4.1. Placement and removal of psammoids in the lab: sample in element test (a), model test with placement (b) and with excavation plus placement (c). Numbers denote the sequence

grain skeletons can lose their uniformity by shear localization or decay. Some localizations may be captured with polar quantities (Sect. 8.2), but strange attractors for such critical phenomena are not well understood (Sect. 16.3).

In a *model test* a psammoid may be placed under water in a solid vessel alongside with a solid body (Fig. 10.4.1b, again with numbers for steps of the evolution). Composition and state of skeleton and solid should be produced so that the subsequent response is the same in repeated tests with the same boundary conditions. This can be achieved with different kinds and sequences of placement steps, but not *ad libitum*. For instance, pumping in a granular mud and driving in a solid body can lead to a loose skeleton with an embedded solid at an equilibrium so that variations of this procedure do not change the subsequent behaviour. A denser skeleton with an embedded solid can be produced by different kinds of filling and shaking so that the subsequent response is the same. Differences in the skeleton near field around the solid can be swept out by suitable motions of the embedded solid. The independence of the subsequent behaviour on details of placement steps indicates that the thus produced state of the skeleton is an *attractor in the large*.

As far as such attractors are attained the placement of skeletons and solids can be simulated by means of constitutive models. In the simplest variants skeleton and solid are first assumed to be weightless with a uniform isotropic pressure p_{so} and a desired initial void ratio e_o , then gravity is slowly imposed so that a field of skeleton and solid stress and void ratio is generated by means of *elp* or *hyp* and boundary conditions. Improvements could be achieved by this procedure with simplified steps, and also by suitable boundary conditions during and after these steps. For instance, one may subdivide the placement into three steps and impose few small displacement cycles. Hydrostatic pore water may be assumed for simplicity. Comparative simulations could show how differences of assumed steps influence the subsequent behaviour, e.g. for the resistance of the skeleton to shift the solid towards it. The average void ratio in the near-field is more important than its spatial distribution (Sects. 13.1 and 14.4). Test results could be reproduced if the placement leads to the same void ratio field, in particular near an embedded solid.

Such attractors in the large are heuristic and may be justified by physical arguments without mathematical rigour. Actual placements may imply localizations and fluidized zones which can scarcely be modelled. What counts is the resulting shape and state of the skeleton. The placement can lead to a rather erratic spatial distribution of skeleton stresses. This *force-roughness in the large* is rather indeterminate and can be swept out in subsequent evolutions. Suitable initial void ratios and boundary conditions can then lead to limit or cyclic state fields. Such attractors in the large do not agree with those by placement in general, ranges of attraction can only be explored by comparative experiments and simulations. Fields with uniformly high relative void ratio ($r_e \geq 1$) can hardly be produced because of collapse without seepage, whereas those with low r_e ($0 < r_e < \text{ca. } 0.3$) and low force-roughness could be reproduced by moderate shaking likewise in experiments and simulations.

Removals may also be carried out with different steps in model tests with psammoids and solids under water. For instance, psammoids may be excavated along a retaining wall with a supported head (Fig. 10.4.1c, again with numbers for steps). The wall foot and a neighboured less embedded solid should not move too much by the full intended excavation. Intermediate slopes should have a lower than critical inclination so that avalanches cannot occur. Even careful lab dredging can lead to temporary suction, however, or to fluidized beds. An attractor in the large is achieved in experiments if different sequences of such excavations lead to the same displacements of wall foot and neighboured solid within certain accuracy bounds. The psammoid can be placed before or after the wall in model tests, but the said attractor should work with different successions. This cannot be achieved *ad libitum*, again the average r_e by placement is more important than its spatial distribution, whereas an initial force-roughness is swept out with the excavation (Sect. 13.6).

The indicated excavation could be simulated with *elp* or *hyp* by reducing the weight of vanishing parts in slow steps so that skeleton accelerations and non-hydrostatic pore pressures are avoided. The deformability of the wall and the second solid could be taken into account, e.g. by elastic or elastoplastic relations, and stick-slip relations could represent the wall roughness (Sect. 10.3). Such simulations could also be carried out with several supports of the wall and adequate excavation steps, and with removal and replacement of neighboured solids. Then size and sequence of steps would matter, particularly if the evolution is not plane-parallel or axi-symmetric. Limit and cyclic state fields could be attained by removals and cyclic deformations imposed by the wall, respectively, so that initial fluctuations of void ratio and stress do not matter. As placement-induced fluctuations are partly due to critical phenomena which cannot yet be modelled (Sect. 16.3) their indeterminacy could thus be ruled out.

Various kinds of placement and removal can occur *in situ* with psammoids under water, Fig. 10.4.2. A natural ground consisting of different psammoid zones is changed by moving water (a). Granular masses are placed and displaced by sedimentation, erosion and avalanches. Their relative void ratio can get high ($r_e \geq 1$ by granular flow) or low ($r_e < \text{ca. } 0.3$ by shaking). Such evolutions can hardly be modelled, so composition and relative void ratios have to be estimated by field investigations. Skeleton stress fields may be generated by imposing gravity as outlined further above.

Hydraulic heights h_w are rarely constant (i.e. hydrostatic), particularly during natural displacements of psammoids (Fig. 10.4.2b). A natural ground-water flow may be modelled by assuming h_w along a fictitious boundary (cf. Fig. 10.2.7d). Seepage forces from waves in the free water can densify the skeleton near its surface or produce a fluidized bed (Fig. 10.3.3) which can flow easily. Avalanches settle at their tail with a reduction of h_w by release of water. Dense skeletons can collapse at steep slopes by erosion, then h_w is temporarily lower by dilation. Such hydraulic effects can hardly be taken

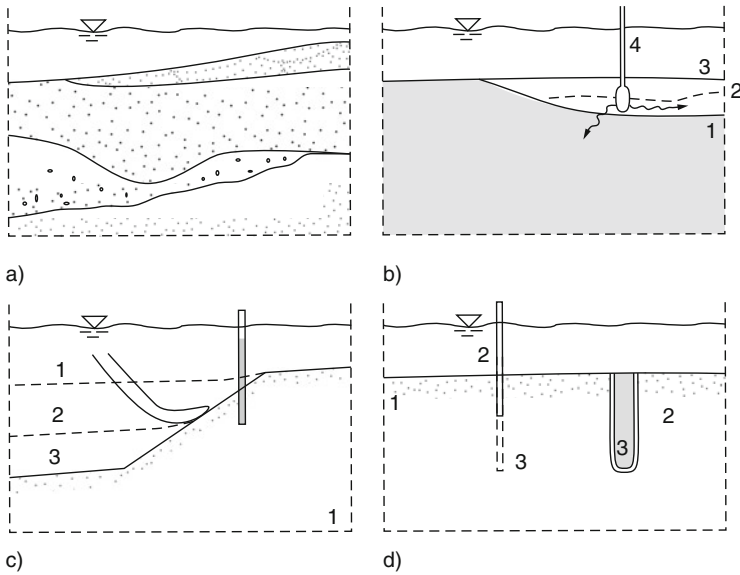


Fig. 10.4.2. Placement and removal of psammoids *in situ*: natural formation (a), influence of free water (b), dredging (c), penetration or boring (d). Numbers denote the sequence

into account in simulations of placement and removal, steps therein should therefore be chosen with caution.

Seismic waves can enhance changes of free skeleton surfaces and of their vicinity. A fluidized bed can arise and avalanches can be triggered at slopes. Below their surface and off slopes skeletons can be densified by repeated earthquakes, but not in zones of the ground where the skeleton decays by shaking (Sect. 11.4). Temporarily fluidized zones in the ground can produce mud volcanos (Sect. 16.3). All that can hardly be taken into account in simulations of seismic psammoid displacements. One may at best estimate how seismic shaking could mobilize a psammoid body (Sect. 12.5).

Psammoid *fills* under water are first loose from granular flow, therefore they are densified by vibrations or impacts (Fig. 10.4.2b). Such evolutions can hardly be simulated as they imply complex interactions of accelerated solids and skeletons with fluidized zones (Sects. 10.3 and 14.3). Skeleton states after placement and densification may again be generated by imposing gravity with given new psammoid zones and void ratios. Technogeneous waves in the surrounding ground can as yet only be controlled by monitoring and countermeasures. Fictitious boundaries of near- and far-fields are of little use, and simulations for far-fields beyond elastic waves would be too expensive. One can as yet only judge empirically whether vibrations and impacts leave back skeleton changes outside tolerated ranges of action.

Excavations of submerged psammoids can likewise not be modelled in detail (Fig. 10.4.2c). Dredging by suction or cutting causes dilation or cracking

with temporary reduction of h_w in the near-field of tools. If slopes are cut steeper than critical skeletons nearby collapse into avalanches (Sect. 12.4). As fluidized zones cannot be totally avoided a superficial part of the remaining skeleton gets looser (and should be densified before or during the placement of structures). The influence of excavations on the surroundings may be simulated by a slow reduction of gravity in the removed part. Far-field hydraulic changes by excavation can thus not be captured, they should be avoided anyway.

The *placement of solids* upon and in saturate psammoid ground causes various changes of skeleton shape and state (Fig. 10.4.2d, numbers for steps of the evolution). It is usually accompanied by excavation, fill and densification. Solid bodies can be placed in excavated holes with displacements of the skeleton, or cast in situ by pumping in and curing of cementitious mud. Such evolutions may be simulated in simplified steps as far as structures are gradually placed upon the ground, combined and back-filled. Skeleton state fields after placement of solids may be generated by imposing gravity to a ‘wished-in-place’ structure upon and in the ground. Near-field changes by penetration may at best be captured with axial symmetry (Sect. 14.3). Near-field changes by other penetrations of solids, e.g. caissons or shields, may partly be estimated and should be controlled by monitoring and counter-actions. Far-field changes of position and state may be simulated with psammoid models, but boundary conditions at penetrating solids and excavation fronts are partly arbitrary and debatable (Sect. 10.3).

The *removal of solids* from submerged psammoid ground can likewise not be captured in detail. Structures upon the ground can be lifted in parts or blasted, stones are usually left in the ground and pits are filled. If parts of structures are pulled out and leave back dilated near-fields, if parts remain in the ground their stress field differs from the far-field. Simulations with simplified steps may help to estimate changes of the surroundings. Skeleton stress fields left back by removals may be generated by reducing weight and stiffness of structural parts in a single step, composition and void ratios should be given from ground investigations for such initial states of subsequent evolutions. The inherited force-roughness is thus not captured, but is often swept out in the sequel so that only the onset of the subsequent evolution is indeterminate.

Evolutions with *combinations* of placement and removal are evidently more complex and less determinate. Heuristic attractors in the large are needed to control them and are often tacitly assumed. Acceptable technologies depend on sufficiently confined near-fields. Far-field changes by seepage, seismic waves or even collapse should be avoided anyway. Size and order of operation steps should be of minor importance for the surroundings, particularly for the skeleton state after the operation. This is not the case in general, skeletons and structures at them feel size and order of steps as such systems are not elastic. This can be shown with hyp (Sects. 12.4, 13.5 and 13.6) and is evident with exaggerated steps. The generic term ‘attractor in the large’ is to indicate that fine resolutions of operations with placement and removal into many steps are

not needed. As long as skeletons do not get lost this could be demonstrated by comparative calculations with *elp* or *hyp*, state limits and state cycles of RSEs therein are necessary. Apart from the numerical expenditure strange attractors delimit such approaches, in particular with localization or collapse.

Placement and removal with psammoids are influenced by capillary effects if the ground contains gas and/or is exposed to the air. *Gas* bubbles between grains increase the compressibility of the pore fluid (Sect. 6.2), this weakens pressure waves and has little influence otherwise. Gas pockets matter also little, whereas gas-filled macropores make the skeleton collapsible so that operations with inclined ground surface and embedded structures can get impossible. Then minor disturbances can trigger a collapse so that size and order of operation steps are no more an issue.

With open *gas channels* in a psammoid the capillary skeleton pressure p_{cs} enables bigger steps with steeper than critical free surfaces (Sects. 10.1, 13.4 and 14.2). Loose humid skeletons should be densified as they could collapse if pore gas gets trapped so that the suction $p_a - p_w$ gets lost. The skeleton can be densified by an increase of total pressure and with so moderate reversals, vibrations or impacts that p_w does not exceed p_a . The placement of humid skeletons could be simulated by imposing gravity section-wise, r_e and p_{cs} have to be assumed empirically. Excavations may be simulated with p_{cs} by reducing gravity, cracks should be avoided. The placement of solids is eased by p_{cs} , their removal can leave back macropores. As far as p_{cs} does not get lost by drying or wetting simulations with it are easier as skeletons are kept together at free surfaces. More than without p_{cs} operations need not be subdivided into many steps, but monitoring and counteractions are needed to avoid a collapse. The skeleton stress field after operations may be generated as a new initial state by imposing gravity in one step, as without p_{cs} void ratios should then be given by investigations in situ, their evaluation may be supported by simulations (Sect. 14.3).

While the progress of placement and removal with dry or humid psammoids is dominated by the one of external actions, *saturated peloids* have also thermally caused intrinsic times due to skeleton viscosity and diffusion of pore water. Both can be controlled in the lab so that an indeterminacy is avoided due to attractors, Fig. 10.4.3. Peloid *elements* (a) can be achieved in testing devices with suitable boundary conditions. Samples can be pre-consolidated elsewhere, cut and placed rapidly so that they can hardly swell or shrink. Pore pressure and void ratio are more rapidly equalized without drainage than with it. Creep and relaxation enhance the equalization of the skeleton state so that an RSE may be assumed with a uniform initial state (0–1). The uniformity gets lost temporarily during a subsequent drainage (1–2), and even with perfect boundary conditions by localization.

The placement in *model tests* is easier with the objective of a constant void ratio e than of a constant hydraulic height h_w . A soft uniformly mixed peloid can be placed under water in a vessel together with a solid so that its void ratio e remains rather uniform (Fig. 10.4.3b). Free water is driven out,

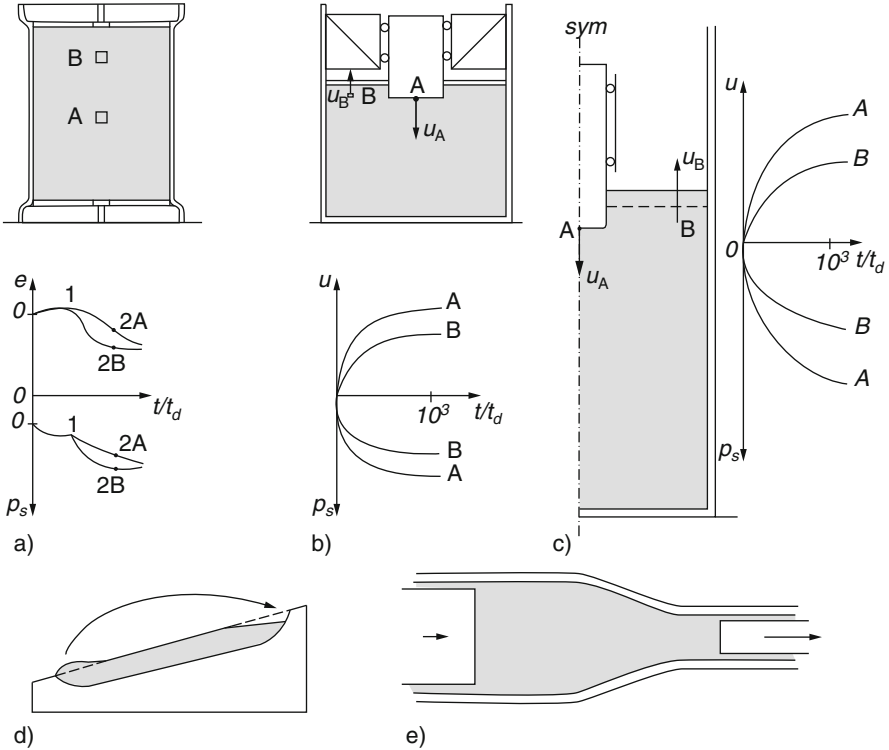


Fig. 10.4.3. State limit fields of undrained peloids in lab experiments: element test (a), guided settling block (b), punching (c), creeping slope layer (d), extrusion (e)

with short waiting times only a negligible fraction of the peloid swells near free surfaces (Sect. 10.1). With gravity and a guided solid the peloid approaches an equilibrium if the system of peloid and solid tends to stabilize. This implies a reduction of the consolidation ratio p_e/p_s so that the rates of creep and relaxation dwindle as they are proportional to $(p_s/p_e)^{1/I_v}$ (Sect. 3.2). During an isochoric rearrangement of the skeleton its equivalent pressure p_e decreases by relaxation of the placement-induced stress obliquity and force-roughness. In case of a low initial p_e/p_s the skeleton pressure p_s decreases by creep with gravity, and the hydraulic height h_w of the pore water rises to a constant value (hydrostatic state).

Swelling near a free surface can be avoided by closing it with a membrane. If pressure differences by its curvature are negligible h_w could be changed uniformly by changing the external pressure, this would not change the skeleton as its particles are neutral with respect to the pore water pressure p_w . After the stabilization of the skeleton its state does not depend on size and order of placement steps, thus the subsequent behaviour is unique and tests are repeatable. This state is an endogenous attractor in the large which is attained

by thermal activation under gravity. The positions of the free skeleton surface and the solid are slightly changed by the stabilization, this change may be negligible in a good model test. Endogeneous attractors of peloid RSEs by creep and relaxation are necessary for an attractor in the large. Whether they are also sufficient could be shown by comparative calculations with v-elp or v-hyp, a more rigorous proof will be difficult.

With less precision saturated peloids and solids can also be placed in model tests without seepage so that *isochoric state limit fields* are approached spontaneously and independently of size and order of placement steps. For instance, an almost stationary flow with axial symmetry can be achieved with a guided solid and enough peloid under it, Fig. 10.4.3c. A perfect flow equilibrium could be produced with far distant base and wall by removing peloid at the free surface so that this moves like the solid. Stationary isochoric creep could also be produced with an inclined long rough basin wherein peloid is added with the same rate above as it flows out below so that the free surface does not change (d). These are thought experiments as free peloid surfaces cannot simultaneously be closed for seepage and adapted by adding or removing peloid. As far as geometrical effects and diffusion of pore water can be excluded the attained fields of skeleton velocity \mathbf{v}_s and stress \mathbf{T}_s do not depend on size and order of placement steps, and the pore water attains a stationary h_w . Such flow equilibria could likewise be achieved with excavation and other shapes of vessels and guided solids, e.g. by extrusion (e).

State limit fields could also be generated by simulations with v-elp or v-hyp as these imply isochoric state limits. Peloid and solid may be added and/or removed in arbitrary steps and order until a free peloid surface is kept in a stationary position. Boundaries and guided solids have to be suitably chosen so that stationarity can be achieved. The attained attractor in the large is argotropic due to skeleton viscosity. The convected skeleton is close to a critical state everywhere, thus its stress obliquity is determined by the field of stretching direction $\hat{\mathbf{D}}$ (Sect. 3.9). The mean skeleton pressure p_s is determined by void ratio e and amount of stretching D . p_s is thus not uniform, and convected RSEs experience changes of p_s . Edges should be rounded as in Fig. 10.4.3c to avoid singularities which could produce cavitation. Argotropic isochoric state limits of RSEs are necessary for such attractors, rigorous sufficient conditions cannot be formulated as easily (Winter 1979).

State cycle fields can be produced after the placement of peloids and solids without seepage in model tests so that size and order of placement steps do not matter. They could be achieved by cyclic deformations of the vessel and of the solid with its guide. This would lead to deformation cycles of the peloid for systems like in Fig. 10.4.3b which would tend to a thermodynamic equilibrium without deformation cycles. RSEs would attain argotropic symmetric skeleton stress cycles (Sect. 5.2). Displacement and deformation cycles of solid boundaries lead to stationary ratcheting in systems like in Fig. 10.4.3c, which would tend to a flow equilibrium without cycles. RSEs could attain asymmetric skeleton stress cycles as far as they are not substantially convected in one

cycle. Erratic cycles with at most moderate amplitudes work like a stronger thermal activation, they could therefore be represented by a seismic temperature (Sect. 5.5). Amplitudes should be kept so low that overcritical skeleton stress obliquities are not reached, otherwise the evolution would get chaotic.

Such *cyclic attractors in the large* could also be generated by simulations with v -elp- α or v -hyp- δ if these relations imply them for RSEs (Sect. 5.5). The previous placement with steps of different size and order could be simulated with the same constitutive relations, and without seepage. Boundaries should be adapted by adding or removing peloid in case of ratcheting so that their average position does not change. More reversals are needed for transitions if the skeleton stress field produced by placement is farther off the average of the attractor, particularly with small amplitudes transitions can therefore be numerically expensive. Cyclic RSE-attractors are necessary for getting asymptotically periodic state fields, again rigorous sufficient conditions could not be formulated as easily.

Turning now to saturated *peloids with seepage*, attractors in the large for different steps could be obtained in model tests and simulations only in exceptional cases, Fig. 10.4.4. The diffusion of the pore water with changes of void ratio e (Sect. 11.1) would only come to an end if the hydraulic boundary conditions enable resting pore water or stationary seepage. This could be approached alongside with an equilibrium of the skeleton with a constant hydraulic height h_w along base and walls of a vessel, a sealed free surface with lower than critical inclination and with peloid with an embedded solid (a). The free surface may be exposed instead to air with such a relative humidity that the seepage there by evaporation does not lead to a capillary entry, but this could not easily be achieved in model tests.

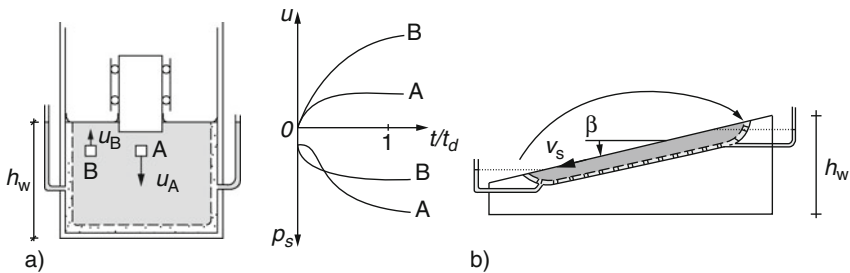


Fig. 10.4.4. State limit fields of drained peloids in model tests: settling solid (a), creeping inclined layer (b)

The placement is usually carried out in steps with such intervals that during it e changes only near draining boundaries. The system should therefore be able to attain an equilibrium with slow creep in each step without seepage as outlined further above with Fig. 10.4.3b. Creep and relaxation are slowed down by densification with release of pore water, i.e. by diffusion, as the

e -equivalent pressure p_e increases. The skeleton pressure p_s decreases and the rate of creep and relaxation is proportional to $(p_s/p_e)^{1/I_v}$ with $0.01 < I_v < 0.05$ (Sect. 3.2). The skeleton approaches a state of rest, and also the pore water if h_w is constant at draining boundaries, after a diffusion time $t_d \approx d\lambda/k_f$ with peloid size d , compression index λ and permeability k_f (Sect. 11.3). The subsequent contractant creep with almost constant h_w is so slow in feasible model tests that it may be neglected.

The same field of skeleton stress and void ratio can be reached after different sizes, orders and intervals of placement steps in the asymptote, this is thus an attractor in the large. The latter could also be generated as a *contractant state limit field* by simulations with v-elp or v-hyp and coupling of skeleton and pore water by the principle of effective stress and seepage (Sect. 11.1). Argotropic contractant state limits of RSEs are necessary to attain them, but the range of attraction cannot be defined with mathematical rigour. With few big steps and intermediate waiting times up to t_d the transition to the attractor can take much more time than with a steadier placement, this is too long for any test. Contractant state limit fields may therefore be postulated in a pragmatic sense and validated by model tests and simulations.

Drained stationary creep could at best be approximately reached with an inclined saturated peloid layer, Fig. 10.4.4b. The inclination must be critical, i.e. $\tan \beta$ by (11.5.4), and the hydraulic height h_w should have the same gradient $\tan \beta$ at the rough pervious base. The latter has to be curved above and below, and peloid should be added above and removed below with suitable e so that the free surface remains plane. The surface may be exposed to the air if its humidity prevents a capillary entry. As peloid has to be added after placement with the same e above while it is removed below this is rather a thought experiment. As in the case of Fig. 10.4.4a shapes and void ratios of intermediate steps have to be chosen so that creep deformations almost without seepage are not too big. The initial void ratios should be higher than the critical ones which are attained in the long run, otherwise the transitory creep would be extremely slow as its rate is proportional to $(p_s/p_e)^{1/I_v}$.

If the indicated precautions are kept the same stationary creep could be reached with different sizes, orders and intervals of placement steps. Corresponding *isobaric state limit fields* could be generated by simulations with v-elp or v-hyp and coupling of skeleton and pore water. This is not quite correct as stationary shearing in the middle part of the slope without lateral changes could occur with different combinations of velocity v_s and void ratio e versus depth (Sect. 11.6), whereas the curved upper and lower base need not suffice to determine the asymptotic v_s . Such attractors in the large may therefore be postulated pragmatically, both in experiments and simulations, so that the range of attraction for different kinds of placement can be defined empirically.

State cycle fields could hardly be produced in drained model tests with saturated peloids as the seepage could not cope with the required changes of

void ratio e . The period duration should exceed the diffusion time to enable substantial changes of void ratio. State cycle fields could be reached with many imposed deformation cycles in reasonable times only without seepage, and could be judged as outlined further above. The subsequent diffusion will be enhanced as the pore pressure is increased by isochoric cycles (Sect. 5.7).

The attractors introduced with Figs. 10.4.3 and 10.4.4 can only be obtained if *critical phenomena* are avoided. The capillary entry was already mentioned, it would lead to a lack of saturation and to cracks (Sect. 6.3). Shear localizations with overcritical skeleton stress obliquities would divide the peloid (Sect. 8.3) and could lead to cavitation, both could hardly be swept out by subsequent deformation and seepage. Loose saturated skeletons with fine hard grains could collapse before they release water. Free surfaces can bulge or get wavy. Such evolutions tend to be chaotic and are hardly predictable (Sect. 16.3), the generic term strange attractor for them is more descriptive than mathematically strict.

The placement in model tests with *unsaturated peloids* may only be mentioned as these can hardly be controlled so that simplified substitutes by means of attractors could be established. Cracks after a capillary entry are rarely regular by extension (Sect. 9.1) and often chaotic by desiccation (Sect. 6.3). Gas-filled macropores soften peloids in a hardly quantifiable manner. Fissures in stiff clays are too irregular at the scale of model tests. Peloids with more uniformly distributed gas channels have so high capillary skeleton pressures and so big channel distances that they are not apt for model tests.

A wider manifold of placement and removal can occur with peloids in situ. Substitutes with simplified steps are needed to simulate such evolutions, heuristic attractors in the large are assumed more or less tacitly. Peloids are often accompanied by psammoids which influence skeleton and pore water via interfaces (Sect. 10.2). It may only be indicated in the sequel for some situations what could be done in such cases.

Natural rearrangements can occur by gravity, seepage forces and tectonic actions. The skeleton state of a thus produced composite may be generated for subsequent evolutions by imposing gravity. Composition, void ratios e and hydraulic heights h_w should be assumed on the base of field investigations, their evaluation could at best be supported by simulating previous rearrangements. Without changes in horizontal directions the vertical skeleton pressure could be calculated by static equilibrium with h_w , and horizontal stresses may be assumed with component ratios as for contractant state limits (Sect. 11.3). The latter is justified by thermally and seismically activated creep and relaxation. With horizontal changes such a stress field may be assumed as point of start with a fictitious horizontal surface. This field could then be corrected by a simulation with adaption of the free surface and of hydraulic conditions. As previous deformations are not of interest and as the force-roughness in situ was or is often ironed out this simplified initial stress field may suffice, together with the given field of e and h_w , to simulate subsequent evolutions.

Technical placements of peloids, often alongside with psammoids, may also be simulated with simplified steps. As with psammoids void ratios and pore pressures after densification have to be assumed empirically. Gravity should be imposed in placement steps with realistic intervals, waiting times and hydraulic conditions so that densification or swelling can occur in simulations. Vibrations for densification may be neglected outside densified zones, inside they enhance relaxation so that the force-roughness from the passage of vibrators may be neglected. Size and order of placement steps are less important for peloids than the conditions for the diffusion of pore water. As outlined further above for model tests, the equivalence of placement variants is justified by attractors in the large as long as critical phenomena (shear localization, cracking, decay and bulging) do not matter.

Excavations of peloids, often alongside with psammoids, may also be simulated in simplified steps. The gravity should be removed section-wise in realistic intervals, hydraulic conditions have to be updated for new free surfaces. As with model tests intervals and waiting times with diffusion of pore water are more important than size and order of excavation steps, and hydraulic boundary conditions play a dominant role. The equivalence of excavation variants is justified by attractors in the large as long as critical phenomena do not matter. As outlined further above for psammoids the near-field of appropriate excavation tools does not matter for the remaining peloid, diffusion and critical phenomena near new free surfaces can be more important without protection (Sect. 10.1).

The *placement of solids*, often alongside with filling and excavation, depends on the kind of operations similarly as with psammoids, but skeleton viscosity and pore water diffusion come additionally into play with peloids. For instance, the installation of a wall or a pile leads to swelling and relaxation or to densification and stressing in the near-field by driving or casting, respectively. This could at best be estimated by simulations, simplified steps are justified for the far-field (Sect. 14.4). Size and order of operation steps matter less than with psammoids, the diffusion of pore water is more important and requires empirically supported boundary conditions (Sect. 10.3). Penetrations with vibration or shocks may at best be simulated with axial symmetry (Sect. 14.3). Critical phenomena, e.g. radial cracking by penetration or fluidization by casting with excavation, should be avoided and could hardly be modelled. Skeleton stress fields after placement may be generated for simulating subsequent evolutions by imposing gravity with given composition, void ratios and pore pressures. This simplification is justified by skeleton relaxation and pore water diffusion with sufficient waiting times.

The *removal of solids* from ground with peloids leads to changes of shape and state in the surroundings which depend on the kind of operation, again skeleton viscosity and pore water diffusion come into play. For instance, if parts of a structure are lifted and others are extracted from the ground its state changes more together with neighboured structures if new ground surfaces are longer exposed to water or air. This could be simulated with skeleton models

and pore water coupling, but one should better keep exposure times short by filling or covering immediately. Then a single step of removal within real time may suffice for simulating the consequences of removal, this is justified by endogeneous attractors as outlined further above for model tests. Critical phenomena should again be avoided.

Various *combinations* of placement and removal with psammoids and peloids could also be captured by simulations with simplified steps which should be justified and delimited by attractors. These are inevitably heuristic, empirical judgment is needed anyway. Moving vehicles upon the ground may be understood as repeatedly placed and removed solids, their effects can also be captured by attractors (Sect. 15.5). The interaction of structures with the ground (SSI) is influenced by placement and removal, simplified steps and adequate intervals could again be defended by attractors in the large which include skeleton viscosity and pore water diffusion.

Closing this rather condensed and long section a remark may be added on *symmetry* (cf. Fig. 10.2.6). The strongest symmetry, namely homogeneity or even isotropy, can be achieved in element tests up to state limits or state cycles and can get lost by shear localization, cracking or decay. One-dimensional evolutions of soil columns may be assumed with suitable boundary conditions including placement and removal, but no more with shear localization, cracking or bulging. Plane-parallel and axisymmetric evolutions can be favoured by suitable placement and removal if state limit or cycle fields arise. Vertical symmetry planes may, apart from pragmatic arguments, also be justified by attractors in the large. Such symmetries can get lost spontaneously by critical phenomena, then strange attractors come into play which cannot easily be specified and impair the predictability (Sect. 16.3).

To *sum up*, simplified boundary conditions on the base of attractors in the large may be employed to capture evolutions with placement and removal, but not *ad libitum*. State limit and state cycle fields can enhance uniqueness and symmetry, such evolutions are favoured by endogeneous attractors due to skeleton viscosity and pore water diffusion. Simplifications of operation steps, sequences and intervals could be justified by observations and simulations. Critical phenomena can impair predictability and technical control, they should be avoided as strange attractors are beyond the present reach. This section is a shortcut of almost the whole book, details as outlined before and after it are needed for better understanding.

ONE-DIMENSIONAL EVOLUTIONS

Except for the desired uniformity of RSEs the highest symmetry is given if all quantities depend only on one co-ordinate. This is the case with so-called soil columns and with radially symmetric evolutions. For preparation the coupling of skeleton and pore water is first considered with foam rubber (Sect. 11.1), Terzaghi's (1925) theory of consolidation is thus introduced. The subsequent sections are focussed on *attractors in the large*. Fields of state limits and state cycles serve to justify simplified calculations, whereas critical phenomena delimit the range of applicability.

Standing soil columns are usually assumed for representations of field data and for simulations of free-field evolutions. Section 11.2 serves to introduce concepts with psammoids and only one spatial co-ordinate. There is more field evidence for the consolidation of peloid layers with draining psammoid neighbours (Sect. 11.3). The propagation of seismic waves can be nearly one-dimensional in sediment basins (Sect. 11.4). Hypoplastic simulations reveal that the unknown initial horizontal stress and intergranular strain are determined by few propagations. Due to such asymptotic cycles an initial state can be identified without hidden variables. Further attractors in the large arise with moderate seismic amplitudes, calculated frequencies and layer separations are confirmed by field data.

Simplified approaches for uniform psammoid slopes are also discussed by means of attractors (Sect. 11.5). We will see that Rankine's (1856) stress fields are at best necessary for stability and can hardly arise. Evolutions with seepage, suction or shaking can also be judged by state limit and state cycle fields. The column symmetry can get lost by surface warping and other critical phenomena. Creep and pore water diffusion occur together generally in peloid slopes (Sect. 11.6). State limits in the large can be attained without or with drainage. Visco-hypoplastic simulations show the dominance of initial consolidation ratios and asymptotic stress obliquities. Shaking can as yet but qualitatively be taken into account, and the predictability is again impaired by critical phenomena.

Radial symmetry can also be justified and delimited by means of attractors in the large (Sect. 11.7). Hypoplastic simulations with this symmetry are confirmed by experiments and serve to evaluate field probing data for getting void ratios. The shrinkage of peloid spheres can likewise be captured, but hardly their swelling. As always there are limitations by critical phenomena.

11.1 A prelude on the diffusion of pore water

Consider a poro-elastic layer (e.g. foam rubber) upon a pervious base with a filter plate on top, Fig. 11.1.1a. Its thickness d may be so small that gravity is negligible. It may be saturated with water under pressure p_w . At top and base the pore water may have atmospheric pressure, $p_w = p_a$, but inside p_w can differ from p_a . The skeleton partial stress T_{s1} may be given at top and base as function of time t , $T_{s1} = -p_o(t)$. In the layer the two partial pressures add up by

$$p_o = -T_{s1} + p_w \quad , \tag{11.1.1}$$

therein both p_o and p_w include p_a . (11.1.1) implies that the solid constituent is neutral with respect to p_w , i.e. it is assumed to be incompressible as the pore water (cf. Sect. 2.2). The volume fractions α_w of water and α_s of solid are complementary,

$$\alpha_w + \alpha_s = 1 \quad , \tag{11.1.2}$$

they change with position x and time t in general.

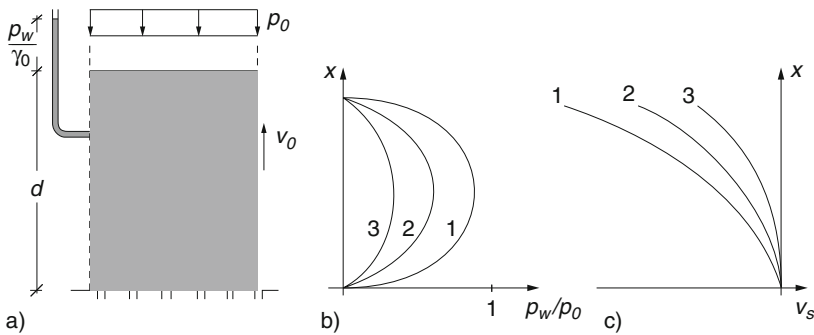


Fig. 11.1.1. Diffusion of pore water in a saturated poro-elastic layer after loading (a), distribution of pore pressure (b) and solid velocity (c) for subsequent times

Leaving aside inertia, (11.1.1) expresses the conservation of linear momentum for a static equilibrium. Neglecting the solid velocity v_s against the average water velocity v_w , Darcy’s law for the seepage may be written

$$v_w = -\frac{k_f}{\gamma_w} \frac{\partial p_w}{\partial x} \tag{11.1.3}$$

with permeability k_f , specific weight of water γ_w and factor -1 as the flow is opposite to the pressure gradient. (One should properly write $v_w - v_s$ instead of v_w , more further below.) The displacement u_s of the solid may be small, $|u_s| \ll d$, so that $v_s = \partial u_s / \partial t \approx du_s / dt$ may be assumed (geometrical linearity). Thus the strain rate is

$$D_1 = \frac{\partial v_s}{\partial t} = \frac{\partial \alpha_s}{\partial t} \approx \frac{d}{dt} \left(\frac{\partial u_s}{\partial x} \right) . \quad (11.1.4)$$

It may be related with the skeleton stress by

$$\dot{T}_{s1} = D_1 E_s \quad (11.1.5)$$

with a stiffness modulus E_s . E_s increases together with $-T_s$ by compaction, so the solid is hypoelastic. Equation (11.1.5) could be substituted by a dependence of α_s on T_s , which is unique if the skeleton is elastic. k_f decreases alongside with α_w , for simplicity $k_f E_s$ is assumed to be constant.

The conservation of pore water mass can be written

$$\frac{\partial \alpha_w}{\partial t} = -\alpha_w \frac{\partial v_w}{\partial x} \quad (11.1.6)$$

as the densities of solid and liquid are constant. Combining (11.1.1) for a constant p_o with (11.1.2), (11.1.4) and (11.1.5) the left side of (11.1.6) (storage term) can be written

$$\frac{\partial \alpha_w}{\partial t} = -\frac{\partial \alpha_s}{\partial t} = -\frac{1}{E_s} \frac{\partial T_{s1}}{\partial t} = \frac{1}{E_s} \frac{\partial p_w}{\partial t} . \quad (11.1.7)$$

Inserting (11.1.3) for the right side of (11.1.6) (transport term) yields

$$\frac{\partial v_w}{\partial x} = -\frac{k_f}{\gamma_w} \frac{\partial p_w}{\partial x} , \quad (11.1.8)$$

therein the variation of k_f with x is neglected. With (11.1.6), (11.1.7) and the abbreviation

$$c_v = \alpha_w \frac{k_f E_s}{\gamma_w} \quad (11.1.9)$$

Equation (11.1.6) can be replaced by

$$\frac{\partial p_w}{\partial t} = c_v \frac{\partial^2 p_w}{\partial x^2} . \quad (11.1.10)$$

The same differential equation describes the diffusion of heat with temperature T instead of p_w , or of a soluble with concentration C . With heat the diffusion constant instead of c_v is conductivity divided by capacity. The equation (11.1.10) for the *diffusion of pore water* was proposed by Terzaghi (1925). He was attacked by Fillunger (1936) because of simplifying assumptions, but these are legitimate up to a certain extent.

The validity of (11.1.10) can be defended in parts. If displacements and deformations are small geometrical corrections may be neglected. As long as E_s and k_f are constant the responses of skeleton and pore water are linear. Even if our layer is poro-elastic, however, E_s and k_f change alongside with the solid volume fraction α_s . One may assume that the product $\alpha_w E_s k_f$ is constant, this yields a nearly constant c_v by (11.1.8) and may hold true as long as changes of α_s are small. The dependence of k_f on α_s means that k_f is a function of x , however, this leads to a term $(\partial k_f / \partial x)(\partial p_w / \partial x)$ by inserting (11.1.3) into (11.1.5). The neglect of this term in (11.1.10) may be justified if the gradient of k_f remains small.

Frame-indifference (Sect. 1.2) requires to replace v_w by $v_w - v_s$ in (11.1.3). The solid velocity is $v_s = -v_w$ for a layer on an impervious base, this is evident from the constant density of solid fraction and of pore water. The same holds true with a pervious base if v_w and v_s are referred to the mid-plane $x = d/2$. $v_w - v_s = 2v_w$ leads to a factor 1/2 for c_v by (11.1.8). Apart from this correction (11.1.10) is a legitimate approach for the diffusion of pore water.

With the dimensionless variables

$$\xi = \frac{x}{d} \quad , \quad \tau = t \frac{c_v}{d^2} \quad , \quad \mu = 1 + \frac{p_a - p_w}{p_o} \tag{11.1.11}$$

Equation (11.1.10) reads

$$\frac{\partial \mu}{\partial \tau} = \frac{\partial^2 \mu}{\partial \xi^2} \tag{11.1.12}$$

The well-known solution with an initial $\mu = 0$ for $\tau < 0$, and the boundary condition $\mu = 1$ for $\tau > 0$ and both $\xi = 0$ and $\xi = 1$, is plotted in Fig. 11.1.2, it

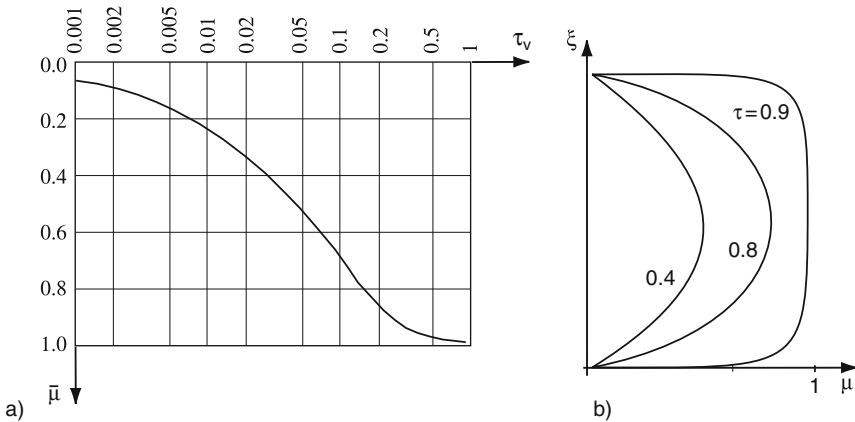


Fig. 11.1.2. Solution of the dimensionless diffusion equation (11.1.12): spatial mean value versus time (a), isochrones of normalized pore pressure (b)

is obtained with a Fourier series. It represents the excess pore pressure $p_w - p_a$ in our layer after loading with p_o . The spatial average

$$\bar{\mu} = \int_0^1 \mu d\xi = \frac{1}{p_o} \int_0^d (p_a - p_w) dx + 1 = 1 + p_a/p_o - \bar{p}_w/p_o \quad (11.1.13)$$

decreases via an S-curve versus $\log \tau$ (a). It may be approximated by

$$\begin{aligned} \bar{\mu} &\approx \sqrt{\tau/\pi} && \text{for } \tau < 1/2, \quad \text{i.e.} \\ (\bar{p}_w - p_a)/p_o &\approx (4\sqrt{\pi})\sqrt{t/t_d} && \text{for } t < t_d/2 \end{aligned} \quad (11.1.14)$$

and

$$\begin{aligned} \bar{\mu} &\approx 1 && \text{for } \tau > 1, \quad \text{i.e.} \\ \bar{p}_w &\approx p_a && \text{for } t > t_d \end{aligned} \quad (11.1.15)$$

with the diffusion time

$$t_d = d^2/c_v \quad . \quad (11.1.16)$$

The distribution of the excess pore water pressure $p_w - p_a$, substituted by μ via (11.1.11), is roughly parabolic (Fig. 11.1.2b). p_w -isochrones, i.e. lines for constant time t , show the gradual decrease of p_w in the course of the diffusion. This solution holds also with an impervious base; then d is replaced by $2d$ in (11.1.11) and one half of the distribution $\mu(\xi)$ is relevant.

This theory is of use for the *consolidation* of peloid layers. The approximate solutions provide estimates of the delay due to the diffusion of pore water. With the non-linear skeleton behaviour and with large deformations more complicated substitutes of (11.1.10) can only be solved numerically, but t_d by (11.1.16) may still be used for scaling t (Sect. 11.3). The motions of skeleton and pore water are coupled in general, this is expressed by the principle of effective stress (11.1.1) and by $v_w - v_s$ instead of v_w in (11.1.3). In case of a constant total pressure after loading one may still speak of the diffusion of pore water (but not of pore pressure dissipation as in the jargon of soil mechanics, this is as incorrect as would be dissipation of temperature instead of heat).

Within the assumed linearity one can also apply (11.1.10) if the load p_o is increased step by step with time. Then solutions are obtained by superimposing the ones for different starting times. Going over to an integration Gussmann (1979) thus worked out a solution for consolidation with controlled displacement, Fig. 11.1.3. The base of the layer is impervious, the top is lowered with a constant velocity v_o (a). With increasing time the top pressure p_{sd} tends to a linear increase, whereas the pore pressure p_{wo} at the base tends to a stationary asymptote (b). For a layer between two filter plates d in t_d by (11.1.15) has to be replaced by $d/2$, and p_{wo} holds in the midplane. This solution can be used to estimate the delayed evolution of skeleton and pore pressures in compression tests with displacement control. It works also

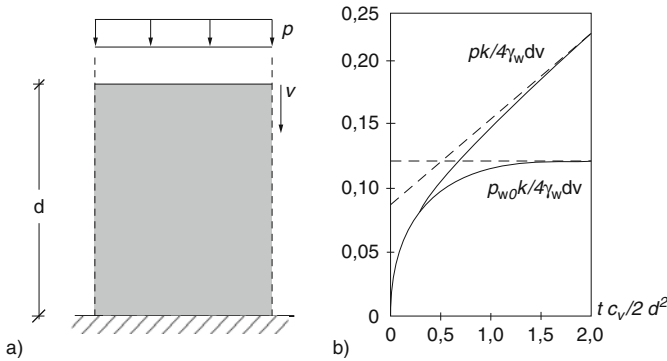


Fig. 11.1.3. Consolidation with constant rate of displacement (Gussmann 1979): **a** system, **b** normalized skeleton pressure above and pore pressure below versus normalized time

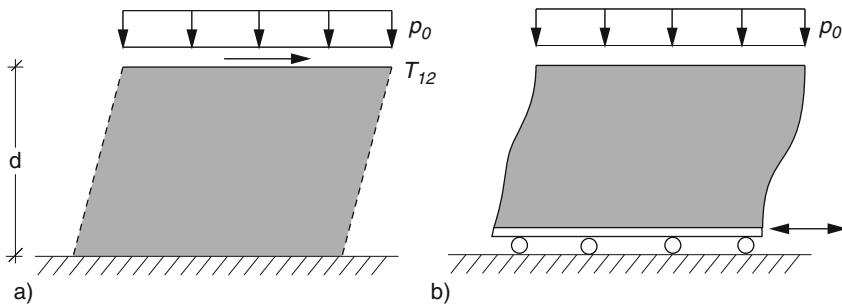


Fig. 11.1.4. Poro-elastic layer with shearing (a) or a shaking base (b)

for a saturated layer with evaporation (Sect. 11.3), this corresponds to heat conduction with a constant heat flux at the surface.

Our poro-elastic layer may now be *sheared* under constant pressure p_0 , Fig. 11.1.4a. The shear-induced reduction of voids may be approximated by

$$\dot{\alpha}_{wd} = \nu \dot{T}_{12} / G_s \quad . \quad (11.1.17)$$

Therein $\dot{\alpha}_{wd}$ denotes the reduction rate of the water volume fraction α_w by shearing, \dot{T}_{12} is the rate of shear stress, G_s denotes a shear modulus and ν a kind of Poisson ratio of the skeleton. This term has to be added to the mass balance (11.1.6), thus (11.1.10) has to be replaced by

$$\frac{\partial p_w}{\partial t} = c_v \frac{\partial^2 p_w}{\partial x^2} + D_w \quad (11.1.18)$$

with the drift term $D_w = \nu \dot{T}_{12} E_s / G_s$. The same equation holds with T instead of p_w for heat flow with an additional heat source, e.g. by microwaves.

Solutions of (11.1.18) for diffusion with drift are available with constant D_w . They are scarcely relevant for soils as a constant drift term can hardly occur with them. If the skeleton tends to dilate or contract by shearing with constant pressure the latter will increase or decrease by isochoric shearing (Sects. 2.10 and 3.8). A kind of pore pressure production may at best be estimated for isochoric shearing (Sects. 4.7 and 5.5), this may be used for the flow of inclined layers (Sects. 11.5 and 11.6). For dilatant or contractant shearing such rather simple relations get invalid as then a constant drift term is not justified. The non-linear coupling of skeleton and water could only be followed up numerically. Nevertheless it can be of use to scale t by means of a diffusion time t_d (Sect. 11.6).

Consider now our poro-elastic layer upon a *shaking base*, Fig. 11.1.4b. Without pore water elastic longitudinal (P-) and transversal (S-) waves could propagate, they would be reflected at the top, repeated waves would lead to a vibration of the layer. With water saturation and a low permeability, i.e. k_f/d far below the frequency f_c , volume changes are negligible during propagations. S-waves get through and induce pulsations of p_w if the skeleton tends to change its volume by shearing. With an elastic pore fluid P-waves are induced by S-waves, the latter are slower than the former (Biot 1965). After such propagations p_w is the same as before. With a linear viscous damping the S-amplitude is reduced and p_w is changed after a propagation.

The anelastic coupling of skeleton and pore water in saturated soils cannot be captured by linear approaches. In psammoid layers (Sect. 11.4) S-waves induce p_w -pulsations of twice the S-wave frequency, and repeated S-waves can cause an accumulation of p_w . The latter can hardly be captured by a drift term as in (11.1.18). The response of peloids to shaking is similarly non-linear, but also argotropic (Sect. 6.3). Layers upon slopes experience an additional drift by gravity as indicated further above. The combined effect of gravity and shaking could at best be modelled numerically (Sects. 11.5 and 11.6). The diffusion of pore water during and after shaking could also be taken into account.

Evolutions of our poro-elastic layer get more intricate if it is partly saturated. With the effects outlined in Sect. 6.2 permeability and compressibility get non-linear. Two different elastic P-waves arise in the solid and the pore fluid (Biot 1965). Due to capillary hysteresis wave propagations can enhance the seepage and can cause a cumulative p_w -increase. Ad- and desorption and reaction play a bigger role than without gas. All that may occur in soils, but is left aside for simplicity.

To *sum up*, the linear theory of pore water diffusion can be of use to estimate certain evolutions of soils. This holds true for monotonous consolidation or swelling although the skeleton behaviour is not linear. The production of excess pore pressures by monotonous or cyclic shearing can hardly be captured by adding a drift term to the diffusion equation. Further non-linear

effects occur by coupling of pore water with gas and skeleton even if the latter is elastic.

11.2 Standing psammoid columns

Psammoid layers with negligible horizontal changes can be represented by a *standing column*, Fig. 11.2.1a. They can be partly identified by a set of material parameters, e.g. hypoplastic ones as introduced in Sect. 2.4. These may be taken as constant in depth sections, thus layers are defined. The material coordinate x_s and the skeleton displacement u_s are referred to the base. The strain rate equals the velocity gradient, $D_1 = \partial v_s / \partial t$ with $v_s = du_s / dt$. The principal skeleton stress components, T_{s1} vertically and $T_{s2} = T_{s3}$ horizontally, are negative.

Readers familiar with conventional soil mechanics may write $\dot{\epsilon}_1$, σ'_1 and σ'_2 instead of $-D_1$, $-T_{s1}$ and $-T_{s2}$. The void ratio e can be substituted by the relative void ratio r_e via (2.2.18). Two further variables are needed in general for the internal state, say the components δ_1 and $\delta_2 = \delta_3$ of the intergranular strain by Sect. 4.5, they require further material parameters for identification. This section is rather preparatory as the assumed symmetry is rarely given in applications and as the considered settlement or heave of sand-like layers is rarely important.

The *pore water* may be assumed to be H_2O , solutes are thus neglected (Sect. 6.2). The water content w can be substituted by the degree of saturation S_r via (6.2.1). The absolute pore water pressure p_w is conventionally substituted by $u = p_w - p_a$ with the atmospheric pressure p_a . Suction, i.e. $p_w < p_a$, can be taken into account for zones with a network of gas channels by means of a capillary skeleton pressure p_{cs} (Sect. 6.2). The water velocity v_w with respect to the base is the volumetric transport rate per cross section of the skeleton. In case of seepage through the layer the filtration velocity $v_f = v_w - v_s$ exceeds v_s normally so much that $v_f = v_w$ may be assumed. With the *hydraulic height* $h_w = x + (p_w - p_a) / \gamma_w$, which is the potential or free energy, Darcy's law can be written as

$$v_w \approx v_f = -k_f \partial h_w / \partial x \quad . \quad (11.2.1)$$

The permeability k_f depends on the porosity $n = e / (1 + e)$ by (6.2.4), but may be considered as constant for simplicity. With gas bubbles between the grains (11.2.1) may also be used, and (6.2.6) may be assumed for the compressibility of the pore fluid. Seepage in zones with gas channels could similarly be captured, but is far slower (Sect. 6.2).

Three *conservation laws* can be formulated as follows (cf. Sect. 1.2). With isochoric grains the condition (2.2.10) for the conservation of solid mass can be written

$$de/dt = \dot{e} = (1 + e)D_1 = (1 + e)\partial v_s / \partial x \quad . \quad (11.2.2)$$

An updating of the material coordinate via $x_s = x + u_s$ is not needed as long as the displacement u_s is minute. With full saturation the condition for the conservation of water mass reads

$$\partial v_w / \partial x = -\dot{e} / (1 + e) \quad (11.2.3)$$

by means of (11.1.2) and (11.2.2) as the densities of water and grains are constant. The more complicated substitute for $S_r < 1$ (Richards 1931) is omitted for simplicity. Without inertia the condition for the conservation of linear momentum reduces to the one of static equilibrium in the vertical direction,

$$\partial T_1 / \partial x - \gamma = 0 \quad , \quad (11.2.4)$$

with the specific weight γ . In case of full saturation, and also if gas bubbles are enclosed by the grains, the defining equations (2.2.5) for the skeleton stress components can be written as

$$T_{s1} = T_1 - p_w \quad , \quad T_{s2} = T_2 - p_w \quad . \quad (11.2.5)$$

Inserting (11.2.5) into (11.2.4) the equilibrium condition for the skeleton can be written

$$\partial T_{s1} / \partial x - (\gamma - \gamma_w) - \gamma_w \partial h_w / \partial x = 0 \quad . \quad (11.2.6)$$

Therein $\gamma - \gamma_w$ is the specific weight minus uplift, and $\gamma_w \partial h_w / \partial x$ is the *specific seepage force* acting onto the skeleton.

For numerical simulations the column is subdivided into *finite soil elements* (FSEs) as indicated in Fig. 11.2.1b. Other than with the representative soil elements (RSEs) employed in Chaps. 2, 3, 4 and 5 velocities and state variables have gradients within an FSE. These are represented by means of interpolation functions, usually so that the skeleton velocities are continuous but state variables are not, and vice versa for the pore water. Kinematic constraints and state quantities for the top and bottom FSEs are part of the boundary conditions. The equations for the conservation of mass and momentum are satisfied in spatial averages, usually via the principle of virtual work. The equations for the increments of position and state of the skeleton are non-linear due to the constitutive relations, so an iterative solution is needed with proper increments. The calculated evolutions can be represented by depth profiles (Fig. 11.2.1c) and by state paths (d) of RSEs. The vertical displacement u_s is related with changes of e by (11.2.3). With a stationary hydraulic height h_w and the assumed rate-independence of psammoids integers suffice as labels to denote the sequence. The evolution of the pore water is assumed in this section to be coupled only via its pressure p_w in (11.2.5).

An *initial state*, labelled by 0 in Fig. 11.2.1c, d, can be generated in different ways. Without seepage p_w is hydrostatic, also above the groundwater table which is defined by $p_w = p_a$. T_1 can be estimated by (11.2.4) with a constant average specific weight $\bar{\gamma}$, (11.2.5) yields T_{s1} . The initial skeleton stress ratio can be estimated by

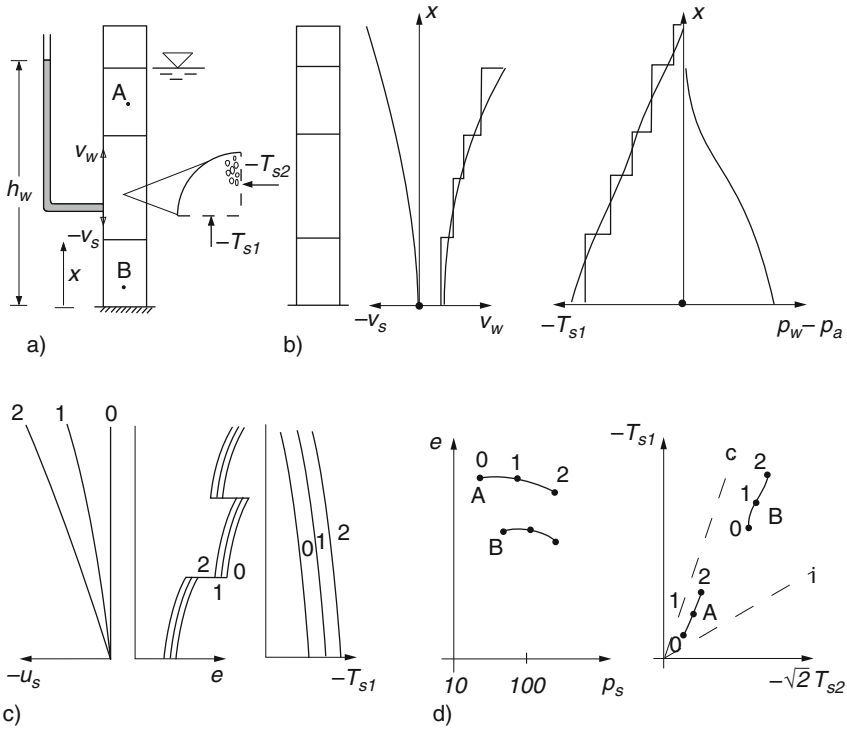


Fig. 11.2.1. Inhomogeneous psammoid column upon impervious base (a), spatial distributions with finite elements (b), distributions of vertical displacements, void ratios and skeleton pressures (c), evolution of void ratios and pressures in two RSEs (d)

$$T_{s2}/T_{s1} = K_o \tag{11.2.7}$$

with the so-called *earth pressure coefficient at rest* K_o . The formula

$$K_o = 1 - \sin \varphi_c \tag{11.2.8}$$

by Jaky (1948) is empirically confirmed for psammoids. Niemunis (2003) derived

$$K_o = a/(3 + a) \quad , \tag{11.2.9}$$

with the constant a depending on φ_c by (2.4.6), from the hypoplastic relation (2.4.3) for a contractant state limit with $\varepsilon_2 = 0$. The initial state is not at such a limit in general, but (11.2.9) is still legitimate: the same T_{s2}/T_{s1} is reached by a proportional compression with other than limit void ratios (SOM-states, Sect. 2.2), and also by shaking (Sect. 4.6).

The resistance to penetration sounding leads to r_e (Sect. 14.3), e can then be calculated with (2.2.18) and (2.4.1). Specific weights can be calculated with the solid specific weight γ_s , e and w or S_r . The capillary skeleton pressure p_{cs}

above the groundwater table can be obtained as tensile strength (Sect. 6.2). The initial intergranular strain may be guessed, e.g. $\delta = 0$ or $\delta = R$ and $\delta_2/\delta_1 = K_o$ (Sects. 4.5 and 11.4).

More insight could be gained by considering possible previous evolutions (Sect. 10.4), but only observable traces of the past are relevant. Sedimentology helps to specify properties and spatial distribution of the grains, thus material parameters and homogeneous zones can be estimated. Hydrological considerations can help to specify S_r (without getting lost by hysteresis and fingering, Sect. 6.2). Pluviation of fine grains can lead to $r_e > 1$ due to capillarity (Sects. 6.2 and 7.2). Granular flow leaves back $r_e \approx 1$, tectonic stretching of the base can also produce zones with $r_e \approx 1$ (Sect. 12.6). Seismic or sea bottom waves can lead to r_e and δ close to zero (Sect. 11.4). T_{s2}/T_{s1} can deviate from K_o by (11.2.8) or (11.2.9), but such deviations can scarcely be specified and are rarely relevant.

Changing boundary conditions lead to changes of position and state as plotted in Fig. 11.2.1. A *surcharge* means an increase of $-T_{s1}$ at the surface beyond p_{cs} if this was free. It is numerically advisable and physically justified to assume at least a small p_{cs} . It was indicated in Sects. 10.1, 10.2 and 10.3 how $-T_{s1}$ can thus increase. The vertical pressure $-T_1$ increases evidently by the same amount in any depth, this results from (11.2.4). As long as changes of p_w due to the surcharge are negligible $-T_{s1}$ increases independently of depth. Changes of further state variables can be obtained by calculations with a constitutive model. Simple hypoplasticity (Sect. 2.4) leads to state paths as plotted in Fig. 11.2.1d, with a nearly constant T_{s2}/T_{s1} if this started with K_o and a stronger reduction of e for lower p_s and h_s and higher r_e . A smaller compression is obtained with low amounts of intergranular strain ($\delta < R$), the evolution of the latter could be plotted by additional state paths (cf. Sect. 4.7). The indeterminacy of δ_1 , δ_2 and T_{s2}/T_{s1} (which is a kind of internal variable in this case) can be erased by a sufficient compression (cf. Sects. 2.4 and 4.7), but the historical element (Darwin 1883, Prologue) due to e can scarcely be ruled out by surcharges in the typical geotechnical range.

Unloading means a reduction of T_1 near the surface. This requires a previous surcharge or an excavation (Sects. 10.1 and 10.4). As with a surcharge T_1 changes by the same amount in any depth, and also T_{s1} as long as the change of p_w is negligible. Further changes of state are obtained with a validated constitutive relation (Sect. 2.6): T_{s2}/T_{s1} grows and can exceed the critical amount by (2.2.17), e increases by a lower amount than it would decrease by the same $|\Delta T_{s1}|$ due to surcharge. Near a totally unloaded surface the skeleton approaches a dilatant state limit (cf. Sects. 2.2 and 2.5). The influence of the intergranular strain components δ_1 and δ_2 is smaller than for a surcharge, the amount $\delta = \sqrt{\delta_1^2 + 2\delta_2^2}$ tends to be reduced.

Hydraulic changes can be imposed from the upper or lower boundary. An upwards seepage is produced by an artesian water pressure p_w . The new $p_w(x)$ -distribution can be calculated by (11.2.1) and (11.2.3) with the new hydraulic

boundary conditions. The increase or reduction of T_{s1} can be calculated by (11.2.5a) or (11.2.6). Other than with a discharge at the surface the skeleton stress increment ΔT_{s1} changes with depth. In the simplest case of constant γ and k_f and a free surface the ratio $\Delta T_{s1}/T_{s1}$ is depth-independent. A hydraulic uplift with $-T_s \rightarrow 0$ is obtained if p_w attains T_1 , then a decay of the skeleton can lead to erosion (Sect. 10.4). Otherwise the increases of T_{s2}/T_{s1} and of e are similar as by unloading. Flooding with constant bottom p_w causes the opposite evolution: downward seepage, increase of $-T_{s1}$ and $-T_{s2}$ and decrease of e as by a surcharge. The transition times depend on k_f , e and S_r , with capillary effects they can at best be estimated (Sect. 6.2).

A vertical psammoid column with plane-parallel *lateral deformations* may now be considered, this can occur approximately in the lab and in situ (Fig. 11.2.2a). Assume rigid smooth lateral walls with varying distance and a uniformly stretched or shortened base so that the horizontal stretching rate D_2 is uniform in the column. The vertical skeleton pressure $-T_{s1}$ may be nearly constant with time, say with $S_r = 1$ and hydrostatic p_w . Which are the attractors with an arbitrary initial distribution of stress and relative void

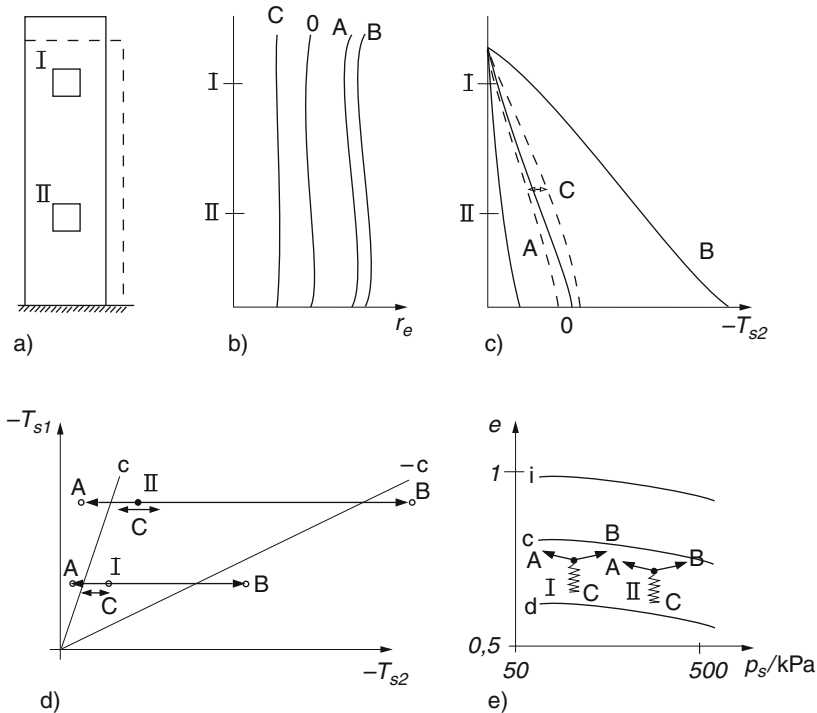


Fig. 11.2.2. Evolution of a drained saturated psammoid column (a) by horizontal shortening (A) or stretching (B): distribution of relative void ratios (b) and horizontal skeleton stresses (c), paths of stress components (d) and void ratios versus pressure (e)

ratio? Evolutions can be represented by depth profiles of state (Fig. 11.2.2b, c), and by paths of skeleton stress and void ratio vs. pressure (d, e) for different RSEs (e.g. I and II).

With slow *monotonous* horizontal stretching (A) or shortening (B) the RSEs in the psammoid column tend to state limits (Sect. 2.2) with a lower or upper bound, respectively, of the horizontal skeleton pressure $-T_{s2}$. A loose skeleton (i.e. $r_e \geq 1$) tends to a critical state with T_{s2}/T_{s1} by (2.7.4) and $e = e_c$ by (2.4.1). This is an attractor in the large which can be represented by a set of state paths for a set of RSEs. It is spoiled by warping of the free surface, more so with shortening than with stretching. A denser skeleton with $r_e < 1$ tends to a dilatant state limit with T_{s2}/T_{s1} by (2.7.5) and an increased r_e due to dilatancy. Even with a uniform initial r_e the peak friction angle φ_{pb} is not uniform. Shear bands evolve in addition to surface waves so that the assumed uniformity gets lost (Sects. 8.2 and 12.6). This pattern formation indicates a strange attractor with loss of column symmetry which can hardly be represented (Sect. 16.2). This means that Rankine's (1856) stress fields (more in Sect. 11.5) could at best be attained with loose sand, and that G. Darwin (1883) was right stating that the historical element eludes mathematical treatment. Or nearly so, the case is not hopeless as we will see now.

The chance for catching an attractor in the large is better with slow horizontal *stretching cycles*. The initial r_e may be arbitrary. With a small amplitude (C in Fig. 11.2.2) the granular column is densified to an r_e just above zero, and the average stress ratio T_{s2}/T_{s1} tends to a constant near K_0 . More precisely speaking, a state cycle field is attained which is almost symmetric in the stress plane and in the intergranular strain plane, and just above the lower bound in the e vs. $\log p_s$ plot. The evolution tends to similar state cycles with moderate amplitudes, then the average r_e and the oscillation of T_{s2}/T_{s1} are somewhat bigger (cf. Sect. 4.3). With a big amplitude state limits are repeatedly attained, this leads to shear banding and surface warping so that a strange attractor would be needed (Sect. 12.6).

A saturated granular column could also be laterally and slowly deformed *without drainage*. In addition to smooth walls and a stretchable base membrane this requires an impermeable membrane at the surface, and a sufficient pressure p_0 above so that the membrane cannot be lifted by $p_w > p_a$. The total volume is constant, but the soil elements can undergo volume changes. Due to the high permeability the hydraulic height h_w remains depth-independent, but it changes with deformations. The equilibrium condition (11.2.6) yields a constant $T_{s1I} - T_{s1II} = (\gamma - \gamma_w)(x_I - x_{II})$. Lateral stretching or shortening leads to contractant state limits of the looser low RSEs, and to dilatant state limits of the initially denser RSEs. The stress ratios T_{s2}/T_{s1} tend to the values for the dilatancy ratios of these state limits, r_e is reduced or increased (cf. Sects. 2.2 and 2.7).

Our saturated psammoid column could be exposed to *stretching cycles without drainage*. The initial relative void ratio r_e should be small enough so that the skeleton will not decay (cf. Sect. 4.2). There is no total volume

change, a cumulative contraction below is compensated by a dilation above. As in the previous case the hydraulic height h_w is depth-independent, and spatial differences of T_{s1} do not change with time. The initial T_{s1} and p_w are given by weight and surcharge, the initial T_{s2}/T_{s1} can deviate from (11.2.7). The stress paths tend to skew butterfly attractors (cf. Sect. 4.4). Paths in an e vs. $\log p_s$ plot would reveal gradual relaxation of p_s and equalization of e .

To *sum up*, uni-axially deformed psammoid columns with pore water and gravity can attain various driven attractors. State limits with contraction are only approached with high initial relative void ratio r_e and/or high pressure p_s . Critical states could be uniformly approached with $r_e \geq 1$ initially, without water or with full saturation and free drainage, only then Rankine's (1856) theory is justified. The column symmetry gets lost by shear localization, this can lead to deterministic chaos (cf. Sects. 8.2, 12.5, 14.7 and 16.3). The symmetry can be regained by suitable monotonous or cyclic deformations.

11.3 Standing peloid and composite columns

A horizontal peloid layer may be represented by a column if transversal changes are negligible. Its limit void ratios are higher with net attraction $p_n < 0$ (Sects. 6.3 and 7.1), although this is usually far smaller than the skeleton pressure p_s . A compression is delayed by the diffusion of pore water, and also by creep if the solid particles are soft. Thus the consolidation ratio p_e/p_s can increase with time and by shrinkage. Swelling is similarly delayed, and is enhanced by shrinkage cracks. A package of peloid and psammoid layers can be represented by a composite column. Its initial state can be estimated more reliably than its composition as psammoid inclusions cannot easily be identified as bands or lenses (Sect. 9.2). Peloid columns with lateral stretching will also be considered in this section.

The *consolidation* of a saturated peloid layer is shown in Fig. 11.3.1. The column may have a pervious base and a filter cap (a). Both may have the same hydraulic height h_w . The skeleton pressure at the cap may be increased from its initial value by a surcharge p_o within a time t_p and then kept constant. Profiles of void ratio, vertical and horizontal skeleton stress (b, c, d) show the evolution with time t after loading. t is referred to the diffusion time

$$t_d = d^2 \frac{\lambda \gamma_w}{\bar{k}_f \bar{\sigma}_s} \quad (11.3.1)$$

with layer thickness d , compression index λ by (2.3.1), specific weight of water γ_w , average permeability \bar{k}_f and average skeleton pressure $\bar{\sigma}_s$. (11.3.1) is taken over from (11.1.6) with (11.1.9) for the linear theory, σ_s/λ is a kind of stiffness modulus $E_s = d\sigma_{s1}/d\varepsilon_1$ (Sect. 2.5). The bars for k_f and σ_s denote averages over space and time, their product is roughly constant for a given peloid. d has to be replaced by $2d$ in (11.3.1) if the base or the top is impervious.

Changes of state of representative soil elements (RSEs) are shown as paths in planes of skeleton stress (e) and of e vs. $\log p_s$ (f), again with labels for t/t_d . The consolidation ratio p_e/p_s can be derived from p_s and the equivalent pressure p_e . p_e is defined as the mean pressure p_s for a state limit with the given e , $T_{s2}/T_{s1} = K_o$ and $D = \dot{\epsilon}_1 = D_r$ (Sect. 3.2). The evolution is also represented by plots of state variables versus t/t_d (g) and $\log(t/t_d)$ (h). The ratios T_{s2}/T_{s1} and p_e/p_s are shown as they will be used further below. A further label can be added for t_d/D_r , the reference strain

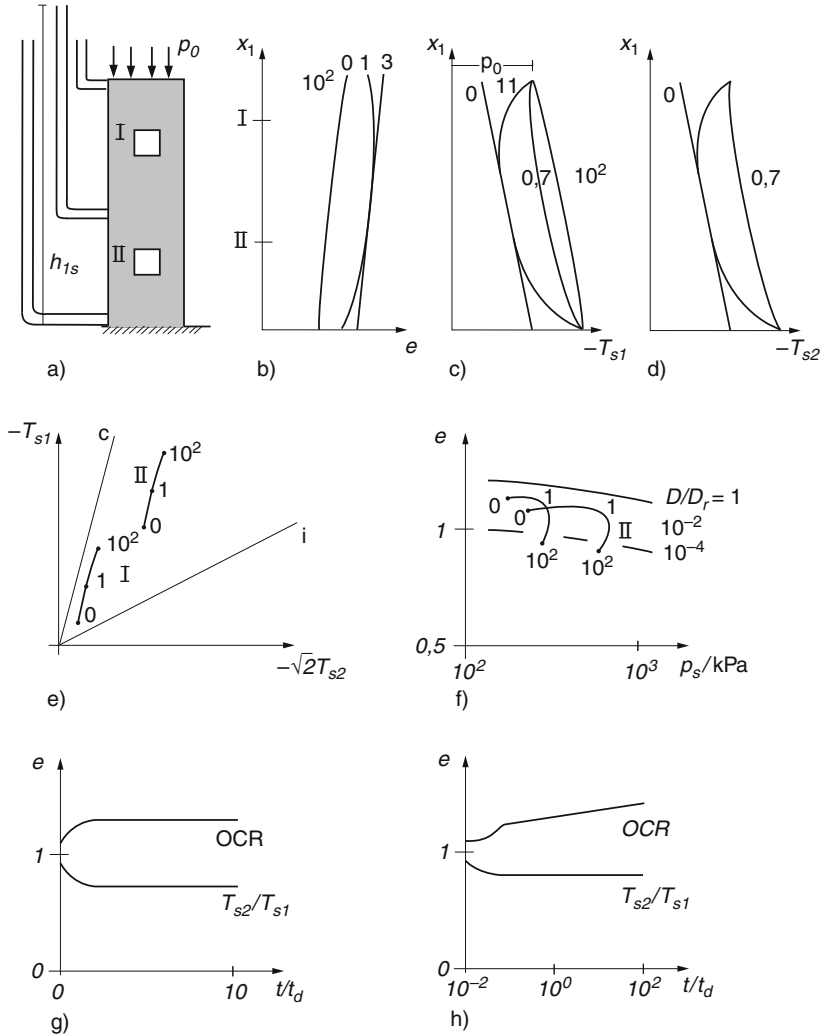


Fig. 11.3.1. Consolidation of a peloid column (a): distributions of void ratios (b), vertical (c) and horizontal skeleton stresses (d); paths of stresses (e) and void ratios versus pressure (f); stress and consolidation ratios versus time (g) and log time (h)

rate D_r means a further time scale due to thermally activated dislocations (Sect. 3.1).

Such evolutions can be simulated numerically. The skeleton may be identified as v-elp or v-hyp by Sects. 3.3 or 3.4 with constant material parameters. Darcy's law (Sect. 6.2) can be written as

$$v_w - v_s = -k_f \partial h_w / \partial x_1 \quad (11.3.2)$$

with the seepage velocity $v_w - v_s$ relative to the skeleton. Changes of k_f with densification can be taken into account, also with the hydraulic gradient $\partial h_w / \partial x$ if shear thinning of bound pore water plays a role (Sect. 6.3). The conservation laws are the same as with psammoids: (11.1.6) for the mass of water in case of full saturation, and (11.2.4) or (11.2.5) for linear momentum.

The column is subdivided into finite soil elements (FSEs), interpolation functions are assumed for skeleton and water as for psammoids (Fig. 11.2.1b). The differential constitutive relation is written with finite differences ΔT_{s1} etc. for time steps Δt , the non-linearity requires caution. Constitutive relations and conservation laws are written for the actual configuration, positions should be updated for large compressions. Time-dependent boundary conditions restrict the freedom of base and top FSEs. Initial state variables are needed for $t = 0$, these are reasonably assumed for Fig. 11.3.1 and will be discussed further below. Evolutions of state can be calculated for a succession of time steps Δt which can get bigger for slower evolutions. Changes of skeleton position, i.e. settlement or heave, are related with changes of void ratio by Fig. 11.2.2. They are needed for updating the configuration and can be plotted versus t/t_d or $\log(t/t_d)$.

The loading time t_p for the increase of the top skeleton pressure may be shorter than t_d by (11.3.1). Then the delay of skeleton compression is mainly determined by the diffusion of pore water. The linear theory yields the average strain rate

$$D_d \approx 1/\sqrt{\pi} t_d \quad (11.3.3)$$

for $t/t_d = 1/2$ by means of (11.1.14). The state paths (Fig. 11.3.1e, f) tend to contractant argotropic state limits (Sect. 3.2). For $t < t_d$ the skeleton pressure p_w increases as the hydraulic height h_w is reduced by diffusion. The stress ratio T_{s2}/T_{s1} approaches K_o by (11.2.9) more rapidly, and p_e/p_s increases significantly with t (Fig. 11.3.1g). During this so-called *primary consolidation* the argotropy of the skeleton is veiled by the diffusion of pore water, but nevertheless effective.

For $t > t_d$ the skeleton stress is almost stationary as then the seepage force is negligible. The so-called *secondary consolidation* can be seen from a further reduction of e and an increase of p_e/p_s with $\log t$ (Fig. 11.3.1f, h). The latter can be approximated by

$$p_e/p_s \approx \left(\frac{1}{\sqrt{\pi}} t D_r \right)^{I_v} \quad \text{for } t > t_d \quad . \quad (11.3.4)$$

This is obtained from the decrease of e with t of an RSE with constant p_s by means of (3.2.6) with an initial D by (11.3.3). This estimate gets better for longer times as then the influence of the initial e and D is more and more swept out. $T_{s2}/T_{s1} = K_o$ and p_e/p_s by (11.3.4) characterize thus an endogenous attractor in the large, provided that the initial p_e/p_s is not too big (say < 1.5).

The assumed surcharge p_o can be produced by filling up a granular layer. If this happens in a longer time than required for the diffusion of pore water, as is typical for a natural sedimentation, the initial evolution differs slightly from the one shown by Fig. 11.3.1. The consolidation is then less delayed by diffusion than by creep, but the attractor is the same. Temporal changes of h_w at bottom and top can also be taken into account, thus the enhancement by drainage can be simulated (cf. Sect.10.1 for filter cakes).

The *shrinkage* by evaporation is a consolidation with a given seepage rate at the top. The column base may be impervious, above $v_w - v_s = v_e$ holds with the rate of evaporation v_e . v_e is determined by the relative humidity in the gas channels of the filter cap (Sect. 6.2). This case may be approximated by the linear theory for the case of Fig. 11.1.3, $v_s = -v_w$ holds due to the mass balance. The rather constant pore pressure at the base and a further increase of the top skeleton pressure for $t > t_d$ may be taken over. Thus the consolidation starts at the top and reaches the base later with a smaller amount. Simulations do not work beyond a capillary entry at the top (Sect. 6.3). The densification cannot go on then without lateral deformation as cracks open and grow.

Swelling could likewise be simulated. The top pressure p_o of the column may be reduced and then kept constant, the hydraulic height at top and bottom may be constant. The diffusion time t_d is shorter as λ has to be replaced by the swelling index $\kappa < \lambda$ in (11.3.1). T_{s1}/T_{s2} and p_e/p_s decrease alongside with unloading and diffusion. In the long run p_e/p_s increases again and T_{s2}/T_{s1} decreases as then compressive creep erases the state at the onset.

Evolutions with swelling vary with initial and boundary conditions. With a low or vanishing pressure p_o at the top the skeleton there can approach a dilatant state limit and can decay thereafter. With a high initial p_e/p_s a rapid unloading can lead to shear bands near the surface, and even to cavitation cracks under water. Wetting a free surface after shrinkage, say without cracks for simplicity, causes swelling up to decay if the skeleton has no net attraction (cf. Sect. 6.3). Thus the validity of simulations with columns is restricted by a loss of symmetry or a phase transition into a suspension.

Cycles of decompression and compression can occur in situ by repeated erosion and sedimentation, and more often by repeated wetting and evaporation. Their simulation with columns is debatable as cracks and shear bands play a major role, this can hardly be captured by means of spatial average values (cf. Sect. 8.3). Slow tectonic effects will be treated further below and in Sect. 12.5. Shear cycles due to seismic waves will be considered in Sect. 11.4, they matter less than in psammoid layers.

A stack of peloid and psammoid layers can be represented by a *composite column*. Jovanovic (2002) produced a sandwich of fine sand and clay by sedimentation in a box (Fig. 11.3.2). The sand bands (a) extended up to filtrating walls, thus they enhanced the diffusion of pore water. After 3 weeks the resistance c_u to vane shearing was proportional to depth (b). This evolution could be simulated by means of an increasing stack of FSEs with impeded lateral drainage (c). Thus the sandwich is simplified with due caution for permeability (cf. Sect. 9.2). The reaction of the vane to torsion can be simulated by means of simple shearing (Sect. 14.6). For longer resting times than the diffusion time this shearing resistance is proportional to depth and p_e/p_s , cf. Fig. 11.3.1.

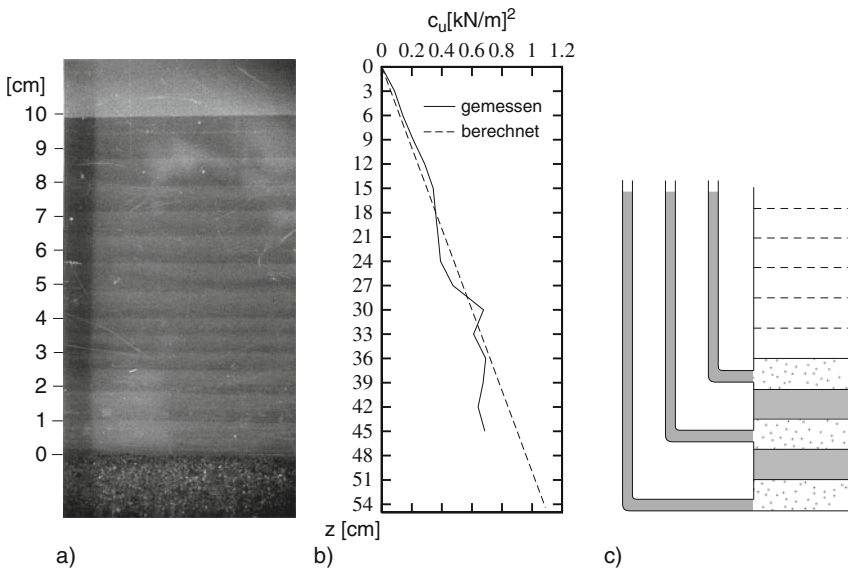


Fig. 11.3.2. Sandwich of peloid and psammoid: vane shearing resistance (b) and bands in a model test (a, Jovanovic 2002), simplified composite for calculations (c)

Natural evolutions are more complex, even without decompression. At the lake of Constance a sandwich of fine sand and silty clay was sedimented upon gravel some thousand years ago. The hydraulic height h_w in the middle of this sandwich was by ca. 1 m higher than hydrostatic due to the low k_f (Scherzinger 1991). The ground of Shanghai consists of sand and clay layers. In some parts h_w is ca. 4 m higher than hydrostatic, and with the thus reduced p_s the p_e/p_s attains ca. 1.3. Up to ca. 400 m thick deposits of silty clay in the Orinoco delta have higher h_w as their diffusion time t_d exceeds their resting time t_g . Tertiary clay layers with resting time $t_g \gg t_d$ have no excess h_w , without decompression their shearing resistance c_u without drainage is

proportional to depth and corresponds to $p_e/p_s \approx 2$ by (11.3.4) after some million years.

The need to simplify composition and initial state for such cases leads to an inevitable indeterminacy of predictions. Deposits in the Lower Renish Basin (Pierschke et al. 1996) may serve as an example. Layers of sand and gravel interchange with seams of clay and lignite, these can be identified as psammoids and peloids. The total pressure was constant while h_w was lowered within two decades. Initial void ratios were determined by borehole logging. They correspond to a relative void ratio $r_e \approx 1/3$ for psammoid and $p_e/p_s \approx 2.5$ for peloid zones. The low r_e may be attributed to earthquakes (cf. Sect. 11.4), the p_e/p_s is also obtained by (11.3.4) with an age $t_g \approx 2 \cdot 10^7$ years. T_{s2}/T_{s1} by (11.2.9) was assumed as outlined with Fig. 11.3.1h. Observed settlements were smaller than calculated. For a better matching thinner sand bands between clay and lignite had to be assumed as hydraulically closed. This indeterminacy (Sect. 9.2) matters more than the representation of lignite as a peloid.

These findings may be generalized as follows. The initial h_w should be measured in situ for cases with $t_g < t_d$. T_{s2}/T_{s1} by (11.2.9) is justified without decompression, this was outlined with Fig. 11.3.1 for peloids and will be defended for psammoids in Sect. 11.4. p_e/p_s may be estimated by (11.3.4), but should also be assessed by vane shearing, penetration sounding or borehole logging. Lab tests with samples from boreholes are needed to get parameters for skeleton and pore fluid. Representative composite columns have to be simplified for numerical simulations. The assumed invariance in horizontal directions causes a further indeterminacy, in particular as psammoid inclusions can more or less work as horizontal drains (Sect. 10.4).

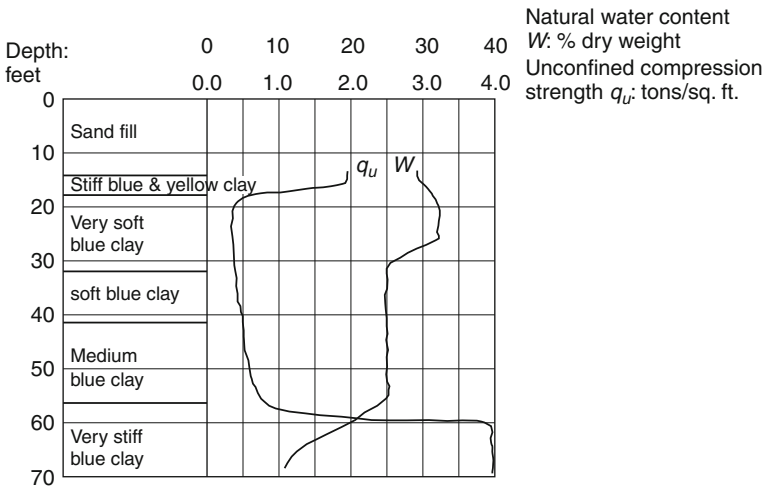


Fig. 11.3.3. Composite ground in Chicago (Wu and Berman 1953); water content and uniaxial strength versus depth

Composites with decompression reveal a wider manifold of compositions and initial states. For instance, a clay in Chicago (Wu and Berman 1953) is differently overconsolidated, Fig. 11.3.3. The p_e/p_s estimated from undrained strength exceeds ca. 4 at the base, this can be attributed to a glacial overburden. A consolidation ratio $p_e/p_s \approx 4$ near the top is due to shrinkage as the surface was temporarily exposed. $p_e/p_s \approx 1.5$ in between may be explained by consolidation under a young sand fill, assuming that the diffusion of pore water was enhanced by cracks. Initial hydraulic height h_w and stress ratio T_{s2}/T_{s1} could not be measured, so both have to be guessed. h_w may be hydrostatic in this case due to cracks, T_{s2}/T_{s1} by (11.2.9) could have been attained by compression and relaxation.

Field situations are often less determined as extended horizontal layers are rather an exception than the rule for composites with decompression. Erosion is never uniform, a re-sedimentation is often accompanied by granular and mud flow. Slow tectonics can lead to faults and to depressions which are later filled (Sect. 12.5). Psammoid inclusions can have lower or higher h_w than due to the groundwater table, h_w can rarely be measured in all details. It is as yet impossible to measure T_{s2}/T_{s1} reliably, so (11.2.8) may suffice as an estimate. Horizontally variable compositions may be estimated from boreholes with the aid of sedimentological and tectonic considerations. Simulations with hypoplasticity could be of use, also if the ground had temporarily slopes. Then plane-parallel symmetry may be assumed, initial states can be generated by simulating a simplified past (Sects. 12.1 and 12.2). Conventional stress and strength ratios can scarcely be defended, let alone Terzaghi's (1925) preconsolidation pressure (cf. Sect. 3.5).

Evolutions with horizontal stretching in situ are more complex. Sedimentation and erosion can occur alongside with tectonic deformations, horizontal uniformity is rarely given. Fractal patterns of shear bands and cracks arise and change with time, hydrostatic pore water pressures are rather an exception (more in Sect. 12.5). Simulations with plane-parallel symmetry could be more realistic (Sects. 12.2 and 12.3).

To *sum up*, evolutions of standing peloid and composite columns can be simulated with different boundary conditions of skeleton and pore water. This can help to understand or even predict consolidation and swelling, and also consequences of horizontal stretching or shortening. The diffusion of pore water dominates the delay of settlement or heave as long as it implies substantial excess pore pressures, thereafter the skeleton viscosity can get dominant. The initial stress and consolidation ratios can be estimated by assuming preceding attractors in the large. The column symmetry can get lost by warping, shear localization or cracking. Substituting packages of peloids and psammoids by composite columns is debatable as the assumed horizontal invariance can rarely be defended. Simplifications of composition, initial state and time-dependent boundary conditions cause an indeterminacy which could hardly be overcome by considering two- or three-dimensional evolutions.

11.4 Standing soil columns with wave propagation

Consider now a package of horizontal layers upon a shaking base from which plane waves are propagated upwards. Neglecting the horizontal variability one may work again with columns, but now also with horizontal displacements. Leaving aside algebraical and numerical aspects we focus on physically revealing cases. This means that the simplifying assumptions are justified, the identification of composition and initial state is tractable, the boundary conditions are realistic, the numerical procedure is verified and that observational data are available for validation.

Lab experiments with soil columns are left aside as they can scarcely be carried out without horizontal gradients. Resonant column tests with torsion imply radial differences of state (Sect. 14.7), the latter occur also with longitudinal waves near the end plates. A propagation of plane longitudinal waves through a column in a confining cylinder can hardly be achieved without wall friction. Tests with laminar shake boxes can at best produce plane-parallel evolutions (Sect. 14.5).

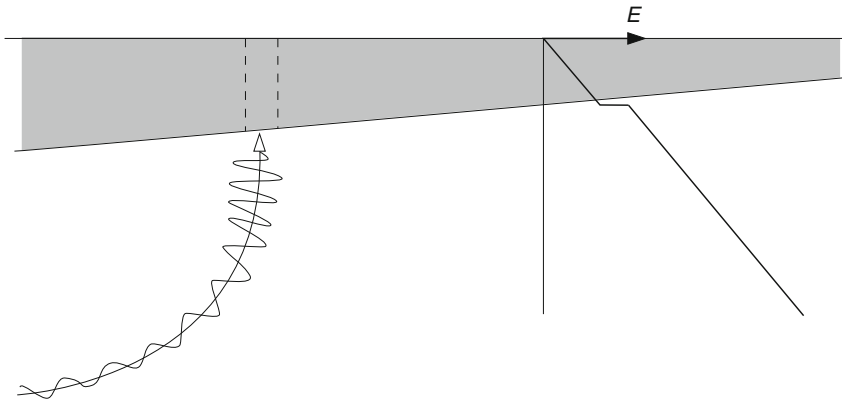


Fig. 11.4.1. Sediment basin with incident seismic wave (*left*) and increasing stiffness versus depth (*right*)

Seismic propagations *in situ* can get almost one-dimensional in sediment basins, Fig. 11.4.1. Soil layers and ground water conditions may be horizontally uniform over distances which exceed by far the package depth. Cemented layers below may behave elastically with a modulus E that increases about linearly with depth. Then seismic longitudinal (P-) and transversal (S-) waves arriving from the rock base tend to vertically propagated plane waves. In the linear range this holds for any monotonous increase of E with depth (Brekhovskikh 1960).

The rims of the basin should be distant enough, and the soil layers should be sufficiently anelastic so that seismic surface waves from the sides cannot

reach the middle of the basin. If all these conditions are satisfied the basin works as an attractor in the large that transforms incident seismic waves from the deeper earth crust into plane ones which are propagated vertically upwards in soil columns. The identification of composition and initial state follows the outline in Sect. 11.3. Deviations from the proposed initial stress ratio T_{s2}/T_{s1} , and also ratios of initial components of the hidden state, fade away with the propagation of a few waves. This was shown numerically for psammoid columns by Osinov and Loukachev (2000) with hyp- δ : after the passage of one or two waves with typical seismic amplitudes skeleton stress and intergranular strain attain asymptotic cycles in each RSE of the column.

Cudmani (2010) points out that an arbitrary initial skeleton stress field, including horizontal gradients, tends to $T_{s2}/T_{s1} = K_o$ by seismic waves. As the latter are rather erratic this can also be understood as a seismically activated creep-relaxation (cf. Sect. 4.7) which is similar to the thermally activated one in peloid layers. The layers should be horizontal as otherwise they would drift sideways, such kind of seismically activated creep will be treated in Sects. 11.5 and 11.6. Formerly or presently active tectonic faults are left aside (Sect. 12.5).

The boundary conditions for the pore water and for the skeleton at the surface can be the same as in Sect. 11.3. The base shaking of the skeleton should be taken from seismograms of boreholes, but only few good data sets are available from arrays. In other cases the seismic history may be substituted by bunches of periodic base shaking. Only S-waves at the base are taken into account as the database for P-waves is insufficient for validations. Constitutive relations may be chosen as explained in Chaps. 4 and 5, but only examples with hyp- δ and v-hyp- δ are given in the sequel as the publications with elp- α are less tractable. Papers with ad hoc relations for cyclic shearing are left aside as these are not frame-indifferent and cannot produce attractors.

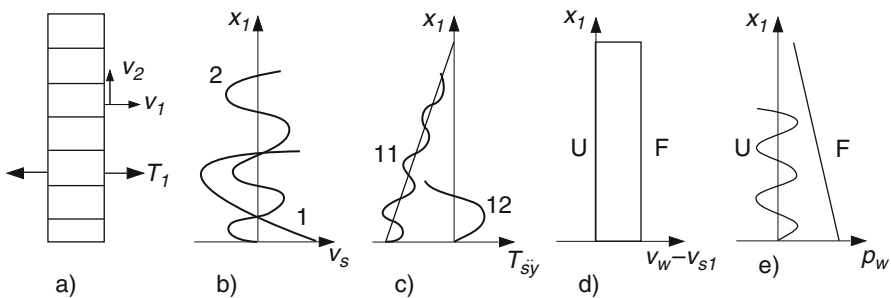


Fig. 11.4.2. Psammoid column with shaking base (a), profiles of horizontal velocities (b), skeleton stress components (c), seepage velocities (d) and pore pressures (e)

General mechanical and numerical features are indicated with a psammoid column, Fig. 11.4.2a. The vertical and horizontal components v_{s1} and v_{s2} of

the skeleton velocity are continuous functions of depth via interpolation functions (b). The skeleton stress components T_{s11} , T_{s12} and T_{s3} (out of plane) can have jumps between the finite soil elements (c), as also the stretching components D_{11} and D_{12} (cf. Sect. 2.9). The vertical seepage velocity $v_w - v_{s1}$ (d) is constant with free drainage (F) and negligible without drainage (U). The pore pressure p_w (e) is stationary in case F and pulsates with propagations in case U. The conservation of linear momentum holds with terms for two components, it is satisfied in the adequate spatial average as the conservation of water mass. The skeleton may be not quite saturated, thus the pore fluid is compressible (Sect. 6.2). The increments of position and state can be calculated via implicit time integration and iterations as the differential constitutive relations of the skeleton are non-linear.

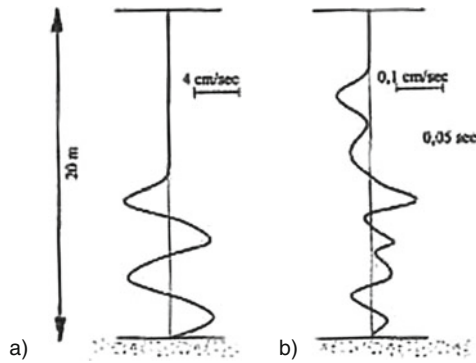


Fig. 11.4.3. Simulated evolution of a freely drained psammoid column with harmonic base shaking (Gudehus et al. 2001): profiles of horizontal (a) and vertical skeleton velocities (b)

Simulation results by means of hyp- δ with a *psammoid* and *hydrostatic* pore water are shown in Fig. 11.4.3. The vertical skeleton pressure is given by (11.2.6) and stationary. The base of the column is shaken horizontally with amplitude $v_a = 0.03$ m/s and frequency $f = 10$ s $^{-1}$, this may represent a rather strong earthquake. 0.05 s after the onset a sinusoidal S-wave can be seen from the profile of the horizontal velocity (a). A less regular and smaller P-wave appears in the profile of the vertical velocity (b). The P-wave propagates with about twice the frequency and speed of the S-wave. With further shaking (not plotted) the waves reach the free surface, there they are magnified but almost not reflected as a major part of the energy is absorbed by friction. With repeated propagations the skeleton is densified up to an asymptotic e just above the lower bound e_d , but not near the free surface where bigger amplitudes cause dilation.

The evolution of an RSE in the middle resembles the one shown in Fig. 4.3.4, case B. A *state cycle* is attained which depends only on the shearing amplitude γ_a . For it two volumetric cycles are induced by one shear cycle,

and the average \bar{e} exceeds e_d more for a bigger γ_a . The transition needs more reversals in case of a higher initial e and a smaller γ_a . Shear waves propagate with a speed c_s which is roughly proportional to $(p_s/p_o)^{1/4}$ by (4.2.1) with $m \approx 1/2$ and $c_s \approx \sqrt{G/\rho}$. They generate P-waves of lower amplitude with about double speed and frequency, this corresponds to Fig. 11.4.3. The kinetic energy is dissipated by hysteretic damping and via the induced P-waves. With a sufficient number of waves the psammoid layer attains an attractor in the large which can be represented by a set of state cycles for a stack of RSEs. The intergranular strain is part of it, i.e. the initial values are swept out.

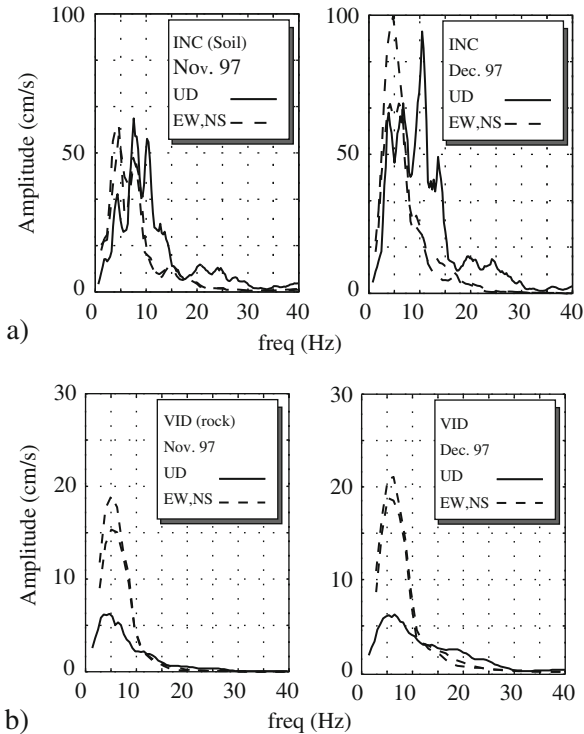


Fig. 11.4.4. Frequency spectra of two earthquakes in Romania (Lungu 2003, Loukachev 2002): one peak of P-waves for the rock base (*below, full lines*), two peaks for a sand layer (*above*); no such difference occurs for S-waves (*dashed*)

Frequency spectra from Romania confirm the double frequency of P-waves, Fig. 11.4.4 (Lungu 2003). At the rock base S- and P-waves had nearly the same spectrum for two moderate earthquakes, with lower P- than S-amplitude, this indicates elastic behavior. Near the surface of the granular sediment the S-spectrum has its peak nearly at the same frequency as the rock base, whereas the P-spectrum has a maximum near the double frequency. With the mod-

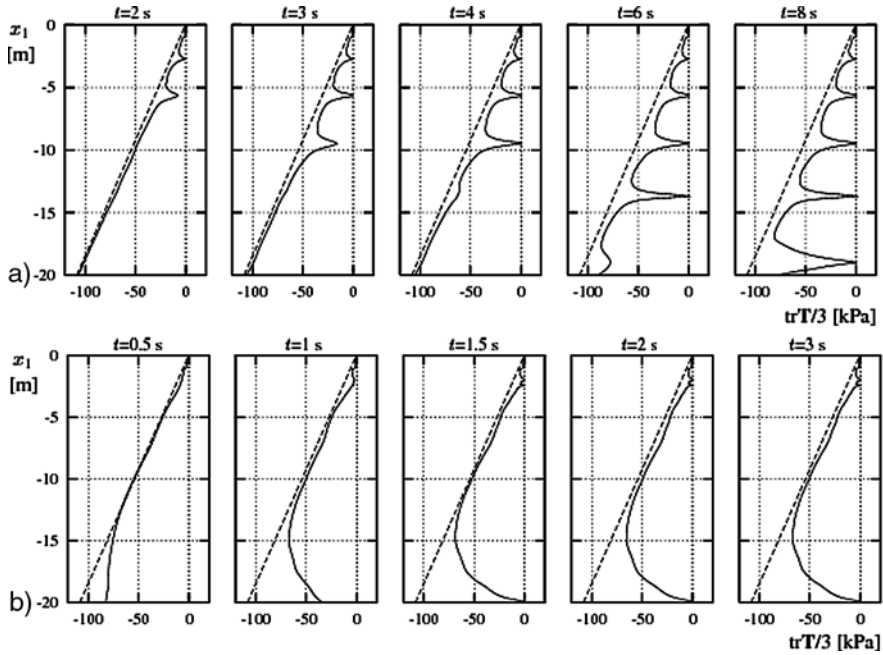


Fig. 11.4.5. Calculated evolution of an undrained psammoid layer with harmonic base shaking (Osinov 2000): skeleton pressures versus depth with moderate (a) and big amplitude (b)

erate magnitude the amplitudes are bigger than at the base. Relative void ratios r_e around 0.3 were determined in the Lower Rhenish Basin (Pierschke et al. 1996) with sand and gravel which experienced many moderate and some strong earthquakes in the past about 10^7 years, though less often than in Romania.

Simulations with an *undrained psammoid* layer are shown in Fig. 11.4.5 (Osinov 2000). With the assumed shaking frequency $f = \omega/2\pi = 5 \text{ s}^{-1}$ seepage was proven to be negligible for permeabilities $k_f \leq 10^{-4} \text{ m/s}$, i.e. for fine sand or silt. Sinusoidal shaking with an initial $r_e \approx 0.5$ and amplitude $v_a = 0.04 \text{ m/s}$ leads to zero skeleton pressure in a succession of depths (a). Shear waves are no more propagated through a decayed skeleton, after ca. 8 s the whole layer is screened from the base. With the same initial r_e and $v_a = 0.1 \text{ m/s}$, corresponding to a stronger earthquake, the skeleton decays near the surface and then at the bottom so that the layer is screened after 3 s (b). Only a minute densification is achieved at the end of shaking so that nearly the same would happen in a repetition.

The evolution of the skeleton in an RSE resembles the one shown in Fig. 4.3.6 (case A). With 98% saturation and without drainage e is almost constant. The asymptotic cycle depends only on the shear amplitude γ_a , then the average p_s is lower for a smaller γ_a . In the transition p_s is more reduced

in case of a higher initial r_e , and more reversals are needed with a lower γ_a . One shear cycle induces two p_s -cycles, so P-waves in the skeleton have the double leading frequency. As always they travel faster than S-waves and there is a second P-wave in the pore fluid, this is not considered here for lack of field data in that respect. For $e > e_{do}$ the skeleton tends to a decay. Near the surface with the biggest amplitude this occurs immediately. Moderate shaking causes the biggest shearing amplitude γ_a somewhat deeper so that there the skeleton decays next, then γ_a gets maximal again deeper and so forth.

This comes up to another attractor in the large. State cycles with low average p_s and temporary decay are attained by a few S-waves, then these are no more propagated upwards. As the subsequent densification is minute this can happen repeatedly, provided that k_f is lower than ca. 10^{-4} m/s and r_e exceeds ca. 0.5 (Osinov 2000). There are many formations of rather loose fine sand in earthquake regions which exhibited a skeleton decay by mud volcanos and spreading. The predicted screening is also validated by observations during the Kobe 1995 earthquake (Iwasaki and Tai 1996). The buildings on the two Port Islands were not damaged except for quay wall structures along the rims. They stand upon a ca. 12 m deep layer of densified sand, the nearly saturated loose sand underneath decayed with the first shear wave so that the following ones could not get through. Although the islands settled by ca. 0.4 m this screening could happen again as only part of the loose sand was thus densified.

Some field data sets are apt for a back-analysis with *composite columns*, Fig. 11.4.6 (Cudmani et al. 2003b). A soil profile from one of the Kobe Port Islands was substituted by a package of psammoids and peloids (a). Using the base shaking measured 1995 the course of horizontal velocities was calculated with hyp- δ and v-hyp- δ for three depths, the overall agreement with observed data is good (b). The calculated reduction of skeleton pressure (c) explains the introduced near-screening ca. 10 s after the onset which was outlined with Fig. 11.4.5. A similar validation was presented by Cudmani et al. (2003b) with data from an earthquake in California 1989.

A *temporary water film* can arise by shaking a saturated psammoid layer which is covered by a peloid layer. If the psammoid is rather permeable and loose its top is rapidly densified and releases water which is caught by the cover. This cannot easily be calculated as the grain skeleton decays near the top and develops erosion channels (cf. Sects. 10.2 and 12.3). It was observed by Kokusho (1999) in a plexiglass cylinder, the kind of shaking does not play a big role. In a coastal plane with a sandwich of sand and clay plates of soil can thus slide seawards just after an earthquake, this happened e.g. at the Corinthian Gulf (Papatheodorou and Ferentinos 1997). Not sliding parts were screened by the water film so that light buildings on top were not damaged. As this can happen repeatedly one can speak of another attractor in the large.

To *sum up*, under certain conditions the response of sediment basins to earthquakes can be captured by means of columns composed of psammoids and peloids. Incident seismic waves from the lithosphere turn into vertically

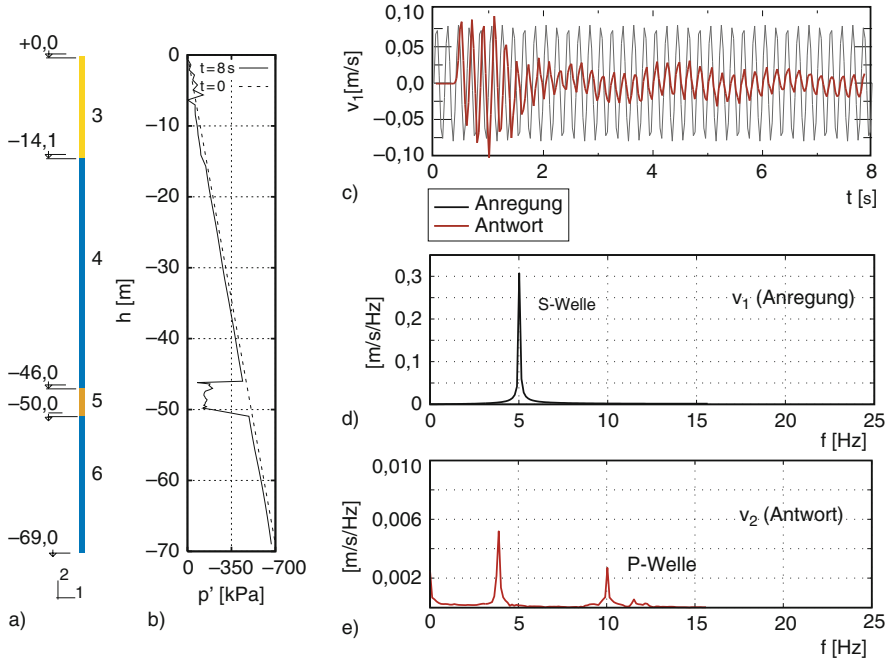


Fig. 11.4.6. Back-analysis of seismic evolutions in Kobe 1995 with hyp- δ and v-hyp- δ (Cudmani et al. 2003b): substitute composite (a), pore pressure (b) before and just after shaking, horizontal velocity (c) versus time at base and surface, velocity spectrum for base (d) and surface (e)

rising plane waves as the stiffness increases with depth. Sufficiently drained psammoid layers tend to a low relative void ratio r_e and remain there with further earthquakes. S-waves produce P-waves of about double frequency and speed. Rather loose, saturated fine-grained psammoids can decay temporarily in different depths so that layers on top are screened against further S-waves. Peloid layers respond more elastically, only with low initial overconsolidation and strong earthquakes the pore pressure can increase and a densification follows. Saturated psammoids with not too low r_e and a peloid cover develop a temporary water film without sliding resistance.

11.5 Psammoid columns in slopes

An inclined psammoid layer with a slope angle β may be so uniform that changes uphill and parallel to the cross section are negligible, Fig. 11.5.1. Then a column (a) with spatial changes along one co-ordinate x_1 may suffice to represent evolutions of shape and state. Pore water can be taken into account without or with seepage. Initial composition and state should be physically attainable. Gravity causes skeleton stress components which increase almost linearly with depth as the specific weight γ is nearly constant (b). Changes of

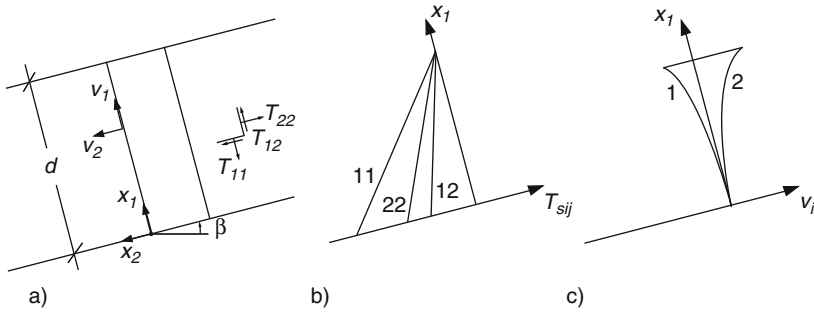


Fig. 11.5.1. Inclined psammoid layer (a), profiles of stress components (b) and velocities (c)

state due to changing boundary conditions can be related with downhill and normal components of skeleton velocity (c). The assumed symmetry can get lost, therefore proper validations are rare, so this section is rather a preparation for subsequent ones.

If a resting psammoid layer is *dry* and has a constant specific weight γ two stress components are given by equilibrium, viz. for $0 \leq x_1 \leq d$

$$\begin{aligned} T_{11} &= \gamma(x_1 - d) \cos \beta \quad , \\ T_{12} &= \gamma(x_1 - d) \sin \beta \end{aligned} \tag{11.5.1}$$

with layer thickness d , therein the atmospheric pressure is omitted. In his treatise ‘On the stability of loose earth’ Rankine (1856) calculated the in-plane stress component T_{22} by means of a limit stress condition. This is shown in Fig. 11.5.2 with stress circles (cf. Fig. 2.9.1). Assuming a limit stress ratio as by (2.7.4) with a constant friction angle φ , there are two stress circles with the given T_{11} and T_{12} . Usually the case with the lower pressure $-T_{22}$ is called active (A), and the other one passive (P). In-plane stress components can be determined via the poles P_A or P_B . The cases A and B coincide for $\beta = \varphi$.

Can such states arise, and are they relevant for stability? Darwin (1883) refuted Rankine’s theory by his experiments and stated that the *historical element* eludes mathematical treatment. His tilted wall prevented the assumed column symmetry, the kind of placement played a role, but the linearity as by (11.5.1) was confirmed (more in Sect. 13.1). A loose layer could be tilted with its rough base until it flows. Except for the vicinity of upper and lower walls a rather uniform and stationary flow can be achieved. With this stationary shearing the psammoid would be in a critical state (Sect. 2.9). A Rankine state would hold with $\beta = \varphi = \varphi_{sc}$. This would be a necessary condition for stationary quasi-static granular flow.

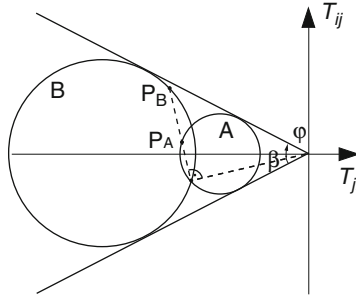


Fig. 11.5.2. Stress cycles of an inclined dry psammoid layer for Rankine states

Equilibrium by (11.5.1) means that inertia is negligible, stationary shearing means $T_{12} = T_{11} \tan \varphi_{cs}$ as by (2.9.6). The onset of granular flow implies an acceleration and is not stationary. An initial Rankine state with $\beta = \varphi_{cs}$ is at best sufficient for stability (i.e. the ability to stand), but not necessary for its loss (i.e. a collapse). A dense granular layer starts to slide when its rough base is tilted up to an inclination $\beta > \varphi_{cs}$. Then a pattern of shear bands appears at the surface (Sect. 12.6) which thus is no more plane. Keeping $\beta > \varphi_{cs}$ the layer accelerates and dilates. A Rankine stress state may be calculated with a friction angle $\varphi > \varphi_{cs}$ due to dilation (Sect. 2.9). The instantaneous relative void r_e should be known and uniform for such a dilatant state limit, but both is not the case. A Rankine state with an assumed $\varphi > \varphi_{cs}$ would at best be necessary for stability, but it is not sufficient. A collapse means a loss of symmetry by shear banding and surface warping. The skeleton stress obliquity at the base is restricted by

$$T_{s12}/T_{s11} \leq \tan \varphi_{si} \quad (11.5.2)$$

with the friction angle φ_{si} of the interface (Sect. 10.3). The psammoid sticks with $<$ and slips with $=$ in (11.5.2).

One could also approach Rankine states in a layer on a rough base with $\beta < \varphi_{cs}$ which is uniformly stretched or contracted. As with $\beta = 0$ (cf. Sects. 11.2 and 12.6) shear band patterns arise in initially dense layers, and the surface buckles by contraction of the base. With this loss of symmetry Rankine states are at best estimates by means of a spatially averaged friction angle $\bar{\varphi}$, but this could hardly be determined. The column symmetry gets lost and minute disturbances would cause rearrangements.

Grains could rain upon a rough incline until they form a layer. This gets denser with a diluter pluviation so that the layer can stand for a short while with a higher than critical inclination, i.e. $\beta > \varphi_{cs}$. Then psammoid chips of different size slide after any minute disturbance as can be seen at the leeward side of dunes. Rankine states may be assumed, but they are at best necessary for a loss of stability. An inclined layer could also be mobilized by shaking its rough base. With $\beta < \varphi_{cs}$ it flows almost like a viscous fluid (Sect. 4.6).

Such seismic effects will be considered further below. A Rankine state could be justified for $\beta = \varphi_{cs}$ with minute shaking.

Finally granular material may flow over a curved base. The relative void ratio is nearly critical, $r_e \approx 1$, due to continuous isobaric shearing. The granulate layer is stretched by passing convex parts of the base and shortened over concave parts, its thickness d varies with position and time. Savage and Hutter (1989) analysed such avalanches by combining active and passive Rankine states in assumed columns for convex and concave parts of an incline with the condition (11.5.2) for sliding along a solid (cf. Sect. 10.3). Evolutions of d with position and time were calculated with equations for the conservation of mass and momentum. This theory was validated by lab experiments.

With the assumed symmetry (11.5.1) expresses static equilibrium, and with a peak friction angle φ for the instantaneous relative void ratio r_e Fig. 11.5.2 conveys upper and lower bounds of the in-slope pressure $-T_{22}$. Thus the possibility of a Rankine state is at best a necessary condition for stability. If, on the other hand, a psammoid layer resting upon an incline can release kinetic energy after a minute disturbance it will collapse. With an arbitrary velocity field as disturbance this would be a sufficient condition for instability. The loss of static equilibrium can imply a loss of symmetry, i.e. a kind of bifurcation.

Osinov and Wu (2005) discuss criteria for the *instability* of rate-independent anelastic bodies. The spontaneous loss of static equilibrium cannot be judged by means of eigenvalues and -vectors as the differential constitutive relations are not linear. Therefore the mathematical well-posedness cannot be recognized algebraically, one cannot decide analytically whether or not a small disturbance results in a weak response (stability in the sense of Lyapunov). The energy condition mentioned above cannot lead to more explicit criteria by working with arbitrary disturbances. Test shear waves cannot pass an emerging shear band with the same normal, this leads to necessary conditions for localization. The impossibility of propagating arbitrary test waves is a necessary condition for instability. All that cannot provide sufficient conditions for static stability, nor can it produce general predictions of further evolutions with localization, bulging and/or collapse.

Simulations with a *shaking base* could be carried out as long as the symmetry of columns is justified. The propagation of each plane wave leaves back an additional downwards displacement, and a depth-dependent change of void ratio $\Delta e(x_1)$ in general. As long as the slope angle is lower than critical, i.e. for $\beta < \varphi_{cs}$, a stationary ratcheting can be expected in the asymptote. The average asymptotic void ratio $\bar{e}(x_1)$ and downwards displacement $\Delta u_2(x_1)$ after each propagation are determined by the acceleration amplitude at the base. The ensemble of asymptotic state cycles is an attractor in the large.

Consider now psammoid columns in slopes with *pore water*. If the column or a part of it is humid with gas channels the skeleton has a capillary pressure p_{cs} (Sect. 6.2). Asymptotic stress circles as by Fig. 11.5.2 are shifted to the right by p_{cs} . This leads to a tensile in-slope stress in case of lateral extension,

i.e. to $T_{22} > 0$ up to a depth which is proportional to p_{cs}/γ . This is often interpreted as the depth of tension cracks, but this kind of cavitation breaks the assumed symmetry so that such an analysis with it is inconsistent. The restriction by cavitation holds also for more elaborate simulations.

If an inclined psammoid layer is submerged in resting water calculations as without water suffice except for the specific weight γ . This is replaced by $\gamma - \gamma_w$, i.e. by subtracting the hydrostatic uplift with $\gamma_w \approx 9.8 \text{ kN/m}^3$ for water. With a groundwater table at the inclined surface (Fig. 11.5.3a) the skeleton gets also the specific seepage force $f_s = \gamma_w \sin \beta$ in the same direction. Thus (11.5.1) is replaced by

$$\begin{aligned} T_{s11} &= (\gamma - \gamma_w)(x_1 - d) \cos \beta, \\ T_{s12} &= \gamma(x_1 - d) \sin \beta \end{aligned} \quad (11.5.3)$$

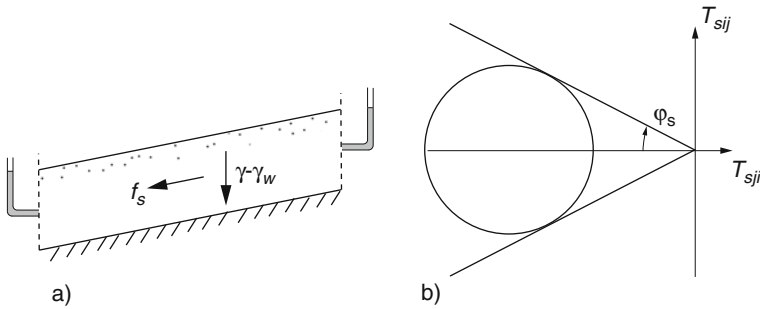


Fig. 11.5.3. Inclined psammoid layer with seepage (a), limit stress circle (b)

for the saturated skeleton. This changes active and passive limit stress circles, and a single one (Fig. 11.5.3b) is obtained for $T_{s12}/T_{s11} = \tan \varphi_s$, i.e. for

$$\tan \beta_s = \tan \varphi_s (1 - \gamma_w/\gamma) \quad (11.5.4)$$

with a friction angle φ_s that depends on the relative void ratio r_e (cf. Sect. 2.9). This statically possible inclination is lower than without downhill seepage. As without or with resting pore water (11.5.4) is necessary for stability, but sufficient only with the critical friction angle φ_{cs} and $r_e \leq 1$.

More often the groundwater *in situ* flows through a lower part of the layer, and the upper part is humid. One could again construct limit stress circles and calculate a statical limit inclination. Evolutions of columns could be simulated with p_{cs} above and p_w below the groundwater table. This would work also for the propagation of plane waves which could be simulated with $\text{elp-}\alpha$ or $\text{hyp-}\delta$. Apart from cavitation cracks critical phenomena with loss of column symmetry can arise by shaking if $\tan \beta$ exceeds the critical value calculated by interpolation of (11.5.1), (11.5.2) and (11.5.4) with φ_{cs} .

The coupling of skeleton and pore water is strongest *without seepage*, in particular for degrees of saturation S_r near 1. This requires shearing times t_s well below diffusion times, say $t_s \leq 10^{-2}t_d$ with t_d by (11.3.1). A saturated psammoid layer *under water* with a high relative void ratio r_e can collapse. This can happen with sediments along a coastal shelf or with flooded mining deposits, with high r_e due to a minute net attraction (Sects. 6.2 and 7.1). With hydrostatic p_w two initial skeleton stress components (a) are given by gravity,

$$\begin{aligned} T_{s11} &= (\gamma - \gamma_w)(x_1 - d) \cos \beta \quad , \\ T_{s12} &= (\gamma - \gamma_w)(x_1 - d) \sin \beta \quad , \end{aligned} \quad (11.5.5)$$

if the specific weight minus uplift $\gamma - \gamma_w$ is constant versus depth. This is obtained from (11.5.1) with a constant hydraulic height. The in-slope components T_{s22} and T_{s33} are statically indeterminate, they may be generated with elp or hyp by imposing T_{s11} and T_{s12} to an RSE with simple shearing from a low initial p_s and a suitable r_e . Rankine states are not justified for the onset, and internal variables may be left aside in case of large monotonous deformations.

An isochoric shearing is related with changes of skeleton stress components which depend mainly on the initial r_e . Very loose psammoid columns collapse with a change of width and height. When the layer slumps it undergoes changes in the downhill direction, thus the assumed column symmetry gets lost. If such a collapse would release more kinetic energy it could arise spontaneously. One can judge such a loss of stability by calculating the excess of kinetic energy with assumed collapse modes (Gudehus 1998). Instead of assuming collapse modes one could generate them numerically by means of a spatial fluctuation of r_e . The suspension flow after a decay of the skeleton and the re-combination of a psammoid will be treated in Sect. 16.3.

A similar collapse can occur with a loose, nearly saturated fine-grained psammoid at the air. This can happen with natural and technical deposits after they are soaked by rain. With 100% humidity and atmospheric pressure p_a the initial pore water pressure is $p_w = p_a + \gamma_w(d - x_1)/\cos \beta$. Two initial skeleton stress components are given by (11.5.1), the further two could be generated by simulation with the given e . They could reveal whether $-T_{s12}$ would decrease by isochoric shearing, this could suffice for a spontaneous collapse. A collapse could occur more easily if more kinetic energy would be released by an isochoric bulging. For $e > e_{co}$ the slope would collapse into a suspension with any inclination $\beta > 0$ and initial p_w .

Gas bubbles can play a role for a collapse without seepage. They can be caught in a flooded or soaked slope (Sect. 6.2) and can render possible high void ratios (Sect. 7.2). Collapse modes are slightly contractant with them, this is controlled by the ideal gas equation. After a decay of the skeleton the gas bubbles rise so that the suspension gets denser. Rising bubbles can unite to a gas cushion under a less permeable cover, this reduces the sliding resistance until the cushion breaks out (Gudehus 1998).

Evolutions of saturated psammoid columns *with seepage* can be induced by changing boundary conditions. If a top layer is imposed and maintained within

times which exceed the diffusion time t_d the slope is densified and sheared. This may be calculated by $\text{elp-}\alpha$ or $\text{hyp-}\delta$ as outlined at the beginning of Sect. 11.3, now also with lateral displacements. Changes of hydraulic conditions could likewise be taken into account, e.g. evaporation above or drainage below. If a collapse can be excluded, which has to be checked without further seepage as outlined above, the assumed one-dimensionality need not get lost. As without shearing the RSEs in stable columns can approach a contractant state limit, this would be an attractor in the large.

A loss of symmetry can occur with *localized dilation*. Suction can lead to nearly vertical cracks near the free surface. This implies a capillary entry in case of full saturation and an extension otherwise (cf. Sect. 6.2). Shear bands can arise not only along the base, but also up to the surface. The localized dilation can cause cavitation of the pore water, near the free surface shear bands can go over into cracks. All that requires a lower than critical initial r_e . Water can rapidly enter via cracks which collapse and can leave back such a high p_w and overall r_e that the slope collapses.

A saturated psammoid layer upon an inclined *shaking base* flows like a liquid. If the void ratio and the slope angle are lower than critical the column symmetry need not get lost by a collapse. Cavitation and shear localization do not occur if the accelerations are not too big. During the propagation of waves through the layer the seepage may be neglected (Osinov 1998) except for the vicinity of a surface and/or base with free drainage. Repeated propagations within a much shorter time than needed for diffusion lead to a higher than initial p_w (a) and ratcheting. This corresponds to Ibsen's (1994) triaxial test results (Fig. 4.2.8) and is captured by $v\text{-hyp-}\delta$ for RSEs in the slope. Detailed simulations could be carried out as proposed by Osinov (2003).

In waiting times without shaking the field of p_w returns to the one given by the hydraulic boundary conditions, and the layer comes to rest with a minute densification. The rapid and strong drainage and densification observed in shakebox tests (Sect. 12.3) due to the breakthrough of channels can be left aside as it requires a suspension which is excluded by lower than critical r_e and β . The intermittent flow (seismic creep) may be estimated by means of seismo-hypoplasticity (Sect. 4.6). This requires model tests to determine scaling factors, and the seismic energy per unit of time and base area is needed for estimating the granular temperature. The influence of r_e and p_w could thus be captured semi-empirically.

Summing up, inclined psammoid layers can be captured by columns as long as inclination β and relative void ratio r_e do not exceed critical values. Without water and with resting water the critical inclination agrees with the critical friction angle, $\beta_c = \varphi_{cs}$. With an inclined groundwater table the statically possible β is reduced by the seepage force. Rankine's (1856) stress states are not sufficient for stability, but may be used for granular flow upon an incline. A saturated psammoid layer with higher than critical β and r_e collapses without seepage, then the assumed symmetry of columns can get lost. The stability can be judged by the release of kinetic energy with a simplified

collapse mode. With a high enough r_e a saturated psammoid turns into a suspension, then gas bubbles can enhance collapse and flow. The assumed column symmetry can get lost by warping, shear localization and/or cavitation.

11.6 Peloid columns in slopes

Peloid columns in slopes can be defined by the same symmetry as with psammoids. We assume full saturation for simplicity, but gas bubbles between the particles could be taken into account (Sects. 6.3 and 7.3). Coupling of skeleton and pore water can occur in many variants. This section is again rather introductory as the assumed symmetry is at best approximately given in situ.

Consider first peloids with *hard grains* so that the skeleton viscosity may be neglected. Their permeability is low, and they can have a net attraction $p_n < 0$ of the skeleton (Sect. 6.3). The contribution of p_n to the skeleton pressure via $p_s = p - p_w - p_n$ may be negligible, i.e. $-p_n \ll p_s$ is assumed, but even then the limit void ratios can be substantially higher due to $p_n < 0$ (Sect. 7.1). As p_n depends on pH and the salt concentration changes of both can have a dramatic influence on the stability, Fig. 11.6.1. The slope (a) may initially be stable with a free surface at the air due to p_n although the void ratio is high. This is possible e.g. with sea water during the sedimentation.

When the salt is leached out by rain and seepage the net attraction $p_n < 0$ can disappear so that the limit void ratio is reduced (b, A \rightarrow B). Thus the void ratio can get higher than critical, whereas the skeleton stress components required for static equilibrium (c) remain the same. Before the loss of p_n an isochoric shearing would meet an increasing resistance (path A), but now it would decrease (B). Then any disturbance would lead to a collapse into an

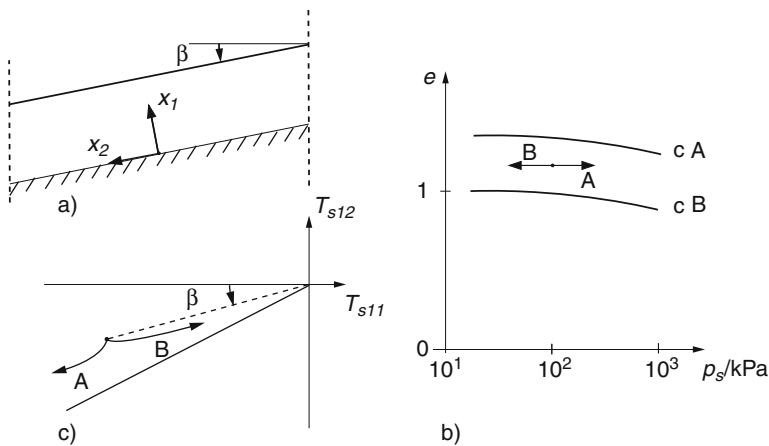


Fig. 11.6.1. Undrained inclined peloid layer with hard grains (a), paths of void ratios versus pressure (b) and stress (c)

avalanche. Such a soil is called *quick clay* (Bjerrum 1955) although its content of clay minerals is low. A similar collapse can occur with mining deposits which are soaked by rain.

The stability can be judged as outlined in Sect. 11.5 for psammoids without seepage. As the dependence of p_n on pH and salt and the one of e_c on p_n cannot be calculated (Sect. 6.3) experiments are needed with the range of expected ionic strength (Sect. 7.1). The further run of an avalanche may be calculated by means of a non-linearly viscous relation, but this cannot capture gas cushions and drainage channels. A stabilization by an increase of $-p_n$ could principally be modelled by means of a decrease of e_c and further limit void ratios with time t . The combined diffusion of pore water and solubles (Sect. 6.3) can as yet hardly be captured, however, therefore a series of e_c -tests with different p_n would be needed.

Turning now to peloids with *soft particles*, the skeleton viscosity has to be taken into account. A collapse as indicated with Fig. 11.6.1 may be left aside as with constant ionic strength and soft particles there is almost no reduction of shearing resistance (loss of ductility) without drainage in the geotechnical range of p_s (except for extremely low or high p_s). *Stationary creep* may be assumed without drainage or for times which are well below the diffusion time t_d , Fig. 11.6.2. This can occur after placement without seepage, by placing a top layer or by removing water above the slope. The void ratio e may be spatially constant for simplicity, together with the inclination β and the water on top it is decisive for the creep rate.

The in-plane total normal and shear stress components increase linearly with depth (Fig. 11.6.2a) by (11.5.1) due to static equilibrium. After a transition the creep velocity v_2 has a gradient that increases non-linearly with depth. This is due to skeleton viscosity: stationary shearing in RSEs with different T_{12} and the same e requires different pressure p_s (b), whereas the stress ratio T_{s12}/T_{s11} is constant (Sect. 3.8). This can be approximated by

$$-D_{12} = \frac{1}{2} \frac{\partial v_2}{\partial x_1} = D_r \left(\frac{-T_{12}}{\tau_r} \right)^{1/I_v} \tag{11.6.1}$$

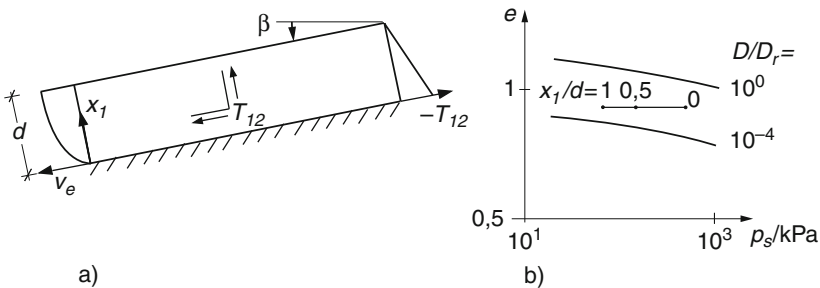


Fig. 11.6.2. Undrained inclined peloid layer (a), critical void ratios versus pressure (b)

with a reference shear stress τ_r which can be determined by an undrained shear test with $D = D_r$. Combination with T_{12} by (11.5.1b) and integration with $v_2 = 0$ for the base $x_1 = 0$ yields

$$v_2 = 2D_r \frac{I_v}{1 + I_v} \frac{\tau_r}{\gamma \tan \beta} \left(\frac{\gamma d \sin \beta}{\tau_r} \right)^{1/I_v + 1} - \left(\frac{\gamma(d - x_1) \sin \beta}{\tau_r} \right)^{1/I_v + 1} \quad (11.6.2)$$

This holds for $0 \leq x_1 \leq d$ and may be simplified by $1/I_v + 1 \approx 1/I_v$ as the viscosity index I_v ranges from ca. 0.02 for 0.05. The creep velocity v_2 is nearly constant for $x_1/d < \text{ca. } 0.2$ with $I_v \leq 0.05$. Therefore (11.6.2) could be validated in a model test with a layer of soft clay upon a rough plate, the slope of which is changed in a much shorter time than the diffusion time t_d .

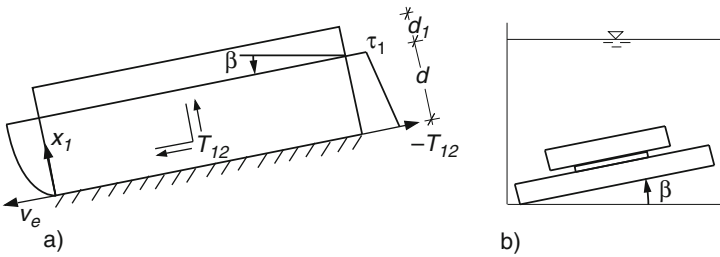


Fig. 11.6.3. Creeping peloid layer with a lid (a), creep test under water (b)

The same approach works also with a top layer, Fig. 11.6.3. With its thickness d_1 and specific weight γ_1 the total normal and shear stresses are bigger by $\gamma_1 d_o \cos \beta$ and $\gamma_1 d_1 \sin \beta$ (a). The creep velocity, which is related again with T_{12} by (11.6.1), has a more uniform gradient due to $-T_{12} > 0$ at the peloid top $x_1 = d$. Integration with $v_2 = 0$ for $x_1 = 0$ leads to

$$v_2 \approx 2D_r I_v \frac{\tau_r}{\gamma \tan \beta} \left[\left(\frac{\tau_o + \gamma d \sin \beta}{\tau_r} \right)^{1/I_v} - \left(\frac{\tau_o + \gamma(d - x_1) \sin \beta}{\tau_r} \right)^{1/I_v} \right] \quad (11.6.3)$$

with $I_v \ll 1$. For $d_o \gg d$ the v_2 -profile gets linear as for simple shearing. The latter case can be validated with a thin submerged layer of clay between two rough impervious plates (b). When increasing the inclination β the velocity of the top plate increases the more suddenly the smaller I_v is. Ignoring the viscosity one would calculate a shear strength c_u from the top weight, the area covered with clay and the inclination β_c required for sliding. A closer look reveals that for each β near β_c there is another stationary v_2 . The covered area could be controlled by choosing a transparent top plate which is smaller than the base and a thin layer which is not squeezed out.

If a drainage is prevented by means of an impervious base and cap the creep motion remains stationary. This is a *state limit in the large* which can be represented by a set of critical states with different stretching rates for different RSEs in a peloid column. The stationary pore water pressure is determined by the total pressure $-T_{11}$ via (11.2.5). The initial skeleton stress states diverge from critical ones, but they get critical by the transition to an argotropic attractor. The transition time t_s is principally determined by the initial state and stretching rate. It cannot be calculated, however, if the initial quantities are not known except for T_{12} and e . The initial stress field caused by the placement need not be uniform in the x_2 and x_3 directions, but even then it tends to the symmetry assumed for columns. This attractor in the large works as long as the layer does not collapse with bulging, and as long as the diffusion of pore water is negligible in case of draining boundaries, i.e. for $t_s \ll t_d$.

The same stationary velocity profile and total stress components are obtained with (3.1.2) and (3.1.23) for an idealized solid. Rübél (2010) simulated *transitions* with a column of finite elements. $T_{22}/T_{11}=T_{32}/T_{11}=K$ was assumed for the statically indeterminate initial stress components with a factor K from 0.8 to 1.2. Assuming an initial state of rest, the calculated velocities tend to a constant velocity profile which agrees with the one by (11.6.2). The statically indeterminate stress components tend to $T_{22} = T_{11} = T_{33}$ in the more deformed lower part. The assumed initial T_{23} and T_{33} remain almost in the nearly undeformed upper part. With a lower viscosity index I_v the transition takes much more time, but about the same rather small deformation. These findings point to an attractor in the large: an argotropic state limit field of shearing (as with a stack of inclined layers) is achieved independently of the initial velocity and stress field. As outlined with Fig. 10.4.3d validations could be achieved with model tests.

Consider now *fully drained creep* which requires shearing times well above the time for pore water diffusion, $t_s \gg t_d$. This could be achieved in the lab with thin layers between filter plates (Balthasar et al. 2006), and can occur in a slope with a thin clay layer upon a pervious base and under a pervious cap. Other than without diffusion the skeleton velocity has two components, v_{s2} tangential and v_{s1} normal. The skeleton stress components T_{s11} and T_{s12} are determined by specific weights, layer thicknesses and hydraulic boundary conditions as for psammoid layers without pore water diffusion (Sect. 11.5). The stress obliquity T_{s12}/T_{s11} may be lower than (A), equal to (B) or bigger than critical (C). The void ratio in an RSE decreases, remains or increases in case A, B or C. It can be substituted by an equivalent pressure p_e , i.e. the p_s for a state limit with the given T_{s12}/T_{s11} and e for the stretching rate $D = D_r$ (Sect. 3.8). $p_s = -T_{s11}$ may be assumed as for isochoric state limits in the calculation of p_e/p_s .

The consolidation ratio p_e/p_s is decisive for the amount of stretching, this changes with stress ratio and time. According to v-elp and v-hyp (Sect. 3.8) the stretching components can be written as

$$\begin{aligned} D_{12} &= -\frac{1}{2}(\partial v_{s2})(\partial x_1) = mD_r(p_s/p_e)^{1/L_v} \\ D_{11} &= (\partial v_{s1}/\partial x_1) = \tan \nu D_{12} \quad . \end{aligned} \quad (11.6.4)$$

Therein the factor m and the dilatancy ratio $\tan \nu$ are determined by the stress ratio T_{s12}/T_{s11} . m is close to 1, whereas $\tan \nu$ has a smaller amount and indicates contractant (A), isochoric (B) or dilatant (C) shearing. The changes of p_s and p_e in the x_1 -direction may be so small that the profiles $v_{s2}(x_1)$ and $v_{s1}(x_1)$ are nearly linear, this is the case with the assumed thin layer which thus undergoes a nearly uniform simple shearing.

With a subcritical stress ratio the creep motion slows down as p_e gets smaller by densification. With a critical stress ratio the creep motion is stationary as there is no change of density. With an overcritical stress ratio the creep motion speeds up as p_e is reduced by dilation. In the third case the drainage gets impeded by the accelerated shearing and by a p_w -decrease. The shearing gets localized (Sect. 8.3) until the slope collapses without further volume change, and cavitation can occur due to suction (Sect. 6.3). The stress ratio is thus decisive for the long-term stability, this can also be expressed by means of argotropic attractors in the large. Contractant or isochoric state limits are attained with subcritical or critical stress ratio. The creep rates are determined by the initial consolidation ratio p_e/p_s . Critical phenomena – viz. localization, cracking and warping – occur with a p_e/p_s -dependent delay. They imply a loss of symmetry, indicate a strange attractor and can hardly be predicted (Sect. 16.3).

Coupled creep and diffusion can only be modelled numerically, at best the stability can be judged analytically. An inclined peloid layer, its base and its cap are identified by dimensions and material parameters. An initial state is specified by profiles of skeleton stress components, pore water pressure and consolidation ratio. The peloid behaviour can be modelled by v-elp or v-hyp (Sect. 3.8), internal state variables are not needed with rather large monotonous deformations (Sect. 5.6). Missing initial skeleton stress components can be generated by imposing gravity up to the given components. The initial consolidation ratio p_e/p_s plays the main role. The permeability k_f is also needed, and its dependence on e can be taken into account (Sect. 6.3). The balance equations for linear momentum and masses and their approximation with finite elements are the same as for psammoids (Sect. 11.2).

Boundary conditions for skeleton and pore water may be specified as imposed evolutions versus time t . The diffusion time t_d estimated by (11.3.1) can be used as reference time. For instance, imposing a top layer can be represented by a simultaneous increase of T_{s11} and T_{s12} at top and base within a loading time. The access of water can be specified by an increase of p_w within a certain time. Drainage below and desiccation above can be specified by a reduction of p_w over a given time. The stress ratio T_{s12}/T_{s11} at the upper and the lower boundary may be stationary and critical, overcritical or subcritical after the proposed changes of boundary pressures.

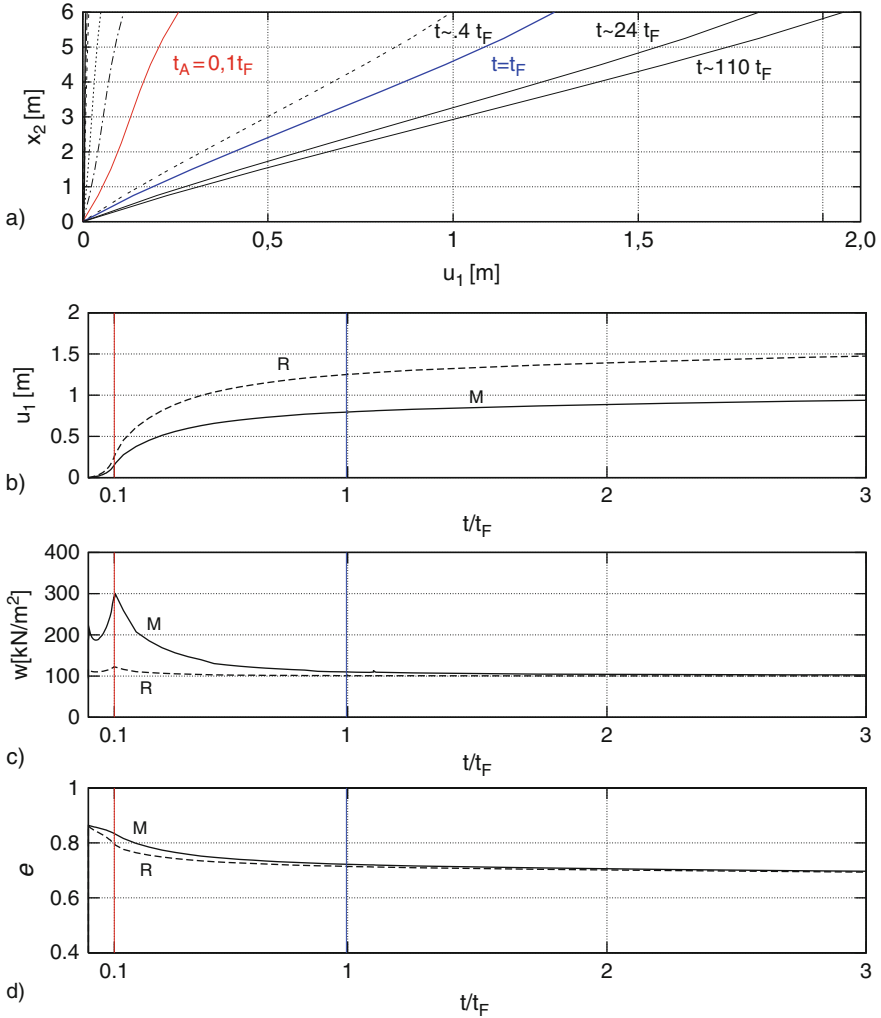


Fig. 11.6.4. Stabilizing creep of an inclined peloid layer with draining boundaries, simulated with v-hyp (Liberos-Bertini 2006): profiles of shear displacement (a); shear displacements (b), pore pressures (c) and void ratios versus time (d) for rim (R) and mid-height (M)

Liberos-Bertini (2006) worked out such simulations for a peloid layer between filter plates. The visco-hypoplastic parameters represent a highly plastic clay, initially the layer thickness is $d = 6$ m, the boundary normal stress is $\sigma_s = -T_{s11} = 1$ MPa, and the pore pressure on top is $p_w = 100$ kPa. With a very low $k_f = 10^{-12}$ m/s, kept constant for simplicity, the diffusion time by (11.3.1) is $t_d \approx 1$ year. The shear stress is increased from zero to a value τ_d within the time $0.1t_d$ and then kept constant, p_w at the boundaries is not

changed. This could represent a clay layer near an excavation (Sect. 12.2), but also a slope with surcharge as details of the increase of σ_s and τ_d are unimportant for the subsequent evolution.

Figure 11.6.4 shows calculated evolutions after *normal consolidation* with *subcritical shear stress*, namely $p_e/p_s = 1$ initially and $\tau_d = 0.55 \sigma_s \tan \varphi_{cs}$ from $t = 0.1t_d$ onwards. The profiles of shear displacement (a) are almost linear. The increase near the upper rim (R) and in the middle (M) of the layer slows down with time (b). The pore water pressure increases by loading and returns to the initial value by diffusion with shear drift (c). The void ratio is more reduced within the diffusion time than thereafter (d). A similar stabilization would occur with any $\tau < \sigma_s \tan \varphi_{cs}$, but slower with a bigger t_d and a bigger initial p_e/p_s .

Figure 11.6.5 shows evolutions calculated after *overconsolidation* with an *overcritical shear stress*, namely with $p_e/p_s = 2.5$ initially and $\tau_d/\sigma_s \tan \varphi_{cs} = 1.4$ from $t = 0.1t_d$ onwards. The profiles of shearing are again nearly linear (a). They are accelerated and diverge at $t \approx 2.7t_d$ (b). The pore pressure is reduced slightly in the beginning and more near the dramatic end (c). The void ratio increases slightly with hardly visible acceleration (d). This destabilization would lead to shear localization and cavitation which cannot be captured by the employed model (Sect. 8.4). It is more delayed with a bigger pre-consolidation and a longer diffusion time.

Seismic waves enhance such evolutions. With a low initial p_e/p_s and a subcritical shear stress propagations produce pore pressure increase and ratcheting, thereafter shearing is slowed down with contraction and diffusion, in the long run the stabilization is stronger than without shaking. With a higher initial p_e/p_s and an overcritical shear stress wave propagations produce ratcheting and minor pore pressure changes, thereafter the time up to a collapse is shorter than without shaking. Such evolutions could be simulated by adding what was said in Sect. 11.4. Big amplitudes have to be excluded as they would lead to cavitation and bulging.

The extension to *composites* of inclined layers is straightforward. Simulations with a fluctuating initial void ratio would lead to more uniformity in case of subcritical stress ratios. Otherwise the fluctuations would enhance critical phenomena as shear localization, cracking and warping so that the assumed column symmetry gets lost. Shaking would enhance diffusion of pore water and creep of the skeleton. This could be captured by asymptotic state cycles with ratcheting in case of periodic shaking. Erratic shaking could be captured by a kind of seismic viscosity, but as yet only in qualitative estimations (Sect. 5.5).

Summing up, peloids with hard grains can be captured nearly as psamoids, but the relative void ratio r_e can be bigger due to a net attraction. If this is reduced by leaching out a peloid slope can collapse into an avalanche. This loss of stability will occur if kinetic energy would be released by any velocity field, then the column symmetry tends to get lost by shear banding and bulging. Water above the slope can stabilize it initially. Undrained peloid

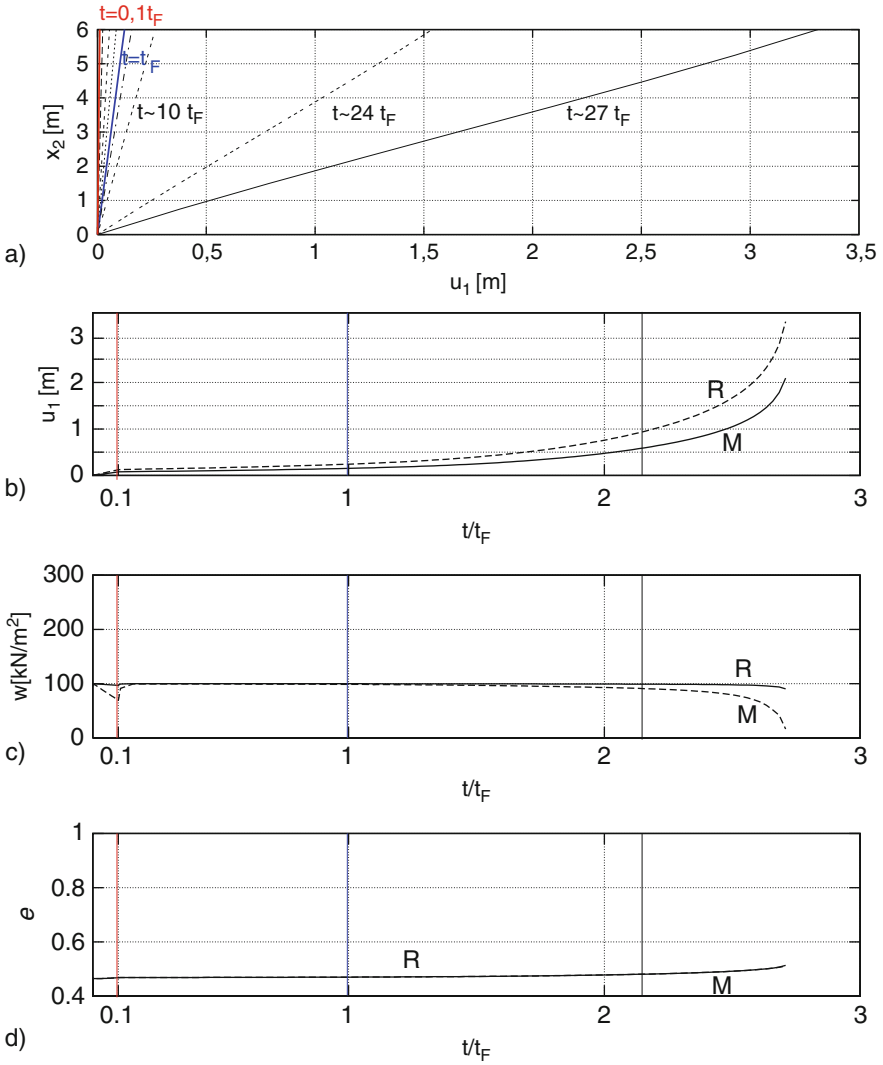


Fig. 11.6.5. Destabilizing creep due to an overcritical stress ratio without instationary pore pressures, otherwise as Fig. 11.6.4; t_F is a reference time for the diffusion of pore water

slopes with soft particles tend to stationary creep. The attained stationary state is an attractor in the large as long as the column symmetry does not get lost.

With drainage the combination of pore water diffusion and shear creep leads to a stabilization if the statically required ratio of shear and skeleton normal stress is subcritical. An attractor in the large is attained more rapidly

with ratcheting by seismic waves. In case of a critical statically required stress ratio the slope tends to stationary shearing with a velocity which is determined by the initial consolidation ratio p_e/p_s . With an overcritical stress ratio the slope collapses sooner or later. The time for stabilization or up to a collapse increases if the initial p_e/p_s and/or the diffusion time t_d of the pore water is bigger, and decreases by seismic waves. Shaking enhances such evolutions, but calculations with it are expensive or rather qualitative.

11.7 Radial symmetry

Radial symmetry, i.e. spatial variation only with radius r , can be spherical or cylindrical. The latter may be assumed e.g. for the *expansion* of a vertical *borehole* in a *psammoid* layer, Fig. 11.7.1. The borehole radius r_o is increased from an initial value r_{oo} over a length of ca. $10r_{oo}$ by inflating a hose (a). The radial skeleton pressure $p_s = p_o - p_w$ increases with the expansion up to an asymptote p_{sa} (b). The pore water pressure p_w does not change because of the high permeability. Vertical displacements and strains may be neglected for the horizontal cross section through the middle of the expander. Similar expansions can be observed in a calibration chamber with controlled placement and pressure under the lid (c). Experiments can also be made with two hard smooth parallel plates (d).

Neglecting the disturbance by installation the initial state for a back analysis with hyp, Cudmani and Osinov (2001) assumed spatially uniform skeleton pressure components and relative void ratio. *In situ* T_{s11} is determined by

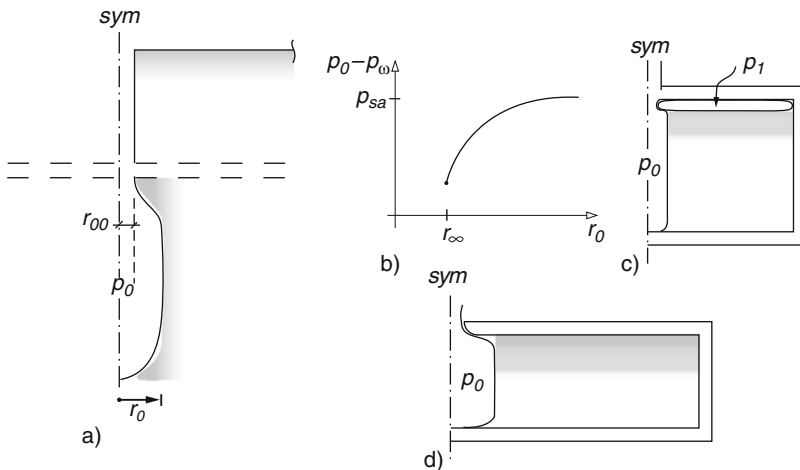


Fig. 11.7.1. Cylindrically symmetric expansion in psammoid bodies: expander in a borehole (a), expansion pressure versus increased radius (b), pressure chamber with controlled top pressure (c) or smooth plates (d)

gravity and T_{s22} may be estimated by (11.2.7), but r_e can at best be guessed by simulating the past (Sects. 11.2 and 11.4). The radial skeleton velocity v_s is given by the expansion, and decreases with the distance so that it may be neglected at a fictitious outer wall with $r_1 = 20r_{oo}$. v_r can be normalized by the rate of radial expansion $\dot{r}_o \equiv dr_o/dt$ as the psammoid is rate-independent. The configuration changes with r_o , and the deformations are big near the expander. r is referred to the initial inner radius r_o . There are two stretching components, viz.

$$D_{rr} = \frac{\partial v_r}{\partial r} \quad , \quad D_{\theta} = \frac{v_r}{r} \quad . \quad (11.7.1)$$

The expansion causes an increase of the radial, circumferential and vertical skeleton pressure components $-T_{sr}$, $-T_{s\theta}$ and $-T_{sz}$ which is smaller for bigger r (b). The evolution is determined by the equation for static equilibrium, viz.

$$\frac{\partial T_r}{\partial r} + \frac{T_r - T_{\theta}}{r} = 0 \quad , \quad (11.7.2)$$

and by the boundary conditions at the expander (given displacement) and at the fictitious outer wall (no displacement).

The inner pressure increases by the expansion with a steeper gradient and up to a higher asymptote if the initial r_e is smaller. The asymptotic pressure p_{sa} is determined by the far-field mean skeleton pressure p_{sf} and relative void ratio r_{ef} , this dependence is influenced by the hypoplastic parameters. This means an attractor in the large: the state of the skeleton near the expander tends to a radial distribution which is only determined by the far-field state. A critical state is attained near the expander with an increase of p_s and a reduction of r_e , whereas RSEs further outside tend to contractant state limits.

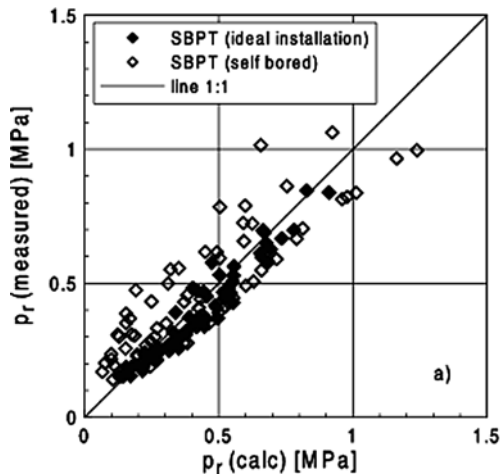


Fig. 11.7.2. Simulated versus observed asymptotic expansion pressures (Cudmani and Osinov 2001)

This calculation model was validated by observations in a calibration chamber, Fig. 11.7.2. Measured asymptotic skeleton expansion pressures are plotted versus those calculated by Cudmani and Osinov (2001). Parameters for the granular material and its initial state were taken over from published reports. The agreement is good for lab tests and acceptable for field tests which reveal more scattering. This is the base for solving the inverse problem, viz. to determine r_e from the asymptotic expansion pressure and the far-field pressure. Samples from the borehole are needed to identify the soil and to determine its hypoplastic parameters. This approach was extended to the penetration of probes (Sect. 14.3).

Evolutions of *peloids* by the expansion of boreholes may be considered as radially symmetric if the degree of saturation S_r is slightly below 1. Thus a radial skeleton velocity $v_s(r)$ can occur in horizontal planes without drainage by compression of gas bubbles (cf. Sect. 6.3). The stretching components by (11.7.1) can be related with changes of the skeleton stress components by v-hyp (Sect. 3.7). The initial state is specified by uniform stress components and a consolidation ratio p_e/p_s (cf. Sect. 11.3). Changes of pore pressure p_w are determined by changes of void ratio via the ideal gas equation (Sect. 6.3), so the equilibrium of the skeleton by (11.7.2) is influenced by a radial seepage force $f_s = -\partial p_w/\partial r$. The radial displacement may be neglected at a sufficiently distant outer cylinder and is prescribed at the inner boundary. The normalized expansion velocity $\dot{r}_o/r_o D_r$ plays a role because of the skeleton viscosity.

The expansion or contraction of *spherical cavities* in psammoids or peloids can be simulated formally as with cylinders. With radial symmetry (11.7.1) remains valid, whereas the second term in (11.7.2) gets a factor 2. The far-field stress should be uniform and isotropic, this excludes in situ applications.

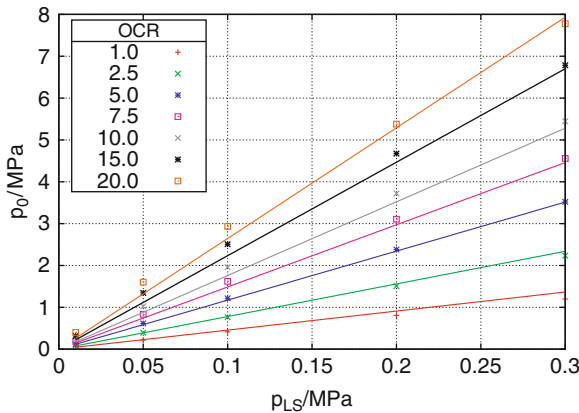


Fig. 11.7.3. Simulated spherical expansion of nearly saturated peloid (Meier 2009): asymptotic expansion pressure versus far-field pressures for different initial overconsolidation ratios

Pressure chambers should be small enough for neglecting gravity and could have an external membrane, and a chamber wall for control of pressure or displacement, but the inner cavity could scarcely be controlled without disturbance of radial symmetry. A spontaneous loss of symmetry can also occur as will be outlined further below.

Meier (2009) worked out simulations with spherical symmetry and realistic in situ input data, Fig. 11.7.3. $S_r \approx 0.97$ was assumed, the initial $p_e/p_s \approx \text{OCR}$ ranges from 1 to 5, the radial velocity is $\dot{r}_o/r_{oo}D_r = 1$. The calculated asymptotic expansion pressures are proportional to the far-field mean skeleton pressure p_{so} and bigger with a higher far-field consolidation ratio p_e/p_s . With another rate of expansion \dot{r}_o than $r_{oo}D_r$ the asymptotic expansion pressure changes by factor $(\dot{r}_o/r_{oo}D_r)^{I_v}$ due to skeleton viscosity (Sect. 3.8). The asymptotic state field near the expander is thus an argotropic attractor in the large which is determined by the far-field state and the rate of expansion. It requires gas bubbles between the particles as the compression is assumed to occur without seepage.

$S_r \approx 0.97$ is a realistic estimate of the gas fraction, deviations from this S_r cause a minor indeterminacy (Meier 2009). A direct validation could not be achieved as sufficiently precise results of expansion tests with clay in a pressure chamber or in situ are not available. Figure 11.7.3 is indirectly confirmed, however, by other field probing results. The resistances to vane shearing and to penetration are also proportional to the far-field p_s and increase likewise with the far-field p_e/p_s (Sects. 14.4 and 14.7). The argotropy and the ratio of both resistances are observed as calculated by Meier (2009) (cf. Sect. 11.3). This is a base to determine p_e/p_s and thus e from the probing resistance (Sect. 14.3).

The outlined evolutions by expansion can get radially symmetric even if they are not at the beginning. Such near-field attractors could be demonstrated by simulations without the assumed symmetry. The proposed methods are limited, however, by a spontaneous *loss of radial symmetry*. This can occur if the circumferential skeleton stress $\sigma_{s\Theta}$ tends to zero by the expansion. A dense psammoid can crack radially with cavitation of the pore water if this develops suction due to insufficient drainage or with gas channels (Sect. 6.2). A loose saturated psammoid can decay by deformation without drainage (Sects. 2.5 and 2.7), then radial cracks can even develop without cavitation of pore water. With pressure control the borehole can also bulge if this bifurcation releases more rapidly free energy than a radially symmetric continuation, in particular with a high r_e or low p_e/p_s and without drainage (cf. Sect. 11.5).

Formally similar calculations could be carried out for *convergent cylindrical cavities*. With radial symmetry they would lead to dilatant state limits with decreasing p_s . Numerical problems arise with low p_s , and validation experiments with a shrinking cylinder and radial pressure measurement are hardly possible. With a controlled inner fluid pressure – with or without membrane or filter cake – the radial symmetry gets lost more easily. Spiral-shaped shear

bands develop from the boundary in case of low initial r_e or high p_e/p_s . The bands can go over into circumferential cracks, then chips fall into the cavity. Without drainage and with high r_e or low p_e/p_s the borehole gets elliptic and closed. Simulations with spatial fluctuation of r_e or p_e/p_s and without radial symmetry could provide insight into such critical phenomena with strange attractors.

Cylindrical bodies of psammoid or peloid could likewise be analysed. As for columns the diffusion of pore water could be taken into account, of course also for the expansion or contraction of cavities. Validation tests could be carried out in a triaxial apparatus with fixed smooth end plates. The circumferential skin could consist of a filter and a rubber membrane, but thus a uniform p_w could scarcely be achieved. Peloid cylinders can have a psammoid core for p_w -control (Rendulic 1937). All that could be done also with *spherical bodies*, but then the radial symmetry is disturbed by an access to the interior. Expansion tests with cylindrical or spherical samples have rarely been made as they appear not rewarding, but a spontaneous loss of symmetry would at least not be so prohibitive as with the convergence of cavities. Experiments with hollow cylinders and spheres could also help to understand patterns of shear bands and cracks.

Shrinkage and swelling of peloid cylinders or spheres can be investigated with *free surfaces*. The boundary condition for shrinkage is the velocity of evaporation v_e , for swelling it is the pore water pressure p_w (cf. Sect. 10.1). Full saturation may be assumed for simplicity, and the suction $p_a - p_w$ at the boundary should not exceed the capillary entry pressure p_{ce} (Sect. 6.3). For neglecting gravity the samples have to be small enough, i.e. $\gamma d \ll \bar{p}_s$ with diameter d and average skeleton pressure \bar{p}_s . In general skeleton and pore water are coupled so that the ratio of diffusion time t_d and waiting time with constant v_e or p_w is important. Thus numerical simulations are required in general (cf. Sect. 11.3).

The *shrinkage of samples* may be considered by means of single RSEs, Fig. 11.7.4. As for a thin layer (cf. Fig. 11.6.3) the stretching components may be assumed as spatially constant. This means $D_{11} = D_{22}$ and $D_{33} = 0$

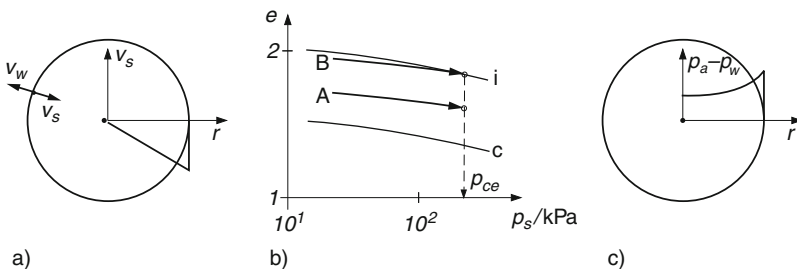


Fig. 11.7.4. Shrinkage of a peloid sphere (a), void ratios versus pressure (b), suction versus radius (c)

for a cylinder (A), $D_{11} = D_{22} = D_{33}$ for a sphere (B) and a linear increase of $-v_s$ with r for both (a). With isochoric solid particles and pore fluid the seepage velocity $v_w - v_s = -2v_s$ is also proportional to r . Evaporation with constant v_e means a nearly stationary stretching, thus p_s increases (b). The suction $p_a - p_w = -T_{sr}$ increases with r because of radial seepage (c). The equilibrium condition $p_a = -T_{sr} + p_w$ can only be satisfied in the spatial average. Beyond a capillary entry with $p_a - p_w = p_{ce}$ this kind of analysis is no more justified.

The evaluation of shrinkage tests can thus yield material parameters for contractant state limits (Külzer 2010, cf. Sect. 2.9). The volume change can be determined via the reduction of weight. The average skeleton pressure \bar{p}_s can be determined by measuring the attainable deviator $\sigma_{s1} - \sigma_{s2}$ under cylindrical shortening: just after the visible capillary entry the sample should be deformed into a cylinder which is shortened between smooth plates, v-hyp provides the initial p_s by a back analysis. Test and evaluation are robust as the evolution tends to an attractor in the large, namely an argotropic contractant state limit. The simplicity gets lost after a capillary entry, cracking suggests a strange attractor (Sect. 16.3).

Swelling of samples cannot be captured as easily. After submerging a saturated sample with suction it gets softer from the skin to the core like a piece of soap. This indicates a pore water diffusion with inwards seepage, therefore the stretching must not be assumed as spatially uniform nor temporally constant. Without a net attraction $p_n < 0$ the sample decays into a suspension (Sect. 6.3). With a p_n estimated from the tensile strength such tests can at best crudely indicate the swelling potential.

To *sum up*, radial symmetry can be achieved by the expansion of cavities in psammoid or peloid. This is due to contractant state limits as attractors in the large, whereas rapid expansions can lead to radial cracks. The radial symmetry can also get lost by bulging, in particular with high relative void ratio r_e or low consolidation ratio p_e/p_s , and more easily by cavity contraction with shear localization and chipping. Coupling of density changes and seepage can principally be taken into account, but it appears that this is hardly worth the effort. Borehole expansions can be used to determine r_e or p_e/p_s in situ. Shrinkage tests with small peloid samples can yield parameters for contractant state limits, swelling tests with a free surface are less promising.

PLANE-PARALLEL EVOLUTIONS WITHOUT SSI

Evolutions which are equal in parallel planes are called *plane-parallel*, this is not always the same as plane strain. Soil-structure interactions (SSIs) are left aside in this chapter, solids occur only as rigid base. Initial and boundary conditions are more complex than in Chap. 11 and more specific than in Chap. 10. Attractors in the large help to justify approaches by calculations and model tests, or at least to delimit their range of validity. Other than with RSEs such asymptotes are non-uniform fields of state variables, but they are again driven (exogeneous) and/or thermally activated (endogeneous). According to the involved RSEs they belong to monotonous deformations (SOM-states and state limits) or cyclic ones and ratcheting (asymptotic state cycles). As state fields are at best compounds of such states our attractors in the large cannot be treated with mathematical rigour. The generic term ‘strange attractor’ will sometimes be used for the spontaneous loss of symmetry by localization or diffuse bifurcation.

Psammoid heaps on a solid base serve for introduction (Sect. 12.1). Even without water they cannot fully be captured by models with grain skeletons as these can arise and decay. With peloids in heaps skeleton viscosity and pore water diffusion play a dominant role (Sect. 12.2). We will see why conventional limit equilibria can at best yield design estimates. As always evolutions are dominated by skeleton stress obliquities and relative void ratios or consolidation ratios, these state quantities change with space and time.

The ground yields usually more when placing fills if it consists partly of peloid (Sect. 12.3). We will meet the same dominant factors also with excavations (Sect. 12.4). Simplified design models will again be discussed. Some field observations support more sophisticated numerical models although the assumed plane-parallelity is rarely given.

We will see in Sect. 12.5 how the same symmetry can be employed for seismically activated evolutions. Hypoplastic simulations are confirmed by shake box tests and field observations, but also delimited by critical phenomena. It is discussed what could be done with seismically activated viscosity and entropic pressures. Slow tectonics are considered in Sect. 12.6, therein initial

and boundary conditions are inevitably artificial as only resulting fault patterns are partly known. Simulations with soil models can thus help to widen their range of application, but there are limitations by critical phenomena in the lithosphere.

12.1 Psammoid heaps upon a solid base

The granular heaps considered in this section may consist of simple grain skeletons in the sense of Sect. 2.2, and may be surrounded by and contain more or less water. Their base may be rigid and fixed if not stated otherwise, and rough or smooth with respect to the grain size (Sect. 10.3). Heaps get shape, density and stress by placement, and can spread or collapse so that shape and state are changed. Such evolutions depend also on the water in the pores and around the heap. Grain skeletons can arise by sedimentation or placement and can get lost by decay or removal (Sect. 12.4), and they can take up or lose pore water. Only evolutions between rise and fall of skeletons can be captured with methods of soil mechanics. For simplicity we assume that heaps can be represented by one cross section and have displacements only in this plane (plane strain).

Dry heaps can be similarly placed in the lab as their counterparts in situ, Fig. 12.1.1. A box may have two transparent smooth hard walls for confinement to plane strain and for observation, and a hard floor which is rough or smooth and horizontal or inclined. Filling via a sieve produces a higher density

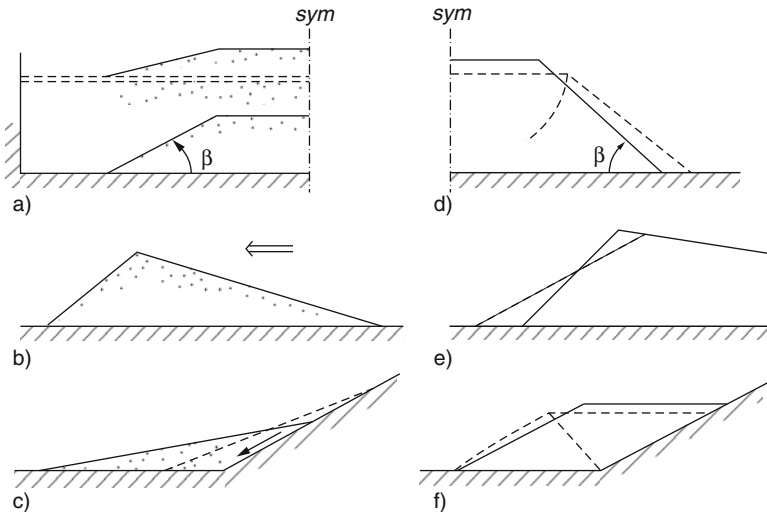


Fig. 12.1.1. Dry psammoid heaps by pluviation without (a) and with wind (b), or from granular flow (c); spreading (d), partial collapse (e) and sliding (f)

with a diluter granular rain as long as the fill does not spread and slide (a). Mining deposits can be similar, but have often softer particles. A fine sand rain with steady wind produces a kind of dam with a dense flat windward and a steep loose leeward slope (b). A barkhan dune has such a cross section and wanders likewise slowly leewards. Granular flow upon an incline leads to a loose heap (c), this may also be coarse debris at a rock slope.

Such heaps undergo evolutions of shape and state, particularly during and just after their formation. A dense pluviated dam spreads with dilation when the slope angle β attains a critical value (d). Parts of a dune near the steep slope collapse every now and then with dilation so that loose sand with low density and slope lies at the foot (e). A heap at an incline can slip past a smooth and shear past a rough base (f). Shear localization occurs in these cases (indicated by a dotted diagonal) if the skeleton was not fully dilated before. Let us see how far such evolutions can be explained or even predicted with the tools of soil mechanics.

Given an initial shape and state of the skeleton, one could principally simulate changes of both due to changing boundary conditions. Our heaps change by and just after placing granular material, the skeleton arises with density and stress and can get lost temporarily by collapse and rapid flow. Mechanical models with skeletons, constitutive relations for them and boundary conditions can only represent parts of such evolutions as initial states have to be assumed, and as the placement can at best be approximated by continuum models (Sect. 10.4).

Similarity rules help to judge calculation models, but such rules will rarely suffice to transfer model test results to cases in situ. The base pressure is proportional to γh with specific weight γ and height h . All stress components are proportional to it if all dimensionless quantities are equal in model and prototype. This implies geometrical and kinematic similarity, i.e. same shape and same ratios of velocities at homologous points. Dimensionless material parameters should be the same in model and prototype, those with the dimension of stress should be proportional to γh . With hypoplasticity (hyp, Sects. 2.4 and 2.11) this means same φ_c , limit void ratios for $p_s = 0$, exponents n , α and β , and granulate hardness $h_s \propto \gamma h$. This can be achieved with grains of same shape, size distribution and friction ratio as in the prototype, but of softer solid in model tests. With elastoplasticity (elp, Sects. 2.3 and 2.11) pressures $p_s \rightarrow 0$ are not captured, and the reference pressure is subjective.

The relative void ratio r_e (Sect. 2.2) should be the same in model and prototype. This is evident with hyp and less precisely defined with elp. The initial r_e due to placement is paramount for any analysis, but cannot be produced with it. Initial stress fields may be generated by means of simulations with elp or hyp as their inevitable arbitrariness does not matter, this will be shown further below. The grain size d_g should be proportional to h if it counts for shear localization (Sect. 8.2). If this leads to a model powder this should not

be cohesive or repulsive and should not develop pore gas pressures deviating from p_a (Sect. 6.2).

Leaving aside mechanisms of placement and rapid granular flow evolutions of granular heaps can thus at best be estimated. We will therefore restrict to *stability*, i.e. the ability of the skeleton to stand during and after placement. Only the following hypoplastic material constants are important,

- critical friction angle φ_c , or φ_{cs} for plane strain,
- exponents n and α for state limits,
- normalized granulate hardness $h_s/\gamma h$ for barotropy.

The ratios e_i/e_c and e_d/e_c are nearly the same for different psammoids, the exponent β is of minor importance near state limits (Sect. 2.4). The mean grain size d_g plays a role for base friction and shear localization. The relative void ratio r_e should be followed up with care as it is the most important state variable. We consider now how fields of skeleton stress and r_e can be related with velocity fields in order to judge the stability.

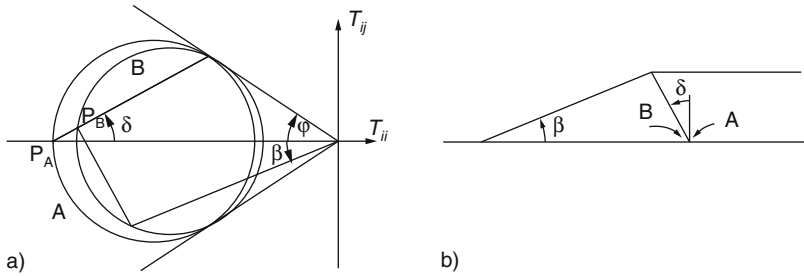


Fig. 12.1.2. Limit stress field of a dry granular fill: stress circles (a) at a thought line (b)

Limit stress fields can be constructed for a dam as indicated in Fig. 12.1.2. A straight line from the shoulder can have such an inclination δ that active Rankine fields right and left of it (Sect. 11.5) are statically compatible. This implies a jump of pressure along the straight line and a stress ratio at the base so that there the friction condition (10.3.1) or (10.3.2) is not violated. The friction angle φ should depend on the instantaneous r_e (Sects. 3.4 and 2.9), but this is not feasible as kinematics and dilation are ignored. One can also construct statically possible stress fields with variable assumed principal stress ratios or directions. Their possibility is only necessary, but not sufficient for stability, so their construction is hardly worth the effort.

Sliding wedges may be assumed as shown in Fig. 12.1.3. A rigid triangle may slide past the base, a second one slides past it and past the other part of the heap which may be fixed (a). A limit equilibrium can be achieved with suitable friction angles φ_i at the base and in the interior (b). The equilibrium of arbitrary wedges with average stress obliquities which are possible for the

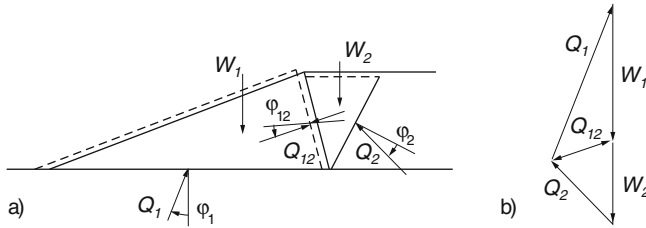


Fig. 12.1.3. Limit equilibrium of a granular fill: wedges (a) and force polygon (b)

material is necessary for stability, but again not sufficient. Stress obliquities at state limits are determined by the spatial averages of r_e along shear zones (Sects. 2.9, 8.2 and 10.3). Equilibria of sliding wedges may suffice for design estimates, but collapse scenarios can thus scarcely be captured.

More insight can be gained with *macro-elements*, Fig. 12.1.4. They can be as high as the heap and may experience a uniform stretching. A single triangle at the shoulder may be assumed with dilatant shearing (a). The statically required average stress obliquity $\tan \varphi_e$ is given by the assumed inclination ϑ . If $\tan \varphi_e$ exceeds the state limit obliquity for simple shearing according to r_e (by Fig. 2.9.2) an equilibrium is impossible, i.e. the shoulder will collapse. This holds for the actual average r_e which is higher than the initial one due to dilation. The latter occurs with any overcritical stress obliquity and is enhanced by any minute disturbance (Sects. 4.3 and 4.6). Thus a slope with $\beta > \varphi_{cs}$

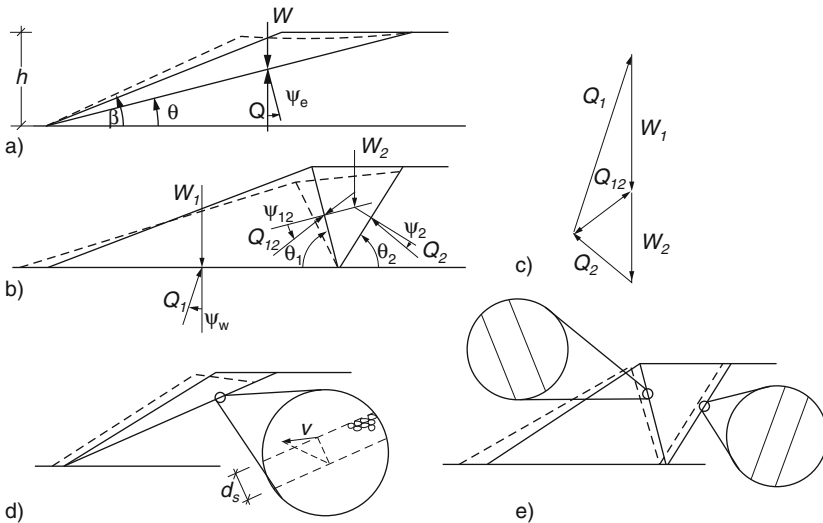


Fig. 12.1.4. Macro-elements for a dry granular fill: deformed wedge (a), two deformed wedges (b), force polygon (c), wedge upon a shear band (d), wedges with shear bands (e)

and $r_e < 1$ may stand for a short while, but collapses with dilated shearing due to minute disturbances. This happens with shear localization which could be captured by an additional macro-element (Sect. 8.2). The shoulder will not collapse with $\beta < \varphi_{cs}$, then its spreading by repeated disturbances causes a stabilization. The latter can scarcely be quantified by macro-elements.

Two macro-elements may be assumed in case of a smooth base, Fig. 12.1.4b. They are sheared simultaneously with dilation, this requires an extension at the base. The obliquity there is the $\tan\varphi_w$ of sliding friction (Sect. 10.3). An equilibrium force polygon can be constructed with weights and two further obliquities (c). The statics is the same as with wedges in Fig. 12.1.3b, but now the obliquities can be related with dilatant shearing that depends on r_e as for the simpler case of Fig. 12.1.4a. It is again necessary for stability that the statically required obliquities are lower than the ones for state limits with the actual average r_e . This can be achieved with different combinations of obliquities. If φ_{sc} is assumed for one of them, and if then the other statically required one exceeds φ_{sc} a collapse will occur with progressive dilation. No collapse can occur with the assumed macro-elements if both statically required obliquities do not exceed φ_{cs} . If this holds also with variation of the assumed angles ϑ_1 and ϑ_2 this would be a sufficient stability condition for this kind of kinematics. A gradual spreading cannot be estimated with macro-elements (Sect. 12.5).

Shear localizations may also be captured with macro-elements. A single plane shear band may be assumed at the shoulder so that a wedge slides down, Fig. 12.1.4d. The band may be thin, $d_s \approx 10d_g \ll h$, uniform shearing is assumed therein (Sect. 8.2). Required and possible average obliquities along the band are determined as outlined with Fig. 12.1.4a. This means again that a delicate equilibrium could be obtained with $\beta > \varphi_{cs}$ for $r_e < 1$, but then a collapse would occur with progressive dilation. A heap with $\beta < \varphi_{cs}$ would spread with stabilization by small disturbances.

In case of a smooth base two plane shear bands may be assumed together with two rigid wedges, Fig. 12.1.4e. The kinematics is determined by sliding along the base and by two dilatancy angles. The latter are related with the average r_e and the obliquities shown in Fig. 2.9.2. Statically required obliquities may be obtained as with Fig. 12.1.4c, the stability may be judged as before. One could combine shear bands with triangles as in Fig. 12.1.4b, but now the latter cannot attain state limits as the shear bands. Therefore this additional kinematic freedom would scarcely improve the judgment of stability.

More detailed calculations can be made with *finite elements*, Fig. 12.1.5. The cross section of the heap is subdivided into triangles or rectangles with velocities v_i of nodes and stress components T_{ij} at integration points (a). The balance of linear momentum is expressed for each node by means of interpolation functions and virtual work, thus it is satisfied in a spatial average. The rates of stress and the stretching can be related by elp or hyp, this leads to non-linear equations for temporal increments which are solved iteratively. Elements along the boundaries satisfy statical and kinematical conditions (b).

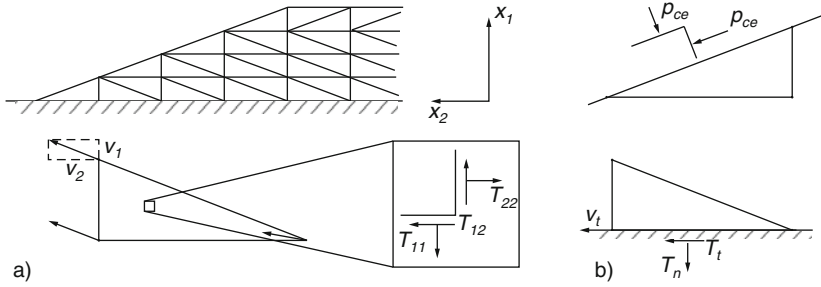


Fig. 12.1.5. Finite elements for a dry granular fill; mesh and element with variables (a), elements at free and rigid boundaries (b)

Along the base the normal and tangential components of velocity and stress are constrained by $v_n = 0$ and v_t by (10.3.1). This excludes opening and implies stick or slip. Along a free surface the stress may be assumed to be isotropic by a capillary skeleton pressure, $p_s = p_{ce}$ (Sects. 10.1).

Coupled evolutions of shape and state can only be simulated with fictitious initial states instead of the real placement (Sect. 10.4). One may assume a weightless heap at the onset with a uniform low isotropic stress $p_s \ll \gamma h$, and an initial e given empirically by the kind of placement. There would be no skeleton without p_s , an initial p_s would hardly change with van der Waals attraction (Sect. 3.2). The arising skeleton gets a void ratio as indicated by Fig. 12.1.1, this has to be assumed. Gravity can then be imposed gradually to the heap as a whole or layer by layer. The simulation produces changes of shape (deformations) and state (stress and void ratio). A loss of equilibrium would be indicated by accelerations without changes of external actions (here only gravity).

The *range of validity* of such simulations could be explored by model tests as indicated with Fig. 12.1.1. Evolutions of shape and void ratio could be observed from the formation of the skeleton up to its collapse, zones of pronounced shearing and dilation could be seen. The evolution of stress fields can at best be observed at the bottom and at confining walls if these are paved with stress cells. The kind of placement has a dominant influence upon the void ratio and its further evolution. With a given shape and void ratio the stress field cannot strongly depend on the order of placement, and such differences could scarcely be observed. It appears that the *historical element* (Darwin 1883) is captured by void ratios in cases like in Fig. 12.1.1. Inertial effects by filling and shaking could principally be taken into account (Sect. 12.5).

Back-analyses with finite elements should focus on spreading and collapse with changes of void ratio as these can be clearly observed. Their simulations will mainly depend on the chosen initial void ratio, whereas the order of imposing gravity is of minor influence. This can be attributed to state limit fields which work as attractors in the large (Sect. 10.4) depending mainly on shape and void ratios. Simulations may be used to judge simplifying assumptions,

e.g. the ones of Figs. 12.1.2, 12.1.3 and 12.1.4. One can at least see how results are changed by variation of assumed distributions. Comparison with model tests could produce a kind of validation. This will remain debatable, however, as real evolutions cannot be observed precisely and as their simulations require assumptions. In particular, shear localization and inertial effects can hardly be captured. Heaps of dry grains are not as simple as they may appear!

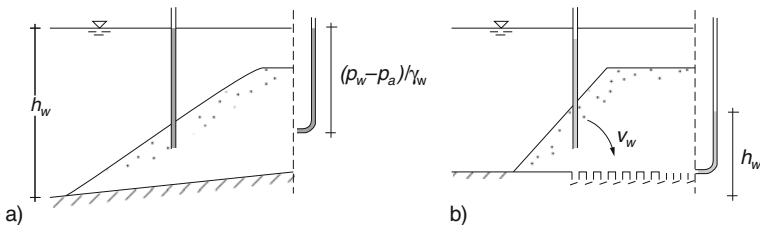


Fig. 12.1.6. Granular fill under water without (a) and with inwards seepage (b)

Turning now to *saturated psammoid heaps*, the pressure p_w or hydraulic height h_w and the velocity components v_{w1} and v_{w2} of the pore water relative to the ones of the skeleton v_{s1} and v_{s2} must be taken into account. Darcy’s law can be written

$$\begin{aligned} v_{w1} - v_{s1} &= -k_f \partial h_w / \partial x_1 \\ v_{w2} - v_{s1} &= -k_f \partial h_w / \partial x_2 \end{aligned} \tag{12.1.1}$$

with the permeability k_f (Sect. 6.2). Total and skeleton stress components are related with p_w via

$$\begin{aligned} T_{s11} &= T_{11} - p_w, & T_{s12} &= T_{12}, \\ T_{s22} &= T_{22} - p_w, & T_{s33} &= T_{33} - p_w. \end{aligned} \tag{12.1.2}$$

The principle of effective stress (Sects. 2.2 and 2.11) states that the skeleton feels only T_{sij} as the grains are neutral with respect to changes of p_w . The gradient of p_w , with components $\partial p_w / \partial x_1$ and $\partial p_w / \partial x_2$, causes a force at the skeleton in addition to gravity and inertia. A skeleton in resting water would only get uplift, otherwise it experiences also a seepage force with components $\gamma_w \partial h_w / \partial x_1$ and $\gamma_w \partial h_w / \partial x_2$. One could easily allow for both if the h_w -field were independent of skeleton displacements, Fig. 12.1.6. With resting water (a) it would suffice to reduce the specific weight for uplift. With a seepage force towards the base the heap can stand with a steeper slope (b).

Observations reveal that this kind of uncoupling is rarely justified. Only with coarse grains placement and subsequent evolution can be rather independent of the surrounding water. Heaps can in fact be placed steeper with seepage towards the middle of the base. This works only with not too coarse grains, however, otherwise the seepage forces can change substantially with turbulent seepage.

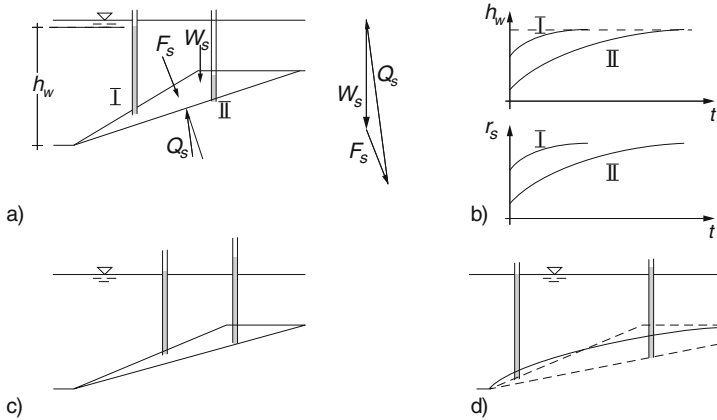


Fig. 12.1.7. Coupling of pore water and granular fills under water: dense macro-element (a), related evolution of hydraulic height and relative void ratio (b), loose macro-element prior to (c) and at the beginning of a collapse (d)

Consider a *macro-element* at the shoulder of a model psammoid dam under water, Fig. 12.1.7. A stable equilibrium with weight minus uplift W_s and resultant skeleton reaction Q_s could be obtained with a steeper slope by means of an inwards seepage force F_s (a). This F_s could be maintained by a bottom drainage as long as the skeleton tends to dilate by shearing. The skeleton would take up water and reduce p_w , thus it could stabilize itself temporarily. Rapid shearing would be almost isochoric so that p_s would increase in case of a low initial r_e .

A steep slope could thus stand for a short while without bottom drainage or after removing a lateral support. The skeleton would immediately decay at the surface, however, as the dilation there is scarcely impeded by the induced inwards seepage. Shear-induced transitions of h_w and r_e are indicated for a point I near the surface and a second one II further inwards (b). The skeleton is stuck by impeded dilation as long as h_w is not equalized by seepage if e is lower than critical. The delayed collapse ends when a slope with $\beta \leq \varphi_{cs}$ is reached so that the remaining skeleton will no more be dilated.

With an outwards seepage from the bottom an equilibrium could only be achieved with $\beta < \varphi_{cs}$. A sufficient outwards seepage force would disintegrate the heap into a suspension (Sect. 10.1). If the skeleton tends to contract by shearing its pressure and shear stress are reduced by isochoric shearing (Sect. 2.9). A macro-element would slump as its shearing causes an increase of h_w and thus an outwards seepage force, Fig. 12.1.7c, d. If the initial void ratio is lower than critical the heap can be stable with a steeper slope as suction arises in a deforming macro-element (d), and as h_w is less reduced by seepage with densification in deeper parts of the sliding region. If the initial e is higher than critical the skeleton decays into a suspension that forms very flat slopes after flowing down.

Submerged granular heaps in situ reveal a similar behaviour. With coarse grains, and a high k_f therefore, only a fast outwards seepage could flatten slopes. Steep slopes can be dredged in dense sand, but they collapse after a short time until $\beta < \varphi_{cs}$ is reached. Loose deposits collapse after a minute disturbance, and very loose ones turn into a suspension temporarily. The stability cannot be judged by means of macro-elements as shear-induced seepage forces can scarcely be estimated.

More insight could be obtained with *finite elements and coupling* of skeleton and pore water. As for one-dimensional cases (Fig. 11.2.1) each node has a p_w or h_w , and each integration point has v_{w1} and v_{w2} in addition to the skeleton variables. Equation (12.1.1) and the balance equations are written with spatial averages. Taking into account hydraulic boundary conditions one could simulate evolutions of shape and state principally as without water. This would be hardly more than an exercise, however, as a suspension flow prior to the birth of a skeleton and after its decay is thus not captured.

The wide variety of *unsaturated* psammoid heaps may only be touched. Gas bubbles in a skeleton make the pore fluid compressible (Sect. 6.2), thus changes of skeleton pressure by shearing without seepage are less pronounced. Bigger gas inclusions can occur in a metastable equilibrium with a surrounding saturated skeleton. They enhance a collapse by shearing and also by an overall compression. Gas channels connected with the atmosphere provide suction $p_a - p_w > 0$ (Sect. 6.2). Then the skeleton can stand with steep slopes and with higher than critical void ratios. This can be captured with a capillary skeleton pressure p_{cs} that depends on d_g , S_r and r_e (Fig. 6.2.3).

A totally submerged heap with gas inclusions is less stable than without them. With subcritical void ratios ($r_e < 1$) it can dilate without seepage, so it stands for a short while with $\beta > \varphi_{cs}$. With $r_e > 1$ it can contract without seepage, therefore p_w increases and $p_s = p - p_w$ decreases with an almost constant total pressure p . Then gas bubbles are released by the collapsing skeleton and rise. A heap with suction throughout is more stable than without as long as gas channels are not closed by contractant shearing.

After being partly submerged by *rising water* a loose granular heap can get collapsible, Fig. 12.1.8a. Any disturbance without seepage causes an increase of p_w with compression of gas bubbles. Thereafter the shearing resistance below can decrease more than it increases above the water table. Thus the heap can slump and turn into an avalanche which runs faster on a gas cushion (Gudehus 1998). A dyke can fail some time after being exposed to high water (b). The suction gets lost in a gradually increasing part by seepage, this leaves back gas inclusions. A loose skeleton can collapse as in the previous case, the air-side foot of a denser dam can be shifted by the seepage force as outlined further above.

Limit equilibria with simplifying statical and kinematical assumptions are at best necessary, but not always sufficient for the stability in such cases. To be on the safe side the relative void ratio r_e and the statically required friction angle should be lower than critical. To get there without collapse the

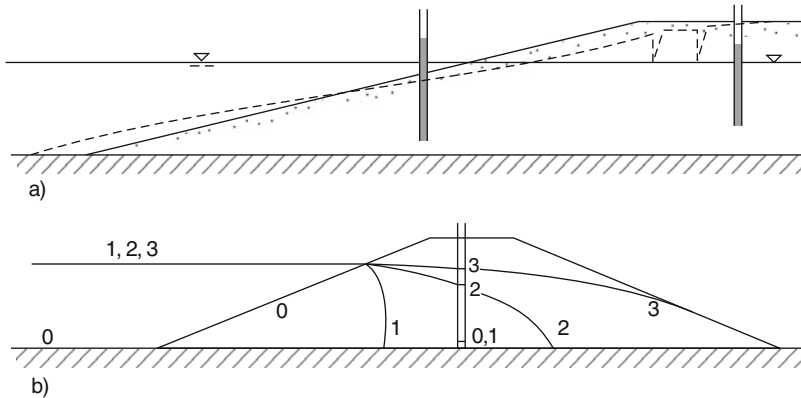


Fig. 12.1.8. Partly flooded psammoid bodies: slumping shoulder of a loose fill (a), gradual wetting of a dam (b). Numbers for the sequence

skeleton should be densified with low water table and injection of air. The disturbance required to trigger critical phenomena of a loose, more or less flooded granular heap cannot yet be estimated, let alone the run of avalanches (Sect. 16.3). Simulations with finite elements and coupling are more debatable with partial saturation as the pore fluid tends to deterministic chaos even if the skeleton is rather fixed (Sect. 6.2).

To *sum up*, some evolutions of psammoid heaps on a solid base can be captured with plane strain and mechanical models for skeleton and pore fluid. The field of the initial void ratio due to the formation has to be assumed. The heap is stable if the relative void ratio r_e and statically required friction angles are lower than critical. It collapses if the slope is steeper than critical which requires a low initial r_e . Roughness, inclination and hydraulic height of the base have to be taken into account. Flooded heaps collapse in case of $r_e > 1$ or with steeper than critical slopes, this is enhanced by gas inclusions. Humid heaps can stand steeper and can be densified without collapse as long as the pore gas is connected with the atmosphere. Limit stress fields are of little use, but statically required friction angles can be reasonably estimated with simplified kinematics. Stable evolutions of shape and state may be simulated with finite elements, whereas collapses with critical phenomena are beyond the present reach, in particular with gas inclusions.

12.2 Peloid and composite heaps on a solid base

Consider first *fully saturated peloid heaps*, Fig. 12.2.1. They may be deposited with a uniform initial void ratio e within a far shorter time than needed for the diffusion of pore water. This may happen layer by layer or at once, without or with temporary support under water (a) or at the open air (b). The heap sticks at a rough base which can be water-permeable or not. It can

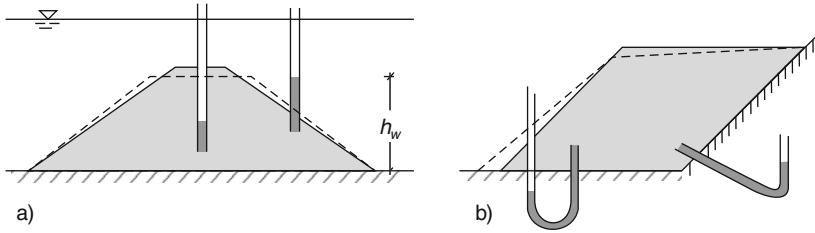


Fig. 12.2.1. Peloid heap after placement under water (a) and at the air (b)

slip along a smooth base which cannot be permeable as the skeleton would stick at drainage openings.

The heap begins to spread without volume change, and its hydraulic height h_w changes as indicated in Fig. 12.2.1. The initial suction $p_a - p_w$, without which lumps could not be piled up, is reduced by surrounding water and also by shear deformation (Sect. 3.8). In a submerged heap (a) h_w is lower in the peloid than the free water level and has an inwards gradient so that the skeleton swells, first near the free surface and last near the middle of an impervious base. At the open air (b) h_w is lower than its position and has an outwards gradient so that the heap shrinks from the free surface towards the middle. At each point h_w increases (a) or decreases (b) in the course of time, respectively, by the diffusion of pore water.

The initial isochoric spreading can be estimated by means of *macro-elements*, Fig. 12.2.2. Velocity fields are assumed with constant stretching in triangular zones so that a single velocity v_o at a suitable point indicates the magnitude. With a single triangle at the shoulder (a) its v_o determines the other velocities v_i and the element-wise uniform isochoric stretching D_{ij} . Two triangles may be assumed for a heap on a rough base and a smooth incline (b). The lower one sticks to the base, the upper one sticks to the lower one and slips along its base so that its volume does not change. Spreading may also be assumed for a fixed middle triangle in contact with two lateral ones which slip along the base (c). With such assumptions any velocity is proportional to a single one, $v_i = \mu_i v_o$ with an assumed vector field μ_i , and the stretching has amounts $D_i = \kappa_i v_o / h$ with height h and factors κ_i ranging from ca. 2 to 3 for each element.

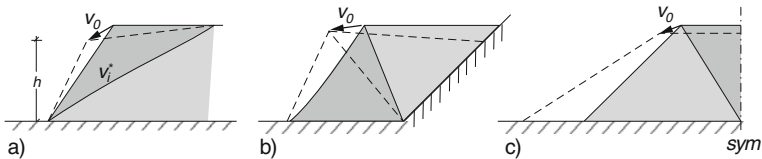


Fig. 12.2.2. Macro-elements for peloid heaps: single triangle (a), two triangles with partly inclined (b) or smooth plane base (c)

The skeleton of a macro-element tends to an argotropic state limit by isochoric shearing (cf. Sect. 3.8), i.e. the amount of shear stress τ tends to the cohesion c_u without drainage,

$$c_u = c_{ur}(D/D_r)^{I_v} = p_{ec} \tan \varphi_{cs}(D/D_r)^{I_v}. \quad (12.2.1)$$

c_u is thus argotropic via reference rate D_r and viscosity index I_v , and pyknotropic via the e -equivalent pressure p_{ec} and the friction angle φ_{cs} for critical states (Sect. 2.3). τ does not change with further shearing after this attractor has been attained, the soil is thus assumed to be ductile. The shear stress at a smooth base is lower, $\tau = c_a = mc_u$ may be assumed with an empirical factor $0 < m < 1$ (Sect. 10.3).

With the assumed velocity field the balance of linear momentum can be written without inertia as (cf. Sect. 1.2)

$$\int_{(V)} \gamma \mu_i dV + \int_{(A)} p_n \mu_i dA = \frac{1}{h} \left[\int_{(V)} \tau \kappa_i dV + \int_{(A)} m \tau \mu_i dA \right] \quad (12.2.2)$$

with the factors μ_i , κ_i and m as introduced above. Multiplied by v_o the first integral is the power of the weight for the assumed velocity field, and the second one is due to the pressure p_A at the free surface. The resisting right hand terms result from shearing of macro-elements and along the base. Equation (12.2.2) may be considered as the principle of virtual work for a static equilibrium, it says that no kinetic energy is produced with the assumed field. The combination of (12.2.1) with (12.2.2) and $\tau = mc_u$ for the base can be written

$$v_o = c_0 D_r h \left(\frac{c_1 \gamma h}{p_{ec} \tan \varphi_{cs}} \right)^{1/I_v} \quad (12.2.3)$$

with dimensionless factors c_0 and c_1 that depend on the assumed velocity field expressed by μ_i and κ_i . For macro-elements as in Fig. 12.2.2 the factor c_0 ranges from ca. 1.5 to 3, and c_1 from ca. 1 to 5. As I_v ranges from ca. 0.02 to 0.05 for lowly to highly plastic clays c_1 matters much more than c_0 .

c_1 depends also on the surface pressure p_A from water or air. For an undrained heap at the open air the atmospheric pressure p_a may be dropped in (12.2.2) as terms with it are cancelled. For a submerged undrained heap the water pressure p_w causes an uplift which is captured by taking $\gamma - \gamma_w$ instead of γ . For a partly submerged heap the partial uplift comes up to a weighted average of γ and $\gamma - \gamma_w$. With a higher water level on one side a bigger c_2 is obtained with (12.2.2) as in the second term the surface pressures from both sides do not compensate each other.

The creep velocity of a characteristic point can also be estimated with (12.2.3) if the cohesion is not uniform in the heap. If this was piled up with different void ratios c_{ur} in (12.2.1) has to be substituted by a spatial average \bar{c}_{ur} which is weighted via (12.2.2) with an assumed velocity field. An average \bar{c}_{ur} may also be used if $c_{ur} = p_{ec} \tan \varphi_{cs}$ decreases by swelling or increases

by shrinkage. The depth d_s of the swollen or shrunk zone increases with the waiting time t roughly via

$$d_s \approx \frac{1}{2}\sqrt{tc_v} \approx \frac{1}{2}\sqrt{tk_f\bar{p}_s/\kappa\gamma_w} \tag{12.2.4}$$

with an average permeability \bar{k}_f and skeleton pressure \bar{p}_s . For shrinkage the swelling index κ has to be replaced by the compression index λ (Sect. 3.3). Equation (12.2.4) follows from (12.3.1) with factor 1/2 for one-sided drainage as by Sect. 11.2, and is at best a crude estimate. As long as only a negligible part of the heap has changed by pore water diffusion, i.e. for $d_s \ll h$, volume changes may be neglected as assumed for (12.2.3).

This approach can be used to judge the *stability* of a saturated peloid heap. If this is submerged the surface water pressure can lead to a low or even negligible initial spreading velocity v_0 by (12.2.3). Swelling causes a gradual reduction of shearing resistance via p_{ec} in (12.2.1). When thus the average shearing resistance \bar{c}_{ur} is reduced, e.g. by 20%, v_0 increases much more with $1/I_v \gg 1$ by (12.2.3), e.g. by a factor ca. $1.2^{1/0.03} \approx 400$. Swelling can thus lead to a collapse with a delay which can be estimated by means of (12.2.1), (12.2.2), (12.2.3) and (12.2.4). The velocity field gets isochoric as the rapid creep prevents a further expansion.

Without adjacent water the initial spreading is much faster if the heap has the same dimensions and initial e . With $\gamma/(\gamma - \gamma_w) \approx 2$ and $I_v = 0.03$ (say) v_0 by (12.2.3) is bigger by factor $2^{1/0.03} \approx 10^{10}$. Thus a lateral support can be necessary until the average shearing resistance has grown by shrinkage. This gradual stabilization can again be estimated by means of (12.2.1), (12.2.2), (12.2.3) and (12.2.4) although the shear deformation is contractant.

The proposed estimates resemble the *bound theorems* for ideal elastoplastic bodies (Koiter 1958). The lower bound theorem says that a collapse cannot occur if an equilibrium stress field exists that nowhere violates the limit stress condition (lower bound). The upper bound theorem says that a collapse will occur if an excess of kinetic energy is obtained with a kinematically admissible velocity field. A proof can no more be given with v-elp or v-hyp, so the bound theorems are at best of heuristic value for peloids.

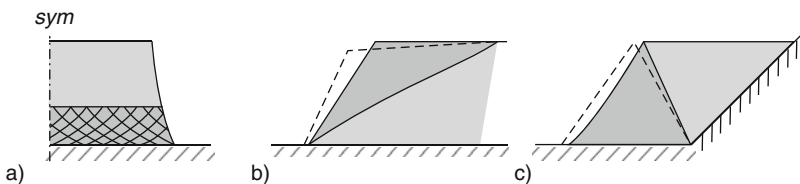


Fig. 12.2.3. Plastic limit states for peloid heaps: stress characteristics (a), single wedge (b), two wedges (c)

A limit stress field for an extruding lower part of a heap is indicated in Fig. 12.2.3a. Its construction is scarcely worth the effort, however, as the argotropy of c_u by (12.2.1) can thus not be allowed for. Upper bounds can be obtained with assumed blocks separated by slip lines (b and c). Application of (11.2.2) can indicate whether a heap would collapse with an assumed rate-independent c_u . Estimates with Fig. 12.2.2 and (12.2.1), (12.2.2) and (12.2.3) may also be considered as upper bounds although they are not based on perfect plasticity. Among different velocity fields with assumed macro-elements the one with the biggest amount v_0 will preferably occur.

Estimates with macro-elements are no more justified with more complex hydraulic conditions, e.g. partial, one-sided or temporary flooding and drainage or sealing along the boundaries. Then simulations with *finite elements* can better serve to the purpose. As with psammoids each node of the mesh has a skeleton velocity v_{si} and a pore pressure p_w , skeleton stress components T_{sij} and pore water velocities v_{wi} are needed at representative integration points. Gradients and rates of these quantities, approximated by means of interpolation functions, are related by Darcy's law (Sect. 6.3) for the pore water and by v-elp or v-hyp for the skeleton. The interaction of both is captured by (12.1.1) and (12.1.2) as for psammoids, the p_w -gradient acting at the skeleton can again be split into hydrostatic uplift and seepage force.

Two quantities or combinations of them have to be given along a boundary. At a free surface under water the skeleton pressure can be estimated from weight and net attraction, and the water pressure is given by the depth. At the open air the suction $p_s = p_a - p_w$ and the rate of evaporation $v_e = v_w - v_s$ are determined by the relative humidity (Sect. 6.3). $v_{si} = 0$ holds at a fixed rough base, p_w is given for a permeable base and the normal seepage velocity v_{wn} disappears at an impervious base. The latter holds together with $v_{sn} = 0$ (no separation) and

$$\begin{aligned} v_{st} = 0 & \quad \text{for} & \quad |T_{st}/T_{sn}| < \tan \varphi_{sw}, \\ v_{st} \neq 0 & \quad \text{for} & \quad |T_{st}/T_{sn}| = \tan \varphi_{sw} \end{aligned} \tag{12.2.5}$$

with normal (n) and tangential (t) components and a friction angle $\varphi_{sw} < \varphi_{cs}$ (Sect. 10.3). In case of slip (12.2.5b) can be substituted by $|T_{sn}| = mc_u$ as outlined further above if the deformation is isochoric. These boundary conditions are expressed with quantities for nodes and integration points by means of interpolation functions.

As always with finite elements the conservation equations for mass and momentum are written for spatial averages around nodes. The constitutive equations relating velocities and rates of state variables are non-linear, so they are solved increment-wise for suitable time steps. One may start with a gravity-free initial state by assuming a given ϵ and a homogeneous isotropic skeleton stress field. Gravity is imposed step by step to groups of elements, thus an artificial heap is piled up gradually. This is justified as far as state limits are thus approached so that only void ratio, shape and boundary conditions

matter for the new initial state with gravity. The inevitable partial arbitrariness of the initial state and the artificial piling up is swept out by an attractor in the large (Sect. 10.4). This reveals already whether the heap can stand near the onset. Finite elements substitute macro-elements and can help to justify them.

Further evolutions of shape and state can be simulated with rather arbitrary boundary conditions for skeleton and pore water. They reveal whether and how the heap tends to a state of rest or to a collapse. The range of validity can be delimited by physical arguments and observations. Swelling can thus only be modelled without decay of the skeleton, and shrinkage without capillary entry (Sect. 6.3). Cavitation under water or at the air and also at the base means another limitation of the model. Validation experiments are easier in the lab than in situ as they require controlled initial and boundary conditions and not too long diffusion times. One can also observe with model dams of sufficient length or between two smooth hard walls whether the evolutions are or get plane-parallel.

Such studies can deepen the understanding and may help to improve the models introduced as yet in this section. One should make sure that the material is captured by v-elp or v-hyp and that it is saturated. Peloids with hard particles will be treated in the sequel, peloids with pore gas thereafter. A net particle attraction $p_n < 0$ can be allowed for via higher limit void ratios (Sect. 7.1). It may be neglected against the effective pressure, $p - p_w \gg -p_n$, except for a free boundary under water where $p_n < 0$ is needed to keep a skeleton.

Saturated peloid heaps with *hard particles* and higher than critical void ratio are less viscous and less ductile without seepage than those with soft particles. They can collapse similarly as loose saturated psammoid heaps, in particular when a net attraction pressure $p_n < 0$ first leads to a high e and then gets lost by a change of the ionic strength (Sects. 6.3 and 7.1). For instance, a heap of Al_2O_3 -powder with $e \approx 2$ in water with pH9 collapses by adding HCl up to pH4. A pile of clay-like mining waste can collapse when an initial $p_n < 0$ gets lost by rain or neutral ground water. A marine sediment with $p_n < 0$ due to NaCl gets a quick clay after tectonic heave and leaching out of NaCl.

Such peloids transform into a suspension with any disturbance if e exceeds e_{co} , i.e. the critical void ratio for $p_s \rightarrow 0$ (Sects. 3.2 and 7.1). One could simulate the change of the ionic strength by diffusion towards $p_n \approx 0$, but the latter and related limit void ratios can only be determined by experiments (Sect. 7.1). Evolutions without skeleton decay could be simulated with finite elements and elp or hyp by taking into account changes of p_n and of limit void ratios (Sects. 6.3 and 7.1). The coupled evolution of the skeleton with diffusion both of pore water and solutes, however, is beyond the reach of present models.

Partly saturated peloids on solid ground are indicated in Fig. 12.2.4. Clay-like sediments in coastal shelves with $p_n < 0$ due to NaCl can contain methane

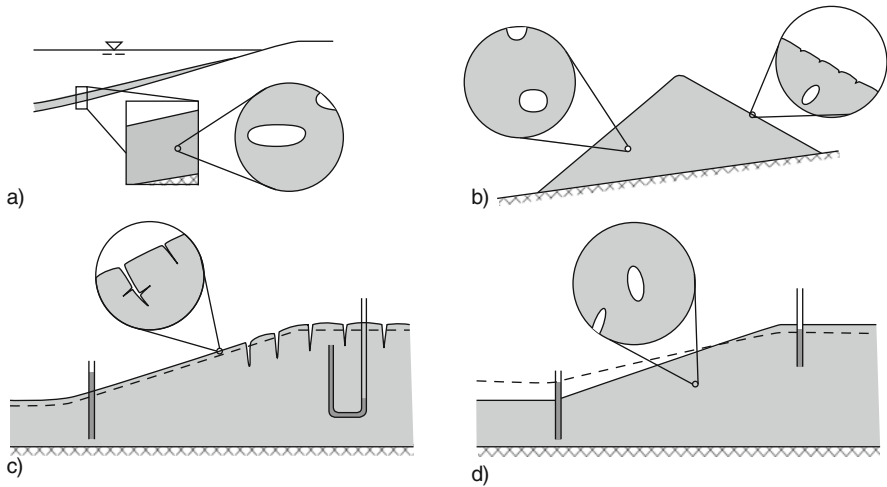


Fig. 12.2.4. Peloids with gas inclusions: submarine slope (a), heap (b), shrinkage cracks (c), slump after rain fall (d)

from organic decay (a). The skeleton is more deformed near CH_4 -bubbles than without them. This could be captured by a kind of composite (Sect. 9.1), but skeleton decay and formation of gas cushions delimit such an approach (Sect. 16.3). Open-air deposits of dust at and with slopes can collapse after the access of rain water so that suction and net attraction get lost (b). Again gas inclusions enhance avalanches which can hardly be captured. Plastic clay at a slope shrinks and cracks in dry seasons (c), and collapses after the access of water (d) due to swelling with loss of suction and net attraction and due to enclosed air. Such cases were already described by Terzaghi (1925) and are still beyond the reach of calculation models.

Composite heaps with more or less saturated psammoid and peloid zones occur in many variants. Natural deposits upon an incline can have inclusions of psammoid in peloid or vice versa. As a result of sedimentation, erosion and flow their void ratios can be nearly critical. The peloid zones can contain methane bubbles from reactions. These enhance a collapse as with Fig. 12.1.8a, but draining psammoid zones would impede it. A dam can consist of a clay core and coarse-grained shoulders with a pervious cover. The core is not saturated if it was compacted from humid crumps. It has suction in dense enough peloids and should not crack (cf. Fig. 12.2.1b). After flooding one side of it gets softer by a gradual loss of suction (cf. Figs. 12.1.8b and 12.2.1a), thus gas bubbles are included. Coarse grains could penetrate into the core, this could be sheared sideways or even eroded. As such evolutions can yet scarcely be predicted one should avoid them by technical means. As with simpler peloid heaps the stability cannot be sufficiently captured by means of a conventional limit state analysis.

To *sum up*, evolutions of peloid heaps on a solid base can be captured with v-elp or v-hyp and plane-parallelity within certain limitations. The gradual spreading is determined by initial shape and void ratio, base roughness and hydraulic conditions. The spreading velocity can be estimated with macro-elements, it increases gradually by swelling and decreases by shrinkage. This substitutes the bound theorems of ideal elastoplasticity. More detailed and complex evolutions can be simulated with finite elements, such approaches could be validated by model tests. Skeleton decay, capillary entry and cracking cannot thus be captured. Peloid heaps with hard particles may be modelled as psammoids with net attraction or repulsion, they are collapsible with higher than critical void ratios. Gas inclusions and gas channels can play a role, but their influence is beyond the reach of present calculation models. Heaps composed of psammoid and peloids may be treated by combining methods of Sects. 12.1 and 12.2. Predictions get less determinate if the composition and the behaviour of interfaces are not well known (Sect. 10.2).

12.3 Heaps upon yielding ground

Instead of a solid the base may now consist of psammoid and/or peloid ground. The heap may be placed and exposed to air and/or water so that it would stand on a rough solid base of the same shape. The ground under the fill yields during and after its placement, as always there is an interplay of skeleton and pore water. Such evolutions of shape and state may be assumed to be plane-parallel if ground and heap have a uniform cross section over lengths of the heap which exceed by far its height.

The simplest case is given by a *psammoid* ground with *constant hydraulic height* h_w , Fig. 12.3.1. Zero skeleton displacements may be assumed along a sufficiently deep base, and only vertical displacements along two smooth fictitious lateral walls. If there is a symmetry line this works like a smooth wall. Initial composition and state can be determined as outlined in Sect. 11.2. Ground water table and relative void ratio r_e are paramount, initial stress ratio and further hidden variables can at best be estimated from the recent history. In a finite element calculation the placement of a heap may be simulated by

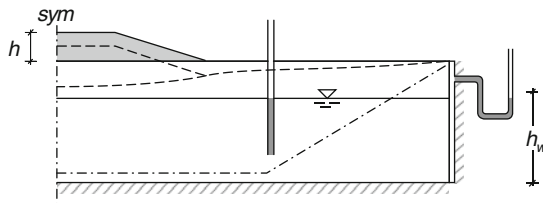


Fig. 12.3.1. Fill upon partly submerged psammoid ground

gradually increasing its gravity. This leads to settlement and spreading of the dam and the neighboured ground alongside with changes of skeleton stress and r_e .

Comparative calculations reveal that the *order of placement* has little influence on the final shape and state (Karcher 2003). This works also in three-dimensional cases so that the assumed plane-parallelity can be justified (Sect. 15.1). Variations of the fictitious fixed boundary can show how far away this should be. Other than with an elastic solid changes of shape and state are confined to a zone of about three times the reflected dam (*nota bene* for a homogeneous psammoid ground with constant h_w). Changes of shape and state after placement can be produced by changing ground water table and by shaking (Sect. 12.4). If the dam would be stable upon a solid base it is also stable in the present case.

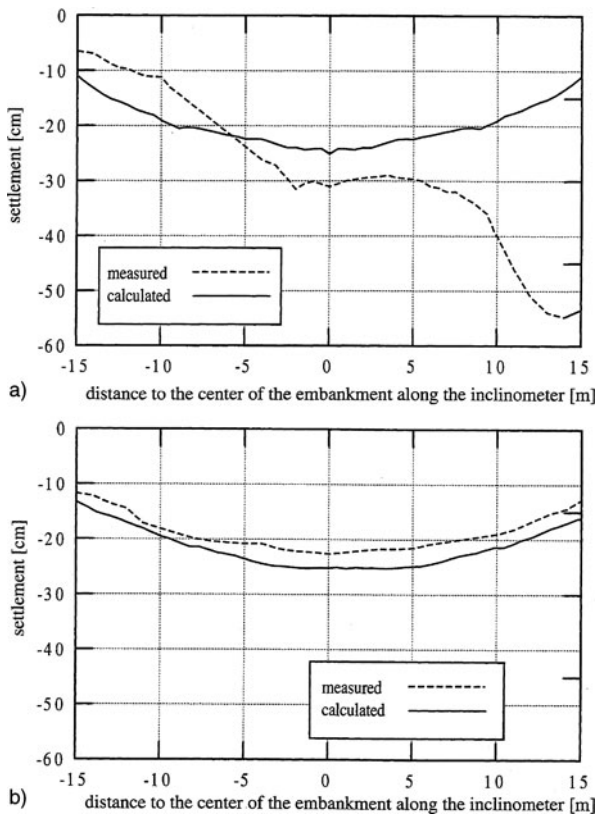


Fig. 12.3.2. Fill upon loose ground with crumps without (a) and with near-surface compaction (b), Nübel (2002)

Such calculations are more than an exercise if the ground consists of a soft psammoid, i.e. if $h_s/\gamma h$ is rather low and/or the initial r_e is higher than critical. A trial dam was placed upon humid lignite mining debris, evolutions were simulated with hyp, Fig. 12.3.2 (Nübel 2002). The low h_s and the high limit void ratios were determined by compression tests (cf. Sect. 9.2), further material constants were estimated empirically. The high initial r_e was determined via penetration sounding (Sect. 14.3), a spatial fluctuation was assumed (cf. Sect. 8.2). Without previous densification the settlement trough was asymmetric and could not be reproduced (a). With densification of the upper 7 m the trough was more regular and could be well reproduced (b). As the agreement was obtained without adaption of parameters to get observed settlements this shows how far such evolutions are predictable.

A loose submerged psammoid ground can be collapsible if it is fine-grained, Fig. 12.3.3. This is also the case for a peloid ground with so hard grains that the viscosity of the skeleton is negligible. As then the time t_d for the diffusion of pore water can be longer than the time t_f for filling the ground gets scarcely denser during and just after it. t_d may be estimated by (11.3.1) with $d = h$ and $\bar{\sigma}_s = \gamma h$ to get the order of magnitude. A part of the heap can slump during or just after placement by pushing aside and upwards part of the ground. This collapse is accompanied by a pore pressure increase and enhanced by gas bubbles and traffic as then p_s decreases by densification without seepage. As with heaps of such material (Sects. 12.1 and 12.2) simplified limit equilibria do not suffice for stability, and realistic finite element simulations are not yet feasible. Machines for filling and densification should only drive therefore on already improved ground.

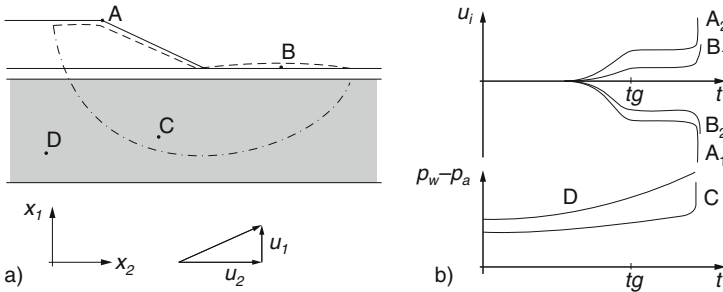


Fig. 12.3.3. Fill upon collapsible ground: (a) slump with slip circle, (b) evolution of displacements and pore pressures

A v-hyp-simulated evolution before and after placing a fill upon a *soft peloid layer* is indicated in Fig. 12.3.4. After an assumed resting time of 5000 years the soft layer is consolidated under the weight of itself and a sand cover (a). p_w is almost hydrostatic after the diffusion time $t_d \approx 400$ years by (11.3.1) with $c_v \approx 10^{-8} \text{m}^2/\text{s}$, the consolidation ratio has attained $p_e/p_s \approx 1.2$ with the chosen visco-hypoplastic parameters. The vertical skeleton stress T_{s1} is given

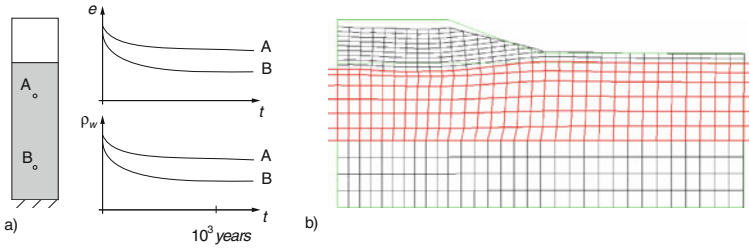


Fig. 12.3.4. Evolution with fill upon soft ground: (a) void ratio and pore pressure versus time, (b) deformation just after placement (exaggerated, courtesy H. Sturm)

by overburden and water table, the stress ratio T_{s2}/T_{s1} has attained $K_0 \approx 0.65$ by (11.2.9). This state before placing the dam would not be changed by other kinds of sedimentation about 5000 years ago, so it is a first attractor in the large (Sect. 11.3). It would be different with a much longer resting time with a temporary pre-load or pre-shaking, and with a crust if pore water could evaporate temporarily.

Placing the dam in $t_f = 15$ days and waiting for 30 days leads to almost isochoric deformations with a higher than hydrostatic p_w . This is a second attractor in the large as the new state and velocity field would not be changed by the sequence of filling in a time $t_f \ll t_d$. It may be imagined as an ensemble of RSEs at argotropic isochoric state limits, connected by a velocity field and static equilibrium. It could not be attained without ductility as will be explained further below.

Isochoric shearing with constant rate leads to an increasing resistance up to an argotropic state limit by v-hyp (Sect. 3.8) which was used in our example. Intermediate psammoid heaps with stable slopes cause far less creep than the complete dam. The travelling load by earth-moving machines is negligible as long as it is well below the weight of intermediate heaps. These assumptions for our heuristic second attractor could be verified by comparative calculations, they are often tacitly assumed in order to simplify the boundary conditions (Sect. 10.4).

The diffusion of pore water sets on along the upper and lower rim of the peloid layer. After 15 days (Fig. 12.3.4b) it reaches only a zone of $d_s \approx 0.1$ m thickness by (12.2.4), this explains the minute settlement at the dam axis and is negligible for the lateral creep. After about 200 years p_w is again almost hydrostatic, but the contractant creep with spreading goes on. The skeleton stress state and the ratios of skeleton velocities at different points remain nearly constant, whereas the void ratios and the amounts of creep velocity decrease. This third attractor in the large is an ensemble of RSEs near argotropic contractant state limits (cf. Sects. 3.8 and 3.9). It would also be attained with another permeability and symmetry as before, and with other sequences of placement and waiting intervals. This could be verified by comparative calculations and is of use for the prediction of long-term deformations.

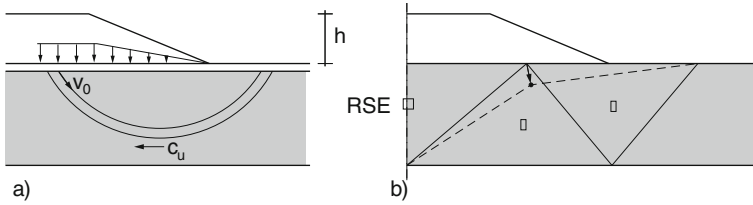


Fig. 12.3.5. Simplified mechanism for fills upon peloid ground: slip circle (a), macro-elements (b)

Design estimates can be obtained with simplifying kinematical and statical assumptions, Fig. 12.3.5. Instead of a slip circle a uniform isochoric shearing may be assumed between two arc sections (a). Substituting the dam by statically equivalent stresses at its base, an initial velocity v_o can be estimated by (12.2.3) with c_0 and c_1 from (12.2.2) as substitute of the equilibrium condition. In other words, the statically required average cohesion \bar{c}_u is related with the shear rate in an assumed shear zone by (12.2.1). Variation of the shear zone until the maximum of \bar{c}_u is found leads to the one with max v_o which could preferably occur. This reminds of an upper bound by ideal plasticity and may help to judge the stability (cf. Sect. 12.2).

Three macro-elements may be assumed for the long-term creep with constant p_w (Fig. 12.3.5b). Their common point may settle and spread with an assumed direction v_{2A}/v_{1A} , this determines the ratios of stretching components in the three triangles. Thus the ratios of skeleton stress components are determined by v-elp or v-hyp for contractant creep (Sects. 3.8 and 3.9). The latter may be calculated for one RSE in each triangle. With a statical estimate of $p_s(=p')$ for each RSE the amount of stretching D may be calculated with v-elp or v-hyp, or read from an e vs. $\log p'$ plot (Sects. 3.2 and 3.8). The reduction of e in the same plot corresponds to the amount of settlement.

Such estimates can at best roughly indicate whether the dam would stand after a rapid placement, and how much it would settle in the long run. The employed kinematical and statical assumptions remain rather arbitrary, and so are the conclusions. Better design estimates could be obtained with a coarse finite element mesh. With a moderate amount of computing such simulations could reveal already crucial points so that further investigations could be adequately chosen. Less uniform ground conditions and different filling procedures could be taken into account. Due to the three attractors in the large proposed further above simplifications of the state before placement and the sequence of it would be justified.

The *range of validity* of this approach is limited for two main reasons. First, composition and state of the ground are never uniform and cannot be detected in all detail. In particular, the peloid layer can have psammoid inclusions and cracks so that its permeability is but vaguely known. Thus the course of pore water diffusion can at best be crudely captured, whereas the creep at the onset and its reduction can be better predicted. Second, the peloid need not

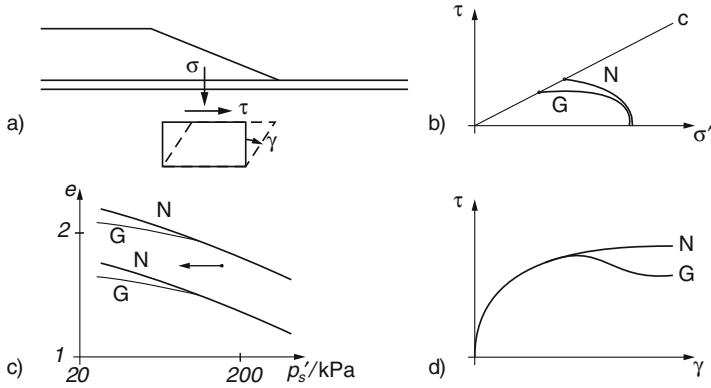


Fig. 12.3.6. Peloid RSE under a fill (a); stress paths (b), void ratio versus pressure (c) and stress-strain curves (d) with different ductility

be ductile as assumed until now. This can lead to a *delayed collapse* as will now be outlined with Fig. 12.3.6.

The velocity field just after placement is nearly isochoric so that an RSE under the dam shoulder is sheared for a while with constant e and rate $\dot{\gamma}$ (a). The skeleton stress path (b) may have reached a maximum of τ , whereas $\sigma' (= -T_{s12})$ is reduced by filling the dam. In a plot of e vs. $\log p_s$ (c) the reduction of p_s with constant e indicates the transition to a critical state. In a plot of τ vs. shear strain γ (d, cf. Fig. 2.9.1) a plateau would be reached in case of ductility, and a peak otherwise. As outlined in Sec. 2.8 and indicated in Fig. 12.3.6, v-elp and v-hyp by Niemunis (2003) predict a ductile response, whereas hyp and v-hyp by Gudehus (2004b) can produce a peak. With a statically required τ a peak would lead to a collapse, i.e. a spontaneous acceleration as the resisting τ is reduced with further shearing.

The crucial extent of *ductility* depends on the p_s -dependence of limit void ratios. With (2.3.1) or (3.3.6) isochoric shearing after consolidation up to $p_e/p_s > \text{ca. } 1.5$ leads to a critical state with about half the initial p_s as a linear decrease of e_c with $\log p_s$ is assumed for any p_s . With (2.4.1) and constant h_s , i.e. constant D by (3.2.2) or (3.4.1), the p_s for critical states can be lower than by CSSM for high enough e . This can lead to a peak, and even to a decay beyond it in case of hard particles. A less marked peak in case of soft particles can also lead to an acceleration if τ is statically given. As with any τ -peak the further shearing gets localized, but this is spread by seepage so that the shear zone cannot get very thin (Sect. 8.3).

A more quantitative analysis could be made with finite elements and v-hyp by Gudehus (2004a) (leaving aside hard grains as with Fig. 12.3.3). A kind of validation could be achieved by means of observations *in situ*. Hunter and Fell (2003) collected and commented a number of field reports. Observed settlements of dams, lateral displacements of the neighbored ground and pore pressures resemble the simulated ones in Fig. 12.3.4. In some cases the dam

slumped with acceleration after resting times from about one day for lowly to one month for highly plastic clay. For some of the reported cases detailed data on composition, state and mechanical properties would suffice for numerical simulations.

A back analysis of a recent case in Germany is represented in Fig. 12.3.7 (Libreros-Bertini 2006). The ground consisted of a highly plastic tertiary clay and a cover of silt with groundwater. The clay had an age of ca. 1 million years, a nearly linear increase of the average penetration resistance with depth indicates that there was no temporary overburden (Sect. 14.3). An initial

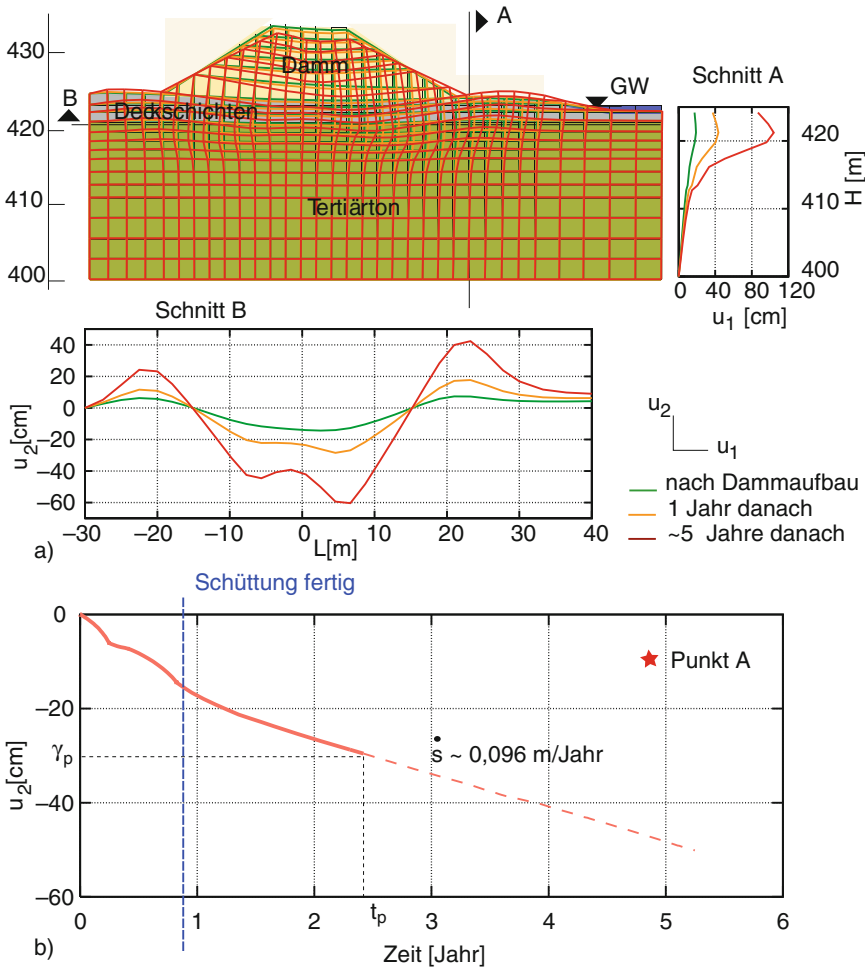


Fig. 12.3.7. Simulation of a delayed collapse by a fill upon overconsolidated clay (Libreros-Bertini 2006): (a) shape and displacement profiles, (b) estimation of collapse time via peak strain

consolidation ratio $p_e/p_s \approx 1.7$ was estimated from the penetration resistance (Sect. 14.3). A simulation for the resting time could not reproduce this p_e/p_s as the influence of cracks is not sufficiently known. A part of the dam collapsed about 1 year after its placement and came to rest after a kind of circular sliding. Material parameters for the dam and the silt layer were estimated empirically. Parameters for the clay were determined from triaxial tests and experience with similar clays.

Creep displacements simulated with v-hyp are shown in Fig. 12.3.7a. The actual placement within 5 months was substituted by imposing gravity in four steps. With a diffusion time $t_d > 200$ years the deformation is nearly isochoric within 5 years. An almost circular shear zone is obtained similarly as observed. Creep displacements in the first year were not registered in situ. The spontaneous acceleration after 1 year could not be calculated with v-hyp and the ductility outlined further above. A delay time from 0.5 to 2 years can be estimated with the calculated shear rate and a peak shear strain from triaxial tests (b).

Turning to *shoulders of fills*, we consider first soft peloid layers below which are embedded in rather loose psammoid, Fig. 12.3.8. ‘Soft’ means marked viscosity and high compressibility. Prior to filling (a) h_w may be hydrostatic, and a slow contractant creep may correspond to a p_e/p_s from ca. 1.2 to 1.5. The equivalent pressure for critical states p_{ec} can be determined from the resistance c_u to vane shearing (Sect. 14.6), whereas initial p_s -values have to be estimated. With given composition and water table an initial field of skeleton velocity and stress can be generated by imposing gravity as for a

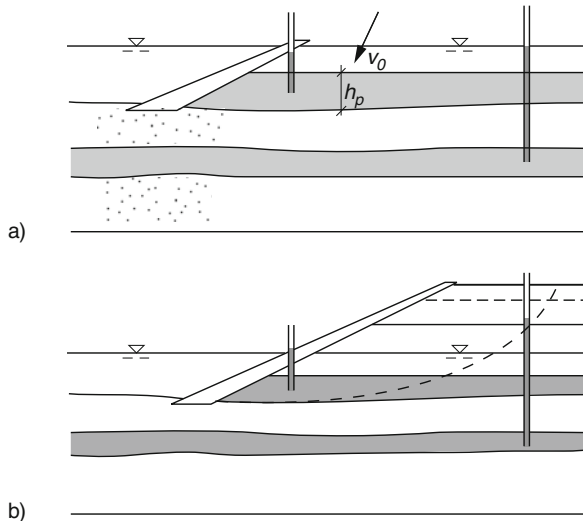


Fig. 12.3.8. Fill with leaning wall upon a partly soft composite ground: prior to (a) and after increase of fill height (b)

heap (Sect. 12.2), or by removing gravity as for an excavation (Sect. 12.4). Therein one may assume a constant h_w , $p_e/p_s = 1$ and a uniform isotropic pressure $p_s \approx (\gamma - \gamma_w)h/2$ at the onset. The obtained attractor in the large is an ensemble of contractant state limits, order and size of filling or excavation steps for its generation do not matter. The attained p_e/p_s , which depends also on stress component ratios (Sect. 3.9), can be checked against a typical creep velocity v_0 known in situ by

$$v_0 \approx h_p D_r (p_e/p_s)^{-1/I_v} \quad (12.3.1)$$

with the layer thickness h_p (Sect. 3.4). Apart from composition and ground-water table the initial consolidation ratio p_e/p_s for the peloid layer, and the initial relative void ratio r_e for the psammoid layer below and above, are paramount for the identification.

As with Fig. 12.3.1 a rigid boundary may be assumed far enough from the slope. A constant h_w and no slip should be assigned to the base, whereas the fictitious wall may be smooth and impervious. A rubble layer upon the slope may be represented by statically equivalent stresses so that its stiffness is neglected and zero skeleton pressures are avoided (Sect. 10.1). Psammoid above the ground water has a capillary skeleton pressure p_{ce} so that its free surface has $-T_{sn} = p_{ce}$ (cf. Fig. 12.1.5b). The additional placement can be simulated by imposing gravity to this part of the finite element mesh within the filling time t_f .

The saturated peloid layer deforms nearly without volume change as long as the time does not suffice for the diffusion of pore water. A second attractor in the large can be attained for times well below the diffusion time, i.e. $t \ll t_d$, as in the cases outlined before it is an ensemble of argotropic isochoric state limits. The amount of shearing, which can be calculated with hyp for the psammoid and v-hyp for the peloid, is biggest along a nearly circular arc, Fig. 12.3.8b. The rate of shearing, visible from a velocity v_0 at the shoulder, is gradually reduced after the end of filling by densification of the peloid layer towards its interior. For times $t > t_d$ the pore water pressure is again nearly hydrostatic, and the peloid experiences contractant creep. Apart from additional fill and changed shape this third attractor in the large equals the first one.

The influence of *shear localization* can only be indicated as it was not yet analyzed with finite elements for such cases. If the peloid is not ductile (cf. Fig. 12.3.6) an isochoric shearing gets localized beyond a peak, but the shear band cannot get very thin as it gets denser by diffusion (Sect. 8.3). If the psammoid on top is denser than critical the shearing therein is localized and dilatant (Sect. 8.2), and can go over into cracking near the free surface (Sect. 8.4). The thickness of the psammoid shear zone may be of minor importance for its resistance as the pressure is nearly constant (cf. Sect. 13.4). A delayed acceleration will occur if the statically required moment for any arc exceeds the resistance of the skeleton for a constant rate of shearing. This delayed loss of equilibrium or creep collapse can at best be estimated as the

numerical problem tends to be mathematically ill-posed. The system tends to a deterministic chaos with unpredictable further evolution (Sect. 16.3).

What about design estimates and validations for such cases? Fellenius (1948) analyzed a collapse with a fill on soft ground at a slope. A row of concrete boxes sunk about one day after filling it, divers detected a heave of the neighboured sea bottom. Assuming a slip circle a limit equilibrium was constructed with horizontal forces between thought vertical slices and a suitable average obliquity $\tan \psi$ along their sliding base. The statically required $\psi \approx 9^\circ$ is lower than the critical friction angle of the peloid skeleton, but the shearing resistance was reduced by higher than hydrostatic pore pressures. Fellenius proposed a limit equilibrium with a pressure-independent shearing resistance c in the peloid zone. He varied slip circles to find the one with the maximal statically required cohesion c , and considered the system as stable if the available c of the soil was bigger than required including a factor of safety.

As with peloid heaps on hard ground (Sect. 12.2) one may estimate a velocity v_0 of undrained creep by comparing such a statically required c with the argotropic shearing resistance c_u by (12.2.1). A velocity field has to be assumed up to a factor v_0 so that $D \approx c_0 v_0 / h_p$ with c_0 from about 2 to 3 as a typical stretching rate. This comes up to (12.2.3) for v_0 , which is a crude estimate as spatial distributions have to be assumed so that the factor c_1 is at best roughly known. A low enough v_0 for unfavourably assumed velocity fields and realistic equivalent pressures p_{ec} would be necessary for stability, and also sufficient if the response to undrained shearing is ductile. As explained further above the latter is not given in general. Even with ductility the assumptions needed to estimate v_0 could only be justified by observations and numerical back-analyses.

If the soil body is stable with a field of excess pore pressures it is even more so with a hydrostatic hydraulic height h_w . Then *deformations* could at best be estimated by means of representative elements, cf. Fig. 12.3.4. The creep velocity v_0 by (12.2.3) is reduced by the increase of the capillary skeleton pressure p_{ce} with the diffusion of pore water, but thus v_0 gets almost unpredictable. The diffusion time t_d by (11.3.1) is quite imprecise not only from the parameters therein, but also as it is influenced by shearing. The long-term contractant creep with constant h_w can likewise only be guessed (cf. Fig. 12.3.4). Even well off the slope the stress ratio T_{s2}/T_{s1} is lower than K_o by (11.2.8) and statically indeterminate. As without a slope the slowing-down settlement and spreading could only be predicted numerically, this works due to the contractant attractor in the large.

The evolution of a *stiff inclined peloid* ground by and after placing a dam is more intricate so that only some aspects may be addressed, Fig. 12.3.9. We leave first aside cracks and gas inclusions. The ground creeps near the slope with seasonal changes by evaporation and wetting. Apart from the composition one can get h_w at the base and c_u -values from probing in situ and undrained shear tests. An initial state field can be generated by imposing or removing gravity above the horizontal ground surface (a). For this simulation

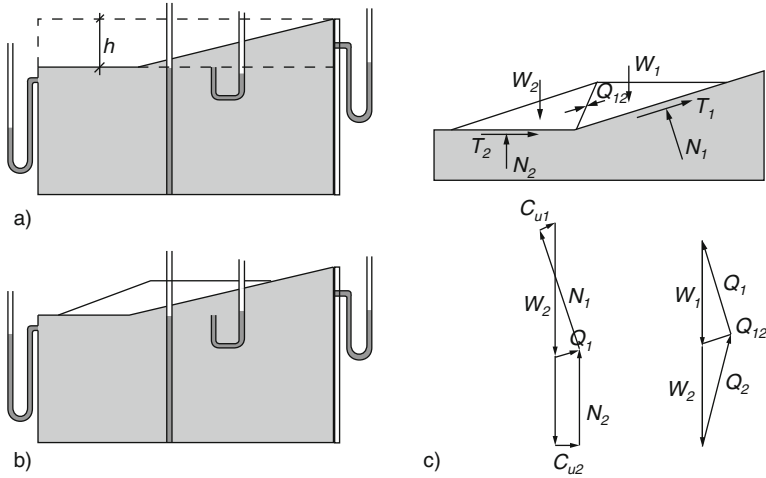


Fig. 12.3.9. Fill upon stiff peloid ground with uneven surface: hydraulic heights before (a) and after placement (b), sliding wedges with force polygons (c)

a gravity-free onset with an isotropic homogenous pressure $p_s \approx \gamma h$ and a field of void ratios adapted to observed c_u -values may be assumed. This simulation produces initial creep velocities which should be small by (12.3.1) as the consolidation ratio p_e/p_s is higher than in the cases of Fig. 12.3.8. This first attractor in the large is a simplified substitute of the seasonally pulsating past evolution which can as yet hardly be captured.

The evolution during and after placing a dam can be simulated as with a softer peloid (Fig. 12.3.9b). The initial deformations are nearly isochoric for a while as the diffusion time is far longer than the filling time. The pore pressure p_w in the markedly sheared peloid region near the dam is less increased or even reduced due to the higher initial p_e/p_s , this prevents a delayed collapse. With drainage from below and evaporation or water access from above the subsequent creep slows down in the average. Seasonal pulsations could also be taken into account. A long-term stabilization is obtained if the dam is stable, i.e. if at most the critical friction angle is statically needed for the peloid at its base.

Simplified limit equilibria may be considered for design, Fig. 12.3.9c. The force between two wedges representing the dam cannot have a lower obliquity than $\tan \varphi_{cs}$. The peloid resistance is bounded by c_u at the onset and by the obliquity $\tan \varphi_{cs}$ in the long run. Thus the capillary skeleton pressure in the dam is neglected, and the suction implied by c_u is neglected for the peloid to be on the safe side. The undrained creep by and just after placement may at best be estimated with (12.2.3). The long-term diffusion and creep could only be guessed without finite element calculations. These cannot substitute monitoring in situ, but can help to plan it and to support technical decisions.

With *partially saturated* peloids the predictability is further reduced. Gas bubbles in peloid skeletons can be captured by assuming a more compressible pore fluid, but thus the changing solubility is neglected (Sect. 6.3). Gas channels of compacted peloid may be captured by suction and higher limit void ratios, but the effect of the ionic strength after wetting can as yet hardly be quantified (Sect. 7.2). Fills of crumps may be captured by composites (Sect. 9.1), but the evolution of cracks is beyond the present reach (Sects. 8.4 and 12.2). Gas inclusions after flooding or from reactions can make the peloid collapsible (Sect. 12.2).

To *sum up*, plane-parallel evolutions of yielding ground by and after placement of heaps can be captured as long as the soil response is ductile, otherwise a possible collapse is beyond the present reach as often is the influence of cracks and gas inclusions. The yielding of not too loose psammoid ground can be predicted, but uneven settlement or collapse in case of higher than critical void ratios are hardly predictable. Fields of stabilizing creep and skeleton stress before and long time after placement may be captured as a contractant state limit in the large. The almost isochoric creep just after placement may also be captured by an attractor in the large, then limit equilibria with slip surfaces can provide design estimates. A delayed creep collapse could be simulated with v-hyp, but the shear localization poses numerical problems. Without saturation only gas bubbles or channels in grain skeletons can as yet be taken into account. The inherent deterministic chaos impedes the consideration of bigger bubbles and cracks.

12.4 Excavations

Evolutions due to the excavation of a *psammoid* body with *constant hydraulic height* h_w can be captured as indicated with Fig. 12.4.1. Below a stationary water table p_w may be hydrostatic, suction above can be represented by a capillary skeleton pressure p_{cs} . The initial relative void ratio field r_e has to be given, the initial skeleton stress field can be determined with specific weight and stress ratio K_o as outlined in Sect. 11.2. The excavation can be simulated by a gradual removal of the weight of finite elements. The skeleton along the new boundary cannot decay above the ground water due to p_{cs} , and can be preserved below by assuming a small p_s (Sect. 10.1). Given stability as outlined in Sects. 12.1 and 12.3, changes of shape and state are negligible beyond a certain distance from the pit. Thus a rigid base may be assumed at a suitable depth, and smooth rigid walls in a suitable distance.

The rigid boundaries should engulf about twice the breadth b and depth h of the pit for $b/d < \text{ca. } 3$, given a symmetry line this means an additional smooth rigid wall. The order and size of excavation steps is of minor importance, the state thereafter may thus be considered as an attractor in the large (Sect. 10.4). These simplifying assumptions are justified by comparative

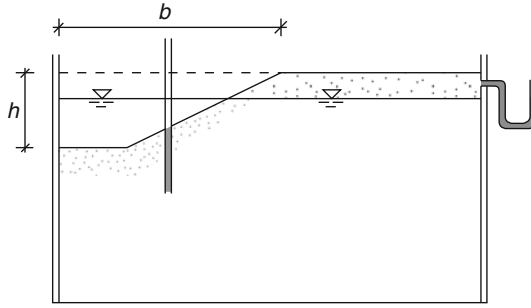


Fig. 12.4.1. Cut in psammoid with hydrostatic pore water

calculations (Karcher 2003), and also by the pragmatic argument that more precise predictions are neither feasible nor necessary in such cases.

Instantaneous hydraulic heights pose no problem if the influence of skeleton changes on h_w is negligible. This may be assumed in cases with lower than critical r_e , small excavator impacts and not too steep slopes. Loose flooded psammoid bodies can hardly be excavated as they would collapse (Sect. 12.1). Strong impacts would increase h_w and prevent a controlled excavation. Slopes under water with more than critical inclination ($\beta > \varphi_{cs}$) collapse after a temporary h_w -decrease (Sect. 12.1).

Slopes above the ground water table with $\beta > \varphi_{cs}$ can *crack* and collapse after a while, Fig. 12.4.2. Details are beyond the reach of present calculation models, so some hints may suffice. The soil near the steep surface falls down if p_{cs} vanishes by drying or wetting (Sect. 6.2). Keeping p_{cs} constant at the surface by a membrane, a crack could start somewhere at the shoulder by horizontal extension, but this localized bifurcation is hardly predictable (Sect. 8.4). The crack could reach the statically possible depth

$$h_c = \frac{p_{cs}}{\gamma} \frac{2 \sin \varphi}{1 - \sin \varphi} \tag{12.4.1}$$

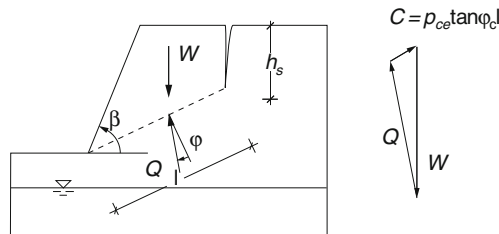


Fig. 12.4.2. Sliding with a crack in a steep humid psammoid slope

with an r_e -dependent friction angle φ . A soil block could just be at equilibrium upon a slip plane from the crack to the pit if the obliquity of the resultant Q in the slip plane does not exceed $\tan \varphi$.

These conventional conditions are at best necessary, but not sufficient for stability. Even if the vapor pressure in the crack is the same as in the skeleton this can dilate gradually so that φ and p_{cs} are reduced. The additional evaporation in an open crack causes a reduction of p_{cs} so that the soil block in front of the crack would collapse, and the shoulder behind it collapses afterwards (cementation excluded).

A collapse by drying would end when the slope has reached $\beta = \varphi_{cs}$ (Sect. 12.1). With an access of water from the surface into a crack this would close due to the loss of p_{cs} . This softening would lead to a collapse of the shoulder, and with further wetting the slope would get flatter than $\beta = \varphi_{cs}$ due to the seepage force (Sect. 12.1). Such evolutions cannot yet be properly simulated (cf. Sects. 6.2, 7.3, 8.4 and 16.3).

Cutting part of a saturated *peloid* layer with soft particles leads to pore water diffusion and creep. This is shown in Fig. 12.4.3 with a *low initial consolidation*, say $p_e/p_s \leq \text{ca. } 1.5$, a dense psammoid below and a constant h_w prior to the excavation. The top layer above the ground water table, consisting of cracked peloid or loose psammoid, may be substituted by a statical equivalent on top of the saturated peloid (cf. Sect. 10.2). The diffusion of pore water in the saturated peloid during a rapid excavation may be neglected. As for filling (Sects. 12.2 and 12.3) the order and size of excavation steps is of minor importance for state and velocity fields just after excavation, i.e. an isochoric attractor in the large may be assumed. Like with peloid heaps (Sect. 12.2) the height of the free water table is decisive for the evolution, and as with heaps upon peloid the degree of ductility plays a role (cf. Fig. 12.3.6).

Without lowering the hydraulic height h_w outside the peloid layer its h_w is reduced by the excavation with such gradients that it takes up water

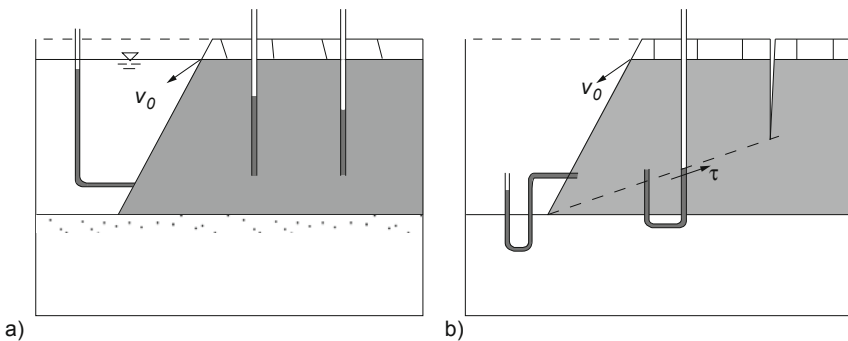


Fig. 12.4.3. Steep cut in peloid under water (a) and at the air (b)

(Fig. 12.4.3a). As with a peloid heap placed under water (Fig. 12.2.1a) a minor part by (12.2.4) is softened during and just after the excavation, whereas the free water pressure at the slope reduces the velocity v_0 of nearly isochoric creep. The initial v_0 can be estimated by (12.2.3) with a macro-element as by Fig. 12.2.2a. The swollen part near the slope slides down, and part of the shoulder can also collapse until the slope is flattened to $\beta \approx \varphi_{sc}$ and h_w is again hydrostatic. The approach to this attractor in the large could be simulated with finite elements and v-elp or v-hyp in order to estimate the lifetime of a cut.

If h_w is lowered outside the peloid layer alongside with the excavation it is more reduced inside, and the peloid loses water by evaporation (Fig. 12.4.3b). As with a peloid heap at the air (Fig. 12.2.1b) the initial creep velocity v_0 by (12.2.3) is far higher than with free water. The suction at the shoulder can lead to a *crack* after a capillary entry with vanishing horizontal skeleton pressure (Sects. 6.3 and 8.4). With the growth of this crack the average shear stress $\bar{\tau}$ below towards the foot of the slope grows so that v_0 increases before it is reduced by shrinkage. This can lead to a collapse, the more if the peloid is not ductile for isochoric shearing (cf. Fig. 12.3.6). Otherwise the peloid near the shoulder can come to rest when the suction has attained an equilibrium with the adjacent vapor in the cover and along the slope (Sect. 6.3). The destabilization by water access and the importance of a ‘skin’ of the peloid need not be explained. Such evolutions are beyond the reach of present simulation models as these cannot capture cracks. Kinematical and statical assumptions as by Fig. 12.4.2 can at best yield a crude necessary condition of stability.

With a *higher previous consolidation*, say $p_e/p_s \geq 2$, peloid layers undergo other evolutions during and after an excavation as they are already fissured, Fig. 12.4.4. The overconsolidation due to shrinkage and/or a temporary natural overburden leaves back a network of cracks (Sect. 8.4). This increases the permeability and reduces the potential suction of the peloid, which is thus a kind of composite (Sect. 9.1). Prior to the excavation such a peloid layer may be saturated with constant h_w , its base may consist of dense saturated

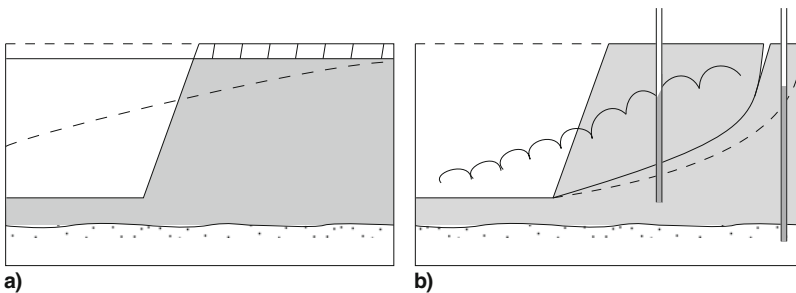


Fig. 12.4.4. Degradation of steep cuts in fissured peloid under water (a) and at the air (b)

psammoid and its cover of loose moist psammoid. The initial vertical stress T_{s1} is given by the overburden and h_w via (11.2.6), in the cover it is higher by p_{cs} . The ratio T_{s2}/T_{s1} of horizontal and vertical skeleton stresses may be taken by (11.2.7) with (11.2.9), except for the cover where $-T_{s1}$ and $-T_{s2}$ are higher by p_{cs} . T_{s2}/T_{s1} can actually be higher near the base if this was not shaken, and in the peloid layer with a temporary geological overburden if the resting time did not suffice for relaxation. This excess of T_{s2}/T_{s1} can hardly be determined, but it does not matter for the response to an excavation (cf. Sects. 3.6 and 15.3). The initial r_e of the psammoid layers can be determined by penetration sounding. The initial p_e/p_s of the peloid layer can be estimated via penetration, vane shearing or lab tests. With a less uniform ground an initial state could be generated by imposing gravity with suitable r_e or p_e/p_s , but this is no attractor in the large in general so that field data are needed.

Near a *steep cut under water* the peloid parts stand at first by suction, but collapse rapidly as the swelling is enhanced by opening cracks, Fig. 12.4.4a. Latent cracks prevent such a strong suction as in the peloid between them, a rapid cavitation enhances the release of vapor and dissolved gas (Sect. 6.3). The opening cracks accelerate the diffusion of pore water, cf. (12.2.4), and are closed after swelling of the adjacent peloid. Thus the steeper part near the shoulder slides down and leaves back a slope with $\beta \leq \varphi_{cs}$ and hydrostatic h_w inside. Transitions to this attractor in the large could hardly be simulated as evolution and influence of cracks cannot yet be captured.

A *steep cut at the air* can have a longer lifetime, Fig. 12.4.4b. A skin at the slope or a humid cover prevent an immediate cavitation if the suction $p_a - p_w$ due to isochoric shearing is not too big. $p_a - p_w$ is determined by the initial p_e/p_s and by the size and shape of the cut. A latent crack opens at the shoulder where $p_a - p_w \approx 0$ is attained and prohibits a stronger suction. The first crack deepens and more cracks develop as $p_a - p_w$ increases in the not yet opened peloid. Similarly as with a humid psammoid (Fig. 12.4.2) shearing is localized along a band towards the foot of a slope. A decomposed peloid mass slides down and comes to rest with a flatter slope. The new steep slope stands until new cracks lead to a retrograde sliding. In the long run a kind of psammoid with soft peloid grains would stand with $\beta \approx \varphi_{cs}$. An access of surface water would enhance the collapse and lead to an avalanche. Such evolutions were first reported by Collin (1846) who realized the role of water. Statical and kinematical assumptions can at best yield a crude necessary condition for temporary stability. Simulations with v-elp or v-hyp and realistic hydraulic conditions could capture the first crack and the subsequent shearing.

A case study by Schulze and Köhler (2003) may help to understand the matter, it reveals also the influence of pore gas and drainage, Fig. 12.4.5. A 20 m deep cut was excavated for a canal about 1925. The ground consisted of a highly plastic, stiff fissured silty clay with an estimated degree of saturation $S_r \approx 0.95$ under the far-field groundwater table in ca. 5 m depth. It was overconsolidated by a temporary ice cover, age and shrinkage, its far-field

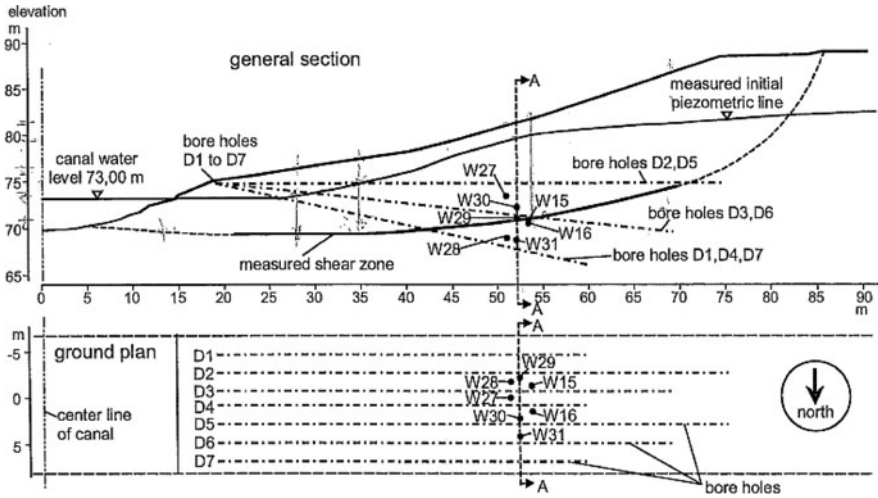


Fig. 12.4.5. Creeping slope with stiff fissured clay (Schulze and Köhler 2003): cross section and ground plan with boreholes for drainage

consolidation ratio p_e/p_s ranged from ca. 2 to 2.5. With the latent cracks its permeability k_f ranged from ca. 10^{-10} to 10^{-9} m/s, without cracks k_f would be at least two orders of magnitude smaller. Sliding started during the excavation so that the slope was flattened. In the course of decades slips led to the profile shown in Fig. 12.4.5. The indicated shear zone was found with an inclinometer in boreholes, it had a thickness of at most 1 m.

The piezometric level with $p_w = p_a$ was measured since 1998 by pore pressure sensors. The dotted upwards continuation of the shear zone led to an offset and a crack which were observed at the surface. Before placing drains the creep velocity v_0 of the shoulder was about 5 mm per month. It was temporarily reduced by a lower air pressure p_a . An observed rise of v_0 by 50% with a reduction of p_a by 3% can be explained: the average e increases by $\Delta e \approx 0.0005$ from S_r and the gas equation, thus p_e decreases by $\exp(-\Delta e/\lambda)$ and v_0 grows by factor $\exp(\Delta e/\lambda I_v) \approx 1/2$ with a typical compression index λ and viscosity index I_v for this soil. The immediate change of the creep velocity v_0 after changes of air pressure is thus an indicator of the skeleton viscosity as proposed in Sect. 3.2.

The magnitude of v_0 and its seasonal fluctuation could not as easily be captured in a back-analysis. An observed lower resistance to the expansion of a flat dilatometer revealed a shear zone of ca. 1 m thickness. The peloid therein could have approached a critical state, but the diffusion time $t_d \approx 1 \text{ m}^2/10^{-9} \text{ m}^2\text{s}^{-1} \approx 30$ years with an empirical $c_v \approx 10^{-9} \text{ m}^2/\text{s}$ of not fissured fat clay indicates an instationary h_w -field. h_w is underestimated by the sensors as they impede a uniform shearing. Higher than observed h_w can also be concluded from a simplified analysis as by Fig. 12.3.9 plus seepage force (cf. Sect. 11.3). An estimate of v_0 by (12.2.3) confirms that the peloid in the shear zone is near a critical state with a somewhat higher than observed h_w .

The strong seasonal fluctuation of v_0 can be attributed to alternating wetting and drying near the ground surface. Water can reach or leave the soil above the shear zone rapidly via fissures. As these are smeared in the shear zone the diffusion of pore water therein takes a longer time as was estimated further above. v_0 by (12.2.3) is strongly changed by minor changes of h_w via c_1 and p_{ec} , i.e. a minor swelling or shrinkage in the shear zone matters a lot for the creep velocity.

A fan of drains was placed in boreholes as shown in Fig. 12.4.5. This lowered the observed hydraulic height h_w by ca. 4 m and reduced the creep velocity v_0 to about 1/10 within 1 year. It appears that the diffusion time was reduced to ca. 1/10 as the fan of drains increased the overall permeability. The reduction of v_0 can be explained by (12.2.3) with an estimated reduction of the average c_2/p_{ce} by 30% and with $I_v \approx 0.05$. A more quantitative calculation would be feasible with v-elp or v-hyp, but delay times could at best be captured by their order of magnitude.

More precise calculations are feasible for *psammoid ground with peloid shear zones*, Fig. 12.4.6. This occurs in the Lower Rhenish lignite mining district with excavation depths up to 300 m and uncommonly detailed investigations (Gudehus and Pierschke 2004). In a simplified cross section (a) a clay layer from the bottom of the pit can reach a fault with a clay smear and an outcrop near the shoulder. The hydraulic height h_w is lowered around the pit, but not outside the fault. The difference of water pressure causes a

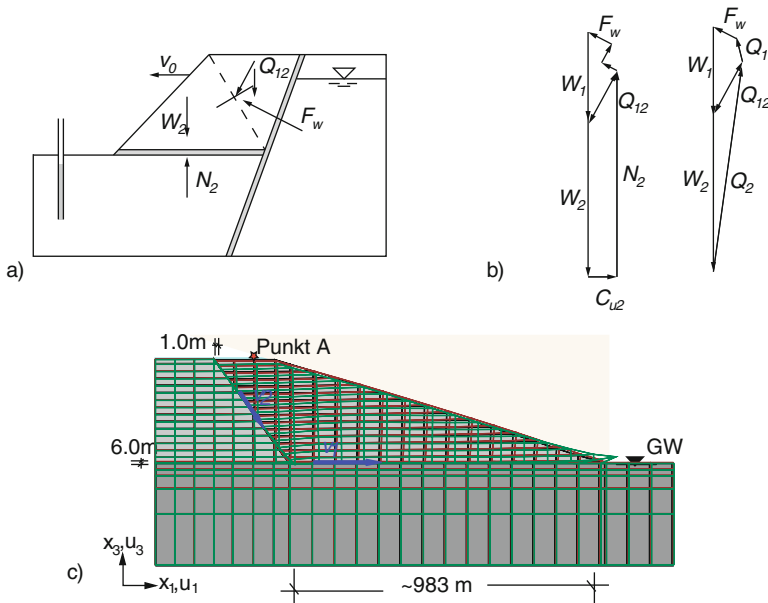


Fig. 12.4.6. Cut in ground with clay bands: sliding wedges (a) and force polygons (b), deformed finite element mesh (exaggerated) 500 days after a rapid excavation (c, Libreros-Bertini 2006)

seepage force F_w in the clay smear which is taken up by the adjacent psam-moid (erosion stability provided, Sect. 8.4).

A simplified stability analysis can be achieved by means of two sliding wedges. Clay layers and smears are natural shear zones, a further shear zone is assumed along a bisectrix (dashed in Fig. 12.4.6a). The resultant force Q_{12} therein cannot have a higher obliquity than $\tan \varphi_{cs}$. Force polygons with Q_{12} , F_w and weights W_1 and W_2 show which forces in the clay zones could prevent accelerations (b). Without diffusion just after excavation a statically required average cohesion \bar{c}_u is obtained (left). After the end of diffusion, when h_w in the peloid is determined by the ones in the adjacent psammoid, a force polygon (right) yields statically required obliquities of resultant skeleton forces Q_1 and Q_2 in the clay bands.

It is necessary for stability that the clay bands have at least the statically required resistance. This is biggest for a certain inclination ϑ of the assumed intermediate shear band, this can be found by variation of ϑ and with a lower obliquity of Q_{12} , its upper bound is $\tan \varphi_{cs}$. The shearing resistance \bar{c}_u is given by (12.2.1) with an assumed distribution of void ratio e and shearing rate D . The latter can be replaced by shear band thicknesses and creep velocity v_0 . This is justified if the peloid is ductile for isochoric shearing as explained with Fig. 12.3.6. Provided that the obtained v_0 is not too big with the required c_u the force polygon is then also sufficient for stability. In the long run a force polygon suffices for stability if the obliquities of Q_1 and Q_s do not reach the $\tan \varphi_{cs}$ of the clay. After the adaption of h_w to the hydraulic conditions the creep is further slowed down by contraction as the stress obliquity is lower than critical (Sects. 3.2 and 3.8).

Kuntsche (1989) reports a case of this kind. Stationary creep was observed in the first 2 years after excavation, this was far below the diffusion time of the clay layer by (11.3.1). A force polygon was obtained with lab c_u -values and $\varphi_{cs} = 12^\circ$ for the thin clay smear in the fault (Sect. 12.6). A minute further cut at the foot caused an increase of creep velocity v_0 by factor 7, with filling at the foot v_0 was reduced again. These changes of v_0 can be explained with (12.2.3) by the minute changes of the statically required c_u .

A finite element simulation with hyp and v-hyp conveys more insight (Fig. 12.4.6c, Librereros-Bertini 2006). The excavation was substituted by removing gravity in a time $t \ll t_d$, the order and size of steps has no influence in the sequel. The deformed mesh indicates rather uniform shearing in the peloid bands and a more diffuse shear zone in the psammoid near the bisectrix. The calculated displacements accelerate during the excavation and slow down afterwards. A more realistic simulation could be obtained with a more detailed mesh, but times for pore water diffusion can only be estimated as shape and permeability of clay layers cannot be determined precisely.

Karcher (2003) has shown that deformations of a *composite ground* due to excavations can be captured by hyp and v-hyp, Fig. 12.4.7. The finite element mesh (a) comprises several layers and faults and is still simplified. A

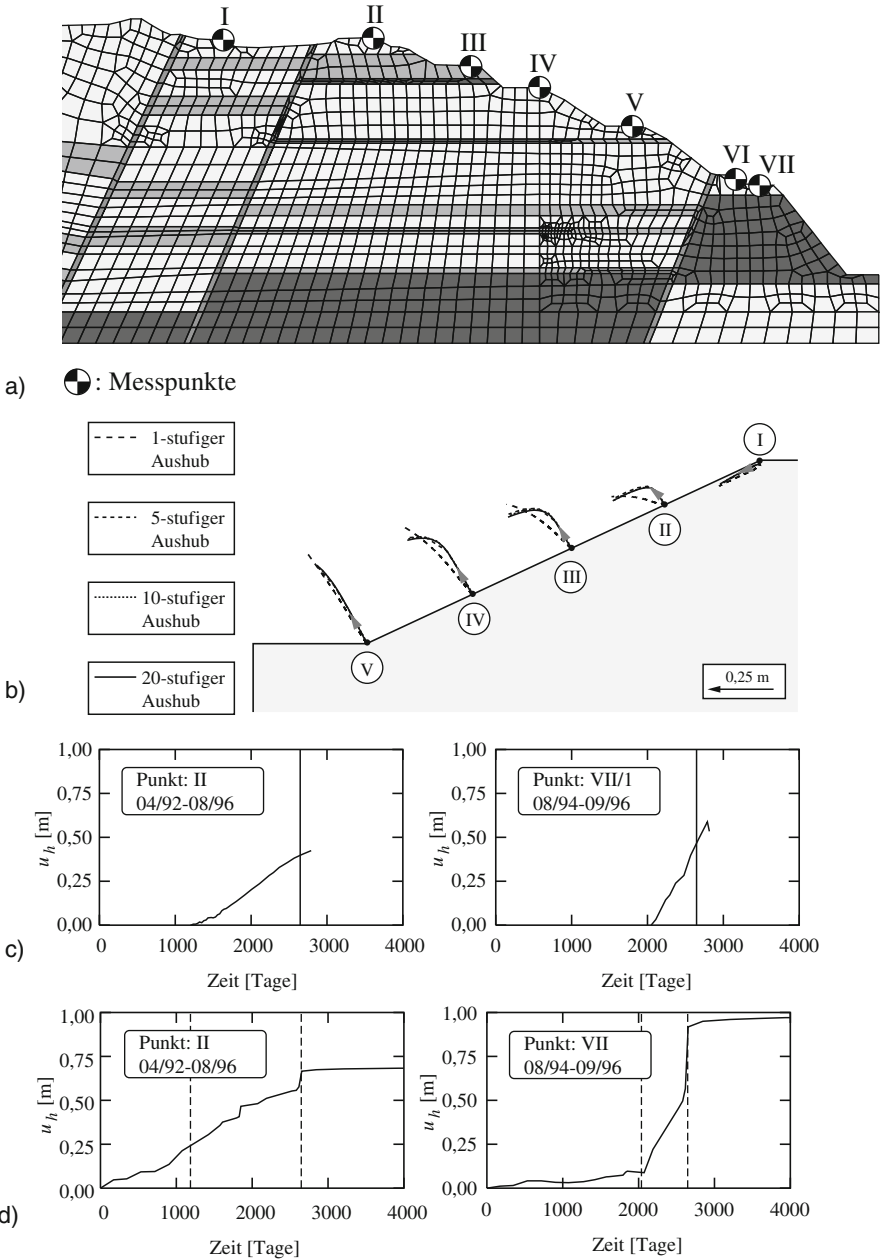


Fig. 12.4.7. Evolution due to a 240m deep excavation (Karcher 2003): finite element mesh (a), influence of excavation steps on displacements (b), calculated (c) and observed displacements (d) versus time of points marked above

field of initial state variables was generated by imposing gravity, and so that void ratios known from boreholes were reproduced. Comparative calculations reveal that size and order of excavation steps had almost no influence on the displacements at the end of and after the excavation (b). The displacement paths of slope points are straighter in case of a fictitious simultaneous removal. Hook-shaped paths due to an excavation layer by layer were in fact observed via boreholes.

Karcher (2003) could also show by comparative calculations that plane strain may be assumed for unsupported trenches which are longer than twice their width. Observed horizontal displacements at the slope due to layer-wise excavation are shown in Fig. 12.4.7c. The good agreement with calculated values (d) is a validation as no parameters were adapted to get a fit. The calculated displacements exceed the actual ones as the observations started somewhat later than the excavation and were not continued after its end.

To *sum up*, excavation-induced evolutions of shape and state can be captured for a variety of ground and water conditions, but critical phenomena delimit the range of predictability. For psammoid ground with subcritical relative void ratio ($r_e < 1$) and slope inclination ($\beta < \varphi_{cs}$ in case of hydrostatic h_w) the displacement at the end of excavation is rather independent of its sequence and time. Cutting fine-grained saturated ground with $r_e > 1$ leads to a collapse. A steep slope ($\beta > \varphi_{cs}$) with gas channels can stand up to a height that can be estimated with the capillary skeleton pressure p_{cs} , but it collapses after drying or wetting. A cut exposing peloid to the air can collapse after a while if it is too steep and high. The gradual opening of cracks and disintegration into crumbs cannot yet be captured. The degradation of slopes cut into stiff fissured clay indicates that the combined diffusion of pore water and creep of skeleton can as yet only be estimated. Better predictions can be obtained with composite ground wherein narrow clay bands work as shear zones.

12.5 In-plane and anti-plane shaking

Boundary conditions for *in-plane shaking* are shown in Fig. 12.5.1. Nearly plane waves propagate through a package of horizontal layers in situ from a shaking base if fictitious lateral walls are suitably specified (a). The propagation would be one-dimensional (Sect. 11.4) if the time-dependent displacements for this case would be imposed to the walls. These displacements are not known in advance, they should be equal for opposite points of the two fictitious walls. This condition works also with inclined layers, then two thought walls are shifted downwards by repeated propagations (b). Velocity v_w and pressure p_w of the pore water are also the same at opposite wall points for this reduction to a one-dimensional problem. In particular, skeleton and pore water can undergo the same motion (no drainage), or the hydraulic height h_w can be independent of the skeleton motions (free drainage).

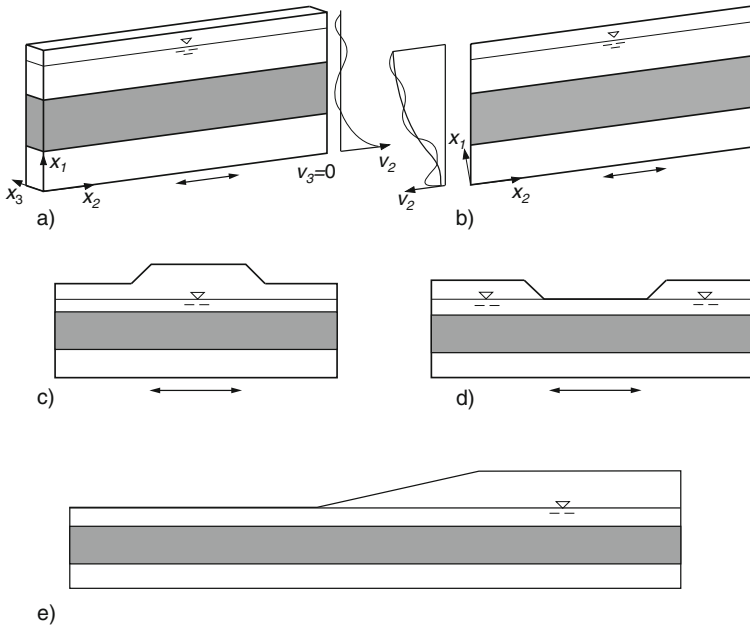


Fig. 12.5.1. Boundary conditions for in-plane shaking: free field with horizontal (a) and inclined layers (b), dam (c) and excavation (d) with layered ground, and different far-field levels (e)

If the ground has a more complex composition and/or an uneven surface conditions for fictitious boundaries cannot be justified as easily. With a symmetric dam (c) or trench (d) and parallel layers otherwise opposite points of walls undergo again the same displacements and have the same pressures. Beyond a sufficient distance from the symmetry line the far-field evolution is no more influenced by the dam or trench. A uniform shaking may be assumed at a sufficiently deep fictitious rigid base (cf. the beginning of Sect. 11.4). The symmetry of opposite walls gets lost with different ground levels on two sides of a slope (e). Evolutions around the slope may be captured by assuming a sufficiently deep rigid shaking base, and two walls with displacements and pore water conditions as for one-dimensional cases with the same ground profile. Comparative numerical calculations could show which distances suffice, analytical estimates are not in sight.

Different *shake boxes* have been used to investigate the range of validity. With rigid walls fixed to the base one-dimensional far-field propagations cannot be approached. This does not matter if the in-plane walls are well-defined and the plane-parallel walls are smooth. Thus the evolutions are plane-parallel and tractable enough for comparing observed and calculated evolutions, although they have no counterpart in situ. A set of laminar stiff frames can confine model soil upon a shaking base. Even if the frames are connected by stiff rods their mutual dislocations cause discontinuous boundary displacements of

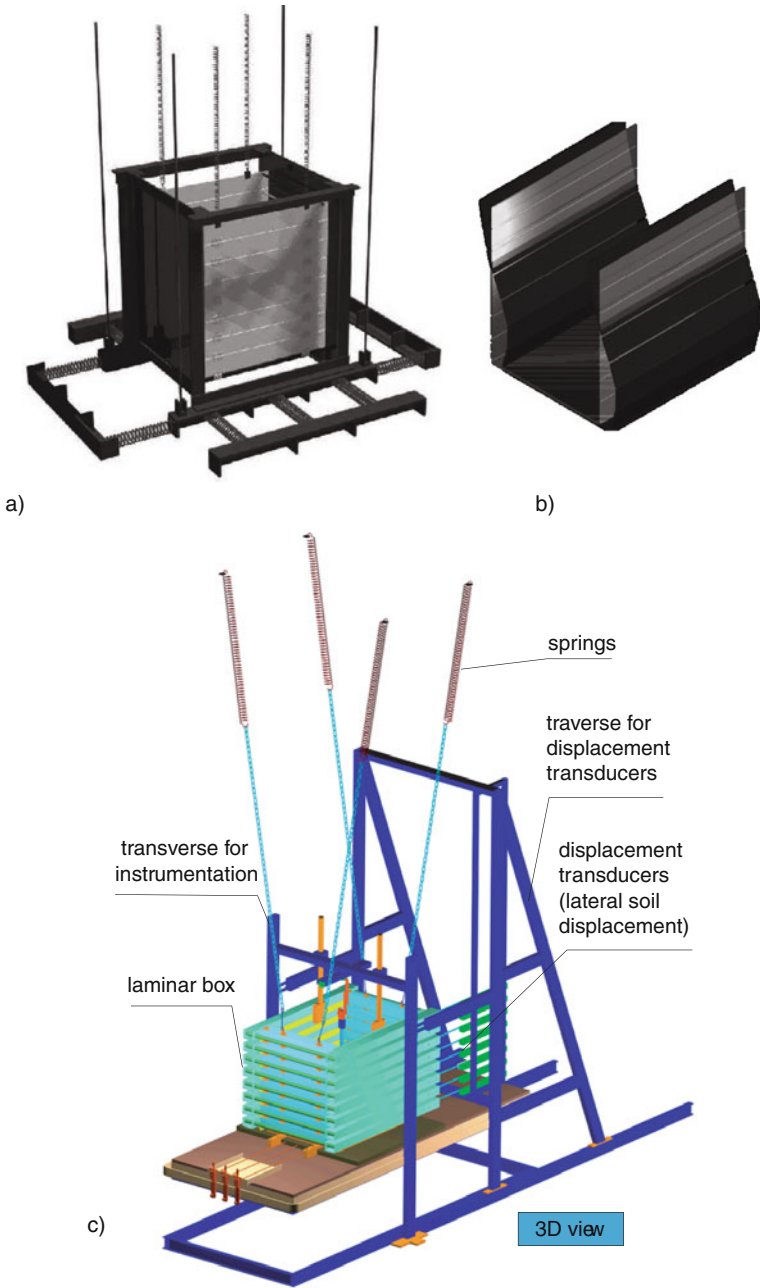


Fig. 12.5.2. Shake box with opposite laminate chains (a, b deformed), and with a jointed stack of frames (c); plots by Bühler (2006)

the soil. These may be smoothed by a membrane, but they lead to localizations which cannot be followed up in the analysis.

Prohibitive dislocations are avoided with *hinged laminar* lateral walls. In the first Karlsruhe shake box (Gudehus et al. 2004) the distance of opposite wall strips is fixed by wires, and the plane-parallel walls are smooth (Fig. 12.5.2a, b). The base is first clamped against springs and then released by cutting a wire. In the second one (Wienbroer et al. 2007) laminar frames with smooth flanks serve to the purpose (c). The base is shaken by a hydraulic drive with prescribed displacement vs. time, periodically or according to a seismic record. Vertical displacements along the in-plane walls are slightly confined by their friction. A membrane is needed between walls and saturated soil. An electro-phoretic water film can be employed instead for a peloid by means of direct current. These boundary conditions are sufficiently defined for back-analyses and resemble cases in situ.

Dry sand with a horizontal surface was investigated with the first Karlsruhe box, Fig. 12.5.3. It was loose at the onset and shaken by releasing the base. The free surface shifted sideways (a) and settled (b) rather uniformly. A back-analysis with hyp- δ (Libreros-Bertini 2006) reproduces this evolution in the essentials. As in the one-dimensional case (Fig. 12.4.2) the transversal waves have the same period as the base, whereas the longitudinal waves exhibit frequency doubling (later in the test and veiled by a shaking mode of the box).

Saturated sand was also tested in the first Karlsruhe box, Fig. 12.5.4. It was loose at the onset, its pore pressure p_w was measured near the base. Shortly after releasing the base the free surface was shifted (a) and settled (b), p_w rose abruptly and returned thereafter (c). The back-analysis with hyp- δ and no drainage in the first seconds reproduced the shift and the p_w -rise, but not the settlement afterwards and the p_w -reduction (Libreros-Bertini 2006). Pore water came out rapidly through spontaneously formed erosion channels (Sect. 8.4), this could be seen from minute volcanos (Sect. 16.3). Seepage is almost excluded in the short propagation time (Osinov 2000), the

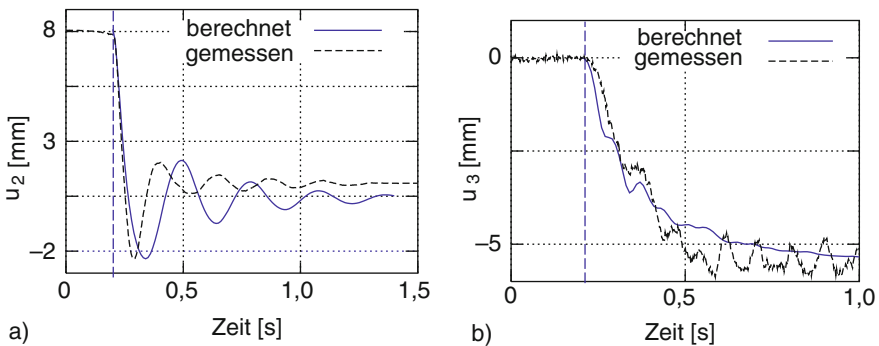


Fig. 12.5.3. Horizontal (a) and vertical (b) displacements of initially loose dry sand in the shake box of Fig. 12.5.2a and simulated with hyp- δ (Gudehus et al. 2004)

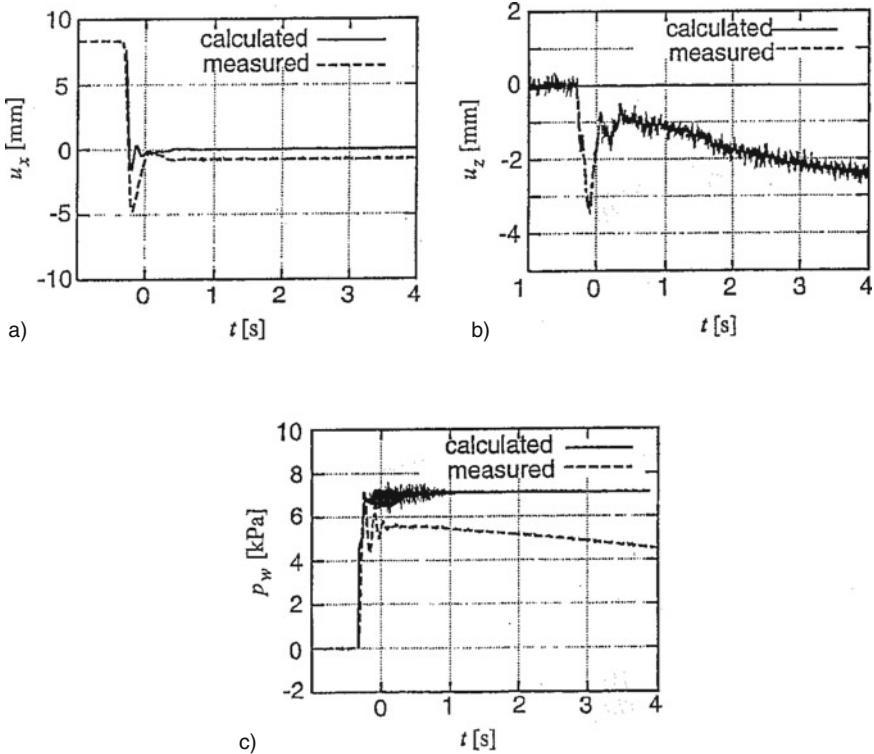


Fig. 12.5.4. Horizontal (a) and vertical displacements (b) and pore pressures (c), observed in the shake box of Fig. 12.5.2a with saturated loose sand and simulated with hyp- δ (Gudehus et al. 2004)

rapid dewatering via channels could not be captured by such a calculation (Kolymbas 1998).

The sand was densified to $e \approx e_d$ by repeated shaking and not shifted anymore. The same was achieved with periodic shaking in the second Karlsruhe box (Wienbroer et al. 2007). This attractor in the large could also be generated by hyp- δ with diffusion of pore water, except for hydrostatic uplift it depends on the amplitude as for a dry psammoid. With big enough amplitudes loose saturated sand expands to a suspension and exhibits gravity waves by strong shaking. The measured p_w reaches the total overburden pressure. This phenomenon and the subsequent formation of dewatering channels are outside the present reach (Sect. 16.3).

A layer of *saturated clay* upon a sand base was also investigated with the first Karlsruhe box. A moderately plastic clay was mixed and placed with a constant initial e so that a consolidation ratio $p_e/p_s \approx 1.5$ was attained near the sand base (Bühler 2006). Repeated shaking was imposed by stressing the box against springs with 1, 2, 4 and 8 mm stretching before release.

The observed response was almost the same in five repetitions, i.e. cumulative changes of state of the clay layer were rather negligible. The horizontal displacements along the wall increased slightly by doubling once and twice the base amplitude, but no more after a further doubling. This screening is confirmed by pore pressures p_w near the sand base. p_w rises slightly for a small amplitude, for a bigger one it reaches the total pressure and is reduced afterwards in some seconds.

These observations can be explained by means of v-hyp- δ . With moderate amplitudes the propagation of an S-wave in a peloid with $p_e/p_s < 1.5$ initially causes a slight reduction of p_s , after this increase of p_e/p_s the response gets nearly hypoelastic. With bigger amplitudes the underlying sand and the adjacent clay get temporarily close to a skeleton decay so that a further propagation is screened. A thin part of the clay layer is densified thereafter with pore water diffusion, this takes only a short time by (11.3.1). Further traces of propagations fade away by relaxation, thus the clay layer is the same as before except for a slight densification near the interface to the sand base. This near-attractor in the large would not occur with big amplitudes as then the clay would dilate in shear bands or crack, and could be transformed into a mud by strong shaking (Sect. 5.5).

Screening of shear waves is achieved by an about 1000 years old Japanese method named *hanshiku*. A mattress of fat clay with loose saturated sand inclusions was placed under important buildings. A strong earthquake causes a decay of the grain skeleton and only a minor subsequent densification, so the mattress which was kept wet served to the purpose repeatedly. Pralle (2002) observed a similar screening with a cushion of a saturated grain skeleton and a membrane (Fig. 12.5.5). The observed reduction of the top amplitude

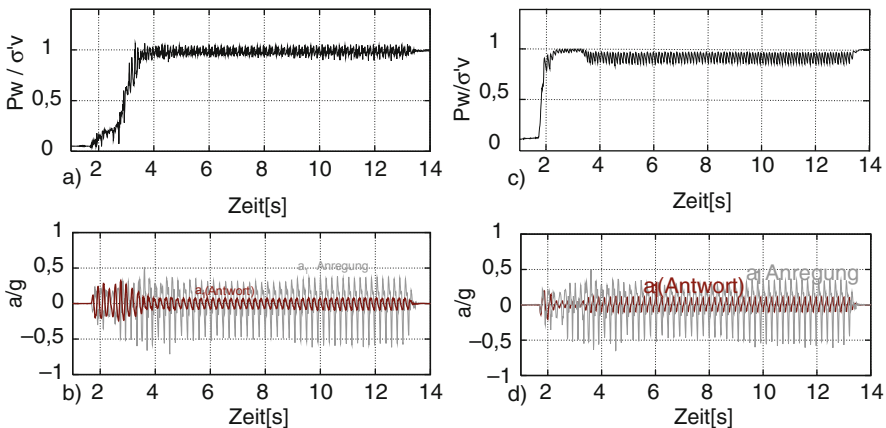


Fig. 12.5.5. Screening by skeleton decay: Pralle's (2002) observed pore pressure (a) and screening (b, inner line, outer zig-zag for excitation), simulation with hyp- δ (c and d) by Librerios-Bertini (2006)

(b) corresponds to the p_w -increase up to skeleton decay (a). Libreros-Bertini (2006) obtained nearly the same response by means of hyp- δ (c, d), this is a further validation.

Figure 12.5.6a shows a psammoid body including a dam under harmonic in-plane or anti-plane shaking (Gudehus et al. 2004, Libreros-Bertini 2006). In the latter case the out-of-plane displacements are equal in parallel cross sections, and the two fictitious walls are fixed and smooth. These boundaries are far enough from the dam, opposite wall points have the same displacements in case of in-plane shaking. Spreading (b) and settlement (c) of the dam calculated with hyp- δ , assuming $r_e = 0.5$ initially and no water, increase almost equally with time for both modes of shaking with amplitude $a_o = 0.2g$ and frequency $f = 3 \text{ s}^{-1}$. After a transition the displacement increases about

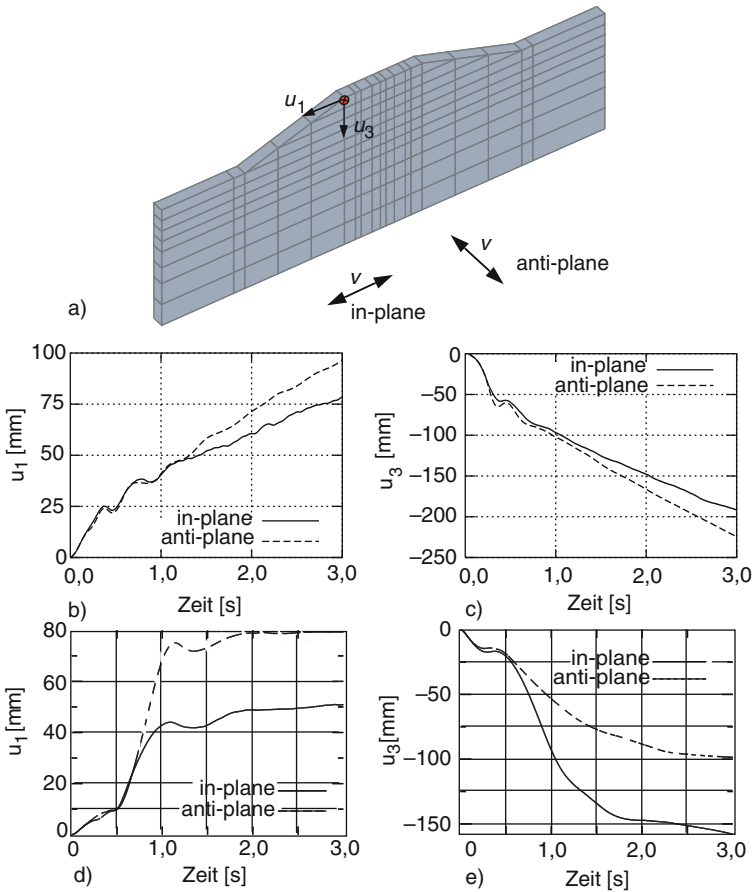


Fig. 12.5.6. Simulated seismic response of psammoid bodies with a dam (Gudehus et al. 2004, Libreros-Bertini 2006): boundary conditions (a), spreading (b) and settlement versus time without pore water (c), same with pore water (d, e)

linearly with the number of cycles, and the ratio of both components is rather constant. The latter is nearly independent of the frequency f , but the rate of growth per cycle is almost 20 times as big for $f = 2 \text{ s}^{-1}$ as for 15 s^{-1} . This magnification has little in common with the resonance of linearly elastic bodies.

The response of such a psammoid body was also calculated with water saturation and without drainage (Gudehus et al. 2004). The latter assumption is justified for some cycles with the assumed data (Osinov 2003), spontaneous channeling can be excluded with an initial $r_e = 0.5$ (rather dense). The cumulative displacements of the dam shoulder are smaller than with dry psammoid (or constant h_w), Fig. 12.5.6d, e. The pore water prevents dilation so that p_s increases, this matters more for in-plane than for anti-plane shaking. The constraint is weaker in the latter case as grain skeletons are softer for out-of-plane path reversals (Sect. 4.7). In the long run the hydraulic constraint is reduced by the diffusion of pore water.

A case with anti-plane shaking of a thin peloid layer was already outlined in Sect. 5.5. The enhanced creep or ratcheting could be captured by v-hyp- δ for lower than critical stress obliquities. A delayed collapse with shear melting and cavitation occurred with an overcritical obliquity. Apart from such critical phenomena the role of seepage can apparently be taken into account realistically for in- and anti-plane shaking of peloids.

A *composite* of psammoid and peloid zones was assumed for a case study, Fig. 12.5.7 (Gudehus et al. 2004, Liberos-Bertini 2006). A breakwater near Kobe was built upon rockfill which partly replaced soft clay, this was represented with finite elements (a). Soil parameters were chosen according to a report by Iai et al. (1998). A seismogram from the Hyogoken-Nanbu 1995 earthquake was taken as base shaking. The calculated pore pressure in the fill (b), mean skeleton pressure at the same place (c), lateral displacement at a surface point (d) and settlement of the breakwater (e) are nearly the same for in-plane and anti-plane shaking. A drainage was almost excluded during the earthquake, subsequent pore water diffusion and creep cause further displacements. The estimated asymptotic settlement of 1.5–2 m engulfs the observed one of 1.8 m.

Cases as presented above could be further investigated with the *seismodynamics* proposed in Sects. 4.6, 4.7 and 5.5. Seismodynamic equilibria were attained with submerged sand in the shakebox of Fig. 12.5.2c (Wienbroer 2010). With continued harmonic shaking the grains get unjammed so that their partial pressure gets isotropic, the void ratio gets close to the lower bound e_d and the mean pore pressure gets hydrostatic. This attractor is determined by the stationary shaking and implies a field of granular temperature T_g , observations could serve to check and quantify the balance of seismic energy by (4.6.7). The densification and the granular relaxation in the transition can at best be estimated with hyp- δ , s-hyp or h-cyc (Sect. 4.5), observations will help to validate and calibrate better theories.

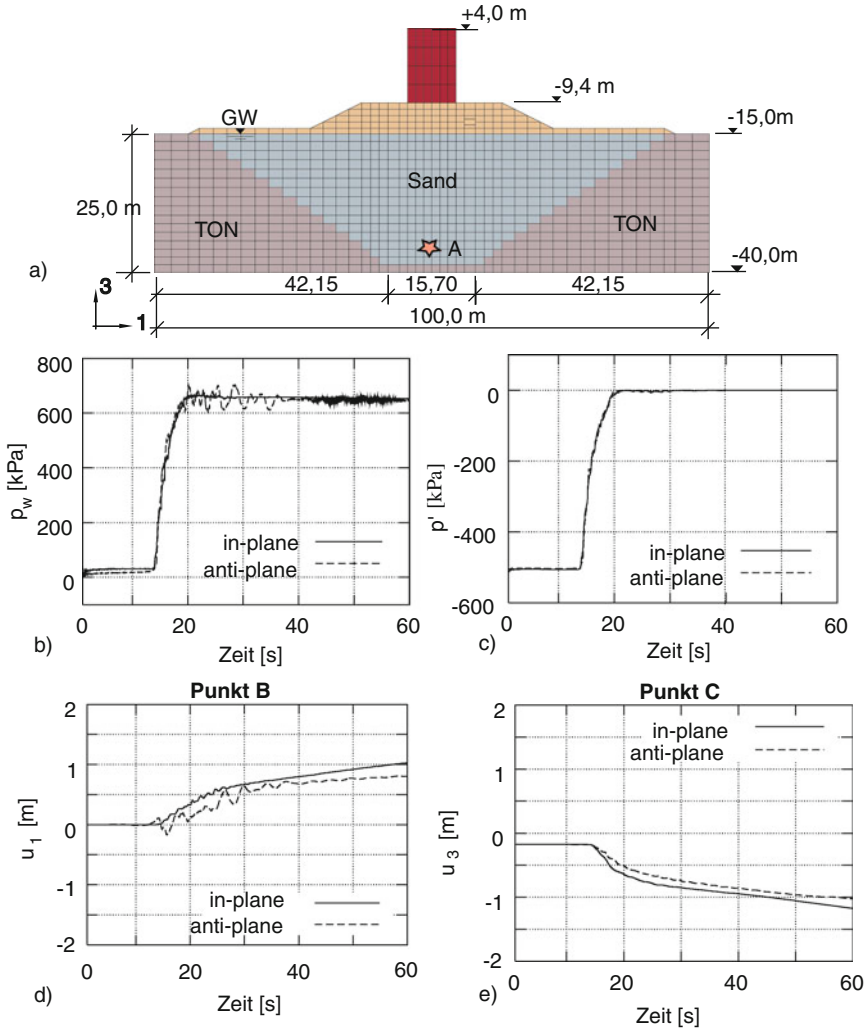


Fig. 12.5.7. Simulation of a breakwater with base shaking (Gudehus et al. 2004, Libreros-Bertini 2006): composition (a), pore pressure (b) and skeleton pressure (c) versus time for point A, horizontal displacement at the rim of fill (d) and settlement of the structure (e) versus time

Another attractor with T_g could principally be obtained by shaking the base of a granular layer with a subcritical inclination, but experiments and calculations will be difficult. In case of stationary ratcheting the grains are not unjammed, and with low T_g entropic and viscous stress fractions may be negligible. The one-dimensionality gets lost at layer rims and by critical phenomena, calculations with the models outlined in Sect. 4.5 can fail by ill-posedness. Earthquakes could produce attractors in the large with sand

which resemble thermally activated ones with peloids (Sect. 12.3), this is indicated by Fig. 12.5.6, but theories beyond hyp- δ , s-hyp and h-cyc will not easily be validated and calibrated. This holds also true for peloids with thermally *and* seismically activated viscous effects (Sect. 5.5), so Fig. 12.5.7 is no more than a promising hint.

To *sum up*, plane-parallel evolutions without structures due to base shaking can be captured by hypoplastic relations as long as critical phenomena do not dominate. Results of shake-box tests with sand are well reproduced by hyp- δ except for the formation of erosion channels after skeleton decay. Some field observations after earthquakes are fairly well reproduced with composites of psammoids and peloids. In these cases a stabilizing creep with pore water diffusion is seismically enhanced. Earth bodies at the verge of stability develop an autogeneous seismicity which indicates the onset of critical phenomena. Even without the latter the seismic mobility cannot be captured by simply assuming a temporarily heated solid.

12.6 Normal faulting

The mechanics of tectonic faulting is based on model tests with soil and on the theory of plasticity (Mandl 1988). Several kinds of fault patterns observed in situ could thus be explained, so it appears that the lithosphere is soil-like in that respect. *Normal faults* resemble shear bands in a biaxial test with horizontal stretching (Sect. 8.2). Following an article by Gudehus and Karcher (2007) it is shown in this section how evolutions of normal fault patterns can be simulated by means of hypoplasticity. As in previous sections of Chaps. 11 and 13 initial and boundary conditions have to be properly specified, now in order to get certain fault patterns. Plane-parallelity is assumed, but will be left aside at the end.

Wolf et al. (2003) obtained normal fault patterns in a model test with dry sand, Fig. 12.6.1. A dense layer was stretched by extending its laminate base via jointed parallelograms. Two out-of-plane walls were rather smooth so that nearly plane-parallel deformations were obtained. Except for the vicinity of the in-plane walls a zig-zag pattern of dilated shear bands arose by stretching (a). The free surface got wavy with steepest slopes at the outcrops of shear bands (b). The inclination of the bands against the horizontal was

$$\vartheta_n \approx 45^\circ + \varphi_p/2 \quad (12.6.1)$$

with a peak friction angle φ_p . The shear band pattern resembles swarms of normal faults (Mandl 1988). It does not arise with initially loose sand.

Nübel (2002) simulated such evolutions by means of hypoplasticity with polar quantities (cf. Sect. 8.2), Fig. 12.6.2. The rough base is extended uniformly, the in-plane walls with increasing distance are smooth and rigid. The initial relative void ratio $r_e = 0.2$ corresponds to a high density. A zig-zag

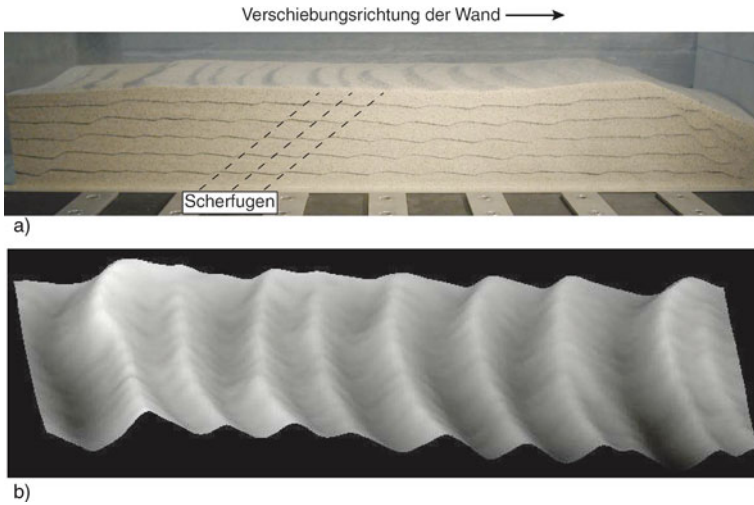


Fig. 12.6.1. Pattern of shear bands (a) and surface warping (b) in an extended model sand layer (Wolf et al. 2003)

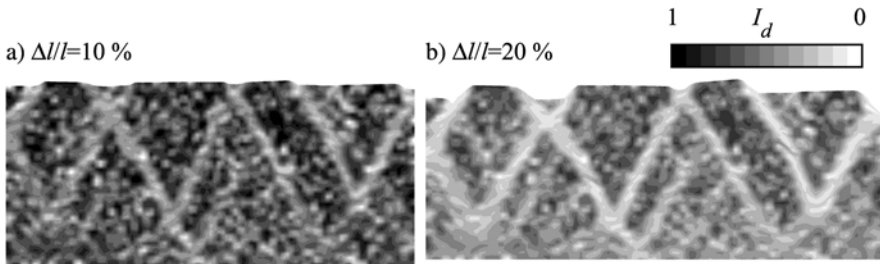


Fig. 12.6.2. Simulated shear band patterns in a sand layer with polar effects by 10% (a) and 20% stretching (b), Gudehus and Nübel (2004)

pattern of dilated shear bands is clearly visible after 10% stretching, and the free surface gets uneven (a). This resembles Fig. 12.6.1a, (12.6.1) is also confirmed. With 20% stretching a secondary pattern of shear bands gets better visible inside the first one, and the slopes at the outcrops reach the critical friction angle (b). The average density is sensibly reduced. An extension beyond ca. 20% could not be simulated as the equations got ill-posed. Similarly as with a biaxial sample between smooth plates (Fig. 8.2.10) the layer tends to an overall critical state with a fractal spatial fluctuation of void ratio and pressure. In the asymptote shear bands can no more be identified, and polar quantities disappear in the average.

Such simulations with polar terms are no more feasible for layers in situ as the number of required finite elements gets too big. Results of simulated stretching without polar quantities are mesh-dependent, Fig. 12.6.3. Shear bands are again produced (a), their initial inclination can be approximated

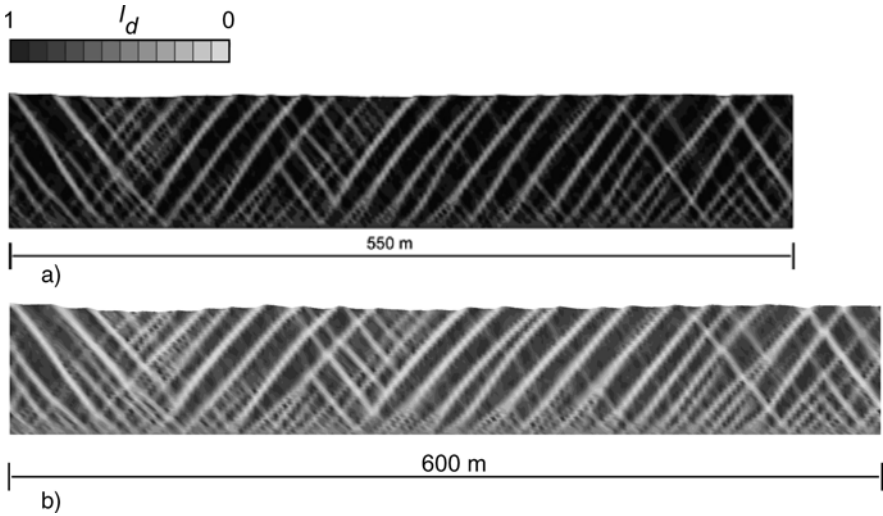


Fig. 12.6.3. Simulated shear band pattern in a sand layer without polar effects after a moderate (a) and a bigger (b) extension (Gudehus and Karcher 2007)

by (12.6.1), their thickness is given by the mesh size and not by the grain diameter. With further base stretching the shear bands get flatter (b). A fractal succession of zig-zag patterns is no more obtained, it is not known whether this lack could be overcome with more finite elements. The free surface gets wavy, and psammoid elements in shear bands tend to critical states. It appears that the layer would attain an overall critical state by continued stretching although this cannot be simulated because of ill-posedness, and that then shear bands could no more be identified.

Uniformly stretched homogeneous granular layers do not occur *in situ*, and even in sophisticated model tests the desired uniformity is spoiled by imperfect walls and bases. Patterns of shear bands or normal faults get different with minor changes of initial fluctuations and boundary conditions. This vicinity of pattern formation and deterministic chaos is typical for critical phenomena (Sect. 16.3). A strange attractor could be represented by a sequence of hatched RSEs. For each size dominating shear bands and offsets at the RSE-boundary can be imagined. Alongside with this fractality (Mandelbrot 1982) there are self-similar spatial fluctuations of skeleton stress. Apart from the cut-off by grain size and layer size there is no preferred RSE-size.

The situation can get conceptually simpler with boundary conditions which produce preferred shear bands, then hypoplastic simulations can yield realistic features of normal faults. Karcher (2003) simulated *synsedimentary tectonic deformations* for a cross section West of Cologne, Fig. 12.6.4. Geological investigations by Knufinke and Kothen (1995) reveal a depression with normal faults near its rim (a, b). The depression was filled with sediments during its formation in the past ca. $2 \cdot 10^7$ years, and stretched with

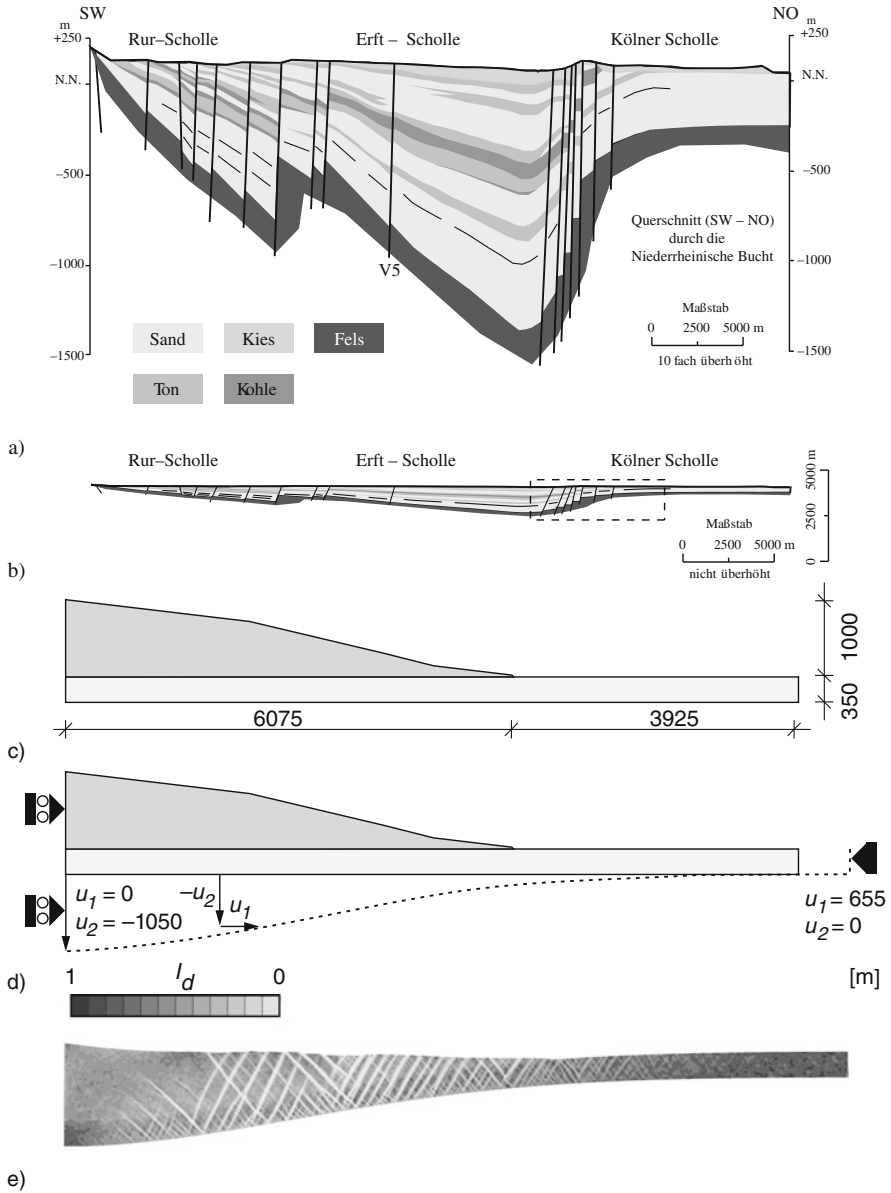


Fig. 12.6.4. Fault pattern in a formation with lignite (Karcher 2003, Gudehus and Karcher 2006): (a) cross section in situ with exaggerated heights, (b) undistorted cross section; onset with an overburden (c) of a depression with simultaneous stretching (d), and shear bands (e) by hypoplastic simulation for a section

simultaneous bending of its shoulders. Only major normal faults with more than about 10m dislocation are depicted, but there are also smaller nested patterns. Major faults appear likewise in the rock base which was deformed by the magma underneath.

Karcher (2003) simulated this evolution with necessarily simplified initial and boundary conditions. He assumed an increasing symmetric depression at the base of an initially uniform psammoid layer, and a simultaneously increasing psammoid fill to compensate for the depression, Fig. 12.6.4c and d. A swarm of shear bands inclined towards the depression is obtained in the region of biggest curvature, and a less marked swarm with the opposite inclination (e). The striking similarity with observed normal faults (a, b) was only obtained with the assumed initial and boundary conditions.

Excavations for lignite mining reveal details which are not captured by this simulation. Off the main faults minor faults and shear bands can be recognized from offsets of layers and brighter dilated zones. Only the main inclination is rather regular, the distances and thicknesses of bands are random. This indicates a strange attractor, so details are not predictable. Along main faults dislocated clay layers are deformed into *clay smears* (Lehner and Pilaar 1995). The faults are wider with bigger dislocations, and swarms of shear bands appear in their vicinity. The band width of clay smears tends to roughly 20% of the source layer thickness with increasing dislocation. This leads to preferred shear zones as assumed e.g. in Fig. 12.4.6.

A simulated evolution of a normal fault with a clay smear is shown in Fig. 12.6.5. A package of two psammoid layers and a thinner peloid layer is dislocated from the base and the fictitious walls with a direction by (12.6.1). With increasing dislocation the shear zone gets wider, whereas the width of the clay smear tends to an asymptote of roughly 20% of the source layer thickness (left). The succession of principal stresses (right) indicates a reduction of mean pressure and an adaption to simple shearing towards the clay smear. This was obtained with constant hydraulic height h_w , i.e. for sufficiently slow deformations. A bigger distance of the fictitious walls and minor modifications of the initial package did not change the results. A closer view reveals the formation of shear bands near the increasing main fault. The bands are mesh-dependent as the ones in Fig. 12.6.3 and can at best indicate the inherent fractality, only their inclinations may be considered as realistic.

A documented clay smear from a hydrocarbon-bearing formation (Weber et al. 1978) has a lot in common with our simulated one. The band thickness in the central part attains ca. 15% of the source layer thickness, this suffices for working as hydrocarbon seal. The adjacent formation reveals shear bands outside of and offsets in the source layer. Lehner and Pilaar (1995) propose a viscous feeding of an increasing clay smear by an assumed pressure gradient towards the fault. We obtain the main features with hypoplastic relations and suitable initial and boundary conditions without assuming anything else in advance for the near-field of faults.

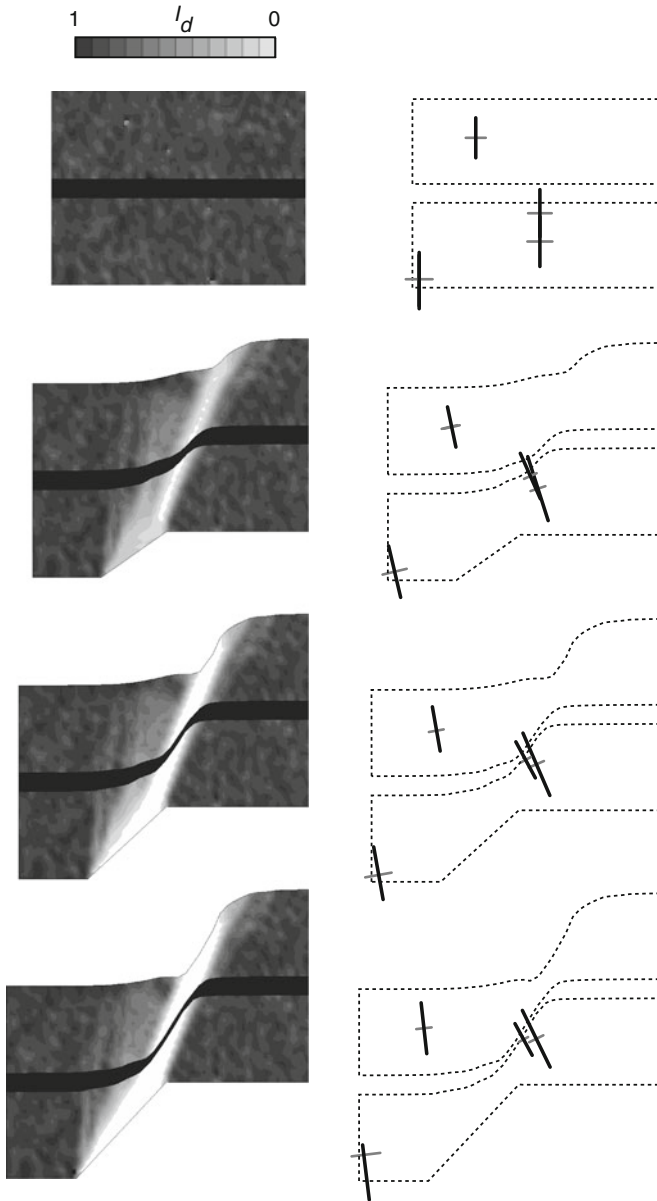


Fig. 12.6.5. Simulated faulting with an arising clay smear (Gudehus and Karcher 2006): composite with dislocation (*left*), principal stresses (*right*)

The assumed initial configurations and boundary conditions suffice to reproduce some key features of observed normal faults. Comparative calculations have shown that minor modifications of these assumptions do not change the major findings. Hypoplastic simulations may therefore be considered as a legitimate tool of structural geology instead of or in addition to model tests. This approach could be extended to other cases than normal faulting, but there are principal limitations.

Such attempts are impeded by mathematical ill-posedness and mesh-dependence. Remeshing alone is no way out, and regularizations need a physical background to avoid numerical artefacts. This could help to understand some critical phenomena in the lithosphere. Patterns of normal faults are never really plane-parallel or axi-symmetric. Model tests reveal swarms of spatially curved narrow shear zones en-echelon along a main nearly vertical fault (Mandl 1988). Ring structures with axi-symmetric initial and boundary conditions (Fig. 14.2.9) could exhibit en-echelon patterns as observed in triaxial tests (Sects. 8.2 and 14.1).

The matter gets more complex with *non-hydrostatic pore water*, in particular with clay smears and comminuted material in faults. In case of over-consolidation p_w can decrease by strong shaking (Sect. 4.2), thus the stress obliquity can get overcritical so that the formation of faults is enhanced. After a weaker consolidation a skeleton decay can occur due to an increasing granular or seismic temperature. A clay smear can get overcritical so that it dilates and cracks with autogeneous seismicity. Thereafter a hydraulic gradient can lead to a breakthrough, the subsequent erosion is enhanced by methane and leads to mud volcanos (more in Sect. 16.3).

To *sum up*, to a certain extent the formation of normal faults can be captured with hypoplasticity. With suitably chosen initial and boundary conditions observed features of synsedimentary faulting and of clay smears are reasonably reproduced. This new tool could also be applied to tectonic deformations with axial symmetry, and even to three-dimensional cases. The formation of fractal patterns and deterministic chaos in the lithosphere cannot thus be captured as the equations get ill-posed.

PLANE-PARALLEL EVOLUTIONS WITH SSI

Soil structure interactions (SSIs) are rarely plane-parallel, but often assumed so for calculations. This chapter leads beyond conventional models, and is more an outline of what could be done than a report on successful applications. Plane-strain model tests with structures are spoiled by parasitary wall forces, structures and ground in situ have rarely the same cross section over lengths which suffice for plane-parallelity. Attractors in the large are employed with the assumed symmetry, but how they can be attained or get lost cannot be judged within this frame (cf. the introduction of Chaps. 12 and 15).

Interactions of rigid walls with psammoids (Sect. 13.1) were first treated by Coulomb (1773). It will be shown how far classical earth pressure theories can be defended, and what can be done beyond including the pore water. The issue gets more intricate with peloids (Sect. 13.2) due to skeleton viscosity and pore water diffusion. We will see that the stability of statical equilibria, i.e. the ability to stand, can hardly be captured by comparing estimated driving and resisting forces. Even shear localizations can be numerically well modelled, polar effects matter only for solids which are not much wider than one grain.

Nearly the same conclusions are drawn for guided strips upon the ground (Sect. 13.3). Design models for shallow foundations can thus be delimited and improved. This is also achieved for nearly rigid structures upon soft ground (Sect. 13.4). Section 13.5 begins with subgrade reaction models although these do not depend on plane-parallelity. The presumed uniform cross sections are more often given with retaining structures (Sect. 13.6) than with skeleton buildings. Validations were achieved with a number of field tests and monitoring data, they are the base of design scenarios.

Cavities and underground structures (Sect. 13.6) are also treated with plane-parallelity, although this symmetry can at best be achieved in model tests and after the end of geotechnical operations in situ. The proposed design scenarios are therefore rather preparatory. Tunnelling with less symmetry will be treated in Sects. 15.2 and 15.4. Plane-parallel evolutions with several reversals are introduced in Sect. 13.7. It is shown how attractors in the large

could be achieved by model tests and calculations. This is rather an outlook, the issue will appear again in the next chapter and deserves further research.

13.1 Psammoids at rigid guided walls

Coulomb (1773) proposed to calculate earth pressures with the following assumptions, Fig. 13.1.1:

- A1: behind a horizontally yielding wall an *active* wedge slides down along a slip plane, the obliquity of the slip plane resultant equals the friction angle φ and the one of the earth pressure E equals the wall friction angle φ_w ;
- A2: the inclination ϑ of the slip plane has a value ϑ_a so that E is a maximum E_a ;
- A3: behind a wall pushed in a *passive* wedge slides up along a slip plane with force inclinations as by A1, but opposite sign;
- A4: in the second case ϑ has a value ϑ_p so that E is a minimum E_p .

In the simplest case of a smooth wall ($\varphi_w = 0$) without deviation α from the vertical and with a horizontal soil surface ($\beta = 0$) the results can be summarized by

$$E_a = \frac{1}{2} \gamma h^2 \tan^2(45^\circ - \varphi/2); \quad \vartheta_a = 45^\circ + \varphi/2 \quad (13.1.1)$$

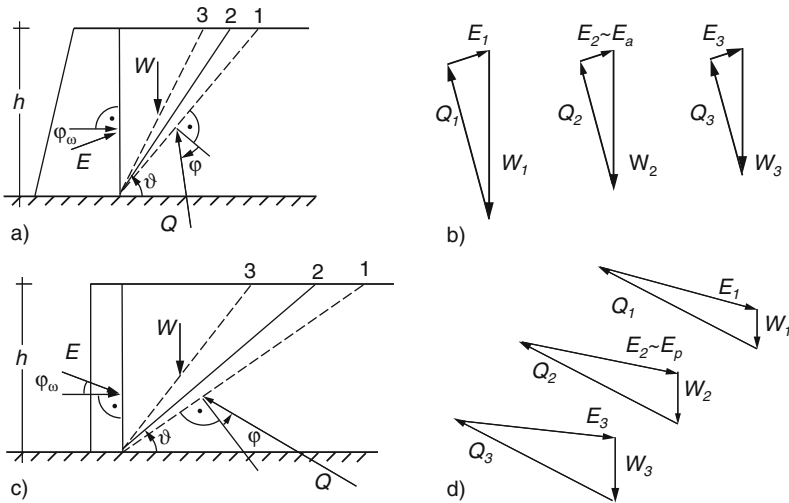


Fig. 13.1.1. Sliding wedges (a) and force polygons (b) assumed for getting Coulomb's active earth pressure; same for the passive case (c, d)

$$E_p = \frac{1}{2}\gamma h^2 \tan^2(45^\circ + \varphi/2); \quad \vartheta_p = 45^\circ - \varphi/2 \quad (13.1.2)$$

with height h and specific weight γ . In general the Coulomb earth pressures can be written as

$$E_a = \frac{1}{2}\gamma h^2 K_a; \quad E_p = \frac{1}{2}\gamma h^2 K_p \quad , \quad (13.1.3)$$

wherein the factors K_a, K_p and the related inclinations ϑ_a and ϑ_p are functions of α, β, φ_w and φ .

Rankine (1856) calculated stresses in a laterally extended or shortened layer, this was shown with Fig. 11.5.2. The stress components increase linearly with depth, their obliquity is maximal and equals $\tan \varphi$ for two normal stress directions. The resultant horizontal force on a fictitious vertical wall at a horizontal layer is E_a or E_p by (13.1.1) or (13.1.2), respectively. With an inclined layer the force upon a fictitious wall with inclination α is the same as by (13.1.3) if $\varphi_w = \beta - \alpha$ is assumed.

When and how can Coulomb’s and Rankine’s theories be justified? G. Darwin (1883) carried out model tests to find an answer. He filled fine dry sand behind a wall with a hinge below, and controlled a weight which pulled a wire at the wall so that the system attained the verge of equilibrium. He concluded that the active earth pressure E_a is proportional to h^2 as by Coulomb and Rankine, but obtained other amounts than these authors when taking the maximal inclination of a slope for φ . He observed different E_a for different sequences of filling and concluded that this *historical element* eludes mathematical treatment (cf. Prologue). His empirical formula for E_a was forgotten, and the historical element is largely ignored until now.

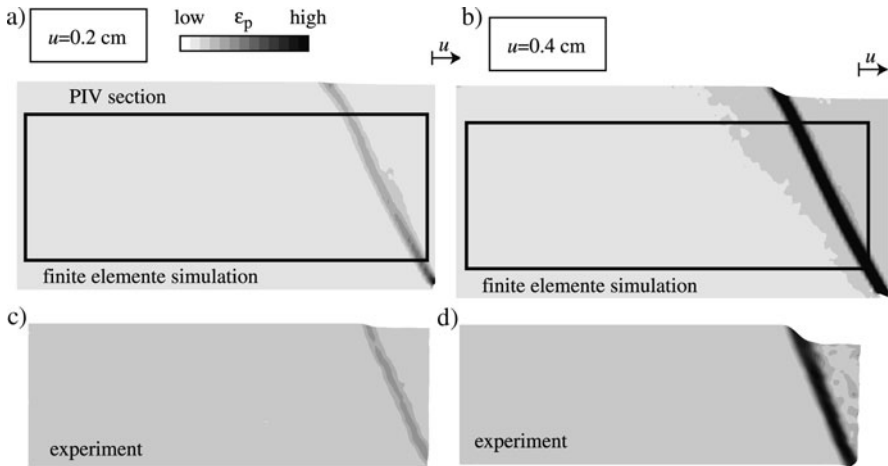


Fig. 13.1.2. Shear bands behind a smooth pulled-back wall (Nübel 2002, Gudehus and Nübel 2004): simulated with polar hypoplasticity (a, b), observed with particle image velocimetry (c, d)

It was shown in Sect. 11.5 that Rankine stress fields can hardly arise and that a density-dependent φ is rather indeterminate. So let us focus on Coulomb's assumptions in the light of modern theories and experiments. Nübel (2002) investigated a smooth model wall that was pulled back from an originally dense dry horizontal sand layer, Fig. 13.1.2 (also in Gudehus and Nübel 2004). Applying a hypoplastic relation with polar terms (p-hyp, Sect. 8.2) a nearly plane shear band was calculated that widened with increasing offset (a, b). The displacements and distortions observed with particle image velocimetry (PIV) are nearly the same (c, d).

Walls rotating around their foot were also investigated, Fig. 13.1.3. The calculation with p-hyp produced three parallel shear bands with marked dilation and offsets at their outcrops after a substantial rotation (a). Similar shear bands with dilation and offsets were observed by means of X-rays (b). For a smaller rotation the calculation yielded an emerging pattern of shear bands (c). This pattern is similarly fractal as for a biaxial test (Fig. 8.2.7) or an extended strip (Fig. 12.6.2). It resembles the lines of maximal stress obliquity by Rankine (1856), but does not reach the wall foot. For the bigger wall rotation two conjugate shear bands appear only just behind the wall (a).

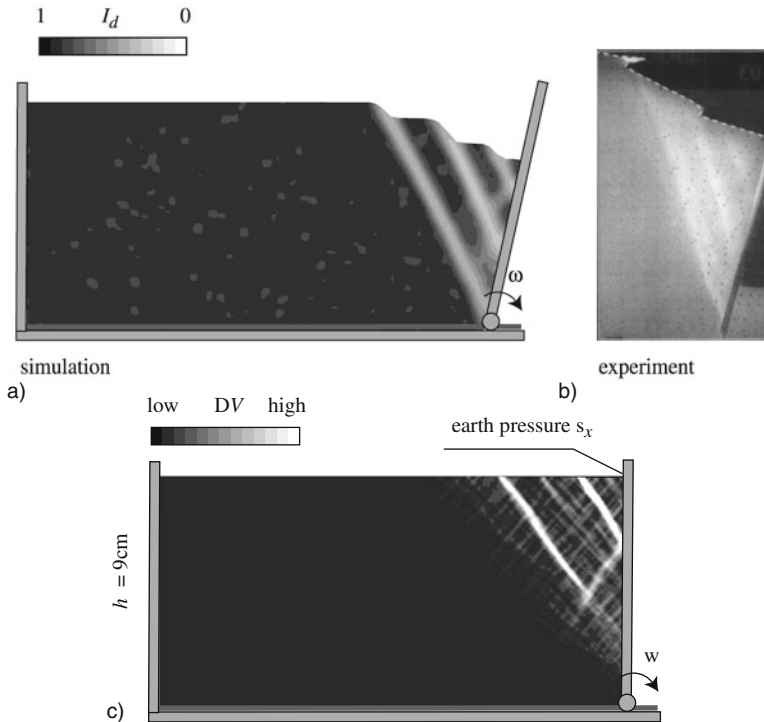


Fig. 13.1.3. Shear bands behind a rotated wall: simulated with p-hyp (a and c, Gudehus and Nübel 2004), observed with X-rays (b, Milligan 1974)

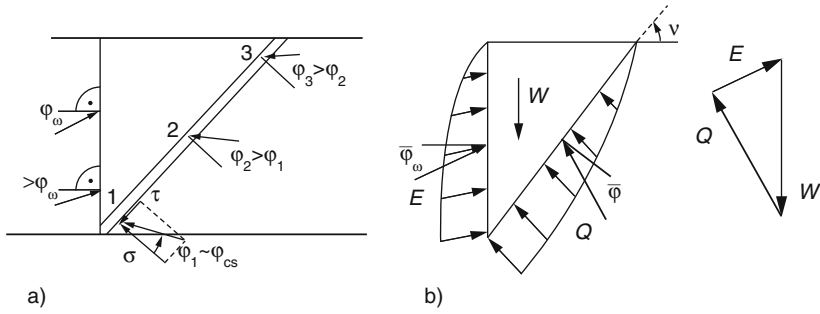


Fig. 13.1.4. Sliding wedge with stress obliquities (a) and distribution (b)

Coulomb’s assumptions A1 and A2 for the *active* case may now be discussed, Fig. 13.1.4. A slip plane from the wall foot is apparently justified if the wall is sufficiently shifted or rotated outwards. The inclination of its resultant force against the normal is not a constant φ , but given by an average peak friction angle that tends to the critical friction angle φ_{cs} by dilation (a, cf. Sect. 2.9). The inclination of the resultant earth pressure is bounded by the wall friction angle φ_w (Sect. 10.3), but need not agree with it. With an observed inclination ϑ and assumed inclination of Q an earth pressure E can be determined by the equilibrium of the triangular zone between shear band and wall (b). As its weight W is proportional to γh^2 (13.1.1a) seems to work with a suitable K_a . But does E really attain a maximum E_a with respect to ϑ as assumed by Coulomb without discussion?

In other words A2 means that given A1, ϑ takes a value ϑ_a so that E attains the highest statically possible value E_a with the assumed force obliquities. This cannot be concluded from equations for the boundary value problem, so it is an ad-hoc hypothesis with at best empirical validity. The consequences (13.1.1), (13.1.2) and (13.1.3) may be used for design estimates with due caution. We will see further below what this means for the assessment of stability, and how deformations and changing densities could be taken into account.

Gudehus and Nübel (2004) present also investigations of a *passive* case which may serve to judge Coulomb’s assumptions A3 and A4, Fig. 13.1.5. In a model test a wall was pushed downwards into partly coloured sand (a). Calculations with polar quantities and hypoplasticity (p-hyp) produced a similarly distorted finite element mesh (b). One can see a curved shear band and distortions on top of it. Dilations reveal the detailed evolution of shear bands, Fig. 13.1.6, both observed with X-rays (a) and calculated with p-hyp (b). At the beginning a shear band grows horizontally from the wall foot (A). This gets stuck and a curved shear band grows up to the surface (B). The band is widened and the skeleton is further dilated with increasing wall shift, and two further shear bands arise from the wall top (C). These findings refute A3 and do not offer a substitute of A4.

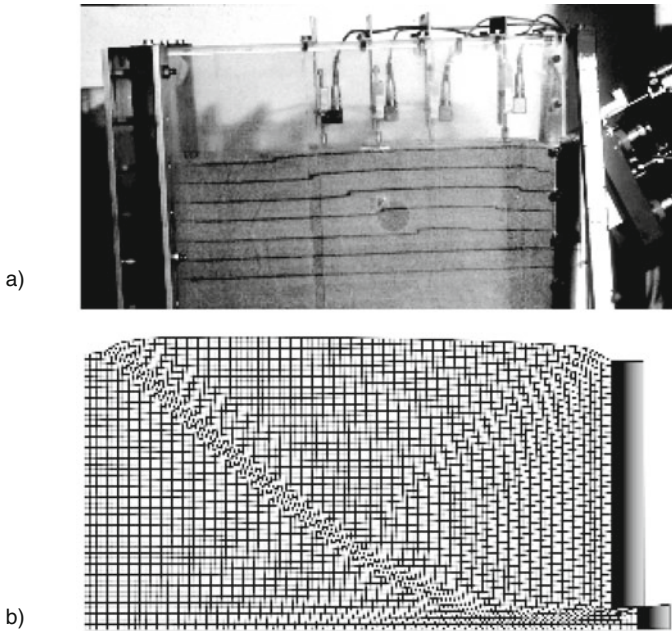



Fig. 13.1.5. Observed (a, courtesy E. Schwing) and calculated (b) deformation behind a pushed-in wall (Gudehus and Nübel 2004)

Two sliding wedges may be considered for design estimates in such cases, Fig. 13.1.7. They are specified by three inclination angles ϑ_1 , ϑ_2 and ϑ_{12} which may first be assumed (a) according to Fig. 13.1.6. Their force obliquities are $\tan \varphi_{cs}$ for the outer bands as these are dilated up to critical states. The inclination of the band from the wall top is bigger by an unknown amount due to dilation, but for caution it should also be taken as φ_{cs} . The inclination of the resultant earth pressure E is lower than the wall friction angle φ_w if the first wedge does not slide along the wall, it may be assumed as zero to be on the safe side. A force polygon for the two wedges yields a limit equilibrium value of E (b). A lower bound of E can be obtained by variation of ϑ_1 , ϑ_2 and ϑ_{12} . Results of such variations (Gudehus 2002) can be captured by (13.1.3b) with K_p -values well below the ones by Coulomb.

This approach gets inconsistent if the wall can also *rotate*. Coulomb (1773) indicated a slightly curved slip surface for the active case and substituted it by a plane, this suffices apparently even if the wall rotates although then a rigid sliding wedge is impossible (cf. Figs. 13.1.2 and 13.1.3). Various approaches have been proposed for the passive case, Fig. 13.1.8. A single curved slip surface can be approximated by a circular arc, then a rigid body on top of it can move together with the wall (a). Assuming a constant stress obliquity $\tan \varphi$ the resultant force Q in the slip surface should have at least the moment

a) X-ray, experiment

b) calculation low ΔV high


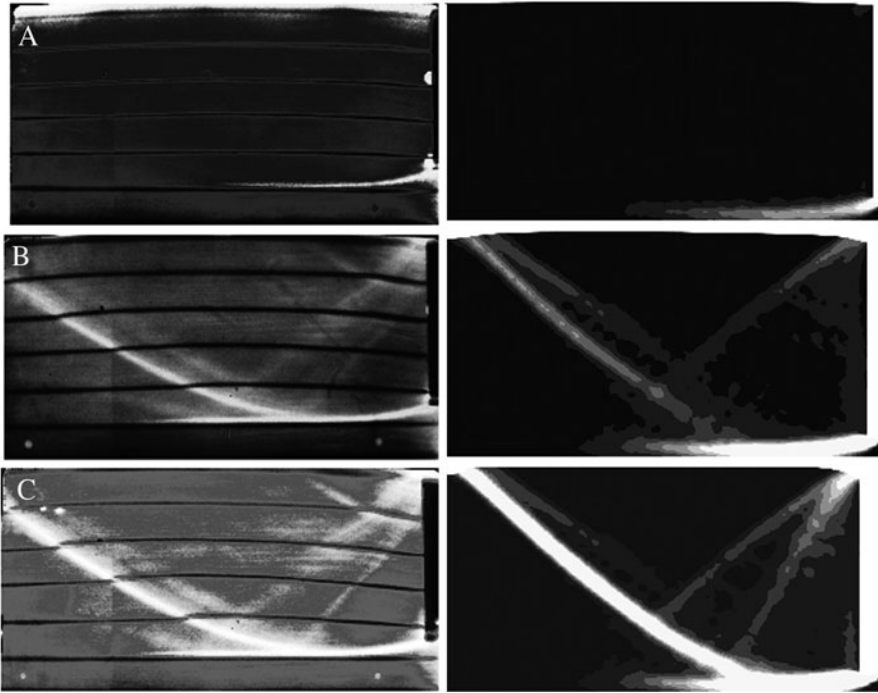


Fig. 13.1.6. Observed (a, courtesy E. Schwing) and calculated dilations (b, Gudehus and Nübel 2004) for the experiment of Fig. 13.1.5

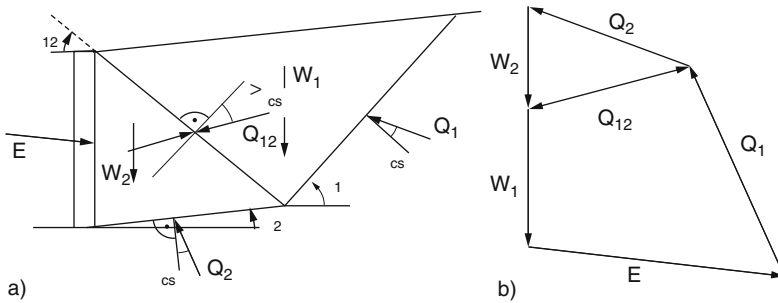


Fig. 13.1.7. Sliding wedges (a) and force polygon (b) Gudehus (1981)

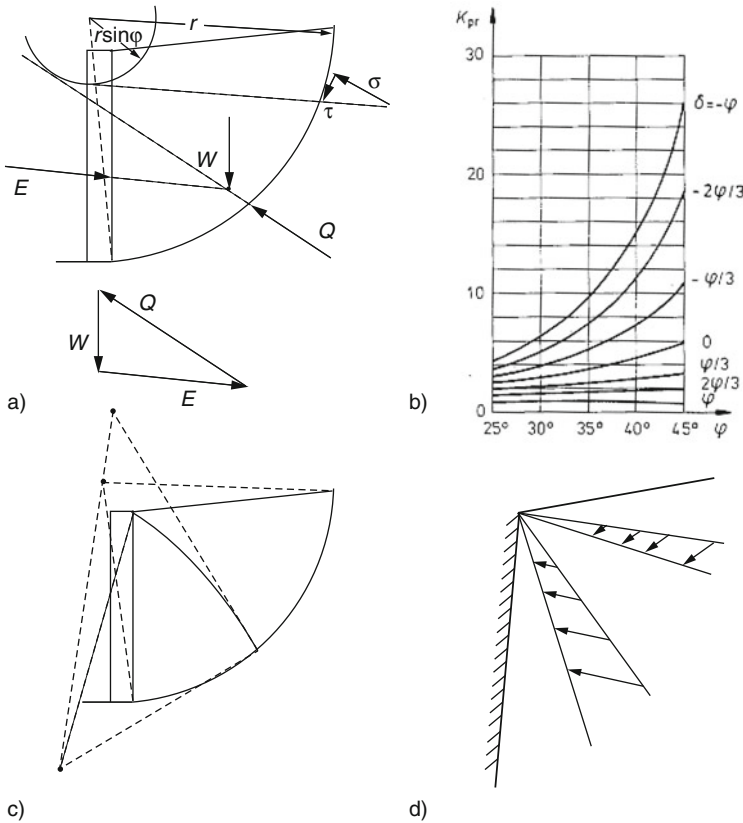


Fig. 13.1.8. Assumptions for passive earth pressures at a rotating wall with a slip circle (a), coefficients of earth pressure (b), three slip circles (c) and radial stress field (d)

$Qr\sin\varphi$ relative to the centre of the arc. Given the direction and position of the resulting earth pressure E , this is determined by the equilibrium with Q and the weight W of the sliding body: E , Q and W go through one point and make a closed polygon. Variation of the arc leads to a lower bound E_p of E . This was calculated and can be expressed by (13.1.3b) with a suitable K_p (Gudehus 2002).

Such K_p -values are plotted in Fig. 13.1.8b. They are lower than the ones for translation, which in turn are lower than the ones by Coulomb. The less constrained the kinematic freedom is by assumed slip surfaces, the lower evidently is the resistance of the psammoid body against the wall. A slightly lower E_p would be obtained with two sliding bodies separated by curved slip lines, Fig. 13.1.8c. Neglecting dilatancy and assuming circular arcs their centres should be on a straight line if the sliding bodies are rigid. With the same assumption for resultant slip line forces as for a single arc a lower bound

E_p can be calculated by variation. This is not needed for design estimates as these are crude anyway.

Purely statical methods may only be mentioned for historical interest. Assuming a radially linear increase from the wall top and a maximal obliquity $\tan \varphi$ of the in-plane stress components, Fig. 13.1.8d, Caquot and Kérisel (1956) calculated K_p values for E_p by (13.1.3b). Sokolovski (1960) dropped the linear increase and obtained slightly lower K_p -values. As with Rankine's (1856) theory (cf. Sect. 11.5) the assumption of a uniform maximal stress obliquity is not justified by observations and sophisticated calculations. Figure 13.1.6 suggests two radial shear bands from the wall top, but a non-uniform obliquity can be concluded from the different degrees of dilation. A radially linear stress increase, as assumed by Caquot and nearly obtained by Sokolovski, is thus not supported by more realistic models.

The *historical element* is ignored in the usual statical and kinematical methods for determining E_a and E_p . Slip lines and stress or force obliquities are assumed without saying how they could arise. Stress distributions have also to be assumed ad hoc, and the highest lower or lowest upper bound for E is only reasonable to get E_a or E_p , respectively, but not necessary. One has to follow up the evolution of shape and state in order to overcome these serious shortcomings. This may first be outlined according to Darwin's (1883) experiments, Fig. 13.1.9. The psammoid can be identified by hypoplastic parameters. The rigid, initially fixed wall imposes a restriction by (9.2) with a friction angle $\varphi_w \leq \varphi_{cs}$. The skeleton is fixed below the wall hinge, along the opposite wall and at the base.

An initial state can be generated by imposing gravity in different orders with suitable relative void ratios r_e (Sect. 10.4). One could simulate different orders of filling as chosen by Darwin, e.g. horizontal layers or inclined ones from or towards the later rotating wall (a). This leads to non-uniformities of stress ratios T_{s2}/T_{s1} and relative void ratios r_e along the wall and the temporary slopes. Tapping or shaking can hardly be simulated, it suffices for the sequel to assume a stress field instead as for a uniform layer (cf. Sect. 11.2) with $T_{s2}/T_{s1} = K_0 \approx 1 - \sin \varphi_c$. The initial density has to be specified by a suitably assumed r_e -field which is the most important state variable.

Shape and state of the psammoid body are now changed by rotating the wall with negligible accelerations (b). Before the system loses its equilibrium one can as well specify steps of the rotation angle ω or the reduction of weight W at a string connected with the wall. Independently of initial fluctuations the stress components along the wall tend to an almost linear increase with depth and according to the slip condition. As in Fig. 13.1.3 shear bands evolve behind the wall. Their thickness and number depends on the chosen mesh (cf. Sect. 12.6), but realistic earth pressures for rotations could be obtained nevertheless. The lack of objectivity could be removed with polar quantities, but such calculations are very expensive and neither feasible nor necessary if the wall is more than ca. 10^3 times as high as the grain size (Tejchman 1997). The average dilation, which is decisive for the evolution of E , could

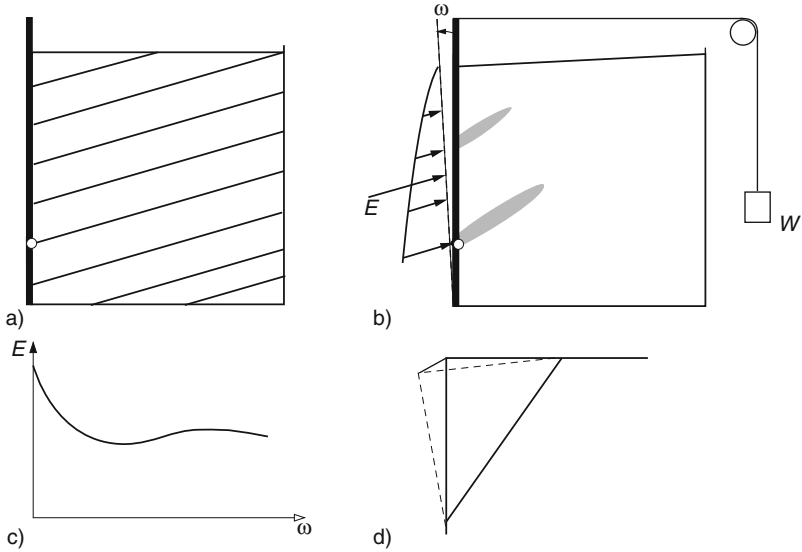


Fig. 13.1.9. How Darwin’s (1883) experiments could be simulated: placement (a), limit equilibrium (b), earth pressure versus rotation (c), macro-element (d)

be captured by a suitable mesh without polar terms. This is legitimate as the mean pressure p_s is hardly influenced by size and rotations of grains in the given case. In a triangular zone above a shear band the forces are given by weight and obliquity (cf. Fig. 13.1.4), the latter is determined in the band by its instantaneous average relative void ratio \bar{r}_e , this is rather mesh-independent.

The state attained by a sufficient wall rotation may be considered as an *attractor in the large*. The stress components along the wall increase about linearly with depth and satisfy the slip condition (10.3.2). Their obliquity is determined by the \bar{r}_e along a plane shear band from the wall foot. This \bar{r}_e in turn is determined by its initial average \bar{r}_{e0} , it gets higher due to dilation during the transition. The wall rotation required to attain the attractor increases with bigger initial non-uniformities of stress ratio and r_e . As long as the initial r_e -fluctuations do not imply higher values along the emerging lowest shear band than the overall average \bar{r}_{e0} the latter determines the earth pressure at the wall. Although the dependence on initial r_e -fluctuations could be investigated by comparative calculations Darwin (1883) was right stating that the determination of earth pressures ‘eludes mathematical treatment’.

Consider now the *stability* of our system. If the wall is further rotated with a slow constant velocity the resultant earth pressure E increases somewhat with rotation ω before it is reduced by the decreasing psammoid height at the wall (Fig. 13.1.9c). Only if the layer is very loose at the onset, i.e. for $\bar{r}_{e0} \approx 1$, such an increase cannot occur. If the wall is kept by a string with a

weight W the system collapses after the minimum of E has been attained, i.e. the equilibrium gets lost with spontaneous acceleration. There is an excess of kinetic energy as the net loss of gravitational energy of the psammoid and the suspended weight exceeds the energy dissipated during an additional wall rotation $\Delta\omega$. This can be estimated by assuming a uniform dilatant shearing in a triangular zone (d). The dilatancy angle ν of this macro-element (cf. Fig. 12.1.4a) is determined by its instantaneous \bar{r}_e via the relations for state limits (Sect. 2.9). The latter determine also the reduction of the stress obliquity by further shearing.

This estimate could be substituted by calculations with finite elements and hyp or p-hyp, but these are cumbersome as even with inertia the equations tend to get ill-posed. This indicates a spontaneous seismicity which was already observed by Darwin (1883). As with heaps and excavations (Sects. 12.1 and 12.4) one should avoid such a collapse by assuming a limit equilibrium according to Fig. 13.1.4 with φ_{cs} . In Darwin's experiments the system attained a new equilibrium with more rotation and a lower psammoid height, but real retaining walls can collapse.

The procedure explained with Fig. 13.1.9 can be transferred to a psammoid fill with a rigid retaining wall which can slide along a plane solid base with friction angle φ_b , Fig. 13.1.10. The wall may be backfilled (a) until it slides. The evolution could be simulated by means of finite elements with different successions and relative void ratios r_e . As before the average \bar{r}_e is decisive for the onset of sliding. This can be captured with a psammoid wedge (b) and a force polygon with limit obliquities (c). A statically possible filling height h_s can thus be determined with an average inclination $\bar{\varphi}$ of the resultant force in the assumed shear band with inclination ϑ . The earth pressure is the intermediate force between wall and soil, $E = Q_{wp}$, with given obliquity $\tan \varphi_w$. Following Coulomb a value ϑ_a may be chosen for ϑ so that E is bigger than for other ϑ . $\bar{\varphi}$ may be taken for an assumed attained average \bar{r}_e in the shear band by means of Fig. 2.9.2 for state limits of simple shearing. It is necessary for stability to avoid this limit equilibrium, but is it also sufficient?

With further sliding φ_b and φ_w do not change, whereas $\bar{\varphi}$ is reduced from a peak value by dilation. The force polygon can no more be closed without inertial forces (dotted in Fig. 13.1.10c). These act in the directions of sliding and are proportional to the sliding masses. They are small at the onset of sliding, substantial accelerations are only reached if the required $\bar{\varphi}$ exceeds φ_{cs} markedly. The system stabilizes itself by reduction of filling height as the psammoid surface gets inclined near the wall. The temporary collapse is triggered by the minutest disturbance, with further sliding the system generates kinetic energy which is dissipated by friction. If the filling height does not exceed h_s determined with $\varphi = \varphi_{cs}$ the system cannot collapse. This is apparently a necessary and sufficient condition for stability, but are the assumptions legitimate and could a collapse be quantified?

Consider finite elements near the corner at the wall foot, Fig. 13.1.10d. Polar quantities are neglected for simplicity. Two triangular elements are needed

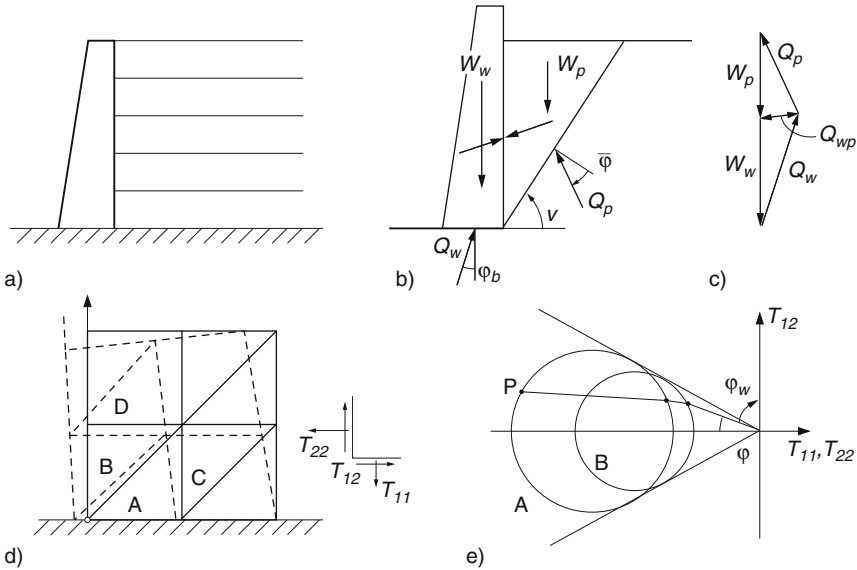


Fig. 13.1.10. Evolution with a sliding retaining wall: placement (a), forces (b) and polygon (c), finite elements (d) and stress circles (e) for the vicinity of the wall foot

at the corner as a single one would lead to statically inconsistent stress states (e). The lower one (A) is more deformed and thus reaches earlier a state limit than the upper one (B), both attain the slip condition. The lateral neighbour (C) is more deformed than the upper one (D), so it is the next one that reaches a state limit. With further wall slip a kind of shear band grows towards the free surface while this rises. This localization depends on the mesh, so this has to be properly shaped to get a realistic inclination. The corner elements should not be deformed too much as otherwise the equations get ill-posed.

When a critical filling height is reached the numerical placement of the next layer gets impossible without acceleration. Thus a collapse is indicated, but not properly captured. The state just before may be an attractor in the large which is mainly determined by the assumed field of the initial relative void ratio r_e after the soil has been placed. As in the case of Fig. 13.1.9 it is hardly possible to quantify the dependence of the average r_e and φ along the shear band on the initial r_e . The mesh-dependence can principally be removed with polar terms, but this is not feasible if the layer height exceeds ca. 10^3 times the grain size. The granular flow during a collapse could at best be simulated in a crude approximation. It appears that there is no way around simplified design models as the one of Fig. 13.1.10b.

Passive cases with a translated and rotated wall are indicated with Fig. 13.1.11. A rigid wall with negligible weight may be pulled by a string via a roll towards a psammoid layer so that the contact of wall and base is just not lost (a). A shear band arises from the wall foot and rises with cur-

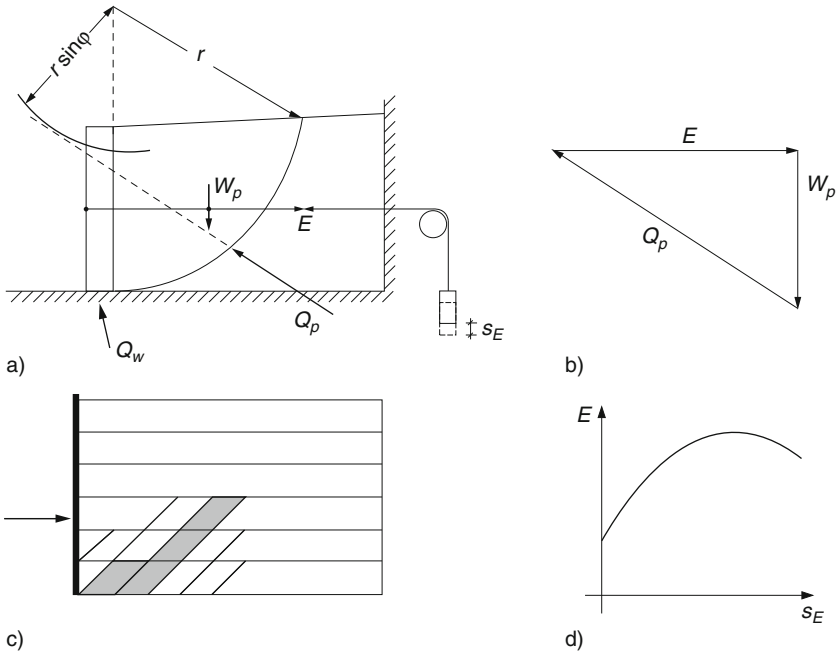


Fig. 13.1.11. Passive cases with rotating wall: slip circle and forces (a), polygon (b), finite elements indicating a shear band (c), wall force versus displacement (d)

vature as in Fig. 13.1.5. Following Fig. 13.1.8a one may assume a circular arc and a resultant force Q in this shear band that touches the circle with radius $r \sin \varphi$. In an equilibrium the string force E , the weight W of the sliding body and Q go through one point and form a closed polygon (b). A collapse would occur with a weight at the string if φ exceeds φ_{cs} . For design it should suffice to keep a given E below E_p by (13.1.3b) with K_p by Fig. 13.1.8b, or not?

Position and inclination of E are given and not assumed a priori as for the calculation of K_p . The moment of Q can exceed $Qr \sin \varphi$, and the required weighted average $\bar{\varphi}$ is as unknown in advance as r_e and the pressure distribution along the shear band. The position of the arc may be determined by minimizing E (Gudehus 2002), but this heuristic approach is debatable as discussed with Fig. 13.1.8. No real wall is weightless, and the force Q_w at its base including friction is not negligible. So how could the mechanical model be improved, in particular with respect to stability?

A finite element mesh could be chosen so that the shear band from the foot is reasonably reproduced even without polar terms, Fig. 13.1.11c. An initial state with a fixed wall can be generated or chosen as outlined with Fig. 13.1.9a. The quasi-static evolution prior to a loss of equilibrium can likewise be driven by pulling with low speed or increasing the weight at the string. The lowest elements near the wall foot slide past the base, sliding

past the wall can be expected near the free surface. The corner elements are strongly deformed, the equations can thus get ill-posed. If the height exceeds about 10^3 grain diameters the relation of string force E and displacement s_E may be reasonably predicted (Tejchman 1997). If the string is pulled by a weight up to a peak of the E vs. s_E curve accelerations arise, but the further course of such a collapse can hardly be calculated. Comparative calculations could at best serve to support assumptions in an updated design model, but thus the more general problem of stability remains unsolved. Following Darwin (1883) one has to state again that this apparently elementary problem with passive earth pressure eludes mathematical treatment.

How could *pore water* be taken into account? With *full saturation* and constant hydraulic height h_w solid partial forces and stresses are obtained by taking the specific weight $\gamma_r - \gamma_w$ instead of γ . This allowance for uplift suffices for submerged psammoids which are so slowly deformed that seepage forces are negligible. As with heaps and excavations (Sects. 12.1 and 12.4) this is no more legitimate with fine grains and for a collapse. As long as the skeleton tends to dilate due to a sufficiently low $r_e < 1$ one may neglect the temporary reduction of h_w for the design of retaining walls on the safe side.

Otherwise temporary changes of h_w can play a role which cannot easily be quantified, Fig. 13.1.12. Pulling back a wall rapidly from a dense, fine-grained psammoid can produce a gap (a). Seepage may be neglected for wall velocities $v_s < 10^2 k_f$ by (6.2.11) as the initial skeleton pressure p_{so} roughly equals $\gamma_w d$ for any depth d . Temporary suction supports the steep skeleton surface and drags water into the gap. After fixing the wall the gap is closed as h_w gets again hydrostatic (cf. Fig. 12.1.7). When a wall is pushed into the same soil the resistance in the growing shear band is increased as the dilation is impeded hydraulically (b). The pore water cavitates if its pressure attains $p_w = 0$ (Sect. 6.2), then the psammoid cracks as long as the wall is not fixed again. A loose, fine-grained saturated psammoid gets a suspension near a wall moved relative to it (c). If the wall is fixed thereafter h_w gets hydrostatic and the re-combined skeleton is slightly densified. These statements are confirmed by the experience with dredging under water. It will be hard work to quantify

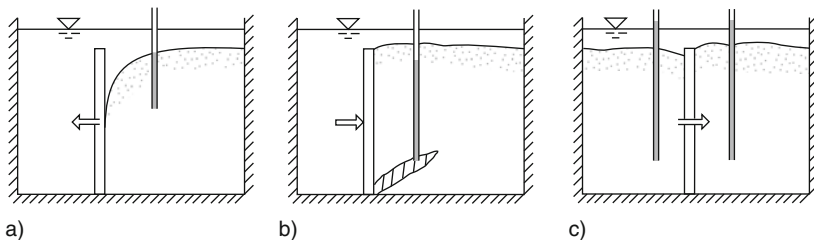


Fig. 13.1.12. Interactions of wall and sand under water: active (a) and passive case (b), embedded wall (c)

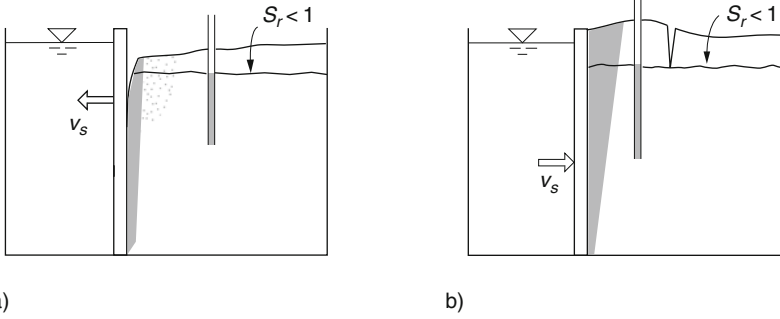


Fig. 13.1.13. Cracking of partly submerged sand behind a wall, active (a) and passive case (b)

them with finite elements, constitutive relations and coupling of skeleton and pore water.

A *capillary entry* can occur by shifting a wall from or into a dense saturated psammoid layer if its surface is initially horizontal and agrees with the groundwater table, Fig. 13.1.13. The shifting velocity v_s may exceed $10^2 k_f$ so that seepage may be neglected by (6.2.11). With this hydraulic constraint of the dense skeleton its pressure p_s increases by deformation so that p_w decreases. When the suction near the free surface attains the capillary entry pressure, i.e. for $p_a - p_w = p_{ce}$, gas channels arise and the surface gets brighter (Sect. 6.2). The skeleton cracks with cavitation of pore water when the increasing grain distance can no more be bridged by (6.1.1) with the attained suction. In the active case (a) the first crack opens behind the wall, in the passive one (b) a sufficient extension at a surface bulge is required for cracking. After fixing the wall water fills extended pores and closes cracks, subsequently the psammoid is softer and cannot develop suction again. Such evolutions could be captured with finite elements, elp or hyp and coupling with pore water, but cracks cause additional difficulties.

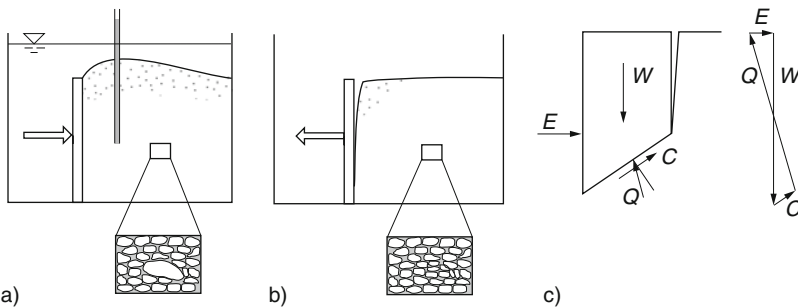


Fig. 13.1.14. Unsaturated psammoid near passive (a) and active wall (b), sliding with crack (c)

With *partial saturation* similar approaches as for heaps and excavations (Sects. 12.1 and 12.4) may be applied, Fig. 13.1.14. Except for bubbles which are far smaller than the grains gas inclusions make the psammoid softer so that it can get a temporary suspension near a wall moved past it (a). With gas channels a gap opens behind a pulled-back wall due to the capillary skeleton pressure p_{cs} (b). The gap closes by evaporation or water access so that an earth pressure arises again. Estimates can be obtained with a second gap and a block that slides on a shear band with friction and cohesion by p_{cs} (c). More sophisticated calculations with coupling are debatable as seepage and suction in psammoids with gas channels can as yet hardly be captured (Sect. 6.2).

To *sum up*, classical methods to determine active and passive earth pressures are partly supported by modern concepts, but even these can hardly capture real evolutions including cracks and collapse. Shear bands evolve so that instantaneous stress distributions and obliquities cannot be estimated and can hardly be calculated. A loss of equilibrium with dead loads and sub-critical relative void ratios can at best be estimated. Except for uplift and capillary skeleton pressure the influence of pore water and gas inclusions is only qualitatively understood and could as yet hardly be quantified.

13.2 Peloids and composites at rigid guided walls

Coulomb (1773) introduced a cohesion, but did not apply it to earth pressures. He noted that the friction of clay is reduced by water, but did not take into account its pressure. For 150 years a cohesion was formally allowed for in earth pressure theories almost without physical background. The latter was substantially improved by Terzaghi's (1925, 1936) principle of effective stress, but his effective cohesion c' due to the bound pore water can no more be defended (Sects. 3.5 and 6.3). Until now earth pressures are widely calculated with assumed φ' , c' and p_w , or with c_u for cases without drainage. Changes of these quantities in the course of time are often ignored, let alone the viscosity of the skeleton. The sequel is more an outline of what could be done better than of what has been improved already.

A rigid wall may be shifted into a *homogeneous saturated* peloid layer with horizontal surface, Fig. 13.2.1. With a shift velocity v_o by (6.2.11) the deformation is nearly isochoric, this occurs preferably in model tests and in building sites due to the low permeability of peloids. A shear zone arises from the wall foot and grows to the surface (a). Its thickness d_s depends on the initial consolidation ratio p_e/p_s , and it has another shape if the wall rotates. Assuming a sliding wedge (b) with an average shearing resistance \bar{c}_u along a slip plane a limit equilibrium (c) yields the passive earth pressure

$$E_p = \frac{1}{2}\gamma h^2 + 2\bar{c}_u h \quad (13.2.1)$$

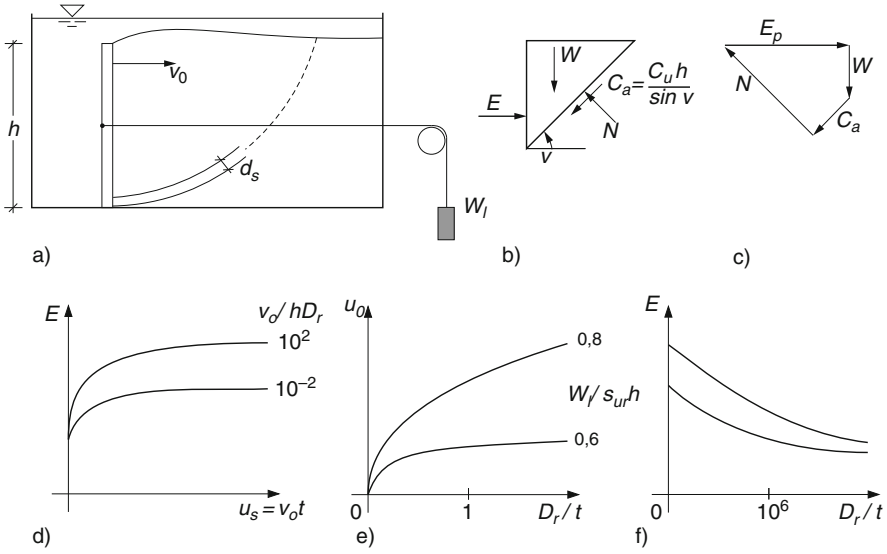


Fig. 13.2.1. Evolutions of an undrained peloid body by a pushing wall: model test (a), sliding wedge (b), force polygon (c), argotropic resistance (d), creep (e) and relaxation (f)

with the minimizing inclination $\vartheta = \vartheta_p = 45^\circ$. Nearly the same E_p is obtained with a curved slip surface, other than with friction the mobility of the wall has apparently little influence. This approach can be extended to more general cases, but is it realistic?

As outlined in Sect. 12.2 the lower bound theorem ignores viscosity and seepage-dependent density changes of peloids. c_u depends on the equivalent pressure p_{ce} and the shearing rate D by (12.2.1). $D \approx v_o/d_s$ may be assumed, but how to get the shear band width d_s ? It is bounded from below by localized densification for an initial $p_e/p_s < \text{ca. } 4$, and by viscosity and polar quantities for localized dilation otherwise (Sect. 8.3). Without an intricate analysis of localization one could take an empirical d_s to capture the argotropy of E_p (Fig. 13.2.1d). A stationary state limit of this kind could nearly be attained with suitable deformations. With a bigger wall shift the assumed geometry and kinematics get invalid. In addition the peloid need not be ductile in the sense of Fig. 12.3.6, this is left aside here for brevity.

The wall may now be loaded via a string and an increasing weight W_l , again in such a short time that the density cannot change. It creeps towards the peloid when W_l is kept constant (e). The creep velocity increases drastically with a higher W_p and tends to an almost stationary value. This can be explained with a statically required c_u by (13.2.1) and by inversion of (12.2.1) with $v_o \approx Dd_s$. Apart from geometrical effects the stationary creep is an endogenous attractor in the large (*nota bene* as long as seepage may be neglected).

The wall may now be fixed after having deformed the peloid up to a state limit. Its resultant force drops in the course of time with a decreasing rate, Fig. 13.2.1f. This relaxation is more marked when it starts with a higher E_p due to a higher previous v_o . Its initial rate \dot{E} may be estimated according to Sect. 3.2 by

$$\dot{E}/E_o \approx D_r(c_{uo}/c_{ur})^{1/I_v}. \quad (13.2.2)$$

Therein c_{uo} denotes the argotropic cohesion for the initial E , and c_{ur} the one for $D = D_r$. With a minute fraction of gas bubbles the pore pressure can get hydrostatic by elastic volume changes (Sects. 6.2 and 6.3) without seepage. Thus the vertical skeleton pressure $-T_{s1}$ returns to the one given by overburden and uplift (Sect. 11.1). In the long run the stress ratio T_{s2}/T_{s1} returns to K_o by (11.2.9) due to relaxation. Apart from displacements of wall and free surface the changes of skeleton stress and pore pressure are forgotten, so this is another endogeneous attractor in the large.

With slow enough wall velocities v_o by (6.2.12) the peloid is deformed with nearly hydrostatic p_w . With this free drainage it tends first to contract by shearing for an initial consolidation ratio p_e/p_s below ca. 4, and to dilate otherwise (Sect. 3.8). With a constant $E = W_l$ via string and weight (dead load) the creep motion is slowed down by densification if W_l is lower than the critical passive earth pressure,

$$W_l < E_{pc} = \frac{1}{2}(\gamma - \gamma_w)h^2K_{pc} \quad (13.2.3)$$

with K_{pc} as by Sect. 13.1 for $\varphi = \varphi_{cs}$. This is an approximate sufficient condition for stability. If (13.2.2) is not satisfied the system tends to accelerate by shear dilation, but the latter is no more possible in a final creep collapse.

When and how could the statements made with Fig. 13.2.1 be quantified beyond design estimates? In a finite element mesh triangles near the wall foot may be chosen as in Fig. 13.1.10d, polar terms have to be dropped as the required number of elements with about three particles size would be far too big. Base and walls may be rough or smooth, along them the skeleton is constrained by (12.2.5). Both are pervious or not and smooth boundaries are impervious, thus either p_w or $v_{wn} = 0$ is given along them. At the free surface the skeleton pressure is $p_s = 0$, or $p_s = p_n$ with net attraction $p_n < 0$ (Sect. 6.3), and p_w is constant according to the free water table. The left wall can be translated with a velocity v_o , without rotation the position of its resultant horizontal force E_h does not matter. The normal and tangential forces between the moving wall and the base have the ratio $\tan \varphi_{wo}$ with $\varphi_{wo} \neq \varphi_w$ in general. A slit at the wall foot is hydraulically closed near an impervious boundary.

The peloid skeleton may be characterized by visco-hypoplastic (v-hyp) parameters, internal variables are not needed for the monotonous evolutions considered there. Ductility may be assumed for simplicity. With a degree of saturation S_r just below 1 for minute gas bubbles the pore fluid is somewhat

compressible (Sects. 6.2 and 6.3). An initial state of the peloid may be assumed with hydrostatic p_w , vertical skeleton stress T_{s1} by the overburden and p_w , and the stress ratio $T_{s2}/T_{s1} = K_o$ with K_o by (11.2.8) or (11.2.9). The initial void ratio e_o may be constant or indirectly given by a constant consolidation ratio p_e/p_s . Less uniform initial states could be generated by simulating previous evolutions with filling and waiting, but they are not of interest for validations with model tests.

For simulations *without seepage* the displacements of skeleton and pore water are equal, $v_{si} = v_{wi}$ ($i=1$ and 2). This may be assumed for sufficiently high wall velocities v_o by (6.2.11). With a constant v_o the peloid is mainly deformed along a shear band growing from the wall foot. p_w increases with a minute densification of the skeleton. The obtained v_o -dependence of wall force E or wall displacement can be used to better quantify Fig. 13.2.1d and c_u with d_s for $D = v_o/d_s$ in (13.2.1).

Undrained creep is obtained by keeping the wall force E_h constant. The mesh is further deformed mainly along a shear band, the obtained v_o increases about exponentially with increasing E_h . With large wall displacements the length of the shear band increases as the free surface bulges, therefore v_o slows down. Rates of undrained creep, depending on E_h referred to the average initial p_e , may thus be quantified. A relaxation with a fixed wall after this was shifted could also be simulated. The bulge at the free surface is negligible as long as it is low. The assumed exclusion of seepage means that the surface is covered by an impervious membrane. Only with this assumption the initial rate of reduction of E_h and its asymptote could be simulated rather easily.

For simulations *with seepage* displacements of skeleton and pore water can be different, i.e. $v_{si} \neq v_{wi}$ holds in general. As shown with Fig. 11.2.1 Darcy's law is written with the p_w at the nodes, and the conservation law of pore water is written with $v_{wi} - v_{si}$ at the integration points. With a rather low initial consolidation ratio, say $p_e/p_s < \text{ca. } 4$, the emerging shear band remains wide by densification as p_w grows more than nearby (Sect. 8.3). With high initial p_c/p_s the skeleton dilates in the shear zone and takes up water so that p_w is lower than nearby. The shear zone thickness d_s is bounded from below by skeleton viscosity and polar stresses. Simulations without polar terms get mesh-dependent, but presumably not too much. Along permeable boundaries, in particular at the free surface, the deformed peloid starts to release or take up water. The latter occurs near the wall foot and afterwards around the outcrop of the simulated shear band for initial $p_e/p_s > \text{ca. } 5$. The time-dependent size of such zones with diffusion may be estimated with (12.2.4).

Such simulations could be carried out with any specified $v_o(t)$ or $E_h(t)$ at the wall. One could substitute the estimates (6.2.11) and (6.2.12) for no and free drainage by more precise conditions. Design estimates for an argotropic E_h and for creep without drainage could thus be improved. The condition (13.2.2) for long-term stability, which is evidently of importance for design, could be validated. For cases with constant E_h without long-term stability delay times up to a creep collapse could be calculated. Their dependence on

the initial consolidation ratio and on the overall diffusion time could thus be quantified. The influence of changing permeabilities on c_u due to changes of density by (12.2.1) could also be taken into account.

Model tests should be carried out for *validation*. The parameters of the model clay have to be well-defined for the p_s -range of the experiments. The free surface should remain under water to avoid shrinkage. The two out-of-plane walls should be smooth, friction of the driven wall along them should be avoided. In simple tests the peloid is placed with a constant initial void ratio and a degree of saturation S_r near 1, and deformed so rapidly that seepage is practically excluded. The influence of gravity could be taken into account without a centrifuge by keeping the initial c_u low enough in the sense of (13.2.1). Argotropy of E_h for different v_o and creep for given E_h can be easily observed. A forced shear localization is visible with markers and a transparent out-of-plane wall. If the driven wall and the base are smooth such model tests resemble biaxial tests except for the influence of gravity.

Model tests with substantial seepage and dominant gravity would take far more time as the k_f of peloids is small, cf. (6.2.4) and (6.2.12). The spatial average initial cohesion \bar{c}_u should be small enough by (13.2.1), a centrifuge is not needed if the net attraction (Sect. 6.3) is negligible against $\gamma_w h$. Tests with pure clay are not feasible due to excessive diffusion times, but a step-wise sedimentation of silty clay leads to a composite with a far shorter diffusion time if the in-plane walls serve for drainage (Fig. 11.3.2a). The vertical permeability can be enhanced by wick drains (Bühler 2006). For both cases an orthotropic composite permeability (Sect. 9.2) should be used in calculations. A constant initial consolidation ratio p_e/p_s up to ca. 1.3 can thus be obtained with acceptable waiting times. A higher nearly constant initial p_e/p_s could be achieved with a shake box (Fig. 12.5.3). The desired constant initial p_e/p_s could be checked with a shear vane (Fig. 11.3.2). The drainage along the boundaries should be controlled.

The response with a constant wall velocity v_o or a constant horizontal force E_h may be observed for some days or even weeks, but asymptotes for $t \rightarrow \infty$ can hardly be concluded. Given acceptable overall diffusion times it is more important to observe when and where the soil contracts or dilates in the course of time. Measurements of p_w are also desirable, but p_w -receivers can influence the evolution by a hardly controllable amount. It is of paramount interest when and how critical states are attained in shear bands. The condition (13.2.3) for long-term stability deserves a careful validation. Creep tests in case that (13.2.3) is not satisfied could serve to check whether calculated delay times up to a collapse after dilation have a realistic order of magnitude.

In active cases with a yielding wall the evolutions can get more complex for two reasons, Fig. 13.2.2. Except for low v_o and low initial p_e/p_s a crack opens behind the wall and can reach its foot (a). The suction at the wall near the free surface can attain the tensile strength of the peloid (Sect. 6.3) if the wall is hydrophilic. As with a steep heap or cut (Sects. 12.3 and 12.4) the gap closes again by swelling and creep after the wall has been fixed. With

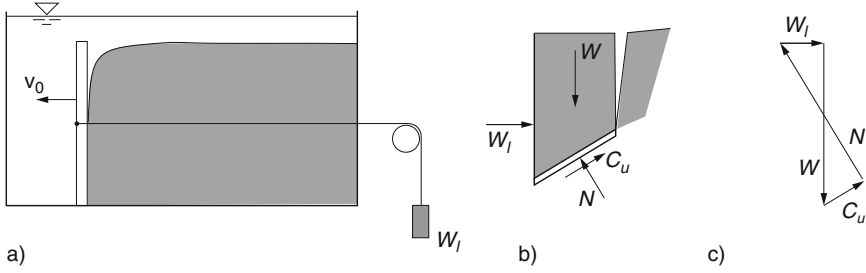


Fig. 13.2.2. Active cases with undrained peloid: model test (a), sliding body (b) and force polygon (c)

a constant low enough E_h at the wall this can accelerate without seepage in the peloid up to a collapse. Then a vertical crack opens off the wall (b), and a shear band from its root to the wall foot gets shorter so that a limit equilibrium (c) gets impossible. If the wall moves slowly enough for an overall diffusion of pore water a localized dilated shearing evolves from the wall foot, and a crack can occur further above. A long-term collapse cannot occur if the supporting E_h is higher than critical,

$$E_h > E_{ac} = \frac{1}{2}(\gamma - \gamma_w)h^2 K_{ac}, \tag{13.2.4}$$

with K_a as by Sect. 13.1 for $\varphi = \varphi_{cs}$.

The influence of a gap at the wall can be fairly well quantified in finite element simulations and controlled in model tests for validation (Bühler 2006). The possible position is known, the depth can be observed and calculated by means of tensile strength tests. A crack off the wall can be observed, in the simulation it may be assumed to start at a surface point where a sufficient extension is attained by creep. Given a crack the evolution of shear bands from its root could be simulated up to a collapse.

Extensions of the outline with Figs. 13.2.1 and 13.2.2 with modified boundary conditions are straightforward. Several shear bands can evolve from a wall if it rotates around its foot (cf. Fig. 13.1.2). If the wall is rotated and translated the shear band is curved from its origin (cf. Fig. 13.1.8). The free surface can be inclined, then the peloid creeps from the very beginning (cf. Sect. 11.6). The stability can be judged by means of two sliding bodies, Fig. 13.2.3. Without seepage a limit equilibrium is obtained by means of c_u (a, b). With free drainage uplift and seepage forces have to be allowed for, and the obliquity of forces in shear bands should be lower than critical (c, d). Thus the passive earth pressure of a fixed wall at a creeping slope can also be estimated (e, f). Evolutions could be investigated in detail with finite elements and v-hyp, and also with model tests for validation.

Evolutions are often more complex due to various *capillary effects*. A cavitation with evaporation of pore water can occur in a passive case with high equivalent pressure p_e and high wall velocity (cf. Sect. 8.4). Extension cracks

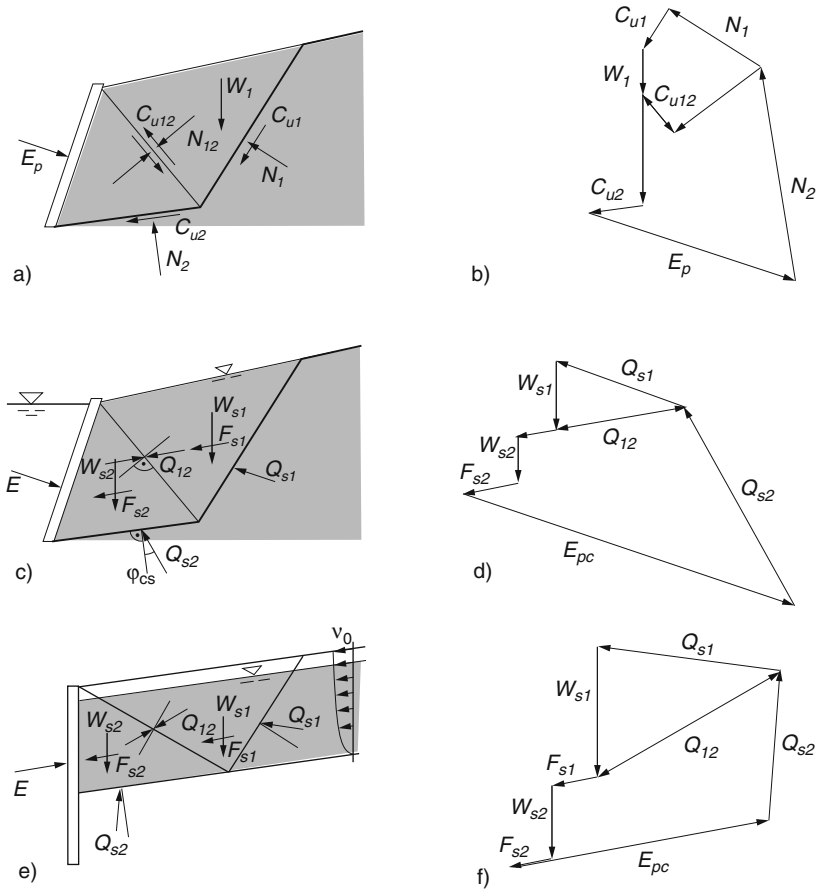


Fig. 13.2.3. Sliding bodies (a) and force polygon (b) for undrained peloid behind a pushed wall; same with seepage (c, d) and a fixed wall at a creeping slope (e, f)

under water may be treated as outlined with Fig. 13.2.2. If the psammoid is exposed to the air it is consolidated by evaporation with increasing suction (Sect. 11.3). With this shrinkage the average cohesion \bar{c}_u can get so high in model tests that these are futile in the sense of (13.2.1) as the influence of gravity gets too small. Air intrudes by capillary entry and via cracks (Sect. 6.3). Clay layers are often fissured and overconsolidated by shrinkage near the transient free surface. They can also reveal patterns of shear bands when they had been distorted by changing overburden and tectonics (Sect. 12.6).

Clays with fissures and shear bands can be captured as *substitute psammoids* (Sect. 9.1). With their typical spacing the required size of RSEs is about 1m, thus model tests are impossible. The overall permeability is increased by fissures even if they are closed by overburden pressure. The capillary entry

pressure is so much reduced that the tensile strength without drainage can get negligible. In zones with previous shearing the fissures are smeared, and the clay is more dilated (cf. Fig. 13.6.5). The overall skeleton behaviour is determined by spatial averages of stress and void ratio, therefore samples of RSE tests should not be too small. The fissures can contain air, then the transition into or from overall suction is decisive.

Interactions of rigid guided walls with fissured and previously sheared clay can principally be judged with composite RSEs. Although there are no validation tests this may help to understand more complex retaining structures. In passive cases a shear band evolves almost as without fissures, but these enhance volume changes. In active cases a gap opens behind the wall, further cracks can arise in the peloid and blocks separated by fissures can topple (cf. Fig. 12.4.4b). A simplified limit equilibrium can be constructed with c_u along a slip plane, thus short-term and long-term creep may be judged. As with excavations drainage and water access play a role, both can hardly be quantified without field monitoring. If the wall is fixed after its displacement the earth pressure tends to an asymptote which can rarely be quantified. A fixed wall at a creeping slope gets passive earth pressure as shown by Fig. 13.2.3e, f in a shorter time because of fissures.

Interactions of rigid guided walls with a *composite ground* consisting of psammoid and peloid zones can be rather complex. In some cases simplified design estimates are justified, also to prepare investigations with finite elements and experiments. Peloid bands at suitable places in psammoid bodies can work as shear zones, Fig. 13.2.4. A plane cut with a clay smear from a peloid layer can serve as sliding base for a granular backfill at a wall (a). The active earth pressure E_a determined via limit equilibrium (b) can be bigger than with other slip planes from the wall foot. Depending on the velocity by (6.2.11) or (6.2.12) the skeleton normal force in the clay smear can be reduced by a resulting excess pore pressure force F_w . With a thin clay layer at the wall foot and a clay smear nearby two sliding bodies can arise by means of an intermediate shear band (c). An active earth pressure can thus be determined (d).

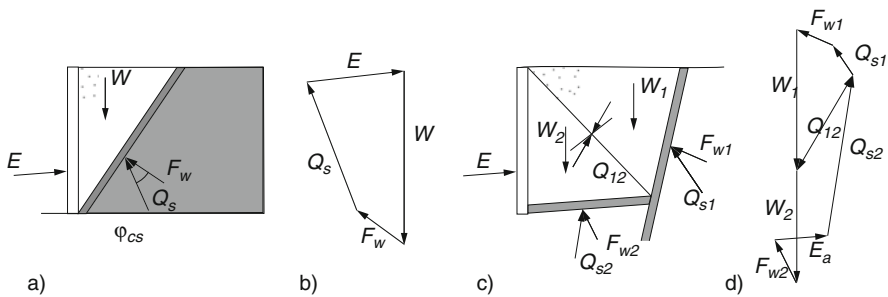


Fig. 13.2.4. Sliding wedge (a) and force polygon (b) with a clay smear; two wedges (c) and polygon (d) with two clay bands

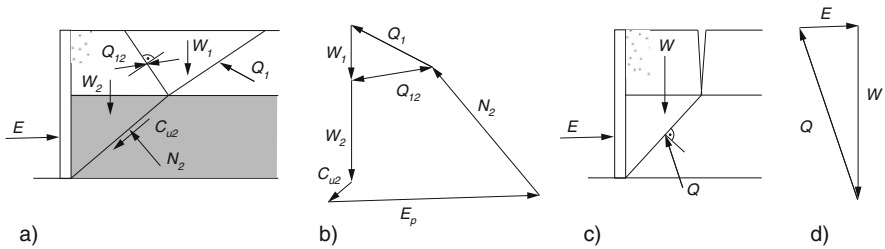


Fig. 13.2.5. Wall pushed into two layers: sliding bodies (a), force polygons (b), sliding body with crack (c), simplified polygon (d)

With two layers a simplified sliding mechanism may also be assumed, Fig. 13.2.5. In a passive case with psammoid on top of peloid, e.g., two sliding bodies (a) serve to determine E_p via a limit equilibrium (b). In an active case with peloid above, e.g., a crack there and a slip plane in the psammoid (c) lead to E_a by equilibrium (d). All this can be done with different hydraulic conditions, in particular without drainage or with free drainage. Several layers may be substituted by one or two with weighted averages. Such composite macro-elements require caution as they cannot replace thin shear or drainage bands.

State limits as by Figs. 13.2.3, 13.2.4 and 13.2.5 may be considered as attractors in the large, but thus the historical element is not ruled out. Without drainage the assumed c_u in peloid shear bands depends on the attained void ratio which is the result of placement and boundary conditions. With assumed free drainage and critical obliquity the pressures depend on the hydraulic conditions, these in turn depend on fissures which are not all smeared out by shearing. Given short term and long term stability, the system tends to a state of rest which works as a contractant state limit in the large. Critical phenomena, viz. spontaneous shear banding, cracking and seismicity, indicate the end of numerical predictability and experimental controllability. Both could be regained with many reversals if asymptotic cycles in the large are attained (Sect. 13.8).

Peloid lumps may be mentioned as they can occur in backfills. These may be treated as psammoids with particles of varying softness according to their density and suction (Sect. 9.2). Such a fill can attain a low E_a and a high E_p when it is dry, but can get a suspension after flooding (which is geotechnically unacceptable).

To *sum up*, the interaction of rigid guided walls with peloids and composites can be predicted and controlled as long as the system is stable in the short and long term. The latter can be judged by means of limit equilibria with simplified sliding mechanisms. Given stability, evolutions could be simulated with finite elements wherein skeleton viscosity and hydraulic conditions are taken into account. Shear bands and cracks could be allowed for with simplifying assumptions concerning their position. Asymptotes of stabilizing evolutions could be estimated, but their progress is less predictable as the permeability

is extremely variable. Spontaneous shear banding, cracking and acceleration can hardly be predicted and controlled.

13.3 Guided rigid strips upon yielding ground

The stability of strip foundations is usually assessed by comparing an assumed or given load with a calculated resisting force of the ground. The latter is only well-defined, however, if the strip follows a certain displacement path. This can be achieved by a guide so that the strip has only one degree of freedom. The resisting force attains a maximum a dead load of the same amount would lead to a collapse. If a rigid body at or in the ground is not guided and if the force at its base is not a dead load, then the stability cannot be judged in the usual way (Sect. 13.4). The issue gets more complex with deformable solids upon the ground (Sect. 13.5). Guided rigid strips are considered for introduction and preparation in this section. The assumed plane-parallelity is justified for long enough strips with uniform cross section, and can be achieved in model tests with fixed smooth out-of-plane walls.

Shear bands arise in dense *dry psammoid* when a strip is punched in vertically, Fig. 13.3.1. This was observed in a model test by Tatsuoka et al. (1990) with marked sand layers (a). Nübel (2002) obtained nearly the same pattern with hypoplasticity including polar terms (p-hyp), stronger shearing is visible by darker strips (b, also in Gudehus and Nübel 2004). A wedge under a strip pushes aside lateral wedges with slightly curved flanks. The initial symmetry gets lost with a minor rotation of the strip in the experiment, and also in the simulation without strip rotation. Shear bands evolve in the course of punching, first along the central wedge and the two adjacent ones. There the skeleton is dilated to a critical state, whereas deeper and more lateral bands are less dilated. Swarms of minor shear bands arise from the strip edges in the simulation, only few of them appear in the experiment.

These findings seem to support conventional limit state approaches, but a closer look reveals deviations. A bearing capacity F_b can be calculated with a central wedge and passive earth pressures E_p at its flanks, Fig. 13.3.1c. Assuming E_p by (13.1.3) it can be expressed by

$$F_b = \frac{1}{2} \gamma b^2 N_\gamma \quad (13.3.1)$$

with a factor N_γ that depends on an angle of friction φ (Terzaghi 1940). This φ is not uniform, however, as it varies alongside with the p_s -dependent relative void ratio r_e (Sect. 2.9) in the shear bands. Thus N_γ should be determined (Gudehus 1981, d) by a weighted average $\bar{\varphi}$ which is not known. In Sokolovski's (1960) purely statical method a uniform stress obliquity φ is assumed for two directions as in Rankine's (1856) theory. Calculated lines of maximal obliquity start from the edges (e), and the resulting force can again be expressed by

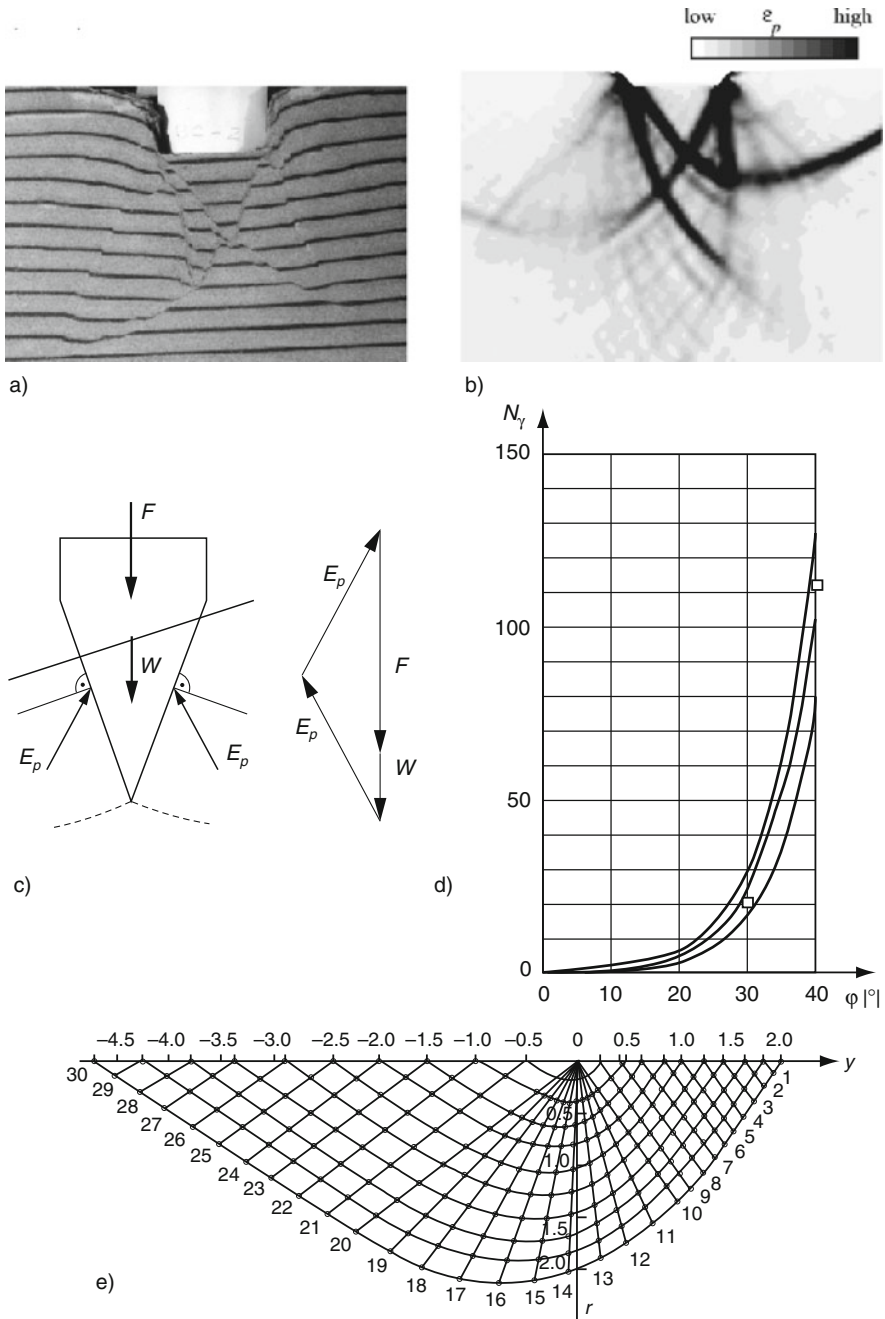


Fig. 13.3.1. Punching of a strip into dry psammoid: model test (a, Tatsuoka et al. 1990), simulation (b, Nübel 2002), wedge and force polygon (c), resistance factor (d), stress characteristics (e, Sokolovski 1960)

(13.3.1). These lines resemble the ones in Fig. 13.3.1b, but the instantaneous stress obliquity is not constant along shear bands.

The historical element is ignored in such conventional approaches, and deformations including volume changes do not appear. φ cannot be lower than the critical value φ_{cs} for shearing, this provides a lower bound for N_γ . Higher N_γ were derived from tests with denser than critical sand (De Beer 1963), and also from centrifuge tests with different pressures and the same initial density (Ovesen 1979). Pyknotropy and barotropy are captured by the dependence of φ on r_e (Sect. 2.9). But how could they be quantified for given initial states, and when may the influence of the mean grain size d_g be neglected?

Tatsuoka et al. (1990) determined force vs. displacement curves with different strip widths b and the same initial e , Fig. 13.3.2a. These can be matched with p-hyp (b, Gudehus and Nübel 2004) and a suitable friction at the strip. Herle and Tejchman (1997) obtained a similar agreement with a rough strip and a variant of p-hyp. The curves reveal a stronger scattering for bigger b/d_g , this is typical for polar effects (Sect. 8.2) and indicates an enhanced granular temperature (Sect. 4.6). The peak resistance F_p and the related displacement u_p increase with lower b/d_g . N_γ -values by (13.3.1) can be calculated from F_p with an increased b due to u_p (c). They decrease with increasing b/d_g and tend to an asymptote for $b/d_g > 10^2$. It appears that beyond this bound polar effects are negligible (Tejchman 1997). For $b/d_g < 10$ they are strong, that's why railway sleepers are kept by ballast. For b/d_g -values in between the resistance is less enhanced by polar effects, in particular in growing and crossing shear bands below the strip (cf. Sects. 8.2, 12.6 and 13.1).

When the strip is shifted further downwards the force F at the base attains a minimum after the peak and grows beyond it with displacements exceeding the breadth, Fig. 13.3.3a. The attained resistance against a monotonous penetration depends on the original and far-field r_e , and less on b/d_g because of

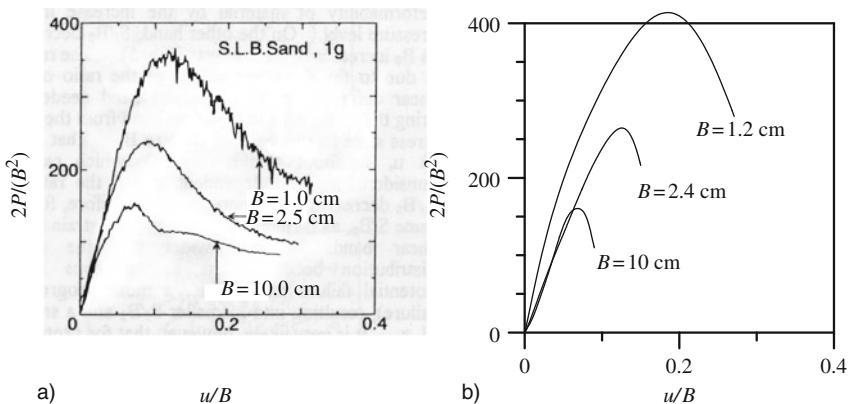


Fig. 13.3.2. Normalized resistance versus punching for different widths: (a) observed (Tatsuoka et al. 1990), (b) calculated with p-hyp (Gudehus and Nübel 2004)

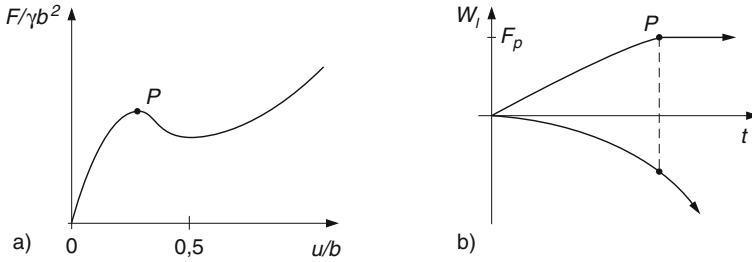


Fig. 13.3.3. Strip upon dry psammoid: force versus penetration (a), dead load and penetration versus time (b)

high pressures. If a strip upon initially dense sand is loaded by an increasing weight W_i the displacement u is the same as for shifting with $W = F$ up to the peak F_p , but then it accelerates with $W_i = F_p$ (b). After this collapse the strip comes to rest with a sufficient penetration. One can identify two attractors: a strange one when fluctuations grow to critical phenomena (Sect. 16.3), and a succession of state limits for a subsequent penetration (Sect. 14.3).

A collapse of a guided strip foundation is avoided by keeping W_i below F_b by (13.3.1) with $\varphi = \varphi_{cs}$. Displacements due to monotonous loading could then be calculated with *finite elements*, Fig. 13.3.4. The edges should be rounded to avoid localizations from the very beginning, near them the mesh should be finer than farther away (a). An initial state may be assumed as for a free layer (Sect. 11.2), spatial fluctuations of stress and density from the placement of the strip can hardly be captured. Fictitious smooth fixed walls may be assumed at a distance of ca. $3b$, and a rough base at a depth of ca. $5b$; these assumptions could be improved by comparative calculations. The skeleton is

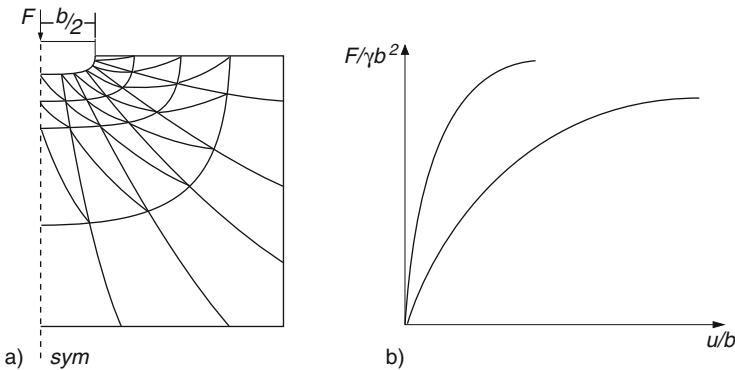


Fig. 13.3.4. Finite element mesh (a) for punching into psammoid, force versus punching (b)

also confined along the vertically shifted strip via (10.3.2). An upper bound of the force F versus displacement u curve (b) could be obtained with hyp- δ by assuming $\delta = 0$ at the onset, i.e. by neglecting the initial force-roughness (Sect. 4.3). A lower bound is obtained with hyp or hyp- δ and $\delta = R$ at the onset, and with a spatial fluctuation of r_e according to the initial average \bar{r}_e (Sect. 8.2). Initial fluctuations are swept out by shifting the strip, but the F vs. u curves do not get parallel to each other. This attractor is determined by the initial average r_e which remains in the far-field. The onset of the F vs. u curve could hardly be predicted more in detail.

A wider range of evolutions is possible with *skew translations*, assuming that rotations of the strip are prevented by a guide. Figure 13.3.5a shows deformations of dense sand after a strip foundation was pushed in by skew

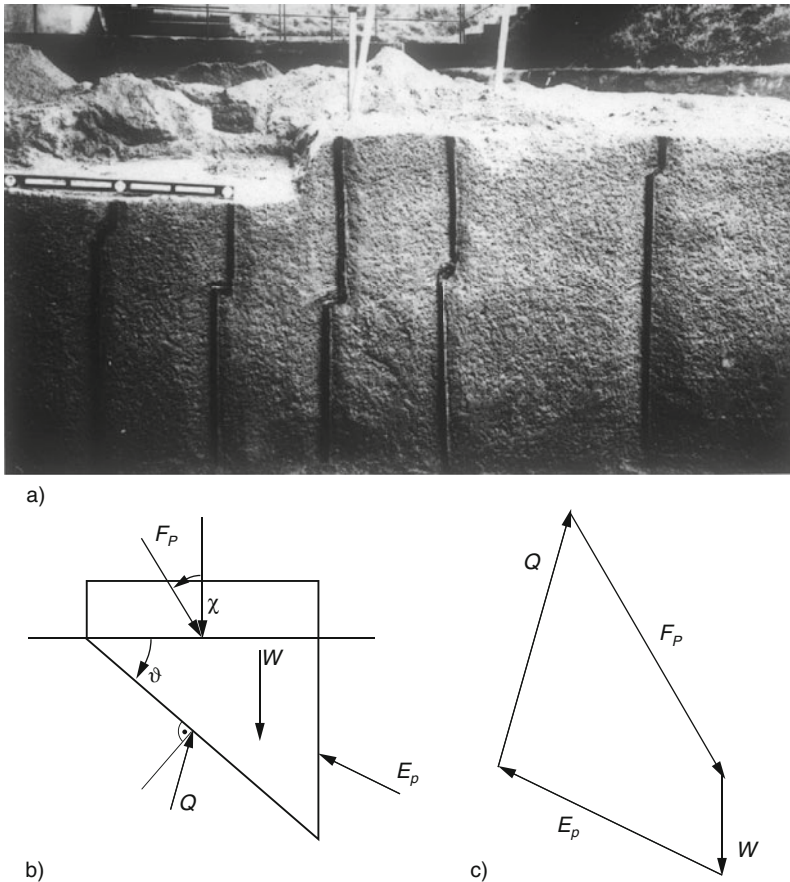


Fig. 13.3.5. Skew punching into psammoid: after a field test (a, DEGEBO Berlin), sliding wedge (b), force polygon (c)

hydraulic jacks. Vertical markers indicate a curved slip surface, but the base of the strip remained horizontal. The skew resisting force F_p can be estimated with a skew wedge that slides upon a shear band together with the strip (b). The inclination χ of F_p should not attain the interface friction angle φ_w as otherwise the strip would slide horizontally. A passive earth pressure E_p , by (13.1.2) with $\delta = \varphi$ and K_p for translation, resists at the steep flank. F_p is obtained with a force polygon (c) by variation of the slip plane inclination ϑ up to a minimal resistance. The result may be described again with (13.3.1), now N_γ is smaller with increasing χ . $F < F_p$ is necessary for stability, but when is it also sufficient, and what about deformations?

As for vertical punching the stress obliquity is not constant along shear bands, thus φ is a weighted average that exceeds the critical friction angle φ_{cs} by an unknown amount. A safe estimate of the peak resistance F_p is obtained with $\varphi = \varphi_{cs}$, the F -minimizing shear band inclination and the minimal K_p , this can be incorporated in N_γ . Finite element simulations could be carried out with elp or hyp, polar effects may be neglected if the mean grain size d_g does not exceed about $b/100$ (Tejchman 1997). They can substitute more expensive tests, this is shown for a dam in Sect. 12.3 and for a block foundation in Sect. 15.1. Between the strip and sufficiently distant fictitious external boundaries the mesh should be chosen so that shear bands can at least roughly be captured. An initial state may be specified as outlined further above, again the field of relative void ratio r_e is decisive and spatial fluctuations cause a hardly avoidable indeterminacy. The strip can be driven without rotation by specifying two of the four quantities F_v , F_h , u_v and u_h , i.e. components of resultant force and displacement (b). Calculated evolutions can be represented by associated paths of forces (c) and displacements (d), by deformed meshes and by iso-lines of mean pressures (e) and relative void ratios (f) for different stages.

As with RSEs (Sects. 2.2 and 4.2) the response is *path-dependent* from the very beginning. This means that the differential response cannot be linearized so that substitute elastic springs are misleading. It means in particular that the force resisting an imposed displacement would lead to another displacement if it would be substituted by a dead load. Attractors in the large can be attained if the strip is shifted with constant velocity: initial fluctuations are partly swept out, the peak resistance is determined by the initial r_e and related with forced shear zones, the asymptotic penetration resistance is determined by the initial r_e and increases with the attained depth. In case of a collapse with dead loads the direction of translation can deviate from the previous one, and spontaneous shear bands arise which differ from the ones in case of a forced translation. The equations can get ill-conditioned, a load test could no more be controlled, a spontaneous seismicity would arise.

Other evolutions occur with guided *rotations*, Fig. 13.3.6. If the strip follows a given circle two sliding bodies may be imagined with circular shear bands (a). Assuming E_p with K_p for rotation at the steep flank, the resisting force F at the strip can be estimated (b) with a force Q in the lower arc that

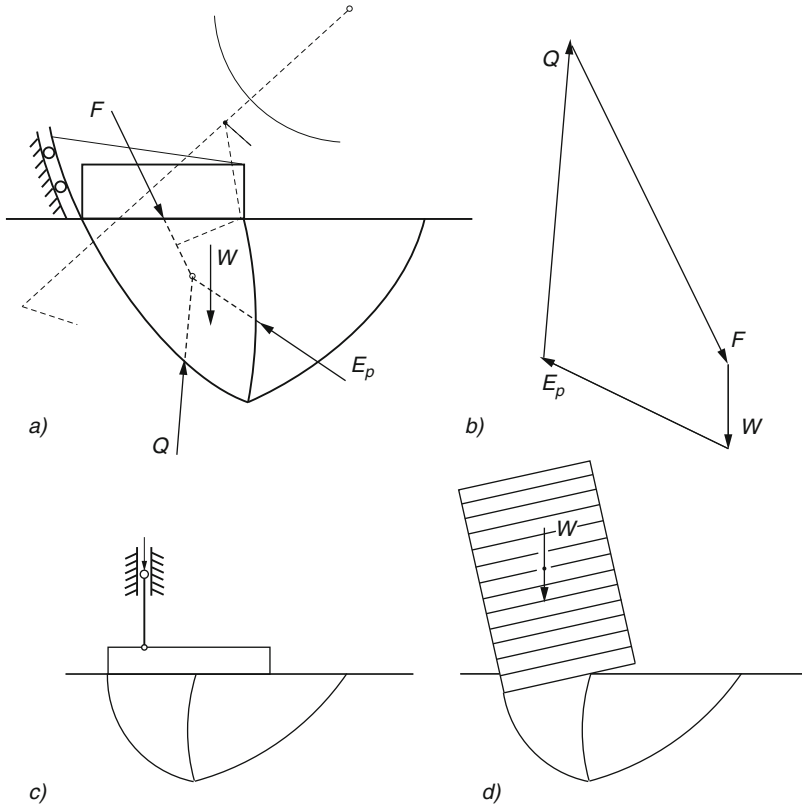


Fig. 13.3.6. Guided punching into psammoid with rotation (a), force polygon (b), sliding bodies (c), toppling (d)

has a moment $Qr \sin \phi$ as in Fig. 13.1.8a. Inclination and eccentric position of F have to be assumed, the result can be expressed by (13.3.1). After variation up to its minimum the obtained N_γ is lower than for translation with the same directions at the onset of rotation. The strip rotates together with part of the ground if it is driven eccentrically via hinges (c). The resisting force may be estimated by assuming a centrally driven smaller substitute strip which rotates when being pushed in. More precise results could be obtained with model tests or finite elements, thus the assumptions required for estimates could be improved.

With a wider kinematic variety the resisting force and its position are again path-dependent. Other than without rotations the changing moments of resulting forces play a role, in particular for a collapse with dead loads. For instance, a strip under a slender weight which is increased disc by disc tilts spontaneously, Fig. 13.3.6d. After this bifurcation the resistance is lower than without it as the eccentricity increases. A collapse occurs at a critical tilt under a dead load which is lower for a higher centre of gravity, and lower anyway than

without rotation. Estimates with kinematical and statical assumptions can at best provide necessary conditions for stability. The loss of equilibrium cannot be captured by a linear analysis of bifurcation as the system is differentially non-linear and history-dependent. The usual comparison of an ‘action’ and a ‘resistance’ has little to do with stability, a way out of this misery will be shown in Sects. 13.4 and 13.8.

Saturated psammoids can be treated almost as dry ones as long as the hydraulic height h_w is constant. The specific weight γ_r for $S_r = 1$ is substituted by $\gamma_r - \gamma_w$ for uplift. Changes of h_w due to skeleton deformations may be neglected if the punching velocity v_o does not exceed the lower bound by (6.2.12). Then a nearly stationary non-uniform h_w -field due to hydraulic boundary conditions could be allowed for by means of seepage forces in the skeleton. The initial pressure p_s and the punching resistance can be increased by a downwards seepage, this is a substitute of centrifuge tests to investigate the barotropy.

The h_w -field is strongly changed if seepage is prevented by rapid punching, i.e. with v_o above the upper bound by (6.2.11), Fig. 13.3.7. A loose skeleton collapses so that the resistance drops to the uplift pressure of a suspension (a). Suction arises in a dense skeleton so that the resistance is bigger than for a much lower v_o (b). Cavitation occurs if $p_w = 0$ is attained (Sect. 6.2). If the water table agrees with the free surface a dense skeleton there loses its saturation by capillary entry. One can see that at the beach, when treading dense sand this gets brighter near the foot. This shows that the seepage should not be neglected in simulations with finite elements. Estimates with kinematical and statical simplifications are rather futeless as then changes of h_w due to skeleton deformations have to be guessed. Upper and lower h_w -bounds due to decay and cavitation or capillary entry, respectively, do not suffice for a quantitative analysis.

Unsaturated psammoids can at best be captured in simple cases (cf. Sects. 11.2, 12.1 and 13.1). Gas bubbles between the grains do not matter

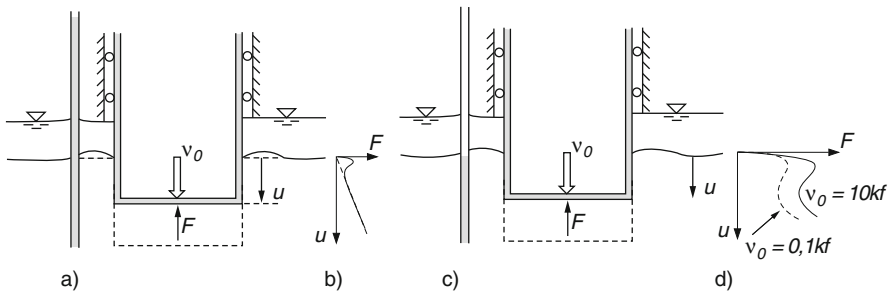


Fig. 13.3.7. Guided punching into loose undrained psammoid (a), force versus penetration (b), same with dense psammoid (c, d)

for low v_o by (6.2.11), they reduce changes of h_w without seepage. Bigger gas inclusions with a sufficient volume fraction can make the ground collapsible (Sect. 7.2). Suction due to gas channels can be taken into account by a capillary skeleton pressure p_{cs} (Sect. 6.2). Estimates with sliding bodies produce a higher resistance with p_{cs} . This gets lost when gas channels are closed by contractant skeleton deformations, and by water access.

Saturated peloids may often be considered as *undrained* according to (6.2.11) as their permeability k_f is low. Assuming ductility their resistance to punching may be estimated with a cohesion c_u if this is spatially uniform, Fig. 13.3.8. With a central wedge and two lateral ones (a) the vertical force under a strip attains

$$F_b = c_u N_c b \quad . \quad (13.3.2)$$

The lowest factor $N_c \approx 5.7$ is obtained if the flanks are inclined by 45° . Prandtl (1920) calculated the pressure difference $p = (2+\pi)c_u \approx 5.1c_u$ along a punched edge by assuming two directions with $\tau = c_u$ (b). The lower bound $N_c = 5.1$ may be related with a freely deformable strip under constant pressure. Somewhat higher N_c are obtained for embedded strips, and lower ones for skew punching.

If c_u is not uniformly distributed (13.3.2) may be used with a spatial average \bar{c}_u . This is not legitimate for $c_u = 0$ at the free surface as by normal consolidation (Sect. 11.3). Even with a uniform void ratio e or e -equivalent pressure p_e the shearing resistance c_u is not uniform as it is argotropic. c_u depends on the stretching rate D approximately by the power law (12.2.1), D in turn is given by the gradient of the velocity field in the peloid. Winter (1979) has proven that with this power law the ratios of velocities at different points do not depend on the one of the punched strip, and that the resistance is

$$F_{ba} = c_{ur} N_c (v_o/bD_r)^{I_v} \quad (13.3.3)$$

with the reference cohesion c_{ur} for $v_o/b = D_r$. Therein N_c is close to 5 as without argotropy although the argotropic c_u is not distributed uniformly as there are zones of pronounced shearing. Winter's proof holds for arbitrary

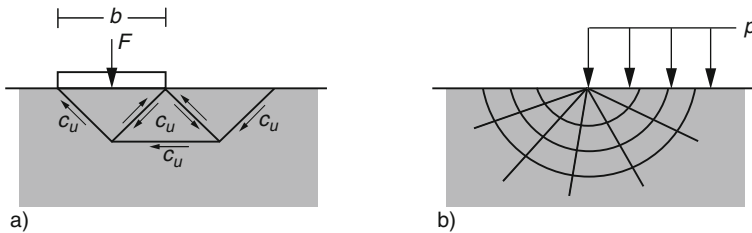


Fig. 13.3.8. Punching into undrained peloid: sliding wedges (a) and stress characteristics (b)

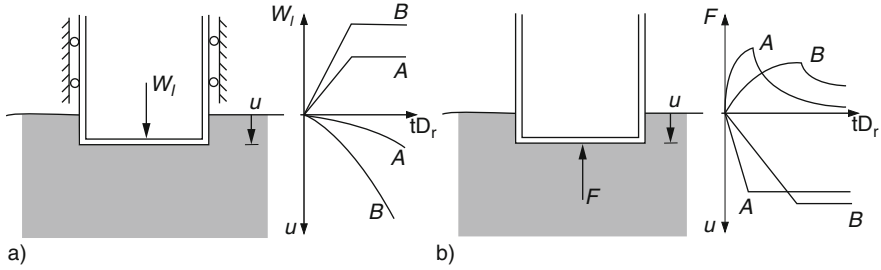


Fig. 13.3.9. Creep (a) and relaxation (b) of undrained peloid after loading or punching of a rigid strip

shapes of strips, bedding depths and directions of penetration, then only N_c has other shape-dependent values. It may also be applied with a non-uniform p_e as long as the viscosity index I_v is constant. Apart from geometrical effects (gained depth and bulged surface) Winter’s solution may be considered as an argotropic attractor in the large (cf. Sect. 10.4).

An undrained ductile peloid under a rigid guided strip exhibits further viscous effects nearly as RSEs, Fig. 13.3.9. With a constant dead load W_l it tends to stationary creep (a) with v_o by inversion of (13.3.3) and W_l instead of F_{ba} . This holds true as long as v_o exceeds the bound (6.2.11) and as long as geometrical effects are negligible. A relaxation occurs under the strip when this is fixed after it had been punched (b). According to v-hyp (Sects. 3.2 and 3.9) the initial rate of force reduction is

$$\dot{F}/F_o \approx m D_r (c_{uo}/c_{ur})^{I_v} \tag{13.3.4}$$

with initial force F_o and related c_{uo} by (13.3.3), and a factor m with the order of magnitude 1. The subsequent relaxation tends to $F = 0$ without seepage if the pore water can also relax due a small fraction of minute gas bubbles. In both cases the evolution tends to an endogeneous attractor in the large.

If v_o is low enough for a *free drainage*, roughly by (6.2.12), a saturated peloid changes its density according to its consolidation ratio p_e/p_s (Sect. 3.2), Fig. 13.3.10. Penetration with constant v_o leads to critical states in zones of pronounced shearing (a), roughly along the bands assumed in Fig. 13.3.1c in the simplest case. The attained resistance can be estimated by (13.3.1) with $N_\gamma = N_{\gamma_c}$ for the critical friction angle φ_{cs} . This works also for an embedded strip and for skew punching. If a lower than critical dead load, i.e. $W_l < F_c = 0.5(\gamma - \gamma_w)bN_{\gamma_c}$, has been imposed slowly enough for consolidation and is then kept constant a contractant creep occurs with decreasing v_o and increasing p_e/p_s (b). With a higher than critical dead load dilatant creep tends to a collapse (c) without further seepage as v_o gets big. This is only possible with a high enough initial p_e/p_s . A higher initial p_e/p_s leads to a higher peak resistance for constant v_o , and to a lower initial creep rate with

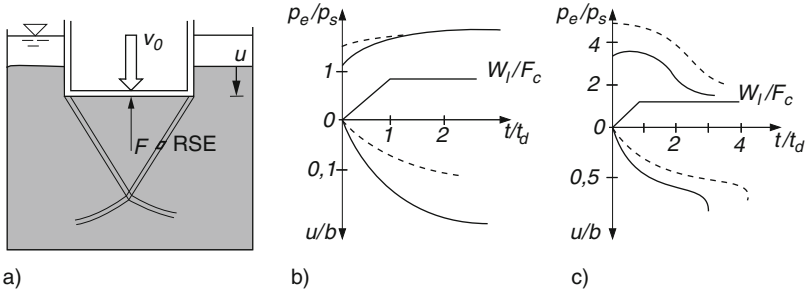


Fig. 13.3.10. Punching of peloid with drainage (a), consolidation ratio and penetration versus time with stabilization (b), same with destabilization (c)

dead loads (dotted lines), but in the long run its influence is swept out. Apart from geometrical effects one can thus identify three further attractors in the large: a driven one for slow enough constant v_o , an autogeneous one for slowly imposed under critical dead loads, and a strange one for overcritical dead loads.

The path-dependence (i.e. the historical element) can no more be represented as for psammoids, the variety is too wide with skeleton viscosity and changing hydraulic heights. The stability can at best be judged as far as no or free drainage may be assumed. The onset of a bifurcation collapse may then be estimated similarly as with Fig. 13.3.6. More insight could be gained with finite elements, v-elp or v-hyp for the skeleton and coupling with the pore water (cf. Sects. 11.3, 12.2 and 13.2). Thus displacements required to approach attractors could be calculated, their dependence on the initial state including fluctuations could be judged, and geometrical effects could be taken into account. The approach to a collapse could also be judged, but its further course can hardly be captured as the equations get ill-conditioned.

Model tests can reveal the range of validity, cf. Sect. 13.2. They are rather easy with a constant void ratio and without drainage. Thus the successive attractors for constant v_o , constant dead load and fixed strip can be determined, and also transitions if the initial states are well defined. A constant initial consolidation ratio p_e/p_s can be achieved with a sandwich produced by sedimentation (Fig. 11.3.2), then experiments with drainage can be carried out in acceptable times. Jovanovic (2002) imposed dead loads to a strip on such a sandwich. After rapid loading the strip sunk with rotation under a sufficient load, and two sliding bodies appeared in the sandwich, Fig. 13.3.11. The collapse load can be estimated by (12.2.2) with a constant c_u in the shear bands, i.e. via the balance of imposed and dissipated work. After slower loading the strip settled without rotation under the same dead load, and the system came to rest by consolidation.

A back-analysis could be carried out with finite elements. Taking v-hyp for the skeleton and an orthotropic composite permeability (Sect. 9.2), the

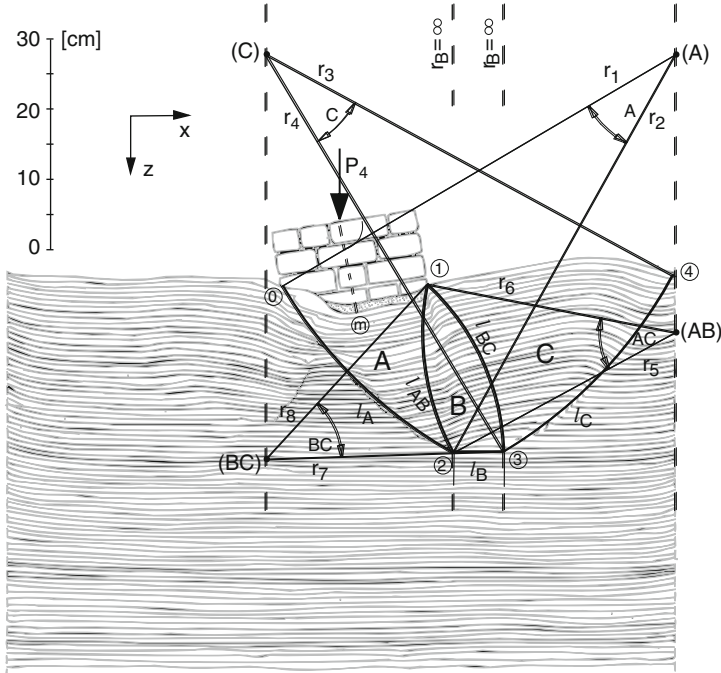


Fig. 13.3.11. Collapse of a strip with dead load upon peloid in a model test (Jovanovic 2002)

contractant creep with diffusion of pore water under a not too big and not too rapidly imposed dead load could be simulated (cf. the example presented with Fig. 13.2.1). This could help to quantify the contractant state limit field and the transition to it. However, the shear localization of Fig. 13.3.11 could thus not be achieved even with more rapid loading. Isochoric shearing leads to a ductile response with Niemunis' (2003) v-hyp, and isobaric shearing likewise if the initial p_e/p_s is lower than about 4 (Sect. 2.8). The clay used by Jovanovic (2002) exhibits a slight lack of ductility in triaxial tests without drainage. This could be captured by Gudehus' (2004b) v-hyp with a sufficiently low initial p_e/p_s , and also with hyp and a sufficiently high initial relative void ratio r_e (Sect. 2.9). These assumptions would lead to localization in a sheared strip (Sects. 8.2 and 8.3).

Without polar terms calculations with finite elements could at best lead to a mesh-dependent localization. When using hyp without viscosity the band width cannot get small as the excess pore pressure leads to a densification with seepage towards the vicinity. With Gudehus' (2004b) v-hyp the band would not get too narrow as the shearing resistance increases due to skeleton viscosity (Sect. 8.3). Comparative calculations with different meshes are cumbersome as the equations can get ill-conditioned. Calculations with polar terms are not

feasible with pore water diffusion and the required mesh size of few particle diameters. Adaptive re-meshing could be of use, but the validation is impeded by smearing of sandwich into shear zones (cf. Fig. 12.6.5).

For the time being the range of predictability is rather restricted with the actually prevailing *composites* in situ. A collapse with rapid loading and localized pore pressure increase can be avoided by a sufficient densification. Permanent loads should be lower than critical with free drainage in order to avoid a delayed collapse after dilatant shearing. Then states attained with contractant creep could be captured, but the related deformations are less predictable as initial spatial fluctuations are rarely known. The delay due to the diffusion of pore water can be captured only crudely if the permeability is not uniform. This is often the case with a sandwich ground which is rarely as regular as in Fig. 11.3.2, and also with stiff fissured clays (cf. Sect. 13.2).

The interaction of guided strips with *unsaturated* peloid ground may only be touched as it has hardly been investigated. A small fraction of minute gas bubbles may be neglected in design estimates, and could be allowed for by assuming a compressible pore fluid (Sect. 6.3). Cavitation of pore water can occur with high initial consolidation and punching velocity, say $p_e/p_s > ca. 10$ and v_o well above the bound (6.2.11). With these conditions a capillary entry occurs at a surface exposed to the air, particularly with evaporation. Cracking at preferred sites may be predicted (cf. Sect. 13.1), but the evolution of crack patterns is hardly predictable (Sect. 6.3). Peloids with gas channels may be captured with suction and suction-dependent limit void ratios, but this approach is debatable (Sect. 7.2). A compacted fill cannot be saturated, but its initial suction can get lost by pressure increase. Its interaction with a strip could be captured with v-elp or v-hyp, a compressible pore fluid and a suitable overall permeability. This approach could work also with stiff fissured clay, but the composite parameters cannot easily be determined as big undisturbed samples are needed (Sect. 9.1). Validation tests are expensive with the required size, and debatable as the hydraulic conditions can hardly be controlled.

Layered ground may be captured with simplifying assumptions, Fig. 13.3.12. Sliding bodies imagined in a peloid layer upon denser than critical psammoid are confined by the latter (a). The pore pressure at the peloid base is given

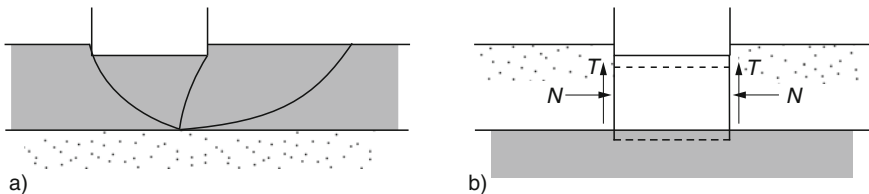


Fig. 13.3.12. Punching with layered ground: sliding bodies (a), punched macro-element (b)

by the one in the psammoid, the pore water diffusion in the peloid is thus enhanced. A psammoid layer is punched into a softer peloid below by a strip if this is wider than the upper layer, vertical shear bands can arise therein (b). The resultant force in the bands is statically indeterminate, its obliquity can only be guessed (as with a trap door, Sect. 12.6). Thus the resistance to punching without seepage exceeds the one from c_u and overburden by a hardly known amount. A better quantification could be obtained with finite elements, polar effects with grain size d_g may be neglected for $b/d_g > 10^2$. Both cases could not be captured with weighted averages, these make sense in case of several layers and are needed for sandwich ground.

To *sum up*, the interaction of rigid guided strips with psammoid or/and peloid ground is predictable as far as contractant or isochoric state limits in the large are approached, otherwise one can at best predict whether critical phenomena could occur. Safe estimates of dead loads for free drainage can be obtained with sliding bodies and critical friction angles. Argotropic resistance and stationary creep are predictable for undrained ductile peloids, and relaxation can be estimated. Stabilizing evolutions of peloid are also predictable, but times for diffusion of pore water can only be estimated. Shear localizations can principally be simulated with finite elements. The onset of cavitation, capillary entry and cracking can only be estimated. Conventional comparisons of statically estimated ‘loads’ and ‘resistances’ calculated with shear parameters have little to do with stability. Simplifying kinematical and statical assumptions may be justified as substitutes for attractors in the large, but the historical element should not be ignored.

13.4 Rigid structures at the ground

Structures in contact with the ground may be idealized as rigid bodies if their deformations are far smaller than the ones of the neighboured ground. They can be placed alongside with excavation and filling, parts of the ground are thus added or removed, the hydraulic conditions can also change. Even in simplified scenarios order, size and duration of stages are important for the evolutions of shape and state. The structure fails if its displacements get too big or accelerate up to collapse, then the requirements are no more satisfied. The historical element should not be ignored in failure scenarios. Some failure mechanisms can be related with attractors in the large and may be simplified for design estimates. Statical and kinematical assumptions could be supported or substituted by numerical simulations with finite elements. This is shown by a number of examples, postponing deformable structures and reversals to following sections.

R. Bisio (in Libreros-Bertini 2006) worked with two-dimensional substitutes of the *Pisa tower* history. Layers of saturated sand and clay were modelled by hyp and v-hyp, the parameters and the initial state were adapted to lab

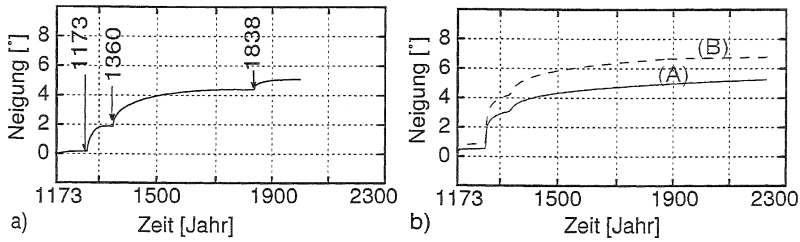


Fig. 13.4.1. Observed (a) and calculated inclination versus time (b) of the Pisa tower (Libreiros-Bertini 2006)

and field data. Lower (A) and upper bounds (B) were assumed for the permeabilities as the k_f -data scatter substantially (cf. Sect. 11.3). The weight of the nearly rigid structure was imposed within 200 years according to the construction stages in Pisa, and then kept constant. Seven hundred years after the onset the structure is substantially tilted and the mesh in its vicinity is markedly deformed. The pore water diffusion times estimated by (11.3.1) range from about 10^2 to 10^3 years for the thickest clay layer. The increase of the calculated tilt with time (Fig. 13.4.1a) agrees fairly well with the observed one (b) for the lower permeability. There is still an excess pore pressure, in particular under the penetrated edge.

Simplified failure scenarios can be obtained by assuming a more uniform ground, Fig. 13.4.2a. A saturated peloid may initially have hydrostatic pore pressure p_w and a constant stress ratio by (11.2.9). The initial equivalent pressure p_e may be constant near the surface and increase linearly with bigger depths due to resting time and temporary evaporation. The permeability may be assumed isotropic and realistically low, or horizontally higher for a composite with sand bands (Sect. 9.2). The weight of the structure is increased disc by disc in desired time steps. With a random fluctuation

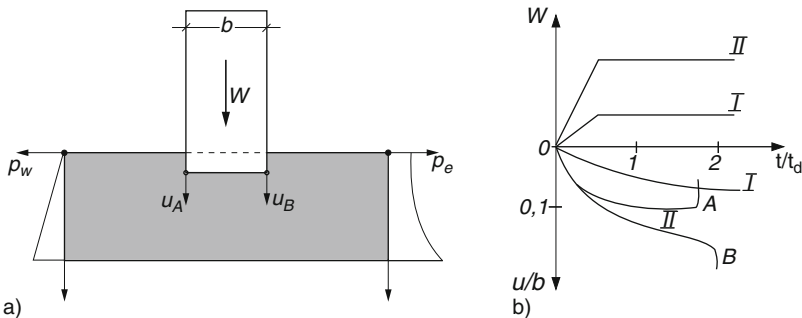


Fig. 13.4.2. Simplified model for a tilting tower upon peloid ground (a), weight and displacements versus time (b)

of p_e a spontaneous tilt sets on immediately, therefore symmetry need not be assumed. A reference diffusion time t_d can be calculated by assuming a vertically guided structure, and crudely estimated by (11.3.1). For loading within times well above t_d contractant creep with nearly constant h_w leads towards a state of rest if the structure is not very slender (b, case I). Otherwise creep with minor diffusion can lead to a toppling collapse when a critical tilt is attained (II). Such simulations could be validated by model tests (cf. Fig. 13.3.11).

Simplifying assumptions could be justified with attractors in the large by means of model tests and finite elements. The critical tilt could be estimated with an eccentric punching via (13.3.3) if the average cohesion \bar{c}_u were known, cf. Fig. 13.3.7. If a previous diffusion of pore water could be neglected the initial c_u by (12.2.1) with $D = v_o/b$ and an acceptable penetration velocity v_o would be a safe estimate. Even then one could not predict the increasing tilt by means of (13.3.3) as the creep is not stationary. The positive feedback up to a loss of stability cannot be captured by assuming essentials of the evolution if these are not known from simulations and/or observations. This is valid even more for the assessment of stabilizing evolutions. The required creep with densification and diffusion could be captured with finite elements, validated constitutive relations and coupling of skeleton with pore water. Even with almost free drainage a slender structure can collapse if it approaches a critical tilt by contractant deformations.

An evolution with a *floating solid* upon soft ground is indicated with Fig. 13.4.3. The initial equivalent pressure p_e may be spatially constant due to temporary evaporation and delayed consolidation, thus the initial pore pressure p_w is lower than hydrostatic near the surface and higher in the depth (a). The average base pressure \bar{p}_o of the structure may be half the bearing capacity

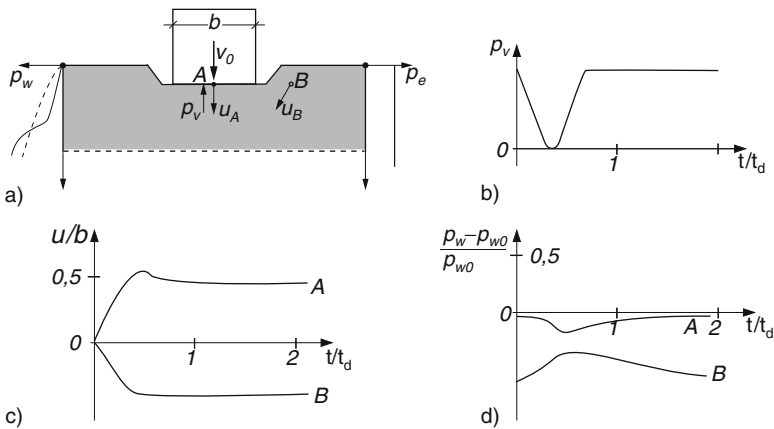


Fig. 13.4.3. Floating structure upon soft peloid ground (a); base pressure (b), displacements (c) and pore pressures versus time (d)

by (13.3.3) without bedding depth, i.e. $\bar{p}_o \approx 2.5c_u$ with c_u by (12.2.1) for an acceptable $D \approx v_o/b$. The structure may be embedded so that \bar{p}_o equals the former overburden pressure γd . The ground may be excavated with slopes, then the building is placed and back-filled. The vertical pressure p_v in the centre at the depth d may thus be reduced in a shorter interval than the diffusion time by (11.3.1) with the same d (c).

With a low slenderness there is no danger of tilting, and the creep velocity v_o would be extremely low by inversion of (13.3.3) even without further consolidation. With the conventional neglect of lateral deformations under the structure this would not settle except for a minor re-compression after swelling due to excavation. A construction planned with this idea in Mexico City (Cuevas 1936) had to be given up when the bottom of the pit rose by 1.4 m. Instead of ignoring the historical element the evolution of shape and state could be simulated with finite elements, v-elp or v-hyp and coupling of skeleton and pore water. This is indicated by displacements and pore pressures in Fig. 13.4.3c, d. Temporary evaporation and water access may be neglected for simplicity. During the excavation the bottom (A) rises, whereas the shoulders (B) cave in due to isochoric creep. p_w may be slightly reduced in the middle, but increases in the flanks. The displacements are not reversed by imposing the previous pressure p_v at the base as with a viscous liquid. In the long run skeleton and pore pressures return to the initial ones if the backfill does not enhance the drainage. This creep-relaxation towards an attractor in the large is accompanied by diffusion of pore water.

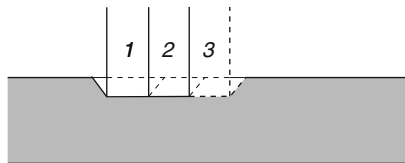


Fig. 13.4.4. Stage construction for the case of Fig. 13.4.3

The isochoric deformation by placing a floating structure can be reduced by working with small sections in short times, Fig. 13.4.4. The first narrow ditch (1) requires a lower average cohesion \bar{c}_u and causes thus a lower v_o by (13.3.3), and with typical rates of digging the creep time is shorter. The creep is almost stopped by placing a part of the structure, then the next section (2) of it can be placed, and so forth. The construction should be completed without delay as otherwise a relaxation of the ground could cause too big forces in a concrete structure after its section-wise curing. Krieg et al. (2004) demonstrate the advantage of this method. They worked with conservative design estimates and monitoring, improvements could be achieved with finite elements and v-hyp. Approaches to argotropic isochoric state limits (i.e. $p_e/p_s \rightarrow (D/D_r)^{I_v}$, Sect. 3.9) should be avoided in order to keep the rates of creep and relaxation

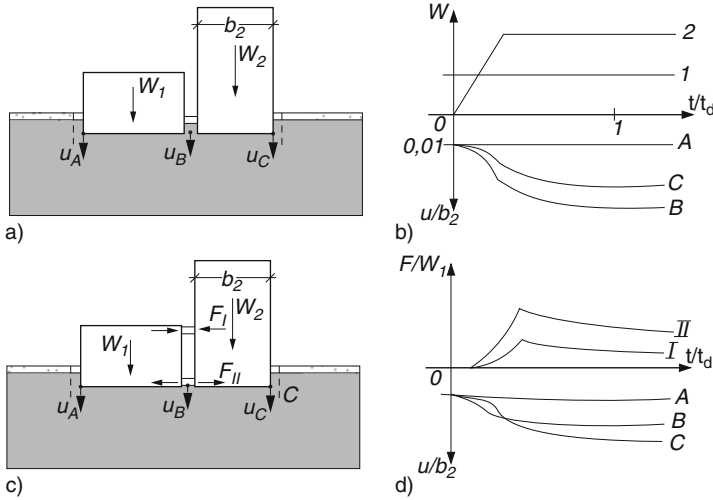


Fig. 13.4.5. Neighboured blocks upon normally consolidated peloid (a), weights and settlements versus time (b); blocks upon overconsolidated peloid (c), forces and displacements versus time (d)

low, both are proportional to $(p_s/p_e)^{1/I_v}$. A variant with stiff retaining walls will be shown with Fig. 13.6.11.

The evolutions are different in case of the *placement of adjacent blocks*, Fig. 13.4.5. The dominant part of the ground may be a stiff clay with an originally constant equivalent pressure p_e that exceeds $\bar{p}_o/N_c \tan \varphi_{cs}$ with the higher one of both average base pressures \bar{p}_o . \bar{p}_o exceeds γd with bedding depth d for both blocks. Even with fissures the overall permeability is low (Sects. 12.2 and 13.2). The isochoric creep due to excavation can be kept small by a supported retaining wall (Sects. 13.6 and 13.7). The first block may stand so long that skeleton creep and pore water diffusion under it have almost attained a state of rest. If the higher new block is placed without a stiff connection to the first one both blocks (a) settle and tilt differently in the course of time (b). The inwards tilt of the first block is due to the pressure increase from the new block, whereas this tilts outwards as there the ground is not further consolidated by the first block. If the second block is firmly connected with the first one (c) both tilt and settle less together, but internal forces increase during this unification and relax partly afterwards (d). Base and pore pressures are gradually redistributed until a new state of rest is attained. In both cases the structures can fail, this could be quantified with validated numerical models.

Evolutions as outlined with Figs. 13.4.1, 13.4.2, 13.4.3, 13.4.4 and 13.4.5 can hardly occur with *psammoids* as their skeleton viscosity is small and their permeability is high. A slender block can nevertheless topple during its construction, its critical height is smaller for a lower density. With over critical void ratios and full saturation, i.e. $r_e > 1$ and $S_r = 1$, blocks could scarcely be placed as they topple in a temporary suspension (cf. Sect. 13.3). Two

neighbouring blocks move past each other, or get internal forces when they are united during the construction. Lowering of the ground water table can hardly cause rearrangements of the grain skeleton as only its mean pressure p_s increases. Flooding with reduction of p_s can matter, in particular if r_e attains or even exceeds 1. Except for collapse such evolutions could be simulated with hyp (cf. Sect. 15.1), but they are of minor practical interest as far as the structures may be assumed to be rigid. Substantial changes of shape and state can occur with few big or many small reversals (Sect. 13.8).

Nearly rigid *retaining walls* interact with *psammoid* ground mainly during the construction. Figure 13.4.6 shows how a collapse can be attained in model tests by increasing backfill or excavation. Dry sand was wetted after each test so that it could be cut due to capillary cohesion. A slender wall of dry masonry upon dense sand toppled by a dense backfill (a). An almost plane shear band rises from the foot, whereas the deformation under it is rather diffuse. A more massive wall upon sand toppled by a backfill with a slope and a minor excavation at its foot (b). Two curved shear bands appear behind the wall, whereas no shear localization is visible under the foot. An L-shaped structure tilted similarly with two curved shear bands behind it and without visible localization below (c).

The stability of such systems can be judged with kinematical and statical simplifications, Fig. 13.4.7. The wall can slide and rotate with a part of the ground, this sliding body is driven by an upper curved wedge and supported by a lower one (a). A limit equilibrium can be obtained with assumed obliquities and moments of the resulting forces in the slip lines (b, cf. Figs. 13.1.2 and Fig. 13.3.7). Variation of slip lines leads to configurations with the lowest possible fill and/or excavation. The findings of Fig. 13.4.6 were thus confirmed with suitable friction angles φ . Such limit equilibria are necessary for stability, and also approximately sufficient if they are possible with the critical friction angle φ_{cs} . The system may be further simplified for design by means of an active earth pressure E_a and a base resistance S (c). E_a by (13.1.3) acts at the lower third point of the back side with inclination φ_w , or on a fictitious rough wall rising from the slab of an L-structure. The resultant S of E_a and the weight W of the central sliding body is determined by equilibrium. S attains F_b by (13.3.1) with the eccentricity and inclination of S . $\varphi = \varphi_{cs}$ should be chosen to be on the safe side.

The gradual shear localization could principally be simulated with polar quantities (cf. Figs. 13.1.2 and 13.3.2), but this is neither feasible nor necessary if the wall breadth b exceeds about 100 average grain diameters d_g (Tejchman 1997). Uplift and seepage forces of pore water can easily be taken into account as long as the hydraulic height h_w is stationary (Sects. 13.1 and 13.3). Design estimates are hardly possible with instationary h_w due to coupling of skeleton and pore water, one should better rule out such effects by technical measures. Unsaturated psammoids with gas channels can be captured with a capillary skeleton pressure p_{cs} (Sect. 6.2), but this varies with density, evaporation and water access in a hardly predictable way. p_{cs} can be needed for steep intermediate slopes and may then be used with due caution (Sects. 12.1 and 13.1).

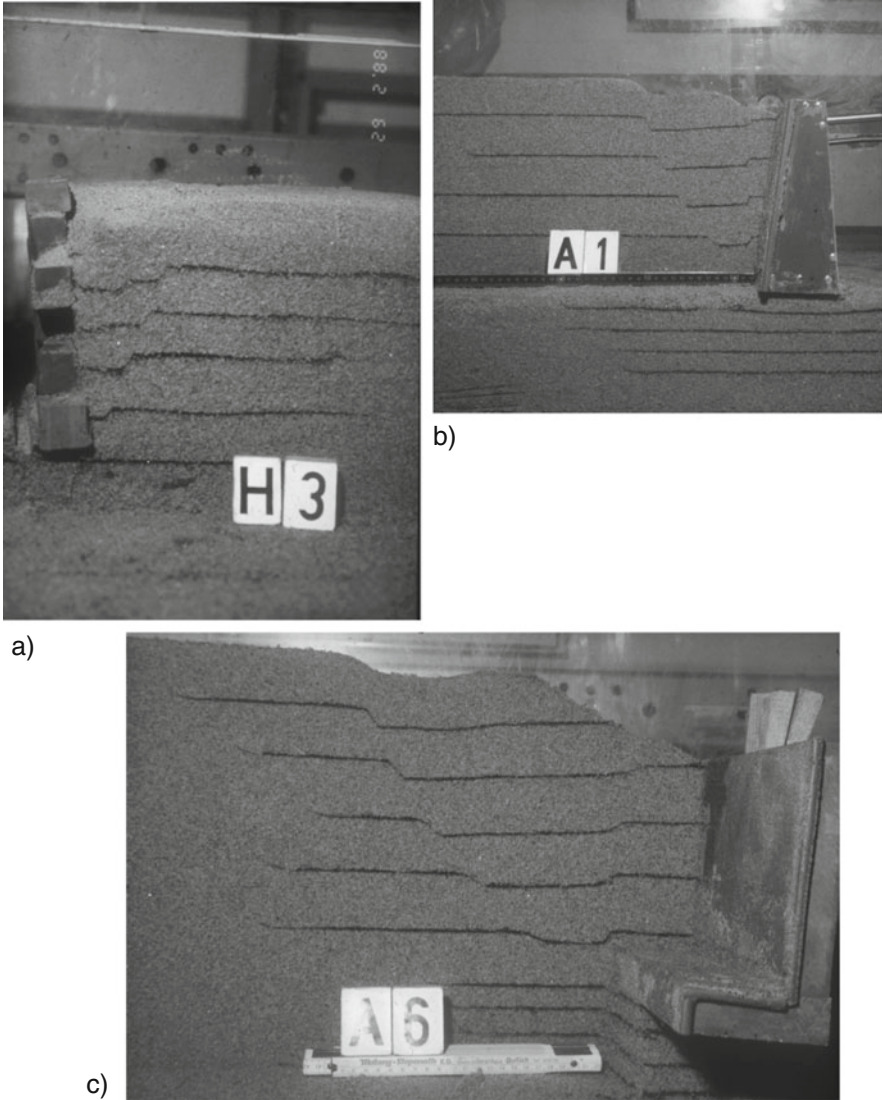


Fig. 13.4.6. Displaced model retaining walls with sand (courtesy E. Schwing): (a) dry masonry, (b) gravity structure, (c) L-structure

Uncompacted non-saturated fills have to be avoided as they slump after water access.

Evolutions of shape and state could be simulated with finite elements and elp or hyp including pore water. The historical element is taken into account via the order, intensity and size of construction stages. For instance, a *terrace in a slope* (Fig. 13.4.8) may be constructed by excavation with steep slopes (1), placing upper and lower walls (2) with drainage (3), backfilling (4) and covering against evaporation and erosion (5). The soil may consist of different

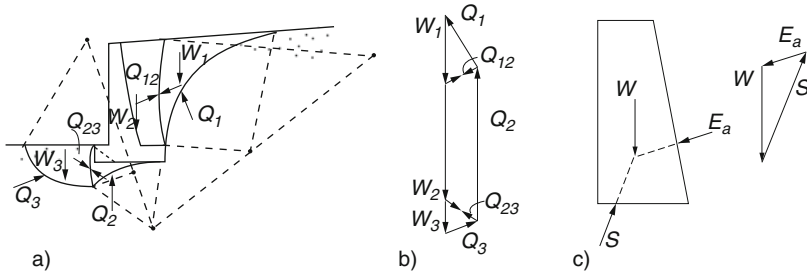


Fig. 13.4.7. Sliding mechanism with L-shaped structure in psammoid (a), force polygon (b), simpler substitute (c)

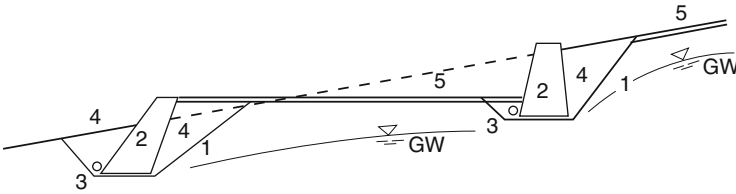


Fig. 13.4.8. Terrace with retaining walls in psammoid ground with seepage. Numbers for the sequence

psammoids, its permeability can vary substantially. Its initial state (0) may be generated as shown in Sect. 11.1, relative void ratios r_e and hydraulic heights h_w are the most important state variables. p_{cs} is needed when finite elements are removed for stage 1 (cf. Sect. 12.3). Gravity is gradually imposed to elements of walls and backfill to simulate stages 2–5. Order and size of simulated construction steps can be chosen differently, but do not matter much for the final shape and state (cf. Sects. 12.1 and 12.3). Failure scenarios up to unacceptable displacements and collapse can thus be generated with realistic imperfections and hydraulic conditions, whereas the geotechnical risk can hardly be quantified with conventional design models.

A *submerged L-structure* in fine sand may serve as further example, Fig. 13.4.9. The initial skeleton state (0) is hardly changed by lowering the ground water table with rows of wells (1). The ground can be excavated with steep slopes (2) due to the capillary skeleton pressure p_{cs} . Suction can also be generated in fine sand without air entry by rows of vacuum wells (1A) if the slopes are properly covered (2A). The base slab is placed (3), the wall is mounted (4) and backfilled (5). After further excavation at the air side (6) the ground and free water tables rise to the previous level (7). Scenarios could be generated up to unacceptable deformations and collapse. Forces in the structure are more important for design than in the previous case, rigidity need not be assumed for their calculation (Sect. 13.5). Hydraulic conditions deserve attention: suction can get lost near the slopes (Sect. 12.3), a pulsating water table causes cumulative effects (Sect. 15.1), the bottom could be softened and eroded by passing free water (Sect. 16.3).

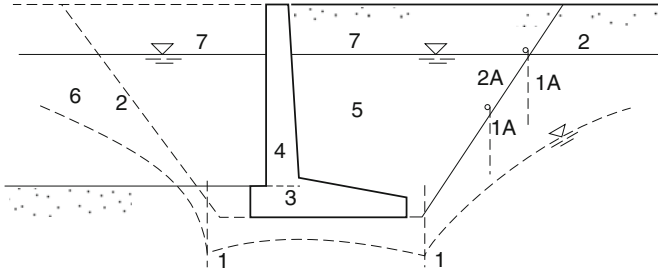


Fig. 13.4.9. L-shaped structure in psammoid ground with excavation, fill and seepage. Numbers for the sequence

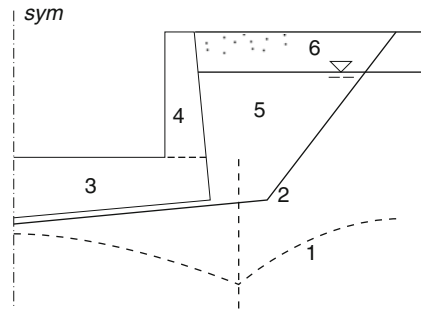


Fig. 13.4.10. Symmetric trough in psammoid ground with fill and seepage. Numbers for the sequence

A *massive trough* in granular, partly flooded ground could similarly be captured, Fig. 13.4.10. After lowering the groundwater (1) and excavation (2) the base slab may be placed (3), then the walls are mounted (4) and backfilled (5), finally the water table rises again (6). Uplift scenarios could be generated with realistic imperfections of structure and ground. The implied earth pressures are neither active nor passive, the obtained heave could be predicted. If the structure is no more assumed as rigid forces in it could be taken into account up to failure (Sect. 13.5). Other evolutions can occur with reversals (Sect. 13.8).

Embedded rigid walls are now considered before dealing with deformable and supported walls in Sects. 13.5 and 13.6. A wall may be driven into submerged gravel and backfilled with densified sand, Fig. 13.4.11a. Conventionally Rankine-like earth pressures are assumed above an assumed centre of rotation, and a horizontal force there instead of the pressures below (b). The bedding depth is somewhat increased for this force, displacements are estimated empirically. A vertical reaction force is assumed at the wall force for equilibrium with wall weight and assumed vertical earth pressure components. The evolution could be captured with finite elements and *elp* or *hyp* (c). The wall foot

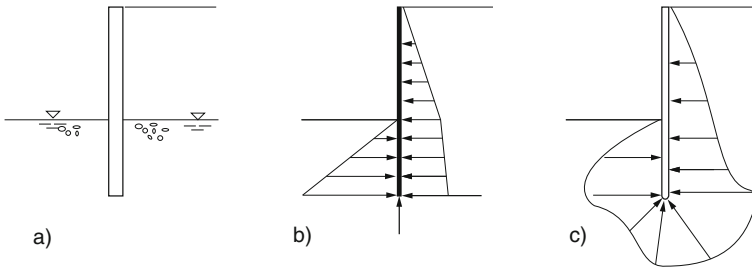


Fig. 13.4.11. Rigid retaining wall in psammoid ground with resting water (a), simplified forces for design (b), displaced wall with stresses (c)

is rounded as otherwise the equations get ill-conditioned (cf. Fig. 13.3.4). The relative void ratio r_e may be assumed in the gravel near the wall due to its placement (Sect. 14.3). Imposing gravity to the sand with given r_e leads to changes of shape and state due to simulated backfilling and excavation. Contact stresses along the wall are part of the results, inner forces of the structure can thus be calculated.

Scenarios could be generated up to failure, i.e. unacceptable displacements or collapse, with realistic initial r_e fields and water levels. The influence of vibratory densification is missed, it may at best be estimated (Sect. 13.8). Other shapes and states are obtained if the ground is excavated. The wall may be placed in a slurry trench, then the sand is excavated at one side. A conventional design of the wall could be the same as before, in addition the stability of the trench would be assessed. Simulations of the placement could be made with *elp* or *hyp*, but are not realistic with plane-parallelity (Sect. 15.3). As long as r_e is not changed by the wall placement deviations from an initial state as without it play a dwindling role with increasing wall displacements. In other words, the skeleton state tends to an attractor in the large which is mainly determined by the initial r_e -field. Initial deviations of the stress field from the one by (11.2.7) enhance the deformations needed to attain this attractor. They play thus a similar role as spatial stress fluctuations for an RSE (Sect. 2.2), one may therefore speak of force-roughness in the large.

The manifold of evolutions is wider for rigid walls in *saturated peloids*, only few cases may be indicated with Fig. 13.4.12. Excess pore pressures and deviations of skeleton pressures from the ones by (11.2.7) due to driving in a wall dwindle by diffusion and relaxation, but a densification can remain near the wall. The lower disturbance from placing the wall in a slurry trench may be negligible, only the interface of concrete and clay is changed by remains of slurry. A simplified state before excavation may be assumed with constant void ratio e , hydraulic height h_w and skeleton stress ratio T_{s2}/T_{s1} . The cohesion may not suffice to keep the unsupported cut (cf. Sect. 12.3) with $v_o \approx k_f$, therefore $c_{uo} = \kappa c_{uf}$ with

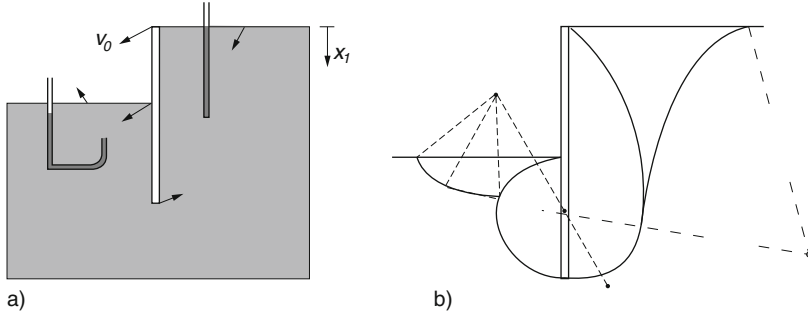


Fig. 13.4.12. Rigid retaining wall in peloid ground with thought piezometric tubes (a), rotating bodies with slip surfaces (b)

$$c_{u,f} = \frac{1}{2} \gamma h (h D_r / k_f)^{I_v} \quad (13.4.1)$$

and $\kappa < 1$ should be avoided.

During and shortly after excavation isochoric deformations tend to a stationary velocity field with non-uniform h_w (a). Ductility may be assumed, and a crack behind the wall may be excluded by adhesion. A statically sufficient average adhesion c_a (Sect. 10.3) can be estimated with a sliding mechanism (b) and the balance of power (12.2.2). It can be expressed by $c_a = m \gamma h$ with a factor $m < 1/2$ that decreases with increasing bedding depth ratio d/h . The creep velocity by (12.2.1) has the order of magnitude

$$v_o \approx D_r h \left(\frac{c_a}{c_{uo}} \right)^{1/I_v} = k_f \left(\frac{2m}{\kappa} \right)^{1/I_v}. \quad (13.4.2)$$

This is a crude estimate as m/κ cannot be determined precisely and as $1/I_v$ exceeds about 20 (Sect. 3.2). The creep slows down by densification if pore water evaporates from the free surfaces, and accelerates by shear-enhanced swelling if the free surfaces are covered with water (Sect. 12.3).

If the initial hydraulic height h_w and the initial consolidation ratio p_e/p_s are constant (cf. Sect. 11.3) the wall could only be placed with external support, and as any machine would stick. The disturbance by placement dwindles to negligible traces if the peloid is ductile. The cohesion without seepage increases with depth x_1 via

$$c_u \approx (\gamma - \gamma_w) x_1 \tan \varphi_{cs} \frac{p_e}{p_s} (D/D_r)^{I_v}, \quad (13.4.3)$$

this was shown in Sect. 11.3. Excavation leads again to isochoric deformations and undrained creep afterwards as long as the diffusion of pore water does not matter. A statically required average adhesion $\bar{c}_a = m \gamma h$ can be estimated with sliding bodies and a linear increase of c_u with x_1 . The creep velocity has the order of magnitude

$$v_o \approx D_r h \left(\frac{\bar{c}_a}{\bar{c}_{uo}} \right)^{1/I_v} \approx D_r h \left[\frac{m/\tan \varphi_{cs}}{1 - \gamma_w/\gamma} \left(\frac{p_{so}}{p_{eo}} \right) \right]^{1/I_v} \quad (13.4.4)$$

with the initial consolidation ratio p_{eo}/p_{so} . This is at best a crude estimate. As with a constant initial c_u , or any other initial distribution, creep is slowed down by evaporation and accelerated by shear-enhanced swelling.

Pressure distributions along the wall after excavation can merely be guessed for design. With a constant initial equivalent pressure p_e suction and cracks arise near the top (A). With a constant initial p_e/p_s the pressure on the active side may increase in proportion with depth (B). At the passive side the pressure could be more uniformly distributed, and would be lower for case A if the creep velocity v_o has the same order of magnitude as for case B. The pressures below the assumed centre of rotation may be substituted by a horizontal force as in Fig. 13.4.11b. The implied average earth pressures can at best be crudely estimated with an assumed v_o (Sect. 13.2).

More insight and quantification could be achieved with finite elements by means of v-elp or v-hyp and coupling with pore water. The state prior to excavation may be generated as for a free-field with pore pressures p_w and e -equivalent pressures p_e from field investigation (Sect. 11.3). Along sufficiently distant fictitious boundaries the skeleton is fixed, and it may move together with the wall. The permeability may be isotropic, or orthotropic for a sandwich (Sect. 9.2), and uniform or variable. Drainage may be assumed or excluded at the solid boundaries. Rates of evaporation or pore pressures p_w are specified along the free boundaries, thus the skeleton pressure p_s is given by suction or net attraction (Sect. 6.3). The excavation can be simulated by removing elements in specified times. The calculated evolution of shape and state with time depends mainly on the ratios $\bar{p}_{eo}/\gamma h$, d/h , t/D_r plus $k_f/D_r h$ and on the material parameters φ_c , I_v and $h_{sr}/\gamma h$, but also on initial spatial distributions. Parametric studies could support understanding and design. Validations could be achieved with model tests (cf. Sects. 12.2 and 12.3), and principally also with field observations (cf. Sect. 13.6).

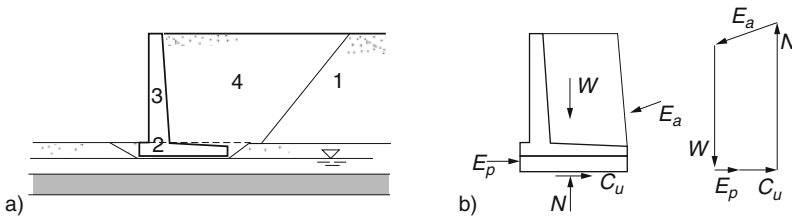


Fig. 13.4.13. L-shaped retaining structure with fill upon composite ground (a), simplified substitute with forces (b). Numbers for the sequence

Examples with backfill, slopes and *composite ground* are briefly considered in the sequel. A fill and a confining L-structure may be placed upon a sand layer with groundwater above a slightly consolidated clay layer upon a solid draining base, Fig. 13.4.13a. A part of the dense humid sand fill is first placed with a slope (1), a slab is placed in an excavation (2), then the wall is mounted (3) and back-filled (4). Design estimates can be obtained for the partial fill as outlined in Sect. 12.3, and for the structure with assumed c_u and earth pressures (b). Settlements far off the structure may be estimated without spreading (Sect. 11.3). The long-term settlement and spreading near the structure attains the same order of magnitude, but cannot be estimated more in detail. The additional yielding of the ground before the clay is further consolidated can scarcely be estimated. The velocity of isochoric creep can attain the order of magnitude

$$v_o \approx D_r d (c_{us}/c_{ur})^{1/I_v} \quad (13.4.5)$$

with clay layer thickness d , statically required cohesion c_{us} and reference cohesion c_{ur} for $D = D_r$. Neither the transition by filling nor the duration of this creep can be calculated as easily.

Sufficiently distant rigid walls have to be assumed for finite element simulations. They are smooth and nevertheless permeable for the transition to far-fields. The initial state is specified as in Sect. 11.3, the hydraulic height h_w is stationary along the peloid layer. The first fill is treated as in Sect. 12.1, thus the state of the ground is also changed outside the slope. The placing of structure and backfill is simulated by imposing gravity in specified times. The obtained evolutions may serve to clarify and improve estimates. Wick drains could be taken into account by means of an orthotropic composite permeability (Sect. 9.2). Obtained contact stresses along the structure determine its internal forces, these could not be calculated realistically with conventional earth pressures. Stiffness and strength of the structure could be allowed for (Sect. 13.5). The influence of vibrations for compaction need not be taken into account, whereas earthquakes can matter a lot (Sect. 13.8).

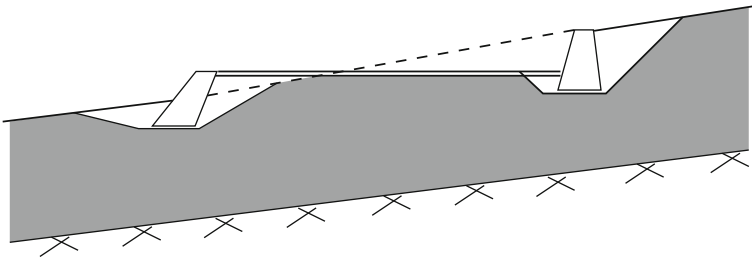


Fig. 13.4.14. Terrace with retaining walls at an inclined peloid layer

A *terrace* in a slowly creeping slope (Fig. 13.4.14) may be similarly constructed as with granular soils only (Fig. 13.4.8), but now skeleton creep and pore water diffusion play a role. The retaining walls may be designed as explained with Fig. 13.4.7. An initial state and velocity field for a finite element simulation may be generated as for an infinite slope (Sect. 11.6), this shows the dominance of hydraulic conditions and supports the identification with field data. Fictitious vertical boundaries far enough from the terrace should have the far-field velocities and pressures which can imply seasonal changes. Construction stages can be simulated as with psammoids only, but now the duration has to be specified and the hydraulic conditions are more important.

As long as the diffusion of pore water with the new conditions does not matter the construction causes isochoric deformations of the peloid and isochoric creep afterwards. This occurs mainly in soil regions behind the walls which do not influence each other. Then the backfills with drainage lead to a densification with diffusion so that the creep motion gets slower than in the far-field. The peloid zone under the terrace is thus not fixed to its base, however, as it is ‘pushed’ and ‘pulled’ by the uphill and downhill zones, respectively. This could scarcely be judged with a mechanism as in Fig. 13.4.13b, and creep deformations could thus not be estimated. Simulated scenarios could support a safe economic design and the execution with monitoring. One could also take into account drainage borings (cf. Fig. 12.4.5), deformable structures (Sect. 13.5) and earthquakes (Sect. 13.8).

Our last case deals with a *fixed structure in a creeping slope*, Fig. 13.4.15. After excavation with steep slopes in a dense peloid with suction (1) a block may be placed in the rock base (2) so that it cannot move. Then it is backfilled with a small wall uphill (3) and a terrace downhill (4), both sides are drained at the base (5). Farther away at fictitious walls (6) the creep motion of the free slope goes on according to the hydraulic conditions with seasonal changes (Sect. 11.5). The pore water diffusion time of the slope may be a few years. The downhill side can be judged with sliding wedges and E_a at the structure, but without knowing pore pressures forces in the peloid can only be guessed. Two wedges uphill lead similarly to an E_p at the fixed part of the backfill (cf. Fig. 13.2.3). Evidently the backfill should be water-insensitive, and the clay smear at the cuts should not swell, but shrink. Finite element simulations

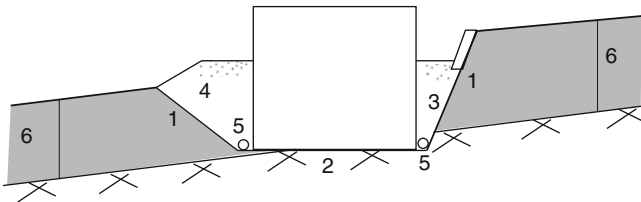


Fig. 13.4.15. Block with backfill in a peloid layer. Numbers for the sequence

could produce scenarios for a safe and economic design. Deformations near both sides of the structure and pressures along its walls could be calculated for differently shaped cuts and backfills, and with different hydraulic conditions.

To *sum up*, simulations with rigid structures upon and at the ground can provide design scenarios where conventional methods do not suffice. With psammoids evolutions of shape and state, which could lead to failure by unacceptable deformations and accelerations, depend mainly on sequence, size and intensity of construction steps. With peloids the viscosity of the skeleton and the diffusion of pore water should also be taken into account. A safe and economic design can be achieved by assuming rigid structures and plane-parallelity, attractors in the large support simplifying assumptions.

13.5 Deformable structures at the ground

Winkler (1867) proposed proportionality of vertical displacement s and base pressure σ ,

$$\sigma = k_s s, \quad (13.5.1)$$

for an elastic beam in order to calculate its internal forces and deformations under loads, Fig. 13.5.1a, c. The coefficient of *subgrade reaction* k_s is chosen empirically, it ranges from ca. 10^2 kN/m³ for soft clay to 10^7 kN/m³ for hard ballast. Equation (13.5.1) leads to maximal bending moments $M_o = \varrho P a / 8$ and displacements $s_o = \omega P / k_s a b$ for a load P with factors ϱ and ω (b and e). These depend on the ratio of beam length a and an *elastic length*,

$$l_e = \sqrt[4]{EI/k_s b}, \quad (13.5.2)$$

with bending stiffness EI and breadth b . For a rigid beam on soft ground, i.e. low l/l_e , $\varrho = 1$ and $\omega = 1$ are approached as for a floating beam. For a flexible beam on hard ground, i.e. high l/l_e , M_o and v_o get small as for a ski on ice.

Winkler's hypothesis (13.5.1) is widely used until now, but when and how can it be justified and quantified, and what could be done otherwise? It means linearity and lateral uncoupling of the ground response. Equation (13.5.2) implies also linear structural behaviour. Assuming an elastic half-space with modulus E in proportion to depth z , i.e.

$$E = E_r z / z_r \quad (13.5.3)$$

with a reference E_r for $z = z_r$, Gibson (1974) obtained (13.5.1) with $k_s = E_r / z_r$, and the same stress fields from surface pressures as for constant E . Lateral uncoupling is also given if the structure rests upon an elastic layer with thickness d far smaller than length a . Then (13.5.1) is evidently valid with $k_s = E/d$. Bending moments and displacements can also be estimated by (13.5.1) for a uniform elastic ground with $k_s = E/d$. The lateral uncoupling

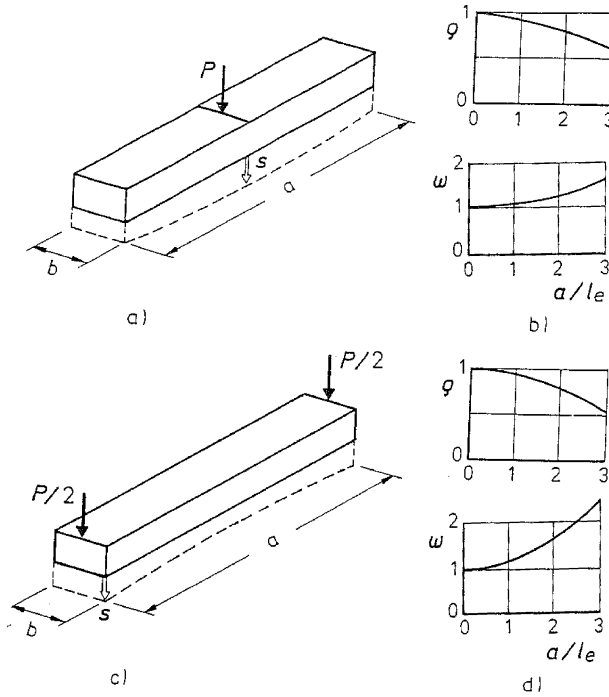


Fig. 13.5.1. Beam upon Winkler subgrade with central load (a), factors for maximal bending moment and settlement (b); same with end loads (c, d)

may thus be ignored, but the assumed linear elasticity and linear distribution of E are hardly realistic. Limitations and substitutes are outlined in the sequel by a number of examples.

Consider a loaded *strip on psammoid* ground. A continuous bedding may substitute the subgrade of a track. Neglecting the strip weight and lateral displacements the differential stiffness E_s by hyp and hyp- δ would increase with depth z by the power law

$$E_s = \frac{d\sigma}{d\varepsilon} = mh_s(\gamma z/h_s)^{1-n} \tag{13.5.4}$$

with a factor m depending on r_e and intergranular strain δ (Sects. 2.4 and 4.5). Equation (13.5.4) would agree with (13.5.3) for $n = 0$ and would mean $k_s = m\gamma$, thus (13.5.1) seems to be justified with a suitable m . Granular soils have $n \approx 0.5$, however, $n = 0$ works at best with soft particles except for $\sigma_s \rightarrow 0$ (Sect. 3.5). Schlegel (1985) showed that bending moments of an elastic beam upon sand can be estimated with a power law

$$\sigma = \sigma_r(u/u_r)^m \tag{13.5.5}$$

instead of (13.5.1) and suitable reference values σ_r and u_r . The lateral uncoupling is justified by model tests in this case, but not the linearity of (13.5.1). Lateral displacements occur under the beam, thus (13.5.4) gets invalid and the parameters in (13.5.5) can scarcely be predicted. Augustin (2002) has shown that the response of ballast depends strongly on its pressure in unloaded states, thus (13.5.4) and (13.5.5) are refuted for reversals. He observed a nearly elastic response after some load cycles, and cumulative effects which are missed by (13.5.1), (13.5.2), (13.5.3), (13.5.4) and (13.5.5), cf. Sect. 13.8.

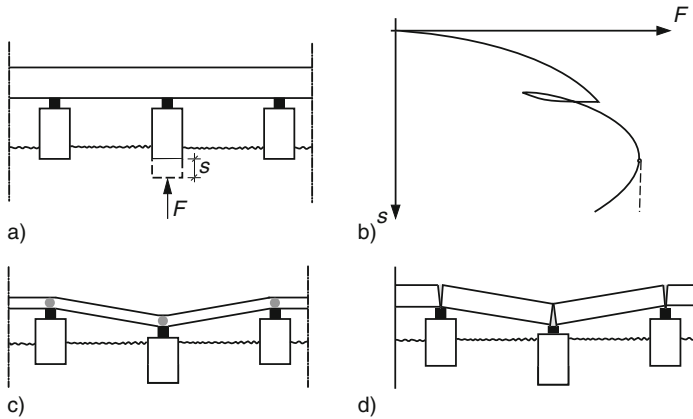


Fig. 13.5.2. Bridge with uncoupled foundations (a), foundation force versus settlement (b), deformation with plastic hinges (c), deformation with cracks (d)

Sufficiently distant foundations under a kind of *bridge* may be assumed as not coupled via psammoid ground, Fig. 13.5.2a. Neglecting lateral displacement and tilt, the response of each foundation may be represented by a plot of vertical force vs. displacement (b). It can principally be predicted (cf. Fig. 13.3.4), and the assumed independence of neighbours could be judged with finite elements. Bridge sections may be placed and coupled thereafter so that bending moments M and transversal forces T by weight arise between the supports. A traffic load P may deform the beam elastically, but the supports react anelastically (c). With sufficient bending stiffness the neighbored foundations are slightly lifted and unloaded. T and N due to P may as well be estimated with rigid supports, a linear subgrade could not produce more realistic results. Cumulative and uneven settlements due to traffic imply path reversals and can at best be estimated (Sect. 13.8).

Collapse scenarios require an *anelastic structural behaviour*. Bending moments can attain limit values in a ductile structure so that plastic hinges arise, Fig. 13.5.2c. This can occur with hardly predictable differential settlements, these would get indeterminate or accelerate if the ground resistance attains a

plateau or a peak, respectively (cf. Sect. 13.3). A brittle bridge would collapse if bending moments attain critical values due to P and differential settlements (d). As at best their order of magnitude could be estimated this failure should be avoided by a sufficiently flexible and ductile structure.

Frames upon psammoid ground may represent buildings with shallow foundations and negligible horizontal displacement, Fig. 13.5.3. A single stiff structure (a) would hardly be stressed by differential settlements during the construction as its stiffness arises alongside with its weight. Deformations by placement are path-dependent as shown in Sects. 13.3 and 13.4, curing of concrete or coupling of structural elements could be taken into account. Further vertical dead loads, as e.g. with a tank or silo, lead to differential settlements and structural forces. Both could be captured with finite elements and elp or hyp , and $elp-\alpha$ or $hyp-\delta$ in case of repeated loading (Sect. 13.8), the sequence of filling and emptying should be allowed for. Such evolutions are missed with (13.5.1), bending moments can thus have a wrong sign and order of magnitude, assumed statically possible distributions of base pressures can be more realistic.

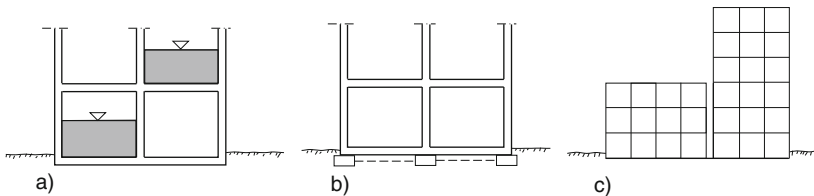


Fig. 13.5.3. Frame structures with shallow foundation on a plate (a) and on strips (b); neighboured structures with shallow foundation (c)

In case of hard-grained dense psammoid ground strip foundations can suffice to keep the deformations small, Fig. 13.5.3b. The interaction of strips via the ground may be neglected although their distance is smaller than for a bridge, this could be justified by comparative calculations with realistic initial fluctuations. Small displacements could be estimated as outlined with Fig. 13.3.4, internal forces may be calculated for design by assuming rigid supports. Bending moments in a base plate needed for water-tightness can be reduced by a soft inlay (dashed). Twin frame structures of different height and stiffness can get bigger deformations (c). As always order and size of construction steps play a role, now curing and coupling of structural parts are also relevant. If one structure stands already it is more affected by the new one than for a simultaneous construction, this is missed by (13.5.1).

A *spreading frame* upon psammoid ground may serve to show further limitations and possible substitutes of usual approaches, Fig. 13.5.4a, this is again idealized with plane-parallelity. It may be constructed upon eccentric strips and used for storage. Conventionally internal forces are calculated with an

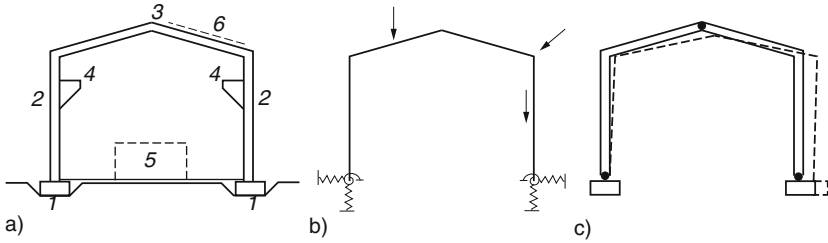


Fig. 13.5.4. Frame upon psammoid ground (a, numbers for sequence), substitute with elastic subgrade (b), frame with plastic hinges (c)

elastic system (b) for ‘ultimate’ and ‘service’ loads, thus cross sections and foundations can be dimensioned. This may suffice for the stability of a ductile system which can get indifferent with plastic hinges and a yielding foundation (c). Excluding brittle systems, service-relevant deformations remain thus indeterminate. Scenarios could be generated with finite elements. The system should be simulated with its step-wise evolution (indicated by numbers in Fig. 13.5.4a). Considerations with single foundations would not suffice as the path-dependence is ignored with unavoidable kinematical and statical assumptions (cf. Sect. 13.3).

Attractors can be of use to justify simplifying assumptions for realistic design scenarios. Initial states including foundations are mainly determined by the zone-wise averages of relative void ratio \bar{r}_e . Spatial fluctuations of r_e and mean skeleton pressure p_s are smaller and play a minor role for low \bar{r}_e , in particular in the near-field (Sects. 8.2 and 10.3). The known advantages of densification could be quantified by comparative calculations. Order, size and intensity of construction steps may be simplified as long as the overall path is monotonous (cf. Sects. 12.4, 13.6 and 13.7). Non-monotonous construction sequences, in particular operations in the ground near a ready structure, would impede the approach to an attractor. The subsequent ground response would thus be softer and less determinate (cf. Sect. 13.3). Scenarios with extreme loads and imperfections of ground and structure imply state limits in the large. These attractors are mainly determined by the initial r_e -field and can substitute plastic limit states (cf. Sects. 11.5, 12.4, 13.1, 13.2 and 13.3). A further attractor is needed for alternating loads in order to estimate cumulative effects (Sect. 13.8).

In addition to the ever-present historical element a ground with *peloid* influences the interaction of deformable structures and ground via skeleton viscosity and pore water diffusion. Structures *floating* in soft ground tend to attractors, Fig. 13.5.5. A not tilting box placed upon mud attains depth and pressure distribution as with a liquid (a). Almost the same happens with a constant initial consolidation ratio p_e/p_s and hydraulic height h_w (b). Independently of permeability the amounts of p_e , p_s and h_w along the box return to the far-field values. The resulting base pressure would be formally obtained

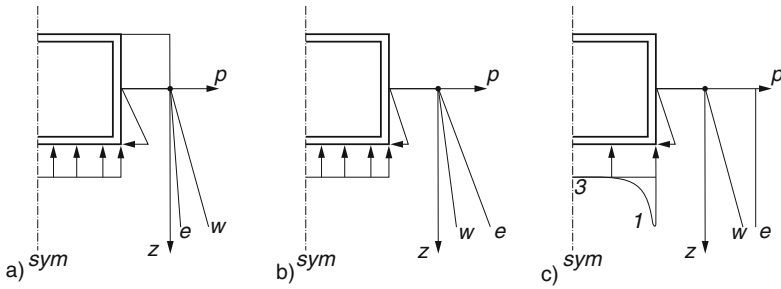


Fig. 13.5.5. Floating box upon mud (a), normally (b) and overconsolidated peloid ground (c). Equivalent (e) and pore water pressures (w) in the free-field versus depth

with (13.5.1), but Winkler's assumption is neither needed nor justified. If a box is placed in excavated stiffer ground as outlined with Fig. 13.4.3 a uniform base pressure is approached by relaxation of the peloid (c). The structure breaks if it attains a plastic or fracture limit. In case of a section-wise construction as by Fig. 13.4.4 a uniform base pressure is more slowly approached. The lower rate of relaxation is due to a higher consolidation ratio (Sect. 3.4), cf. (13.3.4) with (13.3.3). Evolutions of forces in the structure could be quantified with v-elp or v-hyp, such scenarios could support design and execution.

Dams with flexible inlays upon soft ground could similarly be captured, Fig. 13.5.6. Spreading of a light fill is reduced by placing a textile in the excavation (a). A state of rest is attained without diffusion of pore water if the weights of fill and excavation are equal and the earth pressure in the fill is compensated by the inlay. Traffic is harmless as long as the consolidation ratio p_e/p_s near the dam is not reduced below ca. 2 (cf. Sect. 13.8). A dam with more weight than the excavation can be placed more rapidly by means of one or two inlays (b). This kind of mattress is hardly spread, and less bent if the textile encloses the flanks. The dam sinks with decreasing rate due to diffusion of pore water and contractant creep (cf. Sect. 14.3). Scenarios could

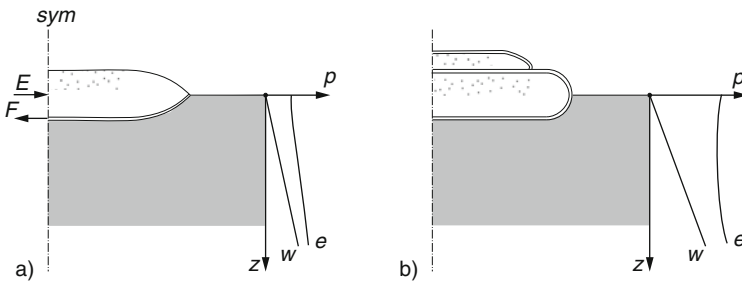


Fig. 13.5.6. Fill on soft ground with a textile mat (a) and textile bags (b). Pressures as in Fig. 13.5.5

be generated with hyp, v-hyp and constitutive relations for inlays and their interfaces with soil (Sect. 10.3).

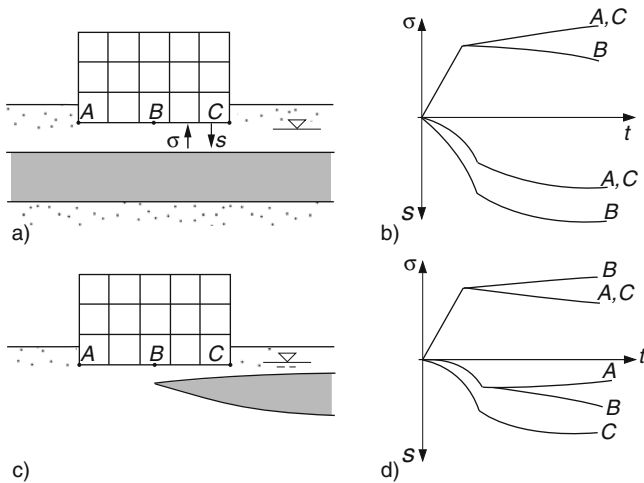


Fig. 13.5.7. Skeleton structures upon ground with a peloid layer (a) and a peloid lense (c); related base pressures and settlements versus time (b, d)

The influence of *peloid layers in psammoid ground* upon deformable structures above is manifold, Fig. 13.5.7. Deformations may be harmless during a uniform bottom-up construction, but can lead to failure afterwards (a). The peloid gets more pressure in the middle and yields more there with contractant creep and diffusion. Thus the structure is gradually deformed and stressed, and can get useless or break after years. This is not obtained with (13.5.1) and also missed with other usual design methods. With peloid under one side the structure is gradually bent with opposite sign (b). Twin buildings bend towards or from each other when they are constructed together or with a long waiting interval, respectively (c). This cannot be quantified by usual methods, whereas scenarios generated with hyp, v-hyp and constitutive relations for structures can lead to a safe and economical design.

Unsupported deformable walls can be treated similarly as rigid ones, Fig. 13.5.8. A row of sheet piles may be driven in sand under water, one side is back-filled and the other one is excavated (a). With a sufficient wall depth a plastic hinge and Rankine earth pressures may be assumed for a pre-design (a). Finite element simulations with elp or hyp and constitutive relations for the wall could supersede such assumptions. A slurry trench wall may be placed in ground with peloid, then one side is excavated (c). Usual design earth pressures (d) are rather arbitrary with partly unknown h_w -changes and vanishing displacements near the foot. Simulations with elp and v-elp or hyp and v-hyp, pore water coupling and wall relations could yield evolutions of

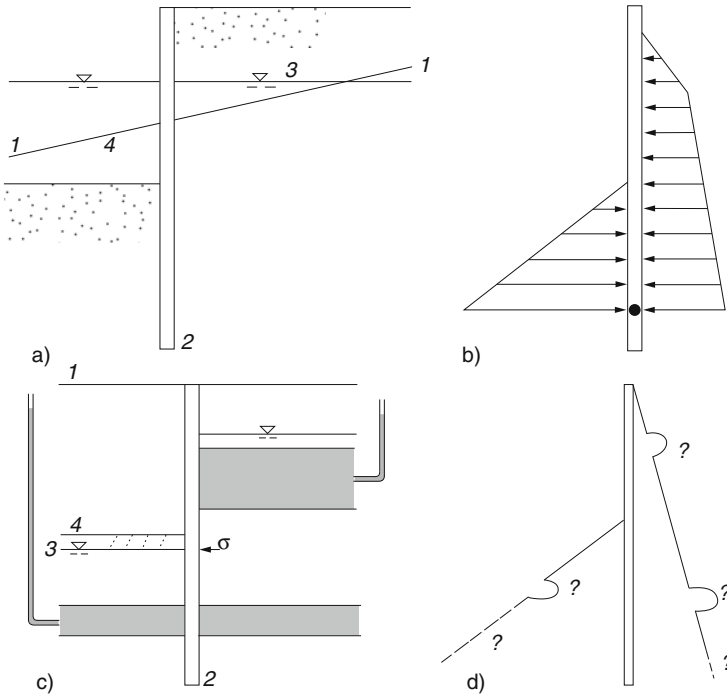


Fig. 13.5.8. Stiff retaining wall in psammoid ground (a), earth pressures (b), same with layered ground (c) and related earth pressures (d). Numbers for stages

shape and state during and after excavation. Except for reversals (Sect. 13.8) scenarios could thus be generated for any ground profile, wall, fill, excavation and hydraulic influence.

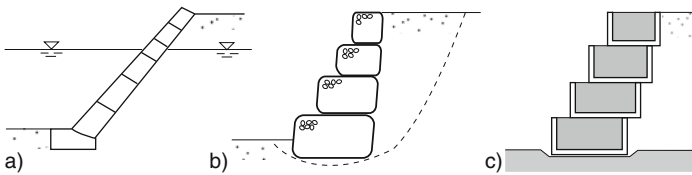


Fig. 13.5.9. Retaining structures with stones (a), rock-filled bags (b) and earth-filled crates (c)

Retaining structures with *dry masonry* are deformable, their anelastic behaviour cannot easily be captured, Fig. 13.5.9. Rigidity as assumed in Sect. 13.4 is no more legitimate if structural deformations can enhance a failure of the system. Blocks in a wall (a) may be represented by rigid bodies with anelastic interaction. Structures with bags of flexible solid and rockfill

(b) could be modelled as composites with elp or hyp (Sect. 9.2). A stack of chests with earth fill (c) requires special finite elements for calculations as such structural parts can destroy each other. Ground, fill and pore water could be modelled as before in design scenarios. Validation tests are needed for constitutive relations representing such structures.

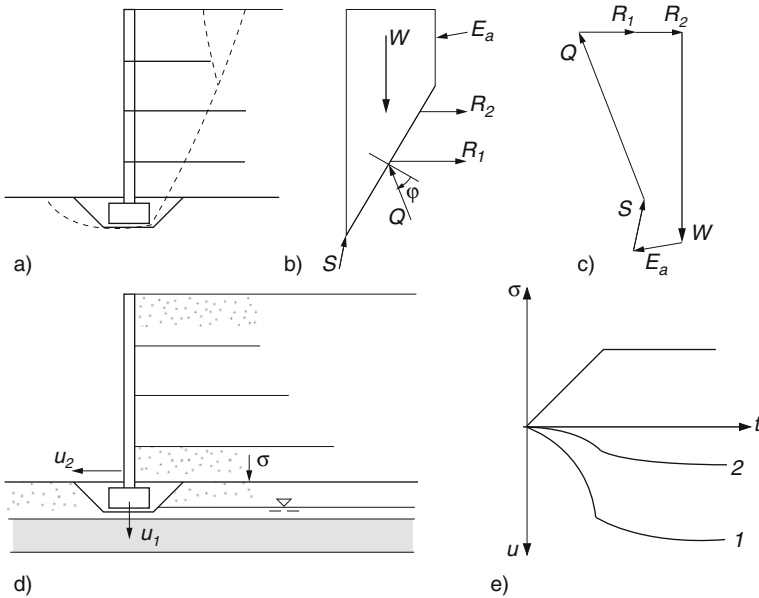


Fig. 13.5.10. Retaining wall with flexible tendons (a), sliding block (b), force polygon (c), wall with tendons upon partly soft ground (d), base pressure and settlement of fill versus time (e)

Structures with flexible inlays could be captured similarly, Fig. 13.5.10. They can be built on stiff ground with steep flanks and almost any height with suitable strips, wall and fill (a). Sliding bodies may be assumed for design with a main slip plane crossing lower strips (b). Their resulting pull-out resistance ΣR_i and a safely estimated resistance S at the wall foot enter the limit equilibrium (c). No such assumptions are needed in stage-wise simulations with elp or hyp and relations for wall and inlays with their interfaces (Sect. 10.3). With softer ground due to a peloid layer this confines the attainable height (d). If the composite structure would be safe according to Fig. 13.5.10b, c it can fail as the peloid in depth yields more in the course of time (e) (cf. Fig. 13.4.13). Longer strips would reduce the spreading of the structure, but not in the ground (cf. Fig. 13.5.6). Usual design estimates could be superseded by scenarios generated with elp and v-elp or hyp and

v-hyp, pore water coupling and relations for structural parts with interfaces. Vibrations and earthquakes could also be taken into account (Sect. 13.8).

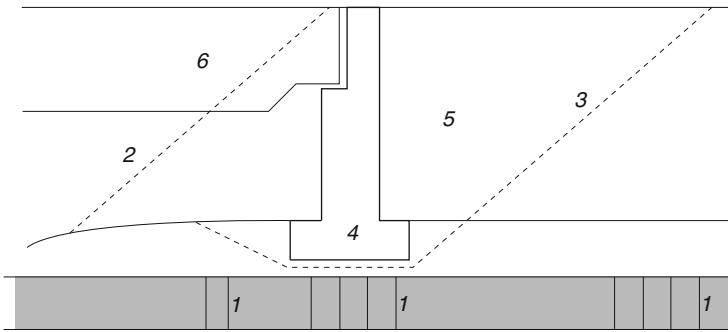


Fig. 13.5.11. Abutment with bridge and fill upon ground with an improved peloid layer. Numbers for the sequence

A two-dimensional substitute of a *back-filled bridge abutment* may finally be considered, Fig. 13.5.11. An extended fill (2) is placed on the rather soft ground after installing wick drains (1) in order to consolidate peloid zones. Part of the fill is removed (3), the abutment is placed (4) and back-filled (5), then a beam is placed (6). The filling could be judged and simulated as shown with Figs. 12.3.4 and 12.3.5, the ground state attained after its removal can also be obtained with elp and v-elp or hyp and v-hyp. Similarly as with Fig. 13.4.3 conventional estimates can at best suffice for pre-designing the abutment. More realistic scenarios are obtained with pore water coupling, stages of construction and use can be simulated within specified times. Failure due to spreading, tilting and differential settlements could thus be safely avoided. Traffic loads, vibrations and earthquakes could also be allowed for (Sect. 13.8).

Attractors in the large are advantageous in cases as illustrated with Figs. 13.5.5–13.5.11, with peloids they are argotropic and/or endogeneous due to skeleton viscosity and pore water diffusion (Sect. 10.4). Except for perfect elasticity and plasticity the asymptotic deformability of structures cannot yet be captured by similar rules. As with rigid structures, however, design estimates and simplifying assumptions for initial and boundary conditions could be justified by means of comparative calculations.

To *sum up*, simulated evolutions of shape and state could supersede conventional design estimates in cases with deformable structures upon and at the ground. The potential of elp and v-elp or hyp and v-hyp with pore water coupling is the same as with rigid structures. The deformability of structures can enhance the approach to unacceptable deformations and collapse. Repeated reversals could principally be allowed for (Sect. 13.8), strutted and back-tied retaining structures will be treated in Sect. 13.6. The general statements of

this section do not depend on plane-parallelity. The latter can be justified or superseded by three-dimensional calculations (Chap. 15), attractors play a key role in capturing the historical element.

13.6 Struted and back-tied retaining structures

Retaining walls can be supported horizontally by struts against an opposite wall, or by back-ties into the ground. They are usually considered as vertical beams with ‘actions’ by earth and water pressure, and ‘resistances’ by passive earth pressure and strength of struts or back-ties. Winkler’s assumption (13.5.1) is often used with horizontal stress σ and displacement u instead of settlement s , and with bounds by Rankine-type earth pressures. This is debatable as actual earth pressures are neither active nor passive in general. Back-ties and soil constitute a composite, vertical components play a role, uncoupling as by (13.5.1) cannot be defended. Thus deformations are missed and the stability is hardly captured. Design estimates of this kind are at best empirically justified, but their range of validity beyond executed cases is unknown.

As shown with other structures in previous sections one can simulate evolutions of shape and state with finite elements, constitutive relations and initial and boundary conditions. This was done in a number of case studies with field data and justified plane-parallelity. As outlined in the sequel hypoplastic models were validated for various retaining structures with granular soils. Less was done until now with clays, but observations indicate that skeleton viscosity and pore water diffusion could also properly be taken into account.

A *struted sheet-pile wall in granular ground* was investigated in detail by von Wolffersdorff (1997). The ground consisted of humid fine sand above and gravel below the water table, both rather dense. Two parallel slits with bentonite smear were installed to keep displacements in one plane. Two opposite walls were driven in by vibrations, one was equipped with earth pressure transducers and strain gages for bending moments. A basin was placed near one wall and filled with water. A row of struts was installed between the walls after partial excavation, this was continued down to the water table. Then the struts were shortened so that their resulting force attained a minimum and the wall yielded. A gap opened behind this wall, and inclinometers indicated a shear localization deeper in the ground. Predictions submitted for this field test missed observed deformations, pressures and structural forces.

After this moment of truth various attempts were made to improve prediction models and to understand their inevitable limitations. Fairly realistic displacements were obtained with *elp* and *hyp* (Wolffersdorff 1997) including the initially ignored capillary skeleton pressure p_{cs} (Sect. 6.2). It was realized that the ground had been partly densified by vibrations, that earth pressures can hardly be observed nor predicted and that bending moments and strut

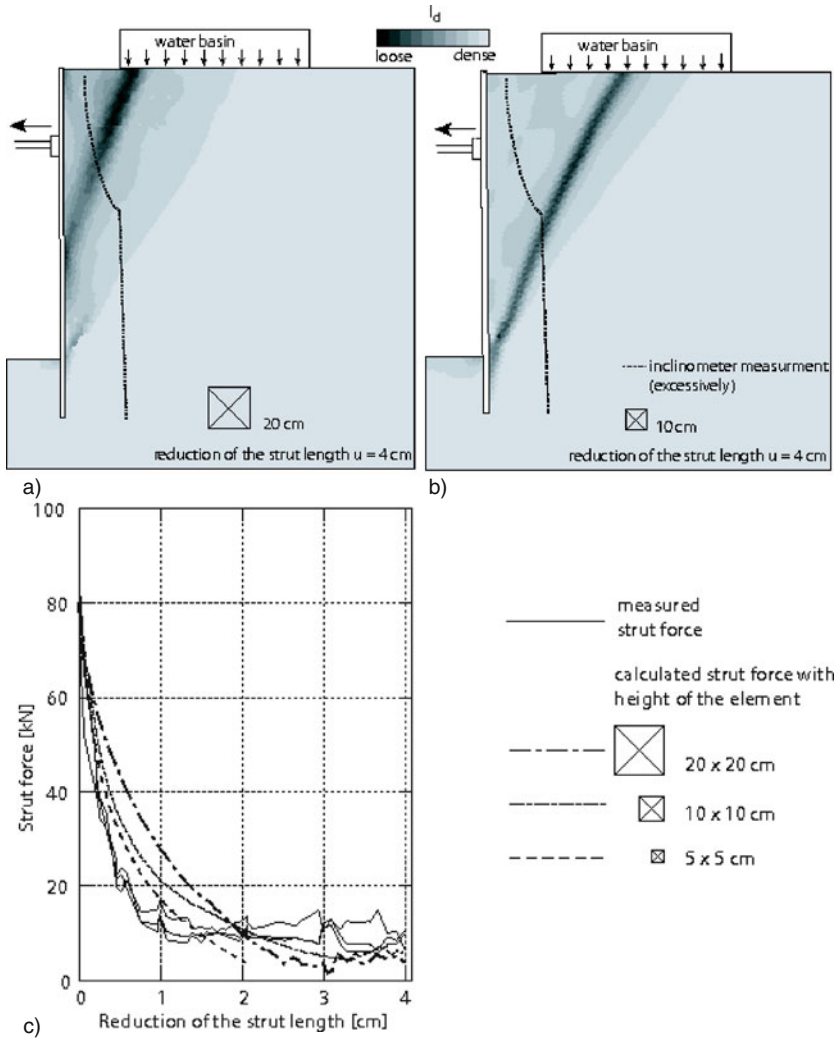


Fig. 13.6.1. Back-analysis of von Wolfersdorff’s (1997) field test by Slominski (2007): localization with coarse (a) and finer mesh (b), strut force versus shortening (c)

forces cannot be captured with the same precision as displacements. This enhanced the development of hypoplasticity, but until recently the observed minimal strut force and shear localization in the ground could not be captured.

Slominski (2007) could remove the last shortcomings with sophisticated calculations, Fig. 13.6.1. A suitable mesh leads to a plane shear band in agreement with the observed dislocation (a, b). The calculated reduction of the strut force with shortening of the struts is realistic with a not too fine or

coarse mesh (c). Polar effects may be neglected as the wall height exceeds by far 100 grain diameters (Sects. 13.1 and 13.3), but a mesh-independence is thus visibly not obtained. As with other case studies discussed in the sequel and in Chaps. 14 and 16 one may nevertheless argue that useful simulations can be obtained with suitable meshes by means of field data.

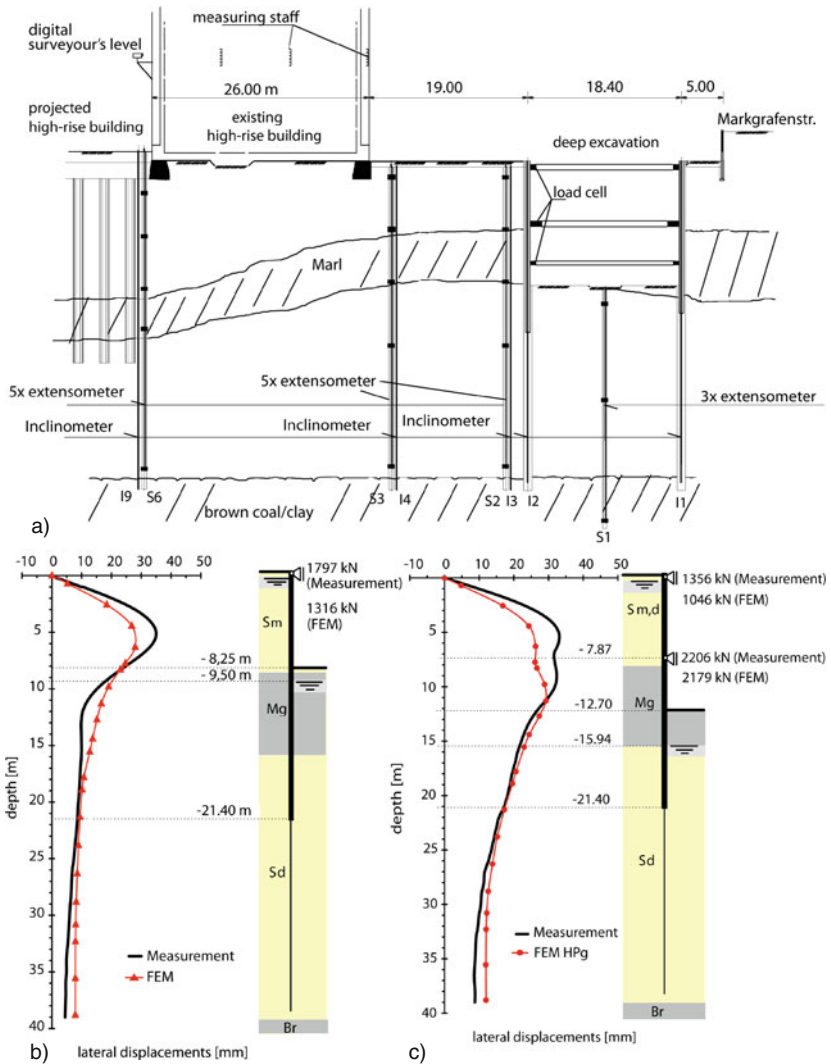


Fig. 13.6.2. Excavation with strutted wall (a), wall displacement and strut forces after half (b) and full excavation (c), Mayer (2000)

A *strutted sheet pile wall* placed in a slurry trench in mainly granular ground was monitored with uncommon precision and back-analysed with hyp- δ , Fig. 13.6.2a (Mayer 2000). The installation of the wall is a three-dimensional evolution (Sect. 15.2), but the ratio of wall length and height suffices for plane-parallelity of the subsequent evolution. The state of the ground before excavation was assumed as without the wall (Sect. 12.2), comparative calculations showed that pressure deviations due to the wall installation had little influence. Excavation, lowering of water table and installation of struts were simulated in steps according to the protocol. The agreement of observed and calculated values is good for horizontal displacements near the wall and acceptable for strut forces both for partial (b) and full excavation (c).

The validations shown by Figs. 13.6.1 and 13.6.2 can be attributed to attractors in the large. A first one for the free field (cf. Sect. 11.3) reveals how far former operations in the ground may be neglected. A second one means that with a vibratory installation a further densification can matter, but that irregular skeleton stress distributions are negligible (cf. Sect. 13.8). A third one means that installation-induced deviations of skeleton stresses from far-field values are swept out by subsequent deformations. The historical element is thus not ruled out, it delimits the predictability as evolutions can never be followed up in all detail.

Design scenarios for strutted walls in psammoid ground can thus be generated as shown with Fig. 13.6.3. With a water table below the excavation (a) sheet pile walls (2) may be installed near buildings (1), an upper row of struts (3) is placed after partial excavation (3), a lower one thereafter (4). Earth pressures as indicated with Fig. 13.5.8 may suffice for a pre-design, but thus deformations and stability cannot be captured sufficiently. Upper bounds of displacements can be obtained with hyp- δ , big initial intergranular strain δ for stress fluctuations, somewhat higher than observed initial r_e with spatial fluctuation, and realistic imperfections of the structure and its installation. Deformation-induced damages of the retaining structure and

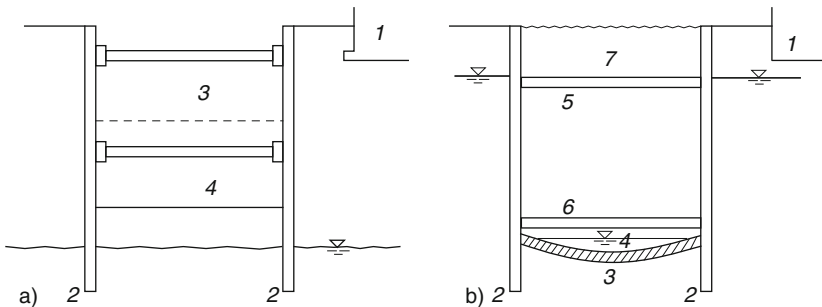
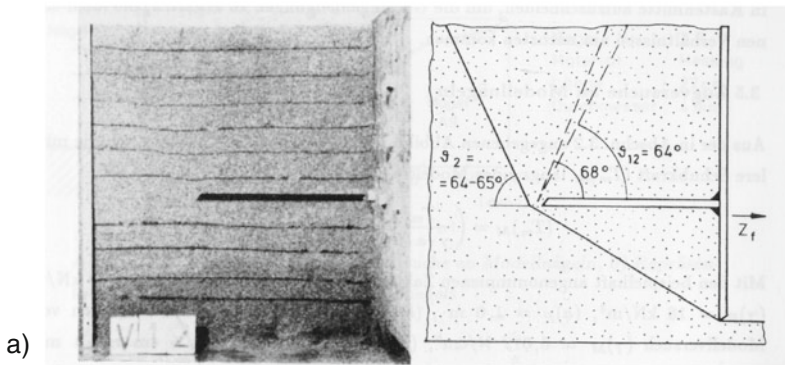


Fig. 13.6.3. Retaining structures in psammoid ground with deep (a) and high water table (b). Numbers for the sequence

neighbourhood buildings can thus better be avoided, monitoring and auxiliary operations can be supported more rationally.

In a second scenario with a high water-table (Fig. 13.6.3b) two slurry trench walls (2) near buildings (1) may be connected by a jet-grouted inverse arc (3). The water table is lowered inside (4), a concrete slab is placed after partial excavation (5), a second one (6) forms a tunnel which is then covered (7). Usual design estimates of structural forces are debatable with such a bottom arc, whereas the evolution of shape and state can again be captured in due order with hyp- δ and relations for structural parts with curing. As for the previous case collapse scenarios require rupture of structural parts (cf. Sect. 13.5). Only then strut forces can change dramatically and shear bands can occur as shown in Fig. 13.6.1.

Experiment



Simulation

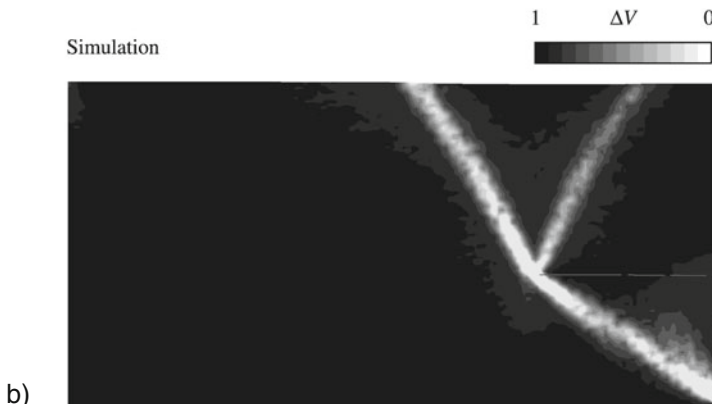


Fig. 13.6.4. Model test with a back-tied wall (a, Gäßler 1987) and its simulation with p-hyp (b, Nübel 2002)

A *back-tied wall* was studied by Gäßler (1987) in a model test with sand, Fig. 13.6.4a. A rough plate was placed behind the fall, then the wall was further back-filled. After releasing the wall a block with the wall and part of the plate slid on a plane shear band, an upper wedge slid with two steeper bands. Nearly the same evolution was obtained by a simulation (b) with polar quantities (Nübel 2002, cf. Sect. 8.2). A limit equilibrium can be generated instead with a mean friction angle (cf. Fig. 13.5.10).

Polar terms are not needed for walls in situ (cf. Sect. 13.5). These are back-tied by rows of anchors or nails and not by an embedded plate. Model tests with dry sand, which was afterwards wetted and cut vertically, reveal similar sliding mechanisms, Fig. 13.6.5. With three rows of anchors, prestressed to the wall by strings, an excavation near the foot leads to a sliding block which is back-tied by the tendons and driven by an upper wedge (b). With several rows of so-called nails, without strings and pre-stress, digging at the foot leads to the same mechanism (a). Neglecting the bending stiffness of anchors or nails the limit equilibrium would be almost the same as in Fig. 13.5.10b, c, with a different resistance S at the wall foot and again a resulting pull-out resistance ΣR_i . This might suffice for design if φ , S and ΣR_i are reasonably assumed, but thus deformations are ignored and the stability is not assessed in case of insufficient ductility.

An anchored sheet-pile wall in a cemented slurry trench in sandy ground, which was first investigated by Mayer (2000), was again back-analyzed with hyp- δ by Slominski (2007), Fig. 13.6.6. The water table inside was lowered above a sealing lignite layer, anchor forces and horizontal displacements in inclinometer boreholes were observed. With a refined mesh around the anchors

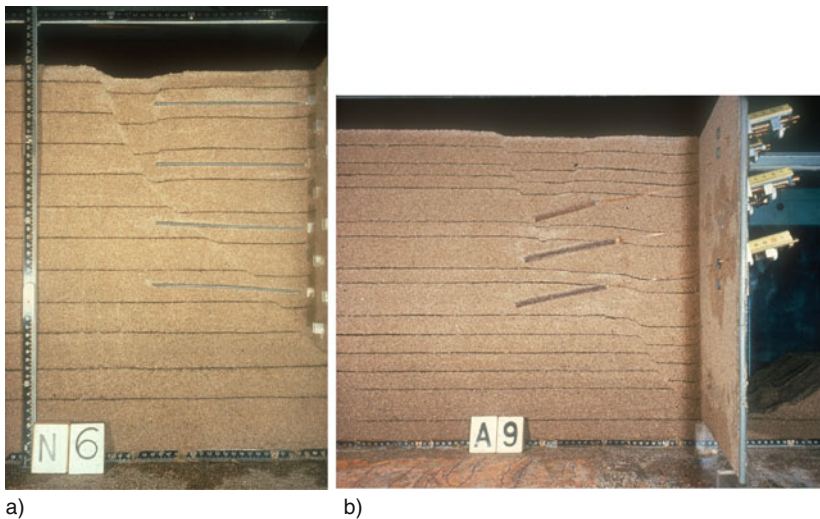


Fig. 13.6.5. Model tests (courtesy E. Schwing) with a nailed (a) and an anchored wall (b)

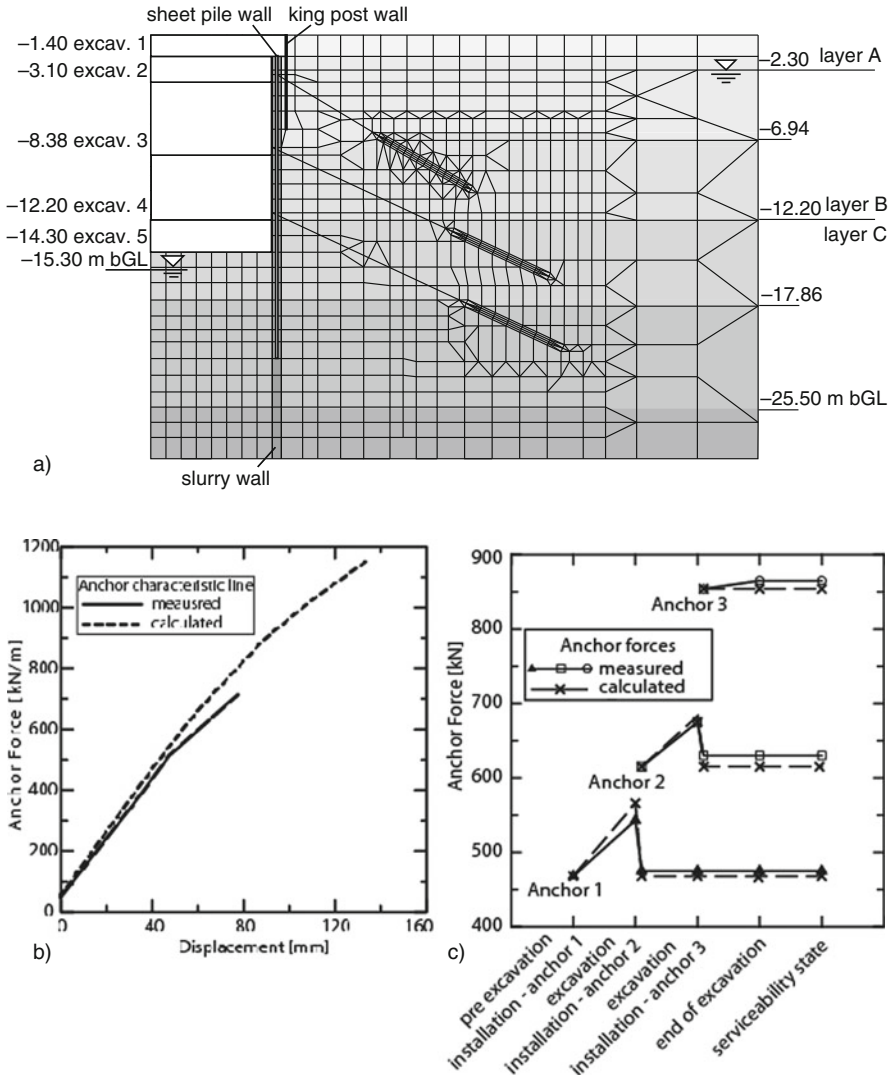


Fig. 13.6.6. Back-analysis (Slominski 2007) of an anchored sheet pile wall in sandy ground (Mayer 2000): cross section with finite elements (a), Pull-out resistance (b), evolution of anchor forces (c)

(a) the observed pull-out resistance was reproduced (b), a substitute anchor plate is thus justified. The evolution of anchor forces with fixing, further stressing by excavation and partial unstressing after installation of the next row is well captured (c). The agreement of observed and calculated horizontal displacements is good for four stages, Fig. 13.6.7a–d. Bigger actual displacements thereafter can be attributed to vibrations in the pit (Sect. 13.8).

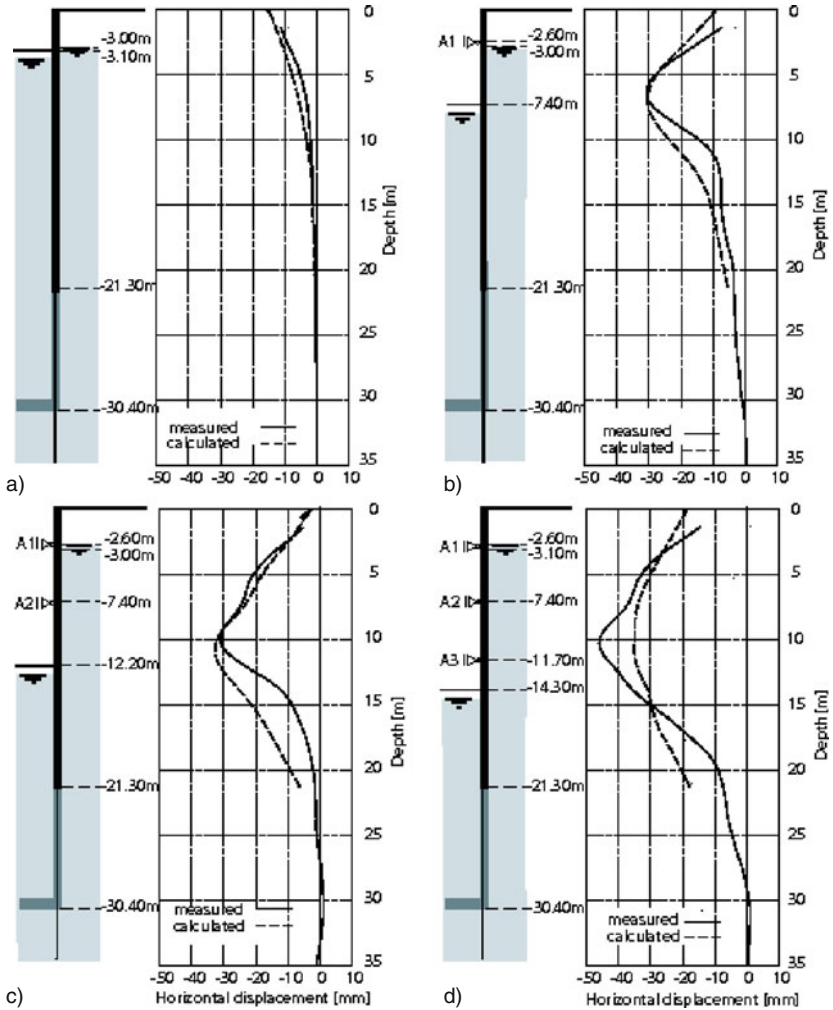


Fig. 13.6.7. Observed and calculated horizontal displacements after little (a), half (b), further (c) and full (d) excavation (Slominski 2007)

A field test with a *nailed wall* was carried out up to a limit equilibrium by Gäbler (1987). Within two vertical clay smears for plane-parallelity the sand behind the wall was loaded via a traverse. Loading and unloading did not lead to a peak in three cycles, but after removing the lowest nails and further excavation it was reached. The observations indicate a limit equilibrium with two sliding bodies, this could be statically explained as with Fig. 13.5.10. Strain gages in nails of the lowest remaining row indicate an increasing tensile force which is almost constant within the sliding block. The system was remarkably ductile, i.e. the resistance at the traverse was only slightly reduced beyond the peak. Strong load cycles caused a substantial ratcheting, but no fatigue.

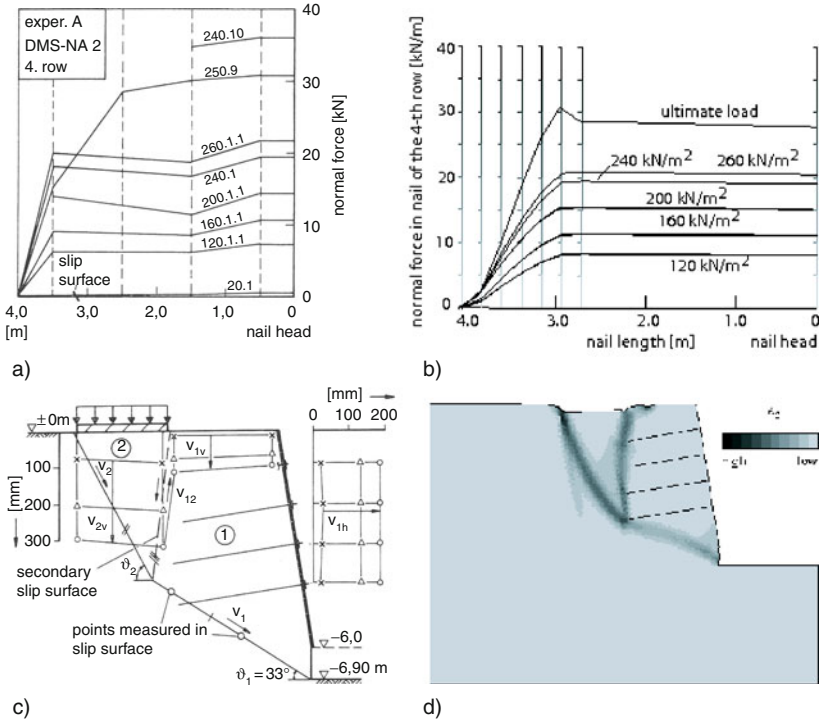


Fig. 13.6.8. Back-analysis of Gäßler’s (1987) field test (Slominski 2007): Observed (a) and calculated (b) forces in lowest nails with increasing traverse load, observed (c) and calculated (d) shear localization after removing a deeper row of nails

In a back-analysis Slominski (2007) could reproduce these findings with hyp. The mesh was finer around the nails and adapted to the step-wise excavation and installation (cf. Fig. 13.6.6). After identification of hypoplastic parameters and initial state a realistic peak of the traverse force was obtained, but an exaggerated ratcheting. The calculated force in the lowest row of nails (b) evolves nearly as observed (Fig. 13.6.8a). Shear zones grew with reloading after removal of the lowest nails and further excavation (c). Two sliding bodies arise similarly in the simulation (d). The calculated shear bands are too thick, but this does not matter for the limit equilibrium as the dilation is hardly impeded. With progressive shearing the sand is dilated to a critical state in the upper steep bands, but not quite in the lower band. The skeleton is no more sheared along the nails. That’s why the system is so ductile, so it would be stable with a dead load below the one determined with the critical friction angle φ_{cs} (cf. Sect. 12.4).

Design scenarios for back-tied structures in psammoid ground can now be conceived as shown with Fig. 13.6.9. Humid fine sand in a gentle slope (1) with buildings (2) may be cut and nailed (3, 4 ...) with a shotcrete skin (a). Limit equilibria have to be assessed for all stages with φ_{cs} , cautious p_{cs} , dead

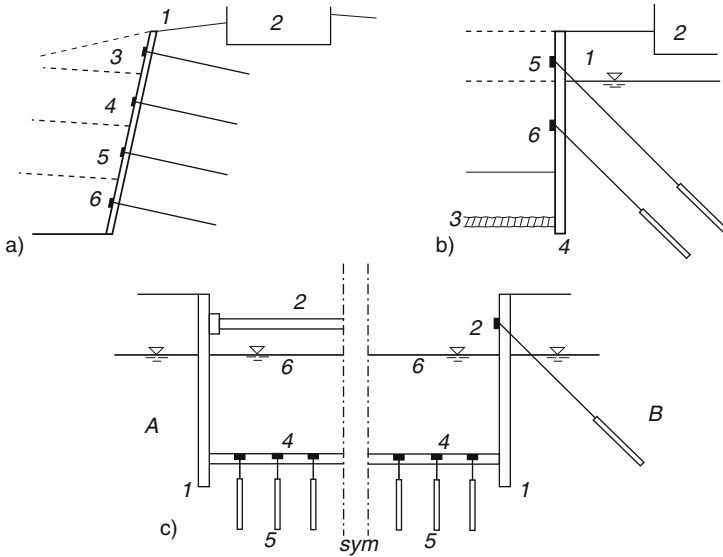


Fig. 13.6.9. Design scenarios for back-tied structures in psammoid ground: nailed wall (a), anchored wall with grouted slab (b), walls with anchored slab (c). Numbers for the sequence

loads and pull-out resistances as in Fig. 13.5.10. Displacements of the building could be predicted with *elp* or *hyp*, p_{cs} and a mesh so that the observed pull-out resistance is reproduced. The sand should be protected against drying and flooding. Prestressed anchors would not do better than nails of the same size as the reinforced soil block ‘forgets’ this prestress in the course of further excavation.

Displacements can be reduced by pre-stressing if anchors reach deeper than the excavation, Fig. 13.6.9b. If the water table (1) must not be lowered under a neighboured building (2) a seal can be injected (3) between tight walls (4) before excavation. The latter is carried out in stages alongside with inside pumping and installation of anchors (5, 6). The structure may be designed with well-defined water pressures and conventional earth pressures. This may suffice for stability, but hardly for deformations. In a simulation with *elp- α* or *hyp- δ* the state after placing the wall could be simplified as for a free field (Sect. 11.3) plus a dead load for the building (Sect. 13.4). The injection may reduce k_f , the cementation in this depth is negligible. The unsupported wall yields slightly during the first excavation, then it is pulled downwards by pre-stressing the first anchors. This yielding goes on with further stages and can affect the building. The pull-out resistance should be well below the strength of brittle tendons so that these cannot break one after another up to a collapse.

Instead of an injection or a natural seal a bottom slab can be back-tied, Fig. 13.6.9c. After placing walls (1) and struts (2A) or anchors (2B) above

soil is excavated under water (3), a plate is cast (4) and fixed by vertical anchors (5), then water is pumped out (6) and the construction is continued. Hydrostatic uplifting (cf. Fig. 13.4.10) is prevented by long anchors and sufficient density of the skeleton in between so that this is lifted together with the plate. Plate and walls may be designed with conventional assumptions as long as the structure is ductile and earth pressures are calculated with φ_{cs} . Deformation tolerances for water-tightness may thus be kept, but empirically unknown variants can hardly be captured. One should better simulate evolutions of shape and state with $\text{elp-}\alpha$ or $\text{hyp-}\delta$, substitute anchor plates and non-linear relations for the structure. This works also with reversals due to changing water tables (Sect. 13.8), whereas cumulative effects are missed by a conventional design.

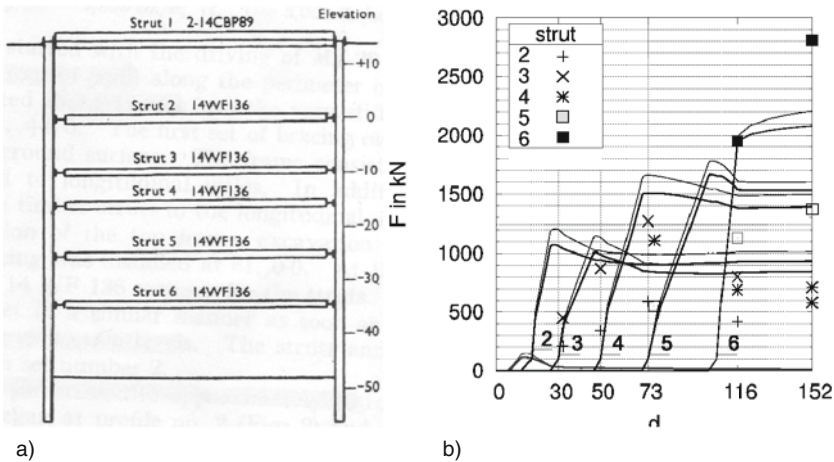


Fig. 13.6.10. Back-analysis (Meier 2009) of a sheet-pile wall (Wu and Berman 1953): cross section (a), strut forces versus time (b)

With *peloids* evolution times are not only determined by construction and subsequent actions, but by skeleton viscosity and pore water diffusion. Leaving aside sandwich soils and artificial drains the diffusion does not matter during the construction (cf. Sects. 13.2, 13.3, 13.4 and 13.5). This was the case for a strutted wall in Chicago (Wu and Berman 1953), Fig. 13.6.10a. Sheet piles were driven into stiff clay with a sand fill above the water table. Struts were inserted in six levels alongside with the excavation. Axial forces observed at them grew during the excavation and slightly also thereafter (b). Horizontal displacements of the wall did not exceed a few cm during the excavation and did not increase thereafter. The structure had been designed for earth pressures estimated with c_u (Sect. 13.2), and the number of struts was adapted to the observed behaviour (Peck 1969).

Meier (2009) carried out a back-analysis with hyp and v-hyp. Composition and initial state were identified as shown with Fig. 11.3.3. Changes due to sheet pile driving were neglected, with a small gas content the minute compression does not matter off the wall. Installation of struts and excavation were simulated with given times, but simplified by plane-parallelity. The calculated evolution of strut forces (also in Fig. 13.6.10b) is close to the observed one, the calculated wall displacements are likewise realistic. Other than with conventional estimates one can therefore predict the evolution of shape and state for such cases. Structural forces and deformations can be kept small enough during and shortly after construction.

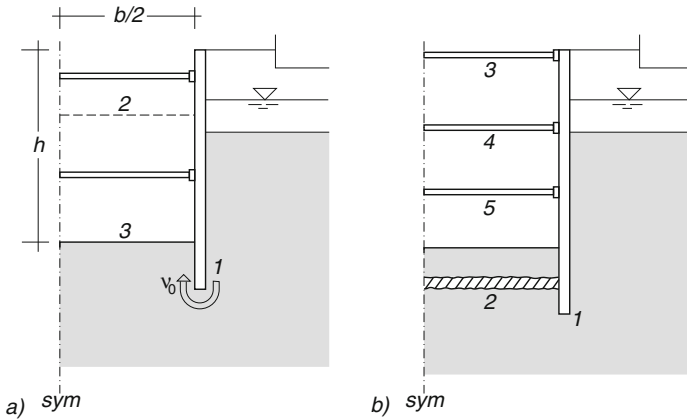


Fig. 13.6.11. Struttred walls in soft ground with open excavation base (a) and grouted slab (b)

For struttred walls in *soft ground* the skeleton viscosity can play a bigger role, Fig. 13.6.11. With an open bottom (a) the soil flows around the wall from a certain excavation depth h onwards. Bjerrum (1973) observed that the excavation depth h could not exceed the critical value

$$h_c = c_u N_c / \gamma \tag{13.6.1}$$

with $N_c \approx 5$ and a lower c_u than from tab tests. This corresponds to the punching resistance by (13.3.2) with the velocity v_o of isochoric creep by inversion of (13.3.3). For a narrow trench, say $b/h < \text{ca. } 1/2$, N_c is higher and v_o is lower with a given h . Structural forces may be estimated with earth pressures from c_u (Sect. 13.2) although the deformations are not suitable. Creep motions and structural forces could be captured with v-elp or v-hyp if the soil is ductile. Otherwise the creep can go over into a collapse, this could be modelled with v-hyp by Gudehus (2004b) (cf. Sect. 3.9).

Deformations are reduced by closing the bottom, but then the structure is more stressed, Fig. 13.6.11b. If a slab is placed after the excavation the

creep after its curing is stopped. This may suffice if the statically required c_u is reduced by means of narrow sections with auxiliary walls, and with rapid construction and curing (cf. Fig. 13.4.4). If a slab is jet-grouted prior to excavation the deformations are small, but structural forces increase more rapidly. This kind of relaxation of the ground enhanced a disaster in Singapore with an under-designed structure (Whittle 2006). For a conservative design pressures at walls and bottom slab may be assumed like in the far-field. As long as the structure is lighter than the excavated ground it rises by creep, thus its bottom pressure is lower than in the far-field. All this could be quantified with v-elp or v-hyp and constitutive relations for the structure, design scenarios should also depend on operation and waiting times.

The diffusion of pore water is not so important for cases as by Figs. 13.6.10 and 13.6.11. With a small gas fraction pore pressures can return to far-field values without seepage, a minor consolidation near structural parts slows down with long-term creep. This neglect is no more legitimate with soft layers above the bottom of excavations. In a field test (Kort 2002) sheet piles were hammered through a soft sandwich ground into sand, after excavation and strutting the wall was plastified by surcharging the ground. Pore pressures rose during the operation and returned to far-field values with densification in a short time. Another test in similar ground was carried out with a slurry trench wall (De Wit and Lengkeek 2002, more in Sect. 15.1). The smaller deformations and excess pore pressures reveal again a rapid diffusion. Both tests could be simulated with hyp, v-hyp and an orthotropic composite (Sect. 9.2), this would support design scenarios.

Back-tied walls at ground with rather soft peloid zones are of geotechnical interest in several variants, Fig. 13.6.12. Anchors or nails can be placed at a cut in stiff fissured clay (a). The composite system deforms almost without pore water diffusion during the construction and by undrained creep for a while thereafter. Later the creep stabilizes by contraction if less than φ_c is needed for any limit equilibrium with the hydraulic conditions, and destabilizes up to a collapse in the opposite case. This could be modelled as outlined in Sect. 12.4, now plus structural elements as shown with Fig. 13.5.10.

If a wall supports a creeping slope and is back-tied in non-viscous ground (Fig. 13.6.12b) the structure gets more stress due to decreasing creep and relaxation of the ground (cf. Fig. 13.2.3e, f). With soft horizontal upper layers (c) the pressures at the wall are reduced as long this yields, and return to the far-field values after fixing the wall. Lower long-term structural forces could be achieved with yielding anchors, but then the system goes on to creep. It stabilizes again if no limit equilibrium needs more than φ_c . Otherwise it collapses sooner or later, all the more if structural parts are not ductile. Design scenarios for such cases could be generated with hyp or hyp- δ , v-hyp or v-hyp- δ and relations for structural elements and their interfaces with soil (Sect. 10.3).

As with other structures (Sects. 13.4 and 13.5) design scenarios for strutted or back-tied retaining walls should imply attractors in the large. Only thus partially unknown fluctuations and imperfections can be mastered without

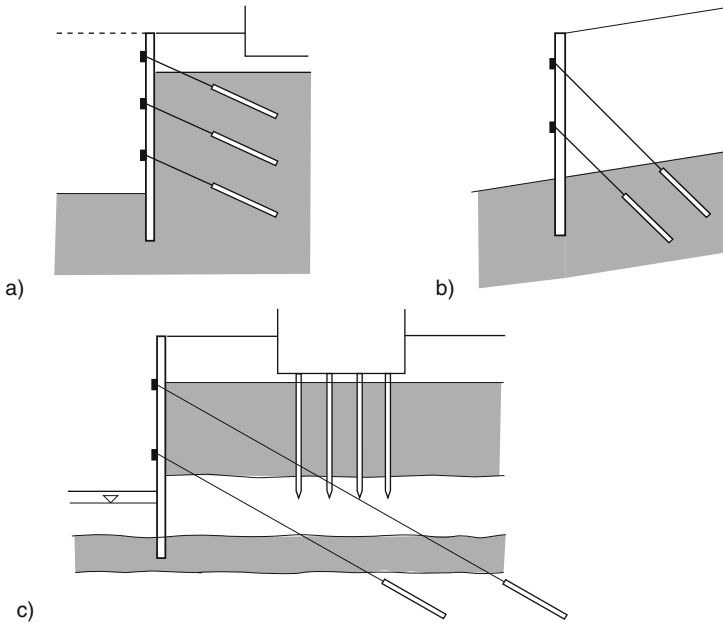


Fig. 13.6.12. Design scenarios with anchored walls in partly viscous ground: fissured clay (a), creeping slope (b), layered ground (c)

ignoring the historical element. With contractant attractors brittle and ductile structures would hardly impede numerical simulations. Contractant state limits in the large are required for stability, otherwise critical phenomena of structure and ground would occur (Sect. 16.3). Attractors for cumulative effects with several reversals will be treated in Sect. 13.8.

To *sum up*, simulations with hyp and v-hyp can supersede usual design estimates for strutted and back-tied retaining structures. This is validated for granular soils by a number of field tests and monitoring protocols. Less validations exist as yet with peloids, but more evidence could be achieved by back-analysing good reports. Fortunately such systems may often be considered as plane-parallel although at least their initial evolution cannot have this symmetry. Overall stability is achieved with contractant attractors, then deformations can also be sufficiently bounded. Creep, relaxation and pore water diffusion can and should be taken into account. Critical phenomena, as e.g. progressive rupture of tendons or struts, can and should be avoided.

13.7 Cavities and underground structures

Cavities in the ground can be supported or expanded by fluids or structures. Alongside with their evolution changes of shape and state in the surroundings can lead to intolerable deformations and collapse. More essentials

than with radial symmetry (Sect. 11.7) can be captured with one cross section, several extensions with less symmetry are straightforward (Sect. 15.2). Plane-parallelity can be achieved in model tests, but hardly in situ, therefore the range of validity of calculation models is not as wide as for retaining walls.

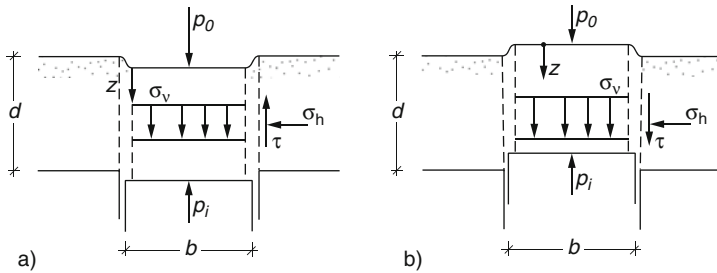


Fig. 13.7.1. Simplest models for active (a) and passive trap door problems (b) with psammoid

Psammoid layers above cavities have often been considered by means of *trap doors*, Fig. 13.7.1. A strip representing a cavity with breadth b underneath can be shifted down (a, active) or up (b, passive) relative to a fixed base. Vertical shear bands may occur above the rims, therein the ratio $K = \sigma_h/\sigma_v$ of horizontal and vertical stresses may be constant. Assuming in addition a uniform distribution of σ_h in every depth z and a constant ratio of shear and normal stress $\tau/\sigma_h = \tan \varphi$ the condition for vertical equilibrium can be written

$$\frac{d\sigma}{dz} = \gamma \mp \frac{2}{b} \sigma_v K \tan \varphi \tag{13.7.1}$$

with $+$ for the active and $-$ for the passive case. This was proposed by Janssen (1895) to calculate pressures in silos.

Integration of (13.7.1) with $\sigma_v = p_o$ for $z = 0$ leads to the cavity pressure p_i for $z = d$, viz.

$$p_i = \gamma/M + (p_o - \gamma/\lambda)\exp(-Mz) \tag{13.7.2}$$

with $M = \pm 2K \tan \varphi/b$, therein $+$ for the active and $-$ for the passive case.

Investigations by Vardoulakis et al. (1981) show that the reality is more complicated, Fig. 13.7.2. In an active case two curved shear bands start from the edges and converge (a), then two nearly vertical bands arise (b). In a passive case two diverging curved bands (c) are followed by two steeper diverging ones (d). These evolutions cannot be captured with constant stress ratios K and $\tan \varphi$ and uniform horizontal stress distributions as with (13.7.1). φ may be close to the critical friction angle φ_{cs} , but K varies within so wide bounds that such statical assumptions cannot be defended. The vertical shear bands assumed with Fig. 13.7.1 may at best substitute a second stage which is not

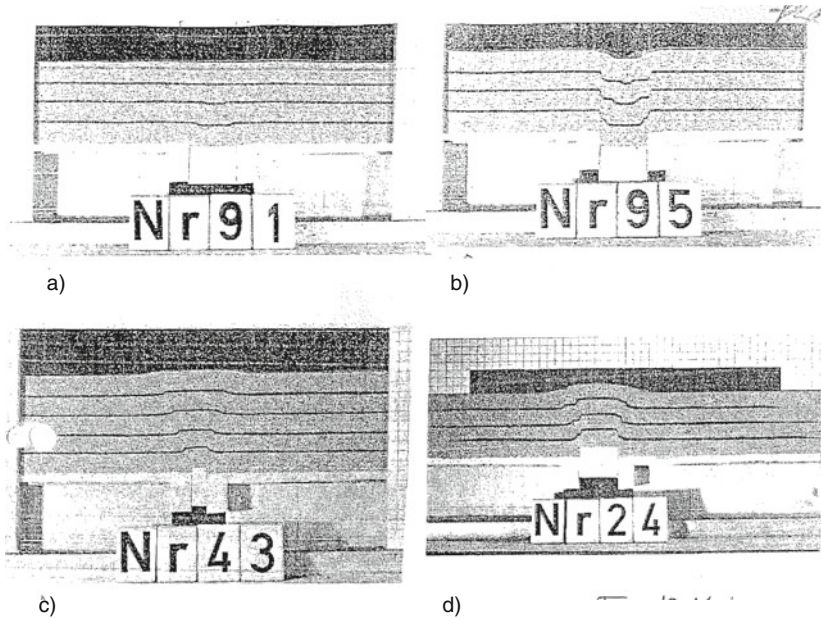


Fig. 13.7.2. Trap door experiments with sand (Vardoulakis et al. 1981): active after small (a) and large displacement (b); same passive (c, d)

influenced by previous converging or diverging bands. This historical element is ignored with (13.7.1).

The assumptions outlined with Fig. 13.7.1 are misleading for deeper trap doors, say $d > 3b$, whereas model test results were captured by hyp with polar terms (p-hyp, Sect. 8.2), Fig. 13.7.3. In an active case a dilated arc observed by X-rays (a, Graf 1984) is reproduced alongside with hardly observable further dilating bands (b, Nübel 2002). In a passive case (same authors) two diverging bands were reproduced (d) including a loss of symmetry.

Tejchman (1997) studied active cases with fixed vertical walls above a trap door by means of model tests and p-hyp, Fig. 13.7.4. With rough walls and loose sand an almost rigid block slides between shear bands (a), whereas a dense skeleton is deformed with sliding (b). For loose sand observed and calculated bottom pressures do not change substantially with bottom displacements. For dense sand the average pressure at the trap door is reduced with its displacement and rises afterwards. The agreement of observed (c) and calculated (d) average bottom pressures is good and shows how inadequate the assumptions presented with Fig. 13.7.1 are. Tejchman (1997) demonstrates that polar terms may be neglected for widths $b > 10^2 d_g$ with grain size d_g even if shear bands (c) thicker than ca. $10 d_g$ are obtained.

Mélix (1987) carried out model tests with *tunnels in humid sand*, Fig. 13.7.5a, c. Sand was placed in a box with almost critical void ratio and a

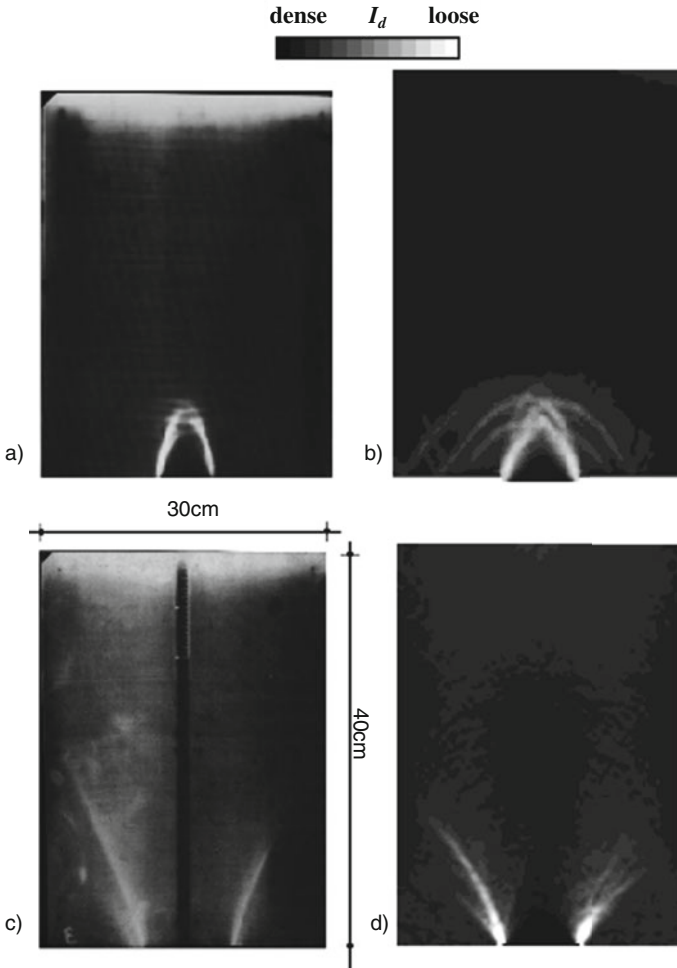


Fig. 13.7.3. Deep trap doors under sand: observed (a, Graf 1984) and simulated shear bands in an active case (b, Nübel 2002), same for a passive case (c, d)

capillary skeleton pressure (Sect. 6.2) $p_{cs} \approx 1$ kPa. After excavation from the side and inserting a rubber hose with a smaller tube inside the tunnel roof collapsed by decreasing the air pressure in the hose, or by increasing the pressure in a cushion on the surface. The falling sand was retained by the tube, got a higher p_{cs} by wetting and was cut vertically. Dark markers indicate a succession of shear localizations as in Fig. 13.7.3a and b up to a collapse if the overburden does not exceed twice the tunnel diameter (a). With sliding bodies (b) Mélix (1987) obtained the statical estimate

$$p_i = p_o + \gamma h - 2c_c h/d \tag{13.7.3}$$

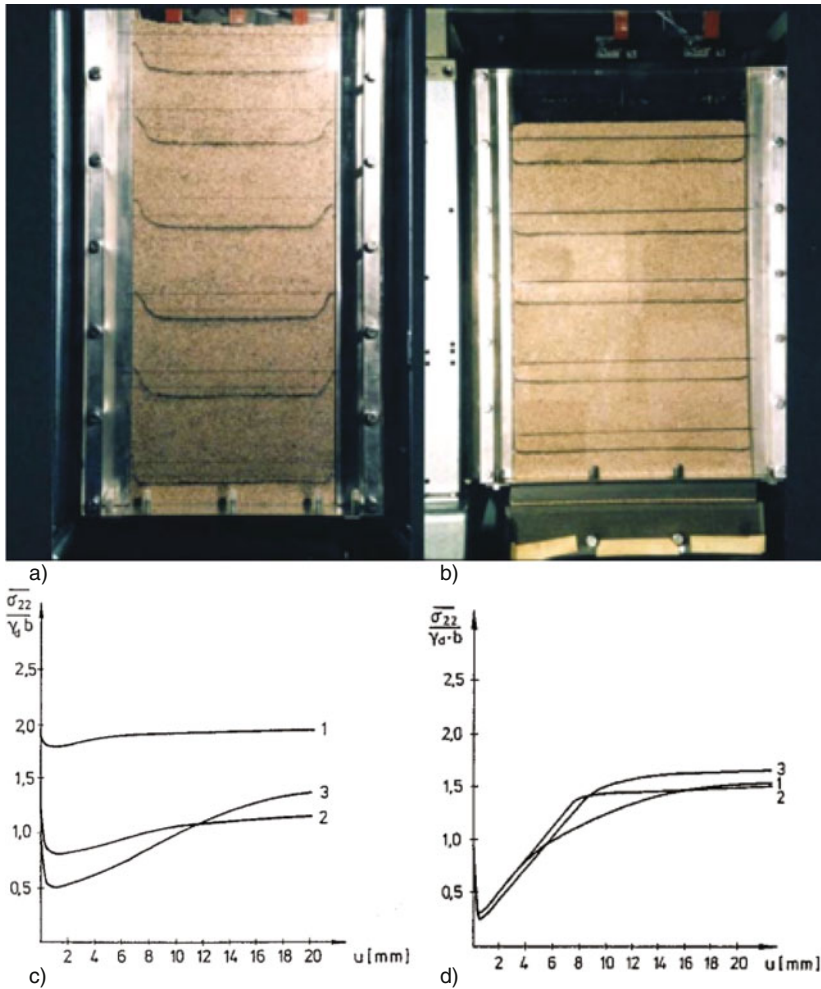


Fig. 13.7.4. Trap door experiments with rough walls (Tejchman 1997): displaced markers in loose (a) and dense sand (b), observed (c) and simulated (d) bottom pressure versus displacement (wall smooth 1, rough 2, very rough 3)

for a collapse, therein c_c denotes the capillary cohesion, $c_c = p_{ce} \tan \varphi$. Other than by Fig. 13.7.1 stress ratios do not enter, and this approach has little in common with block a sliding as by Fig. 12.1.4.

With more overburden than $h = 2d$ only a minor part of the soil collapses into the tunnel, whereas the ground surface settles smoothly, Fig. 13.7.5c. This cannot be captured by sliding bodies, but statical assumptions (d) by Kolymbas (1982) lead again to the supporting pressure by (13.7.3). This estimate may be used for design, but it is neither necessary nor sufficient for stability or collapse, respectively. The bound theorems of perfect plasticity

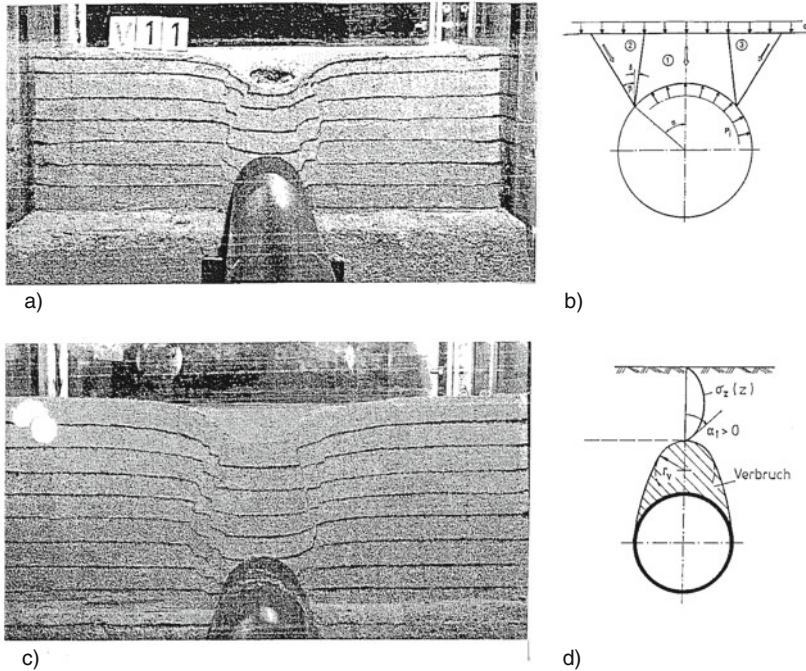


Fig. 13.7.5. Model tests (a, c) and sliding mechanism (b) for tunnels in cohesive sand (Mélix 1987), statical approach (d) by Kolymbas (1982)

(Koiter 1958) are invalid with dry friction. The validation by model tests is debatable as only one sand with a certain void ratio and capillary cohesion was used. Other stabilizations and sequences of excavation than in the model tests are employed for tunnels in granular ground, let alone three-dimensional effects.

Design scenarios could be generated with finite elements, elp or hyp and pore water, Fig. 13.7.6. A flexible shell (a) may be placed (2) on stiff ground (1) and filled laterally (3) and above (4) so that a dead load can be placed anywhere above (5). Leaving aside the initial support for the shell, the state after filling is obtained by imposing gravity with specified relative void ratio r_e and capillary skeleton pressure p_{cs} (cf. Sects. 12.1 and 13.4). Asymmetric filling has to be excluded as then the shell could not stand, p_{cs} can be secured by hydraulic insulation. Placing an eccentric design load and assuming realistic imperfections leads to deformations of shell and free surface which should not exceed tolerance limits. Except for repeated loads (Sect. 13.8) a collapse could thus be excluded, this is not possible with assumed earth pressures and a linear subgrade.

A partly submerged polygonal tube (Fig. 13.7.6b) may be constructed by placing slurry trench walls (1), a jet-grouted inverse arc (2), partial excavation

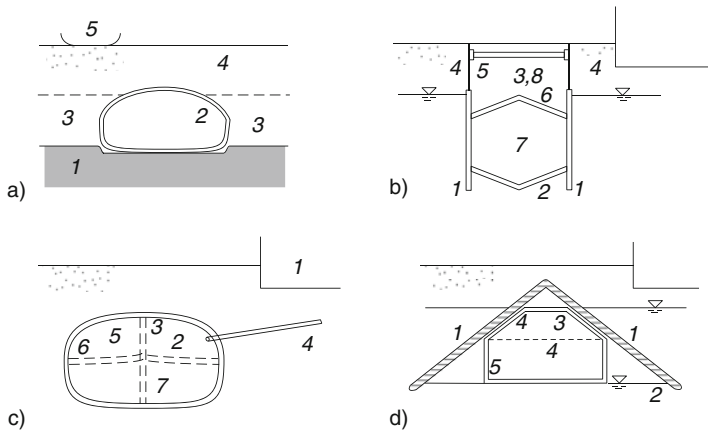


Fig. 13.7.6. Design scenarios for tunnels in psammoid ground: shell with overburden (a), walls with roof and invert (b), section-wise mining (c), mining with grouted or frozen roof (d). Numbers denote the succession

(3) between removable upper walls (4) with struts (b), placing a concrete roof with a ridge (6), excavating below (7) and filling above (8). Starting from the free-field as in Sect. 13.6, this evolution of matter, shape and state could be followed up with realistic imperfections, water tables and surface loads up to acceptable deformations. Whereas the risk can hardly be quantified and controlled with assumed earth pressures and linear subgrade reaction.

Without excavation on top (Fig. 13.7.6c) a tunnel may be constructed near a building (1) in humid and thus cohesive granular ground by mining one quarter (2), placing shotcrete (3) and a row of nails (4), mining (5) and shotcreting (6) the next quarter and likewise the lower half (7). Then the inner concrete ribs are removed, and a further shell is placed if decay of shotcrete and/or access of water cannot be excluded. Variants of this sequence could be simulated up to tolerance limits, now including the neighboured building and a substitute anchor plate as in Sect. 13.6.

Tunnels can be constructed in groundwater near buildings by means of a roof (Fig. 13.7.6d). After its placement (1) by freezing or grouting the water table near the roof may be lowered (2) by air pressure, one half is excavated (3) and concreted (4), then the other half (4, 5). Now the water table inside can rise by lowering the air pressure, the frozen soil may thaw or the grout may decay. All stages could be simulated with times for freezing or grouting, curing and creep and thawing or decay. Combinations of the four examples in Fig. 13.7.6 could also be captured, and other supports and sequences can be taken into account.

Simulation results with *expanders* in psammoid ground are shown in Fig. 13.7.7 (Schauppel 2004). Flexible hoses are placed in boreholes and expanded by grouting with suitable intensity and sequence. In simulations with

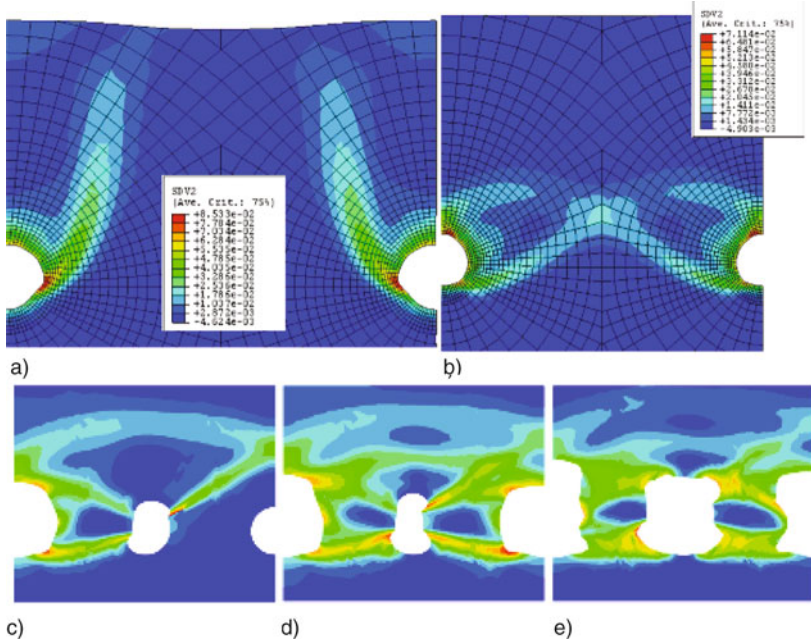


Fig. 13.7.7. Simulated response of initially dense sand to expansion of textile hoses by grouting (Schauppel 2004): simultaneous expansion with big (a) and smaller distance (b); successive expansion of first (c), second (d) and third hose (e). Brighter means more dilated

hyp the expander is an elastic membrane with circular initial shape which gets non-circular by increasing grout pressure. Simultaneous expansion of a row with distance $a = 4d$ leads to separate dilated shear bands and uplift (a). This resembles Fig. 13.7.3c, but the shear bands are thicker due to the element size. With a smaller distance crossing shear bands with dilation arise between simultaneously grouted expanders (b), and the surface is lifted more uniformly.

The ground is less uniformly deformed and more dilated if every third hose is first expanded (Fig. 13.7.7c), then its over next neighbour (d) and finally the one in between (e). These simulations are confirmed by model tests with a centrifuge (Wichmann and Allersma 2004). Dense granular layers could thus be lifted optimally by simultaneous grouting into a row of expanders with not too big distance. Otherwise the layer would be more dilated and less uniformly lifted. With higher initial relative void ratios r_e , alongside with spatial fluctuation of r_e , the skeleton could be densified by alternated grouting of expanders, but then this method would probably not be economical.

Compensation grouting in granular ground can be carried out without expanders by means of pastes, Fig. 13.7.8. The expansion of a cavity by increas-

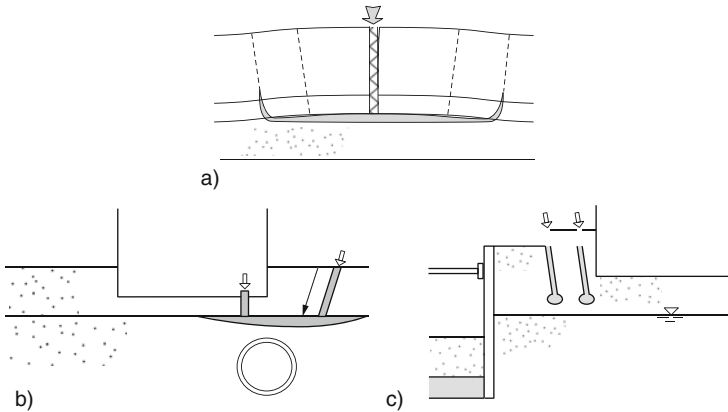


Fig. 13.7.8. Compensation grouting: (a) heave of a layer, (b) heave above tunnel, (c) near a supported open ditch

ing fluid pressure (a) may substitute grouting via a flexible tube with packers. A sufficiently thick paste pushes aside the skeleton (cf. Sect. 10.2) and does not break out. The latter could also be modelled with hyp for the skeleton and v-hyp for the paste, but suitable pastes can only be found by trial experiments. A less permeable layer can be lifted by grouting underneath (a). The grout can break out from the rims of a widened cavity (cf. Fig. 10.2.1). Other than with a passive trap door the bottom pressure can lead to a collapse.

Excluding break-outs, far-field evolutions due to grouting could be captured with hyp or hyp- δ . For instance, scenarios for the compensation of settlements due to tunneling could thus be generated (Fig. 13.7.8b). In a first stage the skeleton near the tunnel can be re-densified by alternating injections, the further expansion can lead to a controlled heave. Settlement and tilt of a building due to a neighboured excavation with a retaining structure can also be compensated (c). The skeleton should first be densified by alternating injections as otherwise the tilt would increase. Monitoring is needed in such cases, but a sufficient control can hardly be achieved without realistic scenarios.

As with structures upon and at granular ground simulations with hyp and hyp- δ can be objective due to driven attractors in the large. State limits in the large, including forced shear localization near cavities, should substitute estimates with hardly defensible statical and kinematical assumptions. The historical element is captured by averages of relative void ratio r_e and simplified construction stages. Due to unknown initial spatial fluctuations displacements and structural forces get better determined with bigger deformations. Pore water effects can be controlled if $r_e > 1$ with $p_w > p_a$ and a loss of p_{cs} by $p_w > p_a$ (Sect. 6.2) are avoided. Critical phenomena, as e.g. roof collapse or break-out, can be avoided with small enough deformations. Asymptotic cycles for repeated reversals will be treated in Sect. 13.8.

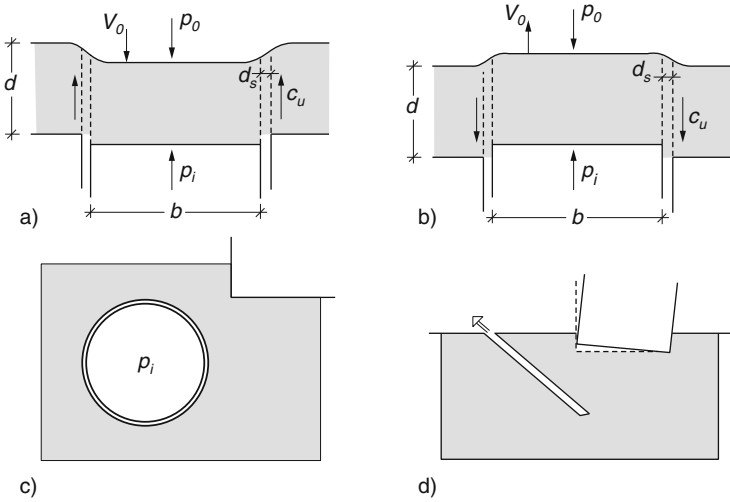


Fig. 13.7.9. Active (a) and passive trap door under peloid (b), tunnel with supporting pressure (c), back-tilting by under-excavation (d)

Turning to saturated *peloids*, the diffusion of pore water around cavities or underground structures may first be left aside, Fig. 13.7.9. One may imagine vertical shear bands above a trap door in the active (a) or passive case (b). Using the cohesion c_u without drainage a limit equilibrium would require the pressure difference

$$p_i - p_o = \gamma d \mp 2c_u d/b \tag{13.7.4}$$

with $-$ for the active and $+$ for the passive case. Assuming a shear zone thickness d_s one can allow for the skeleton viscosity with the viscoplastic relation (12.2.1) and the shearing rate $D = v_o/d_s$. With a low enough initial consolidation ratio, say $p_e/p_s < \text{ca. } 4$, the forced shear zones cannot get very thin (Sect. 8.3), then $d_s \approx 0.1b$ may suffice. With ductility and c_u via a specified v_o (13.7.4) approximates an argotropic isochoric state limit, otherwise a collapse could occur. Equation (13.7.4) may serve as a design estimate for shallow cavities, i.e. $d < \text{ca. } 2b$.

Simple approaches as by (13.7.4) get insufficient for deeper cavities. In an active case (Fig. 13.7.9c) a cylindrical excavation may first be supported by gas pressure p_i , then by a shell. Isochoric deformations during the excavation, creep with constant p_i and subsequent increase of forces in the shell by relaxation of the ground could be simulated with v-elp or v-hyp. This works also for a row of boreholes which are excavated without support in order to re-erect a tilted building (d). In these cases the ground can return to its previous state, but not in case of a cavity with a lighter structure than the excavated soil.

The order of construction stages plays a smaller role than with psammoid ground as its traces dwindle by creep and relaxation. The diffusion of pore water renders possible a wider spectrum of evolutions, all the more with pore

gas. A stiff fissured clay around a tunnel deforms without seepage during and just after construction. Lumps can fall from an unsupported cavity roof after a capillary entry, a hydrophilic supporting fluid can cause swelling and collapse (cf. Sect. 12.4). The pore pressure around an impervious shell returns to far-field values, the system stabilizes by contractant creep of the ground if its relaxation does not destroy the shell. A tunnel with a pervious shell drains the ground and enhances its contractant creep, with low initial consolidation ratio p_e/p_s structures can thus be damaged gradually.

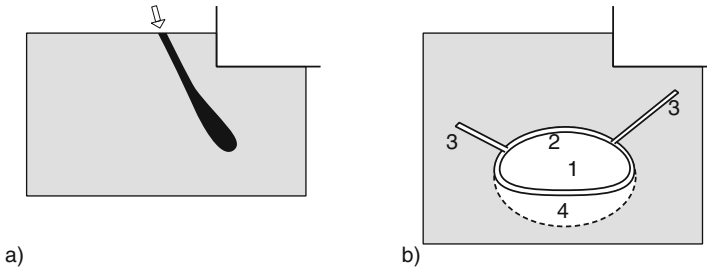


Fig. 13.7.10. Compensation grouting with soft peloid ground (a), tunnelling with anchors (b, numbers for sequence)

Design scenarios could be generated for such cases by v-elp or v-hyp with composite permeability (Sect. 9.2), a fraction of enclosed gas, capillary entry pressure (cf. Sect. 6.3) and relations for the structure and its interfaces. This works also with *compensation grouting* of partly soft ground, Fig. 13.7.10a. Zones with gas bubbles are immediately densified, all the more by alternating injections, in a sandwich ground a rapid diffusion of pore water enhances a subsequent contractant creep. Anchors or nails placed during the construction (b) could be captured as with retaining walls (Fig. 13.6.12). Auxiliary walls or plates installed in the ground near a tunnel via slurry trenches, mixing with cement-lime or jet grouting could also be taken into account, including the curing and the visco-plastic behaviour of such structures. Monitoring and stage-wise adaption are needed in such cases (Peck 1969), but conventional or merely empirical prediction models will not suffice for uncommon situations.

Simulations with v-elp or v-hyp could again be objective due to attractors in the large. These are driven for construction stages as with psammoids, but argotropic and nearly isochoric. For rest intervals during and after construction endogeneous attractors occur due to thermal activation in skeleton and pore water, and also in ductile structures. This should lead to a gradual stabilization with tolerable deformations, spatial fluctuations are less important than for psammoids. Critical phenomena like roof collapse or break-out could occur with delay and can be avoided by keeping deformations tolerable. Asymptotic state cycles for reversals will be treated in Sect. 13.8.

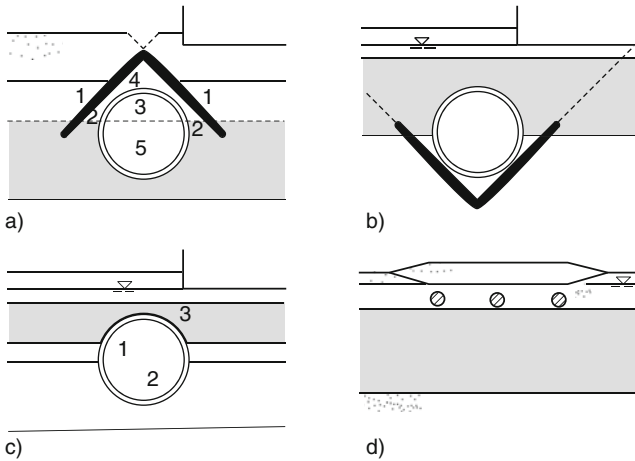


Fig. 13.7.11. Cavities in composite ground: roof (a) and inverted roof (b) against groundwater, tunnel with roof grouting (c), compensation grouting under a dam (d). Numbers for the succession

Extensions to *composite ground* are rather straightforward and may therefore only be indicated by a few examples, Fig. 13.7.11. The lower half of a tunnel may lie in stiff peloid, the upper one in partly submerged dense psammoid with a building on top (a). A roof (1) is first installed by grouting or freezing, the water table under it is lowered (2), the upper half is excavated (3) and gets a provisional shell (4), the lower excavation follows (5), a final shell is installed and the water can rise again. With peloid at the upper part of a tunnel (b) an inverted roof and air pressure can shield the psammoid part. Design scenarios for different construction sequences could be simulated with *elp* and *v-elp* or *hyp* and *v-hyp*, and judged by means of deformation tolerances.

A shield tunnel may be driven into submerged ground with soft layers and neighbored buildings (Fig. 13.7.11c). In a plane-parallel simulation an elastic ring is placed (1), its interior is excavated (2), simultaneously a slit above (3) closes and is widened again by grouting. Excess pore pressures from this operation disappear by diffusion, simultaneously the tunnel rises and is further stressed while the surroundings settle, the rates decrease by densification. Such scenarios can be on the safe side for rapid operations without seepage, and get more realistic with plane-parallelity for long-term evolutions.

A bulge under a dam due to a soft layer may be compensated by filling expanders with cement grout (Fig. 13.7.11d). Similarly as in Fig. 13.7.7 a controlled heave can be achieved by simultaneous expansion with suitable distances and grout masses. The soft layer is deformed without seepage during this operation. Thereafter the dam settles with pore water diffusion due to the added weight. This can be avoided by expanding boreholes with granular

material and by removing pore water simultaneously (Maisch 2000). Simulated variants, also with buildings on top and reacting grouted powders, could help to develop technologies and to support their adaption with monitoring.

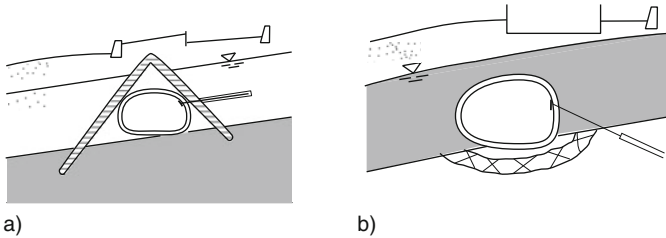


Fig. 13.7.12. Tunnels in composite ground with slope: roof against groundwater (a), creeping peloid (b)

The proposed method could similarly be applied to bigger parts of the earth crust. Design scenarios could thus also be generated for *tunnels in slopes*, Fig. 13.7.12. In case of psammoid with groundwater upon hard peloid (a) one can proceed as outlined with Fig. 13.7.11a. The evolution of shape and state has a downhill trend similarly as in the case of Fig. 13.6.12b. Again back-ties could be incorporated, and usual estimates are inferior. In case of stiff peloid upon dense psammoid on rock with groundwater (b) one could proceed similarly as shown with Fig. 13.7.11b, c. Back-ties can be employed, evolutions are skew as with Fig. 13.6.12. Again the diffusion of pore water may be neglected during and just after construction. In the long run the desirable stabilizing creep with increasing uphill thrust depends on whether the tunnel drains the ground or not.

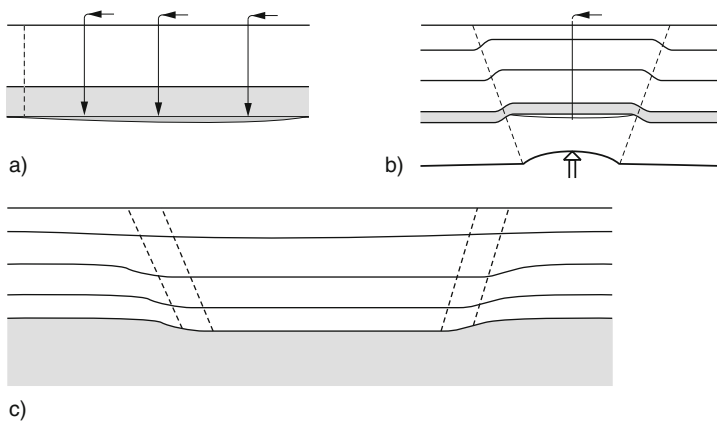


Fig. 13.7.13. Large-scale trap-door problems: (a) grouting, (b) diapir, (c) subsidence

A land subsidence due to the depletion of methane or petrol could be compensated by grouting under a cap layer (Fig. 13.7.13a). A mud-like grout is spread from boreholes, should not break out through shear zones at the rim and hardens by filtration and reactions. Carbon dioxide could be sequestered under a cap seal from a diapir (b). The lifted region is wider above as with a lifted trap door (Fig. 13.7.2c), the fluid should not break through the dilated shear zones. A graben arises above a sinking magma base and is filled by sediments (c). Shear bands as above a lowered trap door (Fig. 13.7.2a) are steeper than normal faults (Fig. 12.6.4). Along them methane could break out and produce mud volcanos (cf. Sect. 16.3). Hypoplastic parameters should be determined for the given range of pressures, stretching rates and temperatures. Cavitation, seismicity and other critical phenomena delimit the predictability (Sect. 16.3).

To *sum up*, evolutions with cavities and underground structures could be captured with elp and v-elp or hyp and v-hyp, pore water coupling and relations for matter placed in the ground should be allowed for. Design scenarios can be generated with attractors in the large, thus simplifications can be justified and delimited. State limits in the large can imply forced shear localizations near the cavity or structure. With peloids stabilizations by densification and pore water diffusion may be interpreted as endogeneous attractors. Collapse and break-out can be avoided by keeping deformations small enough. Such approaches could substitute usual design estimates and can be extended to cases without plane-parallelity.

13.8 SSI with reversals

Plane-parallel evolutions of ground and structures at or in it can be markedly changed by reversals. As with representative soil elements (RSEs, Chaps. 4 and 5) symmetric or non-symmetric *asymptotic cycles* with small or big amplitudes reveal main features. Such periodic attractors in the large are more complex with uneven spatial distributions, structures, pore water and inertia. Some of them are introduced in the sequel, and consequences for examples of previous sections are indicated. The possible use of attractors is indicated with hypoplastic relations, but is not restricted to them (Sects. 4.7 and 5.5).

Consider first *dry psammoids* with *cyclic displacements*, Fig. 13.8.1. A rigid body upon (a) or deeper in (b) granular ground with constant far-field relative void ratio r_e may run through quasi-static displacement cycles. After a transition the ground response gets periodic. This *state cycle field* depends on the shape (mode) and the size (amplitude) of the displacement cycles. It does not depend on the far-field r_e for a shallow embedment (a), whereas for a deep one (b) the average asymptotic skeleton pressure \bar{p}_s is bigger for a lower far-field r_e .

Such attractors could be generated with finite elements by means of elp- α or hyp- δ (Sect. 4.7), and can be represented by ensembles of RSE state cycles

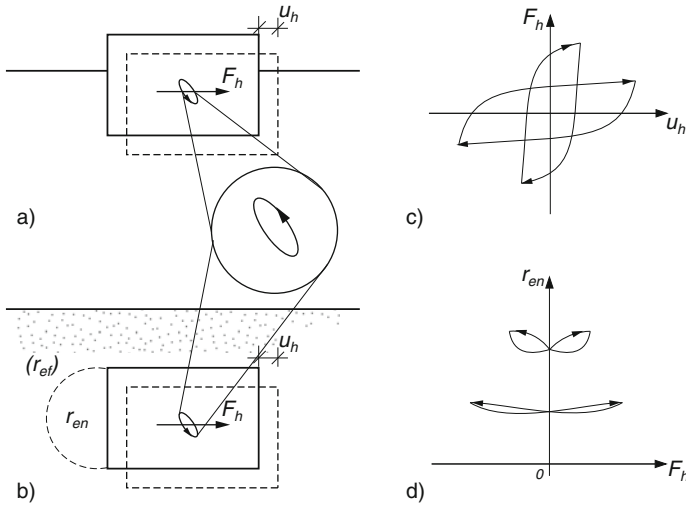


Fig. 13.8.1. Cyclically displaced strip embedded in psammoid (a), asymptotic horizontal driving force versus displacement (b). Buried cyclically displaced strip (c), asymptotic near-field relative void ratio versus driving force (d)

alongside with mode and amplitude. In less comprehensive representations one can plot one component of the resultant force among rigid body and psammoid versus one displacement component (c), or a spatial average of r_e in the near-field (d). These plots are symmetric and reveal an increasing hysteresis for bigger amplitudes (c), and double loops of average state paths (d) as with RSEs (Sect. 4.5). Labels are needed for the far-field r_e in case of a deep embedment. Plots with spatial averages could be obtained with experiments and used for validation.

Plane-parallelity is obtained with in-plane and/or anti-plane displacement and force components (cf. Sect. 12.5). There are four or five different RSE stress components, respectively. *Deformable structures* with shallow or deep embedment can likewise be displaced cyclically past psammoid ground. As with rigid bodies one can specify displacement mode and amplitude of two material points, but now the displacements of other points depend on the deformability of ground and structure. The latter can be elastic and/or plastic, thus stiffness and strength are needed as additional parameters in representations. Fatigue and cracking of solids have to be excluded for getting asymptotic cycles.

The response of dry psammoid ground to *erratic sequences* of displacement cycles of embedded bodies can principally be captured by means of seismohypoplasticity with a granular temperature T_g (s-hyp, Sect. 4.6). Presuming maximal disorder, mode and amplitude are substituted by the input of 'seismic heat'. In case of quasi-static pulsations their average frequency f_c is so low that the system returns to states of rest between the pulses. The attractor for

an erratic energy input implies a zero time-averaged resultant force between solid body and granular ground, this is due to seismic relaxation. The temporal average near-field relative void ratio r_{en} , which is attained by seismic creep up to the asymptote, is lower in case of a lower input of seismic heat-like energy per unit of solid surface and average contact pressure \bar{p}_s . In other words, the pressure-normalized asymptotic skeleton density in the vicinity of the solid body attains an average value which is lower for a higher energy input per cycle.

Model tests could serve to quantify this heuristic approach. A rigid strip with two horizontal degrees of freedom would suffice for the beginning. In-plane and anti-plane shaking should imply the same average energy input per unit of length normal to the cross section plane. This equipartition is necessary for a temperature. It should first be attained by trial and error, then further degrees of freedom could be taken into account. An increasing seismic input could be recognized from an increasing asymptotic r_{en} in the near-field, which could be determined by an averaging geophysical method. A smaller seismic input would lead to a lower asymptotic r_{en} .

Suitable T_g -fields and T_g -dependent parameters could first be adapted by trial and error. This could be done with different skeletons of sufficiently permanent grains (Sect. 7.4), shapes of rigid bodies and degrees of freedom. Thus a seismo-hypoplastic approach could be strengthened beyond RSE-tests before dealing with more complex cases. The T_g -field is principally determined from the balance of seismic energy. The seismodynamics without cumulative displacements resembles the thermodynamics of equilibria, but there are fundamental differences due to the non-conservative granular interactions (Sect. 3.6).

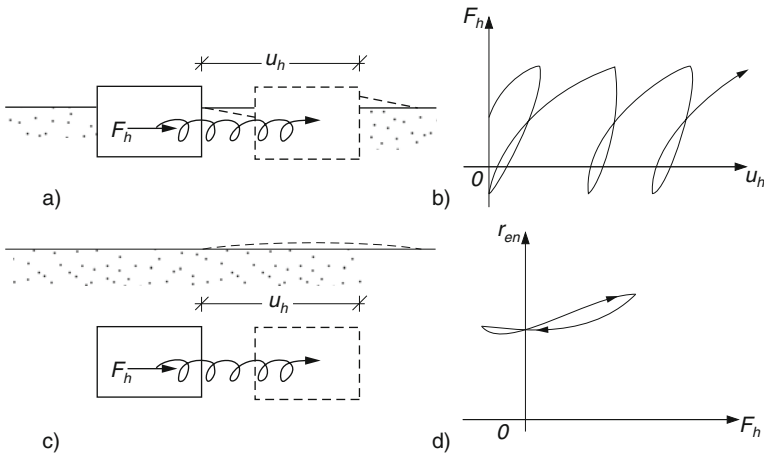


Fig. 13.8.2. Ratcheting of a strip embedded in psammoid (a), horizontal force versus displacement (b). Ratcheting of a buried strip (c), mean relative void ratio of convected near-field versus horizontal force (d)

Ratcheting could also be considered with dry psammoid and horizontal far-field values of surface, Fig. 13.8.2. A rigid strip may be shifted horizontally past (a) or through the ground (b) with super-imposed cyclic displacements. After a transition the response gets periodic and independent of the far-field r_e for a shallow embedment (a), but otherwise (b). This could be calculated with $\text{elp-}\alpha$ or $\text{hyp-}\delta$ and represented by an ensemble of *convected RSE state cycles* plus displacement cycles. Typical ratcheting would appear in a plot of resulting horizontal force F_h versus horizontal displacement (c), but further components should be kept in mind. The attractor can also be represented in an *asymmetric state plot* of F_h vs. r_{en} in the instantaneous vicinity (d). Such plots could be obtained by model tests and used for validation. As with cyclic displacements different degrees of freedom (in- and anti-plane), shapes and deformabilities of structures and granulates should be investigated.

Stationary seismic creep could similarly be achieved by a horizontal average displacement past or through psammoid ground with a horizontal far-field surface. As without average shift the erratic part of displacement should produce an equipartition of the seismic energy input by quasi-static pulsations. Experiments with different input intensities, far-field values of r_e and \bar{p}_s , shapes and deformabilities of solids, degrees of freedom and granular materials could serve to improve the heuristic approach with s-hyp. F_h and the average r_e of the convected vicinity are the main quantities to be captured. Trial and error could again lead to a quantification of the granular temperature T_g and the T_g -dependence of s-hyp parameters. The stationary T_g -field is again determined by the balance of seismic energy.

Similar attractors can be related with a quasi-static *intermittent penetration*, Fig. 13.8.3. In case of a vertical average shift of a rigid wall (a) the vertical resultant force tends to an average \bar{F}_v which increases with depth z independently of the initial embedment (b). The depth-dependent $\bar{F}_v(z)$ is determined by mode and amplitude of superimposed cycles. For a given far-field r_e and z this force is smaller than without reversals as with them the skeleton is more relaxed (cf. Sect. 14.3). F_v is bigger for a lower far-field r_e and for bigger amplitudes. With a sufficient penetration depth and not too big amplitudes the oscillating fraction of the F_v vs. z plot increases so little with

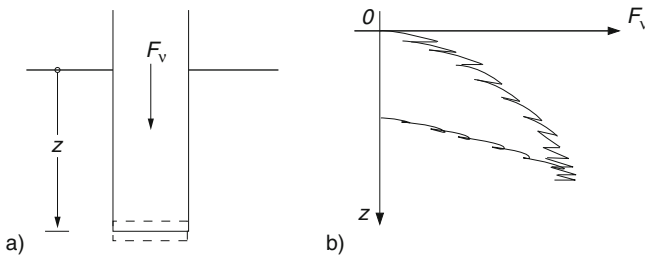


Fig. 13.8.3. Wall penetrating with reversals into psammoid (a), vertical force versus penetration depth (b)

depth that one can identify *quasi-attractors* which depend on depth, mode, amplitude and far-field r_e .

This approach could be extended to deformable solids, e.g. an elastic rod, and to skew penetrations. Anti-plane components could be incorporated as outlined with Fig. 13.8.1. Simulations could be validated and calibrated by model tests with non-abrasive granulates (cf. Sect. 14.4). Erratic non-monotonous displacement fractions could be captured with s-hyp. Model tests and back-analyses of the same kind are recommended before treating the more complex cases indicated in the sequel.

If *forces are imposed* to solid bodies at or in psammoid ground with constant r_e in the far-field attractors could only be attained if the bodies are suitably guided, Fig. 13.8.4. For instance, a rigid wall sinks under a dead load by imposing in-plane and anti-plane horizontal cyclic displacements (a). With constant mode and amplitude the number of cycles per unit of attained depth dN/dz increases with depth z (b). An embedded plate is shifted sideways by a horizontal dead load and lateral cycles (c). If average vertical and anti-plane deviations are prevented a stationary ratcheting can be attained. This implies an asymptotic state cycle in the large for the convected near-field, whereas the penetration implies quasi-attractors as with Fig. 13.8.3. A skew penetration could be captured by a kind of interpolation.

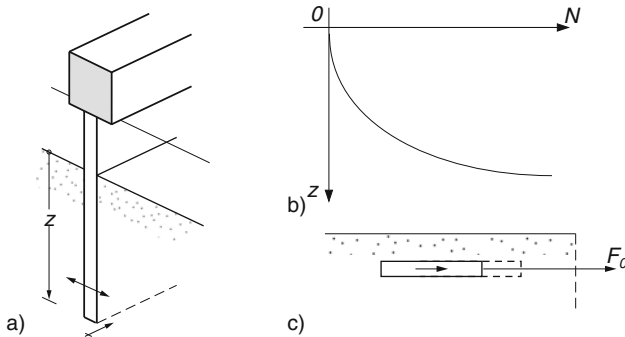


Fig. 13.8.4. Penetration of a cyclically displaced wall into psammoid (a), number of cycles versus depth (b). Ratcheting of a pulled strip in psammoid (c)

A controlled average displacement of solid bodies past granular ground can hardly be achieved without guide. For instance, an embedded strip with horizontal and vertical dead loads rises or sinks gradually when it is shifted by dead loads and load cycles. A slender embedded solid body tilts gradually if it is not suitably shaped and pulled. Erratic cycles could again be captured with s-hyp. The gradual displacement or seismic creep can be stationary (cf. Fig. 13.8.2c), stabilizing (cf. Fig. 13.8.3) or unstable if there is no guide.

Wave effects could be taken into account explicitly. In case of quasi-static pulsations changes of shape and state are propagated by waves, but there are

pauses so that the number of cycles counts, not their frequency. If embedded solid bodies are shaken with higher frequencies f_c the neighbored skeleton cannot rest. In the case of Fig. 13.8.4c a stationary excitation leads to stationary ratcheting with state cycles of the instantaneous vicinity. Calculations with hyp- δ would be more expensive than with plane waves (Sect. 11.4), and cumbersome as the equations tend to get ill-conditioned. Numerical problems should first be overcome for attractors as these represent essentials of system behaviour and could be validated by experiments. Shaking without pauses could also be taken into account (cf. Sect. 14.3). Quasi-attractors are attained which change by increasing depth of penetration. Transitions to quasi-static cases could be investigated by means of excitations with pulses and pauses.

Gradual displacements as in Fig. 13.8.4 can also be achieved with a *shaking base*. A guided wall with a dead load sinks with decreasing rate if the far-field is shaken as without the foreign body (cf. Sect. 12.4). A strip with a horizontal dead load and the same far-field conditions tends to a kind of ratcheting. As with directly excited bodies stable trajectories are only achieved with suitable shapes, guides and tractions.

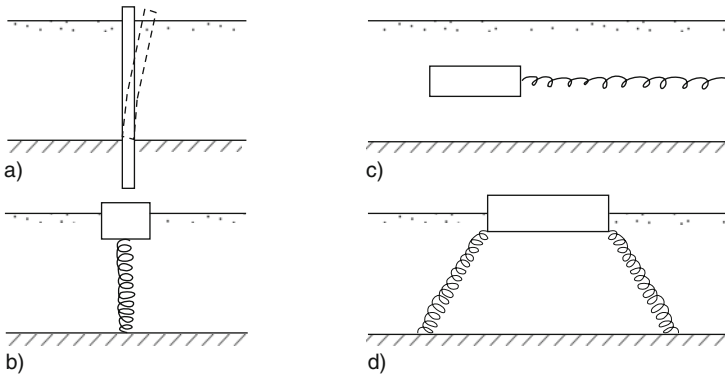


Fig. 13.8.5. Cyclically deformed elastic structures in psammoid: wall (a), embedded strip (b) and buried strip with row of springs (c), strip with two rows of springs (d)

Various asymptotic cycles can be achieved with *embedded elastic bodies*, Fig. 13.8.5. A flexible vertical wall fixed at a solid base may be shaken periodically at its top, or at its base and the lateral far-field boundaries (a). In the asymptote the wall is vertical and the grain skeleton's r_e decreases with depth in the average, details depend on the amplitude. A rigid strip with a horizontal elastic string fixed outside moves laterally by shaking strip or base until the string is relaxed (b). A rigid strip with a vertical string fixed at the base sinks by shaking strip or base until the string is relaxed (c). A flat strip on top of a granular layer, which is fixed to its solid base by two strings, tends to stationary rocking by excitation of strip or base (d). Such attractors could be generated numerically with hyp- δ and by model tests for validation.

Evolutions as indicated by Figs. 13.8.4 and 13.8.5, but with *erratic shaking*, could be captured with s-hyp. Instead of state cycle fields attractors in the large are attained which may be called *seismic state limits*. The excitation is represented by a field of granular temperature T_g , this determines state limits including an entropic pressure p_d (Sect. 4.6). The seismic creep stabilizes by penetration and densification (Fig. 13.8.4b) or gets stationary (c). Seismic creep and relaxation of the skeleton enhance a relaxation of externally fixed elastic structures (Fig. 13.8.5). As with the cases of Figs. 13.8.1, 13.8.2, 13.8.3 and 13.8.4 a heuristic approach with s-hyp could be improved by model tests and trial and error calculations.

Pore water could be taken into account as follows. The hydraulic height h_w of *saturated* skeletons is not affected by pulses and shaking if the skeleton velocity v_s does not exceed ca. $0.1k_f$ by (6.2.12). Pauses between quasi-static pulses suffice for a re-adaption of h_w to the hydraulic boundary conditions. Uplift and seepage forces are hardly influenced by pulses and shaking. During the propagation of waves in the skeleton h_w changes in general as v_s can exceed $0.1 k_f$. The pore water diffusion may be neglected for propagations with

$$v_s \approx \gamma_a c_s > 10^2 k_f \quad . \quad (13.8.1)$$

Therein γ_a denotes shear amplitude and c_s shear wave velocity. This estimate follows from (6.2.11) with $p_{cs} \approx \gamma_w d$ and $v_s \approx \gamma_c c_s$ as with elastic waves for simplification. It is confirmed by Osinov's (2000) calculations (cf. Sect. 11.4).

For repeated wave propagations with $v_s > ca. k_f$ attractors can be influenced by excess pore pressures due to changes of void ratio. In case of $r_e > 1$ the skeleton decays at once so that propagations are only possible in the pore water, the collapse of embedded solid bodies may be related with a strange attractor. For lower void ratios symmetric state cycles as for the cases of Figs. 13.8.1, 13.8.3, 13.8.4 and 13.8.5 are influenced by the ratio $f_c d/k_f$ with characteristic frequency f_c and body size d . Pulsations of h_w , or equivalently of pore pressure p_w , could thus be taken into account in simulations with hyp- δ and in experiments for validation. The average h_w is not influenced by pulsations of void ratio e as without cumulative changes of e there is no average diffusion of pore water. This is also valid for erratic pulses and shaking.

Penetration and ratcheting can involve deviations from the average h_w in the vicinity of gradually shifted solid bodies (cf. Figs. 13.8.2, 13.8.3 and 13.8.4). The convected vicinity is contracted or dilated in the average, this requires an average seepage into or from the far-field and reduces or lifts the average skeleton pressure p_s in the near-field. This hydraulic effect is determined by the ratio \bar{v}_s/k_f (average skeleton velocity \bar{v}_s) and the far-field relative void ratio r_e in addition to $f_c d/k_f$. Quantifications could be achieved again with hyp- δ , s-hyp and model tests.

Unsaturated skeletons could also be captured, though with less precision as the pore gas tends to erratic spatial distributions (Sect. 6.2). Gas bubbles between the grains reduce k_f and enable changes of p_w without diffusion,

otherwise one could proceed as with full saturation. With gas channels p_s increases by the capillary skeleton pressure p_{cs} , otherwise one could work as without pore water. The range in between is rather fuzzy, one should at least catch the phase transition from gas channels to gas inclusions, i.e. from suction to $p_w > p_a$. The suction depends on water content and asymptotic r_e , and can pulsate in case of big amplitudes. Ratcheting and penetration are enhanced by gas inclusions as p_w increases with their pulsation.

Transient interactions of granular ground with structures at or in it may at least be touched by means of some examples from previous sections. Inclined free surfaces can thus be incorporated. Earth pressures and related wall displacements with reversals diverge from those outlined in Sect. 13.1. If a rigid wall is shifted past the ground (cf. Figs. 13.1.1–13.1.8) with quasi-static pulsations the shear localization is less marked than without them (Sect. 8.2), and the average earth pressure is closer to the one at a resting wall. The latter is attained in the average if the wall is shifted cyclically, then the neighboured ground tends to a lower r_e with smaller amplitudes. Pore water effects come into play as outlined above, capillary entry and cracking are less marked with reversals than explained with Figs. 13.1.12, 13.1.12 and 13.1.13.

A wall with a given average force and a slowly pulsating force moves gradually off or into the ground. This kind of seismic creep is more marked if the average force is closer to the active or passive earth pressure E_a or E_p , respectively. The gradual displacement increases with bigger amplitudes and goes over into a collapse if the average force approaches E_a or E_p . Simulations could be carried out with hyp- δ , with a big number of reversals estimates by s-hyp could be more rewarding.

Inertial effects cannot be captured with sliding wedges as these are disintegrated by propagating waves. A few strong impacts could be taken into account by means of hyp- δ , more simplified approaches are not defendable nor needed. Seismic creep and relaxation could be better captured by means of s-hyp in case of many small and rather erratic impacts. This would also work with pore water.

The extension to *shallow rigid strips* (cf. Sect. 13.3) is straightforward. Sliding wedges as in Figs. 13.3.1a, 13.3.2 and 13.3.6a get less realistic by reversals with increasing amplitude. Transitions to the attractors outlined with Figs. 13.8.2 and 13.8.3 are less indeterminate with reversals as with them unknown initial spatial fluctuations are swept out more easily than by monotonous punching. A toppling collapse as sketched in Fig. 13.3.6d is enhanced by reversals. Hydraulic and inertial effects could be taken into account as outlined above for walls.

Rigid structures at psammoid ground (cf. Sect. 13.4) can float gradually due to repeated reversals. Retaining walls as in Figs. 13.4.7, 13.4.8, 13.4.9 and 13.4.11 are shifted and tilted by repeated changes of groundwater table or uphill surcharge. A trough as in Fig. 13.4.10 rises by repeated changes of water table, its pressures at the ground get independent of hardly known initial fluctuations. Few reversals including hydraulic effects could be captured with

hyp- δ . s-hyp could be more rewarding for a big number, seismic activation of creep and relaxation works similarly as thermal activation in the cases indicated with Figs. 13.4.2, 13.4.3 and 13.4.5.

Reversals can lead to a plethora of mechanisms with *deformable structures* at and in granular ground from the simple case of Fig. 13.8.5 to the examples in Sects. 13.5, 13.6 and 13.7. Structures on top as in Figs. 13.3.3 and 13.3.4 experience a kind of creep and relaxation by repeated actions. This can be better captured by hyp- δ or s-hyp than by merely empirical estimates. This is also valid for retaining structures as in Figs. 13.5.8, 13.5.9, 13.5.10, and 13.6.10. Upper and lower pressures along underground structures are lower and higher, respectively, than for monotonous evolutions as outlined with Figs. 13.7.1, 13.7.2, 13.7.3 and 13.7.4. Cavities with pressure support can collapse easier after reversals than outlined with Figs. 13.7.5 and 13.7.6, and break out earlier than shown with Figs. 13.7.7 and 13.7.12. Cavities with supporting structures which are lighter than the excavated ground rise gradually. The complexity of such problems should not be underestimated, so much the more attractors in the large can be of use.

Interactions of structures and *peloid ground* with reversals are additionally influenced by thermally activated skeleton viscosity and pore water diffusion. Due to the low permeability this diffusion can only occur in long enough pauses. Without these the ground under or around a rigid structure as in Fig. 13.8.1 tends to an argotropic symmetric state cycle in the large if the structure is cyclically displaced. This could be simulated by v-hyp or v-hyp- δ and observed in model tests. Erratic displacements without shift could principally be captured by means of a seismic temperature T_s (Sect. 5.5). Asymmetric argotropic state cycles could be obtained for ratcheting as shown with Fig. 13.8.2. Similarly as in Fig. 13.8.4c seismically *and* thermally activated stationary creep could be captured by means of T_s . A gradual penetration leads to argotropic quasi-attractors. Elastic structures embedded in undrained peloid as in Fig. 13.8.5 get relaxed together with its vicinity by repeated reversals or impacts. Model tests should be carried out for validation (cf. Sects. 14.3 and 15.5).

Reversals with diffusion of pore water would require $v_s < \text{ca. } 0.1 k_f$ by (6.2.12), this can often be excluded with the low permeability k_f of peloids. Excess pore pressures due to reversals disappear by diffusion in resting times $t \geq t_d$ by (11.3.1). A small fraction of minute gas bubbles may be taken into account by increasing the compressibility of the pore fluid. Capillary effects in peloids (Sect. 6.3) are left aside as even with full saturation models for peloids with several reversals are still in the make. It would be premature therefore to discuss examples of previous sections with composite ground.

To *sum up*, interactions of structures and ground with several reversals can principally be captured by attractors in the large. Metastable systems can gradually attain a collapse with slumping, toppling, break-in or break-out. Otherwise displacement cycles or ratcheting of embedded bodies lead to symmetric or skew-symmetric state cycles, respectively, of the ground. These

are argotropic and preferably isochoric for peloids. They could be simulated with hyp- δ or v-hyp- δ and observed in model tests for validation. Inertial effects with wave propagations could also be taken into account. Erratic pulses or shaking could be captured by s-hyp, this requires model tests for matching. Seismically activated creep and relaxation can principally be captured by a kind of seismic temperature. Attractors could also be used to check and quantify other than hypoplastic models.

AXI-SYMMETRIC EVOLUTIONS

Axi-symmetric evolutions can occur in the lab and in situ, they are important for validation, design and technologies. Using again attractors in the large, this chapter is less a report on successful applications than an outline of what could further be done. Axial symmetry can arise with suitable initial and boundary conditions and can get lost with bifurcations towards critical phenomena. Axi-symmetric solutions will also serve as a support of interpolations for evolutions with two symmetry planes (Sects. 15.1 and 15.2).

Samples in triaxial tests need not remain uniform, but can exhibit axial symmetry (Sect. 14.1). A loss of uniformity can only be avoided with certain initial and boundary conditions. The symmetry can get lost spontaneously by diffuse and localized bifurcations. Simulations are recommended for improved control and evaluation. Fill and excavation are instructive in the lab and practically important in situ (Sect. 14.2). Ring structures from subsidence and diapirs are also treated in Sect. 14.2.

Penetrations (Sect. 14.3) were successfully modelled with hypoplastic relations. Such approaches are proposed for the evaluation of probing and the control of driving in situ. Axi-symmetric evolutions can also occur if piles are pushed down or pulled up (Sect. 14.4). Although the state after installation is never fully known the proposed attractors could help to improve loading tests and design models.

Silos are often axi-symmetric, and evolutions of their fill can be so. The outline in Sect. 14.5 starts with Janssen's (1895) theory and ends with silo music and quake. Such critical phenomena with inertial effects are still at best qualitatively understood, the proposed models are grossly simplified. Evolutions with torsion are geotechnically more important, but except for one successful model test Sect. 14.6 is rather an outlook. It may help to extend the range of application, to get further validations and to improve technologies.

14.1 Triaxial tests

Axial symmetry can be achieved in so-called triaxial tests if the sample and its boundary conditions have this property. Without gravity the desired homogeneity of state can get lost by forced or spontaneous bulging or necking and by drainage. Shear localization can also lead to a loss of axial symmetry, whereas reversals can improve the uniformity. Simulations could help to conceive and evaluate triaxial tests, and may also serve as exercises before dealing with more complex problems.

Dry psammoid samples can initially have a fairly uniform void ratio e and an isotropic pressure p_s by pluviation and vacuum if they are confined by a membrane and two plates. If these are rough (Fig. 14.1.1) the sample gets bulged by axial shortening (a) and necked by stretching (b). This gradual loss of uniformity cannot be reduced in the middle third by increasing the slenderness h/d as thus a loss of uniformity by spontaneous bulging or necking

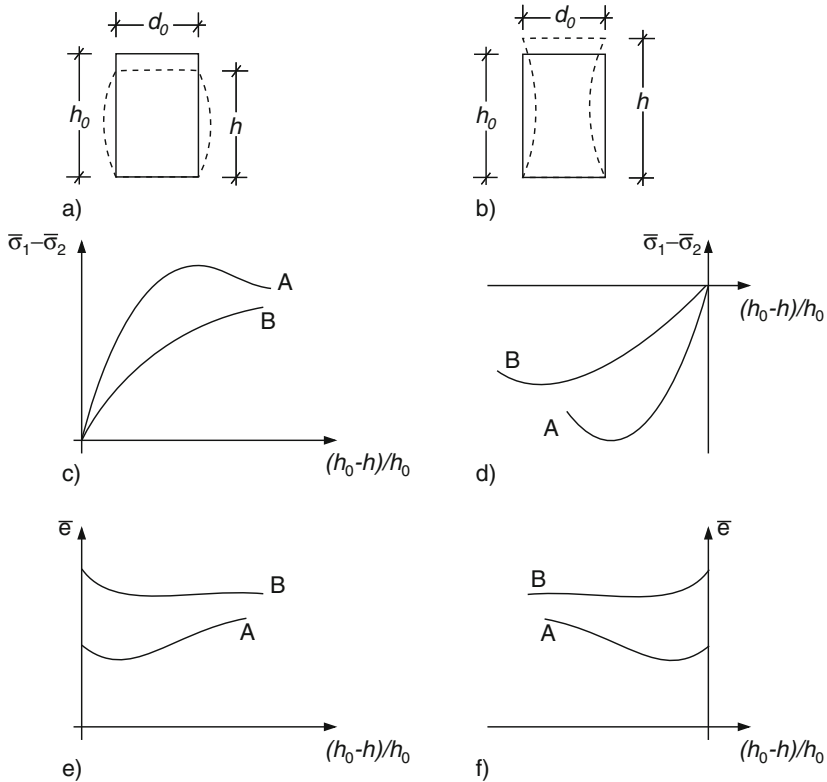


Fig. 14.1.1. Evolution of dry psammoid samples with rough plates and membrane: axial shortening (a) and lengthening (b), mean stress deviator versus axial shortening (c) and lengthening (d), same for mean void ratio (e, f)

(diffuse bifurcation) is enhanced. With constant mean pressure p_s the average deviator $\bar{\sigma}_1 - \bar{\sigma}_2$ attains a peak by shortening (c) in case of a low initial relative void ratio r_e (A), but not otherwise (B). Stretching leads to a peak in both cases (d). The average void ratio \bar{e} indicates less initial contraction and more subsequent dilation by shortening (e) and stretching (f) for a low (A) than for a higher initial r_e (B).

Even averages for the middle third should not be evaluated with mean values because the sample cannot remain uniform as required for RSEs (Sect. 2.2). In finite element simulations with *elp* or *hyp* the skeleton has a pressure $p_g - p_a$ at the elastic membrane, is fixed at one plate and deformed via the opposite one. This leads to evolutions as shown in Fig. 14.1.1 and can reveal more details than experiments. One could also work with spatial fluctuations of stress (force-roughness, Sects. 4.3 and 8.2) and of r_e . Back-analyses of this kind could clarify the range of validity if the experiments are good enough. Shear localization and diffuse loss of axial symmetry cannot thus be captured, however, both will be discussed further below.

A squat sample remains more uniform with smooth plates and central fixing points. With membrane and grease at both plates the adjacent skeleton can have nearly the same r_e as farther off, but it is looser along a smooth hard plate. Even with perfect smoothness the sample gets bulged at the endplates by shortening (e.g. Wu 1992) and necked by stretching. Other than at rough plates the sample diameter is nowhere fixed. A loss of uniformity can occur by a diffuse bifurcation, and can evolve gradually if the sample has spatial fluctuations. Simulations with them and *elp*, *elp- α* , *hyp* or *hyp- δ* could lead to similar evolutions of average stress and void ratio as shown in Fig. 14.1.1. Results depend on the slenderness h/d , deviate from the ones with rough plates and can serve for validation.

A *loss of axial symmetry* can occur without localization if slender samples are shortened. A kind of buckling could also be obtained by simulations with *elp* or *hyp* and initial fluctuations of e if axial symmetry is no more assumed. Desrues et al. (1996) worked with dry sand and vacuum, samples with a uniform grain size $d_g \approx 0.3$ mm had an initial relative void ratio $r_e \approx 0.2$ or 0.8 and $d = h = 0.1$ m. Taking plates with membranes and lubrication, the samples with $r_{e0} \approx 0.8$ (loose) remained uniform after shortening, $\sigma_1 - \sigma_3$ and e attained a plateau which indicates a critical state. The density field was monitored with X-rays. Samples with $r_e \approx 0.2$ (dense) and rough plates were bulged by shortening and exhibited dilation patterns. A horizontal section near one plate (Fig. 14.1.2a) shows radial *shear bands* in an outer ring and a dilated core. At mid-height (b) the radial bands are longer, and a wider core is dilated more uniformly. The void ratios in the bands attain critical values, the lower average \bar{e} evolves as in Fig. 14.1.1e(A).

Alshibli et al. (2000) made similar observations with X-ray computed tomography including vertical sections. Conical bands arose near the plates (Fig. 14.1.2c), off the plates the dilation was small (d). Deman (1975) detected similar cones with rough endplates by means of X-rays and lead shot markers,

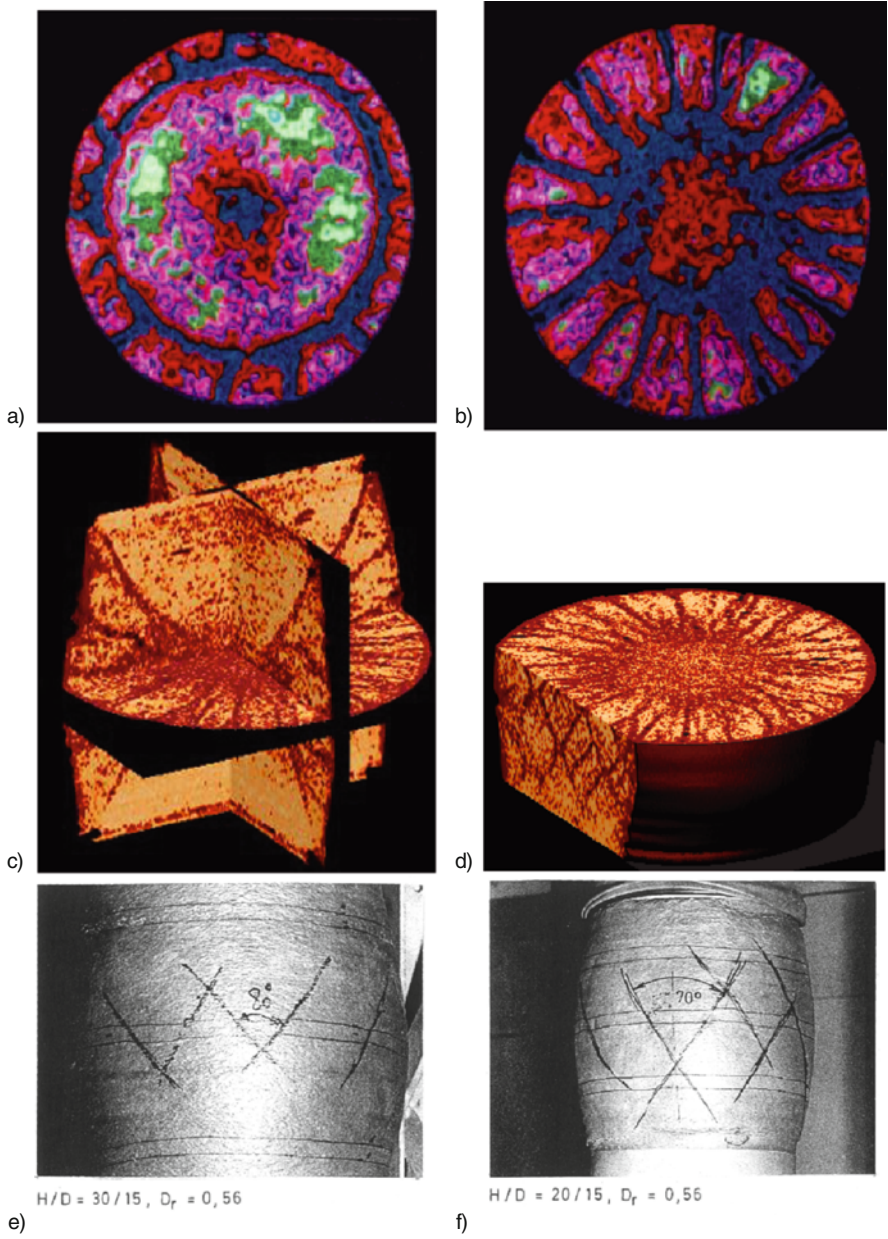


Fig. 14.1.2. Shear band patterns of dry sand samples in triaxial tests : X-ray cross sections (Desrues et al. 1996) near an endplate (a) and near the middle (b), multiple sections (Alshibli et al. 2000) near the middle (c, d); deformed membranes with marked bands (Demman 1975), sample slender (e) and squatter (f)

and noticed shear bands at the membrane. With $r_e \approx 0.5$ and $h/d = 0.2/0.15$ m initially (Fig. 14.1.2e) the pattern at the bulge was similar as with $r_e \approx 0.2$ and $h/d = 0.4/0.15$ (f). How does this suit to the tomographic pictures?

It appears that two families of helical shear bands arise outside of less deformed conical zones. In the course of shortening the axial symmetry goes over into a $2\pi/n$ -symmetry with $n \approx 12$ and 24. This successive pattern formation could principally be captured with polar quantities (Sect. 8.2), thus a strange attractor could be established. A loss of axial symmetry by the dominance of a single shear band could likewise be investigated, and also a collapse with an axial dead load. Bulging and necking with smooth endplates were first described by Roscoe (1970), he concluded that an evaluation of triaxial test results by assuming uniformity can be misleading.

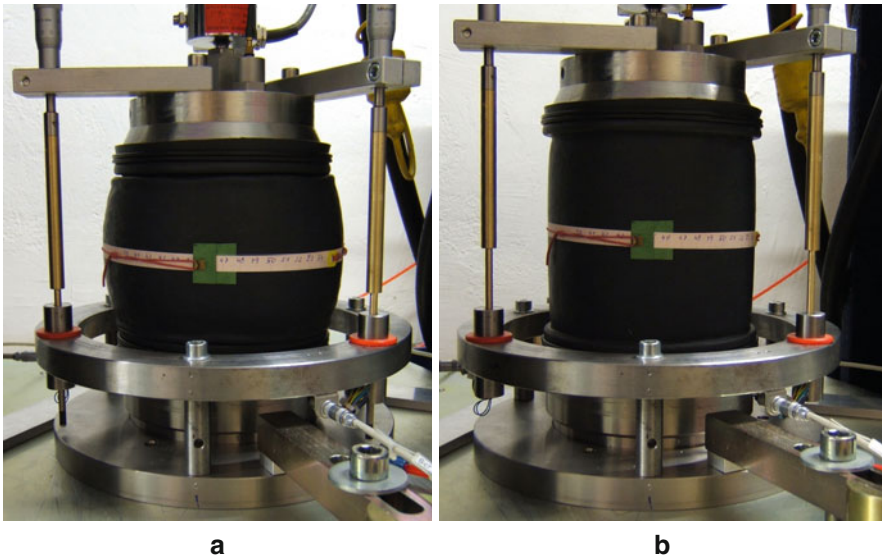


Fig. 14.1.3. Sample of dry corundum granulate with vacuum (courtesy H. Wienbroer) beyond a peak (a), and after stretching with reversals (b)

Reversals can reduce and even compensate the loss of uniformity. Huber and Wienbroer (2005) worked with a corundum granulate to avoid abrasion and with $h = d = 0.1$ m, and teflon membranes at the plates to reduce bulging and necking, Fig. 14.1.3. The radial pressure was kept constant at 50 kPa by vacuum. After an increase of the axial force the sample bulged suddenly and stabilized afterwards (a). A reduction of the axial force with small added reversals removed the bulge almost completely (b). The associated plot of $\sigma_1 - \sigma_2$ vs. ε_1 was used in Sect. 4.6 to introduce seismically activated creep. It appears that this can sweep out emerging shear bands (Gudehus and Nübel 2004) and can re-shape bulged samples. Back-analyses with variants of $\text{elp-}\alpha$

and hyp- δ could clarify their range of validity, and could help to understand asymptotic cycles in the large.

Water-saturated psammoid samples can exhibit a similar behavior as dry ones if they are freely drained. The pore water pressure p_w should be high enough to avoid gas bubbles and cavitation (Sect. 6.2). Higher skeleton pressures $p_s = p - p_w$ than with vacuum are achieved with higher cell pressures p . Gradients of p_w get negligible by keeping the stretching rate v_o/d below the bound (6.2.12). Therein d is the sample size, this presumes drainage along the sample surface. If the sample is drained by central filters in the plates the threshold of v_o is lower, and the simple estimate (6.2.12) can no more be applied.

Without drainage the total volume of a saturated sample is constant, but this does not exclude local seepage. Very loose samples (i.e. $r_e > 1$) can hardly be controlled as they collapse with bulging or necking by skeleton decay. Loose samples with $h \leq d$ and smooth plates can uniformly attain a lower than critical stress obliquity ($\tan \psi_s < \tan \varphi_c$, Sect. 2.6). After this peak of $\tan \psi_s$ the evolution goes on with bulging or necking. Such bifurcations could be simulated with elp or hyp and $e = \text{const}$ by means of density fluctuations in order to reveal the range of validity.

Shear localization without overall drainage was not observed in triaxial tests with sand as in biaxial ones (Sect. 8.2), but can likewise occur. With contractant skeletons, say $r_e \geq \text{ca. } 0.8$, shear bands are widened by pore water diffusion and not marked therefore. Skeletons with lower r_e dilate in bands which get narrower by taking up water from the vicinity. Patterns can arise as shown in Fig. 14.1.2, and could principally be observed and simulated by means of p-hyp (Sect. 8.2) with seepage. Evolutions with partial drainage could likewise be simulated, but the experimental observation of non-uniform pore pressures p_w as desirable for validation is difficult. Reversals would sweep out localizations, but they enhance diffuse bifurcations as p_w increases. Triaxial test results with saturation should not be evaluated by simply assuming uniformity as for RSEs, this has to be justified in exceptional cases.

Triaxial tests with psammoid samples get more complex by gas inclusions (Sect. 6.2). Gas bubbles between the grains make the pore fluid compressible so that the void ratio can change without seepage. Cavitation occurs if $p_w = 0$ is attained. Humid skeletons with gas channels can be looser than critical, and dense ones can get cracks. Gas pockets are irregular and exclude suction, i.e. they have $p_g \approx p_w > p_a$. Evolutions with gas inclusions could principally be observed in experiments and simulated with elp or hyp and relations for the pore fluid, this could deepen the understanding.

Inevitable non-uniformities of *peloid* samples in triaxial tests were not as often reported. Rendulic (1937) worked with saturated remoulded kaolin samples with $h/d = 8/5$ cm initially, an axial sand drain of 0.8 cm diameter and rough plates, Fig. 14.1.4. Keeping the radial pressure σ_2 constant, he changed the average axial stress $\bar{\sigma}_2$ slowly and waited in each step until the

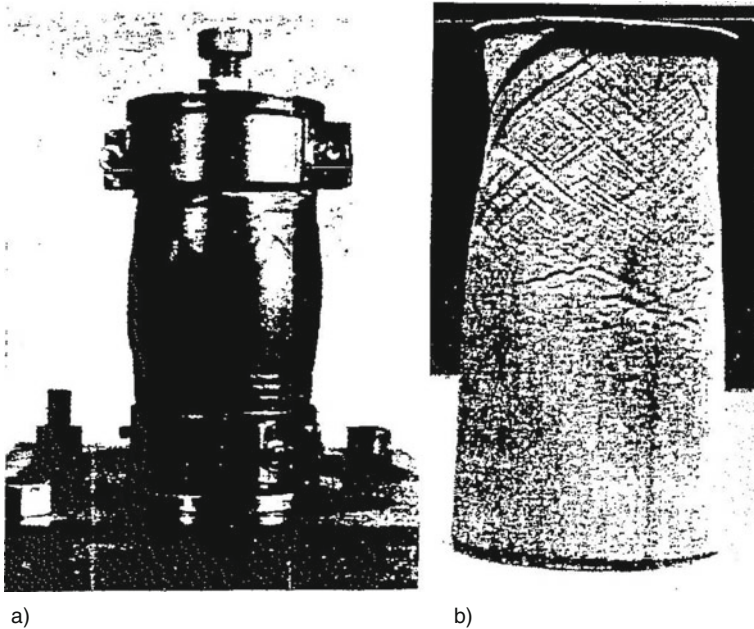


Fig. 14.1.4. Clay samples after experiments (Rendulic 1937) with axial shortening (a) and extension (b)

sample nearly attained a state of rest. With axial shortening the sample bulged (a) so that $\bar{\sigma}_1$ could no more be increased. With axial stretching the sample got a neck (b), $\bar{\sigma}_1 - \bar{\sigma}_2$ could no more be decreased and two families of shear bands appeared at the membrane.

Hvorslev (1937) shortened cylindrical clay samples without a membrane so that the skeleton was only kept by suction. Afterwards the sample was dried and cut, Fig. 14.1.5. It had a bulge and exhibited one marked and one less marked shear band. Slightly different bulges and shear bands were observed with samples which had likewise been consolidated without lateral strain, but with other orientations relative to the sample axis. Rendulic could have produced similar shear bands with his tests, but they are not visible in Fig. 14.1.4a.

Hicher and Wahyudi (1994) shortened samples of kaolin and bentonite without or with drainage after isotropic normal consolidation ($OCR=1$) or overconsolidation ($OCR=10$). Lubricated plates had the same diameter as the sample so that this bulged with any h/d , but the shearing localized only for $h/d > ca. 0.6$. Axial cuts after tests with drainage and $h/d = 2$ initially exhibited shear bands with non-uniform water contents. With $OCR=1$ at the onset the clay was denser in a shear band than outside, with $OCR=10$ it dilated in two bands. Bulging and localization were enhanced by squeezing around the plates. X-ray tomographs were made after the test without

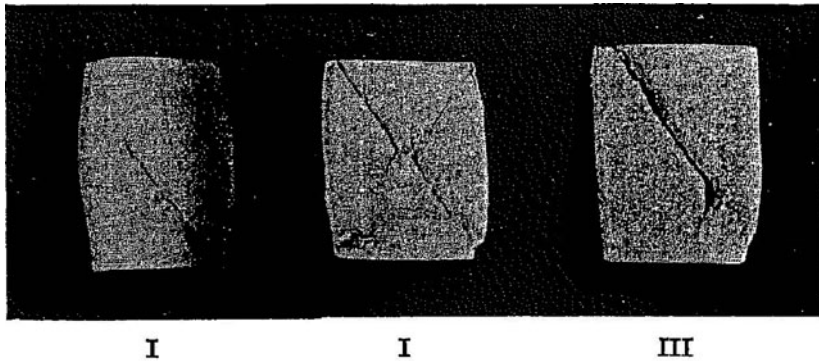


Fig. 14.1.5. Moderately plastic clay samples with suction after unconfined shortening (Hvorslev 1937); previous uniaxial consolidation in the same direction (I), differing by 45° (II) and by 90° (III)

subsequent seepage and cutting. With $OCR=1$ and closed drainage a localized contraction could hardly be seen. This means nearly isochoric shearing with increasing band thickness due to excess pore pressure and seepage into the vicinity (Sect. 8.3). With $OCR=10$ and open drainage the dilation in two bands was more marked. This is due to suction in the bands and seepage towards them so that they got narrower. They got wider with further axial shortening, this can be attributed to punching by the plates. Optical microscopy of cuts revealed narrower bands for $OCR=10$ than for $OCR=1$.

Rübel (2010) carried out experiments with axial shortening of paraffin samples between smooth plates with different rates D (Fig. 8.1.6). For $D < 10 \text{ s}^{-1}$ the sample remained uniform, its response was viscoplastic and ductile as introduced with Fig. 3.1.1a. For $D \approx 10 \text{ s}^{-1}$ two families of shear bands arose, the resistance was bigger and slightly brittle. For $D \approx 10 \text{ s}^{-1}$ the sample was split axially and more brittle. Paraffin is a kind of peloid with polymer particles and oil as pore fluid so that the viscosity is more pronounced and the seepage is slower than with clays. For low enough constant D an argotropic critical state could be attained with the same rate of aggregation and disaggregation. For higher D the then harder particles cause a dilation of the skeleton, but this is confined by the low permeability (Sect. 8.3). For very high D the elevated suction leads to cavitation (Sect. 8.4).

Rübel (2010) worked also with clay minerals and water. Bentonite with water was consolidated uni-axially under 12MPa, cut to $d = h = 8 \text{ cm}$, decompressed to 8 MPa and axially shortened via smooth plates without drainage with $\sigma_2 = 8 \text{ MPa}$ and $D = \text{s}^{-1}$ (Fig. 14.1.6). The sample remained apparently cylindrical up to a slight peak of $\sigma_1 - \sigma_2$ vs. ε_1 . The dismantled sample could be decomposed by hand and revealed a pattern of shear bands (a). One half of a radial pattern appeared at the exposed top (b). Such patterns are typical for stiff fissured clays, these can thus be reconstituted. Capillary entry and cracks occurred after decompression as shear bands and swelling reduced

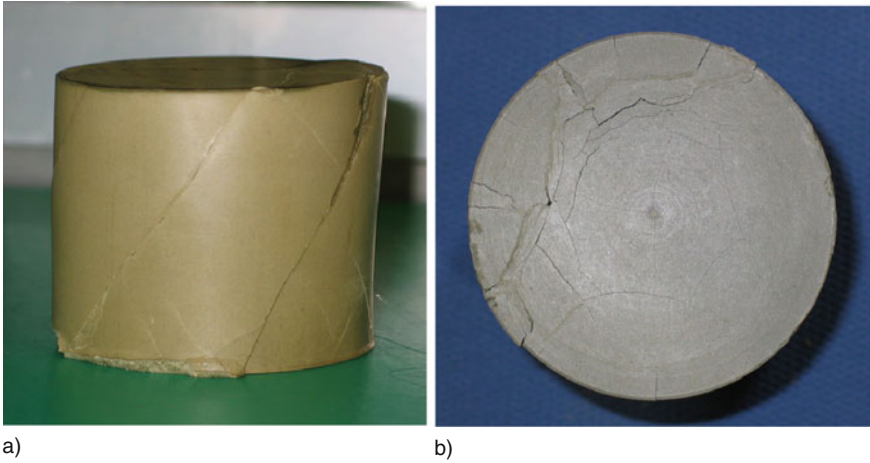


Fig. 14.1.6. Dismantled bentonite sample (Rübel 2010) with shear bands after a triaxial test (a), same from above (b)

the capillary entry pressure (Sect. 6.3). Thus the sample was no more kept together by suction as after the decompression.

In further tests Rübel (2010) consolidated bentonite samples by compressing a slightly humid powder with 150 MPa. Full saturation was attained, this can be concluded from the final stiffness which would be lower with enclosed gas. The decompressed sample (Fig. 14.1.7a) had a suction $-p_w \approx 50$ MPa, this is at equilibrium with vapor by (6.1.5) for a relative humidity $\psi_w \approx 0.5$. A capillary entry would not occur by (6.1.1) with a gap size $d \approx 2$ nm, this is

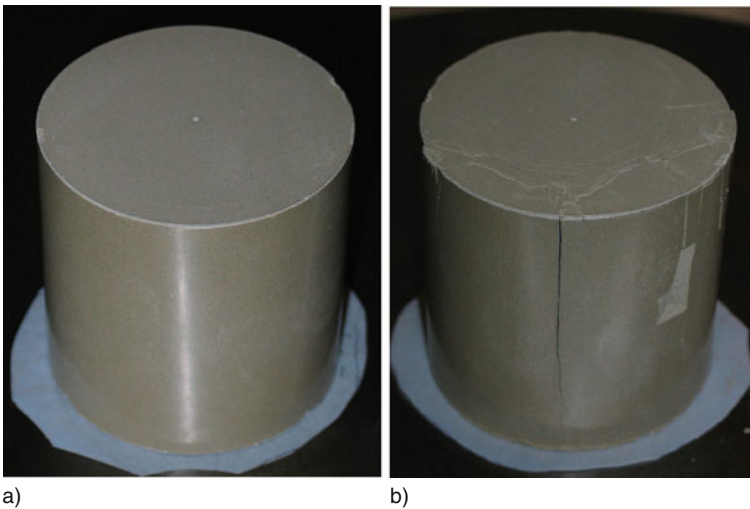


Fig. 14.1.7. Extremely precompressed bentonite sample (Rübel 2010) after decompression (a) and split by axial shortening (b)

about the thickness of layer silicates. To my knowledge a higher suction was nowhere reported. Uniaxial shortening afterwards with $D \approx 10^{-5} \text{ s}^{-1}$ led to a marked peak of σ_1 vs. ε_1 and to axial splitting (b). This cavitation occurred as the extreme suction got impossible in widening pores.

Before turning to back-analyses a physical interpretation of the findings presented with Figs. 14.1.4, 14.1.5, 14.1.6 and 14.1.7 may be added. Composition and state of saturated peloid samples may be uniform at the onset. *Without seepage* the uniformity gets evidently lost by axial shortening or stretching if the plates are not smooth or not big enough. Otherwise bulging or necking occurs with big enough slenderness h/d and relative deviator $|\sigma_1 - \sigma_2|/p_{eo}$ (initial equivalent pressure p_{eo}). During such diffuse bifurcations spatial fluctuations of state grow spontaneously if h/d and $|\sigma_1 - \sigma_2|/p_{eo}$ are critical, Fig. 14.1.8. A uniformly continued evolution gets metastable, i.e. bulging (a) or necking (b) releases more rapidly kinetic energy than a uniform continuation. This implies a peak in the plot of $\sigma_1 - \sigma_2$ vs. $h - h_o$ (c) wherein h_o denotes the initial height, σ_2 the confining pressure and $\bar{\sigma}_1 = 4F_1/\pi d_o^2$ the nominal axial pressure.

Still with closed drainage, smooth plates and central fixing points, the radial symmetry can get lost if such continuations with constant shortening or stretching rate \dot{h}/h release more rapidly kinetic energy, Fig. 14.1.9. A slen-

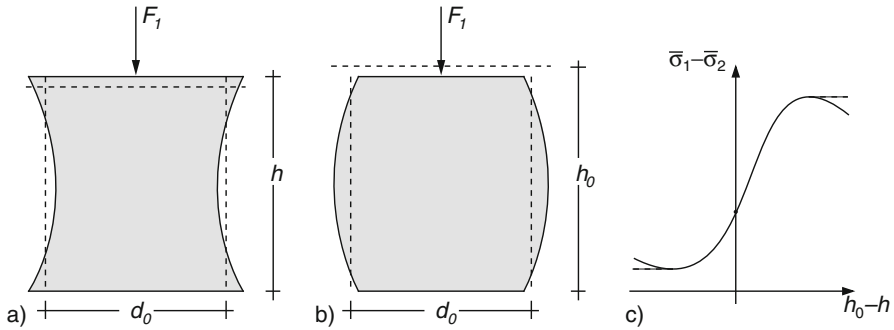


Fig. 14.1.8. Diffuse bifurcation of peloid samples with extension (a) and shortening (b), apparent stress-strain curves (c)

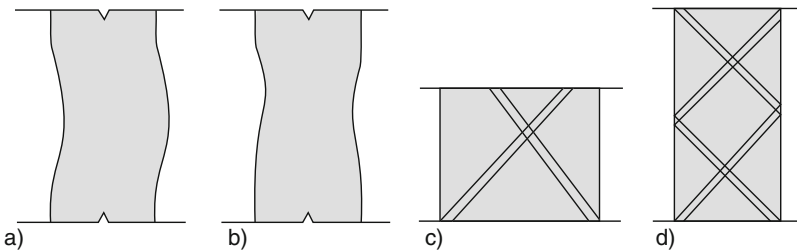


Fig. 14.1.9. Bifurcation of peloid samples with buckling (a), skew necking (b) and shear bands (c, d)

der sample can buckle by shortening (a), stretching can lead to asymmetric necking at any height (b, cf. Fig. 14.1.4b). Shortening with $h \approx d$ can lead to two crossing plane shear bands (c). A single band occurs if the sample is squeezed over the rim of a too small plate. Stretching with $h \approx 2d$ could lead to two pairs of crossing shear bands (d). Such shear localizations require a low enough consolidation ratio p_e/p_s so that the skeleton pressure is reduced by isochoric shearing (Sect. 8.3). Bands can arise alongside with bulging or necking and are enhanced by rough or small plates.

The spectrum of bifurcations is wider *with seepage*. Without drainage pore water can be redistributed in the sample, in particular during a shear localization (Sect. 8.3), so that the time for pore water diffusion plays a role in addition to the argotropy of the skeleton. With a low initial consolidation ratio, say $p_e/p_s < \text{ca. } 4$, the pore water pressure p_w increases in a shear zone so that this releases water and gets wider. Otherwise, say for $p_e > p_s > \text{ca. } 6$, p_w decreases in a shear band so that this takes up water and gets narrower. The threshold $p_e/p_s \approx 5$ is not precise, therefore it may also hold with the overconsolidation ratio *OCR* although this is not the same as p_e/p_s (Sect. 3.2). Shear bands cannot get arbitrarily thin due to polar effects, and tend to fractal patterns in case of suitable boundary conditions. This is visible in Fig. 14.1.4b where p_s was reduced by stretching, and in Fig. 14.1.6b as p_e/p_s was big enough after decompression.

Evolutions as shown by Figs. 14.1.4–14.1.9 can principally be *simulated*, but there are numerical and physical limitations. Higo (2003) investigated prismatic samples of saturated clay for axial shortening via rough plates. He obtained similar bulging and shear banding in experiments and simulations, e.g. Fig. 14.1.10. A visco-elastoplastic relation was used for the skeleton and

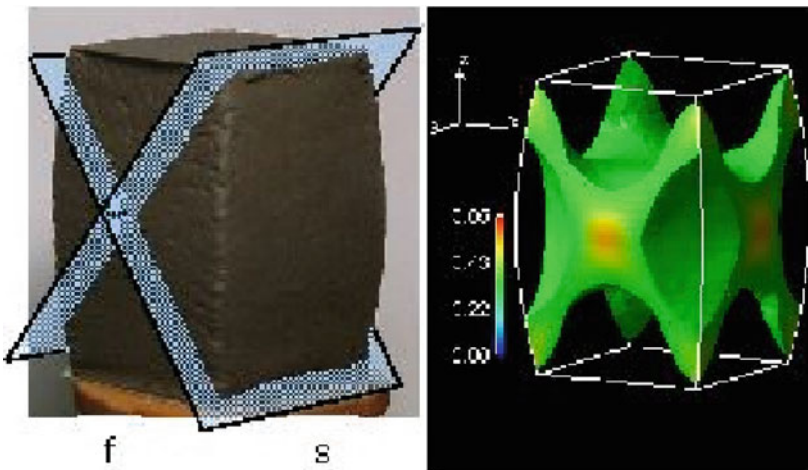


Fig. 14.1.10. Shear localizations in cuboidal peloid samples with $\sigma_2 = \sigma_3$ (Higo 2003): test results (*left*) and simulation (*right*)

extended by gradient terms for shear localization. Seepage in the skeleton and drainage at the boundary were taken into account. This could also be done with initially cylindrical samples and with smooth plates which are wider than the initial sample.

Such simulations could as well be carried out with v-hyp as it implies similar state limits as v-elp (Sect. 3.9). Feasible mesh sizes suffice to capture bulging, squeezing, necking and shear banding as long as the initial consolidation ratio p_e/p_s is low enough to enhance a spreading of pore water. Otherwise polar terms are principally more suitable than gradient terms to capture narrow shear bands (Sect. 8.3). This would require re-meshing in a fractal succession. As cavitation and capillary entry can also play a role one is far from reproducing patterns as in Figs. 14.1.4b or 14.1.6a.

Reversals have rarely been investigated with clay samples in triaxial tests, let alone a forced or spontaneous loss of uniformity. They could suppress diffuse and localized bifurcations as with psammoids. Kuntsche (1982) reports on triaxial tests with normally consolidated samples which were shortened and stretched via smooth plates. Isochoric strain reversals reduced the pore pressure (cf. Sect. 5.2) which was measured with a needle placed at the axis up to the centre. The maximal deviator $|\sigma_1 - \sigma_2|$ attained by subsequent monotonous shortening or stretching is somewhat smaller than without reversals. This could not be captured with a single φ_c and p_e as for cuboidal tests (Sect. 2.5), it may be attributed to non-uniformities near the needle which could be taken into account as for penetration (Sect. 14.3).

Triaxial tests with *gas inclusions* in clay samples have hardly been considered with respect to non-uniformities. Minute gas bubbles between solid particles may be captured by an elevated compressibility of the pore fluid (Sect. 6.3) as long as they are not dissolved by a sufficient p_w . Gas channels may principally be taken into account by means of composites with suction, but this could as yet not even be quantified with assumed uniformity (Sects. 7.3 and 9.1). Gas pockets and gas-filled cracks are beyond the present reach. Net attraction (Sect. 6.3) and cementation (Sect. 7.3) are not considered here.

To *sum up*, the forced or spontaneous loss of uniformity and axial symmetry observed in triaxial tests could principally be simulated with numerical models in order to check them. Rough plates restrict deformations in conical zones and enhance bulging or necking. Smooth plates with fixing central points, and sufficient size to avoid punching, cannot prevent spontaneous bulging, necking, buckling and shear localization. Such bifurcations are enhanced and could be simulated by means of spatial fluctuations. Helical patterns of narrow shear bands in denser than critical sand samples could be captured by constitutive relations with polar or gradient terms. Such patterns arise also in clay samples with a sufficient consolidation ratio, but observation and simulation are more difficult as the bands are thin. Without localizations skeleton viscosity and seepage may be captured numerically. Reversals can reduce a spontaneous loss of homogeneity.

14.2 Fills, excavations and ring structures

Axially symmetric evolutions with fills and excavations differ from plane-parallel ones (Sects. 12.1, 12.2, 12.3 and 12.4) by hoop effects: outward displacements are enhanced and inward ones are confined by circumferential pressures. Interactions with structures are different therefore from the ones outlined in Chap. 13. Ring structures and diapirs in the lithosphere can be nearly axi-symmetric. Axial symmetry occurs at best approximately in the lab and in situ and can get lost spontaneously. Therefore the following outline is kept short, all the more as only a few cases have been investigated in detail.

Dry psammoids favour the formation of conical heaps or holes, Fig. 14.2.1. A sandpile can be placed upon a rough rigid base (a) with low or high relative void ratio r_e by slow or fast precipitation. Filling by slow granular flow from a central tube leads to critical states with $r_e = 1$ and a critical stress obliquity along the free surface. As there the hoop effect is negligible against gravity, i.e. $|T_\theta|/r \ll \gamma$, the principal stresses T_I and T_{II} in the cross section and their directions are given by the slope angle $\beta = \varphi_c$ (b, cf. Fig. 11.5.2). $T_\theta = T_{III}$ may be assumed as for cylindrical shortening (Sect. 2.2), this was proposed by Haar and von Kármán (1909). Thus φ_c can be determined (Sect. 2.11).

Assuming limit stress obliquities and $T_\theta = T_{III}$ everywhere stress fields can be calculated (Cox et al. 1961). These are as arbitrary as Rankine fields (Sect. 11.3), in particular critical obliquities cannot arise uniformly. Near the axis the relative deviator $\tan \psi_s$ (Sect. 2.11) is lower than critical and can even

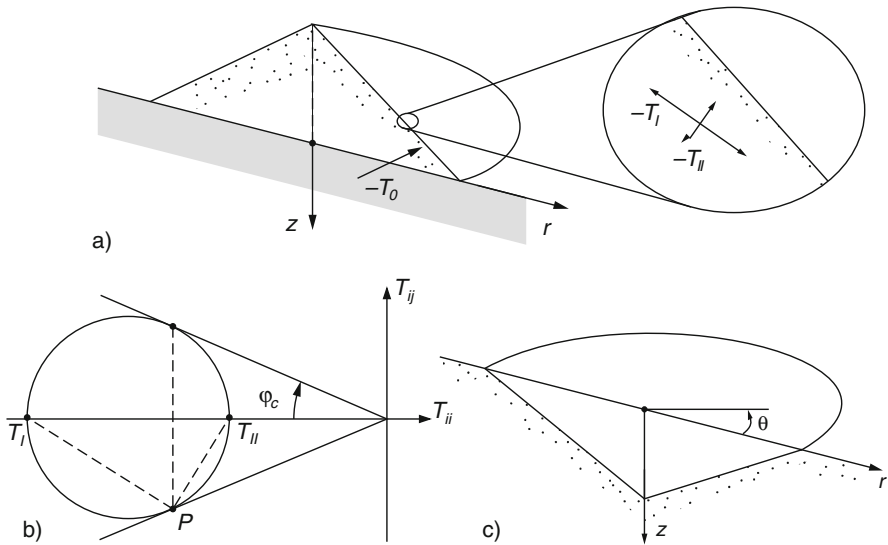


Fig. 14.2.1. Psammoid heap (a), stress circle near its surface (b), conical hole in psammoid (c)

disappear. Near the surface $\tan \psi_s$ could be overcritical for a short while with $r_e < 1$, then the heap is collapsible and avalanches occur in a rather chaotic fashion. This was observed by adding grains to a pile upon a scales (Bak et al. 1987) and triggered a euphoria with ‘self-organized criticality’. Avoiding such critical phenomena (Sect. 16.3) by means of subcritical slopes, axially symmetric evolutions of heaps could be simulated with *elp* or *hyp* (cf. Sect. 12.1). Model experiments with focus on r_e could be carried out for validation, low pressures p_s have to be taken into account in back-analyses.

Starting with a horizontal free surface, an excavation can lead to a conical heap or hole. In the second case (Fig. 14.2.1c) radial symmetry can be achieved with a suction tube. The hoop effect is again negligible near the free conical surface. Assuming $T_\Theta = T_I$ for inwards displacements as Haar and v. Kárman (1909) one can calculate limit stress fields (Cox et al. 1961), these are less realistic farther off the cone because of lower stress obliquities. The critical friction angle equals the attainable slope of a loose skeleton, $\varphi_c = \beta$ for $r_e = 1$. This corresponds to cylindrical stretching, and the same observed slopes as with heaps confirm that φ_c is the same as for shortening (Sect. 2.2). Critical phenomena occur again with $\beta > \varphi_c$, otherwise evolutions could be simulated with *elp* or *hyp* and observed in validation experiments.

With *pore water* the preference for conical heaps and holes gets lost in general, Fig. 14.2.2. Only with full saturation and resting water, i.e. constant

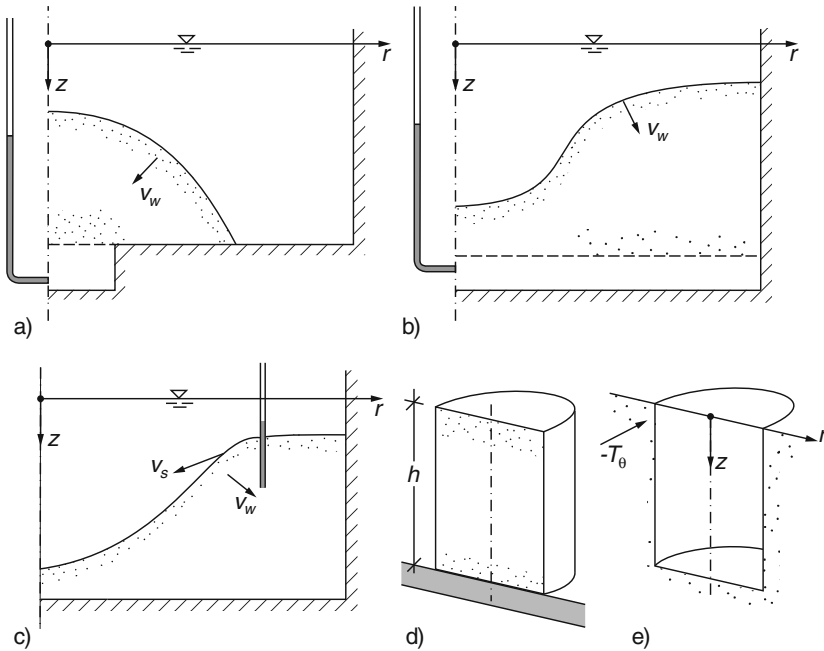


Fig. 14.2.2. Psammoid heap (a) and hole (b) with inward seepage, hole in dense submerged psammoid (c), column of (d) and hole in humid psammoid (e)

hydraulic height h_w , evolutions are the same as without water except for the reduction of the body force by hydrostatic uplift. A steeper axi-symmetric heap can be achieved by an inwards seepage (a). It grows from a uniform precipitation the intensity of which determines r_e by means of a lower h_w at a bottom filter. An opposite seepage would flatten the heap and lead to erosion. A hole can be excavated steeper and deeper with downwards and inwards seepage towards a bottom filter (b). Such evolutions could be simulated with *elp* or *hyp*. The skeleton would collapse and decay with an opposite seepage.

Without or with an initial hydraulic gradient h_w gets instationary if the grain skeleton is deformed in shorter times than needed for the diffusion of pore water (cf. Sect. 11.1). Seepage may be neglected for skeleton velocities v_s beyond the bound (6.2.11). Heaps and holes with loose skeletons slump and can hardly be controlled. Resting dense skeletons are stabilized by their tendency to dilate, this favours model tests and their back-analysis for validation. Thus a steep hole can stand just after its rapid excavation (Fig. 14.2.2c), but it collapses gradually when h_w returns to a constant value. Such cases may be simulated with *elp* or *hyp* and coupling with seepage. This is no more justified if the axial symmetry gets lost by bulging, shear localization or decay.

Gas inclusions can be taken into account by assuming a compressible pore fluid if the skeleton contains bubbles between the grains (Sect. 6.2). With bigger bubbles or gas pockets axial symmetry can hardly be attained. With gas channels connected to the atmosphere slopes can be steeper due to the capillary skeleton pressure p_{cs} . A cylinder (Fig. 14.2.2d) can thus stand up to a height of roughly (cf. Sect. 12.4)

$$h_c \approx \frac{p_{cs}}{\gamma} \frac{2 \sin \varphi_c}{1 - \sin \varphi_c}. \quad (14.2.1)$$

This necessary condition is obtained from the critical stress condition (2.2.15) for $\sigma_1 > \sigma_2 = \sigma_3$ with $p_s = (\sigma_{s1} + 2\sigma_{s2})/3 = p_{cs}$. It does not suffice for looser than critical skeletons and for so slender cylinders that these can buckle. Sand castles can thus stand as long as p_{cs} does not get lost by wetting, drying or cracking.

A cylindrical hole can stand in humid psammoid deeper than by (14.2.1) due to the hoop stress, Fig. 14.2.2e. Limit stress fields (Cox et al. 1961) have little relevance for stability as skeleton stress obliquities off the hole can hardly be guessed. Simulations with *elp* or *hyp* could be more rewarding with p_{cs} if this can be controlled in situ and in validation model tests. The most important parameters are r_e , φ_c and a grain size d_g that characterizes capillary bridges (Fig. 6.2.2). Such calculations get invalid by cracking of the skeleton or by closing of gas channels, such critical phenomena lead to a loss of axial symmetry.

The spectrum of shapes and states of psammoids is wider with *supporting shells*. (Storage bins will be treated in Sect. 14.5, holes with casing are shown

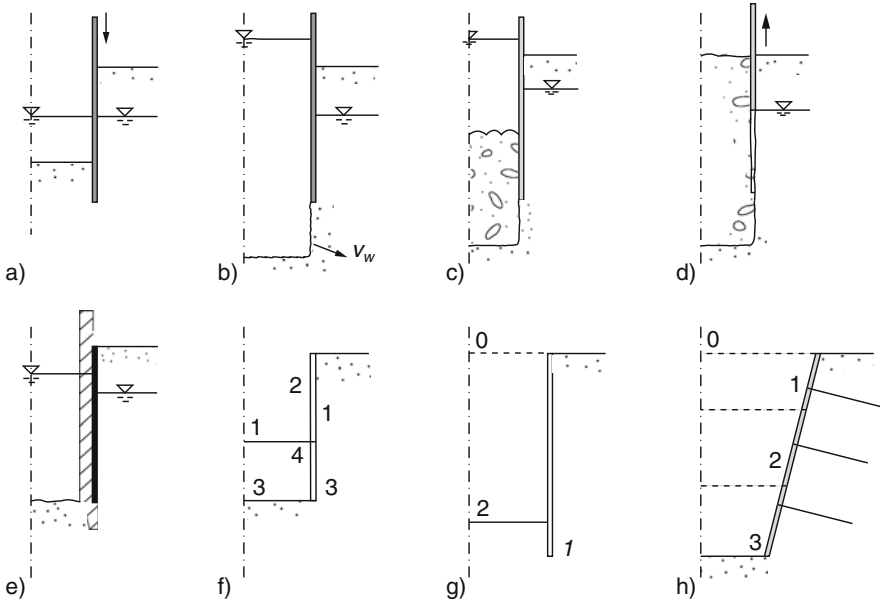


Fig. 14.2.3. Supported holes in psammoid ground: casing without (a) and with seepage (b), concrete mud before (c) and during removal of casing (d), concrete tube with clay smear (e), cylindrical concrete wall after excavation (f), cylindrical trench wall (g), shotcrete and nails around conical hole (h). Numbers for sequence

in Fig. 14.2.3.). A steel tube may first be lowered by dead load and axial shocks, vibrations (Sect. 14.3) and cyclic torsion (Sect. 14.6). The skeleton under and around the tube is densified by its placement, but the far-field stress is hardly changed. The skeleton inside the tube after partial excavation (a) is less densified near its free surface and is stressed (this may be considered as inverted silo problem, Sect. 14.5). After a deeper excavation than the casing the skeleton remains nearly in place with an outwards seepage due to a higher h_w inside than outside (b). Otherwise the skeleton would be dilated during the excavation and could be eroded by inward seepage.

After reaching a desired depth the hole can be filled with granular material or fresh concrete (c). Both can be densified and supplemented while the tube is pulled out with axial or torsional vibrations or shocks (d). This leads to a granular column in compacted ground or to a pile after curing. The tube can consist of sections, the lowest one can have a conical edge and an offset for grouting a smear (e, more on suspensions further below). Humid psammoid ground can be supported by a shell which is placed after the gradual excavation of a shaft (f, numbers for sequence). A wider shaft can be stabilized by a slurry trench wall (g) or by shotcrete and nails (g).

Such cases could be captured by simulations with elp or hyp and relations for supporting structures. Design estimates could thus be obtained,

these would be more realistic than usual statical assumptions. As with plane-parallelity (Chap. 13) attractors in the large play a key role for defining initial states and simplifying conditions at changing boundaries, and for quantifying failure scenarios. The assumed axial symmetry could be justified by state limits in the large, this requires three-dimensional simulations (Sects. 10.4 and 15.5) and observations. A collapse can cause a spontaneous loss of axial symmetry, e.g. ovalization of casing or uneven bottom heave.

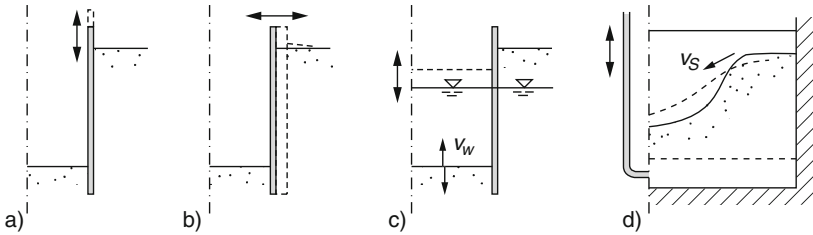


Fig. 14.2.4. State cycle fields can arise in psammoid by axial cycling (a) and pulsating diameters of a wall (b), or by pulsating water table with (c) and without casing (d)

Reversals in psammoid ground could principally be simulated with $elp-\alpha$, $hyp-\delta$ or $s-hyp$ (cf. Sects. 12.5 and 13.8). Asymptotically cyclic state fields are advantageous for validation model tests, but only few of them could be realized with axial symmetry, Fig. 14.2.4. A supporting tube could be shifted axially in cycles (a) until the ground response gets periodic. This could also be attained with a ‘breathing’ cylindrical wall (b) and would be enhanced by means of shaking (Sects. 4.7 and 13.8). More variants could be achieved with torsion (Sect. 14.6). Cycling hydraulic heights at boundaries could lead to asymptotic state cycles if the system can stabilize itself. This could be achieved with an excavation and a supporting shell (c), but hardly without it (d). In the latter case the skeleton flows gradually and can accelerate by dilation, let alone erosion. Penetration with reversals implies near-attractors (Sect. 14.3). Erratic shaking of the base flattens a heap or a hole. Such experiments could help to quantify the seismically activated creep (Sect. 4.6).

Unsupported heaps and holes with *peloids* evolve spontaneously due to thermally activated skeleton rearrangements and seepage, Fig. 14.2.5. A column with an initial cohesion c_{ur} (Sect. 3.2) can be placed upon a smooth hard base (a) with a height up to

$$h_c = 2 \frac{c_{ur}}{\gamma} \left(\frac{D}{D_r} \right)^{I_v} \tag{14.2.2}$$

if it is not so slender that it buckles. This implies spreading near the base by isochoric creep with a stationary stretching rate D as long as seepage

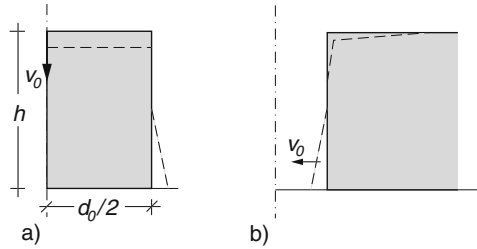


Fig. 14.2.5. Creep of a standing peloid cylinder (a) and around a vertical hole in peloid (b)

is negligible. Assuming uniform stretching near the base for simplicity the inversion of (14.2.2) leads to the downward creep velocity

$$v_o \approx d_o D_r \left(\frac{\gamma h}{2c_{ur}} \right)^{1/I_v} \tag{14.2.3}$$

of the cylinder with initial diameter d_o . As outlined in Sect. 12.2 this v_o decreases by shrinkage at the air and increases by swelling under water, and γ has to be replaced by $\gamma - \gamma_w$ for uplift. Further quantifications could be obtained with v-elp or v-hyp and coupling with seepage, also with other than cylindrical shapes. State limits in the large are argotropic via skeleton and pore water, they can be validated by model tests. Cracking after capillary entry or buckling after swelling mean a spontaneous loss of symmetry.

A borehole gets narrower by creep after its excavation, Fig. 14.2.5b. As long as the diffusion of pore water may be neglected the isochoric creep is almost stationary, but nowhere plane-parallel. Rübél (2010) obtained radial velocities v_o by simulations with v-hyp which can be represented by

$$v_o = r_o D_r \left(\frac{p_f - p_i}{c_{ur}} \right)^{1/I_v} \kappa. \tag{14.2.4}$$

Therein $p_f = \gamma h$ denotes the far-field pressure at the depth h , p_i a hydrostatic supporting pressure at depth h and κ a factor depending on r_o/h . Equation (14.2.4) is a variant of (13.3.3) with the power law as by (14.2.3) and as for an RSE, this similarity was proven by Winter (1979). The stationary field is an argotropic attractor in the large, this works as long as the geometrical stabilization due to the closing hole is negligible.

Without seepage the axial symmetry can get lost spontaneously by ovalization of the hole, and also by shear localization if the material is not ductile for isochoric shearing (Sect. 8.3). This is also the case for other axi-symmetric holes which converge by (14.2.4). With seepage the convergence is slowed down by shrinkage and accelerated by swelling. This could be simulated with v-elp or v-hyp and coupling with seepage. The axial symmetry gets lost by cracking or ovalization, respectively.

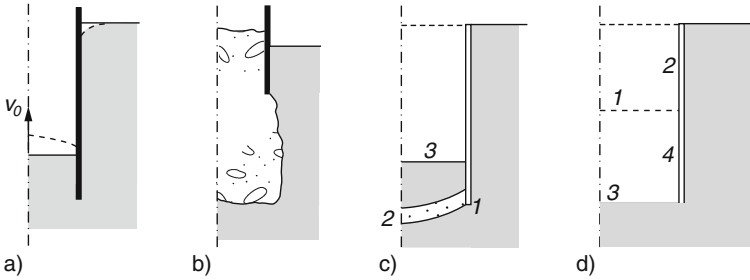


Fig. 14.2.6. Supported holes in peloid with casing (a), fresh concrete (b), wall and invert (c) or a wall placed after excavation (d). Numbers for sequence

Supported excavations in peloid ground are shown in Fig. 14.2.6. A tube (casing) can be placed in advance as outlined in Sects. 14.4 and 14.6. After the excavation (a) and prior to the diffusion of pore water the bottom rises by isochoric creep. This gets nearly stationary for a while if the soil is ductile, and could be simulated by v-elp or v-hyp. The velocity v_o of heave could be expressed by (14.2.4) with a numerically determinable factor κ , except for the vicinity of the bottom the external pressure on the tube tends to the far-field value. Creep and relaxation are slowed down by shrinkage and accelerated by swelling.

A fill of granular material or fresh concrete after partial removal of the tube can push aside the peloid (b), in particular if the internal pressure is elevated and the peloid has a low initial consolidation ratio p_e/p_s . A rapid expansion can produce vertical radial cracks in the peloid so that it can release pore water in a short time. Otherwise consolidation and relaxation of the peloid occur after removal of the tube. Fresh concrete releases water into the peloid with high initial p_e/p_s and fissures, and also upwards after skeleton decay with gas bubbles. Such and similar evolutions could be captured by simulations with axial symmetry, but at best crudely as this can get lost. Therefore monitoring is needed for control, and probing in situ for specifying composition and state afterwards (Sect. 14.4).

Peloid ground at wider excavations can be supported by a cylindrical wall and an inverted lid. In case of low initial p_e/p_s both should be placed prior to the excavation in order to reduce deformations during and just after it (c, numbers for sequence). Wall and lid are stressed by relaxation of the ground. This could be simulated with v-elp or v-hyp, coupling with pore water and relations for the structure. Radial symmetry is better apt for stabilization than plane-parallelity (Sect. 13.4). With a high initial p_e/p_s wall and lid can be placed alongside with the excavation (d). Creep and relaxation are harmless if opening of latent cracks and shear dilation are avoided. This could be quantified by simulations including crack-enhanced capillary entry and seepage. This could also be done with further supporting structures, e.g. ring beams

or anchors (ring discs for rows). Axial symmetry should be favoured by the operation, a spontaneous loss of it should be avoided.

Reversals with peloids could principally be treated as outlined for psammoids with Fig. 14.2.4. Simulations with v-elp- α or v-hyp- δ and validation model tests would be rewarding with argotropic attractors for cyclic changes of structure height (a) or diameter (b), similar attractors will be treated in Sects. 14.3 and 14.6. Cyclic hydraulic boundary conditions with (c) or without structure (d) can also lead to attractors, then the product of frequency and diffusion time determines the influence of shrinkage and swelling. As in triaxial tests (Sect. 14.1) reversals enhance axial symmetry, but cannot exclude its spontaneous loss.

Cases with *composite ground* as shown e.g. with Figs. 13.4.13, 13.5.10 and 13.5.11 or 13.6.12 can also be captured with axial symmetry. Other than with plane-parallelity simplifying kinematical or statical assumptions could hardly be defended without validation simulations by which they get obsolete. Psammoids with filter cakes are important composites in cases with axial symmetry. A shown in Sect. 10.1 a peloid is fixed to a psammoid filter cake by inward seepage, this requires suitable hydraulic conditions which in turn can depend on the filter cake. The psammoid at the cake has a skeleton pressure that equals the water pressure difference at the cake.

A psammoid hemisphere under a suspension can thus be kept in place by seepage towards a central drain (Fig. 14.2.7a). This works also with other shapes, such experiments and their back-analyses could help to quantify filter cakes. A lab experiment with a hole in psammoid under a suspension and a filter base with a lower hydraulic height h_w (b) would also be worth the effort. A borehole in partly flooded psammoid ground can stand by means of a suspension with a higher level in a tube (c). This suspension support works also with a psammoid layer between peloid layers (d), but not with a psammoid lense in peloid (e) as then there is no radial seepage. Simulations for cases c and d could substitute hardly defensible design estimates and support the control.

Axi-symmetric cavities and underground structures can be treated similarly as plane-parallel ones (cf. Sect. 13.7). With psammoids the punching of trap doors may be simplified as in Fig. 13.7.1, but model test results resemble more those in Figs. 13.7.2, 13.7.3 and 13.7.4. A cylindrical shaft can be built as shown in Fig. 13.7.6b except for a ring beam instead of struts. Axi-symmetric cavities can be built as in Fig. 13.7.6 by means of access shafts or tunnels. Injection of grout from a vertical borehole with casing would lead to an increasing bubble as in Fig. 13.7.7a, this can lose its symmetry and break out along the casing. Grouting under an injected layer as in Fig. 13.7.8a leads to spreading and heave, but a break-out will not be axi-symmetric.

With peloid ground trap doors may be considered as with Fig. 13.7.9a and b. Grouting under an axially guided body (cf. Fig. 13.7.10a) can lift it, but this sinks if it was already close to an indifferent state (Kudella 1994). A cavity with a cross section as in Fig. 13.7.10b can be built from

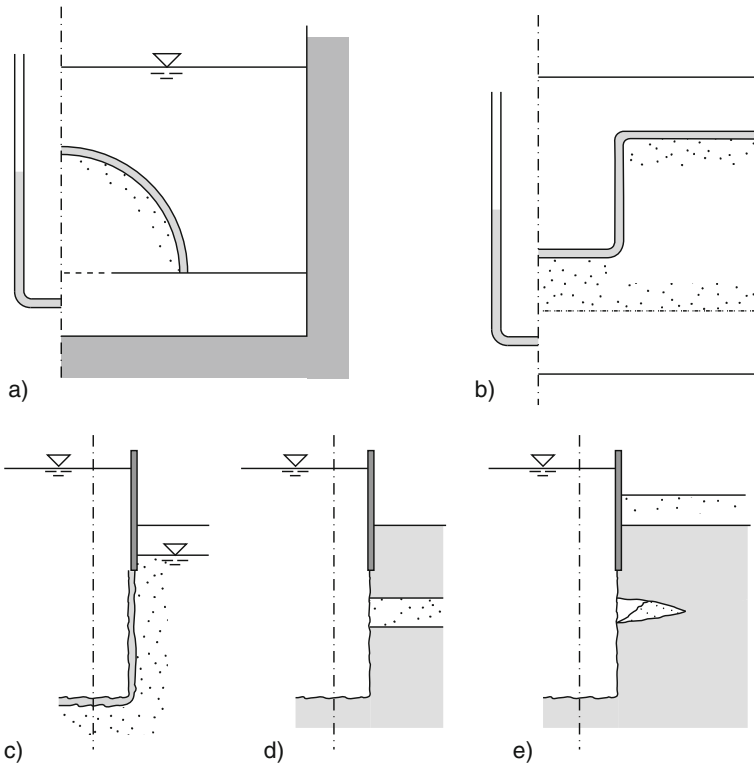


Fig. 14.2.7. Psammoid with supporting filter cake: (a) hemisphere, (b) hole, (c) hole with casing, (d) psammoid band, (e) psammoid lense after collapse

an access shaft or tunnel. Axi-symmetric cavities with cross sections as in Fig. 13.7.11a, b may also occur. Heaving injections can have cross sections as in Fig. 13.7.13a.

Stazhevskii (2005 and 2006) investigated *ring structures* which are generated by axi-symmetric lowering of the base of horizontal layers. He observed first a conical and then a cylindrical shear localization in cross sections of active trap door tests with dry sand, Fig. 14.2.8a, b. In some tests the free surface exhibited axi-symmetric offsets (d, e). Similar axi-symmetric evolutions could be generated with elp or hyp, except for hoop terms cross sections and finite element calculations could be the same as in plane-parallel cases (Sect. 13.7). Polar effects may be neglected for the overall behaviour if the layer size exceeds ca. 100 grain diameters (Tejchman 1997). Details of shear localization could principally be captured by re-meshing with polar terms. In other model tests the axial symmetry got lost spontaneously (e, f), this indicates a succession of helical shear bands (cf. Fig. 14.1.2).

Stazhevskii (2005, 2006) demonstrates that similar ring structures occur in the earth crust and on the Moon with diameters from ca. 10 to 10^3 km. The

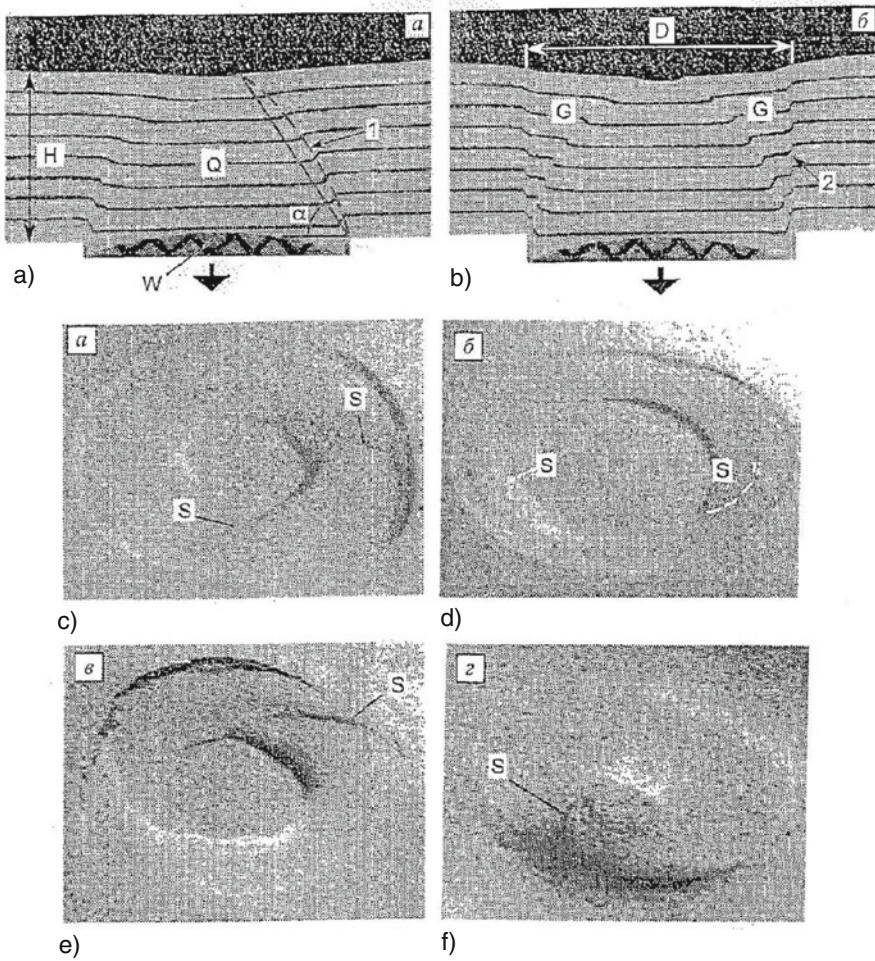
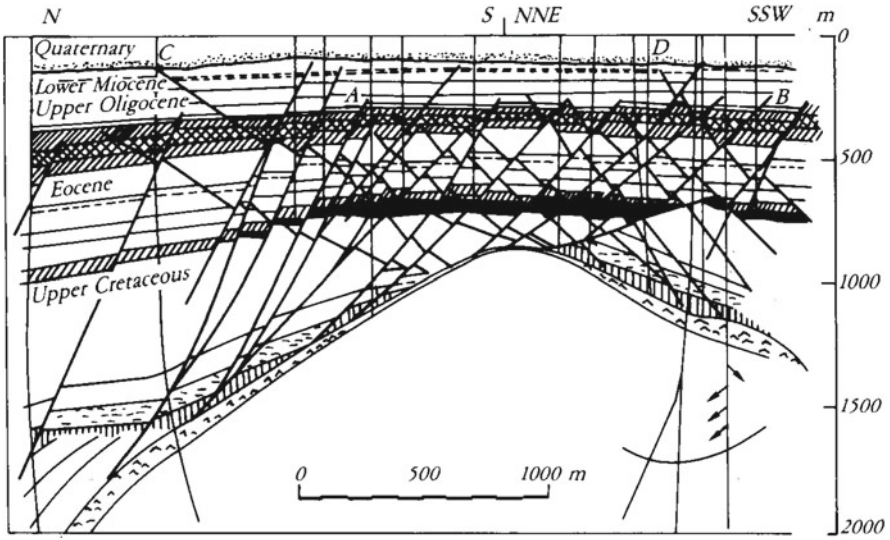


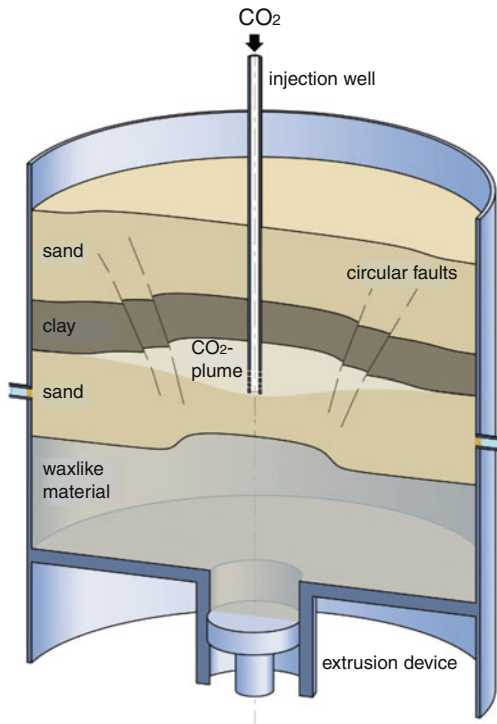
Fig. 14.2.8. Ring structures in model tests (Stazhevskii 2006): cross sections of two stages (a, b), axi-symmetric sinkholes (c, d), helical sinkholes (e, f)

shear zones are dilated and more permeable so that pore fluid can rise along them. The seismic activity is shown to be concentrated along the conical shear zones. It resembles quakes observed in silos which are related with successive shear localizations, stress jumps and stick-slip (Sect. 14.5).

Similar phenomena occur in the earth crust with *diapirs*, Fig. 14.2.9. Swarms of normal faults arise in regions of radial extension (a). The dislocation of layer packages leads to clay smears (cf. Fig. 12.2.4) which can work as hydrocarbon seals. Such evolutions could similarly be observed in model tests (b). Other than in passive trap door tests the inner part of the bottom can be lifted by a viscous paste. Mechanical similarity can be achieved with



a)



b)

Fig. 14.2.9. Ring structure above a diapir (a, Mandl 1988), model test with diapir and injection (b, Rübel 2010, courtesy K. Balthasar)

realistic proportions of lengths, solid hardnesses (cf. Sects. 2.2 and 3.2) reduced as lengths, and the same relative void ratios and consolidation ratios as in situ for psammoids and peloids, respectively. The argotropy of skeletons is achieved with the same viscosity index as in prototypes. Times for pore water diffusion are scaled as the square of length by (11.1.16) and far shorter therefore.

To *sum up*, axi-symmetric fills and excavations without or with support can be captured in a number of geotechnically important cases. Simulations with *elp* or *hyp* for psammoids, without or with ground water, can be validated by model tests and can substitute hardly defensible conventional estimates. The same holds true for peloids with skeleton viscosity and pore water diffusion, and for composite ground. State limits and state cycles are of use as attractors in the large. The axial symmetry can get lost by ovalization, shear localization or cracking, such critical phenomena are beyond the present reach.

Ring structures in the lithosphere may be explained as axi-symmetric active or passive trap door problems. This was shown with model tests and could be supported by simulations with *elp* or *hyp*. Shear localizations can be helical or even less symmetric, however, so that simulations of faulting by a nearly circular subsidence or diapir are beyond the present reach.

14.3 Penetration

A ground with horizontal psammoid and peloid layers can experience axi-symmetric evolutions of shape and state through the vertical penetration of solid cylinders without or with reversals. For a number of cases hypoplastic simulations have been carried out and validated by experiments. For some of them inertial effects were taken into account, and drainage was either excluded or assumed to be free. The penetrating cylinders are often assumed as rigid for simplicity. Such evolutions can be captured with attractors, these work also for extensions and help to understand limitations.

Cudmani (2001) proposed a finite element mesh with a smooth neck under the cylinder and a fictitious thin tube under it, Fig. 14.3.1. He avoided thus a singularity at the tip and showed that neither the slope at the neck nor the thin tube diameter influences the main results. The grid is pushed aside and deformed by the penetration, and the thin tube is consumed. A fictitious rigid base and a likewise fictitious cylindrical wall are chosen sufficiently far off the solid cylinder. Calculations with such substitutes were first carried out with *hyp* and *hyp- δ* for *dry psammoids*. For validation initial and boundary conditions were chosen as in calibration chamber tests, and hypoplastic parameters were adapted to oedometer and triaxial test results for the employed sands. Sliding or sticking was assumed for the interface of skeleton and solid with a friction angle $\varphi_w < \varphi_c$ (Sect. 10.3).

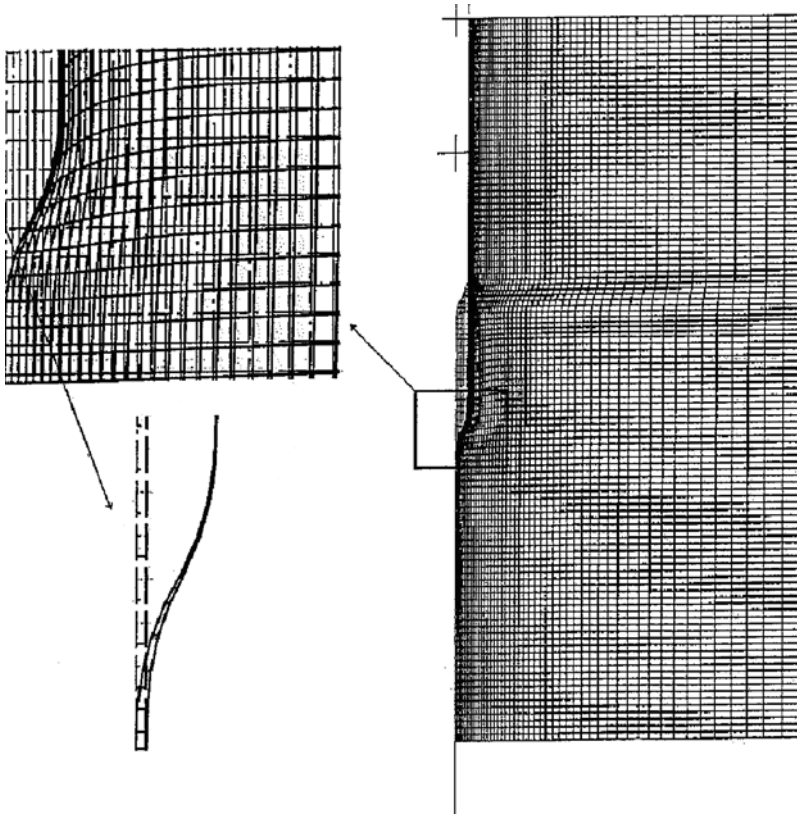


Fig. 14.3.1. Finite element mesh for penetrations (Cudmani 2001)

Monotonous slow penetrations are represented in Fig. 14.3.2. Independently of the position the cone resistance F_c increases with the depth z of penetration (a). F_c is hardly influenced by slope and smoothness of the assumed neck. It gets bigger with rough hard grains of uniform size in a dense skeleton, i.e. with high φ_c , h_s and α (Sect. 2.4) and low relative void ratio r_e . Calculated cone resistances $q_c = F_c/(\pi d^2/4)$ agree fairly well with observed ones for dense quartz sands (b, Cudmani and Sturm 2006). q_c -values for low far-field pressures p_{cf} are underestimated as h_s -values adapted for higher p_s are too low, for high p_{cf} the resistance q_c is overestimated as grain crushing is not taken into account. q_c depends on r_e and the far-field pressure p_{sf} at the same depth as for radially symmetric expansions (Sect. 11.7). Cudmani (1996) proposed a correction factor for the transition from radial to axial symmetry so that data from probing in situ can be evaluated for the far-field relative void ratio r_{ef} .

Figure 14.3.3 shows a calculated state field near the tip during a monotonous penetration into initially dense sand. The mean pressure p_s rises by more

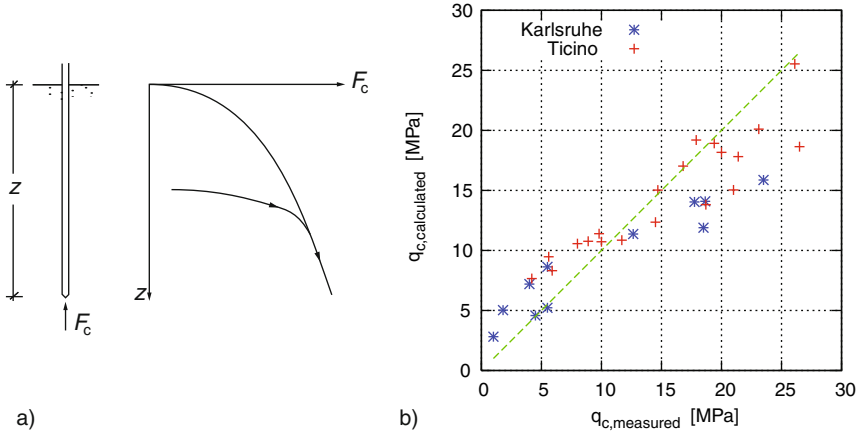


Fig. 14.3.2. Resistance of psammoid ground to penetration: (a) qualitative depth-dependence, (b) calculated versus observed tip resistance (Cudmani and Sturm 2006)

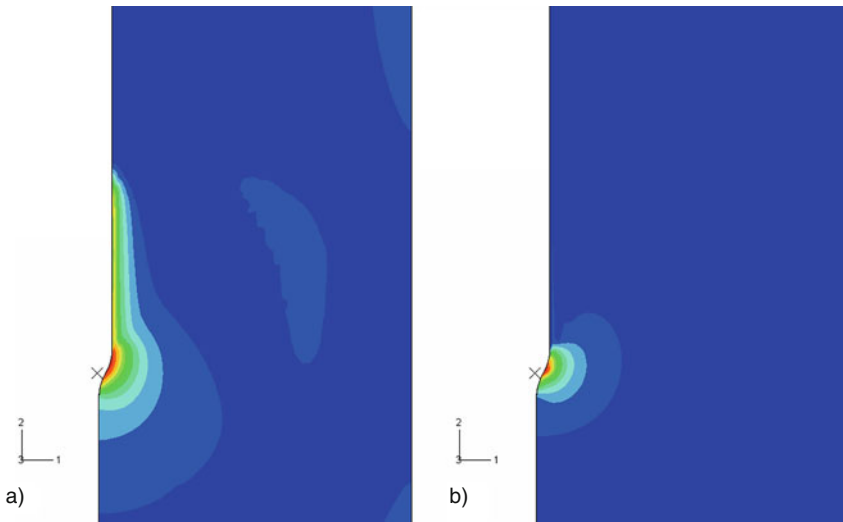


Fig. 14.3.3. Calculated fields of mean pressure (a) and relative void ratio (b) for penetration in dense sand. Darker means lower pressure or higher density, respectively (courtesy H. Sturm)

than two decades at the tip, i.e. this is strongly jammed together with the neighbored sand. The relative void ratio (b) rises up to $r_e = 1$ near the tip, there a critical state is approached with e near e_c for the high near-tip pressure. The monotonous deformation leads to SOM-states (swept-out of memory, Sect. 2.5) in the near-field, and almost to an isochoric state limit at

the tip by a kind of granular flow. Grain crushing would reduce the pressure increase by more contractant shearing.

Such convected *state limit fields* are attractors in the large. For a given depth they are determined by the initial and far-field relative void ratio r_{ef} . Initial position and stress field do not matter, they are swept out by a penetration of about 4 to 2 rod diameters for high or low initial r_e , respectively. The dominant hypoplastic parameters are granulate hardness h_s , critical friction angle φ_c and exponent α (which reflects the capacity for dilation, Sect. 2.4). The penetration depth enters via the far-field pressure p_{sf} , so the ratio p_{sf}/h_s counts for unit-invariance (Sect. 2.2). Cudmani (2001) found that the penetration resistance increases with p_{sf}/h_s as for a spherical expansion which can more easily be calculated. Thus the original relative void ratio, which is the most important state variable, can be determined from the penetration resistance if the far-field pressure and a few hypoplastic parameters are known. This works also with uniform layers if these are thicker than about 4 rod diameters, thinner layers produce more scattering.

Mahutka et al. (2006) investigated also the field above the tip due to a monotonous penetration, Fig. 14.3.4. Other than at the cone the resistance

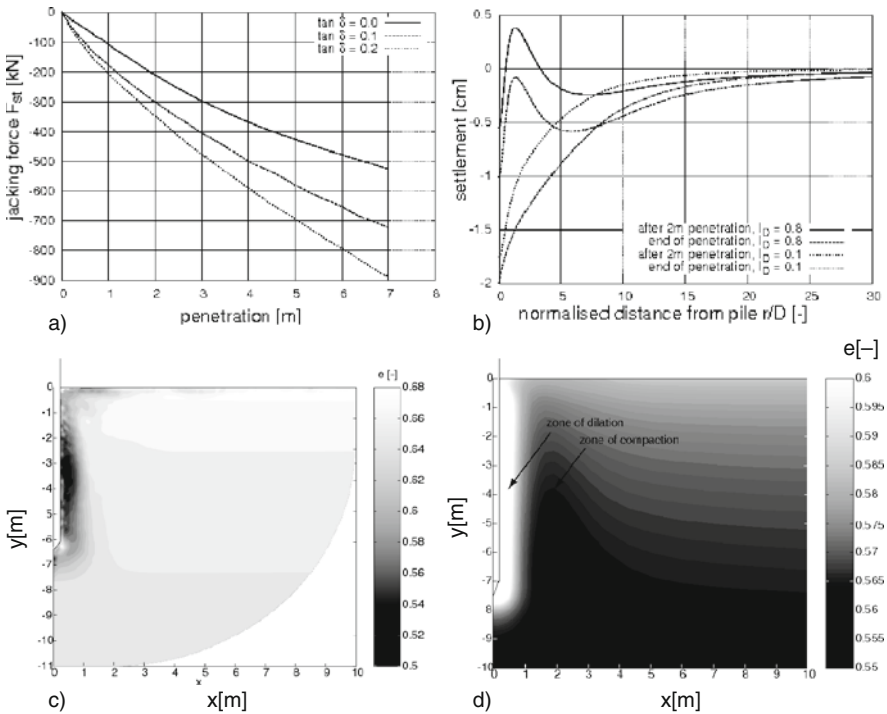


Fig. 14.3.4. Hypoplastic simulation results for penetration into psammoid ground (Mahutka et al. 2006): (a) resistance versus depth, (b) vertical surface displacements, void ratio field with initially loose (c) and dense ground (d). Darker means denser

at the shaft increases with its roughness, and almost linearly with depth (a). The free surface rises by dilation near the rod if the ground is initially dense, and settles otherwise (b). With further penetration the overall settlement goes on. The void ratio is reduced near the shaft if the skeleton was loose before (c), and gets higher by dilation in the opposite case (d). In the transition to the far-field the skeleton is slightly densified by shearing. These findings could be represented by fields of p_s and r_e as in Fig. 14.3.3. The state fields near the shaft and wall above the tip do not change with further penetration. They are determined by the rod and the initial relative void ratio (if this is uniform) and are thus attractors in the large. Apart from the minor continued settlement they are not convected as the field near the penetration tip. State limits are attained and maintained near the shaft.

Cudmani (2001) and Cudmani and Sturm (2006) investigated *alternating penetrations* in dry sand, i.e. a kind of quasi-static ratcheting, Fig. 14.3.5. Simulations (a) reveal that the cone resistance q_c gets zero temporarily if the upwards displacement exceeds about half the downwards one in a cycle. For this *cavitative mode*, i.e. if the skeleton at the cone gets temporarily stress-free, the q_c vs. displacement curve has loops, otherwise it has saw-teeth. Nearly the same was observed in a pressure chamber (b), this validates the employed model.

Experiments and simulations indicate that the loops or saw-teeth are determined by the far-field pressure $p_{s,f}$ and relative void ratio $r_{e,f}$ for a given depth if r_e was uniform before the penetration. The alternating penetration can start at any depth with any near-field of stress, this influences only the transition. The attained state cycle fields depend on the amplitude of downwards and upwards steps. The average near-field relative void ratio \bar{r}_e is lower than for a monotonous penetration. The skeleton is densified more easily and p_s rises less than without reversals.

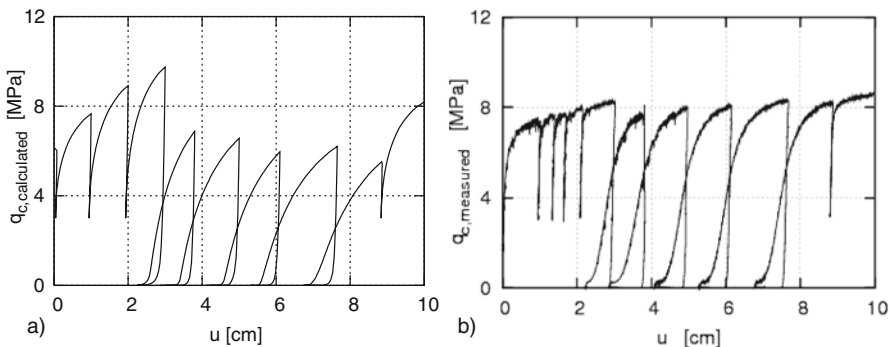


Fig. 14.3.5. Tip resistance versus penetration with reversals in psammoid ground (Cudmani and Sturm 2006): simulation (a) and observation (b)

The near-field just above the tip could be represented by a succession of state cycle fields. As for monotonous penetrations the influence of depth can be subsumed by plotting the normalized shaft force $F_s/(2\pi\gamma dz)$ versus an average near-field \bar{r}_e . The distribution of shear stress versus depth is nearly linear (cf. Sect. 14.4). \bar{r}_e is lower and F_s is smaller than for a monotonous penetration as the skeleton is densified and the more relaxed by reversals the smaller the amplitudes are (cf. Sects. 4.2 and 4.6). Therefore the free surface settles more and is nowhere lifted. As with monotonous penetrations the state cycle field for alternating penetrations is convected near the tip and stationary further above.

By definition inertial effects play a role for *dynamic penetrations*. They are substantial for the penetrating cylinder, but smaller for the ground. Only a minor part of the latter experiences relevant accelerations under the penetrating cone as waves in this zone are strongly damped. Along the shaft kinetic energy is dissipated in phases with sliding, and radiated off with hysteretic damping otherwise. Apart from ejection of surface grains and heating near cone and shaft this could be simulated with elp- α or hyp- δ . State limit and SOM-fields of the skeleton are modified by inertia as this widens the near-field, this means a higher rise of p_s and a lower reduction of r_e than farther away.

Cudmani and Sturm (2006) simulated penetrations with rapid reversals in dry sand, Fig. 14.3.6. An almost rigid cylinder was driven in by a vibrator and a dead load on top. The plot of tip force versus displacement exhibits a cavitative mode (a, cf. Fig. 14.3.5) for a low dead load, but not for a higher one (b). Cavitative modes are obtained at a lower depth with different dead loads both in the experiment (c) and its simulation (d). The associated plots of cone velocity versus displacement show quite similar observed (e) and simulated (e) loops. Further validations were presented by Cudmani et al. (2002). A satisfactory agreement was obtained with different far-field relative void ratios and diameters so that such penetrations can be predicted.

These plots indicate that a few reversals with a small shift (compared with the diameter) suffice to attain convected state cycle fields. These differ little from the ones for quasi-static alternating penetrations as average inertial forces in the near-field are smaller than the skeleton weight. Therefore attained pressures and densities are similar as without inertial effects in the ground, thus vibratory probing works and can yield void ratios for bigger depths than with other kinds of penetration.

Cudmani (2001) observed also shear forces along the shaft in vibratory driving tests, Fig. 14.3.7. With diameter $d = 0.15$ m, depth $z = 6$ m and frequency $f_c \approx 10 \text{ s}^{-1}$ the height-averaged shear stress $\bar{\tau}$ attains the same maximal amount for downwards and upwards sliding (a). This means shear ratcheting with big amplitude along the shaft and a minor radiation of shear waves in intervals with sticking. With $d = 30$ m, $z = 10$ m and $f_c = 30 \text{ s}^{-1}$ the ratcheting is slower and the $\bar{\tau}$ vs. z plot is less symmetric because the

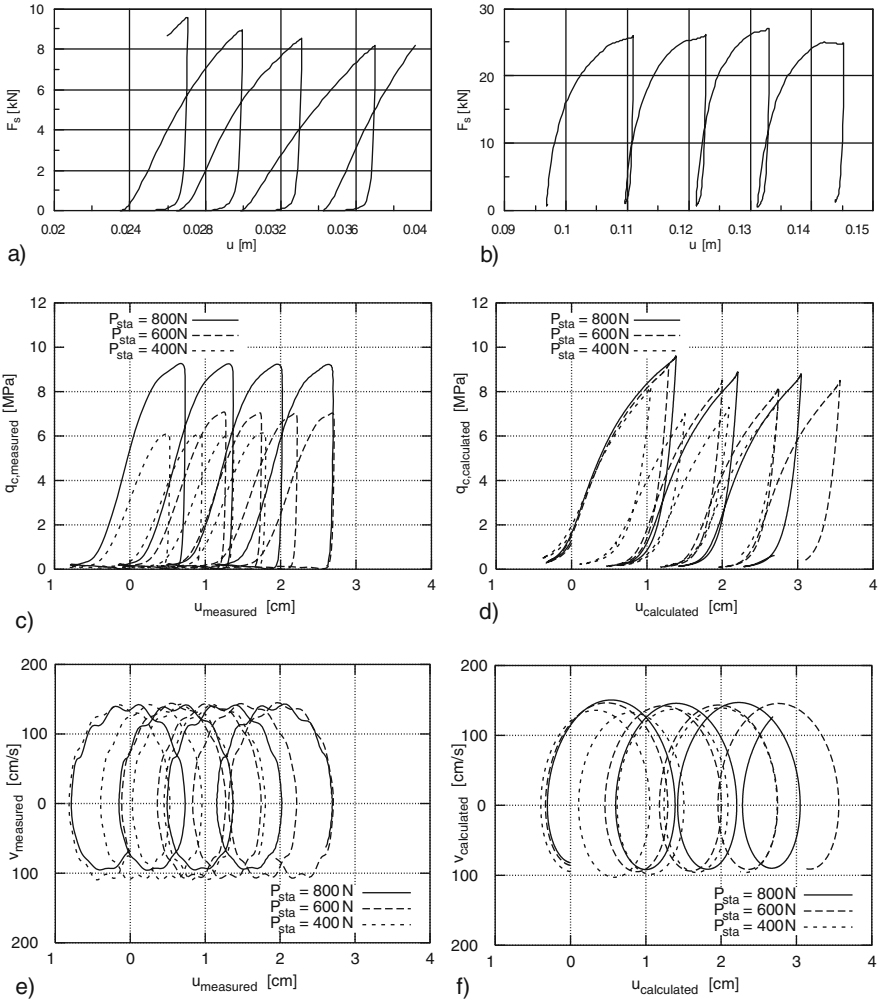


Fig. 14.3.6. Rapid alternating penetration in psammoid ground (Cudmani and Sturm 2006): simulated tip force versus vertical displacement with (a) and without temporary loss of tip contact (b), observed (c) and calculated tip force versus shift (d); observed (e) and simulated tip velocity versus shift (f)

fraction of slip intervals is smaller (b). On this base Cudmani (2001) proposed a simplified model for dynamic penetrations. Therein parameters for tip and shaft resistance are taken from in situ probing data for quasi-static or dynamic penetrations.

Pile driving by repeated blows was simulated by Mahutka et al. (2006) with $hyp-\delta$ and the same soil data as for Fig. 14.3.4 with monotonous penetration. With diameter $d = 2\text{ m}$ and penetration depth $z = 6\text{ m}$ the radial pressure at

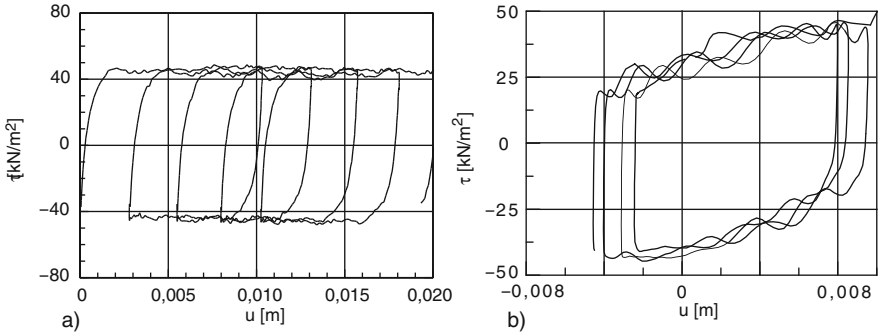


Fig. 14.3.7. Shaft force versus penetration in psammoid ground with (a) and without temporary state limit (b), observed by Cudmani (2001)

the shaft is higher near the tip and lower further above than before driving, Fig. 14.3.8a. A higher initial pressure due to a previous surcharge is swept out, and the skeleton further below is also relaxed near the shaft by almost cyclic shearing (cf. Sect. 4.6). Closer to the tip the skeleton gets jammed by the penetration, more so with a lower void ratio, but not as much as for a monotonous penetration.

Calculated void ratios are more reduced after driving if the skeleton was medium dense (b) than if it was dense initially (c). Similarly as in Fig. 14.3.4c the free surface settles near the pile except for a bulge with radius $r \approx 2d$ in case of a high initial density (d). The more marked dilation by shearing near the pile for an initially denser skeleton can be seen from the e -contour plot (c). The radial skeleton pressures after driving are markedly higher than before below and near the tip, less with an initially medium dense skeleton (e) than if it was dense (f). The skeleton near the tip is less jammed than by monotonous penetration (cf. Fig. 14.3.2). Along the shaft the skeleton is relaxed further above (cf. a), and farther off it is not changed (cf. c, d).

These findings can be interpreted, generalized and simplified by means of attractors in the large. The near-field around the tip resembles the one for a non-cavitative alternating penetration (cf. Fig. 14.3.3), i.e. the skeleton is the more jammed and dilated the denser it is initially, but less than for a monotonous penetration. Further above around the shaft the skeleton goes through state cycles with the smaller amplitudes the smoother the shaft is and the smaller its amplitudes are. The propagation of pressure waves from the tip and of shear waves from the shaft influences the asymptotic response (cf. Sect. 11.4). Simplified models as those proposed by Cudmani (2001) are justified by these attractors.

Under certain conditions the vibratory driving can get *chaotic*. Vielsack and Hartung (1999) observed period-doubling and a chaotic end of penetration in model tests with dry sand and a vibrator upon a rod for certain dead loads and initial densities. Simplifying to a model with one degree of freedom and

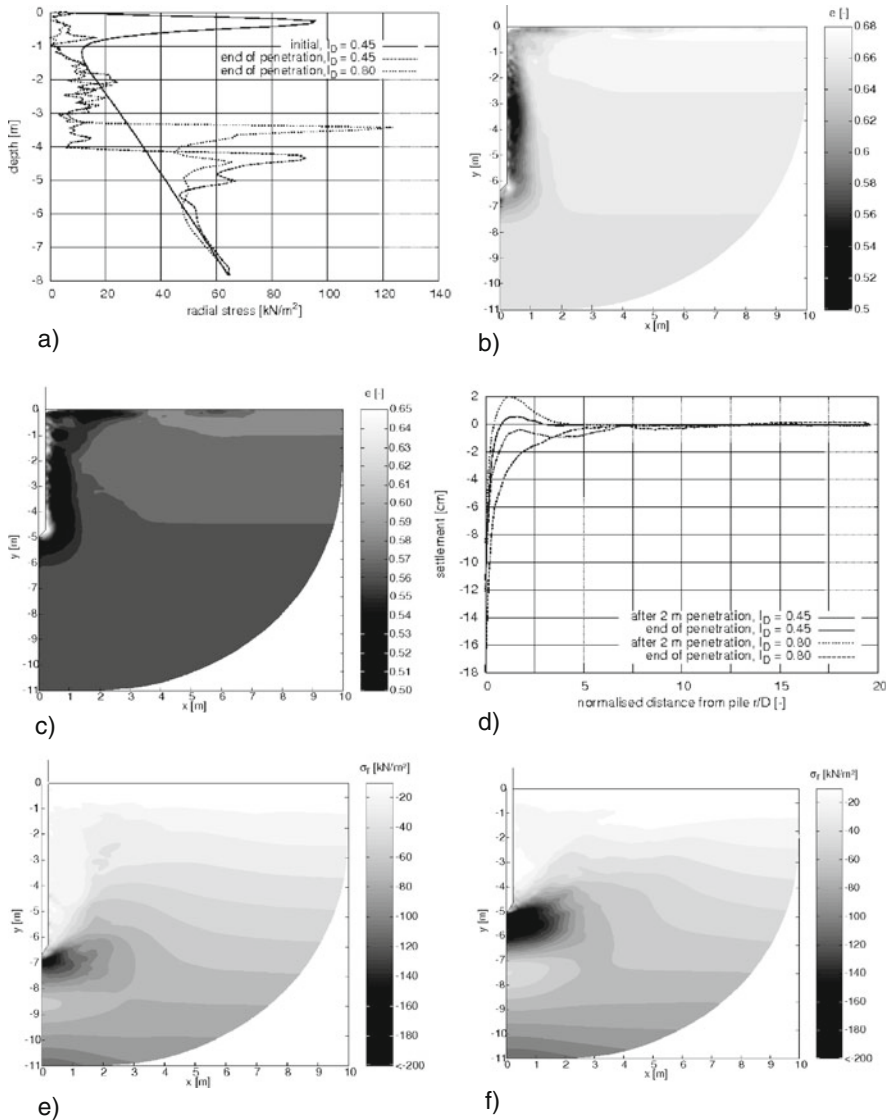


Fig. 14.3.8. Simulated dynamic pile driving in psammoid ground (Mahutka et al. 2006): radial shaft stress versus depth (a), void ratio field after penetration in initially medium dense (b) and dense ground (c), vertical surface displacements (d), radial stress field after penetration with medium (e) and high initial density (f)

a hysteretic interaction of rod and sand they could catch this behaviour by means of a strange attractor (Sect. 16.3).

It may at least briefly be indicated how penetrations in dry psammoid can be changed by the *deformability* of solid cylinders, Fig. 14.3.9. A slow monotonous penetration ends (a) when a further vertical displacement Δu with fixed tip (b) wakes a further shearing resistance $\Delta\tau$ (c) which adds up to the additional internal normal force ΔN , i.e. for

$$\Delta N = \frac{\pi d^2}{4} E_s \frac{\Delta u_0}{z_0} = \pi d \int_0^{z_0} \Delta\tau dz \quad (14.3.1)$$

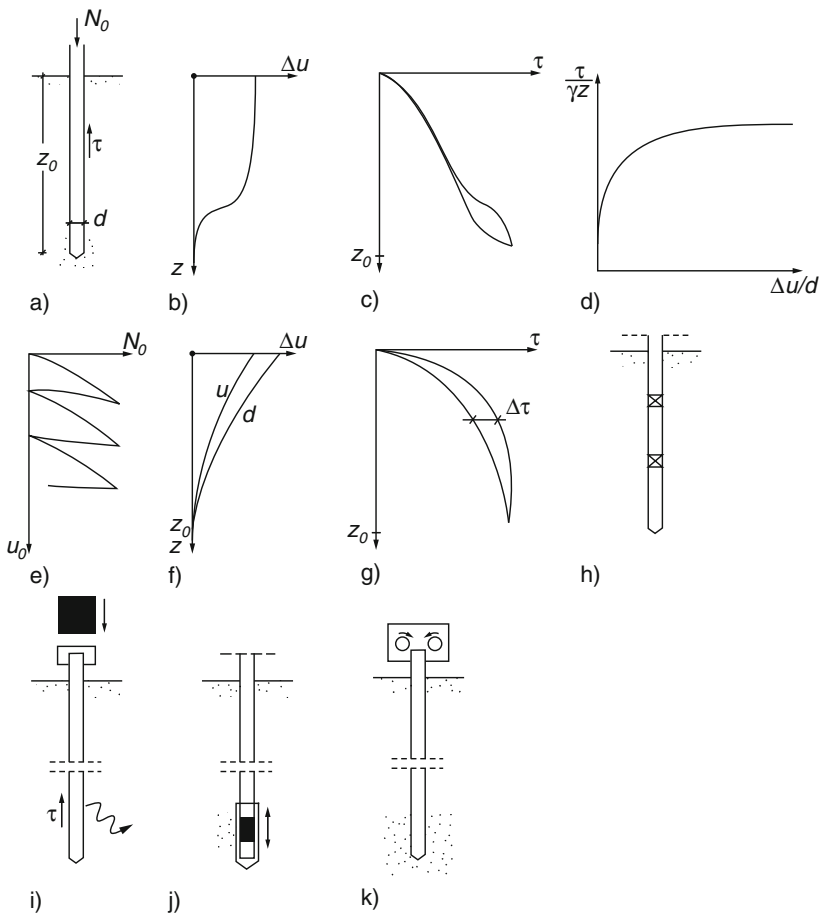


Fig. 14.3.9. Penetration of an elastic rod in psammoid ground (a): displacement (b) and shaft resistance versus depth (c) and versus each other (d) for a monotonous penetration; ratcheting (e) and bounds of displacement (f) and shaft resistance (g) for a slowly pulsating head force; rod with expanders (h); driving by blows at head (i) or tip (j) or by a head vibrator (k)

with solid modulus E_s , top displacement Δu_0 and end depth z_0 . As plotted $\Delta\tau$ can only arise near the tip, but not exactly there if this does not move, nor farther above as stationary sliding goes on there. This dead end could be calculated with elp- α or hyp- δ , z_0 may also be estimated with (14.3.1) and relations of $\Delta\tau$ with Δu (d) as proposed by Cudmani (2001). The penetration ends with $z_p < z_0$ if the top normal force reaches the plastic limit of the solid.

A quasi-static ratcheting at the top (e) does not reach the tip with downward (d) and upward (e) displacement increments (f) if the incremental top force ΔN is absorbed by the incremental shear stresses (g) as by (14.3.1). This can lead to a shallower dead end than without reversals. The bound by plastification of the cylinder is less relevant with smaller amplitudes as then the axial forces are smaller. A ‘peristaltic’ penetration could get deeper by means of axial expanders above and near the tip (h). This can drive the tip with reversed shaft friction as reaction, can draw thereafter the upper shaft with reversed friction near the tip, and so on. More expanders can ease the penetration, earth-worms do a similar job.

The depth of dynamic penetrations is also reduced by the deformability of solid cylinders. The longitudinal wave due to an impact (i) can be damped by friction and radiation of shear waves along the shaft so that the tip remains at its place. The returning wave may be used to judge the integrity of the cylinder. The penetration before may be simulated with elp- α or hyp- δ and elastic or elastoplastic relations for the cylinder. This can also be achieved with simplified ground reactions (Dierssen 1994), but solutions of the inverse problem in order to identify the ground reaction are debatable. Blows from a drive near the tip (j) render possible a deeper penetration as with a ‘peristaltic’ motion the shaft friction alternates above and below the drive. With vibrator and dead load on top (k) longitudinal waves in the cylinder are again damped by shaft friction and radiation. This can lead to a dead end with periodic propagation and to state cycles in the ground. Simulations with elp- α or hyp- δ would be expensive, whereas those with simplified ground reactions are debatable. It is not yet known how much a vibrator near the tip could ease the penetration.

The *degradation of grains* can play a role for the cone resistance as high pressures can occur. One could principally take it into account by updating constitutive parameters (cf. Sect. 7.3). Degradation bounds and simple substitutes are needed for applications with elp- α , hyp- δ or simpler soil reaction models. Cudmani (2001) found hemispherical cemented bodies under a rod pushed into dry sand. They arose from crushing of grains and baking of fresh powder. Such hemispheres are wider than the cylinder and break with further penetration. The cone resistance gets thus temporarily bigger and scatters more with a monotonous penetration.

Pore water in psammoids can easily be taken into account as long as its hydraulic height h_w does not change by the penetration. This may be assumed

for quasi-static cases as far as the grains are not very fine and the skeleton is not collapsible. Then it suffices to reduce the weight of soil and rod by hydrostatic uplift, and to work with a slightly lower granulate hardness due to the diminished surface energy with water (Sects. 6.1 and 7.3). Changes of h_w due to the diffusion of pore water in fine-grained psammoids can influence penetrations considerably. The ratio of tip velocity v_0 , or its average \bar{v}_0 over several reversals, and the permeability k_f get relevant (Sect. 6.2).

For rapid penetrations in the sense of (6.2.11) the seepage may be neglected so that skeleton deformations are isochoric in case of full saturation. The resistance to monotonous penetration is thus enhanced in dense and reduced in loose skeletons. Low or high relative void ratios r_e have a similar effect on penetrations with reversals and big amplitudes. With small amplitudes the average skeleton pressure \bar{p}_s is reduced, therefore higher frequencies can be of use. Such cases could be simulated with elp- α or hyp- δ , attractors in the large would support validations and simplifications as without water or with constant h_w .

With seepage and considerable seepage forces, i.e. for v_0 or \bar{v}_0 between the bounds by (6.2.11) and (6.2.12), the ground reaction depends on the delayed diffusion of pore water. Simulations with elp- α or hyp- δ and coupling with seepage would get expensive. Validations should be focused therefore on attractors in the large, simplified approaches could thus be justified. The h_w -field near the tip can be estimated by assuming an access of water through the tip with $v_w = v_0$ or \bar{v}_0 , Fig. 14.3.10. h_w rises approximately by

$$\Delta h_w \approx \frac{1}{8} dv_0 / k_f \tag{14.3.2}$$

at the tip, and nearly in proportion to $(d/2r)^2$ further away. Densification of the skeleton causes a slightly bigger Δh_w . p_s is reduced by ca. $\gamma_w \Delta h_w$ through seepage.

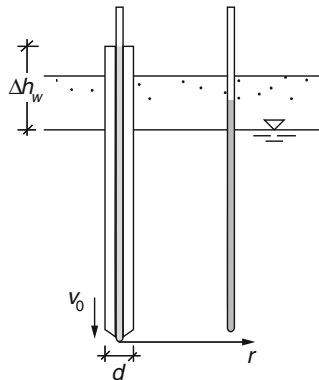


Fig. 14.3.10. Increased hydraulic heights by penetration into psammoid ground

Gas inclusions can be taken into account by a compressible pore fluid in case of bubbles between the grains (Sect. 6.2). A capillary skeleton pressure p_{cs} can be used if gas channels are connected with the atmosphere. With the closure of gas channels by densification of the skeleton h_w and p_w rise suddenly, also if gas pockets are left back. The related decrease of p_s by $\Delta p_w = \gamma_w \Delta h_w$ enhances the penetration more than by hydrostatic uplift, at least if Δh_w by (14.3.2) is considerable.

Injection of fluids through the tip eases the penetration as thus p_s is reduced in the near-field. This may be estimated by (14.3.2) with a lower k_f and the average infiltration velocity \bar{v}_f at the tip instead of v_0 . In more precise and expensive calculations the upward seepage along the shaft could be taken into account. Penetrations with blows or a vibrator can be enhanced by injection, but the influence of coupled pressure waves in skeleton and pore water can as yet hardly be quantified. Injections of suspension can further reduce the shaft friction if a filter cake can arise. Injection of air reduces p_s and enhances the penetration if the psammoid has open gas channels. The reduction $\Delta p_s = \gamma_w \Delta h_w$ can be estimated by (14.3.2) with average velocity \bar{v}_g and permeability k_g for gas. Injected air reduces the shaft friction at saturated fine-grained psammoids. Calculations for injections are only of qualitative value as the axial symmetry gets lost by a break-out (Sect. 16.3).

Penetrations into *peloid ground* are usually so fast by (6.2.11) that the seepage may be neglected. Meier (2009) simulated monotonous ones with *v*-hyp, different velocities v_0 , different spatially constant initial consolidation ratios p_e/p_s and degrees of saturation S_r around 0.95, Fig. 14.3.11. The chosen S_r in the range observed in situ prevents bulging of the free surface, and

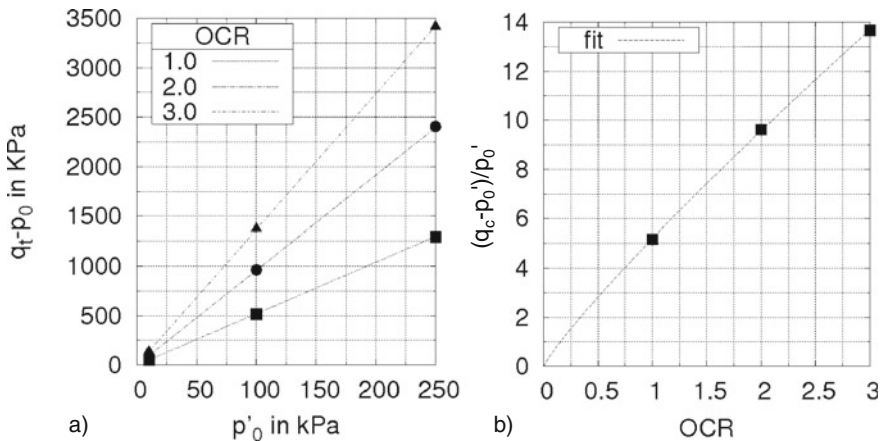


Fig. 14.3.11. Slow penetration into peloid ground, simulated with *v*-hyp by Meier (2009): (a) tip pressure versus far-field pressure, (b) pressure ratio versus initial overconsolidation ratio

its variation in a realistic range has little influence on the penetration resistance $q_c = F_c/(\pi d^2/4)$. In the asymptote q_c is proportional to the far-field pressure p_{sf} and increases with the initial p_e/p_s (a). The same dependence on the far-field values of p_s and p_e is obtained for the expansion of a spherical cavity (cf. Sect. 11.7). The ratio of both asymptotic pressures increases with the far-field consolidation ratio $p_e/p_s \approx OCR$ (c), this can be approximated by

$$q_c/p_i = a(p_e/p_s)^b \quad (14.3.3)$$

with $a \approx 10$ and $b \approx -0.1$. The argotropy enters via the one of the asymptotic spherical expansion pressure p_i , this is proportional to $(v_0/d_0 D_r)^{I_v}$ (Sect. 11.7).

q_c is proportional to the cohesion c_u without drainage (cf. Sect. 3.2) which can be determined in situ by torsion of a vane (Sect. 14.6). This is valid as both q_c and c_u are proportional to the far-field p_s . Combining Fig. 14.3.11 with c_u for the same data leads to q_c/c_u from ca. 15 to 20 for far-field consolidation ratios p_e/p_s from 1 to 3. This q_c/c_u is known empirically for clayey layers which are consolidated by their weight only, i.e. which have $p_e/p_s = \text{const}$ (e.g. Senneset et al. 1982). Based on this validation one can transform probing data from a penetrometer into those with a vane, and can determine p_e from one of the two data sets (Meier 2009). This works also if p_e/p_s varies with depth as long as p_s can be estimated via h_w (Sect. 11.3). For example, Cudmani and Sedlacek (2006) evaluated penetration data from Oslo, Fig. 14.3.12. Adaption of calculated and observed penetration pressures q_c (a) leads to a consolidation ratio which is higher above and constant below (b). This profile can be attributed to evaporation above and creep below the ground water table (Sect. 11.3).

The near-field by penetration with constant velocity v_0 is an argotropic attractor in the large. It is determined by the far-field values of p_s and p_e , the penetration velocity v_0 , the diameter d and the smoothness (Sect. 10.3) of the cylinder. After stopping a monotonous penetration the peloid relaxes and h_w gets hydrostatic if it was so before. The e -equivalent pressure p_e gets and p_s remains higher than in the far-field. An alternating penetration leads to a succession of argotropic state cycles. These can imply cavitation at the tip and may help to simplify approaches for the ground resistance. After such penetrations skeleton and pore water relax again, but towards a higher p_e and a lower p_s than after monotonous penetrations.

Vibratory driving with dead load and repeated impacts in peloid ground can also lead to successions of state cycles. They are distorted with respect to slow alternating penetrations by the propagation of waves, and by argotropy as the stretching rate varies over many decades. Caution is needed therefore with simplified approaches and with data transfer for different modes of penetration. Particle bridges and gas inclusions could principally be taken into

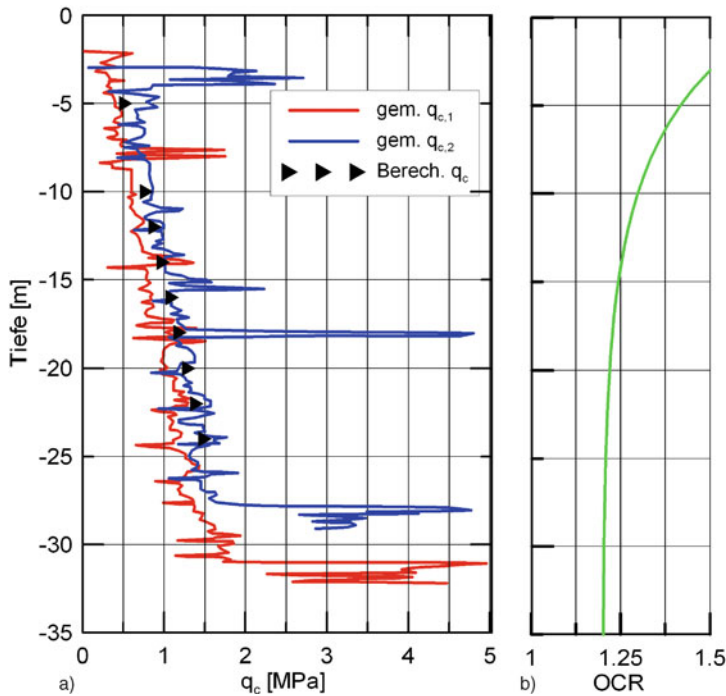


Fig. 14.3.12. Observed (*zig-zag lines* for two sites) and calculated (*triangles*) penetration resistance in peloid ground (a), estimated overconsolidation ratio versus depth (b) (Cudmani and Sedlacek 2006)

account (Sects. 7.1 and 7.2). Vibratory driving can get chaotic and the axial symmetry can get lost by radial cracks.

Penetrations in *composite ground* could be calculated by combining the methods outlined for psammoid and peloids, but transitions between layers require attention. A tip in a psammoid region feels a peloid layer ahead and vice versa, and the previous layer influences the entry into a new one. Such cases could be captured by combined attractors, these may help to establish simplified approaches. In a sandwich of many thin layers the penetration resistance is dominated by such transitions and cannot be predicted as precisely as with a more uniform ground. A simpler substitute composite (Sect. 9.2) may at best suffice to capture average penetration resistances, but hardly without adaption by field monitoring.

To *sum up*, various kinds of penetration can be captured by axi-symmetric simulations and attractors. The latter help to validate and simplify mechanical models for predictions and back-analyses. Such approaches were validated for monotonous, slow alternating and dynamic penetrations. Extensions are possible for deformable cylinders and for psammoids with excess pore pressures and degradation of grains. Monotonous penetrations in peloids can be

captured by argotropic attractors, extensions to alternating and dynamic penetrations are feasible.

14.4 Piles

Vertical piles can be placed in horizontal ground layers by filling (Sect. 14.2) and/or driving (Sect. 14.3), they can be pushed down and/or pulled up via structures at the pile head. For a plethora of cases their interaction with the ground can be captured by axially symmetric models, and attractors are of use to judge the range of validity and simplifications. For simplicity the pile may be cylindrical with flat or conical foot, and elastic or elastoplastic. The interface of pile and ground is defined by roughness and permeability (Sect. 10.3). A narrow zone near the pile can have another composition due to placement than the neighboured ground, which has another state due to the installation of the pile than farther away in the same depth.

Substitute boundary conditions are needed for numerical simulations and could be justified by comparative studies, Fig. 14.4.1. For capturing the field around the shaft a smooth rigid wall may be assumed, plus a rigid base and a smooth tube from the pile foot down to the bottom (a). A wall diameter $a \geq \text{ca.}10d$ may suffice for a single pile, uniform pile groups with smaller distance a can be represented by cells moving together (b). A bottom depth $d_b > \text{ca.}5d$ suffices instead of deeper ground, *nota bene* as far as the ground reaction along the shaft is concerned. A nearer and rougher wall and a shallower bottom can be chosen for validation tests, then the lowest part of the pile should be smooth. For geotechnically relevant axial displacements $|u| < \text{ca.} d/5$ an assumed smooth shaft section of the same height has almost no effect on the total shaft force (positive downwards into the ground)

$$F_m = \pi d \int_0^h \tau dz, \quad (14.4.1)$$

with vertical shaft shear stress τ and embedded pile depth h . The total foot force

$$F_f = 2\pi \int_0^d \sigma_f r dr, \quad (14.4.2)$$

with vertical pressure σ_f at the foot level $z = h$, may be calculated with a smooth shaft and a kind of hourglass instead of the tip for a driven pile (c). As for penetration (Fig. 14.3.1) singularities at apex and cone edge are thus avoided. Details of this substitute have little influence on F_f , this suffices for cones of driven piles which may aswell consist of soil compacted by driving. A convex foot without edge and a smooth shaft can represent bored piles with respect to F_f (d). Thus a singularity at the tip is avoided, and near-field

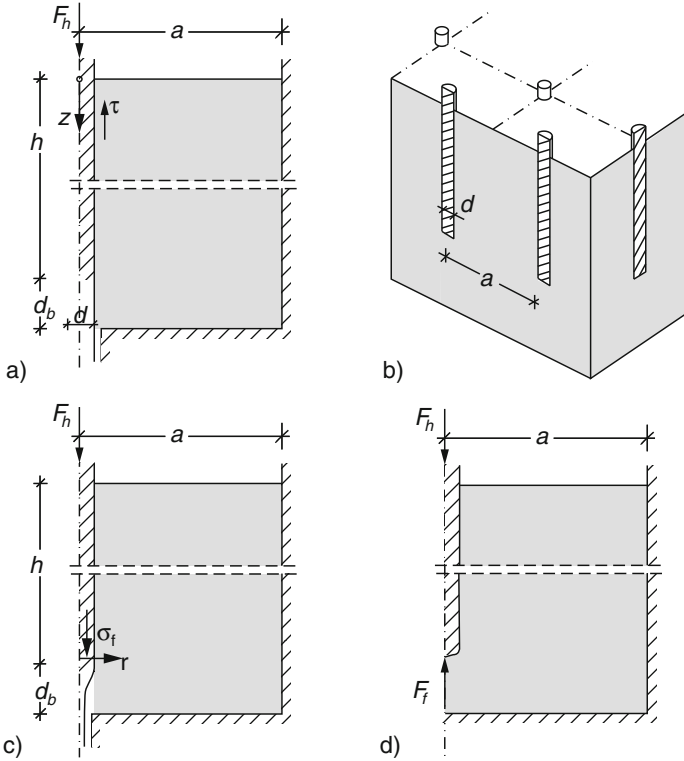


Fig. 14.4.1. Substitute boundary conditions for a pile shaft (a), a vertical pile group (b), and for the foot of a driven (c) or bored pile (d)

deformations can be followed up for allowable displacements. $F_f = 0$ suffices if the pile is pulled up.

For quasi-static evolutions head force F_h plus pile weight W_p equal the resistance of shaft and foot,

$$F_h + W_p = F_m + F_f. \tag{14.4.3}$$

For pulling up this holds with $F_f = 0$ and $F_m < 0$. Both F_m and F_f are slightly underestimated for pushing down with the simplifications by Fig. 14.4.1. For pulling up $|F_m|$ is thus also a little bit too small, and smaller than F_m for pushing down. The installation can lead to $F_f > W_p$ and $F_m < 0$ before imposing F_h , e.g. by grouting or inflating a cushion at the foot. During alternating pile displacements F_m can change its sign, and F_f can alternate between zero and an upper bound. Piles are rarely so deformable that the head can be displaced if the foot is fixed as shown in Fig. 14.3.9. With impacts or vibrations F_m and F_f are changed by inertial effects so that (14.4.3) is no more valid, such cases will only be touched in the sequel.

The response of *dry psammoid* ground to slow monotonous axial pile displacements u is mainly determined by the near-field relative void ratio r_{en} . This is lower than the initial and far-field value r_{ef} for a driven pile except for very low r_{ef} , Fig. 14.4.2a (cf. Fig. 14.3.8). The pressures at the pile (b) and the shear stresses along its shaft (c) can differ from original and far-field values after the installation (subscript i) and are then confined by $F_m + F_f = 0$. They change alongside with r_{en} by pushing down (label A) or pulling up (B). This can also be represented by plotting head force F_h versus head displacement u_h (d, with labels f for foot and m for shaft). The spatial average of r_e for $r \leq d$ may be taken as a representative r_{en} .

The *initial state* due to the installation of a pile cannot be determined in detail, but it can be estimated by means of attractors depending on the kind of operation (Sect. 14.3). Near the pile the skeleton tends to a state limit field

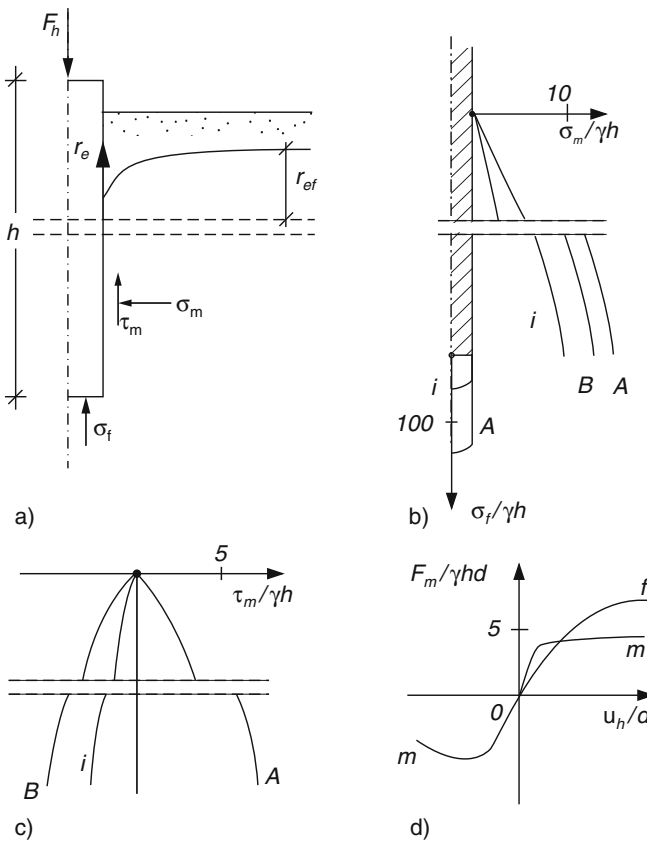


Fig. 14.4.2. Pile with monotonous loading in psammoid ground (a), distributions of shaft and foot pressure (b), profiles of shaft shear stress (c), shaft and foot forces versus displacement (d)

by a monotonous axial pile displacement, this field is determined by the far-field pressure p_{sf} and by the near-field average relative void ratio r_{ef} . In other words, this attractor means that the ground response is determined by shaft geometry and ground density close to it, whereas details of skeleton stresses due to the installation are swept out with the pile displacement. Rebstock (2006) showed that by means of comparative calculations with hyp- δ and found that only the average r_{en} of the initial r_e in the range $r \leq d$ counts. As this can hardly be determined in situ r_{en} has to be adapted by back-analysis of pile loading tests, the results of which can then be transferred to other loading conditions.

Figure 14.4.2 shows evolutions for an originally medium dense skeleton which was densified near the pile by its installation. For pushing down (A) F_m can almost attain a plateau, whereas a peak of F_f vs. u_h can at best be reached with a hardly tolerable displacement and a low r_{en} . The skeleton near the shaft is radially stressed as its dilatant shearing is impeded by the surrounding ground. Near the foot the skeleton is mainly densified and only dilated with excessive displacements. For pulling up (B) the negative F_m attains a flat peak with $\max |F_m|$ well below the positive F_m . The dilated shearing near the shaft is less impeded by the surrounding ground when the nearest part of it is lifted, thus shear softening by dilation occurs after a smaller pile displacement than for pushing down.

For a bored pile with the same geometry and far-field the ground resistance is lower as the skeleton is more dilated near the pile during its placement. This means a lower initial r_e and radial pressure and a negligible initial shaft shear stress. F_f and $|F_m|$ are smaller than for a driven pile for pushing down, and for pulling up with a smaller difference of $|F_m|$. Due to the higher r_{en} the skeleton near the pile is less jammed by confined dilation near the shaft and more compressed at the foot than with a driven pile.

Rebstock (2004) back-analyzed *tension pile* lab tests with dry sand by means of finite elements and hyp, Fig. 14.4.3. Wernick (1978) had pulled up a rough rod in a cylinder filled with dense sand (a). The finite element mesh is finer near the pile, and a small surface pressure was added to avoid $p_s = 0$ (b). The elements along the shaft are as thick as the observed shear zone. Calculated and observed force-displacement curves agree in the asymptotes, but observed peaks are not reproduced (c). The deviation cannot be attributed to polar effects at the shaft (Sect. 8.2) as the ratio of pile and grain size $d/d_g \approx 75/0.25 = 300$ exceeds the bound of influence by Tejchman (1997), cf. Sect. 14.1. This indicates a seismically activated relaxation (Sect. 4.6, Rebstock 2010).

Rebstock (2004) simulated also a pull-out test in situ, Fig. 14.4.4. The piles had been placed by boring in medium dense sand under water (a). Their diameters had been increased from 0.15 to ca. 0.20 m by grouting. The mesh has fictitious rough outer boundaries and thinner elements along the shaft (b). Observed and calculated pull-out curves agree with a realistic r_e near the shaft (c). Hydrostatic uplift and pile deformability were taken into account. Com-

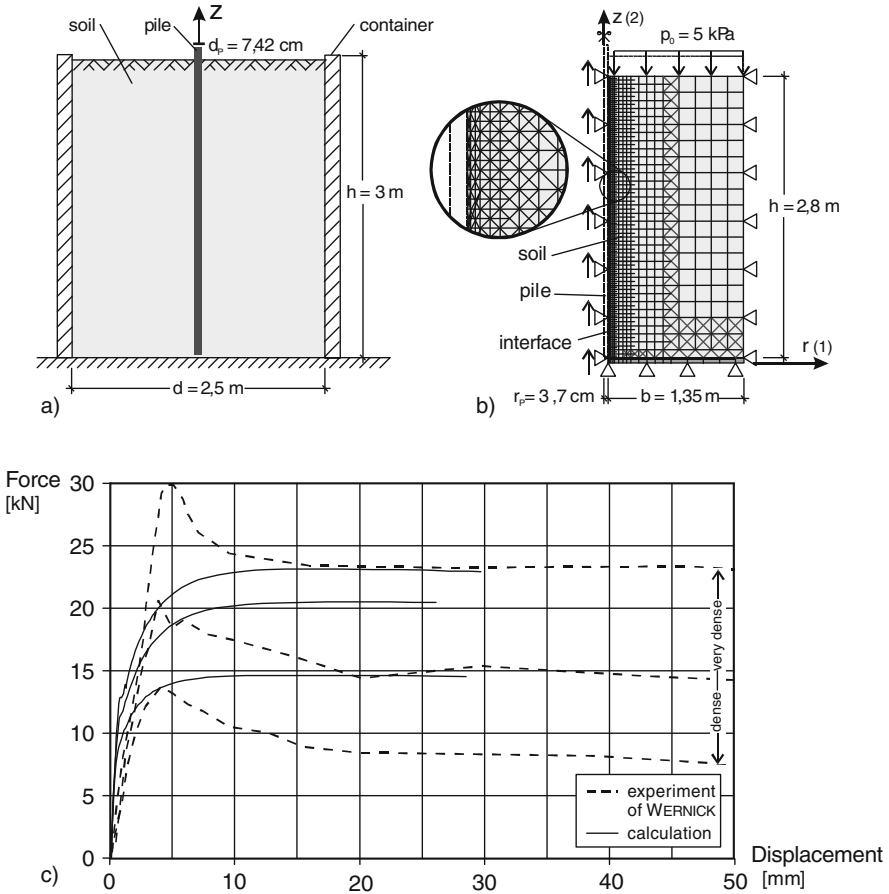


Fig. 14.4.3. Back-analysis of Wernick's (1978) tension pile tests with sand by Rebstock (2004) : setup (a), mesh (b), forces versus displacement (c)

parative calculations reveal that the expansion pressure after grouting may be neglected as it is swept out by shearing. The shaft resistance is determined by the far-field p_s and the near-field r_e , and increases with the hypoplastic parameters φ_c (friction), h_s (hardness) and α (dilatancy). The piles were so rough that slip along them can be excluded.

Interactions of piles with dry psammoid ground for slow displacements with *reversals* can be judged by means of asymptotic state cycles, Fig. 14.4.5. Consider representative soil elements (RSEs) near the shaft (A) and the foot (B) which are sheared (a). With axial pile displacement cycles the state paths in plots of two stress components (b) and of e vs. $\log p_s$ (c) tend to butterflies (cf. Fig. 14.3.6). The average r_e is determined by the amplitude, the average

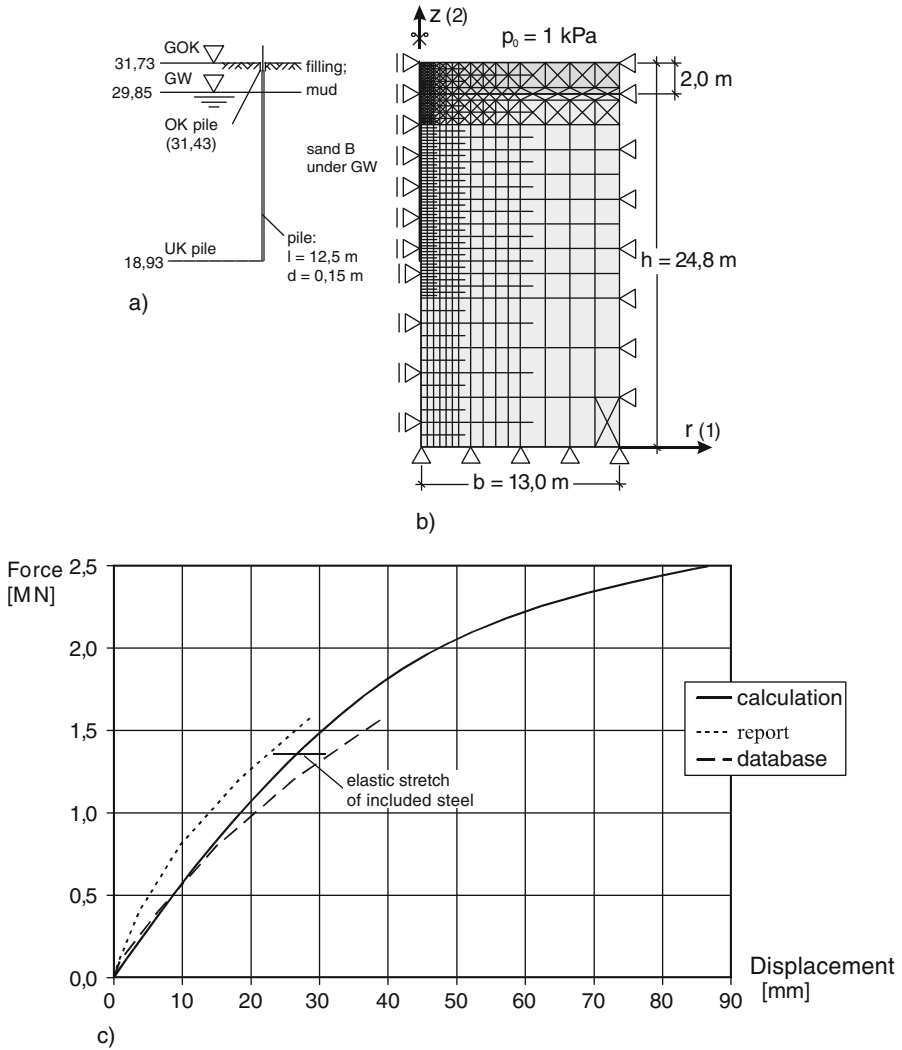


Fig. 14.4.4. Simulation of pull-out tests with sand in situ (Rebstock 2004): situation (a), mesh (b), force versus displacement (c)

p_s is close to the far-field value. For ratcheting the asymptotic cycles are loops with higher average r_e , again with average p_s nearly as in the far-field. Such attractors in the large could be generated with hyp- δ and observed in model tests. They mean that the near-field state due to placement can be swept out in periodic asymptotes.

Some observations confirm this concept. Mazurkiewicz (1968) reports that model piles in dense sand can be more easily pulled out with reversals, and concludes that anchor piles for repeatedly emptied dry docks require a more

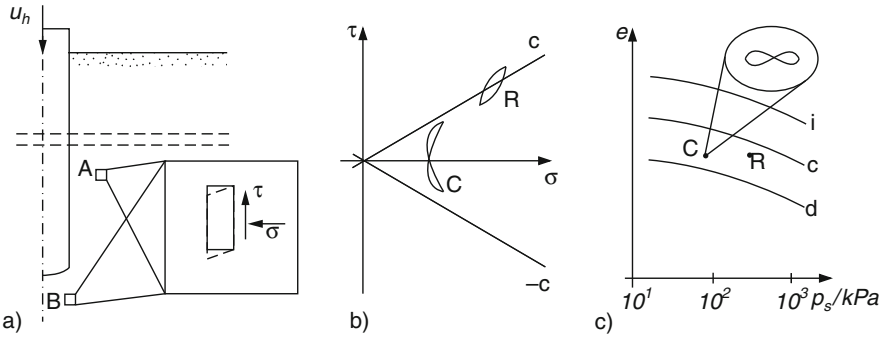


Fig. 14.4.5. Pile with reversals in psammoid ground (a), asymptotic cycles of stress (b) and void ratio versus pressure (c) of RSEs near the pile for cyclic displacements (C) and ratcheting (R)

conservative design than for monotonous loading. Rebstock (2010) found that these model tests cannot be simulated with hyp- δ due to polar and seismic effects. His simulations are more realistic for pile tests with ratcheting by Schwarz (2002), and for the anchored and repeatedly emptied mud vessel of a sewage plant. This kind of seismically activated relaxation and creep may be qualitatively explained with s-hyp or h-cyc (Sect. 4.6), but quantifications require an energy-based approach.

Inertial effects can principally be taken into account as for penetration (Sect. 14.3), but simulations and validation studies are not at hand. An axial impact could be imposed to the pile head or at the bottom of a cylindrical test bin. It could be repeated until a periodic response indicates an attractor. Axial vibrations could likewise be imposed up to a periodic response. Stochastic impacts from above or below with axi-symmetric averages could be captured with s-hyp and model tests (cf. Sect. 13.8).

The *pore water* of psammoid ground at piles may often be assumed to have a stationary hydraulic height h_w . With full saturation, and also with gas bubbles between the grains, this means hydrostatic uplift for resting groundwater, and well-determined seepage forces in case of stationary flow. With gas channels connected to the atmosphere the skeleton pressure p_s is higher by the capillary skeleton pressure p_{cs} (Sect. 6.2). p_{cs} is often negligible for the resultant forces at shaft and foot F_m and F_f in situ, but not in model tests with fine grains, and is of use near the free surface to avoid $p_s = 0$ and dust. Changes of h_w due to pile displacements can play a role alongside with inertial effects (cf. Sect. 13.8), but have not yet been investigated.

Interactions of piles with *peloid* ground are argotropic due to skeleton viscosity and pore water diffusion. Thus the state at the onset of loading does not only depend on the kind of installation, but also on the waiting time thereafter. The rate of skeleton relaxation \dot{p}_s/p_s after installation is proportional to $(p_s/p_e)^{1/I_v}$ by (3.2.7), and thus high for the reduced consolidation

ratio p_e/p_s which arises near the pile by its installation. The rate of pore pressure adaption \dot{p}_w/p_w by diffusion is proportional to k_f/d_w^2 by (11.1.4), with permeability k_f and drainage length d_w . Thus shear stresses due to the installation may be neglected for initial states after installation, but not excess pore pressures in general. Only if the diffusion of pore water is avoided during the installation it can hardly play a role in waiting times, but the pore water can then relax due to the ever-present gas fraction. Otherwise, in particular if changes of void ratio during the installation are enhanced by cracks, diffusion times can be shorter than acceptable waiting times.

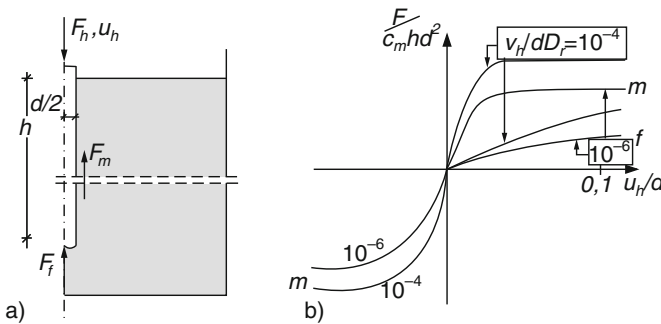


Fig. 14.4.6. Monotonously loaded pile in peloid ground (a), forces versus displacements (b)

Leaving aside relaxation and diffusion, interactions *without seepage, reversals and inertia* may be considered first, Fig. 14.4.6. A pile may stand in peloid ground and may be loaded at its head with control of axial force or displacement (a). The far-field may have a constant hydraulic height h_w , skeleton stress ratio T_{s2}/T_{s2} and consolidation ratio p_e/p_s due to its resting time (Sect. 11.3). Near the surface h_w could be lower (suction), and p_e/p_s could be higher (after shrinkage or geological unloading) than further below. After an installation without swelling or shrinking the near-field may have returned to the original state field. The weight difference of pile and displaced ground may be neglected, or imposed as permanent head load. The pile surface may be rough and remain in contact with the ground, the pile may be rigid. As outlined with Fig. 14.4.1 the forces F_m and F_f at shaft and foot can be calculated by assuming a smooth cylinder under or above the foot, respectively. F_m and F_f result from total stresses including pore pressures which are changed by loading.

With a given head velocity v_h the resistance is argotropic, Fig. 14.4.6b. This can be expressed by

$$F_m/F_{mr} = F_f/F_{fr} = (|v_h|/D_r d)^{I_v} \tag{14.4.4}$$

with reference values F_{mr} and F_{fr} for shaft and foot in case of $|v_h| = D_r d$. This results from the non-linear skeleton viscosity (Sect. 3.2) and agrees with Winter's (1979) relation (13.3.3) for a stationary asymptotic response. The latter has the same amount for pushing down (A) as for pulling up (B) as the asymptotic response to shearing near the pile is determined by the void ratio and the shearing rate (Sect. 3.2).

The foot resistance F_f can at best attain a plateau after an acceptable displacement u_h with a driven pile as then the ground close to the foot can reach an isochoric state limit before (cf. Sect. 14.3). The displacement needed to attain a stationary shaft resistance F_m is often acceptable with driven and bored piles. The reference value F_m in (14.4.4) can then be approximated by

$$F_{mr} \approx \operatorname{sgn}(v_h) \pi d_s h \bar{c}_{ur} \quad (14.4.5)$$

with the cohesion \bar{c}_{ur} averaged over the shaft for undrained shearing with rate $D = D_r$. This implies a shear zone of thickness d_s along the shaft. The stationary reference foot resistance for (14.4.4) can be approximated by

$$F_{fr} \approx m_f \pi \frac{d_s^2}{4} \bar{c}_{uf} \quad (14.4.6)$$

with the average cohesion \bar{c}_{uf} near the foot for $D = D_r$. The factor m_f depends on the far-field consolidation ratio p_{ef}/p_{sf} at depth h used in Fig. 14.3.11 for penetration.

The near-field of piles which are monotonously shifted past peloid ground tends thus to an argotropic state limit in the large. This could be simulated with v-elp or v-hyp for an axi-symmetric initial state field which depends on far-field and pile placement. Similarly as with psammoid ground the resistance is dominated by the near-field void ratios. As shown in Fig. 14.4.6b the displacement required to reach this attractor is hardly argotropic. It cannot as easily be estimated as the limit resistance, and is at best as determinate as the near-field void ratios after placement.

With a constant head force F_h the pile tends to stationary *creep* as long as pore water diffusion may be neglected. The asymptotic creep velocity of the pile head can be estimated by inversion of (14.4.4) with (14.4.5) and (14.4.6). The transition to this thermally activated attractor is at best as determinate as the initial near-field, simulations with v-elp or v-hyp could demonstrate this indeterminacy. *Relaxation* towards the initial near-field would occur after complete unloading or stopping the pile. This second endogeneous attractor could also be obtained by simulations, but the transition can at best be estimated.

Interactions of rigid piles with peloid ground, again first without seepage and/or inertia, are different with *reversals* of axial displacements u , Fig. 14.4.7. With axial pile displacement cycles and constant amount of velocity $|v_h|$ the ground tends to argotropic state cycles, and so do the resultant forces F_m and F_f at shaft and foot (a). The plot of F_m vs. u is symmetric in the asymptote,

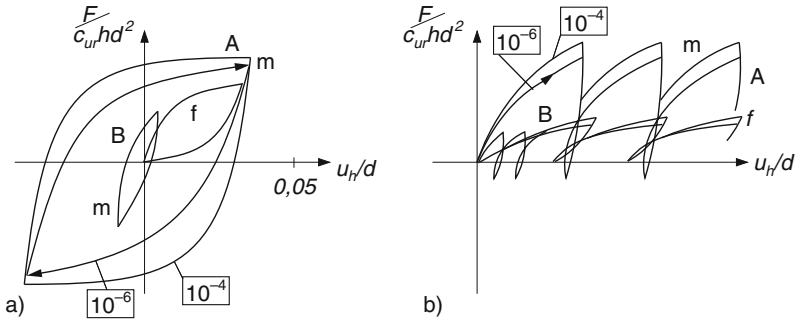


Fig. 14.4.7. Forces versus displacements for cyclic displacements (a) and ratcheting (b) of a pile as in Fig. 14.4.6a

the one of F_f is asymmetric. The amounts attain the ones for monotonous displacements with big amplitudes (A), otherwise they are smaller (B). The average near-field skeleton pressure \bar{p}_s gets closer to the far-field value p_{sf} for smaller amplitudes. This is understandable with cyclically sheared RSEs near the pile (cf. Sect. 3.8).

Ratcheting of a rigid pile with constant $|v_h|$ leads to other argotropic state cycles of the ground. These can be partly represented by plots of F_m and F_f vs. u_h (Fig. 14.4.7b). The ones of F_m are asymmetric, those of F_f are one-sided nearly as before. The amounts attain the ones for monotonous displacements in case of big amplitudes with dominant downwards fraction (A). Otherwise the amounts are smaller (B), and the averages over one cycle are closer to the far-field values. This response can be justified by means of RSEs near the pile (cf. Sect. 3.8). The argotropy of F_m and F_f could be approximated by (14.4.4), this is evident for so big amplitudes that state limits are attained as without reversals.

Step-wise *creep* occurs with dead loads in intervals where F_m attains amounts related with significant head velocities by (14.4.4), and where F_f attains values by (14.4.6) for penetration, Fig. 14.4.8 (A). Otherwise (B) the cumulative displacement is often negligible. With periodic loading at the pile

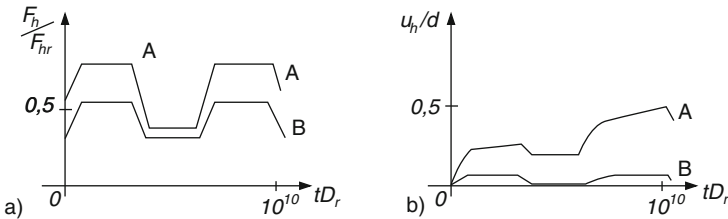


Fig. 14.4.8. Creep of a pile as in Fig. 14.4.6a with pulsating loads: head forces (a) and displacements versus time (b)

head the near-field attains again state cycles, but now the related stretching rates D vary by orders of magnitude within one cycle. A *relaxation* occurs in the ground near the shaft, and also near the foot if it is fixed. Then the skeleton state returns to the one in the far-field, this occurs faster if the near-field consolidation ratio is low, say $p_e/p_s < \text{ca. } 1.5$.

The *deformability* of piles could be taken into account by elastic or elastoplastic relations for the solid. As with penetration (Fig. 13.3.9) it reduces the ground resistance under and near the foot as this is less displaced than the head. *Inertial* effects influence evolutions with impacts or vibrations imposed from the pile head or the deeper ground. As with penetrations the diffusion of pore water is first negligible, and for rapid monotonous pile displacements the soil inertia may often be neglected. The radiation of shear waves from the shaft and of pressure waves from the foot plays a role for repeated impacts or vibrations, both can lead to asymptotic state cycle fields. The propagation of longitudinal waves in elastic piles is damped by soil hysteresis and radiation of waves.

The *diffusion of pore water* matters for durations of pile loading that reach or exceed the diffusion time t_d . This is shorter if the ground is drained via the pile. The diffusion may be neglected for the vicinity of the shaft as far as the pore water can get relaxed due to a small gas content. The foot resistance F_f increases by consolidation for times reaching or exceeding t_d . With dead loads over times $t > t_d$ creep velocities can thus be reduced considerably. With long-term negative dead loads and initial consolidation ratios $p_e/p_s > \text{ca. } 4$ a suction with respect to the far-field, $p_{wf} - p_{wn} > 0$, is reduced by dilation. This shear-enhanced swelling can lead to a pull-out collapse after loading times $t > t_d$. Reversals with small amplitudes in between enhance the consolidation for durations $t > t_d$, with big amplitudes they enhance the average dilation up to a collapse.

Gas inclusions can play another role than during the placement by penetration (Sect. 14.3) due to the solubility (Sects. 6.1 and 6.3). Minute gas bubbles between solid particles can be taken into account by assuming a compressible pore fluid with allowance for the p_w -dependent solubility. Cavitation may be assumed at the pile foot for $p_w = 0$ as imperfections prevent more suction there, this yields a lower bound for F_f if the foot is pulled up. Gas channels can arise by opening of latent fissures and along shafts pulled up, this reduces suction and enhances swelling with diffusion. The influence of partly dry crack systems or other gas channels above the groundwater table cannot yet be quantified.

Except for gas channels evolutions with piles in peloid ground could be simulated with v-elp or v-hyp for monotonous pile displacements, and with v-elp- α or v-hyp- δ if there are reversals. Given axial symmetry, such simulations would be the more realistic the better initial composition and state after placement are known. Validations could be obtained with good data sets, these could more easily be attained with lab model tests than with load tests in situ.

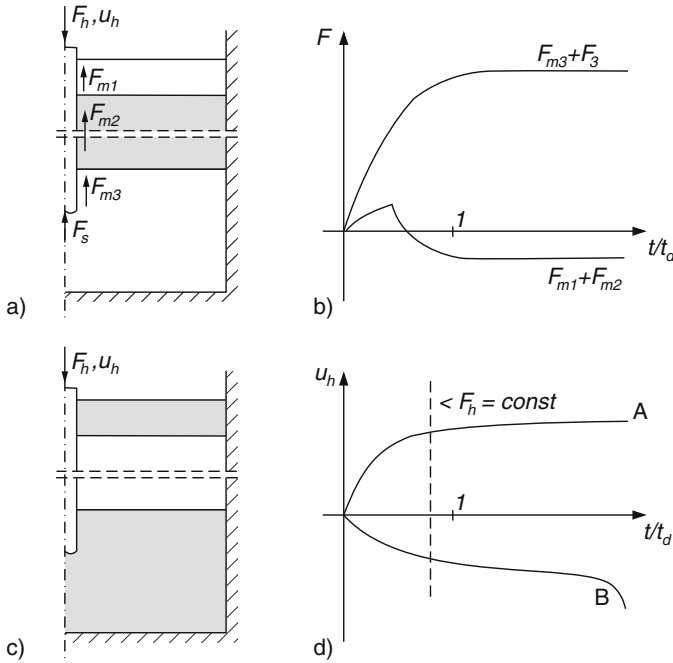


Fig. 14.4.9. Pile in composite ground with soft peloid (a), forces versus time (b), same with sand layer in stiff clay (c, d)

Axi-symmetric interactions of piles with *composite* ground cannot be captured as precisely as when the ground consists of psammoid or peloid only. Two cases with three layers may illustrate what can happen, Fig. 14.4.9. A pile may stand in dense psammoid under unconsolidated peloid with a young psammoid cover in groundwater, and may carry a permanent positive dead load (a). After placement and loading the on-going consolidation of the peloid layer by pore water diffusion and skeleton creep (Sect. 11.3) causes a *negative shaft friction* in the peloid and the psammoid on top, $F_{mc} < 0$ and $F_{m2} < 0$. The pile sinks further therefore into the competent base layer, but how much in the course of time?

The downward displacement of ground relative to the pile after its loading is zero at the peloid base and biggest at the top layer. Therefore the drag shaft forces F_{m1} and F_{m2} increase up to nearly stationary values (b), while the resistance $F_{m3} + F_{f3}$ of the competent layer increases (otherwise F_{m1} and F_{m2} would not get negative). The pull-out resistance F_{m1} can be determined as explained with Fig. 14.4.2. The initial one of the peloid can be determined without seepage as explained with Fig. 14.4.6. With the initial shear reversal near the shaft of a driven pile the required relative displacement up to stationary F_{m1} and F_{m2} is bigger than without it as for a bored pile. Excess pore pressures after loading the pile may be excluded by drainage and waiting

time. The negative F_m cannot further increase thereafter although the shearing resistance would increase due to densification with constant shearing rate D as it would decrease with constant e by decreasing D due to stabilizing creep. Thus the pile tends to a state of rest if it is not plastified near the foot.

An opposite layering, which may include a peloid crust, leads to other evolutions, Fig. 14.4.9c and d. With a positive permanent dead load (A) creep goes on in the base layer, and is slowed down by consolidation under the foot. This enhances the upper shaft resistances F_{m1} and F_{m2} as the far-field base of these layers does not subside, but both cannot exceed their stationary asymptotes. With a negative permanent dead load (B) the upwards creep of the pile is impeded by negative friction $F_{m1} < 0$ and $F_{m2} < 0$ as long as their amounts increase, the far-field base of these layers is not lifted.

Such cases could be simulated by combining elp and v-elp or hyp and v-hyp for monotonous evolutions, coupling with pore water requires further boundary conditions (Sect. 10.3). With reversals elp- α and v-elp- α or hyp- δ and v-hyp- δ could similarly be employed. Shaft and foot forces may be determined separately as indicated with Fig. 14.4.1, but similar simplifications for interfaces of layers are not advisable as their consequences can hardly be judged. Packages of several layers may be substituted by composites (Sect. 9.2), in particular for sandwich ground. As thus a layered ground cannot be captured as well as homogeneous ones caution and judgment are required in evaluations of load tests and predictions for design.

To *sum up*, interactions of vertical piles with horizontal layers for axial loads can be captured with axial symmetry, and attractors are of use for simplifications and validations. Shaft and foot resistances F_m and F_s of psammoid ground are enhanced by low relative void ratios r_e and hard grains. F_m and F_f have lower amounts with reversals, the more if the amplitudes are small. F_m and F_f are smaller with peloid ground as its particles are softer, and argotropic so that creep and relaxation can occur. Monotonous pile displacements can lead to state limits in the near-field, with reversals state cycles can be attained. The approach to these attractors is less determinate with layers. Axi-symmetric near-fields can be attained by axial loading and can hardly get lost by shear localization or cracking.

14.5 Silos

Storage and flow of soil-like materials in axi-symmetric vessels or silos can be axi-symmetric, but this symmetry can get lost spontaneously. Attractors are of use for such cases to strengthen mechanical models, to validate them by experiments, to understand limitations and to improve them.

Beginning with *dry psammoids*, slow motions in rigid cylinders may first be considered, Fig. 14.5.1. In a setup (a) a rigid bottom may be attached to

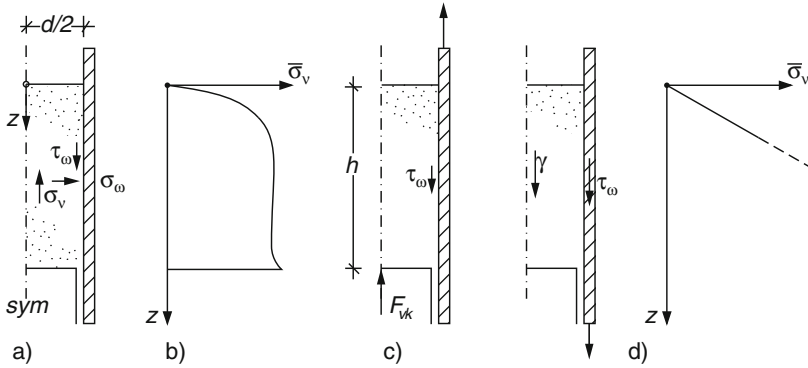


Fig. 14.5.1. Cylinder with granular fill (a), wall pressures with lifted cylinder (b), near-wall shearing with lifted and lowered cylinder (c), jamming (d)

a force transducer, the wall may be movable and smooth or rough (cf. Sect. 10.3), and granular material may be placed with a horizontal free surface and a desired density (cf. Sect. 12.1). During and after filling the skeleton is partly suspended by wall friction so that its stress state is independent of depth z except for the vicinity of base and free surface (b). As outlined with Fig. 13.7.1 the horizontally averaged vertical pressure σ_v can be approximated by Janssen’s (1895) formula

$$\sigma_v = \frac{\gamma}{M} [1 - \exp(-Mz)] \tag{14.5.1}$$

with the constant factor $M = 4K \tan \varphi_w / d$. Therein the wall friction angle φ_w may be given by wall roughness and critical friction angle φ_c (Sect. 10.3), whereas relative void ratio r_e and stress ratios are determined by shearing at best along the wall (Sect. 8.2). The ratio $K = \sigma_h / \bar{\sigma}_v$ of normal wall pressure σ_h and average vertical pressure $\bar{\sigma}_v$ is not likewise determined as it depends on the filling procedure. This historical element could principally be captured by means of the initial void ratio e_o at the rising free surface (cf. Sect. 12.1). Settling leads to shearing of a narrow zone along the wall and determines e there, whereas it is reduced from e_o by the increase of the mean pressure p with depth which may be estimated by (14.5.1). But how to get K , and when and where will sliding occur with the average amount of shear stress $|\bar{\tau}| = \sigma_h \tan \varphi_w$?

A slow *granular flow* can be produced by lifting the wall relative to the fixed bottom, Fig. 14.5.1c. The resultant bottom force $F_{vh} = \sigma_{vh} \pi d^2 / 4$ can be measured for different filling heights h . Back-analyses with (14.5.1) can thus lead to K and can confirm the uniformity of state over the major part of depth (Tejchman 1997). A stationary granular flow could as well be produced by opening a bottom sieve and adding grains through a top sieve with the same mass flow. With such a generation and decay of the grain skeleton its state will differ near top and bottom from the one produced without sieves, but

hardly over the major part of depth. This kind of attractor could be observed by measuring resultant forces at bottom and/or cylinder with different filling heights h and initial relative void ratios r_{eo} . Higher r_{eo} are obtained by bigger intensities of pluviation, e.g. via wider sieves (cf. Sect. 12.1).

The grain skeleton can be *jammed* into the cylinder by pulling this down relative to the bottom, Fig. 14.5.1d. As with a passive trap door (Fig. 13.7.1b) wall shear stress τ_w and specific weight γ act in the same direction. Janssen's (1895) assumption and the equilibrium of discs as by (13.7.1) would lead to an exponential increase of the horizontally averaged vertical pressure $\bar{\sigma}$ from the free surface downwards, i.e. (14.5.1) would hold with $+$ instead of $-$. This can at best be valid up to a certain depth as the mean bottom pressure $\bar{\sigma}_{vh}$ is bounded by the capacity of the device to pull the cylinder. Janssen's approach gets invalid for the major part of the fill as this does not slide past the cylinder.

Slow axial *displacement cycles* of the bottom relative to the cylinder lead to state cycles in the skeleton, Fig. 14.5.2a. The latter may be represented as in Sect. 4.4 for cyclic shearing of a boundary zone of thickness d_s (insert). This substitutes a zone with polar quantities (Sect. 8.2), so d_s and attainable stress ratio $|\tau_w|/\sigma_w$ increase with grain size d_g , wall roughness d_w and neighboured relative void ratio r_e . With a big amplitude (A) and a rough wall ($d_w \approx d_g$) the stress path near the wall (b) approaches an asymptotic cycle temporarily. Downward shearing of the skeleton past the wall jams a not too loose skeleton more than upwards shearing, in both cases the dilation is impeded. Upward shearing can lead to monotonous granular flow, downward shearing causes a stronger stressing up to states as explained with Fig. 14.4.1d.

With a small amplitude (B) state limits with overcritical stress ratio $|\tau|/\sigma$ and impeded dilation are never reached. If the skeleton is not very dense after filling it gets denser in the transition to such asymptotic cycles. The average asymptotic stress ratio $|\bar{\tau}|/\sigma_w$ over a cycle is lower than $\tan \varphi_w$. This means that the average vertical pressure $\bar{\sigma}_v$ increases almost linearly with depth, and that the skeleton is compressed by its weight (cf. Sect. 11.1). In other words, small cycles relax the skeleton and reduce thus the average wall friction. This resembles the response of a saturated RSE to cyclic shearing without drainage (Sect. 4.2). There skeleton deformations are constrained by the pore water, here by the cylinder.

A stationary *ratcheting* of the cylinder upwards past the base (14.5.1c), with a low frequency f_c so that inertial effects may be neglected, leads also to asymptotic state cycles. With a big amplitude (A) stress cycles near the wall (d) can attain dilatant state limits in upwards sections if the fill is not loose and the wall is rough. Thus the skeleton is repeatedly stressed as its dilation is impeded by its hardly deformed interior part. In upwards intervals a state limit can be attained near the wall as for monotonous granular flow, in downwards intervals the skeleton gets jammed as explained with Fig. 14.5.1d. This means that a stationary ratcheting of the cylinder downwards past the bottom is not possible.

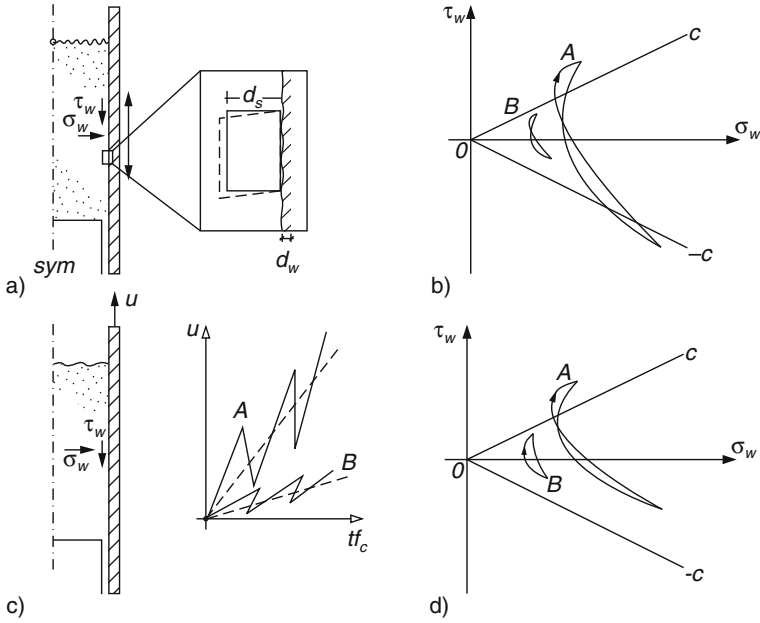


Fig. 14.5.2. Cylinder with granular fill and cyclic displacement (a), attained stress cycles near the wall (b), same with ratcheting (c, d)

With a small amplitude (B) the asymptotic stress cycles are still asymmetric, but dilatant state limits are never attained. Thus the skeleton is not stressed by the gradually increased shearing along the wall, and its average stress ratio $|\bar{\tau}_w|/\sigma_w$ over one cycle is well below the wall friction ratio $\tan \varphi_w$. Even with a rough wall the average vertical pressure $\bar{\sigma}_v$ increases therefore almost linearly with depth as without wall friction. A similar ‘cyclic mobility’ occurs with a saturated undrained RSE (cf. Fig. 4.3.7) where skeleton rearrangements are confined by the pore water, here average radial strains are prevented by the wall.

Other slow evolutions would occur with *deformable walls*. These can be punctuated and scratched by hard grains so that φ_w increases, but φ_w can also decrease by creep if the wall material is viscous (cf. Sect. 3.1). The cylinder is expanded by an increasing wall pressure σ_w , thus the dilation by shearing along the wall is less impeded. With reversals of the fill the cylinder could swell and shrink, this would modify the asymptotic cycles. With big amplitudes jamming would occur after a bigger displacement than with a rigid wall due to bulging.

Slow evolutions as indicated with Fig. 14.5.1 can be observed in model tests, and could be *simulated* with elp or hyp without and elp- α or hyp- δ with reversals. Polar effects should be taken into account if the cylinder diameter does not exceed about 100 grain diameters, i.e. for $d < \text{ca. } 100d_g$ (Tejchman

1997). Then the wall roughness enters the boundary condition (Sect. 8.2), otherwise $|\tau|/\sigma$ cannot exceed $\tan \varphi_w$ at the wall (Sect. 10.3). The granulate hardness h_s should be lower in model tests by the same scaling factor as lengths in order to get the same strains as in prototype silos. The density after filling can be controlled by a top sieve. Axial forces and displacements could be used for validation if the attractors outlined with Figs. 14.5.1 and 14.5.2 are attained both in experiments and simulations. Local pressures can hardly be measured without disturbance, but asymptotic void ratios could be observed via X-ray tomography.

Inertial effects could also be investigated with dry psammoid in a rigid cylinder, Fig. 14.5.3. Axially symmetric motions with relevant accelerations of the skeleton can be imposed via cylinder or bottom, and can also arise spontaneously. Extending Janssen's (1895) idea we consider wall stresses, average axial stresses \bar{T}_z and displacements \bar{u}_z of a representative disc (a). The balance of axial momentum requires

$$\frac{d\bar{T}_z}{dz} - \frac{\gamma}{g} \frac{d^2 \bar{u}_z}{dt^2} + \gamma - 4 \frac{T_{zrw}}{d} = 0. \tag{14.5.2}$$

Therein the wall shear stress T_{zrw} may be proportional to the axial one via

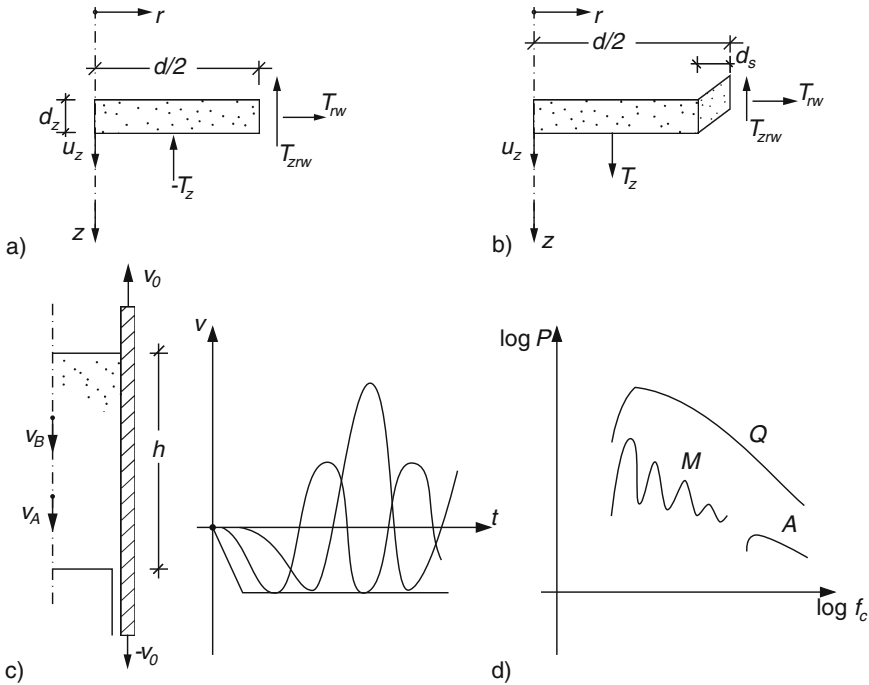


Fig. 14.5.3. Cross section of a granular disc (a) and of a disc with ring (b), longitudinal waves (c), power spectra (d)

$$T_{zrw} = -\text{sgn}\left(\frac{d\bar{u}_z}{dt}\right) K\bar{T}_z K \tan \varphi_w \tag{14.5.3}$$

in case of monotonous shearing past the wall. The axial deformability is sufficiently determined by \bar{T}_z and e only if the skeleton was initially at a state limit. Other than in a free-field (Sect. 11.4) the longitudinal wave propagation is damped by wall friction, the energy input required for a certain reach of propagation could thus be estimated. Numerical simulations with (14.5.2), (14.5.3) and adapted elp or hyp parameters are at most worth the effect if a single propagation can be achieved with wall slip in an experiment for validation.

Equation (14.5.3) gets invalid for other than monotonous evolutions, with or without wall slip, as the stress ratios T_r/\bar{T}_z and T_{zrw}/T_{rw} switch during a propagation. In a less simplified approach one may assume representative discs with sheared rings which are uniform with respect to states and deformations, Fig. 14.5.3b. Less specified and without inertia this was similarly assumed in the explanations above with Figs. 14.5.1 and 14.5.2. With $d > 100 d_g$ to avoid polar effects, and with a shear zone thickness $d_s/d_g \approx 2$ to 10 (Sect. 8.2) according to wall roughness and void ratio, weight and inertia of the shear zone may be attributed to the disc or neglected (cf. Sect. 14.3). The following outline is rather qualitative and refers to the simpler disc-ring model. Quantifications could principally be achieved by simulations with hyp- δ and p-hyp, but these could only be justified by more general axi-symmetric simulations and validation experiments.

Lifting the cylinder relative to the bottom with a constant velocity v_o can lead to stick-slip, and thus to repeated longitudinal waves in the psammoid column, Fig. 14.5.3c. With suitable combinations of diameter d , height h , grain size d_g , wall roughness d_w , initial relative void ratio r_{eo} and upwards wall velocity v_o this can lead to a rather periodic *silo music* (Tejchman 1997). Outside this range chaotic *silo quakes* can occur, or a stationary flow without such autogeneous shocks. This response has characteristic power spectra in

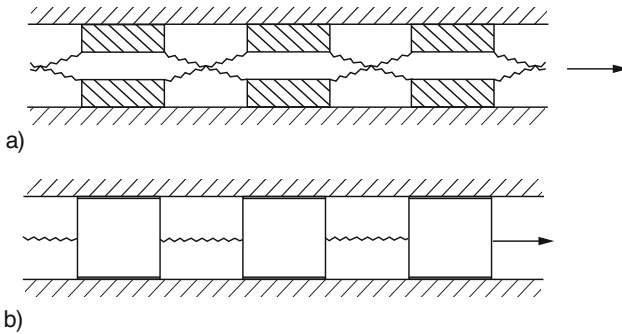


Fig. 14.5.4. Stick-slip models with (a) and without (b) changing transversal pressure

a double-log plot, Fig. 14.5.3d. The leading frequency of the music (M) is inversely proportional to the column height, $f_c \sim 1/h$, the spectra of higher frequencies are weaker and tend to a white noise. The power spectrum of silo quakes (Q), i.e. of autogeneous chaotic motions, has $P \sim 1/f_c$ as known for earthquakes. The acoustic emission of a stationary motion (A) has also $P \sim 1/f_c$, but with a far higher upper bound of f_c which increases with $1/d_g$.

Similar spectra can also be generated with simpler models, Fig. 14.5.4. A chain of elastic elements (a) with Coulomb wall friction (Tejchman 1997) works like a cork shifted past the neck of a bottle. A narrow zone between an elastic column and the wall (b) can melt by shearing and freeze by sticking (Persson 2000b), like colophonium at the string of a violin. Such substitutes could lead to qualitatively realistic spectra although barotropy and pyknotropy of psammoids are ignored.

Simulations with hyp- δ and disc-ring elements (Fig. 14.5.3b) could be more realistic, but are numerically intricate as the equations can get ill-posed. They should yield three kinds of attractors as in experiments: state limits, state cycles and strange attractors. The latter are as hard to capture numerically as the transition from dynamic pattern formation (music) to deterministic chaos (quakes) in experiments. A qualitative agreement could at best be achieved with suitable ratios of disc and ring sizes, but at least the influence of dominant parameters could thus be identified.

Rapid cycles of axial cylinder displacements relative to the bottom can lead to a periodic response. With a small amplitude or/and a smooth wall the wall stress obliquity $|\tau_w|/\sigma_w$ is always subcritical. As outlined with Fig. 14.5.2a for quasi-static motions the skeleton remains in the contractant regime, so it is densified and relaxed in the transition. The asymptotic cycles resemble the ones without inertia, but are distorted due to the repeated wave propagation (cf. Sect. 11.4). With a bigger amplitude and a rough wall the skeleton can approach dilatant state limits as part of state cycles (cf. Fig. 14.5.2b). With too big amplitudes and rough walls the response gets chaotic due to repeated jamming.

Rapid ratcheting can be obtained with suitable amplitudes and frequencies. As for quasi-static cases (cf. Fig. 14.5.2c), i.e. with low frequencies or waiting intervals, a cumulative downward motion of a rough wall relative to the bottom is prevented by jamming. Otherwise asymptotic cycles of representative discs and rings are similar as without inertia (Fig. 14.5.2d), but distorted by wave propagations. With low frequencies, big amplitudes and rough walls, so that dilatant state limits are approached repeatedly, the response can get chaotic with repeated jamming. Autogeneous frequencies arise in addition to imposed ones. As with penetration (Sect. 14.3) period-doubling can indicate a deterministic chaos (cf. Vielsack and Hartung 1999).

Evolutions with displacement cycles or ratcheting can principally be simulated with disc-ring elements and hyp- δ . Jamming and autogeneous stick-slip are numerically as intriguing as experimentally. Quasi-static evolutions are comprehended, for them reversals are transmitted by propagations of waves

and separated by waiting intervals. Simulations with disc-ring elements are debatable as the assumed shear zone thickness is actually part of the solution. More adequate models with polar quantities are hardly feasible with the big required number of finite elements. Tejchman's (1997) finding that polar effects are negligible for $d/d_g > \text{ca. } 10^2$ may also be questioned. Investigations with cylindrical silos may help to understand the dynamics of shear bands along walls beyond what is proposed in Sects. 8.2 and 10.3.

The response to *irregular reversals* could be qualitatively explained by means of seismo-hypoplasticity (Sect. 4.6). The cylinder may be shaken chaotically without (A) or with cumulative axial displacement (B) relative to the bottom. Irregular torsion with zero average may be included so that shearing along the wall is as erratic as upon an incline (cf. Fig. 4.6.1). Weak shaking without average displacement implies substantial average shearing amplitudes at the wall. This means a high granular temperature T_g and a substantial entropic pressure p_d (Sect. 4.6). Similarly as with pore water the skeleton pressure p_s enabling friction is reduced to $p_s - p_d$, with this kind of wall lubrication the average vertical pressure can get almost hydrostatic. This was observed by Tejchman (1997) with a hanging cylinder and a bottom plate on a scales: after some kicks at the cylinder the bottom took over the weight of the granular column.

If the cylinder slides monotonously upwards past the granular column and the bottom the acoustic emission from the ring shear zone represents a basic or reference granular temperature T_g . It may be estimated with (14.5.1) and a factor K adapted to experiments. The required shear zone thickness d_s , which increases with the wall roughness d_w and the relative void ratio r_{eo} off the wall, can be estimated as outlined above with Fig. 14.5.1. If the cylinder is shaken with high energy and without average displacement T_g pulsates with the imposed frequency f_c . An entropic pressure p_d arises with the same rhythm and reduces the wall friction via $p_s = p - p_d$. Back-analyses of such experiments with s-hyp may be of use to quantify relations for T_g (cf. Sect. 4.6).

An axi-symmetric *convergent flow* of dry psammoids can be achieved with suitable silos, Fig. 14.5.5. In a kind of hourglass the wall is smooth and rounded along the neck (a). The lower cylinder can have any height h_l as its extension would not change the state of convected granular discs. Without a bottom the discharge velocity v_o is determined by the diameter d_l via

$$v_o = \kappa \sqrt{gd_l} \quad (14.5.4)$$

with $g = 9.81 \text{ m/s}^2$ and an empirical factor κ (Wieghardt 1952). The skeleton leaves the neck with the p_s -dependent critical void ratio $e = e_c$ as it is strongly deformed. It would be dilated with shear localization if it enters the neck with $e < e_c$. A succession of helical shear bands (as in a triaxial test, cf. Fig. 14.1.2) would lead to a loss of axial symmetry. The repeated come and go of shear bands leads to pressure jumps at the confining neck. Stationary flow can be achieved therefore only if the psammoid is filled with $e \approx e_{co}$ for $p_s = 0$. The

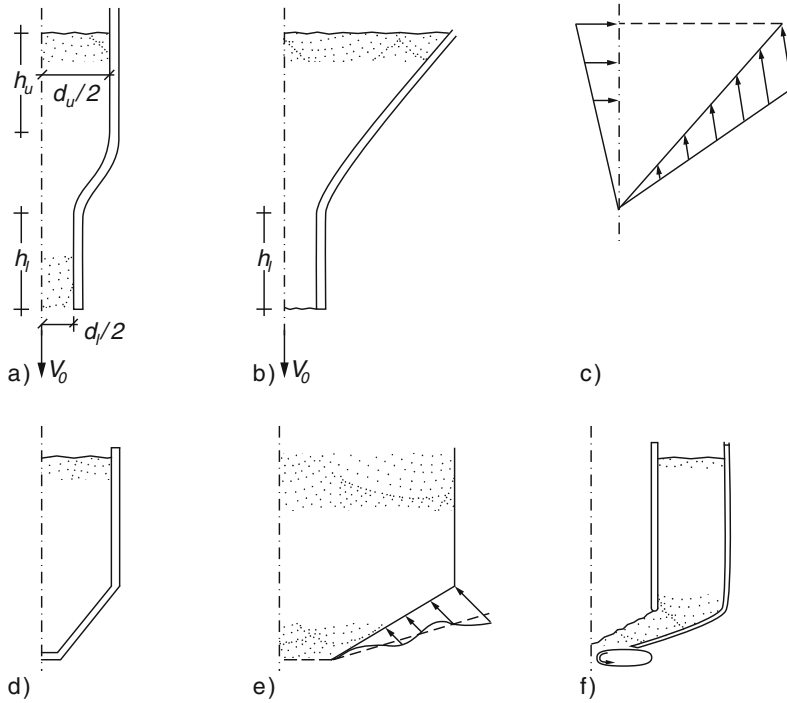


Fig. 14.5.5. Convergent granular flow: hourglass (a), funnel (b), radial stress field (c), hopper (d), pressures by flow (e), ring hopper (f)

pressure level above the neck is given by the upper diameter d_u and does not depend on the upper height h_u , this is expressed by (14.5.1).

A steady discharge can also be obtained with a funnel, Fig. 14.5.5b. The wall should be smooth and rounded at the transition to the cylinder below. The rate of discharge is given by (14.5.4), the lower height h_l does not matter. As with an hourglass a uniform convergent flow is only obtained with loose filling, i.e. $e \approx e_c$ at the onset (Revushenko 2006). Otherwise a helical flow appears at the surface (Fig. 14.2.8), and shear bands can be traced by means of markers. A radial limit stress field may be assumed for $e \approx e_c$ with $p = 0$ at the fictitious apex (c). With two equal major principal stress ratios (cf. Sect. 14.2) one can thus estimate wall pressures and allowable combinations of cone angle β and wall friction angle φ_w (Jenike 1964). This is no more justified with $e < e_c$ as then the axial symmetry gets lost and the wall pressures jump, and as overcritical stress ratios change with space and time (cf. Fig. 13.3.2a).

A usual hopper consists of a cylinder, a cone and a discharge unit, Fig. 14.5.5f. The latter serves to extract granular material with a controlled rate and is also called dosimeter. It is rarely axi-symmetric, but above it the granular flow can be so if the void ratio in the cylinder is about critical.

Then an almost radial limit stress field can arise in the cone and remain during a continued discharge. Near the transition to the cylinder, however, the skeleton pressure p can be bigger and irregular (e) even with $e \approx e_c$. This so-called *switch* can be reduced by a smooth constriction of the wall (Tejchman 1997). With $e < e_c$ near the neck the granular flow cannot get stationary, and pressure jumps can damage the vessel. Silo music or quakes can arise in the cylinder. A more regular granular flow may be achieved by vibrations, shocks or injection of air, but such attempts can fail.

A ring hopper renders possible a better control, Fig. 14.5.5h. Conveyers and a free conical slope near the conical wall can produce an almost axi-symmetric uniform discharge. The walls should be smooth, the transition to the cone should be rounded. The filling device should again produce $e \approx e_c$ as otherwise flow and pressures get irregular.

Evolutions of dry grain skeletons as indicated with Fig. 14.5.5f may be simulated with elastoplastic or hypoplastic relations, but axial symmetry cannot be taken for granted. The walls should have $\varphi_w < \varphi_c$ so that stick or slip is captured by (10.3.2), polar effects should be avoided with small enough grains. Strong curvatures of walls should be avoided as otherwise singularities would cause insurmountable numerical problems. An initial state can be generated by imposing gravity to a loose skeleton (cf. Sect. 12.1). A stationary granular flow may be achieved by maintaining a very low skeleton pressure at stationary free surfaces above and below. With this substitute of filling and emptying, i.e. rise and loss of skeleton, a kind of state limit field could be achieved with suitable shapes of silos. Such attractors could be delimited and validated by model tests, they could reveal whether elp or hyp is more competitive (Tejchman 1997) and when radial limit stress fields or pressures by (14.5.1) are justified.

The equations can get ill-conditioned so that numerical simulations are impossible. Inertial terms may improve ('regularize') them, but this is no more legitimate for a rapid granular flow as then the skeleton goes over into a granular fluid or gas. Jamming due to unsuitable walls may be obtained realistically, but subsequent quakes can hardly be captured as they imply strong fluctuations of pressure and density. With lower than critical void ratios shear localizations cause also mesh-dependence and ill-posedness. Alongside with a regularization by polar terms the axial symmetry has to be abandoned, strange attractors are outside the present reach.

The *pore fluid* of psammoids in silos is more often a gas than a liquid. (6.2.11) and (6.2.12) may be used to estimate the influence of pore gas diffusion, which evidently plays a bigger role with finer grains and more rapid flow. Other than with saturation by a liquid a granular flow without seepage of gas is not isochoric, and changes of void ratio and pore pressure are related by the gas equation. The elastic pore gas can enhance silo music or quakes during a discharge (Tejchman 1997).

Pressurized pore gas can suddenly evade via channels with erosion if the skeleton is loose, such localizations (cf. Sect. 8.4) mean a spontaneous loss

of symmetry. With a small fraction of a suitable pore liquid the capillary skeleton pressure p_{cs} (Sect. 6.2) renders possible cavities after partial discharge (cf. Sect. 14.2). Lumps can fall repeatedly and damage lower parts of the vessel. Such a deterministic chaos can hardly be captured (Tejchman 1997) and should better be avoided by technical means.

Peloids in silos are more often dry than wet. Without pore liquid and net interparticle forces (cf. Sect. 6.3) a dry fine powder with soft grains is pyknotropic, barotropic and argotropic like clays (cf. Sect. 3.2), but more compressible than saturated clay without seepage. After filling and a sufficient resting time the powder is consolidated, after opening the dosimeter it can flow without further seepage. If it was not consolidated too much the outflow is enhanced by the decrease of skeleton pressure $p_s = p - p_g$ as the skeleton tends to contract (cf. Sect. 3.2). The elasticity of the pore gas enhances silo music and quakes during the outflow. This can reduce p_s along the walls up to a skeleton decay and the formation of a granular gas so that the pressure in the lower part rises and gets nearly isotropic.

Such evolutions could at best partly be simulated with v-elp or v-hyp without and v-elp- α or v-hyp- δ with reversals in the skeleton. Coupling with the elastic pore gas could be taken into account with diffusion for waiting times and without it for flow. Model tests can serve for validation, the solid hardness h_s (cf. Sect. 3.4) should be reduced as lengths for getting deformations as in prototype silos. A mechanically similar compressibility of the pore gas is obtained by reducing its average pressure by the same factor as lengths. Diffusion times are proportional to the square of length by (11.1.16) and shorter therefore in small-scale tests.

The convective acceleration in a convergent flow is approximately

$$a \approx v_o^2/h_n \tag{14.5.5}$$

with outlet velocity v_o and neck height h_n , Fig. 14.5.6. A desired ratio of inertial force and weight a/g can thus be achieved via v_o , which in turn is

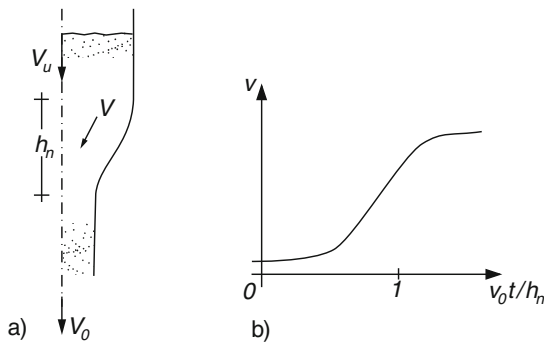


Fig. 14.5.6. Convergent peloid flow (a), flow velocity versus time (b)

controlled mainly by the input void ratio and the outlet width. Limit state fields with negligible or moderate inertial effects may thus be captured.

Asymptotic cyclic state fields can principally be attained by displacement cycles or ratcheting of a cylinder relative to a bottom. In case of sinusoidal motions accelerations may be estimated from amplitude and frequency. The propagation velocity of longitudinal waves can be estimated by means of gas pressure and void ratio as it is dominated by the elasticity of the pore gas. One may thus delimit quasi-static evolutions for which waves come to rest in intervals between reversals. Simulations with disc and ring (Fig. 14.5.3a) may be of use for identifying state cycles. Silo music or quakes could thus also be captured without a spontaneous loss of axial symmetry.

Powders with *net repulsion* ($p_n > 0$, Sect. 6.3) due to equal electrical charge of particles can lead to interesting extreme cases in silos. Free surfaces get horizontal as the repulsive force of each particle exceeds its weight. For all that the material is not a liquid as anisotropic pressure states of rest can exist in a skeleton with purely normal contact forces. Thermal oscillations cannot mobilize particles of more than ca. 10^{-6} m size. The granular temperature T_g can play a similar role as the ordinary one if the total pressure is transmitted by repulsion so that there is no dissipation at solid contacts. Then the skeleton has a seismic heat capacity, seismic heat is conducted as ordinary heat in a liquid, and mechanical energy is dissipated as in a viscous liquid. Avoiding free surfaces by top and bottom plates, silo model tests with such materials may thus be worth the effort.

The discharge of powders with substantial *net attraction* ($p_n < 0$) from silos can hardly be controlled. Void ratios are higher by consolidation after filling than without p_n , which can result from an excess of van der Waals forces or from capillary bridges due to a low liquid content (cf. Sects. 6.2, 7.1 and 7.3). If $-p_n$ attains about $\gamma d_l/4$ with specific weight γ and outlet size d_l cavities can just stand or collapse (cf. Sect. 14.2). The discharge can be enhanced by vibrations, shocks or injection of air, but successfully at best by trial and error. This is not further outlined here as strange attractors with the required loss of axial symmetry are out of reach.

A stationary flow of *pastes* can be achieved in silos if the e -equivalent pressure p_e does not exceed about $\gamma d_l/4$, Fig. 14.5.7. The weight of the upper cylinder with diameter d and height h is compensated by the wall adhesion

$$\tau_a = \gamma d/4. \quad (14.5.6)$$

τ_a attains the cohesion c_u without drainage at a rough wall and is lower otherwise (Sect. 10.3). c_u is proportional to $p_e \tan \varphi_c$ and to $(D/D_r)^{I_v}$ by (13.2.1), the rate of shearing may be estimated as $D \approx v_o/10d$ with flow velocity v_o . The extrusion by weight has a velocity

$$v_o \approx \kappa d_l D_r (\gamma d_l / p_e \tan \varphi_c)^{1/I_v} \quad (14.5.7)$$

with a prefactor κ depending on dimensionless geometrical and material parameters. This corresponds to (13.3.3) and means that a minor change of e

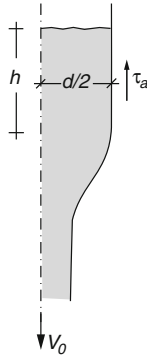


Fig. 14.5.7. Convergent peloid flow

causes a drastic change of discharge velocity. The rate of discharge can be controlled by a dosimeter, then an argotropic state limit can be attained both in experiments and simulations. This works also with a low gas content and related changes of pressure and density without seepage (cf. Sect. 12.2). Sensitive peloids (cf. Sect. 3.2) and higher gas contents are left aside as with them the axial symmetry gets lost easily.

To *sum up*, storage and flow in silos could be captured with elastoplastic or hypoplastic relations and axial symmetry in a number of cases, this may be judged by means of attractors. Stationary flow can be achieved with suitable silo shapes and not too low void ratios by filling, only then stress fields in cylindrical and convergent parts may be statically estimated. Dry powders can be captured as peloids with an elastic pore fluid. Asymptotic state cycles can be achieved by moving cylinders past a bottom with reversals, the average wall friction is more reduced with small amplitudes. If the fill tends to dilate by shearing a slow convergent flow leads to helical shear bands and strong pressure fluctuations. Stick-slip during a discharge can lead to silo music or quakes. Such critical phenomena imply a spontaneous loss of axial symmetry and impede likewise technical operations and numerical simulations.

14.6 Torsion

Axi-symmetric evolutions can be produced by torsion of solid bodies past psammoid or peloid. The following outline begins with plane-parallel evolutions, i.e. with spatial variations only along the radius r . Other than with radial symmetry as treated in Sect. 11.7 there are circumferential velocities v_Θ and hoop shear stresses $T_{r\Theta}$. Plane-parallel state limits and asymptotic cycles could be worth the effort. The axial symmetry can get lost spontaneously.

A ring-shaped *dry psammoid* body can be twisted in a kind of Couette device, Fig. 14.6.1. The grain skeleton is fixed at an outer cylinder ($r = r_b$), sheared by a rough inner one ($r = r_a$) and axially confined by a smooth rigid

base and a smooth top ring (a, b). The latter is kept with a transducer for the resulting axial skeleton force

$$F_z = -\pi \int_a^b T_{zz} r dr \tag{14.6.1}$$

so that the height h (I) or the axial force F_z (II) is constant. The initial state may be uniform with the stress components $T_{rr} = T_{zz} = K_o T_{zz}$ as in an oedometer (Sect. 2.5), and a relative void ratio r_{eo} . The skeleton weight may be negligible, i.e. $-T_{zz} \gg \gamma h$ holds throughout.

The angular position Θ of the inner cylinder may be slowly changed without reversal (A), with cycles (B) or by ratcheting (C). The torque

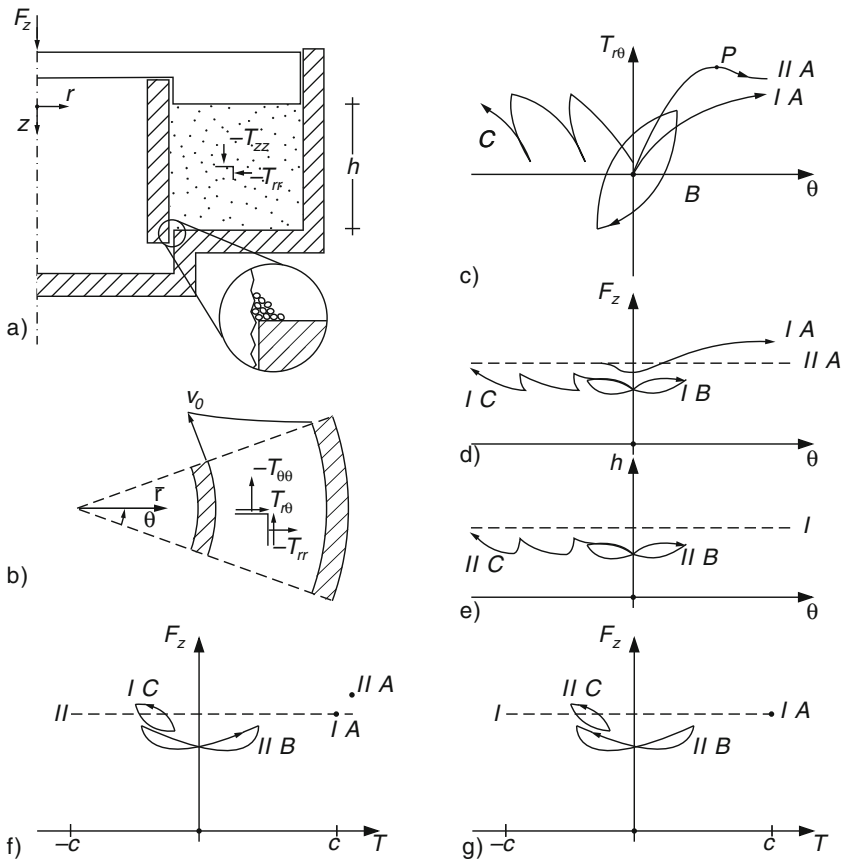


Fig. 14.6.1. Torsion of an annular psammoid sample (a, b); evolution of torque (c) and axial force (d) or height with torsion (e); asymptotes of axial force (f) and height (g) versus torque

$$T = 2\pi h r_a T_{r\theta a} = 2\pi h r_b T_{r\theta b} \quad (14.6.2)$$

at the inner or outer cylinder changes with Θ (c). For monotonous torsion it attains a plateau (I) or a peak (II), with Θ -cycles T vs. Θ tends to a periodic hysteresis, with ratcheting the plot tends to saw-teeth. These asymptotic responses indicate attractors, i.e. the skeleton state field tends to state limits or state cycles. With constant height (I) the related axial force F_z (d) gets stationary (A), F_z vs. Θ tends to a butterfly (B) or to a garland (C). With constant F_z and $|\dot{\Theta}|$ the height (e) gets stationary (IA), h vs. Θ tends to a butterfly (B) or to a garland (C).

The attractors can also be represented by limit state points (A) or asymptotic cycles (B, C) in plots of F_z vs. T (f) and h vs. T (g) with labels for the mode. With $h=\text{const}$ and a dense hard-grained skeleton, i.e. with low r_{eo} and high h_s (Sect. 2.2), the mean pressure p can grow so much by monotonous torsion that grains break. With $h=\text{const}$ and high h_s , but bigger r_{eo} the skeleton would decay by reversals with small amplitude (cf. Sect. 4.2), this is excluded here. With $F_z=\text{const}$ the height h , which substitutes the average void ratio \bar{e} via r_e and e_o (Sect. 2.2), attains a critical value h_c by monotonous torsion. With reversals the average \bar{h} over one cycle tends to an asymptotic value which is lower without ratcheting, $\bar{h}_B < \bar{h}_C$, and for lower amplitudes. The stress components of convected and co-rotated RSEs are stationary.

State limit fields could be calculated straightforward or via evolutions. The stress components of convected and co-rotated RSEs are stationary. The radial distribution of all stress components is determined by the pressure p_a at the inner cylinder, this implies (14.6.2). The r -dependence of the circumferential velocity v_Θ is confined by boundary values. Transitions to such attractors start at the inner cylinder with the onset of its rotation. They imply radial displacements off the walls, and axial ones in case of a constant axial force F_z except for the base. This means a radial redistribution of the void ratio e , with constant average \bar{e} for $h=\text{const}$ and with an adaption of \bar{e} for $F_z=\text{const}$. Starting with any initial $e(r)$ and $T_{ij}(r)$, numerical simulations should lead to stationary state limit fields.

Calculations of asymptotic cycle fields would be more expensive. Cyclic stress paths of RSEs should be similar for different r due to equilibrium. They resemble symmetric butterflies for cyclic torsion and skew lenses for ratcheting. The asymptotic cycles are determined by zero accumulation for each one of them. Combined with the conservation laws and boundary conditions this leads to a set of implicit equations for r -dependent asymptotic cycle fields with reversals. They depend on the amplitudes and on the initial average void ratio \bar{e} for $h=\text{const}$ or the given F_z as outlined with Fig. 14.6.1c, d.

Calculating transitions to such asymptotic cycle field gets the more expensive the more the initial average pressure \bar{p} (I) or void ratio \bar{e} (II) deviates from the asymptotic values. With small amplitudes the required number of reversals to attain the periodic asymptote can get big. Caution is needed to

avoid the numerical accumulation of rounding errors, steps between reversals should be small because of the material non-linearity (cf. Sect. 4.6).

Numerical studies of this kind could be of use before turning to attractors without plane-parallelity. Validation experiments require sensitive gaps between the annular disc and the walls as shown in the insert of Fig. 14.6.1a. A control of the axial force F_z could safeguard that the skeleton does not decay and the grains are not crushed. The main objective should be to get asymptotic responses. The annular disc has to be fixed against torsion as a minor friction along it (and likewise along the base) cannot be avoided. The resultant frictional torque at the disc should be measured and taken into account as a circumferential mass force in back-analyses.

Pore water could be added in such tests and allowed for in simulations. The rough walls can be open or closed for seepage, the smooth discs are impervious. With full saturation the pore water pressure p_w could be kept constant, then only the granulate hardness h_s (Sect. 2.2) is reduced by wetting (Sect. 6.2). Without wall drainage p_w is r -independent as long as skeleton velocities are far smaller than the permeability, i.e. for $|v_\theta| \ll k_f$. Then p_w changes by torsion, can be measured at the outer cylinder and influences the skeleton pressure via $p_s = p - p_w$, while the sample height h is constant. With gas inclusions h can change without drainage, their spatial distribution can be non-uniform (Sect. 6.2).

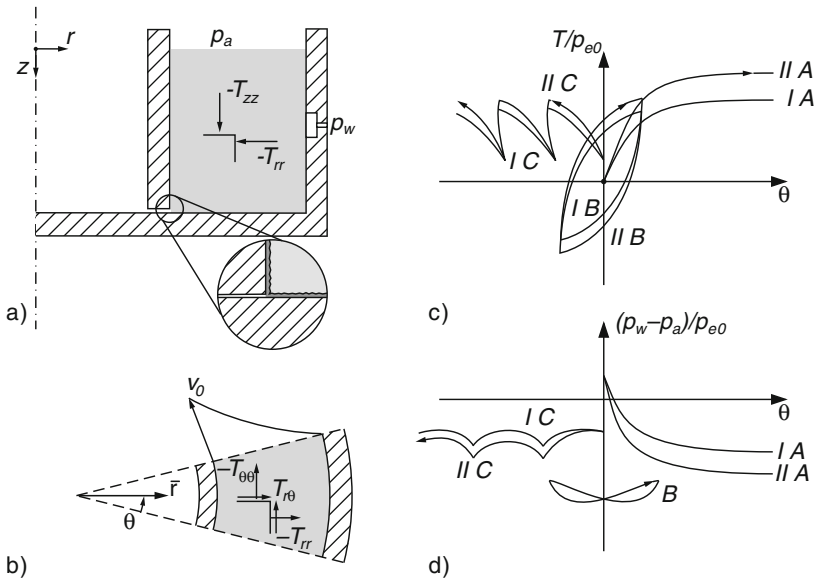


Fig. 14.6.2. Torsion of an annular peloid sample (a, b), stress ratios (c) and pore pressures (d) versus torsion

Plane-parallel torsion tests with saturated *peloids* can be simpler than with psammoids as long as drainage can be excluded, Fig. 14.6.2. The top ring could even be omitted, the rough walls are impervious, p_w can be measured at one of them (a). At the beginning the ring-shaped sample should have a uniform e and $p_s \approx -p_w \gg \gamma h$ by suction, evaporation can be avoided by short exposure times. Torsion by changing the angular position Θ of the inner wall (b) may again be imposed monotonously (A), cyclically (B) or with ratcheting (C). The argotropy is revealed by different responses to slow (I) and fast twisting (II). This can be expressed for the attractors by

$$T = T_r \left(\left| \dot{\Theta} \right| / D_r \right)^{I_v} \quad (14.6.3)$$

for the torsional resistance T , with $T = T_r$ for $\left| \dot{\Theta} \right| = D_r$.

In the plot of T vs. Θ (c) monotonous torsion leads to an asymptote (A) with $T = T_c$ depending on $\dot{\Theta}$ by (14.6.3). Ductility is thus assumed. The skeleton pressure would be (cf. Sect. 3.8)

$$p_s = p_e \left(\left| \frac{\partial v_\Theta}{\partial r} \right| / 2D_r \right)^{I_v} \quad (14.6.4)$$

with the shearing rate $D = \frac{1}{2} \partial v_\Theta / \partial r$ and only tangential velocity v_Θ , i.e. $v_r = v_z = 0$. With the conservation laws the limit state field and the related velocity field are thus determined. The asymptote of p_w at $r = r_b$ (d) is determined by the initial e -equivalent pressure p_{e0} , the initial suction $p_w < p_a$ (Sect. 6.3) is swept out during the transition.

Cyclic torsion (B) leads to a symmetric hysteresis loop in the T vs. Θ plot (c), and to a symmetric butterfly in the p_w vs. Θ plot (d). Both plots reveal argotropy via (14.6.3), the amplitudes are proportional to p_{e0} . The hysteresis is reduced with smaller amplitudes and is big if state limits are repeatedly attained. Ratcheting (C) leads to garlands of T and p_w vs. Θ , both are argotropic with amplitude-dependent shape.

Implicit equations for asymptotic fields could also be obtained, now with skeleton partial stress, conservation and boundary conditions. Transitions to such state limit or state cycle fields start from the inner cylinder and finally attain the outer one. Their numerical simulation is the more expensive the more the initial average field deviates from the asymptotic one. Validation experiments should be focussed in the attractors as the initial states are not known in detail, only the initial average void ratio can be easily controlled.

Other torsion tests with initially uniform annular samples and negligible gravity cannot produce plane-parallel evolutions, therefore their investigation is more difficult, Fig. 14.6.3. In a ring shear device with smooth cylinders and a rough annular disc twisted past a rough base (a) the shearing is concentrated near the top. This localization can be attributed to the inevitable wall friction, it can be shifted to the middle height by means of horizontally split

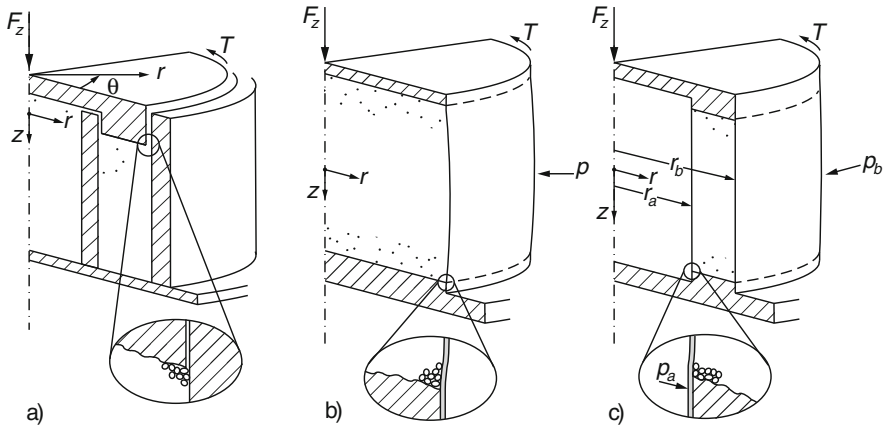


Fig. 14.6.3. Torsion of annular (a), cylindrical (b) and tube-shaped (c) granular samples

cylinders (Hvorslev 1937). Asymptotic responses as shown in Figs. 14.6.1 and 14.6.2 could be obtained with psammoids and peloids. Simulations are difficult as pressures and velocities change with r and z , in particular with forced localizations including seepage (Sect. 8.3).

A cylindrical sample can be twisted via rough plates and supported via a circumferential membrane (b). Shearing increases roughly in proportion to r in the middle, but less near the plates and more near their rims. Monotonous torsion could lead to a state limit field, principally also in expensive simulations. The axial symmetry can get lost spontaneously, however, due to shear localization and uneven bulging (cf. Sect. 14.1). Cyclic torsion can lead to axi-symmetric asymptotic cycles, these are generated with propagating waves in resonant column devices (cf. Sect. 4.2). Torsional ratcheting could be imposed as long as the membrane is not wrinkled. Except for big amplitudes shear localizations are suppressed by reversals (cf. Sects. 8.2 and 14.1). r - and z -dependent asymptotic cycle fields can principally be simulated, this could be of use for validations.

Hollow cylindrical samples can be twisted via rough base and top rings, and are usually supported via inner and outer membranes, Fig. 14.6.3c. With small ratio $(r_b - r_a)/r_a$, suitable external pressure ratio p_b/p_a and small amplitudes uniform deformations may be assumed as in RSE-tests (cf. Sects. 2.8 and 3.8). The axial symmetry can get lost by shear localization and uneven bulging, but less with moderate reversals. Leaving aside such strange attractors, investigations of r - and z -dependent asymptotic cycle fields could be worth the effort.

Helical motions of cylindrical psammoid bodies could be generated in devices as shown in Fig. 14.6.3, but hardly up to attractors. Ring shearing with

axial shortening or lengthening would lead to jamming or decay, respectively. Massive cylindrical samples would get a bulge or neck with axial shortening or lengthening, respectively, by torsion without or with reversals. As in triaxial tests (Sect. 14.1) the axial symmetry can get lost with helical shear bands, and also with wrinkles of the membrane. State limit and state cycle fields could hardly be attained by twisting hollow cylindrical samples beyond critical stress obliquities, so simulations of such evolutions would be less promising.

Torsion of a solid cylinder in homogeneous ground was investigated with dry psammoid by Cudmani (2001), Fig. 14.6.4. A rough steel tube was rotated past the base, the ring space up to a fixed outer cylinder was filled with sand of initially low density (a). Torsion cycles led to densification and settlement which were stronger near the inner tube than farther away (b), and the growth of settlements slowed down with the number of cycles (c, d). Simulations with hyp- δ led to similar settlements after some cycles (e), and to state cycles of near-field RSEs (f).

Further attractors could be obtained with similar devices, and calculated with hypoplastic relations for validation. Monotonous torsion leads to limit state near-fields with forced shear localization at the rotated cylinder, polar effects may be neglected for $d < 100 d_g$. Less rough walls and/or lower initial density would lead to a narrower near-field. Bigger torsional cycles would likewise enhance shear localization, smaller rapid ones would widen the near-field by wave propagations. Torsional ratcheting would lead to more or less narrow one-sided asymptotic near-field cycles. All that could also be done with pore water and *in situ*, but the increasing complexity could impede validations.

Such investigations are also possible by twisting non-cylindrical solid bodies which are axially fixed in psammoid ground, Fig. 14.6.5. A cone (a) could first be penetrated into the ground, and then rotated without or with reversals until the response gets stationary or periodic, respectively. This could also be done with a cylinder and a conical tip (b), then the attractors would mainly depend on the initial near-field produced by the previous penetration (Sect. 14.3). Club-like bodies with a driving rod (c) could thus more easily be embedded than pushed down for installation. The attractors depend again on the near-field due to placement of the solid body, therefore back-analyses for validation are more difficult. Pore water could also be taken into account.

Evolutions as indicated by Figs. 14.6.4 and 14.6.5 could also be investigated with *peloids*. Other than in Couette devices the fields around rotated cylinders are no more plane-parallel because of gravity. Below a depth $z \approx 5d$ this further symmetry may be assumed as long as seepage during torsion and disturbance by placement are negligible. For the evaluations of *vane shear* tests the torsion of an enclosing rough cylinder may be assumed, and a shearing resistance τ at upper and lower horizontal planes that increases in proportion to r , Fig. 14.6.6. The torque in a ductile peloid tends to

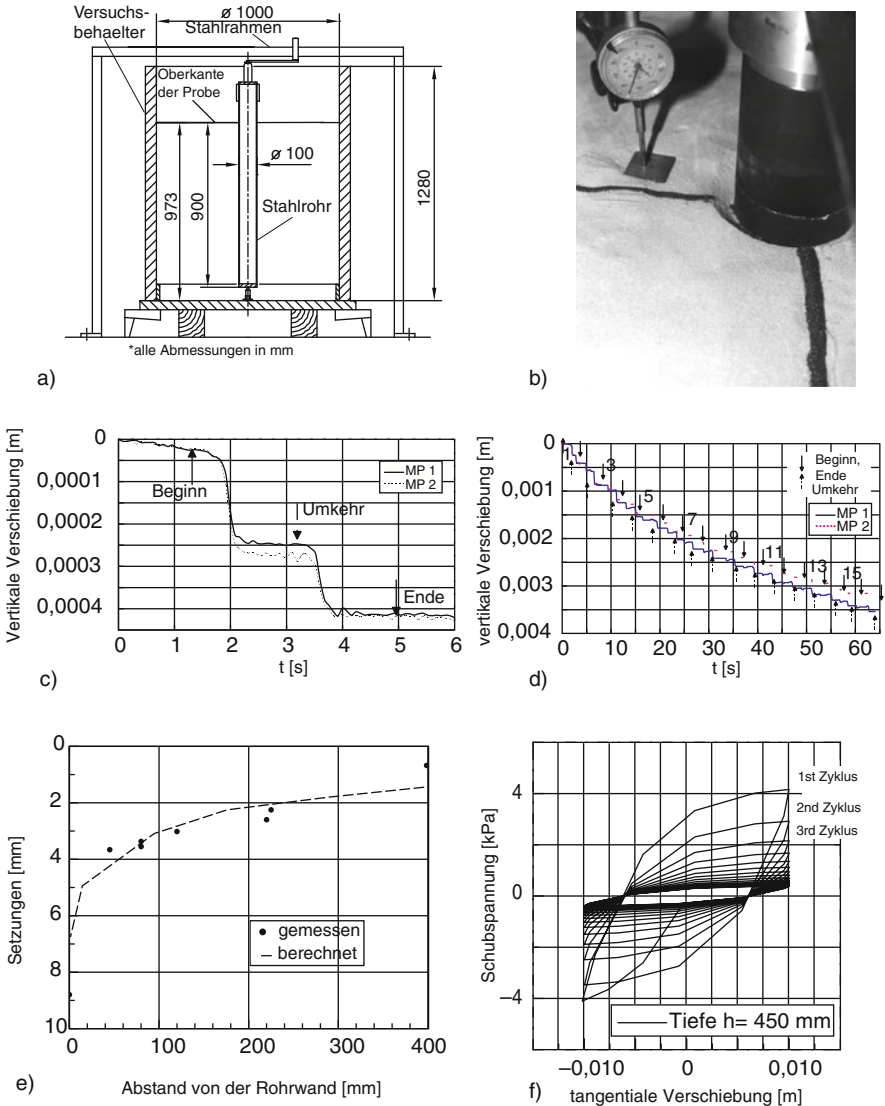


Fig. 14.6.4. Torsion of a tube past surrounding sand (Cudmani 2001): setup (a), surface near the pile (b), observed near-field settlement (c, d), observed and calculated settlement versus radius after 16 cycles (e), calculated wall shear stress versus cyclic torsion (f)

$$T \approx 3.5c_u d^3 \tag{14.6.5}$$

with the usual aspect ratio $h/d = 2$. The argotropy of c_u by (11.2.1) can be taken into account with the shearing rate $D \approx \dot{\theta}$, this implies a shear zone of thickness $d/2$ and may suffice for applications.

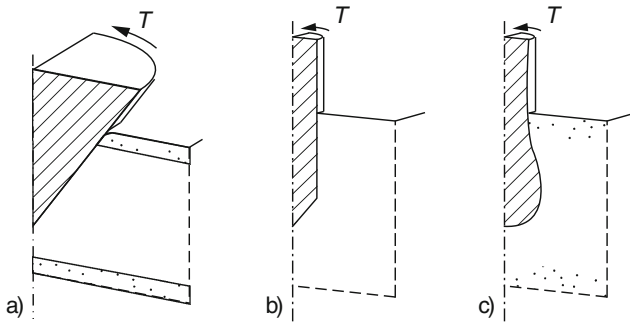


Fig. 14.6.5. Penetration with torsion: cone (a), cylinder with tip (b), club (c)

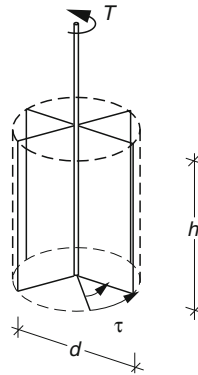


Fig. 14.6.6. Shear vane in peloid

As always with peloids attractors for torsion are argotropic. They may be approximated by (14.6.3). Creep and relaxation play a role with resting intervals after placement and during reversals, this should be taken into account in simulations and validation experiments. Even asymptotically stationary or periodic evolutions get more complex with the diffusion of pore water, let alone cavitation with loss of axial symmetry.

Helical motions of axi-symmetric solid bodies in psammoid or peloid ground can lead to attractors with suitable initial and boundary conditions. Monotonous (A) or alternating torsion (B) can be combined with penetration (I), whereas axial lifting (II) could lead to a skeleton decay. A cylinder can be screwed up or down through a hole in a solid bottom (Fig. 14.6.7a) so that the state in the surrounding ground gets stationary or changes periodically. Evolutions of the skeleton can be represented by associated paths of twist Θ vs. shift u (b) and torque T vs. axial force F (c). The attractor is a point (A) or a skew lense (B) in the plot of a skeleton force vs. torque. As with penetration (Sect. 14.3) a plot of average near-field void ratio vs. pressure serves as a further representation. Such attractors could be generated with hyp- δ and observed in validation tests, the feasibility was shown by Cudmani (2001).

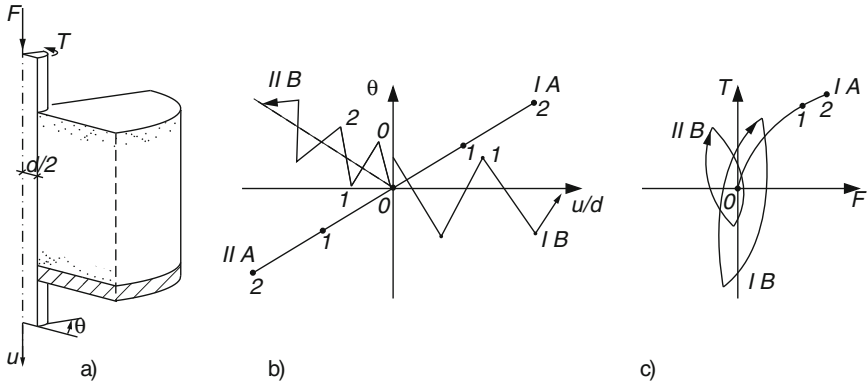


Fig. 14.6.7. Torsion of a cylinder with penetration through a layer (a), torsion versus axial displacement (b), torque versus axial force (c)

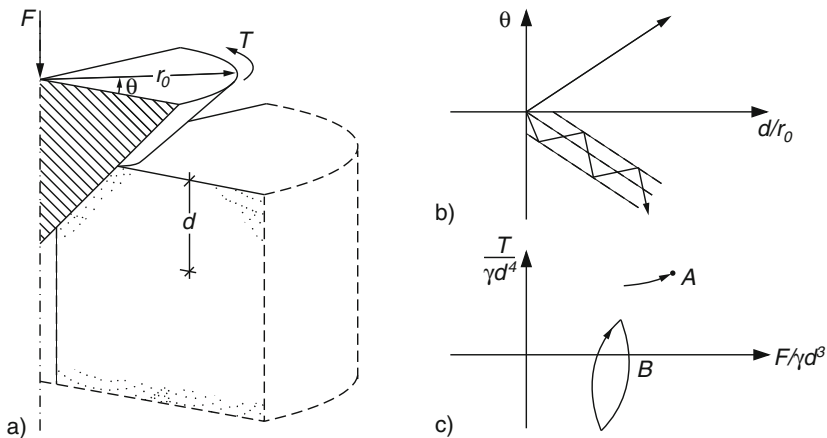


Fig. 14.6.8. Torsion and penetration of a cone (a), torsion versus displacement (b), torque versus axial force (c)

A cone can more easily be pushed into the ground with monotonous or alternating torsion, Fig. 14.6.8a. Associated paths of twist vs. shift (b) and torque vs. force (c) can again exhibit attractors. The shape of them depends on the ratio of average rates of penetration and rotation and on the amplitude of alternations. The similarity of near-fields for increasing penetration depth d can be used by referring torque and axial force to γd^4 and γd^3 , respectively. The initial relative void ratio plays a major role. Gravity enters via γ , and polar effects matter at the onset as then d does not exceed $100 d_g$. For a homogeneous peloid without seepage torque and force can be referred to $p_{eo}d^3$ and $p_{eo}d^2$ with initial equivalent pressure p_{eo} , respectively, and are argotropic by (14.6.3). The singularity at the tip can be avoided in simulations

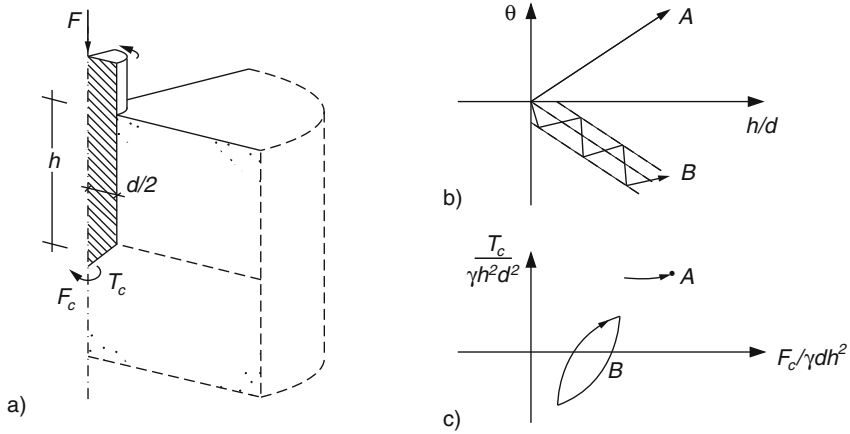


Fig. 14.6.9. Penetration of a pile with torsion (a), torsion versus displacement (b), torque versus axial force (c)

by a fictitious thin tube as in Fig. 14.3.1. Validation tests are simpler than calculations, resting intervals matter for peloids.

A cylinder with cone penetrates more easily with monotonous or alternating torsion, Fig. 14.6.9a. As shown in Fig. 14.3.1 without torsion one can separate torsional and axial resistances at shaft and cone. The shaft resistance increases with depth h and can be captured as shown with Fig. 14.6.7. The resisting torque T_c and axial force F_c at the cone are no more self-similar for different penetration depths as in Fig. 14.6.8. Associated paths of twist vs. shift (b) and of T_c vs. F_c (c) can exhibit attractors, however, if T_c is referred to $\gamma d^2 h^2$ or $p_{eo} dh$ and F_c to pdh or $p_e dh$, respectively, for psammoids or peloids. The shapes depend on the ratio of average penetration and rotation rates, and on the amplitude for alternations. The tip singularity can again be avoided in simulations by a thin tube below, but calculations are still expensive. They will pay after validation tests by improved applications in situ.

It is known that a tube penetrates more easily with torsion, Fig. 14.6.10a. A cyclic torque is imposed above quasi-statically or with blows, then the solid weight can suffice as axial drive. The soil in the tube is partly excavated, the remaining part is twisted past its base. The outer shaft resistance could be captured as shown with Fig. 14.6.7. Associated paths of twist vs. shift (b) and of edge torque T_e vs. force F_e (c) can exhibit attractors if T_e is referred to $\gamma h d^2 t$ or $p_{eo} d^2 t$ and F_e to $\gamma h d t$ or $p_{eo} d t$, respectively, for psammoids or peloids, with wall thickness t and instantaneous depth h . The resistance of the soil in the tube can be captured as shown further below with Fig. 14.6.11. Asymptotic cycles of normalized edge resistances (d) reveal the influence of progress per cycle and amplitude. Pore pressure and argotropy can be taken into account, and principally also inertial effects. Simulations of such helical

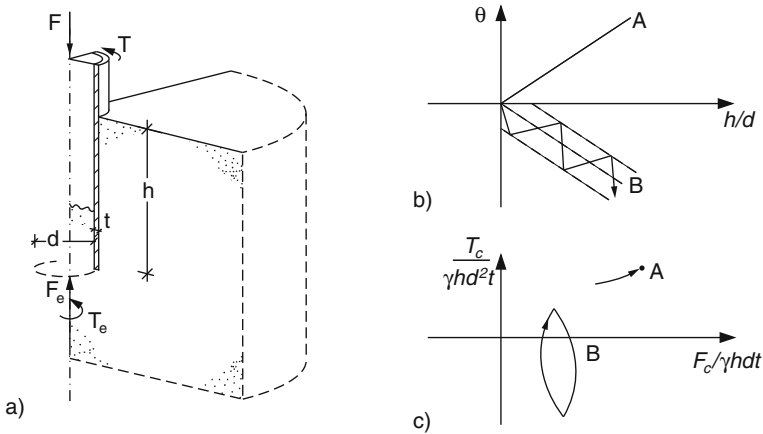


Fig. 14.6.10. Penetration and torsion of a tube (a), torsion versus displacement (b), torque versus axial force (c)

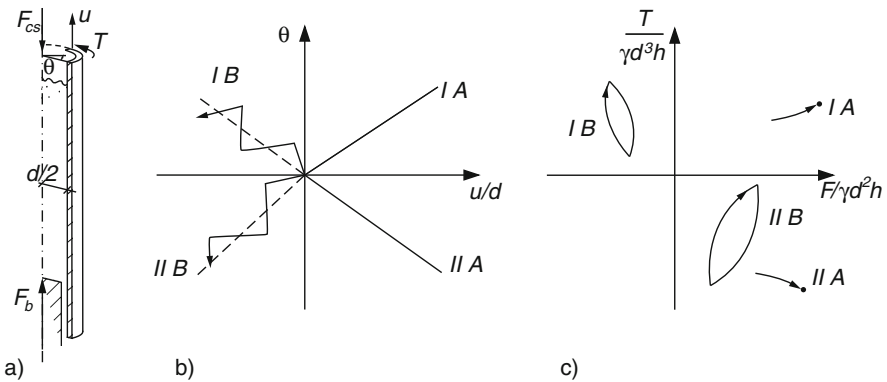


Fig. 14.6.11. Torsion of a cylinder past its base (a), torsion versus axial displacement (b), torque versus axial base force (c)

evolutions would be expensive, but could be rewarding with validations for improved technologies.

The fill in a *cylindrical silo* can be twisted by rotating the wall past the base, Fig. 14.6.11a. The cylinder is simultaneously shifted axially past the base. For psammoids associated paths of twist vs. shift (b) and of torque $T/\gamma d^3 h$ versus base force $F/\gamma d^2 h$ (c) can reveal attractors. The initial relative void ratio r_{eo} and the wall friction angle φ_w are important parameters (cf. Sect. 14.5). For monotonous helical upward (I) or downward (II) motions (A) the axial resistance is reduced so much by twisting that jamming can be overcome. In case of helical ratcheting (B) the lenticular state cycle for upward shifting (I) is nearly the skew-symmetric counterpart of the one for

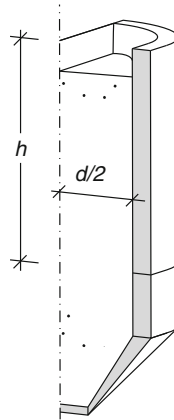


Fig. 14.6.12. Vessel for twisting of a granular fill by torsion of a cone past a cylinder

upward shifting (II). Simply speaking the axial resistance by wall friction is partly consumed by torsion, but changes of radial pressures enter as without torsion (cf. Sect. 14.5). As for the counterpart with psammoid outside the wall (Fig. 14.6.7) investigations of such helical evolutions are recommended before treating more complex cases.

A *silo with cylinder and cone* can be better controlled by means of torsion, Fig. 14.6.12. One can twist the lower part cyclically past the upper one via an elastic ring. This can lead to a pulsating discharge with helical ratcheting, and to a nearly radial average stress field without switch and quakes (cf. Sect. 14.5). Associated paths of twist vs. shift and torque vs. axial force at the transition from cylinder to cone exhibit amplitude-dependent asymptotic cycles. Numerical simulations and verification tests with such helical attractors could help to improve technologies of granular storage and flow. Similar investigations could be made with peloids, e.g. for a torsion-enhanced extrusion.

To *sum up*, axi-symmetric evolutions of psammoid and peloid bodies due to torsion of adjacent solid bodies can be captured by attractors in a plethora of cases. In Couette devices state limit and state cycle fields depend spatially only on the radius r , this additional symmetry eases simulations and validation tests. Otherwise such attractors depend also on the axial coordinate z , therefore spatial averages are preferable for graphical representations. The argotropy due to soft particles can easily be taken into account, capturing the one due to the diffusion of pore water is more expensive. Shear localization, cavitation and skeleton decay can lead to a spontaneous loss of axial symmetry.

LESS SYMMETRIC EVOLUTIONS

The search for symmetry means scientific economy in the sense of Mach (1912), without it the nature (*φύσις*) of soils could hardly be captured. Geotechnical engineers will feel at home with several examples treated in this chapter, they are used to assume symmetry for design. Some examples may appear rather academic, but they are helpful for understanding. We will see how symmetry can arise with the approach to state limits, SOM-states or state cycles in the large, and how it can get lost by critical phenomena. This is again more an outline of promising approaches than a report on successful applications.

Vertical symmetry planes may be assumed for a number of natural and technical evolutions. With two of them interpolations between plane-parallel and axial symmetry can be of use, this is shown without (Sect. 15.1) and with interactions of soil and structures (SSI, Sect. 15.2). More often a single symmetry plane may be justified, therein SSIs can be simple (Sect. 15.3) or complex (Sect. 15.4). Some validations can be presented for such cases, further simulations will be rewarding.

Tumbling and driving can lead to periodic SSIs (Sect. 15.5). Such an *orbital symmetry* can arise by repeated motions of solids past soil bodies along a circle or an endless straight line. Then neighboured RSEs can go through state cycles during each passage. Tumbling and driving can also lead to spatial and temporal patterns, or to deterministic chaos without any symmetry.

15.1 Two symmetry planes without SSI

Several cases of geotechnical interest may be simplified by assuming two symmetry planes which are vertical and orthogonal to each other. This will be outlined first without soil-structure interaction (SSI), also by means of attractors. In two case studies in-situ data and simulations with hypoplasticity led to a validation. A kind of interpolation between plane-parallel and axi-symmetric evolutions may sometimes be assumed. Other cases can be captured similarly as long as a spontaneous loss of symmetry can be excluded.

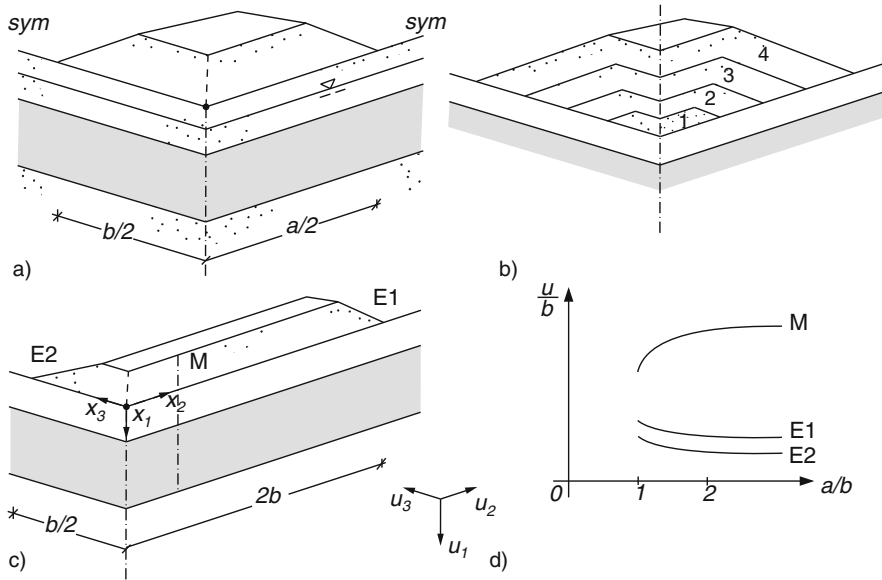


Fig. 15.1.1. Dam with free ends (a), filling steps (b), slender heap (c), interpolation between axi-symmetric and plane-parallel results (d)

A *fill* can be shaped like a dam with free ends, Fig. 15.1.1. Two symmetric cross sections (a) may exhibit the same ground profile and two generally different widths. The slopes may have the same inclination everywhere. The ends of the dam may be substituted by parts of cones so that conical heaps (Sect. 14.2) are implied as special cases. Plane-parallelity may be assumed for middle cross sections if the ground plan of the dam is sufficiently slender. With this assumption settlement and spreading are overestimated for ratios of length and breadth $a/b > \text{ca. } 4$. This could be justified and quantified by simulations with two symmetry planes. The spreading of the dam ends is enhanced by hoop stresses, but as for heaps with slope edges this effect is minor.

Initial and boundary conditions can be specified for psammoids and peloids as outlined in Sects. 12.1 12.2 12.3 and 14.2. The *sizes and intervals of filling steps* (b) could be varied in comparative calculations, but as with plane-parallel or axial symmetry the sizes are of minor importance. One may as well assume a uniform growth of gravity within the time of filling which matters with respect to times needed for the diffusion of pore water. A further adaption to actual sizes, intervals and orders of filling steps would exclude the assumed symmetry, but would not be worth the effort as long as the pore water diffusion takes far less or more time than the filling time.

An *interpolation* between plane-parallel and axi-symmetric evolutions can be rewarding for dams with a squat ground plan, say $a < \text{ca. } 3b$. It requires one plane-parallel plus one axi-symmetric simulation, which together are less

expensive than one simulation with two symmetry planes. The interpolation is evidently monotonous. It works also for a single free end (c). Further off the end than ca. $2b$ plane-parallelity may be assumed for cross sections. The reduced settlement u_1 and the enhanced spreading u_2 at one end may thus be captured. This provides an asymptote for the interpolation of u_1 and u_2 versus a/b (d). Polyhedral ends may be substituted by conical ones with the same volume.

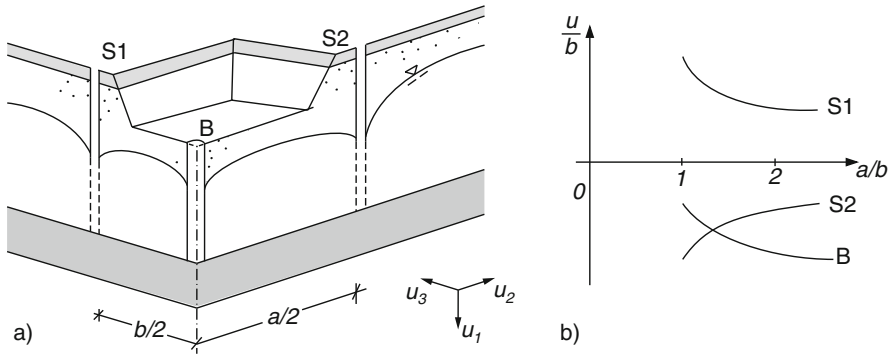


Fig. 15.1.2. Excavation in layered ground (a), interpolation between axial and plane-parallel symmetry (b)

Similar approaches can be employed for *excavations*, Fig. 15.1.2. Two cross sections suffice with horizontally layered ground (a). The groundwater table may be partly lowered with the same symmetry. The slopes may have a uniform inclination, polyhedral ends may be substituted by parts of cones. The displacements at the bottom (heave $-u_{1B}$ and caving $-u_{2B}$) and the shoulder (subsidence u_{1S} and caving $-u_{2S}$) are reduced by hoop stresses. Initial and boundary conditions can be specified as outlined for plane-parallel and axi-symmetric evolutions in Sects. 12.4 and 14.2. One could quantify by comparative calculations how the sizes of excavation steps influence more the paths of bottom and rim displacements than their final values (cf. Sect. 12.3). This is also valid for peloid ground with thermally activated redistributions of skeleton and pore pressures as long as these occur mainly after the end of excavation.

Plane-parallelity may be assumed for aspect ratios $a/b > 2$. Karcher (2003) demonstrated by a case study (cf. Fig. 12.4.7) that this is justified already with $a/b \approx 2$ in the light of ever-present horizontal variations of ground profiles. End effects can be captured by interpolating results of plane-parallel and axi-symmetric evolutions (Fig. 15.1.2b), this works also for one end of a long ditch. Symmetric corners will be treated in Sect. 15.3, and prograding excavation windows in Sect. 15.4. Simulations without such symmetries are only needed if exceptional risks would otherwise be missed.

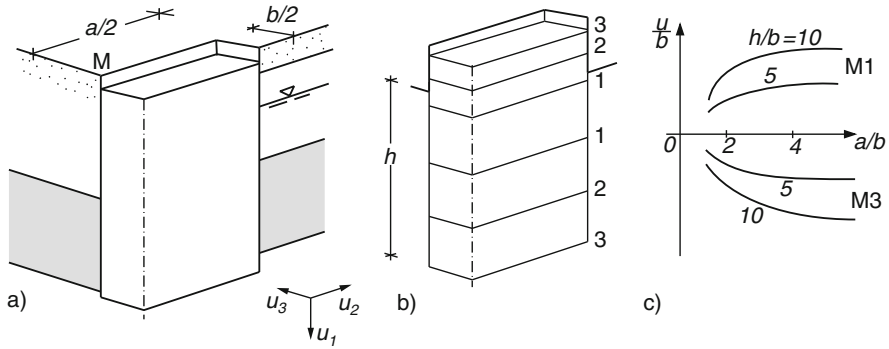


Fig. 15.1.3. Slurry trench in layered ground (a), excavation with an elevated supporting suspension (b), interpolation as before (c). Numbers for stages

Hydraulic boundary conditions can be taken into account for double-symmetric fills and excavations as explained in Sects. 12.1, 12.2, 12.3, 12.4 and 14.2. A *slurry trench* with rectangular horizontal cross sections can thus be captured, Fig. 15.1.3. The ground can have horizontal layers and variable hydraulic far-field heights, auxiliary retaining walls can be taken into account (a). A cured concrete wall at one side impairs the two-fold symmetry, it may be neglected (on the safe side) for simplicity. Exchanging soil blocks section-wise by slurry substitutes the excavation, during which the slurry surface can rise above the ground (b). As outlined in Sects. 10.2, 12.4 and 12.2 a filter cake at a psammoid wall requires an outward gradient of hydraulic height h_w . Swelling of peloids can be sufficiently avoided by rapid working and by hydrophobic additives (Sect. 6.3), so that the diffusion of pore water is negligible during the operation. The subsequent filling with fresh concrete and its curing can also change the neighboured ground.

As far as long trenches with the same cross section are stable subsidence u_{1M} and caving $-u_{2M}$ in the middle of the long rim of the excavation may be captured by interpolation between a circular shaft and a long narrow trench with axial or plane-parallel symmetry, respectively (Fig. 15.1.3c). The displacements are bigger for a deeper trench, the relative depth h/b enters therefore as parameter. The rim displacements of the short walls may be assumed as the ones for $a = b$. As with more symmetry (Sects. 12.4 and 12.2) the two-fold symmetry can get lost if the saturated soil is not ductile without seepage (Sects. 2.2 and 3.2). Apart from such a collapse the stability could better be judged by the evolution of displacements with two symmetry planes than with arbitrary statical and kinematical assumptions.

Schäfer and Triantafyllidis (2004) investigated a field test by Di Biaggio and Myrvall (1972) in *peloid ground* by means of v-hyp, Fig. 15.1.4. The ground profiles exhibit a uniform post-glacial clay with high groundwater table and low consolidation ratios p_e/p_s due to ca. 10^3 years resting time (cf. Sect. 11.3). The finite element mesh (a) has two symmetry planes for one

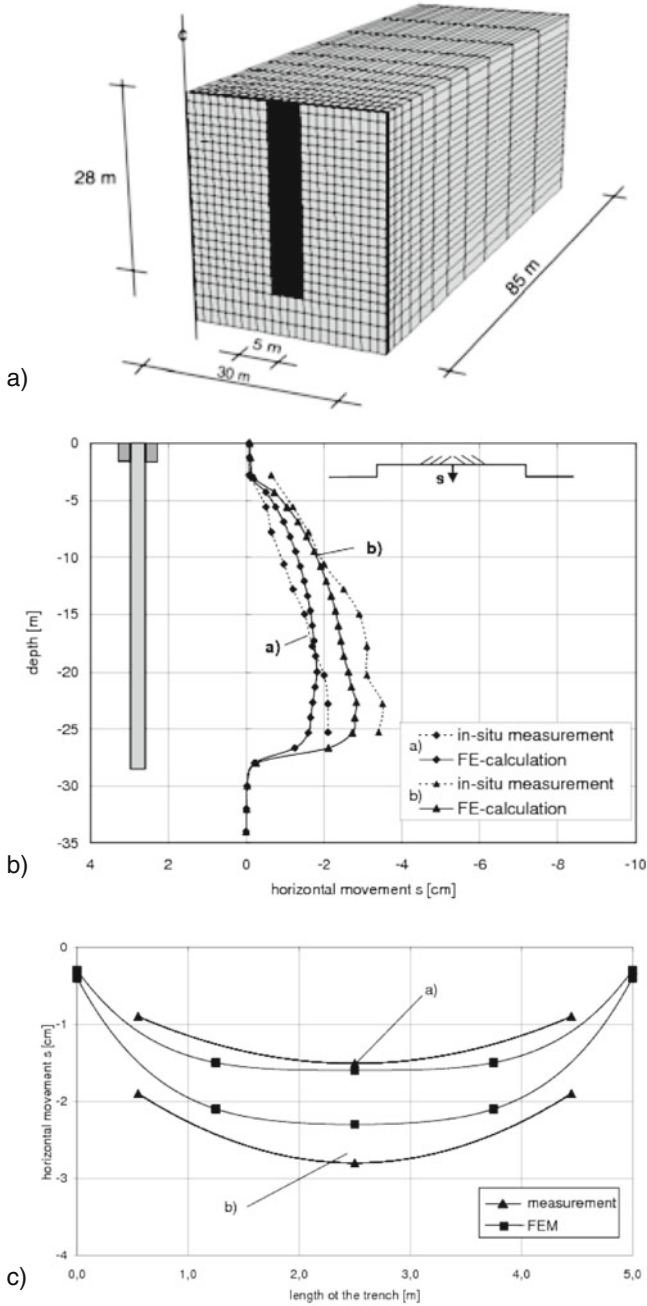


Fig. 15.1.4. Back-analysis of a field test by Di Biaggio and Myrvall (1972) with a slurry trench in soft clay (Schäfer and Triantafyllidis 2004): mesh (a), horizontal displacements at mid-height (b) and rim of the long wall (c)

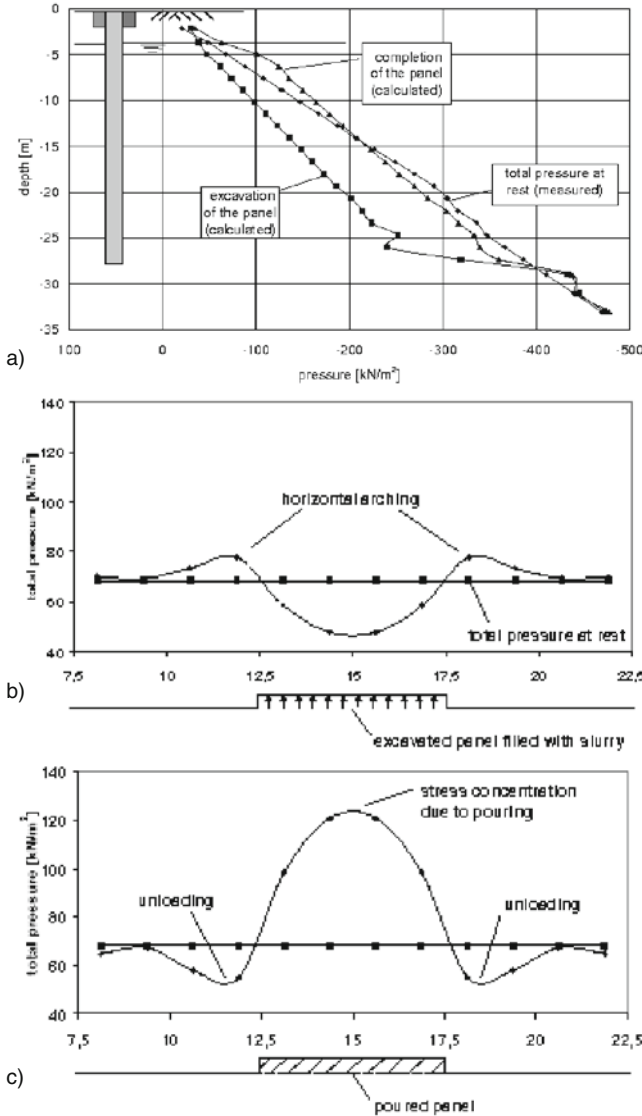


Fig. 15.1.5. Pressures along the vertical axis of the slurry trench of Fig. 15.1.4 (a), long-wall pressures after excavation (b) and with fresh concrete (c)

panel (not for the progression of panels, Sect. 15.3). Specific weights, level and gradual placement of slurry and concrete during and after excavation were adapted to the test protocol. Seepage with swelling or consolidation was neglected as in the operation time the diffusion of pore water could not exceed $0.5\sqrt{tc_v} \approx 0.5\sqrt{24 \cdot 3600 \text{ s} \cdot 10^{-8} \text{ m}^2\text{s}^{-1}} = 15 \text{ mm}$ by (12.2.4), i.e. far less than the panel width. Isochoric deformations and stress redistribution occurred

mainly during the change of boundary conditions, the subsequent creep and relaxation was minor in the observation time.

Horizontal displacements along the middle height of the long wall (b) are well reproduced both with water and slurry in the hole. The same good agreement was obtained for horizontal displacements along the long rim (c). Calculated pressures along the vertical axis exhibit a decrease by excavation with slurry at the panel (Fig. 15.1.5a). Calculated pressures along a horizontal axis decrease by excavation (b) and increase by filling with fresh concrete (c). The neighboured ground experiences other pressure changes, this kind of arching is not the same at other depths.

De Wit and Lengkeek (2002) report on a field test in soft *composite ground*, Fig. 15.1.6. In the upper 13.5 m the ground consists of loose psammoid and soft peloid layers under groundwater. Horizontal displacements slightly off the middle of a trench (a) were small with about zero average just after excavation with slurry support. The fresh concrete mud pushed aside soft layers between the crust and a harder base. Simultaneously the ground surface subsided along

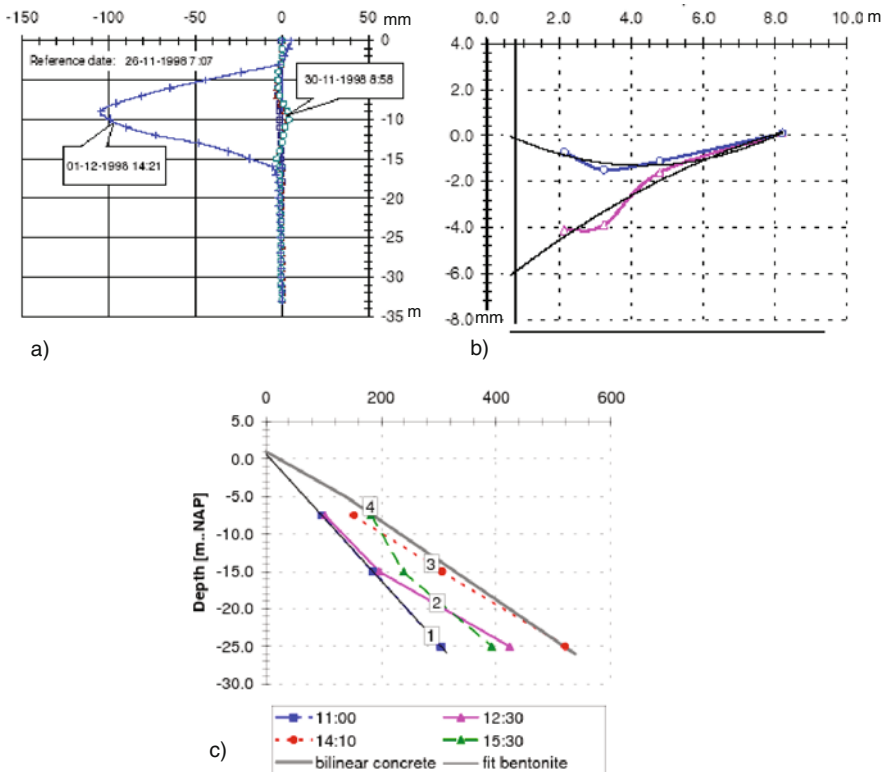


Fig. 15.1.6. Field test with a slurry trench in soft layered ground (De Wit and Lengkeek 2002): horizontal displacements versus depth (a), vertical surface displacements versus distance (b), pressures in the trench (c)

the shorter cross section (b), this indicates a densification in the near-field. Piezometers along the middle long wall exhibit an increase from a hydrostatic slurry pressure to the pressure of heavier fresh concrete (c), which is first hydrostatic and then reduced by curing.

De Wit and Lengkeek (2002) report also on simulations with two-fold symmetry, an elastoplastic relation and seepage. Observed lateral displacements could be reproduced with an adaption of soil stiffness, but a heave of the ground surface was obtained instead of the observed subsidence. The diffusion of pore water may be neglected for the operation time in the peloid layers. In the psammoid layers with free drainage, however, the pore water is already mainly diffused during the input of fresh concrete. The loose grain skeleton is contracted so much by sideways shearing (Sect. 2.9) that it is shortened vertically so that the surface subsides. This could be reproduced with hyp and v-hyp for psammoid and peloid layers, respectively, and with coupling of skeleton and water. In view of the actual deviations from two-fold symmetry an interpolation between axial symmetry as by Fig. 15.1.3c and plane-parallelity could suffice.

Evolutions in the ground during and after the curing of concrete could also be simulated with two symmetry planes, but have not sufficiently been observed *in situ*. The double symmetry is less relevant as prograding panels have at best one symmetry plane (Sect. 15.3). Shape and state of psammoid ground would hardly be changed by curing as the concrete remains almost undeformed. Skeleton stresses do change by the progression of panels, but this does not matter for subsequent evolutions with excavation and support (Sect. 13.6). The near-field of peloid layers tends to far-field values by relaxation of the skeleton and diffusion of the pore water. The latter should be minor after careful trenching, the former matters only if the ground has a low consolidation ratio p_{ef}/p_s in the far-field (cf. Sect. 15.2). Otherwise the near-field progrades with the panels, but this does not matter afterwards in case of careful trenching. The assumed symmetry would get lost by a collapse if the soil is not ductile (Sects. 2.2 and 3.2), but then trenching with slurry would be too dangerous anyway.

The prograding excavation of a *tunnel* can exhibit two symmetry planes, Fig. 15.1.7. As supporting structures (Sect. 15.2) are left aside for introduction the ground should have a sufficient cohesion, whereas an excess air pressure $p_g > p_a$ may be applied for support. Psammoid with open gas channels has a capillary skeleton pressure p_{cs} which can keep the free wall and roof (Sect. 6.2). p_{cs} is not reduced by $p_g > p_a$ and the skeleton pressure p_s is increased by outwards seepage forces. Saturated peloid, which may include minute gas bubbles, develops suction ($p_g - p_w > 0$, Sect. 6.3) at new free surfaces if the initial consolidation ratio p_e/p_s exceeds ca. 2 so that p_s increases by isochoric deformations (Sect. 3.2). The excavation may prograde with the full cross section and a dome at the front (a). It could proceed in smaller steps if p_{cs} or p_e/p_s and $p_g > p_a$ would not suffice, then supporting structures are indispensable.

A ground with layers and ground water is specified by profiles of composition and state (Sect. 11.3). The moving tunnel boundary is specified by replacing the initial pressure along it (Sect. 10.1) in realistic steps and intervals (Sect. 12.3). Pneumatic and hydraulic conditions should be specified off the tunnel, they could include drains installed before. As always fictitious walls and a fictitious rigid base are assumed sufficiently far off. Evolutions of shape and state could be simulated with elastoplastic or hypoplastic relations plus coupling with pore gas or water. The time scale for psammoids is determined by the rate of excavation, and also by the flow of pore gas for $p_g > p_a$. The skeleton viscosity of peloids means a further time scale via D_r (Sect. 3.2), whereas the diffusion of pore water may be neglected during usual opening times.

Simulations could again be reduced to axi-symmetric and plane-parallel ones by means of an *interpolation*. This is shown in Fig. 15.1.7b for vertical displacements at the front roof (A), at the surface above it (B), at the roof far off the front (C) and above it (D). This interpolation works also for other points and displacement components, and for different rates of excavation. Plane-parallelity may be assumed for $a/b > ca. 2$. The interpolation is no more legitimate with non-symmetric loads or buildings at the ground surface. The symmetry would also get lost by a collapse if the soil is not ductile, but then such an excavation should be avoided anyway.

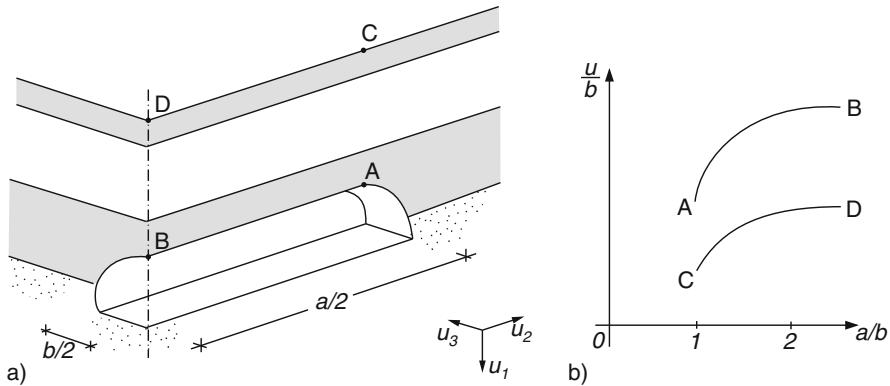


Fig. 15.1.7. Excavation of a tunnel without support (a), interpolation as Fig. 15.1.1b (b)

Tectonic *ring structures* can be similar as for axial symmetry with an elliptic shape in the ground plan and two symmetry planes (cf. Figs. 14.2.8 and 14.2.9), Fig. 15.1.8. Above a diapir (a) funnel-like faults may be imagined with layer dislocations, the free surface remains horizontal by erosion and sedimentation. Above a depression (b) an elliptic dome may be imagined with a succession of near-conical faults. A superimposed horizontal stretching of

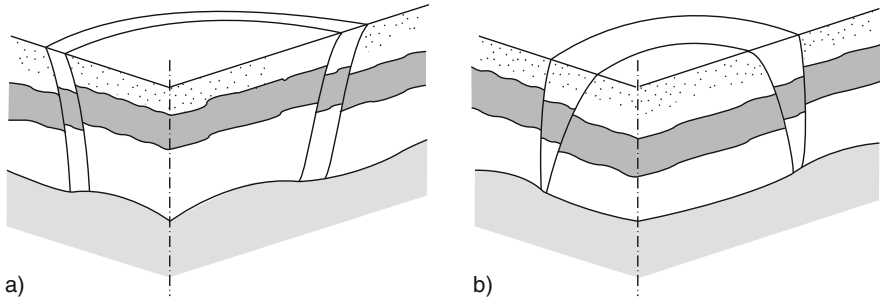


Fig. 15.1.8. Ring structures above a diapir (a) and a depression (b)

the subsiding base, which may be orthotropic with the same symmetry, would lead to flatter fault cones, the free surface could again remain horizontal. The indicated conical faults may consist of several rather normal and less marked antithetic faults with clay smears (cf. Sect. 12.6).

As with axial symmetry (Sect. 14.2) such evolutions could be simulated with hyp and v-hyp, mechanically scaled model tests with elliptical vessels could serve for visualization and validation. Shear localizations cannot be captured down to bands of some grain diameters thickness, they would also mean a loss of symmetry. Instead of a two-fold symmetry interpolations between plane-parallel and axi-symmetric evolutions could reduce the amount of calculations. A few simulations with two symmetry planes could suffice to quantify the transition to plane-parallelity. Such simplifications could be of use before reducing the assumed symmetry as tectonic and sedimentary initial and boundary conditions have to be guessed anyway.

Psammoid and peloid bodies as shown in Figs. 15.1.1 to 15.1.7 can experience *reversals*. Cyclic filling and excavation with two symmetry planes would be of merely academic interest, but cyclic hydraulic conditions or pulsations from the base can be practically important. Wetting and drying cycles can lead to stabilization or collapse, Fig. 15.1.9. If a fill is exposed to periodic rain and drought (a) a zone near the free surface can attain diffusion cycles of pore fluid (cf. Sects. 6.2, 6.3 and 10.1). The skeleton of mineral particles in this zone will gradually slide down the slope. This kind of ratcheting can get minute if the skeleton is densified by an excess of evaporation versus imbibition, and by small amplitudes. Otherwise a near-surface zone can dilate by shearing and swelling until an avalanche arises.

If a free water table in an excavation changes periodically (Fig. 15.1.9b) a near-surface zone can experience diffusion cycles, ratcheting or collapse. The pore water of psammoids is temporarily and partly depleted, its seepage force shifts the skeleton downslope. A rapid dewatering at a fine-grained psammoid ground can cause it to slump without seepage (cf. Sect. 12.1), the more if the skeleton had been dilated before. Peloid ground can remain saturated except for minute gas bubbles as long as shrinkage does not lead to cracks (cf.

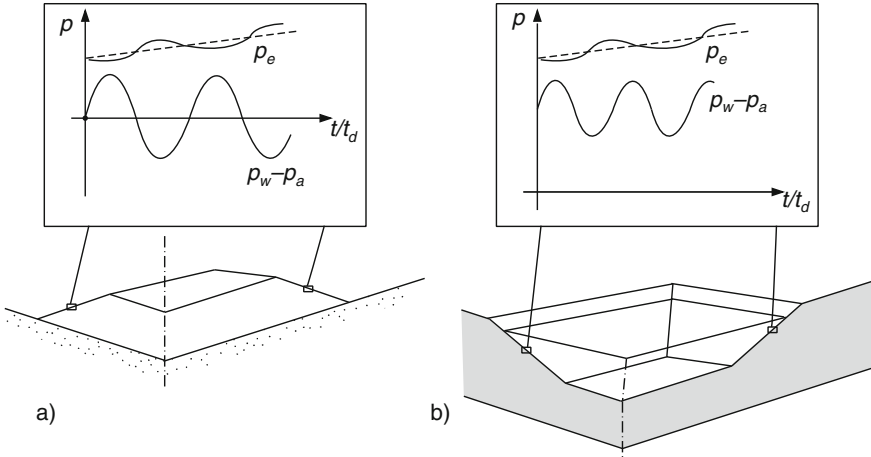


Fig. 15.1.9. Slopes with pulsating humidity (a) and water table (b)

Sects. 6.3 and 12.2). A densified crust can then arise with release of pore water if wet intervals do not last too long, otherwise swelling can lead to slump and avalanches.

Such coupled evolutions of skeleton and pore fluid are beyond the reach of present prediction models, particularly as capillary effects with reversals are not yet properly understood (Sects. 6.2 and 6.3). Model tests with axial symmetry would be of use, but models with less symmetry will be needed for applications. In experiments with psammoids repeated flooding and depletion could reveal conditions for a nearly asymptotic response with so minute ratcheting that changes of shape are negligible.

Slow tectonic actions can also exhibit reversals, but hardly so often that the response gets periodic. Model tests with cyclic orthotropic extension and contraction of the base together with pairs of confining walls could nevertheless be rewarding. The focus should again be on conditions for a nearly periodic response as long as overall geometrical changes are minor. Such experiments could also be made with fills and excavations, one should start with plane-parallel and axi-symmetric evolutions.

Sections of the earth crust including fills or excavations with *seismic actions* can exhibit two symmetry planes, Fig. 15.1.10. Repeated shaking in one of the principal directions leads to gradual spreading of a fill (a) and caving of a hole with free slopes (b). Leaving aside a collapse due to overcritical slope inclinations or void ratios without seepage (cf. Sect. 12.3), the ground state can get nearly periodic by repeated base shocks as long as the slopes are not flattened by shaking.

Random shaking with stationary average spectrum can lead to spreading or caving up to a slump (cf. Sects. 4.7,). The directions of such seismically activated motions are more determined by the shape of the hill or the hole

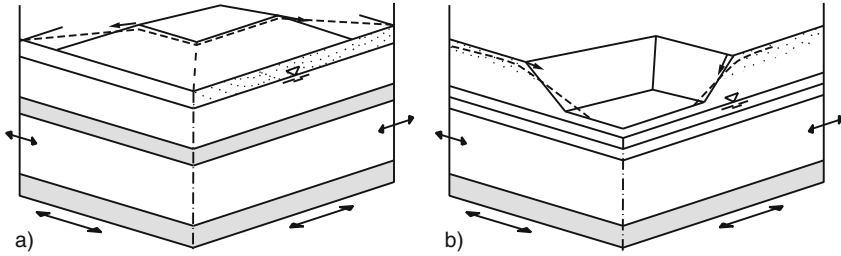


Fig. 15.1.10. Spreading of a hill (a) and caving of a hole (b) by earthquakes

than by preferred directions of random shaking. The intensity of a cumulative flow increases with the average kinetic energy, this works thus like a higher temperature. A repeated propagation of waves from the far-field can lead to an amplification or attenuation near the free surface, according to shape and amplitude. The response to repeated shocks with rest intervals can be nearly rate-independent, suitable leading frequencies can cause a kind of resonance. Tectonic ring structures can be ironed out by earthquakes, i.e. higher stress obliquities and void ratios due to confined dilation are reduced. Stazhevskii (2005) showed that ring structures are seismogeneous, an autogeneous seismicity would also be obtained with hills or holes if the slopes are steeper than critical.

Models for such evolutions are not yet at hand, but not out of reach and certainly worth the effort. Scaled model tests with dry psammoids and isochoric peloids will help to identify and quantify the main factors of geometry, material parameters, initial state variables and shaking. Axi-symmetric shaking could be generated by periodic or stationary random torsion. Such evolutions could be simulated with the same expenditure as for plane-parallelity, with hyp- δ or v-hyp- δ for periodic and s-hyp for random shaking. Even axi-symmetric bodies retain at best two symmetry planes in case of uni-directional base shaking. Simulations with the latter symmetry should be focussed on cases with asymptotically periodic response, which can be identified by model tests and could thus enable validations.

Attractors determine how far evolutions as outlined in this section could be captured. State limit fields can arise in and under fills, around excavations, without or with fluid inside and with elliptic ring structures. A two-fold symmetry could be attained with suitable geometrical and boundary conditions even in case of initial spatial irregularities of state. If the latter have much shorter wavelengths than hills, holes or ring structures such fluctuations could be swept out by changing or maintained boundary conditions. Only then monotonous model tests can be repeated, and simulations can be numerically robust so that validations could be attained.

Asymptotic state cycle fields can arise with repeated reversals as outlined with Figs. 15.1.9 and 15.1.10. Such attractors in the large can arise as long as geometrical changes are small (cf. Sect. 14.3), they render possible repeatable

model tests and robust simulations. Again non-symmetric initial spatial fluctuations with small wavelengths are ironed out. The numerical generation of asymptotic cycle fields would be expensive (cf. Sect. 15.5), but this should be mastered before turning to less symmetric evolutions.

A spontaneous loss of two-fold symmetry can occur at *critical points* (Sect. 16.3). Collapsing heaps and holes with saturated skeletons of high relative void ratios or low consolidation ratios can get skew with one-sided avalanches. Helix-like shear bands can arise at spreading or caving corners in a rather fractal succession. Cracks, which can preferably arise at spreading corners of heaps or caving longer walls of holes, would also break an initial two-fold symmetry. Ring structures may at best exhibit two symmetry planes in a coarse-grained view. This symmetry gets lost with further faulting and seismic emission, collapsing heaps or holes can release quakes (cf. Sect. 14.5). Hydraulic localizations due to different hydraulic heights along the boundary (cf. Sect. 8.4) could not exhibit two symmetry planes, particularly if mud volcanos rise in ring structures.

To *sum up*, evolutions related with hills, holes or ring structures can be captured with two symmetry planes and judged by means of attractors. Monotonous displacements could be estimated by interpolation of results from plane-parallel and axi-symmetric simulations. Periodically changing hydraulic boundary conditions or base shaking can lead to asymptotic cycle fields if the system is stable. The symmetry gets lost by slumping, shear banding, cracking and autogeneous seismicity.

15.2 Two symmetry planes with SSI

Two-fold symmetry may more often be assumed in geotechnical engineering with structures than without them. Their interaction with the ground (SSI) occurs via interfaces with contact stresses and relative displacements (Sect. 10.3). The structures may be modelled as rigid, elastic or elastoplastic. As without SSI (Sect. 15.1) an interpolation between plane-parallel and axi-symmetric simulations may often suffice. Only few case studies and model test reports are apt for validation. As without SSI the symmetry can get lost, now also due to structural failure.

The subsidence of a *rigid block* upon horizontally layered ground may be simulated with two symmetry planes as far as imposed displacements or forces have the same symmetry, Fig. 15.2.1. The structure could have other shapes with two vertical symmetry planes. Composition and initial state have to be specified (cf. Sects. 13.3, 13.4, 14.2 and 14.4) for one quarter (a). A fictitious rough rigid base and fictitious smooth rigid walls may be assumed closer to the block than with plane-parallelity, sufficient distances could be found by comparative calculations. Along the interface of block and ground both may have the same displacements, thus slips and gaps are left aside. The soil near the base may be improved, this can be captured by the composition. A softer

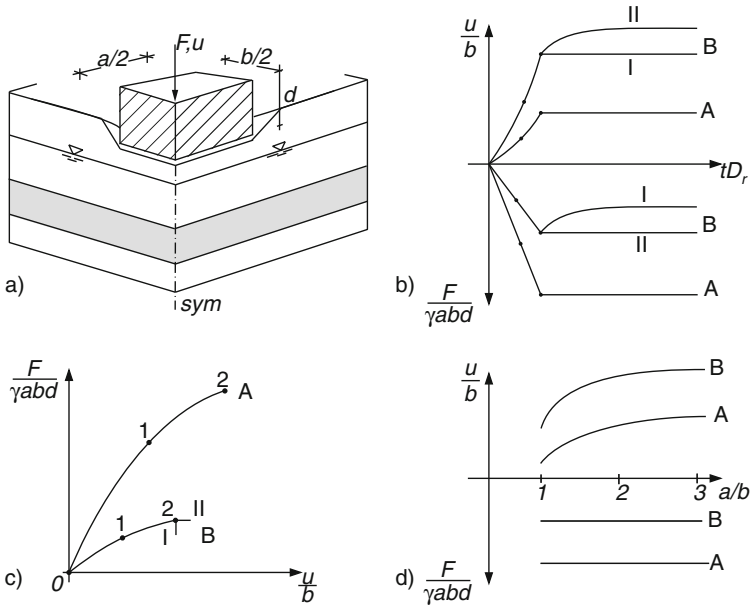


Fig. 15.2.1. Block upon layered ground (a), evolution of settlement and force (b), relation of both (c), interpolation as Fig. 15.1.1b (d)

elastic material may be assumed near the edge as otherwise the equations get ill-posed, the finite element mesh can be coarser farther off the edges (cf. Fig. 13.3.4).

A *monotonous* increase of the subsidence s with time t can be imposed, or produced by an increase of the resultant vertical force $F(t)$ with time (b). The block weight W after construction means $F(t = 0) = W$. With a psammoid ground and constant hydraulic height h_w the relation of F and s (c) will be rate-independent (A). It is non-linear and can attain a peak with $dF/du = 0$, a collapse beyond it is left aside (cf. Sect. 13.3). With peloid layers without seepage (B) the relation of F with u is argotropic due to the skeleton viscosity (cf. Sect. 13.4). Relaxation occurs after fixing the block (I, b below), and creep under a constant force (II, b above). With seepage a diffusion of pore water in peloid layers (hardly in psammoid) occurs alongside with a densification or dilation of the skeleton. The time-dependence is then influenced by the hydraulic boundary conditions at the free surface and the fictitious far-field boundaries. Relaxation or creep for constant block position or load, respectively, are now determined by skeleton viscosity plus pore water diffusion. The time t may as well be referred to a diffusion time t_d by (11.3.1), then the reference stretching ratio D_r (Sect. 3.2) enters via $t_d D_r$.

Simulations with double symmetry require numerically adequate increments of u and F for psammoids, and also of t with peloid layers. Initial spa-

tial fluctuations of density and stress with wavelengths well below the block size may be neglected as they are ironed out during a monotonous subsidence. This approach of a state limit field strengthens predictions, but an initial uncertainty cannot be avoided (cf. Sects. 13.3 and 14.4). As without a block one can interpolate displacements for given forces and times between those for plane-parallel and axi-symmetric evolutions with the same cross section, Fig. 15.2.1d. The required same average block base pressure is achieved by the same $F/\gamma abd$ and by taking $4F/\pi\gamma d^2b$ instead, respectively, for the two limit cases with only two co-ordinates. Plane-parallelity may be assumed for $a/b > \text{ca. } 2.5$, this restriction of interpolation curves could be further quantified by comparative calculations with two symmetry planes.

Such calculations may suffice for applications if the ground is horizontally uniform, the structure is very stiff and horizontal and eccentric loads are negligible (otherwise Sect. 15.4). Validations could preferably be obtained by model tests as natural ground is rarely that well-defined, and as installation and vertically guided loading of nearly rigid blocks in situ are expensive. A pressure level as in prototypes could be obtained with a centrifuge, but with them inevitable vibrations cause additional seismic creep. Tests with $1g$ are less expensive and can still be representative if stiffness and strength are scaled down as the lengths.

For *psammoids* this means that only the granulate hardness h_s should be reduced for $1g$ model tests, whereas the dimensionless hypoplastic parameters (φ_c, n, α and β , Sect. 2.4) should be the same as in the prototype. This could be achieved with softer grains of nearly the same shape and size distribution. Minor deviations do not matter as the actual dimensionless parameters can be used in the back-analysis. Laudahn (2005) reduced h_s by adding a minute fraction of synthetic grains to quartz sand, Fig. 15.2.2e and f. Thus the buckling of force chains is enhanced (Fig. 4.3.2) so that the skeleton yields easier. With a medium relative void ratio ($r_e \approx 1/2$) the obtained increase of settlement s with average base pressure $p = F/b^2$ of a block (b) is roughly the same as in a large scale experiment (a).

The prototype block was quadratic and not embedded ($d = 0$), quartz sand had been densified with a vibrator, the block was guided and loaded by a jack (Leussink et al. 1966). Laudahn's (2005) model block had $b = 0.1$ m and $d = 0$, sand was placed by pluviation, h_s was reduced to about 1/10 by adding ca. 0.2% polystyrene. Settlements s and base pressures p were scaled up by factor 10 for comparison with the prototype. Having in mind the indeterminacy of states after placement the agreement is good enough for validations and predictions. With a low initial r_e the upscaled p versus s is overestimated by about 40%, a peak was only obtained in one model test (Fig. 15.2.2b). The deviation can be attributed to a reduction of h_s by grain crushing in the large scale test. Model tests with moderate (c) and low (d) density show how this matters. The influence of shear localization near the edges is small as the ratio of b and grain size d_g exceeds 1,000 (Tejchman 1997). The advantage of such model tests is evident.

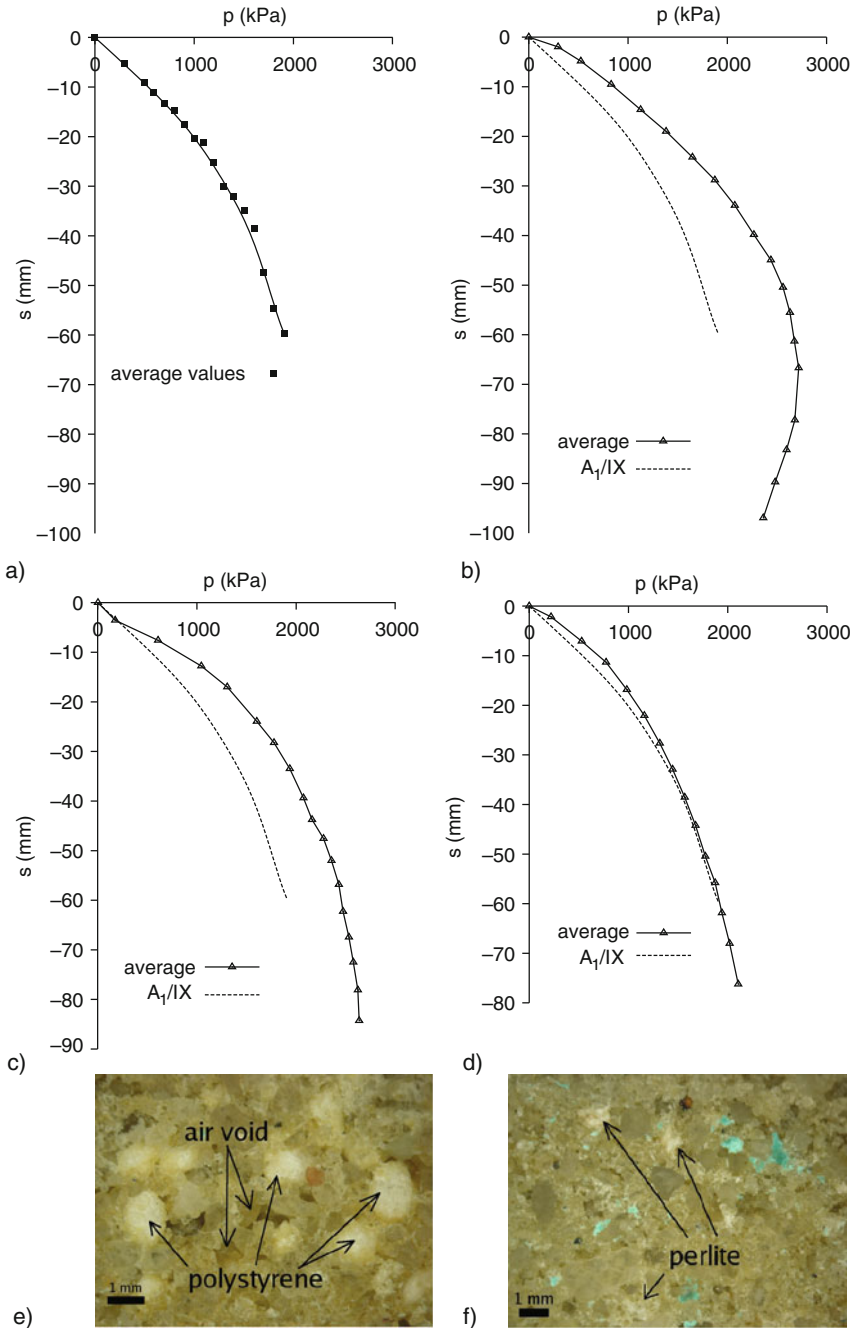


Fig. 15.2.2. Tests with blocks upon dry sand: (a) base pressure versus settlement with big size and high density (Leussink et al. 1966); small size (Laudahn 2005) with high (b), medium (c) and low density (d), scaled up with reduced hardness by adding polystyrene (e) or perlite grains (f). A₁/IX denotes one corner

Model experiments with *peloids* are more elaborate because of skeleton viscosity and pore water diffusion. As shown with plane-parallelity (Fig. 13.3.11) the similarity laws could be satisfied for both effects without a centrifuge. Complete similarity is not required with suitable model peloids and hydraulic conditions, however, if the actual visco-hypoplastic parameters and state variables are taken for back-analysis. Further validations could be obtained by means of model tests with composite ground as in Fig. 15.2.1, sandwich-like soil may be simplified for calculations (Sects. 9.2 and 11.3).

Interactions of *deformable structures* with shallow foundation in layered ground could similarly be captured with two symmetry planes, Fig. 15.2.3. Initial composition and state of the ground can be identified as in a free field (Sect. 11.3). The structure may be placed in an excavation, with slopes, basement box and skeleton with ceiling and wall plates (a). Weight W and stiffness S of the structure grow with time (b), the structure is backfilled. Structural forces and deformations increase during the construction, and change thereafter by payloads and by creep and relaxation in structure and ground, also by diffusion of pore water and heat. Internal forces and deformations should not exceed tolerance limits.

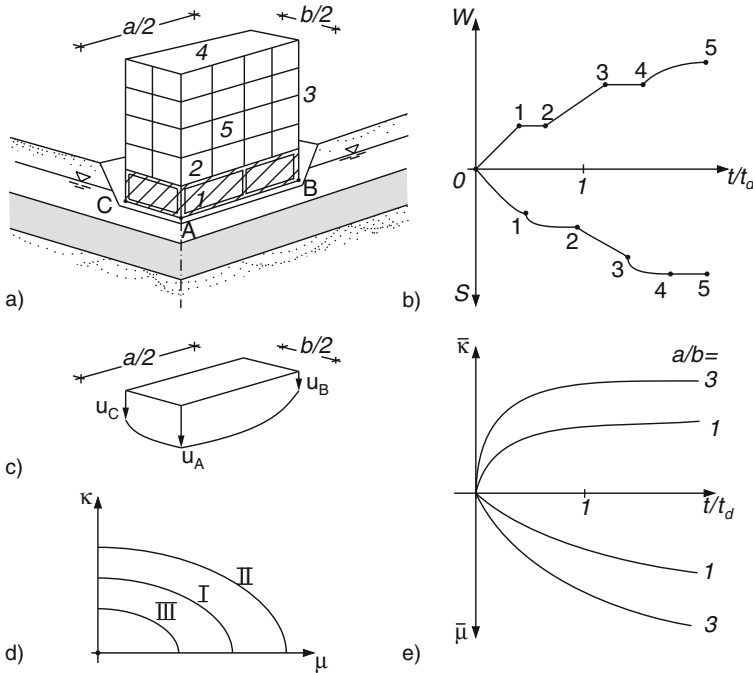


Fig. 15.2.3. Deformable structure upon composite ground: excavation and placement (a, numbers for sequence), growth of weight and stiffness (b), subsidence trough (c), tolerance bounds (d), interpolation as Fig. 15.1.1b (e). Numbers for stages

Avoiding hardly defensible assumptions, simulations with validated models can secure for design that tolerance bounds are not trespassed. These can be expressed by means of an average relative settlement

$$\mu \approx \frac{2}{3}(u_B + u_c - 2u_A)/\sqrt{ab} \tag{15.2.1}$$

and a relative curvature

$$\kappa \approx \sqrt{\frac{u_A - u_B}{a} + \frac{u_C - u_A}{b}} \tag{15.2.2}$$

with settlements u_A, u_B, u_C along the axes and a parabolic distribution otherwise, Fig. 15.2.3c. Both can be combined to a measure of ground and structural deformation

$$\varepsilon_{gs} = \sqrt{f_W \mu^2 + (1 - f_W) \kappa^2} \tag{15.2.3}$$

with a weighting factor f_W . Thus tolerance bounds are ellipses in a plot of μ vs. κ (d) which are wider for construction (I) and extreme actions (II) than for regular use (III), cf. Boscardin and Cording (1989).

Simplifications are justified as only overall changes of shape count and as tolerance limits are rarely precise. This could be quantified by comparative calculations and could serve to specify investigations and monitoring. The assumed double symmetry is needed for construction and use to keep the building upright, and should not get lost anyway. An interpolation between axi-symmetric and plane-parallel simulations for the evolution of relative settlement and curvature μ and κ (e) with time t may suffice in simpler cases (cf. Fig. 15.2.1d). The structure has to be substituted by rings or strips, respectively, thus neglected stiffening corners are minor. One cross section would suffice with plane-parallelity for $a/b > 2$ to 3, an interpolation could be quantified by comparative calculations.

Structures upon *vertical pile groups* can be captured similarly, Fig. 15.2.4. After an excavation the piles are driven or cast in boreholes (Sect. 14.2). Subsequent construction, use and other actions may be the same as before (a).

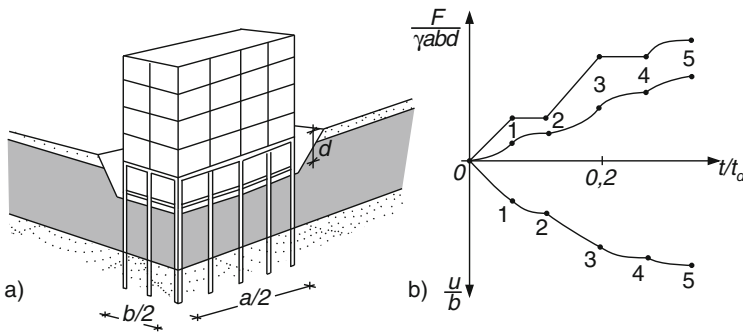


Fig. 15.2.4. Structure upon a vertical pile group in layered ground (a), evolution of forces (weight above, piles together below) and settlement with time (b). Numbers for stages

In case of squat buildings the evolution of settlement $u(t)$ and average pile force $F_p(t)$ alongside with the total weight $W(t)$ during and after construction (b) may suffice for design considerations. The near-field ground is specified by spatially averaged pile and soil properties (Sect. 14.4). These could be more simplified for $u(t)$ than for $F_p(t)$, therefore the structure should be so robust that inevitable redistributions of pile forces do not matter. A further simplification by interpolation between axi-symmetric and plane-parallel simulations is hardly feasible as the substitution of pile rows by walls is not sufficiently clarified. A loss of double symmetry by spontaneous tilting should hardly play a role with a competent pile foundation.

Validations have been obtained with two high-rise buildings. Kudella and Reul (2002) present a back-analysis with hyp- δ for *psammoid* ground, Fig. 15.2.5. The finite element mesh (a) represents one quarter of the ground with fictitious walls and base. The mesh was refined for the near-field with

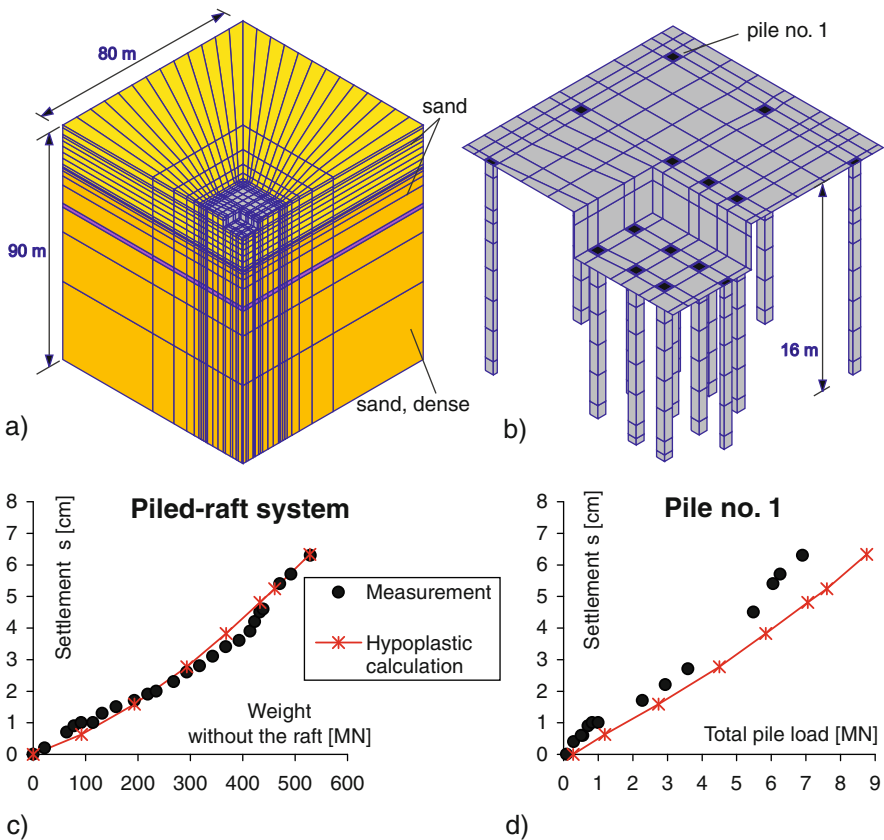


Fig. 15.2.5. Back-analysis for a building with piles in sand (Kudella and Reul 2002): mesh (a), structural mesh (b), settlement versus weight (c), corner pile force versus building weight (d)

piles and superstructure (b). The ground was identified by means of boreholes, lab tests and penetration probing (cf. Sect. 11.2), the structure was assumed as elastic. The ground state after placing piles and basement was generated by imposing gravity with the given low r_e . Grouting around the bored piles after their installation was also taken into account. The further construction was simulated by increasing weight and stiffness of the superstructure. The calculated increase of settlement with weight agrees with the observed one (c), *nota bene* without further adaption of parameters. The increase of a corner pile force with total weight was also captured satisfactorily (d).

Garcia et al. (2006) investigated a tower upon piles in *peloid* ground, Fig. 15.2.6. Piles and raft were placed in an overconsolidated clay (a) which was modelled by v-hyp with a consolidation ratio from 1.6 to 2.1. A deeper limestone base was captured by elp. Various receivers had been installed for monitoring (b). Because of four symmetry planes the mesh comprised only 1/8 of structure (c) and ground (d). Pile forces versus depth along the inner, middle and outer ring of piles are well reproduced (Fig. 15.2.7a). The likewise reproduced redistribution of forces after the end of construction is minor. Settlements are also well captured (b), they increased by ca. 1/3 within 8 years due to creep (c), temporary increases of pore pressure were negligible. As no parameters were adapted afterwards this is a validation.

Supported excavations can also exhibit two symmetry planes, Fig. 15.2.8. In a representative quarter (a) the ground may be composed of horizontal *psammoid* layers (1) and carry neighboured buildings (2). After installing a wall (3) and partial excavation (4) upper struts (5) may be placed. After further excavation under water (6) vertical anchors may be installed (7) in order to fix a bottom plate (8), then the water above is pumped out (9). Structural forces and displacements at representative points evolve with these steps (b) and should not exceed tolerance limits. Apart from construction and curing times (let alone shaking) the evolution is rate-independent as long as the soil grains are hard and the structure is elastic. Variants of supporting structures and ground treatments may be considered similarly (cf. Sect. 13.6), subsequent changes of boundary conditions and superstructures can also be taken into account.

Simulations could be organised as outlined in Sect. 13.6 and with Fig. 15.2.5. Back-analyses of well-documented field cases could be used for validation. Transitions to plane-parallelity in a *prograding supported trench* could likewise be captured, this is shown in Fig. 15.2.8c with lowered groundwater and a top slab that first works like struts (cf. Fig. 13.6.3). For aspect ratios $a/b > \text{ca. } 2$ to 3 of the prograding structure the consideration of cross sections may suffice, but evidently only for a part of the evolution. An interpolation between axi-symmetric and plane-parallel simulations can provide design estimates of representative forces and displacements. This is legitimate as long as the interpolation can be shown to be monotonous and on the safe side. Transitions from wider to narrower supported excavations and crossings with ramps could be captured similarly.

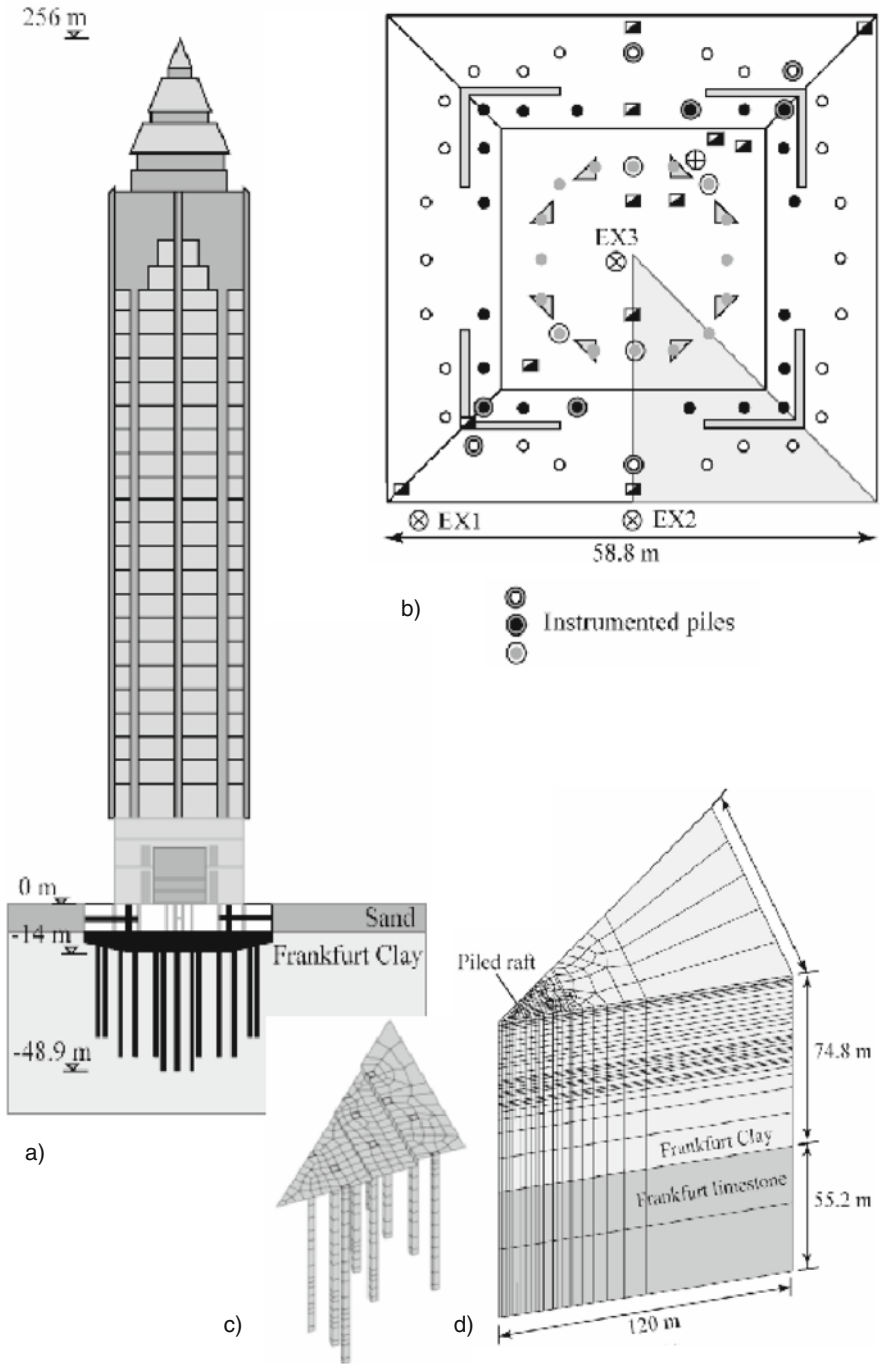


Fig. 15.2.6. Building with piles in clay (Garcia et al. 2006): overview (a), receivers (b), meshes of structure (c) and ground (d)

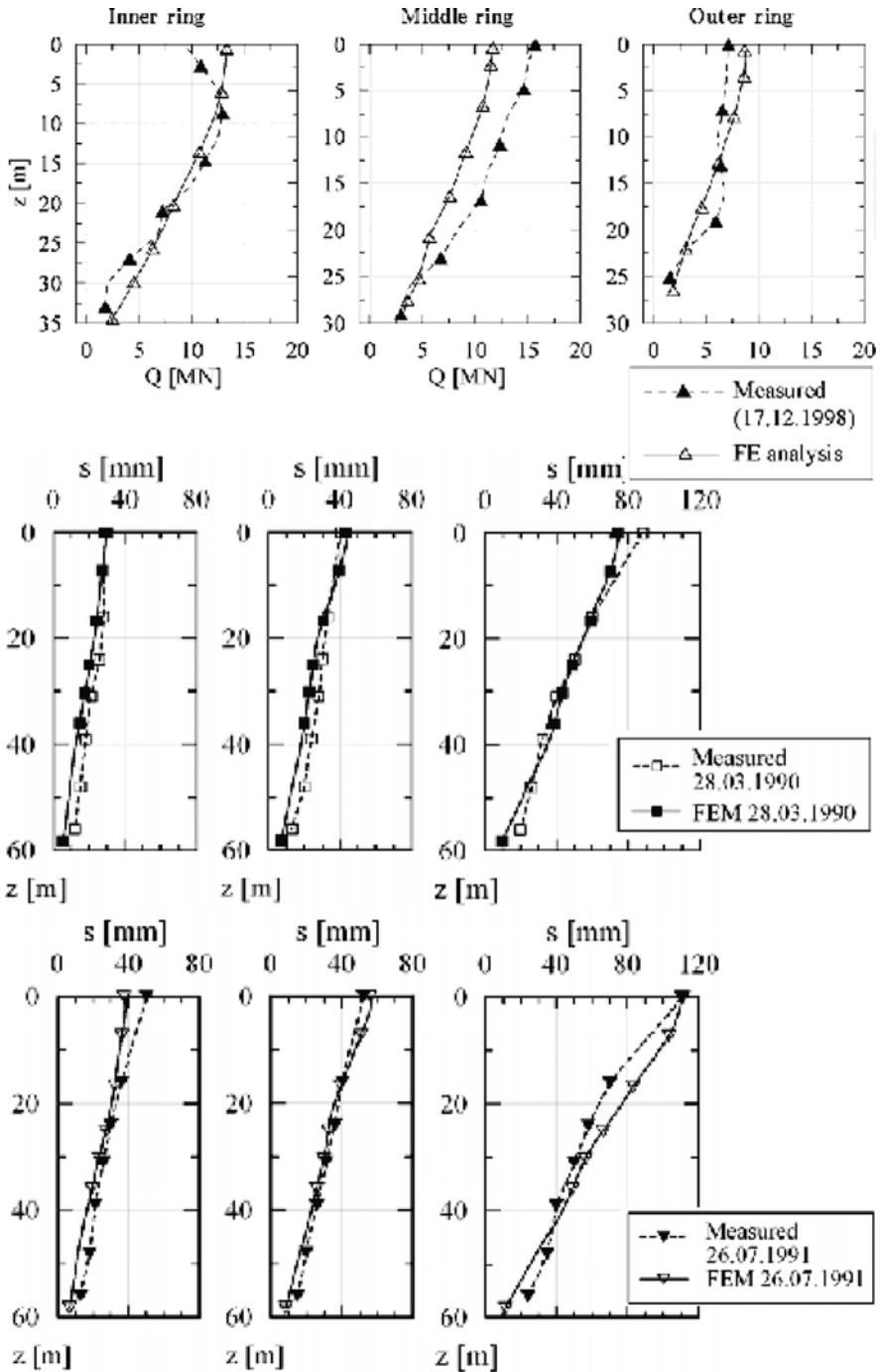


Fig. 15.2.7. Back-analysis for the building of Fig. 15.2.6: axial pile force versus depth (a), settlements just after construction (b) and 8 years later (c)

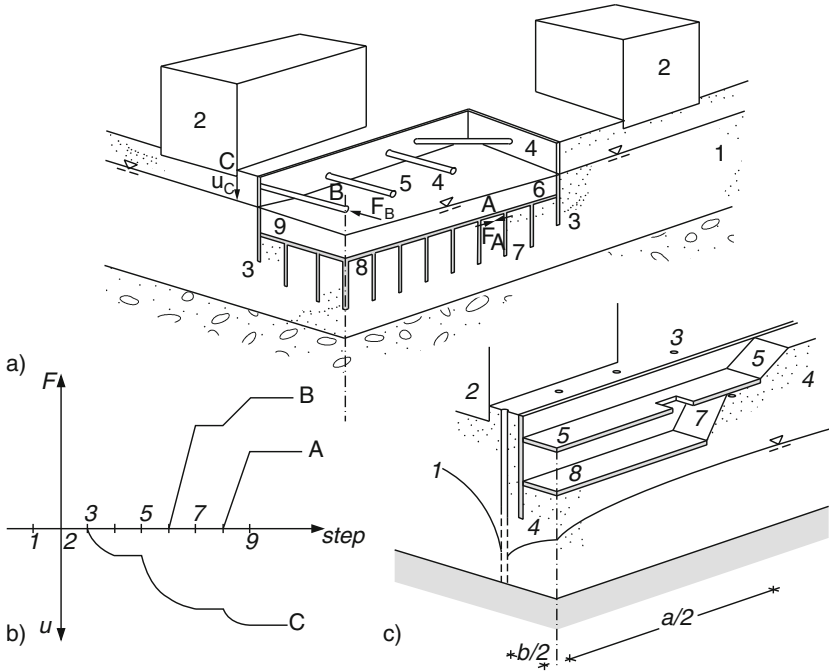


Fig. 15.2.8. Supported excavation in psammoid ground (a), evolution of structural forces and displacements (b), transition to plane-parallelity with a prograding trench (c). Numbers for stages

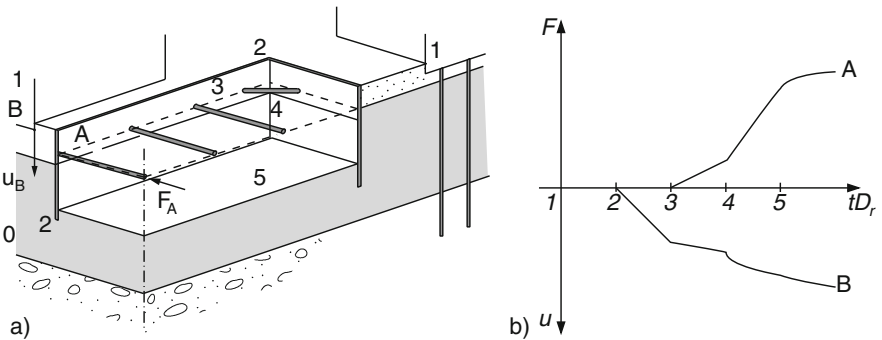


Fig. 15.2.9. Supported excavation in composite ground (a), evolution of structural forces and displacements (b). Numbers for stages

Supported excavations in *peloid* and *composite* ground could be treated with the same symmetry. For instance (Fig. 15.2.9a), a sheet pile wall may first be driven in (1), after partial excavation (2) a first row of struts (3) is installed, this is repeated down to the bottom (4 etc.). The evolution of strut

forces and displacements with time (b) goes on after the last installation due to skeleton viscosity, and in the long run also by diffusion of pore water. The report by Wu and Berman (1953) could be used for validation beyond the one for a middle cross section presented by Fig. 13.6.10. Comparative calculations could yield a sufficient aspect ratio a/b for plane-parallelity. An interpolation between axi-symmetric and plane-parallel evolutions is legitimate as these are monotonous. Corners instead of thus assumed rounded ends could be modelled in addition with one symmetry plane (Sect. 15.4). Transitions to narrower excavations and crossings can be treated similarly.

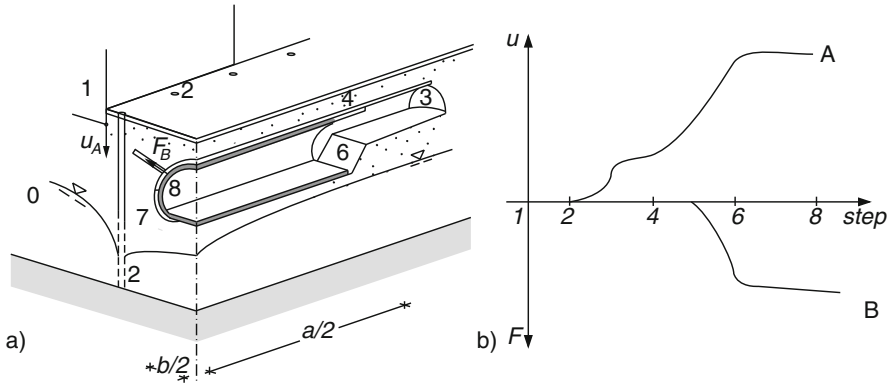


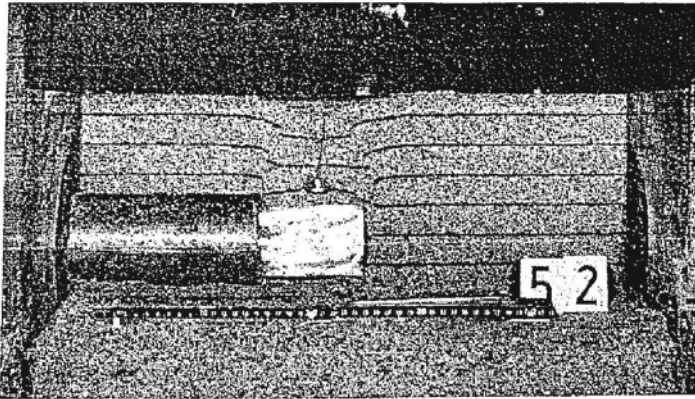
Fig. 15.2.10. Driving of a tunnel with support in psammoid ground (a), evolution of displacements and structural forces (b). Numbers for stages

The driving of *supported tunnels* could also be captured with two symmetry planes. For instance, in *psammoid ground* (Fig. 15.2.10a) the water table may first be lowered (2) to get capillary cohesion, this may suffice for the front of a smaller roof tunnel (3) with subsequent shotcrete shell (4) and anchors (5), then the lower part is excavated (6) and supported by shotcrete (7), thereafter a concrete tube is installed (8). Characteristic displacements and structural forces (b) evolve with these construction steps and should not exceed tolerance bounds. The time scale is determined by construction and curing times as far as ground and hardened structural parts are rate-independent. Variants can similarly be considered, e.g. with grouted shells, excess air pressure (cf. Fig. 13.7.6) and/or a supporting shield with roof grouting and subsequent tubings.

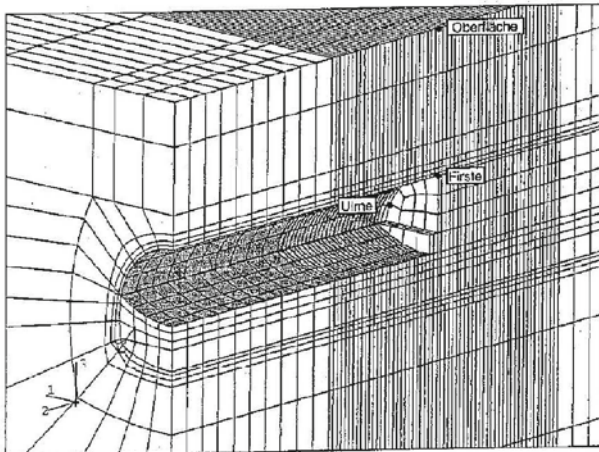
Simulations could be organized as with plane-parallelity (Sect. 13.7), but now the evolution along the tunnel axis is included so that more geometrical variants are possible. A transition to plane-parallelity may be assumed for aspect ratios $a/b > 2$ to 3, this could be further quantified by comparative calculations. This is a tractable substitute of hardly defensible usual assumptions to catch the longitudinal arching for design. Interpolations between axi-symmetric and plane-parallel simulations are legitimate for displacements at the ground surface as they change monotonously with a/b . Therein

axi-symmetric walls replace the actual excavation front, and anchor rows are represented by plates (cf. Figs. 13.6.4 and 13.7.6). Variants as indicated above can likewise be simulated. A similar interpolation is less justified for internal forces of supporting structures as these do not change monotonously with the progression in general. The possible damage to neighboured buildings could be judged by combined tolerances of stretching and tilt (Boscardin and Cording 1989), cf. Fig. 15.2.3d.

The range of validity can be better judged by model tests than by observations *in situ* as there the conditions are rarely regular enough. Mélix (1987) bored a tube into humid sand in a box (Fig. 15.2.11a) and produced a roof



a)



b)

Fig. 15.2.11. Roof collapse in a model test with sand (a, Mélix 1987), mesh for back-analysis with a tunnel (b, Bliem 2001)

collapse at the front by increasing the pressure on the ground surface (cf. Fig. 13.7.5). This could be modelled with a gradually emptied and completed mesh (b) as proposed e.g. by Bliem (2001). His back-analysis of a tunnel constructed in humid sand did not produce realistic surface settlements. A fair agreement was obtained with *elp* only by a fitted soil stiffness. Displacements were overestimated with *hyp*, they would be smaller with *hyp- δ* as the evolution implied reversals and small deformations (Sect. 4.2). An impending roof collapse could be captured except for shear localizations (Sect. 13.7).

The assumed double symmetry is certainly not always given, and can get lost spontaneously. With a row of buildings on one side only, or with two equal tunnels constructed one after another, e.g., displacements and structural forces would be underestimated by assuming a longitudinal symmetry plane. Only a transversal one may be justified for a sufficient aspect ratio a/b . Excavation and installation of structures without longitudinal symmetry would be detrimental otherwise and may be excluded. Caving with shear localization and cracking would break an initial double symmetry, but this can be avoided by keeping forces and displacements within tolerance bounds.

A double symmetry may also be assumed for supported tunnels in ground with *peloid* layers. For instance (Fig. 15.2.12a) the ground may consist of *psammoid* and *soft peloid* layers under groundwater (1), and buildings may stand in rows near both sides of the tunnel axis (2). A shield (3) may be driven with a supporting slurry (4) at the excavation front (5), the slit above the shield is grouted (6) and the subsequent tube (7) is installed by placing tubings. Displacements of representative points and internal structural forces (b) evolve with time by the prograding construction, and afterwards due to skeleton viscosity and pore water diffusion, both should not exceed tolerance bounds. Variants of shield driving, tube placement and grouting (cf. Sect. 12.7) could be represented similarly.

Simulations could be organized as with more symmetry (Sects. 13.7 and 14.2), with time steps according to viscosity and diffusion plus steps of excava-

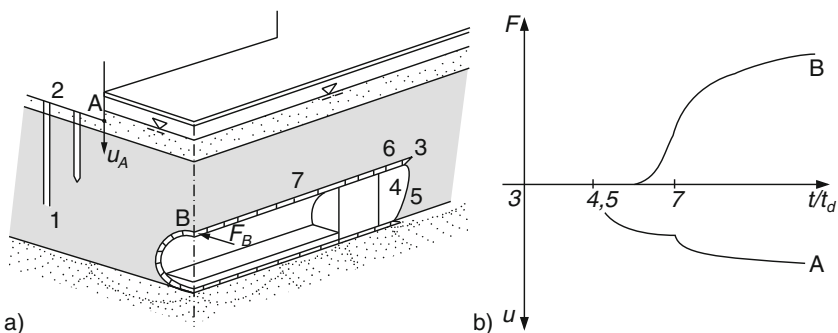


Fig. 15.2.12. Excavation of a tunnel with support in soft ground (a), evolution of displacements and structural forces with time (b). Numbers for stages

tion and placement of structural parts. Details of cutting at the front cannot and need not be modelled for getting key displacements and forces. Combined stretching and tilting tolerances (cf. Fig. 15.2.3d) of neighbour buildings (Boscardin and Cording 1989) justify a simplified composition of ground and support. This is also valid for supporting structures which have to be robust anyway, i.e. insensitive against inevitable redistributions. Axial symmetry may be assumed to judge the stability of the initial cavity (Sect. 14.2), and plane-parallelity is justified for long-term displacements and structural forces. Interpolations of displacements and forces for different times between axi-symmetric and plane-parallel simulations could substitute hardly defensible assumptions.

Limits of validity arise due to a forced or spontaneous loss of double symmetry. A construction without longitudinal symmetry would magnify displacements and structural forces and should be avoided if the tolerances are tight. Otherwise a two-fold symmetry could be attained after construction by skeleton viscosity and pore water diffusion. The symmetry can get lost by a slump during the construction, particularly if the soil is not ductile (Sects. 2.2 and 3.2), and by structural buckling or cracking, in particular with delay due to viscosity and diffusion (cf. Sect. 13.7). Such failures can and should be avoided by keeping tolerance limits. Validations are feasible as far as good data from ground investigation and monitoring are available.

For *stiff ground* with dense psammoid and peloid layers less risky tunnel constructions by mining with weaker structural support may likewise be quantified with double symmetry. For instance (Fig. 15.2.13a), with overconsolidated clay (1), previously drained sand (3) and buildings at the surface (2) the front may be partially open (4), then shotcreted (5), widened (6) and further shotcreted up to the base (invert 7), then the final tube is placed (8) and the groundwater table rises again (9). Variants can be similarly represented,

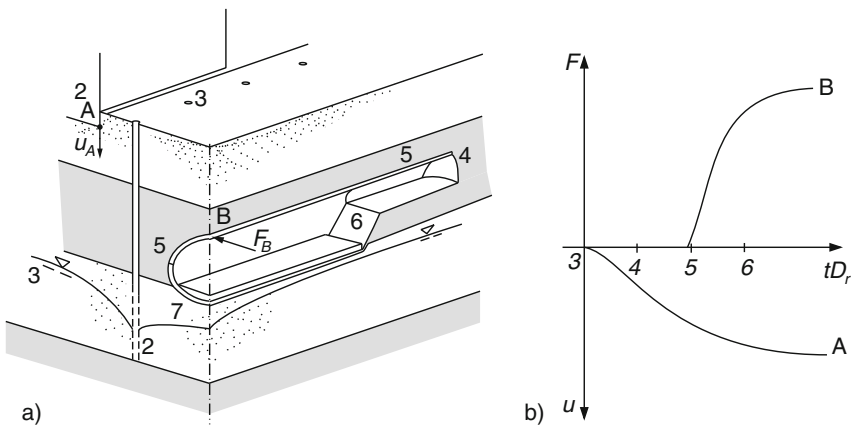


Fig. 15.2.13. as Fig. 15.2.12, with stiff ground

e.g. with grouting or freezing, excess air pressure (cf. Sect. 13.7) and drainage by suction or electrophoresis (Sect. 6.3).

Displacements and internal forces (Fig. 15.2.13b) at representative points evolve with time during the construction, and afterwards due to skeleton viscosity and pore water diffusion. Combined tolerance limits of stretching and tilts for neighbour buildings (Boscardin and Cording 1989) justify again simplified substitutes of ground and structure and related space-time steps. A similar approach may be applied for supporting structures as long as their tolerance bounds are not trespassed during and after construction. Simulations could be organized as before (cf. Sect. 13.7), interpolations between axial symmetry and plane-parallel calculations could again substitute hardly defensible assumptions. Validations are feasible on the base of case reports, these may include well-documented collapses (e.g. Masin 2009) as far as a loss of symmetry can be separated.

Evolutions with *reversals* can be principally captured as without structures, cf. Sect. 15.1. A periodic diffusion of pore water near free soil surfaces may be left aside as it can be avoided by short exposure times and covering. Periodic changes of groundwater table or payloads after the end of construction cause a further increase of displacements and a redistribution of time-averaged structural forces. This can and should lead to a stabilization by densification of near-by ground, and to a periodic response of ground and structure afterwards.

Such asymptotic state cycle fields can principally be simulated as outlined in Sects. 14.1 and 15.1, whereas transitions to them could at best be estimated as initial states are never sufficiently known. This works also with temperature cycles imposed to structures or ground as long as heat-dependent phase transitions in them can be excluded. Repeated wave propagations from above or below can and should likewise lead to stabilization and asymptotic cycles, and not to unacceptable deformations or structural fatigue. Simulations will be expensive even for few propagations, cumulative deformations and redistributions can at best be estimated (cf. Sect. 12.5). Random actions with stationary average can be principally captured by s-hyp (Sect. 4.6), but this approach could only be quantified by means of model tests and field data (cf. Sects. 13.8 and 15.2).

Evolutions as outlined in this section can be judged by means of attractors. Monotonous ones can lead to SOM-states and state limits in the near-field so that initial spatial fluctuations are swept out. This is necessary for predictions and delimits their precision, transitions to attractors are less determinate. Deformable structures can bridge spatial fluctuations with smaller wavelengths, and can help to smooth them in the course of construction and time, but inevitably with deformations. A two-fold symmetry can be gained in the course of construction and use, even if it is not given initially and intermediately.

Asymptotic state cycles due to actions with repeated reversals were introduced further above. These attractors require a stabilization by densification and stress redistribution. Many reversals with small amplitudes in between

work like thermally activated creep and relaxation, they can also enhance the diffusion of pore water (Sects. 6.2 and 6.3) and the two-fold symmetry. This could similarly be achieved with random actions, seismically activated creep and relaxation (Sect. 4.6) can even restore it.

A spontaneous loss of symmetry by tilting, caving, buckling or cracking would indicate deterministic chaos (Sect. 16.3). Such critical phenomena are hardly predictable, one should avoid them by suitable design, execution and monitoring. This can be achieved with sufficiently ductile ground and structure, and with protective construction and use, then the technical control is supported by a better predictability.

To *sum up*, interactions of ground and structure with two symmetry planes can be captured by means of elastoplastic and/or hypoplastic relations and can be judged by means of attractors. The double symmetry can be achieved during and after construction with monotonous or alternating actions, then numerical predictions can be realistic and may be reduced to interpolations between axi-symmetric and plane-parallel simulations. Thermally and seismically activated redistributions of shape and state should also be kept within tolerance bounds. Thus critical points with a spontaneous loss of symmetry can be avoided.

15.3 One symmetry plane and simple SSI

A vertical symmetry plane can occur in evolutions with filling, excavation and other actions which are often called loading or unloading. Embedded structures may be assumed to be rigid or freely deformable so that their interaction with the soil (SSI) is simple. The evolutions can be monotonous or alternating with thermal and/or seismic activation. The need to keep deformation measures within specific bounds helps to simplify simulations. State limits and state cycles can lead to an objective approach, validations are available or feasible. As before limitations by critical phenomena will only be indicated.

The *corner of a fill* upon layered ground can have a diagonal vertical symmetry plane, Fig. 15.3.1. A flexible structure on top with payload and the same symmetry can be damaged by settlement and spreading near the corner. Damage bounds of deformation can be defined by a combined measure ε_{st} of stretching $\varepsilon = (u_{2A} - u_{2B})/b$ and tilt $\psi = (u_{1A} - u_{1B})/b$, viz.

$$\varepsilon_{st} = \sqrt{f_w \varepsilon^2 + (1 - f_w) \psi^2} \quad (15.3.1)$$

with a weighting factor $0 < f_w < 1$. Following Boscardin and Cording (1989) one can represent damage bounds as ellipses in a plot of ε vs. ψ , cf. Fig. 15.2.3d.

Predictions of ε_{st} are needed to judge design variants, and also for execution and control. They can be achieved by means of elp- α and v-elp- α or hyp- δ and v-hyp- δ for psammoid and peloid layers. The composition of the ground may be simplified as ε_{st} is an integral measure (cf. Sect. 11.3), but

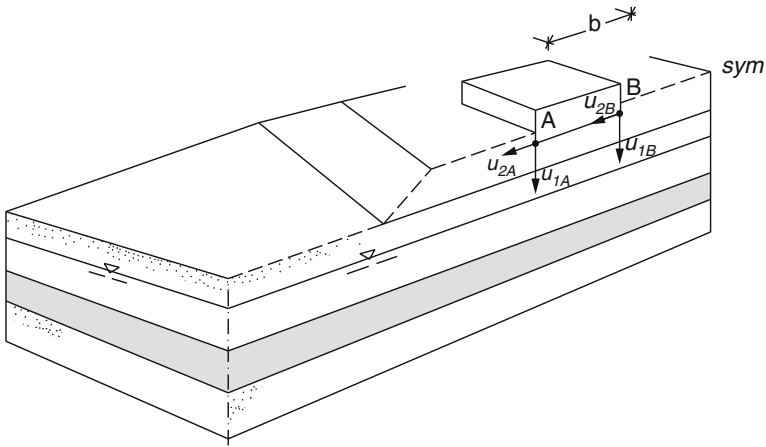


Fig. 15.3.1. Corner of a fill with a building

permeabilities should be substituted with caution (Sect. 9.2) as they determine the duration of pore water diffusion (Sect. 11.1). As always the initial relative void ratios and consolidation ratios should be well established as they dominate the evolutions. Simpler design models with more symmetry and statical or kinematical assumptions could thus be justified with physical and economical arguments. Validations can be achieved with 1g model tests and softer particles than in situ (cf. Sect. 15.2). Model tests are also needed for quantification of rather heuristic seismo-hypoplastic approaches (cf. Sects. 4.6, 12.5, 13.5 and 14.2).

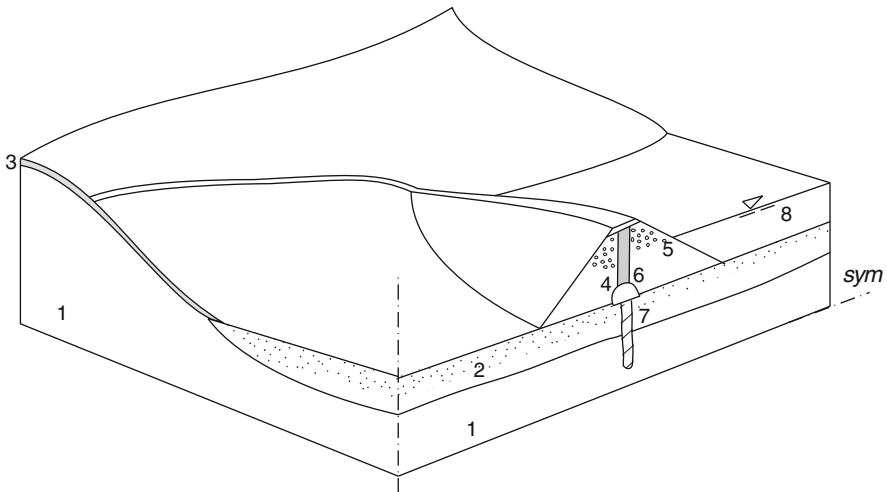


Fig. 15.3.2. Curved dam in a valley. Numbers for stages

The better performance of a *curved dam* than of a straight one can be quantified with a vertical symmetry plane, Fig. 15.3.2. As for a typical valley the ground may consist of a groove-shaped rock base (1), granular sediments from the river (2) and clayey soil along the slopes (3). After removing part of the latter the dam may be built with a tunnel (4), rockfill (5) and a flexible impervious core (6). After sealing the sediment and too pervious rock by grouting (7) the basin is filled with water (8), partly emptied via a separate tunnel, re-filled and so on. Many small and few strong earthquakes may occur. The dam should not trespass tolerance bounds of a deformation measure $\bar{\varepsilon}$ which can be defined as by (15.3.1) with more than two components, viz.

$$\bar{\varepsilon} = \sqrt{\sum f_i \varepsilon_i^2} \quad (15.3.2)$$

with deformation components ε_i and weighting factors f_i ($\sum f_i = 1$).

For simulations with elastoplastic or hypoplastic relations the system has first to be identified by means of a simplified composition and state within sufficiently far off fictitious lower and lateral boundaries. Simplifications can be justified by comparative calculations with tolerance bounds for $\bar{\varepsilon}$ by (15.3.2) for judging the accuracy. As always constitutive parameters have to be assessed for the given soils. Rockfill may be modelled as a psammoid with a moisture-dependent granulate hardness and sufficient permanence (Sect. 7.3). Its placement can be simulated by a slow increase of its gravity with a realistic initial void ratio (cf. Sect. 12.1). Attached structures may be modelled as elastic or elastoplastic, their interfaces with rockfill and ground can be captured as shown in Sects. 10.3 and 12.1. The grouted zone may be modelled as a cemented soil (Sect. 7.3). The obtained field of stress and density in ground, dam and attached structures suffices as initial state for subsequent simulations.

Leaving aside creep, relaxation and pore water diffusion as they should be negligible for a good dam, relevant changes of shape and state can occur by water storage and earthquakes. Hydraulic boundary conditions are imposed

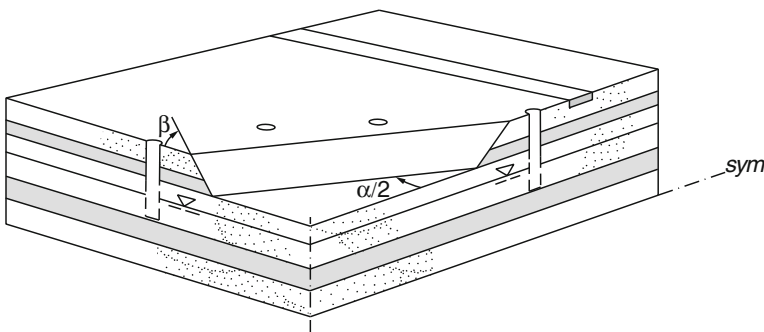


Fig. 15.3.3. Corner of an excavation near a line building

along the basin within design times. Because of seepage the duration of quasi-static hydraulic changes can matter. Strong earthquakes can be substituted by in-plane and anti-plane shaking (Sect. 12.5), because of reversals an internal skeleton variable is needed as with $\text{elp-}\alpha$ or $\text{hyp-}\delta$. Many small earthquakes could instead be captured by s-hyp (Sect. 4.6) with model tests for quantification (cf. Sect. 12.5). Cracking and erosion can be avoided by keeping deformations by (15.3.2) below tolerance bounds, and by filter rules (Sect. 10.2).

The near-field of *excavation corners* can be simulated with a diagonal symmetry plane, Fig. 15.3.3. The slope angle β may be uniform, the angle α made by the two slope edges may range from ca. 60° to 140° . The ground may be composed of horizontal psammoid and peloid layers (the assumed

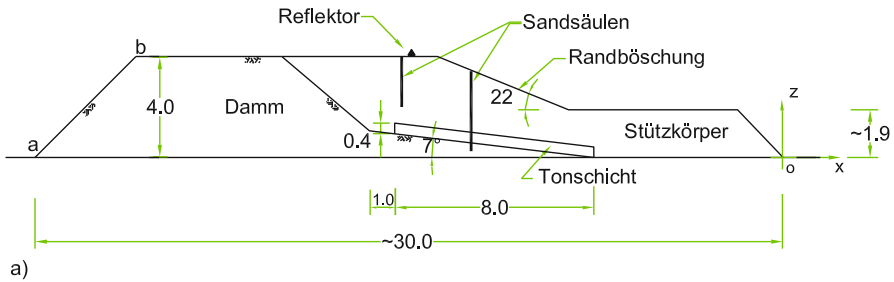


Fig. 15.3.4. Large scale test with an excavation window (Lizcano 2004): (a) cross section, (b) end of excavation and surface markers

symmetry can hardly occur with faults or filled erosion channels). The groundwater may be at rest or have a variable hydraulic height with the same symmetry. Structures in and upon the ground (e.g. wells and roads) may have a negligible resistance against deformations relative to the one of the ground. Deformations of them by (15.3.2) should not exceed tolerance bounds during and after the excavation, waiting times should be taken into account for pore water diffusion and creep (Sect. 12.4).

In addition to a sufficiently deep base fixed smooth walls should be assumed so far off that plane-parallelity is obtained near them. Karcher (2003) found that a base depth of three times the excavation depth and a wall dis-

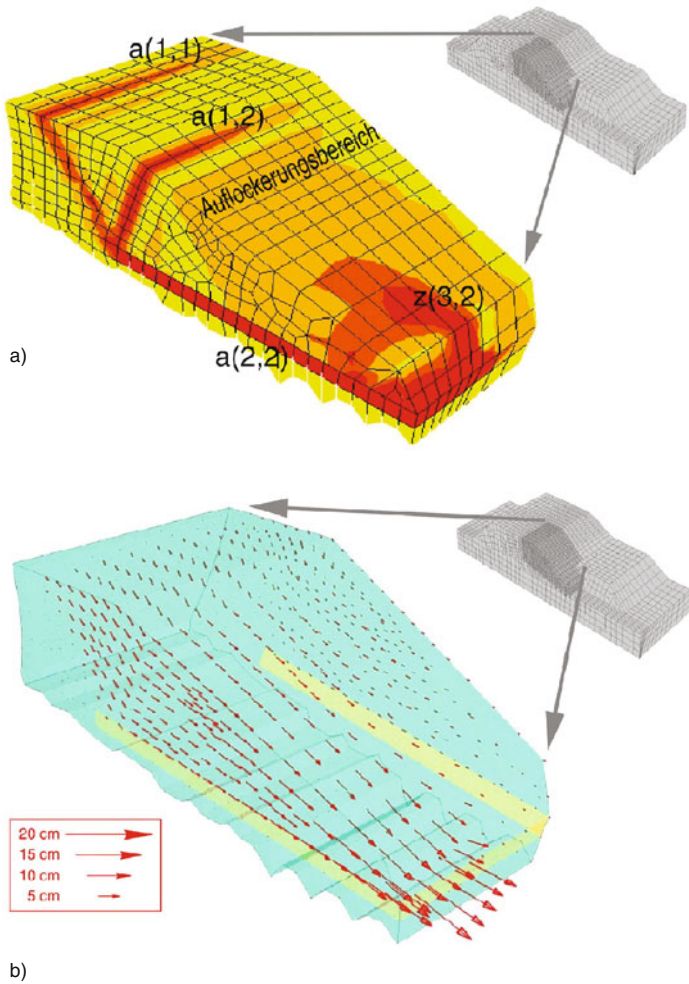


Fig. 15.3.5. Simulated shear zones (a) and displacements (b) for the test of Fig. 15.3.4 (courtesy M. Bühler)

tance from the corner of ca. 2.5 times the base depth suffice for open pit lignite mining. As with plane-parallelity (Sect. 12.4) the displacements after full excavation can be captured by assuming a uniform reduction of gravity for the excavated part, but intermediate displacement paths are missed as they depend on the sequence of excavation. Karcher (2003) calculated reduction factors for displacements relative to plane-parallel ones. These factors depend mainly on the corner angle α and the relative position of displaced points, but hardly on the slope angle β and the relative void ratio.

A so-called *excavation window* with a vertical symmetry plane was investigated by means of a field test, Fig. 15.3.4 (Lizcano 2004). A layer of saturated clay was placed upon a slightly inclined base and covered by a dam of humid sand (a). A window was then excavated in the slope (b) until the neighbored sand slid so that arching cracks arose. Photogrammetric markers at the free surface and thin columns of dyed sand indicated the range of caving and zones of intensive shearing.

In a back-analysis with hyp and v-hyp Bühler (internal report) could reproduce the essential findings, Fig. 15.3.5. With the given void ratios and water contents he first produced an initial state of dam and clay base by removing shoulders. Opening then the window led to realistic zones of intensive shearing (a). The simulated displacements (b) have realistic directions, but too small amounts. The deviation may be attributed to cracks which were not allowed for in the calculation and make the ground softer.

This field test served also to validate a calculation model by Goldscheider and Lizcano (2004), Fig. 15.3.6. An exploded view shows blocks and wedges which act together in a sliding mechanism. Statical equilibrium conditions with directions of friction forces from the relative sliding velocities lead to a required cohesion c_u . Its maximum was determined by variation of the mechanism (cf. Sect. 12.4). This was confirmed by the field test although the assumed shear bands occurred only in the symmetry plane. Comparative calculations with this method revealed that for typical configurations of lignite mining a local deeper cut (window) does not reduce the stability of a long slope (plane-

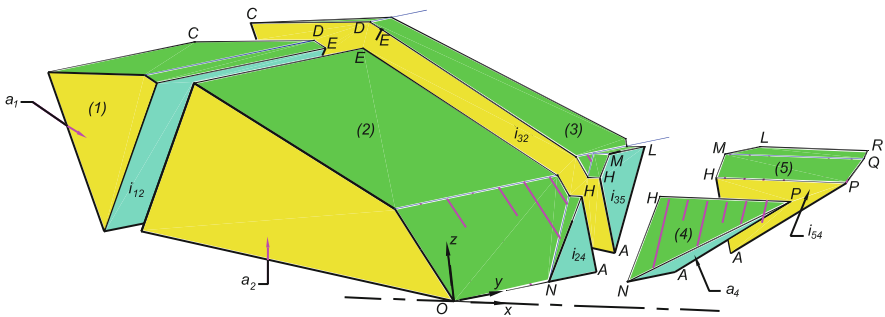


Fig. 15.3.6. Sliding bodies for an excavation window (Goldscheider and Lizcano 2004)

parallel). This simplification is justified as long as the soil is ductile (Sects. 2.2 and 3.2).

The installation of a *slurry trench wall* in *psammoid* ground was investigated by Mayer and Gudehus (2001) with a longitudinal vertical symmetry plane, Fig. 15.3.7. The initial composition and state varied only with depth (Sect. 11.2), groundwater table and penetration resistances were given. The finite element mesh (a) was prepared for some panels in a row with sufficient distance from fictitious base and walls. Excavation with supporting suspension, pouring in and curing of concrete were simulated according to the site record. Sand layers were represented by hyp- δ , a marl band was captured by elp, lab tests served to determine constitutive parameters. Calculated horizontal displacements agree satisfactorily with those observed by inclinometers (b). They approached tolerance limits of near-by facilities, this was the reason for the investigation.

Comparative calculations were carried out with different sequences of production. Characteristic displacements were smaller with a more regular order than with the actual rather erratic jumping of machines. This shows once more the *path-dependence* of grain skeletons (cf. Sects. 2.2 and 12.4): smooth operations pay off. Skeleton stresses at a trench section are similarly distributed as shown in Fig. 15.1.5, but redistributed by the progression of excavation and casting. This leads to more reversals for less steady operations, and thus to bigger deformations. The near-field of the ready panels is not uniform and rather indeterminate anyway. This force-roughness does not matter for the subsequent excavation with support as long as the surrounding ground is not dilated (the ground would be stiffer after vibrating in a wall, Sect. 13.6).

The progressive installation of a *slurry trench wall in peloid ground* was observed by Di Biaggio and Myrvall (1972), and back-analyzed with v-hyp- δ by Schäfer and Triantafyllidis (2004) with a vertical symmetry plane, Fig. 15.3.8. The ground was identified as explained with Fig. 15.1.4a, sequence and intervals of excavation and casting panels were taken from the record. The mesh (a) was adapted to the given geometry, sufficiently distant fictitious walls and base were chosen by means of comparative calculations. Without further adaption of parameters calculated and observed displacements agree satisfactorily. The near-field pressures change with the progression (b) in fair agreement with available data, more precision in that respect is not achievable nor required.

Time enters via skeleton viscosity, whereas curing of concrete and diffusion of pore water are negligible in the considered period. In the long run both lead to a stabilization with minor deformations by densification and pressure redistribution. Stability is given during the operation if the ground and embedded structures are ductile. Structures are on the safe side as long as deformation bounds are not trespassed (cf. Fig. 15.2.3). Saturated undrained soil can be sensitive, i.e. not ductile with high void ratio and rather hard particles (Sects. 2.2 and 3.2). With skeleton viscosity and/or minute repeated disturbance the ground could then collapse some time after trenching. Cudmani and Sedlacek (2006) report on such a case. The version v-hyp by Gudehus

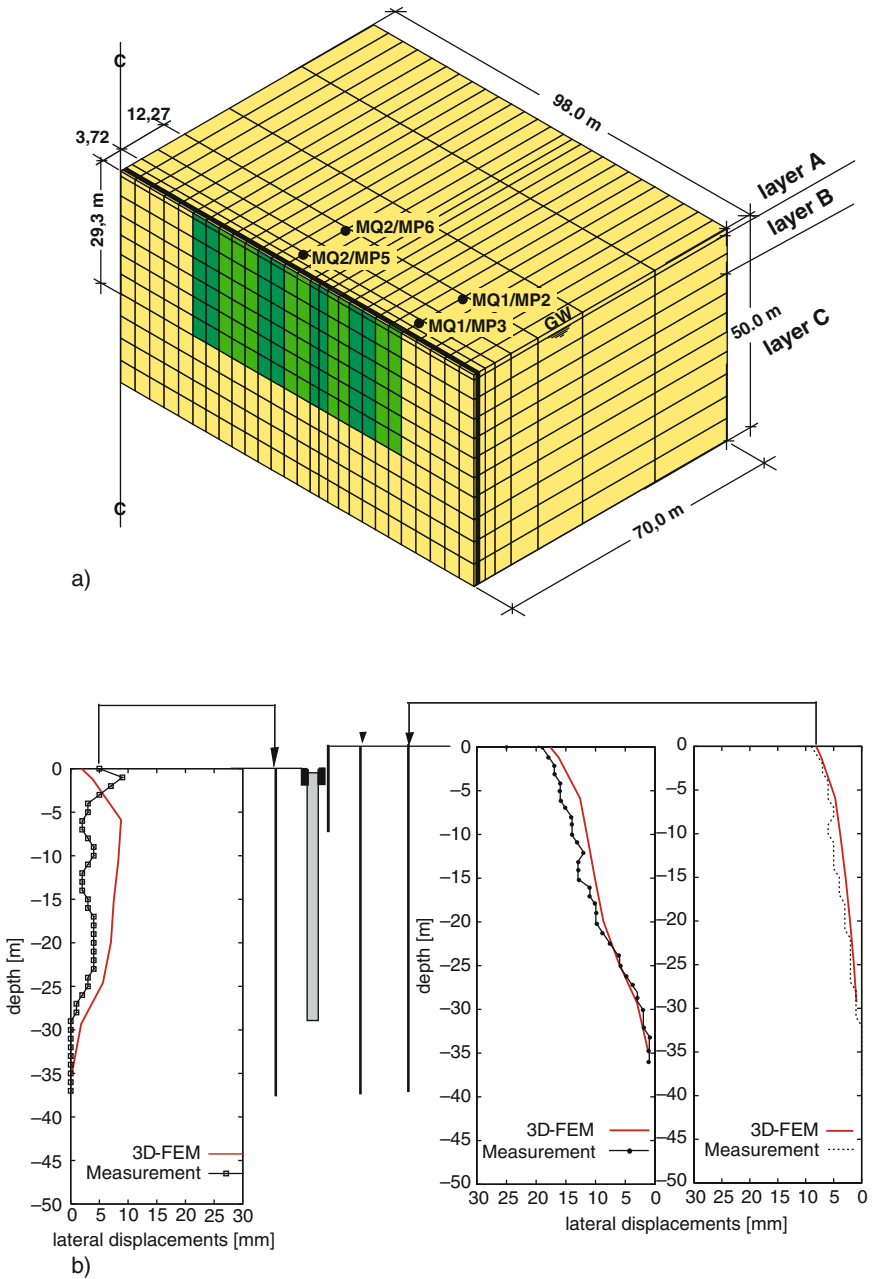


Fig. 15.3.7. Installation of a slurry trench wall in sand (Mayer and Gudehus 2001): mesh (a), calculated and observed displacements (b)

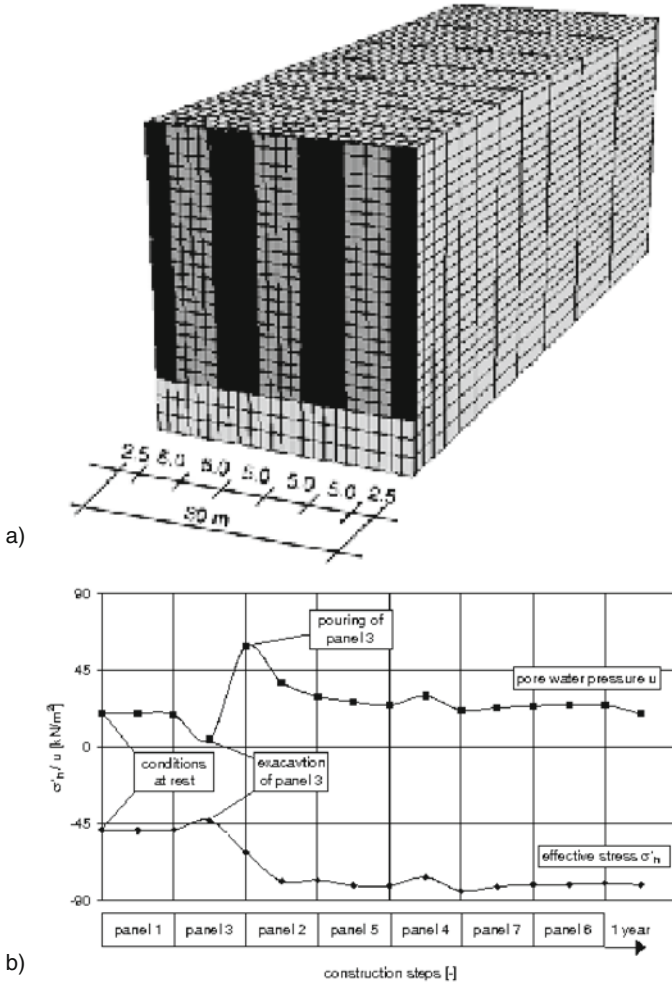


Fig. 15.3.8. Simulated progression of a slurry trench in peloid ground (Schäfer and Triantafyllidis 2004): (a) mesh with panels, (b) evolution of pore pressure (*upper curve*) and horizontal skeleton pressure (*lower curve*) with construction steps

(2004a) embraces a possible loss of ductility (Sect. 3.4), monitoring should then include pore pressures and vibrations.

Wolffersdorff (1997) investigated a *block upon sand* with a skew load, Fig. 15.3.9. The block was placed upon the same ground as for the field test with a sheet pile wall introduced by Fig. 13.6.1, and loaded via a jack and an anchored tripod (a). The mesh with a vertical symmetry plane implies sufficiently distant fictitious walls and base (b). A simulation with hyp and capillary skeleton pressure p_{cs} (Sect. 6.2) produced realistic displacements

(c). Deviations at the onset indicate rather indeterminate initial fluctuations of skeleton stress due to placement. They could principally be reduced by means of hyp- δ as far as the placement is well defined (cf. Sect. 13.3). The loading could not be continued after one anchor failed. It would be difficult to simulate up to a limit state because of shear localizations evolving from the edge (cf. Sect. 13.3). A gap arose at the block with loading both in the simulation and in situ (d).

Similar field tests with *blocks upon peloid* or composite ground have apparently not been made. They could be back-analysed as with plane-parallelity or two symmetry planes (Sects. 13.3 and 15.2). The main obstacle for validations and predictions would be partly unknown sand bands and lenses so that the time needed for pore water diffusion gets rather indeterminate. Hydraulic reversals can principally be treated as outlined in Sects. 12.4, 14.2 and 15.1,

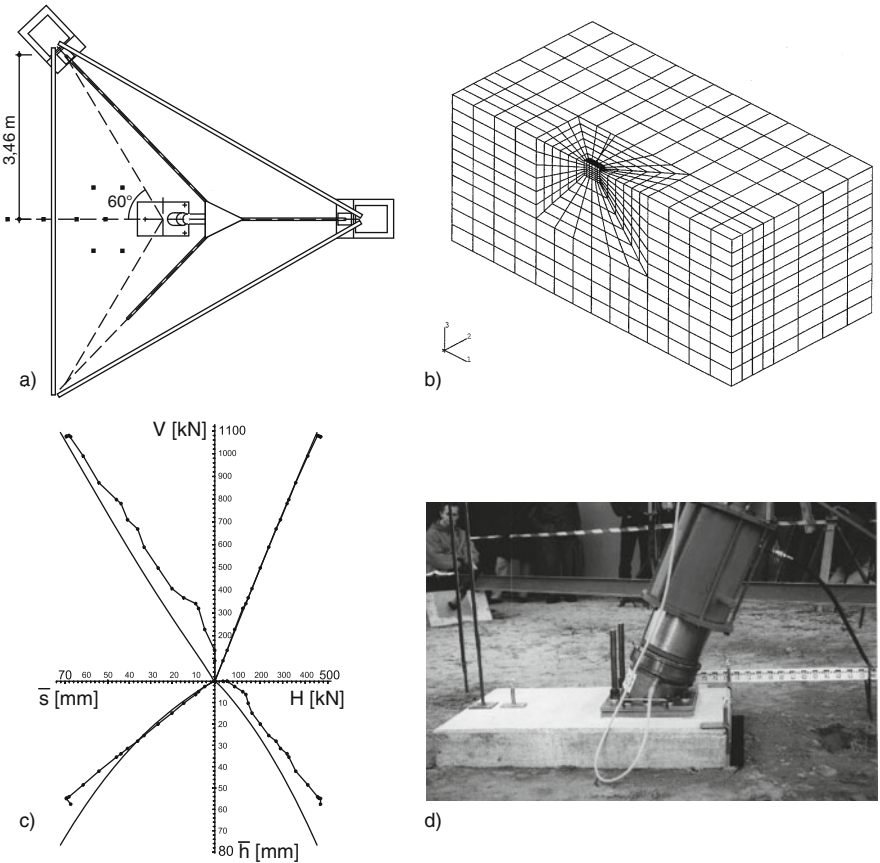


Fig. 15.3.9. Field test with a loaded block upon sand (a), mesh for simulation (b), observed and calculated horizontal and vertical displacements versus imposed forces (c), tilted block (d); von Wolfersdorff (1997)

but model tests and back-analyses should be postponed until at least axisymmetric cases are well understood.

Consider now *blocks with reversals*. To begin with, assume a rather dense psammoid ($r_e \approx 0.5$), resting pore water ($h_w = \text{const}$), a vertical dead load by weight ($W = \text{const}$) and symmetric horizontal load cycles with subcritical amplitude and low frequency ($H = H_a \cos \omega t, H_a < W \tan \varphi_c, \omega^2 b \ll g$), Fig. 15.3.10. The block may have a square base ($a = b$), a shallow bedding ($d \ll b$) and a rather low tetrapod ($h/b < W/6H_a$) for horizontal loads in one symmetry plane (a). The displacement response (b) is neither symmetric nor harmonic, but gets periodic after a transition (dashed lines). In the average the top settles so that d increases (ratcheting, cf. Sect. 13.8), and the block is slightly shifted and tilted.

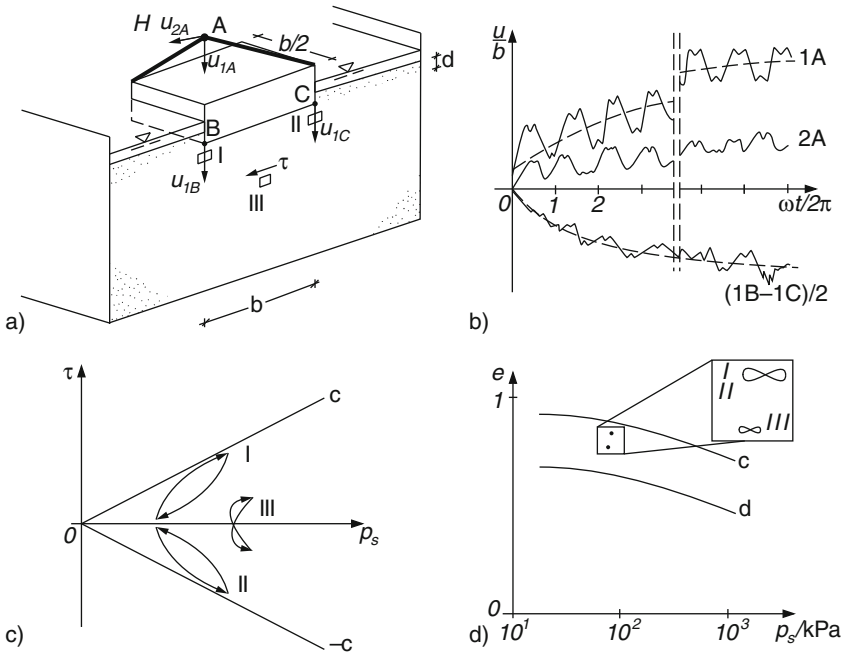


Fig. 15.3.10. Block upon psammoid ground with alternating loads (a), displacements versus time (b), asymptotic cycles of stress (c) and of void ratio versus pressure (d) for some RSEs

The skeleton state tends to state cycles which can be visualized by paths of RSEs under the left (I) and right edge (II), and somewhat deeper under the middle (III). In a plot of shear stress τ (only one component for simplicity) versus mean pressure p_s (c) the paths I and III resemble a pair of lenses, whereas I is butterfly-like. In a plot of e vs. $\log p_s$ (d) minute skew butterflies indicate repeated dilation near the edges (I \approx II with $1/2\omega$ delay)

and a lower average e under the middle. The related average growth of settlement Δu_{1A} per cycle is slightly reduced by the increase of bedding depth d . This attractor in the large can be represented by an ensemble of RSE state cycles which change slightly by the change of bedding depth and tilt. These geometrical effects may be neglected as also the bulge of the near-by free surface.

Simulations and validations should be focussed on the proposed attractor as it exhibits an objective response. Initial partly indeterminate near-field deviations by placement are swept out at the beginning. The transition needs the more H -cycles the more the initial r_e near-field differs from the average asymptotic one. Calculations with hyp- δ get more robust with a soft elastic inlay along the edge, polar effects may be neglected. Model tests with $1g$ and softer grains can more easily represent a prototype than with natural grains and a centrifuge (cf. Fig. 15.2.2). Shear localizations near the edge can be reduced by an elastic inlay as in calculations, polar effects are minor with a grain size $d_g < 100b$ (cf. Sect. 13.4).

Extensions with symmetric loading can be treated similarly if limitations are kept in mind. Blocks may have other shapes with two symmetry planes including ground and loading. Many H -cycles in packages, each one with another constant amplitude in one of the principal directions, can lead to a succession of attractors. Overcritical amplitudes H_a/W and heights h/b would lead to excessive sliding and tilt with shear localization near the edges so that the assumed symmetry gets lost. The pore water is no more hydrostatic if its diffusion time t_d exceeds one load cycle time t_l , then its coupling with the skeleton should be taken into account. In resting intervals the pore water can get hydrostatic by diffusion. The assumed symmetry can get lost by decay of loose skeletons or by cavitation in dense ones. Inertia matters with high frequencies so that repeated propagations distort asymptotic cycles (cf. Sect. 11.4).

The response of a system as in Fig. 15.3.10a to asymmetric horizontal load cycles can be represented similarly within suitable limits, Fig. 15.3.11.

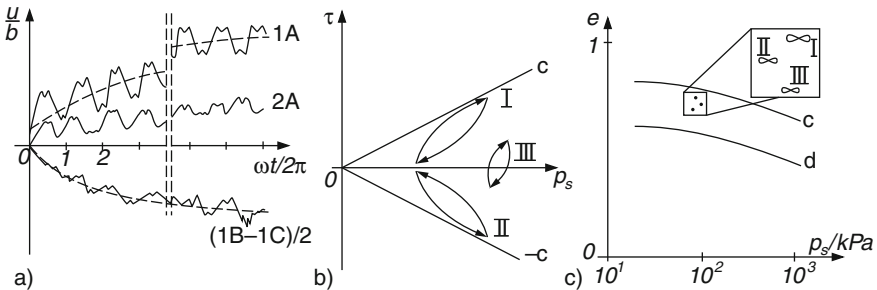


Fig. 15.3.11. Evolution with a foundation block on psammoid ground as in Fig. 15.3.10a with asymmetric alternating loads: displacements versus time (a), asymptotic cycles of stress (b) and void ratio versus pressure (c) of some RSEs

Assume again $r_e \approx 0.5$, initially $h_w = \text{const}$, $W = \text{const}$, $a = b$, $d \ll b$ and $h/b < W/6H_a$, but $H = 0.5H_g(1 + \cos \omega t)$ with $H_a < W \tan \varphi_c$ and $\omega^2 b \ll g$. Displacements (a) may indicate a slight stabilization, shift and tilt tend to nearly stationary ratcheting as long as the tilt is not too big. Asymptotic stress cycles of RSEs positioned as before (b) are no more symmetric pairs for opposite edges, and are skew in the middle. Asymptotic cycles in the e vs. $\log p_s$ plot (c) are less regular and have a higher average than for symmetric loading with the same H_a/W , h/b and initial r_e .

Simulations and model tests could be carried out similarly as with symmetric loading. Focussing again on attractors additional settlements, shift and tilt per cycle belong to the main features. These could be used to estimate cumulative displacements, and the tilt beyond which it would grow faster by the moment of W (cf. Fig. 13.4.1). Extensions for other shapes, packages of load cycles, changing h_w and inertial effects can be achieved principally as for symmetric loading. A tilted block can *turn back* with smaller and/or more symmetric load cycles (Sturm 2009), but then it settles in the middle and can only be shifted back by an opposite average H .

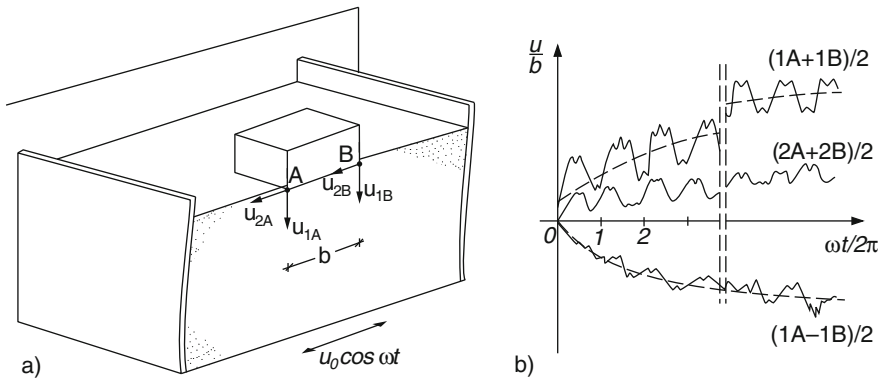


Fig. 15.3.12. Block upon shaken psammoid ground (a), displacements versus time (b)

The response of blocks upon psammoid ground to *base shaking* could also be captured by asymptotic cycles, Fig. 15.3.12. Sufficiently distant base and opposite movable walls undergo free-field shaking with one symmetry plane, whereas two fictitious in-plane walls are smooth (a, cf. Sect. 12.5). Repeated wave propagations can lead to oscillating and cumulative displacements of the block up to a periodic asymptotic response (b). With a horizontal free surface a nearly stationary vertical ratcheting is attained as long as the block is not toppled. Stress paths and e vs. $\log p_s$ paths of RSEs tend to similar state cycles as with cyclic loading (cf. Fig. 15.3.10c, d), but now far-field RSEs get more engaged.

Simulations and validation tests could be carried out similarly as with plane-parallel shaking (Sect. 12.5). They are more expensive with only one symmetry plane, and cannot be simplified by interpolations (cf. Sects. 15.1 and 15.2) as an axial symmetry gets lost by regular shaking. Other block shapes, packages of shaking and changing pore pressures could be taken into account, cumulative displacements can at best be estimated because of partly indeterminate onsets.

Responses to random shaking from below or above may be estimated by s-hyp (Sect. 4.6, cf. Sects. 12.5, 13.3 and 14.3) with the aid of model tests. Imagining the shaken ground like a temporarily heated viscous fluid may help to understand and avoid gradual sinking, sliding and tilting, whereas a substitution of earthquakes by cyclic horizontal loads and a simplified subgrade can hardly be defended. The asymptotic state cycles proposed above fail for toppling and bulging, and also by dislocations and break-outs along faults (Sect. 16.3).

Blocks upon *peloid* ground with reversals can also be judged by means of asymptotic state cycle fields. These are argotropic due to skeleton viscosity, and constrained as the time needed for the diffusion of pore water exceeds usual loading times by orders of magnitude (Sects. 11.4 and 12.5). With small amplitudes the response is more elastic than with psammoids, but big ones can lead to skeleton decay or cavitation which enhance toppling. Simulations with v-hyp- δ and model tests without seepage should be focussed on asymptotic state cycles for cyclic displacements and ratcheting.

Evolutions with blocks upon *composite ground* and reversals are more complex, but often met. Again an objective response is exhibited by state cycles in the large, but this approach is still too complex for design. Simplifications may be attained after validations with one symmetry plane, but hardly as far as widely assumed at present (more in Sect. 15.4).

To *sum up*, evolutions with a vertical symmetry plane and almost rigid or very flexible structures can be captured by means of attractors. Partly indeterminate initial spatial fluctuations can be swept out by sufficiently big monotonous deformations or by many repeated reversals. Some validations have been obtained by in situ tests where asymptotic state fields were approached, and further ones could be attained by model tests with reversals up to state cycles. Cumulative displacements can at best be estimated, particularly if the diffusion of pore water comes into play. The proposed approach for psammoid and peloid ground is limited by localizations and skeleton decay.

15.4 One symmetry plane and complex SSI

A vertical symmetry plane may often be assumed for piles and pile groups with lateral loads. It works with various superstructures and also with granular columns instead of piles. The interaction of soil and structure (SSI) is complex as the structural forces can vary for constant loads. Subgrade models may work

at best for monotonous evolutions, whereas alternating ones can be captured by asymptotic cycles. Some validations are at hand and others are attainable, limitations by critical phenomena should be kept in mind.

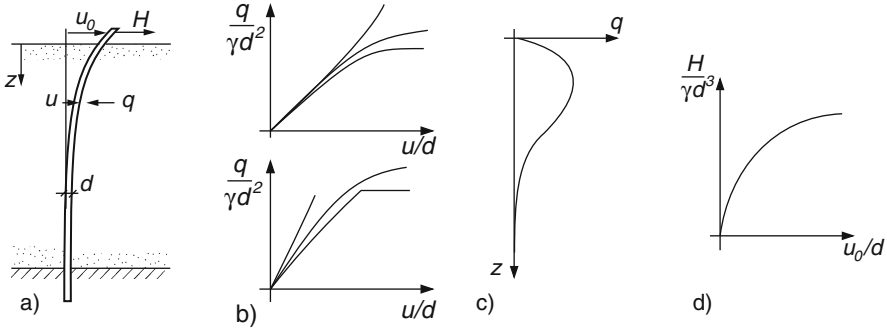


Fig. 15.4.1. Psammoid ground and single pile with horizontal load (a, bending exaggerated), lateral subgrade model (b), lateral ground resistance versus depth (c), top load versus displacement (d)

Consider first a vertical pile in psammoid ground with monotonous top loading, Fig. 15.4.1. It may be clamped in the base and free at the top (a), but it could also have a yielding base support and could be constrained by a top structure. The resulting lateral ground resistance q per unit of depth is horizontal with a smooth shaft, and may be assumed thus for simplicity if the shaft is rough. Replacing the ground by a horizontal subgrade means that q is assumed to be a unique function of the horizontal pile displacement u , viz. $q = f_q(u)$. This depends on depth z and may be linear, bi-linear or monotonous with a horizontal asymptote (b). The increase of stiffness with z may be captured by a factor for f_q which increases with the far-field pressure p_{sf} (Sect. 11.2), e.g. via

$$q = (p_{sf}/\gamma d)^m f_{qr}(u/d) \tag{15.4.1}$$

with pile diameter d , specific weight γ , an exponent m in the range $0 < m \leq 1$, and a reference subgrade function f_{qr} of u/d . γ is replaced by γ' for uplift if the ground is submerged.

The distribution of q vs. z (c) is thus a unique image of the pile bending line $u(z)$. Both get wider with an increasing horizontal top force H . With a subgrade reaction by (15.4.1) and an elastic bending stiffness the increase of top displacement u_0 with H (d) can be calculated numerically. Load test data can be used to adapt parameters in (15.4.1), other conditions at base and top can as well be captured. This works also with layered ground and parameters which can be adapted by means of borehole expansion tests (Sect. 11.7). The assumptions in (15.4.1) are often defended with the argument

that pile bending moments and transversal forces do not vary substantially with inevitable variations of parameters, but is that legitimate?

More insight could be gained by simulations with a vertical symmetry plane, Fig. 15.4.2. The opened system (a) exhibits the pile (round and smooth or rough and elastic) and a base (rigid), fictitious walls (rough or smooth and sufficiently far off), a top force H (increasing from zero, slightly above ground) and RSEs in front (I), sideways (II) and behind (III). The far-field depends only on depth x_1 (Sect. 11.2), the initial near-field after placement is axi-symmetric (Sects. 14.2 and 14.3). As with axial loading (Sect. 14.4) the relative void ratio r_{en} in the near-field is of major importance, the unknown initial stress near-field is swept out by monotonous deformations whereas the initial response is less determinate. This can be represented by paths of two principal stress components (b, with assumed principal directions for simplicity) and by plots of e vs. $\log p_s$ (c) for RSEs. With low r_{en} the RSE I is more stressed and less dilated than II, whereas III is unstressed and more dilated than II.

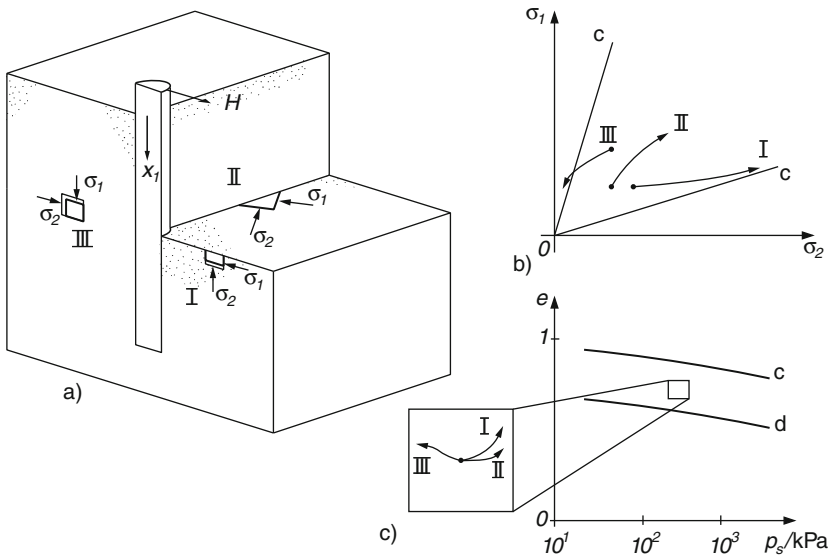


Fig. 15.4.2. Model instead of Fig. 15.4.1 (a), paths of stress (b) and void ratio versus pressure (c) for RSEs near the pile

Simulations with hyp (or with elp if it reproduces dilation, contraction, stressing and unstressing for cuboidal deformations and shearing, Sects. 2.7, 2.8, 2.9 and 2.10) could yield ensembles of state paths for finite elements. They would tend to SOM-state and state limit near fields which are attained by sufficient monotonous deformations. Validations could be obtained by 1g

model tests with reduced granulate hardness and the same dimensionless loads so that realistic in situ deformations are obtained (cf. Sects. 14.4 and 15.2). Comparative calculations could reveal the main factors of influence and the inevitable inaccuracy, and would delimit simplified assumptions as (15.4.1). Extensions for pore water could be achieved as outlined in Sects. 15.1 and 15.2, cavitation behind the pile could be taken into account as shown with Fig. 15.3.9, skeleton decay and spontaneous localization delimit the range of validity.

Vertical piles with *horizontal reversals* in psammoid ground can no more be captured by subgrade models. Consider a pile as in Fig. 15.4.1a, but now with slow cyclic head displacements in the symmetry plane, Fig. 15.4.3. After a sufficient number of reversals the H vs. u_o relation for the top gets periodic with more hysteresis for bigger amplitudes (a). The pile is bent with lateral ground reactions q , these have signs which do not always agree with the ones of lateral displacement u (b). The sections of deviating signs are not the same for other amplitudes, nor for transitions to a periodic H vs. u_o response. The relation of H with u_o is path-dependent, and the one of q with u is no more unique so that subgrade models get invalid.

The path-dependence of the top response arises due to the changing state of pile and neighboured skeleton, which may be considered as hidden (cf. Sect. 4.2) when focussing on the pile head. This indeterminacy can be overcome by means of periodic state fields associated with a periodic relation of H with u_o . They can be represented by an ensemble of RSE state cycles which can be obtained by finite element simulations with hyp- δ (or elp- α with validated state cycles, Sect. 4.4). Some cycles are indicated for RSEs by plots of principal stress components (c, with assumed principal directions) and of e vs. $\log p_s$ (d).

With a moderate amplitude, so that state limits are never reached in the RSEs of Fig. 15.4.2a, the skeleton in front (I) tends to the same stress cycles as the opposite one (III) except for a phase shift. Average pressures and void ratios are lower than for monotonous bending with a low initial r_{en} , whereas the sideways RSE (II) is more relaxed and less dilated. The average asymptotic near-field void ratios and pressures are determined by the top amplitude (and of course by skeleton and pile properties), and do not depend on the initial near-field or on the far-field.

Ratcheting of the pile head can lead close to asymptotic state cycles in the ground. Apart from the bending resistance without ground the plot of H vs. u_o gets periodic (e) as long as strong bending and surface bulging do not matter. Stress paths of RSEs as in Fig. 15.4.2a tend to cycles (f). The skeleton in front (I) tends to a higher average pressure and void ratio than the opposite one (III), but not as high and low, respectively, as for monotonous bending with low initial r_e . A lateral RSE (II) tends to asymmetric stress cycles with intermediate average pressure and void ratio. The asymptotic near-field void ratios are lower for lower forward and backward amplitudes $\Delta u_f/b$ and $\Delta u_b/b$, and are also independent of the onset.

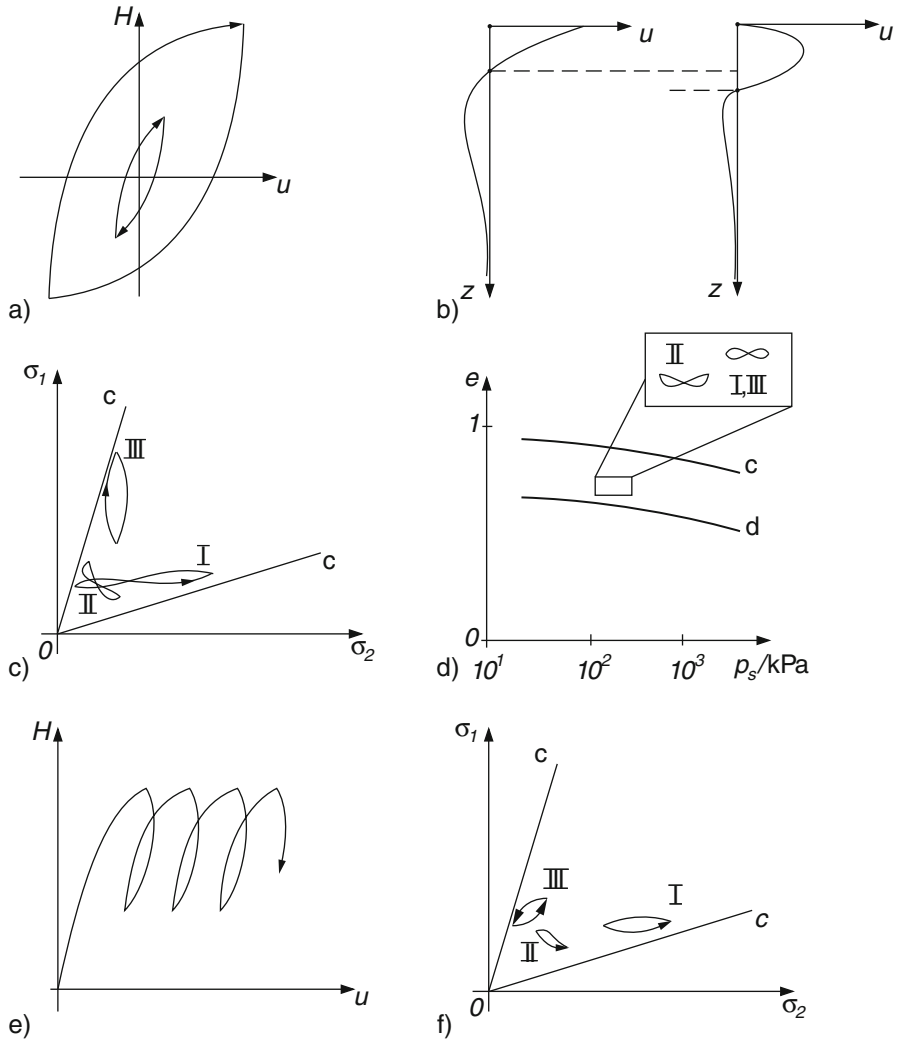


Fig. 15.4.3. Response of a single pile to horizontal head displacements with reversals: head force versus cyclic displacement (a), lateral pile displacement and ground resistance versus depth (b), asymptotic RSE-paths of stress (c) and void ratio versus pressure (d); head force versus displacement for ratcheting (e), related asymptotic stress cycles of some RSEs (f)

Simulations with hyp- δ (or elp- α with realistic attractors, Sect. 4.4) could produce such attractors and transitions to them. $1g$ model tests with soft grains can serve for validation and help to quantify cumulative effects. Transitions could be further quantified by successions of cyclic displacements and ratcheting with different amplitudes. One could change the loading direc-

tion in the ground plan, then a new vertical symmetry plane is attained after a transition. Piles with other cross sections and end conditions could be treated likewise. Pore water could be taken into account, limitations by critical phenomena should be kept in mind.

Inertial effects could also be captured by attractors and transitions to them, but one should begin with simple cases in order to master the increasing complexity. The psammoid should be dry, or saturated with so fine grains that the diffusion of pore water is negligible. If the pile head with an attached mass is shaken with big amplitudes the neighboured ground responds almost quasi-statically, whereas with small amplitudes a bigger part of the kinetic energy is radiated off. Asymptotic cycles deviate more from quasi-static ones in the latter case. If the base and opposite walls are shaken state cycles of RSEs are distorted by inertia. The response depends on the mass attached to the pile head, as with shallow foundations (Fig. 15.3.12) it cannot be captured by means of substitute top loads.

Model tests may also be used to quantify seismo-hypoplastic estimates (cf. Sects. 4.6 and 15.2). The pile and the neighboured ground return to a relaxed state with low r_e by erratic shaking of the head or the base in case of low amplitudes. This seismo-viscous state limit field can be calculated with v-hyp by means of viscosity parameters depending on the granular temperature T_g . Crude estimates of T_g suffice if relaxation and densification are safely attained, but T_g -differences for head and base shaking should not be ignored. The response with bigger amplitudes could principally be captured with a T_g -dependent entropic pressure.

A *peloid* ground with a single pile could be treated similarly as with psammoids. The response is argotropic due to skeleton viscosity, this could be captured by v-hyp or v-el ρ without and by v-hyp- δ or v-el ρ - α with reversals. As pore water diffusion times t_d are typically far longer than loading times seepage may often be neglected. This does not exclude density changes due to a small volume fraction of minute gas bubbles. The initial void ratio field, which can be substituted by equivalent pressures p_e or consolidation ratios p_e/p_s , is of major importance as it is not swept out by nearly isochoric transitions. In waiting intervals without horizontal head loads ground and pile are relaxed (faster with lower p_e/p_s), and both p_s and p_e tend to far-field values by pore water diffusion. Permanent head loads lead to creep, for times $t \ll t_d$ this occurs without seepage and is later reduced by densification in case of subcritical loads (cf. Sect. 13.2). Asymmetric oscillating loads lead to creep and ratcheting, an erratic shaking enhances relaxation and diffusion with density changes.

Model tests for validation can be carried out with constant e and almost full saturation without a centrifuge if the material can be captured by the chosen constitutive relation in the given range. For instance, Bühler (2003) investigated a pile in clay with a constant load in one horizontal direction and an oscillating transversal load, Fig. 15.4.4. The elastic pile was fixed at the base, the clay was homogeneous and could not swell or shrink in the load-

ing time. The loading device and its vicinity (a) were represented by finite elements (b), farther off the mesh was coarser. The observed head displacements (d) are reproduced (c) in all essentials. An almost stationary ratcheting was attained already after the first cycle because of the rather big amplitude, and maintained for the following cycles due to the low pile bending stiffness. This is a validation as no parameters were adapted to fit the model test results.

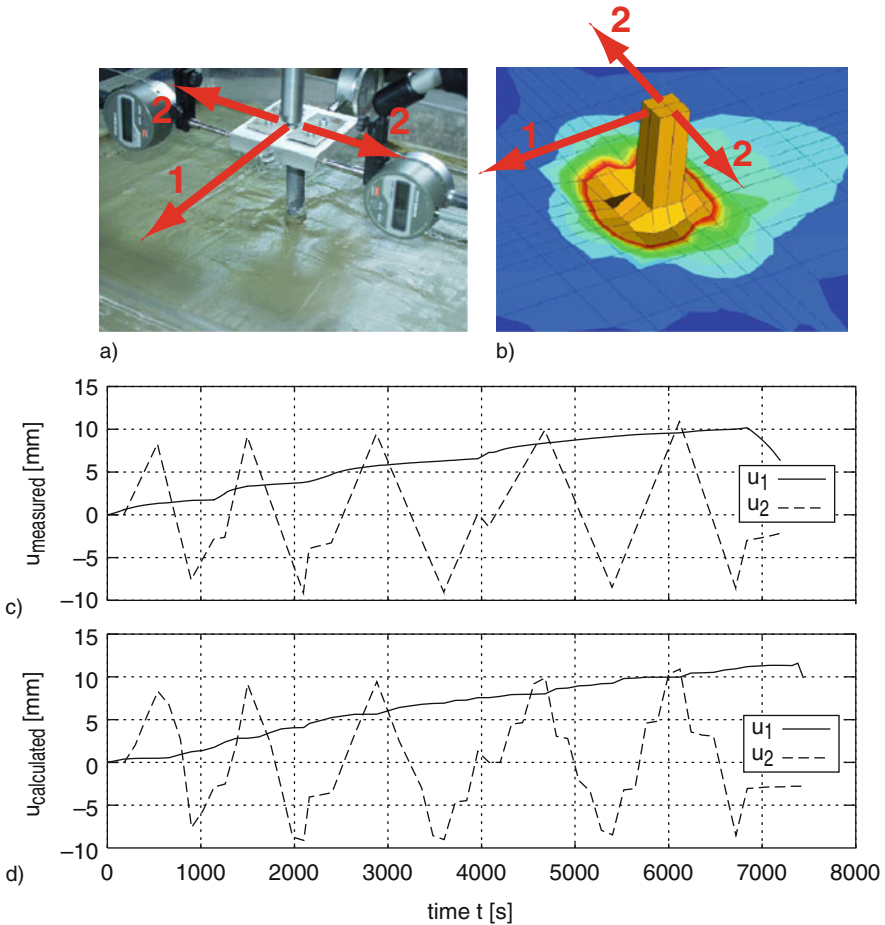


Fig. 15.4.4. Model test with ratcheting of a pile head in clay (Bühler 2003): pile head with vicinity (a) and substitute mesh (b), calculated (c) and observed head displacements (d) versus time

Similar validations could be attained with other kinds of clays, piles and loading. Argotropic and endogeneous attractors and transitions to them could

be investigated with different initial states and waiting intervals. Thermally and seismically activated creep and relaxation could be studied, also with pore water diffusion via changes of density. Limitations by localizations and liquefaction should be quantified. Such studies could help to establish simplified design models which are more justified than those with a lateral subgrade.

Evolutions with bending of a vertical pile in *composite ground* are more complex, but often composition and loading may be simplified and a vertical symmetry plane may be assumed. If a single pile carries also a permanent axial load, e.g. from a mast or a windmill, it should stand in a competent layer so that it does not sink too much. The soil near the surface should not be nor get too soft so that it can take over temporary horizontal loads. This can be achieved by a dense enough psammoid or peloid top layer if this is not too much dilated or cracked and not liquefied. The pile should not break or lose its foothold by strong actions (survival), and the near-field should return to the previous state (healing). Survival can be assessed by means of state cycles with not too big amplitudes, healing by thermal and seismic activation should occur prior to the next strong impacts.

Bühler (2006) investigated single piles in *model tests* with the shake box of Fig. 12.5.2c, Fig. 15.4.5. A pile with transducers stood in saturated sand and/or clay (a) and was shaken from below (cf. Sect. 12.5). The system was modelled with finite elements (b), an interface between pile and soil as by Fig. 15.4.6b, a symmetry plane and hyp- δ or v-hyp- δ for sand and clay, respectively. Displacements and internal forces were reproduced almost up to liquefaction, i.e. near ground surface and pile the soil was gradually transformed into a suspension. This occurred with a clay and shaking as the Loma Prieta earthquake (c). After consolidation with wick drains liquefaction and partial uncoupling of pile and ground was more delayed with the same base shaking (d). The uncoupling occurred earlier with loose than with dense sand, and earlier than with consolidated clay. This validation of hypoplastic models with reversals and pore water coupling is limited by liquefaction.

For further validation Bühler (2006) back-analyzed an *offshore pile test* by Cheang and Matlock (1981). Two piles were pushed and pulled past each other via jacks in traverses. The horizontally layered ground with fine sand and clay was identified as a composite of psammoid and peloid layers. The material constants for hyp- δ and v-hyp- δ were determined from reported triaxial test results. Initial skeleton stresses were estimated as outlined in Sect. 11.3, initial void ratios were determined from penetration resistances (Sect. 14.3), the influence of pile driving on the near-field was neglected. Permeabilities k_f were estimated by means of particle size distributions (cf. Sect. 6.2). The finite element mesh (Fig. 15.4.6) enclosed one pile and a smooth symmetry plane (a). Fictitious confining walls were chosen so far off by means of comparative calculations that they did not influence the ground response of the piles. Opening and closing gaps at a pile were captured with a contact model (b). The diffusion of pore water was neglected for the peloid layers as it could

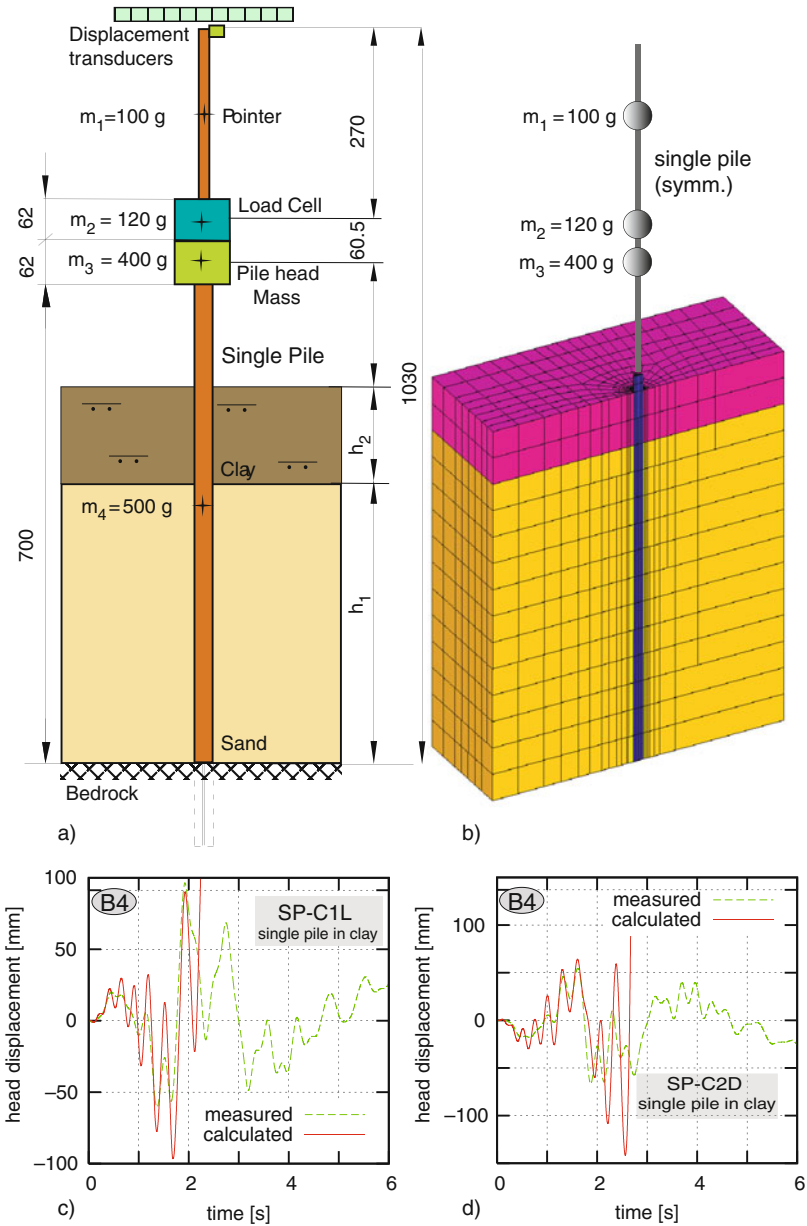


Fig. 15.4.5. Model test with a pile in saturated soil and a shake box (Bühler 2006): (a) setup, (b) mesh and substitute pile, (c) head displacements versus time by harmonic base shaking with clay, (d) same after consolidation

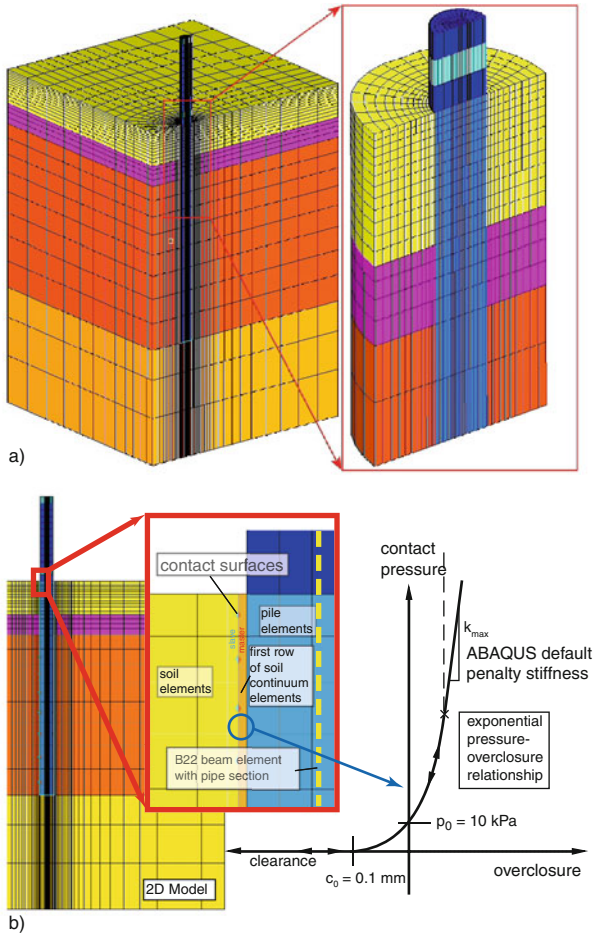


Fig. 15.4.6. Finite element mesh (a) for simulation of offshore pile tests (Bühler 2006), contact model (b)

scarcely occur in the loading time, which had to be estimated for the viscous response.

In one test the pile head was clamped so that it moved horizontally without rotation. Without further adaption of parameters the observed relation of horizontal head force and displacement with some reversals was reproduced in detail (Fig. 15.4.7a). Calculated bending moments for the load steps 1–7 (b) were rather close to observed ones (c). A fair agreement was also obtained with free head rotations of the loaded piles. This is a validation for evolutions without seepage, i.e. when the pore water diffusion time exceeds by far the loading time. The latter is typical for offshore structures during strong actions, so this validation strengthens the assessment of their survival.

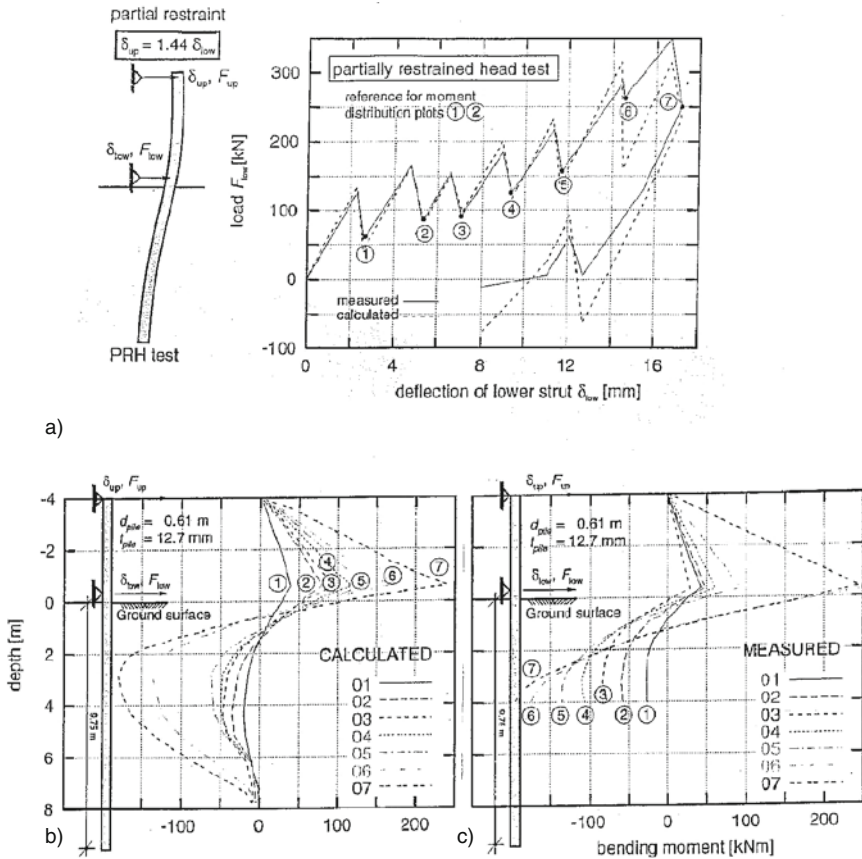


Fig. 15.4.7. Simulation results by Bühler (2006) of an offshore pile test by Cheang and Matlock (1981): (a) head forces versus displacement, calculated (b) and observed (c) bending moments versus depth

Various kinds of *horizontally loaded pile groups* in layered ground can be captured with a vertical symmetry plane, Fig. 15.4.8. This can be identified in a rectangular array (a), but an anti-plane symmetry as in an elastic system cannot arise with the anelastic ground response. (A polygonal array is better apt if horizontal loading or shaking can occur in arbitrary directions.) Infinite rows of piles are often assumed for retaining structures (b), such systems are composed of equal slices and can get in-plane or anti-plane loading or shaking (cf. Sect. 12.5). This can be legitimate with a slope or a cut which is uniform over a sufficient length. Opposite points of fictitious walls separating the slices experience the same displacements. An infinite array of piles with equal ground and loads may be assumed for the interior of pile groups. Rims and corners of such arrays are no more symmetric as piles are more or less deformed than interior ones under a flexible or stiff superstructure, respectively.

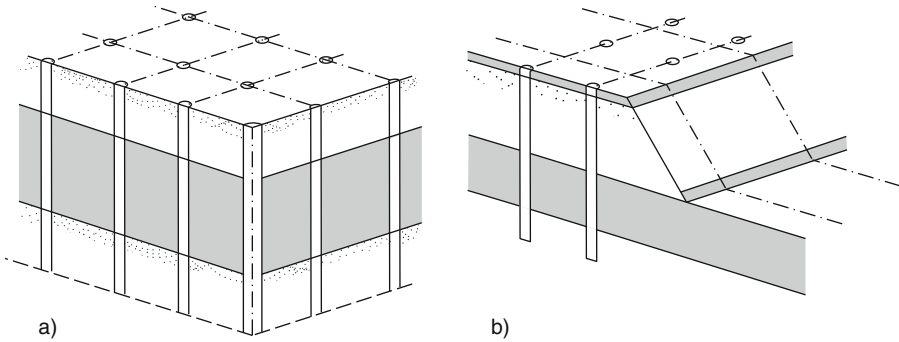


Fig. 15.4.8. Groups of vertical piles with horizontal ground surface (a) and near a slope (b)

A symmetry as in Fig. 15.4.8 may also be assumed with *granular columns* instead of piles. Their near-fields due to installation are nearly axi-symmetric (Sect. 14.2). What counts for the overall behaviour is the average diameters and spacing of the columns, and the average void ratios of columns and ground between them. Cemented columns can be treated as soft piles. A ground with many equal piles or columns can be modelled as a composite, this requires calculations with suitable unit cells and deformations in the expected range (Sect. 9.2).

Tetrapods of piles have often been investigated in model tests with sand, but only few of them are apt for validation. Usually the grains were too hard and big, initial states and boundary conditions were not well-defined and/or the evolutions were not sufficiently monitored and documented. Bühler (2006) worked with saturated clay which was shaken by a laminate box (cf. Fig. 12.5.2c), Fig. 15.4.9. One of the four piles was equipped with strain gauges, otherwise the setup (a) was the same as with one pile. The finite element models had again a vertical symmetry plane (b). With loose sand observed and calculated head displacements agree fairly well up to the second base cycle (c). Clearer than with one pile a response fraction with twice the excitation frequency indicates a double cycle in the ground as in RSEs (cf. Fig. 15.4.3c). An even better agreement was obtained with consolidated clay (d). As with one pile (cf. Fig. 15.4.5) the calculations end by liquefaction.

Pile dowels in creeping slopes may be considered as endless rows. A simplified model (Gudehus 1984) serves for the design, Fig. 15.4.10. The velocity profile of the creeping layer (cf. Sect. 11.6) is substituted by a step function, i.e. shearing is assumed to be localized at the base (a). The lateral thrust H at each pile (b) is taken as a bi-linear function of the displacement of the soil relative to the pile, with different amounts above and below the shear zone (c). With the pile bending stiffness and the creep velocity before installation of piles this subgrade model can be transferred to a creeping ground with pile dowels (d). After their installation the creep velocity is reduced by the

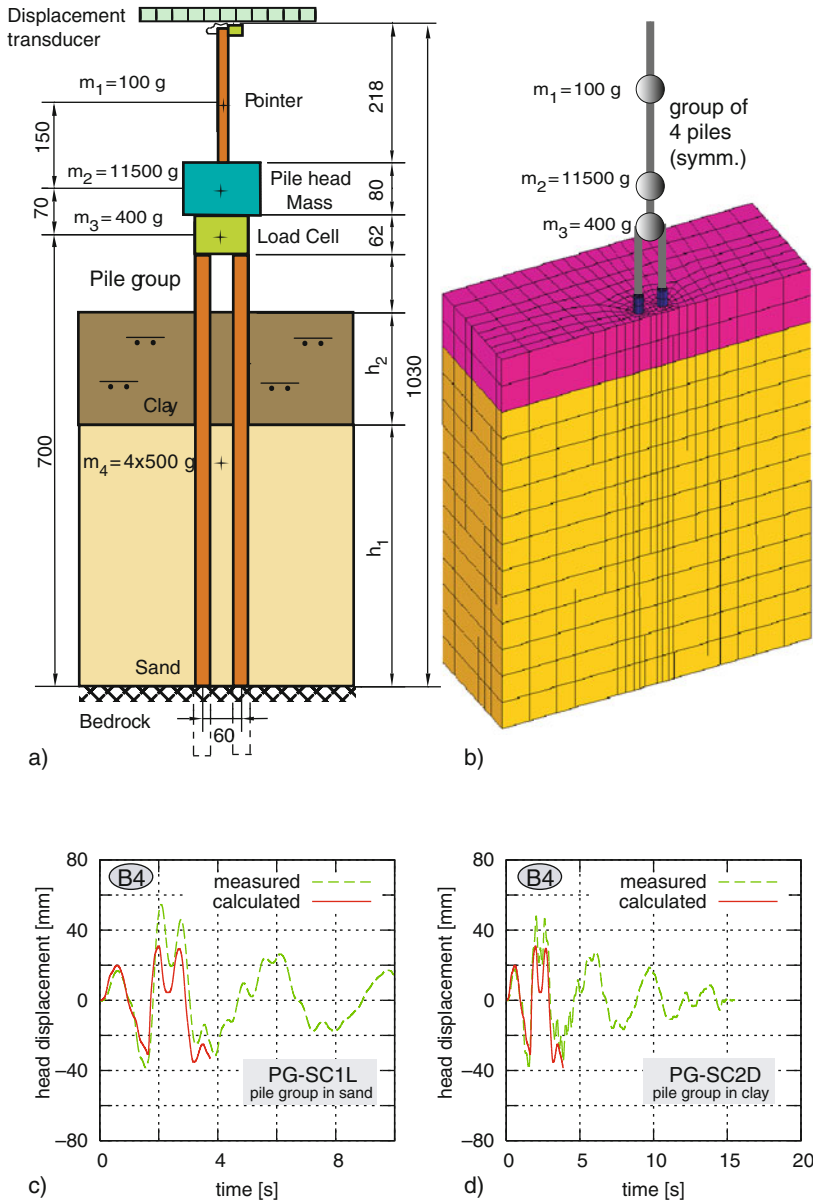


Fig. 15.4.9. Model test with four piles and a shake box (Bühler 2006): (a) setup, (b) mesh with structure (one half), head displacement versus time with dense sand (c) and consolidated clay (d)

increasing transversal pile resistance (e). Deformation tolerances of piles can be kept by predictions for the lifetime.

This concept was technically improved and applied, Fig. 15.4.11. In one case (Schwarz 1987) sliding bodies could be identified in a middle cross section (a). After installing two concrete pile rows the creep was slowed down as shown in Fig. 15.4.10e. In another case (Lippomann 1988) a creeping slope

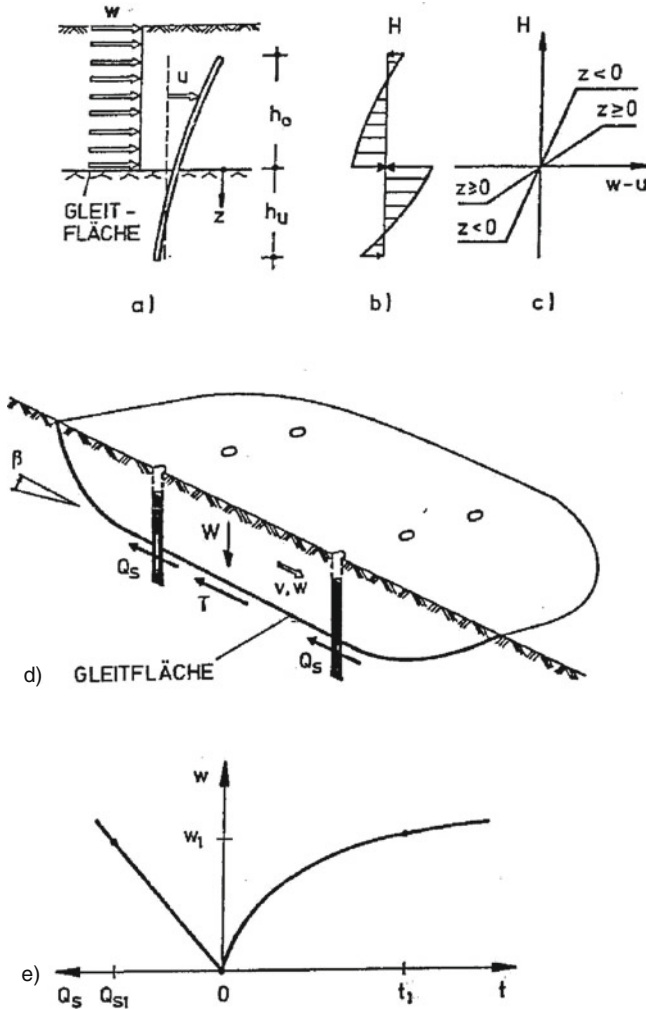


Fig. 15.4.10. Pile dowels in a creeping slope (Gudehus 1984): simplified velocity profile (a), lateral force per unit of depth between pile and soil versus displacement past the ground (b), lateral force versus displacement (c), sliding soil with pile dowels, displacement (d) versus time after installation of piles (right) and versus transversal pile forces (left)

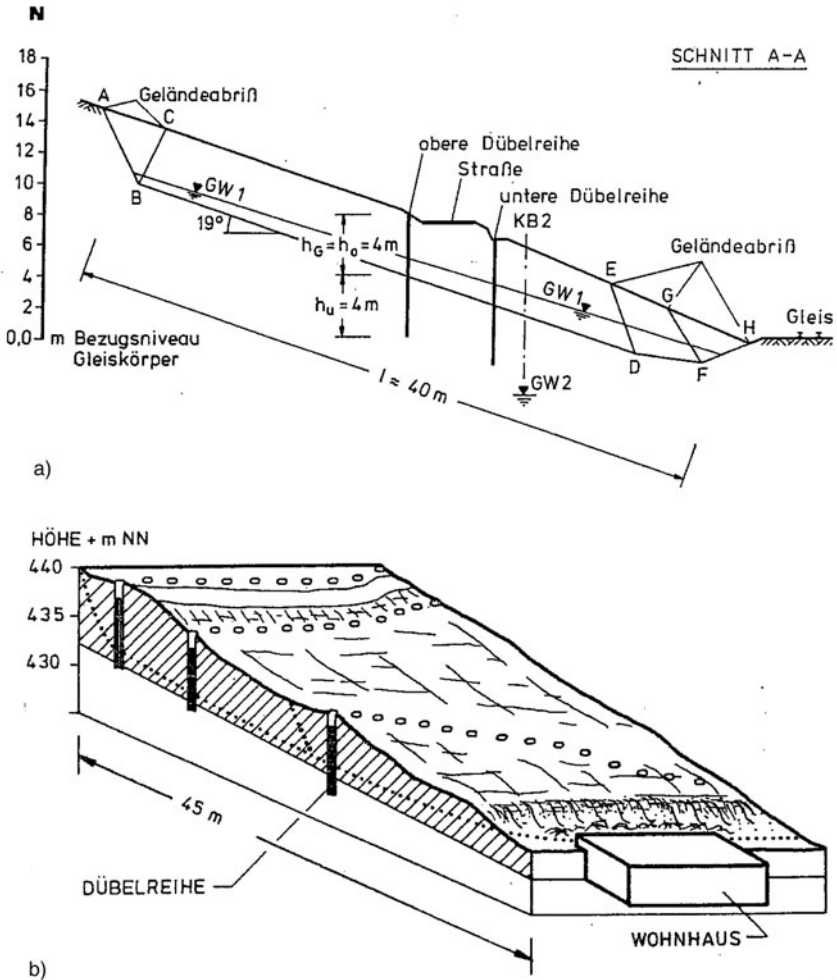


Fig. 15.4.11. Applications of model by Fig. 15.4.10: (a) sliding bodies above a railway (Schwarz 1987), (b) pile dowels behind a house (Lippomann 1988)

had damaged part of a dwelling house (b). After placing three rows of piles the creep was slowed down slightly more than predicted so that the house could be used again.

Inclined piles occur in groups with a vertical symmetry plane, Fig. 15.4.12. A foundation block for a rope can be anchored by a symmetric group of tension piles with different inclinations (a, ground partly removed for visibility). The total pull-out resistance can be estimated by assuming a sliding block with earth pressures, but displacements and distributions of forces could as yet only be captured with hyp (cf. Fig. 15.2.5) or with hyp- δ in case of alternating

loads. A pile group for a mast or a bridge implies battered piles (b) if the upper soil cannot take over horizontal loads, one symmetry plane may be assumed. The piles have bending stiffness, therefore they get bending moments by displacements relative to the ground. Subgrade reaction models may at best serve for a pre-design, whereas the response to extreme and repeated actions could be captured with hypoplastic relations.

Rows of tension piles or anchors behind retaining walls may be replaced by plates (Sect. 13.6), but more details are revealed with a vertical symmetry plane (Fig. 15.4.12c). As with rows of vertical piles (Fig. 15.4.8b) opposite walls of fictitious slices experience the same in-plane and no out-of-plane displacements. The state field after installation of tendons may be generated by taking production-dependent near-field void ratios as with axial symmetry (Sect. 14.3) plus unchanged far-field values, and to impose gravity (cf. Sect. 13.6) plus expansion for grouting. Deviations from this serial symmetry could hardly be detected and are swept out in the further evolution. This can thus be simulated in order to improve installations and to justify substitute

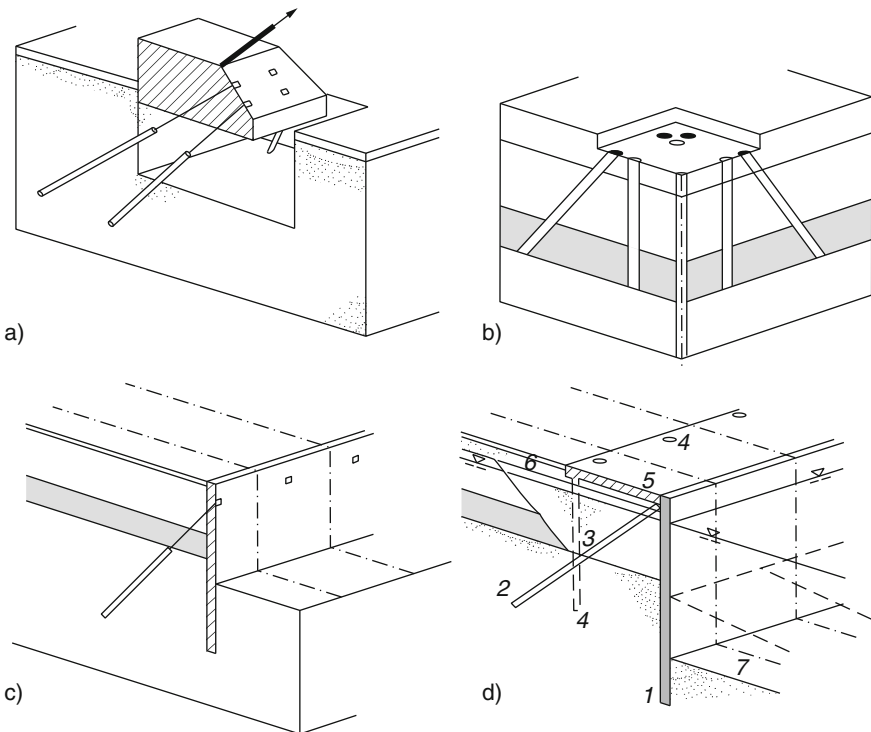


Fig. 15.4.12. Anchor block with battered piles (a), foundation block with differently inclined piles (b), back-tied retaining wall (c), quay wall structure (d). Numbers for sequence

anchor plates. A similar approach can be applied for embedded flexible strips (cf. Fig. 13.5.10).

Quay wall structures can have the same symmetry, e.g. Fig. 15.4.12d. After driving a sheet pile wall (1) and inclined piles (2) to fix the head part of the soft ground is replaced by sand (3) which is densified by deep vibration. Then a second row of piles (4) is driven vertically, plates are placed on top (5), the ground behind is filled up (6) and a part of the ground in front is excavated (7). This evolution can be captured with plane-parallelity by means of plates instead of piles (Sect. 13.5), but simulations with a row of symmetric slices provide more insight. The interaction of piles with the ground and substitute plates can thus be quantified, details of installation can be simplified as indicated further above. This approach works also with further pile rows and composite or wavy walls.

Mardtfield (2005) achieved a validation, Fig. 15.4.13. The complete system consisted of natural and filled sand (modelled by hyp), a soft clay layer (elp), steel wall and piles (elp) and concrete plate and piles (elp). The mesh for a slice was refined for the structure and the neighboured ground. An initial state was generated by imposing gravity with given void ratios and water level. Simulations of further earth movements led to deformations of the structure (a, exaggerated) and to changed earth pressures. Observed displacements agreed with calculated ones, even defaults of earth pressure measurements were revealed. Axial forces of the inclined anchor piles were reproduced realistically (b). It could be shown that the composite system was ductile with the attained deformations, which could not be judged with conventional models.

Raju's et al. (2002) report on *earthquake* damages of a quay wall structure may be used to show what could and should be done. A platform had been placed on vertical piles bored through a marine clayey silt into rather dense gravel, Fig. 15.4.14. Sand was filled up landwards, warehouses in a row were founded on vertical and inclined piles. The slope under the plate got steeper by sedimentation of further silt. During the Bhuj earthquake 2001 anti-plane shaking produced up to ca. 2 m/s^2 platform accelerations over 90 s (Rao 2001). The warehouses crumbled and several pile heads were damaged. Within the next 3 months the ground settled up to ca. 0.4 m behind the platform, and this was partly damaged.

This evolution could be simulated with hyp- δ and v-hyp- δ for the ground and elp plus fracture bounds for the structure by means of a row of slices. The fresh sediment after installation creeps past piles, and is thus retained so that bending moments arise (cf. Fig. 15.4.10). Anti-plane shaking could be imposed to the base and the fictitious walls of a slice (cf. Sect. 12.5) so that opposite points have equal displacements. If forces at the pile heads attain fracture bounds the warehouse can still be destroyed by inertial forces transmitted by inclined piles. The pore pressure in the silt is increased by shaking (cf. Sect. 12.5), this leads to creep and further structural deformations, and to densification with dwindling excess pore pressures by diffusion in the long

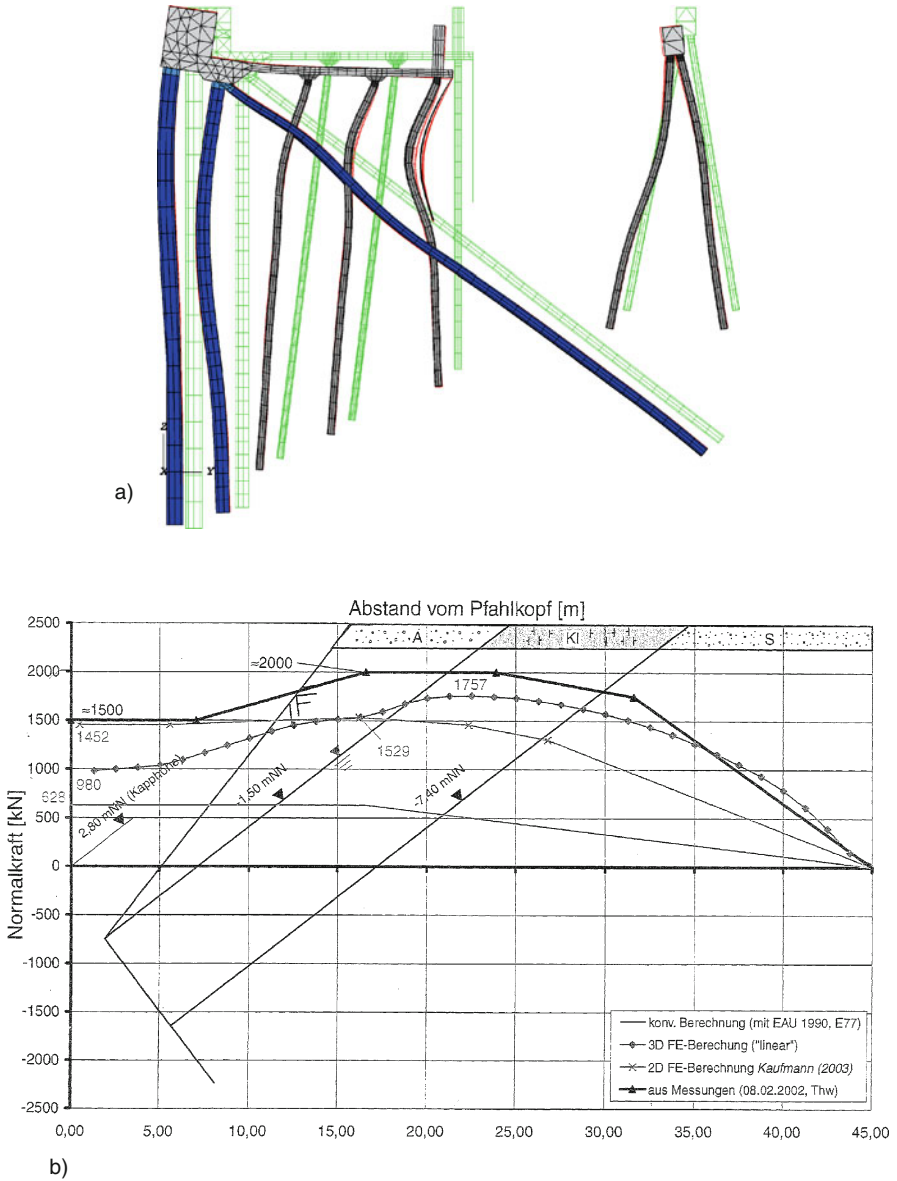


Fig. 15.4.13. Back-analysis of a quay wall structure (Mardtfeld 2005): (a) deformed structure (exaggerated) after back-filling and excavation, (b) observed (*upper curve*) and calculated (*dotted line*) axial force of anchor pile

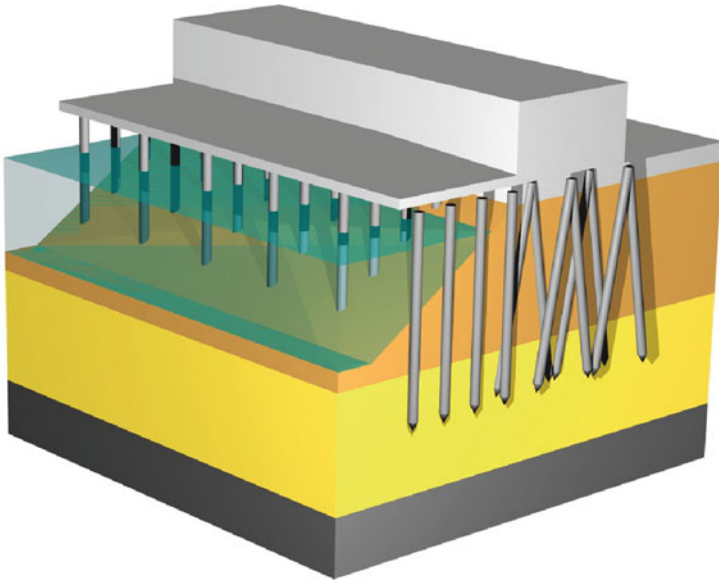


Fig. 15.4.14. M. Bühler's representation of a quay wall structure which was damaged by an earthquake (Raju et al. 2002)

run. Such a simulation could lead to a validation although the data are not as comprehensive as in the case of Fig. 15.4.13.

Such damages could be avoided with only vertical piles, a more ductile structure and a hidden dam of improved ground, this could be assessed by simulations with slices. Houses upon vertical piles or granular columns can survive earthquakes (cf. Fig. 15.4.7). Sideways creep and settlement can be sufficiently reduced by granular columns, after their installation the neighboured ground is also denser. A hidden dam of densified sand and stone columns would prevent damages as in Kobe 1995 (cf. Sect. 12.5), and could be simulated by means of slices. The reduction of excess pore pressures by the columns and the desired rise in partly loose sand could thus be captured, simplified design models could also be established.

To sum up, complex interactions of structures with the ground can sometimes be captured with a vertical symmetry plane, this can be justified by means of attractors. SOM-state, state limit and state cycle fields could be generated for monotonous and alternating actions, respectively, and deformations can be fairly well predicted. The partial indeterminacy of initial states can thus be mastered, validations by model tests and field observations get feasible, and simpler design models can be delimited and improved. Limitations due to shear localization or cracking and liquefaction with erosion should be regarded by means of deformation bounds.

15.5 Tumbling and driving

Tumbling and driving in uniform ground can exhibit spatial and temporal symmetry and can principally be captured by asymptotic state cycle fields. It is briefly outlined how such evolutions could be simulated and how validations could be achieved by model and field tests. Limitations due to critical phenomena are indicated, these can lead to a loss of control.

Wichtmann (2005) reports on experiments with dry sand in a *tumbling cylinder*, Fig. 15.5.1a. The fixed base was rough, a confining membrane was

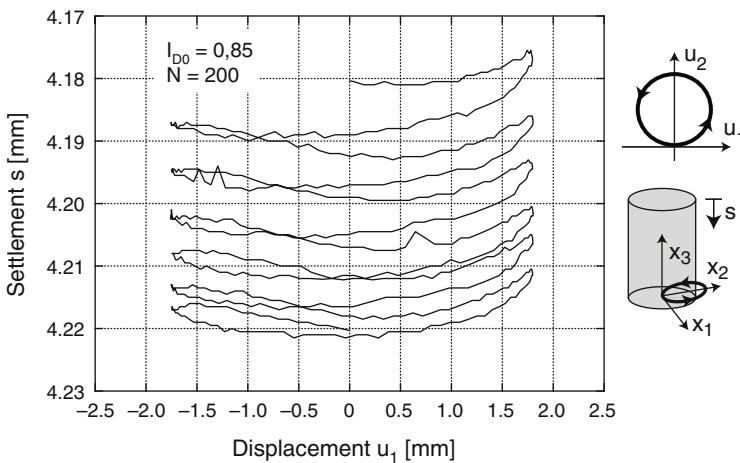
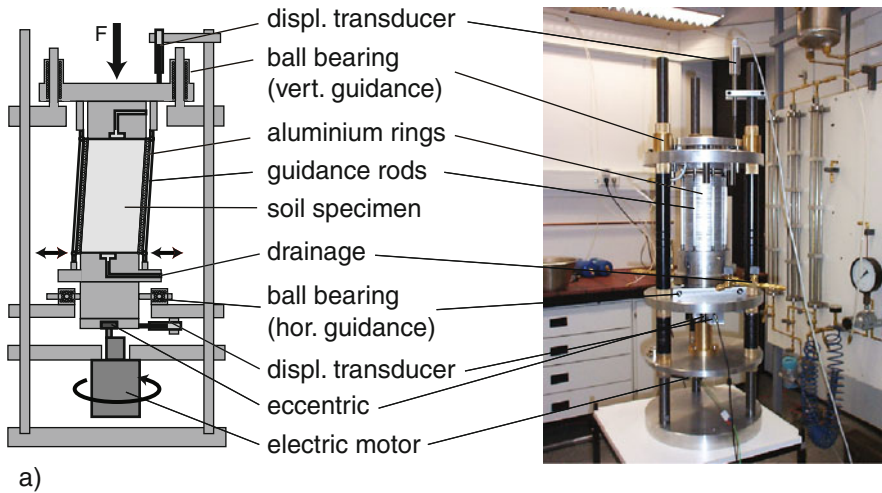


Fig. 15.5.1. (a) Tumbling device by Wichtmann (2005), (b) observed evolution of sample height with torsion for initially dense sand

reinforced by parallel rods, these tumbled together with the rough top plate which could not tilt and had a constant vertical force. The evolution of the height with the torsion angle indicates a transition to a periodic response after some revolutions (b). The number of revolutions needed to attain such state cycles is bigger for smaller deviations from the cylindrical shape and for higher initial relative void ratios r_{eo} .

Revushenko (2006) reports on similar tumbling experiments with sand and a free surface, Fig. 15.5.2. A confining group of rods was kept above by a fixed ring and twisted by a ring below (a). After one test the distortion was visualized by means of a dyed zone and fixing glue (b). Revushenko does not report more results of these promising experiments. Presumably patterns of shear bands appear at the surface of a distorted dense sample, and disappear after cyclic torsion with small amplitude. Changing sample heights indicate again changing average void ratios.

Such evolutions could be simulated with $\text{elp-}\alpha$ or $\text{hyp-}\delta$, other than outlined for torsion (Sect. 14.6) without axial symmetry, Fig. 15.5.3. The initial skeleton state may be uniform, gravity may be neglected. The skeleton boundaries move together with the rough plate (with fixed eccentricity α and increasing rotation angle β) and the distorted wall. The latter is deformed in the ground plan and by penetrating grains, but confined by the rods. As in experiments a constant height is less difficult than a constant axial force for which an adaption of the upper rim is needed. Shear localizations can be avoided by not too big amplitudes. Calculations should be focussed on asymp-

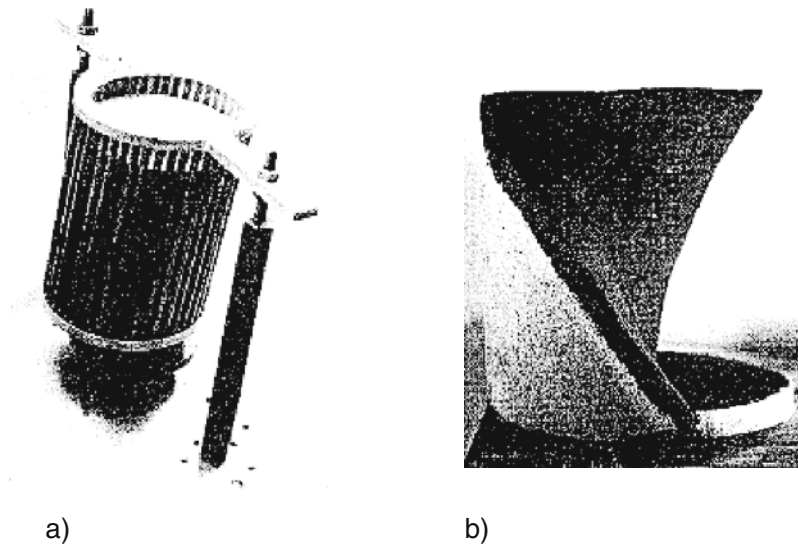


Fig. 15.5.2. (a) Tumbling device presented by Revushenko (2006), (b) glued and marked sample after a test

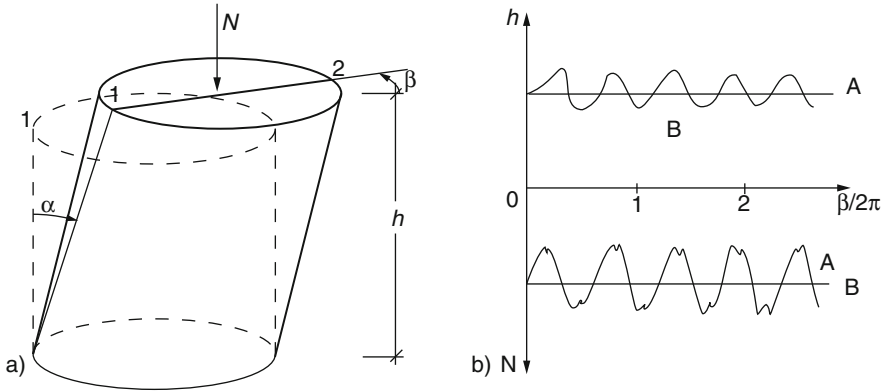


Fig. 15.5.3. Simulated tumbling (qualitative): (a) distorted psammoid cylinder, (b) asymptotic pulsation of normal force with constant height (A) and of height with constant normal force (B)

otic cycles (cf. Fig. 14.5.1) as these can provide validations and a base for more complex tumbling. They exhibit *orbital symmetry*, i.e. they are invariant with respect to changes of β by $2\pi/n$ with integer n (b).

With a fixed height h (A) the normal force N pulsates twice with each full revolution. With constant N (B) two cycles of h are smaller with respect to the mean value. Simply speaking, each revolution means one shear cycle of convected RSEs. The induced double cycle of pressure or density for constant h or N , respectively, is characteristic of psammoids (Sects. 2.11 and 4.7). There will be further cycles with higher frequency and smaller amplitude so that the pulsations are not harmonic.

Bobriakow et al. (1990) made experiments with *open sand columns* in a torsional device, Fig. 15.5.4a. The average height of the free surface tended to periodic changes (b) with four times the tumbling frequency (cf. Fig. 15.5.3b, case B). It represents the spatially averaged void ratio, the asymptote of which is determined by the amplitude. The smaller this is the denser gets the skeleton. The torque at the discs with elliptic holes which impose the tumbling motion to the confining tube could be measured for quantification of asymptotic cycles. Simulations with hyp or hyp- δ and gravity would be straightforward: the rather smooth lateral boundary moves periodically, the skeleton is fixed at the base and the stress-free surface. A loss of orbital symmetry by shear localization (cf. Fig. 14.1.2) and surface warping (cf. Figs. 12.6.1 and 12.6.2) could be avoided by small enough amplitudes, thus further validations could be achieved.

Shemyakin (1993) observed a *pattern formation* in such a device at the surface by means of partly dyed sand, Fig. 15.5.5. Starting with in one half dark cylinders (a), several revolutions led to a Yin and Yang pattern (b). This indicates slip at the wall and distortion by the revolving double bulge.

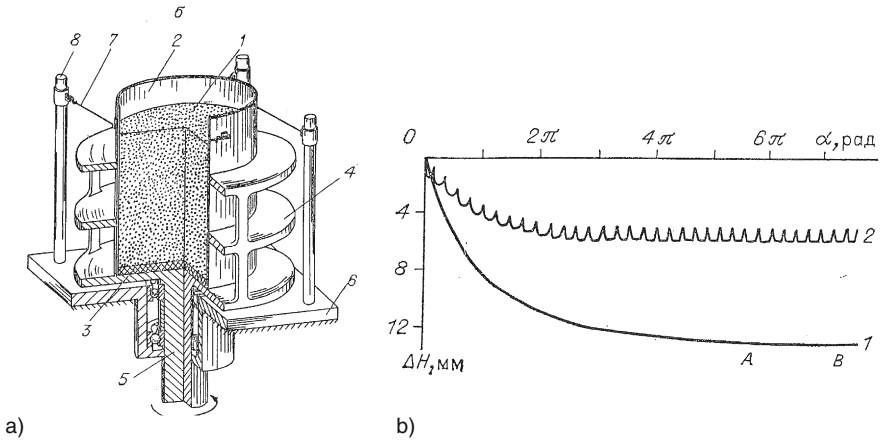


Fig. 15.5.4. Evolutions of a sand column with free surface by twisting its cylindrical wall (Bobriakow et al. 1990): device (a), height decrease versus rotation with an initially loose sand (b) with small (below) and bigger (above) eccentricity of the elliptic tube

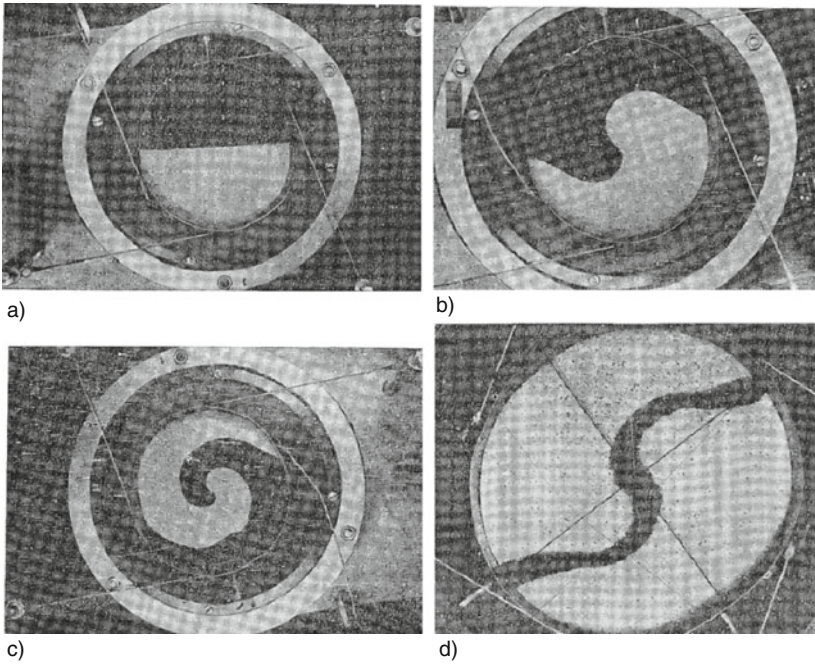


Fig. 15.5.5. Pattern formation (Shemyakin 1993) by distortion of sand in the device of Fig. 15.5.4a: onset with *bright and dark half cylinders* (a), pattern after some (b), further (c) and many revolutions (d)

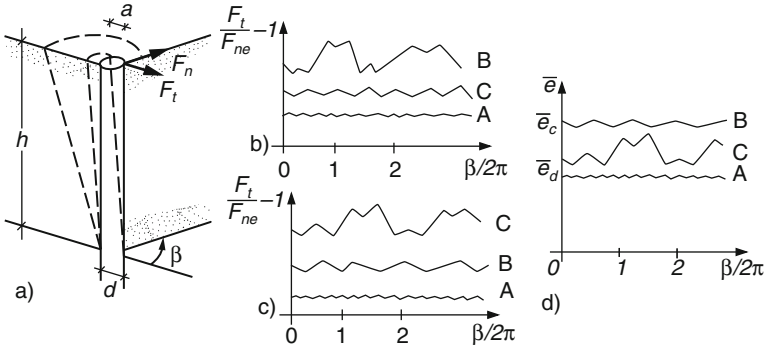


Fig. 15.5.6. Tumbling of a flexible rod in psammoid: setup (a), tangential (b) and radial head force (c) and mean void ratio (d) versus revolution

With further revolutions of the confining cylinder dislocations of the black-white boundary (c) indicate shear localizations. The shear bands could be helical (cf. Fig. 14.5.3), they cannot arise near the confining base. After many revolutions the black-white boundary changes its topological order (d), mixing occurs so that particles migrate outwards and inwards. As this was also observed with clay-like materials one can conclude that the topology of psammoids and peloids as proposed in this book is no more legitimate for excessive deformations. Investigations as indicated with Figs. 15.5.1 to 15.5.5 could also be carried out with seepage and skeleton viscosity.

Tumbling with gravity can be obtained with an elastic rod, Fig. 15.5.6. In a model test with psammoid (a) an elastic tube of diameter d and height h with strain gauges inside can be clamped at the base and slowly rotated at the top. Plots of normal (b) and tangential head force (c) and of average near-field void ratio \bar{e} in a cone with radius d versus rotation angle (d) tend to orbitally symmetric responses. These are determined by the top eccentricity a (amplitude) and do not depend on the initial and far-field void ratios (except for an average initial surface rise or sink near the tube which is of minor influence). With small amplitudes (say $a/d < 10^{-2}$, A) F_t and F_r exceed hardly the elastic values without psammoid ($F_{te} = 0$ and $F_{ne} = 4aEI/h^2$), and \bar{e} approaches the lower bound e_d for $p_s = \gamma h/2$ (Sect. 2.2). With moderate amplitudes (say $10^{-2} < a/d < 10^{-1}$, B) F_t and F_n get markedly bigger than the bending resistance F_n , and the near-field average void ratio \bar{e}_n exhibits stronger orbitally symmetric, i.e. periodic pulsations. With big amplitudes (say $a/d < 10^{-1}$, C) F_t and F_n do not exceed the elastic resistance so much and fluctuate less regularly than with smaller amplitudes. Then \bar{e} approaches the critical value e_c for $p_s = \gamma h/2$ with fluctuations, and a kind of granular turbulence arises in a conical neighbourhood.

Simulations of such evolutions will be a straining and frustrating exercise, but should be attempted before turning to more complex cases. They should

be focussed on asymptotic cycles as only these are apt for validation and as only then a kind of symmetry can be used. One should begin with low a/d and r_e , and increase both values gradually in order to get along with low numbers of transition head cycles. The same orbitally symmetric attractors can easily be attained with arbitrary onsets in model tests, but at best after many attempts in simulations. Polar effects could be enhanced by grain sizes $d_g > \text{ca. } 10^{-2}d$, but should be left aside for the beginning. The limit of psammoid approaches is attained with big amplitudes when the grain skeleton loses its topological order (cf. Fig. 15.5.5) and goes over into a turbulent granular mass. This could be recognized by means of markers in experiments and will be indicated by unavoidable numerical failures.

Extensions of tests as in Fig. 15.5.6 and related validations will be revealing and are recommended before treating more complex cases. Water-saturated psammoids can exhibit non-hydrostatic pore pressures which can produce skeleton decay or cavitation. Humid skeletons with sufficient capillary pressure p_{cs} and high initial r_e can produce a hollow cone with a bulge running around with the tube. Peloids with low initial consolidation ratio p_e/p_s can remain in contact with the rod, but not for bigger amplitudes which can also lead to liquefaction (cf. Figs. 15.4.5 and 15.4.9). Higher initial p_e/p_s and lower degrees of saturation S_r can lead again to a hollow cone with a running bulge.

Tumbling with inertia occurs *in situ* with deep vibrators. After driving down the machine its upper cylindrical part is fixed by the ground, and its lower part connected by a hinge is driven around by an eccentric motor. With air flushing an initially loose humid psammoid ground is compacted and pushed aside so that a cavity with a running bulge can arise. Submerged psammoid ground is transformed into a suspension near the tumbling part, but densified farther off. The response gets periodic, and longitudinal waves with twice the leading frequency of transversal waves due to the tumbling vibrator can be observed. The compaction is accompanied by downwards granular flow, thereafter the machine is lifted.

Fellin (2003) simulated the onset of such complex evolutions with hyp- δ . With precautions to avoid numerical artefacts the computer capacity did not enable quantitative calculations. Cudmani et al. (2003a) got farther with simplifying assumptions, Fig. 15.5.7. Substituting the tumbling vibrator by a plane-parallel system with cylindrical expansion and contraction, simulations with hyp- δ led to radial (a), circumferential (b) and vertical stress cycles (c) in the asymptote for a given depth and amplitude. Imposing such stress paths to RSEs at different distances r produced r -dependent reductions of the void ratio with time up to an asymptote (d). The penetration resistance was calculated with these asymptotic void ratios by means of Cudmani's (2001) model (cf. Sect. 14.3). This was done for different assumed distances of vibration points; the best agreement with the observed resistance was obtained with the actual distance $2r = 3$ m (e). This approach was improved by Meier (2009).

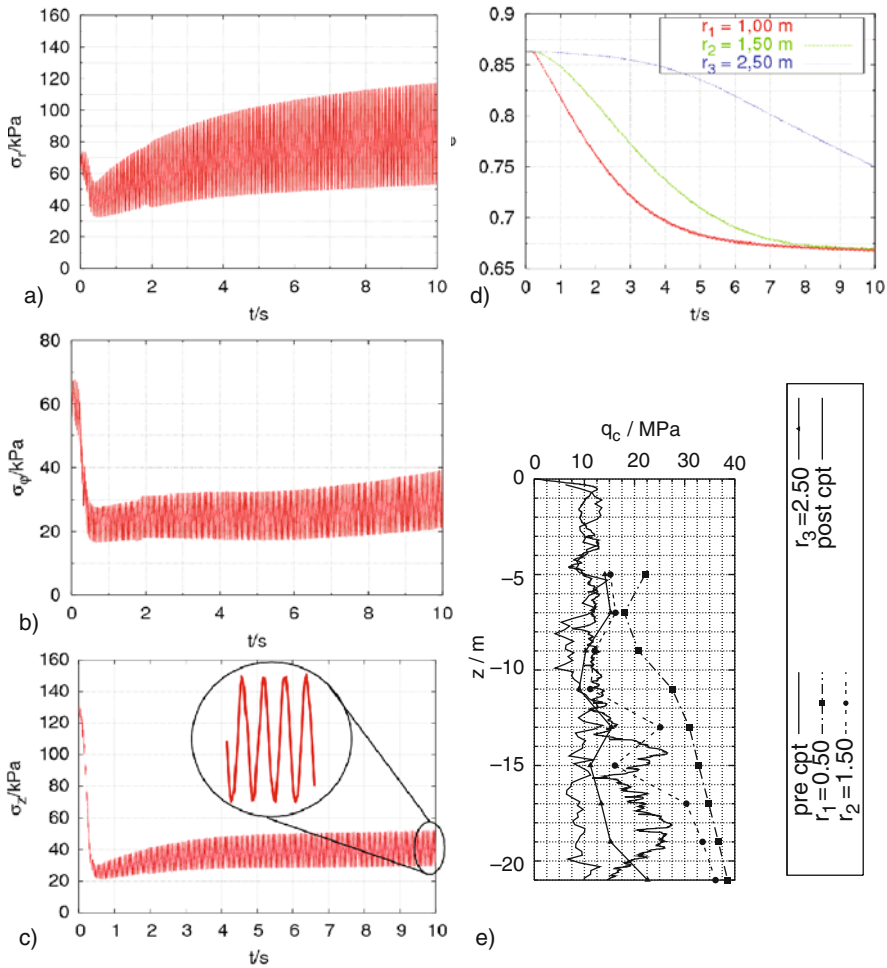


Fig. 15.5.7. Simulated evolution by vibro-flotation (Cudmani et al. 2003a): radial (a), circumferential (b) and vertical (c) skeleton stress of a near-field RSE versus time; void ratio versus time for differently distant RSEs (d) and penetration resistance versus depth (e), observed before and after compaction and simulated with differently assumed distances of vibrator axes in an array

It is recommended to focus simulations of tumbling on state cycle fields of skeleton stress and void ratio. These asymptotes with orbital symmetry are not easily obtained with arbitrary onsets and without initial symmetry, but advantageous for validation and control. The asymptotic response can only get independent of the far-field and periodic if the system does not get chaotic.

Driving of a roller over level ground may be considered with plane-parallelity for simplicity's sake. It serves to compact sand-clay mixtures with

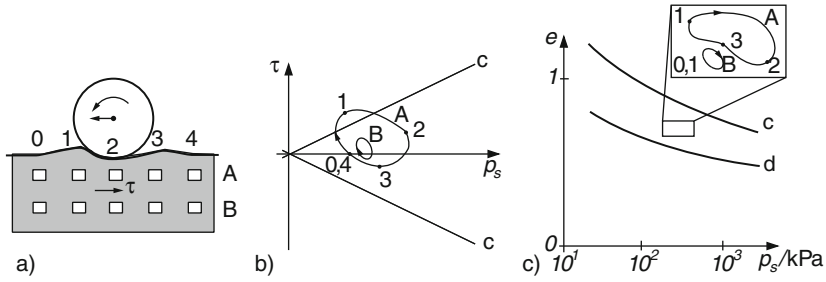


Fig. 15.5.8. Driving of a roller (a), paths of stress (b) and void ratio versus pressure (c) for adjacent RSEs during a passage after some repetitions

gas channels by repeated passages. Continued quasi-static rolling (Fig. 15.5.8) causes a running bulge (a) with periodic changes of the ground. With repetitions RSEs tend to state cycles of skeleton stress components (b, only one shear stress τ and mean pressure p_s for simplicity) and of void ratio e vs. $\log p_s$ (c). A shallow RSE (A) is nearly isotropic by a capillary skeleton pressure p_{cs} (Sects. 5.2 and 5.3) and has a low relative void ratio r_e (Sects. 2.2 and 3.2) before it feels the roller (stage O). In front of the roller (1) it is sheared and dilated, below (2) it is compacted with less shearing, behind (3) it is decompressed and again sheared with some dilation, after the passage (4) it does not feel the roller. A deeper RSE (B) experiences smaller amplitudes and lower maximal pressures. Below a depth of about twice the contact breadth b the ground is hardly changed after passages.

Plane-parallel simulations with S_r - and e -dependent p_{cs} and hyp- δ or v-hyp- δ should be focussed on asymptotic state fields as these are most important for validation and control. Initial state fields (stage O) should be adapted in iterations until they are obtained again after a passage (stage 4, cf. Fig. 14.6.1). Width and stress distribution of the travelling contact strip are part of the solution, likewise the shape of the two bulges and the depression between them, only forces and horizontal velocity of the roller are given. Big deformations with repeated dilation occur with too low p_{cs} with respect to the roller weight (Sect. 13.3), then rolling would not pay as the process can get chaotic. Increased pore pressures by enclosing pore gas (Sect. 7.3) should be avoided as they would lead to excessive deformations.

If a roll is not pulled with constant low speed, but driven via a second smaller roll in a kind of *car* the surface can more easily get wavy by repeated passages, Fig. 15.5.9. The contact normal forces are given by the distribution of weights, the tangential ones are opposite with equal amount which should not attain the sliding resistance of the smaller roll. The wavelength is given by the vehicle, neighboured RSEs tend to more complex state cycles than with one roll. The surface waves need not disappear by repeated passages although the ground resistance can be smaller in a crest than in a valley. This positive feedback is more marked with softer ground and higher loads. Periodic waves

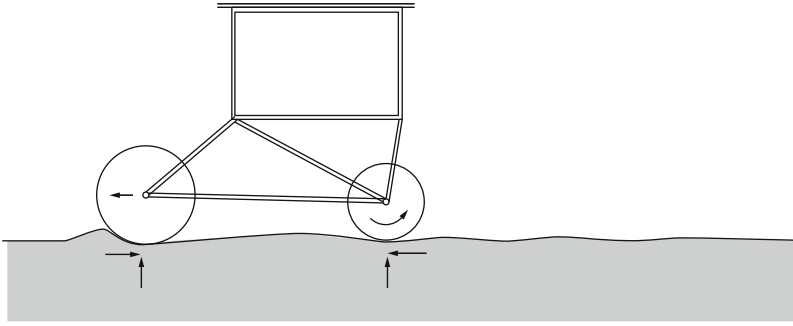


Fig. 15.5.9. Idealized driving car

arise thus in originally uniform ground from small fluctuations, so there is a pattern formation (more further below).

Plane-parallel simulations with p_{cs} and hyp- δ or v-hyp- δ should be focussed on periodic state fields. These imply changing *ripples* of given length, amplitude and shape have to be adapted in iterations alongside with the ground free-field until they are no more changed by a passage. This should first be done without seepage and with a small gas fraction and variable pore pressures as then model tests for validation are easier. Thereafter the seepage of pore gas may be taken into account, then tests require a control of vapor pressure and should avoid cracking (Sects. 6.2 and 6.3). The attained periodic asymptotes indicate an orbital symmetry as repeated passages work like endless circulation.

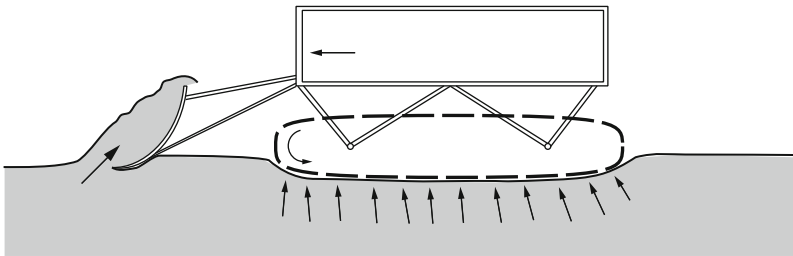


Fig. 15.5.10. Idealized driving bulldozer

Plane-parallel simulations and model tests can also help to understand the passage of a kind of *bulldozer*, Fig. 15.5.10. The ground may be horizontally uniform, sufficiently dense and suitably saturated so that its skeleton does not decay under the caterpillar. Its progression is like a succession of laterally connected strip foundations with vertical forces from the weight and horizontal ones from the resistance of shovel and front bulge. Repeated passages without shovel lead to state cycles as explained with Fig. 15.5.8. With a grading shovel

state cycles can also be obtained, they can imply waves as in Fig. 15.5.9. A cutting shovel shifts and dilates the soil ahead like a guided wall (Sect. 13.1). It can produce a convected state limit field (cf. Sect. 14.5) if the soil flowing off the shovel is removed. Except for shear localization, cracking and mixing at the shovel such evolutions could be simulated and validated as indicated further above.

These are preparations for the more complex driving of *cars with wheels*. To begin with, a single wheel with weight may be pulled horizontally over initially uniform ground. If the axle is fixed laterally by convected strings this can lead to a straight trace so that there is a vertical symmetry plane. With shifted contact and bulge and without localizations this could be simulated as outlined further above. An attractor with contact, bulge and state cycles in the ground could be generated numerically and observed in tests. A steady traction can lead to periodic changes of state and to a wavy trace. This kind of pattern formation (Sect. 16.2) may principally be simulated as indicated with Fig. 15.5.9. A steady traction can also lead to a deterministic chaos (Sect. 16.3) and thus to a loss of control, however, one could at best predict under which conditions this can happen.

Such evolutions were observed in tests by Augustin (2002), Fig. 15.5.11. A circular track of an unsaturated silt was placed in a ring of 1m diameter. A



Fig. 15.5.11. Model test with a roller upon a circular track (Augustin 2002)

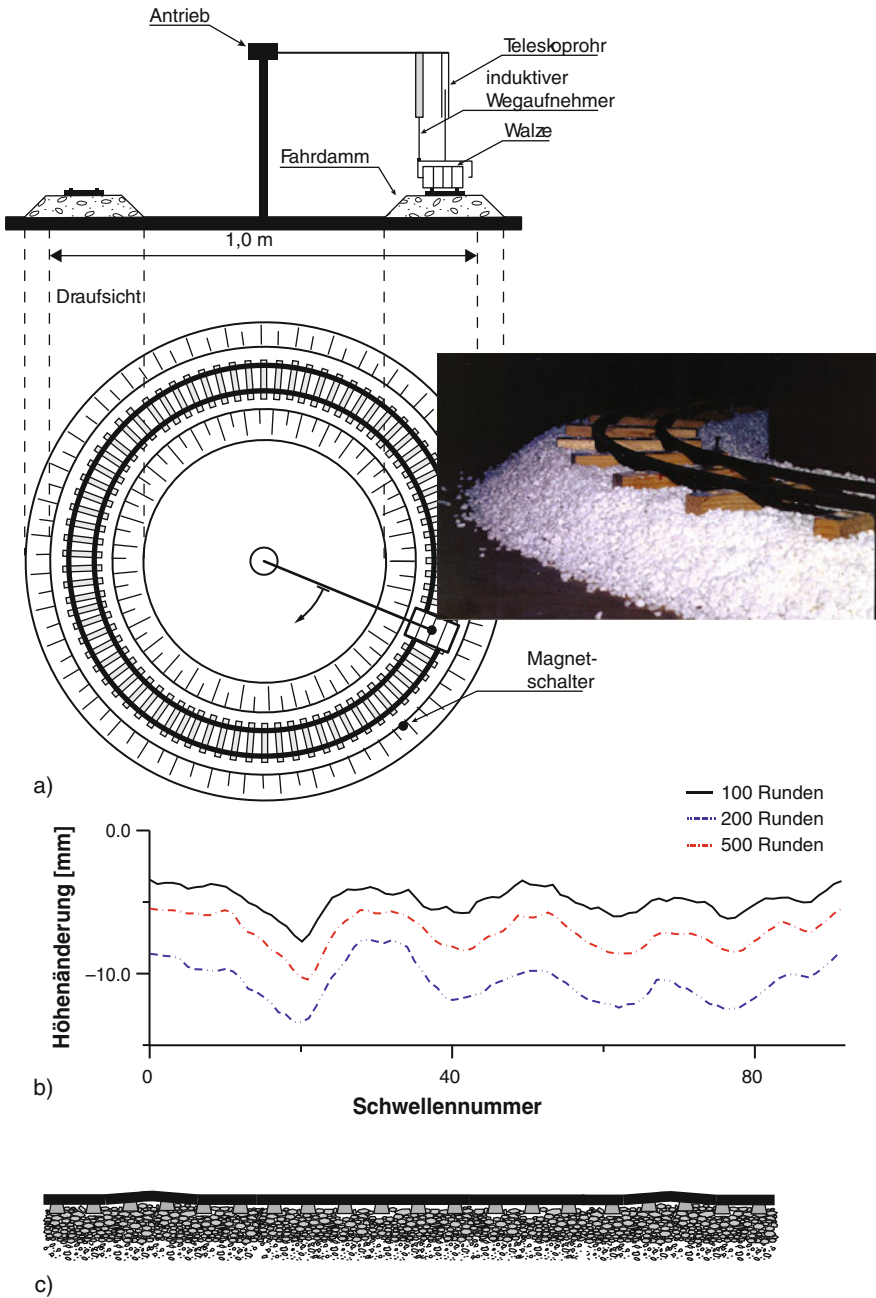


Fig. 15.5.12. Model test with a railway track (Augustin 2002): setup (a), reduction of track height versus number of sleepers after 100, 200 and 500 passages (b), circumferential section (c, qualitative)

roller was driven around by a radial guide with small accelerations. The track got wavy after some rounds, the more the faster the roller was driven. The ripples were not uniform over the track, and after some tracks they did not grow any more. This kind of orbital symmetry could also be attained with a straight track and a driven roller which enters and leaves it repeatedly. A slowly driven roller could iron out ripples as their crests yield more than the valleys by cohesion. Then a single mould would travel together with the roller with about $3/2$ roller diameter length (Fig. 15.5.8). With faster driving the vertical acceleration releaves a crest and pushes down a valley. Starting with minor imperfections, this positive feedback enhances moulds with a length given by the roller. Osinov (2001) obtained a similar pattern formation with an elastoplastic subgrade model. Surface ripples are slowly shifted sideways by the roller.

Pulling a cart with two wheels and a traverse over a horizontally uniform ground can lead to two straight traces with a vertical symmetry plane. This can be observed in tests and represented by a state cycle field for stationary RSEs, and could be simulated with psammoid and peloid relations. A spontaneous loss of symmetry can lead to lateral and vertical oscillations or to deterministic chaos. A bicycle driven over a ground with sufficient capillary cohesion p_{cs} can produce a straight trace so that a vertical symmetry plane can be identified, then RSEs can tend to state cycles. With lower p_{cs} the trace is deeper, and can get wavy or chaotic so that driving gets impossible.

A repeatedly passing car with four wheels can likewise cause straight traces upon a ground with sufficient p_{cs} so that a symmetry plane and state cycles can be identified. With lower p_{cs} it can tumble and the passage can get chaotic. A single driven wheel sinks and a pair of wheels tilts when both are rotated sideways. A *navigation* gets impossible, this can also happen with a bulldozer. Simulations of car driving on ground should be focussed on state cycles, models with a simple subgrade (Sect. 13.5) cannot serve to the purpose.

The evolution of *tracks* for increasing vehicle sizes and speeds was a never-ending battle with pattern formation and deterministic chaos. Railways with sleepers and some simplifications may serve for illustration. Augustin (2002) worked with a model railway upon coarse sugar with a revolving loaded roll (Fig. 15.5.12a). After several revolutions the initially level track got wavy with wavelengths of about 20 sleeper distances (b). There is a positive feedback as the subgrade yields more at initially free valleys than at always pressurized crests (c), and a preferred wavelength arises according to the stiffness of rails and ground. This pattern formation depends also on inertial effects and is visibly close to a deterministic chaos.

Schünemann (2006) simulated the passage of trains with a simplified track, Fig. 15.5.13a. Ballast upon elastic ground was modelled as a row of RSEs with $\text{hyp-}\delta$, the sleepers could temporarily lose contact (b), the idealized car (c) had different velocities. The ends of a section with 40 sleepers experienced the same displacement and internal forces, so the track was endless like a ring. Starting with level sleepers and small fluctuations repeated passages led to a wavy track

(d). With a higher initial void ratio the track settled more by passages, the waves got higher and somewhat longer (e). More settlements were obtained with initial fluctuations of void ratio or position, and the waves were somewhat shorter. Other than with Fig. 15.5.12 and in situ the waves grew only little with higher vehicle speeds. This shortcoming may be attributed to the neglect of grain crushing.

The *horizontal penetration* through horizontally uniform ground can lead to state cycles or strange attractors. If an elastic rod is pushed forward

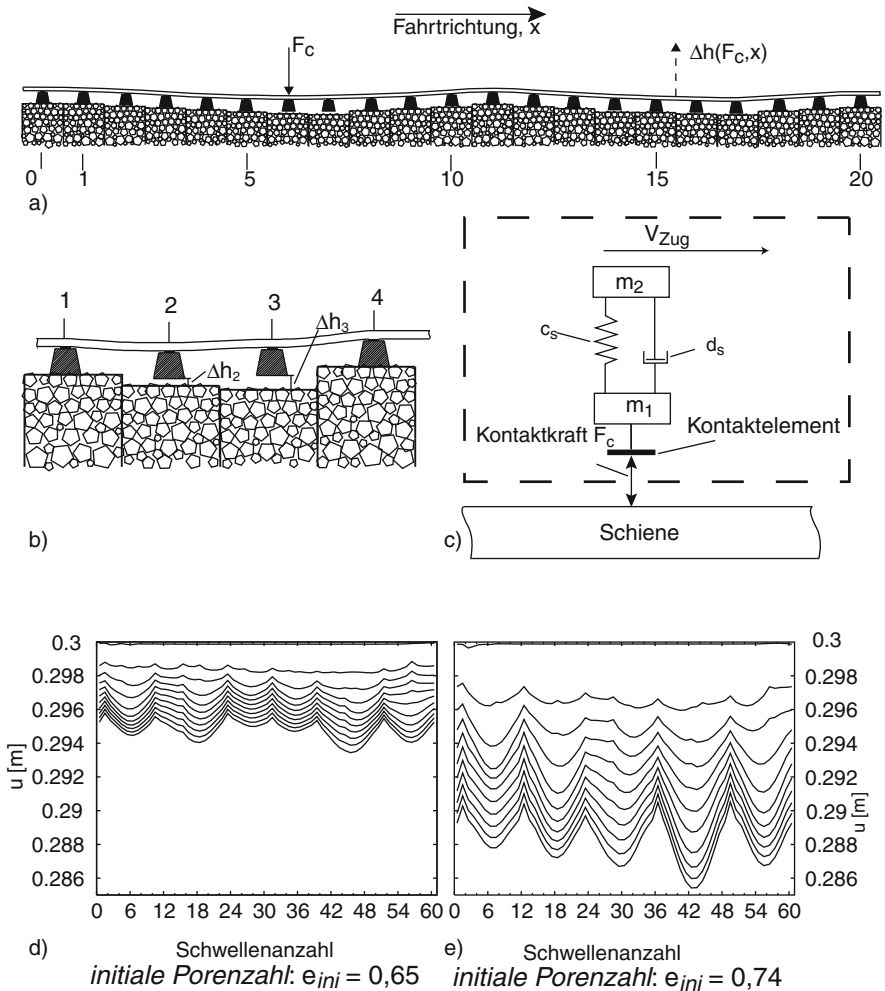


Fig. 15.5.13. Simulated evolution of an endless railway track (Schünemann 2006): longitudinal section (a), closer view (b), idealized car (c), settlement versus number of sleepers with initially dense ballast after 1.000–10.000 passages (d), same with initially loose ballast (e)

monotonously it deviates inevitably. With torsion and an eccentric tip the axial resistance is smaller and deviations can be corrected. Flushing at the tip can ease the penetration, but can also lead to a loss of control. With alternations the resistance to penetration is smaller (cf. Fig. 14.3.2), and deviations can be reduced. Longer penetrations require a head drive, e.g. by a so-called earth rocket: A pneumatic hammer blows an anvil behind the tip so that this is pushed ahead, whereas the device is fixed by the ground when the hammer returns. A kind of navigation can be achieved with an eccentric tip by rotating the tube behind the rocket. Flushing with air, water or suspension enhances the penetration, but can also lead to deterministic chaos (loss of control, breakout). Simulations may at best be achieved with a vertical symmetry plane, but are beyond the present reach otherwise.

The *horizontal boring* with tube and excavation in horizontally uniform ground can likewise get steady or chaotic. For diameters $d < \text{ca. } 0.5 \text{ m}$ a continuous auger with a bit and a twisted tube can serve to the purpose. Deviations cannot be avoided with bigger lengths. With $\text{ca. } 1 \text{ m} < d < \text{ca. } 4 \text{ m}$ tube sections can be pushed ahead from a shaft by jacks and a front cutting edge. Groundwater can be kept off by excess air pressure, the shaft friction can be reduced by a suspension grouted from the cutting edge. Longer tubes require expander stations so that a shorter group of sections progrades at a time. Even with adapted cutting edge, excavation and grouting the navigation can get impossible. For $d > \text{ca. } 4 \text{ m}$ shield machines can be pushed by jacks against tubings which are placed behind the tail. The ground inside of the cutting edge can be excavated by a wheel with bits, and supported by suspension and/or compressed air. Even with several control tools the navigation is not always successful.

Simulations and model tests could improve the understanding, quantifications require monitoring in situ so that predictions remain semi-empirical. Simulations with symmetry planes (Fig. 15.2.11) may suffice to estimate far-field effects if boundary conditions at the front and the tube are properly assumed. Forces at the tube and the drive may be estimated for design. A regular progression can be better understood by means of state cycle fields in the ground. Spontaneous deviations from horizontal drive may be retrieved, but this will be no more than a first step towards a reliable simulation-supported navigation.

Inclined and curved borings can also principally be captured by model tests and simulations, but both would over-extend the presently available capacity. The penetration of a screw may be captured by attractors in some cases. With a vertical progression soil is pushed aside and densified if pore water can get out in time. This is enhanced by alternating deformations of neighbored RSEs and by cracking. A steady response can be obtained with a horizontal drive, but it can get chaotic by shear localization and cracking, let alone deviations of the auger. If the latter is used for transporting soil ahead or backwards the topological order of skeletons gets lost (cf. Fig. 15.5.2) so that psammoids or peloids are no more justified. This happens also with a plough which dilates and stirs part of the ground.

To *sum up*, some cases of tumbling and driving may be captured by simulations and tests with the aid of attractors. State cycle fields can arise after several rotations or passages. Driving can lead to spontaneous pulsations or to deterministic chaos, but such critical phenomena are beyond the present reach.

CRITICAL PHENOMENA

As announced in the Prologue it was shown in several chapters how and when monotonous and cyclic attractors (which were called SOM states, state limits and state cycles) can serve to capture the nature of soils. A comparable outline of methods for *critical phenomena*, i.e. pattern formation and deterministic chaos, cannot be offered. This last chapter is to convey what is meant without a unified concept, so my book has an open end and not a finale like a symphony.

Critical phenomena were mainly investigated for thermodynamic equilibria, less often for systems which are little or far off such states. Some snapshots in Sect. 16.1 may indicate what kinds of pattern formation and deterministic chaos can occur and what they have in common. Some in-depth approaches are just mentioned as until now they could not be transferred to soils.

The outline of *pattern formations with soils* in Sect. 16.2 is likewise rather descriptive. Some observations and few simulations indicate that fractal patterns of shear bands can be predicted for suitable initial and boundary conditions. One is inclined to model such cases by mean-field theories, i.e. by relations with spatial averages. This was repeatedly proposed in the present book, but readers should be aware that patterns in soils cannot always be captured by such approaches.

Critical phenomena with soils are practically more important if they imply *deterministic chaos*. This is discussed in Sect. 16.3 by means of examples. It was outlined in previous chapters that and why prediction methods cannot capture catastrophic evolutions. We have to accept that such cases can hardly be controlled by means of conventional design models, and that sophisticated numerical methods can at best indicate critical points. Subsequent catastrophic evolutions are beyond the scope of this book as skeletons of solid particles can no more be identified.

16.1 Critical phenomena off soil mechanics

If an ensemble of molecules in a *thermodynamic equilibrium* is at a critical point phase transitions occur without transition energies (second order phase transitions). For instance, liquid and vapor coexist at a critical pressure p_c and a critical temperature T_c . As the transition energy disappears bubbles and drops arise spontaneously in pulsating configurations (Bruce and Wallace 1989). With a constant pressure $p = p_c$ the density ϱ decreases from the critical one ϱ_c with increasing temperature T by a power law, viz.

$$\varrho_c - \varrho \sim (T - T_c)^n \quad (T \geq T_c) \quad (16.1.1)$$

with an exponent $0 < n < 1$. Such relations work also for other critical phenomena near equilibria, e.g. with condensation and evaporation at solid surfaces or with magnetization. The exponents n do not depend on the size and shape of the system. This was proven with the so-called renormalization group method for patterns which are similar for different blow-ups, it is typical for fractals (Mandelbrot 1982). As for any thermodynamic equilibrium the method requires *conservative* interactions of molecules.

Small deviations from equilibrium can be captured by linear relations of thermally activated fluxes with gradients. The coefficients can have the same T -dependence, thus the ones for viscosity and for diffusion of heat are proportional to each other (Einstein's relation). More generally fluxes and gradients are coupled by linear relations (fluctuation-dissipation theorem). The matrix of coefficients is symmetric (Onsager's relation). If its eigenvalues are positive the system returns to equilibrium after a slight disturbance, so it is stable. Otherwise fluctuations evolve into periodic pulsations or increase chaotically.

For instance, *convection cells* can arise in a basin with two not mixable liquids heated from below. If one constituent has a lower density than the other one with the bottom temperature, but is heavier for the upper T , it rises and returns repeatedly. Stochastically stationary patterns arise if the sign of the density difference changes at the mid-height T . Otherwise the heavier fluid assembles in a lower layer, and only heat flows due to the gradient of T . The size of convection cells depends on the surface energy of interfaces without which the constituents would get mixed. This is an example of pattern formation.

We now turn to systems which are so *far off equilibrium* that linear relations get invalid. Except for phase transitions exponential relations of flows and gradients can be established, e.g. for dislocations in solids due to thermal activation (Sect. 2.1). Consider now a system with two non-linearly viscous liquids. If a lower liquid layer gets lighter and less viscous than the upper immixable one by heating from below it rises in *diapirs*. First the interface warps in a rather fractal pattern, then the biggest warp grows into a kind of finger that reaches the surface. The diameter of the finger depends on the surface energy, its position is random and it grows faster with lower viscosities. This is an example of deterministic chaos.

A steady wind produces periodic running *surface waves* in initially resting water. A slight wind warps only the skin with its surface energy so that this determines the small wavelengths (capillary waves). The amplitude increases as a crest gets more shift from the wind than a valley, but is bounded by damping. With moderate wind the same feedback leads to longer gravity waves which are no more pulled back by the surface energy. With strong wind this pattern formation goes over into a deterministic chaos. Then the spectrum of waves is rather fractal and solitons can arise.

Particles in a liquid sink straightway if there is an excess of weight versus uplift and if they are so far from each other that the laminar velocity near-fields do not interfere. With moderate distance and negligible mutual attraction or repulsion the particles dance laterally so that the suspension density fluctuates. With a bigger solid mass fraction the particles assemble in sinking clouds so that the upward flow in between is impeded. The higher energy dissipation than for more uniformly arranged particles enhances such *convection cells*. The size of the clouds depends on the overall viscosity which is bigger than without particles.

Turbulent flow depends on inertia and viscosity and can produce various critical phenomena. For instance, periodic eddies can arise behind an obstacle, whereas with a higher entrance velocity the flow gets chaotic. The overall dynamics can be captured by a ‘turbulent’ viscosity. The overall diffusion of heat or solubles can be modelled by a ‘turbulent’ diffusion coefficient. Experiments reveal that both parameters are proportional to each other. This analogy to Einstein’s relation suggests a turbulent temperature T_t which is proportional to the chaotic part of the kinetic energy. This can be estimated by model tests or computer simulations for different boundary conditions. The observed linear overall viscosity and diffusion suggest that the fluctuation-dissipation theorem holds, but there is no ‘turbulent heat capacity’.

Lightnings are an example of deterministic chaos so far off equilibrium that molecules are broken temporarily. In a thunderstorm ions move down from charged clouds along zig-zag paths in the air where the fluctuating conductivity is higher. There the gas is ionized by the temperature increase as the released heat cannot be dissipated in the short time. The positive feedback by increasing conductivity produces an exponential growth of ion transport until the electric gradient decreases by discharge of the cloud. One can at best estimate conditions for the critical point when lightnings arise, but cannot predict their position and course.

Many *music instruments* work by spatio-temporal pattern formation. If they are blown the leading frequency is determined by the size of the chamber where acoustic waves travel to and fro. The positive feedback is due to the elasticity of a solid opening (e.g. mouth or flute). The intensity is given by the air supply, a sound arises if this remains between suitable bounds. In a string instrument the bow sticks to the string via colophonium as long as this does not melt, and slips back until the re-hardened colophonium can again take over a shear force. The positive feedback towards oscillations is due to a loss

of sliding resistance and its regain in stick intervals. A too slow passage of the bow produces periodic pulsations with silent intervals as the string released by melting colophonium returns earlier than within half its own period. No tone is produced with such a fast passage that the colophonium cannot harden in time.

Stick-slip can be periodic or chaotic during the *sliding friction* of solid blocks along plane solid surfaces (Persson 2003b). A block with mass m may transfer a constant normal force N , and a spring with a constant c attached to it may be driven with constant velocity v . The interface exhibits nano-sized asperities which constitute contact islands. Their average area is proportional to N , they oscillate with high frequencies and fluctuate with shear melting and re-crystallization. With a low v the block sticks and slips with irregular intervals, with a moderate v it oscillates periodically with frequency $f \approx \sqrt{c/m}$, and with a high v it slides uniformly.

There are more examples and models for pattern formation and deterministic chaos, but little of them can as yet be transferred to critical phenomena in the *lithosphere*. These are driven by convection cells in the magma base and the hotter interior which are usually attributed to heat flow and T -dependent variations of density and viscosity, combined with the daily rotations of the earth. The convection is enhanced by periodically changing gravity fields (Shemyakin 1993). Patterns can hardly be identified in shapes and motions of continental plates. Tectonic processes along their interfaces can exhibit a spontaneous order, but are more often chaotic.

Slow tectonics imply normal faulting (Sect. 12.6), ring structures (Sect. 14.2) and other kinds of shear localization (Mandl 1988). Earthquakes can be accompanied by a humming noise, but more often their spectra are typical of deterministic chaos. They are usually attributed to stick-slip dislocations along faults. In the light of real compositions of the lithosphere simple models, as proposed e.g. by Shkoller and Minster (1997), are debatable. Crack patterns are far more intricate than in lab tests (Sect. 8.3), so their opening and closing *in situ* can at best be crudely estimated. Diapirs in saline formations resemble the one of Fig. 14.2.9, volcanic outbursts are more intricate.

The surface of the lithosphere is also shaped by wind, water and ice, and close to it soils come into play. The self-similarity of coast lines is a known example of fractality (Mandelbrot 1982), but erosion models for its generation are hardly available. A weathered little dam of humid sand can resemble a mountain ridge, Fig. 16.1.1, this indicates common features of rock and soil.

To *sum up*, a plethora of critical phenomena is known, and the better understood the more conservative the involved interactions are. Thermodynamic equilibria can only exist with conservative interactions, these can produce order or chaos at critical points. Linearly dissipative evolutions near equilibria can similarly get critical. Models get more intricate with interfaces of solid, liquid and gas, and more so for systems far off equilibrium. This is particularly the case for the lithosphere with its complex composition.

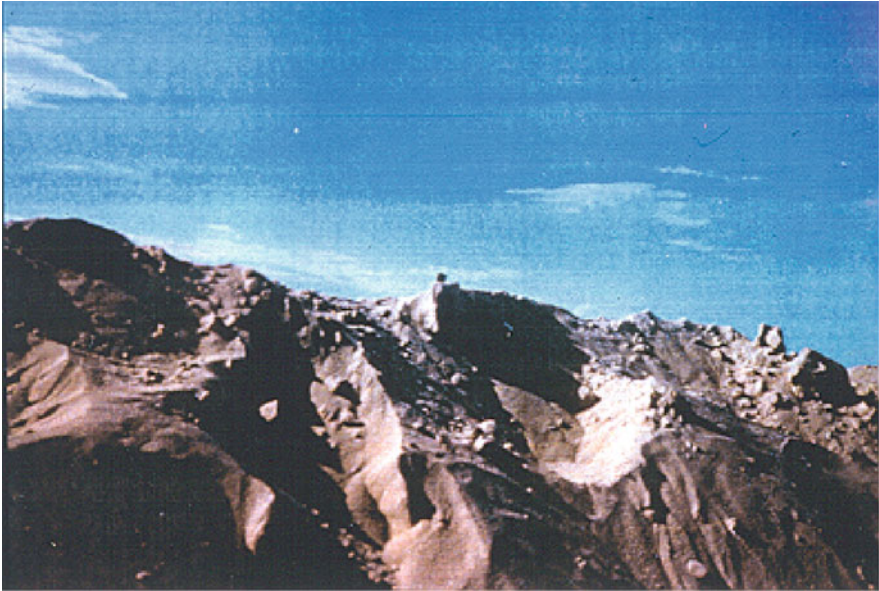


Fig. 16.1.1. Weathered sand dyke of ca. 0.3 m height (photo by R. Gudehus)

16.2 Pattern formation with soils

Cases with pattern formation which were outlined in previous chapters have something in common with the ones indicated in Sect. 16.1. Patterns in soils will only be indicated as models for them are preliminary due to the complexity with non-conservative interactions.

As shown in Sect. 8.2 *shear bands* in psammoids can evolve in patterns in rectangular RSEs with suitable boundary conditions. Observations in biaxial tests and simulations with polar quantities indicate a fractal sequence of nested patterns. At the beginning the self-similarity (i.e. same angles in triangles of characteristic pattern points) is clearly visible. An asymptotic overall critical state cannot be identified in this manner as then the shear band thickness gets indeterminate (Fig. 8.2.5). Patterns of void ratios and pressures resemble the ones of thermodynamic equilibria in the bulk at a critical point. Thus the name ‘critical state’ proposed by Casagrande (1936) seems to be adequate.

Considering boundary conditions of RSEs, critical states imply apparently a contradiction in terms. Spatial and temporal fluctuations cannot be stationary along sample boundaries in real experiments, and could at best be approached iteratively in simulations. (Deceiving artefacts can also be obtained with conservative molecular interactions, in particular with periodicity from the boundary distances.) Psammoid patterns get frozen if the boundaries are fixed, or patterns are swept out by continued deformations.

Axi-symmetric psammoid samples can produce $2\pi/n$ -symmetric shear band patterns in triaxial tests (Figs. 14.1.2 and 14.1.4). Even short samples with smooth plates which remain fairly cylindrical are then no more uniform. Cubical samples could do better, but shear band patterns in them cannot be uniform (Fig. 8.2.10). Patterns could be reconciled with spatial uniformity ('smeared') if sites and directions of shear bands were randomly distributed. RSEs with shear bands may be considered as composites (Sect. 9.1).

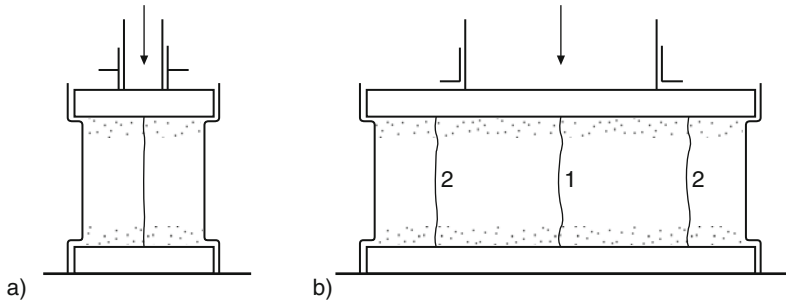


Fig. 16.2.1. Splitting of a slender (a) and a squat (b) very dense psammoid

Crack patterns may be imagined in very dense biaxial psammoid samples, Fig. 16.2.1. As with dry masonry shortening by smooth plates with confining pressurized membranes could lead to a kind of axial splitting (a). This could occur in a fractal succession in a flat sample (b) so that composite RSEs with such cracks could be justified. As postulated for simple psammoids (Sect. 2.2) this kind of cracking may be considered as an anomalous shear localization with uniaxial stress for a lower bound void ratio e_d . One may also speak of a granular phase transition from a dry masonry to a grain skeleton, and of a critical point as there is no transition energy. Such states can at best be approached, but not be reached in experiments. Snap-throughs of granular force chains (Fig. 4.3.1 and 4.3.2) suggests more chaos than order.

Psammoid RSEs with *pore water* can exhibit similar critical phenomena, but thermally activated phase transitions come additionally into play. Loose saturated skeletons are left aside as they tend to deterministic chaos (Sect. 16.3). The reduction of pore pressure in dilating shear bands can produce gas bubbles and cavitation cracks (Sect. 6.2). Crack patterns as in Fig. 16.2.1 can also occur in humid dense skeletons, these can thus get loose by openings where capillary bridges are torn apart. With fine grains the succession of such crack patterns can exhibit a fractal self-similarity (Mandelbrot 1982).

Peloid RSEs could be captured similarly, now the argotropy of the skeleton due to thermally activated dislocations (Sects. 3.1 and 3.2) comes into play. Thus a pattern of shear bands produced in a triaxial test can disappear after a sufficient resting time. A similar kind of self-healing can be produced in a sample by many small erratic deformations. A crack pattern generated in

a shortened dense clay sample with confining pressure could be healed by resting. The cavitation of pore water by suction is thus reversed with less suction, and the surface energy of water-gas interfaces is regained.

Shear patterns in layers can be similar as in RSEs, but they are influenced by gravity and layer size. This was shown with psammoids in Fig. 12.6.2 for a kind of normal faulting by stretching of the base. Rectangular RSEs of arbitrary size can no more be identified precisely as the skeleton experiences a succession of shear dislocations. The vertical uniformity is disturbed at the base and the surface. A hard base prevents dislocations, whereas these produce a wavy surface. A more uniform pattern of shear bands could hardly be obtained as a softer base would get wavy and a stiff cap layer would suppress dislocations. Patterns in situ are never that uniform as composition and boundary conditions are more complex.

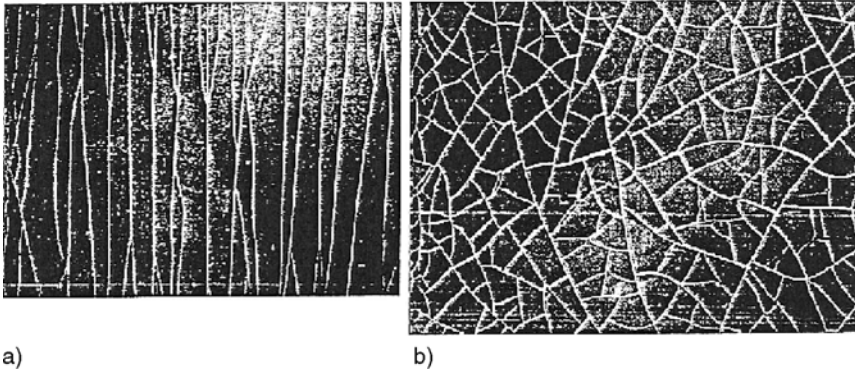


Fig. 16.2.2. Cracking of a peloid layer upon a membrane (Revuzhenko 2006) by uniaxial (a) and biaxial extension (b)

Crack patterns of various kinds can arise in peloid layers. Revuzhenko (2006) expanded a thin layer of a paste via an elastic membrane upon a plane base, Fig. 16.2.2. A succession of parallel cracks starts from the middle if the membrane is pulled in one direction (a). Equal extension in two directions leads to a pattern of polygons without orientation and with less order (b). Such evolutions could be simulated with v-hyp and capillary entry pressure p_{ce} (Sects. 6.2 and 6.3). Starting with realistic spatial fluctuations of void ratio, the cracks due to $p_w = p_{ce}$ would have zig-zag shapes. With a uniaxial extension the first crack arises in the middle, then two cracks arise in the middle of each half and so on. Shrinkage cracks arise in soft saturated peloid by evaporation. Cracks and shortening near the surface cause shingles so that the surface gets uneven. This evolution is more complex than the diffusion-controlled growth of dendrites which is often used to illustrate fractals.

Clay layers in situ have complex fabrics if they had repeatedly been exposed to drought and rain. After many repetitions an upper part of them can

go through state cycles as long as erosion and sedimentation do not come into play. Changes of temperature or salinity play also a role, evidently if they lead to freezing and thawing or to variable aggregation, respectively. There is no way around substitute composites, the identification requires judgement (Sect. 9.1). The assumed state should be consistent with gravity, hydraulic conditions and age by means of v -hyp.

Surface waves of horizontally layered soils can occur under various conditions. Wrinkles by shear band patterns can be produced in the lab (Figs. 12.6.1 and 12.6.2), but in situ they are swept out by erosion or covered by sedimentation. Tracks with sufficient capillary skeleton pressure or a structure on top can get wavy by traffic (Figs. 15.5.11, 15.5.12 and 15.5.13). The positive feedback for this pattern formation can result from another soil resistance of crests than of valleys, also with accelerations. Horizontal forces lead to a slow shift of the ripples, but without traffic these are frozen. The dominant wavelength is mainly determined by the vehicle and/or the distance of sleepers and by the stiffness of rails. High velocities would lead to deterministic chaos.

Erosion and sedimentation can lead to travelling ripples at the surface of psammoid ground if this is exposed to a uniform current of water or air. The near-field of air velocity produces erosion uphill and sedimentation with granular flow downhill. This works only with medium sand and a certain range of wind velocities, then the pattern is rather stable. With higher uniform far-field velocities dunes travelling on a plane can evolve into groups of barchans. Schwämmle and Herrmann et al. (2003) have shown with validated simulations how the asymptotic shape and size is determined by the wind velocity.

The transport of coarser grains along a solid surface by water is understood in hydrodynamics, but critical phenomena of the adjacent sediment have not been investigated. With finer grains and peloid particles colloidal interactions come into play. A net attraction leads to flocs which sink faster in resting water, it causes a higher void ratio of the sediment (Sect. 7.1) and impedes the erosion near the surface. Without net attraction or with net repulsion, which can be achieved by rain water when dissolved salt before provided a net attraction, the erosion proceeds faster and with little order. A dense peloid can temporarily stand with a steep slope due to suction (Sect. 12.3). This can enhance the formation of meanders with a positive feedback by higher velocities along outer downstream curves.

Composite sediments of psammoids and peloids can get rather uniform by annual floods due to the slower sinking of finer particles (e.g. Fig. 11.3.2a). More often such formations are wavy or disturbed due to ripples, dunes and/or erosion channels. Such arguments may be used to identify initial compositions and states for geotechnical purposes. Composites (Sect. 9.2) can have a fractal self-similarity, otherwise element sizes could not be chosen according to geotechnical sizes. The indeterminacy of the composite permeability is inevitable if the genesis was partly chaotic.

The *acoustic emission* of soils is more often chaotic than ordered, and is apparently negligible for peloids. The humming noise of dunes has a

frequency of ca. 100 s^{-1} and can be heard some km away. Andreotti (2004) observed granular discs sliding down slopes on an air cushion. The humming frequency can be explained with the speed of shear waves and the size of discs, but a positive feedback could not yet be found. Other than with a wind-instrument the disc is not an elastic solid, but is disintegrated after a few seconds. A hooping noise during the discharge of polymer grains from a silo is described by Tejchman (1997). It disappeared after placing rough strips along the wall.

To *sum up*, pattern formations with soils can arise similarly as with other matter, but are not as well understood. Patterns of shear bands can evolve in a rather fractal succession, the ground surface can get wavy, but seldom periodically, the acoustic emission can exceptionally be periodic. The onset of such evolutions was captured theoretically in some cases, but these are not yet strange attractors in a strict mathematical sense.

16.3 Deterministic chaos with soils

Stability of earthworks and structures denotes their ability to stand, but not necessarily at a thermodynamic equilibrium. A loss of stability with spontaneous acceleration means deterministic chaos. At best the onset may be captured with elastoplastic or hypoplastic models and with coupling of skeleton and pore water. The stability of stationary and periodic evolutions implies the one of state limit or state cycle fields, respectively. As without soils pattern formation and deterministic chaos can be close to each other in space and time, but without conservative interactions evolutions are more complex, particularly at and near critical points.

Consider first evolutions with *dry psammoids*. Steady states with closed boundaries can at best be achieved by torsion of annular bodies via axisymmetric solid bodies. Rotation of two rough cylinders with two smooth plates in the device of Fig. 14.6.1 could lead to radial symmetry if gravity does not matter with the given pressure and size. If both diameters are close to each other and their difference exceeds by far the grain size the shearing should get uniform and steady. Could a uniform critical state be achieved in a torsional device with suitable materials and initial states?

Yes and no. Imagine non-abrasive grains placed with a uniform void ratio e in a range so that the skeleton does not decay or attain such a high pressure that grains are crushed. Imagine devices to measure the torque between the cylinders and the normal force between the plates so that the solid deformations are negligible. Using stress component ratios as by elp or hyp one could thus determine a mean pressure p_s related with $e = e_c$ and a critical friction angle φ_c from stationary values of torque and force. More detailed measurements would reveal fluctuations of stress and void ratio, however, and a multi-fractal acoustic emission. All that suggests that uniform critical states can be attained at best in the average.

More details could be achieved by following up individual grains. Sophisticated experiments and granular-dynamic simulations could reveal systematic deviations from the desired uniformity and topological order. Marker grains would indicate migrations into and out of the interior. One should keep in mind that critical states are latently chaotic and deserve this name. Simulations could lead to fractals, but would also get more difficult with them. Loose skeletons could decay with extreme fluctuations, and dense ones could be ground without becoming a uniform mixture. Bigger ratios of boundary diameters in torsional devices could lead to r -dependent critical states, or to uncontrolled circumferential fluctuations. Such a loss of symmetry would more easily occur with a control of the axial force.

Ring shear devices (Fig. 2.9.9) can at best produce axially symmetric evolutions, but changes in the axial direction impede attempts towards a stationary response. With more kinematic freedom the skeleton can more easily lose an initial uniformity when it approaches a critical state. Shear localizations with hardly known distribution prevent the determination of critical void ratios. Torsional devices with membranes (Fig. 2.9.10) cannot produce a monotonous stationary response because of shear localization, bulging and wrinkling (Sect. 14.6).

Stationary evolutions of psammoid bodies with gravity can only be achieved in exceptional cases as a spontaneous loss of symmetry can rarely be avoided. A *flow equilibrium* can be produced in an hour-glass with a smooth wall if the running out granular matter is continuously filled above with a suitable low density. Other kinds of silos can hardly produce a stationary flow (Sect. 14.5). Pulling out or twisting a pile past a bottom hole and surrounding loose psammoid (Sects. 14.4 and 14.6) can also lead to stationary flow in the vicinity. It is not yet known for such conditions whether and how the evolution can get stationary.

Except for a constant hydraulic height h_w evolutions of psammoids are different with *pore water*. With full saturation ($S_r = 1$) and high relative void ratio ($r_e > 1$) the skeleton decays, with low r_e suction can lead to cavitation, and even with an initially critical $r_e = 1$ and inevitable fluctuations around critical states a deterministic chaos can be enhanced by pore water. Transitions from and into open gas channels are always disordered. Humid granular materials can get homogeneous by mixing, but then the assumptions by which psammoids are defined can no more be defended.

Stationary responses of *peloid* bodies can be obtained with a wider range of initial states than with psammoids. Due to softer and smaller particles the range of void ratios between decay and cavitation is wider. The argotropy requires constant boundary velocities for stationarity. If these are as low as the permeability seepage can play a role throughout the peloid body. With higher consolidation ratios ($p_e/p_s > \text{ca. } 5$ initially) shearing is localized to so thin bands that seepage towards them can occur (Sect. 8.3). As then suction can also lead to cavitation evolutions with controlled total pressure tend to more chaotic than stationary features.

Critical phenomena can be investigated by *thin layer shearing* (Fig. 2.9.8). The psammoid or peloid sample is sheared between two filter plates with such a small distance that the free rim has little influence upon the major part of the interior. So this may be assumed to be and remain uniform as long as changes of pore pressure p_w are negligible in the time of shearing. With a constant normal force and monotonous shearing up to a stationary response the skeleton pressure p_s would then be given by the sheared area, a critical void ratio e_c and a critical friction angle φ_{cs} could thus be determined (cf. Sects. 2.9 and 3.8).

Higher than critical obliquities ($|T|/N > \tan \varphi_{sc}$) require lower than critical void ratios. If both ratios belong to a dilatant state limit (Sects. 2.9 and 3.8) continued shearing leads to localization with polar quantities so that the initial uniformity gets lost (Sects. 8.2 and 8.3). For shearing with constant velocity v of the top plate the shear force $|T|$ goes through a peak alongside with maximal dilation and acoustic emission. Seismic and thermal activation lead to a dilatant state limit and can cause cavitation.

Other so-called *element tests* with overcritical stress obliquities can at least in principle be treated similarly, but the often assumed uniformity of a single RSE can rarely be defended. Cylindrical homogeneous RSEs were assumed in Sects. 2.2 and 3.2 for the ease of introduction, but even short samples with smooth plates experience a loss of symmetry at critical points in triaxial tests (Sect. 14.1). Biaxial and cuboidal devices with nested smooth plates can produce a better uniformity up to critical points, so they are of use to validate assumed state limits (Sects. 2.7 and 3.7) and can indicate critical phenomena (Sects. 8.2 and 8.3). Samples sheared up to overcritical stress obliquities get less uniform already before a peak the more stress components are controlled by the device (Sects. 2.9 and 3.8).

Without the defining uniformity of RSEs evolutions with overcritical stress obliquities evolve through the psammoid and/or peloid body in the course of time. Simulations should take into account shear localizations with polar quantities and cracking with cavitation from the very beginning, and also phase transitions from or into skeletons in general. As this would be too expensive or not feasible one has to put up with a partial indeterminacy.

The *guided driving* of solid bodies past soil need not lead to critical phenomena if edges and too high average stress ratios are avoided. It appears that only thin layer shearing can produce a controllable evolution up to a critical point. Otherwise deviations from a mesh of simple psammoid and peloid elements may at best be kept small in an engineering sense. Rounding of edges or insertion of elastic strips there could suppress critical phenomena so that they are negligible for tolerable deformations. Further driving with free or pressure-controlled soil surfaces, however, leads inevitably to critical phenomena.

A loss of symmetry in the course of dilatant creep, in case of slender structures also by a geometrical feedback, impedes simulations and again localizations cannot be captured properly. So how can the *stability* of statical

equilibria be sufficiently assessed? And how can assumed symmetries be defended if they can get lost with a collapse? How could simplifying assumptions be defended and how could a sufficient ductility be warranted?

One way out of this misery could be achieved by simulations with disturbances. These could be represented in design scenarios by increased void ratios, and by increased viscosity exponents I_v which represent thermal and seismic activation (Sects. 3.2, 4.7 and 5.5). If simulations with legitimate symmetries yield a stabilization by densification and redistribution of skeleton and pore water pressures the system may be considered as ductile. Then calculated characteristic deformations may be used to judge the capability of involved structures. A loss of stability means the release of kinetic energy with a sudden growth of seismicity. If a destabilization is indicated by spontaneous accelerations the design should be changed, and a monitoring system should be employed so that an impending collapse could be recognized early enough.

There are no simple recipes for *early warning systems* as the features of deterministic chaos can be complex. Observed deformations may be used to judge elastic and brittle structures, but are hardly relevant for soils as for them deformations are no state variables. Monitoring of void ratios and mean skeleton pressures in significant regions would be desirable. Pore pressures can more easily be measured, their spontaneous rise in significant regions would indicate danger. A loss of stability could be recognized from pore pressure rises and increasing acoustic emissions, but interpretations of such fingerprints are still rather subjective. A decreasing propagation of shear waves could also indicate an impending collapse.

A skeleton decay would be indicated by an isotropic total pressure. It can occur in contractant saturated soils with low permeability, also with gas inclusions, and even without pore water. The subsequent flow of a suspension, which can be enhanced by the segregation of water or gas into cushions (Gudehus 1998), is outside the scope of this book. In a kind of sudden freezing solid particles can be recombined into skeletons, this happens typically alongside with outbursts from water or gas cushions.

A skeleton decay can lead to an *internal erosion*. In a simulation with hyp a loose psammoid layer was exposed to an upwards hydraulic gradient (Fig. 16.3.1). With a fluctuating void ratio (cf. Sect. 8.2) the seepage is concentrated in randomly distributed wider pore channels. These are widened by transversal seepage forces (cf. Sect. 14.2) so that the localized discharge of pore water is enhanced. This positive feedback, which resembles the one with a lightning (Sect. 16.1), leads to erosion and sand volcanos. A similar breakthrough occurs with a peloid layer kept above by a coarse filter with a critical gradient of hydraulic height h_w , $|i| = |\partial h_w / \partial x| = i_c$ (Sect. 8.4). The i_c of overconsolidated peloid can exceed 10^3 and is reduced by shear bands (Zou 2000).

Model tests with a hard-grained loose peloid with gas bubbles led to *mud volcanos*, Fig. 16.3.2. The peloid had first an inclined surface and slumped after slow pulsations of air pressure above the water table. The peloid was

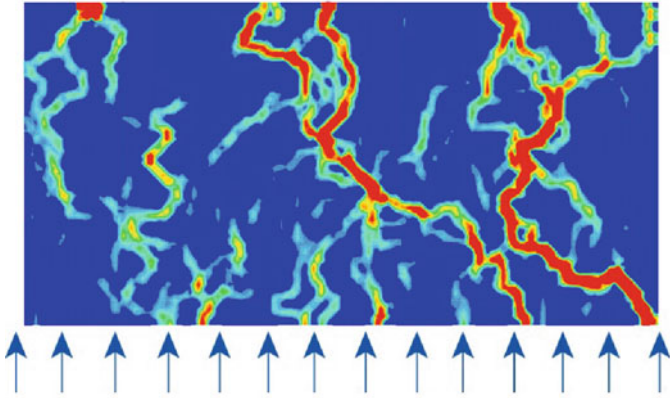


Fig. 16.3.1. Simulated hydraulic break-through in loose psammoid (courtesy K. Nübel and T. Wilhelm)

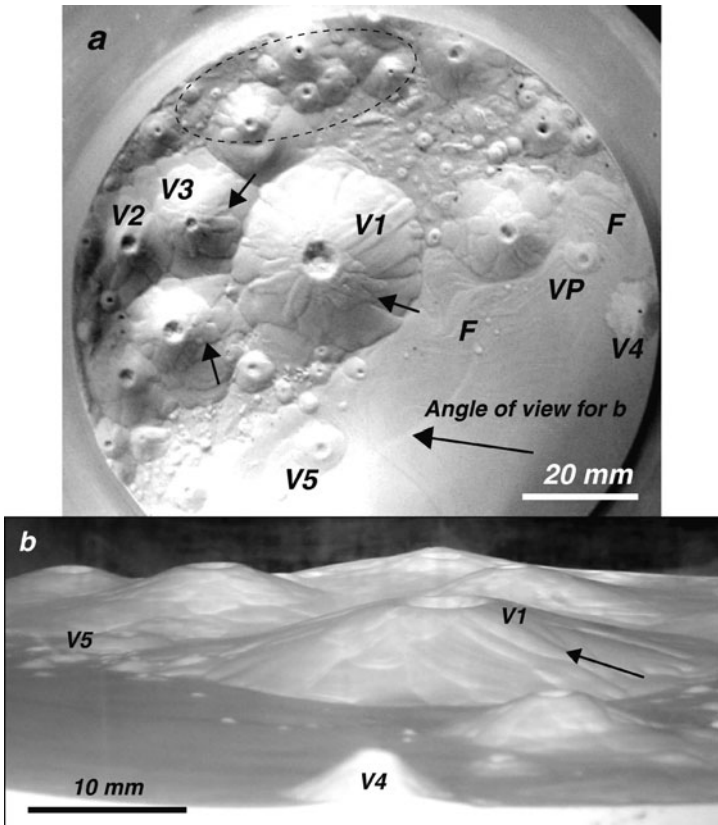


Fig. 16.3.2. Mud volcanos in a model test (Pralle et al. 2003)

thus densified and brought to skeleton decay, then the gas bubbles were no more kept and rose together with water and solid particles. As with diapirs (Fig. 14.2.9) the position of the break-out cannot be predicted, at best state conditions could be specified for such a critical point. In the case of Fig. 16.3.2 the skeleton was collapsible due to an overcritical void ratio, and also due to a minute net attraction (Sect. 6.2) which got lost by disturbance.

More dramatic outbursts can occur at faults. A clay smear (cf. Fig. 12.6.5) can sustain high hydraulic gradients with the aid of adjacent coarser gauge material from tectonic shearing. With sufficiently rapid changes of boundary conditions (e.g. depletion or earthquake) the critical gradient i_c can decrease, and the actual hydraulic gradient i can increase. With $i = i_c$ erosion channels evolve and release mud into the fault above, therein this rises up to the surface so that mud volcanos arise.

With *reversals* (cf. Sect. 4.7) evolutions can get more or less ordered than without. A stabilization can be obtained with so low amplitudes that the skeleton stress obliquities ($\tan \psi_s$ by Sects. 2.11 and 3.9) are always subcritical. With periodic boundary conditions the system can tend to state cycle fields without or with ratcheting, respectively. In transitions the skeleton is densified with seepage which is enhanced by reversals. With bigger amplitudes, and thus with temporarily overcritical stress obliquities, the evolutions get chaotic. With repeated shear localization, cracking and/or skeleton decay such evolutions are outside the reach of psammoid and peloid models as the topological order of skeletons can get lost by mixing and segregation.

To *sum up*, evolutions with overcritical stress ratios and/or skeleton decay can lead to deterministic chaos which cannot be captured by the models outlined in this book. State limits and state cycles may at best be approached with the aid of confining solid boundaries. Otherwise, and particularly if void ratios are near the bounds for given mean pressures, shear localization, cavitation or skeleton decay can evolve with increasingly disordered spatial and temporal distributions, and the topological order can get lost. One should avoid such losses of stability by design, execution and monitoring.

EPILOGUE

This book is voluminous, but far from complete as that is impossible with a living science. Applications require investigations in the lab and *in situ*, estimates for design and numerical simulations, and monitoring for technical operations and use. You can read a lot about all that elsewhere, and will make more of it with a better physical understanding. I will be grateful for criticism, more freely available software and further validation examples which could improve a next edition.

Research is going on. In the article ‘Seismo- and thermodynamics of granular solids’ (Gudehus et al. 2010) a theory named Granular Solid Hydrodynamics (GSH) is modified and strengthened with arguments from this book. Jiang and Liu (2009) worked before with uncommon liquids and call sand ‘singularly intricate’. The energy plays the key role, with the seismic part of it a granular temperature T_g and a specific granular entropy s_g are conjugated like their thermodynamic counterparts T and s . T_g is proportional to s_g , thus the microseismic energy is proportional to T_g^2 and to the density ρ . At thermodynamic equilibria with $T_g = 0$ the total skeleton and elastic stress tensors agree ($\sigma_{ij} = \pi_{ij}$), but then the field of ρ and σ_{ij} is not determined by conservation laws, elastic relations and boundary conditions. Seismodynamic equilibria have no elastic stress, but only an entropic pressure p_d , and exhibit stationary gradients of T_g . For suitable boundary conditions both kinds of equilibria are attractors with a minimum of the total free energy as far as stability is secured.

The evolution equations by GSH for π_{ij} , σ_{ij} , T and T_g imply the transition of seismic energy into heat and enable the fastest approach to the named equilibria. For uniform rather slow monotonous deformations they lead to SOM-states and nearly hypoplastic relations, whereas just after a reversal with a short rest the response by GSH is differentially elastic. This supports hyp and hyp- δ more than elp and elp- α , and provides a substitute of s-hyp and h-cyc. State limits can be approached with GSH, but not reached as then the elastic energy is no more a convex function of elastic strain and density. Realistic state cycles can be obtained asymptotically by GSH with slow cyclic

deformations and ratcheting, this supports elp- α and hyp- δ as far as these are confirmed by experiments. These validations indicate an energy-based substitute of the rather arbitrary and intricate constitutive relations used in this book. Observed attractors will be of use to calibrate and improve GSH.

Roscoe used to say ‘uniform critical states are an Eldorado, a golden country where you can never get’. The GSH-equations exclude uniform steady states, a slow stationary granular flow requires gradients. Such ‘flow equilibria’ cannot be critical as they imply dynamic stability. At the verge of static stability by GSH the elastic energy is no more a convex function of elastic strain and density. At such a critical point the imposed energy is fully transformed into seismicity, increasing fluctuations lead to pattern formation or chaos. Such critical phenomena are not yet captured by GSH, polar quantities are needed, but one can state already that critical points do not agree with conventional critical states.

Boundary value problems with GSH can be judged by means of the total free energy F of interacting granular and solid bodies. The gravitational part *in situ* exceeds by far the elastic part, and this exceeds even more the seismic part by T_g . Seismic activations matter nevertheless as they are focused on a minute fraction of the grain molecules near the grain contacts. Stabilizations with shaking boundaries (seismostats) mean a decelerating reduction of F by rearrangement (seismic creep) and a stress redistribution (seismic relaxation). Accelerating reductions of F with stationary seismostats mean a loss of stability (i.e. convexity of F as a functional of the field of elastic strain and density) with spontaneous growth of T_g in granular chain reactions. It appears that GSH can replace heuristic methods like s-hyp and h-cyc in Sects. 4.6 and 4.7, and that extensions of GSH will provide a more systematic approach to critical phenomena than throughout this book.

In general GSH does not imply constitutive relations for so-called simple materials in the sense of Truesdell and Noll (1965). Jiang and Liu (2009) refer to a paper by Temmen et al. (2000) which supersedes the Cauchy stress as independent variable and resolves the uncertainty of ‘co-rotational stress rates’. As indicated above an extension by polar terms is needed in general, this requires further boundary conditions (cf. Chap. 8). Decay and recombination of skeletons (i.e. granular solids) mean rather fractal transitions to and from suspensions or dust. All that calls for a revision of continuum approaches beyond this book, the consequences will be substantial in particular for evolutions beyond critical points.

This promising theory for dry hard-grained materials can be easily extended for pore water in case of full saturation. Its further quantification for applications will take years, however, and granular phase transitions are not strictly captured by the present GSH. In other words, this theory may first help to delimit elastoplastic and hypoplastic models for psammoids, and extensions could later deepen the understanding of critical phenomena. Soft particles with thermally activated viscosity could also be captured by an extended GSH, therein argotropic state limits can again be defined by the

verge of energetic convexity. The elastic stress can relax by T and T_g , this could help to support and substitute v-elp- α and v-hyp- δ . The stability could again be judged by means of the total free energy, now with simultaneous thermal and seismic activation. Argotropic SOM-states and state cycles could be used to check and calibrate such extensions. Shear localizations and other phase transitions including hydraulic, capillary and electrocapillary effects will pose harder problems.

The half-life of this book will hardly be shorter than anyway by GSH and its extensions. Deservedly energies will play a key role and attractors will remain useful, thus soil mechanics can get closer to the mainstream of physics. Numerical models should be Eulerian with gradient terms, and design assessments should refer to the total free energy. However, even further extensions of GSH will not answer all the open questions addressed in this book – and others which arise. The unification of seismo- and thermodynamics from particulate dynamics up to critical phenomena including capillary effects is a great task. Let us hope that mathematicians will provide suitable tools, in particular for attractors and in order to capture the mechanical roughness beyond Mandelbrot's fractal geometry. All that can enrich various branches of engineering and geo-science, the heat-like seismic energy is certainly not only relevant for soils. God knows when and how this will lead to a completely revised edition of the present book.

Even Newton said that he was standing on the shoulders of giants, but scientific work depends also on hands and hearts which deserve thanks. Demetrios Kolymbas, Mario Liu and Theodoros Triantafyllidis acted as reviewers. Andrzej Niemunis and his group created tools for numerical element tests and applied them in many examples for this book. David Masin and Arcesio Lizcano provided good advice, Toshihisha Adachi, Yannis Dafalias and David Muir Wood (to name only a few) were likewise open-minded partners. Gerhard Huber, Mauro Poblete, Daniel Rebstock and Hendrik Sturm helped me with the computer. My successor Th. Triantafyllidis granted technical support: Sigrid Rausch for typewriting, Maria Gödel for references, Svetlana Ayalowa for figures and layout. Springer gave professional advice. Friends and family tolerated my absent-mindedness, in particular my wife Soula. God helped with His blessings. Words cannot suffice to express my gratitude.

Symbols and Acronyms

Italic scalars

<i>A</i>	intensity factor for anelastic stretching
<i>a</i>	factor for hypoplasticity by (3.4.6)
<i>b</i>	breadth
<i>c</i>	cohesion
<i>D</i>	amount of stretching rate and tensor
<i>d</i>	diameter or thickness
<i>E</i>	modulus of elasticity, energy or earth pressure
<i>e</i>	void ratio
<i>F</i>	force
<i>f</i>	factor or function
<i>H</i>	step function
<i>h</i>	height, or force-roughness
<i>I_v</i>	viscosity index
<i>K</i>	ratio of horizontal and vertical stress components
<i>k</i>	factor (Darcy k_f , Boltzmann k_B)
<i>l</i>	length
<i>m</i>	factor or exponent
<i>N</i>	factor or normal force
<i>n</i>	exponent
<i>P</i>	power
<i>p</i>	pressure
<i>Q</i>	resultant force in slip surface
<i>q</i>	deviatoric stress of cylindrical RSE
<i>r</i>	radius
<i>r_e</i>	relative void ratio
<i>S_r</i>	degree of saturation
<i>T</i>	temperature
<i>u</i>	displacement or pore pressure
<i>V</i>	vertical force

v	velocity or specific volume
W	weight
w	water content
x, y, z	Cartesian coordinates

Greek scalars

α	fraction, exponent, angle or back-stress
β	exponent or angle
γ	shearing, angle or specific weight
Δ	difference
δ	angle or intergranular strain
ε	strain
θ	angle
κ	swelling index
λ	exponent or compression index
ν	Poisson ratio or dilatancy angle
σ	normal stress
τ	shear stress
φ	friction angle
χ	factor or angle
ψ	angle of stress obliquity
ω	frequency

Vectors, tensors and matrices

α_{ij}	back stress
D	stretching tensor
D_{ij}	components of stretching tensor
δ_{ij}	intergranular strain
h_{ij}	force-roughness
L_{ij}	matrix in linear part of hypoplastic relation
N_i	vector in nonlinear part of hypoplastic relation
σ_{ij}	components of stress tensor
T	stress tensor
v	velocity vector

Subscripts

a	air, adhesive or active
b	barotropy
c	critical or capillary
d	dense

e	equivalent or void ratio
ϵ	strain
$\dot{\epsilon}$	strain rate
f	flow or failure
g	granular or gas
h	force roughness
i	isotropic
n	net
p	peak or passive
r	reference, residual or radial
s	skeleton, seismic, stress or shear
u	undrained
v	volumetric or viscous
w	water
α	back stress
σ	stress

Superscripts

a	anelastic
e	elastic
p	plastic
v	viscous
'	effective
*	deviator

Acronyms

CSSM	Critical State Soil Mechanics
elp	elastoplastic, v- visco-, $-\alpha$ with back stress
h-cyc	high-cyclic
hyp	hypoplastic, v- visco-, $-\delta$ with intergranular strain
OCR	overconsolidation ratio
s-hyp	seismo-hypoplastic
SOM	swept-out memory
RSE	representative soil element

References

- Adachi T. and Oka F. Constitutive equations for normally consolidated clay based on elasto-viscoplasticity. *Soils Found.*, 22: 57–70, 1982.
- Airey D.W. and Wood D.M. An evaluation of direct simple shear tests on clay. *Géotechnique*, 37(1):25–35, 1987.
- Alonso E.E., Gens A., and Josa A. A constitutive model for partially saturated soils. *Géotechnique*, 40(3):405–430, 1990.
- Alonso-Marroquin F. and Herrmann H.J. Ratcheting of granular materials. *Phys. Rev. Lett.*, 92(5):054301, 2004.
- Alshibli K.A., Sture S., Costes N.C., Frank M.L., Lankton M.R., Batiste S.N., and Swanson R.A. Assessment of localized deformations in sand using X-ray computed tomography. *Geotech. Test. J.*, 23(3):274–299, 9 2000.
- Andersen K.H. Behaviour of clay subjected to undrained cyclic loading. In *Proceedings of the International Conference on Behaviour of Offshore Structures*, pages 392–403, Delft, 1976.
- Andersen K.H. and Berre T. Behaviour of a dense sand under monotonic and cyclic loading. In *Proceedings of the 12th ECSMGE, Geotechnical Engineering for Transportation Infrastructure*, pages 667–676, 1999.
- Andreotti B. The song of dunes as a wave-particle mode locking. *Phys. Rev. Lett.*, 93:238001, 12 2004.
- Arthur J.R.F. and Menzies B.K. Inherent anisotropy in a sand. *Géotechnique*, 22(1):115–128, 1972.
- Åstroem J.A., Herrmann H.J., and Timonen J. Granular packings and fault zones. *Phys. Rev. Lett.*, 84, 638–641, 2000.
- Atkinson J.H., Richardson D., and Stallebrass S.E. Effect of recent stress history on the stiffness of overconsolidated soil. *Géotechnique*, 40(4):531–540, 1990.
- Augustin S. *Untersuchungen zur Lagestabilität des Schotteroberbaus*. PhD thesis, Institute of Soil Mechanics and Rock Mech., University of Karlsruhe, Heft 154, 2002.
- Babuska I. and Oden J.T. The reliability of computer predictions: can they be trusted? *Int. J. Numer. Anal. Model.*, 3:255–272, 9 2006.

- Bak P., Tang C., and Wiesenfeld K. Self-organized criticality: An explanation of $1/f$ noise. *Phys. Rev. Lett.*, 59(4):381–384, 1987.
- Balthasar K., Gudehus G., Külzer M., and Libreros-Bertini A.B. Thin layer shearing of a highly plastic clay. *Nonlin. Proc. Geophys.*, 13:671–680, 11 2006.
- Barden L. Time-dependent deformations of normally consolidated clays and peats. *J. Soil Mech. Found. Div., ASCE*, 95(1):1–31, 1969.
- Barden L. and Khayatt A.J. Incremental strain rate ratios and strength of sand in the triaxial test. *Géotechnique*, 16:338–357, 1966.
- Barkan D.D. *Dynamics of Bases and Foundations*. McGraw-Hill Book Company, New York, 1962.
- Bauer E. Conditions for embedding Casagrande's critical states into hypoplasticity. *Mech. Cohes. Frict. Mater.*, 5:125–148, 2000.
- Bauer E. *Zum mechanischen Verhalten granularer Stoffe unter vorwiegend ödometrischer Beanspruchung*. PhD thesis, Institute Soil Mechanics and Rock Mechanics, University of Karlsruhe, Heft 130, 1992.
- Bauer E. Calibration of a comprehensive hypoplastic model for granular materials. *Soils Found.*, 36(1):13–26, 1996.
- Been K. and Jefferies M.G. A state parameter for sands. *Géotechnique*, 35(2): 99–112, 1985.
- Been K. and Sills G.C. Self-weight consolidation of soft soils: an experimental and theoretical study. *Géotechnique*, 31(4):519–535, 1981.
- Behringer R.P. and Miller B. Stress fluctuations for sheared 3D granular materials. In *Powders and Grains 97*, pages 333–336. A.A. Balkema: Rotterdam, 1997.
- Biot M.A. *Mechanics of Incremental Deformations*. Wiley, New York, 1965.
- Bishop A.W., Green G.E., Garga V.K., Andresen A., and Brown J.D. A new ring shear apparatus and its application to the measurement of residual strength. *Géotechnique*, 21(4):273–328, 1971.
- Bjerrum L. Stability of natural slopes in quick clay. *Géotechnique*, V(1):101–119, 3 1955.
- Bjerrum L. Problems of soil mechanics and construction on soft clays. In *State-of-the-Art Report to Sess. IV, 8th Int. Conf. Soil Mech. Found. Engg.*, pages 1–53. Moscow, 1973.
- Bjerrum L. and Landva A. Direct simple-shear tests on a Norwegian quick clay. *Géotechnique*, 16(1):1–20, 1966.
- Bliem C. *3D Finite Element Berechnungen im Tunnelbau*. PhD thesis, University of Innsbruck, Institute of Geotechnics and Tunnelling, Austria, Heft 4, 2001.
- Bobriakow A.P., Kosych V.Z., and Revushenko A.F. On temporal structures and processes of the deformation of granular matter. *Acad. Sci., Siberian Branch, All Union Sci. J., Phys. Tech. Probl. Mining*, 2:29–40, 1990. In Russian.
- Bogdanova-Bontcheva N. and Lippmann H. Rotationssymmetrisches ebenes Fließen eines granularen Modellmaterials. *Acta Mech.*, 21:93–113, 1975.

- Boscardin M.D. and Cording E.J. Building response to excavation-induced settlement. *J. Geotech. Eng. Div., ASCE*, 115(1):1–21, 1 1989.
- Bowden F.P. and Tabor D. *The Friction and Lubrication of Solids*. Clarendon Press, Oxford, 2nd edition. 1954.
- Brekhovskikh L.M. *Waves in Layered Media*. Academic Press, New York, 1960.
- Brooker E.W. and Ireland H.O. Earth pressures at rest related to stress history. *Can. Geotech. J.*, II(1):1–15, 2 1965.
- Brown S.F., Lashine A.K.F., and Hyde A.F.L. Repeated load triaxial testing of a silty clay. *Géotechnique*, 25(1):95–114, 1975.
- Bruce A. and Wallace D. *Critical Point Phenomena: Universal Physics at Large Length Scales*. The New Physics. Cambridge University Press, Cambridge, MA, 1989.
- Buchholtz V. and Pöschel T. Force distribution and comminution in ball mills. In *Friction Arching, Contact dynamics*, page 265. World Scientific, Singapore, 1997.
- Budhu M. Lateral stresses observed in two simple shear apparatus. *J. Geotech. Eng., ASCE*, 111(6):698–711, 6 1985.
- Bühler M.M. Ratcheting of a model pile in clay. Technical report, Institut für Bodenmechanik und Felsmechanik University of Karlsruhe, 2003.
- Bühler M.M. *Experimental and Numerical Investigation of Soil-Foundation-Structure Interaction during Monotonic, Alternating and Dynamic Loading*. PhD thesis, Institute of Soil Mechanics and Rock Mechanics University of Karlsruhe, Heft 166, 2006.
- Buisman A.S.K. *Grondmechanica*. Waltman, Delft, 1941.
- Butterfield R. A natural compression law for soils. *Géotechnique*, 29:469–480, 1979.
- Callisto L. and Rampello S. Shear strength and small-strain stiffness of a natural clay under general stress conditions. *Géotechnique*, 52(8):547–560, 2002.
- Calvetti F., Viggiani G., and Tamagnini C. Micromechanical inspection of constitutive modelling. In *Constitutive Modelling and Analysis of Boundary Value Problems in Geotechnical Engineering*, pages 187–216. Hevelius Edizion:, Benevento, 2003.
- Campanella R.G. and Vaid Y.P. Triaxial and plane strain creep rupture of an undisturbed clay. *Can. Geotech. J.*, 11(1):1–10, 2 1974.
- Caquot A. and Kérisel J. *Traité de Mécanique des Sols*. Gauthier-Villars, Paris, 1956.
- Carman P.C. *Flow of Gases Through Porous Media*. Academic Press, New York, 1956.
- Casagrande A. Characteristics of cohesionless soils affecting the stability of slopes and earth fills. *J. Boston Soc. Civil Eng.*, 23:257–276, 1 1936.
- Casagrande A. On liquefaction phenomena. *Géotechnique*, 22(3):197–202, 1971.
- Castro G. Liquefaction and cyclic mobility of saturated sands. *J. Geotech. Eng. Div., ASCE*, 101(GT6):551–569, 1975.

- Chang C. and Whitman V. Drained permanent deformation of sand due to cyclic loading. *J. Geotech. Eng. Div., ASCE*, 114(10):1164–1180, 1988.
- Cheang L. and Matlock H. Static and cyclic lateral load tests on instrumented piles in sand. Technical report, The Earth Technology Corporation and California Institute of Technology, Los Angeles, CA, 10 1981.
- Chu-Chung H. and Mladen V. Dynamic and cyclic behavior of soils over the wide range of shear strains in NGI-type simple shear testing devices. *Research Report UCLA ENG-02-228*, 1 2002.
- Chu J. and Lo S.-C.R. Asymptotic behaviour of a granular soil in strain path testing. *Géotechnique*, 44(1):65–82, 1994.
- Chu J., Lo S.-C.R., and Lee I.K. Strain softening and shear band formation of sand in multi-axial testing. *Géotechnique*, 46(1):63–82, 1996.
- Collin A. *Landslides in Clays*. University Press, Toronto, 1956. French original 1846, translation by W. R. Schriewer.
- Cornforth D.H. Some experiments on the influence of strain conditions on the strength of sand. *Géotechnique*, XIV: 143–167, 1964.
- Cornforth D.H. One-dimensional consolidation curves of a medium sand. *Géotechnique*, 24:678–683, 1974.
- Cosserat E. and Cosserat F. *Théorie des corps déformables*. Herman et fils, Paris, 1909.
- Coulomb M. *Essai sur une application des regles des Maximis et Minimis a quelques Problemes de Statique, relatifs a l'Architecture*. Editions Science et Industrie, Paris, 1773. reprint 1971.
- Cox A. D., Eason G., and Hopkins H.G. Axially symmetric plastic deformation in soils. *Phil. Trans. Roy. Soc.*, 254:1–45, 1961.
- Cudmani R. Anwendung der Hypoplastizität zur Interpretation von Drucksondierwiderständen in nicht-bindigen Böden. *Geotechnik*, 19(4):266–273, 1996.
- Cudmani R. *Statische, alternierende und dynamische Penetration in nicht-bindigen Böden*. PhD thesis, Institute Soil Mechanics and Rock Mechanics, University of Karlsruhe, Heft 152, 2001.
- Cudmani R. Fundamental aspects of soil response and soil-structure interaction during strong earthquakes, 2010. monography, under preparation.
- Cudmani R. and Osinov V.A. The cavity expansion problem for the interpretation of cone penetration and pressuremeter tests. *Can. Geotech. J.*, 38:622–638, 2001.
- Cudmani R. and Sedlacek G. Analytische und numerische Standsicherheitsanalyse der Schlitzwandherstellung in einem weichen marinen Ton in Oslo, Norwegen. *Geotechnik*, 29(3):272–288, 2006.
- Cudmani R. and Sturm H. An investigation of the tip resistance in granular and soft soils during static, alternating and dynamic penetration. In *Proceedings of the International Conference on Vibratory Driving and Deep Soil Compaction*, pages 221–231. 2006.
- Cudmani R., Huber G., and Gudehus G. A mechanical model for the investigation of the vibro-drivability of piles in cohesionless soils. In A.

- Holeyman et al., editor, *Proceedings of the International Conference on Vibratory Driving and Deep Soil Compaction*, pages 45–52. Louvain, 2002.
- Cudmani R., Meier T., and Wehr W. Entwicklung und Verifikation eines Verfahrens zur Bemessung von Rütteldruckverdichtungsmaßnahmen. In D. Fellin and W. Kolymbas, editors, *Bodenverdichtung. Experimente-Modellierung-Geräteentwicklung-Baustellenberichte-F+E-Bedarf*, pages 61–82. Innsbruck, 2003a.
- Cudmani R., Osinov V.A., Bühler M. M., and Gudehus G. A model for the evaluation of liquefaction susceptibility in layered soils due to earthquakes. In *Soil and Rock America*, pages 969–976. Glückauf, Essen, 2003b.
- Cuevas J.A. The floating foundation of the new building for the National Lottery of Mexico: An actual size study of the deformations of a flocculent-structured deep soil. In *Proceedings of the International Conference on Soil Mechanics and Foundation Engineering*, volume 1 pages 294–301. Cambridge, MA, 1936 (Volume 4).
- Cundall P.A., Drescher A., and Strack O.D.L. Numerical experiments on granular assemblies; measurements and observations. In *IUTAM Conf. Deformation and Failure of Granular Materials*, pages 355–370. Delft, 1982.
- D’Addetta G.A., Ramm E., Diebels S., and Ehlers W. A particle center based homogenization strategy for granular assemblies. *Eng. Computations*, 21(2/3):360–383, 2004.
- Dantu P. A contribution to the mechanical and geometrical study of non-cohesive masses. In *Proceedings of the 4th International Conference on Soil Mechanics and Foundation Engineering*, volume 1, pages 144–157. 1957.
- Darwin G.H. On the horizontal thrust of a mass of sand. In *Minutes of the Proceedings Institution of Civil Engineering*, pages 350–378. 1883.
- De Beer E.E. The scale effect in the transposition of the results of deep-sounding tests on the ultimate bearing capacity of piles and caisson foundations. *Géotechnique*, 13:39–75, 1963.
- De Josselin De Jong G. Rowe’s stress-dilatancy relation based on friction. *Géotechnique*, 26(3):527–534, 1976.
- Demian F. *Achsensymmetrische Spannungs- und Verformungsfelder in trockenem Sand*. PhD thesis, Institute of Soil Mechanics and Rock Mechanics University of Karlsruhe, Heft 62, 1975.
- Den Haan E.J. and Kamao S. Obtaining isotache parameters from a c.r.s. k_o -oedometer. *Soils Found.*, 43(4):203–214, 8 2003.
- Derjaguin B.V. Investigation of the properties of water II. *J. Colloid Interface Sci.*, 38 (4):415–426, 1971.
- Derjaguin B.V. and Churaev N.V. Nature of anomalous water. *Nature*, 244: 430–431, 8 1973.
- Derjaguin B.V., Karasev V.V., and Khromova E.N. Thermal expansion of water in fine pores. *J. Colloid Interface Sci.*, 109 (2):586–587, 1986.

- Desrues J., Chambon R., Mokni M., and Mazerolle F. Void ratio evolution inside shear bands in triaxial sand specimens studied by computed tomography. *Géotechnique*, 46(3):529–546, 1996.
- De Wit J.C.W.M. and Lengkeek H.J. Full scale test on environmental impact of diaphragm wall trench installation in Amsterdam. *Proceedings of the International Symposium on Geotechnical Aspects of Underground Construction in Soft Ground*, 2002. available online.
- Di Biaggio E. and Myrvoll F. Full scale field test of a slurry trench excavation in soft clay. In *Proceedings of the 15th European Conference Soil Mechanics and Foundation Engineering*, pages 461–471, Madrid, 1972.
- Dierssen G. *Ein bodenmechanisches Modell zur Beschreibung des Vibrationsrammens in körnigen Böden*. PhD thesis, Institute of Soil Mechanics and Rock Mechanics, University of Karlsruhe, Heft 133, 1994.
- Dijkstra M., Hansen J.-P., and Madden P.A. Statistical model for the structure and gelation of smectite clay suspensions. *Am. Phys. Soc.*, 55(3): 3044–3053, 1997.
- Duttine A., Tatsuoka F., Kongkitkul W., and Hirakawa D. Viscous behaviour of unbound granular materials in direct shear. *Soils Found.*, 48 (3):297–318, 2008.
- Edwards S.F. and Oakeshott R.B.S. Granular matter: An interdisciplinary approach. *Physica A*, 157:1080, 1989.
- Evans R. Fluids adsorbed in narrow pores: Phase equilibria and structure. *J. Phys. Condens. Matter*, 2:8989–9007, 1990.
- Fam M. and Santamarina J.C. Coupled diffusion-fabric-flow phenomena: An effective stress analysis. *Can. Geotech. J.*, 33:515–522, 1996.
- Fellenius W. *Erdstatische Berechnungen*. Ernst und Sohn, Berlin, 2 edition, 1948.
- Fellin W. RDV-online: ein Qualitätssicherungssystem für die Rütteldruckverdichtung. In J. Grabe, editor. *Bodenverdichtung. Experimente – Modellierung – Geräteentwicklung – Baustellenberichte – F+E-Bedarf*. Veröff. Fachbereich Geotechnik und Baubetrieb/TU Hamburg-Harburg 5, pages 199–214, 2003.
- Feynman C. and Goodstein J.R. *Feynman's Lost Lecture: The Motion of Planets Around the Sun*. Norton, W.W. and Company Inc., New York, 2000.
- Feynman R.P., Leighton R.B., and Sands M. *The Feynman Lectures on Physics*; volume I. Mainly Mechanics, Radiation, and Heat, Addison Wesley, California, 1966.
- Fillunger P. *Erdbaumechanik?* Buchdruckerei F. Jasper, Wien, 1936.
- Finno R.J., Harris W.W., Mooney M.A., and Viggiani G. Shear bands in plane strain compression of loose sand. *Géotechnique*, 47(1):149–165, 1997.
- Franke E., Kiekbusch M., and Schuppener B. A new direct simple shear device. *Geotech. Test. J.*, 2(4):190–199, 1979.
- Fredlund D.G. and Rahardjo H. *Soil Mechanics for Unsaturated Soils*. Wiley, New York, 1993.

- Fujiwara H., Ue S., and Yasuhara K. Secondary compression of clay under repeated loading. *Soils Found.*, 27(2):21–30, 6 1985.
- Gäßler G. Vernagelte Geländesprünge – Tragverhalten und Standsicherheit. PhD thesis, *Veröff. Inst. Boden-u. Felsmech. Univ. Karlsruhe*, Heft 108, 1987.
- Gajo A. and Muir Wood D. Severn-Trent sand: A kinematic-hardening constitutive model: The q-p formulation. *Géotechnique*, 49(5):595–614, 1999.
- Garcia F., Lizcano A., and Reul O. Numerical modelling of the case history of a piled raft with a viscohypoplastic model. In T. Triantafyllidis, editor, *Numerical Modelling of Construction Processes in Geotechnical Engineering for Urban Environment*, pages 265–272, Bochum, 2006.
- Garcia-Rojo R. A general micromorphic theory of kinematics and stress in granular media. In *Powders and Grains 05*, pages 129–133. Taylor & Francis Group, London, 2005.
- Garga V.K. and Infante Sedano J.-A. Steady state strength of sands in a constant volume ring shear apparatus. *Geotech. Test. J.*, 25(4):131–148, 12 2002.
- Gelb L.D., Gubbins K.E., Radhakrishnan R., and Sliwinska-Bartowiak M. Phase separation in confined systems. *Rep. Prog. Phys.*, 62:1573–1659, 1999.
- Gibson R.E. The analytical method in soil mechanics. *Géotechnique*, 24:115–140, 1974.
- Goddard J.D. A general micromorphic theory of kinematics and stress in granular media. *Powders Grains 05*, 1:129–134, 2005.
- Goldscheider M. Dilatanzverhalten von Sand bei geknickten Verformungswegen. *Mech. Res. Commun.*, 2:143–148, 1975.
- Goldscheider M. Grenzbedingung und Fließregel von Sand. *Mech. Res. Commun.*, 3:463–468, 1976.
- Goldscheider M. True triaxial tests on dense sand. In I. Vardoulakis, G. Gudehus, F. Darve, editors, *Constitutive Relations for Soils*, pages 11–54. Balkema, Rotterdam, 1984.
- Goldscheider M. and Böisinger E. Bestimmung der Scherfestigkeit von Ton-schichten im Bereich tiefer Tagebaurandböschungen. *Neue Bergbautechnik*, 19,2(3):87–90, 3 1989.
- Goldscheider M. and Gudehus G. Rectilinear extension of dry sand: testing apparatus and experimental results. In *Proceedings of the 8th International Conference on Soil Mechanics and Foundation Engineering*, volume 1/21 143–149, 1973.
- Goldscheider M. and Lizcano A. Standsicherheitsuntersuchung für ein räumliches Böschungsmodell (Teil 2). *Bautechnik*, 1:9–16, 2004.
- Graf B. *Theoretische und experimentelle Ermittlung des Vertikaldrucks auf eingebettete Bauwerke*. PhD thesis, Institute of Soil Mechanics and Rock Mechanics, University of Karlsruhe, Heft 96, 1984.

- Grandas-Tavera C.E. *Dynamische Konsolidierung von granularen wassergesättigten Böden*. PhD thesis, Institute of Soil Mechanics and Rock Mechanics, University of Karlsruhe, 2010, Under preparation.
- Griffith A.A. The phenomena of rupture and flow in solids. *Phil. Trans. Roy. Soc.*, 221:163–198, 1921.
- Gudehus G. Lower and upper bounds for stability of earth-retaining structures. *Proceedings of the 5th European Conference on Soil Mechanics and Foundation Engineering*, 1:21–28, 1972.
- Gudehus G. A comparison of some constitutive laws under radially symmetric loading and unloading. In W. Wittke, editor, *Proc. 3rd Int. Conf. Num. Meth. Geomech.*, pages 1309–1323. Balkema, Aachen, 1979
- Gudehus G. *Bodenmechanik*. Ferdinand Enke, Stuttgart, 1981.
- Gudehus G. Seitendruck auf Pfählen in tonigen Böden. *Geotechnik*, 7:73–87, 1984.
- Gudehus G. A comprehensive concept for non-saturated granular bodies. In *Proceeding of the 1st International Conference on Soil Mechanics on Unsaturated Soils*, pages 725–737, Paris, 1995.
- Gudehus G. A comprehensive constitutive equation for granular materials. *Soils Found.*, 36(1):1–12, 1996.
- Gudehus G. On the onset of avalanches in flooded loose sand. *Phil. Trans. R. Soc. Lond. A*, 356:2747–2761, 1998.
- Gudehus G. *Earth Pressure Determination*, volume 1: Fundamentals, pages 407–436. Ernst und Sohn, Berlin, 2002.
- Gudehus G. Seismic decay of psammoids and peloids with and without hypoplasticity. In T. Triantafyllidis, editor, *Cyclic Behaviour of Soils and Liquefaction Phenomena*, pages 11–20. Balkema, Bochum, 2004a.
- Gudehus G. A visco-hypoplastic relation for soft soil. *Soils Found.*, 44(4):11–25, 8 2004b.
- Gudehus G. Seismo-hypoplasticity with a granular temperature. *Granular Matter*, 8(2):93–102, 2006.
- Gudehus G. and Karcher C. Hypoplastic simulation of normal faults without and with clay smears. *J. Struct. Geol.*, 29:530–540, 2007.
- Gudehus G. and Mašin D. Graphical representation of constitutive equations. *Géotechnique*, 2, 2010.
- Gudehus G. and Mikulitsch V. Materialverhalten zementierter Korngerüste. *Der Bauingenieur*, 71:119–126, 1996.
- Gudehus G. and Nübel K. Evolution of shear bands in sand. *Géotechnique*, 54(3):187–201, 2004.
- Gudehus G. and Pierschke K.-J. Landslides with natural pre-existing slip planes. *World Min. Surf. Undergr.*, 56(6):430–441, 2004.
- Gudehus G. and Wichter L. Case study of a landslide in jointed and layered red marl. In Assoz. Geot. Ital., editor, *Proceedings of the International Symposium on Geotechnical Complex Formations*, pages 269–280. Capri, 1977.

- Gudehus G., Goldscheider M., and Winter H. *Mechanical Properties of Sand and Clay and Numerical Integration Methods: Some Sources of Errors and Bounds of Accuracy*, pages 121–150. Balkema, Rotterdam, 1977.
- Gudehus G., Loukachev I., and Pralle N. Inelastic behaviour of grain skeletons with propagation of shear waves. In Y. Kishino, editor, *Powders and Grains 4*, pages 125–128. Sendai, Japan, 2001.
- Gudehus G., Cudmani R., Libreros-Bertini A.B., and Bühler M.M. In-plane and anti-plane strong shaking of soil systems and structures. *Soil Dyn. Earthquake Eng.*, 24:319–342, 2004.
- Gudehus G., Jiang Y., and Liu M. Seismodynamics and thermodynamics of granular solids. *Granular Matter*, 2010, accepted.
- Günther W. Zur Statik und Kinematik des Cosseratschen Kontinuums. *Abh. Braunschweig. Wiss. Ges.*, 10:195–213, 1958.
- Gussmann P. Verschiebungsgesteuerte Konsolidationsprobleme. *Acta Mechan.*, 34:271–278, 1979.
- Guyon E. and Troadec J.-P. *Du sac de billes au tas de sable*. Odile Jacob, Paris, 1994.
- Haar A. and von Karman Th. Plastic deformations in soils. *Nachr. Ges. Wiss. Gött.*, page 204, 1909.
- Haff P.K. Grain flow as a fluid-mechanical phenomenon. *J. Fluid Mech.*, 134:401–430, 1983.
- Hambly E.C. Plane strain behaviour of remoulded normally consolidated kaolin. *Géotechnique*, 22 (2):301–317, 1972.
- Hardin B.O. and Black W.L. Vibration modulus of normally consolidated clay. *J. Soil Mech. Found. Eng. Div., ASCE*, 94 (2):353–368, 1968.
- Hardin B.O. and Drnevich V.P. Shear modulus and damping in soils; ii. design equations and curves. *J. Soil Mech. Found. Div., ASCE*, 98 (SM7):667–692, 7 1972.
- Henkel D.J. The effect of overconsolidation on the behaviour of clays during shear. *Géotechnique*, VI:139–150, 1956.
- Henkel D.J. The relationships between the strength, pore-water pressure, and volume-change characteristics of saturated clays. *Géotechnique*, 9(3): 119–135, 1959.
- Henkel D.J. The relationships between the effective stresses and water content in saturated clays. *Géotechnique*, 10:41–54, 1960.
- Herle I. and Gudehus G. Determination of parameters of a hypoplastic constitutive model from properties of grain assemblies. *Mech. Coh. Frict. Mater.*, 4:461–486, 1999.
- Herle I. and Tejchman J. Effects of grain size and pressure level on bearing capacity of footings on sand. *Deform. Prog. Fail. Geomech.*, 781–786, 1997.
- Herrmann H.J. On the thermodynamics of granular media. *J. Phys. II France*, 3:427–433, 1993.
- Hicher P.Y. and Lade P.V. Rotation of principal directions in k_0 -consolidated clay. *J. Geotech. Eng. Div., ASCE*, 113(7):774–787, 7 1987.

- Hicher P.Y. and Wahyudi H. Microstructural analysis of strain localisation in clay. *Comput. Geotech.*, 16:205–222, 1994.
- Hidalgo R.C, Grosse C.U., Kun F., Reinhardt H.W., and Herrmann H.J. Evolution of percolating force chains in compressed granular media. *Phys. Rev. Let.*, 89, 10 2001.
- Higo Y. *Instability and Strain Localization Analysis of Water-saturated Clay by Elasto-viscoplastic Constitutive Models*. PhD thesis, Soil Mechanics, Department of Civil Engineering, Kyoto University, 2003.
- Hirschfeld R.C. and Poulos S.J. High-pressure triaxial tests on a compacted sand and an undisturbed silt. *ASTM, Lab. Shear Test. Soils, Tech. Publ.*, 361:329–339, 1963.
- Hong W.P. and Lade P.V. Elasto-plastic behavior of k_o -consolidated clay in torsion shear tests. *Soils Found.*, 29(2):127–140, 6 1989.
- Horn R.G. Surface forces and their action in ceramic materials. *J. Am. Ceram. Soc.*, 73(5):1117–1135, 1990.
- Howard D.A. *Einstein's Philosophy of Science*. 2004. available via Internet.
- Howell D.W., Behringer R.P., and Veje C. T. Fluctuations in granular media. *Chaos*, 9 (3):559–572, 1999.
- Hsu C.-C. and Vucetic M. Dynamic and cyclic behavior of soils over the wide range of shear strains in NGI-type simple shear testing devices. Technical report, 2002.
- Huang W. and Bauer E. Numerical investigations of shear localization in a micro-polar hypoplastic material. *Int. J. Numer. Anal. Meth. Geomech.*, 27: 325–352, 2003.
- Huber G. Asymptotic behaviour of sand in resonant-column tests. *Granular Matter*, 2010. under preparation.
- Huber G. and Wienbroer H. Vibro-viscosity and granular temperature of cylindrical grain skeletons-experiments. In M.J. Herrmann, R. Garcia-Rojo and S. McNamara, editors, *Powders and Grains 05*, pages 287–290. Balkema, Rotterdam, 2005.
- Hungr O. and Morgenstern N.R. High velocity ring shear tests on sand. *Géotechnique*, 34: 415–421, 1984.
- Hunter G. and Fell R. Prediction of impending failure of embankments on soft ground. *Can. Geotech. J.*, 40:209–220, 2003.
- Hvorslev M. J. *Ueber die Festigkeitseigenschaften gestörter bindiger Böden*. Number 45. Danmarks Naturvidenskabelige Samfund, Ingeniorvidenskabelige Skrifter A, 1937.
- Hvorslev M.J. Physical components of the shear strength of saturated clays. *Res. Conf. Shear Strength and Cohesive Soils*, page 169. Colorado, 1960.
- Hyde A.F.L. and Ward S.J. A pore pressure and stability model for a silty clay under repeated loading. *Géotechnique*, 35(2):113–125, 1985.
- Hyodo M., Murata H., Yasufuku N., and Fujii T. Undrained cyclic shear strength and deformation of sands subjected to initial static shear stress. In *Proceedings of the 4th International Conference on Soil Dynamics and Earthquake Engineering*, pages 81–103. Mexico City, 1989.

- Hyodo M., Yasuhara K., and Hirao K. Prediction of clay behaviour in undrained and partially drained cyclic triaxial tests. *Soils Found.*, 32(4):117–127, 12 1992.
- Hyodo M., Hyde A.F.L., Yamamoto Y., and Fujii T. Cyclic shear strength of undisturbed and remoulded marine clays. *Soils Found.*, 39(2):45–58, 4 1999.
- Iai S., Ichii K., Liu H., and Morita T. Effective stress analyses of port structures. *Soils Found.*, Special Issue(2):97–114, 9 1998.
- Ibsen L.B. The stable state in cyclic triaxial testing on sand. *Soil Dyn. Earthquake Eng.*, 13:63–72, 1994.
- Ibsen L.B. and Praastrup U. The Danish rigid boundary true triaxial apparatus for soil testing. *Geotech. Test. J.*, 25(3):254–264, 9 2002.
- Ippolito I., Annic C., Lemaitre J., Oger L., and Bideau D. Granular temperature: Experimental analysis. *Phys. Rev. E*, 52(2):2072–2075, 8 1995.
- Irwin G.R. Analysis of stresses and strains near the end of a crack. *J. Appl. Mech.*, 24:361, 1957.
- Ishihara K. Liquefaction and flow failure during earthquakes. *Géotechnique*, 43(3):351–415, 1993.
- Ishihara K. and Towhata I. Sand response to cyclic rotation of principal stress directions as induced by wave loads. *Soils Found.*, 23(4):11–26, 1983.
- Israelachvili J.N. *Intermolecular and Surface Forces*. Academic Press, London, 2 edition. 1995.
- Iwan W.D. A distributed-element model for hysteresis and its steady-state dynamic response. *J. Appl. Mech.*, 893–900, 12 1966.
- Iwasaki Y. and Tai M. Strong motion records at Kobe Port Island. *Soils Found.*, Special Issue(2):191–205, 1996.
- Iwasaki T., Tatsuoka F., and Takagi Y. Shear moduli of sands under cyclic torsional shear loading. *Soils Found.*, 18(1):39–56, 1978.
- Jaeger H.M., Nagel S.R., and Behringer R.P. Granular solids, liquids, and gases. *Rev. Modern Phys.*, 68(4):1259–1273, 10 1996.
- Jagau H. *Verhalten unvorbelasteter tonig-schluffiger Böden unter zyklischen Einwirkungen*. PhD thesis, Institute of Soil Mechanics and Rock Mechanics, University of Karlsruhe, Heft 118, 1990.
- Jaky J. Minimum values of earth pressure. In *Proceedings of the 2nd International Conference on Soil Mechanics and Foundation Engineering*, volume 1, pages 103–107. 1948.
- Janssen H.A. Versuche über Getreidedruck in Silozellen. *Zeitschr. d. Vereines deutscher Ingenieure*, 1045, 1895.
- Jefferies M.G. Plastic work and isotropic softening in unloading. *Géotechnique*, 47(5):1037–1042, 1997.
- Jenike A.W. Steady gravity flow of frictional-cohesive solids in converging channels. *J. Appl. Mech.*, 31:5–11, 3 1964.
- Jennings J.E.B. and Burland J.B. Limitations to the use of effective stresses in partly saturated soils. *Géotechnique*, XII:125–146, 1962.

- Jiang Y. and Liu M. Granular solid hydrodynamics. *Granular Matter*, 11, 2009.
- Johnson K.L. *Contact Mechanics*. Cambridge University Press, Cambridge, MA, 1985.
- Jovanovic M. *Historische Holzgründungen – Tragverhalten in weichem Baugrund*. PhD thesis, Institute of Soil Mechanics and Rock Mechanics, University of Karlsruhe, Heft 153, 2002.
- Kadanoff L.P. *Chaos and Complexity: The Results of Non-linear Processes in the Physical World*, volume 57, pages 127–139. Springer, Berlin etc., 1991.
- Kagawa T. Moduli and damping factors of soft marine clays. *J. Geotech. Eng., ASCE*, 118(9):1360–1375, 1992.
- Kaliakin V.N. and Dafalias Y.F. Theoretical aspects of the elastoplastic-viscoplastic bounding surface model for cohesive soils. *Soils Found.*, 30(3):11–24, 9 1990.
- Karcher C. *Tagebaubedingte Deformationen im Lockergestein*. PhD thesis, Institute of Soil Mechanics and Rock Mechanics, University of Karlsruhe, Heft 160, 2003.
- Katzenbach R. and Festag G. Material behaviour of dry sand under cyclic loading. In *International Conference on “Cyclic Behaviour of Soils and Liquefaction Phenomena”*, pages 153–158, Bochum, 2004.
- Kirkgard M.M. and Lade P.V. Anisotropic three-dimensional behavior of a normally consolidated clay. *Can. Geotech. J.*, 30:848–858, 1993.
- Klobe B. *Eindimensionale Kompression und Konsolidation und darauf basierende Verfahren zur Setzungsprognose*. PhD thesis, Institute of Soil Mechanics and Rock Mechanics, University of Karlsruhe, Heft 128, 1992.
- Knufinke H.V. and Kothen H. Die Tektonik der Niederrheinischen Bucht vor, während und nach der Hauptflächenbildung. *Braunkohle*, 473–479, 1995.
- Koeppe J., Enz M., and Kakalios J. Avalanche segregation of granular media. *Powders and Grains*, 443–446, 1997.
- Koiter W.T. General theorems for plastic solids. *Prog. Solid Mech.*, 165, 1958.
- Kokusho T. Formation of water film in liquefied sand and its effect on lateral spread. *J. Geotech. Geoenv. Eng.*, 125(10):817–826, 1999.
- Kolmogorov A.N. Über das logarithmisch normale Verteilungsgesetz der Dimensionen der Teilchen bei Zerstückelung. *Dokl. Akad. Nauk SSSR*, 31:99–101, 1941.
- Kolymbas D. *Ein nichtlineares viskoplastisches Stoffgesetz für Böden*. PhD thesis, Institute of Soil Mechanics and Rock Mechanics, University of Karlsruhe, Heft 77, 1978.
- Kolymbas D. Vereinfachte statische Berechnung der Firste eines Tunnels in massigem Fels. *Rock Mech.*, 14:201–207, 1982.
- Kolymbas D. An outline of hypoplasticity. *Arch. Appl. Mech.*, 61:143–151, 1991.
- Kolymbas D. Behaviour of liquefied sand. *Phil. Trans. Roy. Soc. Lond. A*, 356:2609–2622, 1998.

- Kondic L. and Behringer R.P. Elastic energy, fluctuations and temperature for granular materials. *Europhys. Lett.*, 67(2):205–211, 2004.
- Kort D.A. *Steel Sheet Pile Walls in Soft Soil*. PhD thesis, Technical University Delft, Delft, 2002.
- Krieg S. *Viskoses Bodenverhalten von Mudden, Seeton und Klei*. PhD thesis, Institute of Soil Mechanics and Rock Mechanics, University of Karlsruhe, Heft 150, 2000.
- Krieg S., Lächler W., and Siebler G. Geotechnische Besonderheiten bei einer grossen Baugrube mit Randbebauung in Konstanzer Seeton. Technical Report 36, Lehrstuhl und Prüfamf für Grundbau, Bodenmech. und Felsmech. der TU München, 2004.
- Kudella P. *Mechanismen der Bodenverdrängung beim Einpressen von Fluiden zur Baugrundverfestigung*. PhD thesis, Institute of Soil Mechanics and Rock Mechanics, University of Karlsruhe, Heft 132, 1994.
- Kudella P. and Reul O. Hypoplastic analyses of piled rafts. *Numer. Meth. Geotech. Eng.*, 389–396, 2002.
- Külzer M. *State Limits of Peloids*. PhD thesis, Institute of Soil Mechanics and Rock Mechanics, University Karlsruhe, 2010, under preparation.
- Kuntsche K. Response of kaolin to reversals of strain path in undrained triaxial tests. In G.N. Pande and O.C. Zienkiewicz, editors, *Int. Symp. Soils Cycl. and Trans. Loadg.*, pages 179–186. Swansea, 1980.
- Kuntsche K. *Materialverhalten von wassergesättigtem Ton bei ebenen und zylindrischen Verformungen*. PhD thesis, Institute of Soil Mechanics and Rock Mechanics, University of Karlsruhe, Heft 91, 1982.
- Kuntsche K. Beurteilung der Standfestigkeit einer tiefen Tagebau-randböschung bei maximaler Lagerstättennutzung. *Neue Bergbautechnik*, 19(2):83–86, 1989.
- Kuroda M. and Tvergaard V. A phenomenological plasticity model with non-normality effects representing observations in crystal plasticity. *J. Mech. Phys. Solids*, 49:1239–1263, 2001.
- Kuwano R. and Jardine R.J. On the applicability of cross-anisotropic elasticity to granular materials at very small strains. *Géotechnique*, 52(10):727–749, 2002.
- Lade P.V. Elasto-plastic stress-strain theory for cohesionless soil with curved yield surfaces. *Int. J. Solids Struct.*, 13:1019–1035, 1977.
- Lade P.V. and Duncan J.M. Cubical triaxial tests on cohesionless soil. *J. Soil Mech. Found. Div., ASCE*, 99(10):793–812, 1973.
- Lagioia R. and Nova R. An experimental and theoretical study of the behaviour of a calcarenite in triaxial compression. *Géotechnique*, 45(4):633–648, 1995.
- Lam W.-K. and Tatsuoaka F. Effects of initial anisotropic fabric and σ_2 on strength and deformation characteristics of sand. *Soils Found.*, 28(1):89–106, 3 1988.
- Lanier J. and Zitouni Z. Development of a data base using the Grenoble true triaxial apparatus. In A.S. Saada and G.F. Bianchini, editors, *Constitutive*

- Equations for Granular Non-Cohesive Soils*, pages 47–57. Balkema, Rotterdam, 1988.
- Lanier J., Di Prisco C., and Nova R. Étude expérimentale et analyse théorique de l'anisotropie induite du sable d'Hostun. *Rev. Franç. Géotech.*, 57, 59–74, 1991.
- Lätzel M., Luding S., and Herrmann H.J. Macroscopic material properties from quasi-static, microscopic simulations of a two-dimensional shear-cell. *Granular Matter*, 2(3):123–135, 2000.
- Laudahn A. *An Approach to 1g Modelling in Geotechnical Engineering with Soiltron*. PhD thesis, University of Innsbruck, Institute of Geotechnics and Tunnelling, Austria, Heft 11, 2005.
- Lehner F.K. and Pilaar W.F. The emplacement of clay smears in synsedimentary normal faults: Inferences from field observations near Frechen, Germany. *Hydrocarbon Seals*, 39–50, 1995.
- Leinenkugel H.J. *Deformations- und Festigkeitsverhalten bindiger Erdstoffe, experimentelle Ergebnisse und ihre physikalische Deutung*. PhD thesis, Institute of Soil Mechanics and Rock Mechanics, University of Karlsruhe, Heft 66, 1976.
- Leussink H., Blinde A., and Abel P.-G. Versuche über die Sohldruckverteilung unter starren Gründungskörpern auf kohäsionslosem Sand. Technical report, Institute of Soil Mechanics and Rock Mechanics, University of Karlsruhe, Heft 22, 1966.
- Lewin P.I. and Burland J.B. Stress-probe experiments on saturated normally consolidated clay. *Géotechnique*, 20(1):38–56, 1970.
- Libreros-Bertini A.B. *Hypo- und viskohyoplastische Modellierung von Kriech- und Rutschbewegungen, besonders infolge Starkbeben*. PhD thesis, Institute of Soil Mechanics and Rock Mechanics, University of Karlsruhe, Heft 165, 2006.
- Lippmann R. *Ingenieurgeologische Kriechhangsicherung durch Dübel*. PhD thesis, Institute of Soil Mechanics and Rock Mechanics, University of Karlsruhe, Heft 111, 1988.
- Lizcano A. *Standardsicherheitsberechnungen symmetrischer Böschungssysteme mit räumlichen Bruchmechanismen*. PhD thesis, Institute of Soil Mechanics and Rock Mechanics, University of Karlsruhe, Heft 161, 2004.
- Loukachev I. Dilatanzverhalten und Schichttrennung bei Wellenausbreitung in sandigen Böden. PhD thesis, *Veröff. Inst. Boden- u. Felsmech. Univ. Karlsruhe*, Heft 155, 2002
- Lungu D.A. Hazard and risk mitigation. In *Vrancea Earthquakes: Tectonics (Near-Surface Geology Aldea und Dynamic Properties of Soil Layers in Bucharest)*. Kluwer Academic Publisher, Germany, 2003.
- Luong M.P. Mechanical aspects and thermal effects of cohesionless soils under cyclic and transient loading. In *Proceedings of the IUTAM Conference on Deformation and Failure of Granular Materials*, Delft, pages 239–246, 1982.
- Maatouk A., Leroueil S., and La Rochelle P. Yielding and critical state of a collapsible unsaturated silty soil. *Géotechnique*, 45(3):465–477, 1995.

- Mach E. *Die Mechanik in ihrer Entwicklung, historisch-kritisch dargestellt*. Brockhaus, Leipzig, 7 edition. 1912.
- Mahutka K.-P., König F., and Grabe J. Numerical modelling of pile jacking, driving and vibratory driving. In T. Triantafyllidis, editor, *Numerical Modelling of Construction Processes in Geotechnical Engineering for Urban Environment*, pages 235–246. Bochum, 2006.
- Maisch K. *Bodenstabilisierung durch Einpressen von Trockengranulaten*. PhD thesis, Institute of Soil Mechanics and Rock Mechanics, University of Karlsruhe, Heft 149, 2000.
- Mandelbrot B.B. *The Fractal Geometry of Nature*. W.H. Freeman, New York, 1982.
- Mandl G. *Mechanics of Tectonic Faulting, Models and Basic Concepts*. Elsevier, Amsterdam, 1988.
- Manzari M.T. and Dafalias Y.F. A critical state two-surface plasticity model for sands. *Géotechnique*, 47(2):255–272, 1997.
- Mardfeldt B. *Zum Tragverhalten von Kaikonstruktionen im Gebrauchszustand*. PhD thesis, Technische Universität Hamburg-Harburg, Arbeitsbereich Geotechnik und Baubetrieb, Germany, Heft 11, 2005.
- Mašin D. and Khalili N. A hypoplastic model for mechanical response of unsaturated soils. *Int. J. Numer. Anal. Methods Geomech.* 32(15): 1903–1926, 2008.
- Masing G. Eigenspannungen und Verfestigung beim Messing. In *Proceedings of the 2nd International Congress of Applied Mechanics*, pages 332–335. Zurich, 1926.
- Matsui T., Bahr M.A., and Abe N. Estimation of shear characteristics degradation and stress-strain relationship of saturated clays after cyclic loading. *Soils Found.*, 32(1):161–172, 3 1992.
- Matsui T., Ohara H., and Ito T. Cyclic stress-strain history and shear characteristics of clay. *J. Geotech. Eng. Div., ASCE*, 106(GT10):1101–1121, 10 1980.
- Matsushita M., Tatsuoka F., Koseki J., Cazacliu B., di Benedetto H., and Yasin S.J.M. Time effects on the pre-peak deformation properties of sands. In *Int. Conf. Pre-Failure Deform. Char. Geomat.*, pages 681–689. 1999.
- Mayer P.-M. *Verformungen und Spannungsänderungen im Boden durch Schlitzwandherstellung und Baugrubenaushub*. PhD thesis, Institute of Soil Mechanics and Rock Mechanics, University of Karlsruhe, Heft 151, 2000.
- Mayer P.-M. and Gudehus G. Ermittlung von Bodenverschiebungen infolge Schlitzwandherstellung. *Bautechnik*, 78(7): 490–502, 2001.
- Mazurkiewicz B.K. Skin friction on model piles in sand. Technical Report 25, Danish Geotechnical Institute, Copenhagen, 1968.
- McManus K.J. and Davis R.O. Dilation-induced pore fluid cavitation in sands. *Géotechnique*, 47(1):173–177, 1997.
- Meier T. *Application of Hypoplastic and Viscoplastic Constitutive Models for Geotechnical Problems*. PhD thesis, Institute of Soil Mechanics and Rock Mechanics University of Karlsruhe, 2009.

- Mélix P. *Modellversuche und Berechnungen zur Standsicherheit ober-flächen-naher Tunnel*. PhD thesis, Institute of Soil Mechanics and Rock Mechanics, University of Karlsruhe, Heft 103, 1987.
- Mesri G. Coefficient of secondary compression. *J. Soil Mech. Found. Div., ASCE*, 99(SM1):123–137, 1973.
- Mikulitsch V. and Gudehus G. Uniaxial tension, biaxial loading and wetting tests on loess. In E.E. Alonso & P. Delage editors, *Proceedings of the 1st International Conference on Unsaturated Soils*, Paris 1995. Volume 1, pages. 145–150, 1995.
- Milligan G.W.E. *The Behaviour of Rigid and Flexible Retaining Walls in Sand*. PhD thesis, University of Cambridge, Engineering Department, 1974.
- Miner M. Cumulative damage in fatigue. *Trans. Am. Soc. Mech. Eng.*, 67:A159–A164, 1945.
- Mitchell J.K., Campanella R.G., and Singh A. Soil creep as rate process. *J. Soil Mech. Found. Div., ASCE*, 94:231–253, 1 1968.
- Miura S. and Toki S. A sample preparation method and its effect on static and cyclic deformation-strength properties of sand. *Soils Found.*, 22(1):61–77, 3 1982.
- Miura K., Maeda K., Furukawa M., and Toki S. Mechanical characteristics of sands with different primary properties. *Soils Found.*, 38(4):159–172, 12 1998.
- Mogami T. and Kubo, K. The behaviour of soil during vibration. In *Proceedings of the 3rd International Conference on Soil Mechanics and Foundation Engineering*, volume I, Switzerland, 1953.
- Mohr O. *Abhandlungen aus dem Gebiete der Technischen Mechanik*. Ernst und Sohn, Berlin, 2 edition. 1914.
- Mokni M. and Desrues J. Strain localization measurements in undrained plane-strain biaxial tests on Hostun RF sand. *Mech. Cohes. Frict. Mater.*, 4:419–441, 1998.
- Morgenstern N.R. and Tchalenko J.S. Microscopic structures in kaolin subjected to direct shear. *Géotechnique*, 17:309–328, 1967.
- Mróz Z. On the description of anisotropic work hardening. *J. Mech. Phys. Solids*, 15:163–175, 1967.
- Mühlhaus H.-B. *Berücksichtigung von Inhomogenitäten im Gebirge im Rahmen einer Kontinuumstheorie*. PhD thesis, Institute of Soil Mechanics and Rock Mechanics, University of Karlsruhe, Heft 106, 1987. Habilitation.
- Mühlhaus H.-B. Application of Cosserat theory in numerical solutions of limit load problems. *Ingenieur-Archiv*, 59:124–137, 1989.
- Mühlhaus H.-B. and Vardoulakis I. The thickness of shear bands in granular materials. *Géotechnique*, 37(3):271–283, 1987.
- Nakai T. and Matsuoka H. Shear behavior of sand and clay under three-dimensional stress condition. *Soils Found.*, 23(2):26–40, 6 1983.
- Nasuno S., Kudrolli A., and Gollub J.P. Sensitive force measurements in a sheared granular flow with simultaneous imaging. In *Powders and Grains 97*. Balkema, Rotterdam, 1997.

- Niemunis A. *Extended Hypoplastic Models for Soils*. Polytechnica, Gdansk, Poland, 2003. monography.
- Niemunis A. A visco-plastic model for clay and its FE- implementation. In *Resultats Recents en Méchanique des Soils et des Roches*, pages 151–162. XI Colloque Franco-Polonais, Politechnica Gdanska, 1992.
- Niemunis A. and Cudny M. On hyperelasticity for clays. *Comput. Geotech.*, 23:221–236, 1998.
- Niemunis A. and Herle I. Hypoplastic model for cohesionless soils with elastic strain range. *Mech. Cohesive-Frict. Mater.*, 2:279–299, 1997.
- Niemunis A. and Prada F. Lessons from FE-implementation of SaniSand and hypoplasticity. Submitted to *Acta Geotechnica*, 2010.
- Niemunis, A., Wichtmann T., and Triantafyllidis Th. A high-cycle accumulation model for sand. *Comput. Geotech.*, 32(4):245–263, 2005.
- Niemunis A., Wichtmann T., and Triantafyllidis Th. Spatial stress fluctuations: Acoustic evidence and numerical simulations. In *Int. Symp. Numer. Models Geotech.*, Rhodos, 2007.
- Niemunis A., Grandas-Tavera C.E., and Prada-Sarmiento L.F. Anisotropic visco-hypoplasticity. *Acta Geotechnica*, 4: 293–314, 2009.
- Norton F.H. *The Creep of Steel at High Temperatures*. McGraw-Hill, London, 1929.
- Nübel K. *Experimental and Numerical Investigation of Shear Localization in Granular Material*. PhD thesis, Institute of Soil Mechanics and Rock Mechanics, University of Karlsruhe, Heft 159, 2002.
- Oda M. and Kazama H. Microstructure of shear bands and its relation to the mechanism of dilatancy and failure of dense granular soils. *Géotechnique*, 48(4):465–481, 1998.
- Oda Y. and Mitachi T. Stress relaxation characteristics of saturated clays. *Soils Found.*, 28(4):69–80, 12 1988.
- Oka F. Elasto/viscoplastic constitutive equations with memory and internal variables. *Comput. Geotech.*, 1:59–69, 1985.
- Oka F., Kodaka T., Kimoto S., Ishigaki S., and Tsuji C. Step-changed strain rate effect on the stress-strain relations of a clay and constitutive modeling. *Soils Found.*, 43(4):189–202, 8 2003.
- Osinov V.A. On the formation of discontinuities of wave fronts in a saturated granular body. *Continuum Mech. Thermodyn.*, 10:253–268, 1998.
- Osinov V.A. Wave-induced liquefaction of a saturated sand layer. *Continuum Mech. Thermodyn.*, 12(5):325–339, 2000.
- Osinov V.A. On permanent long-wave distortions of a railway track due to the moving vehicle load. *Arch. Appl. Mech.*, 71:418–425, 2001.
- Osinov V.A. Cyclic shear of saturated soil: the evolution of stress inhomogeneity. *Continuum Mech. Thermodyn.*, 14(2): 191–205, 2002.
- Osinov V.A. Cyclic shearing and liquefaction of soil under irregular loading: an incremental model for the dynamic earthquake-induced deformation. *Soil Dyn. Earthquake Eng.*, 23:535–548, 2003.

- Osinov V.A. and Loukachev I. Settlement of liquefied sand after a strong earthquake. In *Compaction of Soils, Granulates and Powders*, pages 297–306. 2000.
- Osinov V.A. and Wu W. Instability and ill-posedness in the deformation of plastic solids: Some correlations through simple examples. *Trends Appl. Math. Mech.*, 361–370, 2005.
- Ovesen N.K. The use of physical models in design. In *Proceedings of the 7th European Conference on Soil Mechanics and Foundation Engineering, Brighton, Vol. 4, Discussion.*, pages 319–323. 1979.
- Papatheodorou G. and Ferentinos G. Submarine and coastal sediment failure triggered by the 1995, Ms= 6.1 R Aegion earthquake, Gulf of Corinth, Greece. *Int. J. Mar. Geol. Geochem. Geophys.*, 137:287–304, 1997.
- Pearce J.A. A new true triaxial apparatus. In R.H.G. Parry, editor, *Stress-Strain Behaviour of Soils*, pages 330–339. Foulis, Henley-on-Thames, 1972.
- Peck R.B. Advantages and limitations of the observational method in applied soil mechanics. *Géotechnique*, 19(2):171–187, 1969.
- Pena A.A., Lizcano A., Alonso-Marroquin F., and Herrmann H.J. Biaxial test simulations using a packing of polygonal particles. *Int. J. Numer. Anal. Meth. Geomech.*, 1145:1–12, 2006.
- Persson B.N.J. On the role of inertia and temperature in continuum and atomistic models of brittle fracture. *J. Phys. Condens. Matter*, 10:10529–10538, 1998.
- Persson B.N.J. Theory of time-dependent plastic deformation in disordered solids. *Phys. Rev. B.*, 61(9):5949–5966, 2000a.
- Persson B.N.J. *Sliding Friction - Physical Principles and Applications*. Springer, Berlin, 2 edition. 2000b.
- Persson B.N.J. and Brener E.A. Crack propagation in viscoelastic solids. *Phys. Rev.*, 71:036123–1/8, 2005.
- Pestana J.M. and Whittle A.J. Formulation of a unified constitutive model for clays and sands. *Int. J. Numer. Anal. Meth. Geomech.*, 23:1215–1243, 1999.
- Pestana J.M., Whittle A.J., and Gens A. Evaluation of a constitutive model for clays and sands: Part 2 – clay behaviour. *Int. J. Numer. Anal. Meth. Geomech.*, 26:1123–1146, 2002a.
- Pestana J.M., Whittle A.J., and Salvati L.A. Evaluation of a constitutive model for clays and sands: Part 1 – sand behaviour. *Int. J. Numer. Anal. Meth. Geomech.*, 26:1097–1121, 2002b.
- Pierschke K., Gudehus G., Hügel H., and Niemunis A. Vorhersage und Steuerung von Bodenverformungen infolge Tagebauaktivitäten. In *Vorträge der Baugrundtagung 1996 in Berlin*, pages 361–370. 1996.
- Popper K.R. *The Logic of Scientific Discovery*. Hutchinson, London, 1959.
- Pöschel T.H. and Luding S.T. *Granular Gases*. Springer, Berlin, 2001.
- Prada F. *Improvement of Small Strain Stiffness Behavior in the Hypoplasticity*. PhD thesis, Institute of Soil Mechanics and Rock Mechanics, University of Karlsruhe, 2010.

- Pradhan T.B.S., Tatsuoka F., and Horii N. Simple shear testing on sand in a torsional shear apparatus. *Soils Found.*, 28(2):95–112, 6 1988a.
- Pradhan T.B.S., Tatsuoka F., and Horii N. Strength and deformation characteristics of sand in torsional simple shear. *Soils Found.*, 28(3):131–148, 9 1988b.
- Pradhan T.B.S., Tatsuoka F., and Sato Y. Experimental stress-dilatancy relations of sand subjected to cyclic loading. *Soils Found.*, 29(1):45–64, 3 1989.
- Pralle N. *Mechanisms in Nearly Saturated Sandy Soils Under Quasi-static and Dynamic Loading*. PhD thesis, Institute of Soil Mechanics and Rock Mechanics, University of Karlsruhe, Heft 158, 2002.
- Pralle N., Külzer M., and Gudehus G. Experimental evidence on the role of gas in sediment liquefaction and mud volcanism. *Geol. Soc. London, Spec. Publ.*, 216:159–171, 9 2003.
- Prandtl L. Ueber die Härte plastischer Körper. *Nachr. Ges. d. Wiss., Math. Phys. Kl., Göttingen*, 74, 1920.
- Prandtl L. Ein Gedankenmodell zur kinetischen Theorie der festen Körper. *Zeitschr. Angew. Math. Mech.*, 8(2):85–106, 1928.
- Prashant A. and Penumadu D. Effect of overconsolidation and anisotropy of kaolin clay using true triaxial testing. *Soils Found.*, 45(3):71–82, 6 2005.
- Radjai F., Wolf D.E., Jean, M., Roux, S., and Moreau J.J. Force networks in dense granular media. In *Powder and Grains 97*, 1996.
- Raju V.S., Gudehus G., and Narasimha Rao. Earthquake damage and repair in the Kandla harbour/India. In *Proceedings of the 12th Danube-European Conference*, pages 287–290. Passau, 2002.
- Ramana K.V. and Raju V.S. Constant-volume triaxial tests to study the effects of membrane penetration. *Geotechn. Test. J.*, 4(3):117–122, 9 1981.
- Rankine W.J.M. On the stability of loose earth. *Phil. Trans. Roy. Soc. London*, 147(1): 9–27, 1856.
- Rao K.S. The Bhuj earthquake. *Bull. Indian Geotechn. Soc.*, 5–7, 1–3 2001.
- Rao V.V.S. Scherfestigkeit von Sand bei dynamischer Beanspruchung. *Die Bautechnik*, 12, 1966.
- Rebstock D. Hypoplastic simulation of piles and column foundations. In H. Brandl and F. Kopf, editors, *16th Eur. Young Geot. Engineers Conf.*, pages 303–312. Vienna, 2004.
- Rebstock D. Kleinbohrpfähle unter statischer und zyklischer Belastung – hypoplastische Simulationen. *Pfahl-Symposium 2005*, 80:349–365, 2005.
- Rebstock D. Versagensmechanismen von Pfählen unter zyklischer Belastung. *29. Baugrundtagung 2006, Forum für junge Geotechnik-Ingenieure*, 2006. available online.
- Rebstock D. *Stressing and Relaxation of Sand*. PhD thesis, Institute of Soil Mechanics and Rock Mechanics, University of Karlsruhe, 2010, under preparation.
- Rendulic L. Ein Grundgesetz der Tonmechanik und sein experimenteller Beweis. *Der Bauingenieur*, 18(31/32):459–467, 8 1937.
- Revuzhenko A.F. *Mechanics of Granular Media*. Springer, Berlin, 2006.

- Richards L.A. Capillary conduction of liquids through porous mediums. *Physics*, 1:318–333, 11 1931.
- Richart F.E., Hall J.R., and Woods R.D. *Vibrations of Soils and Foundations*. Prentice-Hall, New Jersey, 1970.
- Richter S. *Mechanical Behavior of Fine-Grained Model Materials During Cyclic Shearing*. PhD thesis, Institute of Soil Mechanics and Rock Mechanics, University of Karlsruhe, Heft 167, 2006.
- Richter S. and Huber G. Time-dependent behavior of fine-grained model material in resonant column experiments. *Granular Matter*, 6(4):195–206, 2004.
- Ridley A.M., Dineen K., Burland J.B., and Vaughan P.R. Soil matrix suction: some examples of its measurement and application in geotechnical engineering. *Géotechnique*, 53(2):241–253, 2003.
- Roesler S. Anisotropic shear modulus due to stress anisotropy. *J. Geotech. Eng. Div., ASCE*, 105(GT7): 871–880, 7 1979.
- Roscoe K.H. The influence of strains in soil mechanics. *Géotechnique*, 20(2):129–170, 1970.
- Roscoe K.H. and Burland J.B. On the generalized stress-strain behaviour of ‘wet’ clay. *Eng. Plast.*, 535–609, 1968.
- Roscoe K.H., Schofield A.N., and Wroth C.P. On the yielding of soils. *Géotechnique*, 8:22–53, 1958.
- Rouainia M. and Muir Wood D. A kinematic hardening constitutive model for natural clays with loss of structure. *Géotechnique*, 50(2):153–164, 2000.
- Rowe P.W. The stress-dilatancy relation for static equilibrium of an assembly of particles in contact. In *Proceedings of the Royal Society*, pages 500–527. 1962.
- Rübel S. *Evolution of State and Shape of Viscous Formations*. PhD thesis, 2010, under preparation.
- Rutledge P.C. Recent developments in soil testing apparatus. *J. Boston Soc. Civil Eng.*, 22(4): 223–250, 10 1935.
- Sangrey D.A., Henkel D.J., and Esrig M.I. The effective stress response of a saturated clay soil to repeated loading. *Can. Geotech. J.*, 6:241–252, 1969.
- Savage S.B. and Hutter K. The motion of a finite mass of granular material down a rough incline. *J. Fluid Mech.*, 199:177–215, 1989.
- Schäfer R. and Triantafyllidis T. Modelling of earth and water pressure development during diaphragm wall construction in soft clay. *Int. J. Numer. Anal. Meth. Geomech.*, 28:1305–1326, 2004.
- Schauppel F. Numerische Optimierung einer Einpresstechnologie zum Wiederanheben setzungsgeschädigter Verkehrswege. Master’s thesis, Institute of Soil Mechanics and Rock Mechanics, University of Karlsruhe, 2004.
- Scherzinger T. *Materialverhalten von Seetonen – Ergebnisse von Laboruntersuchungen und ihre Bedeutung für das Bauen in weichem Baugrund*. PhD thesis, Institute of Soil Mechanics and Rock Mechanics of University of Karlsruhe, Heft 122, 1991.

- Schlegel T. *Anwendung einer neuen Bettungsmodultheorie zur Berechnung biegsamer Gründungen auf Sand*. PhD thesis, Institute of Soil Mechanics and Rock Mechanics, University of Karlsruhe, Heft 98, 1985.
- Schofield A. *Disturbed Soil Properties and Geotechnical Design*. Thomas Telford, London, 2005.
- Schofield A. and Wroth P. *Critical State Soil Mechanics*. Mc Graw-Hill, London, 1968.
- Schulze R. and Köhler H.-J. Stabilisation of endangered clay slopes by unconventional pore pressure release technique. In F. Myrsvoll, editor, *Field Measurements in Geomechanics*, pages 347–353, Oslo, 2003.
- Schünemann A. *Numerische Modelle zur Beschreibung des Langzeitverhaltens von Eisenbahnschotter unter alternierender Beanspruchung*. PhD thesis, Institute of Soil Mechanics and Rock Mechanics, University of Karlsruhe, Heft 168, 2006.
- Schwämmle V. and Herrmann H.J. Geomorphology: Solitary wave behaviour of sand dunes. *Nature*, 426:619–620, 12 2003.
- Schwarz P. *Beitrag zum Tragverhalten von Verpressfählen mit kleinem Durchmesser unter axialer zyklischer Belastung*. PhD thesis, Lehrst. und Prüfamf für Grundbau, Bodenmech. und Felsmech. der TU München, München, 2002.
- Schwarz W. *Verdübelung toniger Böden*. PhD thesis, Institute of Soil Mechanics and Rock Mechanics, University of Karlsruhe, Heft 105, 1987.
- Senneset K., Janbu N., and Svano G. Strength and deformation parameters from cone penetration tests. In *Proceedings on the 2th European Symposium Penetration Testing*, pages 863–870. Rotterdam, 1982.
- Shahinpoor M. Statistical mechanical considerations on storing bulk solids. *Bulk Solids Handl.*, 1(1):31–35, 1981.
- Shemyakin E.I. On deformations of a rotating planet. *Vestnik Mosc. Univ. Math.-Mech.*, 1(3): 63–72, 1993. in Russian.
- Shibata T. and Karube D. Influence of the variation of the intermediate principal stress on the mechanical properties of normally consolidated clays. In *Proceedings of the 6th International Conference on Soil Mechanics and Foundation Engineering*, volume I. 1965.
- Shimizu M. Effect of overconsolidation on dilatancy of a cohesive soil. *Soils Found.*, 22(4):121–135, 12 1982.
- Shkoller S. and Minster J.-B. Reduction of Dietrich-Ruina attractors to unimodal maps. *Nonlin. Processes Geophys.*, 4:63–69, 1997.
- Skempton A.W. Residual strength of clays in landslides, folded strata and the laboratory. *Géotechnique*, 35(1):3–18, 1985.
- Slominski C. Validierung von Rechenmodellen zur Scherzonenentwicklung mit Versuchen im Labor und in situ. PhD thesis, *Veröff. Inst. Boden- u. Felsmech. Univ. Karlsruhe*, Heft 169, 2007.
- Sokolovski V.V. *Statics of Soil Media*. Butterworths Scientific Publications, London, 1960. Translation by Jones and Schofield.
- Sridharan A. and Venkatappa Rao G. Effective stress theory of shrinkage phenomena. *Canad. Geotech. J.*, 8(4):503–513, 1971.

- Sridharan A. and Venkatappa Rao G. Mechanisms controlling volume change of saturated clays and the role of the effective stress concept. *Géotechnique*, 23(3):359–382, 1973.
- Stallebrass S.E. and Taylor R.N. The development and evaluation of a constitutive model for the prediction of ground movements in overconsolidated clay. *Géotechnique*, 47(2):235–253, 1997.
- Stazhevskii S.B. On the contribution of ring structures to the stress-strain state of the lithosphere and to metallogeny. *Fysicheskaya Mesomechanika*, 8:65–70, 2005. In Russian.
- Stazhevskii S.B. Ring structures as a source of seismicity. *Fysicheskaya Mesomechanika*, 9:23–32, 2006. In Russian.
- Sturm H. *Stabilisation Behaviour of Cyclically Loaded Shallow Foundations for Offshore Wind Turbines*. PhD thesis, University of Karlsruhe, 2009. URL <http://uvka.ubka.uni-karlsruhe.de/>.
- Suklje L. *Rheological Aspects of Soil Mechanics*. Wiley, London, 1969.
- Sun D., Sheng D., and Xu Y. Collapse behaviour of unsaturated compacted soil with different initial densities. *Can. Geotech. J.*, 44:673–686, 2007.
- Taiebat M. and Dafalias Y.F. SANISAND:simple anisotropic sand model. *Int. J. Num. Anal. Meth. Geomech.*, 32(8):915–948, 2007.
- Tatsuoka F., Sakamoto M., and Kawamura T. Strength and deformation characteristics of sand in plane strain compression at extremely low pressures. *Soils Found.*, 26(1):65–84, 3 1986.
- Tatsuoka F., Nakamura S., Huang C.C., and Tani K. Strength anisotropy and shear band direction in plane strain tests on sand. *Soils Found.*, 30(1):35–54, 1990.
- Tavenas F., des Rosiers J.-P., Leroueil S., La Rochelle P., and Roy M. The use of strain energy as a yield and creep criterion for lightly overconsolidated clays. *Géotechnique*, 29(3):285–303, 1979.
- Taylor D.W. *Fundamentals of Soil Mechanics*. Wiley, New York, 1948.
- Tejchman J. *Modelling of Shear Localisation and Autogeneous Dynamic Effects in Granular Bodies*. PhD thesis, Institute of Soil Mechanics and Rock Mechanics, University of Karlsruhe, Heft 140, Habilitation, 1997.
- Tejchman J. and Gudehus G. Shearing of a narrow granular layer with polar quantities. *Int. J. Numer. Analyt. Meth. Geomech.*, 25:1–28, 2001.
- Tejchman J. and Niemunis A. FE-studies on shear localization in an anisotropic micro-polar hypoplastic granular material. *Granular Matter*, 8(3–4):205–220, 2006.
- Temmen H., Pleiner H., Liu M., and Brand H.R. Convective non-linearity in non-Newtonian fluids. *Phys. Rev. Lett.*, 84, 3228, 2000.
- Temperley H.N.V. and Chambers LL.G. The behaviour of water under hydrostatic tension. *Proc. Phys. Soc.*, 58:420–443, 1946.
- Terzaghi K. New facts about surface friction. *Phys. Rev.*, 16(1):54–61, 1920.
- Terzaghi K. *Erdbaumechanik auf bodenphysikalischer Grundlage*. Deuticke, Leipzig and Wien, 1925.

- Terzaghi K. The static rigidity of plastic clays. *J. Rheol.*, 2(3):253–262, 1931.
- Terzaghi K. The shearing resistance of saturated soils and the angle between the planes of shear. In *Proceedings of the 1st International Conference on Soil Mechanics and Foundation Engineering*, volume I, pages 54–56, 1936.
- Terzaghi K. *Theoretical Soil Mechanics*. J Wiley, New York, 1940.
- Thiers G.R. and Seed H.B. Cyclic stress-strain characteristics of clay. *J. Soil Mech. Found. Div., ASCE*, 94(SM2):555–569, 3 1968.
- Thornton C. and Sun G. Numerical simulation of general 3D quasi-static shear deformation of granular media. In I.M. Smith, editor, *Numerical Methods in Geotechnical Engineering*, pages 143–148. 1994.
- Tillemans H.-J. and Herrmann H.J. Simulating deformations of granular solids under shear. *Physica A*, 217:261–288, 1995.
- Topolnicki M. *Observed Stress-Strain Behaviour of Remoulded Saturated Clay and Examination of Two Constitutive Models*. PhD thesis, Institute of Soil Mechanics and Rock Mechanics, University of Karlsruhe, Heft 107, 1987. Habilitation.
- Topolnicki M., Gudehus G., and Mazurkiewicz B.K. Observed stress-strain behaviour of remoulded saturated clay under plane strain conditions. *Géotechnique*, 40(2):155–187, 1990.
- Towhata I., Kuntiwattanakul P., and Kobayashi H. A preliminary study on heating of clays to examine possible effects of temperature on soil-mechanical properties. *Soils Found.*, 33(4):184–190, 12 1993.
- Triantafyllidis T. Dynamic stiffness of rigid rectangular foundations on the half-space. *Earthquake Eng. Struct. Dyn.*, 14:391–411, 1986.
- Truesdell C. and Noll W. The non-linear field theories of mechanics. In *Handbuch der Physik*, volume III/3. Springer, Berlin, 1965.
- Valanis K.C., Peters J.F., and Gill J. Configurational entropy, non-associativity and uniqueness in granular media. *Acta Mech.*, 100, 79–93, 1993.
- Van Eekelen H.A.M. and Potts D.M. The behaviour of Drammen Clay under cyclic loading. *Géotechnique*, 28(2):173–196, 1978.
- Vardoulakis I., Goldscheider M., and Gudehus G. Formation of shear bands in sand bodies as a bifurcation problem. *Int. J. Numer. Anal. Meth. Geomech.*, 2:99–128, 1978.
- Vardoulakis I., Graf B., and Gudehus G. Trap-door problem with dry sand: A statical approach based upon model test kinematics. *Inst. J. Numer. Anal. Meth. Geomech.*, 5:57–78, 1981.
- Vardoulakis J. and Georgopoulos J.-O. The “stress-dilatancy” hypothesis revisited: Shear-banding related instabilities. *Soils Found.*, 45(2):61–76, 4 2005.
- Verdugo R. and Ishihara K. The steady state of sandy soils. *Soils Found.*, 36(2):81–91, 6 1996.
- Vermeer P.A. A double hardening model for sand. *Géotechnique*, 28: 413–433, 1978.

- Vermeer P. A five-constant model using well-established concepts. In F. Darve G. Gudehus and I. Vardoulakis, editors, *Constitutive Relations for Soils*, Balkema, pages 175–198. 1984.
- Vielsack P. Pseudoviskosität bei trockener Reibung. *Geotechnik*, 14(1):11–15, 1991.
- Vielsack P. and Hartung A. An example for the orbital stability of permanently disturbed non-smooth motions. *Zeitschr. Angew. Math. Mech.*, 79(6): 389–397, 1999.
- von Wolffersdorff P.-A. A hypoplastic relation for granular materials with a predefined limit state surface. *Mech. Cohesive-Frict. Mater.*, 1:251–271, 1996.
- von Wolffersdorff P.-A. *Verformungsprognosen für Stützkonstruktionen*. PhD thesis, Institute of Soil Mechanics and Rock Mechanics, University of Karlsruhe, Heft 141, Habilitation, 1997.
- Weber K.J., Mandl G., Pilaar W.F., Lehner F.K., and Precious R.G. The role of faults in hydrocarbon migration and trapping in Nigerian growth fault structures. In *Proceedings of the 10th American Offshore Technology Conference*, pages 2643–2653. Houston, 1978.
- Wernick E. *Tragfähigkeit zylindrischer Anker in Sand unter besonderer Berücksichtigung des Dilatanzverhaltens*. PhD thesis, Institute of Soil Mechanics and Rock Mechanics, University of Karlsruhe, Heft 75, 1978.
- Wheeler S.J. A conceptual model for soils containing large gas bubbles. *Géotechnique*, 38:389–397, 1988.
- Whittle A.J. *Role of Soil Modelling in Geotechnical Predictions*. Columbia University Press, New York City, 2006.
- Whittle A.J. and Kavvas M.J. Formulation of MIT-E3 constitutive model for overconsolidated clays. *J. Geotech. Eng. Div., ASCE*, 120(1): 173–198, 1 1994.
- Wichman B.G.H.M. and Allersma H.G.B. Onderhogen van zandbed in geocentrifuge. Technical report, 2004.
- Wichtmann T. *Explicit Accumulation Model for Non-cohesive Soils Under Cyclic Loading*. PhD thesis, Institut Grundbau und Bodenmech. Ruhr-Univ., Bochum, Germany, Heft 38, 2005.
- Wichtmann T., Niemunis A., and Triantafyllidis T. Experimental evidence of a unique flow rule of non-cohesive soils under high-cyclic loading. *Acta Geotech.*, 1:59–73, 5 2006.
- Wieghardt K. Ueber einige Versuche an Strömungen in Sand. *Ing.-Archiv*, 20:109–115, 1952.
- Wienbroer, H. *Zustandsgrenzen und Grenzyklen von Sand*. PhD thesis, Institute of Soil Mechanics and Rock Mechanics, University of Karlsruhe, 2010. under preparation.
- Wienbroer H., Rebstock D., and Huber G. Shake-box tests. In *Int. Symp. on Strong Vrancea Earthquakes and Risk Mitigation*, pages 226–238. Bucharest, 2007.
- Winkler E. *Elastizität und Festigkeit*. Dominicus, Prag, 1867.

- Winter H. *Fliessen von Tonböden: Eine mathematische Theorie und ihre Anwendung auf den Fließwiderstand von Pfählen*. PhD thesis, Institute of Soil Mechanics and Rock Mechanics, University of Karlsruhe, Heft 82, 1979.
- Wolf H., Koenig D., and Triantafyllidis T. Examination of shear band formation in granular material. *J. Struct. Geol.*, 25:1229–1240, 2003.
- Wood D.M. Explorations of principal stress space with kaolin in a true triaxial apparatus. *Géotechnique*, 25(4):783–797, 1975.
- Wood D.M., Drescher A., and Budhu M. On the determination of stress state in the simple shear apparatus. *Geotech. Test. J.*, 2(4):211–221, 1979.
- Wu T.-H. and Berman S. Earth pressure measurements in open cut: Contract D-8, Chicago subway. *Géotechnique*, 3(6):248–258, 1953.
- Wu W. *Hypoplastizität als mathematisches Modell zum mechanischen Verhalten granularer Stoffe*. PhD thesis, 1992.
- Wu W. and Bauer E. . A hypoplastic model for barotropy and pyknotropy of granular soils. In D. Kolymbas, editor, *Modern Approaches to Plasticity*, pages 225–246, 1993.
- Wu W., Bauer E., Niemunis A., and Herle I. Visco-hypoplastic models for cohesive soils. In Kolymbas, editor, *Modern Approaches to Plasticity*, pages 365–383. Elsevier, Amsterdam, 1993.
- Xue W. and Grest G.S. Shear-induced alignment of colloidal particles in the presence of a shear flow. *Phys. Rev. Lett.*, 64(4):419–422, 1 1990.
- Yamada Y. and Ishihara K. Undrained deformation characteristics of loose sand under three-dimensional stress conditions. *Soils Found.*, 21(1):15–31, 3 1981.
- Yamada Y. and Ishihara K. Yielding of loose sand in three-dimensional stress conditions. *Soils Found.*, 22(3), 9 1982.
- Yashima A., Leroueil S., Oka F., and Guntoro I. Modelling temperature and strain rate dependent behavior of clays: One dimensional consolidation. *Soils Found.*, 38(2):63–73, 6 1998.
- Yasuhara K., Hirao K., and Hyde A. Effects of cyclic loading on undrained strength and compressibility of clay. *Soils Found.*, 32(1):100–116, 3 1992.
- Youd T.L. Compaction of sands by repeated shear straining. *J. Soil Mech. Found. Eng. Div., ASCE*, 709–725, 7 1972.
- Zou Y. A non-linear permeability relation depending on the activation energy of pore liquid. *Géotechnique*, 46(4):769–774, 1996.
- Zou Y. *Der Einfluss des gebundenen Wassers auf die Leitfähigkeit und die mechanischen Eigenschaften feinkörniger Böden*. PhD thesis, Institute of Soil Mechanics and Rock Mechanics, University of Karlsruhe, Heft 144, 1998.
- Zou Y. Der vom Spannungszustand und Bodengefüge abhängige Erosionsdurchbruch bindiger Böden. *Wasserwirtschaft*, 90(11):554–559, 2000.

Index

- Acoustic emission, 245
- Activation energy, 114
- Adhesion, 420
- Amplitude, 106
- Argotropic, 10
- Argotropic response polar, 118, 126
- Argotropic solid hardness, 125
- Argotropic state limits, 116–117, 124
- Attractor in the large, viii, 424, 548
- Attractors, v, 33, 36

- Back stress, 197
- Back stress direction, 227
- Barotropic, 6
- Barotropy, 27
- Biaxial, 66
- Biaxial tests, 71, 363
- Boundary condition, 3
- Boundary zones, 398
- Bound pore water, 293, 306, 309
- Brittle, 333
- Bubble models, 276
- Bubbles, 428

- Cam clay, 137
- Cap, 39
- Capillary condensation, 297
- Capillary entry, 300, 405
- Capillary hysteresis, 300, 327
- Capillary skeleton pressure, 302
- Cavitation, 304, 310
- Cavitative mode, 664
- Cementation, 332, 384
- Channelling, 380

- Clay smears, 535
- Collapsible, 135
- Compensation grouting, 620
- Composite column, 454
- Composition, 7
- Composites of psammoids and peloids, 393
- Compression index, 37
- Compression test, 134
- Conservation laws, 3, 444
- Conservative, vi
- Consolidation, 441, 450
- Consolidation ratio, 127, 146
- Contact elements, 419
- Contractant state limit fields, 432
- Convection cells, 790
- Couple stress, 345
- Crack, 410
- Crack patterns, 381, 794
- Creep, 113
- Creep rupture, 160
- Critical friction angle, 30
- Critical phenomena, x
- Critical points, x, 58
- Critical state soil mechanics, 37
- Critical states, vii
- Critical void ratio, 31
- Cuboidal, 64
- Cutting, 422
- Cyclic attractor in the large, 431
- Cyclic mobility, 209
- Cyclic torsional shear tests, 209
- Cylindrical shear, 89

- Delayed collapse, 372, 507
 Deviatoric flow rule, 68
 Diapirs, 658
 Diffusion of pore water, viii
 Dilatancy angle, 82
 Direct shear tests, 176
 Dislocation units, 114
 Drained stationary creep, 432
 Drained strength, 136
 Driven attractors, 36
 Ductile, 35, 135
 Ductility, 20, 137, 507
- Earth pressure coefficient at rest, 446
 Effective cohesion, 137
 Effective shear strength, 136
 Effective stress, 28
 Eigenstress, 195
 Elastoplastic, 18, 21
 Elasto-plastic relation, 21
 Electro-capillary, 296
 Electrophoresis, 308
 Element test, 799
 Equivalent pressure, 127
 Excavation window, 746
 Explicit accumulation models, 281
 Explicit constitutive relations, 288
 Extended argotropic critical states, 369
 Extended state cycles, 362
 Extended state limits, 346, 356
- Fabric tensor, 386
 Failure, 6, 31
 Failure conditions, 66
 Faults, 395
 Filter cake, 401
 Filter criteria, 411, 419
 Fingering, 300
 Finite elements, 490, 499
 Finite soil elements, 445
 Flow equilibrium, 798
 Fluidized bed, 400
 Fluidized zones, 417, 420
 Force chains, 218
 Forced polarization, 347
 Force-roughness, viii
 Force-roughness in the large, 424
- Gas bubbles, 428
 Gas channels, 299
 Gas cushions, 409, 420
 Gas inclusions, 409
 Gradual relaxation, 214
 Granular entropy, 250
 Granular flow, 400
 Granular fluids, 245
 Granular gas, 244
 Granular phase transitions, 5, 367
 Granular solids, 2, 245, 253
 Granular temperature, 244
 Granulate hardness, 44
- Hanshiku, 527
 High-cycle accumulation model, 249
 Historical element, vi, 3, 464, 491
 Hydraulic breakthrough, 383
 Hydraulic height, 9, 444
 Hypoelastic, viii, 39
 Hypoplastic, 18
 Hypoplastic relation, 23, 46
 Hysteresis, 18
 Hysteresis ratio, 108
- Identification, 12
 Induced and inherent anisotropy, 390
 Inherent anisotropy, 77
 Initial state, 3
 Inner shear bond, 345
 Interface zones, 421
 Intergranular strain, 236
 Intermittent creep, 224
 Intermittent relaxation, 224
 Internal erosion, 800
 Internal strain, 198
 Isobaric creep, 129
 Isobaric state limit fields, 432
 Isochoric creep, 130
 Isochoric ratcheting, 99
 Isochoric state limit fields, 430
 Isotachs, 125
- Limit stress fields, 488
 Limit void ratio, 31, 125, 315
 Limit water contents, 191
 Liquefaction, 37
 Localization in the pore fluid, 382
 Localization, ix

- Localized bifurcation, 347
 Lode parameter, 101
- Macro-elements, 489, 493, 496
 Macropores, 305, 322, 409
 Mats, 399, 401
 Mean skeleton pressure, 27
 Mechanical annealing, 349
 Mechanical roughness, 255
 Membranes, 401, 417, 420
 Miner's rule, 196
 Mixtures, 393
 More geometrico, v
 Mud volcanos, 800
- Navigation, 784
 Negative shaft friction, 686
 Net attraction, 314, 384
 Net repulsion, 288, 304, 314
 Normal faults, 531
- Orbital symmetry, 775
 Osmotic repulsion, 296
 Overconsolidation ratio, 38
 Overcritical, 30
- Path-dependence, 747
 Path dependent, 568
 Paths, 20
 Pattern formation, 775
 Pavements, 403
 Peak states, 30, 54
 Penetration, 422
 Percolation, 45
 Permanence of solid particle, 338
 Permeability, 300, 306, 308
 Phase transition of pore water, 372
 Pisa tower, 576
 Plastic clays, 191
 Polar quantities, 343, 355
 Polar stresses, 9
 Polywater, 123, 293
 Pore water pressure, 9
 Primary consolidation, 163, 452
 Principle of effective stress, viii, 28
 Psammoids, vii, 10, 16
 Pyknotropic, 6
 Pyknotropy, 28
- Quasi-attractor, 630
 Quick clay, 471
- Ratcheting, 22, 36, 121
 Rate-independence, 10
 Relative void ratio, 31
 Relaxation, 113, 131
 Representative elements, 7
 Representative soil elements, 3
 Residual strength, 179
 Resonant column tests, 206
 Response polars, 21, 46
 Reversals, 35
 Ring shear, 90, 176
 Ring structures, 657, 721
- Sandwich, 392
 Secondary consolidation, 158, 163, 452
 Seepage velocity, 8
 Seismically activated, 245
 Seismic creep, 243
 Seismic pressure, 250
 Seismic state limits, 632
 Seismic temperature, 243, 288
 Seismodynamic equilibria, 250
 Seismodynamics, 250
 Seismo-hypoplastic, 245
 Seismostats, 249
 Shake boxes, 523
 Shear band patterns, 388
 Shear band thickness, 358
 Shear bands, 410, 416, 639
 Shear localization, 490
 Shear mixing, 408
 Shear thinning, 297
 Shrinkage, 453
 Shrinkage cracks, 311
 Shrinkage limit, 310
 Silo music, 692
 Silo quakes, 692
 Similarly rules, 487
 Simple peloids, 111
 Simple psammoids, 26
 Simple shear apparatus, 88, 93
 Skeleton decay, 37
 Skeleton partial pressure, 298
 Skeleton stress tensor, 9
 Skeleton, 7
 Skin, 401

- Slickenside, 369
- Sliding wedges, 488
- Slurry trench, 716
- Soil-structure interaction, 415
- Solute transport, 321
- Specific seepage force, 445
- Spontaneous polarization, 347
- Stability, 6
- Standing column, 444
- State boundary curve, 38
- State boundary surface, 68
- State cycle fields, 430, 432, 626
- State cycles, v, 22
- State limits, v, 30
- State parameter, 38
- Stationary creep, 471
- Stationary seismic creep, 629
- Stick-slip condition, 416
- Strain rate obliquity, 29
- Strange attractor, vi
- Stress-dilatancy, 34, 66
- Stress direction, 85
- Stress obliquity, 101
- Stretching tensor, 8
- Subcritical, 30
- Subgrade reaction, 590, 755
- Suction, 299
- Surface waves, 796
- Swelling, 453
- Swelling index, 39
- Swept out memory, VII
- Symmetry, 13, 435
- Sysendimentary tectonic deformation, 533
- Thermal activation, 155
- Thermally activated dislocation, 113
- Thick-walled cylinders, 93
- Thick-walled cylindrical, 181
- Thin layer shear, 179
- Thin layer shear tests, 89
- Torsional cyclic shear, 275
- Torsion of thick-walled tubes, 92
- Trap doors, 614
- True triaxial tests, 70
- Undrained cohesion, 134, 142
- Undrained creep, 155
- Validation, 2, 12
- Verification, 2
- Visco-elastoplastic, 116, 175
- Visco-hypoplastic, 116, 145, 175
- Viscosity factor, 116, 127
- Viscosity index, 113, 125
- Viscous effects, 260
- Viscous strain rate, 282
- Void ratio, 28
- Volumetric strain, 29
- Water film, 408